CONF-800782
SLAC-239
(T/E)
UC-34d

PROCEEDINGS

OF

SUMMER INSTITUTE ON PARTICLE PHYSICS

July 28 - August 8, 1980

THE WEAK INTERACTION

Program Directors

Gary J. Feldman

Frederick J. Gilman

David W. G. S. Leith

Ed. by Anne Mosher

Sponsored by Stanford University and Stanford Linear Accelerator Center
under contract with the U.S. Department of Energy. Contract DE-AC03-76SF00515

January 1981

Printed in the United States of America. Available from National Technical Information Service, U.S. Department of Commerce, 5285 Port Royal Road, Springfield, VA 22161. NTIS price codes:
Printed copy, A99
Microfiche copy, A01

PREFACE

The SLAC Summer Institute on Particle Physics held its eighth session on July 28-August 8, 1980, and the focus of the meeting was The Weak Interaction. Following the now traditional format, the first seven days of the Institute were spent with the mornings given to pedagogic lectures on the experimental and theoretical foundations of the topic. This year we had a very stimulating and successful series on the physics of particle detectors. In the afternoons we had seminars on the various experimental tools being designed or constructed to further probe the Weak Interaction, followed by lively discussion of the morning's lectures. Again, following our usual format, the "school" led into a three-day topical conference at which the most recent theoretical and experimental results were presented and discussed.

Three hundred and seventy physicists participated (some more, some less) in this year's Institute, and representatives of fifteen foreign countries attended. This year attendance had over one hundred and fifty participants from out of state. It was a lively and stimulating meeting.

Once again Anne Mosher was the Coordinator for the Institute and Editor of the Proceedings. We are indebted to her and her staff for the smooth and effective running of the meeting.

Gary J. Feldman
Frederick J. Gilman
David W. G. S. Leith
Program Directors

Table of Contents

GAUGE THEORIES OF WEAK INTERACTIONS

Martin J. Veltman

1. Introduction

The purpose of these notes is to produce an introduction to the presently popular standard model of weak and electromagnetic interactions. This model has a number of ingredients, leptons, quarks, vector bosons, photons and finally also Higgs scalars, and of these only the leptons and photons are directly observed particles. The evidence for quarks comes from another domain of physics, namely strong interactions supposedly described by quantum chromodynamics. The massive vector bosons as well as the Higgs particles are theoretical inventions, and while few people doubt the existence of vector bosons, many are sceptical with respect to the Higgs system.

Meanwhile, theorists have gone beyond the standard model, and speculations on possible grand unified schemes have emerged. Also there are speculations on the possible compositeness of quarks and leptons, or Higgs particles. In these notes we will not discuss grand unified theories, and the question of physics beyond 1 TeV (where compositeness may show up) will be touched upon only sketchily.

Our metric is such that $k^2 < 0$ if k is a timelike vector.

2. The Four-Fermion Interaction

In 1957, Marshak and Sudarshan, and Feynman and Gell-Mann[1] proposed the V-A theory. These latter authors then also introduced the current-current theory. In this theory the interaction between fermions is written as the product of two currents that carry a charge. If we restrict ourselves to muons, electrons and their neutrinos then the interaction Lagrangian is:

$$\mathscr{L}_{cc} = G_F j_\alpha^+ j_\alpha^- \tag{2.1}$$

$$\begin{aligned} j_\alpha^- &= i(\bar{\nu}_e \gamma^\alpha (1+\gamma^5) e) + i(\bar{\nu}_\mu \gamma^\alpha (1+\gamma^5) \mu) \\ j_\alpha^+ &= i(\bar{e} \gamma_\alpha (1+\gamma^5) \nu_e) + i(\bar{\mu} \gamma^\alpha (1+\gamma^5) \nu_\mu) \ . \end{aligned} \tag{2.2}$$

Thus:

$$\begin{aligned} \mathscr{L}_{cc} = -G_F [& (\bar{\nu}_e \gamma^\alpha (1+\gamma^5) e)(\bar{e} \gamma^\alpha (1+\gamma^5) \nu_e) \\ & + (\bar{\nu}_e \gamma^\alpha (1+\gamma^5) e)(\bar{\mu} \gamma^\alpha (1+\gamma^5) \nu_\mu) \\ & + (\bar{\nu}_\mu \gamma^\alpha (1+\gamma^5) \mu)(\bar{e} \gamma^\alpha (1+\gamma^5) \nu_e) \\ & + (\bar{\nu}_\mu \gamma^\alpha (1+\gamma^5) \mu)(\bar{\mu} \gamma^\alpha (1+\gamma^5) \nu_\mu)] \ . \end{aligned} \tag{2.3}$$

We thus have four basic interactions, and they all go with the same coupling constant (see Fig. 1).

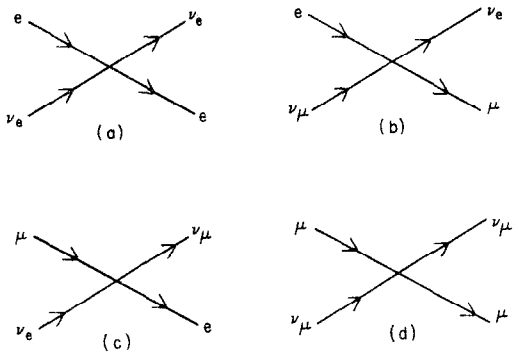

Figure 1

Vertices b and c are relevant for μ^+ and μ^- decay respectively.

Using the expression corresponding to vertex c we may compute the muon lifetime as a function of the fermi coupling constant G_F.

$$\frac{1}{\tau_\mu} = \frac{m_\mu^5}{96\pi^3} G_F^2 \ . \tag{2.4}$$

Comparing this with the experimentally known lifetime we find

$$G_F = 8.2297 \times 10^{-12} \ \text{MeV}^{-2} = \frac{1.0246}{m_p^2 \sqrt{2}} \times 10^{-5} \tag{2.5}$$

where m_p is the proton mass. To good approximation $G_F \sim 10^{-5}/m_p^2\sqrt{2}$. In the literature one often writes $G_F/\sqrt{2}$ in front of the interaction rather than G_F, as we did, and consequently values quoted may differ by $\sqrt{2}$ from the value that we give here.

At this level the current-current theory produces a prediction for ν_e-e scattering. The lowest order amplitude is:

$$- (2\pi)^4 iG_F(\bar{e}\gamma^\mu(1+\gamma^5)\nu_e)(\bar{\nu}_e\gamma^\mu(1+\gamma^5)e) \tag{2.6}$$

which, after a Fiertz transformation is equivalent to

$$(2\pi)^4 iG_F(\bar{\nu}_e\gamma^\mu(1+\gamma^5)\nu_e)(\bar{e}\gamma^\mu(1+\gamma^5)e) \tag{2.7}$$

This leads to the total cross section:

$$\sigma^{tot}_{\nu_e e} = \frac{16}{\pi} G_F^2 \frac{m^3 E_\ell^3 (E_\ell + \frac{1}{2}m)}{E^4 E_\nu} \tag{2.8}$$

m = electron mass,

E_ν = neutrino energy,

E_ℓ = total lab energy = $E_\nu + m$

E = c.m. energy = $\sqrt{2mE_\ell + m^2}$.

If E_ℓ and E large with respect to m we may approximate $E_\ell = E_\nu$ and $E^2 = 2mE_\ell$. The result is then:

$$\sigma^{tot}_{\nu_e e} \simeq \frac{4}{\pi} G_F^2 \, mE_\ell \simeq \frac{2}{\pi} G_F^2 \, E^2 \, . \tag{2.9}$$

We will not analyze here to what extent this prediction agrees with the data obtained from low energy reactor experiments. As a matter of fact, it seems that there is no conflict with the measurements. However, the above equation shows a strong dependence on energy; the cross section grows indefinitely with increasing energy. This is not acceptable; at some point one gets into conflict with conservation of probability. Stated differently, above a certain energy the formula for the cross section violates unitarity, and thus must be wrong. In the following section we will analyze this problem.

3. The Unitarity Limit

The fact that Eq. (2.9) for the total cross section violates unitarity actually implies that we have not made a correct calculation. We must include radiative corrections, and they will restore unitarity. From the fact that at high energy the cross section (2.9) violates unitarity by an arbitrarily large amount we deduce that the radiative corrections become very large at high energies. Since we have no data at high energy, that cannot be excluded. However, it may well be that some of these radiative corrections are also large at low energies, in which case they are of immediate interest.

To study this we must introduce a cut-off in the theory. Instead of the Fermi constant G_F we will use the expression

$$\frac{g^2}{q^2 + \Lambda^2} \tag{3.1}$$

where q is the four-momentum transfer between the currents. Thus in the process under consideration it is the momentum as indicated in Fig. 2. In our metric q^2 is positive for spacelike q. If we choose g and Λ such that $g^2/\Lambda^2 = G_F$ then at low energies there will be no difference with the original interaction.

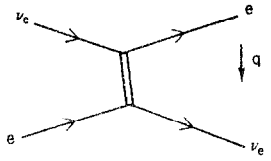

Figure 2

The lowest order radiative corrections to the above process correspond to a number of diagrams, and the relevant diagrams are shown in Fig. 3.

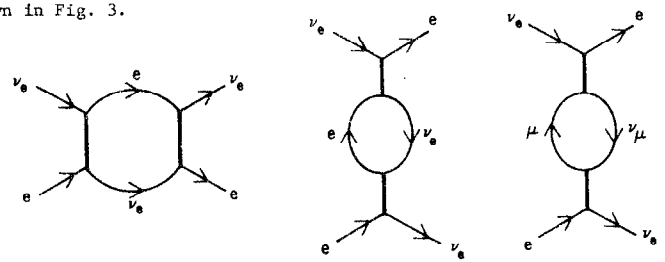

a b c

Figure 3

All of these diagrams give large contributions at high energies. At low energies all these diagrams lead to effects that can be eliminated by redefining g and Λ.

However, there is also μ-decay. The relevant diagrams to this decay are shown in Fig. 4.

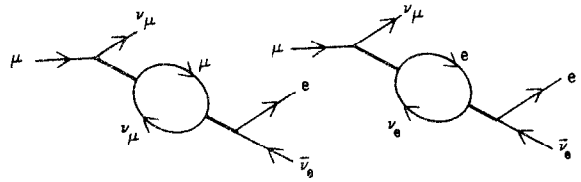

Figure 4

Again, the above diagrams can be eliminated by redefining g and Λ. However, this redefinition evidently differs from that needed for ν_e-e scattering, as there is no equivalent of diagram a of Fig. 3 in the case of μ-decay. This diagram will therefore induce a difference between

the rate for μ-decay and the ν_e-e scattering cross section relative to the lowest order predictions.

The contribution of diagram a of Fig. 3 can be computed. It is given by:

$$\int d_4q \, \frac{g^4}{(q^2+\Lambda^2)^2 q^4} \cdot \{\bar{\nu}_e \gamma^\mu (1+\gamma^5)(-i\gamma q)\gamma^\nu (1+\gamma^5)\nu_e\} \times \{\bar{e}\gamma^\mu (1+\gamma^5)(+i\gamma q)\gamma^\nu (1+\gamma^5)e\} \tag{3.2}$$

where we neglected the electron mass as well as the external momentum dependence. Averaging over directions amounts to the replacement $q_\alpha q_\beta \to \frac{1}{4} q^2 \delta_{\alpha\beta}$, and furthermore using the formula

$$\gamma^\mu\gamma^\alpha\gamma^\nu = \gamma^\mu\delta_{\alpha\nu} + \gamma^\nu\delta_{\mu\alpha} - \gamma^\alpha\delta_{\mu\nu} + \varepsilon_{\mu\alpha\nu\lambda}\gamma^5\gamma^\lambda$$

we obtain:

$$\begin{aligned} &\int d_4q \, \frac{12 g^4 q^2}{(q^2+\Lambda^2)^2 q^4} (\bar{\nu}_e\gamma^\mu(1+\gamma^5)\nu_e)(\bar{e}\gamma^\mu(1+\gamma^5)e) \\ &= 12 g^4 \cdot i\pi^2 \cdot \frac{1}{\Lambda^2} (\bar{\nu}_e\gamma^\mu(1+\gamma^5)\nu_e)(\bar{e}\gamma^\mu(1+\gamma^5)e) \qquad (3.3) \\ &= 12 i\pi^2 \, G_F^2\Lambda^2 (\bar{\nu}_e\gamma^\mu(1+\gamma^5)\nu_e)(\bar{e}\gamma^\mu(1+\gamma^5)e) \, . \end{aligned}$$

The addition of this to the lowest order amplitude Eq. (2.7) shows that we have a radiative correction to ν_e-e scattering (relative to μ-decay) given by a factor

$$1 + \frac{3}{4\pi^2} G_F\Lambda^2 = 1 + \frac{\Lambda^2}{(1365\ m_p)^2} \tag{3.4}$$

to the amplitude.

Clearly, in the limit $\Lambda \to \infty$ the relation between μ-decay and ν_e-e scattering gets completely lost. Of course, one should also take into account still higher order corrections, and in fact they give again arbitrarily large corrections.

If we assume that the four-fermion theory remains valid up to some energy then we see that this energy must be less than 410 m_p if the correction to the amplitude is to be less than 9%.

The above example shows in full clarity the following fact: in a non-renormalizable theory relations between coupling constants may be strongly affected.

The model described above is incomplete in many respects: no quark currents have been included, and also current-current interaction involving neutral currents have not been considered. A more complete discussion[2] along these lines leads to a limit on the validity of the four-fermion theory of about 150-300 GeV. We refer to the literature for more extensive and/or alternative discussions relating to these matters.[3]

4. Gauge Theories

The discussion of the previous section resulted in the statement that the four-fermion theory of weak interactions cannot be true to all energies. The real question is then this: how to modify the four-fermion theory in such a way that the low energy results remain unaffected, and furthermore such that radiative corrections remain small. One of the basic ingredients in such a construction is the introduction of a symmetry. For instance, one introduces a symmetry that guarantees the equalness of the μ-decay and ν_e-e scattering coupling constants, and tries to arrange things such that most interactions respect this symmetry. Invariably such considerations lead to the same result, namely a gauge theory of weak interactions. We will give here the standard theory[4] of weak and electromagnetic interactions, and describe in detail the options available within the framework of that theory.

The first choice is the choice of the symmetry. Here this is $SU_2 \times U_1$. Thus there is a two-dimensional complex space and a one-dimensional complex space. SU_2 is the collection of 2×2 unitary matrices with determinant 1 defined in the two-dimensional space, and U_1 is the collection of 1×1 unitary matrices in the one-dimensional space. Alternatively one may see U_1 as matrices in n×n space differing from the unit matrix by a phase factor.

Having chosen the symmetry the vector particle content of the theory is fixed. There are as many vector particles as degrees of freedom in the symmetry. An SU_2 matrix may be written in the form

$$S = e^{-i\rho_a \frac{\tau^a}{2}}, \quad a = 1,2,3 \tag{4.1}$$

where the τ^a are the Pauli matrices and the ρ_a are three real numbers. For the U_1 matrices we may write

$$e^{-i\rho_o \frac{\tau^o}{2}} \tag{4.2}$$

involving one real number ρ_o and the unit matrix τ^o.

Next we define vector boson fields B_μ^α, $\alpha = 1,2,3$ and C_μ^o, and vector boson matrices:

$$b_\mu = -\frac{i\tau^\alpha}{2} B_\mu^\alpha ; \qquad c_\mu = -\frac{i\tau^o}{2} C_\mu^o \ . \tag{4.3}$$

With every SU_2 and U_1 transformation we will associate a transformation of the vector boson matrices. Let S be an SU_2 matrix of the form (4.1). With this matrix we associate a vector boson transformation involving an arbitrary constant g:

$$b'_\mu = S\, b_\mu S^\dagger + \frac{1}{g} S\, \partial_\mu S^\dagger \ . \tag{4.4}$$

This defines b'_μ. If we write b'_μ as a function of new vector boson fields B'_μ just like in Eq. (4.3) for b then, after some work, one finds the relation between the B' and B. Just for completeness we quote this relation:

$$B'^a_\mu = U_{ab} B^b_\mu - \frac{1}{g} \left(\frac{U-1}{\overline{\Lambda}} \right)_{ab} \partial_\mu \rho^b \tag{4.5}$$

where $\overline{\Lambda}$ and U are matrices:

$$\overline{\Lambda}_{ab} = -f_{cab}\rho^{c}$$
$$U = e^{\overline{\Lambda}} \tag{4.6}$$

and the f are structure constants:

$$\left[\frac{-i\tau^a}{2}, \frac{-i\tau^b}{2}\right] = f_{abc}\frac{-i\tau^c}{2} . \tag{4.7}$$

In the case at hand $f_{abc} = \varepsilon_{abc}$, the completely antisymmetrical tensor in three dimension.

A similar transformation holds for c_μ with respect to the U_1 transformations (4.2).

We now can write down the vector boson Lagrangian. Define the matrix $g_{\mu\nu}$:

$$g_{\mu\nu} = \partial_\mu b_\nu - \partial_\nu b_\mu + g[b_\mu, b_\nu] . \tag{4.8}$$

If we decompose

$$g_{\mu\nu} = -\frac{i\tau^a}{2} G^a_{\mu\nu} \tag{4.9}$$

Then we deduce:

$$G^a_{\mu\nu} = \partial_\mu B^a_\nu - \partial_\nu B^a_\mu + g f_{abc} B^b_\mu B^c_\nu . \tag{4.10}$$

The SU_2 vector boson Lagrangian is now:

$$\mathscr{L} = -\tfrac{1}{2}\,\mathrm{Tr}(g^\dagger_{\mu\nu} g_{\mu\nu}) = -\tfrac{1}{4}\, G^a_{\mu\nu} G^a_{\mu\nu} \tag{4.11}$$

where Tr stands for trace. To this we must add the U_1 vector boson Lagrangian constructed in the same way. However, there the commutator part of $g_{\mu\nu}$ is zero, thus no further coupling constants enter in the theory.

We will now show some important results, namely that two successive transformations with matrices S_1 and S_2 give the same result as one transformation with a matrix S_3, where $S_3 = S_2 S_1$. Secondly we show that the Lagrangian (4.11) is invariant under the transformation (4.4).

(i) Let

$$b''_\mu = S_2 b'_\mu S_2^\dagger + \frac{1}{g} S_2 \partial_\mu S_2^\dagger$$

with b'_μ related to b_μ as shown in Eq. (4.4) with S_1 for S. We find:

$$\begin{aligned} b''_\mu &= S_2(S_1 b_\mu S_1^\dagger + \tfrac{1}{g} S_1 \partial_\mu S_1^\dagger) S_2^\dagger + \tfrac{1}{g} S_2 \partial_\mu S_2^\dagger \\ &= S_3 b_\mu S_3^\dagger + \tfrac{1}{g} S_3 (\partial_\mu S_1^\dagger) S_2^\dagger + \tfrac{1}{g} S_2 \partial_\mu S_2^\dagger \\ &= S_3 b_\mu S_3^\dagger + \tfrac{1}{g} S_3 \partial_\mu S_3^\dagger \end{aligned}$$

where we used

$$\partial_\mu S_3^\dagger = \partial_\mu (S_1^\dagger S_2^\dagger) = (\partial_\mu S_1^\dagger) S_2^\dagger + S_1^\dagger \partial_\mu S_2^\dagger$$

and

$$S^\dagger = S^{-1} .$$

(ii) From (4.4) and (4.8) we deduce:

$$\begin{aligned} g'_{\mu\nu} &= \partial_\mu b'_\nu - \partial_\nu b'_\mu + g[b'_\mu, b'_\nu] \\ &= \partial_\mu S\, b_\nu S^\dagger + S\, b_\nu \partial_\mu S^\dagger + S \partial_\mu b_\nu S^\dagger - \partial_\nu S\, b_\mu S^\dagger - S\, b_\mu \partial_\nu S^\dagger - S\, \partial_\nu b_\mu S^\dagger \\ &\quad + \tfrac{1}{g}\partial_\mu (S\, \partial_\nu S^\dagger) - \tfrac{1}{g}\partial_\nu (S\, \partial_\mu S^\dagger) + \tfrac{1}{g} S[b_\mu, b_\nu] S^\dagger \\ &\quad + [S\, \partial_\mu S^\dagger, S\, b_\nu S^\dagger] + [S\, b_\mu S^\dagger, S\, \partial_\nu S^\dagger] + \tfrac{1}{g}[S\, \partial_\mu S^\dagger, S\, \partial_\nu S^\dagger] . \end{aligned}$$

With

$$\partial_\mu S = -S(\partial_\mu S^{-1})S = -S(\partial_\mu S^\dagger)S$$

one obtains

$$g'_{\mu\nu} = S(\partial_\mu b_\nu - \partial_\nu b_\mu + g[b_\mu, b_\nu])S^\dagger = S\, g_{\mu\nu}\, S^\dagger .$$

Now the Lagrangian (4.11) contains the trace of $g_{\mu\nu}g_{\mu\nu}$, and if we use the property Tr(ABCD) = Tr(BCDA) then we see that $\mathrm{Tr}(g'_{\mu\nu}g'_{\mu\nu}) = \mathrm{Tr}(g_{\mu\nu}g_{\mu\nu})$. This is precisely what we mean by invariance of the Lagrangian under the transformations (4.4).

For completeness we write explicitly some equations for the U_1 field c_μ. Under a transformation (4.2) the transformation law (4.4) simplifies for the 1×1 matrix c_μ to

$$c'_\mu = c_\mu + \frac{1}{g}\, i\, \frac{\tau^0}{2}\, \partial_\mu \rho_0 \qquad (4.12)$$

and Eq. (4.5) becomes:

$$C'^0_\mu = C^0_\mu - \frac{1}{g}\, \partial_\mu \rho_0 \qquad (4.13)$$

For convenience we also give some equations that are useful for the derivation underlying the connection between Eqs. (4.4) and (4.5). A useful trick is to write:

$$\frac{U-1}{\bar{\Lambda}} = \int_0^1 dy\; e^{y\bar{\Lambda}}\ , \quad U = e^{\bar{\Lambda}}\ . \qquad (4.14)$$

Other useful equations are (A and B are matrices):

$$e^{-A}\, B\, e^{A} = B + [B,A] + \frac{1}{2!}\,[[B,A],A] + \ldots \qquad (4.15)$$

If A is a matrix depending on x:

$$e^{-A}\,\frac{d}{dx}\,e^{A} = A' + \frac{1}{2!}\,[A',A] + \frac{1}{3!}\,[[A',A],A] + \ldots$$

where A' is the matrix whose elements are the derivative of the elements of A. Equations like these are proven by substituting A = yA and subsequently working out d^n/dy^n of the left-hand side to obtain a power series in y. For instance:

$$\frac{d}{dy}\left\{e^{-yA}\, B\, e^{yA}\right\} = e^{-yA}[B,A]\, e^{yA}\ .$$

For y = 0 the expression on the right is the coefficient of y in the series expansion. So we get the second term in Eq. (4.15).

5. Strong Interactions

In the previous section we introduced vector-boson matrices b and c. They may be combined elegantly into one matrix $\underline{b}$:

$$\underline{b}_\mu = b_\mu + c_\mu = -\frac{i}{2}\begin{pmatrix} C^o_\mu + B^3_\mu & B^1_\mu - iB^2_\mu \\ B^1_\mu + iB^2_\mu & C^o_\mu - B^3_\mu \end{pmatrix} .$$

The Lagrangian is now simply $-\mathrm{Tr}(\underline{g}_{\mu\nu}\underline{g}_{\mu\nu})/2$ where $\underline{g}_{\mu\nu}$ is defined analogous to Eq. (4.8).

The identification with physical particles goes by establishing the mass eigenstates, and also by charge (or other quantum number) eigenstates. Such things become well defined only after coupling of the vector-bosons to fermions and Higgs fields, where then the latter generate masses for the vector bosons. Things will be arranged such that off-diagonal fields represent quantum eigenstates. Along the diagonal things may be more complicated. There the mass-eigenstates may be combinations of the fields found along the diagonal, but that can be established only after mass generation by the Higgs system is worked out.

The physical fields in the $SU_2{\times}U_1$ standard model will be denoted by $W^{\pm}_\mu$, W^o_μ and A_μ, where W^o_μ is the neutral vector boson (often called the Z^o) and A_μ is the photon field. The fields B^3_μ and C^o_μ are linear combinations of W^o and A:

$$B^3_\mu = c_\theta W^o_\mu + s_\theta A_\mu$$
$$C^o_\mu = -s_\theta W^o_\mu + c_\theta A_\mu$$
$$c_\theta = \cos\theta \qquad s_\theta = \sin\theta .$$

The as yet unspecified angle θ is the weak mixing angle. In terms of the physical fields the vector boson matrix is:

$$\underline{b} = -\frac{i}{2}\begin{pmatrix} (c_\theta - s_\theta)W^o_\mu + (c_\theta + s_\theta)A_\mu & \sqrt{2}\,W^+_\mu \\ \sqrt{2}\,W^-_\mu & -(c_\theta + s_\theta)W^o_\mu + (c_\theta - s_\theta)A_\mu \end{pmatrix} .$$

If $\mathscr{L}$ was properly normalized with respect to the B and C then this will also be the case for the W and A.

Quantum chromodynamics is presumably described by an SU_3 symmetry. This amounts to writing 3×3 matrices λ^a instead of the 2×2 matrices τ^a. The vector bosons of QCD are called gluons, and may also be grouped in a matrix. A gluon is characterized by two colors (or one color and one anticolor), and in terms of these color states the gluon matrix is

$$g_\mu = -\frac{i}{2}\begin{pmatrix} g^w + \frac{1}{\sqrt{3}}g'^w & \sqrt{2}\,g^r_g & \sqrt{2}\,g^r_b \\ \sqrt{2}\,g^g_r & -g^w + \frac{1}{\sqrt{3}}g'^w & \sqrt{2}\,g^g_b \\ \sqrt{2}\,g^b_r & \sqrt{2}\,g^b_g & -\frac{2}{\sqrt{3}}g'^w \end{pmatrix} .$$

The subscripts r,g,b refer to the colors red, green and blue, and the superscript to their anticolors. There are two "white" gluons that may be considered also as combinations of red-antired, green-antigreen and blue-antiblue.

The Lagrangian now simply gets an extra term involving the gluon fields completely analogous to the b fields as described before. One may combine the weak, electromagnetic and gluon vector bosons by introducing a 5×5 matrix made up from the 2×2 b matrix and the 3×3 g matrix:

$$\begin{pmatrix} b & b & 0 & 0 & 0 \\ b & b & 0 & 0 & 0 \\ 0 & 0 & g & g & g \\ 0 & 0 & g & g & g \\ 0 & 0 & g & g & g \end{pmatrix} .$$

The Grand Unified Theory of Georgi and Glashow is obtained by assuming the existence of 6 new vector bosons at the locations with zeroes in the above matrix. Moreover, the U_1 part of $SU_2 \times U_1$, represented by C^o, is redefined as a multiple of the matrix with 1,1,-2/3,-2/3,-2/3 along the diagonal. It is no longer a U_1 symmetry, but part of the SU_5 symmetry.

On the face of it this SU_5 symmetry is quite far from the reality of physics. The new vector bosons must be very heavy, or else they would have been observed either directly or indirectly. Furthermore, in a Lagrangian defined with such a matrix as in Eq. (4.11) we have only one free parameter, the coupling constant g as shown in Eqs. (4.8) and (4.10), while at low energies we observe 3 different coupling constants for electromagnetic, weak and strong interactions. However, it may be shown that the apparant experimental differences arise from radiative corrections. The calculation of these corrections involves one new parameter, inherent to the renormalization procedure. It turns out that there exists one choice for this parameter such that the radiative corrections, starting from one coupling constant, give rise to about the experimentally observed coupling constants. Stated differently, two parameters may be chosen such that three quantities fit the data. In these notes we will not discuss SU_5 any further, we will focus attention on other areas of interest.

6. The Fermions

In constructing the fermion Lagrangian, including the coupling to vector bosons, one must assign SU_2 and U_1 transformation properties to these fermions. With respect to SU_2 the popular view is that the left-handed fermions are SU_2 doublets while the right-handed fermions are singlets under SU_2. The transformation properties with respect to U_1, always given by phase factors, are fixed such that the proper coupling to the photon results.

Consider a left-handed fermion doublet, denoted by f_i^+, $i = 1,2$. Under an SU_2 transformation X_{ji}, with X of the form (4.1), the f_i transform as

$$f_i'^+ = X_{ij} f_j^+ \quad . \tag{6.1}$$

Once the fermions are chosen to be doublets there is no freedom in this transformation assignment. The requirement is that the matrix X corresponding to an SU_2 transformation as in Eq. (4.1) must be of the form

$$e^{-i\rho_a \frac{t^a}{2}} \quad , \quad a = 1,2,3 \tag{6.2}$$

where the t^a have the same commutation rules as the τ^a, and apart from trivialities this has only the solutions $t^a = \tau^a$ or $t^a = 0$. The situation is quite different with respect to the U_1 symmetry. Corresponding to the U_1 transformation (4.2) we have a transformation

$$e^{-i\rho_o \frac{t^o}{2}} \tag{6.3}$$

and the requirement that t^o commutes as τ^o gives only that t^o must be a multiple of the identity. In other words, the U_1 transformation takes

the form

$$e^{-ig_1\rho_o \frac{\tau^o}{2}} \tag{6.4}$$

with g_1 as arbitrary constant.

Formally, the right-handed counterparts of the left-handed doublet may also be written as a doublet, ℓ_i^-, i = 1,2. These right-handed fermions are singlets under SU_2, i.e., the transformation matrices X for the f^- are given by an expression of the form (6.2) with $t^a = 0$, which is the unit matrix. With respect to t^o we now may take any hermitean 2×2 matrix, and denote that by T^o.

The coupling of the vector bosons to the fermions is dictated by the fact that the covariant derivative D_μ must involve the vector bosons in such a way that $D_\mu \ell$ transforms precisely as ℓ under $SU_2 \times U_1$. Consider f^+. Under an SU_2 transformation S we have:

$$f'^+ = Sf^+ \tag{6.5}$$

and

$$\partial_\mu f'^+ = (\partial_\mu S)f + S\partial_\mu f \ .$$

We define (compare Eq. (4.4))

$$D_\mu = \partial_\mu + gb_\mu \ .$$

Note that D_μ is a 2×2 matrix. The ∂_μ part is ∂_μ times the unit matrix. We have:

$$\begin{aligned} D'_\mu f'^+ &= (\partial_\mu + gb'_\mu)f'^+ \\ &= (\partial_\mu + gSb_\mu S^\dagger + S\partial_\mu S^\dagger)Sf^+ \\ &= S(\partial_\mu + gb_\mu)f^+ + (\partial_\mu S)f^+ + S(\partial_\mu S^\dagger)Sf \ . \end{aligned}$$

Since

$$\partial_\mu S^\dagger = - S^\dagger(\partial_\mu S)S^\dagger$$

we see that

$$D'_\mu f'^+ = SD_\mu f^+ \ .$$

With respect to the U_1 transformations we must use t^o instead of τ^o in the use of the vector boson matrix. In other words, let

$$\bar{c}_\mu = - \frac{i}{2} t^o C_\mu = t^o c_\mu$$

(compare Eq. (4.3)). Then, including also the SU_2 part of the correct definition for D is:

$$D_\mu = \partial_\mu + gb_\mu + g\bar{c}_\mu \ .$$

For the right-handed SU_2 singlet doublet we have the definition

$$D_\mu = \partial_\mu + g\bar{\bar{c}}_\mu \ , \qquad \bar{\bar{c}}_\mu = T^o c_\mu$$

where now in the definition of $\bar{\bar{c}}$ the T^o occurring in the transformation rule of f^- is to be used.

The above shows how the SU_2 fields b and the U_1 field c appear in several different combinations. In a truly unified theory this would not happen.

The Lagrangian for the fermion fields can now be written:

$$\mathscr{L}_f = - \overline{f^+}\gamma^\mu D_\mu f^+ - \overline{f^-}\gamma^\mu D_\mu f^- \ .$$

D_μ involves t^o in the f^+ term and T^o in the f^- term. Several arbitrary parameters (relating to the behaviour under U_1) remain to be fixed. This is done requiring that the electromagnetic field has couplings as required. This amounts to the following

(i) Leptons. Consider the ν_e e system. The left- and right-handed doublets are:

$$f^{\pm} \to \ell^{\pm} = \tfrac{1}{2}\,(1 \pm \gamma^5)\begin{pmatrix}\nu_e\\ e\end{pmatrix} \quad .$$

For t^o and T^o

leptons: $\quad t^o = -\dfrac{s_\theta}{c_\theta}\,\tau^o, \qquad T^o = -2\,\dfrac{s_\theta}{c_\theta}\begin{pmatrix}0 & 0\\ 0 & 1\end{pmatrix}$

must be used. The construction decouples the neutrino from the photon, and the interaction between photon and electron is parity conserving (equal for left- and right-handed electrons).

(ii) Quarks. Consider the u-d system. The left- and right-handed doublets are

$$f^{\pm} \to q^{\pm} = \tfrac{1}{2}\,(1 \pm \gamma^5)\begin{pmatrix}u\\ d\end{pmatrix}.$$

Now one must take

quarks: $\quad t^o = \dfrac{1}{3}\,\dfrac{s_\theta}{c_\theta}\,\tau^o\ , \quad T^o = \dfrac{s_\theta}{c_\theta}\begin{pmatrix}4/3 & 0\\ 0 & -2/3\end{pmatrix}.$

7. Higgs Couplings

In order to get a realistic model we must have mass terms for the vector bosons and the fermions. This is to be generated using the Higgs mechanism. This amounts to introducing scalar particles that must transform according to some $SU_2 \times U_1$ representation. The simplest non-trivial choice is a doublet, much like the left-handed fermion doublet. Thus we assume a complex doublet K:

$$K = \begin{pmatrix}K_1\\ K_2\end{pmatrix} \equiv \begin{pmatrix}\sigma_0 + i\phi^3\\ -\phi^2 + i\phi^1\end{pmatrix} \quad . \tag{7.1}$$

Now σ_0, ϕ^1, ϕ^2 and ϕ^3 are real fields. We have written things in this way because now (7.1) can also be written as:

$$\begin{aligned} K \equiv M\begin{pmatrix}1\\ 0\end{pmatrix} &= \begin{pmatrix}\sigma_0 + i\phi^3 & \phi_2 + i\phi_1\\ -\phi_2 + i\phi_1 & \sigma_0 - i\phi^3\end{pmatrix}\begin{pmatrix}1\\ 0\end{pmatrix} \\ &= \left\{\sigma_0\tau^o + i\phi^a\tau^a\right\}\begin{pmatrix}1\\ 0\end{pmatrix}. \end{aligned} \tag{7.2}$$

This notation is sometimes advantageous. We now establish the $SU_2 \times U_1$ properties of K. Under SU_2, $K' = SK$, with S an SU_2 transformation as before, and under U_1 we have a transformation involving a t_0 that must be a multiple of the identity τ_0. All this is precisely like for the fermion doublet. The Lagrangian for the Higgs system is now:

$$\mathscr{L}_H = -\tfrac{1}{2}\,(D_\mu K)^+(D_\mu K) - \frac{\mu}{2}\,(K^+K) - \frac{\lambda}{8}\,(K^+K)^2 \tag{7.3}$$

where we have added two terms that are $SU_2 \times U_1$ invariant and furthermore of a renormalizable type. Two arbitrary parameters μ and λ are involved. Further

$$D_\mu = \partial_\mu + g b_\mu + g \underline{c}_\mu \tag{7.4}$$

with $\underline{c}_\mu = -\frac{i}{2} g_1 \tau^o C^o_\mu$. Also g_1 is a new parameter, to be fixed by requiring the proper behaviour for electromagnetic interactions.

The state of lowest potential energy corresponding to the Lagrangian (7.3) is not necessarily the state with $K = 0$. In fact we may write:

$$\frac{\mu}{2} (K^+K) + \frac{1}{8}\lambda (K^+K)^2 = \frac{\lambda}{8} \left\{(K^+K) + \frac{2\mu}{\lambda}\right\}^2 - \tfrac{1}{2} \frac{\mu^2}{\lambda} . \tag{7.5}$$

This potential will have a minimum if $\lambda > 0$ (remember that $\mathscr{L}$ = kinetic-potential energy). If $\mu > 0$ then the minimum is for $K = 0$, which is not what we want. If $\mu < 0$ then we have a minimum for $(K^+K) = -2\mu/\lambda$. This happens for some K. By performing an $SU_2 \times U_1$ transformation this K may be turned such that it is of the form:

$$\begin{pmatrix} F\sqrt{2} \\ 0 \end{pmatrix} .$$

Let us now rewrite the potential substituting $\sigma_0(x) = F\sqrt{2} + H(x)$ in the expression for K. Writing

$$K = \begin{pmatrix} F\sqrt{2} \\ 0 \end{pmatrix} + \underline{K} \quad , \qquad \underline{K} = \begin{pmatrix} H + i\phi^3 \\ -\phi^2 + i\phi^1 \end{pmatrix} \tag{7.6}$$

we find for the potential (7.5)

$$\frac{\lambda}{8} \left\{(\underline{K}^+\underline{K}) + 2HF\sqrt{2} + 2F^2 + 2\frac{\mu}{\lambda}\right\}^2 - \tfrac{1}{2}\frac{\mu^2}{\lambda} .$$

In the following we will ignore the term $-\mu^2/2\lambda$. Introducing the new parameters

$$M = \frac{g}{\sqrt{2}} F \ , \quad m_H^2 = 2\lambda F^2 \ , \quad \beta = \mu + \lambda F^2, \ \alpha = \frac{m_H^2}{4M^2} \tag{7.7}$$

we get:

$$\frac{g^2 m_H^2}{32M^2} \left\{(\underline{K}^+\underline{K}) + \frac{4M}{g} H + \frac{8\beta M^2}{g^2 m_H^2}\right\}^2 . \tag{7.8}$$

Choosing $F^2 = -\mu/\lambda$ corresponds to $\beta = 0$. For $\beta = 0$ we have only one quadratic term, namely

$$\tfrac{1}{2} m_H^2 H^2 . \tag{7.9}$$

What happened to the $SU_2 \times U_1$ invariance? We used this invariance to write things in a convenient way. But the symmetry is of course unaffected.

At this point one may fix the U_1 constant g_1 involved in the Lagrangian (7.3) through D_μ as given in (7.4). Writing out this Lagrangian the constant part in K gives rise to vector boson masses, and g_1 must now be chosen such that the photon remains massless. This gives $g_1 = -s_\theta/c_\theta$.

It should be noted that we have turned things upside down. What happens is that the Higgs system involves a certain constant g_1. Then one rewrites the vector boson fields, introducing an angle θ such that one of the fields remains massless. This θ is then found by solving $s_\theta/c_\theta = -g_1$. In other words, the coupling constant g_1 of the Higgs system defines the weak mixing angle.

The Higgs Lagrangian can now be worked out. In doing so we will use the charged fields $\phi^\pm$ instead of ϕ^1, ϕ^2 and ϕ^o instead of ϕ^3:

$$\phi^\pm = \frac{1}{\sqrt{2}} (\phi^1 \mp i\phi^2), \ \phi^0 = \phi^3.$$

8. Higgs-Fermion Couplings

Up to now also the fermions are massless, and we now use the Higgs fields to also generate fermion masses. This amounts to constructing $SU_2 \times U_1$ invariant Higgs-fermion couplings. Here we must be particularly careful with respect to the U_1 behaviour. This is most easily done by considering the right-handed fermions separately, thus no longer artificially written as doublets. Under a U_1 transformation $\exp(i\rho^0)$ any fermion field requires a factor $\exp(i\kappa\rho^0)$ with κ varying from field to field. For a given fermion field the associated value of κ will be called the U_1 hypercharge of that field. For a U_1 invariant term the sum of the U_1 hypercharges of the fields in that term must be zero.

In addition we will also consider strange, charmed, bottom and top quarks. As a matter of notation we introduce a generation index a. Thus there exist three quarks u_α with charge 2/3 and three quarks d_α with charge -1/3. In addition there is still the three-fold color degeneracy, but that is a trivial complication here. At this moment we will not introduce the names, up, charm, top, etc., since there is a matter of mixing involved. Similarly there are three lepton families, denoted by ν_α and ℓ_α.

The U_1 and SU_2 properties of the fermion multiplets are:

$\ell^+ = (\nu,e)_+$	$\kappa = -t_\theta$	SU_2 doublet
ν^-	0	singlet
e^-	$-2t_\theta$	singlet
$q^+ = (u,d)^+$	$1/3\ t_\theta$	doublet
u^-	$4/3\ t_\theta$	singlet
d^-	$-2/3\ t_\theta$	singlet
K	$-t_\theta$	doublet

In this table $t_\theta = \tan_\theta = s_\theta/c_\theta$. Note that for antiparticles the U_1 properties are simply the opposite of the ones given above. Furthermore, if the particle doublets transform under SU_2 with S then the antiparticles transform with $S^\dagger$, for example

$$K' = SK\ , \qquad K'^\dagger = K^\dagger S^\dagger\ .$$

Interaction terms that are invariant under $SU_2 \times U_1$ may now be written down. First we do this assuming one generation only

$$\mathscr{L}_{fH} = \mu_1(\bar{\ell}^+\nu^-K) + \mu_2(\bar{\ell}^+e^-K^\dagger) + \lambda_1(\bar{q}^+u^-K) + \lambda_2(\bar{q}^+d^-K^\dagger) + \text{herm. conj.}$$

The SU_2 properties have not yet been considered. Here we need the completely antisymmetrical tensor in two dimensions, ε_{ij}. This tensor is invariant under SU_2:

$$S_{ki}S_{\ell j}\varepsilon_{ij} = \varepsilon_{k\ell}\cdot\det(S) = \varepsilon_{k\ell}\ .$$

Writing explicitly SU_2 indices we then have

$$\mathscr{L}_{fH} = \mu_1(\bar{\ell}_i^+\nu^-)K_i + \mu_2(\bar{\ell}_i^+e^-)K_j^\dagger\,\varepsilon_{ij}$$

$$+ \lambda_1(\bar{q}_i^+u^-)K_1 + \lambda_2(\bar{q}_i^+d^-)K_j^\dagger\,\varepsilon_{ij} + \text{herm. conj.}$$

Remember that the superscripts ± refer to factors $\frac{1}{2}(1 \pm \gamma^5)$ in front.

In the first instance we are interested in the mass terms only. Then only the constant part of K, i.e., $K = (F\sqrt{2},0)$ needs to be considered. Thus only $K_1 \neq 0 = 2M/g$. The result is

$$\mathscr{L}_{fH} = \frac{2M\mu_1}{g}(\bar{\nu}^+\nu^-) - \frac{2M\mu_2}{g}(\bar{e}^+e^-)$$

$$+ \frac{2M\lambda_1}{g}(\bar{u}^+u^-) - \frac{2M\lambda_2}{g}(\bar{d}^+d^-) + \text{herm. conj.}$$

Noting that $\nu^- = \tfrac{1}{2}(1+\gamma^5)\nu$, $\bar{\nu}^+ = \tfrac{1}{2}\bar{\nu}(1-\gamma^5)$, etc., we get:

$$\mathscr{L}_{fH} = \frac{M}{g}\left\{\bar{\nu}(\mu_1 + \mu_1^* + (\mu_1 - \mu_1^*)\gamma^5)\nu\right\}$$

$$- \frac{M}{g}\left\{\bar{e}(\mu_2 + \mu_2^* + (\mu_2 - \mu_2^*)\gamma^5)e\right\}$$

$$+ \text{similar quark terms.}$$

Actually, $\mu_1 \ldots \lambda_2$ may be taken to be real. This is because a phase factor in these parameters may be turned away by multiplying ν^-, e^-, etc., with a constant phase factor. Such a space-time independent phase factor leaves $\bar{\nu}^- D_\mu \nu^-$, etc., invariant.

Having done that we see that we can give an arbitrary mass to neutrino and electron. Assuming zero neutrino mass we thus take:

$$\mu_1 = 0\,, \qquad \mu_2 = \frac{gm_e}{2M}$$

$$\lambda_1 = \frac{gm_u}{2M}, \qquad \lambda_2 = \frac{gm_d}{2M}\,.$$

Things get more complicated if we consider three families. We will **explicitly treat** the quark sector.

Since all quark generations have the same behaviour under $SU_2 \times U_1$ we may use an arbitrary superposition of generations everywhere. In all generality the quark-Higgs couplings are then:

$$(\bar{q}_{i\alpha}^+ \Lambda_1^{\alpha\beta} u_\beta^-)K_i + (\bar{q}_{i\alpha}^+ \Lambda_2^{\alpha\beta} d_\beta^-)K_j^\dagger \varepsilon_{ij} + \text{herm. conj.}$$

In here Λ_1 and Λ_2 are arbitrary complex 3×3 matrices.

The Quark -W part of the Lagrangian is diagonal with respect to the generation index:

$$-(\bar{q}_\alpha^+ \not{\partial} q_\alpha^+) - (\bar{u}_\alpha^- \not{\partial} u_\alpha^-) - (\bar{d}_\alpha^- \not{\partial}\, d_\alpha^-)\,.$$

Any unitary transformation U in generation space of q^+, u^- or d^- leaves this invariant, provided U is constant as a function of space time. For instance, if $q' = Uq$, with $U^+ = U^{-1}$ then

$$(\bar{q}'_\beta \not{\partial} q'_\beta) = (\bar{q}_\alpha U^+_{\alpha\beta} \not{\partial} U_{\beta\gamma} q_\gamma) = (\bar{q}_\alpha U^+_{\alpha\beta} U_{\beta\gamma} \not{\partial} q_\gamma) = (\bar{q}_\alpha \not{\partial} q_\alpha)\,.$$

Only the generation structure is shown.

We may use this freedom to simplify the Λ-matrices. First we perform a unitary transformation on u^- and another one on d^- so that Λ_1 and Λ_2 become hermitean. Thus we use the property that for arbitrary complex matrix Λ there exists a unitary matrix T such that ΛT is hermitean. Proof: consider the hermitean matrix $\Lambda^+\Lambda$. A suitable unitary transformation diagonalizes $\Lambda^+\Lambda$, thus $(e_i U^+ \Lambda^+ \Lambda U e_j) = \mu_i \delta_{ij}$, where the μ_i are

the positive real eigenvalues and the e_i the normalized basis vector. Now define the vectors $v_i = Ue_i$. The last equation reads then $(v_j v_i) = \mu_i \delta_{ij}$. Thus the v_i are an orthogonal (but not normalized) system. There exists a unitary transformation V that turns the orthogonal v_i along the e_i, thus $Vv_i = \sqrt{\mu_i}\, e_i$, or $V\Lambda U e_i = \sqrt{\mu_i}\, e_i$. Thus there exist unitary matrices V and U such that $V\Lambda U$ is diagonal and real positive, and evidently hermitean. But then also $V^\dagger V\Lambda UV = \Lambda UV$ is hermitean, and UV is the desired matrix T.

Thus Λ_1 and Λ_2 may be taken to be hermitean. Next we transform q^+, u^- and d^- all with the same unitary matrix U such that Λ_1 diagonalizes with positive real eigenvalues. The matrix Λ_2 remains hermitean.

Finally we perform a unitary transformation of the form

$$U(\phi) = \begin{pmatrix} e^{i\phi_1} & 0 & 0 \\ 0 & e^{i\phi_2} & 0 \\ 0 & 0 & e^{i\phi_3} \end{pmatrix}$$

to all fields. This leaves the diagonal matrix Λ_1 unchanged. The hermitean matrix Λ_2 changes; the off diagonal elements get phase factors of the type $e^{i(\phi_a - \phi_b)}$. There are 2 independent differences, $\phi_1 - \phi_2$ and $\phi_2 - \phi_3$, and thus two of the three arbitrary phases in Λ_2 may be turned away. After all this work Λ_2 is a hermitean matrix with only one complex phase. We may write

$$\Lambda_2 = CM^d C^{-1}$$

where M^d is diagonal, and C is of the form

$$C = \begin{pmatrix} c_1 & -s_1c_3 & -s_1s_3 \\ s_1c_2 & c_1c_2c_3 - s_2s_3e^{i\delta} & c_1c_2s_3 + s_2c_3e^{i\delta} \\ s_1s_2 & c_1s_2c_3 + c_2s_3e^{i\delta} & c_1s_2s_3 - c_2c_3e^{i\delta} \end{pmatrix}$$

where $c_i = \cos\theta_i$, $s_i = \sin\theta_i$, and $\theta_1 \ldots \theta_3$ and δ are undetermined angles. They must be found from experiment.

If we substitute everywhere for the $d_\alpha^\pm$ the combination $C_{\alpha\beta} d_\beta^\pm$ then the d mass term becomes diagonal in the generation index. This is then what we call down, strange, and bottom quarks. But at various places we will see the generalized Cabibbo matrix C, in particular in the interaction of the charged vector bosons with u-d pairs.

9. Field Theory

The Lagrangian constructed so far is invariant under $SU_2 \times U_1$ transformations. Before one arrives at Feynman rules that permit the calculation of radiative corrections, some further pieces must be added. Here we will not discuss this at length, but will just give the prescription.

First a gauge fixing part must be defined. To this purpose one must introduce 4 functions F_0, F_1, F_2, F_3 that are not invariant under the $SU_2 \times U_1$ transformations. Then $\mathscr{L}_{gf}$ is given by:

$$\mathscr{L}_{gf} = -\tfrac{1}{2}(F^a)^2 \ , \quad a = 0,\ldots,3 \ .$$

We will choose:

$$F^o = -\partial_\mu A_\mu$$
$$F^i = -\partial_\mu W^i_\mu + M\phi^i \qquad i = 1,2$$
$$F^3 = -\partial_\mu W^o_\mu + \frac{M}{c_\theta}\phi^3 \ .$$

Next the Faddeev-Popov ghost Lagrangian is to be constructed. It is obtained by subjecting the F to an infinitesimal $SU_2 \times U_1$ transformation generated by infinitesimal parameters ρ_0, ρ_1, ρ_2 and ρ_3. To first approximation one will have:

$$F^a \to F^a + M^{ab}\rho_b \ .$$

The Faddeev-Popov Lagrangian is then

$$\mathscr{L}_{FP} = \bar{X}^a M^{ab} X^b$$

where $X^o \ldots X^3$ are four ghost fields with the wrong statistics, meaning that a minus sign must be given for every closed X loop in a Feynman diagram.

Instead of $X^o \ldots X^3$ we will use X^+, X^-, Y^o and Y^a:

$$X^3 = c_\theta Y^o + s_\theta Y^A$$
$$X^o = -s_\theta Y^o + c_\theta Y^A$$
$$X^1 = \frac{1}{\sqrt{2}}(X^+ + X^-)$$
$$X^2 = \frac{i}{\sqrt{2}}(X^+ - X^-) \ .$$

10. The Complete Lagrangian

The complete Lagrangian is the sum of all previously described parts.

$$\mathscr{L}_{tot} = \mathscr{L}_W + \mathscr{L}_H + \mathscr{L}_{gf} + \mathscr{L}_f + \mathscr{L}_{fH} + \mathscr{L}_{FP}$$

$\mathscr{L}_W$, $\mathscr{L}_H$ and $\mathscr{L}_{gf}$ were discussed in Sections 4, 7 and 9. (n.b., $\alpha = \frac{m_H^2}{4M^2}$)

$$\begin{aligned}
\mathscr{L}_W + \mathscr{L}_H + \mathscr{L}_{gf} = & -\partial_\nu W_\mu^+ \partial_\nu W_\mu^- - M^2 W_\mu^+ W_\mu^- - \tfrac{1}{2}(\partial_\nu W_\mu^o)^2 - \tfrac{1}{2}\frac{M^2}{c_\theta^2} W_\mu^o W_\mu^o - \tfrac{1}{2}(\partial_\nu A_\mu)^2 \\
& -\partial_\mu \phi^+ \partial_\mu \phi^- - M^2 \phi^+ \phi^- - \tfrac{1}{2}(\partial_\mu \phi^o)^2 - \tfrac{1}{2}\frac{M^2}{c_\theta^2}\phi^o\phi^o \\
& - \tfrac{1}{2}(\partial_\mu H)^2 - \tfrac{1}{2} m_H^2 H^2 \\
& -\beta\left\{\frac{2M^2}{g^2} + \frac{2M}{g} H + \tfrac{1}{2}(H^2 + (\phi^o)^2 + 2\phi^+\phi^-)\right\} + \frac{2M^4\alpha}{g^2} \\
& -igc_\theta[\partial_\nu W_\mu^o (W_\mu^+ W_\nu^- - W_\mu^- W_\nu^+) - W_\nu^o (W_\mu^+ \partial_\nu W_\mu^- - W_\mu^- \partial_\nu W_\mu^+) \\
& \qquad + W_\mu^o (W_\nu^+ \partial_\nu W_\mu^- - W_\nu^- \partial_\nu W_\mu^+)] \\
& -igs_\theta[\partial_\nu A_\mu (W_\mu^+ W_\nu^- - W_\mu^- W_\nu^+) - A_\nu (W_\mu^+ \partial_\nu W_\mu^- - W_\mu^- \partial_\nu W_\mu^+) \\
& \qquad + A_\mu (W_\nu^+ \partial_\nu W_\mu^- - W_\nu^- \partial_\nu W_\mu^+)] \\
& - \tfrac{1}{2} g^2 W_\mu^+ W_\mu^- W_\nu^+ W_\nu^- + \tfrac{1}{2} g^2 W_\mu^+ W_\nu^- W_\mu^+ W_\nu^- \\
& + g^2 c_\theta^2 (W_\mu^o W_\mu^+ W_\nu^o W_\nu^- - W_\mu^o W_\mu^o W_\nu^+ W_\nu^-) \\
& + g^2 s_\theta^2 (A_\mu W_\mu^+ A_\nu W_\nu^- - A_\mu A_\mu W_\nu^+ W_\nu^-) \\
& + g^2 s_\theta c_\theta \left\{A_\mu W_\nu^o (W_\mu^+ W_\nu^- + W_\nu^+ W_\mu^-) - 2A_\mu W_\mu^o W_\nu^+ W_\nu^-\right\}
\end{aligned}$$

$$\begin{aligned}
& - \alpha g M\left\{H^3 + H(\phi^o)^2 + 2H\phi^+\phi^-\right\} \\
& - \tfrac{1}{8} g^2 \alpha\left\{H^4 + (\phi^o)^4 + 4\phi^+\phi^-\phi^+\phi^- + 4(\phi^o)^2\phi^+\phi^- \right. \\
& \qquad \left. + 4H^2\phi^+\phi^- + 2(\phi^o)^2 H^2\right\} \\
& - gMW_\mu^+ W_\mu^- H - \tfrac{1}{2} g \frac{M}{c_\theta^2} W_\mu^o W_\mu^o H \\
& - \tfrac{1}{2} ig\left\{W_\mu^+(\phi^o \partial_\mu \phi^- - \phi^- \partial_\mu \phi^o) - W_\mu^-(\phi^o \partial_\mu \phi^+ - \phi^+ \partial_\mu \phi^o)\right\} \\
& + \tfrac{1}{2} g\left\{W_\mu^+(H\partial_\mu \phi^- - \phi^- \partial_\mu H) + W_\mu^-(H\partial_\mu \phi^+ - \phi^+ \partial_\mu H)\right\} \\
& + \tfrac{1}{2} g \frac{1}{c_\theta} W_\mu^o (H\partial_\mu \phi^o - \phi^o \partial_\mu H) \\
& - ig \frac{s_\theta^2}{c_\theta} M W_\mu^o (W_\mu^+ \phi^- - W_\mu^- \phi^+) + igs_\theta M A_\mu (W_\mu^+ \phi^- - W_\mu^- \phi^+) \\
& - ig \frac{1-2c_\theta^2}{2c_\theta} W_\mu^o (\phi^+ \partial_\mu \phi^- - \phi^- \partial_\mu \phi^+) + igs_\theta A_\mu (\phi^+ \partial_\mu \phi^- - \phi^- \partial_\mu \phi^+) \\
& - \tfrac{1}{4} g^2 W_\mu^+ W_\mu^-\left\{H^2 + (\phi^o)^2 + 2\phi^+\phi^-\right\} \\
& - \tfrac{1}{8} g^2 \frac{1}{c_\theta^2} W_\mu^o W_\mu^o\left\{H^2 + (\phi^o)^2 + 2(2s_\theta^2 - 1)^2 \phi^+\phi^-\right\} \\
& - g^2 s_\theta^2 A_\mu A_\mu \phi^+\phi^- \\
& - \tfrac{1}{2} g^2 \frac{s_\theta^2}{c_\theta} W_\mu^o \phi^o (W_\mu^+ \phi^- + W_\mu^- \phi^+) \\
& - \tfrac{1}{2} ig^2 \frac{s_\theta^2}{c_\theta} W_\mu^o H (W_\mu^+ \phi^- - W_\mu^- \phi^+) \\
& + \tfrac{1}{2} g^2 s_\theta A_\mu \phi^o (W_\mu^+ \phi^- + W_\mu^- \phi^+) \\
& + \tfrac{1}{2} ig^2 s_\theta A_\mu H (W_\mu^+ \phi^- - W_\mu^- \phi^+) \\
& - g^2 \frac{s_\theta}{c_\theta} (2c_\theta^2 - 1) W_\mu^o A_\mu \phi^+\phi^- \quad .
\end{aligned}$$

The fermion Lagrangian contains 3 lepton generations (e,μ,τ) and three quark generations. We assume zero neutrino mass, and label generations with an index α, β..., and colors with the index i:

$$\begin{aligned}
\mathscr{L}_f = & -\bar{e}^\alpha(\not{\partial} + m_e^\alpha)e - \bar{\nu}^\alpha \not{\partial} \nu^\alpha \\
& - \bar{u}_i^\alpha(\not{\partial} + m_u^\alpha)u_i^\alpha - \bar{d}_i^\alpha(\not{\partial} + m_d^\alpha)d_i^\alpha \\
& + igs_\theta A_\mu\left\{-(\bar{e}^\alpha\gamma^\mu e^\alpha) + \tfrac{2}{3}(\bar{u}_i^\alpha\gamma^\mu u_i^\alpha) - \tfrac{1}{3}(\bar{d}_i^\alpha\gamma^\mu d_i^\alpha)\right\} \\
& + \frac{ig}{4c_\theta} W_\mu^o\left\{(\bar{\nu}^\alpha\gamma^\mu(1+\gamma^5)\nu^\alpha) + (\bar{e}^\alpha\gamma^\mu(4s_\theta^2-1-\gamma^5)e^\alpha)\right. \\
& \qquad \left. + (\bar{d}_i^\alpha\gamma^\mu(\tfrac{4}{3}s_\theta^2-1-\gamma^5)d_i^\alpha) + (\bar{u}_i^\alpha\gamma^\mu(1-\tfrac{8}{3}s_\theta^2+\gamma^5)u_i^\alpha)\right\} \\
& + \frac{ig}{2\sqrt{2}} W_\mu^+\left\{(\bar{\nu}^\alpha\gamma^\mu(1+\gamma^5)e^\alpha) + (\bar{u}_i^\alpha\gamma^\mu(1+\gamma^5)C_{\alpha\beta}\bar{d}_i^\beta)\right\} \\
& + \frac{ig}{2\sqrt{2}} W_\mu^-\left\{(\bar{e}^\alpha\gamma^\mu(1+\gamma^5)\nu^\alpha) + (\bar{d}_i^\alpha C^{-1}_{\alpha\beta}\gamma^\mu(1+\gamma^5)u_i^\beta)\right\}
\end{aligned}$$

$$\begin{aligned}
\mathscr{L}_{fH} = & -\frac{i}{2\sqrt{2}} g \frac{m_e^\alpha}{M}\phi^+(\bar{\nu}^\alpha(1-\gamma^5)e^\alpha) \\
& + \frac{i}{2\sqrt{2}} g \frac{m_e^\alpha}{M}\phi^-(\bar{e}^\alpha(1+\gamma^5)\nu^\alpha) \\
& - \tfrac{1}{2} g \frac{m_e^\alpha}{M}(\bar{e}^\alpha e^\alpha)H - \frac{i}{2} g \frac{m_e^\alpha}{M}(\bar{e}^\alpha\gamma^5 e^\alpha)\phi^o \\
& - \frac{i}{2\sqrt{2}} g \frac{m_d^\beta}{M}\phi^+(\bar{u}_i^\alpha C_{\alpha\beta}(1-\gamma^5)d_i^\beta) \\
& + \frac{i}{2\sqrt{2}} g \frac{m_u^\alpha}{M}\phi^+(\bar{u}_i^\alpha C_{\alpha\beta}(1+\gamma^5)d_i^\beta) \\
& + \frac{i}{2\sqrt{2}} g \frac{m_d^\alpha}{M}\phi^-(\bar{d}_i^\alpha C^\dagger_{\alpha\beta}(1+\gamma^5)u_i^\beta) \\
& - \frac{i}{2\sqrt{2}} g \frac{m_u^\beta}{M}\phi^-(\bar{d}_i^\alpha C^+_{\alpha\beta}(1-\gamma^5)u_i^\beta) \\
& - \tfrac{1}{2} g \frac{m_u^\alpha}{M}(\bar{u}_i^\alpha u_i^\alpha)H - \tfrac{1}{2} g \frac{m_d^\alpha}{M}(\bar{d}_i^\alpha d_i^\alpha)H \\
& - \frac{i}{2} g \frac{m_d^\alpha}{M}(\bar{d}_i^\alpha\gamma^5 d_i^\alpha)\phi^o + \frac{i}{2} g \frac{m_u^\alpha}{M}(\bar{u}_i^\alpha\gamma^5 u_i^\alpha)\phi^o
\end{aligned}$$

$$\begin{aligned}
\mathscr{L}_{FP} = & \bar{X}^+\partial^2 X^- - M^2\bar{X}^+X^- + \bar{X}^-\partial^2 X^- - M^2\bar{X}^-X^- + \bar{Y}^o\partial^2 Y^o - \frac{M^2}{c_\theta^2}\bar{Y}^oY^o + \bar{Y}^A\partial^2 Y^A \\
& -igs_\theta W_\mu^+(\partial_\mu\bar{X}^+Y^A - \partial_\mu\bar{Y}^AX^-) + igc_\theta W_\mu^+(\partial_\mu\bar{Y}^oX^- - \partial_\mu\bar{X}^+Y^o) \\
& -igs_\theta W_\mu^-(\partial_\mu\bar{Y}^AX^+ - \partial_\mu\bar{X}^-Y^A) + igc_\theta W_\mu^-(\partial_\mu\bar{X}^-Y^o - \partial_\mu\bar{Y}^oX^+) \\
& -igs_\theta A_\mu(\partial_\mu\bar{X}^-X^- - \partial_\mu\bar{X}^+X^+) - igc_\theta W_\mu^o(\partial_\mu\bar{X}^-X^- - \partial_\mu\bar{X}^+X^+) \\
& -\tfrac{1}{2} gM(\bar{X}^+X^+H + \bar{X}^-X^-H + \frac{1}{c_\theta^2}\bar{Y}^oY^oH) \\
& + ig\frac{(1-2c_\theta^2)}{2c_\theta}M(\bar{X}^+Y^o\phi^+ - \bar{X}^-Y^o\phi^-) + ig\frac{M}{2c_\theta}(\bar{Y}^oX^-\phi^+ - \bar{Y}^oX^+\phi^-) \\
& -igs_\theta M(\bar{X}^+Y^A\phi^+ - \bar{X}^-Y^A\phi^-) - ig\frac{M}{2}(\bar{X}^-X^-\phi^o - \bar{X}^+X^+\phi^o) \ .
\end{aligned}$$

11. Discussion of the Lagrangian

The Lagrangian written down represents a large amount of experimental data. If we take the mass of the vector boson as energy scale, then all of the data are at very low energy.

Further, in constructing the Lagrangian, certain choices have been made. For instance, not having any direct information on the Higgs system, we have employed the simplest choice that covers our needs, namely an SU_2 doublet. This could be used to generate both vector boson and fermion masses. Other choices for the Higgs system lead to differences that are usually not observable at low energies, with one exception, namely the ratio of charged and neutral vector boson mass. In the quoted Lagrangian this ratio is equal to $\cos\theta_W$. If one allows also a Higgs triplet then the ratio depends on the choice of parameters in the Higgs sector, and may vary from 0 to $\cos\theta_W/\sqrt{2}$. This ratio may be changed by complicating this Higgs sector, but this is at the price of new hypothetical scalar particles.[5]

Experimentally one observes that the ratio is very close to $\cos\theta_W$. We will elevate this observation to an assumption: for calculations at low energy one may assume the simplest Higgs system, and we call this the Higgs $\Delta I = \frac{1}{2}$ rule.

It is a very difficult question to establish what is and what is not tested in this model. To a large extent this depends on one's cynicism with respect to the theory. For instance, at this time no top quark has been observed, and we do not know if the b quark is part of an SU_2 doublet. Also, it is quite possible to modify the vector boson structure without changing the low energy behaviour. We will know for sure only as soon as the vector bosons have been observed.

The situation with respect to the Higgs sector is even more obscure. The difference is that even in this simplest model the Higgs mass remains a free parameter. Moreover, there are theoretical suspicions with respect to the Higgs system.

Now it must be understood that the standard model is a system that, unlike the four-fermion theory, needs no cut-off. It is conceivable that this model describes physics up to 10^{19} GeV, the threshold where gravitation becomes important. In this sense it is a much better theory than the four-fermion theory. This fact is a consequence of the renormalizablility of the standard model.

There is however another aspect of the present situation. While the standard model is internally consistent, it nevertheless leaves many things unexplained. For instance, we may remember that the U_1 coupling for the various multiplets entered as a completely free parameter. Why should this coupling arrange itself such that the neutrino has zero charge? and so that the electromagnetic interactions conserve parity? In other words, the unification of weak and electromagnetic interactions is really a very superficial one in this model. All the time one must adapt parameters to the observed properties. In this respect grand unified theories represent progress, although a certain amount of arbitrariness remains.

The question of the observed fermion spectrum remains largely unanswered. Why are there three, or more, generations? Why do they have the particular $SU_2 \times U_1$ multiplet assignment as observed? Are the masses arbitrary parameters?, etc., etc.

In the remainder of these notes we will study some of these questions. The tools that we use are the radiative corrections in the standard model. The following results can be obtained

(i) There is a limit on new, as yet not observed generations.

(ii) The screening theorem: even if the Higgs mass is very large, which implies that the Higgs has strong interactions, no significant effects can be seen at low energies.

The screening theorem opens the door for all kinds of speculations on the Higgs system. To this author it is very plausible that the Higgs particle is really not a fundamental particle, but may be a bound state, or may be not even that but a system of new strong interactions. In itself, the idea that the Higgs is composite was advanced already some time ago[6]; through the screening theorem this idea gains credibility. We want to go further, and allow for the possibility that there is not even a well defined particle corresponding to the physical Higgs particle in the standard model.

12. Calculation of Radiative Corrections

In view of the complexity of the Lagrangian it is in general a considerable task to compute radiative corrections. However, for the two points cited the effort needed is rather small. Mainly one must first have a clear understanding of the renormalization procedure, after which the calculations are simple.

As in quantum electrodynamics, also in the standard model, infinities appear in the process of calculating radiative corrections. Therefore one must have a regularization scheme, that is a calculational scheme where everything is finite and where the actual model can be obtained by taking some limit. Thus we will introduce a parameter Δ, and the standard model obtains in the limit $\Delta \to \infty$. It is a property of renormalizable theories that the physical results are independent of Δ, and consequently the limit $\Delta \to \infty$ becomes trivial, at least insofar as experimentally observable results are concerned.

The standard model contains a number of parameters, and one must first have a number of data points such that the parameters can be fixed. Given the parameters new results can be computed and compared with experiment.

In the Lagrangian for the standard model we have as free parameters

- the coupling constant g
- the weak mixing angle θ_W
- the mass of the charged vector boson M
- the mass of the Higgs particle m_H

- the three angles θ_1, θ_2 and θ_3 in the generalized Cabibbo matrix as well as a phase angle δ
- the masses of the quarks and leptons.

Not all data points will be equally sensitive to all these parameters. For example, without neutral current experiments it would be very hard to determine θ_W to any precision. For the moment we will concentrate on the first four parameters.

Thus let g, θ_W, M and m_H denote the four parameters occurring in the Lagrangian. Comparison with the data points (four numbers, $d_1,\ldots,d_4$) fixes these parameters, for a given choice of Δ. Thus, for example:

$$g = g(d_1,d_2,d_3,d_4,\Delta) \ .$$

Having established g, θ_W, etc., we can now compute other experimentally observable effects. In these computations one must use the same Δ. But the final result will be independent of Δ provided the same Δ is used in fixing the parameters and in producing the new results.

A very simple example, with interesting physics consequences, will now be considered. Consider the standard model, as given before. This includes the Higgs $\Delta I = \frac{1}{2}$ assumption. Let us assume that all one-loop corrections have been computed. Let us furthermore assume that the following data points are used in determining the parameters g, $\sin^2\theta$ and M:

- μ decay
- the electric charge (e-μ scattering at zero momentum transfer)
- the ratio of $\bar{\nu}_\mu e$ to $\nu_\mu e$ total cross sections.

Of course, also the masses of electron, muon, etc., are used as input.

As experimentally testable consequence we will take the $\nu_\mu e$ total cross section.

Imagine the calculation has been done (actually, it has been done, see Ref. 7). We now pose the following question: imagine that there exists a new generation of quarks and leptons, with large masses, except for a **massless** neutrino. What would be the consequence of this new generation to the $\nu_\mu e$ prediction?

To find the result we must compute the influence of this new generation on all four processes mentioned above. Now it happens that the only way that such new fermions can contribute is through self-energy insertions in the vector boson propagators. Roughly speaking such diagrams produce radiative corrections to the vector boson masses, and these corrections violate the rule $M_0 = M/c_\theta$. In lowest order the three data points mentioned are independent of the mass of the neutral vector boson. The computed number (the $\nu_\mu e$ cross section) depends on this mass M_0, and the measurement is a test for the rule mentioned. And the new leptons and quarks produce deviations of this rule, so that experimental results give us information on these new particles.

The calculational work involved amounts to computing the contribution of vector boson self-energy graphs involving these new particles. Let us restrict ourselves to the new lepton doublet, ℓ and ν_ℓ. The following graphs need to be computed (see Fig. 5).

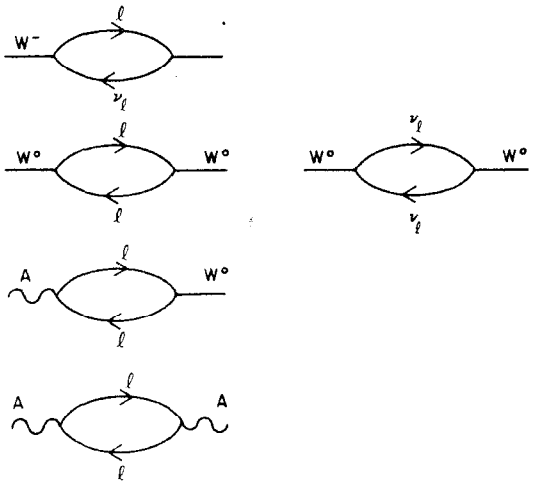

Figure 5

The calculation simplifies even further if we realize that we need the results only at low energy. In most cases, with the exception of photon self-energy diagrams, one can straight away set the external momentum to zero.

The actual calculation has been written down in great detail elsewhere.[8] The result is rather plausible. Denote the contribution of the W^+ and W^0 self-energy diagrams by A^+ and A^0. Then the prediction for the $\nu_\mu e$ total cross section is modified by a factor

$$\left(\frac{1}{1-8G_F\delta}\right)^2 \qquad \delta = \frac{1}{(2\pi)^4 ig^2}\,(A^0 c_\theta^2 - A^+) \quad . \tag{12.1}$$

Thus insofar as the correction follows the Higgs $\Delta I = \frac{1}{2}$ rule it is invisible. To give an idea of the quantities A^+ and A^0 we quote the expression for A^+. Consider the expression:

$$g^2\int d_4q\,\frac{Tr\{\gamma^\mu(1+\gamma^5)(-i\gamma q+m)\gamma^\nu(1+\gamma^5)(-i\gamma q)\}}{(q^2+m)q^2} = g^2\int d_4q\,\frac{2\{-8q_\mu q_\nu + 4\delta_{\mu\nu}q^2\}}{(q^2+m^2)q^2}$$

$$= g^2\left\{-16B_{22}(0,m,0) + 8A(m)\right\}\delta_{\mu\nu} \quad .$$

The coefficient of $\delta_{\mu\nu}$ is the desired function A^+. We introduced the standard functions B_{22} and A defined by:

$$\int d_4q\,\frac{1}{q^2+m^2} = A(m^2) \tag{12.2}$$

$$\int d_4q\,\frac{q_\mu q_\nu}{(q^2+m_1^2)((q+k)^2+m_2^2)} = B_{21}(k,m_1,m_2)k_\mu k_\nu + B_{22}(k,m_1,m_2)\delta_{\mu\nu} \quad .$$

Working out the expressions for A^+ and A^0 one finds for δ:

$$\delta = \frac{m^2}{64\pi^2} \quad . \tag{12.3}$$

The correction is:

$$\left(\frac{1}{1-8G_F\delta}\right)^2 \simeq 1 + G_F\frac{m^2}{4\pi^2} \quad .$$

Thus the correction grows like the square of the lepton mass. Comparison with the experimental data leads to the constraint $m < 300$ GeV.

It seems that the pattern of new generations cannot continue much further, or else we would have seen this in neutral current cross sections as deviations from the standard model.

For completeness we note that in the general case the observed correction grows proportionally with the square of the mass differences in the new SU_2 multiplets. Thus new generations in which all masses would be about the same (including the neutrino mass) are not constrained by the present data.

13. The Screening Theorem[9]

We now focus attention on the Higgs system. The first question that arises is this: do we have any objective indication that it is there? Or stated differently: is there an upper limit to the Higgs mass from experimental data?

To a large extent this question is the same one as discussed in the 4-fermion theory, Section 2. From experiment an upper limit on Λ, the cut-off, could be established from low energy data (the equalness of the coupling constants of μ decay and neutron decay).

Here we have the following. Without the Higgs boson the theory is non-renormalizable. That is like the 4-fermion theory. The Higgs boson with finite mass is the equivalent of our Λ cut-off with finite Λ in the 4-fermion theory.

Thus in the limit of large Higgs mass there is a unitarity limit. This limit is actually around 1 TeV. Thus if there exists no Higgs then the theory becomes a strong interaction theory above 1 TeV. This is another way of stating that the radiative corrections are of the same order of magnitude as the lowest order results for energies above 1 TeV.

However, nothing is known at 1 TeV. For all we know there is no Higgs boson, but as an alternative strong interactions. If there is a Higgs boson with mass below 1 TeV then there is no unitarity problem, and no strong interactions are indicated.

The great problem is this: if there is no Higgs, would we note anything at low energies? We thus are led to study radiative corrections at low energies as a function of the Higgs mass. The question is if

there are big corrections in the limit $m_H \to \infty$. We will consider here the most likely candidate for such corrections, namely the mass ratio $M/M_0 = c_\theta$.

We must go again through the whole procedure outlined before, and establish Higgs dependence in the relation between data points and parameters in the Lagrangian. After that we can establish Higgs dependence in some experimentally verifiable number.

In inspecting the Lagrangian of the standard model we observe that the Higgs H is not coupled to neutrinos, and that the coupling to electrons and muons is suppressed by a factor m_e/M or m_μ/M, which are of order 10^{-5} resp. 10^{-3}. We can safely ignore the Higgs-fermion couplings. So now we are back to a situation similar to that of the previous section: we need to consider only vector boson self-energy diagrams. Given that the external lines may be either a W^- or W^o the relevant diagrams are given in Fig. 6.

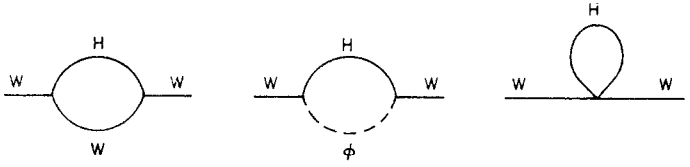

Figure 6

Besides, Higgs mass dependent contributions could come through tadpole type diagrams, Fig. 7.

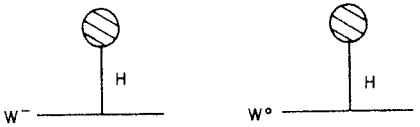

Figure 7

Some example of tadpole diagrams are given in Fig. 8.

Figure 8

The diagrams of Fig. 8 derive from HHW^o and H^3 terms in the Lagrangian. The contribution of these tadpoles to the masses derives from the W^-W^+H and W^oW^oH terms. But if we look to these latter terms we see that they have coefficients that are in the same ratio as the mass terms:

Mass terms: $$-M^2 W^+_\mu W^-_\mu - \tfrac{1}{2} \frac{M^2}{c^2_\theta} W^o_\mu W^o_\mu$$

WWH terms: $$-gMW^+_\mu W^-_\mu H - \tfrac{1}{2} g \frac{M}{c^2_\theta} W^o_\mu W^o_\mu H \quad .$$

For this reason the tadpole terms do not lead to any deviation from the rule $M/M_0 = c_\theta$.

Another contribution is the third diagram of Fig. 6. This derives from the terms of the type W^+W^-HH and W^oW^oHH. These are:

$$-\frac{1}{4}\,g^2 W^+_\mu W^-_\mu H^2 - \frac{1}{8}\,g^2\,\frac{1}{c_\theta^2}\,W^o_\mu W^o_\mu H^2 \quad .$$

Again no deviation from the mass rule results. The contributions of the other diagrams must be computed, but that is an easy matter. Again, there is a contribution δ to an observable effect in $\sigma_{\nu e}$ scattering (see Eq. (12.1)), where now A^o and A^+ refer to contributions of the two first diagrams of Fig. 6. Now one finds:

$$A^o = g^2\,\frac{M^2}{4c_\theta}\,B_0(0,m_H,M_0) + g^2\,\frac{1}{2c_\theta}\,B_{22}(0,M_0,m_H)$$

$$A^+ = g^2M^2B_0(0,m_H,M) + g^2B_{22}(0,M,m_H) \quad .$$

Working this out one finds the contribution to δ:

$$\delta \to \delta - \frac{3}{64\pi^2}\,M^2\,\frac{s_\theta^2}{c_\theta^2}\,\ell n\, m_H^2 \quad .$$

All m_H independent terms, or terms becoming small for large Higgs mass, have been dropped.

The important point is that there is no contribution to δ proportional to m_H^2. The dependence is only logarithmic, and even for m_H = 3 TeV the effect is only 0.8% on $\sigma_{\nu e}$. For an effect of 2% a mass of about 700 TeV is required. These calculations are relative to $m_H^2 = M^2$.

This insensitivity to the Higgs mass is called the screening theorem. The effect persists also in other situations: the dependence on the Higgs mass is very weak and not visible at low energies even for very large Higgs mass.

The conclusion is this: if the Higgs mass becomes very large there will be new strong interactions in the TeV region. This follows because of the unitarity limit. But there is no substantial effect at low energies. In other words, because of the screening theorem it is quite possible that there are new strong interactions at the TeV level without this being visible at low energies.

Various authors, in particular Susskind and collaborators, have made models and conjectures concerning these possible new interactions. In these models an analogy with the usual strong interactions, quantum chromodynamics, is often made, and the new strong interactions are termed technicolor. The subject is quite open, and will not be discussed any further here.

14. Other Radiative Corrections

Various other radiative corrections have been computed, and the most interesting of these is the calculation of the corrections to the masses of the neutral and charged vector boson. In the spirit of the previous discussion the mass of the neutral vector boson is defined as the location of the resonance in e^+e^- annihilation. This must not be identified with the value of the parameter M, or $M_0 = M/c_0$ in the Lagrangian. It is simply another observable number.

With $s_\theta^2 = 0.238$ the lowest order calculation gives the values 76.5 and 87.6 GeV for M and M_0. Including radiative corrections the values shift by + 2.0 and 2.5 GeV.[10,11] These values differ from those quoted in Ref. 10 due to a calculational error in Ref. 7.* The results of Ref. 7, being part of the total, and quoted as 120 and 140 MeV, are in fact -940 and -690 MeV.

References to other calculations are given in Ref. 7 and 10. Similar calculations have also been done by Sirlin and Marciano, see Ref. 12.

* There is a sign error in the equation for F_1, Section 5. Instead of $-\frac{1}{2} k^2$ one must have $+ \frac{1}{2} k^2$.

References

1. For references on this and related subjects, see R. Marshak, Riazuddin and C. Ryan, Theory of Weak Interactions in Particle Physics, Wiley, New York (1969).
2. M. Veltman, Varenna lectures (1977).
3. J. Bjorken, Phys. Rev. D19 (1979) 335; Proc. Moriond Conference (1978); International Conference on Neutrinos, Bergen (1979). A. Haatuft and C. Jarlskog, editors. Contributions by J. Sakurai, P. Langacker and M. Roos.
4. S. Bludman, Il Nuovo Cim. 9 (1958) 433; S. Glashow, Nucl. Phys. 22 (1961) 579; S. Weinberg, disc. remark at 1967 Solvay conference, talk of H. P. Durr; Phys. Rev. Lett 19 (1967) 1264. S. Glashow, J. Iliopoulos and L. Maiani, Phys. Rev. D2 (1970) 1285. C. Bouchiat, J. Iliopoulos and Ph. Meyer, Phys. Lett. 42B (1972) 91.
5. D. Ross and M. Veltman, Nucl. Phys. B95 (1975) 135.
6. R. Jackiw and K. Johnson, Phys. Rev. D8 (1973) 2386. J. M. Cornwall and R. Norton, Phys. Rev. D8 (1973) 3338.
7. M. Green and M. Veltman, Nucl. Phys. 169B, Erratum, Volume 173B.
8. M. Veltman, Nucl. Phys. B123 (1977) 89; Cargese lectures 1979. M. Chanowitz, M. Furman, I. Hinchliffe, Phys. Lett. 78B (1978) 285.
9. M. Veltman, Acta Phys. Pol. B8 (1977) 475; Phys. Lett. 70B (1977) 253. T. Appelquist and R. Shankar, Nucl. Phys. B158 (1979) 317.
10. M. Veltman, Phys. Lett. 91B (1980) 95.
11. F. Antonelli, M. Consoli and G. Corbo, Phys. Lett 91B (1980) 98.
12. W. Marciano, Phys. Rev. D20 (1979) 1274; A. Sirlin, Preprint Inst. Adv. Study, Princeton, March (1980). W. Marciano and A. Sirlin, Rockefeller University preprint, July (1980).

NEUTRINOS AND NEUTRINO INTERACTIONS

Frank Sciulli
California Institute of Technology
Pasadena, California

Contents:

INTRODUCTION - THE FORCES

My charge is to summarize the world of neutrino physics in three lectures. This is a broad charge, which cannot possibly be accomplished in so short a time. I will attempt to cover a few topics that are most interesting to me. My apologies to those who feel that some important topics have not been adequately discussed. Much of the current situation will be discussed in the topical conference next week. I will try to place some of that information in context without upstaging the speakers by overly anticipating their results. We begin today with a review of our knowledge of the interactions that produce the neutrinos and through which they are influenced. Following this is a brief discussion on the nature of the neutrinos themselves.

The common garden-variety neutrino that has been in the physics consciousness for the longest time is the electron neutrino. The second type, the muon neutrino, ν_μ, has been studied for almost twenty years. There is a likely new arrival in the past few years, the tau neutrino, ν_τ. As far as we know all of these neutrinos interact through a V-A charged current and a Weinberg-Salaam-Ward neutral current. Fig. 1 shows the diagram representing the standard picture of muon decay, $\mu^+ \to e^+ + \nu_e + \bar{\nu}_\mu$, in which the muon emits a muon-neutrino and a virtual intermediate vector boson of high mass, which in turn quickly transforms to a lepton pair (electron and electron-neutrino).

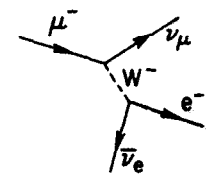

Fig. 1: Decay of the muon pictured as occurring through the action of a high mass virtual intermediate boson.

An extremely important question, even (or especially) in this time of strong theoretical predispositions, is "How well-verified is this V-A picture of the charged-current weak interactions?" We are now strongly enmeshed in prejudice, mainly formed by precedent, that forces are carried by spin-one particles, and therefore that couplings between spin-1/2 particles are vector or axial-vector in nature. The best precedent for this is that lone force-carrier which has actually been observed in isolation from matter: the spin-1 photon. All evidence is consistent with electromagnetic theory being a parity-conserving vector theory up to corrections that arise from neutral current effects. The weak neutral current itself is very likely a combination of vector and axial-vector, although the tests are not so strong as those involving the electromagnetic and weak charged-currents. The V,A nature of the weak charged current is seen in many processes. Perhaps the best verification of its nature comes from the decay of the charged pion.

$$\pi^+ \rightarrow \mu^+ + \nu_\mu \qquad (1)$$

Here the charged pion, which has $J^P = 0^-$ disappears into the 0^+ vacuum, while a muon, muon-neutrino pair is created. This can happen through either a psuedo-scalar or axial vector current. As is well known, the vector propagators prefer the final-state leptons to have total angular momentum of one unit, while scalar propagators would allow the final state to have zero angular momentum, equal to that of the initial pion. This helicity suppression in the V,A case then gives a substantially lower rate that depends on the velocity of the emitted charged lepton. The predicted rates for pion decay into electron leptons and muon leptons differ by about four orders of magnitude for the two different assumptions: Psuedoscalar or Axial Vector. The latter is the only form consistent with experiment.[1] Hence, we know that the charged weak current is dominantly vector and axial-vector.

This experiment, indeed most weak interaction measurements, do not differentiate between V-A and V+A combinations. For V-A, neutrinos (antineutrinos) always have negative (positive) helicity; for V+A, the helicities are reversed. Therefore, the prediction for π-decay would be the same for any combination of V and A. As we shall see, there are two, and only two, experiments that tell us that the preferred combination is V-A.

The world of weak interactions as seen by us <u>is</u> dominantly V-A. Is this asymmetry an intrinsic part of the physical world, or is it just the piece that we observe with our limited view at low energies? Where is the V+A current that would restore some semblance of symmetry? With the discovery of the tau-lepton, it was conjectured that this new charged lepton and its (presumed) neutrino, ν_τ, might demonstrate the elusive V+A current. Fig. 2 shows the point-of-view one might take: the tau emits a ν_τ with a virtual weak boson at a

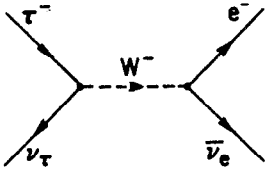

Figure 2: Decay of the τ. In the analysis described, the right vertex is assumed V-A. The composition of the left vertex is considered unknown.

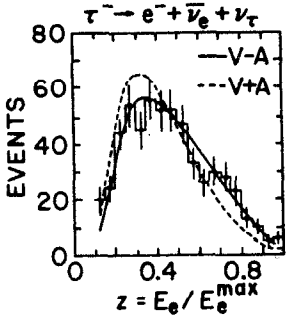

Figure 3: The electron spectrum from τ-decay. The curves are for the two extreme assumptions at the τ-vertex.

vertex that could be V-A, V+A, or a mixture. We presume that the boson will interact via V-A at the electron vertex (i.e., the boson is of the usual type). Fig. 3 shows the normalized electron spectrum of the decay of the τ.[2] It turns out that a combination with less than 80% V-A is unlikely. This rules out the V+A interaction as mediated through the same bosons that mediate the V-A interactions, at least in a simple way. At present energies all known neutrinos prefer, or interact most strongly through the V-A interaction.

The usual form for an effective Hamiltonian mediating the charged-current interaction is

$$H^{CC} = \frac{G}{\sqrt{2}} j_\lambda j_\lambda \quad \text{e.g. } j_\lambda{}^{(\mu)} = \bar{\mu}\gamma_\lambda(1+\gamma_5)\nu_\mu \qquad (3)$$

This explicitly shows the interaction as the product of two lepton currents. Suppose that there were another weak interaction that was opposite-handed, and of comparable dimensionless coupling as the V-A interaction. Its effect could be small as we observe it if the boson that carries the right-handed force were more massive than the usual left-handed boson. Effectively, the Fermi-constant for the right-handed case would be much smaller. In the usual picture the value of G_F for invariant 4-momentum transfers, Q^2, much smaller than the boson mass, M_-^2, is given by

$$G_F = \frac{g^2}{Q^2+M_-^2} \approx \frac{g^2}{M_-^2} \qquad (4)$$

where g is some dimensionless coupling of order the electromagnetic coupling, $\alpha = 1/137$. In a case where there exists a V+A boson which does not mix with the V-A boson, the effective Hamiltonian would be[3]

$$H^{cc} = \frac{G_F}{\sqrt{2}} j_\lambda j_\lambda + \frac{G_F'}{\sqrt{2}} j_\lambda' \; j_\lambda' \qquad (5)$$

where the primed currents are V+A, or $(1-\gamma_5)$, and the new Fermi constant, G_F', is given in terms of the new boson mass, M_+, as

$$G_F' \approx \frac{g^2}{M_+^2} \qquad (6)$$

If the right-handed boson were more massive than the left-handed boson the effect of the second term in (5) could be small.

EXPERIMENTS SENSITIVE TO V+A CHARGED CURRENTS

One of the two low energy experiments sensitive to right-handed currents is the measurement of electron helicity in nuclear β-decay. For example, in

$$Co^{60} \rightarrow Ni^{60} + e^- + \bar{\nu}_e \qquad (7)$$

the helicity is negative of magnitude $\beta = v/c$ if the interaction takes place through V-A currents. A small admixture of V+A, acting though the auspices of a heavier vector boson of mass, M_+, would give a helicity of magnitude

$$\frac{|h|}{\beta} \approx 1 - 2\left(\frac{M_-}{M_+}\right)^4 \qquad (8)$$

Fig. 4 shows the schematic of how such experiments are done.[4] The electrons from a source are analyzed by an electrostatic spectrometer in which the particle spin is rotated by a different amount than the momentum. Helicity information is obtained by scattering from a thin foil. The analyzing power can be calculated, and also can be calibrated using double scattering. Fig. 5 shows some experimental measurements[4,5] of helicity as a function of the particle velocity. The data are consistent with the straight-line relationship of unit slope.

The results of many such experiments over the years give an accuracy for this measurement

$$|h|/\beta = 1.0 \pm .012 \qquad (9)$$

which implies that, at the two standard deviation level

$$M_+/M_- > 3 \qquad (10)$$

So, for example, if the V-A boson were to have a mass of 80 GeV then this V+A boson would be heavier than about 240 GeV.

The second measurement directly sensitive to V+A currents is the asymmetry of electrons from polarized muon decay. These muons are the product of the pion decay. The electron angular distribution is given by

$$d\Gamma = K d\Omega \left[f_1(x) + \xi P \cos\theta \; f_2(x)\right] dx \qquad (11)$$

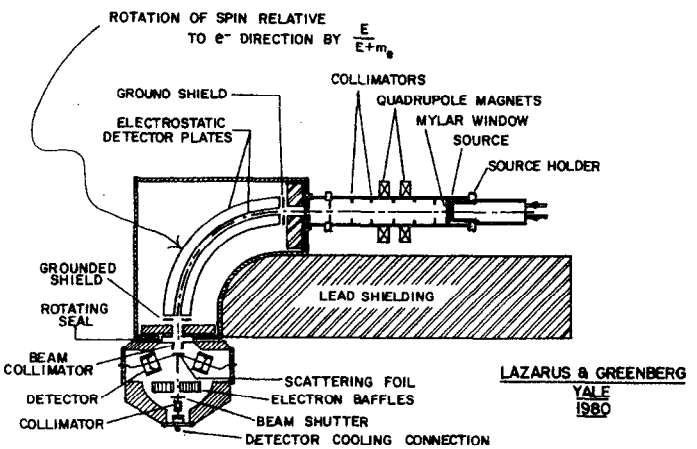

Figure 4: Longitudinally polarized electrons are bent through an electrostatic field to provide a large component of transverse polarization at the scattering foil. The electromagnetic scattering at the foil produces a detectable asymmetry. (See Ref. 4)

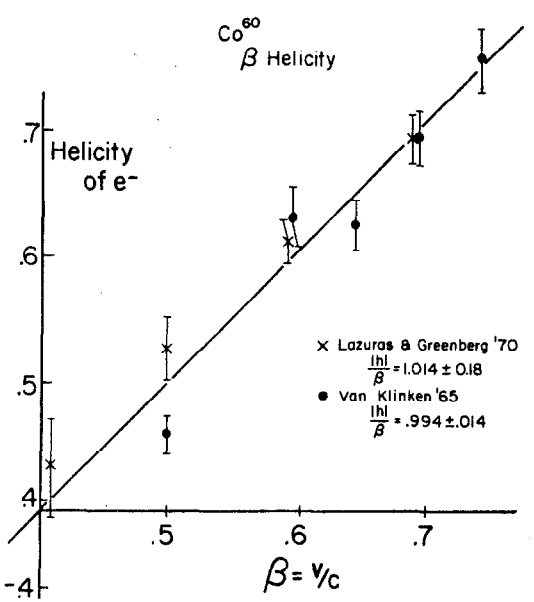

Figure 5: Results of measurements of β-helicity from two experiments (see refs. 4 and 5)

where the functions $f_1(x)$, $f_2(x)$ are known functions of $x=E_e/E_{max}$ and of the μ-decay parameters, η, ρ, δ, and include known first-order radiative corrections. The quantity ξ reflects the handedness character of the weak interaction underlying the muon decay, and is equal to one for pure V-A currents. The quantity, P, is the polarization of the muon, which reflects the handedness character of the pion decay products; it is 1 if V-A is the only operative current in that process. A V+A admixture shows in both factors. In this case, the product of the factors is given by

$$\xi P \approx 1-4\ (M_-/M_+)^4 \qquad (12)$$

Fig. 6 shows a schematic of an experiment[6] performed with emulsions to measure this fundamental number. A polarized muon beam is incident on an emulsion stack. As the muon is stopped, a very large magnetic field is applied whose purpose is to preserve the state of polarization until the muon decays. The asymmetry of electrons is then measured by scanning and analyzing the emulsion trajectories. Fig. 7 shows the angular distribution of decay electrons both along and opposite to the magnetic field direction. The experimenters conclude (2 standard deviations)

$$\xi P = .975 \pm .030 \qquad (13)$$

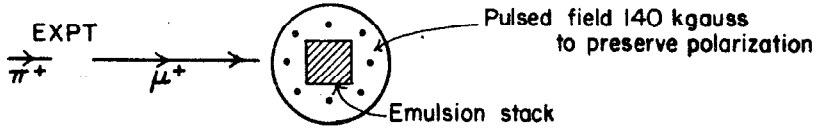

Figure 6: Measurement of electron asymmetry from polarized muon decay. The high magnetic field preserves the component of polarization along the field.

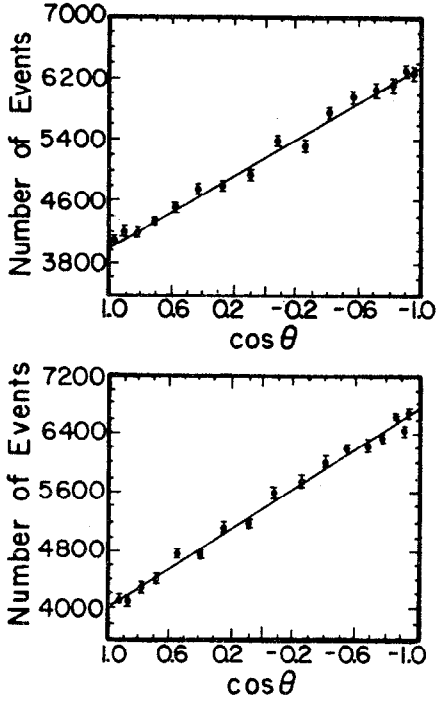

Figure 7: Distribution of decay electrons along and opposite to the magnetic field, respectively. (See Ref. 6)

which implies

$$M_+/M_- \gtrsim 3 \qquad (14)$$

giving the same restriction as that seen in the beta decay helicity experiments.

These are not very stringent limits. Indeed, some of the assumptions made in quoting these limits on right-handed boson mass may be questioned. For example, if the right-handed neutrinos coupled to this boson were somewhat heavier than present neutrinos, e.g., $M_{\nu_R} > 500$ MeV, then no evidence for the current could be seen in any experiment on the weak decays of particles or nuclei. We would also not have seen it in neutrino experiments, since we always begin with left-handed beam neutrinos. The experiments with electron and muon beams would not have observed it, because at present energies such interactions are overwhelmingly dominated by photon exchange. We look forward to experiments with beams of high energy electrons colliding with high energy protons, which will be able to extend the limits from decay experiments in any case, and will be sensitive to more general possibilities, like massive neutrinos.

Another logical possibility is that the coupling to quarks for right-handed currents is different from that of left-handed currents. For example, if the right handed interaction were to couple the quarks to a new set of more massive quarks, or if the coupling to present

quarks were substantially different than that of the V-A current, the sensitivity of these experiments would be at least dramatically reduced. One postulate is that the role of the Cabibbo angle in V-A could be reversed for V+A currents.[7] This would have the u-quark coupled in the V+A case by $\cos\theta_c$ to s-quark, and by $\sin\theta_c$ to d-quark. A sensitive test of this hypothesis would be a careful comparison of the muon helicities for $K \to \mu+\nu_\mu$ and $\pi \to \mu+\nu_\mu$. At present, the muon helicity from the kaon decay has only been measured at the 20% level.[8]

We conclude that the V-A interaction of the charged currents stands in good stead. It is probably correct at the few percent level or better. We can certainly use the Hamiltonian (3) as a tool to describe the neutrino-fermion charged current force in this energy region with little concern about its ultimate limitations.

EXPERIMENTS SENSITIVE TO NEUTRAL CURRENTS

Until the end of the last decade, it was thought that neutrinos only manifested themselves through charged current interactions. They were then predicted[9] to interact through a neutral current mechanism, and today that prediction (SU2xU1) stands as the theoretical framework that best describes them. There was no opportunity to see the neutral current in decay processes, because any decay which could occur through neutral weak currents would be overwhelmed at such low energies by electromagnetic decays. They were initially seen and studied in processes initiated by neutrinos: for example

$$\begin{aligned} \nu_\mu + N &\to \nu_\mu + X \\ \nu_\mu + e^- &\to \nu_\mu + e^- \\ \nu_\mu + p &\to \nu_\mu + p \end{aligned} \qquad (13)$$

The SU2xU1 current-current picture at present energies would describe these interactions by a Hamiltonian of a form that preserves the left-handed character of neutrinos; i.e.,

$$H^{nc} = \frac{G_F}{\sqrt{2}}\sqrt{\rho}\left[\bar{\nu}_\mu \gamma_\alpha(1+\gamma_5)\nu_\mu\right]\left[\bar{T}\gamma_\alpha(g_V^T+g_A^T\gamma_5)T\right] \qquad (14)$$

where the couplings, g_V^T and g_A^T depend on the quantum numbers of the target particle, T:

$$g_V^T = I_3^T - 2Q_E^T \sin^2\theta_w \qquad (15)$$

$$g_A^T = I_3^T$$

Here I_3^T and Q_E^T are the component of weak isospin and charge, respectively, of the target, T. θ_w, the Weinberg angle, is expected to be process and energy independent. In the Weinberg-Salam-Ward (WSW) model, the normalizer ρ equals 1 identically, and is proportional to the ratio of the vector-boson masses of charged and neutral currents. The general form for the cross sections of processes like (13), in which scattering occurs from a

free target whose mass is small compared to the incident neutrino energy, E, is

$$\frac{d\sigma}{dy} = \frac{G_F^2 M_T E}{2\pi}\left[(g_V+g_A)^2 + (g_V-g_A)^2(1-y)^2\right] \quad (16)$$

$$\frac{d\bar{\sigma}}{dy} = \frac{G_F^2 M_T E}{2\pi}\left[(g_V+g_A)^2(1-y)^2 + (g_V-g_A)^2\right] \quad (17)$$

Equation 16 refers to scattering of neutrinos from fermion targets or antineutrinos from antifermion targets; equation 17 refers to the other two possible cases. The first term in each equation is the V-A term; the second is the V+A term. Here the parameter, y, which we will discuss later at length, is related directly to the center-of-momentum scattering angle of the outgoing fermions:

$$1-y = \frac{1+\cos\theta^*}{2} \quad (19)$$

For the charged current case already discussed, we would have $g_V^T=g_A^T=1$, giving the standard formulas of charged-current scattering. (See Table V later.)

In the neutral current case, equation 15 gives for the couplings (with $\sin^2\theta_w=1/4$) the values shown in Table I. The process gives about equal amounts of V-A and V+A for scattering from electrons, but is dominantly V-A for scattering from nucleons. Table II shows a recent compilation of various ratios obtained in neutrino scattering experiments.[10] The best values of the parameters, ρ and θ_w, come from fitting these ratios in

TABLE I

$\sin^2\theta_w = 1/4$

Examples of Targets	I_3	Q_E	g_A	g_V	V-A g_V+g_A	V+A g_V-g_A
electron	-1/2	- 1	-1/2	0	-1/2	+ 1/2
quarks u,c	+1/2	+2/3	+1/2	+ 1/6	+2/3	- 1/3
quarks d,s	-1/2	-1/3	-1/2	-1/3	-5/6	+ 1/6

TABLE II

Reaction	Quantity Measured	Data ± 1σ		WSW prediction with $\rho = 1$ $\sin^2\theta_w = .232$
$\nu N \to \nu X$	R_ν	0.307 ± 0.008		0.305
		0.30 ± 0.04		0.325
		0.28 ± 0.03		0.304
$\bar{\nu} N \to \bar{\nu} X$	$R_{\bar{\nu}}$	0.373 ± 0.025		0.386
		0.33 ± 0.09		0.365
		0.35 ± 0.11		0.399
$\nu N \to \nu X$	g_L^2	0.32 ± 0.03		0.298
$\bar{\nu} N \to \bar{\nu} X$	g_R^2	0.04 ± 0.03		0.030
$\nu p \to \nu X$	R_ν^p	0.52 ± 0.06		0.448
		0.48 ± 0.17		0.414
$\bar{\nu} p \to \bar{\nu} X$	$R_{\bar{\nu}}^p$	0.42 ± 0.13		0.383
$\nu \frac{n}{p} \to \nu X$	$R_\nu^{n/p}$	1.22 ± 0.35		1.12
$\bar{\nu} \frac{n}{p} \to \bar{\nu} X$	$R_{\bar{\nu}}^{n/p}$	0.64 ± 0.18		0.935
$\nu N \to \nu \pi^{\pm} X$	$R_\nu^{+/-}$	0.77 ± 0.14		0.84
$\bar{\nu} N \to \bar{\nu} \pi^{\pm} X$	$R_{\bar{\nu}}^{+/-}$	1.65 ± 0.33		1.16
		$1.27 \; {}^{+0.36}_{-0.27}$		1.01
$\nu_\mu e \to \nu_\mu e$	σ/E	$2.4 \; {}^{+1.2}_{-0.9}$	(a)	1.52
		1.8 ± 0.8	(a)	1.52
		1.1 ± 0.6	(a)	1.52
$\bar{\nu}_\mu e \to \bar{\nu}_\mu e$	σ/E	2.2 ± 1.0	(a)	1.32
		$1.0 \; {}^{+1.3}_{-0.6}$	(a)	1.32
$\bar{\nu}_e e$ (low E)	σ	7.6 ± 2.2	(b)	6.37
$\bar{\nu}_e e$ (high E)	σ	1.86 ± 0.48	(b)	1.21

(a) units of 10^{-42} E_ν (cm^2/GeV)
(b) units of 10^{-46} cm^2

addition to others not shown: specifically measurements of the Q^2-dependence of quasi-elastic scattering and of the dependence of the parity-violating interference term in inelastic electron-nucleon scattering. The result is

$$\rho = 1.00 \pm .019 \qquad (20)$$

$$\sin^2\theta_w = .235 \pm .016 \qquad (21)$$

As the table illustrates, there is very good agreement among all the various parameters that have been measured. The agreement of the parameter, ρ, with the WSW prediction $\rho = 1$ also stands evident. The case for ρ set to one gives as the best value for the angle

$$\sin^2\theta_w = .232 \pm .009 \qquad (22)$$

There are predictions for this angle based on a higher symmetry (SU5) (it also predicts lifetimes for the free proton that are within the range of experimental expectations) which give $\sin^2\theta_w = .20$. There seems to be good evidence that the angle is different from this prediction.

The only conflict that exists in this entire picture of the weak neutral current are certain atomic physics experiments. A typical such experiment involves the measurement of the angle of rotation of the plane of polarization of laser light which occurs by passing it through a sample. This parity-violating effect is of

order 10^{-8}, presenting a formidable experimental task. Table III shows experimental results that have been reported. Discrepancies are apparent in identical transitions; there is clearly some controversy remaining regarding these measurements.

Generally, we must conclude that the simple WSW prescription for neutral currents looks very good!

TABLE III

EXPT	ATOM	LINE (nm)	DATA/WSW	
Oxford	Bi	648	0.2-0.5	P.G.G. Baird et al PRL 39, 798(1977)
Seattle	Bi	876	0.2-0.3	L.L. Lewis, et al PRL 39, 795(1977) N. Fortsan, ν'78 (Purdue), P. 417.
Commins	Ti	293	$2.3^{+3.1}_{-1.4}$	P. Conti, et al PRL 42, 343 (1979)
Barkov	Bi	648	1.07±.14	L.M. Barkov and M.S. Zolotory PL 85B, 308(1979)

PROPERTIES OF NEUTRINOS

The spin and charge of neutrinos were part of the original postulate of their existence by Pauli. During the last decade, it was found that there were two types of neutrinos. Now we believe that there are at least three: these are associated with the three known charged leptons. Are there more? We only know that there are likely not any additional charged leptons of mass probed at the limits of present accelerators, so the masses of any additional charged leptons are probably higher than about 15 GeV. The cosmologists have had something to say in recent years about neutrinos; one statement is that there are unlikely to be more than one or two additional low mass neutrinos.

It is also well verified that the three known neutrinos are separated into different families: electron, muon, and tau. These families are labelled by three separately-conserved quantum numbers: electron number (L_e), muon number (L_μ), and tau number (L_τ).

There was for some time the logical possibility that an alternative might prevail: that the sum of the individual quantum numbers was conserved, and that the parity of each was separately conserved.

$$\sum_i L_i = \text{constant} \qquad (-1)^{L_i} = \text{const} \quad i=e,\nu,\tau \qquad (23)$$

This would permit both of the following decay schemes for the muon:

$$\mu^+ \to e^+ + \nu_e + \bar{\nu}_\mu \qquad \mu^+ \to e^+ + \bar{\nu}_e + \nu_\mu \qquad (24)$$

whereas if L_e, L_μ, and L_τ were individually conserved, the second of these could not occur. A recent measurement has concluded that[11]

$$\frac{\text{Rate}(\bar{\nu}_e p \to e^+ n)}{\text{Rate}(\nu_e n \to e^- P)} < .098 \qquad (25)$$

for electron neutrinos from decays of muons at LAMPF. It follows that the standard picture of separately-conserved lepton numbers is the only one of the alternatives which is viable.

An important recent question about neutrinos, and one which will be with us for a long time, is the question of whether the neutrinos have a finite rest mass. There are those who question whether there is any fundamental reason why the neutrinos need to have precisely zero rest mass, for example; contrast the photon whose (probably) zero rest mass is thought to be a consequence of charge conservation. Again, our cosmologist friends have entered the fray with interpretations of astronomical anomalies that could be interpreted with neutrinos of finite rest mass. The experimental mass limits that presently exist are shown in Table IV along with the reactions from which these limits are typically set. The smaller the energy release in a process, the smaller will be the mass limit that can be set on the neutrino.

How these measurements are made in the case of the electron-neutrino is shown in Fig. 8.[12] The Kurie plot would have a linear dependence, intercepting the abscissa at a calculable endpoint if (a) the neutrino were massless, (b) the resolution of the spectrometer used to measure the electron spectrum were perfect, and (c) there were only a single final-state atom. The effects of the last two effects are to broaden the spectrum at the high energy end, while the effect of a massive neutrino is to shrink the distribution at that end. Usually there is more than one final atomic state and there is always finite experimental resolution so the data will project with positive curvature to higher energies. Deviations from this expected shape in the other direction are taken to be an indication of finite neutrino mass.

A recent paper has discussed just such an effect.[13] Fig. 9 shows the data. The experiments see a deviation

TABLE IV

Neutrino	Mass Limit	Reaction	p_ν
ν_e	<60 ev	$H^3 \rightarrow He^3 + e^- + \nu_e$	<18 kev/c
ν_μ	<0.57 MeV	$\pi \rightarrow \mu + \nu_\mu$	37 MeV/c
ν_τ	<250 MeV	$\tau^- + \nu_\tau e^- \bar{\nu}_e$	<750 MeV/c

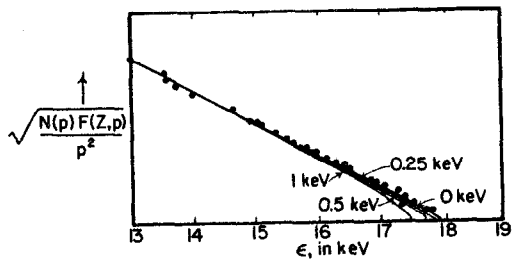

Figure 8: Examples of the effect of large neutrino rest mass on the end point spectrum of tritium decay.

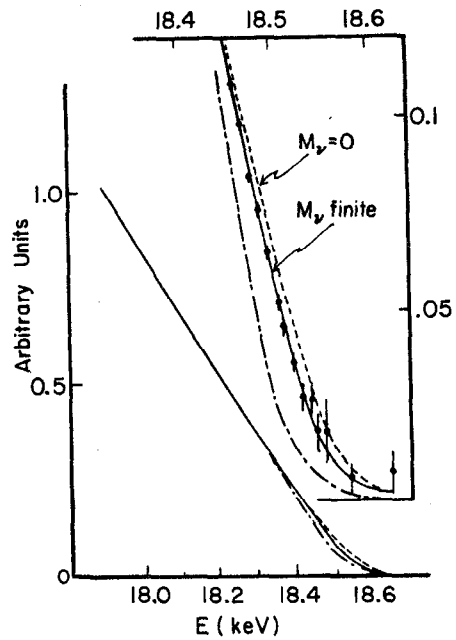

Figure 9: Recent data indicating a small, but finite, rest mass for electron neutrinos (see Ref. 13)

from the curve expected with zero mass neutrinos. If interpreted this way, they would conclude that the electron-neutrino mass is between 14 and 46 eV. Clearly this and other such experiments will continue. They are very difficult, and it may be some time before we know definitely whether this mass range for neutrinos is correct.

With cosmological and laboratory data indicating the possibility of massive neutrinos in the region of several electron volts, another possibility presents itself. The different neutrino types may have different mass. This seems a reasonably likely possibility, since their associated charged leptons have very different masses. We have no good idea why the latter occurs, so we have no good reason to think that their uncharged counterparts will behave differently.

Lepton-number violations are also possible. With theoretical searches for a grand scheme to imbed present understanding of all the forces, we have come to question some previously held sacred cows. We are told that baryon-violation at a very low level is a distinct possibility. Experiments are being constructed to investigate this question at sensitive levels. Why not lepton-type number violation also at a low level? If there were such a process, and neutrinos of different types had a finite mass difference, the various neutrinos could mix in a similar way that the K^o-$\bar{K}^o$ system mixes due to a very small second-order weak interaction.[14]

There are logically very different kinds of neutrino mixing that may occur. The three known neutrinos may mix among themselves or with neutrinos that are still unknown.[14] This implies interactions that simultaneously violate two kinds of lepton number. On the other hand, the neutrinos could mix with their corresponding anti-neutrinos.[15] This would require a change in the lepton number of that neutrino by two units, and would have the closest analogy to the K^o-$\bar{K}^o$ case. A left-handed neutrino would spontaneously evolve into a left-handed antineutrino. We will return to the signatures for the these and other types of mixing.

The algebra of mixing is the algebra of two- or more-state systems. Take a simple case as an example: the mixing between ν_e and ν_μ. The mass eigenstates of the system are defined as $|\nu_1\rangle$ and $|\nu_2\rangle$, of laboratory energies E_1 and E_2, respectively. The physically created states in weak processes are

$$\begin{pmatrix} \nu_e \\ \nu_\mu \end{pmatrix} = \begin{pmatrix} \cos\theta & \sin\theta \\ -\sin\theta & \cos\theta \end{pmatrix} \begin{pmatrix} \nu_1 \\ \nu_2 \end{pmatrix} \qquad (26)$$

The "mixing matrix" involves an angle, θ, which has the physical range $0<\theta<\pi/4$, the upper limit corresponding to the full-mixing case. Then, an initially pure beam of ν_μ after time, t, will have an admixture of ν_e given by

$$N_{\nu_e} = N_o \sin^2 2\theta \ \sin^2\left(\frac{\Delta E}{2} t\right) \qquad (27)$$

where $E=E_2-E_1$. Assuming that the neutrino energies are always large compared to the mass, then $\Delta E \simeq \Delta^2/2E$, where $\Delta^2=m_2^2-m_1^2$. Fig. 10 shows a schematic of how such oscillations might be detected. The detector located a distance L≈ct from the source looks for, as example, $\nu_e + N \rightarrow e^- + X$ events. Then the number of electron neutrino events observed at the detector is

$$N_{\nu_e}=N_o \sin^2 2\theta \ \sin^2\left[1.27\Delta^2\frac{L}{E}\right] \qquad (28)$$

where Δ^2 is in ev^2, L is in meters (km), and E is in MeV(GeV).

A maximal effect is obtained when the last argument in equation 28 is equal to $\pi/2$. Fig. 11 shows the effect versus $\Psi = (2.54\Delta^2/\pi)(L/E)$, over 4 decades of this argument. The sensitivity of an experiment is related to two items: the best value of Ψ that can be obtained for fixed Δ^2 and to the largest value of N_o, corresponding approximately to the total of ordinary interactions. The latter is sometimes limited in practice by backgrounds. As a rough idea of the ranges of sensitivity at, say $\Delta^2 = 1\ ev^2$, high energy accelerators cover the lowest two decades with "ordinary" event rates ∽ 1000/hr, reactors cover the middle two decades with rates ∽ 2 ev/hr, and deep mine experiments go off-scale to the right at rates approximately equal to .02 ev/hr. Hence, the high-energy accelerators might expect to best cover the larger mass-differences and small mixing angles.

There are several different kinds of signatures for oscillations that may be sought. "Exclusive" signatures

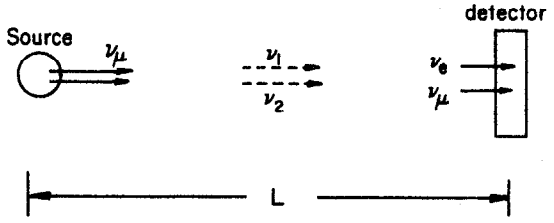

Figure 10: An example of oscillation detection. An exclusive experiment would defect $\nu_e + N \rightarrow e^- + X$ as indication that ν_e spontaneously exist in an initially pure ν_μ beam. An inclusive experiment might detect the sinusoidal variations of ν_μ through the L/E variation in the detection of $\nu_\mu + N \rightarrow \mu^- + X$.

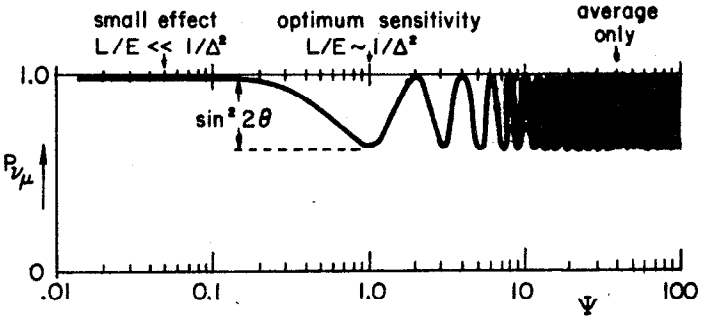

Figure 11: Magnitude of the oscillation effect as a function of $\Psi = (2.54\ \Delta^2/\pi)/(L/E)$.

involve a positive indication of different neutrinos in an initially pure beam. For example, as above, one may start with an almost pure beam of ν_μ from π-decay and seek reactions of the form $\nu_e + N \to e^- + X$ or $\nu_\tau + N \to \tau^- + X$. In this example, "inclusive" signatures might be a sinusoidal variation of the $\nu_\mu + N \to \mu^- + X$ rate which would result from oscillation of ν_μ into any other kind of neutrino, including those that would produce only charged leptons of very high mass, or into antineutrinos of the wrong helicity to produce either the charged or the neutral current reaction. Since all left-handed neutrinos interact equally in the process, $\nu + N \to \nu + X$, then all low mass neutrinos of the correct helicity would produce this reaction with equal rate. This reaction could be especially useful for distinguishing mixing into higher lepton states and mixing into neutrino or anti-neutrino states that do not couple to usual V-A W or Z bosons.

During the topical conference, you will hear of some contemporary information on these subjects, including some possible indications of neutrinos mixing in new data. I believe this is the beginning of a topic of which you will hear much more over the coming years.

POINT-LIKE STRUCTURE OF NUCLEON CONSTITUENTS

An important and substantial effort has taken place over the past decade which utilizes the inelastic scattering of charged and neutral leptons from nucleons to investigate nucleon structure. We had come to think of neutrons and protons as made of quarks, because this idea produced great successes in explaining and predicting the spectroscopy of hadrons. But there remained a serious question: "Were quarks 'real' or were they just a good idea to explain this spectroscopy?" The reality of quarks would become firmer if their properties were well-defined and reproducibly measurable. The tried and true methods of measuring the properties (e.g., spin and charge) of elementary particles did not work for quarks because they simply would not be removed from the hadrons. Hence, they cannot be passed through electric or magnetic fields, and the parameters describing the decay of free quarks cannot be measured.

The new technique involved the elastic scattering of the quarks bound inside the nucleons. The assumption is that a weak or electromagnetic interaction at high energies produces an incoherent scatter from a single quark. This upsets the nucleon bound-state wave function, so that the final hadronic state will generally contain many hadrons, but these final-state interactions do not substantially prejudice the measurements involving the primary scatter. In the "scaling limit," we treat

the quark as if it were free (see Fig. 12). Then the scattering is described by the same Hamiltonian as that expressed in equation (3):

$$H^{cc} = \frac{G_F}{\sqrt{2}}\left[\bar{\mu}\gamma_\alpha(1+\gamma_5)\nu_\mu\right]\left[\bar{T}'\gamma_\alpha(1+\gamma_5)T\right] \qquad (29)$$

where T(T') is the target (recoil) quark. In terms of the center-of-momentum scattering angle, θ^*, this cross-section is isotropic for the scattering of the left-handed neutrino from the left-handed quark, or for the scattering of the right-handed antineutrino from the right-handed antiquark. Recall that the V-A Hamiltonian (29) forces only left-handed fermions and right-handed antifermions to interact as the velocity of the interacting particles approaches light speed. When a left-handed neutrino interacts with a right-handed antiquark, their spins are aligned into a total angular momentum of one unit, so that the distribution takes on the typical spin-one character, as shown in Table V. This table gives the cross-section per unit solid angle, as derived directly from (29) for the case of all kinematic energies large compared to masses or binding energies.[16]

In the description of deep-inelastic scattering, a somewhat different notation has conventionally been used. The scaling variable, y, is illustrated in Fig. 13. It is directly related to the center-of-momentum scattering angle through relation 19: $1-y=(1+\cos\theta^*)/2$, which can be measured directly in any scattering process by knowledge of the laboratory energies of the leptons involved in the

TABLE V: V-A cross-sections

Beam	Example Constituent	$\frac{d}{d\Omega^*}$ V-A cross-section	$\frac{d\sigma}{dy}$ cross-section y-notation
ν_μ $\bar{\nu}_\mu$	(A)Spin 1/2 particle (B)Spin 1/2 anti-particle	$\frac{G^2ME}{\pi}$	$2\frac{G^2ME}{\pi}$
ν_μ $\bar{\nu}_\mu$	(B)Spin 1/2 anti-particle (A)Spin 1/2 particle	$\frac{G^2ME}{\pi}\left(\frac{1+\cos\theta^*}{2}\right)^2$	$2\frac{G^2ME}{\pi}(1-y)^2$
ν_μ $\bar{\nu}_\mu$	(C) Spin 0	$\frac{G^2ME}{\pi}\cos^2\frac{\theta^*}{2}$	$2\frac{G^2ME}{\pi}(1-y)$
ν	Other Spins	Linear Combinations of Above	

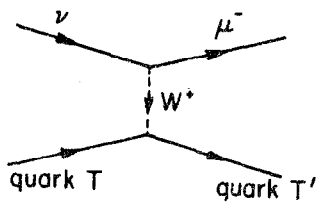

Figure 12: The scaling assumptions: scattering from a free quark, T.

Figure 13: The scaling variable, y. All energies taken equal in c.m. system (equal to ε).

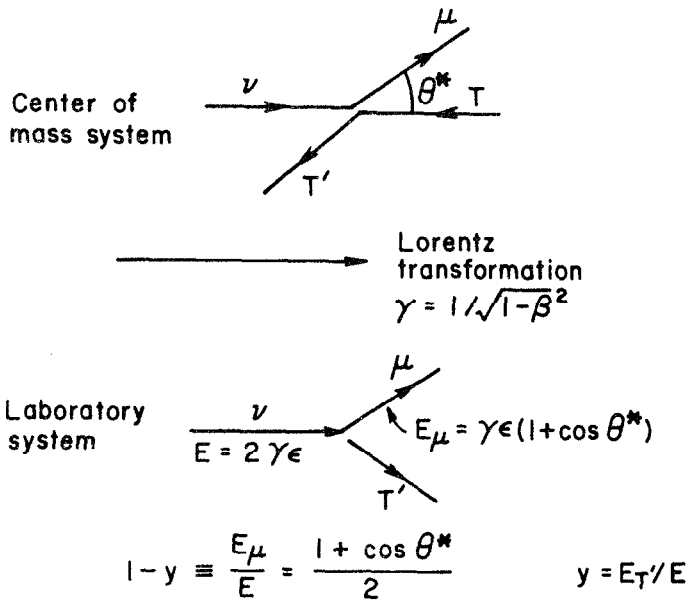

collision. The second column in Table V gives the cross-section per interval of y. The well-defined y-dependence anticipated for deep-inelastic scattering is seen to be a direct consequence of the character of the exchanged force and of the spins of the interacting constitutents. Furthermore, relationships between neutrino and anti-neutrino scattering directly follow. In general, these cross-sections are given for an isoscalar target by

$$\frac{d\sigma^{\nu}}{dy} = \frac{G^2 s}{\pi}\left[A + B(1-y)^2 + C(1-y)\right] \qquad (30)$$

$$\frac{d\sigma^{\bar{\nu}}}{dy} = \frac{G^2 s}{\pi}\left[A(1-y)^2 + B + C(1-y)\right] \qquad (31)$$

where s=square of the c.m. energy, or $s=2M_T E_\nu$ for a target of mass M_T at rest.

Some general features of these forms can be used to make specific predictions. First of all, the laboratory energy dependence of all cross sections should be linear. In particular, the total integrated cross sections should have this dependence to the accuracy of the assumptions that we have made. More than six years ago, the first high energy cross sections showed this qualitative linear dependence on neutrino energy.[17] Nowadays, this behaviour is so expected that we plot the slope (cross-section divided by energy) as shown in Fig. 14.[17-22] There are new results on these fundamental numbers that will be presented in M. Shaevitz' talk during the topical conference. At the present level of precision, there is

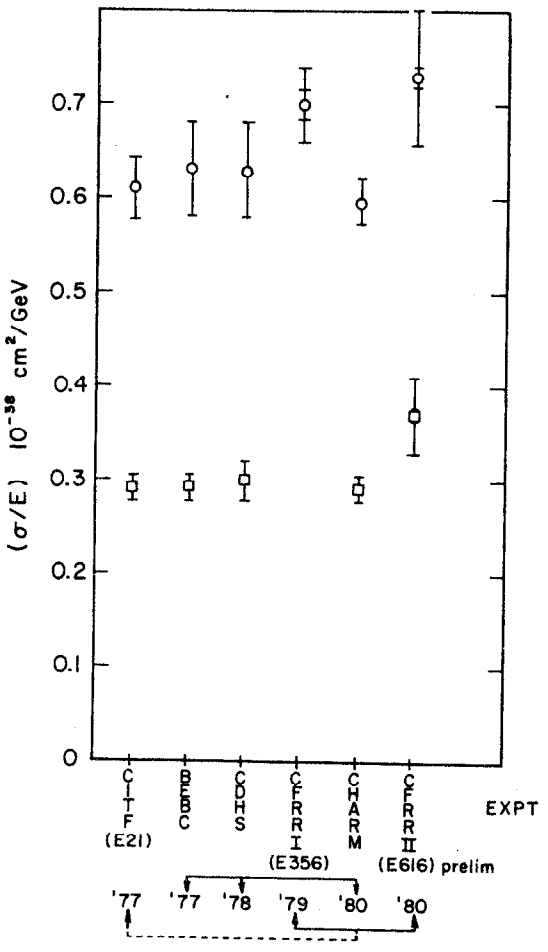

Figure 14: Slopes of neutrino and antineutrino cross-sections.[17-22] Experiments with common flux measuring apparatus are linked by solid lines. Experiments with common group membership are shown dashed.

no controversy that the dependence is linear. However, there are discrepancies among various measurements that remain to be resolved at the 20% level. It has generally been felt that the model assumptions can also produce deviations of 20%. As we will see, more sophisticated ideas involving quark-quark forces should also produce some discrepancy from the simple predictions. So, even though the various measurements are not yet in agreement, the size of the discrepancies are not large enough to place the quark idea in jeopardy.

An interpretation and prediction that follows from equations 30-31 is that the magnitude of the parameter C should be small compared to the others. In a free quark model, this parameter comes from the interaction of neutrinos with non-spin 1/2 constituents of the nucleon. We will see that this parameter has not been well measured, but we do agree that C/A is not bigger than 0.2, on the average.

The parameter, A, gets its contribution from quarks, and the parameter, B, from the antiquarks. Since the nucleon must obtain its net baryon number from three (valence) quarks, we anticipate that B will be substantially smaller than A. The antiquark composition must come from a sea of quark-antiquark pairs, whose net quantum numbers will be zero.

Fig. 15 shows the y-distributions measured in a recent experiment.[22] The curves drawn according to equations 30-31 assume $B/(B+A)=0.15$. As can be seen, the curves describe the data well. By integrating these

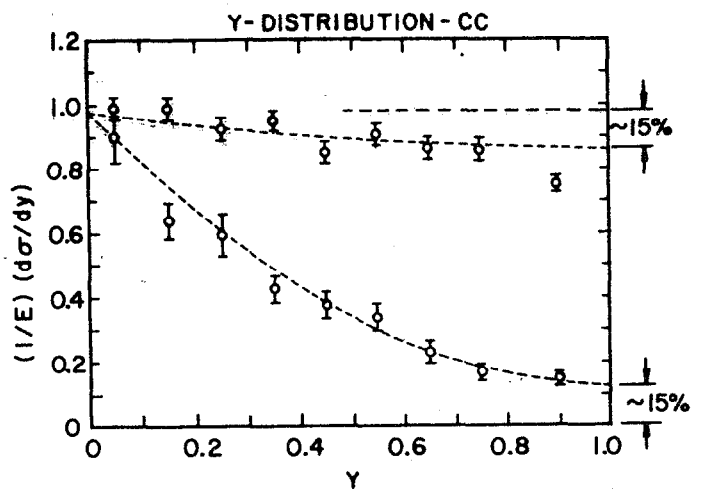

Figure 15: y-distributions, after radiative corrections, from the CFRR experiment.[22]

equations, we obtain predictions for the ratio of anti-neutrino to neutrino cross sections, as well as average y-values for neutrino distributions and antineutrino distributions. Figures 16, 17, and 18 illustrate again that these simple formulas agree well for B/A 0.2. All experiments[17-22] are in agreement that these qualitative features are there.

An interesting point is illustrated in Fig. 19 with regard to the neutral currents that we discussed earlier. This shows the y-distributions of neutral current events (NC) and those from charged-current events(CC). If there were a difference between these, it could come from that small part of the NC process that is V+A. Indeed, a small difference is seen, as the figure shows, which is consistent with that predicted from the Weinberg angle discussed earlier.

Even though equations 30-31 give the correct general behaviour of the y-distributions and energy dependence of the cross-sections, we have cheated a bit in arriving at it. The fact that the quarks are moving inside the nucleon, particularly that they have longitudinal momenta, is important to the interpretation of data. Fig. 20 shows the neutrino incident on the target quark in the center of momentum of the neutrino-quark system. In this frame the proton has total momentum, P, and the quark has a fraction, ξ, of this. The frame then defines the neutrino to have the same momentum as the struck quark, ξP. The cross-section is proportional to $s_{\nu q}$, the

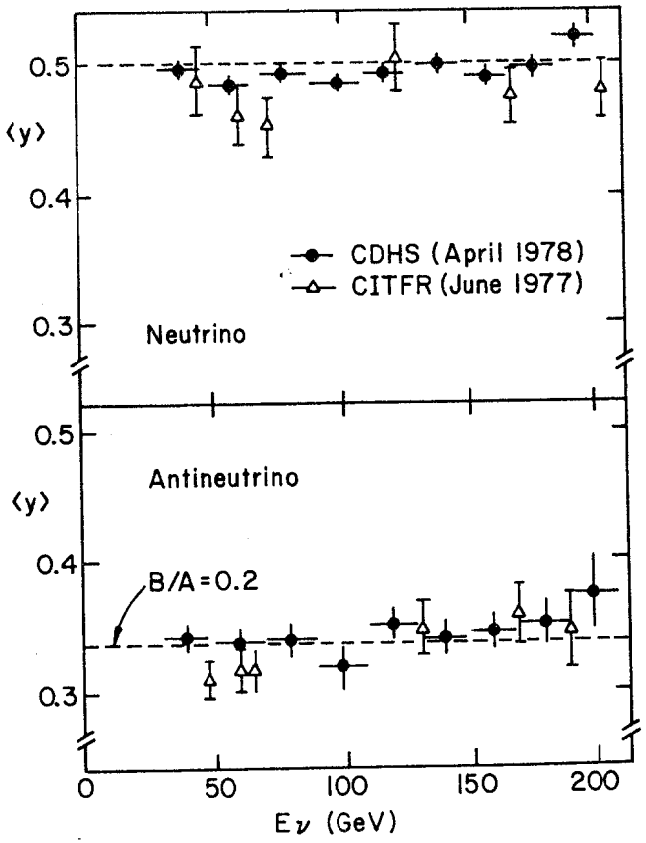

Figure 16: Mean y for neutrino events vs E_ν.
Figure 17: Mean y for antineutrino events vs E_ν.

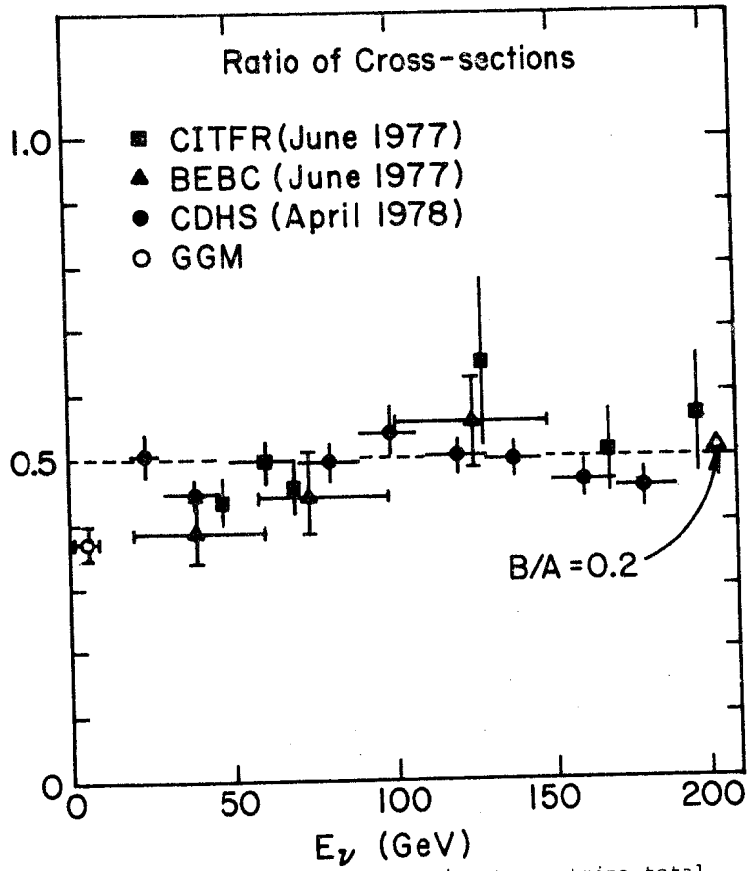

Figure 18: Ratio of anti-neutrino to neutrino total cross-sections versus incident laboratory energy.

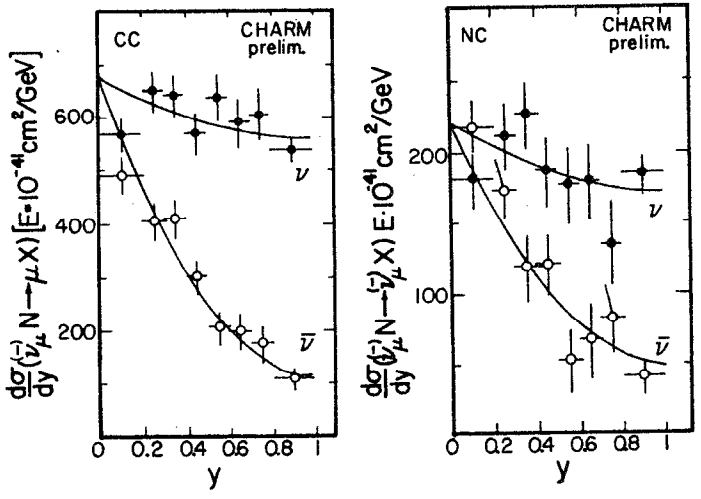

Figure 19: The y-distributions for charged and neutral current events.[21]

Figure 20: Neutrino incident on struck quark in the center-of-momentum frame of the neutrino-quark.

square of the total four-momentum for the neutrino-quark. This is just $s_{\nu q}=(2\xi P)^2$. The square of the four-momentum for the entire system is $s=(\xi P+P)^2-(\xi P-P)^2 = 4\xi P^2$. Hence, $s_{\nu q}=\xi s$. The differential cross-section for neutrinos, for example, scattering from such quarks is then just

$$\frac{d\sigma}{dy} = \frac{G_F^2 \xi s}{\pi}\rho(\xi)d\xi \qquad (32)$$

where $\rho(\xi)d\xi$ is the probability for finding such a quark in a frame in which the proton has high momentum with the struck quark fraction between ε and $\varepsilon+d\varepsilon$. The forms for the cross-sections expressed in equation 30-31 are then appropriate if we keep in mind that A, B, and C are actually functions of this variable, ξ, appropriate to quarks, antiquarks, etc. One of the really important ideas that has helped us interpret deep-inelastic data is the one that gives us an experimental handle on this variable. Refer to Fig. 21, where the scattering of the virtual boson from the quark is shown in the frame in which the (timelike) energy of the boson is zero. By energy conservation, the outgoing massless quark must have final-state energy equal to its initial state energy. The spacelike momentum of the propagator must then just equal $q=\pm 2\xi P$. It follows that ξ is related to a ratio of Lorentz scalers as

$$\xi = x \equiv \frac{-q^2}{2P\cdot q} \approx \frac{E_\nu E_\mu \theta_\mu^2}{2M\nu} \qquad (33)$$

Figure 21: The scaling variable, x.

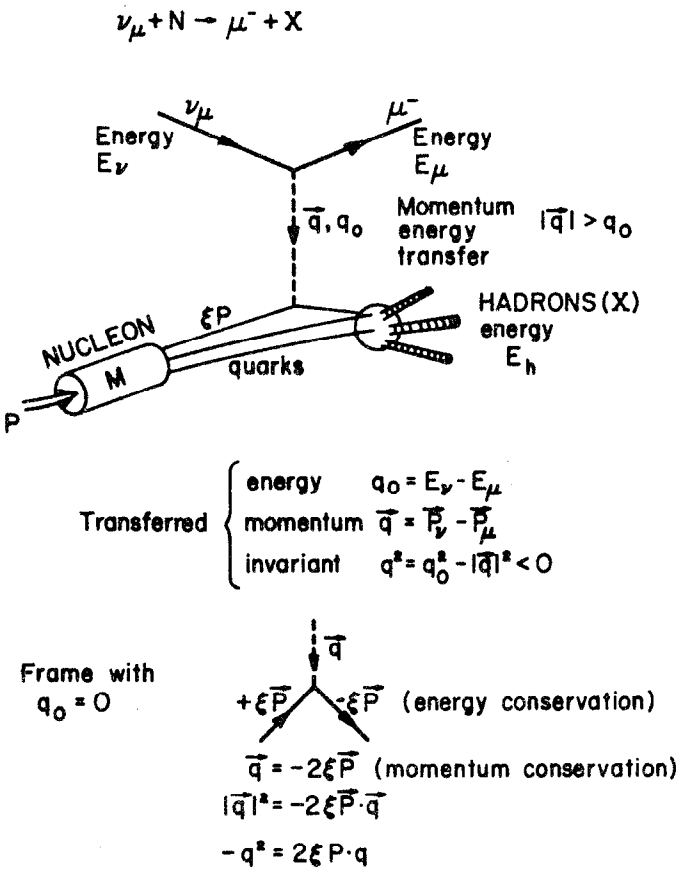

Hence, we can measure laboratory quantities: neutrino energy, E_ν; outgoing muon energy, E_μ; the difference equal to the laboratory hadron energy ν; and the outgoing muon angle relative to the incident neutrino direction, θ_μ. These define the scaling variable, x, which will approximate the fractional momentum of the struck quark. Of course, this will only be really true in the scaling limit; that is, all energies in the c.m. large compared to all masses, all binding energies, and all internal momenta.

This provides the following very general form for the cross-sections of neutrinos and antineutrinos from an isoscalar target in this scaling limit:

$$\frac{d^2\sigma^\nu}{dxdy} = \frac{G_F^2 ME}{\pi}\left[q(x) + \bar{q}(x)\,(1-y)^2 + K(x)\,(1-y)\right] \qquad (34)$$

$$\frac{d^2\sigma^{\bar{\nu}}}{dxdy} = \frac{G_F^2 ME}{\pi}\left[q(x)\,(1-y)^2 + \bar{q}(x) + K(x)\,(1-y)\right] \qquad (35)$$

where $x=Q^2/2M\nu$ and $y=\nu/E_\nu$. Here $Q^2 \approx E_\nu E_\mu \theta_\mu^2$ and $\nu = E_\nu - E_\mu$. Also, $q(x)=u(x)+d(x)$ refers to the quark fractional momentum distribution in the proton multiplied by that momentum. If we wish to be even more general and take into account scale-breaking processes that may take place at the hadron vertex, we can write for the sum and difference of the neutrino and antineutirno cross-sections, respectively,

$$\frac{d^2(\sigma^\nu+\sigma^{\bar{\nu}})}{dxdy} = \frac{G_F^2 ME_\nu}{\pi}\left[F_2^{\nu N}(x,Q^2)\left\{1+(1-y)^2\right\} - F_L^{\nu N}(x,Q^2)y^2\right] \qquad (36)$$

$$\frac{d^2(\sigma^{\nu} - \sigma^{\bar{\nu}})}{dxdy} = \frac{G_F{}^2 ME_{\nu}}{\pi} \; xF_3{}^{\nu N}(x,Q^2) \left\{1-(1-y)^2\right\} \qquad (37)$$

Here the structure functions in our previous notation are given by

$$F_2{}^{\nu N}(x,Q^2) = q^{\nu}(x,Q^2) + \bar{q}^{\nu}(x,Q^2) + K^{\nu}(x,Q^2) \qquad (38)$$

$$xF_3{}^{\nu N}(x,Q^2) = q^{\nu}(x,Q^2) - \bar{q}^{\nu}(x,Q^2) \qquad (39)$$

$$F_L{}^{\nu N}(x,Q^2) = K^{\nu}(x,Q^2) \qquad (40)$$

$$R = F_L{}^{\nu N}/(F_2{}^{\nu N} - F_L{}^{\nu N}) \qquad (41)$$

The scaling limit corresponds to these functions having no dependence on Q^2. The simplest quark model predicts that R=0.

The same properties of nucleon structure are measured in inelastic electron scattering. Fig. 22 illustrates that similarity. The electromagnetic structure functions include the mean-square charge of the scattered nucleon constituents. The formula for the scattering cross section has a direct analogy to the sum formula (36) in the neutrino case:

$$\frac{d^2\sigma^{eN}}{dxdy} = \frac{8\pi\alpha^2}{Q^4}\left[F_2{}^{eN}(x,Q^2)\left\{1+(1-y)^2\right\} - F_L{}^{eN}(x,Q^2)y^2\right] \qquad (42)$$

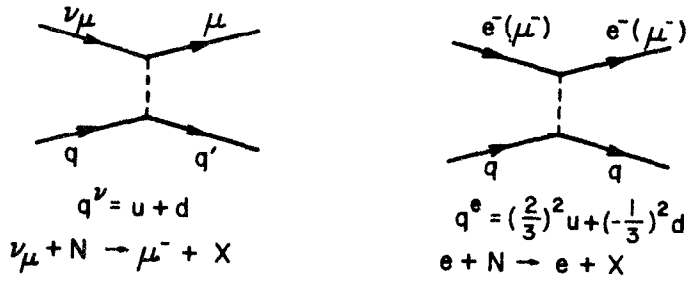

Figure 22: Similarity between neutrino and electron scattering from quarks. Both measure the momentum distribution of constituent quarks, but the electromagnetic coupling gives a different normalization, dependent upon the mean square quark change.

There is no analogous formula to (37), since the difference between neutrino and antineutrino scattering isolates the parity-violating part of the interaction. This does not exist in the electromagnetic case. For an isoscalar target consisting of valence quarks only, the ratio of structure functions is

$$\frac{F_2^{eN}}{F_2^{\nu N}} = \frac{\frac{4}{9} N_u + \frac{1}{9} N_d}{N_u + N_d} = \frac{5}{18} \quad \text{for } N_u = N_d \qquad (43)$$

which is just the mean-square charge of the constituents scattered. By contrast, the ratio for integer charged constituents would generally be larger than 1/2. Fig. 23 shows that this ratio is consistent with that expected for quark charges, and is inconsistent with expectations of integral charges.

There are many other qualitative features of deep-inelastic scattering that verify the quark-like nature of the constituents. Comparison of the scattering cross-sections between neutron and proton targets, for example, gives the correct ratio (2 for neutrino beams and 1/2 for antineutrino beams), as expected for the constituency dominated by the valence quarks.[23]

LIMITATIONS OF THE SIMPLE QUARK MODEL

We have seen several qualitative successes of a very simple model which assumes that free quarks inside nucleons are the participants in the weak/electromagnetic

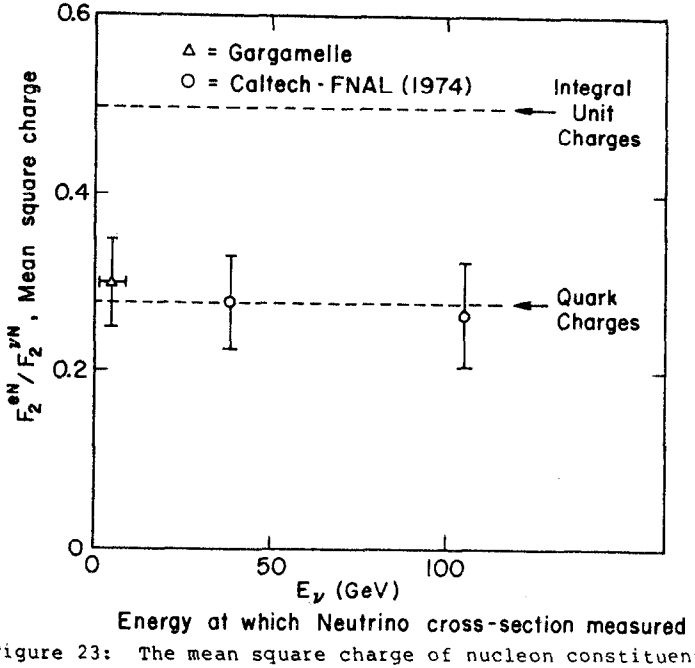

Figure 23: The mean square charge of nucleon constituents as obtained from the ratio of structure functions obtained in electron scattering and neutrino scattering. The ratio does not change substantially with neutrino energy.

interactions with leptons:

(a) The neutrino and antineutrino cross-sections rise linearly with laboratory energy, to the 20% level, in agreement with the expectations of point-like structure of the nucleon.

(b) The y-dependence of the cross-sections shows the qualitative features expected for scattering dominantly from point-like spin-1/2 constituents.

(c) The comparison of deep-inelastic scattering using weak and electromagnetic probes agrees with the constituents having fractional charge, and does not agree with the constituents exhibiting integer charge. The logical possibility exists that these fractionally charged objects are bound states of several integrally charged fields that act coherently at present energies. Such a possibility would become apparent only at energies large enough to fragment the bound states.

(d) Comparisons between scattering from neutron and proton targets show the qualitative features expected if the nucleon is dominantly a bound state of u and d quarks.

(e) Several important features not mentioned, like the jet-like structure of the final-state hadrons in neutrino or electron (muon) deep-inelastic scattering, are expected for point-like constituents, and some of the detailed behaviour (e.g., leading particle behaviour) is qualitatively as predicted for scattering of u and d quarks. Such structure is also visible in the final states at large transverse momentum from hadron-hadron and electron-positron collisions.

However, there are some problems with this model. We do not really expect it to be more than qualitatively correct; for example, the quarks are actually bound into states of the nucleon and we have ignored this binding. Since the quarks are not visible outside of hadronic matter, there clearly must be very strong forces between the quarks, at least at long range, to accomplish their confinement. In addition, the nucleon target has finite mass. We would naively expect deviations from the simple picture at least at the level of $\approx 1\ \mathrm{GeV}^2/Q^2$.

Another important fact is not explained by this model. From equation 38, we see that the integral of the F_2 structure function is precisely the fraction of the total nucleon momentum, in a frame in which the nucleon has high momentum, that is carried by the constituents that interact with the neutrino. Experimentally, this number turns out to be about 0.5. So roughly half the nucleon momentum is carried by components that do not interact with either electrons or neutrinos. We assume that this momentum is carried by the uncharged, spin-one fields responsible for the quark-quark force (i.e., the gluon fields). These fields could be operative at short range as well as long range.

Recent theoretical developments have led to some specific predictions for the short-range properties of this field. The theory of QCD (Quantum Chromodynamics), expressed in a perturbative expansion, has a coupling

constant which decreases approximately logarithmically with energy. In first order, this coupling constant is

$$\alpha_s(Q^2) = \frac{12\pi}{33-2n_f} \log \frac{Q^2}{\Lambda^2} \qquad (44)$$

where n_f = number of quark fields (=4) above threshold, and Λ is a free parameter of the theory. It sets the scale of the strong interactions. The zeroth order terms in the perturbation series are just the "free quark" expressions of the simple model that we have discussed. The leading order terms in α_s would provide an approximately logarithmic dependence of the structure functions as a function of Q^2 at fixed x. Higher orders can be calculated but it is difficult, especially at low Q^2 where α_s is large. The theory is not well enough developed that it can be used to calculate the bound-state nucleon wave functions, or the related behaviour at low Q^2 of the structure functions . . . behaviour due to the finite transverse momenta or binding energies of the bound quarks. Nowadays, this behaviour is called a "higher twist" contribution to the structure functions. As in the days before QCD, it is expected to fall like a power of $1./Q^2$, and will have an uncertain dependence on the x-variable. Specific mechanisms predict specific x-dependences, but there are no definitive predictions for how much of each mechanism is operative in a particular reaction.

The data, as we have seen, do not precisely obey the free quark model. In other words, the x-distributions do not exactly scale; i.e., they are not independent of Q^2 at fixed x. This is true now and it has been true since the first deep-inelastic scattering experiments were performed over ten years ago. During the past decade, the approximate nature of scaling has been a dramatic enough revelation to completely revamp the picture that we had of nucleon structure. It gave reality to our picture of quark-like nucleon constituents. In the early days of these experiments, it was even conjectured that the scaling behaviour might become exact if we measured the structure functions at Q^2 that were high enough. There were many mechanisms that could be invented to explain deviations from exact scaling; these would give behaviour approximately as $(1.0\ \mathrm{GeV}^2)/Q^2$, as described above. All theories would have such effects at low Q^2: they were anticipated and probably observed, long before the advent of QCD.

With the inception of a candidate theory for the strong interactions, one generally thought to be a beautiful theory in which experimental predictions are possible, we no longer expect precise scaling at high Q^2. However, the problem of interpreting low Q^2 data has changed little. Some forms for specific higher twist terms can be anticipated, but we cannot now unambiguously make predictions from theory about the $1./Q^2$ behaviour. If we take a skeptical, objective attitude we must view "corroborations" of QCD from structure function data as follows: so long as one can explain data in terms of corrections to the structure functions that go like $1./Q^2$, or as was done ten years ago,[24] describe the data

in terms of a scaling variable that differs from the asymptotic variable, $x=Q^2/2M\nu$, by corrections to the variable of order $1./Q^2$, then we cannot categorically state that we are observing scaling violations that are anything other than those due to low-Q^2 mechanisms.

A very important point should be made with regard to the variable used to describe the structure functions. We have reproduced a derivation for the variable, x, as representing the fractional momentum of the struck quark. This derivation is only unambiguously valid in the limit $Q^2>>M^2$. There is no proof, to my knowledge, that parametrization in terms of x is in any sense more correct at low Q^2 than some other variable that approaches x at large Q^2. There have been arguments that some specific higher twist scale-breaking mechanisms are more naturally described in terms of different variables than by additional functions of the x-variable.[24,25] No unique variable has been proposed to describe completely all scale-breaking at low Q^2.

Once we arrive at Q^2-values that are large enough to be insensitive to terms of $1./Q^2$, there are unambiguous predictions that QCD makes about the Q^2-dependence of the structure functions. (Although precisely what values of Q^2 are above this critical point is, and will be, argued strenuously.) At those very high energies, the behaviour is to be dominated by the diagrams shown in Fig. 24. The leading terms in the perturbation expansion come from terms that are analogous to QED bremsstrahlung and pair-

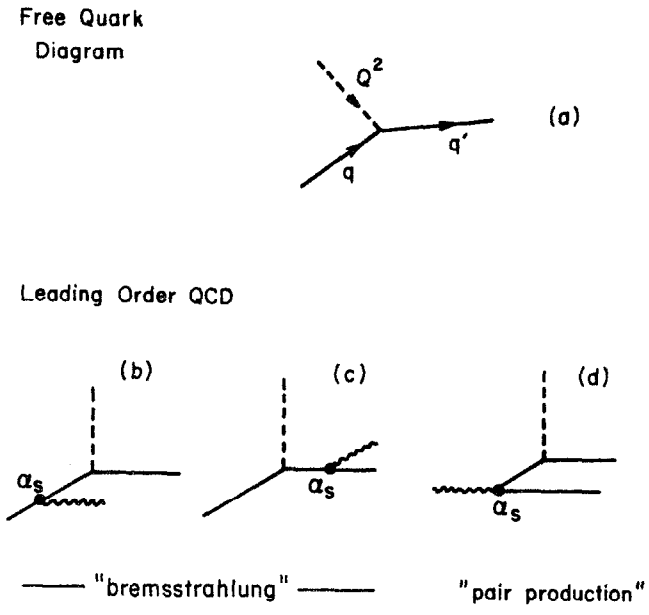

Figure 24: Hadronic vertex to lowest (a) and first (b-d) order in QCD. The free quark vertex (a) is modified by diagrams with external gluon lines in (b-d).

production. The effects of these terms are to cause the logarithmic Q^2-development of the structure functions, and to induce a finite value of the R-parameter defined previously in equation 41. We will return to the structure functions, but let us digress momentarily to look into this question of the R-parameter.

THE LONGITUDINAL STRUCTURE FUNCTION (R-PARAMETER)

The R-parameter attains positive values by scattering from quarks that are not colinear with the incident neutrino. This effect should depend on the mean transverse momentum of the scattered quark, $\langle p_T^2 \rangle$, and on the four momentum of the propagator. It should fall approximately as $\langle p_T^2 \rangle / Q^2$. Another anticipated higher-twist effect is that due to the scattering from a quark bound tightly with another quark (diquark system).[26] This induces a behaviour of the form

$$R \sim \left[\frac{1}{Q^2(1-x)}\right]^n \qquad (45)$$

which would produce perverse values at large x. All such effects, which depend on the wave functions of initial and final state quarks, should disappear at very large Q^2, but "very large" may depend on the value of the x-variable.

At large Q^2, there is an anticipated contribution from QCD that falls much more slowly with Q^2. This comes effectively from the diagrams shown in Figures 24b and 24d. The formula is

$$F_L(x,Q^2) = \frac{\alpha_s(Q^2)}{2\pi} x^2 \left[\int_x^1 \frac{dz}{z^3} \frac{8}{3} F_2(z,Q^2) + \int_x^1 \frac{dz}{z^3} 16\left(1-\frac{x}{z}\right) G(z,Q^2) \right] \qquad (46)$$

where the first term, from Fig. 24b, is the contribution from the probability for an incident quark to bremsstrahlung a gluon. The second term, from Fig. 24d, is proportional to the gluon momentum distribution inside the nucleon (G). Note that these effects are proportional to the quark-gluon coupling constant, α_s, parametrizing the strength of the first vertex in both diagrams. Both mechanisms provide the scattered quark with a transverse momentum that rises linearly with Q^2, but falls with log Q^2. Fig. 25 shows the approximate x-dependence of R expected asymptotically. Because of the integrands in equation 46, the contribution is biggest at small x, but falls dramatically at large x.

Equation 46 can be integrated over all x-values to give the average contribution to F_L from this mechanism. We obtain terms proportional to the momentum carried by quarks and gluons, respectively. Assuming that they carry approximately equal momenta (for which there is some evidence) we obtain [27]

$$\langle R(Q^2) \rangle = \frac{\int F_2(x,Q^2)dx}{\int 2xF_1(x,Q^2)dx} \approx \frac{20}{9} \frac{\alpha_s(Q^2)}{2\pi} \approx \frac{0.5}{\log Q^2/\Lambda^2} \qquad (47)$$

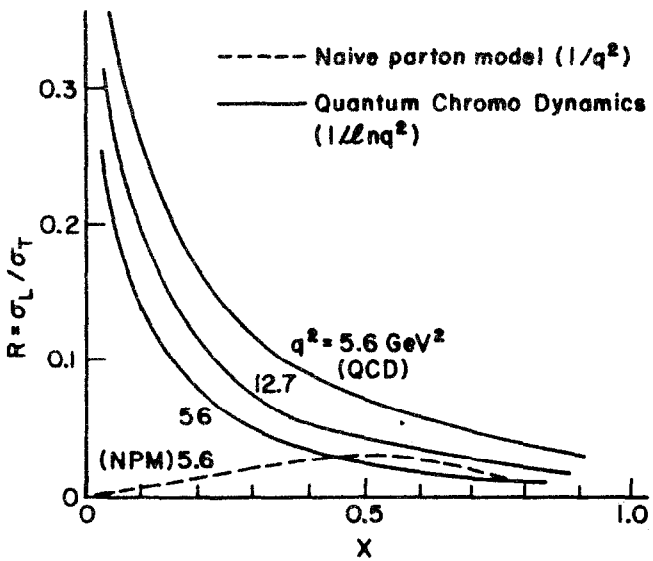

Figure 25: QCD predictions for the x-dependence of R at several Q^2 -values.

which is illustrated for two values of Λ^2 in Fig. 26. We see that a non-trivial value for R is expected from the perturbative QCD effects alone. Nonperturbative, higher-twist effects may make the value of R different from this at low Q^2.

Table VI shows some average R-values obtained in several experiments.[28-35] There is a tendency toward positive numbers, but the errors are very large. There is some indication[29] (see Fig. 27) of very large values at small x. This may be indicative of the QCD effects mentioned above, but they are measured at very small Q^2, where higher twist contributions are expected. The dependence on x and Q^2 are shown in Fig. 28 at larger x-values,[28] but still low Q^2; a finite value of R is indicated, but no dramatic dependence on either x or Q^2 is visible. Recent data[35] from neutrino scattering (in Fig. 29) show a finite average value, but still no clear dependence on either Q^2 or x. Note that the Q^2 range is considerably higher than that of the previous data.

We require more precise data on this very important parameter. It will constitute a very important corroboration of the ideas of QCD if the value of R shows a dependence that is substantially slower than $1./Q^2$ and falls with x. At present, we can only say that the value is finite; its dependence on x and Q^2 may be more complicated than the simple prediction (46).

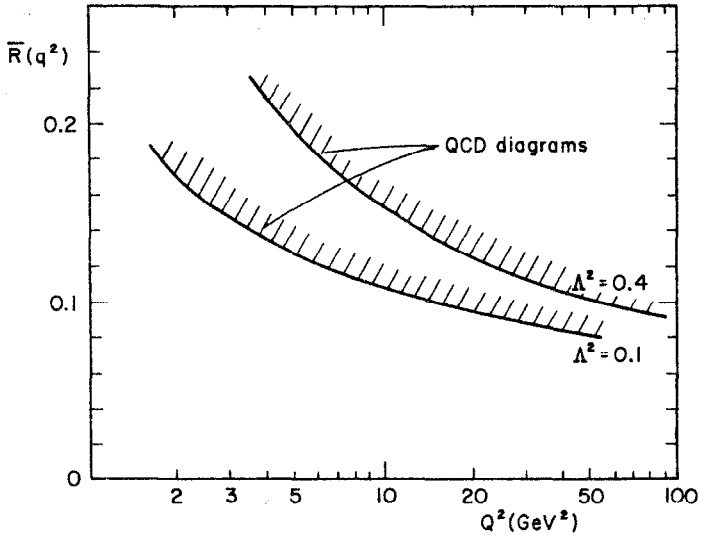

Figure 26: The mean value of R, averaged over x, as a function of Q^2 in QCD. The slow Q^2 dependence and sharp x-dependences of Fig. 25 are characteristic of perturbative QCD.

TABLE VI: Measurements of Averaged Values of R

GROUP-TECHNIQUE		x-range	Q^2-range	R
SLAC-MIT	eN	.1 - .9	2-20 GeV^2	0.20±0.10
Hrv, etc	μN	0. - .1	1-12.5	0.44±0.25±0.19
BEBC	νN	0. - 1.	.1-50	0.15±0.10±0.04
CDHS	νN	0. - 1.	2-200	- 0.03± .05
CDHS	νN	0. - 1.	2-200	0.03±.05±.1
HPWF	νN	0. - 1.	2-200	0.18±.06±.04
CDHS	νN	0. - 1.	2-200	0.10±.025±.07

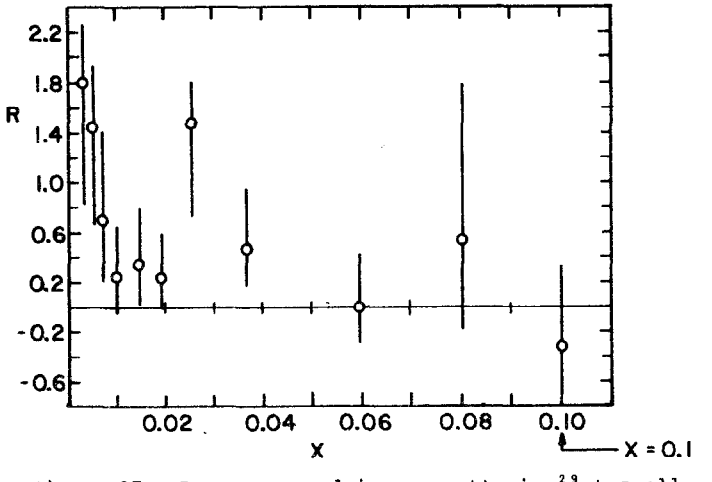

Figure 27: R as measured in μp scattering[29] at small x-values. The average is the second item of Table VI.

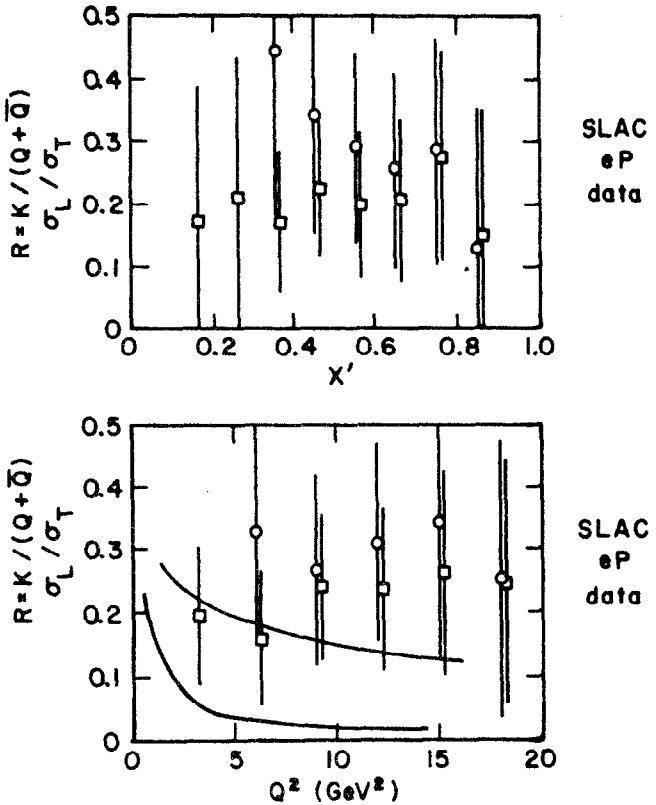

Figure 28: The low energy ep data[28] on R. Although the Q^2 dependence is slow, the x-dependence is not structured as expected from asymptotic QCD.

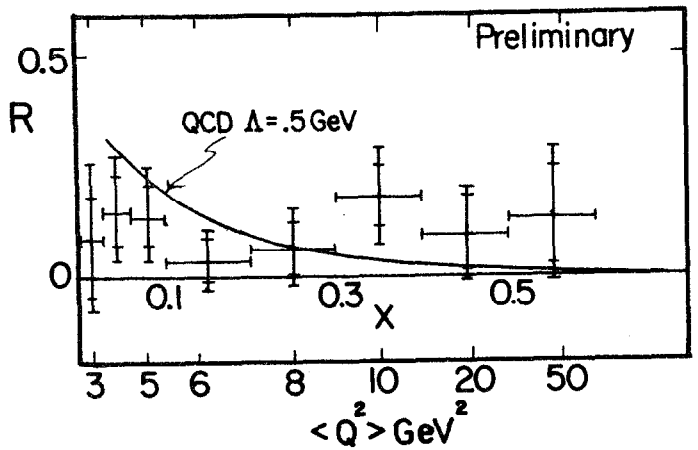

Figure 29: Recent νN data on the R-parameter.[35] The x and Q^2 -dependence do not yet show striking QCD-like behaviour. Previous measurements by these experimenters gave values of R that were somewhat smaller.[31, 32, 33]

THE Q^2 EVOLUTION OF THE STRUCTURE FUNCTIONS

The structure functions are expected to have explicit dependence on Q^2 that comes from either higher twist effects and/or from perturbative QCD effects. The former are not calculable unambiguously; the latter are highly predictable. The evolution equation in the case of xF_3 is particularly simple. This structure function represents the difference between quark and antiquark distributions. Hence, there is no contribution to xF_3 from "pair production" diagrams like those in Fig. 24d. The evolution equation is[36]

$$\frac{\partial xF_3(x,Q^2)}{\partial \ln Q^2} = \frac{\alpha_s(Q^2)}{3\pi}\left[\left\{3 + 4\ln x\right\} xF_3(x,Q^2) + \int_x^1 dw\, \frac{2}{1-w}\left\{(1+w^2)\frac{1}{w}xF_3\left(\frac{x}{w},Q^2\right) - 2xF_3(x,Q^2)\right\}\right] \quad (48)$$

and requires only the distribution of xF_3 at a specific value of Q^2. By contrast, the evolution of the F_2 structure function requires knowledge of the gluon distribution as well as of the F_2 structure function at a particular Q^2. There has been quite a bit of attention[23] paid in the last few years to utilizing the moments of the xF_3 structure function. The ratios of moments have a predictable dependence on Q^2 that depends only on the number of quark fields in the problem. Some qualitative success has been found with such tests, but the technique has not had great success in obtaining a unique value of Λ that is process and energy independent. There is some danger in this approach, since obtaining a moment from data requires the complete x-distribution at each Q^2; one must typically extrapolate to x regions not sampled in the data and/or use data at very low Q^2 which is unlikely to be dominated by perturbative QCD.

An alternative technique is to fit the evolution equations directly. This requires an empirical parametrization of the x-distributions at one value of Q^2, which is then evolved through the appropriate equations. In the process, unknown parameters for the shapes of the distributions at that Q^2 are determined from the data. More recent data from neutrino scattering and from muon scattering will be presented during the topical conference. I will not try to prejudice your response to it by showing the raw data at this stage. I will present the results of their fits, shown in Table VII, to provide some overview. While all experimenters do see scale-breaking, there is some contention regarding the degree of scale-breaking, and even more stimulated discussion about the value of Λ that best fits the data. Table VII shows values of Λ that have been quoted. The moment methods have given rather large values by comparison. The more recent data give progressively smaller values of Λ. We hope that this situation will settle down over the next several years. These experiments are very difficult and, if Λ keeps getting smaller, they will get more difficult. Indeed, it is worrisome that as the experiments get better and the energies get higher, there may be a trend toward

Table VII

Fits for Λ from deep-inelastic data (some differences in experiments and models assumed)

Moments Technique (xF_3)	Variable	Λ
BEBC-GGM (1979)	Nachtmann	.72 ± .13 GeV
CDHS (1979)	Nachtmann	.33 ± .15
CDHS (1979)	x	.60 ± .15

Evolution Equations	Particles	Function	Λ
CDHS (1979)	νN	F_2	.47 ± .11 ± .1
CDHS (1979)	νN	xF_3	.55 ± .15 ± .1
CDHS (1980)	νN	F_2+xF_3	.5 ± .05 ± .1
CDHS (1980)	νN	xF_3	$.3\ ^{+.17}_{-.13}$
EMC (1980)	μN	F_2	.1 ± .1
MSU-F(1980)	μN	F_2	$\sim$ .1

smaller values of Λ and smaller values of the coupling constant, α_s. So long as this fundamental number cannot be reproducibly measured in several different processes, we cannot conclude that we are yet measuring it.

Although the degree of non-scaling as expressed by the magnitude of the QCD parameter, Λ, is the subject of some controversy, the situation is not so terrible if indeed we are measuring the effects of perturbative QCD. Fig. 30 shows the dependence of the quark-gluon coupling constant as a function of Λ in first-order. Although there are questions about Λ over the range 0.1 - 0.6 GeV, the value of α_s (evaluated at 20 GeV^2) changes only by about a factor of two over this same range. Perhaps we are converging on the perturbative region.

The worrisome and nagging concern is that we are not yet measuring asymptotic effects. Several years ago, when the first glimpses into QCD showed that the qualitative features of the theory were such as to shrink the x-distributions as Q^2 increased, it was thought that perhaps most of the scale-breaking already seen was dominated by these effects. As the data have become more precise and extended to higher Q^2, some of the qualitative features have become less trustworthy. For example, at small x the value of F_2 rose with Q^2 up to about 5-10 GeV^2, but more recent data at higher Q^2 do not show this dramatic rise. There are also calculations that indicate that charm production could be a major contribution to scale-breaking in this region.[37]

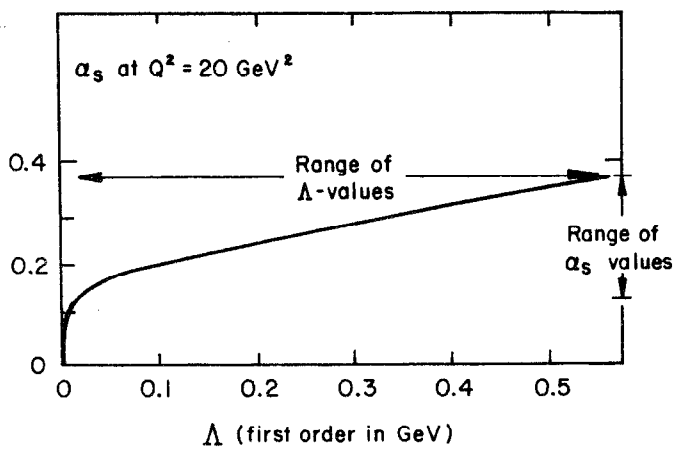

Figure 30: $\alpha_s(Q^2)$ versus Λ^2 at Q^2=20 GeV^2 using the first-order formula for α_s (equation 44).

At higher x-values, where the structure functions appear to fall with Q^2, data at higher Q^2 continue to fall, although in more recent data the dependence is less dramatic. As we have seen, there are higher twist effects that can produce perverse behaviour at large x.

It should also be mentioned that higher twist effects described by a different variable may show very different behaviour at different x-values. For example, take the following arbitrary choice as the representative variable

$$x' = x/(1+g(x)/Q^2) \qquad (49)$$

where g(x) is some unknown function of x of approximate magnitude 1 GeV^2. (The old Bloom-Gilman variable corresponds to $g(x)=M_N^2 x$.) Such a variable would cause non-scaling behaviour that differs at different x-values. In the extreme case of exact scaling at very high Q^2, the structure function is given by $F_o(x)$. Then, expanding to first order,

$$F(x,Q^2) = F_o(x) \left[1 + D/Q^2\right] \qquad (50)$$

where the scale-breaking parameter is given by

$$D = - \frac{F_o'(x)}{F_o(x)} x g(x) \qquad (51)$$

For $F_o(x) = (1-x)^3$, this has the form

$$D = \frac{3xg(x)}{1-x} \qquad (52)$$

D is sketched in Fig. 31 for several different forms for g(x). While only a representative example, it does illustrate that a change in the x-variable by a term of order $1./Q^2$ can produce an "effective" scale-breaking parameter that can be larger in certain x-regions by an order-of-magnitude.

CONCLUSION

We conclude, then, that the quark model for nucleon constituents stands well-verified. There are scale breaking effects in the structure functions, and the value of the R-parameter is very likely nonzero. We are not yet at the point that we can state unambiguously that these effects are dominated by perturbative QCD; indeed, there are some indications that higher-twist effects are strong in the lower part of the Q^2 region presently available. Resolution of these questions can only come with more precise data in the present energy regions, and from data at even higher Q^2. The FNAL Tevatron gives promise to be very important in resolving this question. Fig. 32 shows computer generated data points in present and Tevatron energy regimes. The shaded region could be suspect, because higher twist effects may well be important there. The Tevatron will substantially increase the Q^2 region in

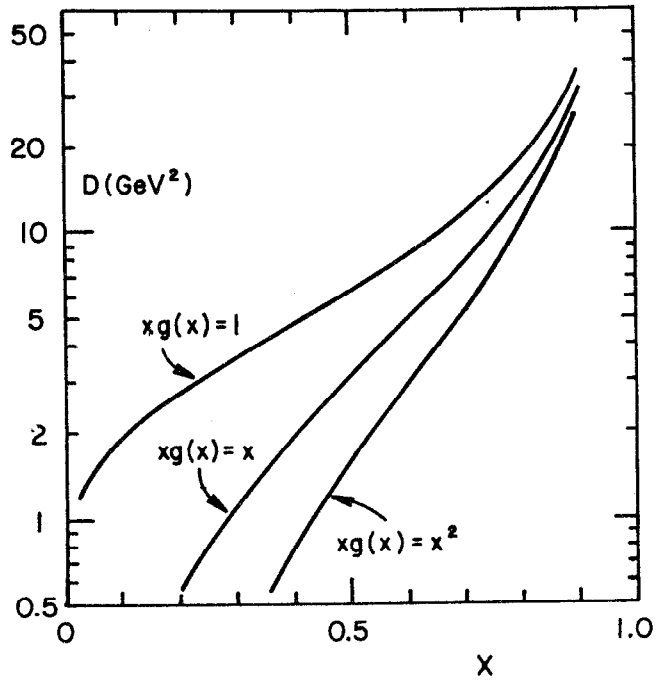

Figure 31: The effective scale breaking parameter D, in GeV^2, as a function of x for a change in the form of the scaling variable. (see text)

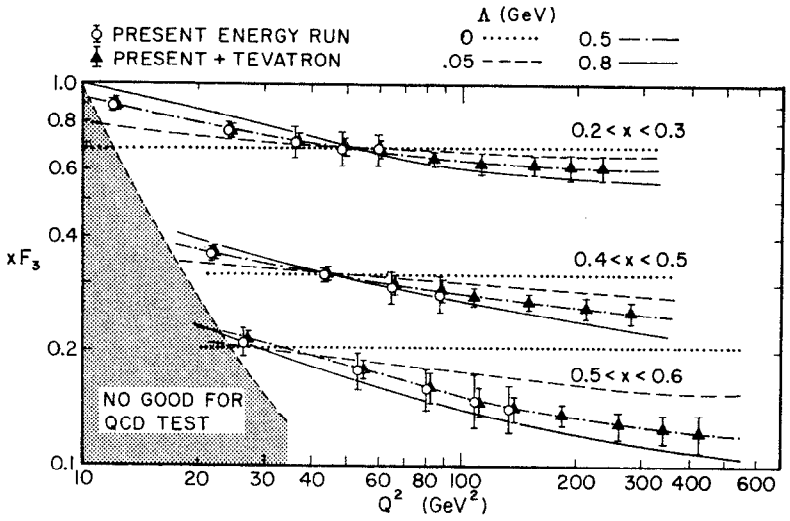

Figure 32: Computer-generated data illustrating statistical errors possible from runs of approximately four month duration using present 400 GeV accelerators, and the increased Q^2 range available from adding 1000 GeV data. Very small values of Λ should be measurable.

which QCD tests can be performed. We anticipate that, with time and energy, we will be able to resolve many of these questions.

REFERENCES

1. See, e.g., D.H. Perkins, Introduction to High Energy Physics, Addison-Wesley, 1972, p. 153.
2. W. Bacino, et al, PRL 42, 749 (1979).
   J. Kirby, Proceedings of the 1979 Int'l Symposium on Lepton and Photon Interactions at High Energies, Batavia, Illinois, p. 107.
3. For a more general case, see B. Bég, et al, PRL 38, 1252 (1977).
4. Lazarus and Greenberg, PR D2, 45 (1970).
5. J. vanKlinken NP 75, 145 (1970).
6. Akhmanov, et al, Soviet Journal of Nuclear Physics 6, 230 (19).
7. J.D. Bjorken, Proceedings of Neutrino '77 (Moscow 1977), p. 414.
8. D. Cutts, et al, PR 184, 1380 (1969).
9. S. Weinberg, PRL 19, 1264 (1967). A. Salaam, Elementary Particle Theory, N. Svartlom, ed, Almquist and Forlag A.B., Stockholm, 1968.
10. J.E. Kim et al, "A Theoretical and Experimental Review of the Weak Neutral Current: A Determination of its Structure and Limits on Deviations from the Minimal $SU2_L$ x Ul Electroweak Theory," U. of P. preprint UPR-158T (1980), submitted to Rev. of Mod. Physics.

11. S.E. Willis, et al, PRL 44, 522 (1980) erratum PRL 45, 1370 (1980).
12. L. Langer and R. Moffatt, PR 88, 689 (1952). See also ref. 1, p. 132.
13. V.A. Lubimov, et al, PL 94B, 266 (1980).
14. See, e.g. S.M. Bilenky and B. Pontacorvo, Physics Reports 41, 225 (1978).
15. T.P. Cheng and L.-F. Li, preprint COO-3066-152 (June 1980).
V. Barger, et al, PRL 45, 692 (1980).
16. See, e.g., E. Commins, Weak Interactions.
17. B.C. Barish, et al, PRL 39, 1595 (1977).
18. P.C. Bosetti, et al, PL 70B, 273 (1977).
19. J.G.H. deGroot, et al, Z. Physik C1, 143 (1979).
20. B. Barish, et al, preprint CALT 68-734 (1979).
21. M. Jonker, et al, contribution to Wisconsin conference.
22. M. Shaevitz, et al, contribution to Wisconsin conference and to SLAC Topical Conference.
23. See, e.g., A. Para, Proceedings of the Int'l Symposium on Lepton and Photon Interactions at High Energies, Fermilab, 1979, p. 349.
24. E. Bloom and F. Gilman, PRL 25, 1140 (1970).
25. A. deRujula, et al, PL 64B, 428 (1977); Ann Phys 103, 315 (1977).
26. L.F. Abbott, et al, SLAC-PUB-2327, 2400 (1979).
27. My appreciation to R. Field for pointing this out.
28. M. Mestayer, PhD thesis, SLAC Report No. 214.
29. B.A. Gordon, et al, PRL 41, 615 (1978).
30. P.C. Bosetti, et al, Nucl. Phys. B142, 1 (1979).
31. See ref. 19.
32. A. Savoy-Navarro, et al, Proceedings of Neutrino '79, Bergen, p. 253.
33. J. Wotshack, et al, EPS Int. Conf. on High Energy Physics, Geneva, 1979.
34. A. Benvenuti, et al, PRL 42, 1317 (1979).
35. J.G.H. deGroot, et al, contribution to Madison Conference and to SLAC Topical Conference.
36. R.M. Barnett, PRL 36, 1163 (1976).
37. J.J. Aubert, et al, contribution to the Madison Conference.

WEAK DECAYS OF STRANGE AND HEAVY QUARKS

David G. Hitlin

California Institute of Technology
Pasadena, California 91125

ABSTRACT

Weak decays of strange, charmed, bottom and top quarks are discussed in the context of the Kobayashi-Maskawa six quark model. Determination of the K-M mixing angles is reviewed. Experimental information on weak decays of charmed particles and bottom mesons is summarized. The resulting phenomenology is shown to be inconsistent with the naive light quark spectator model of charmed particle decay, and some of the consequences of alternative models are considered. Explicit QCD based estimates of decay diagrams are discussed, with emphasis on the origin of the $\Delta I = 1/2$ rule, understanding of Cabibbo-suppressed charm decays and CP violation. Further experimental results which are necessary to arrive at a clear understanding of these weak decay processes are considered.

I. Introduction

In the five years since the discovery of explicitly charmed particles, evidence for their production in e^+e^- annihilation, photoproduction, neutrino reactions and hadron induced reactions has accumulated. More recently, evidence for the existence of particles containing bottom quarks has also been found. The study of the weak decays of these particles presents an area in which the phenomenology of the current-current structure of the weak interactions can be tested with new quarks and at higher momentum transfer. Ideas such as the $\Delta I = 1/2$ rule and non-leptonic enhancement, developed in the context of strange particle decays, can be extended to new laboratories. The exciting possibility of seeing CP violation in other than the $K^o - \bar{K}^o$ system is raised.

While many of the new experimental results are easily understood by extension of older ideas, there have been several recent measurements which are difficult to understand on the basis of the most naive ideas. In particular, measurements of substantially differing lifetimes for the D^o and D^+ mesons, and the values of certain Cabibbo-allowed and suppressed branching ratios make it unlikely that the initially favored light quark spectator model for charm decays can be correct. We will discuss here the experimental situation, the underlying phenomenological structure of weak decay theories and new ideas which have been presented in an attempt to understand the recent results. This will be done in the context of the Kobayashi-Maskawa six quark model, which appears to be in accord with all data except the absence of a t quark, and which naturally admits the possibility of CP violation. We will begin the discussion with a treatment of the K-M model and the determination of its mixing angles. We will then review measurements of charmed particle lifetimes, and semileptonic and non-leptonic branching ratios. This will be followed by a treatment of the theoretical situation in charm and b quark decays and a discussion of CP violation in heavy quark systems.

II. The Kobayashi-Maskawa Model

Our discussion of the phenomenology of strange and heavy quark decays will take place in the context of the Kobayashi-Maskawa [Kobayashi 73] six quark model. This is a natural extension of the earlier four quark model of Glashow, Illiopoulos and Maiani [Glashow 70] which came to prominence with the discovery of charmed hadrons. The extension to three left-handed doublets of quarks and leptons allows incorporation of the τ lepton and its neutrino, and the new (b) $Q = -1/3$ quark which comprises the Υ family. It is the great phenomenological success of this model which has led to the eager anticipation of the discovery of the (t) $Q = +2/3$ partner of the b quark, and conversely, the absence to this point of any evidence for the t quark which constitutes the greatest weakness of the Kobayashi-Maskawa scheme. We will briefly discuss possible alternatives in a later section.

While left-handed quarks and leptons appear as doublets:

$$\begin{pmatrix} u \\ d \end{pmatrix}_L , \quad \begin{pmatrix} c \\ s \end{pmatrix}_L , \quad \begin{pmatrix} t \\ b \end{pmatrix}_L$$

$$\begin{pmatrix} \nu_e \\ e^- \end{pmatrix}_L , \quad \begin{pmatrix} \nu_\mu \\ \mu^- \end{pmatrix}_L , \quad \begin{pmatrix} \nu_\tau \\ \tau^- \end{pmatrix}_L ,$$

right-handed objects are singlets:

$$(u)_R,\ (d)_R,\ (c)_R,\ (s)_R,\ (t)_R,\ (b)_R,\ (e)_R,\ (\mu)_R,\ (\tau)_R.$$

The structure of the theory is that of an $SU(2) \otimes U(1)$ renormalizable gauge theory with $W^{\pm}$, Z^o and γ gauge bosons and in its simplest form a complex isodoublet of Higgs scalar fields which are responsible for spontaneous symmetry breaking and allow incorporation of CP violation. The gauge bosons connect states within a multiplet; mixing between doublets is described by a set of mixing angles, in a generalization of Cabibbo mixing. In general, the weak gauge group doublet eigenstates which diagonalize the weak interaction are not identical to the quark mass eigenstates. Thus there exists an $n \times n$ unitary quark mixing matrix (in an n doublet model) which relates the mass and gauge group eigenstates. Note that this distinction between two types of eigenstates may also apply to the lepton sector, leading to neutrino oscillations, μ - e transitions and related phenomena.

A general $n \times n$ unitary matrix has n^2 parameters. $2n - 1$ of these are unmeasurable relative phases of the quark fields, which leaves $(n-1)^2$ parameters. Since an orthogonal $n \times n$ matrix has $n(n-1)/2$ real parameters, we are left with $(n-1)^2 - n(n-1)/2$ measurable phases. A four quark model is thus characterized by one mixing angle ($\theta_{Cabibbo}$) and no phases, while a six quark model has three mixing angles and one complex phase. A particular choice of representation of these parameters is called the K-M model, although it should be noted that there are different phase conventions in use in the literature. It should also be noted that Cabibbo and Maiani [Cabibbo 79] have introduced an altogether different parametrization of the six quark model. The charged and neutral currents are given by

$$J_\lambda^+ = (\bar{u},\ \bar{c},\ \bar{t})\ \Gamma_\lambda^+\ V \begin{pmatrix} d \\ s \\ b \end{pmatrix} = (\bar{u},\ \bar{c},\ \bar{t})\ \Gamma_\lambda \begin{pmatrix} d' \\ s' \\ b' \end{pmatrix}$$

$$J_\lambda^o = (\bar{d}',\ \bar{s}',\ \bar{b}')\ \Gamma_\lambda^o \begin{pmatrix} d' \\ s' \\ b' \end{pmatrix} = (\bar{d},\ \bar{s},\ \bar{b})\ \Gamma_\lambda^o\ V^+ V \begin{pmatrix} d \\ s \\ b \end{pmatrix} .$$

The non-existence of flavor-changing neutral currents implies $V^{+}V = 1$, so that the neutral current structure is

$$J^{o}_{\lambda} = \bar{d}\,\Gamma^{o}_{\lambda} d + \bar{s}\,\Gamma^{c}_{\lambda} s + \bar{b}\,\Gamma_{\lambda} b \ .$$

Note that the absence of flavor-changing neutral currents involving the b,t quarks is at this point an assumption. In our convention, the K-M matrix is given by

$$V = \begin{pmatrix} c_1 & s_1c_3 & s_1s_3 \\ -s_1c_2 & c_1c_2c_3 - s_2s_3e^{i\delta} & c_1c_2s_3 + s_2c_3e^{i\delta} \\ -s_1s_2 & c_1s_2c_3 + c_2s_3e^{i\delta} & c_2s_2s_3 - c_2c_3e^{i\delta} \end{pmatrix}$$

where

$$\left.\begin{aligned} s_i &= \sin\theta_i \\ c_i &= \cos\theta_i \end{aligned}\right\} \ i = 1,\ 2,\ 3$$

The transformation is then

$$\begin{pmatrix} d' \\ s' \\ b' \end{pmatrix} = \begin{pmatrix} V_{ud} & V_{us} & V_{ub} \\ V_{cd} & V_{cs} & V_{cb} \\ V_{td} & V_{ts} & V_{tb} \end{pmatrix} \begin{pmatrix} d \\ s \\ b \end{pmatrix} \ .$$

In the Cabibbo-GIM model

$$|V_{ud}|^2 + |V_{us}|^2 = 1$$

$$|V_{cd}|^2 + |V_{cs}|^2 = 1$$

and

$$\frac{V_{us}}{V_{ud}} = -\frac{V_{cd}}{V_{cs}} \ .$$

The requirement $V^{+}V = 1$ implies

$$V_{tb} = 1$$

and

$$V_{td} = V_{ts} = V_{ub} = V_{cb} = 0 \ .$$

That is, all transitions involving the t quark are $t \to b$ and the b quark is stable. Two Fermilab experiments [Vidal 78, Cutts 78] have shown, however, that $\tau_b < 5 \times 10^{-8}$ sec, and the recent JADE results [Yamada 80] improve this limit to $\tau_b < 3 \times 10^{-11}$ sec. In addition, in the SU(3) limit, the two Cabibbo suppressed decays $D^{\circ} \to K^{-}K^{+}$ and $D^{\circ} \to \pi^{-}\pi^{+}$ would have equal branching ratios:

$$\frac{\Gamma(D^{o} \to K^{-}K^{+})}{\Gamma(D^{o} \to K^{-}\pi^{+})} = \frac{\Gamma(D^{o} \to \pi^{-}\pi^{+})}{\Gamma(D^{o} \to K^{-}\pi^{+})} = \left|\frac{V_{us}}{V_{ud}}\right|^2 = \left|\frac{V_{cd}}{V_{cs}}\right|^2 \ .$$

As we shall discuss in detail later, the Mark II has shown that these decays differ in rate by a factor of 3. Thus it is clear that there are non-zero matrix elements between the (t,b) doublet and the four older quarks and that the Kobayashi-Maskawa generalization is non-trivial.

A. Determination of the Kobayashi-Maskawa Angles

In an extension of the original Cabibbo angle determination procedure several authors have explored the values or limits which can be placed on the K-M angles [Shrock 78, Shrock 79, Shrock 79a, Barger 79, Suzuki 79, Gaiser 80]. We will next discuss these procedures.

1. $|V_{ud}|$

$|V_{ud}|$ can be obtained by comparing rates for μ decay with nuclear β decay, on the assumption that there is no mixing between the leptons. The lifetime for the purely leptonic μ decay is given by

$$\tau_\mu^{-1} = \frac{G_\mu^2}{192\pi^3} f\left(\frac{m_e^2}{m_\mu^2}\right)\left[1 - \frac{\alpha}{2\pi}\left(\frac{\pi^2 - 25}{4}\right)\right],$$

where

$$f\left(\frac{m_e^2}{m_\mu^2}\right) = f(x) = 1 - 8x + 8x^3 - x^4 + 12x^2 \ln\left(\frac{1}{x}\right).$$

With the measured muon lifetime, this expression yields a value

$$G_\mu = (1.43582 \pm 0.00004) \times 10^{-49} \text{ erg cm}^3 .$$

This coupling constant is then to be compared with that derived from the Ft values for the super-allowed $0^+ \to 0^+$ Fermi transitions in ^{14}O and ^{26m}Al. When the Ft values are corrected for Coulomb distortion and radiative effects, the coupling constant is given by

$$G'_\mu = \frac{\pi^3 \ln 2}{Ft\, m_e^5}$$

The values obtained for these two transitions are

$$G'_\mu = 1.4128 \pm 0.0005 \times 10^{-49} \text{ erg cm}^3$$

and

$$= 1.41248 \pm 0.00044 \times 10^{-49} \text{ erg cm}^3 .$$

The K-M matrix element is then just

$$|V_{ud}| = \left[\frac{G'^2_\mu}{G_\mu^2(1 + \delta_W)}\right]^{1/2},$$

where δ_W is essentially a correction to the ratio of the measured nucleon decay to free quark decay. This is done using the Weinberg-Salam model, resulting in a very slight dependence on $\sin^2\theta_W$.

The result is

$$|V_{ud}| = |\cos\theta_1| = 0.9737 \pm 0.0025 .$$

2. $|V_{us}|$

$|V_{us}|$ is determined by the study of the rates of strangeness changing semileptonic decays. This can be done using either semileptonic hyperon decays or K_{e3} decays.

a) Hyperons

The extraction of $|V_{us}|$ from $\Delta S = 1$ semileptonic hyperon decays is complicated by the fact that the baryon current contains six form factors and by the necessity of simultaneously fitting for $\alpha_D = \frac{D}{D + F}$, where D and F are the symmetric and antisymmetric SU(3) reduced matrix elements for the axial vector current. The six form factors are fixed by relating them to nucleon electromagnetic form factors through the octet property of the V, A currents, and by using PCAC and generalized Goldberger-Treiman relations. Radiative corrections must also be incorporated. Two fits have in fact been made. The first, to six $\Delta S = 1$ decays yields

$$|V_{us}| = 0.220 \pm 0.003$$

$$\alpha_D = 0.654 \pm 0.008$$

with a χ^2 of 6.9 for 6 degrees of freedom.

The second, which also includes the two $\Sigma^+ \to \Lambda e \nu_e$ $\Delta S = 0$ decays, yields

$$|V_{us}| = 0.222 \pm 0.003$$

$$\alpha_D = 0.645 \pm 0.008$$

with a χ^2 of 14.8 for eight degrees of freedom. A theoretical uncertainty of ~5% is estimated for this procedure.

b) K_{e3}

The use of K_{e3} decays for the extraction of $|V_{us}|$ has the advantage that since only the vector current contributes, radiative corrections can be done more reliably and that the effects of SU(3) and SU(3) × SU(3) symmetry breaking can be explicitly incorporated. Only the $f_+(q^2)$ form factor is involved and its q^2 dependence is well measured, but a larger range of q^2 than in hyperon decays is involved and the SU(3) predictions are strictly valid only at $q^2 = 0$. From the decay $K^+ \to \pi^o e^+ \nu_e$, the value $|V_{us}| = 0.221 \pm 0.003$ is obtained, while the decay $K_L^o \to \pi^- e^+ \nu_e$ yields $|V_{us}| = 0.212 \pm 0.005$.

The weighted average of the two approaches is

$$|V_{us}| = 0.219 \pm 0.002 \text{ (statistical)}$$
$$\pm 0.011 \text{ (theoretical + statistical)}$$

With these values we have

$$|\sin\theta_3| = 0.28 \begin{matrix} + 0.13 \\ - 0.28 \end{matrix} \text{ (statistical)}$$
$$\begin{matrix} + 0.21 \\ - 0.28 \end{matrix} \text{ (statistical + theoretical) .}$$

The possibility of a reasonably large θ_3 complicates the extraction of θ_2 and δ, since procedures which set θ_3 to zero are no longer justified [Ellis 77].

Combining the values of $|V_{ud}|$ and $|V_{us}|$ we have

$$|V_{ud}|^2 + |V_{us}|^2 = 0.996 \pm 0.004 .$$

Thus, $|V_{ub}| = 0.06 \pm 0.06$, indicating the possibility of b quark mixing.

c) $|V_{cd}|$

$|V_{cd}|$ can be obtained from an analysis of the $K_L - K_S$ mass difference or by using $K_L \to \mu^+\mu^-$ decay.

The $K_L - K_S$ mass difference has its origin in the $\Delta S = 2$ transition shown in Fig. 1. The matrix element for this transition is

$$\langle \overline{K^o} | \mathscr{L}_{eff} | K^o \rangle = -\frac{2}{3} \frac{G_F^2 \sin^2\theta_1 \cos^2\theta_1}{4\pi} m_c^2 \, X \langle \overline{K^o} | (\bar{d}_L \gamma_\mu s_L) | \, | (\bar{d}_L \gamma_\mu s_L) | K^o \rangle$$

where

$$X = \frac{1}{\sin^2\theta_1 \cos^2\theta_1} \left[\left(V_{cs} V_{cd}^* \right)^2 + \left(\frac{m_t^2}{m_c^2} \right) (V_{ts} V_{td}^*)^2 \right.$$
$$\left. + V_{cs} V_{cd}^* V_{ts} V_{td}^* \frac{2m_t^2}{m_t^2 - m_c^2} \ln \left(\frac{m_t^2}{m_c^2} \right) \right]$$

The real part of the matrix element is proportional to the mass difference. The expression can be written in terms of $\Gamma(K^+ \to \mu^+ \nu_\mu)$:

$$m_{K_L} - m_{K_S} = \frac{4}{3\pi} \frac{m_c^2}{m_K} \cos^2\theta_1 \left[\frac{m_K}{2} \frac{}{m_\mu} \Gamma(K^+ \to \mu^+ \nu_\mu) \right] X .$$

Evaluation of the local four quark operator between K^o and $\overline{K^o}$ states is subject to theoretical uncertainty. The simplest approach is to insert a complete set of intermediate states and assume it to be saturated by the vacuum. Shrock and Treiman [Shrock 79b] have done an MIT Bag model computation of the matrix element, obtaining a value which is 40% of the naive calculation. The result is also clearly dependent upon the (unknown) value of the t quark mass. Further issues involving leading log computation of coefficients and dependence on the renormalization point have also been discussed [Gaiser 80].

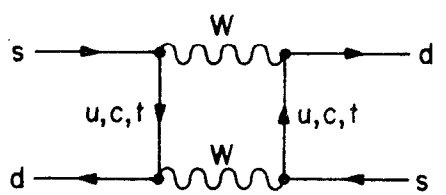

Fig. 1 Diagram for the $K_L - K_S$ mass difference.

An approach using the $K_L^o \to \mu^+\mu^-$ decay [Shrock 79a], is not subject to these uncertainties in the evaluation of the matrix element since no two-current matrix element is involved. The branching ratio has the experimental value:

$$B(K_L^o \to \mu^+\mu^-) = (9.1 \pm 1.8) \times 10^{-9} .$$

The absorptive part of the contribution of the $\gamma\gamma$ intermediate state to this process can be related by unitarity to the measured $K_L \to \gamma\gamma$ rate:

$$\Gamma(K_L \to \mu^+\mu^-)_{abs} = 1.2 \times 10^{-5}\, \Gamma(K_L \to \gamma\gamma)$$

$$= (5.9 \pm 0.6) \times 10^{-9}\, \Gamma(K_L \to \text{all}) .$$

Thus the dispersive part of the contribution must be

$$\Gamma(K_L^o \to \mu^+\mu^-) = (3.2 \pm 2.4) \times 10^{-9} .$$

The short distance (sd) contribution to the dispersive part can be calculated in the K-M model via the diagram of Fig. 2. Normalized to $\Gamma(K^+ \to \mu^+\nu_\mu)$ the result is

$$\frac{\tau(K^+)}{\tau(K_L^o)} \frac{B(K_L \to \mu^+\mu^-)_{sd}}{B(K^+ \to \mu^+\nu_\mu^-)} = \frac{G_F^2}{2\pi^4} \frac{(1 - 4m_\mu^2/m_K^2)^{1/2}}{(1 - m_\mu^2/m_K^2)^2} \frac{\left[\sum_{i=c,t} \mathrm{Re}(V_{is}^+ V_{id}) m_i^2\right]^2}{|V_{us}|^2}$$

The bound follows from the condition

$$B(K_L \to \mu^+\mu^-)_{sd} \leq B(K_L \to \mu^+\mu^-)_{disp} \leq 5.6 \times 10^{-9} .$$

Determination of a lower bound on $B(K_L \to \mu^+\mu^-)_{sd}$ is complicated by the neglect of long distance contributions to the dispersive part. The condition does, however, imply the inequality

$$|\cos\theta_2\, (\cos\theta_1 \cos\theta_2 - \sin\theta_2 \tan\theta_3 \cos\delta)\, m_c^2$$

$$+ \sin\theta_2\, (\cos\theta_1 \sin\theta_2 + \cos\theta_2 \tan\theta_3 \cos\delta)\, m_t^2 | < 57\ \text{GeV}^2$$

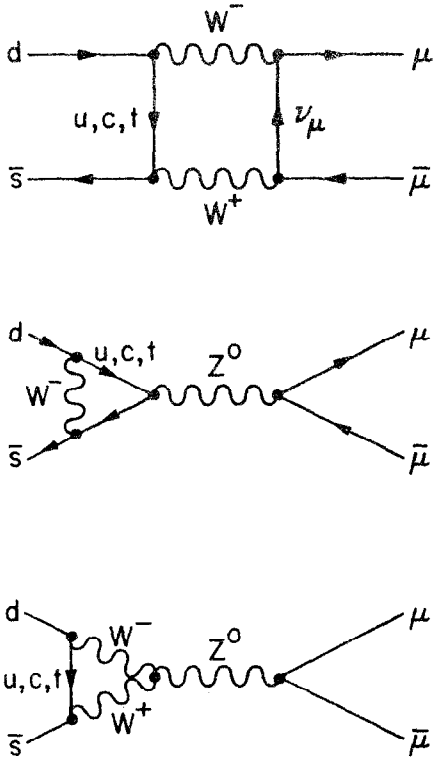

Fig. 2 Short distance contributions to the dispersive part of the $K_L^o \to \mu^+\mu^-$ transition.

Since $m_t^2 >> m_c^2$ the first term can be neglected for purposes of the bound. Then, taking the value of $\cos\theta_1$ determined above, there is a relation between the t quark mass, $|\sin\theta_3|$ and the upper bound for $|\sin\theta_2|$ which depends on $\xi \equiv \text{sgn}(\cos\delta) = \pm 1$. This is shown in Fig. 3. For comparison, the bound determined from $m_{K_L} - m_{K_S}$ [Shrock 79] is also shown.

A more recent analysis of the K-M angles, by Gaiser, Tsao and Wise [Gaiser 80] includes QCD corrections in leading log approximation. The dependence of the QCD effects on the renormalization point is explicitly exhibited in Fig. 4, which shows their results for $\sin\theta_2$ and $\sin\delta$ as functions of $\sin\theta_3$. From $|V_{ud}| \equiv \cos\theta_1 = 0.9737 \pm 0.0025$ and $|V_{us}| \equiv |\sin\theta_1 \cos\theta_3| = 0.219 \pm (0.002, 0.011)$, we can determine

$$\sin\theta_3 = 0.28 \begin{matrix} +0.21 \\ -0.28 \end{matrix} .$$

There are thus two possible solutions. For $\cos\delta > 0$,

$$|\sin\theta_2| \simeq 0.18 \begin{matrix} +0.12 \\ -0.04 \end{matrix}$$

$$|\sin\delta| \simeq 9 \times 10^{-3} ,$$

while for $\cos\delta < 0$,

$$|\sin\theta_2| \simeq 0.45 \begin{matrix} +0.18 \\ -0.15 \end{matrix}$$

$$|\sin\delta| \simeq 4 \times 10^{-3} ,$$

with only a slight dependence on the renormalization point. These results assume the reduced bag model value of 0.4 for the $K^o - \overline{K^o}$ insertion. If the vacuum insertion value 1.0 is used, somewhat smaller values of $\sin\theta_2$ and larger values of $\sin\delta$ are found, with a greater dependence on the renormalization point.

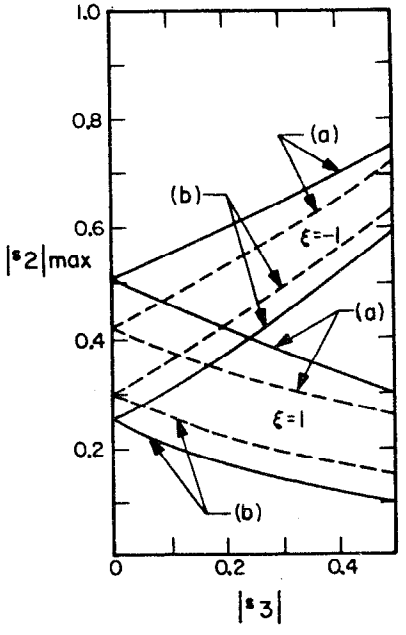

Fig. 3 Upper bounds on $|\sin\theta_2|$ from $K_L \to \mu\bar{\mu}$ decay (solid line) as a function of $\sin\theta_3$ for a) m_t = 15 GeV and b) m_t = 30 GeV. Dashed lines are bounds from the $K_L - K_S$ mass difference approach [Shrock 79a].

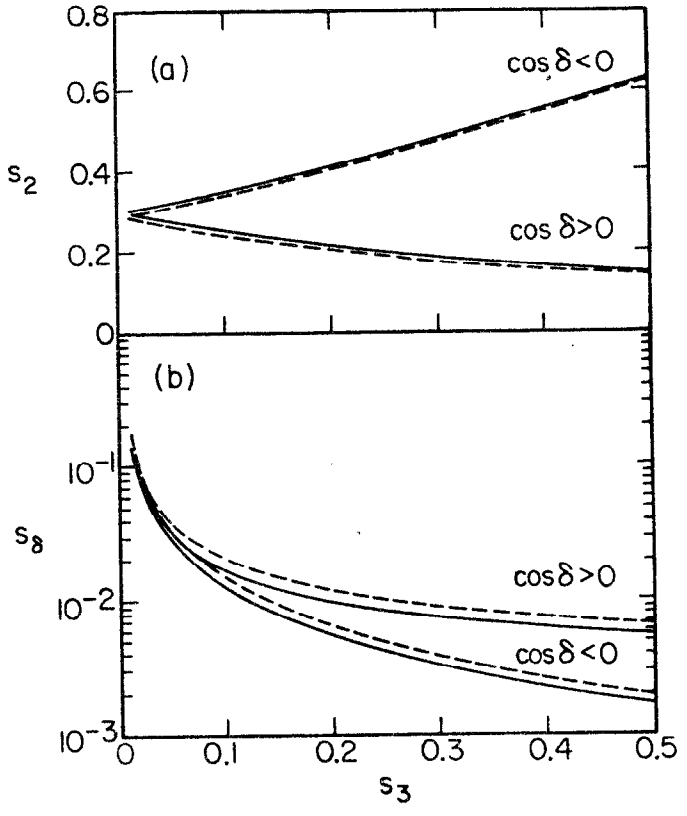

Fig. 4. Relation between $\sin\theta_2$, $\sin\delta$, and $\sin\theta_3$, when δ lies in the upper half plane. Dashed line is for Λ^2 = 0.1 GeV^2, solid line for Λ^2 = 0.01 GeV^2. A t quark mass of 30 GeV and the bag model estimate of the $K^o - \bar{K}^o$ matrix element are used [Gaiser 80].

Using our parametrization of the Kobayashi-Maskawa matrix, we can take the central value of the mixing angles and determine the two possible linear combinations for the physical quark states. These are:

for $\xi = +$, $0 \leq \theta_{1,2,3} \leq \pi/2$

$$d' = .97d + .22s + .064b$$

$$s' = -.22d + (.87 - 4.5 \times 10^{-3}i)s + (.44 + 1.6 \times 10^{-3}i)b$$

$$b' = 0.41d + (.44 + 2.5 \times 10^{-3}i)s + (-.90 - 8.5 \times 10^{-3}i)b$$

while for $\xi = -$, $0 \leq \theta_{1,2,3} \leq \pi$

$$d' = .97d + .22s + .064b$$

$$s' = -.20d + (.96 - .50 \times 10^{-3}i)s + (-.19 + 1.7 \times 10^{-3}i)b$$

$$b' = -.10d + (.17 + 1.0 \times 10^{-3}i)s + (.98 - 3.4 \times 10^{-3}i)b$$

In either case, the diagonal matrix elements are the largest and the values decrease with distance from the diagonal, indicating that flavor mixing is indeed small and that the quarks maintain much of their original identity. This means, for example, that b quark decays should be predominantly $b \to c$ and not $b \to u$, while t quarks should decay to b quarks. We will discuss the experimental evidence for this in a later section. It is also possible to calculate average particle lifetimes with this mixing scheme. The result is $\sim 10^{-13}$ sec for charm and $\sim 10^{-14}$ sec for b quarks.

III. Measurement of Charmed Particle Lifetimes

A crude estimate of the lifetime of charmed particles follows immediately by inspection of Fig. 5. The W^+ radiated in the $c \to s$ transition can form three colors of $u\bar{d}$ quarks, $\mu\nu$ or $e\nu$. Thus we expect a semileptonic branching ratio $B(D \to e \text{ or } \mu, \nu X)$ of the order of 20% in the absence of non-leptonic enhancements. It is then a simple matter to scale from the μ decay lifetime:

$$\Gamma_{TOT} \simeq 5 \left(\frac{m_c}{m_\mu}\right)^5 \times \frac{1}{2} \times \Gamma(\mu \to e\nu\bar{\nu})$$

$$\simeq \left[1.5 \times 10^{-12} \text{ sec}\right]^{-1} ,$$

for $m_c = 1.5$ GeV. The factor of 1/2 accounts for phase space differences.

This estimate can be refined in two ways [Chanowitz 80]. First, the coefficients f_+ and f_- can be calculated in QCD in leading log approximation, and the result predicts a small non-leptonic enhancement

$$\Gamma_{NL}(D) = \frac{2f_+^2 + f_-^2}{3} \Gamma_{NL}(c) \simeq \frac{5}{3} \Gamma_{NL(c)} .$$

Second, there are first order radiative gluon corrections to the semi-leptonic decay (discussed in detail below), such that

$$\Gamma_{SL}(D) = \left(1 - \frac{1}{2}\alpha_s(m_c)\right) \Gamma_{SL}(c) \simeq \frac{2}{3} \Gamma_{SL}(c)$$

Taken together, these corrections result in a predicted semileptonic branching ratio of about 10% and a $\Gamma_{TOT} \simeq [1.2 \times 10^{-12}\text{sec}]^{-1}$.

Lifetimes in the range 10^{-12} - 10^{-13} seconds can be directly measured with emulsions or high resolution bubble chambers. These techniques are discussed in detail in the article by Mulvey in these Proceedings [Mulvey 80]. We will limit the treatment here, therefore, to a brief summary of experimental results.

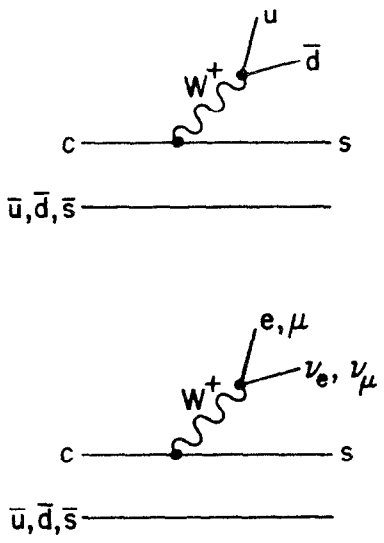

Fig. 5 Diagrams contributing to charmed meson decay in the light quark spectator model.

Over the past decade, bare emulsion, bubble chamber or high pressure streamer chamber experiments, using cosmic rays, neutrino or hadron beams were able to establish that charmed particle lifetimes were in the range of a few $\times 10^{-13}$ seconds. It has only been within the past year or so that emulsion experiments utilizing downstream spectrometers or large bubble chambers for particle identification and accurate momentum measurement have been able to quote reasonably precise values for individual charmed particle lifetimes. Two experiments using neutrinos at FNAL, E531 [Ushida 80, Ushida 80a] and E564 [Ammar 80], have presented results, as have two at CERN, WA17 [Angelini 79] in the ν beam and WA58 [Aston 80] using photoproduction. The results of these four experiments are summarized in Table I. While statistics are small and the internal consistency for the various experiments is not great, it seems clear that D^o, F^+ and Λ_c^+ lifetimes are equal to within a factor of two and are much shorter than the naive estimate, and that the D^+ lifetime is longer, by as much as a factor of 5 to 10, in agreement with the estimate.

The ratio of D^o to D^+ lifetimes can be measured in e^+e^- annihilation. This has been done by the Mark II [Lüth 79, Schindler 80] and DELCO [Kirkby 79, Bacino 80] groups. The technique follows immediately from a simple observation. By inspection of Fig. 5 it is clear that

$$\Gamma(D^o \to \ell\nu X) = \Gamma(D^+ \to \ell\nu X)$$

Now, the semileptonic branching ratios are defined as

$$B(D^o \to \ell\nu X) = \frac{\Gamma(D^o \to \ell\nu X)}{\Gamma_{TOT}(D^o)}$$

$$B(D^+ \to \ell\nu X) = \frac{\Gamma(D^+ \to \ell\nu X)}{\Gamma_{TOT}(D^+)}$$

TABLE I. *Summary of Recent Direct Lifetime Measurements of Charmed Particles*

Reference	Beam	Detector	Number of Events	Lifetime ($\times 10^{-13}$ Sec)
Ushida 80, 80a	$\nu,\bar{\nu}$	Emulsion + Spectrometer	10 D^0	$1.01\ ^{+0.43}_{-0.27}$
			5 D^+	$10.3\ ^{+10.5}_{-\ 4.1}$
			5 Λ_c^+	$1.36\ ^{+0.84}_{-0.46}$
			2 F^+	$2.2\ ^{+2.8}_{-1.0}$
Ammar 80	$\nu,\bar{\nu}$	Emulsion + 15 ft. Bubble Chamber	1 F^+	1.4
Angelini 79	ν	Emulsion + BEBC	3 neutral (prob. D^0)	$0.53\ ^{+0.57}_{-0.25}$
			4 charged (D^+, F^+, Λ_c^+)	$2.5\ ^{+2.2}_{-1.1}$ (assumed D^+)
			1 Λ_c^+	7.3
Aston 80	γ	Emulsion + Omega Spectrometer	2 D^0	0.84, 0.45
			1 Λ_c^+	0.57
			D^-	1.0

thus:

$$\frac{\tau(D^+)}{\tau(D^0)} = \frac{\Gamma_{TOT}(D^0)}{\Gamma_{TOT}(D^+)} = \frac{B(D^+ \to \ell\nu X)}{B(D^0 \to \ell\nu X)}$$

Both measurements are made at the ψ'' (3.77) resonance. Both depend on the fact that D's are produced in pairs at the ψ''. The Mark II measures the branching ratio by identifying correct sign electrons in the particles recoiling against D's reconstructed into particular hadronic modes: $D^0 \to K^-\pi^+$, $K^-\pi^+\pi^-\pi^+$ and $D^+ \to K^-\pi^+\pi^+$, $K_s^0\pi^+$. Table II shows the results, including wrong sign events which are a measurement of background due to misidentification. The lifetimes are not equal, the result being

$$\frac{\tau(D^+)}{\tau(D^0)} = 3.1\ ^{+4.2}_{-1.4}$$

DELCO cannot reconstruct hadronic decay modes, but has extremely clean electron identification. Their procedure is to compare one and two electron events. Figure 6 shows the results. As there are differences in the electron spectra for $D \to Ke\nu$ and $K^*e\nu$ decays, efficiencies differ and the two parts of the figure show the results under the two extreme assumptions. No clear signal from D^0's is seen, resulting in a ratio quoted as

$$\frac{\tau(D^+)}{\tau(D^0)} > 4.3 \text{ @ } 95\% \text{ CL}\ .$$

Thus the two e^+e^- results are consistent, showing a clear difference in the D lifetimes, albeit a smaller difference than that measured directly in emulsions. It should be noted that the ratio technique can be extended to F^+ and Λ_c^+ decays when their semileptonic branching ratios are measured.

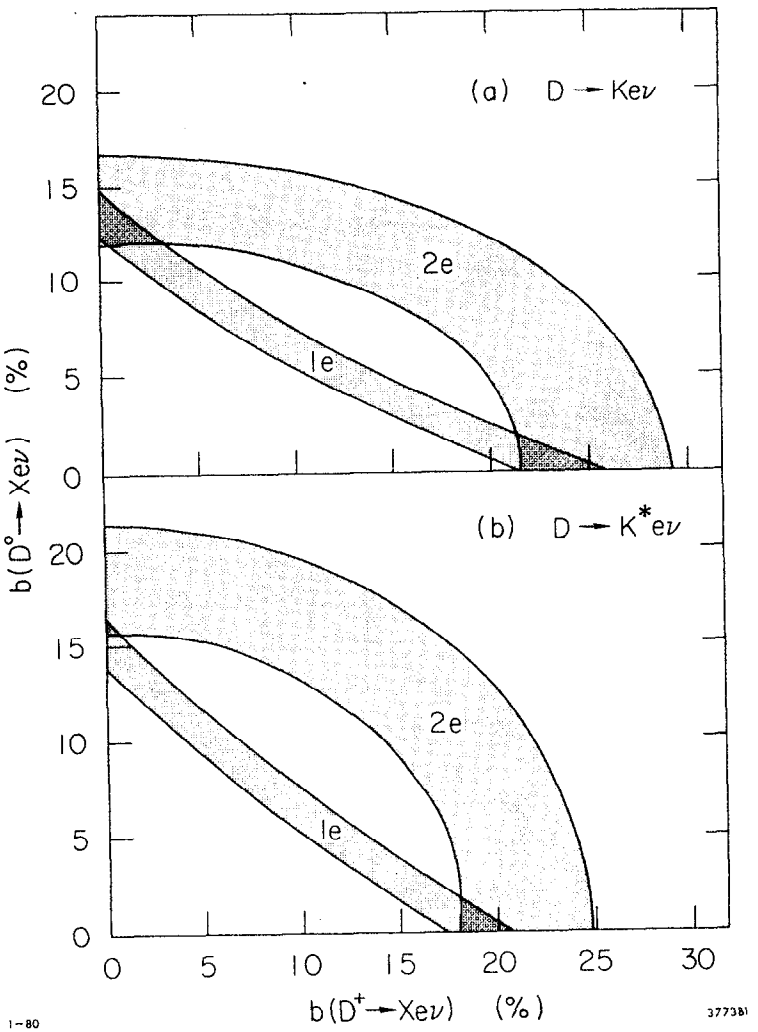

Fig. 6 D^0 and D^+ semi-electronic branching ratios obtained by DELCO from one and two electron events. Curves are ± one standard deviation, for a) D → Keν assumed and b) D→K^*eν assumed for calculation of efficiency [Bacino 80].

TABLE II. Mark II Data on Semileptonic Branching Ratios of the D Mesons at the ψ" (3.77) Resonance

	D^0		D^+	
Total tagged sample	536		330	
Background	59		35	
Net tagged sample	477		295	
	Right sign	Wrong sign	Right sign	Wrong sign
Observed electrons	36	18	39	4
Expected from hadron misidentification	17.4 ± 1.0	11.8 ± 0.9	16.3 ± 1.0	4.2 ± 0.5
Electrons after subtraction for hadron misidentification	18.6 ± 6.1	6.2 ± 4.3	22.7 ± 6.3	$0^{+2.1}_{-0.0}$
Net right sign electrons (right sign - wrong sign)	12.4 ± 7.5		22.7 ± 6.6	
Net contribution from leptonic K decays, $K^-\pi^+$ mislabeling, and false tags	-0.1 ± 1.0		+0.6 ± 0.8	
Net electrons	12.3 ± 7.6		23.3 ± 6.7	
Semileptonic branching fraction (%)	5.5 ± 3.7		16.8 ± 6.4	

IV. Semileptonic Decays of Heavy Quarks

The semileptonic decays of heavy quarks provide a clean laboratory for the study of weak hadronic transitions, in that the matrix element factorizes into a product of weak hadronic and leptonic currents. There has been a great deal of experimental and theoretical effort devoted to the study of $K \to \pi e\nu$ and $\pi\mu\nu$ decay. This work has provided justification for the pole dominance approximation to the q^2 dependence of form factors, and has yielded experimental support for the validity of PCAC techniques.

Semileptonic decays of charmed and bottom quarks are particularly interesting, in that the maximum momentum transfer is large (as much as 1.3 $(GeV/c)^2$ for $D \to Ke\nu$) [Ali 78, Ali 79, Bletzacker 77, Buras 76, Gavela 79, Glück 79, Gronau 77, Yamada 80a, Pasupathy 78]. For $D \to K\ell\nu$ or the Cabibbo suppressed mode $D \to \pi\ell\nu$, the matrix element can be written in terms of two form factors:

$$\langle q|V_\lambda|Q\rangle \propto f_+(q^2)(p_Q + p_q)_\lambda + f_-(q^2)(p_Q - p_q)_\lambda \ ,$$

where

$$q^2 = (p_Q - p_q)^2 .$$

In practice the extraction of the f_- form factor is difficult, as it enters into the rate expression with a coefficient proportional to m_ℓ^2.

The f_+ form factor can then be written in terms of a once-subtracted dispersion relation

$$f_+(q^2) = \frac{f_+(0)}{1 - q^2/m_{F^*}^2} \ , \quad \text{or}$$

expanded in powers of q^2:

$$f_+(q^2) = f_+(0)\ (1 + \lambda_+ q^2 + \ldots .) \ .$$

λ_+ or m_{F^*} can then be extracted from a study of the Dalitz plot distribution of the decay, although this has not yet been done experimentally. The expected q^2 dependence of the f_+ form factor is shown in Fig. 7.

Analysis of $D \to K^*\ell\nu$ (or $\rho\ell\nu$) is complicated by the vector nature of the final state hadron [Barger 77, Kane 80, Kane 79a]. For the K^* case the matrix element has four non-negligible form factors:

$$M \propto \langle q|V_\lambda + aA_\lambda|Q\rangle \ ,$$

$$\langle q|A_\lambda|Q\rangle = F_1^A(q^2)\varepsilon_\lambda + F_2^A(q^2)(p_Q \cdot \varepsilon)p_{q\lambda} + F_3^A(q^2)(q \cdot \varepsilon)q_\lambda$$

$$\langle q|V_\lambda|Q\rangle = iF_1^V(q^2)\ \varepsilon_{\lambda\sigma\mu\nu}\ \varepsilon^\sigma p q^\mu q^\nu \ ,$$

where ε_λ is the polarization of q (e.g., K^*).

Experimental work to this point has been limited to measurement of inclusive semileptonic branching ratios of the D's and the inclusive electron spectrum. Measurements of semileptonic branching ratios are shown in Table III. The world average of 8.0 ± 1.1% indicates that there is indeed a non-leptonic enhancement of a factor of 2, much smaller than that in strangeness changing decays. The separate measurements of D^+ and D^0 branching ratios are discussed in more detail in the section of charmed particle lifetimes.

Figure 8 shows the inclusive electron spectrum for D's at the $\psi''(3.77)$ as measured by DELCO. It will be seen that the data are well fit by a mixture of $Ke\nu$, $\pi e\nu$ and $K^*(890)e\nu$ final states. Form factors have been assumed independent of q^2.

Recently, several authors have calculated the lepton spectrum in heavy quark decay, including order α_s corrections, within QCD [Ali 79a, Cabibbo 79a]. Relevant first order diagrams are shown in Fig. 9.

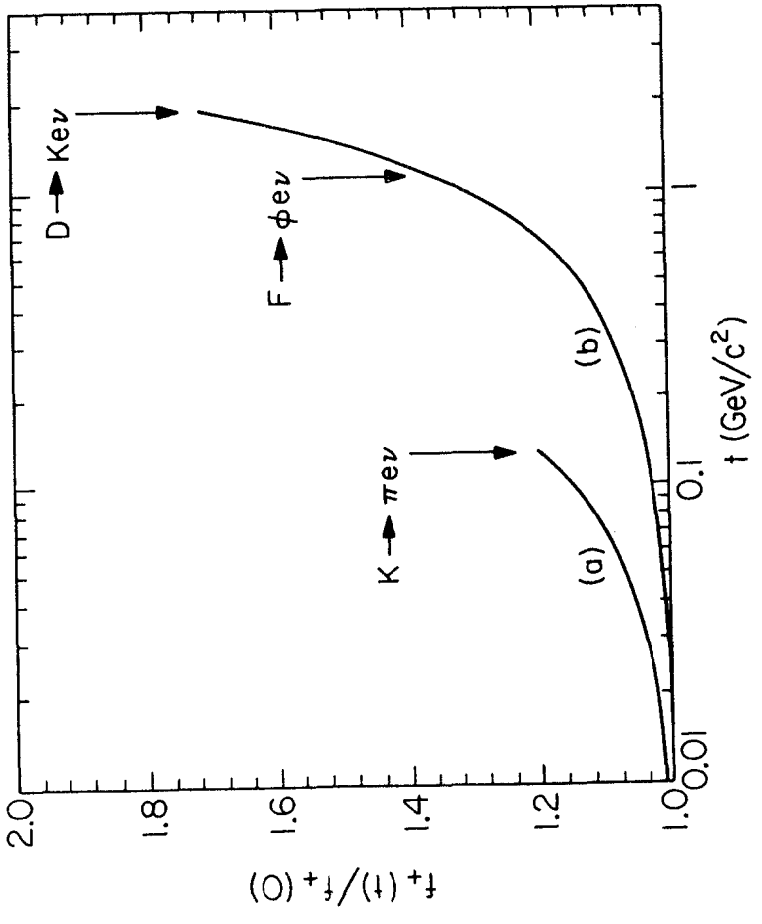

Fig. 7 t dependence of the f_+ form factor for a) $K \to \pi e\nu$ ($K^*(890)$ pole) and b) $D \to Ke\nu$, $F \to \phi e\nu$ (F^* pole).

TABLE III. D Semileptonic Branching Ratios

Group	$\Gamma(D \to eX) / \Gamma(D \to all)$
DASP	8.0 ± 2.0 %
Pb-Glass Wall	7.2 ± 1.8
DELCO	8.0 ± 1.5
Mark II	10.0 ± 3.2
Average	8.0 ± 1.1 %

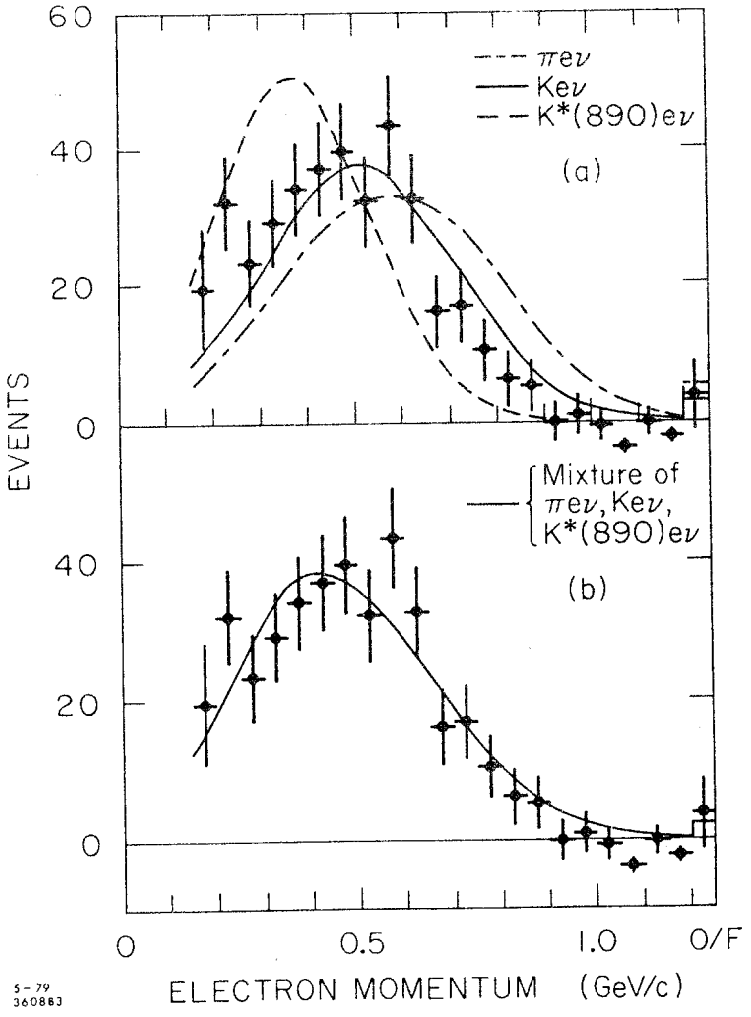

Fig. 8 Inclusive electron spectrum in D decay, from DELCO. Data can be adequately fit by mixture of $\pi e\nu$, $Ke\nu$ and $K^{*}e\nu$ contributions.

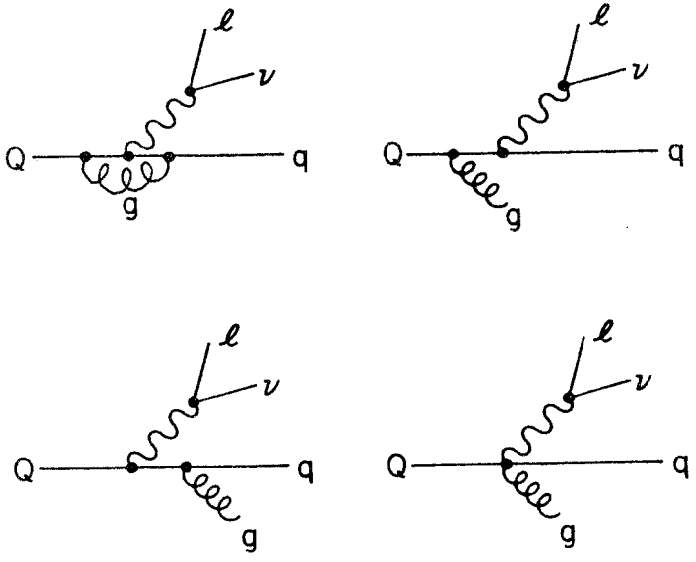

Fig. 9 Order α_s corrections to $Q \to q\ell\nu$ decay.

This approach is complementary to that discussed above, in that it should average the effects of multibody hadronic final states in the sense of duality, much as the QCD corrected value of R gives the average hadronic cross section in e^+e^- annihilation. The calculation is essentially identical to the radiative corrections to μ decay with the identifications:

$$(\mu^-, e^-, \bar{\nu}_e, \nu_\mu) \longleftrightarrow (Q, q, \ell, \nu_\ell) \text{ for } Q = 2/3$$
$$\longleftrightarrow (Q, q, \nu_\ell, \ell) \text{ for } Q = -1/3 \ .$$

One would expect that this approach would be better suited to $b \to c\ell\nu$ than to $c \to s\ell\nu$ decay, but it appears to work well even for the lepton spectra in D decay. Figure 10 shows the fit of Ali and Pietarinen to the DELCO electron spectrum. Figure 11 shows their prediction of the lepton spectrum in b decay. The important test of these ideas will occur when it is possible to make a full Dalitz plot analysis of both the lepton and hadron spectra in semileptonic decay, since the QCD analysis yields a parameter-free prediction of the distribution. It will, of course, be necessary to use information of fragmentation functions to relate quark to hadron spectra.

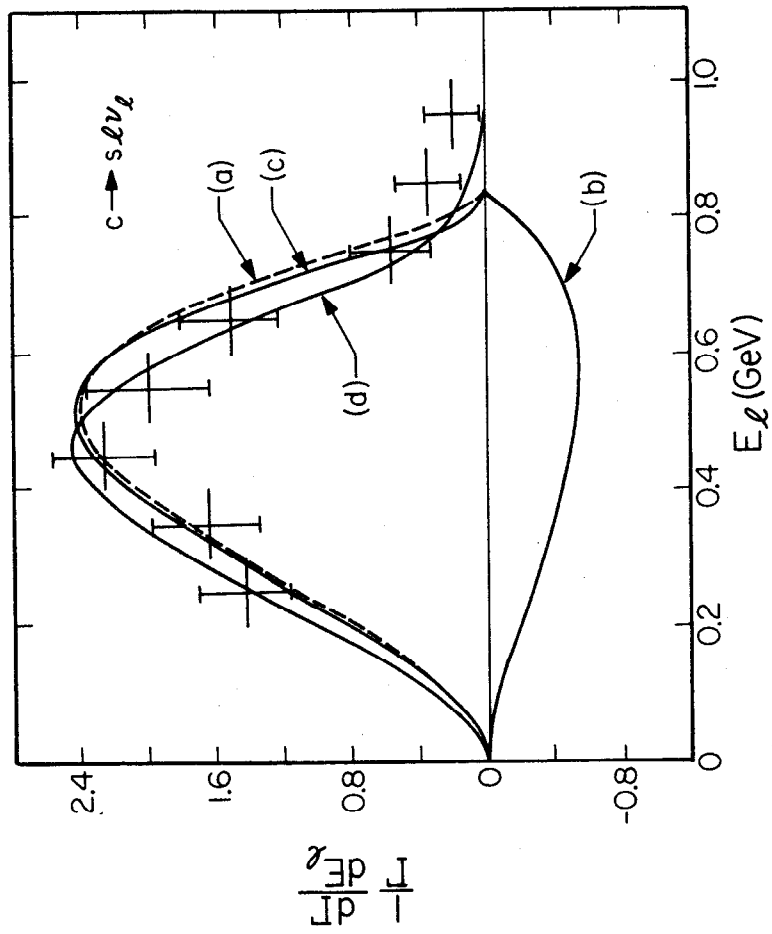

Fig. 10 Inclusive lepton spectrum from c quark decay. a) Free quark model; b) $\theta(\alpha_s)$ corrections; c) $\theta(\alpha_s)$ corrected spectrum, and d) combined effect of one gluon and c quark Fermi motion corrections. [Ali 79a]. Data is from DELCO.

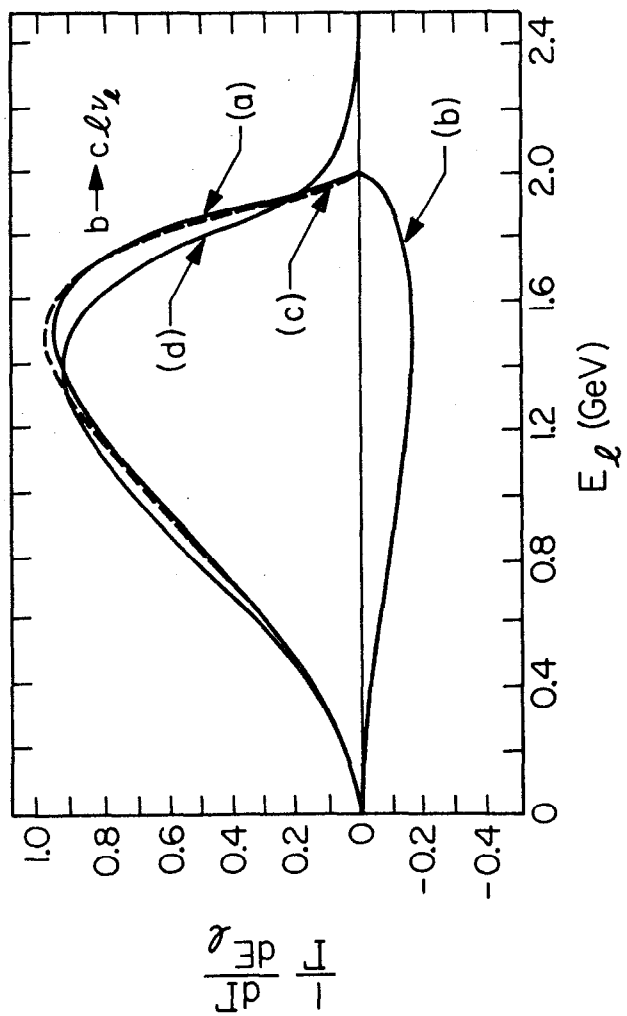

Fig. 11 Inclusive lepton spectrum from b quark decay. a) Free quark model; b) $\theta(\alpha_s)$ corrections; c) $\theta(\alpha_s)$ corrected spectrum, and d) combined effect of one gluon and b quark Fermi motion corrections.

V. Experimental Review

The existence of families of new mesons and baryons stable against strong and electromagnetic decay is a natural consequence of extensions of the old three quark model to include charmed, bottom and top quarks. Each new quark generates a family of stable hadrons in combination with the older generations. Figures 12 through 14 show the expected new mesons and baryons in the six quark model. As of this writing, only indirect evidence, via observation of leptons from semileptonic decays, exists for mesons or baryons containing b quarks. This data will be discussed in a later section. A good deal of experimental information on charmed mesons and baryons exists, however, and this will be reviewed in some detail. Charmed particles have been observed in e^+e^- annihilation, photoproduction and hadron and neutrino induced processes. The emphasis here will be on understanding of the weak decay mechanism, and not on the details of the production process.

The lowest lying charmed mesons are an isodoublet of D mesons ($c\bar{u}$ and $c\bar{d}$) and a singlet F^+ meson ($c\bar{s}$). Both the D° and D^+ mesons have been studied in depth. Little is known about either F^+ production or decay. The lowest charmed baryon state was the first explicitly charmed particle to be observed. There is also evidence for two higher charmed baryon states observed in neutrino reactions.

A. D Mesons

The existence of the ψ'' (3.77) $^3D_1$ resonance [Bacino 78, Rapidis 77, Schindler 80a] in e^+e^- annihilation has made it possible to study the decay properties of D mesons in a particularly fruitful way. As the ψ'' resonance decays into $D^\circ\bar{D}^\circ$ and D^+D^- pairs of low momentum, constrained

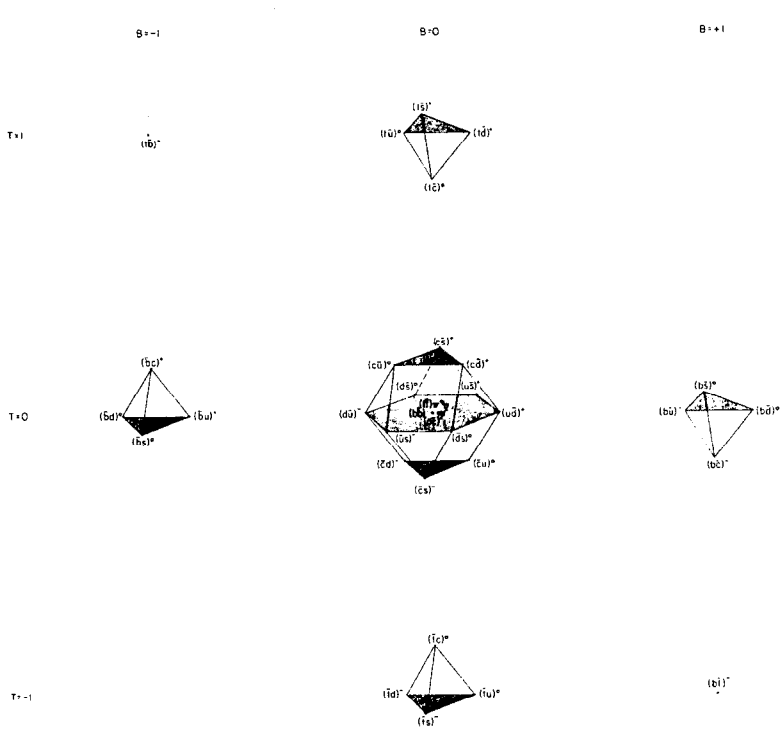

Fig. 12 Weight diagrams for the 0^+ mesons in the six quark model, (Figures 12-14 courtesy C. Quigg).

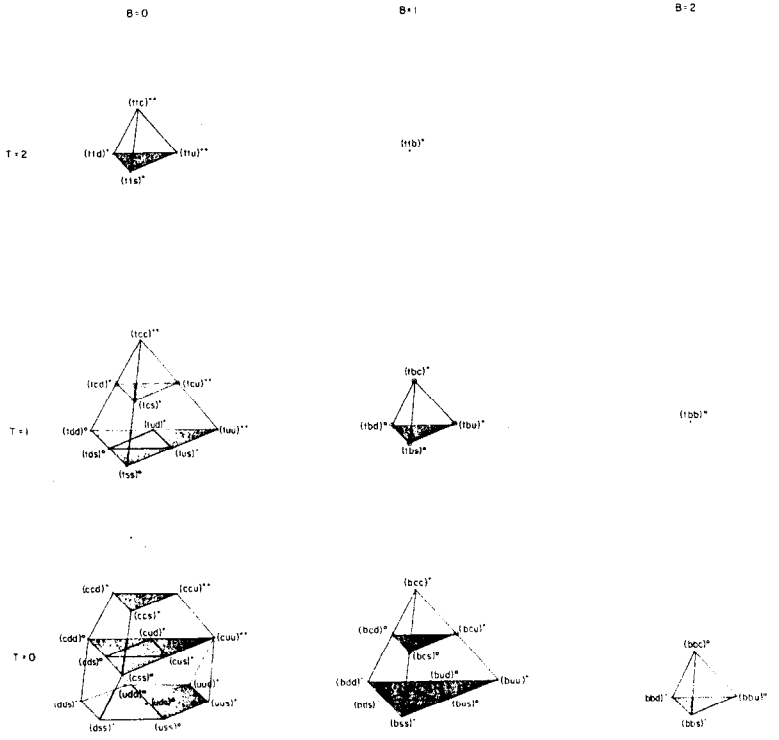

Fig. 13 Weight diagrams for the $\frac{1}{2}^+$ baryons in the six quark model.

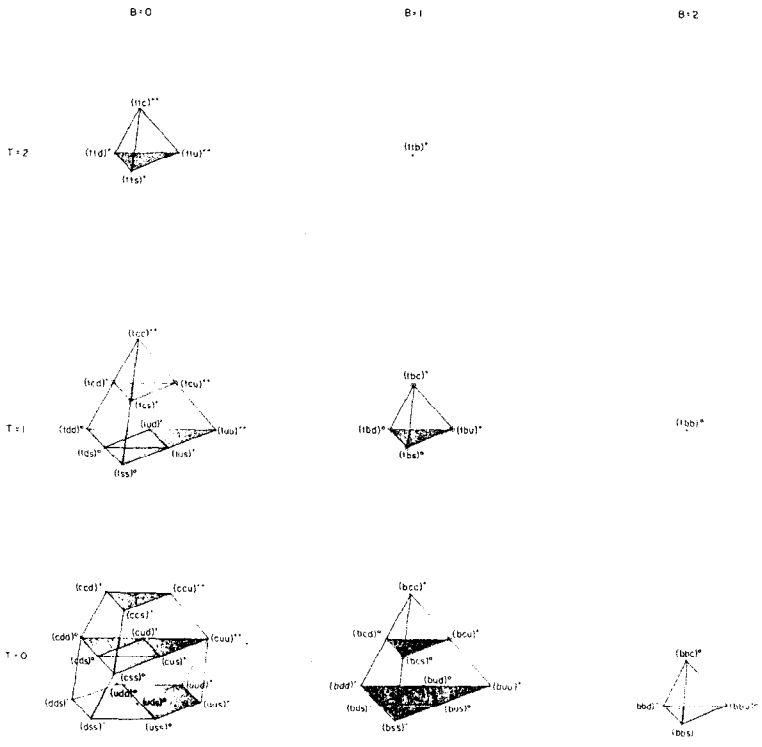

Fig. 14 Weight diagrams for the $\frac{3^+}{2}$ baryons in the six quark model.

kinematic fitting is useful, resulting in excellent mass resolution ($\sigma \simeq$ 2-3 MeV). In addition, secondaries have low momentum, permitting good particle identification by time-of-flight. The result is exclusive state mass reconstruction with good signal to noise ratios. The ψ'' energy is below D^*D thresholds; thus one can be sure that a reconstructed D meson must be accompanied by another. This unique property of the ψ'' has made possible studies of inclusive decay properties of D's via the recoil spectrum. While beam constraint techniques can be applied to the study of charmed baryons, to date data taken have been sufficiently far above threshold so that the many advantages enjoyed in the D studies are not as fully realized.

A good deal of evidence for charmed particle production in hadronic collisions has been compiled [Olsen 80]. A single experiment [Drijard 79] has reported reconstruction of an exclusive state: $D^+ \to K^*(890)\pi^+$. A differential cross section $\frac{d\sigma}{dx}$ $(x > 0.3) \approx 55$ μb (±5%) is seen. This implies a total cross section of .1-1 mb, depending on assumptions concerning x dependence.

$\bar{D}^o$ production has been seen with the Omega spectrometer in a 40-70 GeV photon beam [Aston 80]. Both $K^+\pi^-$ and $K^+\pi^-\pi^o$ modes have been observed. Using branching ratio data from e^+e^-, a total cross section of $\sigma_{\bar{D}^o} = 525 \pm 140$ μb is found. Interestingly, if charmed baryons are assumed to be more centrally produced than charmed mesons, their data can be used to extract a model-dependent cross section for $\bar{D}^o$ production via $\gamma p \to c\bar{D}X$, which is $\sigma_{\bar{D}^o} = 525 \pm 160$ μb. The close agreement implies that most $\bar{D}^o$ are generated by associated production.

Two examples of D^* production by neutrinos with subsequent $D^* \to D\pi$ decay have also been reported [Blietschau 79].

1. Inclusive Properties

A great deal of experimental effort has gone into the study of inclusive properties of charmed particle decays. In most situations, such as in hadron-induced reactions, signal to noise considerations restrict these inclusive studies to leptonic final states. An improvement in signal to noise can be achieved by studying lepton-missing energy (neutrino) correlations [Diament-Berger 79]. The properties of the $\psi''(3.77)$ in e^+e^- annihilation which decays ~50% of the time to $D\bar{D}$ pairs, allow more detailed inclusive properties to be measured, by using "tagged events." The Mark II procedure has been to study the properties of the system recoiling against reconstructed $K^+\pi^-$, $K^-\pi^+\pi^+$ and $K^-\pi^+\pi^+\pi^+$ events. About 300 D^+ tags and 480 D^0 tags with a signal to background ratio of ~3:1 have been employed in these studies [Schindler 80].

Observed and acceptance corrected charged particle multiplicity distributions in the recoil spectrum are shown in Fig. 15. The mean multiplicities, 2.47 ± 0.08 for D^0 and 2.16 ± 0.11 for $D^\pm$ are in good agreement with the previous determination of 2.3 ± 0.3 for both D^0 and $D^\pm$ [Vuillemin 78]. They are, however, in substantial disagreement with early statistical model predictions [Quigg 78].

Measurement of the strange particle content of the recoil spectrum provides a test of the GIM model and of more detailed characteristics of the weak current. Given that a D or $\bar{D}$ has been reconstructed including a kaon of definite strangeness, a Cabibbo-allowed decay of its partner via the GIM scheme will produce a kaon of opposite strangeness. A

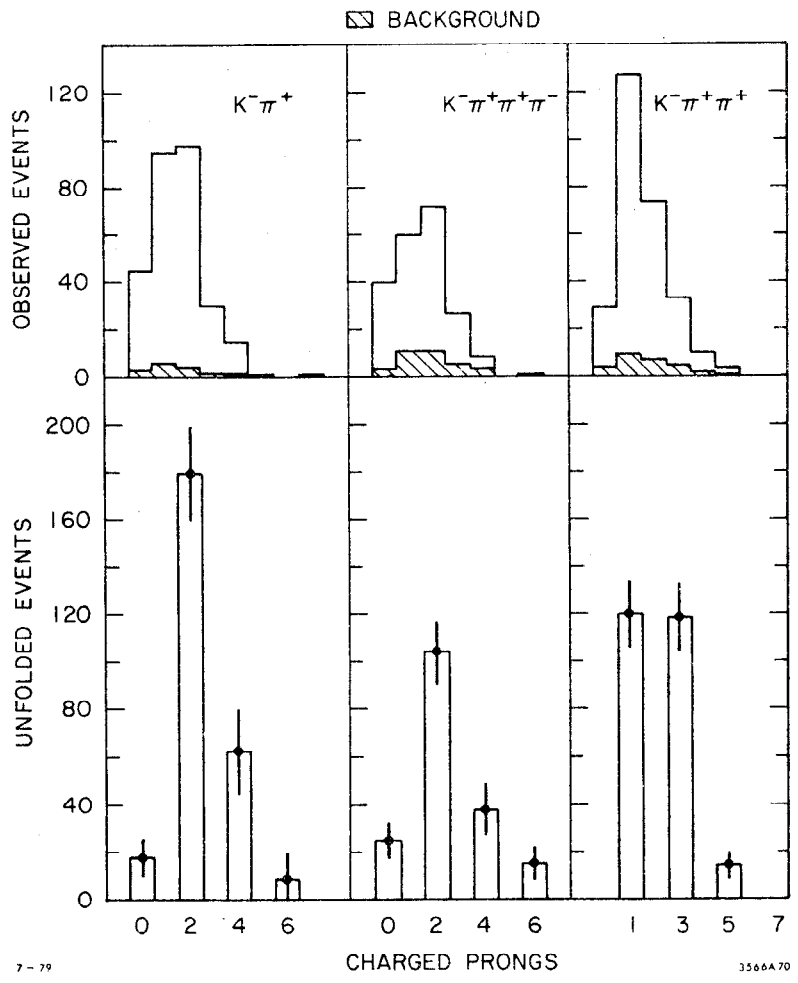

Fig. 15 Observed and corrected charged multiplicities in the recoil spectrum against reconstructed D's at the ψ'' resonance. Mark II data [Schindler 80].

Cabbibo-suppressed decay of the recoil D will yield either no strange particles or two of opposite strangeness. Both doubly Cabibbo-suppressed decays and $D^0\bar{D}^0$ mixing can produce equal strangeness recoils, although these are expected at a level far below the sensitivity of present experiments. Charged kaons are identified in the Mark II by time-of-flight with an efficiency of ~.4, while neutral kaons are identified with lower efficiency (~.09) by the decay $K_s^0 \to \pi^+\pi^-$. Table IV shows the resulting inclusive strange particle branching fractions for the Mark II and earlier Mark I-Pb Glass Wall [Vuillemin 78] experiments. Agreement is generally good within rather large uncertainties. Overall kaon multiplicities are 0.92 ± 0.16 for D^0 decays and 0.77 ± 0.19 for D^+. These are not entirely attributable to Cabibbo-allowed $c \to s$ transitions, however, as a significant fraction have "wrong" strangeness. On the assumption that there are equal numbers of neutral and charged kaons with wrong strangeness and that each kaon of wrong strangeness is accompanied by a kaon of correct strangeness that is not due to a $c \to s$ transition, it is possible to correct the raw results to conclude that kaon multiplicities attributable to the $c \to s$ transition are 0.60 ± 0.20 for D^0 and 0.53 ± 0.22 for D^+. These are to be compared to a fraction 0.90 expected in the naive light quark spectator model. As we shall discuss later, the inclusion of additional diagrams can reduce expected kaon multiplicities.

Inclusive electrons are identified in tagged events by a combination of time-of-flight and shower counter energy distribution information. Electron identification efficiency averages ~.7 while misidentification averages ~.05. Since GIM transitions produce specific strangeness kaons from D decays, it is possible to measure backgrounds by identifying

TABLE IV. Comparison of Strange Particle Branching Fractions Measured by the Mark II (Schindler 80a) and the Lead Glass Wall Experiments (Vuillemin 78)

		D^0(%)	D^+(%)
$B(D \to K^-)$	Mark II	55 ± 11	19 ± 5
	Pb Glass Wall	36 ± 10	10 ± 7
$B(D \to K^+)$	Mark II	8 ± 3	6 ± 4
	Pb Glass Wall	---	6 ± 6
$B(D \to \bar{K}^0$ or $K^0)$	Mark II	29 ± 11	52 ± 18
	Pb Glass Wall	57 ± 26	39 ± 29

"wrong sign" electrons in the recoil spectra. Table II summarizes the Mark II results on inclusive electrons at the ψ''. It is unlikely that D^o and D^+ semileptonic branching ratios are equal. Although their average is consistent with a small-nonleptonic enhancement of a factor of two. The semileptonic partial widths of the D isodoublet are expected to be equal since the decay amplitude has I = 0. Thus the ratio of semileptonic branching ratios also measures the ratio of charged and neutral D lifetimes, as discussed in more detail above. DELCO also measures inclusive electron spectra, identifying electrons very cleanly by means of a large acceptance Čerenkov counter. They find semileptonic branching ratios of <4% at 95% CL for D^o and $22.0\%^{+4.4\%}_{-2.2\%}$ for D^+. Lepton energy spectra from these experiments and two earlier ones are consistent, and indicate approximately equal branching ratios $D \to$ KeV and $K^*(890)$eV.

2. Exclusive Final States of D Mesons

The Mark II collaboration has now identified six hadronic Cabibbo-allowed D^o decays, and five allowed D^+ decays. In addition, two Cabibbo-suppressed D^o decays have been seen and upper limits placed on another allowed D^+ decay and five Cabibbo-suppressed modes. These measurements are made at the $\psi''(3.77)$ resonance [Schindler 80, Abrams 79]. The fundamental measurement is of cross section times branching ratio ($\sigma \cdot B$), but using independent knowledge of the inclusive D meson production cross sections, it is possible to calculate absolute branching ratios. The results are summarized in Tables V - VII. In addition to all charged particle modes, decays involving K^o_s's and π^o's have been seen. K^o_s and π^o candidates are required to satisfy a one-constraint fit in which momenta and angles of the tracks are adjusted to obtain the correct masses.

TABLE V. Cross Section Times Branching Ratio ($\sigma \cdot B$) and Branching Ratio (B) for Cabibbo-favored D Decays as Measured by the Mark II Collaboration (Schindler 80a). The Charge Conjugate Mode is Included. The Error on the Number of Signal Events Includes the Uncertainty in the Background Shape. The Upper Limit is at the 90% Confidence Level.

Mode	Signal	Efficiency	$\sigma \cdot B$(nb)	B(%)
$K^-\pi^+$	263.0 ± 17.0	.386	0.24 ± 0.02	3.0 ± 0.6
$\bar{K}^o\pi^o$	8.5 ± 3.7	.017	0.18 ± 0.08	2.2 ± 1.1
$\bar{K}^o\pi^+\pi^-$	32.0 ± 7.7	.037	0.30 ± 0.08	3.8 ± 1.2
$K^-\pi^+\pi^o$	37.2 ± 10.0	.019	0.68 ± 0.23	8.5 ± 3.2
$K^-\pi^+\pi^+\pi^-$	185.0 ± 18.0	.095	0.68 ± 0.11	8.5 ± 2.1
$\bar{K}^o\pi^+$	35.7 ± 6.7	.090	0.14 ± 0.03	2.3 ± 0.7
$K^-\pi^+\pi^+$	239.0 ± 17.0	.221	0.38 ± 0.05	6.3 ± 1.5
$\bar{K}^o\pi^+\pi^o$	9.5 ± 5.5	.004	0.78 ± 0.48	12.9 ± 8.4
$\bar{K}^o\pi^+\pi^+\pi^-$	21.0 ± 7.0	.015	0.51 ± 0.18	8.4 ± 3.5
$K^-\pi^+\pi^+\pi^-\pi^+$	< 11.5	.021	< 0.23	< 4.1

TABLE VI. A comparison of σ.B measured by the Mark II [Schindler 80a] and the Lead Glass Wall (Mark I) experiment, [Peruzzi 77, Scharre 78].

Mode	σ.B (nb) Mark II $E_{c.m.}$ = 3.771 GeV	σ.B (nb) Pb Glass Wall $E_{c.m.}$ = 3.774 GeV	Difference
$K^-\pi^+$	0.24 ± 0.02	0.25 ± 0.05	-0.01 ± 0.05
$\bar{K}^o\pi^+\pi^-$	0.30 ± 0.08	0.46 ± 0.12	-0.16 ± 0.14
$K^-\pi^+\pi^o$	0.68 ± 0.23	1.4 ± 0.6	-0.72 ± 0.64
$K^-\pi^+\pi^+\pi^-$	0.68 ± 0.11	0.36 ± 0.10	0.32 ± 0.15
$\bar{K}^o\pi^+$	0.14 ± 0.03	0.14 ± 0.05	0.00 ± 0.06
$K^-\pi^+\pi^+$	0.38 ± 0.05	0.36 ± 0.06	0.02 ± 0.08

TABLE VII. Measurements on Cabibbo-suppressed D decays by the Mark II. Upper limits are at the 90% confidence level.

Mode	Number of Signal Events in the Suppressed Mode	Ratio of Efficiencies	Ratio of Branching Ratios
$\frac{\Gamma(\pi^-\pi^+)}{\Gamma(K^-\pi^+)}$	9.3 ± 3.9	1.19	0.033 ± 0.015
$\frac{\Gamma(K^-K^+)}{\Gamma(K^-\pi^+)}$	22.1 ± 5.2	0.84	0.113 ± 0.030
$\frac{\Gamma(\pi^o\pi^+)}{\Gamma(\bar{K}^o\pi^+)}$	< 7.5	1.03	< 0.30
$\frac{\Gamma(\bar{K}^oK^+)}{\Gamma(\bar{K}^o\pi^+)}$	5.6 ± 3.0	0.71	0.25 ± 0.15
$\frac{\Gamma(\pi^-\pi^+\pi^+)}{\Gamma(K^-\pi^+\pi^+)}$	< 21.6	1.12	< 0.084
$\frac{\Gamma(K^-K^+\pi^+)}{\Gamma(K^-\pi^+\pi^+)}$	< 18.0	0.56	< 0.14
$\frac{\Gamma(\pi^-\pi^-\pi^+\pi^+)}{\Gamma(K^-\pi^-\pi^+\pi^+)}$	< 32.2	1.28	< 0.21

The mass resolution of a few MeV is obtained by exploiting the properties of the $\psi''(3.77)$. Since D meson production of the ψ'' occurs only through $D\bar{D}$ final states, it is possible to improve the mass resolution by constraining the sum of measured energies to that of the beam (E_b). For particle combinations with measured total energy with 40-60 MeV of E_b, the invariant mass is written as

$$M_D = \left[E_b^2 - P_D^2\right]^{1/2} .$$

At the ψ'', the D^o and D^+ have momenta of 288 and 255 MeV/c, respectively, with typical uncertainties of <15 MeV/c, while the spread in E_b is typically ~1.3 MeV. Thus the uncertainty in M_D can be dramatically reduced. Detection efficiencies are calculated by a detailed Monte Carlo in which generated events are passed through the same analysis programs as are the data. Figures 16 through 18 show the invariant mass plots for three D^o decays, three D^+ decays and three decays involving π^o's, respectively. Figure 19 shows the two identified Cabibbo-allowed D^o decays, together with the $D^o \to K^-\pi^+$ decay used for normalization. Table VI includes a comparison with previously published $\sigma \cdot B$ determinations [Peruzzi 77, Scharre 78]. With the exception of the $K^-\pi^+\pi^+\pi^-$ mode, there is good general agreement. Absolute branching ratios differ from earlier determinations primarily in that σ_{D^o} and σ_{D^+} at the ψ'' by the Mark II are ~30% smaller than previous values. From the point of view of understanding the D decay mechanism, the large value of $B(D^o \to \bar{K}^o\pi^o)$ will prove most important. D meson masses as determined by the Mark II and previous SPEAR results are summarized in Table VIII.

There is now sufficient data on three body modes from the Mark II to allow study of the Dalitz plot distribution, which are shown in Fig. 20.

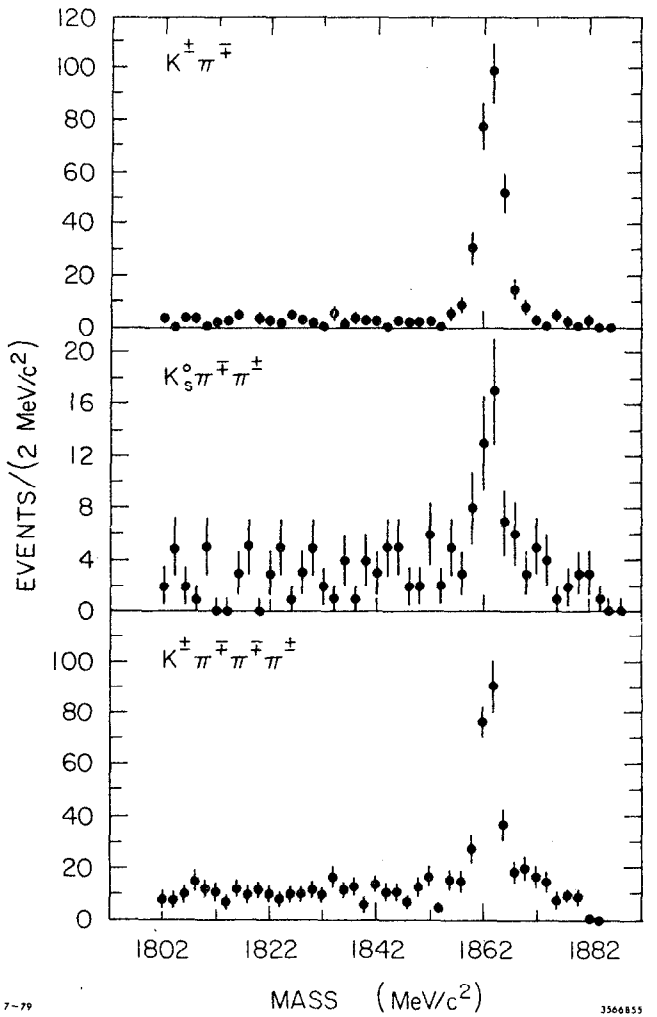

Fig. 16 Invariant mass plots from the Mark II collaboration for three D^o decay modes.

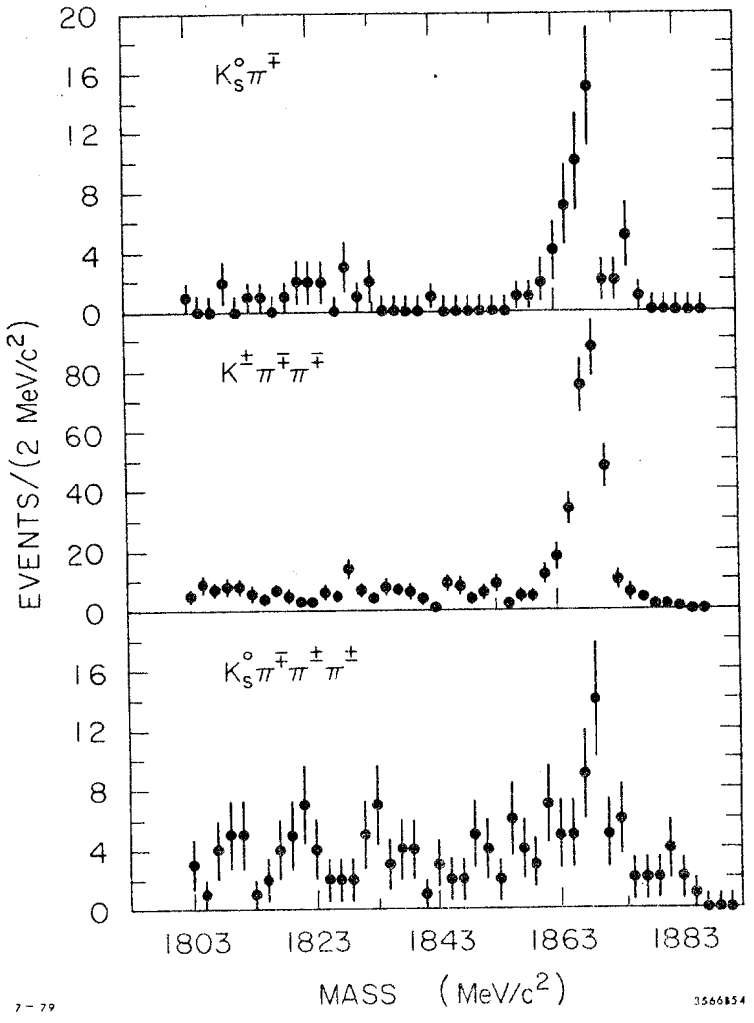

Fig. 17 Invariant mass plots from the Mark II collaboration for three D^{+} decay modes.

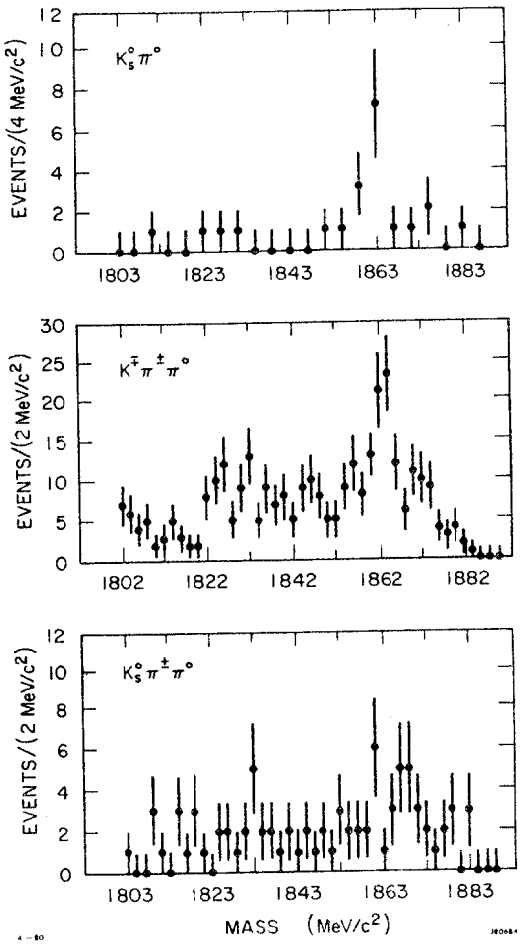

Fig. 18 Invariant mass plots from the Mark II collaboration for three D decays containing π^{o}'s.

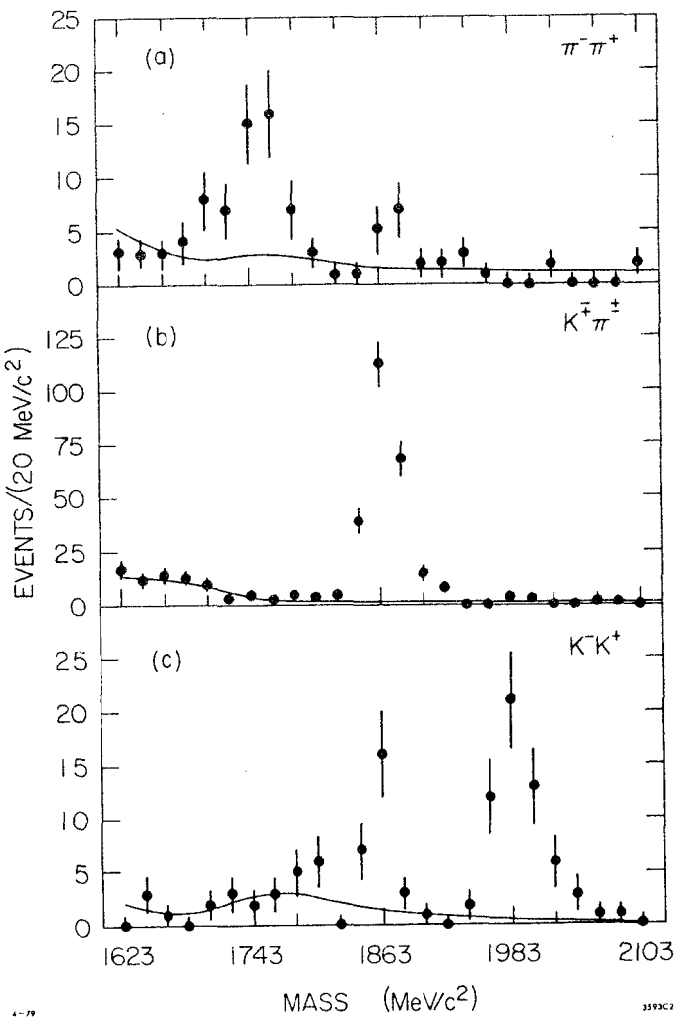

Fig. 19 Invariant mass plots from the Mark II collaboration for two Cabibbo suppressed decays of the D^o, together with $D^o \to K^\mp\pi^\pm$ mode used for normalization.

TABLE VIII. Mass of D mesons determined by the Mark II (Schindler 80a) and by the Lead Glass Wall (Mark I) experiment (Peruzzi 77). The errors include all uncertainties except the 0.13% uncertainty in the SPEAR energy calibration which is common to both experiments. With the SPEAR energy calibration the mass of the ψ is 3095 GeV/c^2.

Measurement	Mark II	Mark I
M_{D^o} (MeV/c^2)	1863.8 ± 0.5	1863.3 ± 0.9
M_{D^+} (MeV/c^2)	1868.4 ± 0.5	1868.3 ± 0.9
$M_{D^+} - M_{D^o}$ (MeV/c^2)	4.7 ± 0.3	5.0 ± 0.8

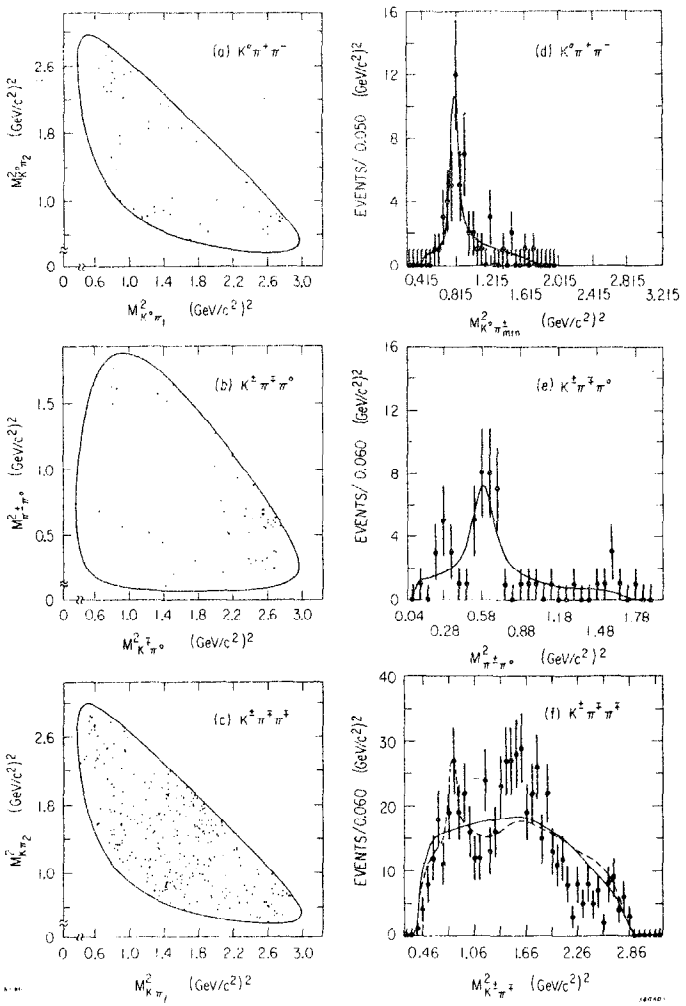

Fig. 20 Dalitz plots for c) $D^o \to K^o_S\pi^+\pi^-$, b) $D^o \to K^-\pi^+\pi^o$ and c) $D^+ \to K^-\pi^+\pi^+$ decays and d) - f) projections of these plots. Data from Mark II collaboration [Schindler 80].

The fraction of these decays resulting in quasi-two-body final states is of special interest, for they allow isolation of the $I = \frac{1}{2}$ and $I = \frac{3}{2}$ components of the final states. The extraction of K^* and ρ components is accomplished by fitting to p-wave Breit-Wigner shapes. The non-resonant component is assumed to be uniformly distributed over the Dalitz plot. Results are summarized in Table IX.

There are significant differences among the Dalitz plots for the three decay modes studied. The $\bar{K}^o\pi^+\pi^-$ shows significant K^{*o} but no ρ^o structure, while the $K^-\pi^+\pi^o$ decay shows a large ρ^+ enhancement. No significant structure is observed in the $K^-\pi^+\pi^+$ Dalitz plot. There are not enough events in the $K_S\pi^+\pi^o$ mode to allow study of the $\bar{K}^o\rho^+$ mode. The amplitudes containing ρ's in the final state are related by the triangle relation

$$A(D^o \to K\bar{\rho}^+) + \sqrt{2}A(D^o \to \bar{K}^o\rho^o) - A(D^+ \to \bar{K}^o\rho^+) = 0 \quad .$$

This leads to an inequality for the branching ratios:

$$B(D^+ \to \bar{K}^o\rho^+) \geq \frac{\tau(D^+)}{\tau(D^o)} \left\{[B(D^o \to K^-\rho^+)]^{1/2} - [2B(D^o \to \bar{K}^o\rho^o)]^{1/2}\right\} .$$

With the Mark II determination of the D lifetime ratio this yields a 90% confidence level limit of

$$B(D^+ \to K^o\rho^+) > 3.8\% \quad .$$

With the addition of the emulsion lifetime measurements [Ushida 80, Ushida 80a], this bound is

$$B(D^+ \to K^o\rho^+) > 11.6\% \quad .$$

TABLE IX. Summary of psuedoscalar-vector branching ratios (%) measured by the Mark II. The upper limit is at the 90% confidence level.

Mode	$\bar{K}^o\pi^+\pi^-$	$K^-\pi^+\pi^o$
Non-resonant	$1.1\ ^{+0.7}_{-0.6}$	< 1.3
$K^{*-}\pi^+$	$4.0\ ^{+1.1}_{-1.2}$	$1.8\ ^{+2.1}_{-1.2}$
$\bar{K}^o\rho^o$	$0.1\ ^{+0.3}_{-0.1}$	---
$\bar{K}^{*o}\pi^o$	---	$1.4\ ^{+2.1}_{-1.4}$
$K^-\rho^+$	---	$7.2\ ^{+2.1}_{-2.3}$

B. F Mesons

In the spectator ansatz one expects a predominance of $s\bar{s}$ containing mesons in the final state of F decay; that is, decays containing η^o or ϕ^o should be significant. A study of inclusive η^o production in e^+e^- annihilation would thus appear to be a useful approach to understanding F^+ production. Such a study was undertaken by the DASP collaboration [Brandelik 77, Brandelik 79]. Their results are shown in Fig. 21. They appear to show an enhancement in inclusive η^o production at $\sqrt{s} = 4.42$ GeV, amounting to $\sigma(\eta_o) \simeq 4$ nb. If one then plots the $\eta^o\pi^+$ invariant mass versus recoil mass for events containing an additional low energy (<200 MeV) photon (Fig. 22), there is a signal of six events, which has been interpreted as the reaction

$$e^+e^- \to F\bar{F}^* \to F\bar{F} + \gamma(<200\ \text{MeV}) \quad (F \to \eta^o\pi^+,\ \eta^o \to \gamma\gamma) \ .$$

Masses were determined to be

$$m(F^+) = 2.03 \pm 0.06\ \text{GeV}$$

and

$$m(F^*) = 2.14 \pm 0.06\ \text{GeV} \ .$$

The cross section x branching ratio is

$$\sigma_F \times B\ (F \to \eta\pi) = 0.41 \pm 0.18\ \text{nb} \ .$$

In addition, it can be determined that

$$\frac{B(F^+ \to \eta^o\pi^+)}{B(F^+ \to \eta^o X)} = 0.09 \pm 0.05 \ .$$

A subsequent search in this region by the Mark II [Lüth 79] has failed to find a comparable signal in either $\eta^o\pi^+$ or $K^+\bar{K}^o$ modes. The limits set are shown in Table X . A recent scan through this energy region by the Crystal Ball collaboration [Bloom 80], whose detector is

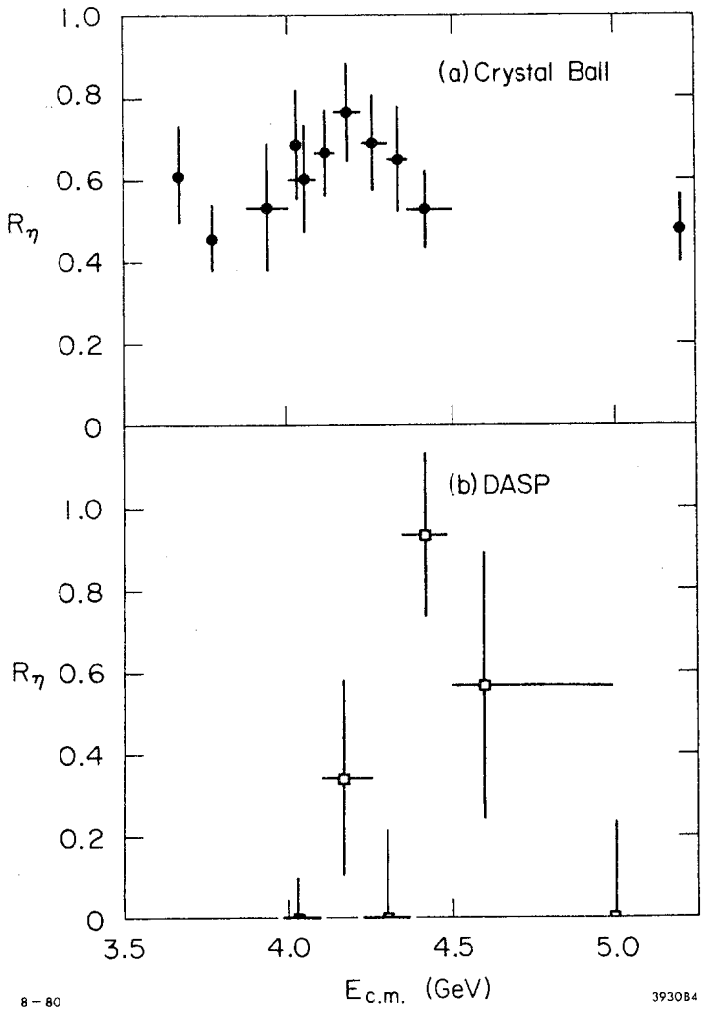

Fig. 21 $R_\eta = \sigma(e^+e^- \to \eta^0 X) / \sigma(e^+e^- \to \mu^+\mu^-)$ vs. $E_{c.m.}$ from a) Crystal Ball and b) DASP.

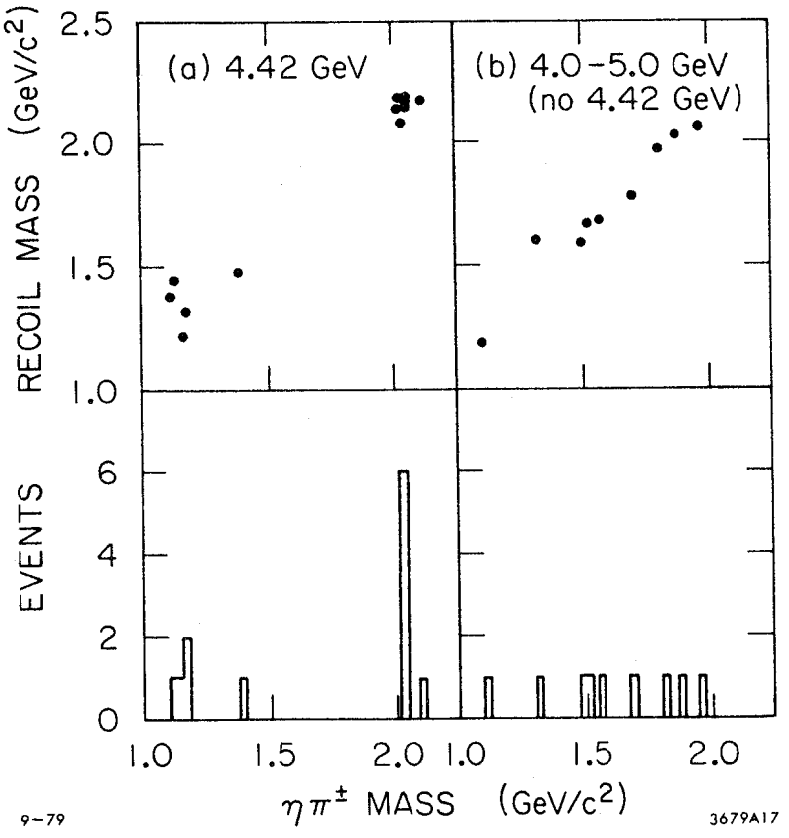

Fig. 22 DASP evidence for the F meson in e^+e^- annihilation.

TABLE X. Mark II limits on $F^{\pm}$ production.

Mode	$\sqrt{s}$	Detection Efficiency (%)	Limit on $\sigma \cdot B$ (95% Confidence)
$\eta^{o}\pi^{\pm}$	4.16	3.1	0.33 nb
	4.42	4.5	0.26
$K^{\pm}\bar{K}^{o}$	4.16	5.8	0.13
	4.42	5.8	0.22

particularly well suited to $\eta^{o} \rightarrow \gamma\gamma$ detection, does find evidence for significant η^{o} production, but this occurs throughout the region $3.68 \leq \sqrt{s} \leq 4.5$ GeV. These data are also shown in Fig. 22. There is no evidence of a peak in η^{o} production in the 4.4 GeV region; the cross section appears flat. There is even significant η^{o} production below charm threshold. The η^{o} signal amounts to ~0.15 η^{o} per hadronic event.

Evidence for F^{+} production does exist in photoproduction and neutrino interactions. The CERN WA4 experiment [Aston 80a] using the OMEGA spectrometer with a 20-70 GeV photon beam has presented preliminary data showing statistically significant potential F^{+} signals in $\eta\pi$, $\eta 3\pi$, $\eta 5\pi$ and $\phi_{\rho}^{o}+$ modes. This experiment employed two triggers, either high multiplicity (4-9 tracks) or a high $p_{\perp}$ photon ($p_{\perp} > 0.6$ GeV/c). Table XI summarizes the WA4 results. No signal was seen in the $\phi^{o}\pi^{+}$ channel ($\sigma \cdot B < 4$ nb). Masses found in all channels are consistent with the DASP value, with $\sigma \cdot B$ in the tens of nanobarn range. The $\eta^{o}\pi^{\pm}$ mass plot, taken with the high $p_{\perp}$ photon trigger, is shown in Fig. 23.

Further evidence on F^{+} production comes from two Fermilab emulsion ν experiments. E531 [Ushida 80a] has two events consistent with an F^{+} hypothesis, while Ammar et al. [Ammar 80] have one. The masses and lifetimes are shown in Table XII.

Thus, while there has as yet been no confirmation of the original DASP inclusive η^{o} result or the observation of FF^{*} production in $e^{+}e^{-}$ annihilation, there is new evidence for the existence of an F^{+} at a consistent mass. It is interesting to note that two of the emulsion events involve four pion final states. These cannot result from W radiation diagrams, but rather are characteristic of the W annihilation process.

TABLE XI. Data on Photoproduction of F Mesons [Aston 80a]

Mode	Mass	σ·B (nb)
$\eta^{o}\pi^{+}$	2.047 ± 0.025	12 ± 3
$\eta^{o}(3\pi)^{\pm}$	2.021 ± 0.015	60 ± 15
$\eta^{o}(5\pi)^{\pm}$	2.008 ± 0.020	20 ± 8

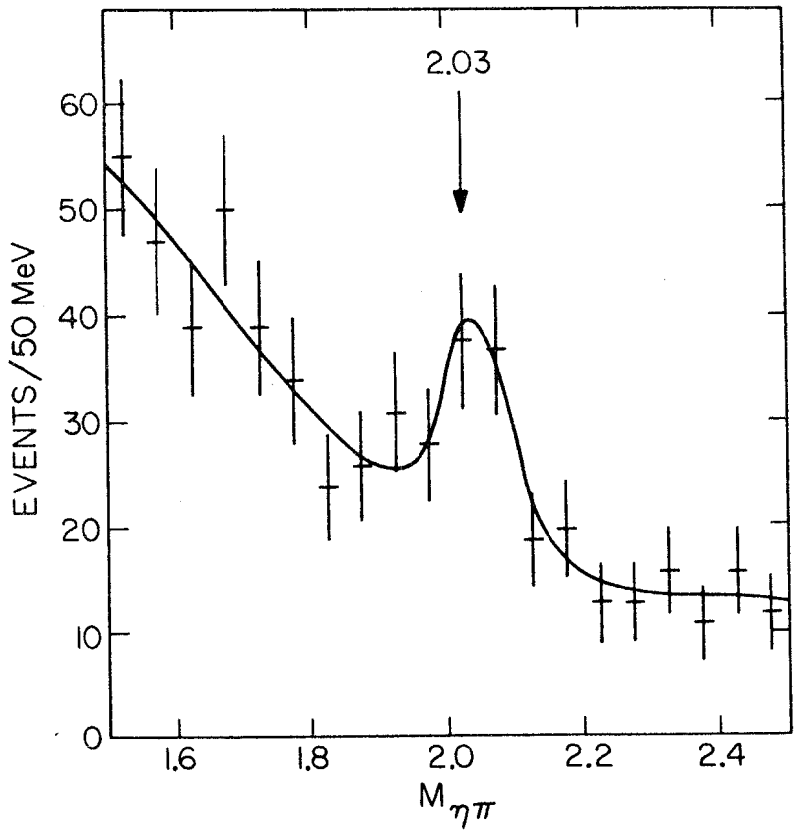

Fig. 23 Evidence for the F meson in the $\eta^{o}\pi^{+}$ channel from the OMEGA photoproduction experiment.

TABLE XII. Masses and Lifetimes of F Mesons Produced in Neutrino Reactions.

Reference	Decay Mode	Mass	Lifetime ($\times 10^{-13}$ sec)
Ushida 80a	$\pi^-\pi^-\pi^+\pi^o$	2.026 ± 0.056	3.70
	$K^+\pi^-\pi^+\bar{K}^o$	2.089 ± 0.121	0.91
Ammar 80	$\pi^+\pi^+\pi^-\pi^o$	2.017 ± 0.025	1.4

C. Charmed Baryons

There is now a large body of experimental evidence for the existence of the Λ_c^+ charmed baryon, and several bubble chamber events which can be interpreted as evidence for the Σ_c^+ and Σ_c^{++}. We will briefly review the data for neutrino, hadron and photoproduction of charmed baryons as well as studies via e^+e^- annihilation.

The first observation of charmed baryons occurred in the BNL 7 foot bubble chamber [Cazzoli 75]. It was an event interpreted as

$$\nu_\mu p \rightarrow \mu^- \Sigma_c^{++}(2.426 \pm 0.012 \text{ GeV}) \rightarrow \Lambda_c^+ \pi^+ \rightarrow \Lambda^o \pi^+ \pi^+ \pi^- ,$$

with

$$m_{\Sigma_c^{++}} - m_{\Lambda_c^+} = 166 \pm 15 \text{ MeV} .$$

Subsequent neutrino results include those from the wideband neutrino beam at Fermilab [Baltay 79] using a heavy neon mix in the 15 foot bubble chamber, in which 20 $\Sigma_c^{++} \rightarrow \Lambda_c^+ \rightarrow$ hadron events were observed. Eight of these are of the type $\Lambda_c^+ \rightarrow \Lambda^o\pi^+$, four were $\Lambda_c^+ \rightarrow \Lambda^o\pi^+\pi^+\pi^-$, seven were $\Lambda_c^+ \rightarrow \tilde{K}^o p$ and one was $\Lambda_c^+ \rightarrow \bar{K}_o p\pi^+\pi^-$. The multipion decay modes showed evidence of $Y^*(1385)$ and $K^*(890)$ enhancements. This experiment found

$$m_{\Lambda_c^+} = 2.257 \pm 0.010$$

and

$$m_{\Sigma_c^{++}} - m_{\Lambda_c^+} = 168 \pm 3 \text{ MeV} .$$

Another bubble chamber experiment, using BEBC with a track sensitive target [Calicchio 80] has presented an event with Λ_c^+ arising from Σ_c^+ production:

$$\nu_\mu p \to \mu^- \Sigma_c^{++} \pi^+ \quad \Sigma_c^{++} \to \Lambda_c^+ \pi^0 \quad \Lambda_c^+ \to K^- p \pi^+$$

In this case the masses found are

$$m_{\Lambda_c^+} = 2.290 \pm 0.003 \text{ GeV}$$

$$m_{\Sigma_c^+} = 2.457 \pm 0.004 \text{ GeV}$$

and

$$m_{\Sigma_c^+} - m_{\Lambda_c^+} = 168 \pm 3 \text{ MeV} \quad .$$

These experiments thus disagree on the Λ_c^+ mass, but would seem to indicate that the Σ_c^{++} and Σ_c^+ masses are likely very close. Other experiments have involved only direct observations of Λ_c^+ production, but these too, show discrepancies in the Λ_c^+ mass.

A signal for $\bar{\Lambda}_c^- \to \Lambda^0 \pi^+ \pi^+ \pi^-$ was reported in photoproduction by experiment E87 [Knapp 76] at a mass of 2.26 ± 0.01 GeV. This observation has not been confirmed in a subsequent experiment of this group, although the decay mode $\Lambda_c^+ \to p\bar{K}_o$ has been reported [Russell 80] at a mass of 2.284 ± 0.001 GeV with a $\sigma \cdot B = 3.2 \pm 0.7$ nb/nucleon (see Fig. 24). Limits (at 90% confidence) were also set on three other decay modes:

$$\Lambda^0 \pi \quad < 0.9 \text{ nb/nucleon} \quad .$$

$$\Lambda^0 \pi\pi\pi \quad < 4.0 \text{ nb/nucleon} \quad .$$

$$pK\pi \quad < 4.5 \text{ nb/nucleon} \quad .$$

With a 2% $\Lambda_c^+ \to pK_s^0$ branching ratio, as suggested by the Mark II (see below), the photoproduction cross section for Λ_c^+ appears to be 150 ± 50 nb/nucleon. This appears to be lower than the F^+ photoproduction

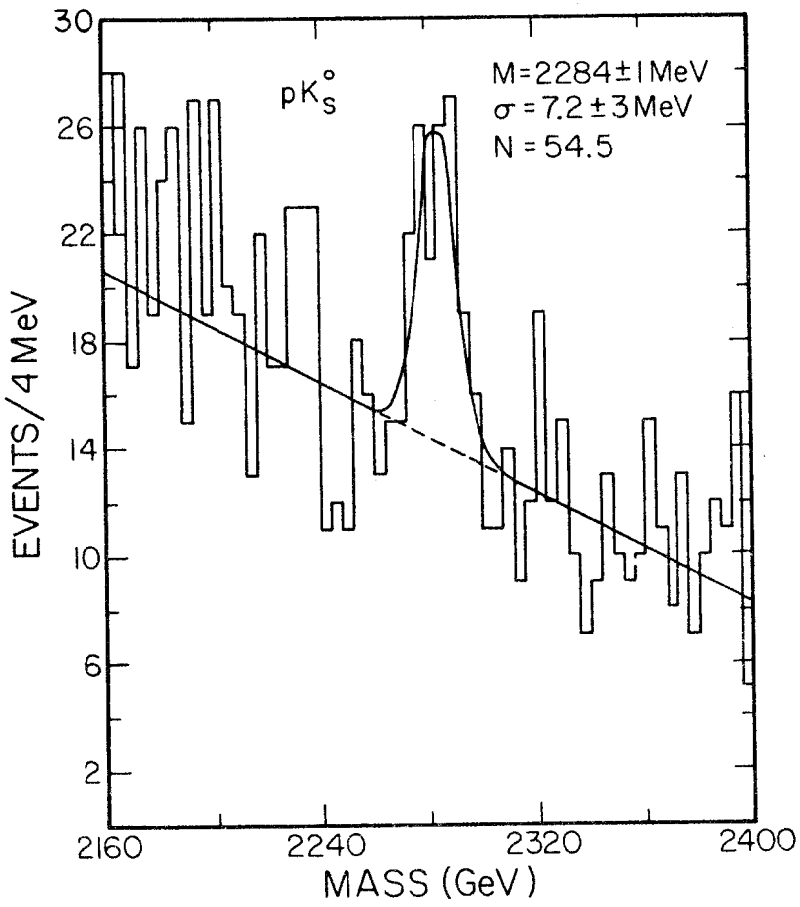

Fig. 24 Evidence for the Λ_c^+ in the pK_s^0 channel from the Columbia-Illinois-Fermilab photoproduction experiment.

results of WA4, assuming (unmeasured) branching ratios of the F^+ of several percent to a typical hadronic mode.

Three experiments at the CERN ISR have reported Λ_c^+ signals in pp interactions. The experiments differ substantially in kinematic acceptance and trigger requirements. The ACHMNR collaboration [Giboni 79] studied diffractive production in the so-called Lampshade magnet. With $0.3 \leq x \leq 0.8$ and $0 \leq p_\perp \leq 1$, they triggered on a single proton in one hemisphere and six or more charged tracks in the opposite hemisphere. They report a 5σ peak consistent with their mass resolution (20 MeV) in $K^-p\pi^+$ and no signal in $K^-p\pi^-$, consistent with a Λ_c^+ decay via the GIM mechanism. The mass is $2.255 \pm 0.002 \pm 0.003$ GeV, with a $\sigma \cdot B = 1.2 < 0.3$ μb. Including uncertainty in efficiency, they conclude $0.7 < \sigma \cdot B < 1.8$ μb. A small signal is also seen in $\Lambda^o\pi^+\pi^+\pi^-$ with $0.3 < \sigma \cdot B < 0.7$ μb. With the Mark II branching ratio this implies $d\sigma/dx \sim 60$ μb (±50%).

Using the Split Field Magnet triggered by a K^- with $p_\perp > 0.5$ GeV/c, the ACCDHW collaboration [Drijard 79a] has observed a peak in $K^{*o}(890)p$ and $K^-\Delta^{++}$. The mass is quoted as $M_{\Lambda_c^+} = 2.26 \pm 0.01$ GeV. $\sigma \cdot B$ values reported are 6.2 and 6.7 μb for the two modes, respectively assuming $d\sigma/dy$ to be constant and 3.0 and 3.3 μb, assuming $d\sigma/dx$ to be constant. Using the $\Lambda_c^+ \to K^-p\pi^+$ branching ratio from the Mark II together with their measured K^* and Δ^{++} fractions, a very large cross section of $d\sigma/dx = 600$ μb from K^*p and 550 μb from $K^-\Delta^{++}$ is implied ($x > 0.3$). Again 50% uncertainties obtain. A nice confirmation of the charmed baryon hypothesis is provided by the fact that a signal in $K^-p\pi^+$ is seen with an electron trigger and none is seen with an e^+ trigger, consistent with diffractive $\Lambda_c^+\bar{D}$ production and subsequent semileptonic decay of the $\bar{D}$.

The third ISR result comes from a UCLA-Saclay group [Lockman 79] at high x ($.75 \leq x \leq .90$). They see peaks in $K^-\pi^+p$ at $2.290 \pm 0.007 \pm 0.008$ GeV ($\sigma \cdot B \approx 2.8 \pm 1.0$ μb) and in $\Lambda^o\pi^+\pi^+\pi^-$ at $2.280 \pm 0.007 \pm 0.008$ GeV ($\sigma \cdot B \approx 2.3 \pm 0.3$ μb). The Mark II $K^-\pi^+p$ branching ratios can again be used to infer $d\sigma/dx \approx 620$ μb (±50%) in this x region.

The three pp production measurements are compared [Olsen 80] in Fig. 25, together with the cross section for Λ^o production. A naive estimate that diffractive Λ_c^+ production should be ~10% of Λ^o production is perhaps borne out, although the consistency of the three results is not great.

A good deal has been learned about the Λ_c^+ from e^+e^- annihilation by the Mark II group at SPEAR [Abrams 80]. Extensive measurements of $R(p + \bar{p}) = \sigma(e^+e^- \to p \text{ or } \bar{p})/\sigma(e^+e^- \to \mu^+\mu^-)$ and $R(\Lambda + \bar{\Lambda})$ indicate threshold behavior characteristic of charmed baryon production in the $4 \leq \sqrt{s} \leq 5$ GeV region. These results, shown in Fig. 26, can be used to estimate branching fraction for specific Λ_c^+ decay modes.

Using 9150 nb^{-1} of data from $\sqrt{s} = 5.2$ GeV and a scan from $\sqrt{s} = 4.5 - 6.0$ GeV, a clean signal is observed in the $K^-p\pi^+$ channel and none in the $K^+p\pi^-$ channel (see Fig. 27). The mass is 2.285 ± 0.006 GeV. A beam constrained fit (which assumes $e^+e^- \to \Lambda_c^+\bar{\Lambda}_c^-$) shows that 26 ± 11% of the signal is produced from $\Lambda_c^+\bar{\Lambda}_c^-$. Dalitz plot projections (Fig. 28) show that $K^-\Delta^{++}$ and K^*p are 17 ± 7% and 12 ± 7% of the $K^-p\pi^+$ signal, respectively. A smaller signal is seen in the $p\bar{K}^o$ mode:

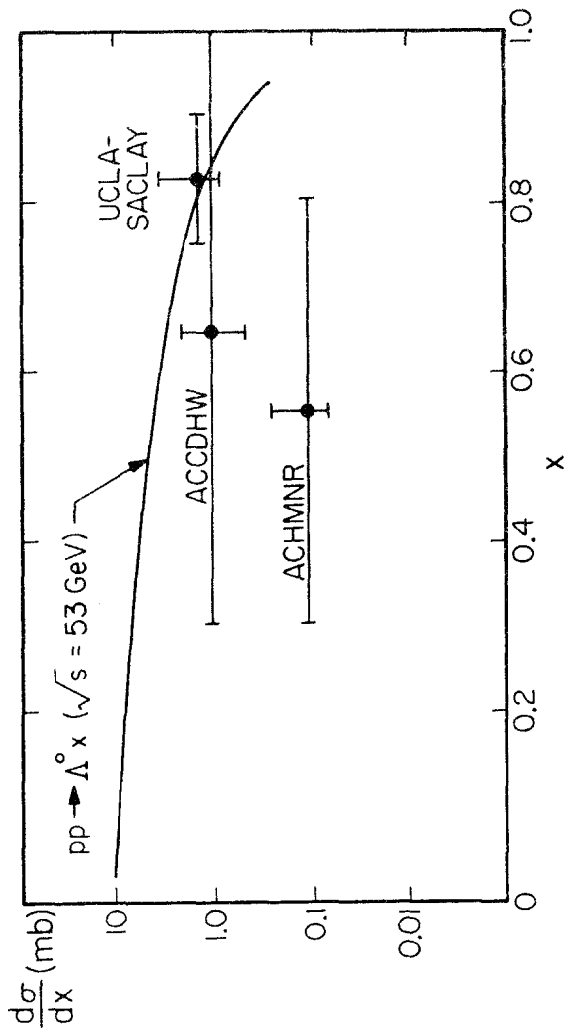

Fig. 25 Charmed baryon production cross sections at $\sqrt{s}$ = 53 GeV compared with inclusive Λ^{o} cross section.

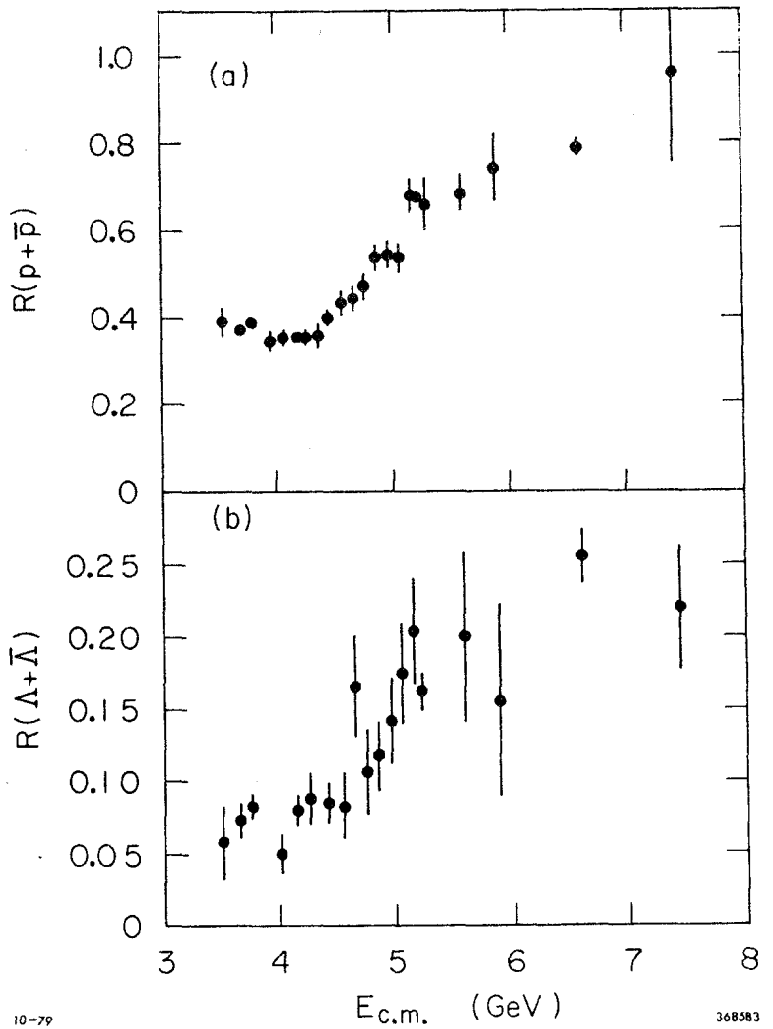

Fig. 26 a) $R(p + \bar{p})$ and b) $R(\Lambda + \bar{\Lambda})$ vs. $E_{c.m.}$ as measured by the Mark II collaboration.

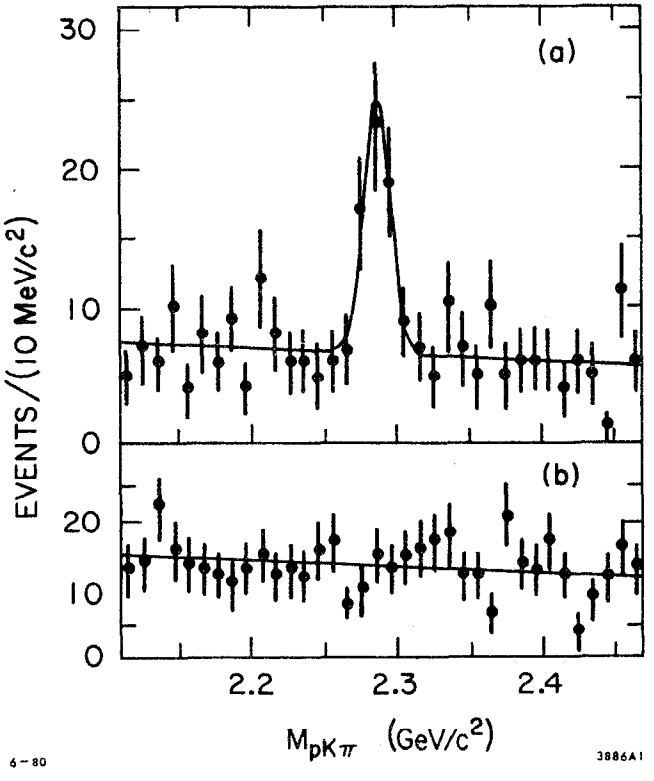

Fig. 27 a) Invariant mass of $pK^-\pi^+$ and $\bar{p}K^+\pi^-$ combinations for recoil masses greater than 2.2 GeV. b) Invariant mass of $pK^+\pi^-$ and $pK^-\pi^+$ and charge conjugates for recoil masses greater than 2.2 GeV. Data of the Mark II collaboration

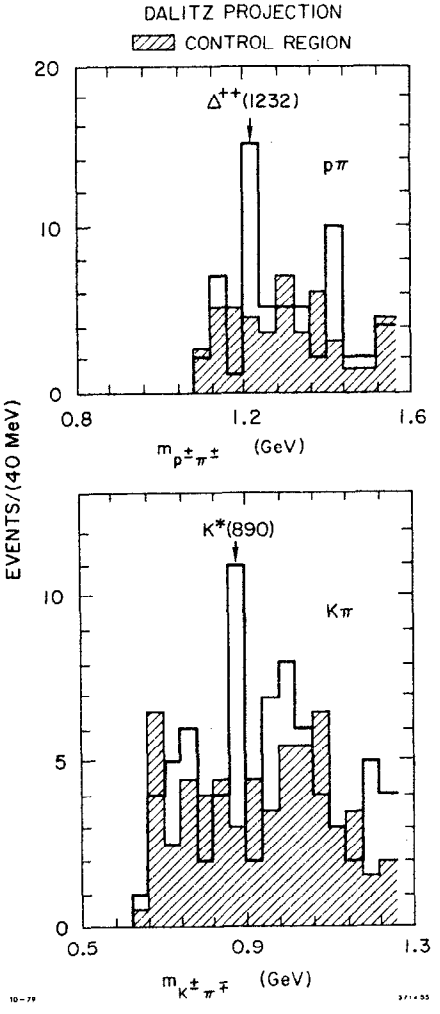

Fig. 28 Dalitz plot projections of the Mark II $\Lambda_c^+ \to pK^-\pi^+$ signal.

$$\frac{B(\Lambda_c^+ \to p\bar{K}^o)}{B(\Lambda_c^+ \to K^- p\pi^+)} = 0.5 \pm 0.25 \quad .$$

90% confidence limits on two other decay modes can also be set:

$$\frac{B(\Lambda_c^+ \to \Lambda\pi)}{B(\Lambda_c^+ \to K^- p\pi^+)} < 0.8$$

and

$$\frac{B(\Lambda_c^+ \to \Lambda^o \pi^+ \pi^+ \pi^-)}{B(\Lambda_c^+ \tau\, K^- p\pi^+)} < 1.4$$

On the assumption that 1) the step in $R(p + \bar{p}) = 0.31 \pm 0.06$ is due entirely to the onset of charmed baryon production, 2) all charmed baryons cascade to the Λ_c^+ state and 3) $\Lambda_c^+ \to p/\Lambda_c^+ \to All = 0.6 \pm 0.1$, we can use the inclusive data and the relation

$$\sigma(\Lambda_c^+ + \bar{\Lambda}_c^+) = \frac{\Delta R(p + \bar{p})}{0.6} \times \sigma_{\mu\mu}$$

to conclude that

$$\sigma(\bar{\Lambda}_c + \bar{\Lambda}_c^+) = 1.7 \pm 0.4 \text{ nb at } \sqrt{s} = 5.2 \quad .$$

Then, individual branching ratios can be extracted:

$$B(\Lambda_c^+ \to K^- p\pi^+) = 2.2 \pm 1.0\%$$

$$B(\Lambda_c^+ \to p\bar{K}o) = 1.1 \pm 0.7\%$$

$$B(\Lambda_c^+ \to \Lambda^o \pi^+) < 1.8\% \text{ @ 90\% confidence}$$

$$B(\Lambda_c^+ \to \Lambda^o \pi^+ \pi^+ \pi^-) < 3.1\% \text{ @ 90\% confidence}$$

From $\Delta R(\Lambda + \bar{\Lambda}) = 0.10 \pm 0.03$, we can also conclude that in charmed baryon decay the ratio $\Lambda/p = 0.41 \pm 0.15$, in good agreement with the theoretical estimate of 0.43 [Körner 79].

The Λ_c mass has been the subject of some controversy. Values have tended to cluster about 2.260 and 2.285 GeV. Figure 29 summarizes the various determinations, in order of date of publication. It appears that the higher mass value is in the ascendency. The exact mass value is of importance not only in and of itself, but because the $\Sigma_c^+ - \Lambda_c^+$ and $\Sigma_c^{++} - \Lambda_c^+$ mass differences are sufficiently close to m_π so that with the higher $m_{\Lambda_c^+}$ value and the bubble chamber $m_{\Sigma_c^+}$ and $m_{\Sigma_c^{++}}$ values, a strong $\Sigma_c - \Lambda_c$ transition could be forbidden. Although there is no clear resolution to this question at this time, it appears likely that the higher Λ_c^+ mass value and a $\Sigma_c - \Lambda_c$ mass difference of ~168 MeV will be found to be correct. Lack of consistency between bubble chamber results makes it impossible to unambiguously resolve the question of the $\Sigma_c^+ - \Sigma_c^{++}$ mass difference.

Study of the recoil spectrum in e^+e^- annihilation above threshold is in principle an excellent way to determine the masses of the excited charmed baryons. Figure 30 shows a recoil mass spectrum from the Mark II. Higher statistics will certainly be required to make this type of study fruitful.

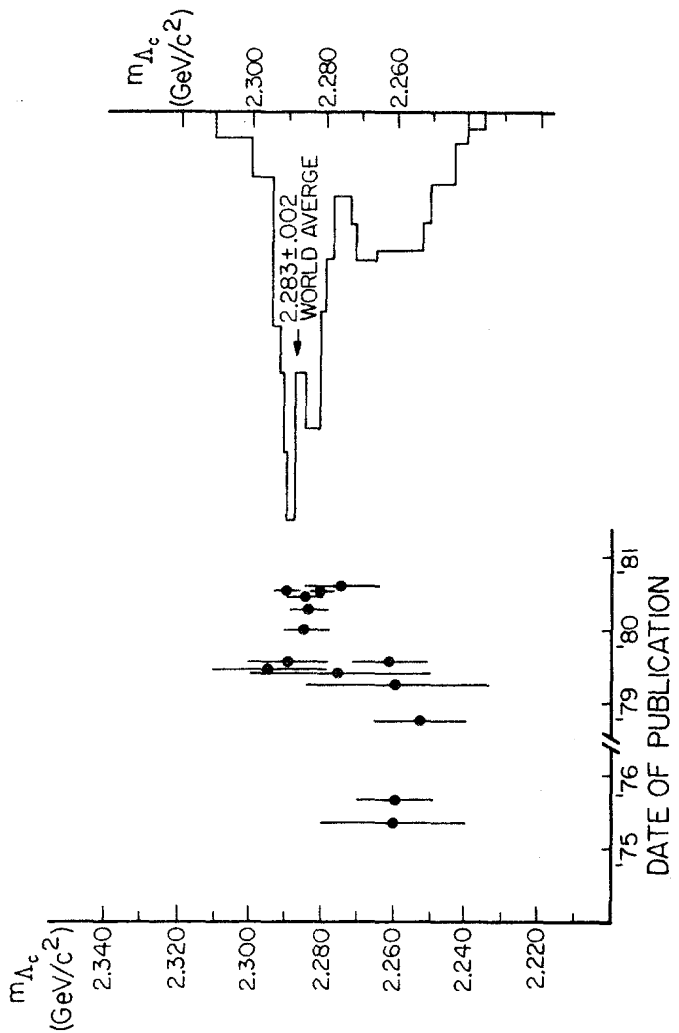

Fig. 29 Measured value of the mass of the Λ_c^+ vs. date of publication and Gaussian ideogram of the mass determinations (courtesy J. Weiss).

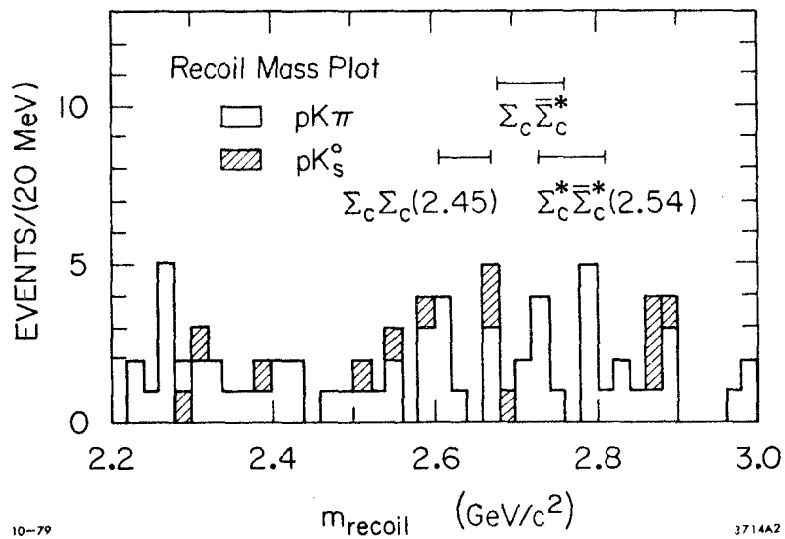

Fig. 30 Mark II recoil mass spectrum against reconstructed $\Lambda_c^+ \to pK^-\pi^+$ and pK_s^o.

VI. The $\Delta I = \frac{1}{2}$ Rule in Strange Particle Decay

While the effective Lagrangian for weak $\Delta S = 1$ transitions

$$\mathcal{L}^{\text{eff}}_{\Delta S=1} \propto (\bar{u}d)(\bar{s}u) + (\bar{u}s)(\bar{d}u)$$

has $|\Delta I| = \frac{1}{2}$ and $\frac{3}{2}$ pieces which are a priori of comparable strength, it is well established experimentally that the $|\Delta I| = \frac{1}{2}$ contribution is dominant. There are many separate pieces of evidence for this; we will briefly list some of them. Perhaps the most striking evidence is the extreme suppression of the decay $K^+ \to \pi^+\pi^o$:

$$\frac{\Gamma(K^o_s \to \pi^+\pi^-)}{\Gamma(K^+ \to \pi^+\pi^o)} \simeq 450 \quad ,$$

indicating that the $\Delta I = \frac{1}{2}$ amplitude is greater than the $\Delta I = \frac{3}{2}$ part by a factor of about 20. Further the $\Delta I = \frac{1}{2}$ property of the Lagrangian leads to predictions for ratios of branching ratios, such as

$$\frac{B(K^o_s \to \pi^+\pi^-)}{B(K^o_s \to \pi^o\pi^o)} = 2 \quad ,$$

$$\frac{B(\Lambda^o \to p\pi^-)}{B(\Lambda^o \to n\pi^o)} = 2 \quad ,$$

and lifetime ratios such as $\tau_{\Xi^o} = 2\tau_{\Xi^-}$, which are experimentally verified. Other consequences are relations between decay asymmetries: $\alpha_{\Xi^o} = \alpha_{\Xi^-}$, $\alpha_{\Lambda \to p\pi^-} = \alpha_{\Lambda \to n\pi^o}$, and symmetries of the Dalitz plots in various $K \to 3\pi$ decays. Table XIII summarizes some of the determinations of $|\Delta I| = \frac{1}{2}, \frac{3}{2}$ and $\frac{5}{2}$ amplitudes in strange particle decay. The size of the $|\Delta I| = \frac{1}{2}$ violations are consistent with an electromagnetic origin. This is unlikely to be the case, however, since electromagnetic couplings, having $\Delta I = 0$ or 1 generate $\Delta I = \frac{1}{2}, \frac{3}{2}$ and $\frac{5}{2}$ amplitudes, while experimentally

TABLE XIII. Evidence for $\Delta I = \frac{1}{2}$ Rule in Strangeness Changing Non-leptonic Decays.

Decay	Amplitudes	Experimental Value
$K \to 2\pi$	$\frac{1}{2}, \frac{3}{2}, \frac{5}{2}$	$\lvert A_{\frac{3}{2}} / A_{\frac{1}{2}}\rvert = 0.45 \pm 0.005$
		$\lvert A_{\frac{5}{2}} / A_{\frac{1}{2}}\rvert = 0.001 \pm 0.003$
$K \to 3\pi$	$\frac{1}{2}, \frac{3}{2}, \frac{5}{2}, \frac{7}{2}$	$\lvert A_{\frac{3}{2}} / A_{\frac{1}{2}}\rvert = 0.06 \pm 0.01$
		$\lvert A(I > \frac{3}{2}) / A_{\frac{1}{2}}\rvert \leq 0.03$
$\Lambda \to N\pi$	$\frac{1}{2}, \frac{3}{2}$	$\lvert A_{\frac{3}{2}} / A_{\frac{1}{2}}\rvert = 0.03 \pm 0.01$ (parity violating) ± 0.03 (parity conserving)
$\Xi \to \Lambda\pi$	$\frac{1}{2}, \frac{3}{2}$	$\lvert A_{\frac{3}{2}} / A_{\frac{1}{2}}\rvert = 0.035 \pm 0.02$ (parity violating), 0.12 ± 0.15 (parity conserving)
$\Sigma \to N\pi$	$\frac{1}{2}, \frac{3}{2}, \frac{5}{2}$	$\lvert A(I \geq \frac{3}{2}) / A_{\frac{1}{2}}\rvert \simeq 0.07 \pm 0.03$

$\Delta I = \frac{3}{2}$ amplitudes dominate the corrections. Thus, it would be necessary to find an explanation for the absence of $\Delta I = \frac{5}{2}$ terms.

Wilson [Wilson 69] proposed that strong interaction corrections could enhance the $|\Delta I| = \frac{1}{2}$ couplings. We can write the $\Delta S = 1$ effective Langrangian as

$$\mathscr{L}^{\text{eff}}_{\Delta S=1} \propto f_1 \mathscr{O}_- + f_+ \mathscr{O}_+$$

where

$$\mathscr{O}_\pm = \frac{1}{2}[(\bar{s}u)_L(\bar{u}d)_L \pm (\bar{s}d)_L(\bar{u}u)_L] \quad .$$

Here

$$(ud)_L = \sum_{\alpha=1}^{3} (\bar{u}_\alpha d_\alpha)_L \quad .$$

The operator $\mathscr{O}_-$ has $I = \frac{1}{2}$, while $\mathscr{O}_+$ has $I = \frac{1}{2}$ and $\frac{3}{2}$ pieces. With the advent of QCD it is possible, in leading log approximation, to calculate the strong interaction corrections to the Lagrangian. In the absence of hard gluon exchange, $f_- = f_+ = 1$. This is modified to

$$f_\pm = \left[\frac{\alpha_s(\mu^2)}{\alpha_s(M_W^2)}\right]^{d\pm} (1 + \alpha_s(\mu^2)) \quad ,$$

where

$$d_- = -2d_+ = \frac{12}{33 - N_F} \quad .$$

For $\mu \sim 1$ GeV we have $f_- = 2.4$, $f_+ = 0.65$. Thus $\left(\frac{f_-}{f_+}\right) \simeq 20$, i.e., there is a $\Delta I = \frac{1}{2}$ enhancement but it is too small to explain the experimental pattern.

There is another class of diagram, shown in Fig. 31 and called a Penguin diagram, which has been proposed as a source of $|\Delta I| = \frac{1}{2}$

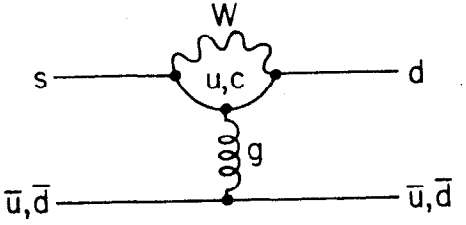

Fig. 31 Penguin diagram which may contribute to the $\Delta I = \frac{1}{2}$ enhancement on strange particle decays.

enhancement [Shifman 77]. Since the gluon carries no isospin, they are pure $\Delta I = \frac{1}{2}$, as well as being Cabibbo-suppressed. Penguin diagrams introduce (V - A) ⊗ (V + A) structure into the Lagrangian:

$$\mathscr{L}^{\text{Penguin}}_{\Delta S=1} \propto (\bar{s}d)_L(\bar{u}u + \bar{d}d + \ldots)_R \quad .$$

Using current quark masses

$$\frac{\langle\pi\pi|(\bar{s}d)_L(\bar{u}u)_R|K\rangle}{\langle\pi\pi|(\bar{s}d)_L(\bar{u}u)_L|K\rangle} \simeq \frac{m_\pi^2}{m_u m_s} \simeq 30 \quad .$$

There is also an MIT Bag model estimate which gives a similar result [Donoghue 80].

We will return to Penguin diagrams in the context of Cabibbo-suppressed D meson decays. Estimates of the matrix elements of Penguin operators are at best semiquantitative and have been controversial. Their relevance to weak decay phenomenology is conjectural, but tantalizing.

VII. Phenomenology of Heavy Quark Weak Decays

A. The Standard Model

Within the context of the Kobayashi-Maskawa model, the dominant weak decay process of charmed particles has the property $\Delta C = \Delta S = 1$. We can write the interaction Lagrangian for non-leptonic decays as

$$\mathscr{L}_{n\ell} = \frac{G}{2\sqrt{2}} c_1(c_1c_2c_3 - s_2s_3e^{i\delta}) \left\{(\bar{u}d)(\bar{s}c) + \text{h.c.}\right\}$$

where

$$(\bar{u}d) = \bar{u}^a \gamma_\lambda(1 + \gamma_5)d_a, \text{ etc.}$$

QCD tells us that these interactions are modified in a calculable way by hard gluon exchange, leading to an effective Lagrangian of the form [Ellis 75, Fakirov 78, Cabibbo 78]:

$$\mathscr{L}_{\text{eff}} = \frac{G}{2\sqrt{2}} c_1(c_1c_2c_3 - s_2s_3e^{i\delta})$$
$$\left\{(f_+ + f_-)(\bar{u}d)(\bar{s}c) + (f_+ - f_-)(\bar{s}d)(\bar{u}c) + \text{h.c.}\right\}$$

The coefficients f_+ and f_- represent the amplitudes which transform as the 6 representation of SU(3) (contained in the 20 of SU(4) and the 15 (contained in the 84), respectively [Einhorn 75]. Using renormalization group techniques, these coefficients can be calculated in leading log approximation:

$$f_\pm = \left[\frac{\alpha_s(m_c^2)}{\alpha_s(M_W^2)}\right]^{d_\pm} \left(1 + \alpha_s(m_c^2)\right) \quad ,$$

where

$$d_- = -2d_+ = \frac{12}{33 - N_F} \quad .$$

N_F is the number of quark flavors and α_s is the QCD coupling constant evaluated at the appropriate value of q^2.

For $N_F = 6$, $m_c \simeq 1.5$ GeV and $\alpha_s(m_c^2) = 0.7$, we have $f_- \simeq 2.15$, $f_+ \simeq 0.68$. It will be useful to define the linear combinations

$$f_1 = \frac{f_+ + f_-}{2} \simeq 1.42$$

$$f_2 = \frac{f_+ - f_-}{2} \simeq -0.74 \ ,$$

as well as the Fierz transformation:

$$(\bar{s}d)(\bar{u}c) = \frac{1}{3}(\bar{u}d)(\bar{s}c) + \frac{1}{2}(\bar{u}\lambda^\alpha d)(\bar{s}\lambda_\alpha c) \ ,$$

which is valid for V-A currents. Here λ^α are color matrices.

The diagrams describing charmed meson decay are then shown in Fig. 32. Diagrams 32c and 32d enter with amplitude 1/3 of 32a and 32b if the color octet piece of the current is ignored. Diagrams 32a-d describe light quark spectator or W radiation processes. Diagram 32e, possible only for D^0 decay, describes a W exchange process, whereas diagram 32f, possible only for F^+ decay, describes a W annihilation process. Early treatments of charmed meson decay [Ellis 75, Fakirov 78, Cabibbo 78] neglected the exchange and annihilation contributions, on the grounds that they were suppressed by a factor of $(m_u/m_c)^2$ due to helicity conservation at the light quark vertex.

In the absence of these diagrams, it is possible to make several unambiguous predictions concerning charmed meson decay. First, if only W radiation contributes, and the light quarks are merely spectators, then the lifetimes of D^0, D^+ and F^+ mesons should be identical. Second, the decay $D^0 \to \bar{K}^0\pi^0$ should be highly suppressed. This is easily seen by referring to Fig. 33. Diagram 33a is proportional to f_1 while diagram 33b is proportional to f_2. Further, the Fierz transformation reduces the

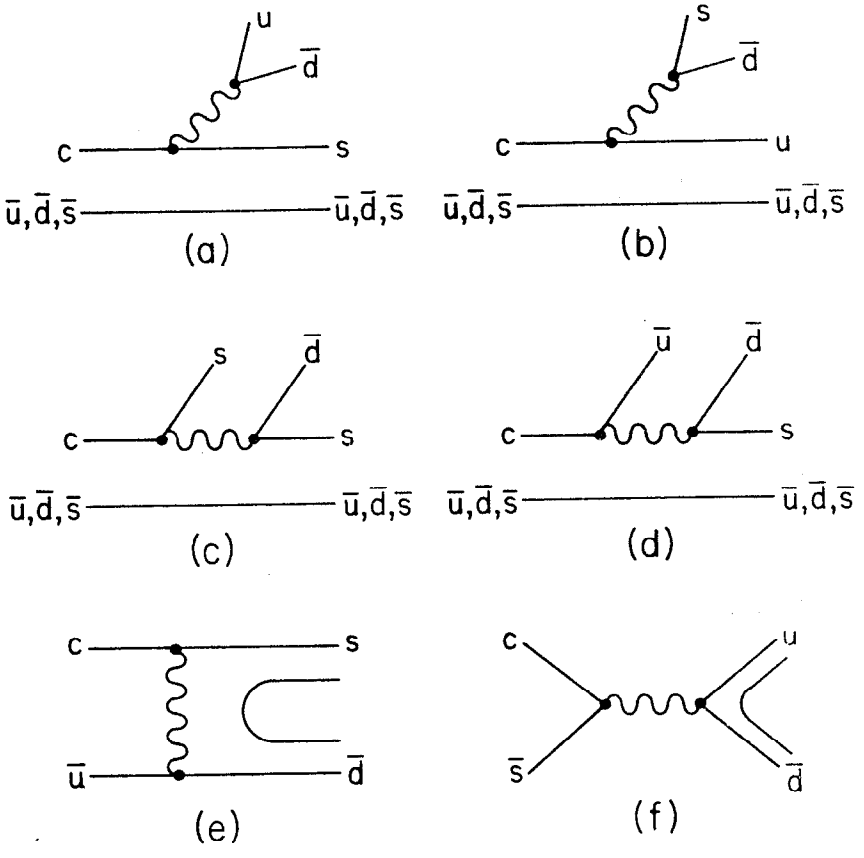

Fig. 32 Possible diagrams describing charmed meson hadronic decay.

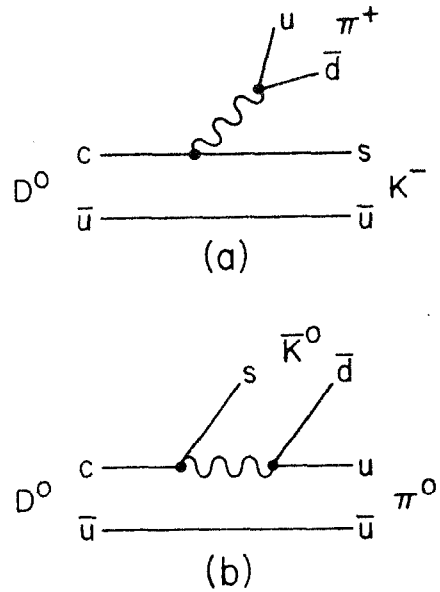

Fig. 33 Spectator diagrams contributing to a) $D^0 \to K^-\pi^+$ decay and b) $D^0 \to \bar{K}^0\pi^0$ decay.

amplitude of 33b by a factor of 3 with respect to 33a. The origin of this suppression is the lack of color matching in the formation of the final state hadrons. Thus, we expect

$$\frac{B(D^0 \to \bar{K}^0\pi^0)}{B(D^0 \to K^-\pi^+)} = \left(\frac{f_2}{f_1}\right)^2 \times \left(\frac{1}{3}\right)^2 \simeq \frac{1}{40} \quad .$$

As we have seen, neither of these predictions is borne out by the data.

Another failure of naive ideas occurs in the Cabibbo-suppressed decays of the D^0. The $\Delta C = 1$, $\Delta S = 0$ piece of the weak Lagrangian can be written as

$$\mathcal{L}_{eff}(\Delta C = 1,\ \Delta S = 0) = \frac{GC}{2\sqrt{2}}\left[(A+B)(\bar{u}c)(\bar{s}s - \bar{d}d) + (A-B)(\bar{u}c)(\bar{s}s + \bar{d}d - 2\bar{b}b)\right] ,$$

where

$$C = c_1(c_1c_2c_3 - s_2s_3e^{i\delta}) = |V_{ud}||V_{cs}|$$

$$A = s_1c_3/c_1 = |V_{us}|/|V_{ud}|$$

$$B = s_1c_1c_2/C = -|V_{cd}|/|V_{ud}|V_{cs}|$$

The diagrams describing Cabibbo-suppressed non-leptonic D^0 decay are shown in Fig. 34. Clearly, up to small corrections for phase space differences, in the SU(3) limit one expects

$$\frac{B(D^0 \to K^-K^+)}{B(D^0 \to K^-\pi^+)} = \frac{B(D^0 \to \pi^-\pi^+)}{B(D^0 \to K^-\pi^+)} \simeq \tan^2\theta_1$$

Data from the Mark II show that these ratios are different by a factor of three. Branching ratios are shown in Table VII. Many explanations have been advanced for this surprising result.

One way to gain insight into Cabibbo-suppressed transitions is to analyze the charm-changing Lagrangian in terms of U spin components:

$$\mathcal{L}_{eff}(\Delta C = 1) = C\left\{U_1^{-1} + \frac{1}{\sqrt{2}}(A+B)U_1^0 + \frac{1}{\sqrt{2}}(A-B)U_0\right\} .$$

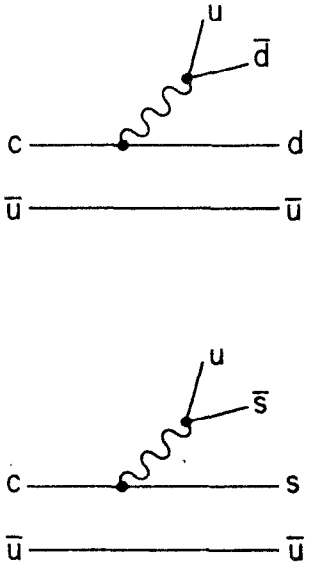

Fig. 34 Spectator diagrams contributing to Cabibbo-suppressed D^o decay.

Letting $\varepsilon = \frac{B}{A}$ and $\rho = \langle \| U_o \| \rangle / \langle \| U_1 \| \rangle$, we have

$$\frac{A(D^o \to K^-K^+)}{A(D^o \to K^-\pi^+)} = \frac{s_1 c_3}{2c_1}\left[(1+\rho) + \varepsilon(1-\rho)\right]$$

$$\frac{A(D^o \to \pi^-\pi^+)}{A(D^o \to K^-\pi^+)} = \frac{-s_1 c_3}{2c_1}\left[(1-\rho) + \varepsilon(1+\rho)\right] \quad .$$

Thus the presence of substantial reduced matrix elements of the U spin 0 component can induce differences in the branching ratios. If $\rho = 1$:

$$\frac{B(D^o \to K^-K^+)}{B(D^o \to K^-\pi^+)} = t_1^2 c_3^2$$

$$\frac{B(D^o \to \pi^-\pi^+)}{B(D^o \to K^-\pi^+)} = \varepsilon^2 t_1^2 c_3^2$$

Wolfenstein [Wolfenstein 79] and, in a more elaborate analysis, Suzuki [Suzuki 79a] have shown that with ρ large and negative (-1.5 to -3) and $\varepsilon \simeq 1.5$, it is possible to produce differences in the K^-K^+ and $\pi^-\pi^+$ branching ratios of the order of a factor of three. Wolfenstein finds that all solutions require a large s_3, which is compatible with the analysis of the first section and requires $\xi = \cos\delta = +1$, thus resolving the ambiguity of the two solutions for the Kobayashi-Maskawa angles.

Interestingly, Penguin diagrams are examples of the U_o portion of the $\Delta C = 1$ Lagrangian. One point of view is that the D^o Cabibbo suppressed decays provide phenomenological evidence for the existence of Penguin diagrams, just as the $\Delta I = 1/2$ rule may provide evidence for these diagrams in $\Delta S = 1$ transitions. The explicit evaluation of Penguin diagrams, however, depends on detailed placement of cutoffs and evaluation of integrals, and has been the subject of a good deal of controversy [Glück 79a, Ishikawa 79, Abbott 79, Fukugita 79, Sanda 79, Finjord 80]. It appears

certain that Penguin diagrams do contribute to the K^-K^+, $\pi^-\pi^+$ rate difference, but perhaps not at a magnitude which can account for the experimentally observed ratio. For example, Finjord estimates

$$\frac{B(D^o \to K^-K^+)}{B(D^o \to \pi^-\pi^+)} = \left[\frac{1 + r(K)}{1 + r(\pi)}\right]^2 \simeq 1 + 0.25\ \alpha_s\ .$$

There is, potentially, an experimental approach to isolating the process responsible for the different Cabibbo-suppressed rates. For example, the decays $D^o \to K^-K^+$ and $D^o \to \pi^-\pi^+$ can, in fact, occur through radiation, W exchange or Penguin diagrams, as is shown in Fig. 35. Other two-body decays occur through some, but not all, of these mechanisms. In $D^o \to \pi^o\pi^o$, the radiation diagram is suppressed by a factor $(f_1/3 + f_2)^2$, so that only exchange and Penguin diagrams should contribute. Were this so, we would expect $B(D^o \to \pi^o\pi^o) \simeq 1/4\ B(D^o \to \pi^+\pi^-)$. In the decay $D^o \to \bar{K}^oK^o$, only the exchange diagram contributes. This decay is further suppressed by the penalty for $s\bar{s}$ pair creation from the vacuum, leading to the expectation $B(D^o \to \bar{K}^oK^o) \simeq 1/4\ B(D^o \to K^-K^+)$.

Without reference to specific decay processes, Wang and Wilczek [Wang 79] have, in enumerating SU(3) relations among decay amplitudes, pointed out that

$$\Gamma(\bar{K}^oK^o) \propto \left\{\left|\frac{V_{us}}{V_{ud}}\right| + \left|\frac{V_{cd}}{V_{cs}}\right|\right\}^2 ,$$

and that

$$\frac{B(D^+ \to \pi^+\pi^o)}{B(D^+ \to \bar{K}^o\pi^+)} = \frac{1}{2}\left|\frac{V_{cd}}{V_{cs}}\right|^2 .$$

Thus measurements of other Cabibbo-suppressed non-leptonic decays can be used to elucidate both the detailed decay mechanisms responsible and provide further insight into the K-M matrix.

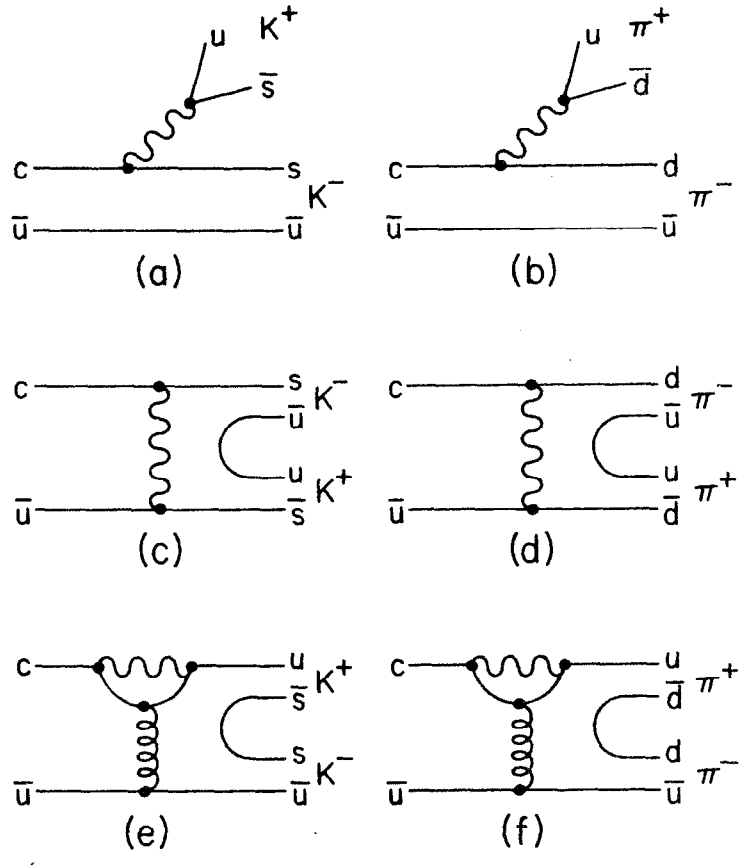

Fig. 35 Examples of Cabibbo-suppressed D^o decays a), b) Spectator diagrams. c), d) Exchange diagrams, and e), f) Penguin diagrams.

It should be pointed out that the cleanest Cabibbo-suppressed D meson decays, from a theoretical standpoint, are the semileptonic processes. Measurements of $B(D^0 \to \pi^- \ell^+ \nu)/B(D^0 \to K^- \ell^+ \nu)$, $B(D^0 \to \rho^- \ell^+ \nu)/B(D^0 \to K^{*-} \ell \nu)$, $B(D^+ \to \pi^0 \ell^+ \nu)/B(D^+ \to \bar{K}^0 \ell^+ \nu)$ and $B(D^+ \to \rho^0 \ell^+ \nu)/B(\bar{K}^{*0} \ell^+ \nu)$, all of which are experimentally accessible in e^+e^- annihilation at the $\psi''(3.77)$ resonance, directly yield information on the basic transitions, unencumbered by the possibility of hadronic final state interactions or details of the decay diagrams themselves.

*Other explanations for the observed phenomenology of the Cabibbo-*suppressed D decays have been proposed. For example, Kane [Kane 79] has investigated a model in which the existence of a doublet of charged Higgs bosons produces couplings proportional to mass, thus enhancing the K^-K^+ mode with respect to $\pi^-\pi^+$. A more conservative approach, due to Barger and Pakvasa [Barger 79], ascribes the observed branching ratios to a combination of effects due to SU(3) breaking as manifested in the leptonic decay constants f_K and f_π and the pattern of K-M angles. These authors point out that the effective Lagrangian between color singlet hadronic states can be factorized as follows, using a Fierz rearrangement. For $D(c\bar{q}) \to M^+(u\bar{\beta}) + P(\alpha\bar{q})$ (the color disconnected diagram):

$$\langle MP|\mathscr{L}_{eff}|D\rangle = \frac{G}{\sqrt{2}} V_{u\beta} V^*_{c\alpha} \chi_+ \langle M|(\bar{u}\beta)|0\rangle \langle P|(\bar{\alpha}c)|D\rangle \quad ,$$

while for $D(c\bar{q}) \to M^0(\alpha\bar{\beta}) + P(u\bar{q})$ (the color connected diagram):

$$\langle MP|\mathscr{L}_{eff}|D\rangle = \frac{G}{\sqrt{2}} V_{u\beta} V^*_{c\alpha} \chi_- \langle M|\bar{\alpha}\beta|0\rangle \langle P|(\bar{u}c)|D\rangle \quad .$$

Here $\chi_\pm = (2f_+ + f_-)/3$.

The single particle matrix elements can then be written in terms of the contribution from the axial current. Relating the meson decay constants to the form factor and assuming pole dominance of the form factor we have

$$A(D \to MP) = \frac{-iG}{\sqrt{2}} V_{u\beta} V^*_{c\alpha} \chi_\pm f_M f_+^{D\to P}(0) \frac{(D^2 - P^2)}{(1 - M^2/s^2)}$$

Each particle's mass is denoted by its symbol; S is the relevant pole mass. f_M is the relevant meson decay constant: $f_M = f_\pi$ for $M = \pi^+$, $f_\pi/\sqrt{2}$ for $M = \pi^0$ and f_K for $M = K^+$ or K^0. Given different decay constants and K-M matrix elements, clearly the rate for $D^0 \to K^-K^+$ can be greater than that for $D^0 \to \pi^-\pi^+$. The results, in fact, are in quantitative agreement with experiment. This approach makes clear predictions for other Cabibbo-suppressed decays, e.g., that branching ratios such as $D^0 \to K^0\bar{K}^0$ and $D^+ \to \bar{K}^0K^+$ will be large, while $B(D^+ \to \pi^0\pi^+)$ will be small.

B. Quark Line Rules

A simple phenomenological description of the charmed meson decay process is given by what are called "quark line rules" [Hayashi 73, Ma 80, Bigi 79, Matsuda 80], which postulate that the total number of quarks and antiquarks is conserved in weak decay processes. This rule can only be approximate, but it serves as a mnemonic for the dominance of I = 1/2 final states in D^0 decay and for the difference of lifetimes. Clearly, the quark line rule prohibits W radiation diagrams, making it the exact antithesis of the light quark spectator approach. The rule allows three diagrams for two-body meson decays (see Fig. 36), corresponding to the three possible ways of including internal W propagators with Q = 2/3, 1/3 quarks. Diagram 36c is Cabibbo-suppressed. For specific charmed meson decays, the Cabibbo-allowed diagrams are shown in Fig. 37. Only the exchange diagram contributes to D^0 decay, only the annihilation diagram to F^+ decay and neither to D^+ decay. Crudely, then, one would expect $\tau(F^+) \simeq \tau(D^0) < \tau(D^+)$. In addition, since the exchange is isovector,

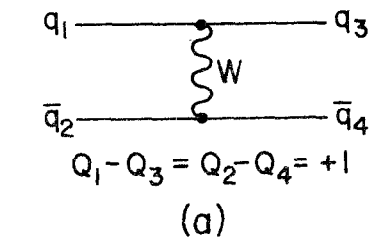

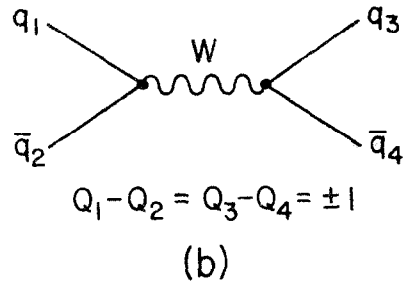

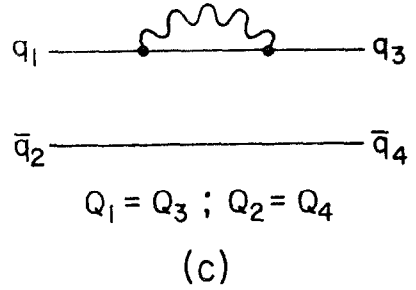

Fig. 36 Diagrams contributing to processes in which the total number of quarks and antiquarks is conserved in the decay.

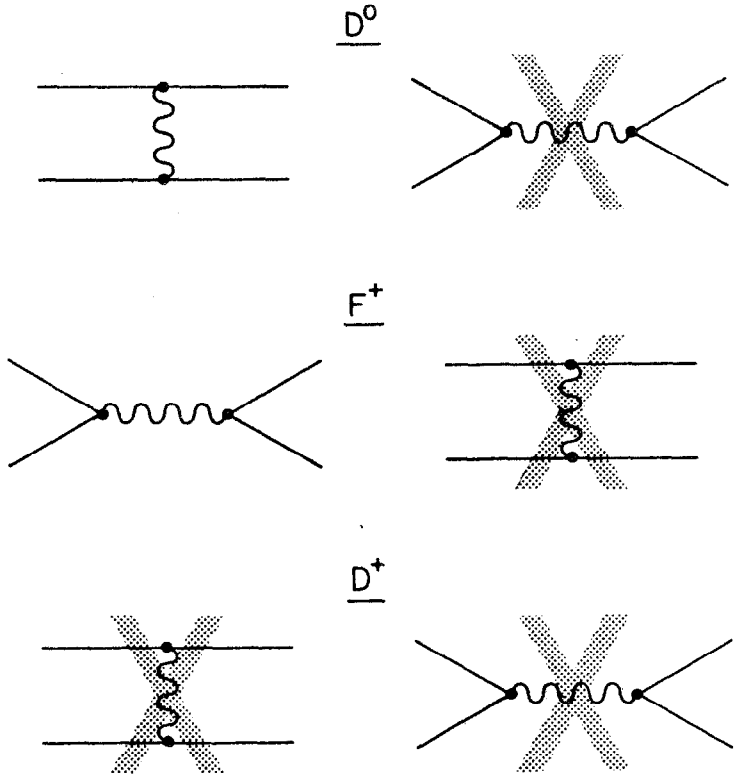

Fig. 37 Diagrams allowed by quark line rule as applied to charm meson decay. Shaded diagrams obey the rule but are not allowed due to specific quark content of the mesons.

the two-body final states of the D^o should be I = 1/2 and those of the F^+ should be I = 1.

The isovector nature of the exchange also has the effect of forbidding the decay $F^+ \to \pi^+\pi^o$. This is easily seen, since $\pi^+\pi^o$ in an s state must have I = 2, while the F^+ is an isospin singlet. Since $\mathscr{L}_{eff}$ transforms as the charged components of an isovector, the decay is forbidden.

Quark line rules cannot be exact. It is interesting to parametrize the contribution of spectator and non-spectator diagrams to ascertain their relative contributions in D meson decays [Barger 80a]. Taking N as the reduced rate for c quark decay, including short distance factors and L as the semileptonic rate, and assuming one effective Cabibbo angle, we can parametrize the spectator contributions as:

$$\Gamma(c \to s\bar{u};\ s\bar{s};\ d\bar{u};\ d\bar{s}) = (\cos^4\theta;\ \cos^2\theta\ \sin^2\theta;\ \cos^2\theta\ \sin^2\theta;\ \sin^4\theta)N$$

$$\Gamma(c \to s\ell\nu;\ d\ell\nu) = (\cos^2\theta;\ \sin^2\theta)L/2$$

Radiative gluon corrections are included in N and L.

The non-spectator diagrams can be parametrized as:

$$\Gamma_g\left(D^o(c\bar{u}) \to s\bar{d};\ d\bar{d};\ s\bar{s};\ d\bar{s}\right) = (\cos^4\theta;\ \cos^2\theta\ \sin^2\theta;\ \cos^2\theta\ \sin^2\theta;\ \sin^4\theta)f_1^2G(D^o)$$

$$\Gamma_g\left(D^+(cd) \to ud;\ us\right) = (\cos^2\theta\ \sin^2\theta;\ \sin^4\theta)f_2^2G(D^+)$$

$$\Gamma_g\left(F^+(cs) \to ud;\ us\right) = (\cos^4\theta;\ \cos^2\theta\ \sin^2\theta)f_2^2G(F^+) \quad ,$$

explicitly allowing for the removal of helicity suppression by radiation of gluons.

The only purely leptonic decay which need be considered is $F^+ \to \tau^+\nu_\tau$:

$$\Gamma_{F \to \tau\nu} = \frac{\cos^2\theta}{8\pi}\, G_F^2 f_F^2 m_F m_\tau^2 (1 - m_\tau^2/m_F^2)^2 \quad .$$

Barger *et al.* assume the rather large value $f_F \approx 430$ MeV. The total decay rates are then:

$$\Gamma(D^o) = L + N + f_1^2 G(D^o)$$

$$\Gamma(D^o) = L + N + f_1^2 \sin^2\theta\ G(D^+)$$

$$\Gamma(F^+) = L + N + f_2^2 \cos^2\theta\ G(F^+) + \Gamma_{F \to \tau\nu} \quad .$$

The bulk of the differences between the reduced rates, the G's, are due to SU(3) breaking, which can be estimated:

$$G(D^o) : G(D^+) : G(F^+) = 1 : 1 : r \quad ,$$

$$r = \frac{|\psi(0)|_F^2}{|\psi(0)|_D^2}\left(\frac{m_F}{m_D}\right)^4\left(\frac{m_u}{m_s}\right)^2 \approx 0.55 \quad .$$

The non-spectator contributions to the total inclusive rate are then in the ratio:

$$\Gamma_g(D^o) : \Gamma_g(D^+) : \Gamma_g(F^+) = f_1^2 : f_2^2 \sin^2\theta : f_2^2 \cos^2\theta\ r$$

$$1.9 : 0.03 : 0.26 \quad .$$

Charmed meson lifetimes can then be related:

$$\frac{\tau(D^+)}{\tau(F^+)} = 1 + \Delta(r\cos^2\theta - \sin^2\theta) + \tau(D^+)\Gamma_{F \to \tau\nu}$$

where

$$\Delta \equiv \frac{f_2^2}{(f_1^2 - \sin^2\theta\ f_2^2)}\left(\frac{\tau(D^+)}{\tau(D^o)} - 1\right) \quad .$$

Figure 38 shows the relation between $\tau(F^+)/\tau(D^+)$ and $\tau(D^+)/\tau(D^o)$ for different $F \to \tau\nu_\tau$ branching ratios. It is therefore expected that the F^+ and D^+ lifetimes will be more nearly equal than the D^+ and D^o lifetimes. On the basis of the limited data on F^+ lifetimes, the expectation does not appear to be well realized.

This analysis can be extended to Cabibbo-suppressed decays alone, predicting that F^+ suppressed decays will lie in the range 4-8%, while D^+ suppressed decays could be larger, as much as 12%. This is in accord with the experimental data on the inclusive kaon content in D^+

and D^o decays. A further consequence of non-spectator diagrams in F^+ decay is the appearance of substantial rates for final states with three or more pions [Nussinov 77]. These could amount to as much as 30% of the total decay rate. It is worth noting that the emulsion events have been of this type.

The non-spectator diagrams also offer a possible explanation for the observed pattern of $D \to K\pi$ branching ratios. This is so because the exchange diagrams do not suffer from color suppression. Barger *et al.* have derived the following triangle inequality which follows directly from the $(I, I_z) = 1$ transformation property of the effective Lagrangian:

$$\frac{1}{2}\left[\left(B(D^o \to K^-\pi^+)\right)^{1/2} - \left(B(D^+ \to \bar{K}^o\pi^+)\,\frac{\tau(D^o)}{\tau(D^+)}\right)^{1/2}\right]^2 \leq B(D^o \to \bar{K}^o\pi^o) \leq$$

$$\frac{1}{2}\left[\left(B(D^o \to K^-\pi^+)\right)^{1/2} + \left(B(D^+ \to \bar{K}^o\pi^+)\,\frac{\tau(D^o)}{\tau(D^+)}\right)^{1/2}\right]^2 .$$

These bounds are, in fact, consistent with experiment.

This type of analysis can be extended to include the Λ_c^+ lifetime. In the case of charmed baryon decay, the exchange process $cd \to su$ is not helicity suppressed, and such diagrams must be included along with the spectator diagram in an estimate of the total rate [Barger 79b]. In Λ and Σ hyperon decays, non-spectator interactions have been found to be necessary to explain the large non-leptonic decay rate and the $\Delta I = 1/2$ rule [Schmid 77, Le Yaouanc 77]. Körner *et al.* [Körner 79] also included exchange diagrams in their calculation of two-body and quasi-two-body branching ratios of charmed baryons. Barger *et al.* calculate the exchange diagram in the free quark model, relating its magnitude to the

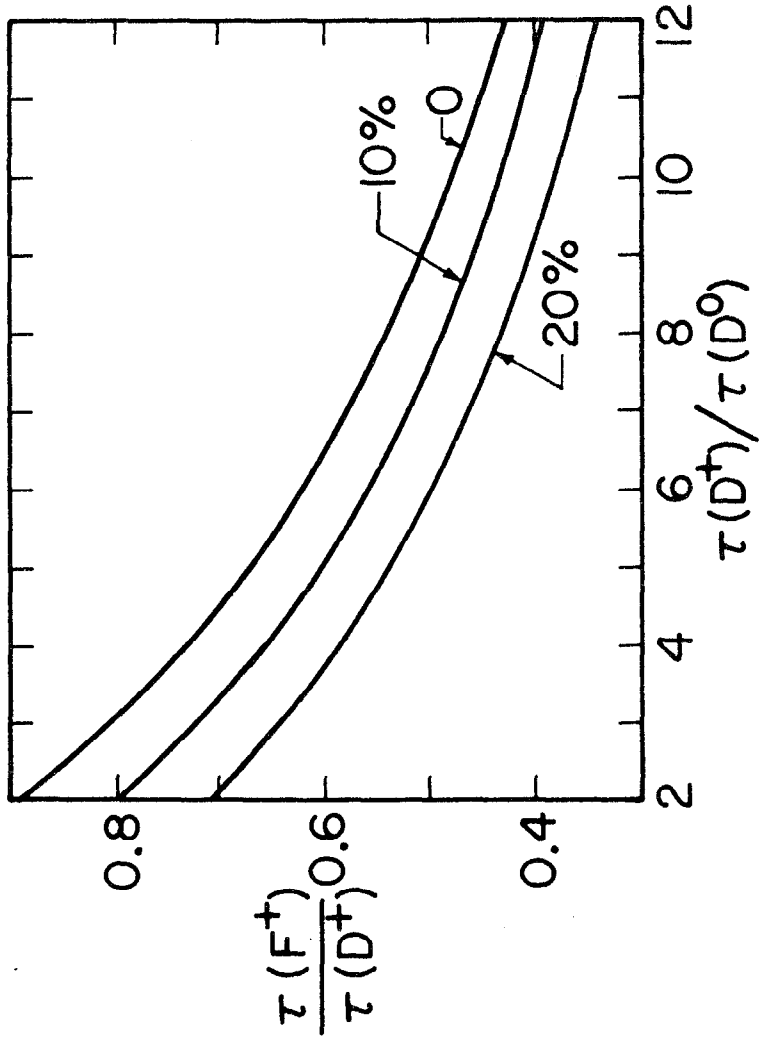

Fig. 38 Relation between lifetime ratios $\tau(F^+) / \tau(D^+)$ vs. $\tau(D^+) / \tau(D^o)$ as a function of $F \to \tau\nu_\tau$ branching ratio [Barger 80a].

$\Sigma_c^+ - \Lambda_c^+$ mass difference. The spectator contribution can be derived from the D^+ lifetime, leading to the relation

$$\tau(\Lambda_c^+) = \frac{\tau(D^+)}{1 + \Gamma_{non\text{-}sp}\,\tau(D^+)} \quad .$$

Numerically, this leads to the expectation that $\tau(D^+)/\tau(\Lambda_c^+) \sim 2\text{-}3$, while experimentally the value is 7-10, although with large uncertainties.

The semileptonic branching ratios can also be related:

$$B_\ell(\Lambda_c^+) = \frac{B_\ell(D^+)}{1 + \Gamma_{non\text{-}sp}\,\tau(D^+)}$$

For the DELCO value of $B_\ell(D^+) = 23 \pm 6\%$, we thus expect $B_\ell(\Lambda_c^+) \simeq 8\text{-}14\%$.

C. Enhanced $\underline{6}$ Dominance

Another approach to understanding the failure of the naive light quark spectator model is the enhanced $\underline{6}$ dominance or enhanced f_- approach [*Guberina 80, Rosen 79*]. *Rather than admitting the possibility of* contributions from exchange and annihilation diagrams, this explanation relies on two rather ad hoc assumptions. The first concerns the renormalized values of f_- and f_+. If we write the $\Delta C = 1$ effective Lagrangian as

$$\mathcal{L}^{eff}_{\Delta C=1} \propto f_- \mathcal{O}^- + f_+ \mathcal{O}^+ \quad ,$$

where

$$\mathcal{O}^\pm = \tfrac{1}{2}(\mathcal{O}_1 + \mathcal{O}_2),$$

with

$$\mathcal{O}_1 = (\bar{c}s)_L\,(\bar{d}u)_L$$

$$\mathcal{O}_2 = (\bar{c}u)_L\,(\bar{d}s)_L \quad ,$$

then the contribution of the two terms to the D^+ and D^o decay amplitudes are:

$$D^+: \quad \mathcal{O}_1|c\bar{d}\rangle = (\bar{d}s) + (\bar{d}u)$$

$$\mathcal{O}_2|c\bar{d}\rangle = (\bar{d}s) + (\bar{d}u)$$

$$D^o: \quad \mathcal{O}_1|c\bar{u}\rangle = (\bar{u}s) + (\bar{d}u)$$

$$\mathcal{O}_2|c\bar{u}\rangle = (\bar{u}u) + (\bar{d}s) \quad .$$

Thus, as can also be seen by referring to Fig. 39, the contributions of $\mathcal{O}^-$ to D^+ decay could cancel coherently, while this is not the case for D^o decay. The non-leptonic widths can be written as

$$\Gamma_{NL}(D^+) = \tfrac{4}{3} f_+^2\,\Gamma_{NL}\ (\text{free quark})$$

$$\Gamma_{NL}(D^o) = \tfrac{1}{3}(2f_+^2 + f_-^2)\,\Gamma_{NL}\ (\text{free quark})$$

Therefore

$$\frac{\tau(D^+)}{\tau(D^o)} = \frac{f_-^2 + 2f_+^2 + \frac{4}{3}}{4f_+^2 + \frac{4}{3}}$$

For the leading log values of f_+, f_- this yields $\tau(D^+)/\tau(D^o) \simeq 2$. Figure 40 shows the lifetime ratio as a function of the value of f_-. Ratios in the range 3-5 require f_- values in the range 2.5 - 3.

D. I, U and V Spin Relations

Our understanding of the structure of the effective weak Lagrangian can be summarized in a series of relations which follow directly from the I, U and V spin transformation properties of the currents [Rosen 78, Rosen 79a, Gavela 79a]. Figure 41 shows the relationship of the three charmed mesons with respect to these transformations.

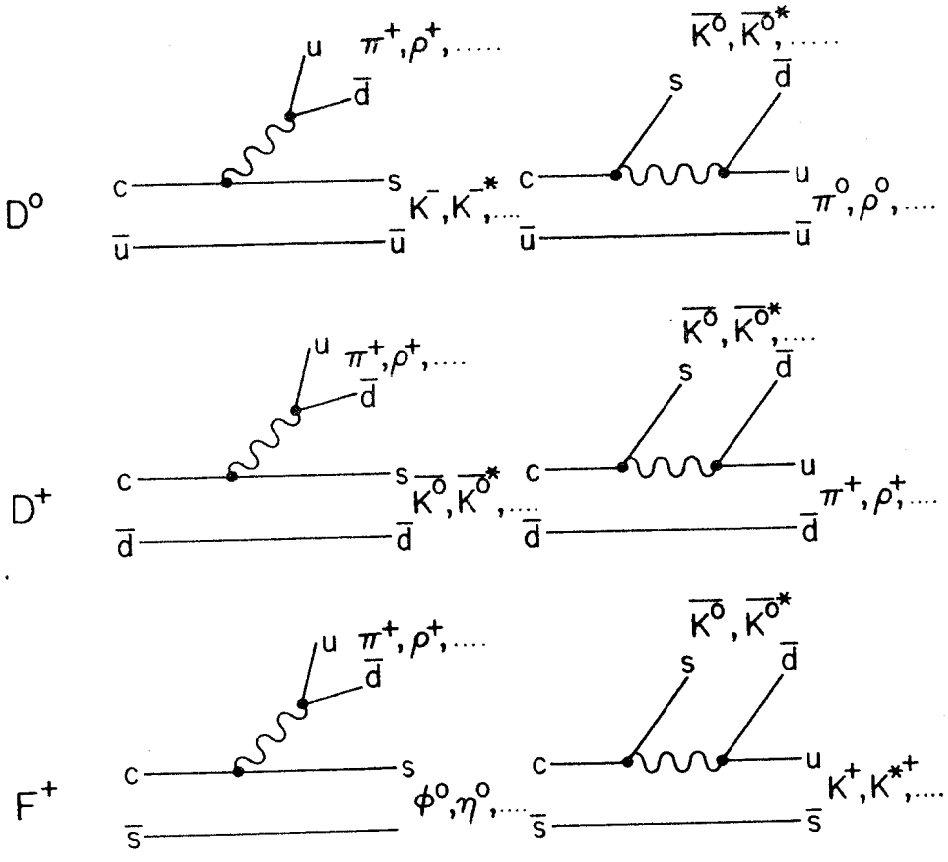

Fig. 39 Spectator diagrams contributing to hadronic decays of D^0, D^+ and F^+. Note that the two D^+ decay diagrams can cancel coherently.

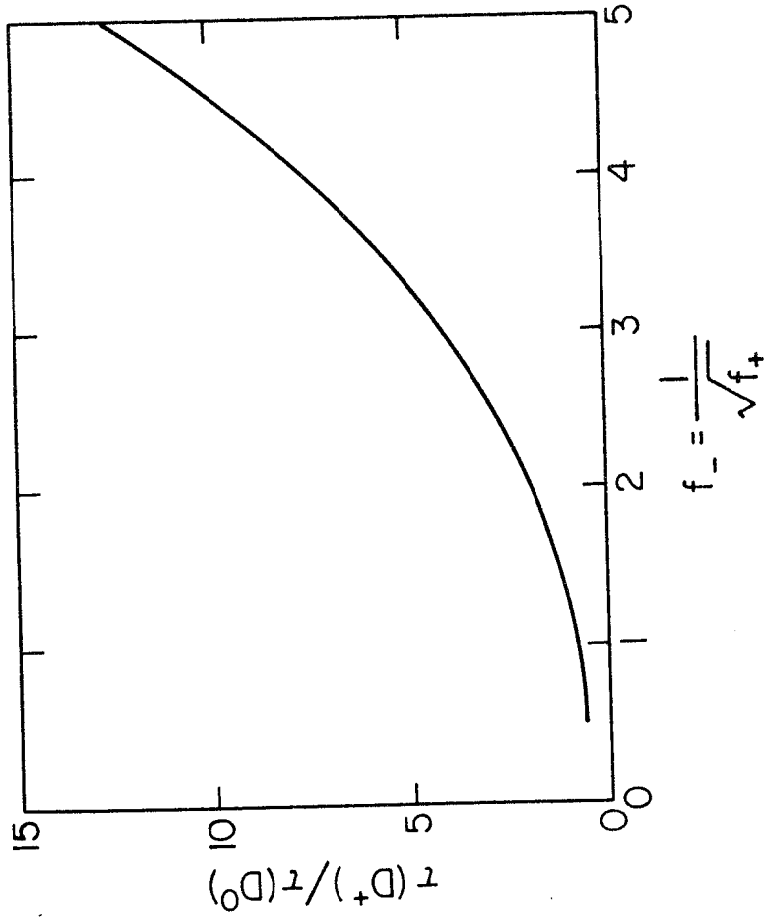

Fig. 40 Lifetime ratio $\tau(D^+) / \tau(D^0)$ vs. f_- in the spectator model.

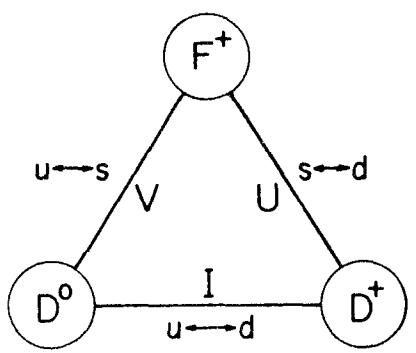

Fig. 41 Relation between charmed mesons with respect to I, u and V spin transformations.

If W exchange is a dominant process in D^o decays, then the final state has I = 1/2. This can be tested in several ways. In general the amplitudes for $D^o \to K\pi$ decays can be written as

$$A(D^o \to K^-\pi^+) = \sqrt{\frac{2}{3}}\, A_{1/2} + \sqrt{\frac{1}{3}}\, A_{3/2}$$

$$A(D^o \to \bar{K}^o\pi^o) = \sqrt{\frac{1}{3}}\, A_{1/2} + \sqrt{\frac{2}{3}}\, A_{3/2}$$

Thus if the final state is I = 1/2, we have

$$\frac{B(D^o \to K^-\pi^+)}{B(D^o \to \bar{K}^o\pi^o)} = 2 \ ,$$

which is consistent with the Mark II data.

If, on the other hand, we seek an explanation solely on the basis of W radiation diagrams (i.e., enhanced 6 dominance), we are forced to assume that there is no color suppression mechanism [Bernreuther 80, Finjord 80]. In that case

$$\frac{B(D^o \to K^-\pi^+)}{B(D^o \to \bar{K}^o\pi^o)} = \frac{2(2f_+ + f_-)^2}{(2f_+ - f_-)^2} \ .$$

For values of f_+, f_- consistent with a lifetime ratio of ~3, this ratio is ~18. Recall that the leading log values of f_+, f_- together with the color suppression factor yield a ratio of ~40. There is a very sensitive interplay between the lifetime ratio and this ratio of branching ratios which is shown in Fig. 42; larger lifetime ratios are more easily reconciled with a small ratio of $D^o \to K\pi$ branching ratios.

This comparison may, however, be complicated by hadronic final state interactions [Lipkin 79]. The isospin decomposition of amplitudes should in fact include phase shifts:

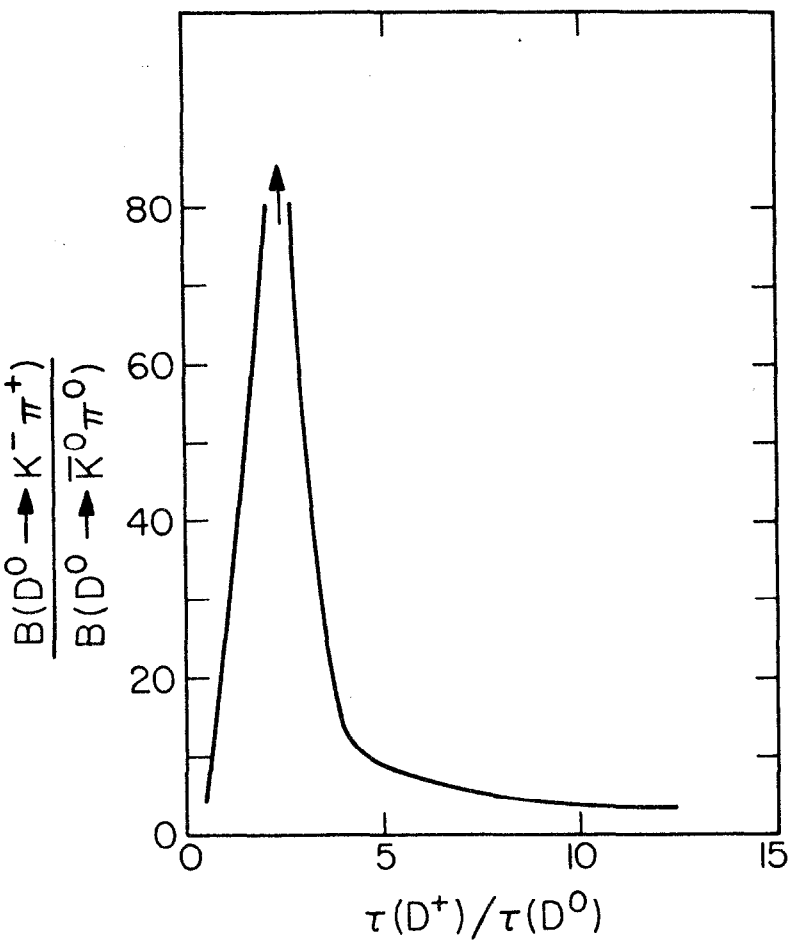

Fig. 42 Relation between $B(D^0 \to K^-\pi^+) / B(D^0 \to \bar{K}^0\pi^0)$ vs. $\tau(D^+) / \tau(D^0)$ in spectator model.

$$A(D^0 \to K^-\pi^+) = -\sqrt{\frac{2}{3}}\, e^{i\delta_1} A_{1/2} + \sqrt{\frac{1}{3}}\, e^{i\delta_3} A_{3/2}$$

$$A(D^0 \to \bar{K}^0\pi^0) = \sqrt{\frac{1}{3}}\, e^{i\delta_1} A_{1/2} + \sqrt{\frac{2}{3}}\, e^{i\delta_3} A_{3/2} \quad .$$

The effect of the phase shifts is clearly illustrated by assuming that the $\bar{K}^0\pi^0$ mode is completely cancelled in the absence of strong interactions, i.e., that $A_{1/2} = -\sqrt{2}\, A_{3/2}$. Then

$$\frac{B(D^0 \to K^-\pi^+)}{B(D^0 \to \bar{K}^0\pi^0)} = \frac{1}{8}\left[9 \cot^2\left(\frac{\delta_1 - \delta_3}{2}\right) + 1\right] \quad .$$

The $\bar{K}^0\pi^0$ mode is suppressed only if $\delta_1 \simeq \delta_3$. Since the I = 3/2 channel is exotic with no known resonances, and the I = 1/2 channel is non-exotic with many K^* resonances, it is far from clear that these phase shifts should be equal. No complete dynamical treatment of this problem exists, so that conclusions based purely on weak interactions with QCD gluon couplings must be viewed with caution.

Since the D^0 and D^+ mesons form an isospin doublet and the weak exchange is isovector, both I = 1/2 and I = 3/2 final states are, in general, allowed. Thus triangle inequalities are the simplest general statements which can be made about these decays. The inequality

$$\frac{1}{2}\left[B(D^0 \to K^-\pi^+)^{1/2} - \left\{B(D^+ \to \bar{K}^0\pi^+)\, \frac{\tau(D^0)}{\tau(D^+)}\right\}^{1/2}\right]^2 \leq B(D^0 \to \bar{K}^0\pi^0)$$

$$\leq \frac{1}{2}\left[B(D^0 \to K^-\pi^+)^{1/2} + \left\{B(D^+ \to \bar{K}^0\pi^+)\, \frac{\tau(D^0)}{\tau(D^+)}\right\}^{1/2}\right]^2$$

is consistent with the Mark II results, accommodating a $B(D^0 \to \bar{K}^0\pi^0)$ branching ratio of from ~.5 to 3%.

Returning to the special case of an I = 1/2 final state, we can extend the relations to include two-body pseudoscalar-vector decays: The prediction is

$$\frac{B(D^0 \to K^{*-}\pi^+)}{B(D^0 \to \bar{K}^{*0}\pi^0)} = \frac{B(D^0 \to K^-\rho^+)}{B(D^0 \to \bar{K}^0\rho^0)} = 2 \quad .$$

Referring to Table IX, we see that the first ratio is satisfied by the data, while the second is not.

For the general case of I = 1/2 and 3/2 final states, we have the triangle relation

$$A(D^0 \to K^-\rho^+) + \sqrt{2}\, A(D^0 \to \bar{K}^0\rho^0) - A(D^+ \to \bar{K}^0\rho^+) = 0 \quad .$$

This can be used to derive the inequality

$$B(D^+ \to \bar{K}^0\rho^+) \geq \frac{\tau(D^+)}{\tau(D^0)} \left\{ \left[B(D^0 \to K^-\rho^+) \right]^{1/2} - \left[2B(D^0 \to \bar{K}^0\rho^0) \right]^{1/2} \right\} \quad .$$

The two D^0 decays have been observed, the D^+ decay has not. Using the measured branching ratios and the Mark II lifetime ratios, we have the 90% confidence level limit:

$$B(D^+ \to \bar{K}^0\rho^+) > 3.8\% \quad .$$

Relations based on U spin or V spin symmetry are not expected to be as solid as those based on isospin. One reason is that the (s,d) and (s,u) mass differences are larger than the (u,d) mass difference. Also, while in the four quark model $\mathscr{L}^{\text{eff}}_{\text{weak}}$ transforms as a pure U spin vector, in the six quark model there is an additional U spin scalar component. This will be seen to be particularly important in Cabibbo-suppressed D decays. Just as is the case with isospin, final state interactions cannot be neglected in tests of U or V spin conservation.

In the SU(3) limit, Cabibbo allowed $\Delta C = 1$ transitions conserve V spin. Since the D^+ is a V spin singlet while $\bar{K}^0(s\bar{d})$ and $\pi^+(u\bar{d})$ are in a V = 1 state, the decay $D^+ \to \bar{K}^0\pi^+$ should be forbidden. It does, however, occur.

Under V spin, the $\underline{6}$ representation ($\alpha f_{\_}$) transforms $u \to s$, while the $\underline{15}$ transforms $u \to -s$. This leads to particular branching ratio relations which can be useful in distinguishing one decay mechanism from another. For example

$$\frac{\Gamma(\Lambda_c \to \Sigma^{*0}\eta^0)}{\Gamma(\Lambda_c \to \Sigma^{*0}\pi^0)} = \begin{cases} 3 \text{ for } \underline{6} \text{ dominance} \\ \frac{1}{3} \text{ for } \underline{15} \text{ dominance} \end{cases} \quad .$$

The most direct utility of U spin comes about in the area of Cabibbo-suppressed decays. In the four quark model, the U spin vector character of $\mathscr{L}^{\text{eff}}_{\text{weak}}$ leads to

$$\Gamma(D^0 \to K^0\bar{K}^0) = 0$$

$$\Gamma(D^0 \to K^-K^+) = \Gamma(D^0 \to \pi^-\pi^+) \quad .$$

U spin relations in the context of Cabibbo-suppressed decays have been discussed above.

E. Calculation of Annihilation or Exchange Diagram Contributions

It appears that the phenomenology of charmed meson decays has led us to the conclusion that a consistent picture requires the existence of substantial (perhaps dominant) contributions from exchange and annihilation processes which were naively thought to be suppressed by helicity conservation at the light quark vertex. Gluon effects can in principle remove the helicity suppression. Quantitative estimates have been made of the size of these effects; there appears, however, to be no consensus as to whether amplitudes large enough to account for the phenomenology can be generated.

Two approaches to these estimates have been made. The first considers soft gluon emission as an explicit radiative process, while the second concerns itself with the gluon content of the quark wave functions. We will briefly describe each approach in turn.

Bander, Silverman and Soni [Bander 80] have estimated the rate of soft gluon emission in terms of f_D. The expression is

$$\Gamma_g \simeq G_F^2 \frac{(5f_+^2 + 3f_-^2)}{8} \alpha_s \frac{f_D^2 m_D^5}{324\pi^2 m_u^2}$$

This is to be compared with the spectator rate

$$\Gamma_S = \frac{G_F^2 m_c^5}{192\pi^3}\left[2 + \frac{(2f_+^2 + f_-^2)}{3} \times 3\right]$$

Thus if the D^o decays via annihilation and the D^+ via radiation, we have

$$\frac{\tau(D^+)}{\tau(D^o)} = 1 + \left(\frac{m_D}{m_c}\right)^5 \frac{16\alpha_s\pi}{27} \frac{f_D^2}{m_u^2} \times \frac{a_8}{2 + 3a_3}$$

where

$$a_3 = \frac{2f_+^2 + f_-^2}{3}\ , \quad a_8 = \frac{5f_+^2 + 3f_-^2}{8} \quad \text{and} \quad \alpha_s = \frac{4\pi}{\ell n\left(\frac{m_D^2}{\Lambda^2}\right)}$$

If α_s is evaluated at $\Lambda = 0.5$ GeV, we have

$$\frac{\tau(D^+)}{\tau(D^o)} = 1 + 0.7 \frac{f_D^2}{m_u^2}$$

For $m_u = 300$ MeV, the ratio takes the values

$$\frac{\tau(D^+)}{\tau(D^o)} \simeq 1.2 - 7$$

for 150 MeV < f_D < 800 MeV.

Should the lifetime ratio settle at the Mark II value, then reasonable f_D values of ~300 MeV would suffice. With large ratios implied by the published E531 results, impractically large f_D values would be required for quantitative agreement. A similar estimate has been made by Fritzsch and Minkowski [Fritzsch 80].

The same authors have also considered the consequences of a significant gluon content in the original meson wave function. In lowest order, the exchange or annihilation process occurs when the initial $c\bar{u}$ or $c\bar{s}$ system emits a gluon, becoming a color-octet system. In higher orders, which should be significant, there can be color-singlet contributions. The relative importance of color singlet and octet terms can be seen by retaining the matrix elements of the λ_α color SU(3) matrices in the Fierz transformation:

$$\mathcal{L}_{eff} \propto f_1(\bar{s}c)(\bar{u}d) + f_2(\bar{s}d)(\bar{u}c)$$

$$= \left(\frac{f_1}{3} + f_2\right)(\bar{s}d)(\bar{u}c) + 2f_1\left(\bar{s}\frac{\lambda_\alpha}{2}d\right)\left(\bar{u}\frac{\lambda_\alpha}{2}c\right) \text{ for } D^o$$

$$= \left(f_1 + \frac{f_2}{3}\right)(\bar{u}d)(\bar{s}c) + 2f_2\left(\bar{u}\frac{\lambda_\alpha}{2}d\right)\left(\bar{s}\frac{\lambda_\alpha}{2}c\right) \text{ for } F^+ .$$

Thus, for example, the non-spectator contribution to D^o decay has both singlet and octet parts:

$$\Gamma_{non\text{-}sp}(D^o) \propto \left(\frac{f_1}{3} + f_2\right)^2 \mathcal{S} + (4f_1^2)\,\mathcal{O}$$

$$= \left(\frac{f_1}{3} + f_2\right)^2 \sum_X |\langle X|(\bar{u}c)(\bar{s}d)|D^o\rangle|^2 + \sum_X |\langle X|\left(\bar{s}\frac{\lambda_\alpha}{2}d\right)\left(\bar{u}\frac{\lambda_\alpha}{2}c\right)|D^o\rangle|^2 ,$$

where the sum is over all final states X.

For the F^+:

$$\Gamma_{non\text{-}sp}(F^+) \propto \left(f_1 + \frac{f_2}{3}\right)^2 \mathcal{S} + 4f_2^2\,\mathcal{O} .$$

The ratio of these two contributions to the decay rates is

$$R = \frac{\Gamma_{\text{non-sp}}(F^+)}{\Gamma_{\text{non-sp}}(D^o)} = \frac{\left(f_1 + \frac{f_2}{3}\right)^2 \mathscr{S} + 4f_2^2 \mathscr{O}}{\left(\frac{f_1}{3} + f_2\right)^2 \mathscr{S} + 4f_1^2 \mathscr{O}} ,$$

$$= \frac{2.19 + 1.38\, \mathscr{S}/\mathscr{O}}{8.07 + 0.07\, \mathscr{S}/\mathscr{O}} .$$

In lowest order, $\mathscr{S}/\mathscr{O} = 0$, implying R = 0.27 [N. B. Barger 80a]. If all colors occur with equal probability incoherently, then $\mathscr{S}/\mathscr{O} = 18$, yielding R = 2.90. For $\mathscr{S}/\mathscr{O} = 9/2$, the ratio is independent of f_1 and f_2, implying $\tau(F^+) = \tau(D^o)$, which is consistent with experiment. Precise measurement of these lifetime ratios can thus provide information on the gluon content of hadronic wave functions.

The semileptonic decay of the F^+ can also provide interesting information, as it can proceed via the annihilation diagram as well as the W radiation diagram. The annihilation rate is proportional to $\mathscr{S}$. Further, the gluon must be emitted from the initial quark, and thus the hadrons accompanying semileptonic F^+ decay could have a rich gluon content. One might then expect large rates for decays such as $F^+ \to (\eta,\eta',\eta_c) + \ell\nu$.

F. Determination of Meson Decay Constants

One of the most fundamental quantities in hadron physics is the coupling constant of the pseudoscalar mesons to vacuum, defined by

$$\begin{array}{c} \langle H|Q\gamma_\lambda\gamma_5\bar{q}|0\rangle = - p_\lambda \frac{f_H}{(2\pi)^{3/2}(2\omega_H)^{1/2}} \\ \| \\ 0^- \text{ meson} = Q\bar{q} \end{array}$$

This is directly measured by the purely leptonic decay rate:

$$\Gamma(H \to \ell\nu) = \frac{G_F^2 |V_{Qq}|^2 f_H^2}{8\pi} m_H m_\ell^2 \left(1 - \frac{m_\ell^2}{m_H^2}\right)$$

In this way f_π has been measured from $\Gamma(\pi \to \mu\nu)$ to be 96 keV and f_K/f_π is known to be 1.28. The nonequality of these constants is a measure of SU(3) breaking. A measurement of a charmed meson decay constant would be very interesting, in that it would yield new information on symmetry breaking. f_D also enters into the estimate of the size of the annihilation contribution to D^o decay via soft gluon emission. Rates for purely leptonic decays of charmed mesons are expected to be quite small due to helicity suppression and, in the case of $D \to \ell\nu$, Cabibbo suppression. The one case in which a measurement could be possible appears to be $F^+ \to \tau^+\nu_\tau$ [Karliner 76, Barger 80]. In this decay the large τ mass minimizes the effect of helicity suppression, and the decay is Cabibbo-allowed. For F^+ lifetimes in the range $2\text{-}4 \times 10^{-13}$ sec, one expects

$$B(F^+ \to \tau^+\nu_\tau) \simeq (.5\text{-}1)\% \times \left(\frac{f_F}{f_\pi}\right)^2 .$$

Many estimates of f_D or f_F exist in the literature. Some of these are shown in Table XIV. Clearly, there is a large uncertainty in this area. Two recent estimates [Suzuki 80a], one based on D and D^* mass differences, yielding $f_D = \left(321\ ^{+141}_{-321}\right)$ MeV, the other based on $\Gamma\left(({}^3S_1\ q\bar{q}) \to \ell^+\ell^-\right)$, yielding $f_D \simeq 150$ MeV are perhaps most reliable. These estimates lead to $F^+ \to \tau^+\nu_\tau$ branching ratios of ~1-8%. Values at the upper end of this range are conceivably measurable, by searching in the recoil spectra of reconstructed F^+ hadronic decays in e^+e^- annihilation for single leptons with large missing energy (three neutrinos). y distributions for leptons and hadrons resulting from F^+ and B decays are shown in Fig. 43.

TABLE XIV. Theoretical Predictions for Meson Decay Constants

f_D/f_π	f_F/f_π	f_K/f_π	Reference
0.974	1.056	1.28	Das and Deshpande, Phys. Rev. D19, 3387 (1979)
0.4	0.4	1.15	Oaks and Sorba, FNAL 77/78-THY
1.015	1.016	1.00096	Gounaris and Sarantakos, Nuovo Cimento 39A, 554, (1977)
1.12	1.34	1.11	Takaiwa, Prog. Theor. Phys. 59, 1625 (1978)
1.517-1.652	1.616-1.892	1.14-1.36	Kandaswamy, Schecter, and Singer, Phys. Rev. D17, 1430 (1978)
1-11.75	1-15.67	1.22	Dominguez, Phys. Rev. D18, 963 (1978)
4.485-5.364	4.765-5.644	1.28	Vaughn, Phys. Rev. D13, 2621 (1976)
(-0.51)-(-3.02)	(-0.37)-(-2.52)	1.08-1.30	Fukuda, Prog. Theor. Phys. 59, 1613 (1978)
1.1	--	--	Preparata, CERN TH-2271 (1977)
0.3	--	--	Quigg and Rosner, Phys. Rev. D16, 1497 (1977)
0-4.8	--	--	Suzuki, UCB - PTH-80/4, Rev.

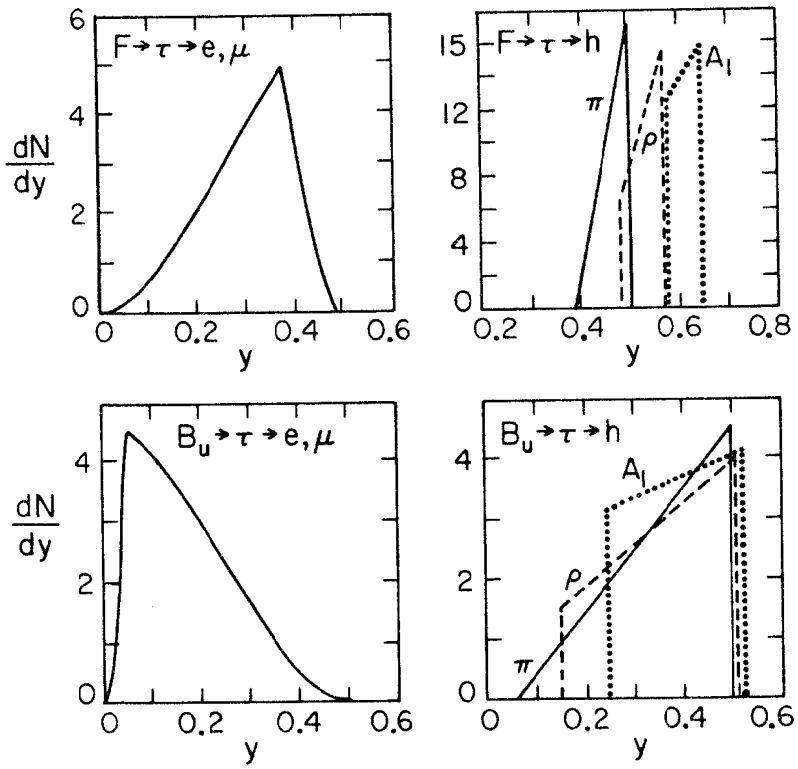

Fig. 43 y distributions for F and B meson decays to τ's. $y \equiv P_h \cdot P_H / m_H^2$, where P_h is the momentum to the charged particle emitted in the τ decay stage of $H \to \tau\nu$ [Barger 80].

VIII. Bottom Mesons

The experimental study of hadrons with bottom quarks is just beginning. At this point, the only experimental evidence is indirect, involving the detection of direct leptons from semileptonic decays of b quark containing mesons. Four B mesons are expected to exist. These are

$$B_u^- = (b\bar{u}),\ B_d^0 = (b\bar{d}),\ B_s^0 = (b,\bar{s}) \text{ and } B_c^- = (b\bar{c}) \quad .$$

The first two are expected to have masses around 5 GeV, the B_s a few hundred MeV higher, and the B_c about a GeV above that. Recent CLEO results allow the placing of a limit on the mass of the lowest B states.

The effective Lagrangian for b decay can be written as

$$\mathcal{L}_{NL}^{eff} = \frac{G}{\sqrt{2}} g_c \left\{ \frac{(f_+ + f_-)}{2} [(\bar{c}b)(\bar{d}u) + (\bar{c}b)(\bar{s}c)] + \left(\frac{f_+ - f_-}{2} \right) [(\bar{c}u)(\bar{d}b) + (\bar{c}c)(\bar{s}b)] \right\} ,$$

where g_c contains the K-M angle factors.

For the dominant transitions, these factors are [Ali 79b]

$$b \to c\bar{d}u : c_1(c_1c_2s_3 + s_2c_3e^{i\delta}) \simeq s_3 + s_2$$

$$b \to c\bar{s}c : (c_1c_2c_3 - s_2s_3e^{i\delta})(c_1c_2s_3 + s_2c_3e^{i\delta}) \simeq s_3 + s_2$$

Two other transitions, $b \to u\bar{d}u$, $u\bar{s}c$ have K-M factors proportional to s_1s_3 and can be neglected for the foreseeable experimental future. It is important to note that all B decays are at least once Cabibbo-suppressed, as they are decays out of the (b,t) doublet.

Hard gluon exchange again causes renormalization of the coefficients, this time evaluated at m_b:

$$f_\pm = \left[\frac{\alpha_s(m_b^2)}{\alpha_s(m_W^2)} \right]^{d_\pm} \left[1 + \alpha_s\ (m_b^2) \right] ,$$

leading to values $f_+ = 0.78$, $f_- = 1.65$. Non-leptonic enhancement for bottom decays is thus expected to be somewhat smaller than that for charm: $2f_+^2 + f_-^2 \simeq 3.9$, versus ~ 5.6 for charm. The relative size of coefficients for color-connected and disconnected diagrams is also expected to be quite different. Color-connected amplitudes are proportional to $\chi_+ = \frac{2f_+ + f_-}{3} = 1.07$, while color-disconnected amplitudes are proportional to $\chi_- = \frac{2f_+ + f_-}{3} = -.03$. With the additional factor of three suppression of the color-disconnected amplitude due to the Fierz transformation, color disconnected transitions should be greatly suppressed in B meson decays.

In the light of the surprises found in c quark decay, we must ask whether the light quark spectator model alone can be used as a guide to the study of non-leptonic B meson decay or whether it will be necessary to include annihilation and exchange diagrams. Since the rate for W radiation processes in Qq decay is proportional to m_Q^5, while that for W exchange or annihilation processes is proportional to $|\psi(0)|^2 \leq m_Q^3$, the dominance of W radiation over other modes should naively be expected to be even greater in the b sector [Suzuki 80a]. Ultimately, this will come down to an experimental question, which can be answered by studying the equality of B meson lifetimes, or by searching for certain specific hadronic decay modes, such as $B^0 \to K^-F^+$ [Bigi 80] (see Fig. 44), which are greatly suppressed via radiation diagrams but which can be fairly prominent in an exchange model. With the exchange mechanism:

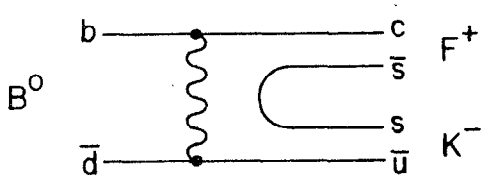

Fig. 44 Example of a B_d^0 decay which proceeds through the W^+ annihilation mechanism.

$$\frac{B(B^0 \to K^- F^+)}{B(B^0 \to \pi^- D^+)} \simeq \frac{1}{4} - \frac{1}{2} \quad ,$$

which is an order of magnitude greater than via the W radiation diagram.

As an example, consider the decay $B_c^-(b\bar{c}) \to c\bar{c} + s\bar{c}$ (e.g., $\eta_c F^-$). Figure 45 shows the four possible W radiation diagrams, two color connected and two color disconnected, and the exchange and annihilation diagrams, together with their renormalized coefficients. This decay is unusual in that all six possible diagrams contribute. In other specific decay modes only one or two classes of diagram enter. Tables XV-XVI show the types of diagrams which enter into various two body and quasi-two body decay modes of B mesons, together with an estimate of rates [Ali 79b]. Measurements of decays such as $B_d^0 \to D^+K^-$ are clean handles on the contribution of non-spectator diagrams.

The study of exclusive non-leptonic B meson decays will be a very difficult experimental task. In most instances, it is necessary to reconstruct a charmed meson through one of its non-leptonic decay modes (typically with a few percent branching ratio) in order to reconstruct a B meson. Rates will typically be quite low. For example, the increase in R due to $b\bar{b}$ production is only $\frac{1}{3}$ unit, and the branching ratio of a B meson to a specific final state containing a D meson is likely to be a few percent, as is the branching ratio of a D to a specific final state. Thus it is likely that of the order of 1 B meson in $\sim 10^4$ can be reconstructed as a particular exclusive hadronic state.

A preliminary report of a peak in the $\psi K\pi$ mass spectrum produced in p intersections [Barate 79] has apparently not held up as the experiment gathered further statistics [Berkelman 80]. The possible prominence of

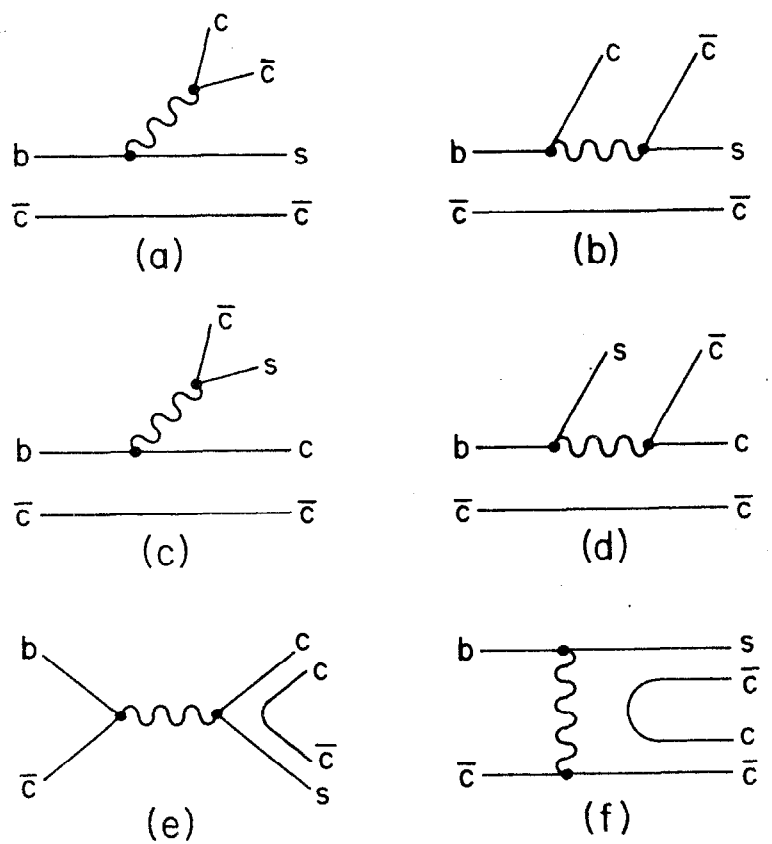

Fig. 45 Diagrams contributing to the decay $B_c^o \to c\bar{c} + s\bar{c}$ (e.g. $\eta_c F^-$).

TABLE XV. B Meson Decays to Two Pseudoscalar Mesons. Color-flavor Coefficients $\chi_\pm$ for the Relevant Diagrams of Figure 45 are indicated. [Ali 79b].

Mode	Diagrams (Fig. 45)		
	a,b	c,d	e,f
$B_u^- \to D^o\pi^-$	χ_-	χ_+	-
D^oF^-	-	χ_+	-
$\eta_c K^-$	χ_-	-	-
$B_d^o \to D^+\pi^-$	-	χ_+	χ_-
D^+F^-	-	χ_+	-
$D^o\pi^o$	χ_-	-	χ_-
$D^o\eta^o$	χ_-	-	χ_-
$D^o\eta'$	χ_-	-	χ_-
$\bar{K}^o\eta_c$	χ_-	-	-
$D^o\eta_c$	-	-	χ_-
D^+K^-	-	-	χ_-
$B_s^o \to F^+\pi^-$	-	χ_+	-
F^+F^-	-	χ_+	χ_-
D^oK^o	χ_-	-	-
$\eta_c\eta^o$	χ_-	-	-
$\eta_c\eta'$	χ_-	-	-
D^+D^-	-	-	χ_-
$D^o\bar{D}^o$	-	-	χ_-
$B_c^- \to \eta_c\pi^-$	-	χ_+	-
$\eta_c F^-$	χ_-	χ_+	χ_+
$\pi^-\pi^o$	χ_-	-	χ_+
K^oK^-	-	-	χ_+
$\bar{D}^oK^-$	-	-	χ_+
D^-K^o	-	-	χ_+

TABLE XV. - Continued

Mode	Diagrams (Fig. 45) a,b	c,d	e,f
$B_c^- \to F^-\eta^o$	-	-	χ_+
$F^-\eta'$	-	-	χ_+
$F^-\eta_c$	-	-	χ_+

TABLE XVI. Prominent Decay Modes of B Mesons. Units are $(\sin\theta_2 + \sin\theta_3)^2 \times 10^{-12}$ sec^{-1}. [Ali 79b].

	PP		PV		VV	
$B_u^- \to$	$D^o\pi^-$	4.16	$D^o\rho^-$	7.34	$D^*\rho^-$	9.72
	D^oF^-	8.00	$D^{*o}\pi^-$	4.29	$D^{*o}F^{*-}$	28.86
			D^oF^{*-}	7.67		
			F^-D^{*o}	4.54		
$B_d^o \to$	$D^+\pi^-$	2.72	$D^+\rho^-$	5.48	$D^{*+}\rho^-$	6.88
	D^+F^-	6.99	$D^{*+}\pi^-$	2.68	$D^{*+}F^{*-}$	25.58
			D^+F^{*-}	6.59		
			F^-D^{*+}	4.34		
$B_s^o \to$	$F^+\pi^-$	3.03	$F^+\rho^-$	5.95	$F^{*+}\rho^-$	6.88
	F^+F^-	7.36	$F^{*+}\pi^-$	2.85	$F^{*+}F^{*-}$	26.38
			F^+F^*	7.15		
			F^-F^{*+}	4.35		
$B_c^- \to$	$\eta_c\pi^-$	4.47	$\eta_c\rho^-$	8.97	$\psi\rho^-$	9.03
	η_cF^-	17.26	$\pi^-\psi$	3.79	ψF^{*-}	49.31
			η_cF^{*-}	20.65		
			$F^-\psi$	7.32		

B meson decays to states involving ψ's had been predicted by Fritzsch [Fritzsch 79].

As with charm, there are expected to be QCD corrections to semileptonic decays, which are calculable in analogy with corrections to μ decay. These have been discussed above. The semileptonic decay can be either $b \to c l\nu$, with a matrix element proportional to $\cos\theta_1\cos\theta_2\sin\theta_3 + \sin\theta_2\cos\theta_3\, e^{i\delta}$, or $b \to u l\nu$, proportional to $\sin\theta_1\sin\theta_3$. From our discussion of the K-M angles, it is clear that $b \to c l\nu$ decay should dominate. Since the B mesons are produced in pairs in e^+e^- annihilation, and the daughter charmed mesons can also decay semileptonically, it is possible to have as many as four leptons in the final state [Ali 79, *Cabibbo* 79]. In fact, the ratio of the numbers of final state leptons is sensitive to the ratios of the K-M angles, and can be used to measure them. It is also worth noting that $b \to c\tau\nu_\tau$ decays are kinematically allowed. The actual isolation of leptons from B decay is complicated by the inevitable background from charm semileptonic decays. This can be eliminated by cuts in the lepton transverse momentum of about 1 GeV/c (see Fig. 46).

CLEO has recently reported the observation of an increase in the inclusive lepton cross section at center-of-mass energies corresponding to the production of the T''' resonance [Mistry 80]. As the width of the T''' has been observed to be greater than that expected from beam energy spread, the T''' is assumed to be above threshold for the production of explicitly bottom quark containing mesons. The observed enhancement of lepton production at the T''' is a confirmation of this hypothesis.

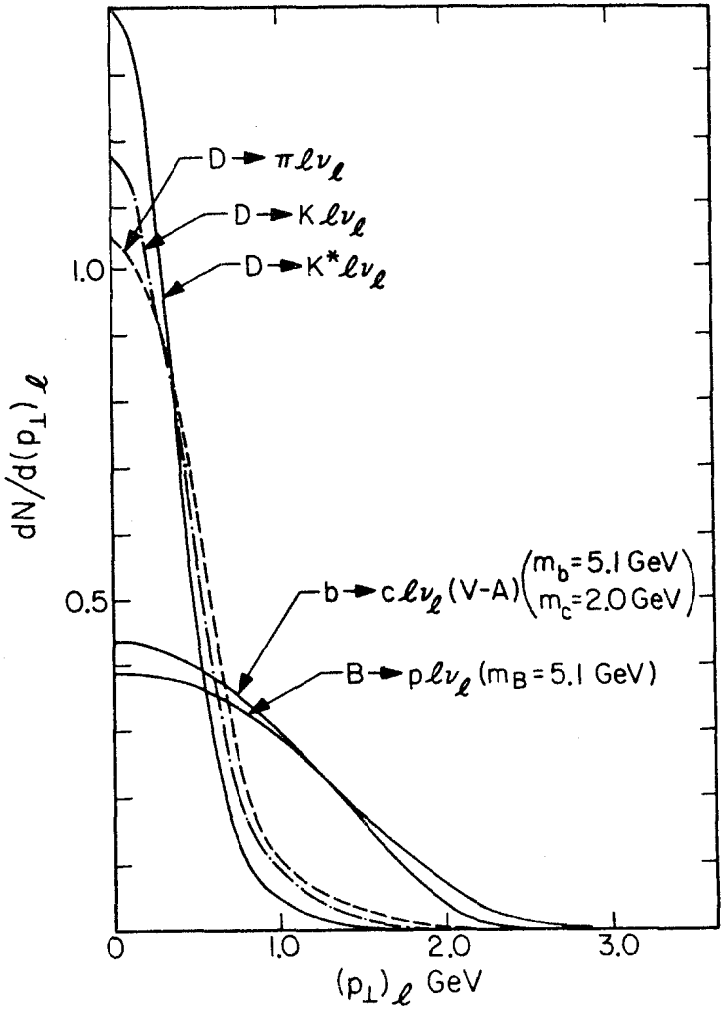

Fig. 46 $P_\perp$ distribution of leptons from D and B semileptonic decays [Ali 79].

The enhancements correspond to $B(B \to e\nu X) = 16 \pm 4 \pm 7\%$ and $B(B \to \mu\nu X) = 7.5 \pm 3.1\%$, indicating a moderate non-leptonic enhancement in the b sector. Figure 47 shows the momentum spectrum of the electrons at the T''', together with a Monte Carlo simulation of electrons resulting from $b \to c l \nu$ decay. There is rough agreement, but statistics are insufficient to exclude a $b \to u l \nu$ contribution.

The PLUTO collaboration [Berger 80] has recently reported results on inclusive muon production in the region $10 \leq \sqrt{s} \leq 31.6$ GeV. These are in agreement with contributions from b and c quark decay and show no evidence of requiring an additional contribution from a top quark.

If the b quark semileptonic decay is $b \to c l \nu$, the subsequent c quark decay should generate a final state rich in kaons. An enhancement in kaon production at the T''' has also been observed by CLEO. Charged K's in the region $0.6 \leq p_K \leq 1.0$ GeV are identified by time-of-flight; K_S^o can also be reconstructed. The results are summarized in Table XVII. With background subtracted, somewhat more $K^{\pm}, K^o$/event are observed than would be predicted by a $b \to c l \nu$ process. This mechanism is clearly favored over $b \to u l \nu$. It has also recently been pointed out [Guberina 80a] that QCD corrections can generate Penguin diagrams involving $b \to s$ transitions, thus directly producing strange particles in B decays not as a result of a cascade through a c quark.

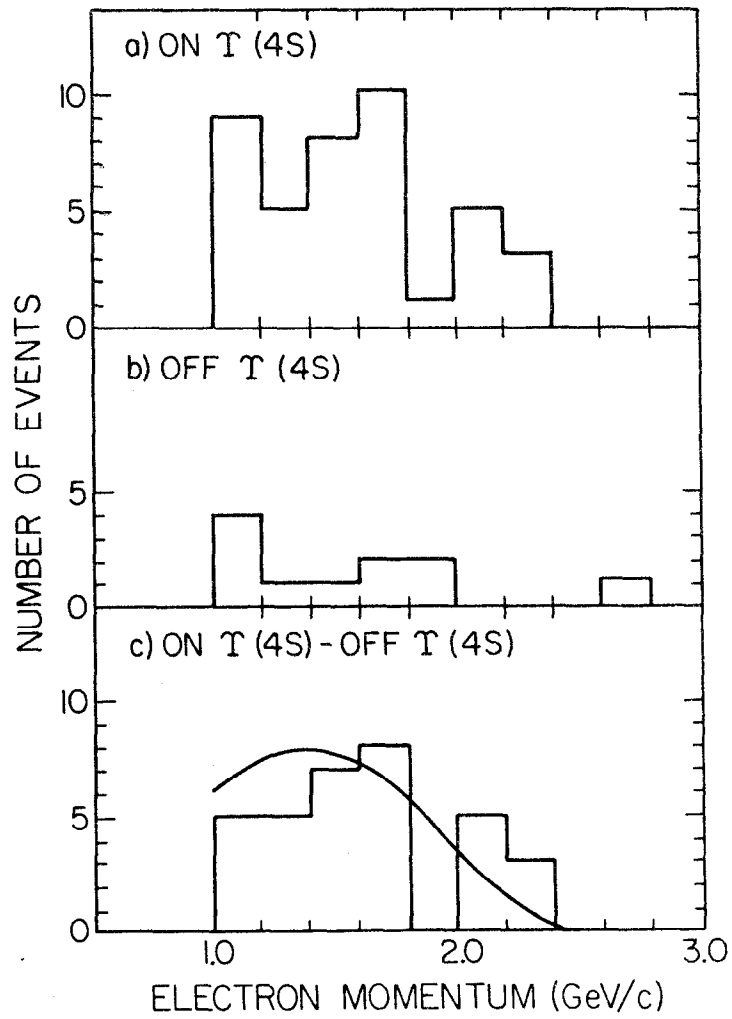

Fig. 47 Electron spectrum on and off the Υ''' resonance as observed at CESR by the CLEO detector.

TABLE XVII. CLEO Results on Strange Particle Content in B Meson Decay.

	$K^{\pm}$ / Event
Continuum (Experiment)	0.06 ± 0.01 ± 0.01
Monte Carlo (Continuum)	0.08 ± 0.02
T''' - Continuum (Experiment)	0.40 ± 0.09 ± 0.02
Monte Carlo $b \to c\ell\nu$	0.22 ± 0.05
Monte Carlo $b \to u\ell\nu$	0.06 ± 0.01

$K^{\pm,o}$/B Decay = 2.4 ± 0.5 ± 0.5

Prediction ≃ 1.7

IX. CP Violation

The possibility of including CP violation into models of quarks and leptons was discussed in general by Kobayashi and Maskawa [Kobayashi 73]. They observed that the then standard weak interaction model of four quarks with a single Higgs doublet did not admit the possibility of CP violation. As we discussed earlier, a six quark model allows one imaginary phase, which can be responsible for CP violation. This has come to be known as the Kobayashi-Maskawa model, although they also outlined other alternatives, such as the inclusion of right-handed currents or the enlargement of the Higgs sector. We will here emphasize the K-M model approach, restricting ourselves to a brief discussion of alternatives at the end.

The problems of mass mixing and CP violation in neutral conjugate meson systems are intimately connected [Carter 80, Ali 79c, Hagelin 79]. Let us denote by $(P^o,\bar{P}^o)$ a pair of such mesons, which may be $(K^o,\bar{K}^o)$, $(D^o,\bar{D}^o)$, $(B^o,\bar{B}^o)$ or $(T^o,\bar{T}^o)$. For the B and T systems, there are more than one pair of such conjugate states. In a strong interaction basis, the time evolution of such a system is given by

$$\mathscr{H}\begin{pmatrix} P^o \\ \bar{P}^o \end{pmatrix} = \begin{pmatrix} \mathscr{M}_{11} - \frac{i}{2}\Gamma_{11} & \mathscr{M}^*_{12} - \frac{i}{2}\Gamma^*_{12} \\ \mathscr{M}_{12} - \frac{i}{2}\Gamma_{12} & \mathscr{M}_{22} - \frac{i}{2}\Gamma_{22} \end{pmatrix}\begin{pmatrix} P^o \\ \bar{P}^o \end{pmatrix}$$

The state of definite mass $\mathcal{M}_{1,2}$ and width $\Gamma_{1,2}$ are given by:

$$P_1 = \frac{(1+\epsilon)P^o + (1-\epsilon)\bar{P}^o}{\sqrt{2(1+|\epsilon|^2)}} \equiv pP^o + q\bar{P}^o$$

$$P_2 = \frac{(1+\epsilon)P^o - (1-\epsilon)\bar{P}^o}{\sqrt{2(1+|\epsilon|^2)}} \equiv pP^o - q\bar{P}^o$$

where

$$\frac{q}{p} = \frac{1-\epsilon}{1+\epsilon} = \left[\frac{\mathcal{M}_{12} - \frac{i}{2}\Gamma_{12}}{\mathcal{M}^*_{12} - \frac{i}{2}\Gamma^*_{12}}\right]^{\frac{1}{2}}$$

Then the mass and lifetime differences between the two eigenstates are given by

$$\Delta m = m_1 - m_2 = 2\,\mathrm{Re}\sqrt{(\mathcal{M}_{12} - \tfrac{i}{2}\Gamma_{12})(\mathcal{M}^*_{12} - \tfrac{i}{2}\Gamma^*_{12})}$$

$$\Delta\Gamma = \Gamma_1 - \Gamma_2 = -2\,\mathrm{Im}\sqrt{(\mathcal{M}_{12} - \tfrac{i}{2}\Gamma_{12})(\mathcal{M}^*_{12} - \tfrac{i}{2}\Gamma^*_{12})} \quad .$$

If a pure P^o state is prepared (as in e^+e^- annihilation) at t = 0, it develops as

$$|\psi(t)\rangle = f_+(t)|P^o\rangle + \frac{q}{p} f_-(t)|\bar{P}^o\rangle \quad ,$$

where

$$f_\pm(t) = \frac{1}{2}\left\{\exp\left[it(-m_1 + \tfrac{i}{2}\Gamma_1)\right] \pm \exp\left[it(-m_2 + \tfrac{i}{2}\Gamma_2)\right]\right\} \quad .$$

Thus for a measurement made at t = ∞, the mixing is described by a parameter ρ:

$$\rho = \frac{\int_0^\infty |f_-(t)|^2 dt}{\int_0^\infty |f_+(t)|^2 dt} = \frac{4(\frac{\Delta m}{\Gamma})^2 + (\frac{\Delta\Gamma}{\Gamma})^2}{2 + 4(\frac{\Delta m}{\Gamma})^2 - (\frac{\Delta\Gamma}{\Gamma})^2}$$

The degree of mixing thus depends on the values of $\Delta m/\Gamma$ and $\Delta\Gamma/\Gamma$. We can make some general statements about the mixing and then apply them to definite conjugate systems. For a model which arranges quarks in doublets:

$$\begin{bmatrix} H(+\frac{2}{3}) \\ L(-\frac{1}{3}) \end{bmatrix} = \begin{bmatrix} c \\ s \end{bmatrix}, \begin{bmatrix} t \\ b \end{bmatrix}, \cdots$$

in general $\Gamma_L < \Gamma_H$. This is so because L must decay out of its doublet, suffering "Cabibbo-suppression," and because phase space further favors the decay of H. Further, Δm is governed by diagrams such as that of Fig. 48, so that for small mixing angles

$$(\Delta m)_{P_L} \propto M_H^2$$

$$(\Delta m)_{P_H} \propto M_L^2 \quad .$$

Thus

$$(\frac{\Delta m}{\Gamma})_{P_H} < (\frac{\Delta m}{\Gamma})_{P_L} \quad .$$

Therefore

$$(\frac{\Delta m}{\Gamma})_{T^o} < (\frac{\Delta m}{\Gamma})_{B^o}$$

and

$$(\frac{\Delta m}{\Gamma})_{D^o} < (\frac{\Delta m}{\Gamma})_{K^o} \quad .$$

A similar pattern holds for $\Delta\Gamma/\Gamma$. We expect, therefore that mixing will be greater in the K^o and B^o systems than in the D^o and T^o systems. Explicitly:

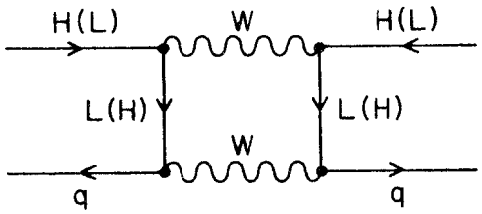

Fig. 48 Diagram for mixing of conjugate neutral mesons containing a heavy (H) or light (L) quark of a doublet.

$$\frac{\Delta m_{K^o - \bar{K}^o}}{m_K} \propto f_K^2 (m_c^2 - m_u^2) \sin^2\theta_1 \cos^2\theta_1$$

$$\frac{\Delta m_{D^o - \bar{D}^o}}{m_D} \propto f_D^2 (m_s^2 - m_D^2) \sin^2\theta_1 \cos^2\theta_1$$

$$\frac{\Delta m_{B_d^o - \bar{B}_d^o}}{m_{B_d^o}} \propto f_B^2 (m_t^2 + m_c^2) \sin^2\theta_1 \sin^2\theta_2 \cos 2\delta$$

$$\frac{\Delta m_{B_s^o - \bar{B}_s^o}}{m_{B_s^o}} \propto f_B^2 (m_t^2 + m_c^2) (\sin\theta_3 + \sin\theta_2 \cos\delta)^2$$

The neutral kaon mass difference is well measured: $\Delta m_K = 3.487 \times 10^{-15}$ GeV. The $D^o - \bar{D}^o$ mass difference can be estimated as

$$\Delta m_D \simeq \Delta m_K \frac{f_D^2}{f_K^2} \frac{m_D}{m_K} \frac{m_s^2}{m_c^2} \simeq 5 \times 10^{-16} \text{ GeV} \quad ,$$

for $f_D \simeq 150$ MeV.

For the widths, $\Gamma_K = \frac{\Gamma_{K_s^o} + \Gamma_{K_l^o}}{2} = 0.56 \times 10^{10}$ sec^{-1}, and $\Gamma_D \simeq 10^{13}$ sec^{-1}. If we take $\Gamma_B \sim 10^{14}$ sec^{-1}, we then have

$$\frac{\Delta m_D}{\Gamma_D} \simeq 7.6 \times 10^{-5} \ll \frac{\Delta m_K}{m_K} = 0.95 \quad ,$$

and

$$\frac{\Delta m_B}{\Gamma_B} \sim 10^{-2} \quad .$$

Taking $\Delta\Gamma \ll \Delta m$, we thus expect rather small mixing in the D^o system, $\rho_D \sim 10^{-8}$. The current limit comes from the observation of same sign

kaon pairs produced at the ψ'' by the Mark I collaboration [Goldhaber 77]

$$\frac{N^{++} + N^{--}}{N^{+-}} \simeq \frac{2\rho_D}{1 + \rho_D^2} < 16 \times 10^{-2} \quad ,$$

which implies $\rho_D < 8 \times 10^{-2}$. This small degree of mixing makes the observation of CP violation in the D system very difficult, even though the CP violating parameter ϵ is comparable in the D^o and K^o systems. In the K-M model, where CP violation occurs explicitly in the mass matrix, ϵ can be related to the mixing angles and the imaginary phase δ:

$$|\epsilon|_{K^o - \bar{K}^o} \sim \sin\theta_2 \sin\theta_3 \sin\delta \sim 2 \times 10^{-3}$$

$$|\epsilon|_{D^o - \bar{D}^o} \sim \sin\theta_2 \sin\theta_3 \sin\delta \sim 2 \times 10^{-3}$$

$$\left.\begin{aligned} |\epsilon|_{B_d^o - \bar{B}_d^o} &\sim \tan 2\delta \\ |\epsilon|_{B_s^o - \bar{B}_s^o} &\sim \left(\frac{\sin\theta_2}{\sin\theta_3 + \sin\theta_2 \cos\delta}\right) \tan 2\delta \end{aligned}\right\} \text{could be } \gg 10^{-3}$$

There have been optimistic estimates of the observability of CP violation in the B system through studies of semileptonic decays, based on the possible large value of $|\epsilon|_B$ [Ellis 77].

The CP violating parameter ϵ can be written in terms of the transition matrix elements:

$$\epsilon = \frac{-\mathrm{Re}\mathcal{M}_{12} + \frac{i}{2}\mathrm{Re}\Gamma_{12} + \left[(\mathcal{M}_{12} - \frac{i}{2}\Gamma_{12})(\mathcal{M}_{12}^* - \frac{i}{2}\Gamma_{12}^*)\right]^{\frac{1}{2}}}{i\,\mathrm{Im}\,\mathcal{M}_{12} + \frac{1}{2}\mathrm{Im}\,\Gamma_{12}}$$

When $\mathcal{M}_{12}$ and Γ_{12} have the same phase, ϵ is pure imaginary. An imaginary ϵ can be transformed away by readjusting the relative phases of the P^o and $\bar{P}^o$ conjugate states, which are undefined, as there is no strong transition between them. Thus the phase of ϵ, as well as its magnitude governs the size of the observable charge asymmetry [Carter 80, Hagelin 80]. In the $K^o - \bar{K}^o$ system, $|\epsilon_K| \simeq \epsilon_K$, making it possible to fairly easily observe CP violation. This is not the case in the $B^o - \bar{B}^o$ system.

Consider $B^o - \bar{B}^o$ production in e^+e^- annihilation:

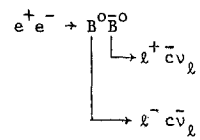

Let us define the ratio of rates to different sign leptons:

$$r = \frac{N(B^o \to \ell^-)}{N(B^o \to \ell^+)} \simeq \left|\frac{1 - \epsilon}{1 + \epsilon}\right|^2 \rho_B$$

$$\bar{r} = \frac{N(\bar{B}^o \to \ell^+)}{N(\bar{B}^o \to \ell^-)} \simeq \left|\frac{1 + \epsilon}{1 - \epsilon}\right|^2 \rho_B \quad .$$

Then a measurement of the charge asymmetry gives us

$$\frac{N^{++} - N^{--}}{N^{++} + N^{--}} \simeq \frac{r - \bar{r}}{r + \bar{r}} = \frac{r/\bar{r} - 1}{r/\bar{r} + 1} \quad .$$

The relation to the phase of ϵ can be seen as follows:

$$\frac{r}{\bar{r}} = \left|\frac{1 - \epsilon}{1 + \epsilon}\right|^4 \equiv \frac{1 - z}{1 + z} \quad ,$$

where

$$z = \frac{-\mathrm{Im}\left(\frac{\Gamma_{12}}{\mathcal{M}_{12}}\right)}{1 + \frac{1}{4}\left|\frac{\Gamma_{12}}{\mathcal{M}_{12}}\right|^2}$$

For the B system $z \to 0$ for $\frac{m_u^2 - m_c^2}{m_b^2} \ll 1$, since in this limit Γ_{12} and $\mathcal{M}_{12}$ have a common phase. Thus, asymmetries are expected to be small, of the order of 10^{-3}. A measurement of this type is further complicated by the corrections which must be made for subsequent semi-leptonic c quark decay:

$$b \to \ell^- \bar{\nu}_\ell c \hookrightarrow \ell^+$$

and

$$b \to \bar{u} d c \hookrightarrow \ell^+ \quad ,$$

and for leptons from directly produced D's. While these can be removed by cuts requiring large lepton energies, with present luminosities it appears unlikely that CP violation in the B system will be observed in the near future.

It has recently been noted that although annihilation diagrams appear to be large in D decay, and therefore possibly in B decay, they do not contribute to the $B^o - \bar{B}^o$ width transition matrix element due to a helicity mismatch in the second order diagram, and thus do not play any role in possible CP violation in this system [Hagelin 80].

If CP violating effects due to mixing in the $B^o - \bar{B}^o$ system are likely to be small, it may still be interesting to look for CP violating interference effects in direct transitions. Several such experiments have been considered [Carter 80]; particular reactions made lead to asymmetries of several percent.

Thus far our discussion of CP violation in the K-M model, originating as it does, purely in the mass matrix, is equivalent to the superweak model. When strong interaction corrections are included, however, imaginary CP violating contributions from Penguin diagrams can cause deviations from superweak predictions.

Diagrams containing heavy quark loops, which arise when the strong interactions are included, both alter the strength of the original (V-A) ⊗ (V-A) couplings and induce new (V-A) ⊗ (V+A) couplings via the imaginary part of the Penguin diagrams. The latter are potentially the larger contribution to CP violation. These diagrams can be evaluated in leading log approximation in QCD. The results can be summarized briefly as

$$|\epsilon| = \frac{(\epsilon_m + 2\xi)}{2\sqrt{2}} e^{i\frac{\pi}{4}}$$

$$|\epsilon'| = \frac{1}{\sqrt{2}} - \xi \left|\frac{A_2}{A_0}\right| e^{i\frac{\pi}{4}}$$

Thus

$$\frac{\epsilon'}{\epsilon} \simeq \left|\frac{A_2}{A_0}\right| \frac{-2\xi}{\epsilon_m + 2\xi} \quad .$$

Here

$$\epsilon_m = 2\sin\theta_2\cos\theta_2\sin\theta_3\sin\delta \; P\left(\theta_2, \frac{m_c^2}{m_t^2}\right)$$

$$\xi \cong \cos\theta_2\sin\theta_2\sin\theta_3\sin\delta \left[f \frac{\ell n(m_c/m_t)}{\ell n(m_c/\mu)}\right] \quad .$$

μ is the renormalization point. There has been some controversy over the value of the coefficient f. Gilman and Wise [Gilman 79, Gilman 79a] found f = 0.75 leading to values of ϵ'/ϵ of from 3×10^{-3} to 3×10^{-2}. Guberina and Peccei [Guberina 80b] found f = .05 - 5, implying ϵ'/ϵ of $1.5 - 3 \times 10^{-3}$. A recent calculation of Galić of some of the higher

order contributions tends to the smaller values [Galić 80]. Current measurements of η_{+-} and η_{oo} yield $\epsilon'/\epsilon = -0.003 \pm 0.014$. Experiments are at present under way at Fermilab and CERN which can push the limit to a few parts in 10^3. These may, then, be able to establish the role of Penguin diagrams in CP violating processes.

Going beyond the K-M model, the presence of explicit right-handed currents can generate CP violation due to interference between the parity violating and parity conserving parts of the effective weak Hamiltonian [Mohapatra 75].

CP violation can also be generated by an enlargement of the Higgs sector. If flavor changing couplings are allowed, then two Higgs doublets can produce large CP violating effects in $D^o - D^o$ and $B^o - B^o$ systems [Lee 73, Sikivie 76]. Without flavor changing couplings, at least three Higgs doublets are necessary. One of these doublets must be charged with a mass of only a few GeV. This type of model [Weinberg 76, Deshpande 79, Ali 79c, Anselm 78] is fairly easily testable, since it predicts a large electric dipole moment of the neutron ($\sim 10^{-25}$ e-cm), and the light charged Higgs bosons can be produced in decays such as $b \to cH^-$. They also enhance the rate for $F \to \tau \nu_\tau$ and $B_c \to \tau \nu_\tau$.

Acknowledgements

I wish to thank G. Feldman, F. Gilman, A. Soni, J. Weiss, M. Wise, and S. Wolfram for helpful discussions.

REFERENCES

[Abbott 79] L. F. Abbott, P. Sikivie, and M. B. Wise
Phys. Rev. D21, 768 (1980)

[Abrams 79] G. S. Abrams, et al.
Phys. Rev. Lett. 43, 481 (1979)

[Abrams 80] G. S. Abrams, et al.
Phys. Rev. Lett. 44, 10 (1980).

[Ali 78] A. Ali and T. C. Yang
Nuovo Cim. Lett. 21, 213 (1978)

[Ali 79] A. Ali
Zeit. Phys. C1, 25 (1979)

[Ali 79a] A. Ali and E. Pietarinen
Nucl. Phys. B154, 519 (1979)

[Ali 79b] A. Ali, J. G. Körner, and G. Kramer
Zeit. Phys. C1, 269 (1979)

[Ali 79c] A. Ali and Z. Z. Aydin
Nucl. Phys. B148, 165 (1979)

[Ammar 80] R. Ammar, et al.
Phys. Lett. 94B, 118 (1980)

[Angelini 79] C. Angelini, et al.
Phys. Lett. 84B, 150 (1979)

[Anselm 78] A. A. Anselm and D. I. Dyakonov
Nucl. Phys. B145, 271 (1978)

[Aston 80] D. Aston, et al.
Phys. Lett. 94B, 113 (1980)

[Aston 80a] D. Aston, et al.
CERN/EP/80 - 189

[Bacino 78] W. Bacino, et al.
Phys. Rev. Lett. 40, 671 (1978)

[Bacino 80] W. Bacino, et al.
Phys. Rev. Lett. 45, 329 (1980)

[Báltay 79] C. Baltay, et al.
Phys. Rev. Lett. 42, 1721 (1979)

[Bander 80] M. Bander, D. Silverman, and A. Soni
Phys. Rev. Lett. 44, 7 (1980)

[Barate 79] R. Barate, et al.
Proceedings of the 1979 International Symposium on Lepton and Photon Interactions at High Energy (Batavia, Ill. 1979)

References - Continued

[Barger 77] V. Barger, T. Gottschalk and R. J. N. Phillips
Phys. Rev. D16, 746 (1977)

[Barger 79] V. Barger, W. F. Long, and S. Pakvasa
Phys. Rev. Lett. 42, 1585 (1979)

[Barger 79a] V. Barger and S. Pakvasa
Phys. Rev. Lett. 43, 812 (1979)

[Barger 79b] V. Barger, J. P. Leveille, and P. M. Stevenson
Phys. Rev. Lett. 44, 226 (1980)

[Barger 80] V. Barger, J. P. Leveille, P. M. Stevenson, and R. J. N. Phillips
Phys. Rev. Lett. 45, 83 (1980)

[Barger 80a] V. Barger, J. P. Leveille, and P. M. Stevenson
Phys. Rev. D22, 693 (1980)

[Berger 80] Ch. Berger, et al.
Phys. Rev. Lett. 45, 1533 (1980)

[Bernreuther 80] W. Bernreuther, O. Nachtmann, and B. Stech
Zeit. Phys. C4, 257 (1980)

[Bigi 79] I. Bigi and L. Stodolsky
SLAC-PUB-2410 (1979)

[Bigi 80] I. I. Y. Bigi and M. Fukugita
Phys. Lett. 91B, 121 (1980)

[Bletzacker 77] F. Bletzacker, H. T. Nieh, and A. Soni
Phys. Rev. D16, 732 (1977)

[Blietschau 79] J. Blietschau, et al.
Phys. Lett. 86B, 108 (1979)

[Bloom 80] E. D. Bloom, et al.
Proceedings of the 1980 SLAC Summer Institute on Particle Physics, A. Mosher, ed., (Stanford 1981)

[Brandelik 77] R. Brandelik, et al.
Phys. Lett. 70B, 132 (1977)

[Brandelik 79] R. Brandelik, et al.
Phys. Lett. 80B, 412 (1979)

[Buras 76] A. J. Buras
Nucl. Phys. B109, 373 (1976)

References - Continued

[Cabibbo 78] N. Cabibbo and L. Maiani
Phys. Lett. 73B, 418 (1978)
Erratum, ibid, 76B, 663 (1978)

[Cabibbo 79] N. Cabibbo and L. Maiani
Phys. Lett. 87B, 366 (1979)

[Cabibbo 79a] N. Cabibbo, G. Corbò, and L. Maiani
Nucl. Phys. B155, 93 (1979)

[Calicchio 80] M. Calicchio, et al.
Phys. Lett. 93B, 521 (1980)

[Carter 80] A. B. Carter and A. I. Sanda
Rockefeller University Preprint, DOE/EY/2232B-205

[Cazzoli 75] E. G. Cazzoli, et al.
Phys. Rev. Lett. 34, 1125 (1975)

[Chanowitz 80] M. Chanowitz
Proceedings of the Conference on High Energy e^+e^- Interactions, R. S. Panvini and S. E. Csorna, eds. (Vanderbilt 1980)

[Cutts 78] D. Cutts, et al.
Phys. Rev. Lett. 41, 363 (1978)

[Deshpande 79] N. Deshpande and E. Ma
Phys. Rev. D16, 1583 (1979)

[Deshpande 79] N. G. Deshpande and D. Iskandar
Phys. Rev. D19, 3457 (1979)

[Diamant-Berger 79] A. M. Diament-Berger, et al.
Phys. Rev. Lett. 43, 1773 (1979)

[Donoghue 80] J. F. Donoghue, E. Golowich, W. A. Ponce, and B. R. Holstein
Phys. Rev. D21, 186 (1980)

[Drijard 79] D. Drijard, et al.
Phys. Lett. 81B, 250 (1979)

[Drijard 79a] D. Drijard, et al.
Phys. Lett. 85B, 452 (1979)

[Einhorn 75] M. B. Einhorn and C. Quigg
Phys. Rev. D12, 2015 (1975)

References - Continued

[Ellis 75] J. Ellis, M. K. Gaillard, and D. V. Nanopoulos
Nucl. Phys. B100, 313 (1979)
Nucl. Phys. B104, 547 (1976) Erratum

[Ellis 77] J. Ellis, M. K. Gaillard, D. V. Nanopoulos, and S. Rudaz
Nucl. Phys. B131, 285 (1977)

[Fakirov 78] D. Fakirov and B. Stech
Nucl. Phys. B133, 315 (1978)

[Finjord 80] J. Finjord
Bern Preprint (1980)

[Fritzsch 79] H. Fritzsch
Phys. Lett 86B, 343 (1979)

[Fritzsch 80] H. Fritzsch and P. Minkowski
Phys. Lett. 90B, 455 (1980)

[Fritzsch 80a] H. Fritzsch and P. Minkowski
Bern Preprint - 80-0092 (1980)

[Fukugita 79] M. Fukugita, T. Hagiwara, and A. I. Sanda
Rutherford Preprint RL-79-052 Rev.

[Gaiser 80] B. D. Gaiser, T. Tsao, and M. B. Wise
SLAC-PUB-2523, (1980)

[Galić 80] H. Galić
SLAC-PUB-2617 (1980)

[Gavela 79] M. B. Gavela
Phys. Lett. 83B, 367 (1979)

[Gavela 79a] M. B. Gavela and L. Oliver
Phys. Lett. 85B, 95 (1979)

[Giboni 79] K. L. Giboni, et al.
Phys. Lett. 85B, 437 (1979)

[Gilman 79] F. J. Gilman and M. B. Wise
Phys. Lett. 83B, 83 (1979)

[Gilman 79a] F. J. Gilman and M. B. Wise
Phys. Rev. D20, 2392 (1979)

[Glashow 70] S. L. Glashow, J. Illiopoulos, and L. Maiani
Phys. Rev. D2, 1285 (1970)

References - Continued

[Glück 79] M. Glück
Phys. Lett. 84B, 459 (1979)

[Glück 79a] M. Glück
Phys. Lett. 88B, 145 (1979)

[Goldhaber 77] G. Goldhaber
Proceedings of the Conference on Weak Interaction Physics,
(Bloomington, Ind. 1977)

[Gronau 77] M. Gronau, C. H. Llewellyn Smith, T. F. Walsh,
S. Wolfram, and T. C. Yang
Nucl. Phys. B123, 47 (1977)

[Guberina 80] B. Guberina, R. D. Peccei, and R. Rückl
Phys. Lett. 91B, 116 (1980)

[Guberina 80a] B. Guberina, R. D. Peccei, and R. Rückl
Phys. Lett. 90B, 169 (1980)

[Guberina 80b] B. Guberina and R. D. Peccei
Nucl. Phys. B163, 289 (1980)

[Hagelin 79] J. S. Hagelin
Phys. Rev. D20, 2893 (1979)

[Hagelin 80] J. S. Hagelin and M. B. Wise
Harvard Preprint, HUTP-80/A070

[Hayashi 73] T. Hayashi, M. Nakagawa, H. Nitto and S. Ogawa
Prog. Theor. Phys. 49, 351 (1973)

[Ishikawa 79] K. Ishikawa
UCLA/79/TEP/20 (1979)

[Kane 79] G. L. Kane
SLAC-PUB-2326 (1979)

[Kane 79a] G. L. Kane, K. Stowe, and W. B. Rolnick
Nucl. Phys. B152, 390 (1979)

[Kane 80] G. L. Kane, W. B. Rolnick, and K. Stowe
Nucl. Phys. B165, 299 (1980)

[Karliner 76] I. Karliner
Phys. Rev. Lett. 36, 259 (1976)

References - Continued

[Kirkby 79] J. Kirkby
Proceedings of the 1979 International Symposium on Lepton and Photon Interactions at High Energies, (Batavia, 1979)

[Knapp 76] B. Knapp, et al.
Phys. Rev. Lett. 37, 882 (1976)

[Kobayashi 73] M. Kobayashi and T. Maskawa
Progr. Theoret. Phys. 49, 652 (1973)

[Körner 79] J. G. Körner, G. Kramer, and J. Willrodt
Zeit. Phys. C2, 117 (1979)

[LeYaouanc 77] A. LeYaouanc, L. Oliver, O. Pène and J.-C. Raynal
Phys. Lett. 72B, 53 (1977)

[Lee 73] T. D. Lee
Phys. Rev. D8, 1226 (1973)

[Lipkin 79] H. J. Lipkin
Fermilab - PUB-79/84-THY

[Lockman 79] W. Lockman, et al.
Phys. Lett. 85B, 443 (1979)

[Lüth 79] V. Lüth
Proceedings of the 1979 International Symposium on Lepton and Photon Interactions at High Energies, (Batavia, 1979)

[Ma 80] E. Ma, S. Pakvasa, and W. A. Simmons
Z. Physik C5, 309 (1980)

[Matsuda 80] M. Matsuda, M. Nakagawa, and S. Ogawa
Prog. Theor. Phys. 64, 264 (1980)

[Mistry 80] N. Mistry
Proceedings of the 1980 SLAC Summer Institute in Particle Physics, A. Mosher, ed. (Stanford, 1981)

[Mohapatra 75] R. N. Mohapatra, J. Pati, and L. Wolfenstein
Phys. Rev. D11, 3319 (1975)

[Mulvey 80] J. Mulvey
Proceedings of the 1980 SLAC Summer Institute on Particle Physics, A. Mosher, ed. (Stanford, 1981)

[Nussinov 77] S. Nussinov
Phys. Rev. D15, 2025 (1977)

References - Continued

[Olsen 80] S. Olsen
Proceedings of Orbis Scientiae 1980 (Miami, 1980)

[Pasupathy 78] J. Pasupathy
CERN.TH.2561 (1978)

[Peruzzi 77] I. Peruzzi, et al.
Phys. Rev. Lett. 39, 1301 (1977)

[Quigg 78] L. Quigg and J. L. Rosner
Phys. Rev. D17, 239 (1978)

[Rapidis 77] P. A. Rapidis, et al.
Phys. Rev. Lett. 39, 526 (1977)

[Rosen 78] S. P. Rosen
Phys. Rev. D18, 2514 (1978)

[Rosen 79] S. P. Rosen
Los Alamos Preprint LA-UR-79-2619

[Rosen 79a] S. P. Rosen
Phys. Rev. D21, 2631 (1980)

[Russell 80] J. J. Russell
Thesis, University of Illinois, (Urbana, 1980), unpublished.

[Sanda 79] A. I. Sanda
Rockefeller Preprint COO-2232B-191

[Scharre 78] D. L. Scharre, et al.
Phys. Rev. Lett. 40, 74 (1978)

[Schindler 80] R. Schindler, et al.
Submitted to Phys. Rev.

[Schindler 80a] R. Schindler, et al.
Phys. Rev. D21, 2716 (1980)

[Schmid 77] C. Schmid
Phys. Lett. 66B, 353 (1977)

[Shifman 77] M. A. Shifman, A. I. Vainshtein, and V. I. Zakharov
Nucl. Phys. B120, 316 (1977)

References - Continued

[Shrock 78] R. E. Shrock and L.-L. Wang
Phys. Rev. Lett. 41, 1692 (1978)

[Shrock 79] R. E. Shrock, S. B. Treiman, and L.-L. Wang
Phys. Rev. Lett. 42, 1589 (1979)

[Shrock 79a] R. E. Shrock and M. B. Voloshin
Phys. Lett. 87B, 375 (1979)

[Shrock 79b] R. E. Shrock and S. B. Treiman
Phys. Rev. D19, 2148 (1979)

[Sikivie 76] P. Sikivie
Phys. Lett. 65B, 141 (1976)

[Suzuki 79] M. Suzuki
Phys. Lett. 85B, 91 (1979)

[Suzuki 79a] M. Suzuki
Phys. Rev. Lett. 43, 818 (1979)

[Suzuki 80] M. Suzuki
UCB-PTH-80/4 Revised

[Ushida 80] N. Ushida, et al.
Phys. Rev. Lett. 45, 1049 (1980)

[Ushida 80a] N. Ushida, et al.
Phys. Rev. Lett. 45, 1053 (1980)

[Vidal 78] R. Vidal, et al.
Phys. Lett. 77B, 344 (1978)

[Vuillemin 78] V. Vuillemin, et al.
Phys. Rev. Lett. 41, 1149 (1978)

[Wang 79] L.-L. Chau Wang and F. Wilczek
Phys. Rev. Lett. 43, 816 (1979)

[Weinberg 76] S. Weinberg
Phys. Rev. Lett. 37, 657 (1976)

[Wilson 69] K. G. Wilson
Phys. Rev. 179, 1499 (1969)

[Wolfenstein 79] L. Wolfenstein
Carnegie-Mellon Preprint C00-3066-134

References - Continued

[Yamada 80] S. Yamada
Proceedings of the XXth International Conference on High Energy Physics, (Madison, 1980)

[Yamada 80a] K. Yamada
Fermilab- PUB 80/36-THY

From the Standard Model to Composite Quarks and Leptons

Haim Harari

Weizmann Institute of Science

Rehovot, Israel

Part I: The Standard Model, its Present Status and its Open Problems

Part II: Composite Quarks and Leptons

Foreword

Particle physics is at an extremely interesting crossroads. Behind us is the marvelous creation of the so-called "standard model" based on the renormalizable nonabelian gauge theory of $SU(3)_C \times SU(2) \times U(1)$, and supported by a long list of successful experimental tests. Ahead of us is a totally unknown territory and several different paths, among which we should soon choose. According to some views we may be about to enter an immense desert, buth other options are, at least, as likely.

These lectures are devoted to those aspects of the physics of quarks and leptons which lie on the frontiers of the standard model and beyond it. The lectures are divided into two parts. Part I starts with a description of the present status of the standard model, proceeds to some open problems and concludes with a short survey of topics such as extensions of the electroweak group, grand unification, the generation puzzle and the connection between quark masses and generalized Cabibbo angles. The material in Part I is not new. It has been discussed in numerous review articles, and it is presented here as a general introduction.

Part II is entirely devoted to the possibility that quarks and leptons are composite. This is a "hot," rapidly developing topic, and the time is not yet ripe for a well-organized review. In fact, the material presented here reflects our thinking in November 1980, when it was written, and it differs in emphasis and in many details from the lectures given at the Summer Institute in August 1980. We start Part II with a discussion of the motivation for, and limitations of composite models. We proceed with a description of some of the general theoretical difficulties and review several published models. We conclude with a description of the dynamical rishon model, a scheme which we have recently proposed (after the lectures were given in August 1980).

Part I

The Standard Model, its Present Status and its Open Problems

1. The Framework of the Standard Model

1.1 The Standard Model: Its Particles and its Free Parameters

The standard model[1] is based on the gauge group $SU(3)_c \times SU(2) \times U(1)$, spontaneously broken into $SU(3)_c \times U(1)_{em}$. It contains 12 gauge bosons (8 gluons, W^+, W^-, Z°, γ), 3 generations of quarks and leptons (u,d,ν_e,e^-; c,s,ν_μ,μ^-; t,b,ν_τ,τ^-) and an unknown number of physical Higgs particles (at least one). All left-handed fermions are in SU(2) doublets and all right-handed fermions are in SU(2) singlets.

The model contains at least 30 free parameters of which 3 are the independent couplings of the three gauge groups, approximately 25 parameters represent masses and mixing angles which arise in the process of spontaneous symmetry breaking, and an unknown number of additional parameters appear in the Higgs potential. Additional "parameters" are the number of quark and lepton generations and the number and classification of the Higgs particles.

Table I summarizes the particles and the parameters of the standard model.

In the following sections we briefly discuss the various sectors of the model, the values of the known parameters and experimental means of studying the undetermined parameters. However, it is clear that a theory with more than 30 free parameters cannot be considered to be completely satisfactory. It is the desire to understand these parameters, as well as the overall pattern, which sends us beyond the standard model.

1.2 The Gauge Boson Sector

While we feel confident that the standard model is essentially correct, we should remind ourselves that we have, so far, directly observed only one of its 12 gauge bosons, and we have yet to detect the 3-boson couplings which are the trademark of a nonabelian gauge theory.

Sector	Particles	Parameters
Gauge bosons	8 gluons	(α_{st} or Λ)
	W^+,W^-,Z°	(α,θ_W or g_1,g_2); (M_W,M_Z)
Fermions	(I) u,d,ν_e,e	Fermion classification: left doublets, right singlets. Number of generations.
	(II) c,s,ν_μ,μ	6 quark masses 3 charged lepton masses
	(III) t,b,ν_τ,τ	3 neutrino masses 3 generalized Cabibbo angles 1 Kobayashi-Maskawa phase
	More?	3 leptonic Cabibbo angles 1 leptonic K-M phase Quark-lepton angles and phases
Higgs particles	ϕ More?	Number of Higgs particles Classification of Higgs particles Higgs masses and couplings

Table I: Parameters of the standard model

Indirect evidence for the existence of gluons has been accumulated for several years and culminated in the discovery of the three-jet events in PETRA[2]. Preliminary evidence for the correct spin of the gluon is now available[3]. The three-gluon coupling has not yet been observed. It probably will be first identified by studying the detailed properties of gluon jets and quark jets, showing that gluon jets are less collimated than quark jets. The single coupling parameter of QCD is Λ, the scale parameter which determined the running coupling α_{st}.

$$\alpha_{st}^{-1}(q^2) = \alpha_{st}^{-1}(\mu^2)\left[1 + \frac{33-2f}{12\pi}\alpha_{st}(\mu^2)\ln\frac{q^2}{\mu^2}\right]$$

Estimates of Λ range all the way from 700 MeV or so down to values around 100 MeV. The absence of observed scaling violations at high-q^2 muon and neutrino scattering[4] points towards very low Λ-values, blaming low-q^2 scaling violations on higher-twist effects. Low Λ-values are also required for the predicted behaviour of elastic form factors. The most direct determination of α_{st} (and Λ) could have come from the rate of three-jet events in e^+e^- collisions. However, large higher order corrections[5] seem to confuse the issue, and the already reliable experimental measurements[6] cannot yet yield a reliable theoretical determination of Λ. Thus-- the QCD coupling is known only approximately.

The masses of the W and Z bosons will not be explicitly known until these particles are discovered, presumably at their predicted masses of 77 GeV and 88 GeV, respectively. The weak mixing angle θ_W has been accurately determined in numerous neutral current experiments[7]:

$$\sin^2\theta_W \cong 0.23$$

A Higgs potential with an arbitrary number of SU(2) Higgs doublets, but no other Higgs multiplets, predicts the famous Weinberg mass relation:

$$\frac{M_W}{M_Z} = \cos\theta_W$$

The ratio M_W/M_Z can be measured by comparing the relative rates of charged and neutral current reactions. The best available values indicate remarkable agreement of this prediction with experiment[7] (within one or two percent). This successful result provides us with two extremely important kinds of constraints on the theory:

(i) All Higgs particles which contribute to the vector boson masses must be in SU(2) doublets. This is an important constraint for any model, especially if one considers the Higgs particles to be composite.

(ii) Radiative corrections to the Weinberg mass relation must be small, thus limiting the allowed spectrum of heavy quarks and leptons[8].

An observation of a W^+W^-Z vertex will have to await accurate measurement of processes such as $e^+e^- \to W^+W^-$, exhibiting the Z°-propagator effect. The $W^+W^-\gamma$ vertex will, of course, be observed if and when the W is discovered.

To summarize: a significant number of very fundamental properties

of the gauge-boson sector of the standard model remain to be observed experimentally. However, there is no cause for any serious worry or alarm, and all indications are in the direction of confirming the model.

It is extremely important to verify experimentally each and every component of the standard model. A future theory of physics at shorter distances may turn the Lagrangian of the standard-model into an effective Lagrangian, and what now appears to be the ultimate theory may become a low-energy approximation of the correct theory. In such a case each aspect of the model and every term in the Lagrangian must be separately tested and verified, and one cannot necessarily deduce the existence of one term from the existence of the other.

1.3 The Fermion Classification[9]

The standard model assumes the existence of three generations of quarks and leptons, each containing two (color triplet) quarks and two (color-singlet) leptons. Left-handed and right-handed fermions are, respectively, in SU(2) doublets and singlets. There is no experimental evidence against these assignments, but much of it is not directly supported by experiments.

There is solid experimental evidence from charged current processes for the assignment of the left-handed u,d,ν_e,e; c,s,ν_μ,μ and ν_τ,τ to SU(2) doublets. There is convincing evidence from neutral current processes for the assignment of the right-handed u,d,e to SU(2) singlets. There is no clear experimental evidence for the assignment of the right-handed c,s,μ into singlets. In order to exclude the possibility of a right-handed doublet including a known "light" fermion and a heavy new fermion, we need neutral current measurements of the third component of the weak isospin. Such measurements have not yet been performed for c,s,μ. The first such experiment will probably be the measurement of the forward-backward asymmetry in $e^+e^-\to\mu^+\mu^-$. Indirect evidence is obtained if we assume the "naturalness" of the absence of flavor-changing neutral currents. In such a case the right-handed c and s must be in singlets.

If ν_e and ν_μ have nonvanishing masses, their right-handed components will also be in SU(2) singlets. If the neutrinos are massless, their right-handed components do not exist.

The missing t-quark is, of course, the most important ingredient yet to be observed in the fermion sector of the standard model. Since its mass cannot be predicted with confidence, there is no cause for any alarm. Needless to say, we have no experimental evidence for the SU(2)x U(1) assignments of the t-quark or, for that matter, the b-quark. However, the recent CESR data[10] are in qualitative agreement with expectations for b-decays in the standard model. The τ-neutrino has not been directly observed, and the assignment of the right-handed τ has not been experimentally determined. However, all data concerning τ are consistent with the standard model.

The overall picture is, again: A large number of ingredients of the standard model remain unconfirmed, but no conflict exists between experiment and the standard model.

2. The Parameters of the Standard Model

2.1 The Masses of Quarks and Charged Leptons

Nine of the free parameters of the standard model represent the masses of the quarks and the charged leptons.

Since quarks are presumably confined, their masses cannot be directly measured. The theoretical definition of the quark masses is somewhat arbitrary and one is led to consider a "running quark mass" in QCD. At very low energies, the so-called "constituent quark masses" presumably play an important role. However, when discussing relations

among quark masses and generalized Cabibbo angles, the so-called "chiral quark masses" or "current quark masses" should be used. They are commonly believed to have the following values in MeV:

$$m_u \sim 4; \quad m_d \sim 7; \quad m_s \sim 150; \quad m_c \sim 1300; \quad m_b \sim 4500; \quad m_t > 18000.$$

The charged lepton masses are, of course, determined by direct observation.

No clear pattern is observed in the fermion mass spectrum and no convincing mass relation has been proposed. One numerological exercise which is not yet completely ruled out is:

$$m_u/m_e \sim m_c/m_\mu \sim m_t/m_\tau \ .$$

The first two ratios are of order 10 (±25%), predicting m_t somewhere between 14 and 22 GeV. A slightly better motivated prediction (discussed in Section 5.3) is[11]:

$$\frac{(m_t-m_c+m_u)^3}{m_t m_c m_u} = \frac{(m_b-m_s+m_d)^3}{m_b m_s m_d}$$

predicting $m_t \sim 14$ GeV in clear disagreement with experiment.

Aside from attempts to understand the numerical values of the quark and lepton masses, we face the problem of understanding the different orders of magnitudes of masses in different generations. For instance, if quarks and leptons are composites of some more fundamental building blocks of matter, one might expect a more evenly spaced spectrum with mass differences corresponding to the distance scale of the hypothetical substructure.

2.2 Generalized Cabibbo Angles and the K-M Phase[12]

The three SU(2) doublets of the left-handed quarks can be defined, for instance, by the u,c,t mass eigenstates. The charge -1/3 SU(2)-companions of u,c,t are, respectively, d',s',b', related to the mass eigenstates d,s,b by the famous 3x3 transformation matrix:

$$A = \begin{pmatrix} c_1 & s_1c_3 & -s_1s_3 \\ -s_1c_2 & c_1c_2c_3-s_2s_3e^{i\delta} & c_1c_2s_3+s_2c_3e^{i\delta} \\ s_1s_2 & -c_1s_2c_3-c_2s_3e^{i\delta} & -c_1s_2s_3+c_2c_3e^{i\delta} \end{pmatrix}$$

where $c_i \equiv \cos\theta_i$; $s_i \equiv \sin\theta_i$; θ_1, θ_2, θ_3 are the three generalized Cabibbo angles; δ is the Kobayashi-Maskawa phase parameter, leading to CP-violation effects[13]. Experimentally, only θ_1 is known. A large number of different weak transitions should enable us to determine (and, then overdetermine) the four parameters of the matrix. Each process measures one or more matrix element of the matrix A. The detailed phenomenology of the A-matrix has been extensively discussed[12]. Here we make only a few brief remarks about each matrix element:

(i) $A_{ud}=c_1$. Well-measured in ordinary β-decay, yielding the standard value: $\theta_1=13.2°\pm0.5°$.

(ii) $A_{us}=s_1c_3$. Well-measured in strangeness changing semileptonic decay. Using the above value of θ_1, A_{us} is consistent with $c_3=1$ (hence $\theta_3=0$). The uncertainty in A_{us} yields the bound $\theta_3 \lesssim 20°$.

(iii) $A_{ub}=s_1s_3$. From the measured values of A_{ud}, A_{us} and unitarity we know that A_{ub} is very small. Direct measurement will have to await the observation of decays such as B→pions+e^-+ν_e. What is required is an absolute measurement of such a rate, unlikely for the next few years.

(iv) $A_{cd}=-s_1c_2$. Could be measured by observing Cabibbo suppressed semileptonic D-decays such as D→ρeν_e, πeν_e, etc. Here again, an absolute rate is necessary, involving separate determinations of the D lifetime and the appropriate branching ratio. Assuming that θ_2 is small, a measurement of A_{cd} will not provide us with a sensitive determination of its value. A_{cd} should be measured mainly in order to confirm the relation $A_{cd}=-A_{us}$ which should be valid for any small θ_2, θ_3.

(v) $A_{cs}=c_1c_2c_3-s_2s_3e^{i\delta}$. Directly measured by the leading semileptonic D-decays such as $D\to K^*e\nu_e$, $Ke\nu_e$. There are no data on these decays, but experiments at SPEAR and DORIS should determine this matrix element within the next few years (using, of course, a separate determination of the D-lifetime). As long as the t-quark is missing, A_{cs} seems to offer the earliest hope for an experimental bound on θ_2.

(vi) $A_{cb}=c_1c_2s_3+s_2c_3e^{i\delta}$. It is very likely, but not absolutely necessary, that $|A_{cb}|>|A_{ub}|$. If so, the leading b-decays involve charmed particles. Preliminary data from CESR[10] are consistent with this hypothesis. An absolute determination of the rate for $B\to De\nu_e$ would yield a value for A_{cb}, and a further constraint on θ_2, θ_3.

(vii) A_{td}, A_{ts}, A_{tb}. These matrix elements can be experimentally determined only if and when the t-quark is discovered. A_{td} would then offer the most direct determination of θ_2, requiring a measurement of the t-lifetime and the branching ratio for $T\to$ pions$+e+\nu_e$.

The δ parameter can be deduced from any CP-violating processes, provided the other angles are known. We must remember that the phenomenology of the A-matrix is based on the assumption that three and only three identical generations of quarks exist and that the phase δ is the sole cause of CP-violation. A fourth generation and/or Higgs-induced CP-violations and/or extensions of $SU(2)xU(1)$ to $SU(2)_L xSU(2)_R xU(1)$ could change the picture.

The attractive aspect of the A-matrix is the fact that the four parameters determine a large number of, otherwise unrelated, weak processes. It would be extremely interesting to see, a decade from now, whether we indeed have independent but consistent experimental determinations of the four parameters.

We return to the question of theoretical, rather than experimental, constraints on the angles in Section 2.4.

2.3 Neutrino Masses and Leptonic Cabibbo Angles

The three SU(2) doublets of the left-handed leptons are defined by the physical electron, muon and τ. Their neutral companions are defined as ν_e, ν_μ, ν_τ. If all neutrinos are massless, the concept of "neutrino mass-eigenstates" becomes meaningless and no transformation matrix between weak eigenstates and mass eigenstates is needed. If, however, the three neutrinos have different masses, the mass eigenstates ν_1, ν_2, ν_3 are, in general, different from ν_e, ν_μ, ν_τ. A transformation matrix, identical in structure to the A-matrix of the quark sector, is then defined, involving three leptonic Cabibbo angles as well as a leptonic K-M phase. Such angles would be extremely hard to measure, although, in principle, each one of them appears in the amplitudes for many different processes.

The present accepted limits on the neutrino masses are (in MeV):

$$m(\nu_e)<6\cdot10^{-5};\quad m(\nu_\mu)<0.5;\quad m(\nu_\tau)<200.$$

The different orders of magnitude of these limits reflect experimental sensitivities which are always related to the mass scale of the accompanying charged lepton. It is entirely possible that all neutrinos are massless or that they have comparable masses, or that their mass ratios are similar to the charged lepton mass ratios, or even that their relative mass values are reversed.

The above limits on the neutrino masses were obtained from measurements of the "endpoint" spectra of the associated charged leptons. A recent experiment claimed[14], for the first time, a finite mass for ν_e. However, the result is yet to be confirmed.

If neutrinos have masses, we expect neutrino oscillations. Starting with a neutrino beam of energy E, in which two neutrinos of masses m_1, m_2 mix, we expect to observe oscillations at distance L of the order of

$$L \sim E/\Delta m^2$$

where $\Delta m^2 = m_1^2 - m_2^2$. At much smaller distances no effect should be observed. For larger distances the oscillations become very rapid and only an average "depletion" of the original beam can be observed.

No experiment has, so far, claimed to have observed actual oscillations. However, several experiments in the last few years found effects which might be interpreted as "neutrino depletion," due to oscillations. Each of these experiments corresponds to specific values of L and E. Since only depletion is claimed (rather than actual oscillations) we can only deduce that, for each such experiment $\Delta m^2 \gtrsim E/L$. Some of the relevant experiments are[15]:

(i) The solar neutrino experiment, sensitive to $\Delta m^2 \gtrsim 10^{-10}$ eV^2.

(ii) Experiments at deep mines, sensitive to $\Delta m^2 \gtrsim 10^{-2}$ eV^2.

(iii) Beam dump experiment, sensitive to $\Delta m^2 \gtrsim 10^{-2}$ eV^2.

(iv) Reactor experiments, sensitive to $\Delta m^2 \gtrsim$ eV^2.

In each of these categories effects have been observed, which can be interpreted in terms of neutrino oscillations. However, in each case, either experimental uncertainties or other possible sources of the observed effect obscure the issue.

Additional, indirect indication, for neutrino masses of the order of 10 eV emerges from astrophysical considerations[16].

We are, thus, in the tantalizing situation of having six independent sources of indications for nonvanishing neutrino masses, but we do not feel that any one of them is sufficiently compelling, at present.

If neutrino masses exist, several interesting theoretical aspects arise:

(i) Right-handed neutrinos should be taken into account in constructing extensions of the standard model. (For instance, the usual SU(5) multiplets have no such component).

(ii) Yet another mass scale is introduced into the already difficult problem of understanding the mass hierarchy of fermions.

(iii) The idea of parity violation by a spontaneous symmetry breaking of a left-right symmetric theory becomes more attractive.

(iv) The number of nonvanishing free parameters of the standard model increases by, at least, seven: Three neutrino masses, three leptonic Cabibbo angles and one leptonic K-M phase.

It will be extremely interesting to follow the experimental developments in this field in the next few years.

2.4 Theoretical Constraints on Generalized Cabibbo Angles

An important bound on the angle θ_2 in the quark sector of the standard model emerges from the following consideration. The original calculation[17] of the K_S°-K_L° mass difference in a four-quark model, yielded the result:

$$M = \text{const.}\ m_c^2 c_1^2 s_1^2$$

where the constant depends on G_F, M_W, etc. The calculation was based on the diagram of Figure 1. Inserting the known experimental values of all

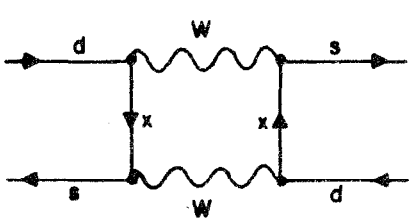

Figure 1: Contribution to K_S°-K_L° mass difference. x = u,c,t.

quantities except m_c, the charmed-quark mass was correctly predicted. It is clear that the diagram of Figure 1 provides us only with a crude approximation. Other diagrams may be important. However, it is generally believed that the above equation is correct to within, say, a factor of two.

If a t-quark exists, it can be exchanged in the diagram of Figure 1. Its contribution to ΔM will include a term proportional to m_t^2. At this point two separate interesting results follow:

(i) Since the calculation of ΔM is approximately correct without the t-quark contribution, the latter must be smaller (or, at most, numerically comparable) to the c-quark contribution. The complete result is[18]:

$$\Delta M = \text{const}\cdot m_c^2\cdot c_1^2 s_1^2[c_3^2 c_2^4 + c_3^2 s_2^4 \eta + 2c_3^2 s_2^2 c_2^2 \frac{\eta \ell n \eta}{1-\eta}]$$

where $\eta = m_t^2/m_c^2$. Requiring that the term in the square brackets is smaller than two we obtain:

$$\tan\theta_2 \lesssim \sqrt{\frac{m_c}{m_t}} \lesssim 0.3$$

This is the best available constraint on θ_2.

(ii) A much more important result, in our opinion, emerges from the assumption that the physics at very low energy cannot depend in any strong way on the existence of an extremely heavy quark[19]. We cannot prove such an assertion, but it can be motivated by observing that large energy denominators make distant levels unimportant; nearby singularities are expected to dominate dispersion integrals while distant singularities are usually neglected; the physics of the lowest lying levels of any simple system does not depend on the existence or the parameters of some very distant high energy level. If we apply this assumption to our case we conclude that ΔM must be determined, to a good approximation, by the c-quark contribution, and a high mass t-quark should not be allowed to influence it too much. In other words, if $m_t \gg m_c$, the K_S°-K_L° mass difference should not be sensitive to whether $m_t \sim 10$ GeV or $m_t \sim 50$GeV or the t-quark does not exist. Considering the nature of our diagram, this can be true if and only if:

$$|A_{td}A_{ts}|m_t \ll |A_{cd}A_{cs}|m_c$$

or, in the approximation of small θ_3:

$$\tan\theta_2 \ll \sqrt{\frac{m_c}{m_t}}$$

Notice that we have obtained this condition without appealing to any experimental values. Our theoretical assumption directly leads to this bound. The result tells us that there must be relations between generalized Cabibbo angles and the quark masses. If the angles do not depend on the masses, the t-quark would dominate ΔM in the limit of large m_t!

A very similar situation, amplifying our argument, exists in the process $\mu \to e\gamma$. Let us assume that, in addition to (ν_e, e^-) and (ν_μ, μ^-) there is a third doublet (ν_x, x^-) where ν_x is extremely heavy. We then have contributions to $\mu \to e\gamma$ from the diagram of Figure 2. The contri-

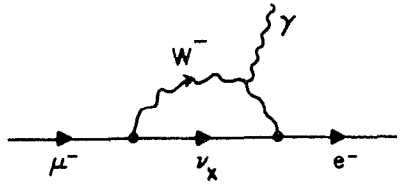

Figure 2: A diagram contributing to $\mu \to e+\gamma$

bution of this diagram is proportional to $A_{e\nu_x} A_{\mu\nu_x}$ and, in the limit $m(\nu_x) \to \infty$, it remains finite[20] ($A_{e\nu_x}, A_{\mu\nu_x}$ are the appropriate matrix element of the leptonic 3x3 matrix and they are explicit functions of the leptonic Cabibbo angles). Here, again, we find that an infinitely heavy neutral lepton will decouple from the low energy process $\mu \to e\gamma$ only if its mixing with the low energy leptons disappears for $m(\nu_x) \to \infty$. We therefore conclude that, in that limit, $A_{e\nu_x} A_{\mu\nu_x} \to 0$. The angles depend, again, on the masses. Distant generations become decoupled, and the mixing angles between light and heavy quarks are somehow related to the appropriate mass ratios.

It should be worthwhile to pursue this line of reasoning and to derive general rules for the relationship between masses and angles. More about this question in Section 4.3

2.5 Quark-Lepton Angles

The generalized Cabibbo angles determine the three-dimensional rotation between the u-c-t axes and the d-s-b axes. The leptonic Cabibbo angles determine the rotation between the e-μ-τ axes and the ν_1-ν_2-ν_3 axes (which are defined only if neutrinos have masses). As long as there is no connection between quarks and leptons and as long as there is no gauge boson which couples a quark to a lepton, we cannot relate the leptonic axes to the quark axes. They remain in different three-dimensional spaces and the concept of a generation is not well-defined. However, if we define the generations by introducing a larger gauge group (such as SU(5) or O(10)) it becomes meaningful to inquire, e.g., which combination of u,c,t belongs to the same generation as the electron. In other words, the Lagrangian of the theory will now contain a term in which a leptoquark couples the electron to a charge +2/3 quark which we define as u_x. Similarly, μ is connected to c_x and τ to t_x. It is now meaningful to define a 3x3 unitary matrix rotating the e-μ-τ axes (which are identical to the u_x-c_x-t_x axes) into the u-c-t axes[21]. Such a matrix will, again, contain new angle parameters which measure the relative orientation of the quark and lepton sectors in generation space. Such angles can, in principle, be determined by measuring branching ratios such as:

$$\frac{\Gamma(p \to \mu^+ + \pi^\circ)}{\Gamma(p \to e^+ + \pi^\circ)}$$

In any theory in which the concept of a generation is well-defined, these quark-lepton angles should be treated on the same footing as the ordinary Cabibbo angles. They also should, presumably, depend on ratios of quark masses and lepton masses.

2.6 Masses, Angles and the Higgs Sector

In the last five sections we have discussed various aspects of the more than 20 parameters which arise through the fermion mass matrix. *This mass matrix is generated by the spontaneous symmetry breaking.* Each of its parameters is determined by the Yukawa couplings and by the vacuum expectation values of the Higgs fields. A complete knowledge of the latter would enable us to completely determine the mass matrix, thus determining its eigenvalues (the physical masses) and eigenvectors (which fix the angles).

Unfortunately, we know almost nothing about the Higgs sector. The successful Weinberg mass relation indicates that all Higgs particles are in SU(2) doublets. This does not help us in the fermion sector. Since all left-handed fermions are in doublets and all right-handed fermions are in singlets, only Higgs doublets can contribute to fermion masses. Hence, the existence or absence of other Higgs multiplets is not directly relevant here.

We do not have any hint for the number of Higgs doublets, except for an "empirical feeling" that it will be very difficult to distinguish

among three generations with only one Higgs doublet. Most attempts to understand the mass matrix assume two or three doublets. However, all other options are definitely open.

The question of Higgs masses is, again, wide open. Fortunately, it does not seem to have a strong impact on the fermion mass matrix, and it seems possible to make progress in understanding the fermion masses and angles without a complete understanding of the Higgs masses and self-couplings.

3. Additional Aspects of the Model

3.1 Conservation Laws in the Standard Model

The only exactly conserved "internal" quantum numbers in the standard model are electric charge and color, reflecting the final, unbroken $SU(3)_c \times U(1)_{em}$ gauge symmetry. Conservation of baryon, lepton or muon number is not an intrinsic part of the model. In principle, all of these quantum numbers need not be conserved. However, the Lagrangian of the standard model contains a finite well-defined set of interaction terms, none of which breaks B or L conservation. If all neutrinos are massless, and if the Higgs sector is sufficiently simple (i.e., one Higgs doublet), there is also no interaction which violates the separate conservation of electron, muon and τ-number. All of these conservation laws are extremely interesting. They are not fundamental symmetries of the gauge group, and they can be violated if we complicate the model by introducing additional fields or additional gauge bosons. In the latter case the overall (broken) gauge group is enlarged, the unbroken gauge symmetry remains unchanged, but the extra conservation laws may be broken.

The direct consequence of this situation is the observation that baryon, lepton and muon number violations probe terms in the Lagrangian which go beyond the standard model, without contradicting it. A hypothetical violation of color or electric charge conservation would be evidence against the standard model. A violation of B, L or muon conservation would be evidence for possible extensions of the standard model (larger gauge group and/or more Higgs particles, etc.). This is the reason for the intimate connection between the search for rare processes such as $p \to e^+\pi^\circ$, $\mu \to e\gamma$, $K^\circ \to e^+\mu^-$ and the physics which lie beyond the standard model.

3.2 Exotic Quarks and Leptons

An extremely important feature of the standard model is the existence of only four color-charge combinations in the fermion spectrum. We find color singlets with charges 0, -1, color triplets with charges 2/3, -1/3 and all the corresponding antiparticles. All other combinations are missing, for no good reason. It is absolutely essential to search for these missing combinations, which we call "exotic" quarks and leptons. We might find:

(i) Charge 1/3, -2/3 color triplets (rather than antitriplets).

(ii) Fractionally charged leptons.

(iii) Integrally charged quarks.

(iv) Doubly charged leptons (or leptons with charge 3,4,...).

(v) Charge 5/3, -4/3 quarks (or quarks with larger fractional charges).

(vi) Color sextet fermions (or larger color multiplets).

(vii) Spin 3/2 quarks or leptons.

Exotic particles of the type (i) would produce fractionally charged hadrons. The experimental limits on the existence of such hadrons are probably quite strong.

Fractionally charged leptons (type (ii)) would not be easy to detect, unless especially searched for. Their contribution to R in e^+e^- is small

(R=1/9 for Q=1/3 lepton). Quark search experiments could probably set the best limits on such objects, which might be stable.

All other types of exotic fermions (types (iii)-(vii)) should be easily detected in e^+e^- collisions, since they contribute large R-values. It is probably safe to assume that no such particles exist with a mass below 18 GeV, with the possible exception of a peculiarly behaved J=3/2 fermion.

The search for exotic quarks and leptons is crucial. If they are found -- we have to "redesign" the standard model. If they are not found, and especially if the third generation is confirmed to have the same structure as the first two, we must be able to explain why the same four color-charge combinations repeat themselves while no other combinations exist. If quarks and leptons are composite, or if they all belong to one multiplet of a large gauge group, the list of allowed color-charge combinations should be the first item to be explained.

3.3. The Standard Model: Summary

Until this point we have discussed various aspects of the standard model itself, usually with an eye towards future developments. Before we move on to discuss the physics which lies beyond the model, let us list some of the open experimental and theoretical questions.

The experimental tasks are:

(i) Find the t-quark.

(ii) Determine the generalized Cabibbo angles and the K-M phase and verify the weak transitions among the six quarks obey the standard phenomenology.

(iii) Detect the τ-neutrino.

(iv) Measure neutrino masses or improve upper limits. Search for neutrino oscillations.

(v) Search for exotic quarks and leptons.

(vi) Find W^+, W^-, Z^0 and their $(W^+W^-Z^0)$ coupling.

(vii) Search for additional generations.

(viii) Probe the Higgs sector: find Higgs particle(s) and study their interactions.

All of these experimental "assignments" would test and verify various aspects of the standard model itself. Other experiments, to be discussed in the following sections, would probe topics which go beyond the model.

The open theoretical problems serve as pointers towards the next steps:

(i) Can we truly unify the three independent interactions of $SU(3)_C \times SU(2) \times U(1)$?.

(ii) What is the connection between quarks and leptons? Why are their charges related? Why do they have a similar pattern? Why does the sum of all fermion charges in each generation vanish, thus rendering the triangle anomaly harmless?

(iii) Can we relate to each other the numerous free parameters of the standard model? In particular, we should be able to relate the Cabibbo angles to fermion mass ratios.

(iv) What is the reason for the redundancy of the three generations? What identifies a generation? How many generations are there?

(v) Can a theory with 24 fundamental fermions, 12 fundamental bosons, an unknown number of Higgs particles and, at least, 30 free parameters, be considered the final word?

These questions lead us towards topics which lie beyond the standard model.

4. Beyond the Standard Model

4.1 Alternative Models?

Before embarking upon our voyage beyond the standard model, we should stop for a moment to inquire whether there are any viable alternative models. The physics of the first two generations of quarks and leptons leaves very little room for any alternatives. However, the absence of the t-quark has led many authors to consider alternatives to the three-generations picture. The most popular among these is the possibility that a sixth quark h will be found, but its charge will be $-\frac{1}{3}$, completing two triplets of quarks, each with electric charges $\frac{2}{3}$, $-\frac{1}{3}$,$-\frac{1}{3}$. In such a case we would have a (u,d,b) SU(3) triplet and a (c,s,h) SU(3) triplet, with the possibility of b↔h interchange[22]. The SU(3) gauge group will have to include flavor changing neutral currents as well as a lack of quark-lepton similarity. Other schemes suggest a color sextet b-quark, a spin $\frac{3}{2}$ b-quark, etc. All such schemes can be completely excluded only when the t-quark is discovered and the t and b weak decays are studied. The preliminary results from CESR indicate that b-decays are probably consistent with the predictions of the standard model[10]. A slight improvement of these results should be sufficient for excluding most alternative models, with the possible exception of a model assigning (u,d,h) and (c,s,b) to two triplets[23]. Such a model would predict dominant b decays into charmed and strange quarks, and much better b-decay data (or finding the t-quark) will be necessary in order to reject it.

In any event, all alternative models are, in our opinion, theoretically unattractive. We hope and expect that the standard model will continue to survive all experimental tests, and we reiterate our view that, at present, there are no experimental difficulties.

4.2 Extensions of the Standard Model

Extensions of the standard model are schemes for which the standard model serves as an adequate low energy approximation, requiring additional ingredients at higher energies. Such extensions can be considered in several directions:

(i) The most trivial extension is, of course, the possible existence of additional generations. This would not change any essential features of the standard model, except for a further increase in the number of parameters and perhaps additional attention to the generation puzzle. We discuss the question of "how many generations" in Section 5.2, but with our present level of understanding, only experiments can tell us whether additional generations are necessary.

(ii) The color gauge group may be extended, for instance, into a spontaneously broken chiral $SU(3)_L \times SU(3)_R$ with an exact "diagonal" $SU(3)_c$ symmetry[24]. Such a possibility cannot be excluded, but we see very little reason to consider it.

(iii) The electroweak gauge group may be extended into a left-right symmetric $SU(2)_L \times SU(2)_R \times U(1)$. This is an attractive possibility which has many important implications for the physics beyond the standard model. We discuss it in the next section and return to it several times in these lectures.

A potentially attractive possibility which does not work is to extend the electroweak group into a simple group, thus allowing for a calculation of the Weinberg angle without reference to the strong interactions. We have explained elsewhere why this does not work, and will not discuss it any further[25].

(iv) Finally there are the grand unification schemes, and their possible extensions into larger groups incorporating several generations in one large multiplet. We will discuss these topics in Section 4.4.

4.3 The Left-Right Symmetric $SU(2)_L \times SU(2)_R \times U(1)$

An attractive extension of the electroweak group of the standard model is the left-right symmetric $SU(2)_L \times SU(2)_R \times U(1)$ scheme[26]. In the unbroken stage we have three independent couplings g_{2L}, g_{2R}, g_1 but the assumption of a discrete left-right symmetry gives $g_{2L}=g_{2R}$, bringing us back to the two-coupling situation of the standard $SU(2) \times U(1)$. In the symmetry limit, parity is conserved. We have seven gauge bosons: $W_L^{\pm}$, $W_R^{\pm}$, Z_1, Z_2, γ. All left-handed fermions are in the $(\frac{1}{2},0)$ representations. All right-handed fermions are in the $(0,\frac{1}{2})$ representations.

The spontaneous symmetry breaking, with the usual Higgs mechanism, provides masses to six gauge bosons and to the fermions. Parity is violated spontaneously, not by introducing different couplings but by introducing different masses for $W_L^{\pm}$ and $W_R^{\pm}$. The vacuum expectation values of the Higgs fields are arranged to give $M(W_L) < M(W_R)$. Thus at low energies, only left-handed currents are observed, the standard model is reproduced, and only the $SU(2)_L$ classification of fermions matters.

The present experimental limits on right-handed charged currents and on deviations from the standard neutral-current phenomenology allow the second set of W^+, W^-, Z to be as low as 200-300 GeV. It could, of course, lie much higher.

The left-right symmetric model has several potentially attractive features:

(i) It allows for a parity conserving theory at short distances.

(ii) The different SU(2) assignments of left-handed and right-handed fermions in the standard model, follow naturally from the simplest symmetric non-trivial assignment in the $SU(2)_L \times SU(2)_R \times U(1)$ model.

(iii) The U(1) "weak hypercharge" is proportional to B-L and is, of course, identical for the left- and right-handed components of the same fermion. In the standard model, the U(1) quantum number has no simple interpretation.

(iv) If neutrinos have nonvanishing masses, the left-right symmetric model becomes even more attractive.

We must remember, however, that:

(i) There is no experimental evidence for the left-right model.

(ii) If neutrinos are massless, the assignments of right-handed leptons become difficult and artificial.

(iii) The group $SU(2)_L \times SU(2)_R \times U(1)$ cannot be incorporated into the most economic grand unification scheme of SU(5) (but it fits naturally within O(10)).

Experiments at the next generation of accelerators could substantially extend our sensitivity to effects due to W_R-particles at masses of a few hundred GeV. Such experiments might give us the first indications for an $SU(2)_L \times SU(2)_R \times U(1)$ gauge theory.

4.4 Grand Unification: General Features

An exciting extension of the standard model is the attempt to unify the three independent interactions under one simple gauge algebra $G \supset SU(3)_L \times SU(2) \times U(1)$. This "grand unification" program leads to several general features which are common to all choices of G.

(i) Quarks and leptons are assigned to the same multiplet of G.

(ii) Consequently, the concept of a generation is now precisely defined, and generation mixing angles (including the quark-lepton angles of section 2.5) are now defined.

(iii) The twelve standard gauge bosons together with, at least, a dozen "leptoquarks" are all in the adjoint representation of G.

(iv) All gauge coupling constants are related in the symmetry limit. In particular, $\sin^2\theta_W$ is determined. If the observed spectrum of quarks and leptons of one generation is assigned to one (possibly

reducible) representation of G, we find $\sin^2\theta_W$=0.375 at the symmetry point.

(v) The rate of logarithmic variation of the QCD coupling together with the size of the electroweak coupling dictates a symmetry point somewhere above 10^{15} GeV. The above prediction of $\sin^2\theta_W$ applies to that energy range. Its value at present energy can be calculated, extrapolating over thirteen orders of magnitude. The obtained values are around 0.2 - 0.27 depending on G.

(vi) The quantization of electric charges for quark and leptons are related, "explaining" why $Q_{e^+}=Q_p$.

(vii) The sum of electric charges of quarks and leptons in one generation must vanish, as required by the anomaly condition.

(viii) Many additional Higgs particles are necessary. (At least 24+5 in the most economic scheme).

(ix) Baryon and lepton number conservation are explicitly violated. Specific combinations such as B-L may remain approximately conserved in some cases. If proton decay occurs in lowest order it, independently, sets the grand unification scale around 10^{15} GeV.

(x) There seems to be a "desert" in which no new physics is to be found between 10^2-10^{15} GeV.

The two strongest candidates for the grand unification algebra G are SU(5) and O(10). Both possess all the above features, but they differ in the symmetry breaking chain, Higgs structure, low-energy extrapolation of $\sin^2\theta_W$, possible fermion mass relations, etc.

A summary of some interesting symmetry breaking patterns of O(10), including SU(5) as a subgroup, is given in Figure 3.

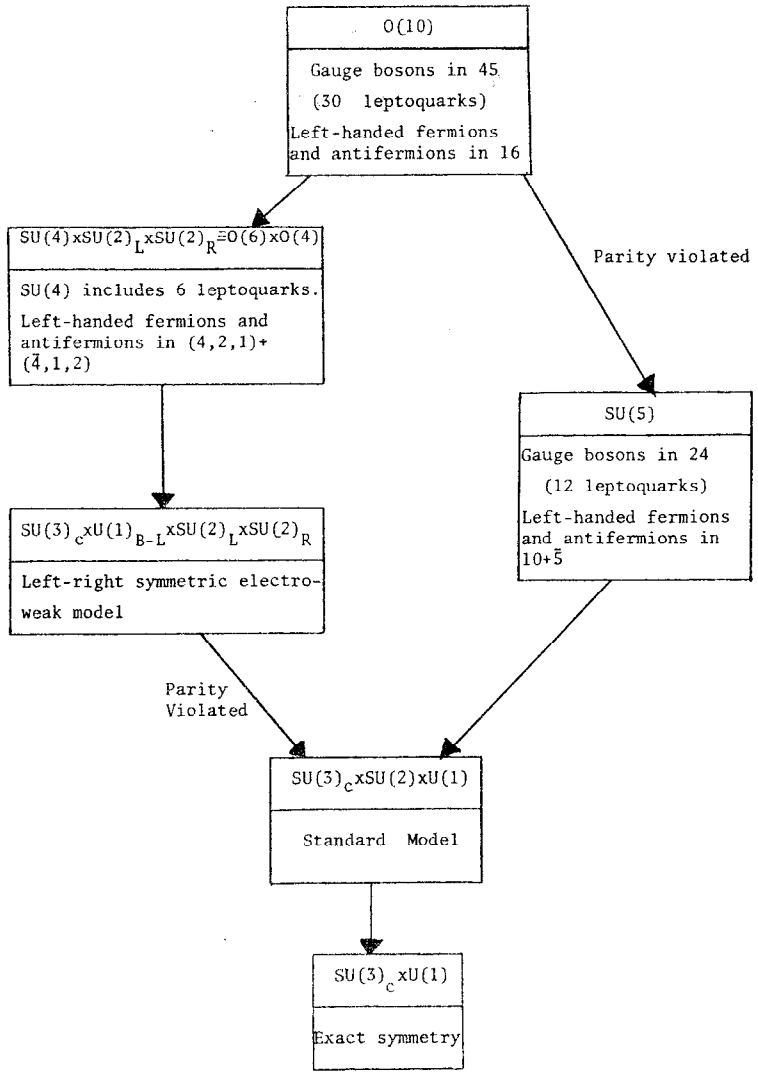

Figure 3: Patterns of Symmetry Breaking in Grand Unification Models

5. The Generation Puzzle

5.1 What Identifies a Generation?

Assuming that quarks and leptons indeed come in three or more identical "generations," we would like to understand the labels which distinguish these generations from each other. As far as we know, all strong and electroweak gauge couplings of the fermions in the three generations are identical. The only measurable difference, so far, are the masses and the related Yukawa couplings of the fermions to the Higgs scalars.

We do not know of any conserved quantum number which distinguishes among generations. The Cabibbo mixing indicates that, even if such a quantum number existed, it could not have been exactly conserved. If the neutrinos are massless, leptons in different generations do not mix. "Electron number" and "muon number" are then automatically conserved by all gauge couplings, simply because no term in the Lagrangian connects e to μ. Even in this case, Higgs scalars could violate these conservation laws, leading to transitions such as $\mu N \to eN$ or $\mu \to e\gamma$.

The full gauge Lagrangian for three generations in the standard $SU(3)_C \times SU(2) \times U(1)$ model, excluding the Higgs couplings, automatically possesses a global U(3) symmetry among the generations. This symmetry must clearly be broken when the fermions acquire their masses. Several situations may be considered:

(i) A discrete symmetry is left unbroken, with each quark, lepton and Higgs field transforming in a well-defined way under the discrete transformation. Such symmetries do not seem to shed too much light on the physics description of the different generations, but they may yield interesting relations among the fermion masses and generation-mixing angle. We discuss these in section 5.3.

(ii) We may have a continuous global symmetry. The simplest would be a U(1) algebra, where each generation transforms with a different phase factor. We could also have an SU(N) algebra, where the three (or more) generations transform according to a three (or more) dimensional representation of SU(N). For three generations, N can only be 2 or 3. For all broken continuous global symmetries, we must face the possible existence of a Goldstone boson which must either exist as a physical particle or should be otherwise removed from the spectrum by some yet unknown mechanism.

(iii) Another possibility is a so-called "horizontal" gauge group[27] which could, again, be $U(1)$, $SU(2)$, $SU(3)$ or perhaps even a larger group. Here, the symmetry breaking would follow the usual Higgs mechanism, and the Goldstone problem is solved. Horizontal gauge bosons must exist, possibly leading to generation-changing neutral currents and to processes such as $\mu \to e\gamma$, $\mu N \to eN$, $K \to e\mu$, $K \to \pi e\mu$ and to new contributions to the $K_S^o - K_L^o$ mass difference[28]. A major problem in this case is that of anomalies. The overall theory must be based on the gauge group $SU(3)_c \times SU(2) \times U(1) \times H$ where H is the "horizontal" group. The absence of anomalies imposes a severe constraint, especially in the case of SU(3) (or any $SU(N)$, $N>2$).

(iv) A final possibility is a very large gauge group which goes beyond grand unification, incorporating several generations of quarks and leptons in one "dynasty" multiplet. Such a group would include the grand unification group SU(5) or O(10) as a subgroup. It is likely, but not necessary, that the "dynasty" group includes $SU(5) \times H$ or $O(10) \times H$ as a maximal subgroup, where H is, again, the "horizontal" gauge group. Models based on SU(7), SU(8), SU(9), O(14), O(18) and larger groups have been proposed[29].

In each of the above cases, fermions of different generations possess certain labels which distinguish them from one another. The Higgs scalars also have such labels and certain Yukawa couplings are

then forbidden. This imposes constraints on the fermion mass matrix (see section 5.3).

Even if a discrete or continuous, global or local symmetry exists among the generations, we would still like to understand the physics which leads to such a symmetry. One possible source could be a composite structure of quarks and leptons, where the generation-labels characterize different excitations of the composite system.

5.2 How Many Generations Are There?

Several indirect arguments seem to limit the number of fermion generations. The arguments are totally unrelated to each other and none of them can be regarded as an absolute limitation.

The arguments include: (i) cosmological bounds on the allowed number of massless (or very light) neutrinos (ranging from 3 to 7, depending on the Helium abundance in the universe)[16]. (ii) The famous requirement of no more than 16 quark-flavors (8 generations) in an asymptotically free $SU(3)_c$ gauge theory. (iii) Bounds on the mass difference between the two quarks or the two leptons in one generation, derived from the smallness of the radiative corrections to the Weinberg mass relations[8]. (iv) Bounds on the fermion masses derived from the Higgs potential[30].

The first two bounds limit the number of generations, but are not very compelling. If all neutrinos have masses and high-generation neutrinos are heavy, the first bound disappears. If asymptotic freedom applies only to the first few generations, we could have many distant generations without spoiling it.

The last two bounds introduce a "reasonable" cutoff of several hundreds GeV on the fermion masses, without explicitly limiting the number of generations. In this case, the number of generations is not a particularly significant parameter.

An interesting "philosophical" question is whether the number of generations is a fundamental parameter of the final theory[19]. If grand unification is the correct approach and if all generations are to be found in a large "dynasty" multiplet, the number of generations must be related to the size of the "dynasty" group. In fact, in that case, the number of generations plays an important role in determining the fundamental symmetry of nature, and all generations are, in some sense, equal in importance.[29]

An alternative possibility is that the number of generations is, more or less, irrelevant to the fundamental symmetry[19]. The number of energy levels of a bound carbon nucleus or the number of N^*-resonances are not important parameters in physics. There may be an infinite number of possible generations, with the physical spectrum being truncated by some cutoff, perhaps at a few hundred GeV. This would almost certainly happen in a composite model of quarks and leptons, but could even happen in other situations. In that case we will not have a dynasty multiplet and no horizontal gauge group (other than, possibly, U(1)) is likely to exist.

We believe that the second possibility is more attractive, but only time will tell.

5.3 Quark Masses and Cabibbo Angles

Most of the parameters of the standard model represent the masses of quarks and leptons and their various mixing angles. All of these parameters emerge in the processes of spontaneous symmetry breaking via the Higgs mechanism. The gauge theory Lagrangian contains Yukawa couplings of the form:

$$g_{ijk}\phi_i\bar{q}_{Lj}q_{Rk}$$

which, after symmetry breaking, result in mass terms:

$$g_{ijk}\lambda_i \bar{q}_{Lj} q_{Rk}$$

where $\lambda_i = \langle \phi_i \rangle$. The element m_{jk} of the quark mass matrix is then given by

$$m_{jk} = g_{ijk}\lambda_i$$

In the case of three generations, we start, in the symmetry limit, with three identical massless doublets of quarks (and, similarly, leptons). We may denote the three doublets by $(u_o,d_o)(c_o,s_o)(t_o,b_o)$, remembering that any set of orthogonal linear combinations of these doublets is an equally adequate starting point. Since electric charge is conserved, only neutral Higgs fields may acquire vacuum expectation values and only equal-charge quarks are connected in the mass matrix. The mass matrix therefore splits into two matrices for the $I_3 = +\frac{1}{2}$ and the $I_3 = -\frac{1}{2}$ quarks, respectively. We have terms of the form:

$$(\bar{u}_o\ \bar{c}_o\ \bar{t}_o)_L\, M_U^o \begin{pmatrix} u_o \\ c_o \\ t_o \end{pmatrix}_R + (\bar{d}_o\ \bar{s}_o\ \bar{b}_o)_L M_D^o \begin{pmatrix} d_o \\ s_o \\ b_o \end{pmatrix}_R + \text{h.c.}$$

In order to obtain the "physical" quark masses and the generalized Cabibbo angles we must diagonalize M_U^o and M_D^o. In general, this is achieved by a bi-unitary transformation for each matrix:

$$\begin{pmatrix} m_u & 0 & 0 \\ 0 & m_c & 0 \\ 0 & 0 & m_t \end{pmatrix} = L_U^{-1}\, M_U^o\, R_U$$

$$\begin{pmatrix} m_d & 0 & 0 \\ 0 & m_s & 0 \\ 0 & 0 & m_b \end{pmatrix} = L_D^{-1}\, M_D^o\, R_D$$

$$C = L_U^{-1}\, L_D$$

The matrix C contains the three independent Cabibbo angles and the Kobayashi-Maskawa phase[13] (see section 2.2).

In the case of a left-right symmetric model, $L_U = R_U$, $L_D = R_D$ and M_U^o, M_D^o are hermitian. In general, they are not.

The total number of free parameters in the quark sector is ten: six masses, three angles and one phase. The matrices M_U^o and M_D^o appear to include more than ten parameters. However, a common unitary transformation of M_U^o and M_d^o does not change any physical quantity. Consequently, many of the parameters are not physical.

A full understanding of the physics of the model would require a complete knowledge of the Higgs potential, the Yukawa couplings and the vacuum expectation values. These would determine the mass matrices M_U^o and M_D^o which would then be diagonalized. If the number of independent Higgs fields and couplings is small, a few parameters would determine the ten physical parameters leading to interesting relations among masses and angles.

Any "explanation" of the generation concept and any symmetry among the generations would, in principle, lead to constraints on the mass matrix. A well-known simple example for a two-generation model is a hypothetical U(1) symmetry under which[11]

$$\begin{pmatrix} u_o \\ d_o \end{pmatrix}_L \to e^{i\alpha} \begin{pmatrix} u_o \\ d_o \end{pmatrix}_L \quad ; \quad \begin{pmatrix} u_o \\ d_o \end{pmatrix}_R \to e^{-i\alpha} \begin{pmatrix} u_o \\ d_o \end{pmatrix}_R$$

$$\begin{pmatrix} c_o \\ s_o \end{pmatrix}_L \to e^{i\beta} \begin{pmatrix} c_o \\ s_o \end{pmatrix}_L \quad ; \quad \begin{pmatrix} c_o \\ s_o \end{pmatrix}_R \to e^{-i\beta} \begin{pmatrix} c_o \\ s_o \end{pmatrix}_R$$

If we have only two Higgs fields, it is easy to show that the two mass matrices must either be diagonal (in which case $\theta_c = 0$) or have the schematic form:

$$\begin{pmatrix} o & x^* \\ x & y \end{pmatrix}$$

In the latter case we obtain the following expression for the Cabibbo

angle:

$$\theta_c = \left| \arctan\sqrt{\frac{m_u}{m_c}} + e^{i\eta} \arctan\sqrt{\frac{m_d}{m_s}} \right|$$

where η is an arbitrary phase. Inserting the standard quark masses, we obtain

$$9^\circ < \theta_c < 16^\circ$$

compared with the experimental value $\theta_c \sim 13^\circ$. In the case of three generations we get additional relations, if we continue to assume that we have only two Higgs fields. One interesting solution has the following form for each mass matrix[11]:

$$\begin{pmatrix} 0 & a^* & 0 \\ a & 0 & b^* \\ 0 & b & c \end{pmatrix}$$

leading to explicit expressions for $\theta_1, \theta_2, \theta_3$ in terms of the six masses and to the mass relation:

$$\frac{(m_t - m_c + m_u)^3}{m_t m_c m_u} = \frac{(m_b - m_s + m_d)^3}{m_b m_s m_d}$$

This relation predicts $m_t \sim 14$ GeV and is, therefore, inconsistent with experiment.

The above examples serve only to indicate the kind of mass-angle relationships which we may expect when we determine the symmetry among the generations and the complete spectrum of Higgs fields. The failure of the above prediction for m_t may simply indicate that we have more than two Higgs fields.

It appears that a full understanding of the quark and lepton masses as well as all the mixing angles requires:

(i) A solution of the generation puzzle.

(ii) An understanding of the Higgs sector.

5.4 What Next?

On the horizon beyond the standard model we see three clouds:

(i) We do not understand the generation structure. What distinguishes among them? Why do they mix? How many are there? Are there any exotic quarks and leptons? If not, why?

(ii) We do not understand the Higgs sector. Are the Higgs fields composite? If so, are they composed of new "technifermions"? If so, do these come in generations, further increasing the number of parameters? Do we have new gauge bosons, connecting fermions to technifermions? How do they get their masses?

(iii) We do not understand the relation between quarks and leptons. Is it governed by a grand unification group, incorporating quarks and leptons in the same multiplet? Do we have composite quarks and leptons, all consisting of the same building blocks?

We believe that all three problems point in the direction of further compositeness. Part II of these lectures is devoted to this possibility.

6. References (Part I)

1. S.L. Glashow, Nucl. Phys. 22, 579 (1961); S. Weinberg, Phys. Rev. Lett. 19, 1264 (1967); A. Salam, Proceedings of the 8th Nobel Symposium, 1968; G. 't Hooft, Nucl. Phys. B33, 173 (1971), B35, 167 (1971). For a review, see e.g. M. Veltman, these Proceedings.
2. Reports from the TASSO, PLUTO, MARK J and JADE Collaborations, Proceedings of the Fermilab Lepton-Photon Symposium, 1979.
3. R. Brandelik et al., TASSO Collaboration, DESY-80/80 preprint.
4. For various reviews of large q^2 deep inelastic muon and neutrino scattering see e.g. Proceeding of the Fermilab Lepton-Photon Symposium, 1979; Proceedings of the SLAC Summer Institute, 1979; Proceedings of the Madison Conference on High Energy Physics, 1980.
5. See e.g. R.K. Ellis, D.A. Ross and A.E. Terrano, Cal. Tech. preprint CALT 68-785 (1980), to be published.
6. See e.g. D.P. Barber et al., MARK J Collaboration, Phys. Lett. 89B, 139 (1979); R. Brandelik et al., TASSO Collaboration, Phys. Lett. 94B, 437 (1980); Ch. Berger et al., PLUTO Collaboration, DESY 80/93 preprint.
7. See e.g. J.E. Kim et al., University of Pennsylvania preprint, UPR-158 (1980), to be published.
8. M. Veltman, Nucl. Phys. B123, 89 (1977); M. Chanowitz, M.A. Furman and I. Hinchliffe, Phys. Lett. 78B, 285 (1978).
9. For a review see e.g. H. Harari, Phys. Reports 42C, 235 (1978).
10. For a review see K. Berkelman, Cornell preprint, to be published in the Proceedings of the Madison Conference on High Energy Physics, 1980.
11. For reviews see e.g. H. Fritzsch, Nucl. Phys. B155, 189 (1979); H. Harari, SLAC-PUB-2363, to be published in the Proceedings of the Jerusalem Einstein Symposium.
12. For a review see e.g. D. Hitlin, these Proceedings; H. Harari, Phys. Report 42C, 235 (1978).
13. M. Kobayashi and K. Maskawa, Progress of Theoretical Physics 49, 642 (1973).
14. Results from the Soviet Union, reported at the Madison Conference on High Energy Physics, 1980.
15. For a review see e.g. F. Sciulli, these Proceedings; V. Barger, Proceedings of the Madison Conference on High Energy Physics, 1980.
16. See e.g. D.N. Schramm, these Proceedings.
17. M.K. Gaillard and B.W. Lee, Phys. Rev. D10, 897 (1974).
18. J. Ellis, M.K. Gaillard, D.V. Nanopoulos and S. Rudaz, Nucl. Phys. B131, 285 (1977).
19. For a discussion see e.g. H. Harari, SLAC-PUB-2363, to be published in the Proceedings of the Jerusalem Einstein Symposium.
20. L.F. Li, Carnegie-Mellon preprint, 1980.
21. C. Jarlskog, Phys. Lett. 82B, 401 (1979).
22. For a review see e.g. B. Stech, Heidelberg preprint HD-THEP-80-4.
23. Y. Achiman, private communication.
24. V. Elias, J.C. Pati and A. Salam, Phys. Rev. Lett. 40, 920 (1978).
25. H. Harari, Phys. Reports 42C, 235 (1978).
26. See e.g. S. Weinberg, Phys. Rev. Lett. 29, 388 (1972); J.C. Pati and A. Salam, Phys. Rev. D10, 275 (1974); R.N. Mohapatra and J.C. Pati, Phys. Rev. D11, 566 (1975).
27. See e.g. F. Wilczek and A. Zee, Phys. Rev. Lett. 42, 421 (1979); A. Davidson, M. Koca and K. C. Wali, Phys. Rev. Lett. 43, 92 (1979).
28. See e.g. R.N. Cahn and H. Harari, Nucl. Phys. B176, 135 (1980).
29. E. Farhi and L. Susskind, Phys. Rev. D20, 3404 (1979); F. Wilczek and A. Zee, Princeton preprint 1979; P.H. Frampton, Phys. Lett. 88B, 298 (1979); H. Georgi, Nucl. Phys. B156, 126 (1979).
30. H.D. Politzer and S. Wolfram, Phys. Lett. 83B, 421 (1979); P.Q. Hung, Phys. Rev. Lett. 42, 873 (1979).

Part II

Composite Quarks and Leptons

1. Motivation

1.1 Too Many Quarks and Leptons

Five quark flavors have been discovered, and we expect at least one more. Five lepton flavors are directly observed and the sixth must exist. The standard gauge theory of the strong, electromagnetic and weak interactions contains a large number of undetermined parameters representing quark and lepton masses as well as Cabibbo-like mixing angles. The observed spectrum of quarks and leptons shows several regularities. The same unexplained pattern (a "generation") seems to repeat three times. Certain combinations of electric charge and color never appear while others appear repeatedly. All of these facts lead us to two simple observations:

(a) It is hard to accept the notion that we already have a "final" theory of the fundamental building blocks and their interactions. There are too many particles and too many parameters.

(b) The entire observed pattern is quite normal for a composite system. It is natural to expect many types of composite objects with a complicated set of mass parameters. It is also quite normal to expect certain composite combinations to be forbidden ("exotic") while others appear in several excited states.

The possibility of composite quarks and leptons is by no means the only one. The notion of grand unification offers an attractive alternative, attempting to reduce the number of principles and parameters, while keeping the quarks and leptons elementary.

Composite models are not necessarily incosistent with grand unification models, but the physical approach is certainly different.

1.2 Are Quarks and Leptons Composed of the Same Objects?

The reasoning outlined above indicates that quarks and leptons may be composite, but no necessary connection is established between their respective constituents. However, an additional major puzzle exists in the world of quarks and leptons. There seems to be a deep relationship between the two types of particles indicating that, if they are composite, they probably contain the same set of constituents.

Both quarks and leptons exhibit the same pattern under the electroweak SU(2)xU(1) group (left-handed doublets and right-handed singlets). Both quarks and leptons seem to exhibit the same pattern of generations. Even more important is the fact that the quantization of electric charges of quarks and leptons is based on related units, leading to the unexplained precise equality between the proton charge and the electron charge and eventually to the electric neutrality of atoms and most matter in general. This crucial and profound property of matter is not explained in the standard electroweak model. It is explained in grand unification models, and it is self-evident and automatic if quarks and leptons are formed by different combinations of the same fundamental building blocks.

Finally, there is the mysterious vanishing of the sum of electric charges of all quarks and leptons in each generation. This sum must vanish if the electroweak theory is to be renormalizable ("the anomaly constraint"). This is the only ingredient in the standard theory which explicitly connects quarks to leptons and which states that the observed leptons could not survive in a self-consistent theory without the observed quarks, and vice-versa. Somehow the quarks and lepton "know about each other," and the remarkable vanishing sum is given by:

$$\Sigma Q_i = 3 \times 2/3 + 3 \times (-1/3) + (-1) + 0 = 0.$$

This can, again, be explained in grand unification schemes where ΣQ_i is the trace of a generator of a simple Lie algebra. In a composite model, ΣQ_i should be rewritten in terms of the constituent charges, and its vanishing may become a trivial consequence of the composition of the

quarks and leptons.

1.3 Composite Higgs Particles

A completely different argument for compositeness follows from the observation [1] that the presence of fundamental Higgs scalars is "natural." The standard electroweak theory would then require tremendously precise "fine tuning" of its parameters. This can be avoided if the scalars are not fundamental fields but are composites of fermion pairs [2]. Since the longitudinal components of W and Z emerge from these scalars, they are also composite in a certain sense. This raises the possibility that the transverse W and Z are composite, although it is not necessary.

The scalar fields may, of course, be composite while the quarks and leptons remain elementary. However, this would introduce new fundamental fermions [2] ("Techniquarks" and "Technileptons"), complicating even further the theory and strengthening our general reasoning in favor of another layer of constituents. It would be much more elegant if quarks, leptons, Higgs fields and possibly W and Z are composites of the same set of fundamental fermions and if the new theory does not require further fundamental scalars.

1.4 Extended Supergravity

Grand unification is an ambitious attempt to unify strong, electromagnetic and weak interactions. Even more ambitious is the desire to unify gravity with the three other forces. The scale is, of course, the Planck mass, and the difficulties are enormous, especially because no self-consistent quantum field theory exists for gravity.

Most recent work in the direction of constructing a quantum theory of gravity, has utilized the ideas of supergravity, where the J=2 graviton is accompanied by a massless J=3/2 "gravitino." Various authors have attempted to go beyond supergravity and to unify all interactions in an "extended supergravity" theory [3] in which one supersymmetry multiplet might contain the J=2 graviton, J=3/2 gravitinos, J=1 vector gauge bosons, J=1/2 quarks and leptons and J=0 scalar particles. The largest group which allows such a multiplet without requiring unwanted J=5/2 particles is SO(8). However, SO(8) does not have enough room for particles such as μ, τ, t, b, $W^{\pm}$. There are simply too many quarks, leptons and gauge bosons. One possible solution to this difficulty is to suggest that gravity is to be unified with the other interactions not at the level of quarks, leptons and W-bosons, but at a more fundamental level of subparticles [4]. If the number of these is smaller, we may have enough room for them in an SO(8) supermultiplet or even in a multiplet of a smaller extended supergravity group.

1.5 Composite Quarks and Leptons

None of the above arguments proves that quarks and leptons are composite. Nevertheless, we believe that the arguments are quite convincing and that the alternative of grand unification leaves too many important questions unsolved (the generation pattern; the composite Higgs fields; number of mass and angle parameters, etc.). The possibility of another layer of fundamental constituents is certainly exciting and we will pursue here its limitations, difficulties and potential successes.

Throughout these notes we will therefore assume that quarks and leptons are composites and will discuss various theoretical ideas and models, aiming at an understanding of the new substructure.

2. Scale Limitations

2.1 How Pointlike is "Pointlike"?

There is a wide range of experiments which lead to the conclusion that quarks and leptons have no inner structure. These include high energy tests of QED, scaling in deep inelastic electron and neutrino scattering, the constant R-value in e^+e^- collisions, and various successful tests of QCD. All of these observations can be directly or indirectly translated into "form factors" for quarks and leptons. In all cases it appears that quarks and leptons have no observable structure down to distances $1/\Lambda$ where Λ is somewhere in the range between 10 and 100 GeV.

Any theory of composite quarks and leptons is therefore limited to energy scales above these Λ-values. This is the only absolutely certain limitation that we have. At present, "pointlike" means smaller than 10^{-15}-10^{-16} cm.

2.2 The Anomalous Magnetic Moments of the Electron and Muon

The limitation of the previous section is based on high-momentum probes. However, internal structure can be observed at zero momentum transfer through anomalous moments. For instance, the compositeness of the proton can be deduced from its $q^2=0$ anomalous magnetic moment, even if large-q^2 form factors are not measured.

The electron and muon have very small anomalous magnetic moments which are fully accounted for by higher order QED corrections (including effects of the known strong and weak interactions). Thus, the $q^2=0$ moments do not give any hint of compositeness.

Can we reach a negative conclusion[5] on the basis of the absence of unexplained moments? In principle, the answer is no. It is possible, but not likely, that a certain internal structure may conspire to contribute nothing to the anomalous moment. Theoretically speaking, we cannot completely exclude a structure at a scale of, say, $\Lambda \sim 100$ GeV which would mysteriously give no measurable contribution to (g-2) of the electron or the muon. However, this appears to be ugly, unnatural and unlikely. No-one has constructed such a scheme.

Barring mysterious conspiracies, we are left with the possibility of a substructure at a scale which is beyond the present accuracy of (g-2) measurements. If we denote by δa the allowed contribution of possible new physics to (g-2), we have: $\delta a_e \lesssim 5\times10^{-10}$; $\delta a_\mu \lesssim 3\times10^{-8}$. The relevant relation for the new scale parameter, in the case of fermion constituents obeying a chiral symmetry is[6]

$$\left(\frac{m_{\text{lepton}}}{\Lambda}\right)^2 \lesssim \delta a_{\text{lepton}}$$

Hence:

$$\Lambda \lesssim 500 \text{ GeV}$$

In the absence of a chiral symmetry one finds[6]:

$$\frac{m_{\text{lepton}}}{\Lambda} \lesssim \delta a_{\text{lepton}}$$

leading to $\Lambda \lesssim 1000$ TeV.

We wish to emphasize that these limits are sufficient but not necessary. However, in the absence of an explicit dynamical model which might teach us how to avoid them, we should probably abide at least by the weaker limit of the chiral symmetry case.

2.3 The decay $\mu \to e+\gamma$[7]

If second generation fermions are excitations of first-generation fermions, decays such as $\mu \to e+\gamma$ need not be forbidden. They may be suppressed by an approximate selection rule or by some dynamical reasons (e.g., small overlap between wave functions). In the absence of such suppression factors we expect:

$$\Gamma(\mu \to e + \gamma) \sim \alpha\, p^3\, \Lambda^{-2}$$

where $p \sim 50$ MeV is the c.m. momentum and Λ^{-1} is the "radius" of the composite lepton. From the present experimental bound on $\Gamma(\mu \to e+\gamma)$, we find $\Lambda \gtrsim 1000$ TeV. This limitation is highly model dependent, since it is valid only if no other suppression mechanisms are at work, and the lepton "radius" is the only controlling factor.

2.4 The Scale of Composite Higgs Fields

If the Higgs fields are composite, and if their vacuum expectation values are to yield the W and Z masses of order 100 GeV, the characteristic scale should be around 1 TeV. This is the case in various technicolor schemes.[2] Higher values of the compositeness scale cannot be excluded, especially if the binding of the fermions in the scalar condensate is not due to the exchange of a new vector gauge particle, but is due to more complex phenomena. If we have a new color group whose confinement radius is involved we might expect it to be somewhere within one or two order of magnitudes above 1 TeV.

2.5 Proton Decay

If quarks and leptons are composites of the same constituents, baryon and lepton number violations are almost unavoidable. The proton may decay through a rearrangement of the constituents in a reaction like:

$$u + u \to \bar{d} + e^+$$

Such a decay may or may not proceed in lowest order of the basic interaction of the fermion constituents. If it proceeds in lowest order, the relevant scale is:

$$\Lambda \sim 10^{15} \text{ GeV}$$

This value cannot be reconciled with the scale of Higgs compositeness, but it is, of course, consistent with all earlier lower bounds on Λ. If proton decay proceeds in second order, Λ should depend on the details of the model, but a crude estimate would place it within one or two orders of magnitude from 10^7 GeV. It is conceivable even that in some composite models baryon number is violated but the proton is stable.

2.6 When Can We Expect to Detect Compositeness?

In the case of proton decay in lowest order, direct experimental detection of the effects of compositeness (other than proton decay itself) is hopeless. However, if proton decay is forbidden, or even if it proceeds in second or third order, we expect the scale of compositeness to be anywhere between 1 TeV and 10^4 TeV. In the lower part of this energy range we may have direct experimentation within one or two decades. Higher energy scales can be probed by rare processes such as $\mu \to e\gamma$, $\mu N \to eN$, $K_L^\circ \to e\mu$, $K \to \pi e\mu$, etc.[8] All of these processes already probe the region around 1-100 TeV, and new precision measurements may push the explored momentum range even further. In the next few years, the only hope of reaching the multi-TeV region seems to be through high sensitivity searches of extremely rare transitions.

3. Theoretical Difficulties

3.1 Massless Composite Fermions

Assuming that the scale of the next layer of physics is above 1 TeV, all quark and lepton masses are small parameters. We may say that the composite quarks and leptons are approximately massless on such a scale.

This can happen if the constituents have masses of the order of the new scale Λ, and their binding energies are such that they precisely cancel the original masses, to give an almost vanishing composite mass. Such a possibility cannot be rigorously excluded, but it is extremely unlikely and unnatural (both in the technical sense and in

the usual, everyday meaning).

A more plausible alternative is the suggestion that the fundamental constituents are massless and their original Lagrangian possesses a chiral symmetry.[9] If that symmetry remains unbroken, certain composite fermions may be massless, their effective Lagrangian being chirally invariant. In such a case, no miraculous cancellations are required, and the masslessness of the composites is established as a result of a symmetry principle.

Two questions immediately arise:

(a) If the fundamental constituents are massless, why don't we see them experimentally?

(b) What determines the scale Λ?

Both questions can be answered in terms of the same hypothesis. We assume that the fundamental constituents possess a new "hypercolor" degree of freedom. They are not observed because they are confined by the hypercolor potential. The scale parameter of the hypercolor coupling constant is Λ_H and the radius of the confining potential is of the order of Λ_H^{-1}. All quarks and leptons are presumably hypercolor singlets and are therefore "observed" at momenta below Λ_H.

3.2 The Generation Gap

If all quarks and leptons are composite, we might expect the second and third generations to be some kind of excitations of the first generation. Two types of excitations can be excluded immediately:

(a) A fermion of a higher generation might consist of the same constituents as its first-generation analog, the level splitting being due to a radial or an orbital excitation. This possibility is totally excluded by the mismatch between the radius of the system (Λ^{-1}) and the mass splittings among generations which are somewhere between 100 MeV and several GeV. All radial and orbital excitations of a composite quark or lepton must have masses of order Λ, somewhere above TeV.

(b) Generations cannot differ from each other by an exactly conserved quantum number. The observed Cabibbo mixing clearly demonstrates that no such quantum number exists.

We are left with the following possibilities:

(i) Generations may differ from each other by the addition of sets of constituents with vanishing quantum numbers. The composite muon may differ from the composite electron by the addition of one or more pairs of fundamental fermion constituents or by the addition of a (hyper)glueball or a scalar Higgs-like meson. In all of these cases it is conceivable that the composites in each generation will have masses which are small with respect to Λ, although no explicit dynamical description for such a situation has been proposed, so far.

(ii) There may be an additional global symmetry or local gauge symmetry identifying a "generation number." Such a symmetry must be broken, to allow for generation-mixing. If it is a broken global symmetry, we must worry about the existence of Goldstone boson. If it is a local gauge symmetry, we must understand its symmetry breaking mechanism and worry about its anomalies.

It is possible to combine the two options, if generations differ from each other by the addition of, say, constituent pairs and the added pairs carry non-vanishing values of some new quantum number which represents a broken symmetry.

3.3 Composite Gauge Bosons?

If quarks and leptons are composite, what about the gauge bosons? If we accept a composite electron or neutrino, should we insist that W and Z are fundamental?[7]

The standard theory contains three types of gauge bosons: photon, gluons and massive weak bosons. Let us study each of these gauge bosons separately:

(i) The photon is massless, representing an exact local gauge symmetry. It exists as a free particle. At least one type of fundamental constituent must possess electric charge and couple to the photon. Among the gauge bosons, the photon is least likely to be composite.

Attempts to construct a composite photon in different contexts have never fully succeeded[10] and the question remains wide open.

We will assume that the photon is not composite.

(ii) The gluons are massless and they also represent an exact local gauge symmetry. They differ from photons at least in three (presumably related) aspects: they do not exist as free particles, they appear in eight species and they couple to themselves.

Various authors have attempted to construct composite gluons[11]. Some of the problems are similar to those encountered in the case of photons. An exciting possibility is to associate the color of quarks not with some intrinsic property of their constituents, but with the particular combinations or "arrangements" of the constituents in the quark[7,12]. In such a case, gluons would not couple to the basic constituents, color would not be defined on the fundamental level of the theory and the gluons would necessarily be composite.

Unfortunately, all attempts to construct an explicit scheme with these features lead to radical departure from the principles of local field theory[13]. Unconventional statistic, violations of CPT and nonlocal effects seem to be necessary, and even then-- serious difficulties remain.

We therefore suspect that composite gluons are unlikely.

(iii) The situation with respect to the massive gauge bosons is quite different. Many of the difficulties encountered in the attempts to construct composite photons or gluons are tied to the masslessness of these particles. The W and Z are exempt from this problem.

If the Higgs scalars are composite, at least the longitudinal W and Z are composite, since they are "born" from the scalars.

The electric charges of $W^{\pm}$ are not the fundamental unit of charge. If there is an economic constituent model, the basic electric charge is likely to be $\frac{1}{3}$, and one might expect all higher charges to be constructed from combinations of such units.

Composite W and Z could apparently mix with an elementary photon without too much difficulty. If SU(2)xU(1) is an effective theory, its broken part could correspond to composite gauge bosons while the surviving exact U(1) symmetry necessitates a fundamental gauge boson.

All the above arguments convince us that, if quarks, leptons and Higgs scalars are composite, the massive weak gauge bosons are probably also composite. This cannot be proved, at present, but we consider it a likely possibility[7].

3.4 "Naturalness"

Let us assume that quarks and leptons are composites of fundamental fermion constituents and that the latter interact via gauge bosons. These include the photon, probably gluons, possibly some "hypergluons" and perhaps even weak bosons. The theory is described by an "underlying" Lagrangian which describes the physics above the new scale Λ. This Lagrangian does not contain any composites. In particular, the quarks, leptons, scalar bosons and possibly the weak bosons do not appear.

At lower energies and larger distances the composite objects are formed. Physics is described by an effective "overlying" Lagrangian in

which the fundamental fermions do not appear, quarks and leptons are present, etc. If the energy scales of the underlying and overlying theories are very different it may be "natural" to assume that the overlying Lagrangian is, by itself, renormalizable without the need to appeal to the more fundamental level of physics[9,14]. In other words-- the high energy dependence of the overlying theory, at energies below the new Λ, is well-behaved.

The requirement that the effective Lagrangian of the composite fields is renormalizable, cannot be proven. At present, it is more a matter of taste. If the new scale Λ is not far from M_W and M_Z, it is not even clear that such a requirement is elegant or simple. However, if Λ is, say, 10^{15} GeV, then it is difficult to imagine a nonrenormalizable composite theory.

If we accept this "naturalness" hypothesis, we obtain extremely powerful constraints on the composite theory, especially with respect to its gauge couplings and the absence of anomalies.

4. Composite Quarks and Leptons: Different Approaches

4.1 Lessons from the Past

The latest triumph of the concept of compositeness is, of course, the quark model. In trying to move towards the next level, many authors have imitated the successful strategy of the quark idea. In the case of hadron physics, the following motivations and circumstances led to our present understanding of quarks:

(i) There were too many hadrons and they had a finite size.

(ii) Several SU(3) multiplets (1, 8 and 10) appeared again and again while others did not exist ("exotics").

(iii) The simplest SU(3) multiplet (the triplet) did not appear in the observed spectrum.

(iv) When the simple quark scheme was proposed, it answered the above questions but violated ordinary statistics.

(v) The simple constituents (the quarks) could not be found experimentally.

(vi) The origin of quark binding was not clear.

(vii) The introduction of color, gluons and finally QCD answered the remaining open questions.

In the case of the quarks and leptons, there is no evidence for a finite size, but the spectrum is as suggestive as the hadron spectrum was twenty years ago. It is not surprising that various authors tried approaches which proved successful in the past: Looking for the simplest representations, inventing counting schemes with wrong statistics, introducing new constituents which are confined by a new color degree of freedom, etc. In this section we briefly review some of these ideas.

4.2 "Factorized" Quantum Numbers

The first published suggestion of composite quarks and leptons is due to Pati and Salam[15] who considered the simplest possible idea. Since quarks and leptons possess color, flavor and a generation label one might introduce four fundamental objects carrying the four colors (the three usual colors and lepton number as a fourth color) and no other attributes. Additional "preons" carry only weak SU(2) quantum numbers and a third set of "preons" carries only the generation label. A red charmed quark will then consist of the "red" preon, the "up" preon and the second-generation preon, etc.

Such a scheme is fairly economical, and it is constructed in such a way that the pattern of identical generations as well as the quark-lepton similarity are guaranteed. All gauge bosons are elementary. At least some of the "preons" are not confined and should be observed,

or be extremely heavy. Unfortunately, this kind of model does not really teach us too much.

Several other authors have suggested variations on the same theme[16]

4.3 Where is the Fundamental Multiplet?

In grand unification schemes, quarks and leptons are usually not assigned into the fundamental representation. One might try to construct the $5+\overline{10}$ of SU(5) from combinations of 5-dimensional representations. In O(10) one may wonder about the role played by the 10-dimensional multiplet. In larger schemes (SU(7), O(14)), etc.) various authors tried to incorporate several generations into one large multiplet of a higher gauge algebra. In all of these cases the fundamental representation does not seem to play any significant role, and no one has succeeded in suggesting a meaningful scheme in which quarks and leptons are constructed from building blocks which transform according to it.

4.4 A Simple "Counting" Scheme: Rishons

The most ecomomic scheme which has been proposed, so far, is the original rishon scheme[7,12]. Quarks and leptons are assumed to be composites of fundamental $J=\frac{1}{2}$ constituents ("rishons") of two types: A charged T-rishon and a neutral V-rishon. The fundamental electric charge of the T-rishon is $+\frac{1}{3}$. All quarks and leptons of one generation are composites of three rishons or three antirishons, according to the following assignments:

$e^+ \equiv TTT$	$\bar{\nu}_e \equiv \bar{V}\bar{V}\bar{V}$
$u \equiv TTV$	$d \equiv \bar{V}\bar{V}\bar{T}$
$\bar{d} \equiv TVV$	$\bar{u} \equiv \bar{V}\bar{T}\bar{T}$
$\nu_e \equiv VVV$	$e^- \equiv \bar{T}\bar{T}\bar{T}$

The three different colors are allegedly formed by three different "arrangements" of the three rishons in a quark (e.g., TTV, TVT, VTT). Gluons and weak gauge bosons must be composites.

As a counting scheme the model is attractive but it fails to answer simple questions such as: What is the interaction which binds the rishons? Are rishons heavy? What kind of statistics do they obey? Why don't we have J=3/2 quarks and leptons? How do we form higher generations? Why do we have only composites of three rishons or three antirishons and not, e.g., two rishons and one antirishon?

Among the attractive features: The absence of "exotic" quarks and leptons is "explained"; the vanishing sum of electric charges of quarks and leptons in one generation follows simply from the fact that they contain $6T+6V+6\bar{T}+6\bar{V}$; the two conserved quantum numbers are the number of T's and the number of V's, or equivalently, the electric charge and B-L (baryon minus lepton number).

In short: a simple counting scheme in search of dynamics, and with several fundamental difficulties.

4.5 Metacolor, Supercolor, Hypercolor, Subcolor

In section 3.1 we referred to the idea that the constituents of quarks and leptons are massless fermions, confined by a new color-like degree of freedom. The overall gauge group would then include an $SU(N)_H$ hypercolor (or metacolor or supercolor or subcolor) group. The underlying theory is based on an $SU(N)_H \times G$ algebra, where G represents all of the "usual" physics, including ordinary color, weak interactions, etc. G may include local gauge symmetries as well as global symmetries.

The fundamental fermions are assumed to be in representations (N,k) under $SU(N)_H \times G$ while all quarks and leptons are hypercolor singlets in $(1,k_i)$ representations.

An immediate disadvantage of such theories is the large number of

fundamental fermions. A severe constraint is imposed by the absence of anomalies in the underlying theory.

A particularly interesting condition was noticed by 't Hooft[9]. He considered a theory with N' fundamental massless fermions transforming like N-dimensional $SU(N)_H$ representations. The theory would then have an $SU(N)_H \times G_F$ symmetry where $G_F = SU(N') \times SU(N') \times U(1)$ is a global chiral "flavor" symmetry (which may eventually include ordinary color, $SU(2) \times U(1)$ and even SU(5)). In the underlying level of the theory the anomalies of the flavor currents do not necessarily vanish, since G_F is not gauged. These anomalies can be, however, computed explicitly from the full structure of the fundamental Lagrangian. In the overlying level of the theory, the composite quarks and leptons ($SU(N)_H$-singlets) appear, while the fundamental fermions are confined and are not part of the effective Lagrangian. The anomalies can, again, be calculated (at least at q=o), and their values in the overlying theory must correspond to the values computed in the underlying theory.

The conditions obtained in this way are severe[9] and the only known solutions correspond to unrealistic schemes which do not exhibit the correct spectrum of quarks and leptons[17].

4.6 Extended Supergravity: A Bold Scheme with Hundreds of Particles

The only serious attempt to construct a composite model of quarks and leptons in the context of extended supergravity is based on the following interesting observation[18]. In an SO(8) theory, the Lagrangian "miraculously" acquires a local SU(8) symmetry[19], larger than the original assumed SO(8). The same Lagrangian possesses an even larger global symmetry based on $SU(8) \times E_{NC}(7)$ where $E_{NC}(7)$ is a noncompact version of the exceptional E(7) algebra[19]. The local SU(8) gauge symmetry involves 63 vector gauge particles which are formed as composites of the original SO(8) "underlying" fields. In that sense, all 63 gauge bosons (including the photon, gluon, W, Z) are composite. The SU(8) algebra contains the standard grand-unified SU(5) and the three remaining directions in the 8-dimensional space allegedly represent the three generations[18].

While the model can accommodate the three generations of quarks and leptons, it contains an enormous array of additional $J=\frac{1}{2}$ fields and J=0 fields. Altogether we count 784 $J=\frac{1}{2}$ composites and 448 J=0 composites, without a clear guideline which might distinguish between the observed physical states and all the additional, unwanted states.

5. A Theoretical Framework

5.1 *A Prescription for Model Building*

Combining all the wisdom expressed in the previous sections, we are now ready to formulate a theoretical framework for a candidate model.

The fundamental gauge bosons should presumably be the photon, the gluons of $SU(3)_C$ and the hypergluons of a hypercolor $SU(N)_H$ group. We assume that the massive weak bosons are composite. The theory would therefore be locally gauge invariant under $SU(3)_C \times SU(N)_H \times U(1)_{em}$. The hypercolor scale Λ_H must be much larger than Λ_C.

The fundamental $J=\frac{1}{2}$ objects should be massless, leading to a certain degree of chiral symmetry, which will later lead to massless composites[9]. The massless building blocks are not observed because they are confined by hypercolor forces. They presumably belong to the fundamental N-dimensional representation of SU(N). Their $SU(3)_C$ assignments are most likely to be singlets and/or triplets but higher multiplets are not completely excluded. The fundamental electric charge is, presumably, 1/3.

Given a set of such constituents, the "underlying" Lagrangian

will possess an additional global chiral symmetry which depends on the number of constituent flavors and on their $SU(3)_C xSU(N)_H xU(1)_{em}$ assignments. This chiral symmetry enables us to define various conserved currents. Certain three-point functions of these currents may contain "triangle anomalies" which can be computed and which need not vanish. The original Lagrangian also conserved parity, by construction.

As the energy decreases below Λ_H, all hypercolor nonsinglets become confined and only $SU(N)_H$-singlets survive as physical particles. In general, such singlets should have masses of order Λ_H. However, because of the chiral symmetry, some composites may be massless. We can predict which composites are massless only if we fully understand the confinement mechanism (but we don't!). However, we can formulate necessary conditions based on the 't Hooft consistency equation[9] which states that the computed anomalies in the overlying effective Lagrangian should be equal to those in the underlying Lagrangian.

In order for the theory to be realistic we must have three generations of massless quarks and leptons, as well as massless composite W and Z bosons (at least for SU(2)xU(1), but possibly for the larger group of $SU(2)_L xSU(2)_R xU(1)$). We must also have composite Higgs fields which will then provide all fermions and composite gauge bosons with masses. The original constituents would remain massless and the theory would not have any fundamental scalar particles.

In the process of symmetry breaking, the chiral "flavor" symmetry as well as parity invariance must be broken. However, the local gauge group of the original Lagrangian would remain unchanged.

Another constraint that we may wish to impose, is to demand that the overlying effective Lagrangian which describes the physics below Λ_H is, by itself, renormalizable[9,14]. This Lagrangian should essentially be the Lagrangian of the standard model, containing the photon, gluons, $W^{\pm}$, Z, quarks, leptons and Higgs fields.

Finally, given that the simplest non-trivial multiplet of $SU(3)_C xSU(N)_H$ contains 3N states, we should insist on a small number of different fundamental constituents, or else we will immediately have too many of them.

The challenge, as we see it, is to construct a model which obeys all the above rules and conditions. In section 6 we describe our best try.

5.2 Dynamical Symmetry Breaking and Composite Quarks and Leptons

We have already noted (in section 1.3) that fundamental scalar particles are not natural and that the simplest way to avoid them would be to suggest that the Higgs particles are fermion-antifermion condensates.

Technicolor models assume the existence of new fermions ("Technifermions"), bound by the gauge bosons of a new color group of a new scale, to form the composite scalars[2]. The scalar particles cannot be formed from $q\bar{q}$ pairs because the energy scale would then be Λ_C, and the masses of W and Z would be too small by three orders of magnitude.

However, if quarks and leptons are composites of fundamental fermions, and the latter are bound by a hypercolor potential of characterisitc scale Λ_H, a totally new situation emerges. The leptons are hypercolor singlets and color singlets. However, "inside" them hypercolor and color forces operate. They are neutralized beyond distances of order Λ_H^{-1} (the effective "size" of the lepton). At distances comparable to Λ_H^{-1}, a residual hypercolor (and color) force will operate between two leptons[20]. This force will be analogous to the hadronic forces. In the same way that hadron-hadron forces are short-range residual color forces between colorless objects, our new lepton-lepton

forces are short-range residual hypercolor forces between singlets of $SU(3)_C \times SU(N)_H$.

This force among leptons (and also among quarks) may or may not be identified with the weak interaction. We believe that such an identification is very attractive[21] and we discuss it in section 6.3. However, independent of such an identification, two leptons at a distance Λ_H^{-1} may bind. We, therefore, have a convenient new mechanism for forming scalar condensates. They may simply be lepton-lepton or lepton-antilepton or quark-antiquark composites, and the neutral combinations may develop vacuum expectation values. The only energy scale is Λ_H and there is no difficulty in generating W and Z masses of order 100 GeV.

Having proposed this idea[20], we may proceed to check whether the obtained Higgs composites possess the correct quantum numbers in order to provide a realistic pattern of symmetry breaking. In the case of the left-right symmetric $SU(2)_L \times SU(2)_R \times U(1)$ model, we find a surprising answer: The most general set of scalar condensates which can be formed from one generation of composite quarks and leptons is identical in all properties[20] to the minimal set of Higgs particles which is needed in order to achieve the following necessary ingredients[22]:

(i) Produce heavy masses for the "right-handed" W and Z, leaving an approximate $SU(2)_L \times U(1)$ symmetry.

(ii) Produce lighter masses for the ordinary W and Z, obeying the Weinberg mass relation.

(iii) Produce fermion masses.

(iv) Produce a Majorana mass for the neutrino, leading to a light left-handed neutrino and a heavy right-handed neutrino.

The details of these calculations are presented elsewhere[20]. Here we only comment that the dynamical symmetry breaking mechanism suggested here is natural and does not add any new particles to the theory.

6. The Dynamical Rishon Model

6.1 The Underlying Lagrangian

Within the general framework established in section 5.1, the simplest candidate for the hypercolor group is SU(3). We therefore propose that the fundamental Lagrangian is locally gauge-invariant under $SU(3)_C \times SU(3)_H \times U(1)_{em}$. The seventeen fundamental gauge bosons are eight gluons, eight hypergluons and the photon.

The most economical set of constituents must include at least one charged particle and one neutral particle. The success of the rishon model[7,12] (section 4.4) as a simple counting scheme encourages us to try two types of fundamental fermions[21]:

(i) A T-rishon in the (3,3) representation of $SU(3)_C \times SU(3)_H$ and with electric charge +1/3.

(ii) A neutral V-rishon in the $(\bar{3},3)$ representation.

The only particles appearing in the underlying Lagrangian are the rishons and the seventeen gauge bosons. All particles are massless. There are no fundamental scalars.

In addition to the local gauge invariance under $SU(3)_C \times SU(3)_H \times U(1)_{em}$, the Lagrangian possesses additional symmetries. Since T, V, $\bar{T}$ and $\bar{V}$ all transform according to different representations of the local gauge group, no "flavor" SU(N) symmetry is present. We have, however, a $U(1) \times U(1) \times U(1) \times U(1)$ chiral group with two vector U(1) factors and two axial U(1) factors. The two vector U(1) groups correspond to separate conservation of T-number $(n_T - n_{\bar{T}})$ and V-number $(n_V - n_{\bar{V}})$. Their sum can be defined as the total "rishon number." Their difference is proportional to B-L (baryon minus lepton number). One of these U(1) factors is coupled to the electromagnet current $\bar{T}\gamma_\mu T$. The other represents a global symmetry.

Of the two axial U(1) factors, one is not conserved. The

divergence of the corresponding current is proportional to a combination of $(F\tilde{F})_C$, $(F\tilde{F})_H$ and $(F\tilde{F})_{em}$. The current is $\bar{T}\gamma_\mu\gamma_5 T+\bar{V}\gamma_\mu\gamma_5 V$. The second axial U(1) factor corresponds to the current $\bar{T}\gamma_\mu\gamma_5 T-\bar{V}\gamma_\mu\gamma_5 V$, whose divergence develops only an electromagnetic anomaly. The corresponding axial charge is conserved[23].

All triangle anomalies vanish except the one involving the conserved axial charge and the two vector currents $\bar{T}\gamma_\mu T+\bar{V}\gamma_\mu V$ and $\bar{T}\gamma_\mu T-\bar{V}\gamma_\mu V$. The underlying Lagrangian is also invariant under parity, since it contains only vector interactions.

6.2 The Composite Fermions

When we consider energies below the hypercolor scale Λ_H, only $SU(3)_H$-singlets survive. The simplest composite fermions consist of three fundamental fermions. Since all rishons are $SU(3)_H$-triplets and all antirishons are $SU(3)_H$-antitriplets, the only allowed composite fermions are made of three rishons or three antirishons (thus answering one of the difficulties in section 4.4).

A TTT state can form a (1,1) lepton of $SU(3)_C xSU(3)_H$, being totally antisymmetric in both color and hypercolor. Fermi statistics then require that the Lorentz part of the three-rishon wave function be totally antisymmetric[21]. This means that the composite lepton must have $J=\frac{1}{2}$ and cannot have $J=\frac{3}{2}$. (This solves two additional difficulties mentioned in section 4.4). The first-generation quarks and leptons are composed by the same combination as in the simple rishon counting scheme[7,12].

Higher-generation fermions may be formed by adding rishon-antirishon pairs to the first generation composites. In order to have all the correct quantum numbers, it appears that one needs composites of five rishons and two antirishons[24]. Independent of details, the higher generations are excitations of the lower ones, but the mass scale has no direct relation to the radial size (Λ_H^{-1}). Generations may differ from each other by a U(1) quantum number which is not exactly conserved[24].

6.3 The Weak Interactions

For each massless three rishon-composite there is a massless three-antirishon composite with the same color, hypercolor and (B-L) quantum numbers. The overlying Lagrangian possesses an $SU(2)_L xSU(2)_R$ symmetry[21] under which these pairs of fermion transform as $(\frac{1}{2},0)$ or $(0,\frac{1}{2})$. Since hypercolor is confined below Λ_H, the overall symmetry of the effective low-energy Lagrangian is $SU(3)_C xSU(2)_L xSU(2)_R xU(1)_{B-L}$, exactly the symmetry group of the left-right symmetric extension of the standard model.

We therefore identify the weak interactions as the short range residual hypercolor interactions among composite hypercolor-singlet quarks and leptons[21]. The W and Z bosons are assumed to be composites of rishons. The three neutral currents of $SU(2)_L xSU(2)_R xU(1)_{B-L}$ exactly coincide with the three conserved U(1) factors of the underlying Lagrangian. The Weinberg angle can be computed and we find[7,21], at Λ_H:

$$\sin^2\theta_W = 0.25$$

Below Λ_H, this value is renormalized downward, in good agreement with experiment[24].

The composite weak bosons, quarks and leptons presumably acquire masses through a Higgs mechanism, governed by scalar condensates of the type discussed in section 5.2. Parity as well as $SU(2)_L xSU(2)_R x U(1)_{B-L}$ are broken symmetries[20]. In fact, all "accidental" symmetries of the underlying and overlying Lagrangians end up being broken, while the original local gauge symmetry of $SU(3)_C xSU(3)_H xU(1)_{em}$ is the only

one which remains exact at all energies.

6.4 Difficulties of the Model

(i) In section 6.1 we mentioned the nonvanishing anomaly in the underlying level. We should be able to calculate the same three-current amplitude in the overlying theory, arriving at the same result[9]. We face a problem only at zero momentum, and there -- only massless particles can contribute poles which would cancel the vanishing of the amplitude and contribute the required nontrivial answer[17]. If all our composite fermions have masses, we obviously do not obey the consistency condition. However, it is not entirely clear how to treat non-vanishing composite masses which are negligible with respect to Λ_H. For instance, if only the u and d quarks are "declared" massless for this purpose, the overlying theory gives exactly the required anomaly[23,24]. Whether this remark is meaningful, we do not know.

(ii) The Higgs condensates and the small renormalization of $\sin^2\theta_W$, both point at Λ_H values somewhere between 1 TeV and 10^4 TeV, but certainly not 10^{15} GeV. Hence, the experimental limit on proton decay may "kill" the model. It turns out that with the proper wave function for the u and d quarks, proton decay is forbidden in lowest order of the theory[24]. It is probably allowed in second order, and an explicit calculation requires much more analysis. Whether the proton lifetime is consistent with the expected value of Λ_H remains to be seen.

(iii) The mechanism which forms the composite W and Z bosons is not at all clear. It remains to be shown that the difficulties encountered in constructing massless composite gauge bosons[10,11] disappear when the bosons acquire masses via scalar condensates.

(iv) It is not at all clear why $\Lambda_H >> \Lambda_C$ and what generates the original $SU(3)_C \times SU(3)_H \times U(1)_{em}$ symmetry. A purist would wish to further unify the three independent gauge groups, not to speak of gravity.

The overall picture that we see is, however, an exciting picture of a rapidly developing field. Whether a final correct theory will resemble any of the ideas presented here remains to be seen, but we are certainly pursuing a worthwhile goal.

7. References (Part II)

1. K. Wilson, unpublished; S. Weinberg, Phys. Rev. D13, 974 (1976); L. Susskind, Phys. Rev. D20, 2619 (1979).
2. L. Susskind, Phys. Rev. D20, 2619 (1979).
3. For a review see e.g. D.Z. Freedman, Proceedings of the Tokyo Conference, 1978, p.535.
4. J. Ellis, M.K. Gaillard and B. Zumino, Phys. Lett. 94B, 343 (1980); H. Harari, Phys. Lett. 86B, 83 (1979).
5. H.J. Lipkin, Phys. Lett. 89B, 358 (1980); M. Gluck, Phys. Lett. 87B, 247 (1979).
6. S. Brodsky and S.D. Drell, SLAC-PUB-2534, to be published; G.L. Shaw, D. Silverman and R. Slansky, Phys. Lett. 94B, 57 (1980).
7. H. Harari, Phys. Lett. 86B, 83 (1979).
8. See e.g. R.N. Cahn and H. Harari, Nucl. Phys. B176, 135 (1980).
9. G. 't Hooft, Proceedings of the Cargese Summer Institute, 1979.
10. See e.g. J.D. Bjorken, Ann. Phys. 24, 174 (1963).
11. T. Eguchi, Phys. Rev. D14, 2755 (1976); See also F.A. Bais and J.M. Frere, CERN TH-2911 preprint, 1980.
12. M.A. Shupe, Phys. Lett. 86B, 87 (1979).
13. S.L. Adler, Phys. Rev. D21, 2903 (1980) and Princeton preprint, to be published in the Proceedings of the 1980 Erice Summer School.
14. M. Veltman, Michigan preprint, 1980.
15. J.C. Pati and A. Salam, Phys. Rev. D10, 275 (1974).
16. See e.g. H. Terazawa, Y. Chikashige and K. Akama, Phys. Rev. D15, 480 (1977); Y. Ne'eman, Phys. Lett. 82B, 69 (1979).
17. S. Dimopoulos, S. Raby and L. Susskind, Stanford University preprint, ITP-662 (1980); T. Banks, S. Yankielowicz and A. Schwimmer, Phys. Lett. 96B, 67 (1980); Y. Frishman, A. Schwimmer, T. Banks, S. Yankielowicz, Weizmann Institute preprint WIS-80/27, Nucl Phys. B, in print.
18. J. Ellis, M.K. Gaillard and B. Zumino, Phys. Lett. 94B, 343 (1980).
19. E. Cremmer and J. Scherk, Nucl. Phys. B127, 259 (1977); E. Cremmer, J. Scherk and S. Ferrara, Phys. Lett. 74B, 61 (1978); E. Cremmer and B. Julia, Phys. Lett. 80B, 48 (1978), Nucl. Phys. B159, 141 (1979).
20. H. Harari and N. Seiberg, "Dynamical Symmetry Breaking and Composite Quarks and Leptons," Weizmann Institute preprint, November 1980 (Phys. Lett., in print).
21. H. Harari and N. Seiberg, Phys. Lett. 98B, 269 (1981).
22. R.N. Mohapatra and G. Senjanovic, Phys. Rev. Lett. 44, 912 (1980) and Fermilab preprint, FERMILAB-Pub-80/61-THY to be published.
23. S. Yankielowicz, Private communication.
24. H. Harari and N. Seiberg, to be published.

INSTRUMENTATION

D. Ritson

Introduction

This is the first and introductory talk in a series of lectures on instrumentation. In this talk I shall describe some of the basic processes that occur when a charged particle passes through a medium. A charged particle traversing a medium loses energy by a number of mechanisms. The most important mechanisms are:

1. Cerenkov radiation: When the velocity of the particle exceeds the velocity of light in the medium, it will radiate via the "Cerenkov" effect.
2. Transition radiation: When the particle traverses a dielectric boundary, it will radiate transition radiation.
3. Ionization losses: Passage of a particle through a medium leads to ionization and excitation of the atoms of the medium. The secondarily produced electrons, in turn, by the same mechanism, lead to further ionization.

Because of time constraints, I shall leave the description of Cerenkov radiation and transition radiation effects to later speakers and will concentrate on ionization losses in this talk.

The intent will be to describe the average energy and spatial distribution of the energies losses, the modifications introduced by the shielding effects of the medium (density effect) and the

fluctuations in these quantities with a view to delimiting the inherent precisions of measurements of positions or velocities based on ionization. Only an overview will be presented and the reader will have to go back to the literature for fine detail.[1,2] Later talks will describe the methods that are used to measure these effects and to categorize particles as to their properties.

1. Ionization Losses in Thin Layers

The standard literature[3] expression for ionization loss of a particle with speed βc, where effects due to the dielectric shielding of the medium are ignored, is

$$\frac{dE}{dx} = \frac{\eta}{\beta^2} \left[\ell n \left(\frac{2mc^2\beta^2 E_M}{I^2(1-\beta^2)} \right) - 2\beta^2 \right] \quad , \tag{1.1}$$

where I is the effective or mean ionization potential and equals approximately 10*Z eV. E_M is the maximum energy delta ray that either can occur physically or can be detected experimentally. The constant η relates directly to the probability P(E) of producing high energy δ-rays in a thickness x_o cms,

$$P(E)\, dE = \eta \, x \, \frac{dE}{E^2} \quad , \tag{1.2}$$

and is given by

$$\eta \left[\text{MeV}\right] = 0.0536 \left(\frac{Z}{A}\right) \rho \left[\text{gm cm}^{-2}\right] \quad , \tag{1.3}$$

where ρ is the density of the medium. (Z/A) applies to the atoms making up the medium.

The energy loss formula can be written as a sum of contributions from the various atomic shells as

$$\frac{dE}{dx} = \frac{\eta}{\beta^2} \sum_i f_i \left[\ell n \left(\frac{2m_e c^2 \beta^2 E_M}{I_i^2(1-\beta^2)} \right) - 2\beta^2 \right] \quad . \tag{1.4}$$

This notation may be unfamiliar. f_i is the fraction of atomic electrons occupying the i-th shell, with ionization potentials of I_i.

During this talk I will give a number of numerical examples for the most commonly used gas, Argon. For Argon at a pressure P,

$$\eta \left[\text{eV}\right] = 123 \, P \left[\text{atm}\right] \quad . \tag{1.5}$$

Bohr, in his original derivation of the energy loss formula, used a model in which the atomic electrons were regarded as free and the energy loss proceeded through the knock-on or delta-ray process. The atomic physics entered his result via the lower limit to the knock-on energy, which was set by atomic physics. If examined in detail, this picture makes little physical sense, as it predicts a spectrum for the secondary produced electrons that peaks at extremely low energies. However, the derivation does give the right result for the average energy loss and, in modified form, is still used.

It was pointed out by Blunk-Leisegang[4] that the effect of the electric field of the ionizing track is to cause photoelectric ionization of the various atomic shells of the atoms of the medium. The secondary energy loss distribution will peak at energies comparable with the binding energy. There is, in addition, just as in the original Bohr picture, a high energy tail of delta-rays with the

standard dE/E^2 distribution.

Blunk and Leisegang also showed that the integrated energy in the photoelectric peak was in fact almost identical to that obtained by Bohr, integrating up to an E_{max} of I_i in Bohr's derivation. Figure 1(a) shows the secondary spectrum that would have been predicted by Bohr's method and Fig. 1(b) the actual discrete atomic distribution that would be seen if instrumentation were available. We can approximately split the energy loss formula into two contributions, a photoelectric (or ionization) term peaking at an energy 1.5 I_i of

Photoionization Contribution

$$\frac{dE_{ion}}{dx} = \frac{\eta}{\beta^2} \sum_i f_i \left[\ln \left(\frac{3m_e c^2 \beta^2}{I_i(1-\beta^2)} \right) - 2\beta^2 \right] \qquad (1.6)$$

and a knock-on contribution extending from 1.5 I_i to E_{max} with an energy distribution dE/E^2

Knock-on Contribution

$$\frac{dE_{K_o}}{dx} = \frac{\eta}{\beta^2} \sum_i f_i \ln \left(\frac{E_M}{1.5\, I_i} \right) . \qquad (1.7)$$

The photoelectric effect will leave the residual atom in an excited state. However for light elements the residual excited atoms predominately lose energy by internal conversion and emission of electrons (the Auger process) and not by x-ray fluorescence. The residual ionizing secondaries therefore start predominately at the site of the original photoionization event.

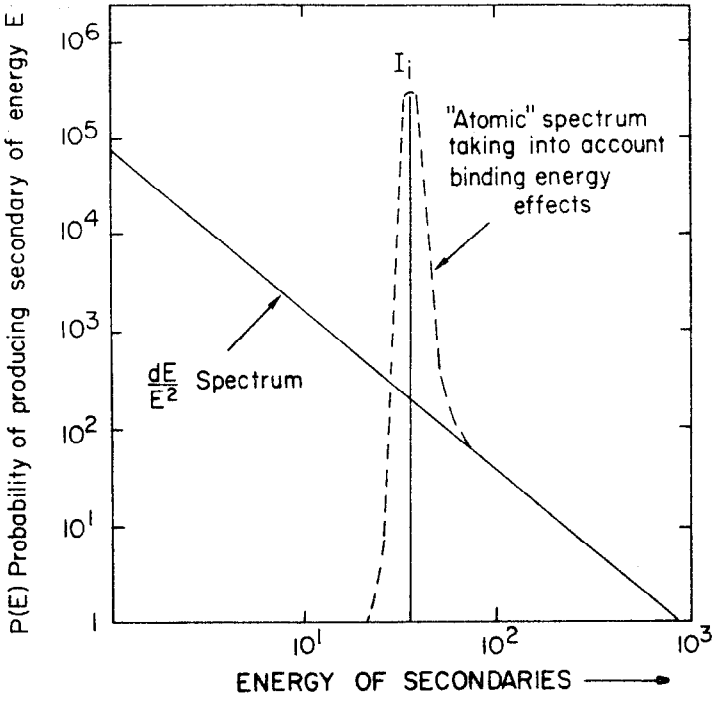

FIG. 1. Diagrammatic representation of (a) "old classical" knock-on spectrum (—) and (b) actual distribution of produced secondaries from a shell with ionization potential I_i. Scales are arbitrary.

Following the method of Chechin[5] (1972), Allison and Cobb[2] have used actual experimental data from synchrotron light experiments on photoelectric absorption to determine with good precision the f_i and I_i for Argon gas and hence predict the precise spectrum emitted in the primary ionization processes. Figure 2 shows results from the recent paper of Allison.

Table IA gives an approximation used by Talman[1] to the f_i and I_i for Argon. The fourth column of Table IA gives the energy loss for each shell in 1 cm-atm. The fifth column divides this average energy loss by the ionization potential to provide a rough measure of the number of ionizing clusters to be expected from each shell for a minimum ionizing particle. Table IB tabulates the number and average energy of the knock-on electrons arising from the various shells. As the events are independent and discrete, we see that we could count the number of primary ionizations; the statistical precision would be approximately $1/\sqrt{31}$ or ~ 18%.

2. Density Effect and Relativistic Plateau

Figure 3 shows energy loss calculated from Eq. (1.1) plotted against the $\beta\gamma$ of the ionizing particle. For low β's the ionization loss is a strong function of β ($\sim 1/\beta^2$). The energy loss has a minimum value at $\beta\gamma \approx 4$ and then increases approximately linearly with $\ell n\gamma$. It at first appears that even for high γ values the velocity can be measured from this "relativistic-rise." However two effects intervene. Firstly E_M, the maximum energy knock-on in the formula, in practice is set by the observing apparatus and becomes constant with increasing energy. The second effect was pointed out by Fermi.[6] The medium

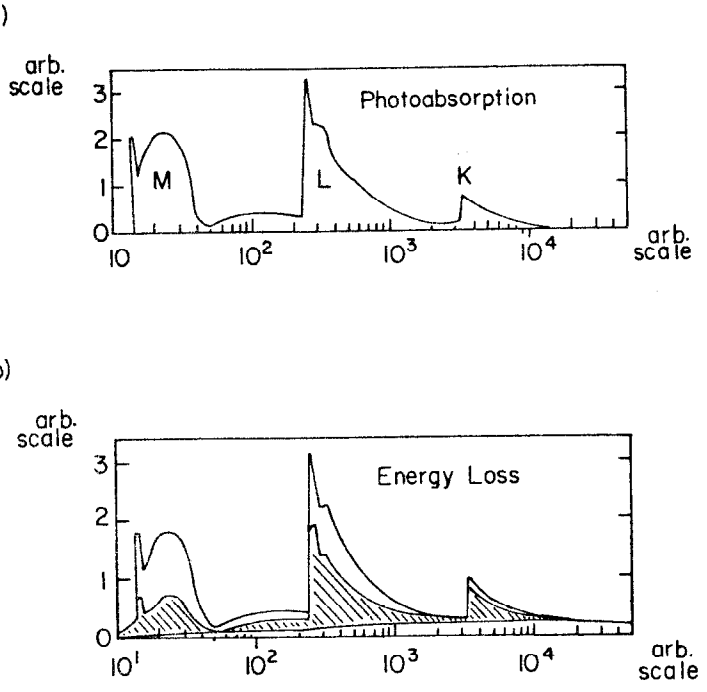

FIG. 2. (a) Measured photoabsorption in Argon gas.

(b) Derived energy loss spectrum. Upper threshold, resonance region, longitudinal term. Shaded, transverse term. Lower unshaded, quasi-free or Rutherford term.

TABLE IA

Fraction of electrons f_i and ionization potentials I_i for 1 cm atm of Argon as given by R. Talman for a particle with $\beta = 0.91$.

Shell	f_i	E_i [eV]	$\frac{dE_i}{dx_i}$ for 1 cm atm	$\frac{1}{E_i}\left(\frac{dE_i}{dx_i}\right)$
1	0.288	20	540	26.7
2	0.123	72	209	2.9
3	0.487	364	692	1.9
4	0.104	4423	110	.025
Totals			1551	31.5

TABLE IB

δ-ray Contributions from the Four Shells

Shell	f_i	<E>	$\frac{dE}{dx}$	<N>
1	0.286		240	2
2	0.123	350	175	.5
3	0.487	1200	240	.2
4	0.104	6000	120	.02
Totals			775	2.7

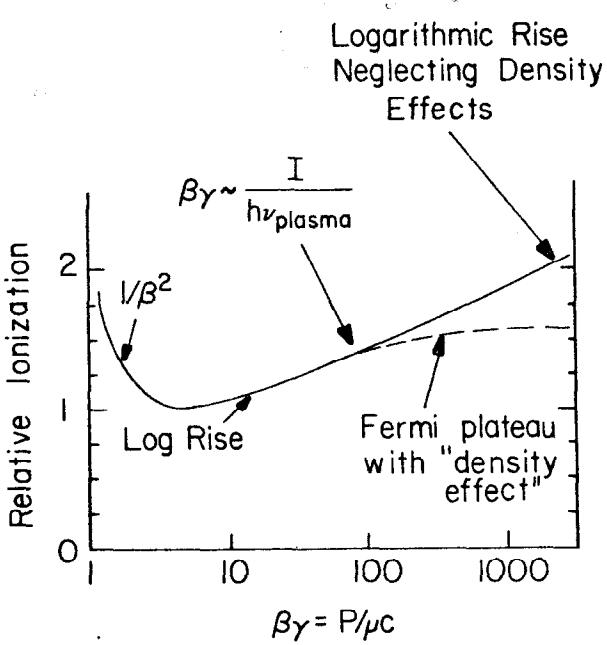

FIG. 3. The typical dependence of ionization on $\beta\gamma$.

through which the particle passes has a finite dielectric constant and this screens out the electric field at large distances. This effect results in a relativistic increase up to some plateau value, and then the ionization curve saturates.

The shielding distance for the electric field can be estimated as follows. Suppose the medium to contain a density N_e of electrons per cm^3. If all the electrons are coherently displaced by x, they will subsequently oscillate with the "plasma-frequency" ω_p.

For a displacement x an electric field E will be set up where (c.f. Fig. 4)

$$E = 4\pi N_e \times e \quad . \tag{2.1}$$

The coherent equation of motion of the electrons is then

$$m \frac{d^2x}{dt^2} = - 4\pi N_e \times e^2 \quad , \tag{2.2}$$

corresponding to a "plasma-frequency" ω_p,

$$\omega_p = \sqrt{\frac{4\pi N_e e^2}{m}} \quad . \tag{2.3}$$

An estimate of the shielding distance b_m for penetration of an electric wave into the medium is

$$b_m = \frac{c}{\omega_p} = \sqrt{\frac{mc^2}{4 N_e e^2}} \quad . \tag{2.4}$$

PLASMA FREQUENCY

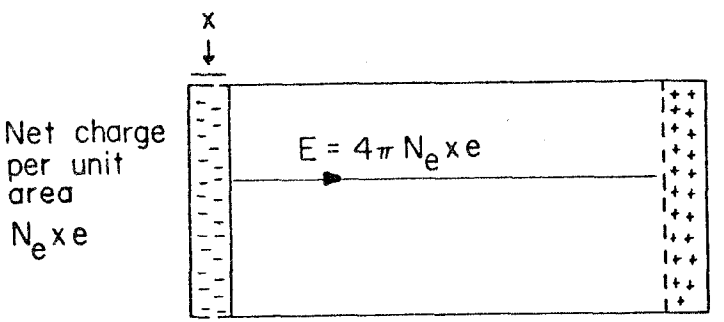

FIG. 4. Diagrammatic representation of material with ALL electrons displaced coherently x.

Using this maximum impact parameter we can derive the energy loss as Bohr did to obtain for large γ's the formula

$$\frac{dE}{dx} = \eta \left[\ell n \frac{mc^2 E_{max}}{(h\nu_{plasma})^2} - 2 \right] \quad \text{when} \left[\begin{matrix} \beta \approx 1 \\ \gamma >> 1 \end{matrix} \right] . \tag{2.5}$$

All electrons make an equal contribution to the energy loss whatever their binding energy. Figure 5 shows for a given electron density in the medium the calculated energy loss curves for electrons with various binding energies. The tighter the binding the larger the difference between minimum ionization and plateau ionization. In the region of the relativistic increase the slopes are identical. Saturation of the curves occurs at γ value given approximately by

$$\gamma \approx \frac{I_i}{h\nu_p} . \tag{2.6}$$

For Argon the plasma frequency ν_p in units of eV as a function of atmospheric pressure is

$$h\nu_p \ [\text{eV}] = .82 \ P^{\frac{1}{2}} \ [\text{atm}] . \tag{2.7}$$

The shielding distance b_m is

$$b_m \ [\text{microns}] \approx 0.23 \ P^{-\frac{1}{2}} \ [\text{atm}] . \tag{2.8}$$

This gives the important result that all the primary ionization is confined within a cylinder of 0.23 microns from the path of the ionizing track. This is much smaller than is measurable with any

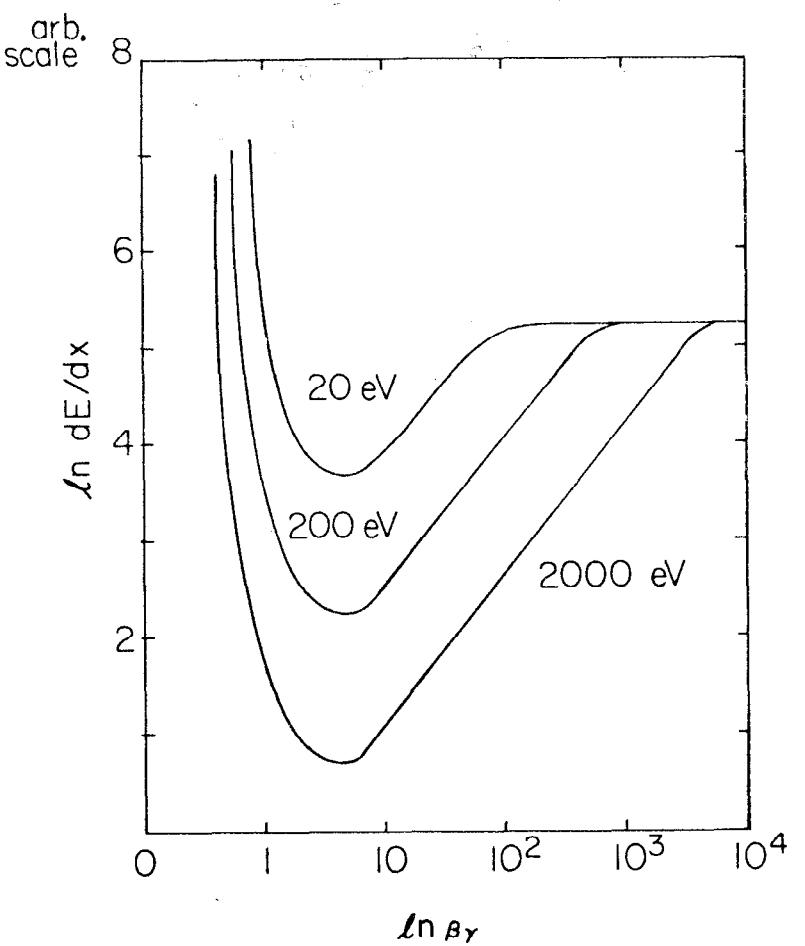

FIG. 5. Energy loss from "single" electrons in the medium with different binding energies (20 eV, 200 eV, 2000 eV).

present techniques.

Although even the most detailed theory involves approximations, agreement with experiment is good.[2] The results can be well approximated by the following formula, which approximates well our previous formula (1.1), for the energy loss but where the density correction is now included.

$$\frac{dE}{dx} = \frac{\eta}{\beta^2} \sum_i f_i \left[\ln \left(\frac{2mc^2\beta^2 E_M}{\left[\frac{I_i^2}{\gamma^2} + (h\nu_p)^2 \right]} \right) - 2\beta^2 \right] \qquad (2.9)$$

Exactly as previously we can split the energy loss into two contributions. The ionization term contains the distant collisions and the logarithmic rise and plateau, and the delta rays are caused by close collisions which are unaffected by the shielding effects.

Photoionization Contributions

$$\frac{dE}{dx} = \frac{\eta}{\beta^2} \sum_i f_i \left[\ln \left(\frac{3mc^2\beta^2 I_i}{\left[\frac{I_i^2}{\gamma^2} + (h\nu_p)^2 \right]} \right) - 2\beta^2 \right] \qquad (2.10A)$$

Knock-on Contributions

$$\frac{dE}{dx} = \frac{\eta}{\beta^2} \sum_i f_i \ln \left(\frac{E_M}{1.5\, I_i} \right) \qquad (2.10B)$$

3. Range Energy Curves for Low Energy Electrons

To obtain range energy curves, we can integrate the ionization loss curve to obtain the track length R. For low energy particles the track is strongly scattered as it comes to the end of its range. It is usual to define the mean effective range R_p.[7] This "practical" range is the geometric distance from the beginning to the end of the track (see Fig. 6). R_p is typically, in the keV range, a factor two or three less than the "track-range" R. Figure 7 shows range energy curves of R and R_p for Argon. A good representation of R_p is given for energies in the keV range by R_p [micron] $\approx 40\, E^{1.72}$ [keV].[7]

While I know of no reference, it would not be hard to Monte-Carlo a set of stopping tracks to obtain R_p and the straggling in R_p. The ionization increases strongly as a track comes to the end of its range, and is therefore predominately at the end of the range.

We can now summarize the history of a minimum ionizing particle traversing one cm of Argon at NTP. It will produce within a 0.2 micron cylinder on the average the following numbers of secondaries with energies and practical ranges tabulated in Table II.

Therefore, in principle, it is possible to locate such a particle by measuring, for instance, drift times of the electrons to much better than 50 micron precision except in one traversal in twenty.

4. Inherent Precision of Ionization Measurements

The previous sections have described the derivation of the formulae for average energy loss.

Figure 8 shows the average energy loss of pions, kaons, and protons in Argon gas as a function of momentum. In principle, provided precise

$R_{practical}$ is the geometric range, R the actual range. The two differ typically by a factor two or three.

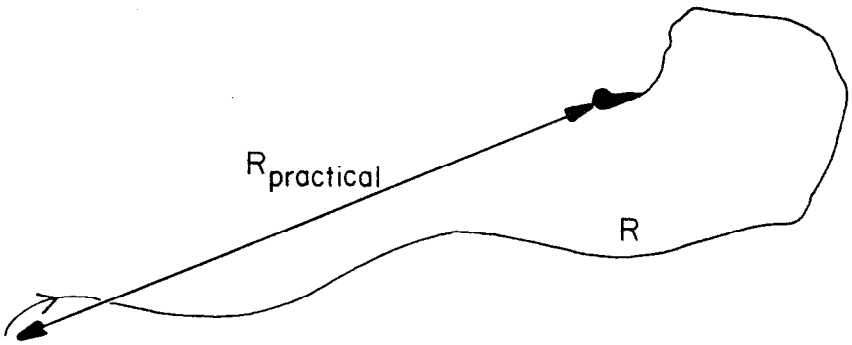

FIG. 6. Diagrammatic representation of a stopping electron.

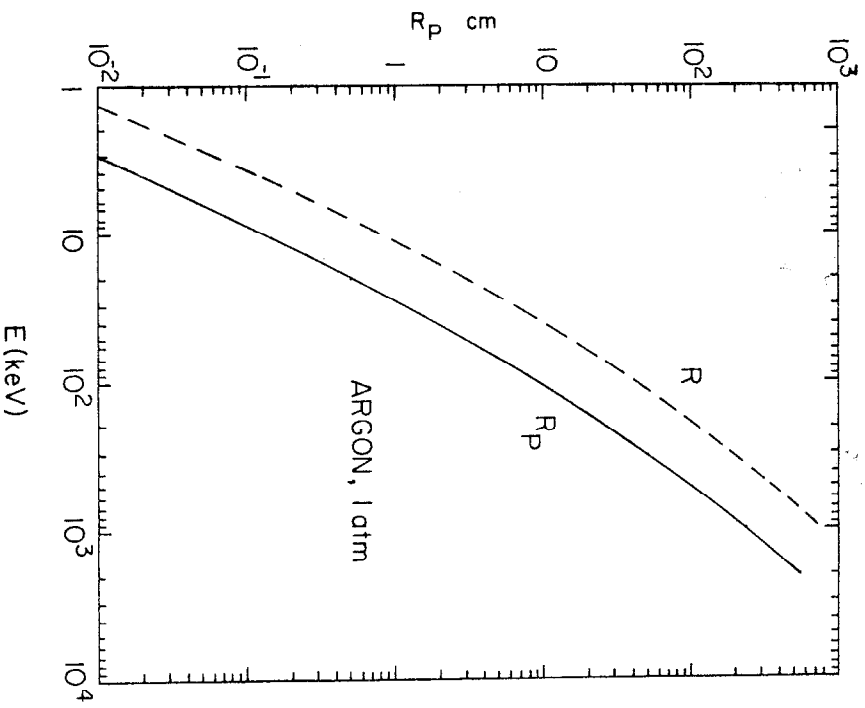

FIG. 7. Range of electrons in Argon, at normal conditions as a function of energy, deduced from measurement in light materials.

TABLE II

Location of Ionization Relative
to an Ionizing Track in Argon

No.	Energy in [eV]	Practical Range in [microns]
27	20	0
3	72	.15
1.9	364	3
.025	4423	150
.025	δ-rays ≥	5 keV 200 microns

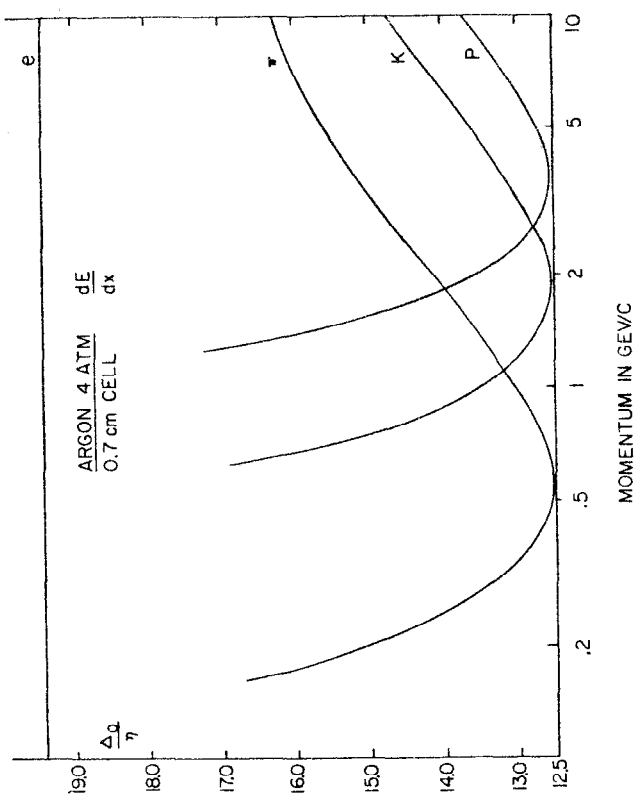

FIG. 8. Ionization loss dependence as a function of momentum.

enough measurements are made, the ionization measurements permit the flavor of the particles to be determined.

Two extreme strategies for ionization measurements are possible, and illustrate the problems involved. One strategy is to measure the number of primary ionization clusters. This is excellent statistically. We have seen that the number of such clusters is on the average 30 per cm at NTP and therefore the rms fluctuation of the measurements is $1/\sqrt{30x}$ where x is the thickness in atm cms. The ionization plateau sets in at comparatively low values of $\beta\gamma$ of ~ 6. For gas at NTP, the curve plateaus at a γ of approximately 30. However the practical difficulties of making such a measurement in a large scale system are intimidating.

Another obvious strategy is to measure the total ionization loss over the track. This leads to an almost invariant distribution of ionization losses independent of track length. The problem with this method is that comparatively high energy delta-rays contribute to the ionization and result in large fluctuations. Doubling the thickness of the layer does not give the canonical improvement because delta-rays of double the energy now contribute to the energy losses. Figure 9 shows calculations by Talman[1] for the fluctuation in relative energy loss as a function of track length. The improvement with thickness is small and effective flavor selection in the region of the relativistic rise would not be possible with these inherent precisions.

Apparently, one method leads to good measurements but is almost impossible to realize, and the other method does not give the necessary precision required to discriminate particle flavors in the region of

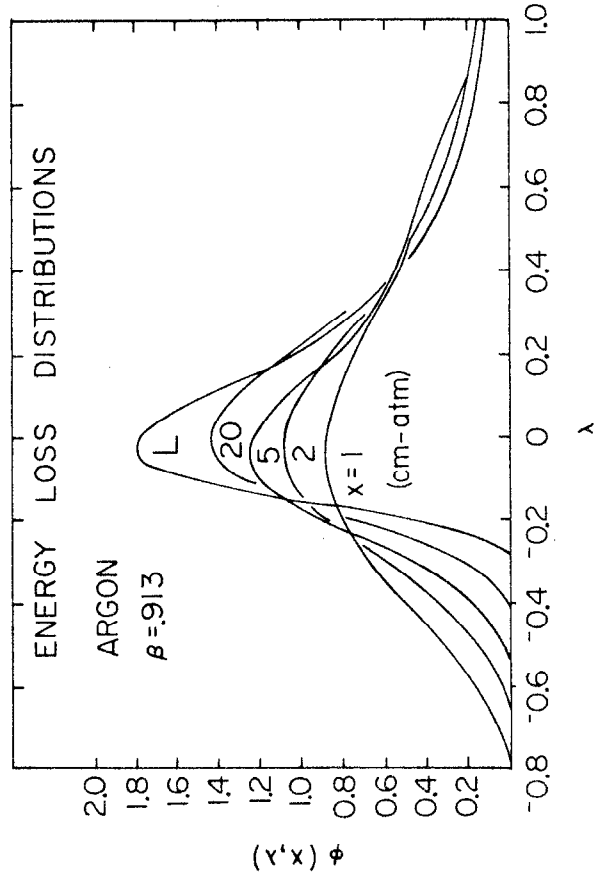

FIG. 9. Probability $\phi(\lambda)$ of a fluctuation $\lambda = \frac{E - \langle E \rangle}{E_{av}}$

the relativistic rise.

The solution adopted in practice is to segment the track and to measure the ionization in each segment (see Fig. 10).

The mean ionization is then determined by making a maximum likelihood fit of the n segments to the best predicted distribution. Predictions are based on the theoretical energy loss distributions combined with Poissonian fluctuations of the primary ionization event. By Monte-Carlo techniques, or with relatively sophisticated statistical theories, predicted curves may be obtained to match observation.

The reader is referred specifically to excellent discussions by Talman and Allison.[1,2] The rule of thumb is that segmentations in excess of one hundred and a total track length in excess of 3 meter-atmospheres are required to obtain the inherent precision required to make good "flavor" separation in the 10 GeV/c momentum range.

5. Fluctuations of Ionization in Sampling Layers

As machine energies increase, electromagnetic and hadronic calorimetry are becoming of increasing importance. It has been argued that for the next generation of machines the measurement of the gross properties of the jets arising from an event are the most important characteristic of the process, and the exact distribution and numbers of hadrons produced in the "dressing" process are of little significance. Whether or not this proves to be true, almost certainly calorimetric type determinations will be of considerable value in the future. These detection techniques will be described in detail by Howard Gordon to you.

Economic constraints almost certainly necessitate detectors of the

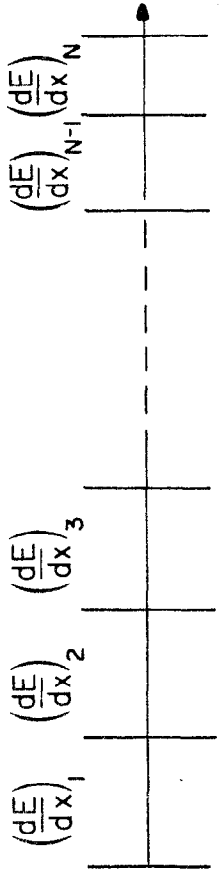

FIG. 10. Diagrammatic representation of a track segmented into N segments.

future (and present) being constructed of passive layers of converters, interspersed with active detection layers. One of the options for constructing these detector layers is to use gaseous detectors. This option has been discussed at length, however, with varying conclusions by many authors. I hope that what I have to say will help clarify the inherent limitations of this technique.

For simplicity the constraints on electromagnetic calorimeters are discussed. Hadronic calorimetry has further complications which need not concern us at this point in the discussion. (The limitations set by thin gaseous sampling layers are similar for hadronic calorimetry.)

The object of the measurements is to obtain the number of tracks crossing the sampling layers due to an initiating particle or jet. To a reasonable approximation, the energy of the initiating object is proportional to the number n of track crossings. The precision of the measurement despite correlations of track crossings is proportional to $1/\sqrt{n}$. The number of particles is not directly measured (except with the Conversi flash tube technique) but is obtained indirectly from ionization measurements and the number of crossings derived from this. For a sampling layer of 1 gm/cm thickness the average energy loss will be 1.7 MeV. A knock-on, however energetic, will only dump at most a comparable amount of energy before passing out of the layer and at worst will cause the track count to be increased by approximately 1. In a thin 1 cm Argon gas layer, however, at NTP a minimum ionizing particle will deposit on the average 1.5 keV. A knock-on with a practical range of 1 cm in Argon will have an energy of about 60 keV (it is slow and heavily ionizing) and will in this extreme case increase the track count by 40. This effect is further aggravated by knock-ons that can in principle run down the sampling layer (see Fig. 11) producing even more ionization. Such geometric effects, however, are much less serious than might appear at first sight. The multiple-coulomb scattering of the path is such as to remove it from the gas after a gap length or so and thus prevent long ranges in the gas.

The mean square fluctuations resulting from ionization measurements have been roughly estimated by integrating the "energy-loss-squared" of the knock-on distribution from the effective E_{min} of the Bohr theory to the E_{max} corresponding to the energy associated with practical ranges commensurate with the gap length.[3]

$$\langle (E-\langle E\rangle)^2\rangle = \int_{E_{min}}^{E_{max}} E^2\, P(E)\, dE$$

$$= \int \eta\, E^2\, \frac{dE}{E^2} = \eta\, E_M \qquad (5.1)$$

For 1 cm Argon at NTP E_M is ~ 60 keV, η/β^2 is ~ 150 eV and the average energy loss is of the order of 2.5 keV. The rms proportional fluctuation is then 1.5. The result of this rough estimate increases the rms error by a factor of about 1.7. The use of thick scintillators or liquid Argon (at a price) avoids this degradation in performance.

6. Overall Conclusions

A good theoretical description now exists which predicts (within

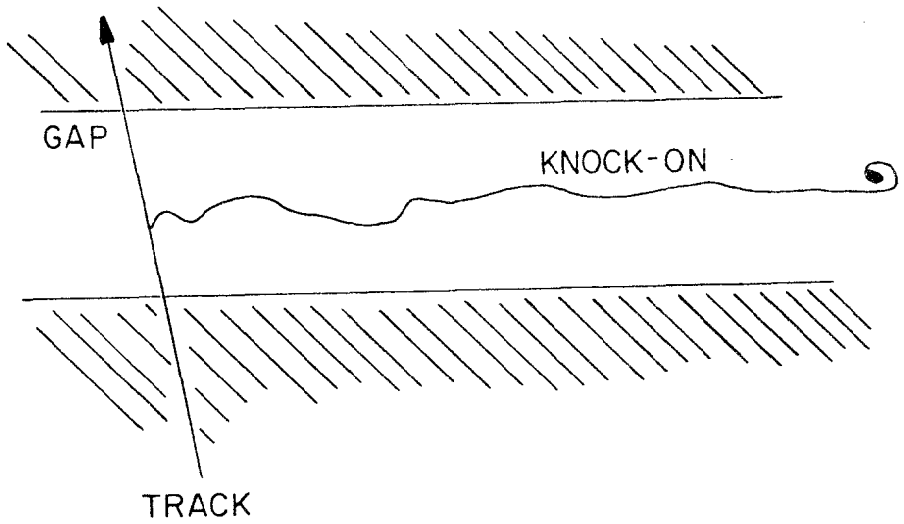

FIG. 11. Worst scenario for a knock-on. (In practice because of multiple scattering probability is very low for this to happen.)

approximations) everything the experimentalist needs to understand: the magnitudes, velocity dependence, spatial distribution and fluctuations inherent in the ionization loss process.

Position determinations are at present limited by the experimental techniques and not by any fundamental limitations.

dE/dx measurements are being forced close to the theoretical precision limits.

REFERENCES

1. Excellent literature summaries are provided by R. Talman, Cornell University Report No. CLNS-386 (1978), and Nucl. Inst. Meth. 159, 189 (1979).

AND

2. W. Allison and J. Cobb, Oxford University, Nuclear Physics Lab Report 13/80.

3. c.f., for instance, D. Ritson, Techniques of High Energy Physics, (New York, Interscience Publishers, 1961) Chapter 1.

4. O. Blunk and S. Leisegang, Z. Phys. 128, 500 (1950).

5. V. Chechin et al., Nucl. Inst. Meth. 98, 577 (1972).

6. E. Fermi, Phys. Rev. Lett. 57, 485 (1940).

7. The literature is summarized in F. Sauli, "Principles of Operation of Multiwire Proportional Chambers," CERN 77-09 (1977).

DRIFT AND PROPORTIONAL TRACKING CHAMBERS *

John A. Jaros
Stanford Linear Accelerator Center
Stanford University, Stanford, California 94305

*Work supported by the Department of Energy, contract DE-AC03-76SF00515.

I. INTRODUCTION

Many techniques have been exploited in constructing tracking chambers, particle detectors which measure the trajectories and momenta of charged particles. The particular features of high-energy interactions — charged particle multiplicities, angular correlations and complex vertex topologies, to name a few — and the experimental environment of the accelerator — event rates, background rates, and so on — accent the importance of certain detector characteristics. In high energy e^+e^-, $\bar{p}p$ and pp interactions the final states are dominated by closely collimated jets of high multiplicity, requiring good track-pair resolution in the tracking chamber. High energy particles deflect very little in limited magnetic field volumes, necessitating good spatial resolution for accurate momentum measurements. The colliding beam technique generally requires a device easily adapted to full solid-angle coverage, and the high event rates expected in some of these machines put a premium on good time resolution. Finally, the production and subsequent decays of the tau, charmed and beautiful mesons will provide multiple vertex topologies. To reconstruct these vertices reliably will require considerable improvements in spatial resolution and track-pair resolution.

This lecture will consider the proportional counter and its descendant, the drift chamber, as tracking chambers. Its goal is to review the physics of this device in order to understand its performance limitations and promises. There are several excellent references on the physics of proportional and drift chambers; the reviews of Charpak,[1] Sauli,[2] and Sadoulet[3] have been especially valuable in preparing this lecture.

The proportional counter dates from 1908, when it was introduced by Geiger and Rutherford. It consists of a thin-walled cylinder with a fine wire on its axis. With an appropriate gas mixture and a high voltage applied between the wire and cylinder, the counter detects ionizing radiation by collecting and then amplifying the electrons left after the passage of the radiation through the gas. The recent popularity of the device derives from Charpak's invention of large multiple-anode wire structures which operate at sufficiently high gain that inexpensive electronics can be used to sense the deposited ionization. The evolution of the technique is shown schematically in Figure 1. Charpak's initial invention, the multi-wire proportional chamber, consists of a sandwich of cathode planes about a layer of fine anode wires (Figure 1(a)). The array serves as a proportional chamber hodoscope. It was recognized that the time between the passage of a charged particle and the appearance of the pulse on the anode wire, the drift time, is a measure of the location of the charged particle's trajectory. By including cathode wires in the anode plane to increase field gradients and demarcate cell boundaries (Figure 1(b)), the multi-wire proportional chamber was successfully adapted for drift time measurements. Figure 1(c) shows another variation of the drift chamber. Here the voltage applied to the main cathode layers is graded to create a nearly uniform collecting field, and thus a uniform electron drift velocity, throughout the cell. Figure 1(d) shows the individual drift-cell geometry common to several of the large solenoidal magnetic spectrometers at PEP and PETRA; and Figure 1(e) shows the "jet chamber" structure adopted for the Jade detector at PETRA. Here we will concentrate on the basic element of all these devices, the simple drift cell in the form of a cylindrical tube with an anode wire on its axis.

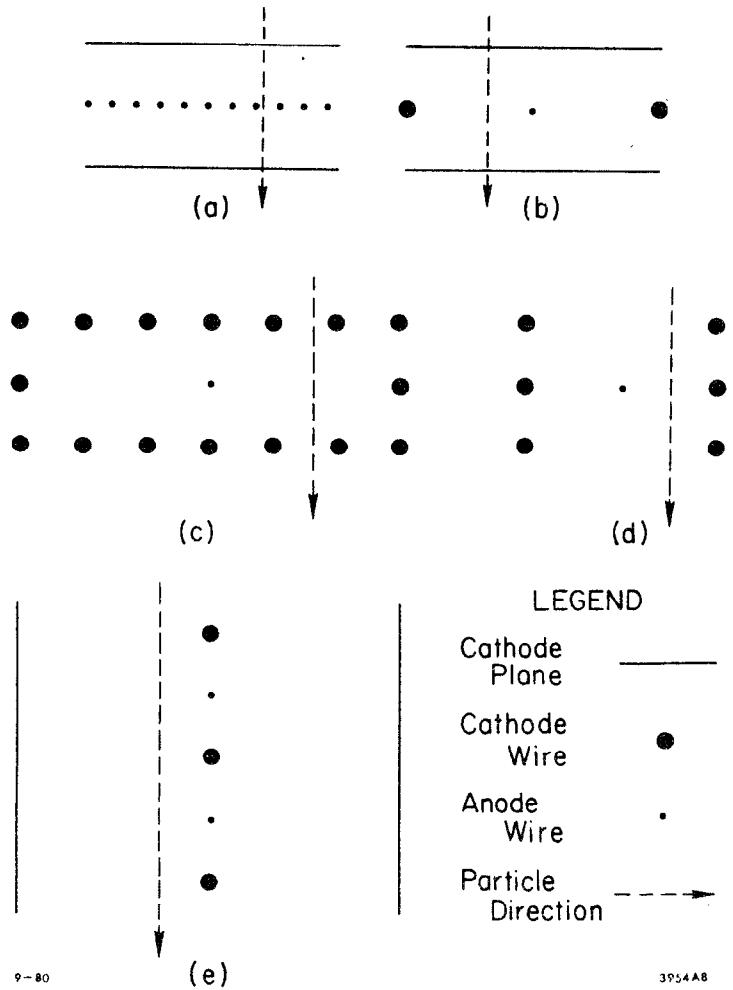

Fig. 1. Electrode arrangements in drift chambers. (a) the multi-wire proportional chamber; (b) planar drift chamber; (c) planar drift chamber with field shaping; (d) Mark II-style drift cell; (e) Jade-style jet chamber.

The plan of the lecture is as follows. We will follow the life history of the electrons released by the passage of a charged particle, reviewing the ionization process, drift and diffusion in electric and magnetic fields, amplification, and pulse formation. We will conclude by summarizing the fundamental limitations to drift chamber performance, especially to spatial resolution, since this is an area where practical improvements can be expected.

II. THE IONIZATION CHANNEL

Professor Ritson[4] has discussed how accurately the electrons ionized by the passage of a charged particle through a gas mark the trajectory of the particle. The picture which emerges is the following. In passing through 1 cm of argon gas at STP, a minimum ionizing particle undergoes about 30 ionizing collisions. Table 1 lists the ionization potentials and number of ionizing collisions for some of the other gases used in proportional chambers. The great majority of the collisions release a single electron with an effective range less than 1μ. Only about .2% of the collisions impart enough energy to the electrons to smear the track definition beyond 1 μ, and many of these δ-rays come to rest within 200 μ or so of the track. Thus the particle trajectory is delineated to the micron level by single electrons marking the collision locations. Only infrequently does a delta ray significantly degrade the resolution. In the organic gases commonly mixed with argon, the δ-ray situation should be even more benign. In any case, the spatial resolution limitations imposed by the ionization process are at the micron level and are well below limitations due to the other effects we shall consider.

The statistical nature of the ionization process already imposes limitations on the accuracy possible in a drift chamber. To study it, we consider a cylindrical proportional tube with a fine anode wire on

TABLE 1

GAS	IONIZATION POTENTIAL (eV)	NUMBER OF ION PAIRS (cm^{-1})
CO_2	13.7	34
CH_4	15.2	16
C_4H_{10}	10,6	46
Ne	21.5	12
Ar	15.7	29.4
Xe	12.1	44

the cylinder's axis. Let us also assume the electron drift velocity is a constant, independent of the distance from the anode. This will accurately approximate the behavior of most chambers near the anode wire.

Consider a track passing the anode wire with an impact parameter b; n electrons per centimeter are distributed along this track. (See Figure 2.) If the electronics is sensitive to the arrival of the first electron, the drift time measures the distance to the electron nearest the anode wire. This distance, ℓ, varies from event to event because of the statistical nature of the ionization process. The probability density for finding the first electron a distance y along the track from the point of closest approach is Poissonian:

$$P(y) = 2ne^{-2ny} \qquad (1)$$

The dispersion in the distance to the anode wire follows and is given by

$$\sigma_e = \sqrt{\frac{5}{16}} \; \frac{1}{n^2 b} \qquad (2)$$

in the limit where $b >> 1/n$. The ionization statistics thus limit the accuracy of drift-time measurements. In practice, these limitations are only important within 1 mm or so of the anode and cathode wires in a typical drift chamber. Figure 3 shows the limiting resolution as a function of the track's impact parameter for the cases $n = 30\ cm^{-1}$ and $n = 60\ cm^{-1}$. Increasing the density of ionization clusters by increasing the pressure or by choosing a gas with large n improves the resolution.

The results above apply to the common situation where the electronics is sensitive to the arrival of the first electron. Other detection

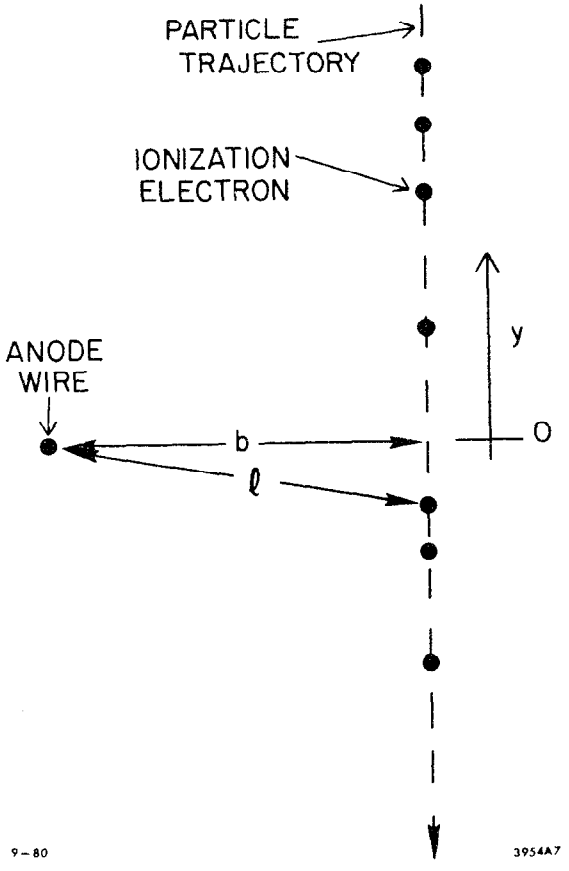

Fig. 2. Ionization deposited in a drift cell.

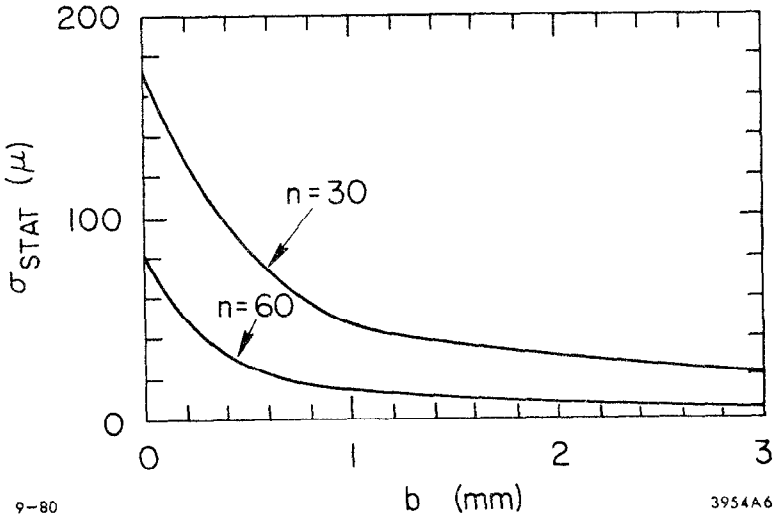

Fig. 3. Spatial resolution due to ionization statistics vs. impact parameter.

strategies are possible and may be desirable, especially in the case of long drift distances.

III. ELECTRON COLLECTION

The electrode structures we have considered in Figure 1 typically provide electric fields in the 1 kV/cm range throughout most of the active area of the drift cell, increasing inversely with the radius near the anode wire. The response of the electrons to these fields is two-fold. First, the electron temperature increases from typical thermal levels to the .1 - 1 eV range, depending on the gas and field strength, with the distribution of electron energies becoming decidedly non-Maxwellian. Second, a slow drift along the field lines toward the anode is imposed on the random thermal motion of the electrons. This drift velocity is an order of magnitude slower than the average thermal velocity of the electrons.

Classical statistical mechanics gives a good description of electron drift in electric fields. Palladino and Sadoulet[3] have applied these methods to the study of drift chamber gases. Reference 2 gives the electron energy distribution, $F(\varepsilon)$, in terms of the field strength E, the mean free path $\lambda(\varepsilon)$, and the fraction of energy lost per collision $\Lambda(\varepsilon)$, as

$$F(\varepsilon) = C\sqrt{\varepsilon}\,\exp\left\{-\int \frac{3\Lambda(\varepsilon)\varepsilon d\varepsilon}{[eE\lambda(\varepsilon)]^2 + 3\varepsilon kT\Lambda(\varepsilon)}\right\} . \qquad (3)$$

The drift velocity as a function of the field strength is

$$W(E) = -\frac{2}{3}\frac{eE}{m}\int \varepsilon\lambda(\varepsilon)\,\frac{\partial\left[F(\varepsilon)u^{-1}\right]}{\partial\varepsilon}\,d\varepsilon \qquad (4)$$

where

$$u = \sqrt{\frac{2\varepsilon}{m}}$$

Using measured values for the mean free paths and inelasticities, they have evaluated these expressions with numerical techniques and found good agreement with the existing data. Note that in the above expressions, the mean free path $\lambda(\varepsilon) \equiv 1/N\sigma(\varepsilon)$, where N is the number of atoms per unit volume and $\sigma(\varepsilon)$ is the collision cross section. Thus λ varies inversely with the gas pressure P. This means that both the energy distribution and the drift velocity depend on the reduced field, E/P.

Drift velocities in common proportional chamber gases[5,6,7] are shown as a function of the electric field in Figures 4, 5, and 6. Argon is a common component in drift chamber gases because it has relatively high specific ionization, shows gain at moderate voltages, and shows good proportionality. It must be used with organic quenchers, however, to obtain high gain. Simple polyatomic organic molecules like CO_2 and CH_4 are photo-absorbers and so prevent the photons released in the avalanching process from initiating new avalanches. More complex organic molecules may polymerize and render a chamber inoperative if it is in a high-rate environment. As the figures indicate, the drift velocity typically increases rapidly as a function of field strength up to fields between 500 and 1000 V/cm at atmospheric pressure, at which point the velocity saturates at a value of order 5 cm/μs. Even these general properties impose some significant limitations on detector performance and design. Drift time measurements must be made with subnanosecond precision to exploit the resolution inherent in this technique. About 200 ns is required to collect the electrons from a 1 cm gap, which obviously limits the maximum rate such a chamber can handle. If the field strength in a cell is kept above the saturation field, the sensitivity of the drift time to small mechanical differences and voltage changes is minimized.

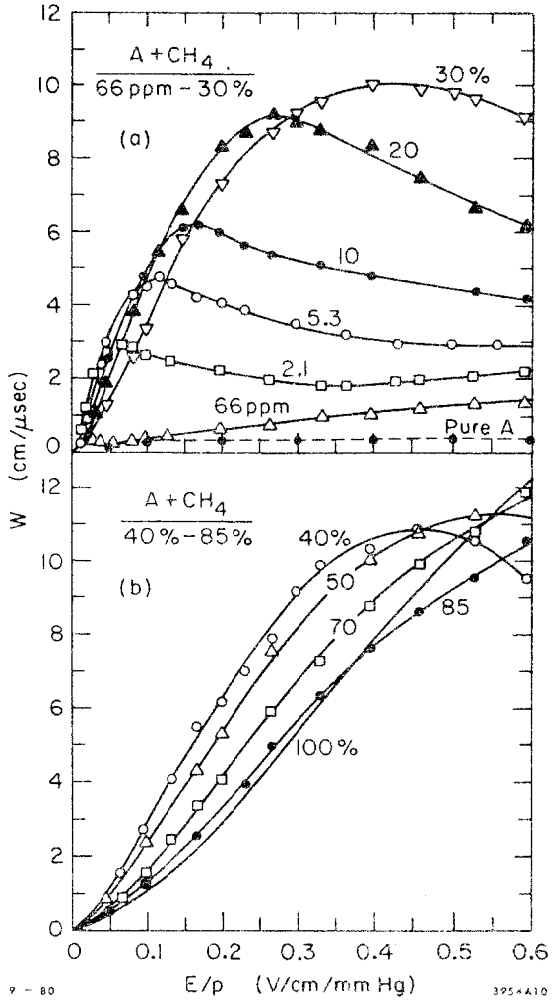

Fig. 4. Electron drift velocity in argon/methane mixtures as a function of the reduced field. Data from Ref. 5.

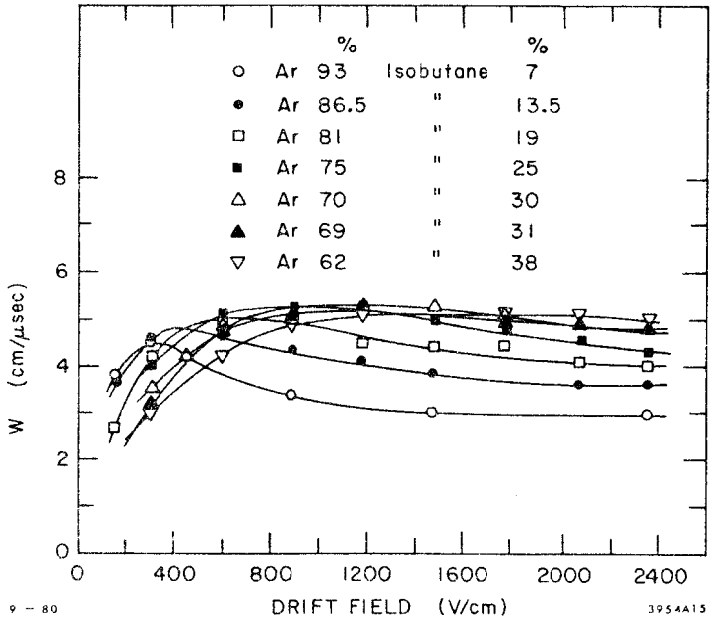

Fig. 5. Electron drift velocity in argon/isobutane mixtures as a function of electric field. Data from Ref. 6.

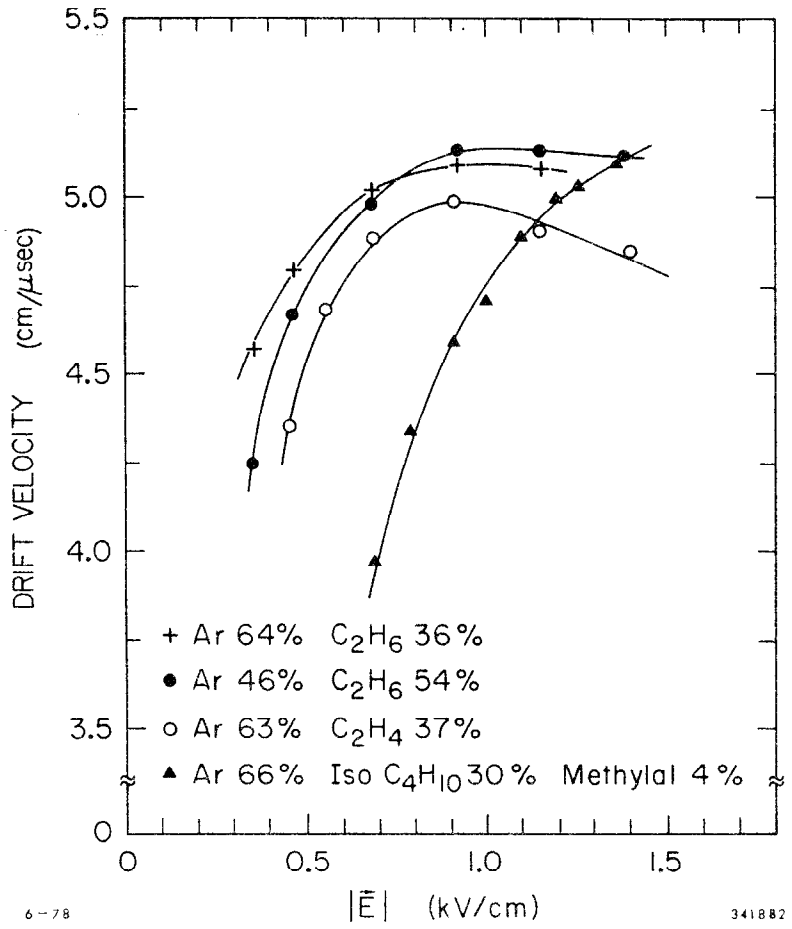

Fig. 6. Electron drift velocity in argon/ethane, argon/ethylene and argon/isobutane mixtures as a function of electric field. Data from Ref. 7.

In the presence of a 1 kV/cm electric field, an electron in an argon/ethane mixture has an average velocity near 10^8 cm/s. It collides with gas molecules every micron or so, its direction being randomized in the process. With the passage of time, the electron "random walks" away from its original location. After 200 ns of collection time it will have undergone about 2×10^5 collisions and diffused by about $1\mu \times \sqrt{2 \times 10^5} = 500\mu$. More precisely, the diffusion transverse to the direction of drift is given in terms of the diffusion constant D and the drift time t as

$$\sigma_T = \sqrt{2Dt} \quad . \tag{5}$$

The diffusion coefficient D is given in terms of the electron energy distribution as

$$D = \frac{1}{3} \int u \, \lambda(\varepsilon) \, F(\varepsilon) \, d\varepsilon \quad , \tag{6}$$

and so is an implicit function of (E/p). Figure 7 gives the root-mean-square of the transverse diffusion after 1 cm of drift for various gases[8] as a function of field strength. Pure argon, with its anomalously low-drift velocity, has $\sigma_T \sim 1000\,\mu$. In the common argon/isobutane 70/30 mixture, σ_T is comparable to pure CH_4, about $250\,\mu$.

The resolution achievable with drift time measurements clearly depends upon electron diffusion and the particular strategy employed in detecting the ionization (e.g., low threshold vs. center of ionization). It has recently been appreciated that longitudinal diffusion, i.e., diffusion in the direction of the drift velocity, is not equal to the transverse diffusion. In fact, as data in pure argon[9] and the data[10] in Figure 8 show, the coefficient of longitudinal diffusion is about a factor of 4 smaller than that for transverse diffusion. Measurements of

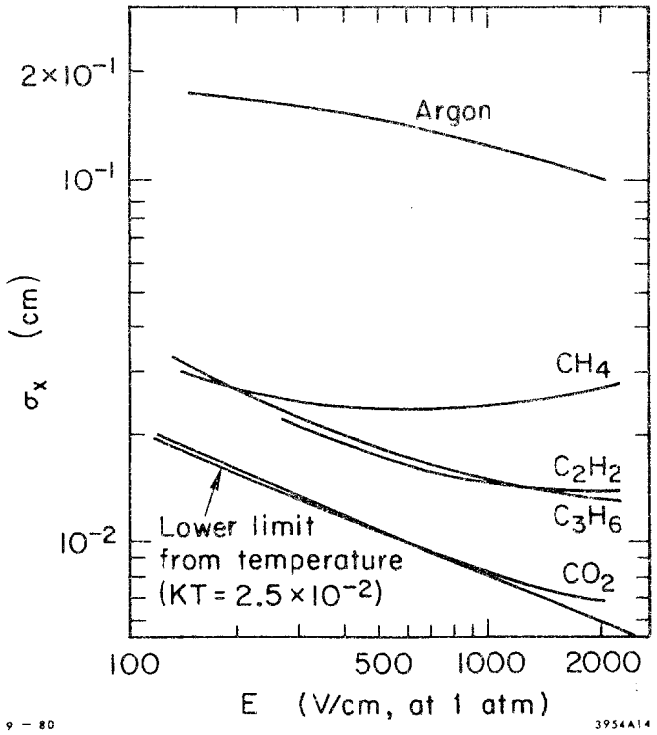

Fig. 7. Spatial resolution due to transverse diffusion after 1 cm drift as a function of the electric field in various gases. Data from Ref. 8.

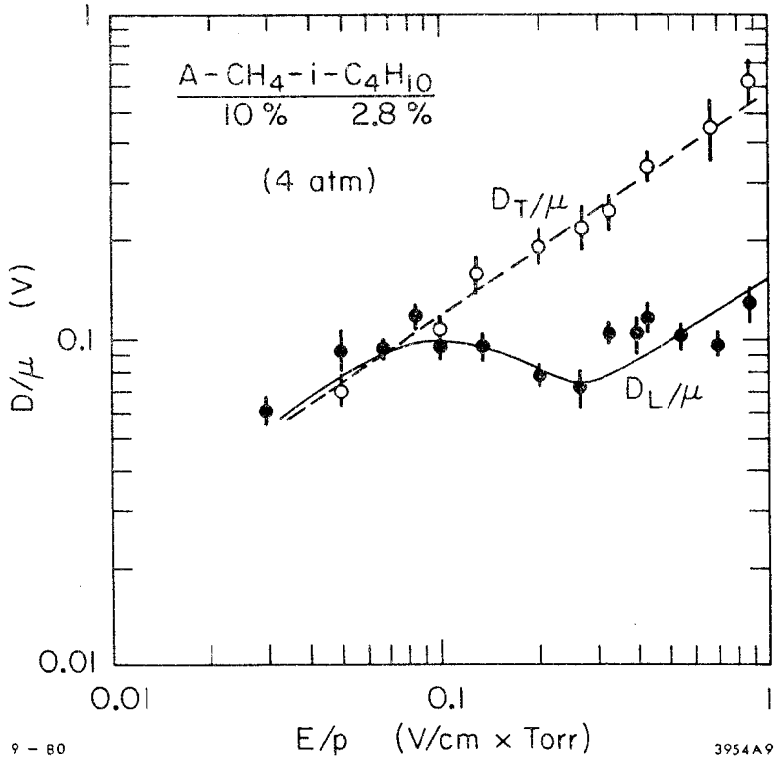

Fig. 8. Coefficients of longitudinal and transverse diffusion as a function of the reduced field. Data from Ref. 10.

longitudinal diffusion have not been made in many proportional chamber gases as yet, so we shall adopt the rule of thumb $\sigma_L = \sigma_T/2$ as a guide in evaluating diffusion effects in drift chambers. Then, we expect the spatial resolution after 1 cm of drift to be limited to ~ 100 μ in argon/isobutane mixtures at one atmosphere. To do substantially better than this, one must increase the pressure or use other gases. Notice that the diffusion constant D varies inversely with the pressure; thus increasing the pressure reduces the diffusion. D also depends on the average electron temperature in the gas. Thus a "cool" gas, like pure isobutane, has considerably lower diffusion than the more common argon/isobutane mixtures. Figure 9 illustrates these points. Note that even over the smallest practical drift distances (~ 1 mm), diffusion significantly limits the resolution inherent in a drift time measurement. For a given permissible resolution, it limits the maximum drift distance unless a new measurement strategy is adopted. Two such techniques should be mentioned. By timing the center of gravity of an n-electron bunch instead of the arrival of the first electron, one could hope to reduce the diffusion by a factor $1/\sqrt{n}$. In practice, this full reduction isn't realized unless the drift-length differences among the electrons are smaller than the expected diffusion. The other technique is to arrange the drift field parallel to an intense magnetic field. In the appropriate gas, this can limit transverse diffusion by forcing the drifting electrons into tight helical paths. Jay Marx's lecture[11] gives the details of this scheme.

The effect of magnetic fields on electron collection in a drift chamber is important in many applications. Chambers have been operated in moderately high magnetic fields (15 kG) with success. Here we shall consider the common situation where $\vec{E}$ and $\vec{B}$ are perpendicular. In this

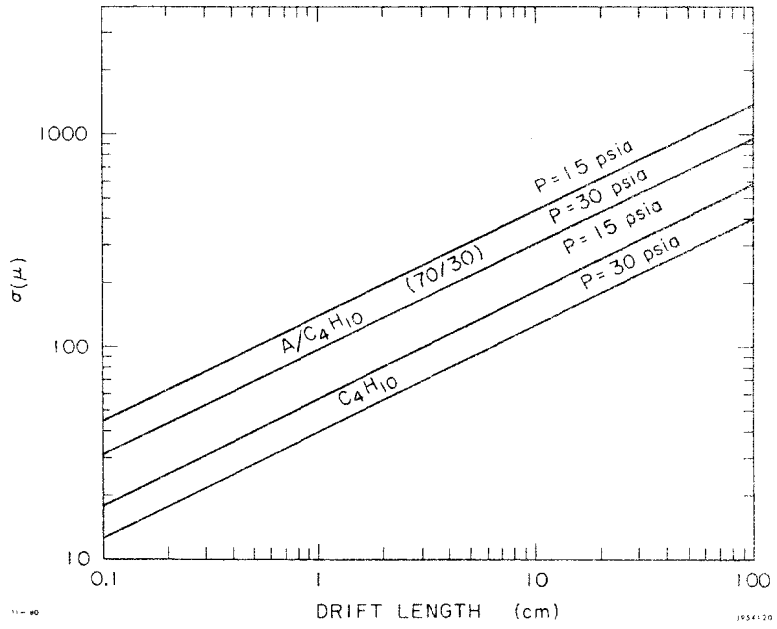

Fig. 9. Spatial resolution due to longitudinal diffusion as a function of drift length in argon/isobutane and in pure isobutane at 1 and 2 atmospheres pressure.

case, there are two effects: (1) the electrons drift at an angle θ with respect to the local electric field direction; (2) the drift velocity is reduced. Figures 10 and 11 illustrate these effects in argon/isobutane/methylal.[12] Notice that the Lorentz angle θ becomes large at high field strengths; argon/xenon mixtures have angles about half those of argon-isobutane and may be useful in very high magnetic fields. As Figure 11 shows, increasing the magnetic field at moderate electric fields decreases the drift velocity. At high electric fields, however, the effect is negligible.

The dependence of the drift angle and drift velocity on the field strengths can be parameterized in terms of two gas-dependent constants, K_1 and K_2, the Larmor frequency $\omega = eB/m_e c$, and the mean time between collisions, τ. Following Reference 13, we write

$$\tau = K_1 \, m_e W_0 / eB \tag{7}$$

$$\theta = \arctan \left\{ K_2 \, \frac{B}{E} \, \frac{W_0}{\left(1+\omega^2\tau^2\right)^{\frac{1}{2}}} \right\} \tag{8}$$

and

$$\bar{W} \cdot \bar{E} = W_0 \Big/ \left(1+\omega^2\tau^2\right) \quad . \tag{9}$$

W_0 is the drift velocity in vanishing magnetic field, and the constants K_1 and K_2 are about 5 for a 90/10 argon/methane gas mixture.

Figure 12, also from Reference 13, shows rather dramatically how a high magnetic field warps the "electron-geodesics." Families of electron trajectories have been drawn for the case where B = 0 (Figure 12(a)) and where B = 15 kG (Figure 12(b)). In the high field case, the space-time relation is strongly angle-dependent and left-right asymmetric. To avoid such complexities, several groups have built chambers like the one shown schematically in Figure 1(e). In these

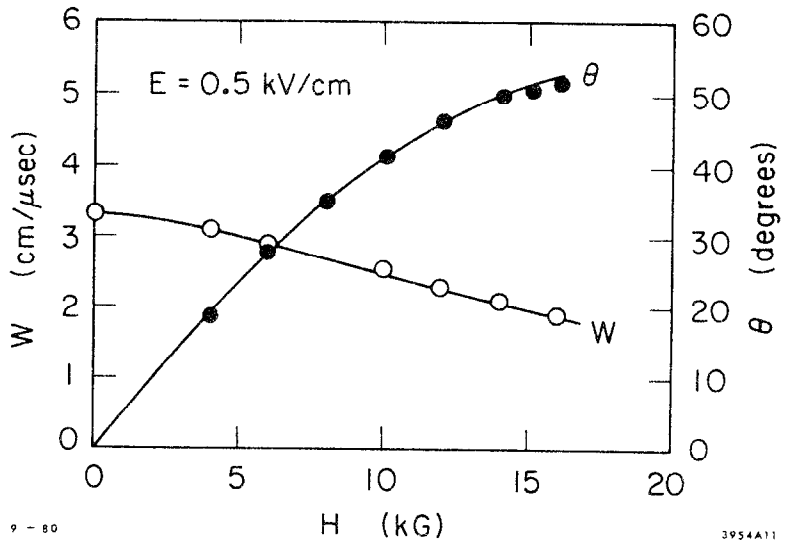

Fig. 10. Dependence of the drift velocity and the Lorentz angle on magnetic field in argon/isobutane at .5 kV/cm. Data from Ref. 12.

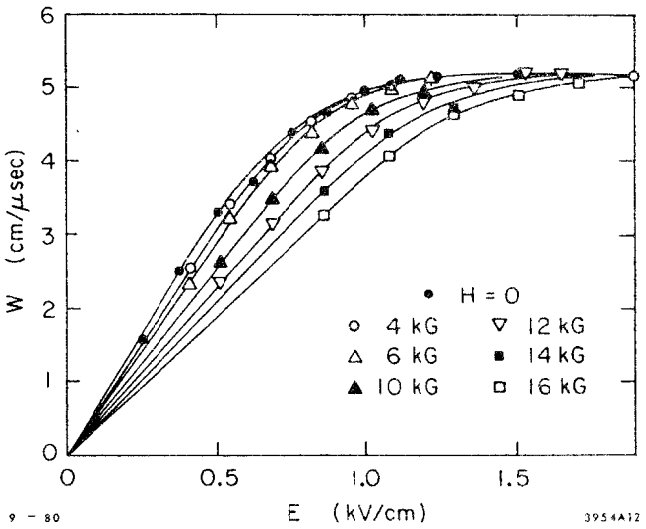

Fig. 11. Dependence of the drift velocity on the electric field for different magnetic fields. Data from Ref. 12.

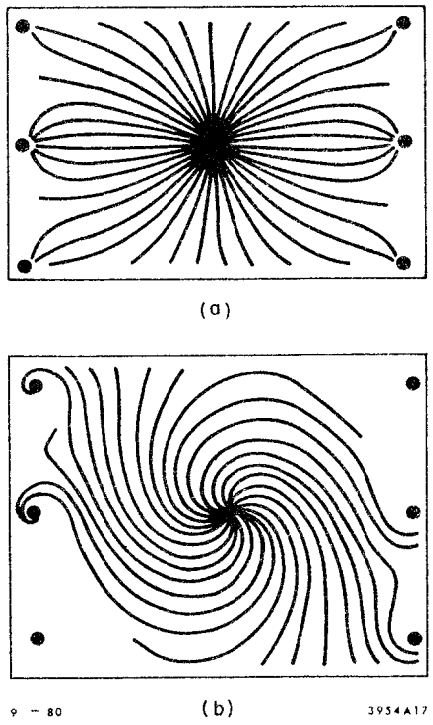

Fig. 12. Electron drift trajectories in the CELLO drift cell with (a) B = 0 and (b) B = 15 kG. Data from Ref. 14.

chambers, the electric field is uniform over much of the active area. Then the electron trajectories are straight lines, tilted with respect to the electric field direction.

IV. AMPLIFICATION AND PULSE FORMATION

Within about 100 μ of the anode wire, the local electric fields are so intense that electrons are accelerated to energies great enough to ionize gas molecules. This frees more electrons, and the process cascades, multiplying the initial 30 or so electrons by a factor of order 10^5 in a typical drift chamber. The process is described in terms of the first Townsend coefficient, α, which is the number of ion pairs produced per centimeter of travel. The amplification factor A can be written

$$A = e^{\int \alpha(r)dr} , \qquad (10)$$

where the integration is over the electron path length. As long as space-charge effects are small, the amplification factor is the same for all the collected electrons. Hence the chamber response is proportional to the amount of initial ionization. Figure 13 shows the first Townsend coefficient as a function of the reduced field in the noble gases.[14] Electric fields near the anode wire are typically in the range $|\vec{E}| = 4000\ (kV/cm)/r(\mu)$; in the amplification region the mean free path for an ionizing collision ranges from about 10 μ to 1 μ, comparable to the classical mean free path for an electron in a gas.

The Rose-Korff parameterization[15] is a handy guide to the rough magnitude of the amplification in a proportional chamber. It is given in terms of the chamber parameters (the voltage V, the anode wire radius r_a, and the wire capacitance per unit length C) and the gas parameters (the rate of change of the ionization cross section with

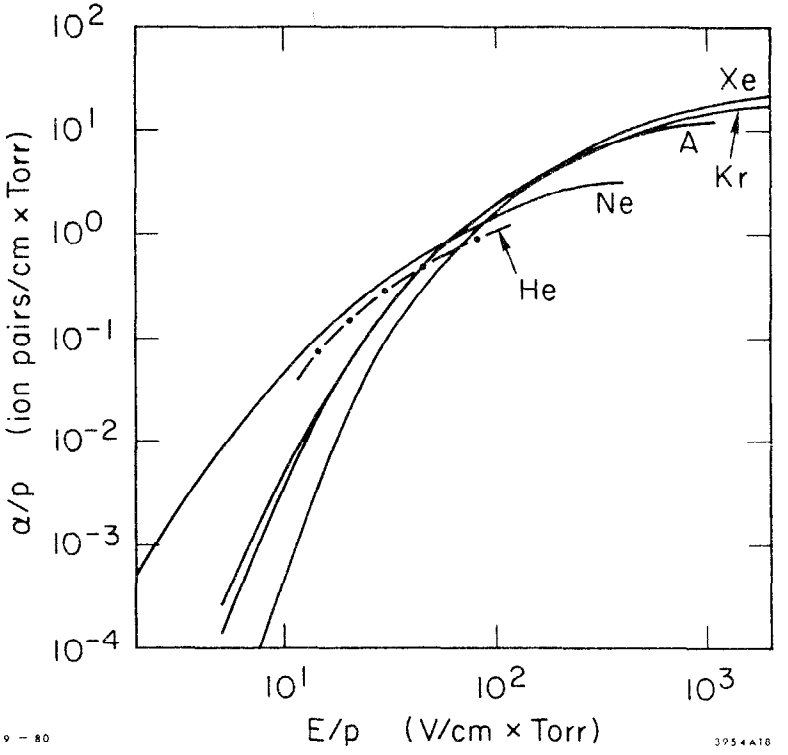

Fig. 13. Dependence of the first Townsend coefficient on the reduced field for the noble gases. Data from Ref. 14.

energy a, the number of gas molecules per unit volume N, and the voltage at which amplification begins, V_T) as follows:

$$A = \exp\left\{2\sqrt{aNCr_a V}\left(\sqrt{\frac{V}{V_T}} - 1\right)\right\} \quad . \tag{11}$$

V_T is treated as a free parameter and determined by fitting the behavior of the amplification at low voltage. When $V \gg V_T$, the amplification is seen to depend roughly exponentially on the chamber voltage; a typical chamber gain doubles in about 150 V. Gains up to 10^5 are common in practice and give rise to signals of order 1 mV/electron. This sets the required level of electronic sensitivity for the detection of single electrons. Higher gains have been achieved in certain gas mixtures, but space-charge effects limit the proportional amplification regime to gains $\lesssim 10^5$.

Amplification is of course a statistical process, so wide variations in the pulse height are expected when single electrons are detected. Curran, Cockroft and Angus[16] have found that the distribution of amplification obeys

$$P(\eta) = \frac{3}{2}\,\eta\,\exp\left\{-\frac{3}{2}\,\eta\right\} \tag{12}$$

where

$$\eta = \frac{A}{\bar{A}} \quad .$$

This distribution is shown in Figure 14; its variance is large, $\sigma_A = \sqrt{\frac{2}{3}}\,\bar{A}$. Such wide variations in the pulse height from a single electron can cause substantial time slewing in the detecting electronics. The mean pulse height must be considerably above the electronic threshold to achieve good timing resolution. Although the pulse height variations from single electrons are large, the variations seen in a typical chamber

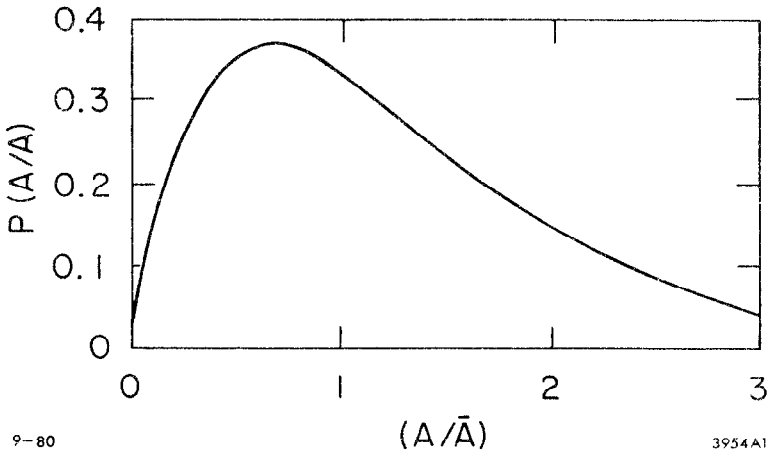

Fig. 14. Distribution of the amplitude of proportional chamber pulses from a single electron.

(where perhaps 30 electrons are collected) are dominated by the ionization statistics, not the amplification process. Letting $\bar{m}$ be the average number of primary electrons and σ_m its dispersion, the net dispersion σ is given by[17]

$$\frac{\sigma^2}{(\bar{m}\bar{A})^2} = \frac{\sigma_m^2}{\bar{m}^2} + \frac{2}{3\bar{m}} \quad . \tag{13}$$

The second term comes from variations in the amplification.

The pulse observed on the anode wire of a proportional chamber is induced by the motion of the charges released in the avalanche. The motion of the positive ions contributes most of the observed pulse. The voltage induced as a function of time is

$$V_+(t) = -\frac{Q}{\ell} \ln\left(1 + \frac{t}{t_0}\right) \quad , \tag{14}$$

where

$$t_0 = \frac{r_a^2 P}{4\mu^+ CV} \quad .$$

Here Q is the total charge of the ions, P the pressure, ℓ the anode wire length, and μ^+ the mobility of the positive ions. The pulse has a very rapid rise followed by a slow logarithmic approach to its maximum value, $-Q/\ell C$, which occurs when the positive ions have been collected at the cathode. This occurs at a time $t = P(r_b^2/r_a^2 - 1)t_0$, where r_b is the radius of the cathode surface. Figure 15 shows V/V_{max} as a function of time. A typical chamber has $t_0 = .5$ ns and a total collection time in the 1 ms range. Notice that about 20% of the signal appears within a few nanoseconds of the avalanche time.

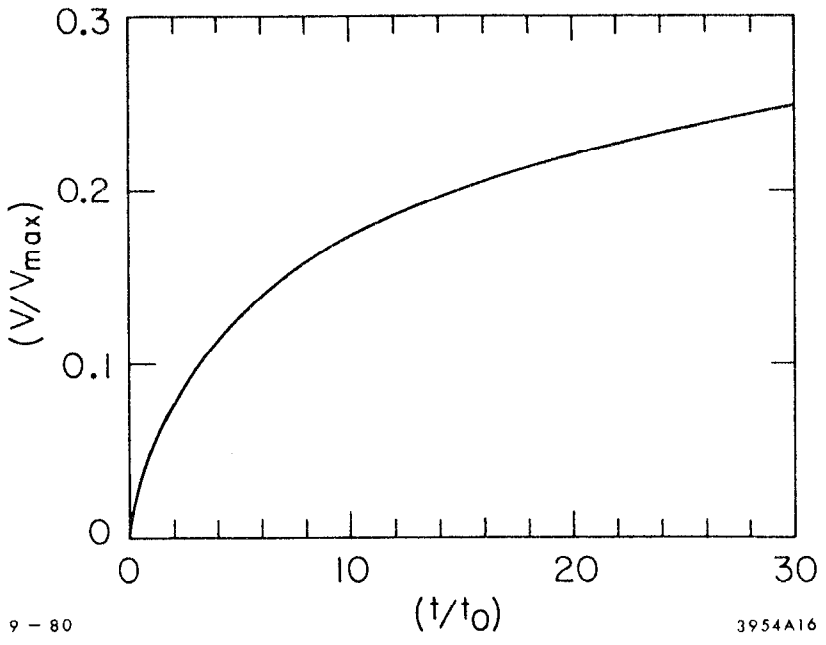

Fig. 15. Time development of a proportional chamber signal.

The expression for $V_+(t)$ applies to the case of arbitrarily high amplifier input impedance; in practice the input impedance is in the 1 KΩ range, which coupled to a typical wire capacitance gives RC' between 10 and 100 ns. The result is the sharp differentiation of the input pulse. The maximum in the differentiated signal appears at $t \approx RC'$ and has a relative amplitude[18]

$$\frac{V}{V_{max}} = \left(\frac{RC'}{t_{col}}\right) \frac{r_b^2/r_a^2}{2 \log\left(r_b/r_a\right)} \quad . \qquad (15)$$

The resulting pulses typically have widths in the 10-100 ns range and pulse heights of order 10-40% of V_{max}. This pulse width of course imposes rate limitations for each wire, and the pulse height loss due to differentiation means that a threshold of order 300 μV is required to see a single electron. Since the rise time of the differentiated pulse is in the few nanosecond range, the electronic rise-times should be comparable so as not to introduce excessive slewing.

V. PERFORMANCE LIMITATIONS IN DRIFT CHAMBERS

High rate capability, good track-pair resolution, and good spatial resolution are the key requirements for tracking chambers in the newly completed or soon-to-be completed colliding beam devices. Rate limitations come about from at least two considerations. The width of the output pulse depends on how sharply the chamber output has been differentiated and on the range of electron arrival times. The width is typically 100 ns and so imposes an upper limit of about 2 MHz per wire. At such high rates, space charge effects become important for chambers operated at gains $\geq 10^5$. The sheath of positive ions migrating away from the anode wire lowers the fields seen by incoming electrons and so reduces the amplification. Breskin et al.,[19] found that wires grew inefficient at rates greater than a few megahertz per meter of wire length.

Track-pair resolution depends of course on the geometry of the drift-cell and the capabilities of the electronics. In simple single-hit cells, the resolution is roughly given by the cell size. Systems with redundant cells offset from one another can obviously do better, but the current practical limit is about 1 cm. Information from two tracks separated by less than this amount is lost. With larger drift spaces and multi-hit electronics, the limit to track-pair resolution comes from the width of the output pulse associated with one track. In the Jade detector at PETRA, a track-pair resolution of 5 mm has been achieved,[20] and in a prototype device, the Charpak group[21] has achieved about 2.5 mm. The corresponding pulse widths are 100 and 50 ns, respectively, very near the limit imposed by the drift-time differences associated with any track.

The fundamental limits to spatial resolution have not been so closely approached. As we have discussed above, the statistical nature of the ionization process and the diffusion of the electrons during the collection time contribute significantly to the spatial resolution. Increasing the gas pressure and choosing a "cool" gas can lead to significant improvements in the resolution as indicated in Figure 16. This technique has been demonstrated by a Heidelberg group,[22] whose data are shown in Figure 17. We have obtained similar results in argon/ethane (50/50) and argon/isobutane (70/30) mixes (Figure 18) for a drift of a few millimeters.

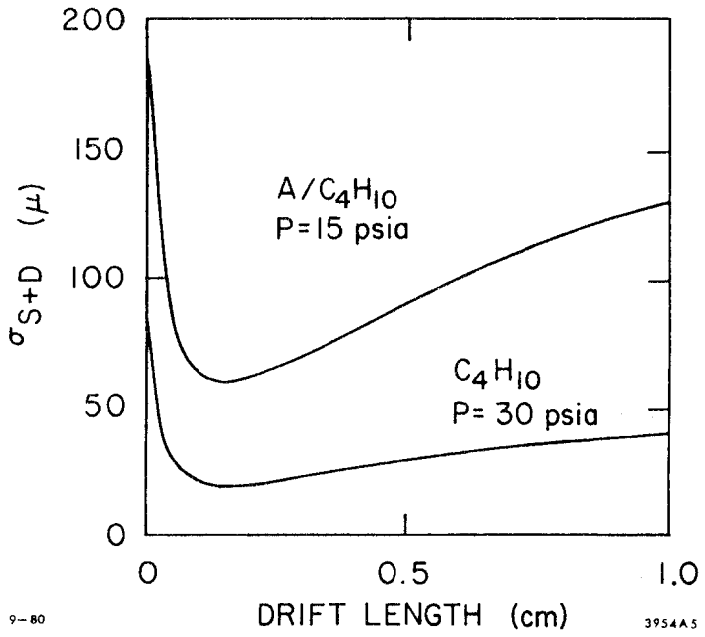

Fig. 16. Spatial resolution due to ionization statistics and diffusion as a function of drift length in different gases.

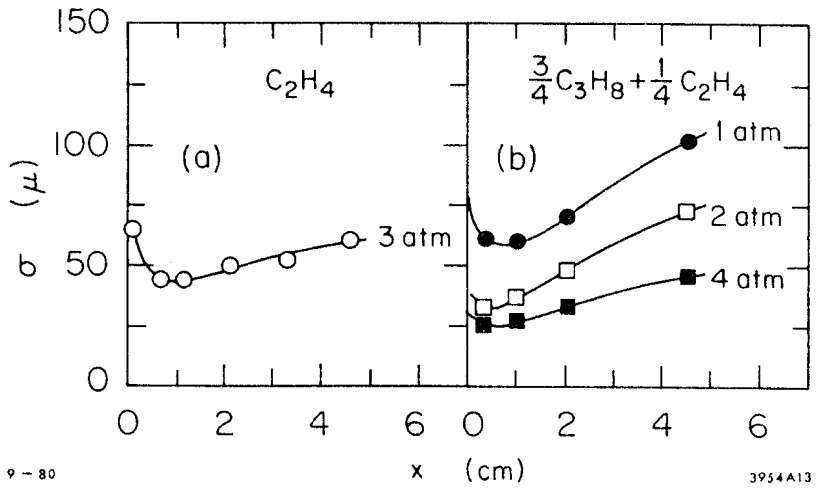

Fig. 17. Measured spatial resolution as a function of drift distance in organic gases at several pressures. Data from Ref. 22.

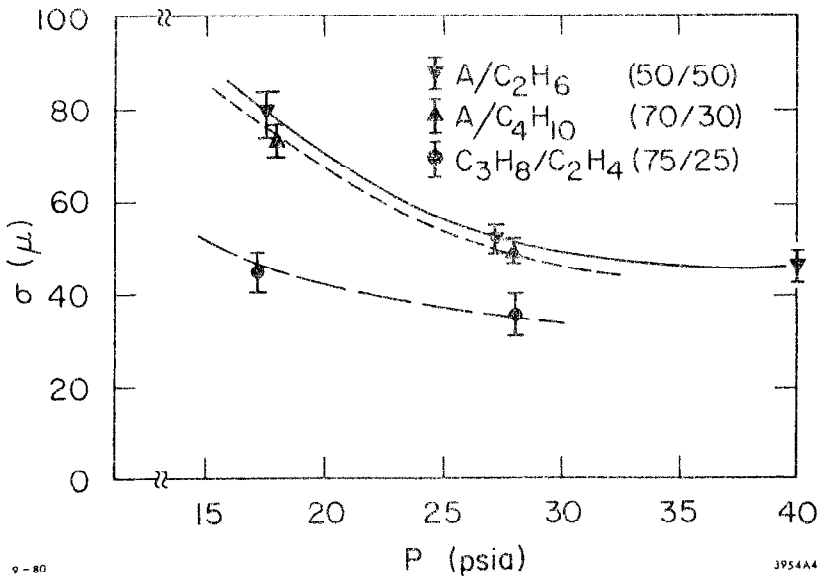

Fig. 18. Measured spatial resolution as a function of gas pressure in several gases for 3 mm drift length.

Spatial resolution depends rather critically on electronic threshold sensitivity. For a fixed threshold, the resolution improves dramatically with increased chamber gain, and only saturates hundreds of volts beyond the beginning of the efficiency plateau, at least for drift lengths ≤ 1 cm. For longer drift distances, where a large number of electrons arrive at the anode at nearly equal times, diffusion effects can be reduced by measuring the arrival time of the nth electron. We have modeled this situation with Monte Carlo techniques with the following assumptions: (1) cylindrical electric field; (2) drift velocity independent of the field; (3) thirty ion pairs produced per centimeter; (4) $\sigma_{DIFF} = 100\mu \times \sqrt{x(cm)}$. Figure 19 shows the spatial resolution as a function of drift length for thresholds corresponding to one, two and four electrons. Pulse height variations and rise-time effects have been ignored, so the graph should only be taken as a rough guide. Still, it indicates the importance of sensitive electronics for the measurement of drifts under 1 cm. Figure 20 shows the improvement in the resolution for short drift lengths that we have observed in propane/ethylene (75/25) as high voltage has been increased beyond the beginning of the efficiency plateau. Resolution improves as the gain increases.

Achieving high spatial resolution in a drift chamber system with a large number of wires requires that considerable attention be paid to many details. Some of these are listed in Table 2 for a high resolution system we have proposed. Sources of error include the mechanical precision in wire placement; timing uncertainties and time-measurement inaccuracies; variations in gas pressure and temperature and chamber voltage; and the more fundamental limitations we have discussed above. Taking these errors into account, it should be possible

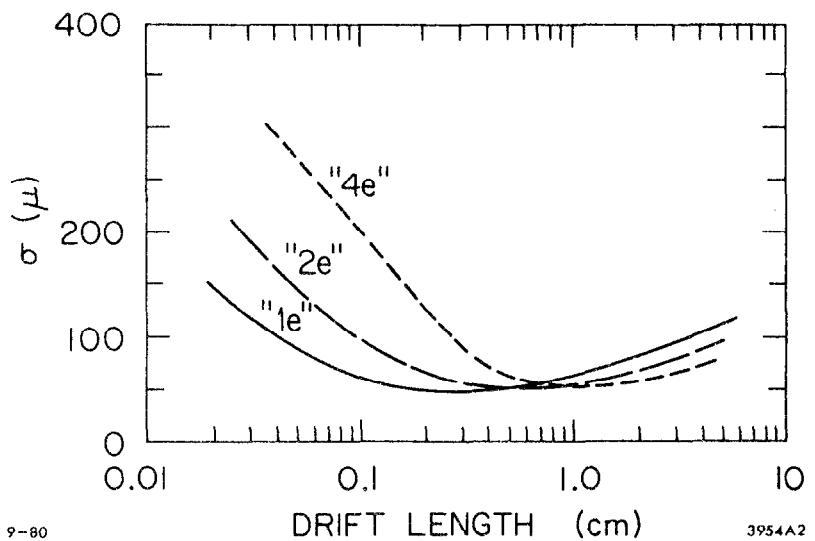

Fig. 19. Modeled dependence of spatial resolution on drift length for various threshold sensitivities.

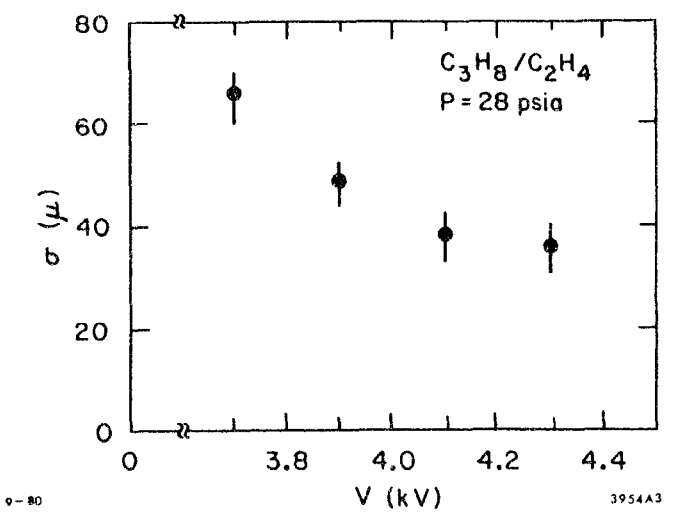

Fig. 20. Measured spatial resolution in propane/ethylene as a function of high voltage.

TABLE 2

	$\sigma(\mu)$
I. MECHANICAL TOLERANCES	
Wire Placement	10
Gravitational Sag (40 μ, corrected knowing Z and tension)	5
Electrostatic Displacement	5
	12
II. TIMING UNCERTAINTIES	
Start-Time (.2 ns)	10
Particle Time-of-Flight to Layer (.1 ns)	5
Signal Propagation (.1 ns, knowing Z)	5
TDC Calibration (.1 ns)	5
TDC Resolution (.2 ns)	10
	17
III. CHAMBER PARAMETERS	
High Voltage Variation (10 V)	10
Temperature Changes (1^{o} C)	10
Pressure Changes (.1 PSI)	10
Cell-to-Cell Gain Variations	5
	18
IV. DRIFT-TIME ACCURACY	
Intrinsic Resolution	40
Space-Time Relationship Uncertainty	20
	45

OPTIMAL SYSTEM RESOLUTION: 50 to 55 μ

using present techniques to construct systems with spatial resolutions in the 50 μ range, i.e., markedly below the 200 μ common to most big systems today.

VI. CONCLUSIONS

Tracking chambers based on drift-time measurements in proportional counters have demonstrated good time, track-pair, and spatial resolution. Diffusion, the statistics of ion formation, and electronic timing jitter limit the spatial resolution to 100-200 μ; by using pressurized gases and operating the chamber well beyond its efficiency threshold, resolutions in the range 25 - 50μ are possible. Even with such improvements, the spatial resolution is more than an order of magnitude worse than that inherent in the ionization process in a gas.

ACKNOWLEDGMENT

It is a pleasure to thank David Ritson and Jay Marx for useful discussions.

REFERENCES

1. G. Charpak, "Evolution of the Automatic Spark Chamber," Ann. Rev. Nuclear Sci. 20, 195 (1970).

2. F. Sauli, "Principles of Operation of Multiwire Proportional and Drift Chambers," CERN report 77-09 (1977).

3. V. Palladino and B. Sadoulet, Nuc. Instru. and Meth. 128, 323 (1975).

4. D. Ritson, talk at this Institute.

5. H. W. Fulbright, "Ionization Chambers in Nuclear Physics," Encyclopedia of Physics, S. Flügge, ed., Springer-Verlag, Berlin, 1958, p. 1.

6. A. Breskin, et al., Nuc. Instr. and Meth. 160, 227 (1975).

7. W. Davies-White, et al., Nuc. Instr. and Meth. 160, 227 (1975).

8. V. Palladino and B. Sadoulet, op. cit.

9. J. J. Lowke and J. H. Parker, Phys. Rev. 181, 302 (1960).

10. A. Wagner et al., "Experience with the Jet-Chamber of the Jade Detector at PETRA," in Proceedings of the Wire Chamber Conference, Vienna, 1980, to be published in Nucl. Inst. and Meth.

11. J. Marx, talk at this Institute.

12. A. Breskin et al., op. cit.

13. W. de Boer et al., "Behavior of Large Cylindrical Drift Chambers in a Superconducting Solenoid," in Proceedings of the Wire Chamber Conference, Vienna, 1980, to be published in Nucl. Inst. and Meth.

14. S. C. Brown, Basic Data of Plasma Physics, MIT Press, Cambridge, Mass., 1959.

15. M. E. Rose and S. A. Korff, Phys. Rev. 59, 850 (1941).

16. S. C. Curran, A. L. Cockroft and J. Angus, Phil. Mag. 40, 929 (1949).

17. D. H. Wilkinson, Ionization Chambers and Counters, Cambridge University Press, 1950, p. 143.

18. D. H. Wilkinson, op. cit.

19. A. Breskin et al., op. cit.

20. A. Wagner, op. cit.

21. A. Breskin et al., op. cit.

22. W. Farr et al., Nucl. Instr. and Meth. 154, 175 (1978).

PARTICLE IDENTIFICATION BY ENERGY LOSS MEASUREMENT AND LONG DRIFT IMAGING CHAMBERS*†

Jay N. Marx

Lawrence Berkeley Laboratory
University of California
Berkeley, CA 94720

A. Introduction

In this review we will discuss two experimental techniques which are the ingredients for a new generation of charged particle detectors. These techniques, particle identification by energy loss measurement and long drift imaging chambers are used separately, or in tandem to configure detector systems (e.g., ISIS, BEBC-EPI, CRIRIS, TPC and others) which can obtain high quality data over large solid angles.

The basic idea of these detectors is to use as much as is possible of the information left as ionization by charged particles traversing a gaseous medium. This residual ionization trail contains trajectory information and, from the distribution of energy loss, velocity information. Since such information is to be collected over a large volume (large solid angle), ionization electrons are drifted in some of these detectors over large distances to sense elements where the information is extracted.

In order to understand in detail the operation and limitations of such detectors, we will discuss the following topics:

- Diffusion of electrons in gases --especially in the presence of electric and magnetic fields.

* Lecture presented at 1980 SLAC Summer Institute.

† Work has been supported by the High Energy Physics Division of the U.S. Department of Energy.

- Drift velocities of electrons in various gases so as to learn the time required to drift long distances.
- Absorption of drifting electrons in various gases under a variety of conditions.
- Particle identification by energy loss sampling techniques.

The reader may wish to keep in mind the Time Projection Chamber (TPC) as a generic example of this type of detector.[1] The TPC will be discussed in some detail later in this lecture.

The basic principles of the TPC which illustrate these techniques involve the detection of ionization trails left in gas by charged particles which contain topological and velocity (dE/dx) information. These ionization electrons are caused to drift up to 1 m by a drift electric field (E/P ≈0.15 V/cm/torr, P ~ 10 Atmospheres).

The ionization electrons are then detected and "measured" at proportional wire instrumented end caps to extract the topological and velocity information for each particle leaving an ionization trail in TPC.

In this lecture we will provide the tools to allow the reader to answer many of the pertinent questions relevant to the operation of such a detector. Examples of such questions are:

1. How much does diffusion smear the drifting ionization trails? What is the resulting limit on spatial resolution?
2. What is the drift time for a 1 m drift (the integration time of the chamber)?
3. How many electrons are absorbed during the 1 m drift? Is extensive information thus lost?
4. How is velocity information extracted from the ionization? Is sufficient accuracy obtained to identify relativistic particles whose momentum is known?

B. Diffusion and Drift of Electrons in Gases

Most figures in this section are taken from reference 2. References 2, 3, 4 contain details on this subject not found in these notes.

I. Diffusion in a Field-free Region

Ionization electrons lose their impluse energy in multiple collisions in the gas. These electrons then assume the thermal energy distribution of the gas (a Maxwellian probability distribution)

$$F(\varepsilon) = C \sqrt{\varepsilon}\, e^{-\varepsilon/kT}$$

$$\langle \varepsilon \rangle = \frac{3}{2} kT \approx 0.04 \text{ eV} \quad \text{at STP} .$$

In the absence of fields a clump of charges diffuses by random, multiple collisions with a Gaussian distribution:

$$\frac{dN}{N} = \frac{1}{\sqrt{4\pi Dt}}\, e^{-(x^2/4Dt)}\, dx$$

where $\frac{dN}{N}$ = fraction of charge in an element dx at a distance x from the origin after a time t. The distribution is characterized by D, the diffusion coefficient, $D = V\lambda/3$ where V = electron thermal velocity, λ = mean free path. The RMS of the distribution is

$$\sigma_x = \sqrt{2Dt} \qquad \sigma_V = \sqrt{6Dt}$$

(Linear Diffusion) (Volume Diffusion)

Figure 1 illustrates the gradual spread of a clump of electrons due to diffusion. For electrons at STP, $V \sim 10^7$ cm/sec, $\lambda \approx 4 \times 10^{-5}$ cm. We can now ask what happens to the diffusion coefficient if we vary the gas pressure.

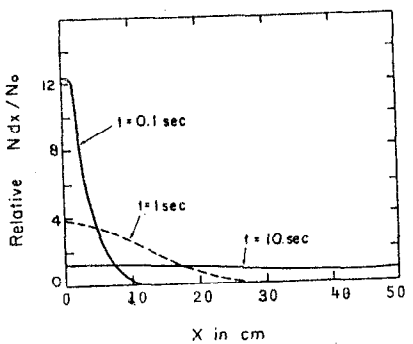

Figure 1. Space distribution of electrons produced in air, at normal conditions, after different time intervals.

Since

$$\sigma_x = \sqrt{2Dt} \qquad \text{and} \qquad D = V\lambda/3$$

then

$$\sigma_x = \sqrt{\frac{2}{3} V\lambda t}$$

where λ, the mean free path is inversely proportional to pressure

$$\lambda \propto \frac{1}{p} .$$

The thermal velocity, V, is dependent on temperature, not pressure. Therefore, for a given time t, the RMS diffusion of a clump of electrons depends on pressure as:

$$\sigma_x \propto \frac{1}{\sqrt{p}} .$$

At increased pressures the RMS clump size after a given time is reduced as the square root of the pressure.

Particle detectors of interest are generally immersed in electric and/or magnetic fields. We must therefore consider diffusion in the presence of such fields of various relative orientations. These matters are considered in the next sections.

II. Diffusion in the Presence of an Electric Field

If we apply an electric field (E) in the gas, the electrons drift in the field and the velocity they gain from the field affects the diffusion coefficient (D) for diffusion in the direction of drift. This effect is illustrated in Figure 2 for drifts of 1 cm at STP in various gases. The RMS longitudinal diffusion of a single electron is plotted as a function of the drift electric field.

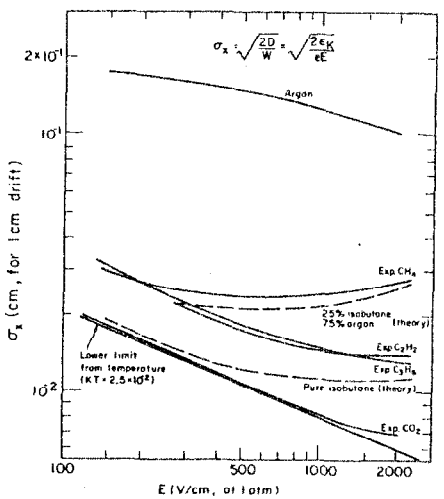

Figure 2. Computed and experimental dependence of the standard deviation of electron diffusion in an electric field for 1 cm drift, in several gases at normal conditions. Reference 2.

III. Diffusion in the presence of Electric and Magnetic Fields

Consider a magnetic field B, which is parallel to the drift electric field E ($E \times B = 0$). The magnetic field has no effect on the drift in the direction along E. However, since it interacts only with the component of velocity perpendicular to E ($E = qV \times B$) it does effect the diffusion in the plane perpendicular to E and B. This effect is easy to see physically.

The drifting electrons try to execute helical orbits around the magnetic field lines (cyclotron oscillations). Collisions in the gas cause these electrons to lose their sense of direction and so terminate a helical trajectory. If the mean time between collisions τ is long compared to the time of a helical revolution (the inverse cyclotron frequency)

$$\omega^{-1} = \left(\frac{eB}{m_e}\right)^{-1} ,$$

the helical trajectories are a significant effect on the drifting electrons. In this case, the electrons hug the lines of B which are parallel to E and so RMS diffusion in the plane perpendicular to the drift direction (and E and B) is reduced. The condition for a significant effect is

$$\omega\tau > 1 .$$

Specifically, the modification of the diffusion due to a magnetic field, B, which is parallel to the drift direction is

$$\sigma_\perp^2(B) = \frac{\sigma_\perp^2(B = 0)}{1 + \omega^2\tau^2} .$$

Thus for high magnetic fields (high ω) or gases and pressures that result in good electron mobility or long mean free paths (high τ), the effect of B on diffusion is large. For example, at STP for argon gas, a magnetic field of ~1T gives $\omega\tau \sim 10$.

Data taken by our group at LBL indicate the effects of a magnetic field ($E \times B = 0$) on transverse diffusion.[5] Figures 3a and 3b depict the RMS diffusion of single electrons as a function of E/p (volt/cm-torr) for various gas mixtures, with $\vec{B} = 0$ and $B = 20.4$ kG. The data were taken at a pressure of 600 Torr with a 15 cm drift distance. From Figure 3, a value of $\omega\tau$ and τ can be extracted as a function of E/p (V/cm-torr) for the various gas mixtures (see Figure 4).

We can summarize these data as follows:

- For $B = 0$, gas with smallest τ gives lowest diffusion (CO_2).
- For $B \neq 0$, gas with largest τ (when $\omega\tau > 1$) gives lowest diffusion (Ar).

When $E \times B \neq 0$, the situation is more complicated. Electrons drift along a trajectory between E and B depending on $\omega\tau$. At low magnetic fields ($\omega\tau << 1$) the electrons tend to follow the electric field. At high fields ($\omega\tau >> 1$) the electrons tend to follow the magnetic field. The locus of drift directions ($\tan\theta = \omega\tau$) is depicted in Figure 5. For $\omega\tau = 1$, the electrons follow a trajectory midway between the electric and magnetic field directions.

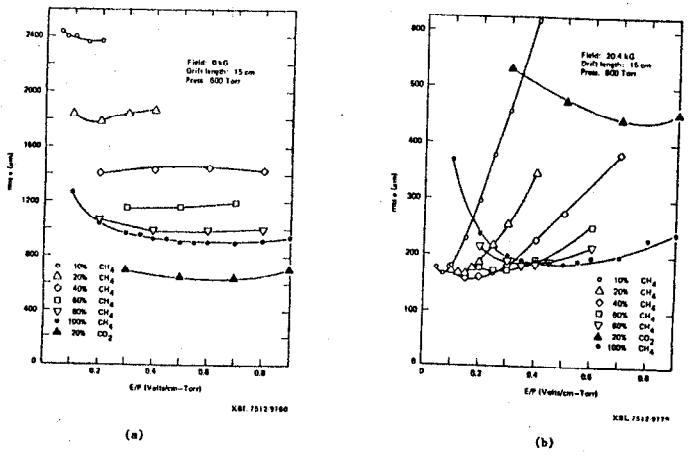

(a) (b)

Figure 3. Transverse diffusion (rms width) for a single electron after drifting 15 cm in various gases. (a) $B = 0$; (b) $B = 20.4$ kG. Note different vertical scales in a) and b). Reference 5.

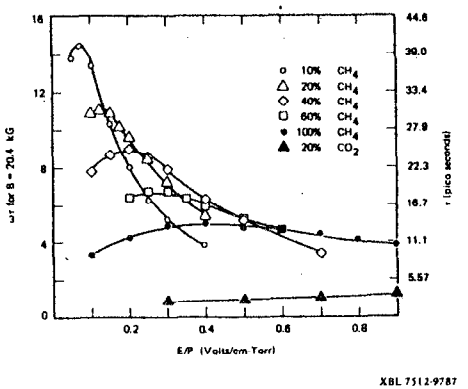

Figure 4. Values of τ, the mean collision time in picoseconds and $\omega\tau$ (dimension less), as extracted from the data of Figure 3. Reference 5.

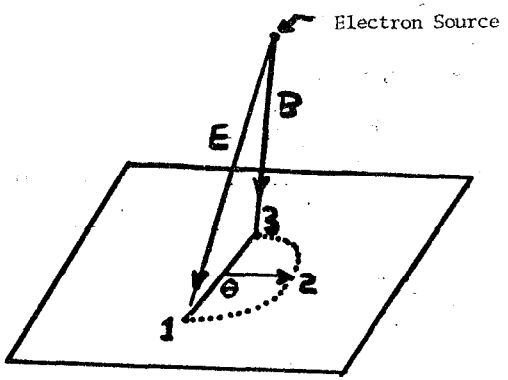

Figure 5. Locus of drift directions when $E \times B \neq 0$ as a function of $\omega\tau$. For point 1: $\omega\tau = 0$; for point 2: $\omega\tau = 1$; for point 3: $\omega\tau = \infty$.

From the discussion above, we see that diffusion of electrons in gases can be reduced by the use of elevated gas pressure, or by suitable magnetic fields with a significant component parallel to the drift electric field.

IV. Drift Velocity of Electrons in Gases

We write the drift velocity of electrons in gases as

$$W = \frac{e}{2m} E\tau$$

where E = electric field

τ = mean collision time

m = mass of electron.

For some gases, $\tau = \tau(E)$ so that $W(E)$ can be a quite complicated function of E. For drift fields of interest, the electron's wavelength can be approximately that of the size of electronic shells in the gas molecules. As a result, complex quantum-mechanical effects such as resonance scattering produce a complicated collision cross section (or τ) as a function of electron drift velocity (or drift field, E). For example, in Argon there is a minimum in the collision cross section σ, at an electron energy of ~0.4 eV (the Ramsauer minimum) as seen in Figure 6. This corresponds to the large value of τ observed at $E/p \sim 0.1$ V/cm/torr in the diffusion data of Figures 3 and 4. This cross section minimum has a large impact on the diffusion coefficient. Additions of small admixtures to argon can substantially change the average electron energy and thus greatly modify the drift velocity (as illustrated in Figure 7) as well as the diffusion coefficient.

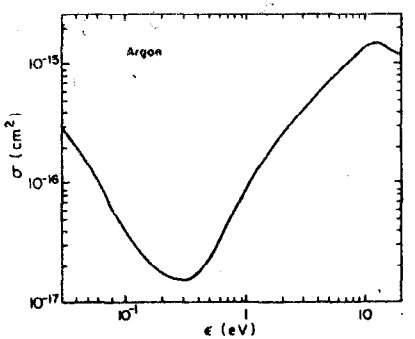

Figure 6. Ramsauer cross-section for electrons in argon as a function of their energy.

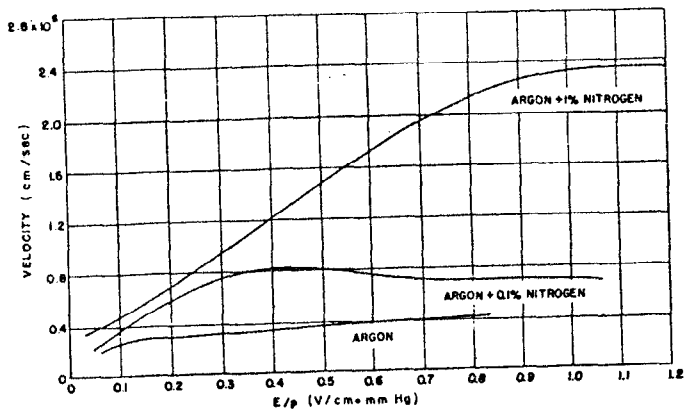

Figure 7. Drift velocity of electrons in pure argon, and in argon with small added quantities of nitrogen. The very large effect on the velocity for small additions is apparent. Reference 2.

Typical drift velocities are ~5 cm/μs for $E/p > 0.2$ (V/cm/torr) for argon with various admixtures. Specific examples are shown in Figure 8 of drift velocities in various gases. The Sauli article contains many more examples of drift velocity curves.

A rigorous theory of electron drift in gases can be found in the work of V. Palladino and B. Sadoulet,[6] and G. Schultz.[7] The major results of these semiclassical treatments are given by the following expressions.

The energy distribution for drifting electrons is

$$F(\varepsilon) = C\ \varepsilon \exp\left[-\int \frac{3\Lambda(\varepsilon)\varepsilon\, d\varepsilon}{(eE\lambda(\varepsilon))^2 + 3\varepsilon kT\Lambda(\varepsilon)}\right]$$

where the collision mean free path $\lambda(\varepsilon)$ is

$$\lambda(\varepsilon) = \frac{1}{N\sigma(\varepsilon)}$$

where N = # molecules per unit volume $= 2.69 \times 10^{19}\ \frac{P(\text{torr})}{760}\ \frac{273}{T(^{\circ}K)}$

$\sigma(\varepsilon)$ is the cross section from the Ramsauer curve of the gas being used.

$\Lambda(\varepsilon)$ is the fraction of energy lost on each impact (the inelasticity) to excite rotation and vibrational levels.

If the approporiate elastic and inelastic cross sections are known, $F(\varepsilon)$ and the drift velocity and diffusion coefficient can be calculated:

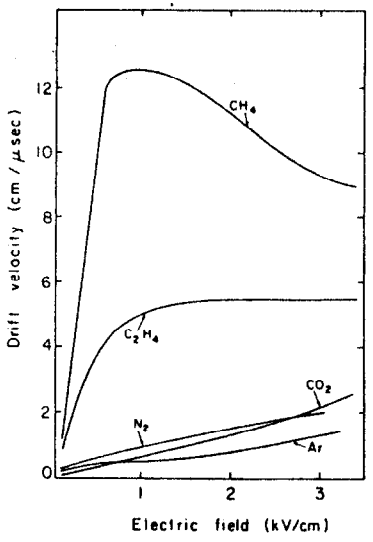

Figure 8. Drift velocity of electrons in several gases at normal conditions. Reference 2.

$$W(E) = -\frac{2}{3}\frac{eE}{m}\int \varepsilon\lambda(\varepsilon)\,\frac{\partial\left(F(\varepsilon)\sqrt{2\varepsilon/m}\right)}{\partial\varepsilon}\,d\varepsilon$$

$$D(E) = \int \frac{1}{3}\sqrt{2\frac{\varepsilon}{m}}\,\lambda(\varepsilon)\,F(\varepsilon)\,d\varepsilon\ .$$

For gas mixtures

$$\sigma(\varepsilon) = \sum_I p_I\,\sigma_I(\varepsilon) \qquad \sigma(\varepsilon)\Lambda(\varepsilon) = \sum_I p_I\,\sigma_I(\varepsilon)\Lambda_I(\varepsilon)$$

where p_I is the relative fraction of a mixture component I. A test of this theory for argon is shown in Figure 9 where, the quantity

$$\varepsilon_k = \frac{eED(E)}{W(E)}$$

is the characteristic energy of the electrons. The agreement between theory and experiment is quite satisfactory when one considers the semiclassical nature of the theoretical treatment.

V. Drift of Electrons in Electric and Magnetic Fields[3]

A magnetic field modifies the drift properties of electrons. The effect is a reduction of the drift velocity w and a drift direction different from that of the electric field (when $E \times B \neq 0$). Electrons will drift in constant fields on the average in a direction at an angle α_β to the field lines with a drift velocity $W_B < W$. When $E \perp B$,

$$\tan\alpha\beta = \omega\tau, \qquad W_B = \frac{W}{\sqrt{1+\omega^2\tau^2}}\ .$$

This model agrees with data as illustrated in Figures 10 and 11.

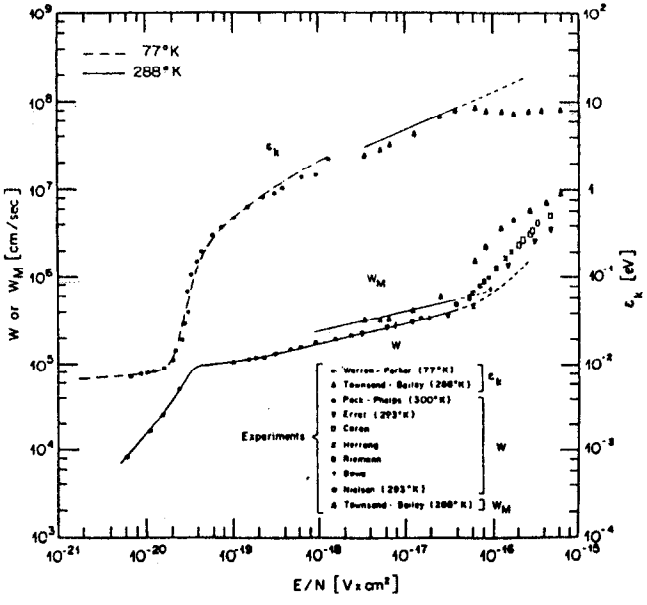

Figure 9. Comparison of measured and computed drift velocities and characteristic energy for argon. Reference 6.

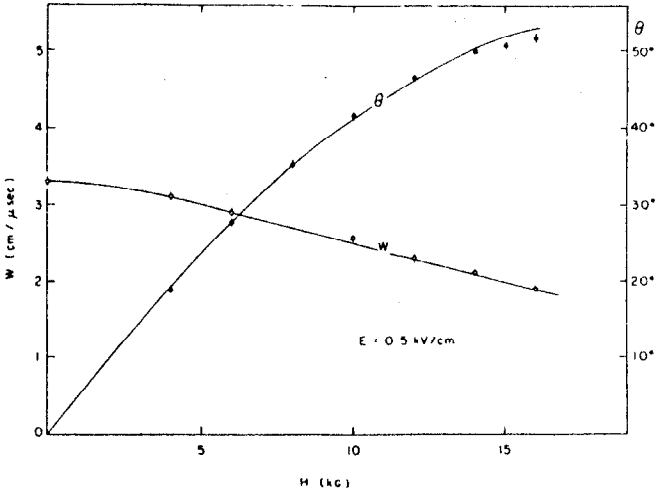

Figure 10. Measured dependence of electron drift velocity and drift angle from the magnetic field for a low value of electric field (500 V/cm), in argon-isobutane-methylal. Reference 2.

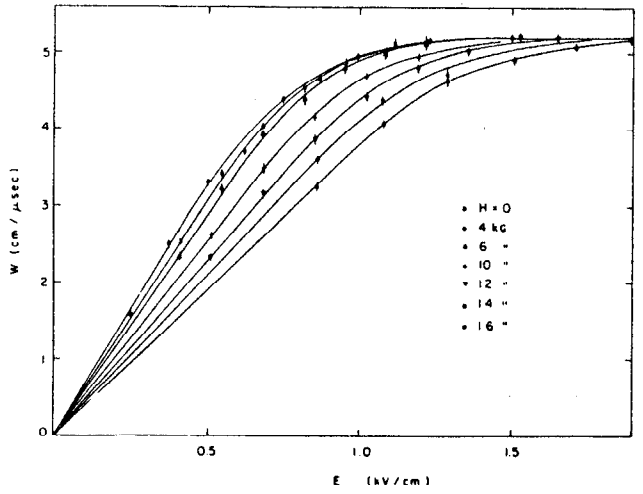

Figure 11. Measured drift velocity of electrons, in the direction of their motion, as a function of electric field for several values of the magnetic field (perpendicular to the plane of drift). Reference 2.

Based on the results given above we conclude that typical drift velocities are several cm/μs resulting in times of tens of μs for electrons to drift 1 meter in gas. The drift direction is modified by magnetic fields and drift velocities are correspondingly reduced.

VI. The Effect of Impurities on Drifting Electrons

When one considers drifting ionization electrons over large distances it is crucial to understand the possible absorption of these electrons by impurities in the gas. The attachment coefficients for several gases at $E = 0$ are given in the following table from refs. 12 18, 21 in Ref. 2.

Coefficient, number of collisions,
and average time for electron attachment
in several gases under normal conditions

Gas	h	N (sec^{-1})	t (sec)
CO_2	6.2×10^{-9}	2.2×10^{11}	0.71×10^{-3}
O_2	2.5×10^{-5}	2.1×10^{11}	1.9×10^{-7}
H_2O	2.5×10^{-5}	2.8×10^{11}	1.4×10^{-7}
Cℓ	4.8×10^{-4}	4.5×10^{11}	4.7×10^{-9}

The cross section for electron capture varies with electron energy (or drift field, E). Examples are given in Figure 12.

We can calculate the absorptive effect of pollutants in a gas on drifting electrons. Oxygen and water are among the biggest offenders in practice. If P is the fraction of pollutants, λ the electron mean free path, μ the electron's instantaneous velocity, then the number of collisions per unit time with pollutants is $\frac{\mu P}{\lambda}$ and the probability of attachment is $\frac{h\mu P}{\lambda W} = \frac{1}{\lambda_c}$ where λ_c is the mean free path for capture. In terms of variables previously defined

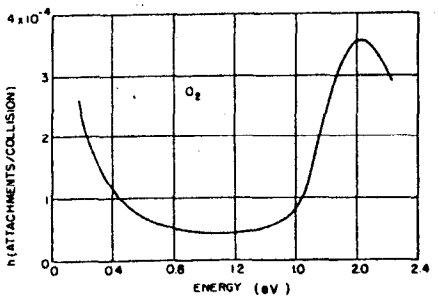

Attachment coefficient for electrons in oxygen, as a function of electron energy . Reference 2.

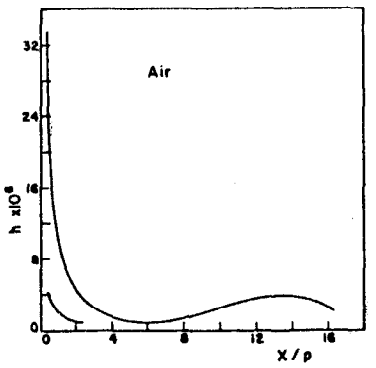

Attachment coefficient for electrons in air as a function of the reduced electric field. Reference 2.

Figure 12

$$\lambda_c = \sqrt{\frac{m}{2\varepsilon}} \frac{W}{Nhp\sigma(\varepsilon)} .$$

The loss of electrons in a swarm of n_o electrons drifting in constant fields across a distance x is:

$$n = n_o e^{-x/\lambda_c} .$$

For pure argon at STP for reasonable conditions $P\lambda_c = 2.5 \times 10^{-2}$ cm. Thus a 1% pollution of air will remove 33% of the electrons in 1 cm of drift. Using this input we conclude that if electrons are to drift one meter in gas at 1 atmosphere, a level of air pollution of a few parts per million results in a 1% absorption probability. It is fairly easy to keep pollutants below this level in typical clean systems with commercial gas purifiers. Of course, other pollutants can be more or less severe in their absorption of electrons, and in some cases (eg., CO_2) can catalyze absorption in the presence of other molecules. Still, we conclude that it is possible to drift ionization electrons over distances of ≈1 meter with minimal absorption of these electrons.

C. Long Drift Chambers - Several Examples

The following example is relevant to the forthcoming discussion of the Time Projection Chamber (TPC). Consider a drift chamber with a 1 meter drift distance with sense wires spaced at 4 mm running perpendicular to the drift direction. What kind of spatial resolution can be obtained with such a chamber as limited by diffusion? What gas purity is required to limit electron capture to 1%? What drift velocity is obtained? To operate such a chamber we consider the following conditions:

1. If there is no magnetic field present we want a filling gas with low mobility to minimize diffusion. If $B \neq 0$ (where B is the component of B parallel to the drift electric field), a gas with high mobility increases $\omega\tau$ and thus minimizes diffusion. High gas pressure

reduces diffusion (if $B = 0$) as $1/\sqrt{p}$, but when $B \neq 0$ it reduces τ and this adversely affects the ability of the magnetic field to reduce transverse diffusion. Thus, elevated pressure can increase transverse diffusion as $\frac{1}{\sqrt{p}} \frac{1}{\sqrt{1 + \omega^2\tau^2}} \simeq \sqrt{p}$ if $B \neq 0$ and $\omega\tau >> 1$ or reduce diffusion as $1/\sqrt{p}$, if $B = 0$.

2. The drifting swarms of electrons should be detected by a method which determines the center of gravity of each clump of electrons (~0.4 mm long) to take advantage of the $1/\sqrt{N}$ statistical factor compared to the RMS single electron diffusion. Here N is the number of electrons detected. If the first arriving electron determines the signal, this advantage is lost.

3. Pollutants must be kept at a sufficiently low level.

Consider the case (relevant for a later discussion of the Time Projection Chamber) where the filling gas is 80% Ar + 20% CH_4 at 10 atmospheres, E/p = 0.2 V/cm/torr and the chamber is bathed in a 2T field ($E \times B = 0$). In this case each 4 mm clump of ionization electrons left by the track contains ~160 electrons. The RMS diffusion for a single electron can be taken from the data presented[5] in Figure 3 by scaling the RMS diffusion by the square root of the drift distance and the pressure for a fixed E/p. Taking $\sigma_x = 150\ \mu m$ for 0.15 m drift of a single electron at 1 atmosphere we find

$$\sigma_x = 150\sqrt{10}\sqrt{\frac{100}{15}}\ \mu m = 1.23\ mm$$

for a single electron. The center of gravity of a 4 mm clump can be found to an accuracy of

$$\langle \sigma_x \rangle = \frac{1.23\ mm}{\sqrt{160}} = 97\ \mu m$$

if the readout method is sensitive to all electrons in the clump. The drift velocity is ~5 cm/μs resulting in a 20 μs drift time for 1 m. To keep electron attachment at <1% over a 1 m drift at 10 atmospheres requires the fraction of air to be $< 3 \times 10^{-7}$.

As a second example of a long drift imaging chamber we consider the ISIS detector[8] (Allison et al., Oxford, Rutherford Laboratory). ISIS is a 7 m long device located following a bubble chamber. The track imaging function in ISIS is performed by drifting ionization trails up to 2 m in 1 atmosphere of 95% Ar + 5% CO_2 to an array of sense wires located in the medium horizontal plane of the chamber. The chamber is depicted in Figures 13 and 14. Multitrack detection in ISIS is shown in the event reconstruction depicted in Figure 15.

Figure 16 indicates the distribution of neighboring track separation (as detected by ISIS) for a uniform beam illumination. When tracks are within 2 cm of one another, they mutually interfere and information is lost. The figure of a few centimeters for full track pair separation is a useful figure of merit for this generic type of detector.

Figure 17 depicts the loss (absorption) of ionization electrons as a function of drift distance in ISIS. About 8% are lost per meter of drift. I understand that more recent runs indicate a substantial improvement in this effect.

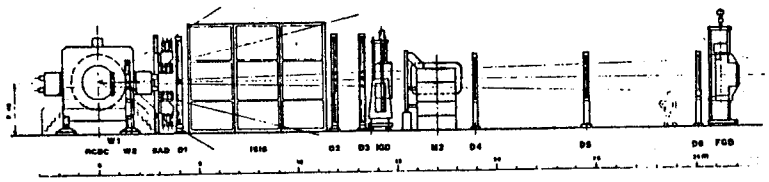

Figure 13. The beam layout of the European Hybrid Spectrometer (EHS) showing the position of ISIS in the first lever arm behind the target bubble chamber (Reference 8).

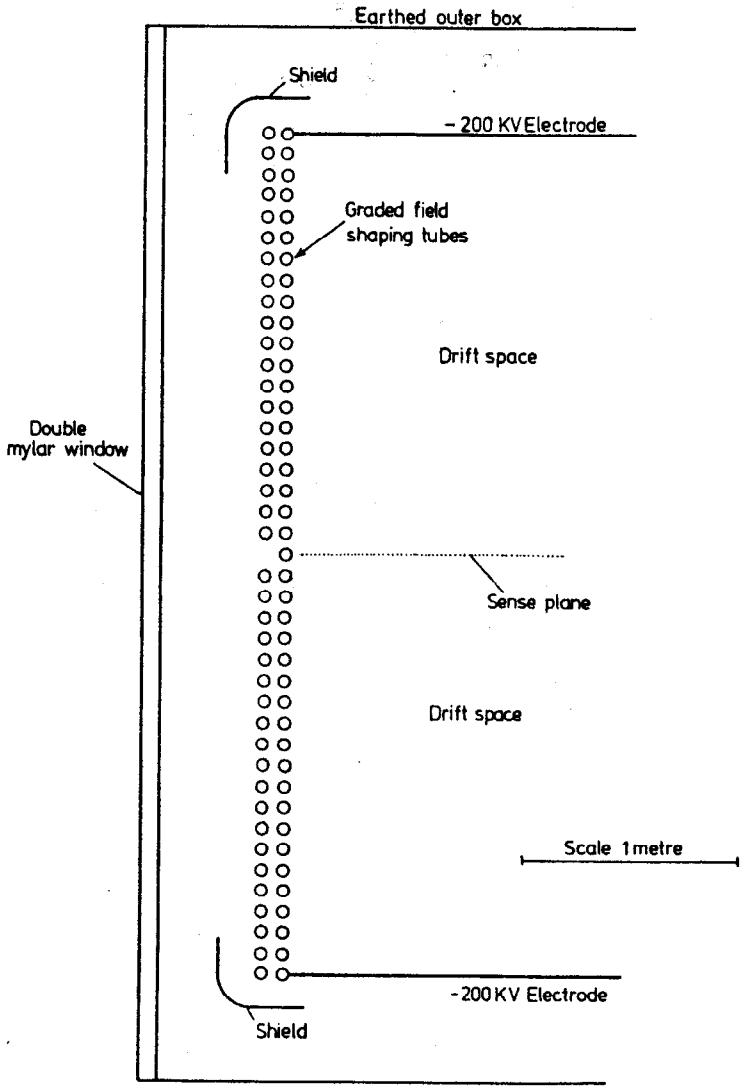

Figure 14. A vertical section through the front of the ISIS 2 chamber parallel to the beam direction. Reference 8.

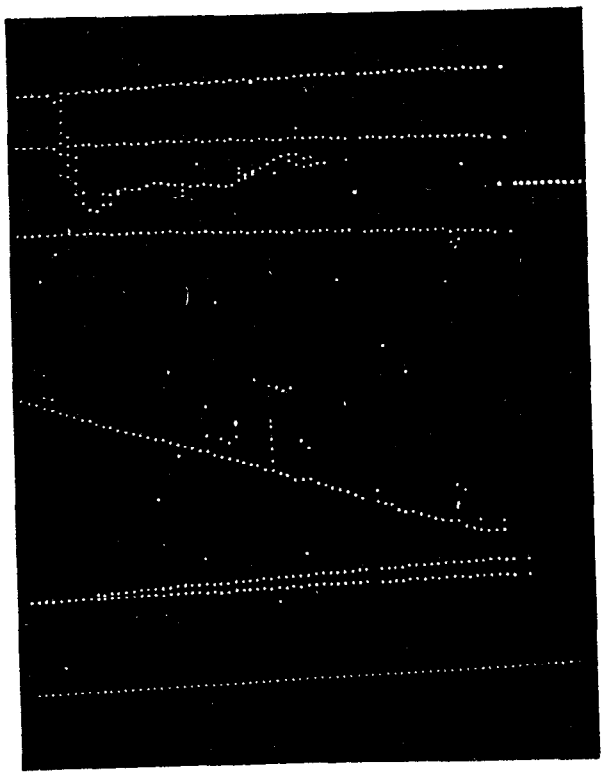

Figure 15. A typical display of data recorded in the ISIS test. The pulse arrival time is vertical and the wire number horizontal. The beam enters from the right. Reference 8.

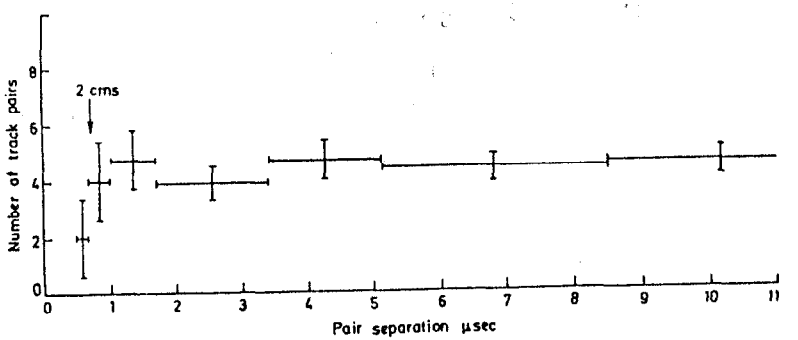

Figure 16. Distribution of the time between random pairs of parallel beam tracks in ISIS-2. Reference 8.

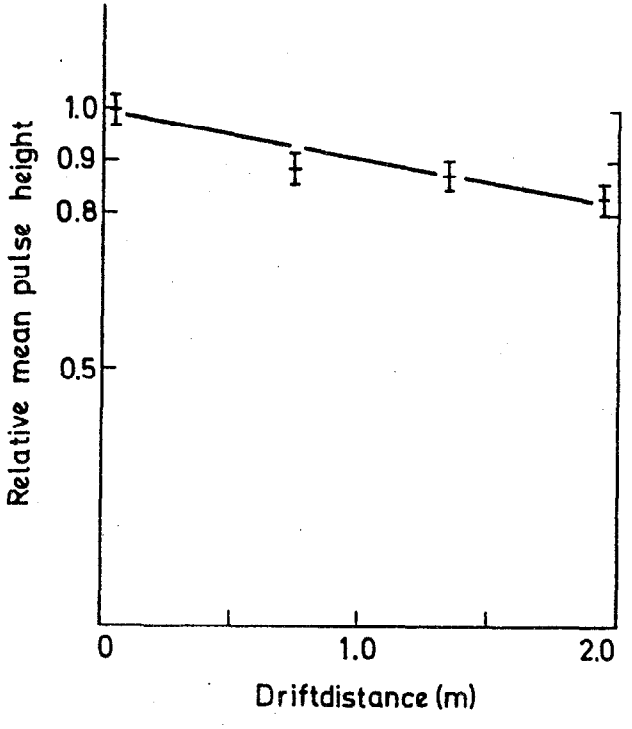

Figure 17. *Variation of observed pulse height with drift distance in ISIS-2. The line indicates a 17% loss over 2 meters. The drift voltage was 120 kV. Reference 8.*

D. Particle Identification by Energy Loss Measurements

A detailed theory of this technique is given in references 9 and 10. This method of particle identification consists of measuring, for each particle, the most probable energy loss (or some other estimator of energy loss) to sufficient accuracy to determine the velocity, β. Then, with knowledge of momentum

$$p = \frac{m\beta}{\sqrt{1 - \beta^2}}$$

one determines m, the mass. This method is useful for $\beta\gamma \leq 300$. For higher velocities the energy loss of all species of particles reaches the saturated value of the Fermi plateau (see below).

A particle traversing a gas is accompanied by a broad spectrum of virtual photons. These photons are detected by their interactions with atoms of the gas (excitation and ionization of atomic levels). The large bandwidth of these photons and the indirect method of observing them through counting ionization electrons leads to large Landau fluctuations in any single measurement. The energy loss fluctuations in a single absorber are large, and do not decrease below ~30% as the absorber thickness increases. As the absorber thickness increases, the probability of large energy losses (δ rays) which have large fluctuations increases in kind. This increasing probability of high energy δ ray production almost cancels the reduction of fluctuations due to the increase in the total number of atomic collisions with increasing absorber thickness. The major difficulty with this method of particle identification is that the difference in most probable energy loss for various species of particles is usually less than the Landau fluctuations observed in a single measurement of energy loss. As indicated in the Figure 18, the range of energy losses

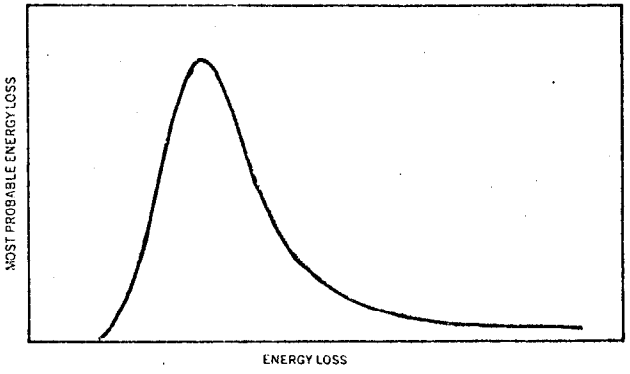

Figure 18. Probability distribution of the energy loss of 1.8 GeV/c pions in 4 cm-atm of 80% argon + 20% methane. The most probable energy loss is approximately 6.7 keV. The "Landau tail" of this distribution extends to 157 MeV. Reference 13.

in a sample of gas (here 4 cm-atm of 90% Ar + 10% CH_4) is large and has a long energy tail extending many orders of magnitude beyond the most probable energy loss.

Figure 19 depicts the slow decrease in the full width of the energy loss distribution as the sample thickness is increased. The typical situation when single energy loss measurements are made for each particle is shown in Figure 20 for 2 GeV/c electrons and 3 GeV/c protons. The difference in most probable energy loss is much smaller than the fluctuations in a single measurement of energy loss. From Figures 18 and 20 we see also that the long tail substantially increases these fluctuations. The "poor" resolution inherent in a single measurement is insufficient to identify particles, but a sufficiently accurate determination of the most probable energy loss by multiple measurements could tell protons from electrons in this case. Obviously, a large number of measurements is required to achieve the requisite accuracy.

Although at this Institute, Professor Ritson[9] has reviewed the theory behind the energy loss distribution, let me remind you of the underlying physical mechanisms responsible.

The distribution of energy loss has two pieces, a Gaussian peak and a long tail extending up to the kinematic limit for δ ray knockons. The peak results from a large number of atomic excitations. For thin gas samples this only involves outer electronic shells whose binding is much less than the most probable energy loss. (This is why Xenon gas is not much better than argon for energy loss measurements. They both have only two loosely bound electrons in their outer shell. The inner shells are bound with an energy comparable to the most probable energy loss.) Excitations come from impacts where the particle is far from the atom being excited. Close collisions result in energetic single ionization events which produce the long Landau tail which goes as $\sim 1/E^2_{particle}$.

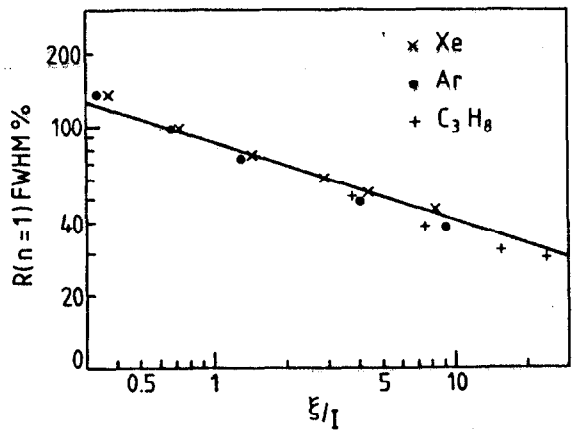

Figure 19. Experimental data on the width of the energy-loss distribution as a function of the scaled sample thickness ξ/I. Reference 11.

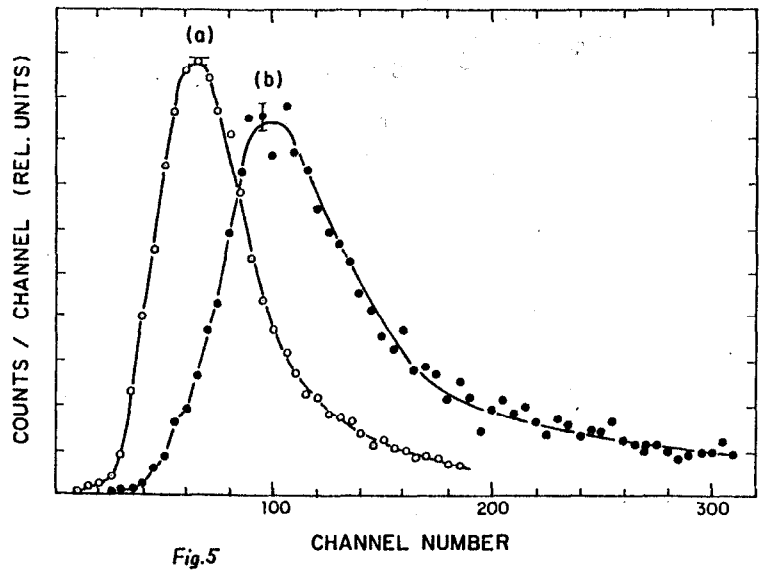

Figure 20. Measured pulse height distribution (energy loss) in 90% Ar + 10% CH_4 at 1 atm. (a) protons 3 GeV/c; (b) electrons 2 GeV/c. Reference 11.

The most probable energy has a dependence on velocity given by the following expression

$$E_{mp} = \frac{0.153 \frac{Z}{A} \rho t}{\beta^2} \left[\ell n \frac{m_e c^2 \, 0.153 \frac{Z}{A} \rho t}{I^2} + 0.891 + 2 \ell n \, \beta\gamma - \ell n \, \beta^2 - \beta^2 - \delta \right]$$

Figure 21 is a plot of E_{mp} as a function of $\beta\gamma$. The three regions of this curve are easy to understand qualitatively. The non-relativistic region has a $1/\beta^2$ dependence which reflects the fact that the slower the particle, the more time it spends near each atom and the higher the collision probability. The logarithmic rise comes from the relativistic expansion of the transverse electric field of the particle. As this field expands, the radial distance from the track at which atoms feel a sufficient momentum impulse from the field to be excited or ionized increases logarithmically. As the transverse field increases, however, the medium eventually becomes polarized and so the continued radial expansion of the high field impulse volume halts. The result is the saturation of the logarithmic rise at the Fermi plateau. Since the plateau is a result of the electric polarization of the medium, it is dependent on density in the expected way. In solids, the total relativistic rise is only a few percent. The dependence on pressure of the level of the Fermi plateau in 90% Ar + 10% CH_4 was measured by Walenta et al.[11] and is depicted in Figure 22.

If we plot the most probable energy loss (E_{mp}) vs momentum (= $m\beta\gamma$) rather than $\beta\gamma$, we get a family of curves, one for each species of particle. If we determine E_{mp} and the momentum to sufficient accuracy we can identify particles by this method as illustrated in Figure 23. Note the places where curves intersect one another. At these points the identity of particles as determined by this method has a two-fold ambiguity.

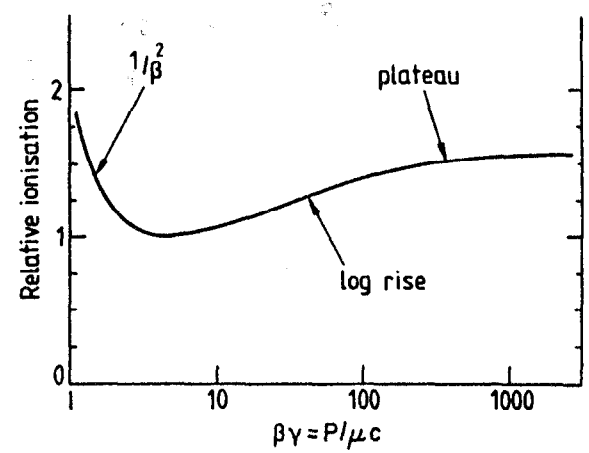

Figure 21. The typical dependence of ionization on $\beta\gamma$.

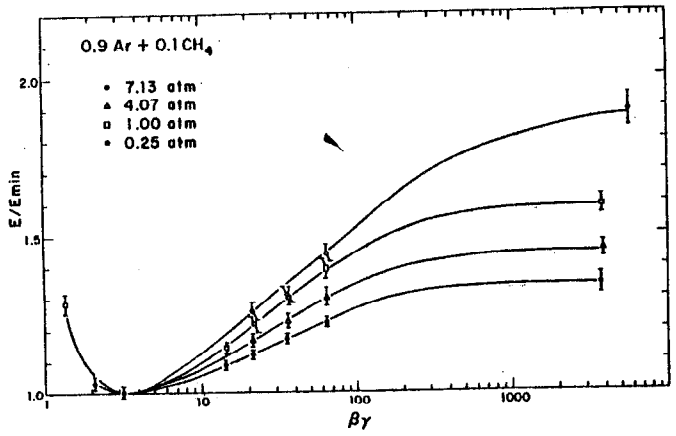

Figure 22. Measured energy loss normalized to the value for protons at 3 GeV/c as a function of pressure of 90% Ar + 10% CH_4. Reference 11.

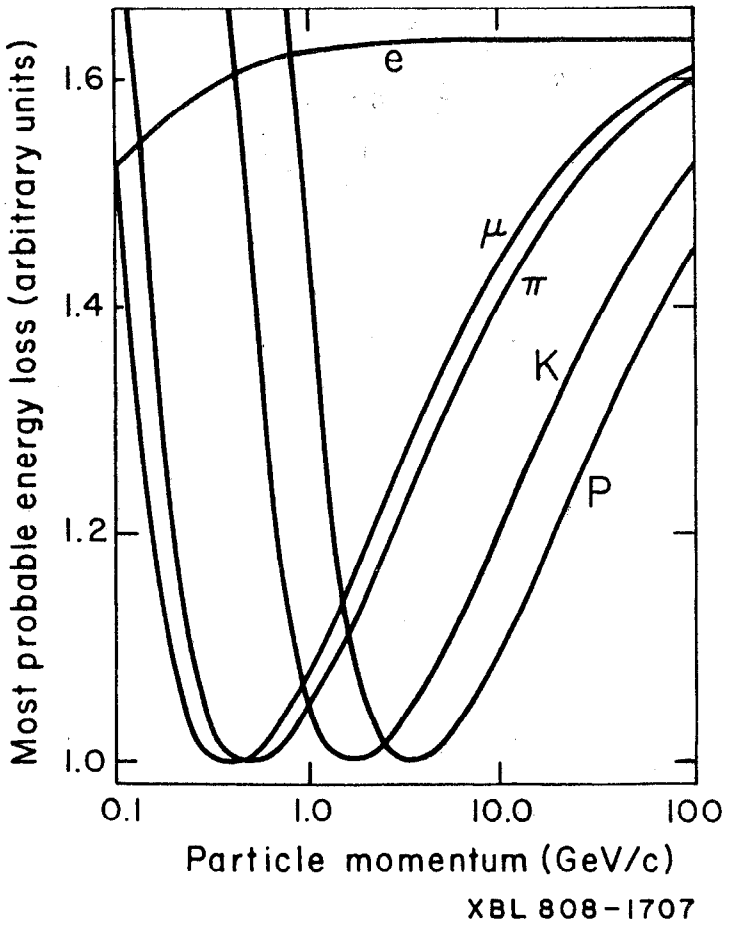

Figure 23. Most probable energy loss of various species of particles in 4 mm of Argon at STP. Note regions of two-fold ambiguity where curves intersect.

To identify particles in the relativistic region we must determine the energy loss to significantly better than 10%. The goal of the energy loss method of particle identification is to determine E_{mp} to a few percent in spite of the large fluctuations in single measurements. This is accomplished by measuring the ionization of a particle many times so as to sample the broad energy loss distribution often enough to determine the peak value to several percent. Many algorithms can be used to determine E_{mp} from the many samples. The simplest is to take the average of the samples in the Gaussian part by throwing away the samples with large pulse height. If, for example, we measure the energy loss 200 times in conditions where the width of the Guassian part is 60% FWHM and we take the mean of the 70% of the samples with the smallest pulse height (the remaining 30% are in the high energy tail), we expect a resolution on E_{mp} of

$$\delta_{E_{mp}} = \frac{60\%}{\sqrt{0.7 \times 200}} = 5\% \text{ FWHM}$$

The experimental problem in designing a system to identify particles by this method is to determine

- What gaseous medium to use
- How many measurements per particle are needed
- How thick each sample should be
- What pressure to use (to keep the detector of finite size and have sufficient relativistic rise).

Allison and Cobb have studied this in detail with Monte Carlo Methods.[10] Their results on the resolution in E_{mp} (FWHM) for pure argon are given in Figure 24 as a function of the number of samples and the total distance in gas traversed by a particle.

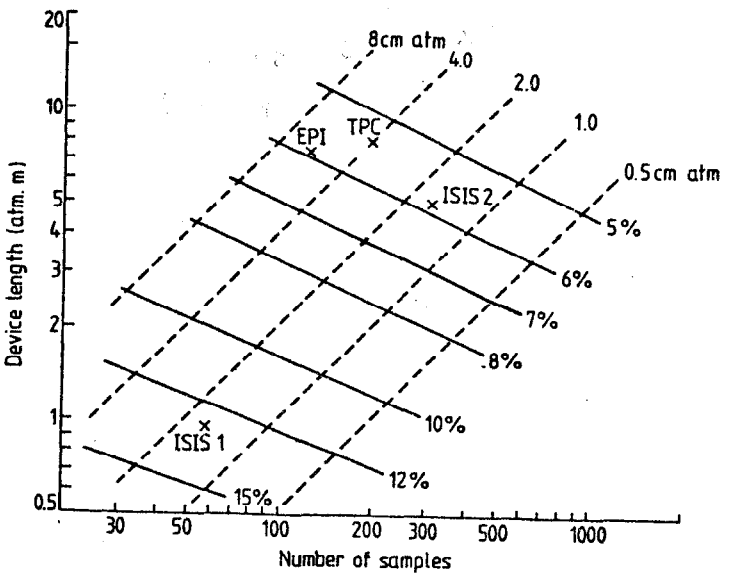

Figure 24. The ionization resolution (% FWHM) of a multisampling detector filled with pure argon calculated for $\beta\gamma = 100$. The dashed lines are loci of constant sample thickness. The devices EPI, ISIS1, ISIS2 and TPC are described in Table II of Reference 10. Figure is from Reference 10.

The expected resolutions (FWHM) of the various detectors employing this method of particle identification are also shown in the Figure 24. ISIS[8] (Allison et al.) has 256 samples each 1.5 cm thick; EPI[12] (Lehraus et al. at CERN) has 128 samples each 6 cm thick, TPC[1] (Nygren et al. at LBL) has 186 samples each 4mm thick at 10 atmospheres.

An interesting result of the Allison studies is a formula for the resolution of a pure argon system as a function of the number of samples and their thickness. The result for pure argon is:

$$\delta_{E_{mp}}\ (\text{FWHM}) \;=\; 96\%\ N^{-0.46}(xP)^{-0.32}$$

where N = # of samples, x = sample thickness in cm, P = pressure in atmospheres. To design a detector, however, you must still determine the particle separation (vs. P) and compare this to $\delta_{E_{mp}}$. This can be determined from the curves of E_{mp} vs. momentum for the gas, pressure and momentum range of interest. Walenta et al.[11] have followed this procedure (using their measurements) to extract the fractional separation of particles (π, K) at 3.5 GeV/c versus pressure for various gases using 56 samples of 2.3 cm. The results are shown in Figure 25. As can be seen from these data, a separation of several standard deviations can be obtained in the relativistic region.

To give an idea of how detectors based on these ideas are doing, Figures 26a,b,c,d are early results from ISIS-1[8] (60 samples), EPI[12] (128 samples), TPC[13] (prototype 192 samples) and the work of Va'Vra at SLAC for the HRS group (41 samples), respectively.

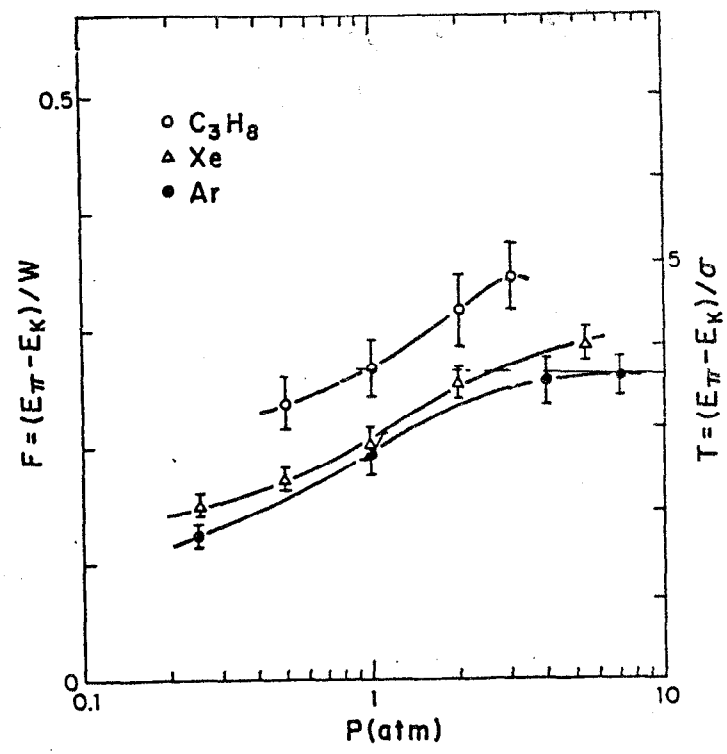

Figure 25. "Figure of merit" for particle separation at 3.5 GeV/c as a function of pressure (for 2.3 cm of gas; left scale). Particle separation for 56 samples of 2.3 cm expressed in standard deviations on the right scale. Reference 11.

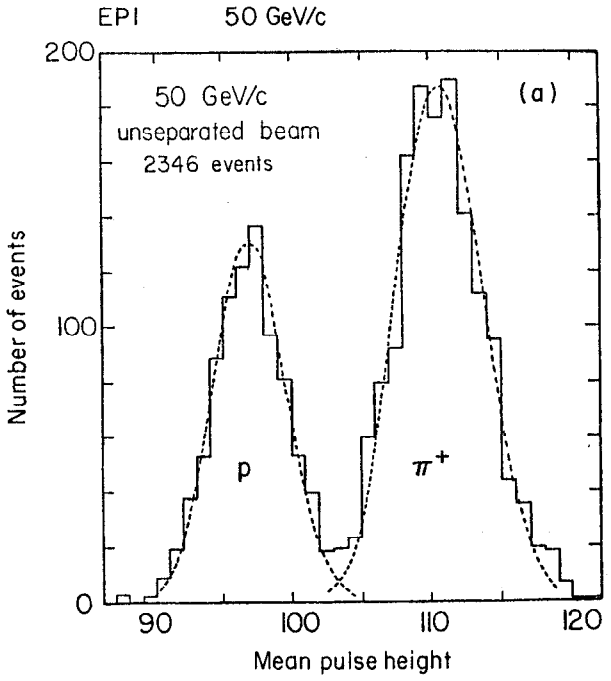

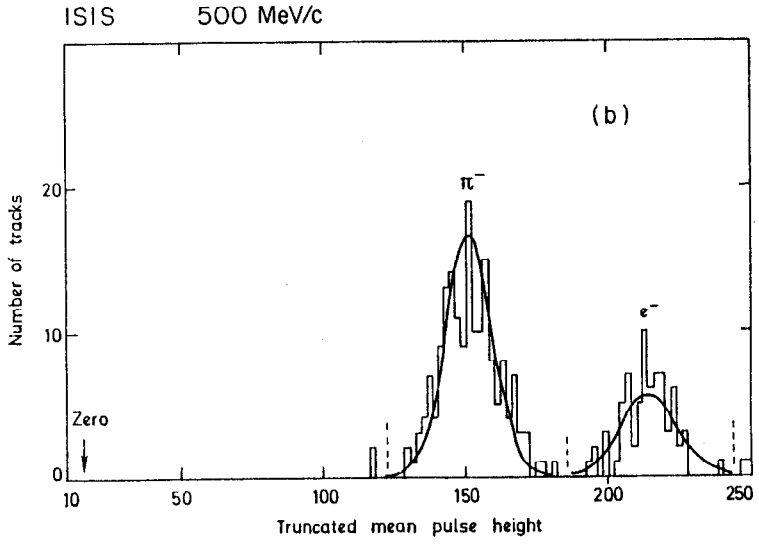

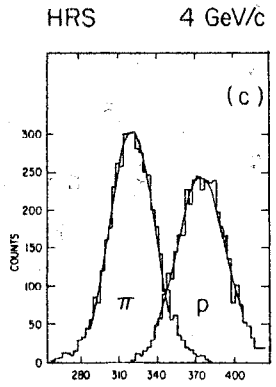

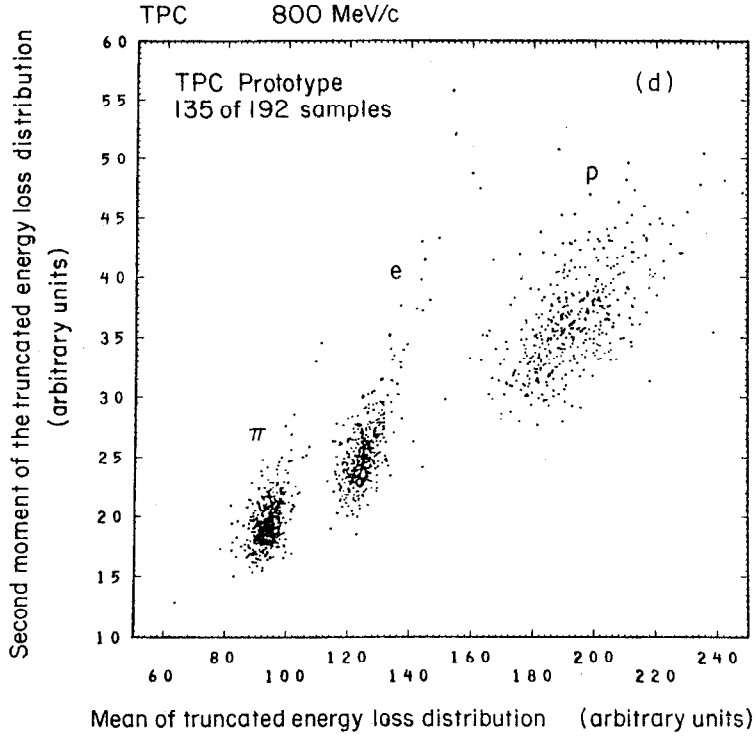

Figure 26. Particle separation in existing detectors or prototypes. (a) EPI, 128 × 6 cm samples, Reference 12; (b) ISIS 1, 60 × 1.6 cm samples, Reference 8; (c) HRS prototype, 41 × 1.6 cm samples, Reference 14; (d) TPC prototype, 192 × 4 mm (10 atmosphere) samples, Reference 13.

From these preliminary results we see that the identification of relativistic particles by multiple sampling of their energy loss is possible in large solid angle detectors. As a rule of thumb, upwards of 100 samples and 5 atmosphere-meters of total track length are needed to achieve useful results. In addition, there are regions of twofold ambiguity in momentum where pairs of species cannot be separated by these methods. The particle identification ability deteriorates within about 50 MeV/c of these ambiguous points.

In order to obtain the precise resolution needed, it is clear that careful control of gain variations in proportional wires and associated electronics as well as intermittent calibration of all components is needed in a large detector. We conclude that the method of particle identification by sampling energy loss can be made to give useful particle separation, but it is damned hard work.

E. Put It All Together - An Example: The Time Projection Chamber

These ideas on long drift imaging chambers and particle identification by energy loss sampling methods are being integrated into several detector systems (ISIS, CRISIS, various TPC's) now under construction or test. Let me briefly describe the most sophisticated example, the Time Projection Chamber being prepared for PEP by Nygren, Marx and coworkers at LBL. The Time Projection Chamber (TPC) is a large volume drift chamber which provides intrinsically three dimensional spatial data by using proportional wires and segmented cathodes to read out the two coordinates orthogonal to the drift direction, and timing information to determine positions along the drift direction.

The chamber is shown schematically in Figure 27. It is embedded in a 1.5 tesla solenoidal magnetic field, and is filled with a mixture of 80% argon and 20% methane at a pressure of 10 atmospheres. The applied voltage of 150 kilovolts over the 1 m drift distance is used to generate the drift electric field in each half of the chamber.

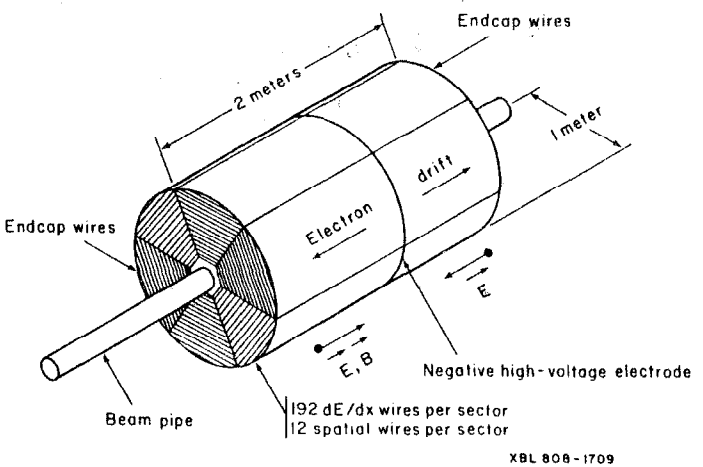

Figure 27. Schematic view of Time Projection Chamber for PEP (Reference 1). Details of endcaps (185 sense wires and 1185 cathode segments per sector) are not shown.

Charged particles originating in beam-beam collisions which take place at the center of the chamber traverse the chamber and ionize the gas along their trajectories. These ionization electrons drift parallel to the axis of the cylinder towards the 185 proportional sense wires in each endcap sector. The drift time of the electrons from the particle's trajectory to the sense wire is measured, and using the known drift velocity of the electrons (~5 cm/sec), one can calculate the axial coordinates of up to 185 points on the trajectory, each with a resolution of ~0.5 mm (rms).

This can be done for many densely clustered particle trajectories in the chamber because each sense wire is connected to an analog shift register (CCD, for charge-coupled device) which records the pulse height information versus time from each wire and cathode segment, taking as many as 455 samples over the total drift time. Thus it is possible with the TPC to topologically sort out all the tracks in a complex event, even with considerable beam induced background present.

The cathode plane under fifteen of the radially-spaced anode sense wires in each endcap sector of the TPC is locally segmented into a strip of square pads (8 mm × 8 mm) under the wire. The process of proportional amplification at the wire induces signals on the nearest cathode pads. The determination of the position of the center-of-gravity of the induced pulses on these cathode pads, which are at a known radial distance, thus gives the radial and azimuthal coordinates of 15 points on each trajectory with an accuracy along the anode wires of 150 microns (rms). The example of a long drift chamber used earlier in this lecture involves TPC operating conditions and indicates that diffusion limits the resolution below the 100 μm level. Since the solenoidal magnetic field bends the tracks in a plane parallel to the endcaps, these coordinates are used to calculate the momentum of the particles to an accuracy of better than $\frac{\Delta p}{p} = 0.5\%\ P$ (GeV/c).

The ionization electrons left along the path of a charged particle in the TPC are not only used to give trajectory information about the particle, but are also used to sample the energy loss of the particle in the gas. Since this energy loss depends on the particle's velocity, this measurement can be used with the momentum measurement to determine the particle's mass.

Each of the 185 proportional sense wires in each of the endcap sectors is used to sample the ionization electrons of each track that drifts onto them. The gas in the TPC is at a pressure of 10 atmospheres to insure that each sample has an adequate number of ionization electrons. With this method, the TPC achieves a resolution in most probable energy loss of better than 3% (rms) and can identify individual electrons, pions, kaons and protons over a momentum range from 100 MeV/c to greater than 15 GeV/c, even in complex multiparticle events.

F. Conclusion

We have shown how techniques for drifting ionization electrons in gas over distances up to several meters can be employed with particle identification methods based on multiple energy loss measurements to design and operate large solid angle detectors which make use of essentially all information contained in the ionization trails left by charged particles in gas. These systems have the capability of high resolution topological reconstruction as well as excellent identification of relativistic charged particles. Several large detectors based on these ideas are currently under construction or being tested in particle beams.

References

1. The Time Projection Chamber, D. Nygren and J. Marx, Physics Today 31, No. 40, October 1978.

2. Principles of Operation of Multiwire Proportional and Drift Chambers, F. Sauli, CERN 77-09, and references therein.

3. "Electrons in Gases J. Townsend, Hutchinson Press, 1947.

4. Lecture at 1980 SLAC Summer Institute, J. Jaros.

5. 1978 PEP Summer Study, D. Nygren et al., p. 126.

6. V. Palladina and B. Sadoulet, NIM 128, 323 (1975).

7. G. Schultz, CERN EP Internal Report 76-19 (1976).

8. W. Allison et al., Multiparticle Identification with ISIS: Tests with Full Aperture ISI-1, Oxford Report 104/78, 1978. Nuclear Physics Laboratory Oxford; Rutherford Laboratory.

9. Lecture at 1980 SLAC Summer Institute, D. Ritson.

10. W. Allison and J. Cobb, Relativistic Charged Particle Identification by Energy Loss, Oxford University, Nuclear Physics Lab. Report 13/30, 1980.

11. A. Walenta et al., Measurement of Ionization Loss in the Region of the Relativistic Rise, BNL Report 25179, 1979.

12. *Performance of a Large Scale Multilayer Ionization Detector*, I. Lehraus et al., CERN, Max-Planck Institute for Physics and Astrophysics, CERN Report CERN/EF/BEAM 77-3, 1977.

13. Performance of a Time Projection Chamber, D. Fancher et al., Nucl. Instr. and Meth. 161, p. 383 (1979).

14. J. Va'Vra, Private communication.

SAMPLING CALORIMETERS IN HIGH ENERGY PHYSICS

H.A. Gordon and S.D. Smith

Physics Department, Brookhaven National Laboratory

Upton, New York 11973

INTRODUCTION

At our current understanding of elementary particle physics, the fundamental constituents are the photon, quarks, gluons and leptons with a few highly forecasted heavy bosons. Calorimeters are essential for detecting all of these particles. Quarks and gluons fragment into many particles-- at high energies, so many particles that one may not want to measure each one separately. This group of both charged and neutral particles can only be measured by calorimeters. The energy of an electron needs to be measured by a calorimeter and muon identification is enhanced by the recognition of a minimum ionizing particle passing through the calorimeter.

There have been many excellent reviews of calorimeters-- in particular, one written last year by S. Iwata,[1] so we will not attempt a complete exposition here. We will limit our attention to sampling calorimeters-- those instruments in which part of the shower is sampled in an active medium sandwiched between absorbing layers. What follows is a very cursory overview of some fundamental aspects of sampling calorimeters. First, the properties of shower development will be described for both the electromagnetic and hadronic cases. Then, examples of various readout schemes will be discussed. Finally, some currently promising new ideas in calorimetry will be described.

Work supported by the Department of Energy under contract DE-AC02-76CH00016

PROPERTIES OF SHOWER DEVELOPMENT

1. Electromagnetic Showers. Sampling fluctuations are usually the largest contribution to the total energy resolution in an electromagnetic calorimeter, since usually a large fraction of the energy is deposited in the inert medium. The energy resolution may be expanded[2] as a power series in energy (E) as follows:

$$(\sigma/E)^2 = \sigma_o^2/E^2 + \sigma_s^2/E + \sigma_{sys}^2 + \text{higher order terms.} \qquad (1)$$

Each of the terms is generally identified with one dominant effect:

σ_o is just the pedestal width which is negligible for high energy showers but limits the minimum signal that may be measured;

σ_s is commonly called the sampling fluctuation term but may include other effects such as photon statistics and excess noise in amplifier gain;

σ_{sys} includes such things as calibration errors amongst the various elements; effects such as shower leakage and saturation contribute to the high order terms.

For calorimeters which use scintillators for sampling, we consider σ_s to be written as follows:

$$\sigma_s^2 = \alpha \, dE/dx \;\; \Delta x + \beta/(dN/dE) \qquad (2)$$

where $dE/dx\ \Delta x$ is the energy loss for a minimum ionizing particle through a single sampling layer in the calorimeter in GeV. α is a semi-empirical constant which depends on the type of shower. For electromagnetic showers it is $\sim$2.5, while for hadron showers the data suggest it is $\sim$10.

While this sampling term determines the resolution for the electromagnetic case, once the sampling goes below 0.02 GeV/sample, nuclear effects dominate the hadronic resolution. dN/dE is the photon light yield in photoelectrons (p.e.) per GeV. β is a constant that differs from 1 to account for the excess noise in the photoelectron amplification process. Excess noise refers to the fact that the pulse height response due to single photoelectrons has a finite width. For example, standard photomultipliers with first dynode gains $\sim$5 have β's $\sim$2.

The p.e. yield can be written as

$$dN/dE = N_o/A(dE/dx)\Delta x \qquad (3)$$

where N_o is the light yield per layer in p.e. per minimum ionizing, and A is an empirical constant equal to ratio between total signal seen from a muon traversing the calorimeter to that amount expected according to dE/dx loss calculations. The signal energy scale is determined from electron showers in that same calorimeter. This number depends on both the showering and sampling media. For example, this number is $\sim$1.3 for uranium and scintillator.

Combining (2) and (3) we obtain

$$\sigma_s^2 = (\alpha + \beta A/N_o)(dE/dx)\Delta x. \qquad (4)$$

Thus for N_o of $\gtrsim$ 1 p.e. per layer per minimum ionizing, photon statistics have a small effect on the energy resolution for the electromagnetic case and $N_o \gtrsim 0.25$ p.e. for the hadron case.

For electromagnetic showers the $(dE/dx)\Delta x$ term in equation (4) is also proportional to $\sqrt{t}$ where t is the number of radiation lengths per sample. This is demonstrated in Fig. 1 in data compiled by Stone et al.[3]

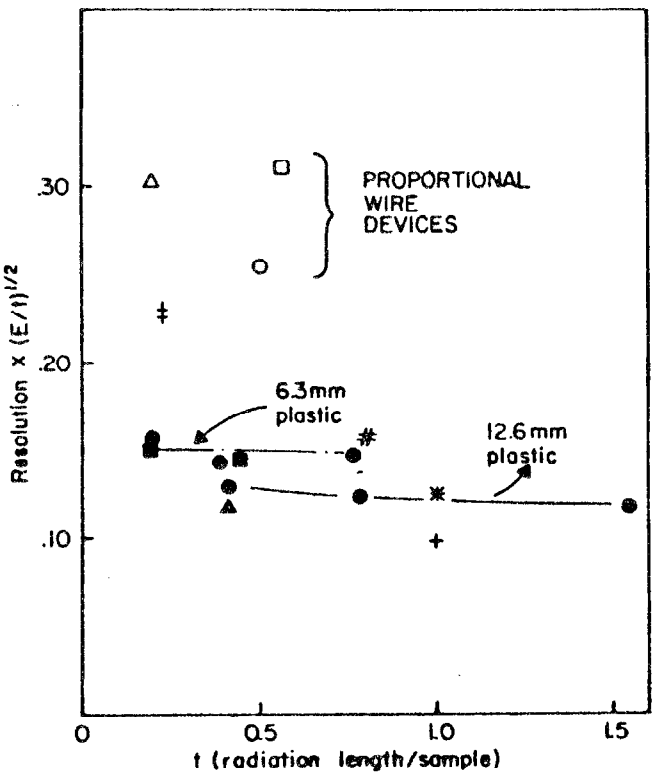

Fig. 1. Energy resolution versus number of radiation lengths per sample in electromagnetic calorimeters.

The lower horizontal group of data is for plastic scintillator and liquid argon sampling. A practical device using plastic scintillator and one radiation length sampling has $\sigma \sim 20\%/\sqrt{E(GeV)}$. Proportional wire devices have typically 50% worse resolution for the same sampling rate. This may be due to the Landau fluctuations of the individual electrons in the shower plus the fact that a wide angle electron can travel a longer distance in gas and, therefore, at times produce a larger signal than if the same electron had gone directly into the inert medium. We will have more to say about attempts to improve these two limitations in proportional wire devices later.

Next the longitudinal and transverse development is discussed. L. Cormell[4] has characterized the average electromagnetic shower shown in Fig. 2. $\nu = n/n_{max}$ is the normalized signal plotted against $\tau = t/t_{max}$, the normalized depth where n is the number of electrons, $n_{max} = 10\ E(GeV)^{0.9}$, t is the distance into the shower in radiation lengths and $t_{max} = 1.08\ \ln\ (E(GeV)/0.05)$. For example for a 10 GeV shower, the peak occurs at 5.7 radiation lengths and 99% of the shower is sampled by 17 radiation lengths. Lower energy showers are contained in a shorter depth. This can be seen in Fig. 3 where the energy resolution as a function of depth sampled is shown.[5] For 0.25 GeV showers, the resolution does not improve (in fact it deteriorates) beyond 12 radiation lengths, whereas for 4 GeV showers the resolution still improves out to 16 radiation lengths. Therefore, in designing an electromagnetic calorimeter, one of the considerations in optimizing the energy resolution is to have sufficient depth.

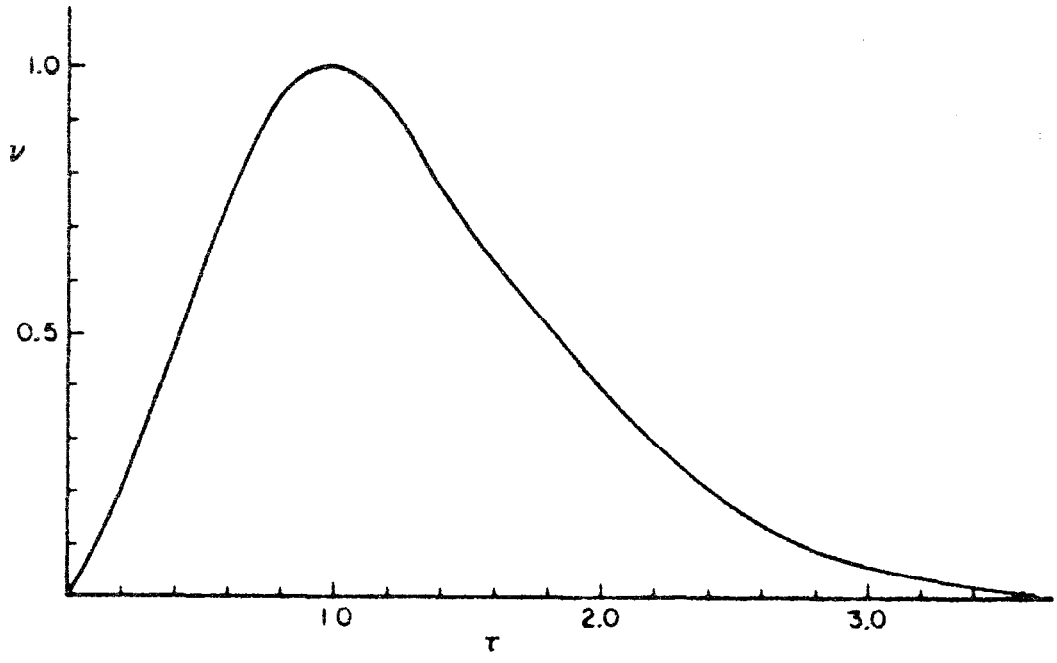

Fig. 2. Universal electromagnetic shower curve $\nu(\tau)$ vs. τ (see text).

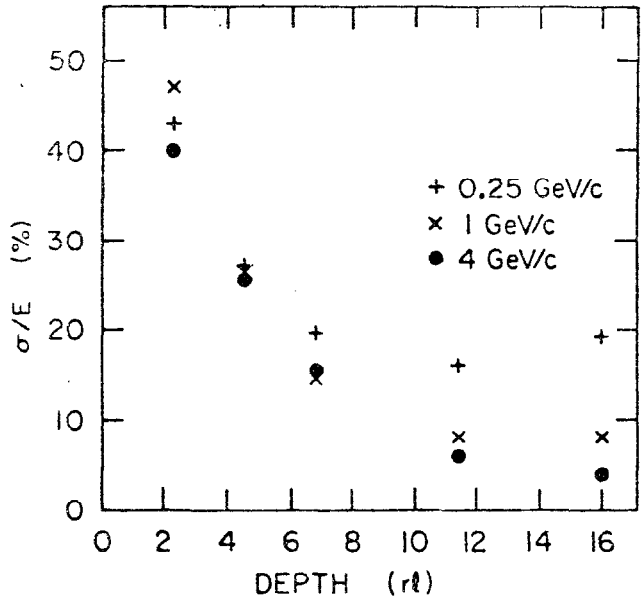

Fig. 3. Energy resolution of electromagnetic showers versus depth sampled.

By contrast, the position resolution is rather independent of energy[5] as seen in Fig. 4. Typically with ∿1 cm transverse strips, position resolution of ∿1-2 mm may be obtained. This becomes an important consideration when designing a device to separate π^o's from single γ's.

Often an electromagnetic calorimeter is called upon to help distinguish electrons from hadrons. Fig. 5 shows data from a study on how to get the best discrimination between π's and e's.[4] The rejection ratio is shown as a function of the energy of the π/e for various minimum energies detected in the calorimeter. The dashed curves show the results using the calorimeter as a whole. An improvement can be obtained by making use of the fact that electrons start depositing energy immediately in a shower whereas even hadrons that deposit a lot of energy through an interaction are more unlikely to do so in the very beginning of the devices. The solid curves indicate the rejection ratios when the additional requirement is imposed of demanding 10% of the total energy in the first 2.57 radiation lengths. To obtain higher e/π rejection, calorimeters must be supplemented by other devices such as Cerenkov counters, transition radiation detectors, or measurements of dE/dx.

2. Hadronic Showers. In contrast to electromagnetic showers where the energy resolution is dominated by sampling statistics, there are many additional complications in hadronic showers. The relative importance of the various processes in a hadron shower in an iron-liquid argon device[6] is shown in Fig. 6. The ionization is due to the energy detected from minimum ionizing particles in the shower. The electromagnetic component comes

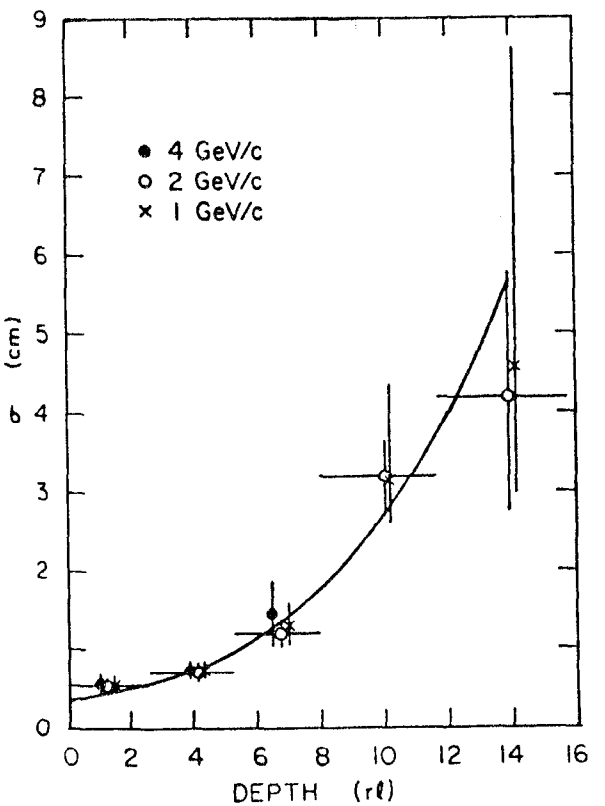

Fig. 4. Position resolution in electromagnetic showers for various energies and at various depths.

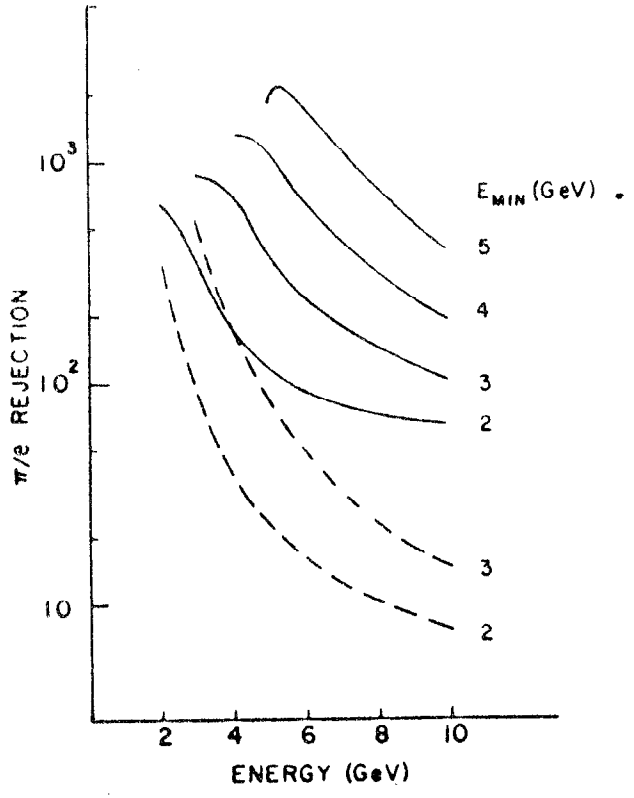

Fig. 5. Pion/electron rejection factors as a function of energy. Curves are given for several different values of the minimum energy required, E_{min}. Solid curves give the results with more than 10% of energy in first 2.6 radiation lengths. Dashed curves show the rejection factors with no ratio cuts.

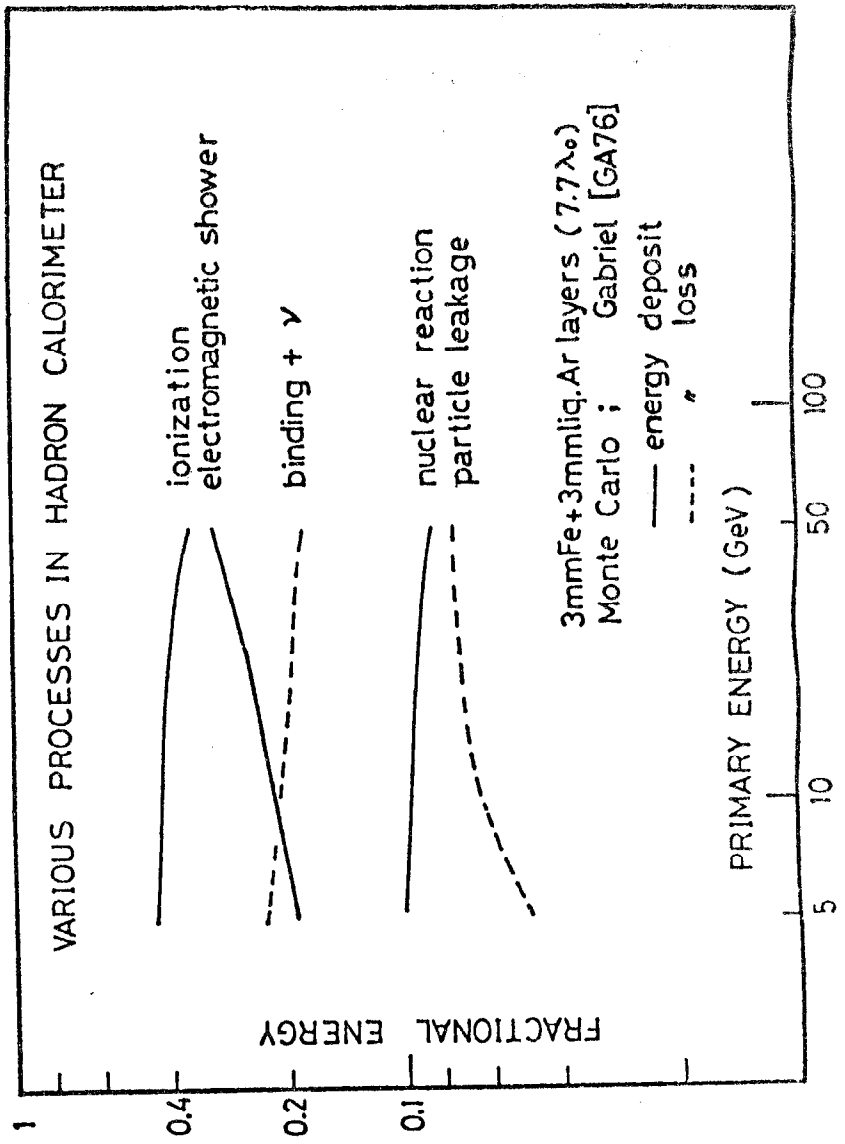

Fig. 6. Components of the hadron shower as a function of energy.

from the production of π^0's and is seen to increase in relative importance with energy. The nuclear reaction part arises from heavily ionizing fragments of the strong interactions of primary or secondary elementary particles in the shower. Liquid argon has a linear response even for these particles. Plastic scintillator saturates for such low energy particles, hence the use of plastic scintillator may lead to slightly worse energy resolution when compared to liquid argon. The dotted curves represent undetected energy in the shower due to binding energy, neutrinos and particle leakage through the boundaries of any finite calorimeter. It is this undetected energy which leads to the fact, shown in Fig. 7, that below $\sim$2 g/cm^2 per sample there is no improvement in the energy resolution.(1) In fact by selecting hadron showers that were primarily electromagnetic, Dishaw was able to show an improvement in the energy resolution.(7) Fig. 8 contains a plot of the energy resolution versus the second moment of the longitudinal energy distribution. Events with a high second moment have a large amount of energy deposited in a small region --large electromagnetic component. The energy resolution improves by $\sim$2 for less than 10% of the showers.

One way to improve the energy resolution of hadron calorimeters suggested by Willis is to use uranium instead of the much less expensive iron.(8) Within the shower some of the particles cause U^{238} to fission which creates photons in the energy region of $\sim$1 MeV which are detected. Therefore, instead of exciting a nucleus which leads to undetected energy, slow neutrons captured in uranium, and other losses previously called "binding energy losses," can lead to detected energy. The

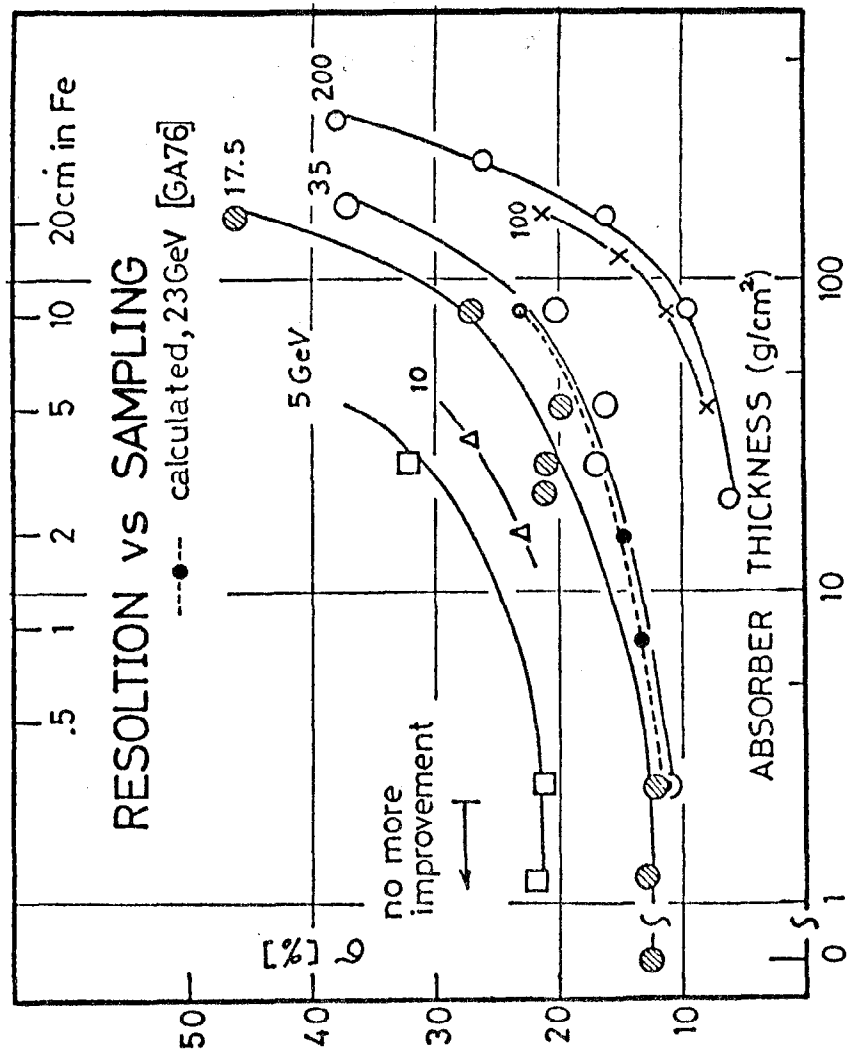

Fig. 7. Energy resolution of hadron showers for various energies as a function of the amount of material per sample in g/cm^2.

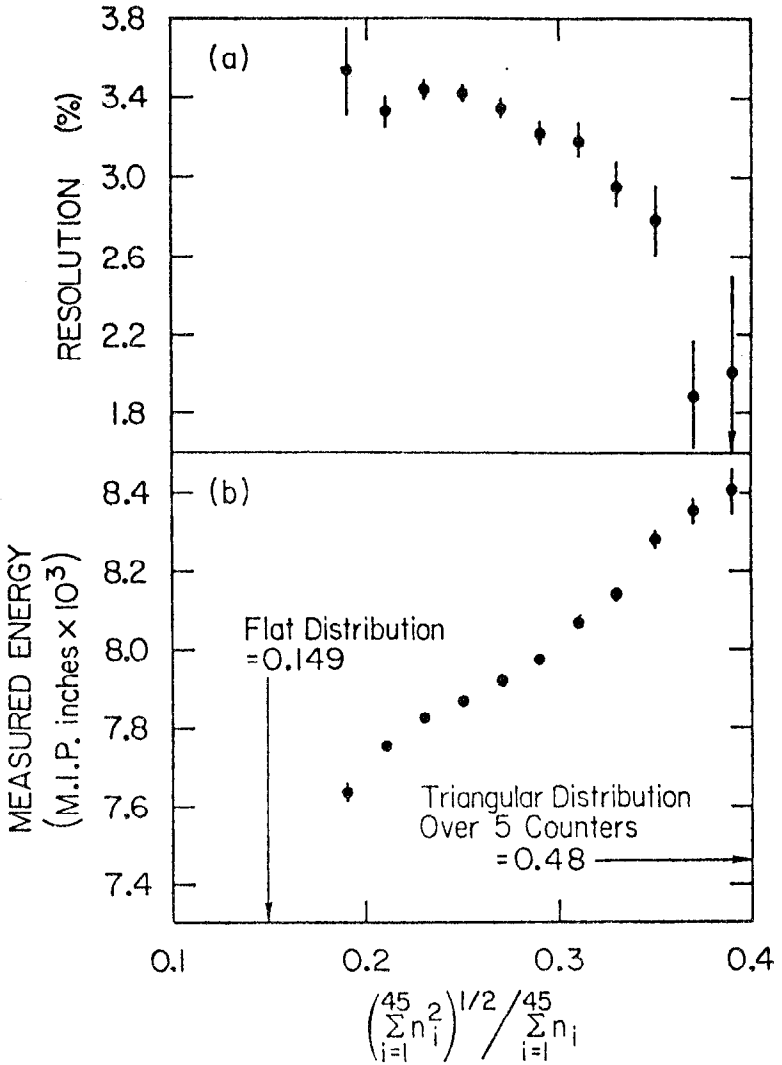

Fig. 8. Energy resolution for different values of the second moment of the longitudinal energy distribution

results of tests using liquid argon sampling are shown in Fig. 9. At 10 GeV, hadrons in iron give ∿70% of the signal obtained from 10 GeV electrons (or π^0's). Using uranium boosts the hadron response while improving the energy resolution by almost a factor of two.

The energy resolution versus the number of interaction lengths of the hadron calorimeter is shown in Fig. 10. At 10 GeV, there is no improvement in the resolution for calorimeters more than ∿5 interaction lengths.[8] However, in designing calorimeters for higher energy machines, selecting the depth of the calorimeter is most critical. Higher energy showers require more absorption lengths but the cost of making a certain size calorimeter deeper can escalate quickly in a storage ring application. Another ameliorating consideration is that most jets fragment into mainly low energy particles-- so if one is optimizing for jets the depth may not need to be as great as if all the energy of the jet were in a single particle. It would be unfortunate if the gain in energy resolution due to using uranium were cancelled by having too shallow a calorimeter.

The transverse size of hadron showers was measured by Sessoms et al.[9] and is shown in Fig. 11. Each of the histograms has a bin width of 2 cm and each plane is approximately one interaction length. Even though hadron showers are substantially wider than electromagnetic showers, there appears to be a narrow electromagnetic core to the average shower. Most hadron calorimeters have not been designed to have fine enough position resolution to be able to separate close hadronic showers. It is important to determine whether the study of the physics

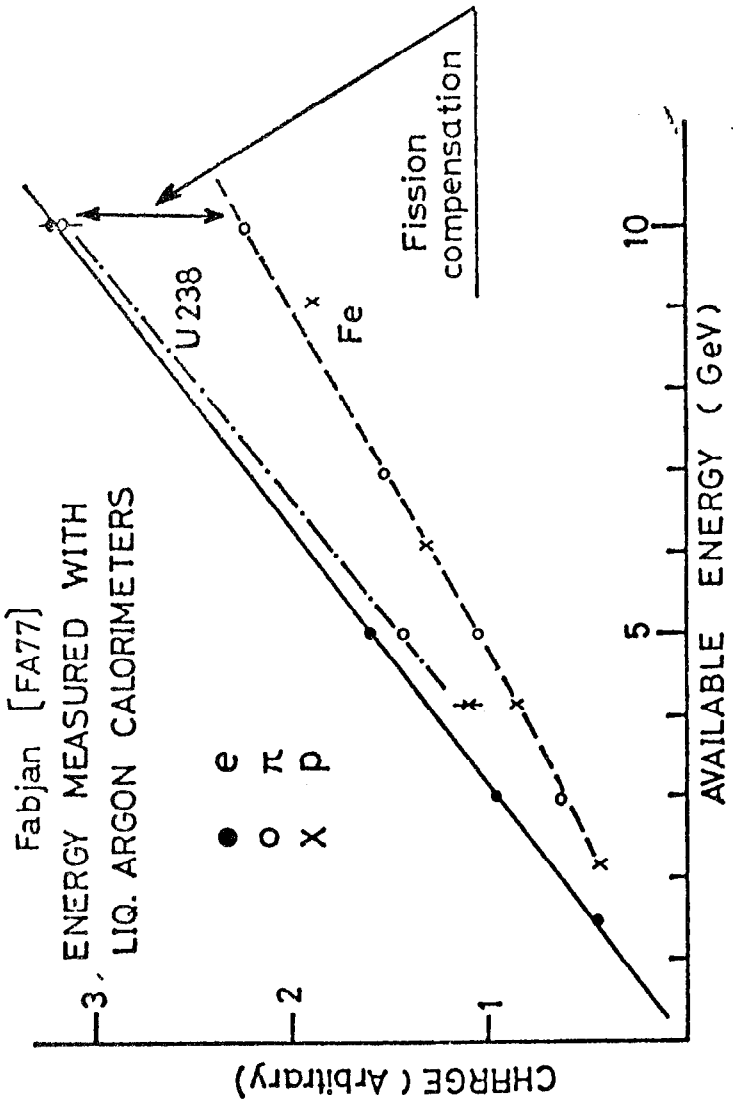

Fig. 9. Energy detected in an iron and uranium-liquid argon detector for pions, electrons and protons.

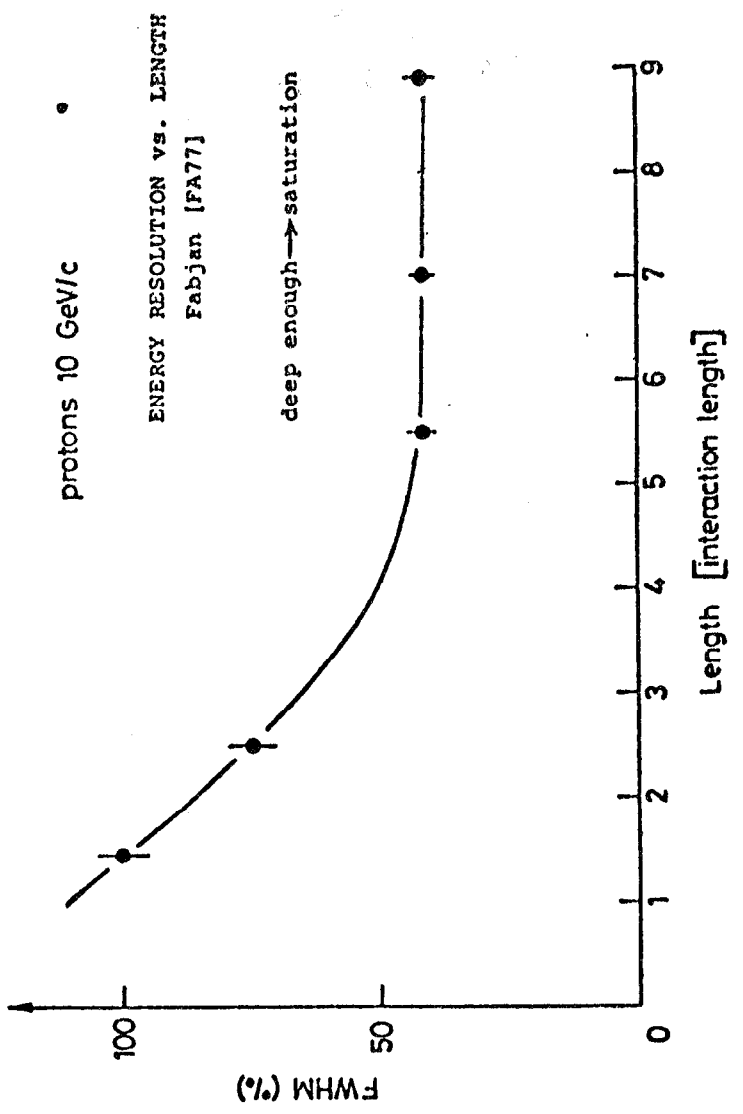

Fig. 10. Hadron energy resolution as a function of number of interaction lengths sampled in an iron-liquid argon calorimeter.

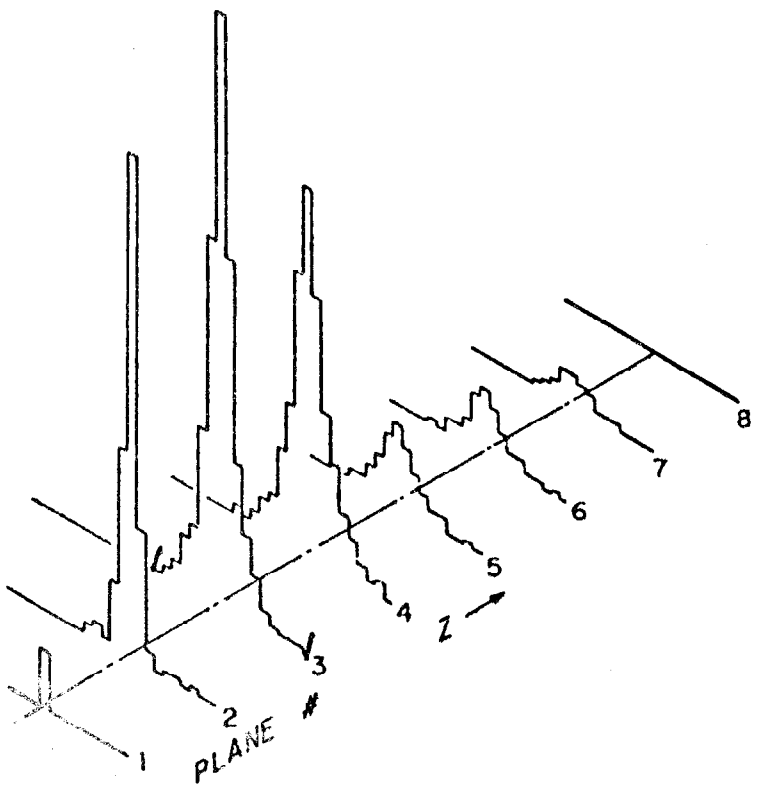

Fig. 11. Transverse size of a typical 20 GeV hadron shower sampled at various depths in an iron liquid argon calorimeter.

of jets is aided by having a calorimeter of optimum position resolution.

The use of a calorimeter as a muon identifier is explored by considering the data of Fig. 12.[10] Pions which do not interact, that is look like muons, fall off with the characteristic interaction length. Therefore, a typical calorimeter of several interaction lengths can do a fairly good job of rejecting π's. A muon passing through a calorimeter will give typically $\sim$1 GeV of apparent energy. Therefore, both momentum of the muon before entering the calorimeter as well as the position the muon has leaving the calorimeter must be measured in order to distinguish muons from the large number of low energy hadrons which would give a similar signal in the calorimeter.

Two practical considerations of the response of calorimeters in high rate environments is found in the data[7] of Fig. 13 from Fermilab. The dashed histogram shows the response of the calorimeter to a low beam rate at 400 GeV. The solid histogram was measured at a high rate (300 kHz) and suffered from pileup from previous events and rate dependent gain variations in the photomultiplier tubes.

TYPICAL CALORIMETERS

For many years sampling calorimeters using scintillator used light guides to couple each layer of scintillator directly to the phototube. A particularly elegant example is the photon detector built by California Institute of Technology and used for a series of experiments at Fermilab.[11] The photon detector, a lead-scintillator-sandwich hodoscope

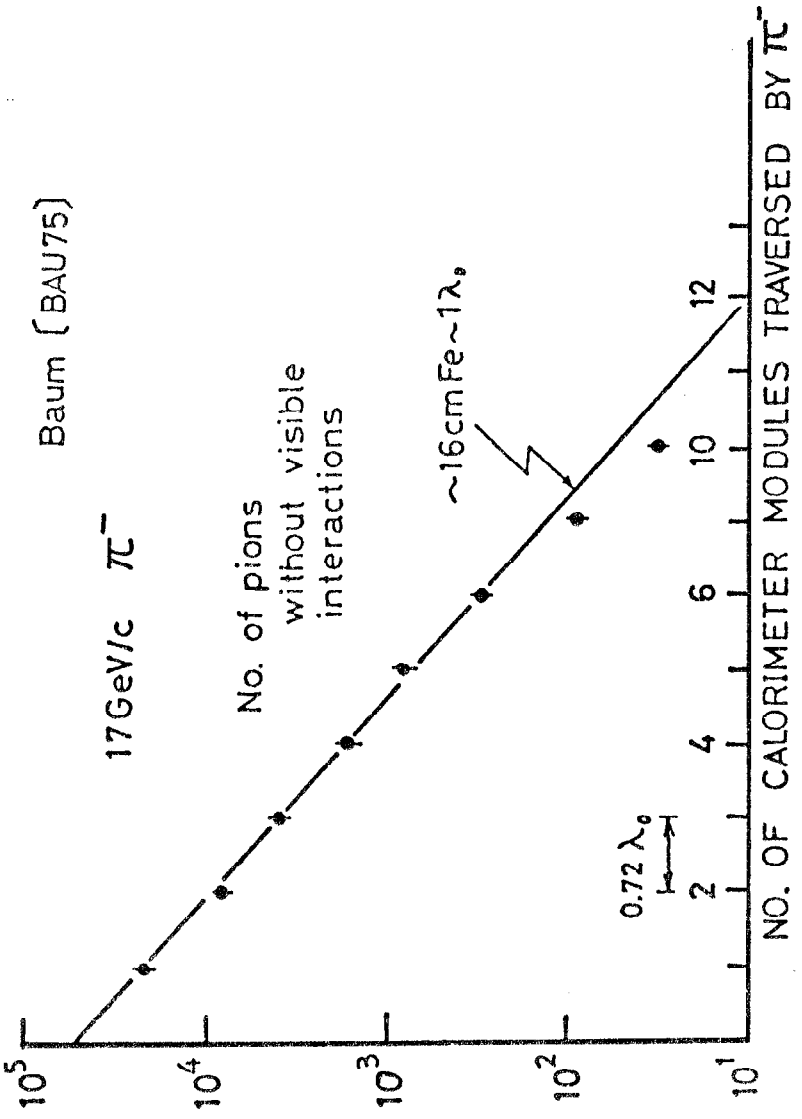

Fig. 12. Pions that do not interact as a function of depth in a hadron calorimeter.

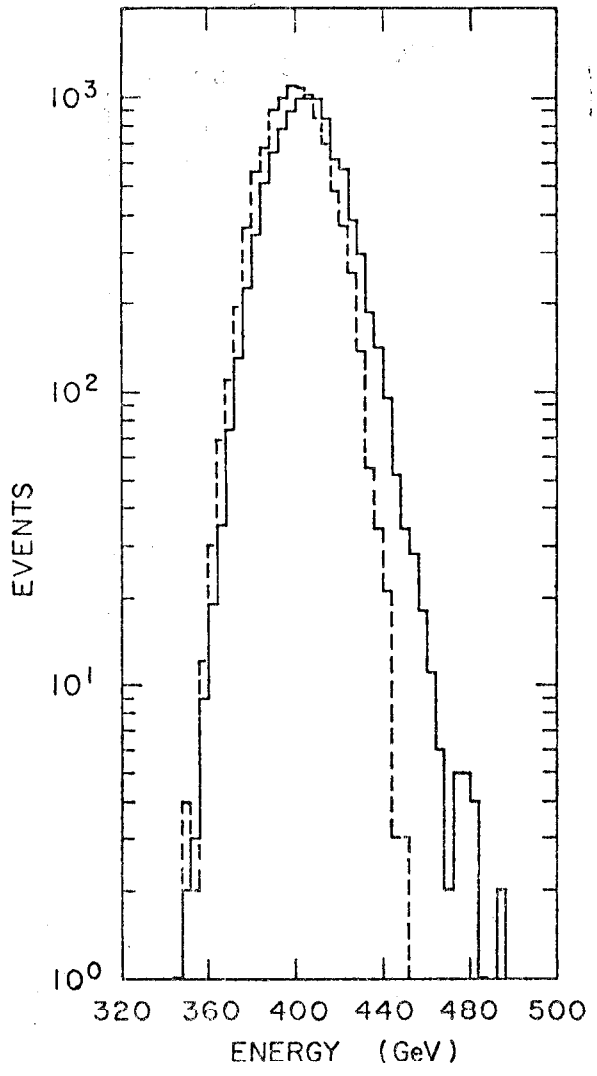

Fig. 13. High intensity measured energy before rate corrections (solid histogram) and low intensity measured energy (dashed histogram).

of 70 horizontal and 70 vertical counters, contains 19 radiation lengths of lead interleaved with long narrow (73.5 x 1.05 cm^2) scintillation rods. The horizontal and vertical rods sample alternate one radiation length lead sheets. Each counter optically joins 8 rods (either horizontal or vertical) to integrate the photon shower longitudinally. The device is homogeneous so the transverse position resolution of ∿2 mm does not depend on where the photon shower originates.

A rather new development is the use of acrylic sheets doped with BBQ to replace the intricate and space consuming light guides of the previous example. The modules of Fig. 14 will be employed in the ISR in the Axial Field Spectrometer.[12] The prototype uses 150 - 20 x 120 cm^2 sheets of acrylic scintillator interleaved with 150 uranium plates 2 mm thick. The BBQ sheets integrate the showers longitudinally. The modules have separate readout for the left and right side of each 20 x 20 cm^2 tower; and for the first 6 radiation lengths and the rest of the ∿4 absorption lengths. The energy resolution for single charged hadrons is $35\%/\sqrt{E}$ with a position resolution (left to right) of ∿2 cm.

An example of using gas as a sampling medium is shown schematically in Fig. 15 in the design of modules for the MAC detector at PEP.[13] D. Ritson discusses the physical principles of using proportional wire chambers in these lectures. Although the energy and position resolution of this device is ∿50% worse than a scintillator-sampled detector, the proportional wire calorimeter has the advantage of much lower cost and greater ease of construction.

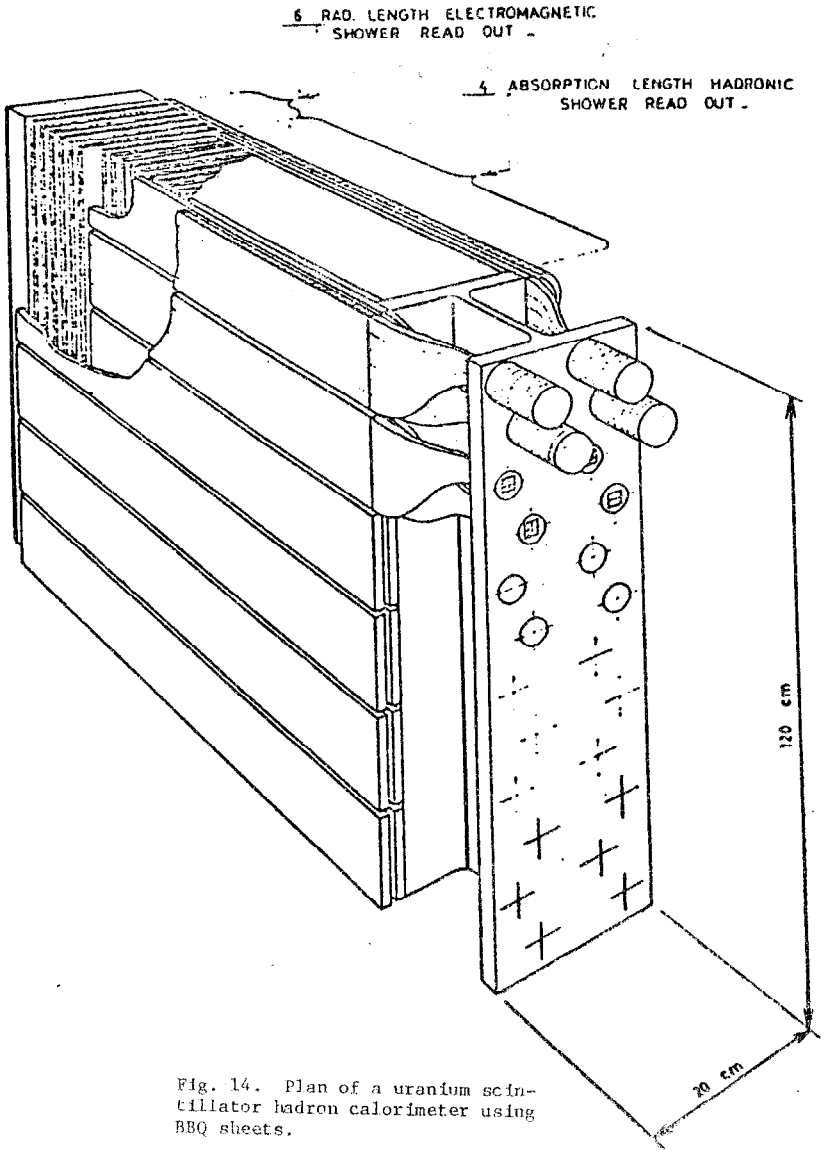

Fig. 14. Plan of a uranium scintillator hadron calorimeter using BBQ sheets.

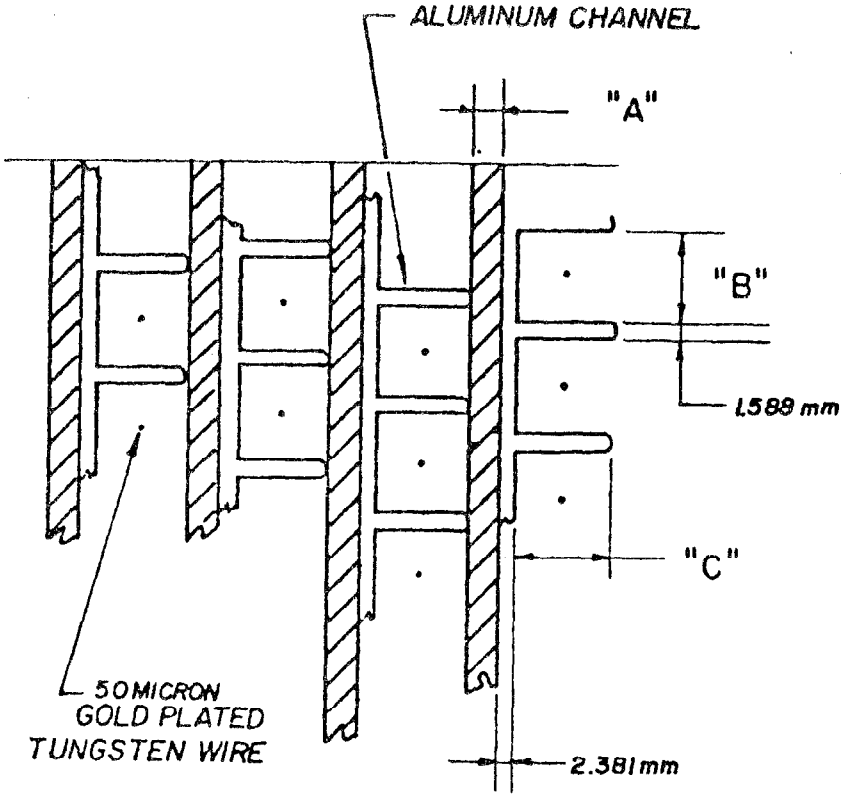

Fig. 15. Cross section showing internal detail of the modules. For the shower chamber, dimension "A" = 2.8 mm of typemetal (83% Pb, 12% Sb, 5% Sn), and "B" = "C" = 9.5 mm. For hadron calorimeter, "A" = 2.7 cm of steel, "B" = 1.75 cm, and "C" = 1.27 cm.

PROMISING NEW IDEAS IN CALORIMETRY[2]

For the last year we have been trying to develop some new ideas in calorimetry for implementation at ISABELLE. Because the time to start construction of a detector is still a little bit off, we have been able to explore several ideas that seem promising, if somewhat speculative. Our goal is a finely segmented electromagnetic and hadronic calorimeter with excellent energy resolution that will operate in a magnetic field of $\gtrsim$ 0.5 Tesla. The next section will discuss the use of scintillators for sampling. The final section presents some new possibilities for gas sampling.

Apart from energy resolution there are a number of other considerations of particular importance to us in designing a calorimeter. They are segmentation and/or position resolution, operation in a magnetic field, cost and high rate capability. In particular, the problem of operating in a field of $\gtrsim$ 0.5 Tesla has led us to consider: 1) using solid state devices or micro-channel plate photomultipliers to measure the light in the field, or 2) using flexible light guides to ship the light to phototubes at a safe distance.

Solid state devices such as avalanche photodiodes (APD)[14] or PIN diodes have high quantum efficiency $\sim$0.8 and are relatively insensitive to magnetic fields. On the negative side these devices have low gain, small size and high cost. APD's which can operate at gains $\gtrsim$ 100 are limited to less than 3 mm diameter and have excess noise factors (β) considerably larger than photomultipliers. PIN's are cheaper and can have larger sensitive areas but are limited to unity gain. The energy

resolution expected from these devices is limited by the noise of the detector and its amplifier, and by their small size. Since the gain is small, one is dealing with small amounts of charge for each photoelectron. Thus, one requires a large number of photoelectrons to make the signal to be well separated from the pedestal σ_o. The electronic noise of the σ_o term in equation (1) contributes at a level which is largely determined by the device capacitance which is in turn proportional to the sensitive area. This minimization of photosensitive area runs counter to the need for high light yield mentioned above. Strand has shown that by cooling a 1 mm (3 mm) APD to -10^oC the intrinsic noise of APD at a gain of $\sim$100 is $\sim$3(7) photoelectrons rms. R. Boie[15] suggests that an equivalent area PIN diode with a GaAs FET low noise amplifier with 100 nsec shaping time could be within a factor of 10 of this noise. To insure that a signal of 100 MeV is observable above noise in these devices requires σ_o to be $\sim$30 MeV. This implies a light yield then 330 photoelectrons per GeV for APD. Such light yields are not unreasonable for scintillator calorimeters, but are made difficult to obtain by the intrinsically small photo-sensitive area of these devices. For example, to match 1 cm strip scintillator elements and the 3 mm diameter APD, the BBQ rod would need to be 0.7 mm thick. To get efficient wave shifting in such thickness will require very high BBQ doping ($\sim$ 250 mg/ℓ). The result is a wave shifter bar with very short attenuation length of its own light. An additional concern in the use of silicon detectors is their extreme sensitivity to charged particles. A single minimum ionizing particle traversing 100 μm of silicon will produce $\sim 10^4$ carriers.

Another approach to map a large area detector to a small photosensitive device that we have considered[16] is shown in Figure 16. Here light from a scintillator without a secondary wave shifter is captured first in a POPOP doped rod in the same plane as the scintillator. Then the shower is integrated longitudinally by a BBQ doped rod running perpendicularly to the scintillator planes. The uniformity of this may be expected to be better than a design using only BBQ rods piercing the scintillator. The main problem here is to obtain enough light for reasonable scintillator thickness so that photon statistics make negligible contribution to calorimeter resolution. We have measured the feasibility of this method as shown in Figure 17. The requirement of 0.25 p.e./layer/minimum ionizing particle can be met with 3 mm of NE111. Two features of this design are notable: the POPOP rods capture light from a large solid angle and the narrowness of the scintillator strips makes the very short wavelengths accessible to the POPOP rod, thus increasing the light yield.

Another aspect of Figure 16 is the use of flexible light guides to bring the signals out of the strong magnetic field to normal phototubes. Since there has been such a revolution in the communications industry, naively one may think it would be easy to find a fiber optics array in this application. However, in the communications field one uses small aperture lasers to launch light so the photon budget is rather plush and whereas in a practical calorimeter the necessary aperture is at least 6-20 mm^2. Table I gives the details of the attempts we have made to come up with a viable flexible light guide.

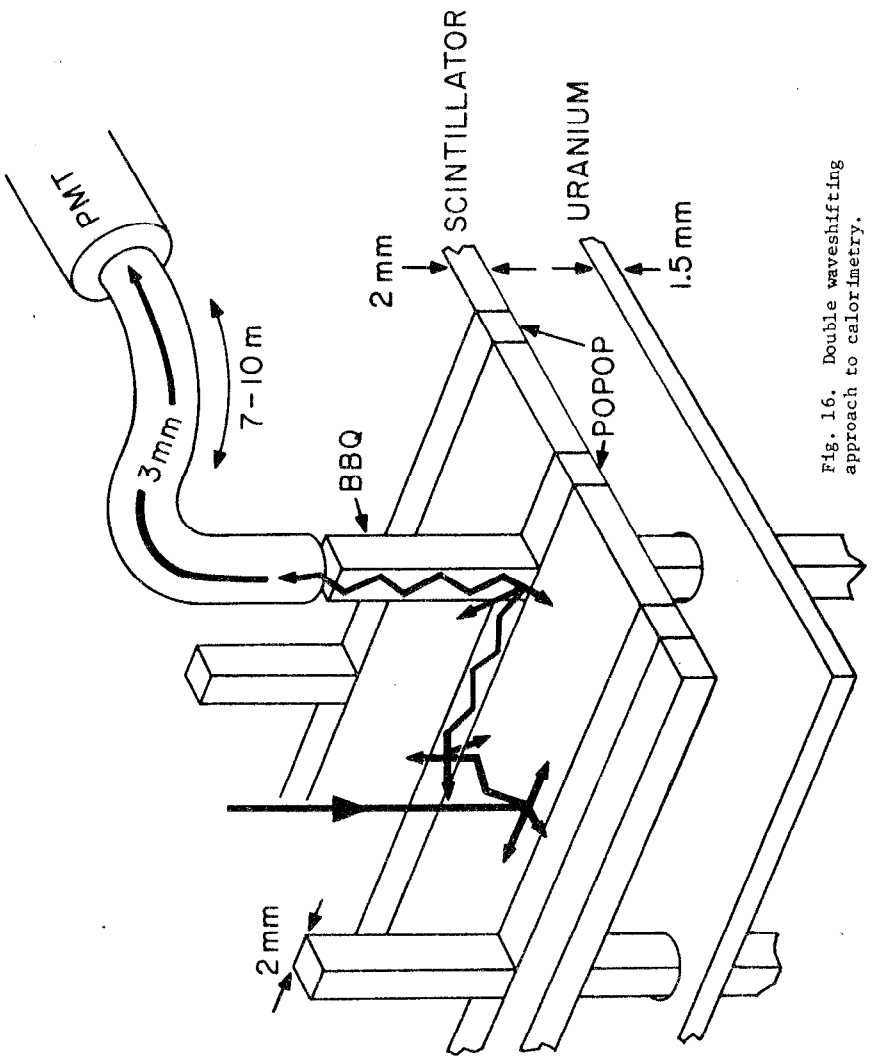

Fig. 16. Double waveshifting approach to calorimetry.

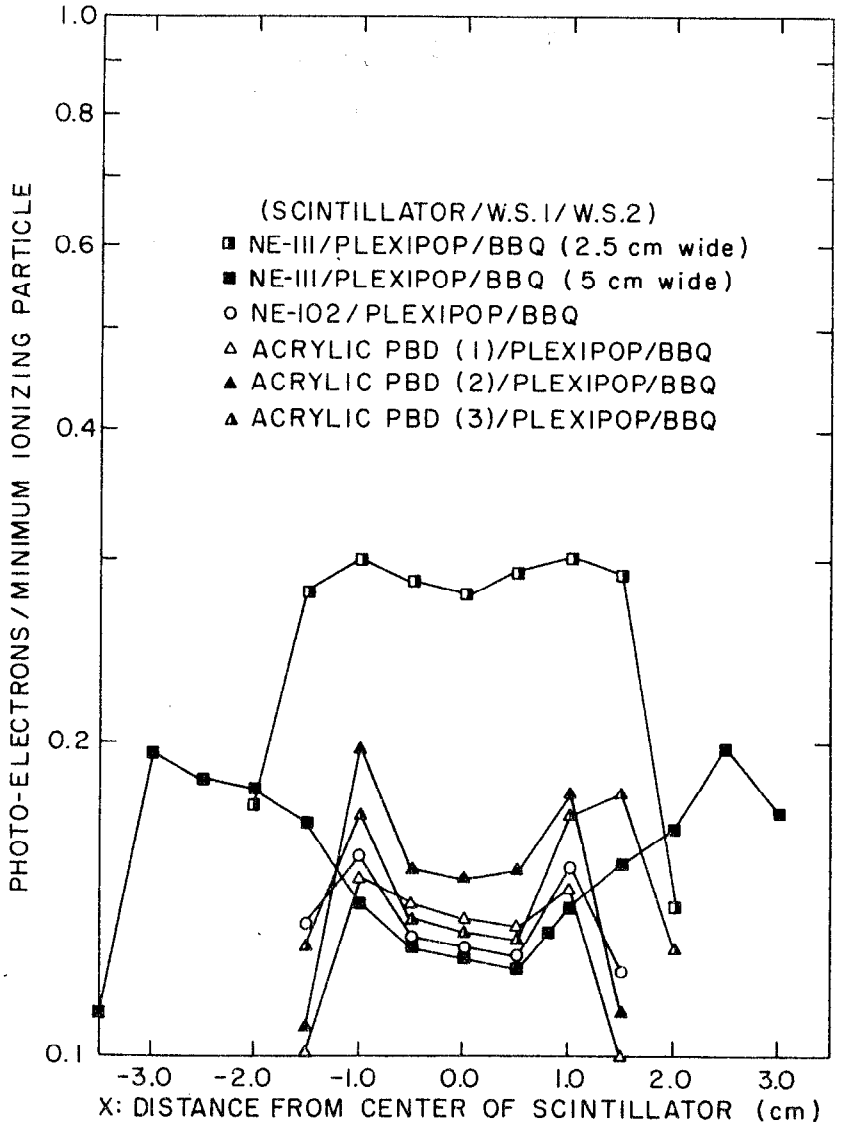

Fig. 17. Light received by Phillips XP2008 phototube in number of photoelectrons by double shifting when a minimum ionizing particle traverses a 3mm thick scintillator.

TABLE I. Properties of Various Media for Flexible Light Guides

Material	Transmission ∿	$\left(\text{Numerical Aperture}\right)^2$	X	(Packing Fraction)	X	(Attenuation (2m) @500nm)	Price	Radiation Hardness
Glass	1/8	$(0.50)^2$		0.75		0.6		∿25 $\frac{db}{m \cdot krad}$
Plastic PVT	1/35	$(0.46)^2$		0.60		0.23		∿20 $\frac{db}{km \cdot krad}$
Quartz	1/100	$(0.22)^2$		0.25		0.93	$$$	∿ 5 $\frac{db}{km \cdot krad}$
$Ce^{+3}La$ doped glass	1/5	$(.5-.6)^2$		0.75+		0.75	$10/m 3mmϕ $30/m 6mmϕ	∿10 $\frac{db}{km \cdot krad}$

At first we tried a glass array. It has a large aperture and moderate attenuation properties. But normal glass is quite sensitive to radiation. We looked to plastic since most light guides are made of plastic if not normally flexible. We chose PVT instead of acrylic on the basis of radiation hardness. Since fibers must be coated, the numerical aperture (N.A.) of a clad fiber is always less than a normal light guide which has air interface. Also, plastic is not very transparent. Quartz fibers seemed to have several desirable attributes. They are certainly the most transparent medium tested and are the most radiation hard. However, the index of refraction of quartz (∿1.5) necessitates a thick silicone cladding which leads to a very low N.A., poor packing fraction and difficulty in assembling couplers. Also, the extreme cost is a disadvantage. We have therefore come back to glass and are now in a contract with Galileo Electro Optics Corporation to produce a lanthanum trivalent-cerium doped boro silicate glass which on paper looks quite promising.

We have been watching closely the developments in microchannel plate photomultipliers. Recently Oba and Rehak[17] have shown how to improve the lifetime of the device and have measured the response in a field up to 0.7 Tesla. Even at this field, as long as the field axis is mainly axial, there is only a small effect on the gain. Although many practical problems need to be solved and the current price is high, this device shows promise. One way to minimize the cost is to have many elements per microchannel plate. With a good system for obtaining the signal from segmented anodes while preserving the linear

response, one could imagine piping many separate signals to the face of one tube via fiber bundles.

If the devices are operated in the saturated mode in order to achieve a low excess noise factor, then there is a recovery time of at least 100 μsec(τ) per microchannel for the best plate in existence. In calorimetry application where the average number of photoelectrons per event ($\bar{n}$) is large, one needs a large number of microchannels per element (N) in order to avoid gain sag at high event rates (F). We can express this requirement as $N >> \bar{n}\ F\tau$. Since for existing microchannel plates $N \sim 10^4/mm^2$, the rate and light yield determine the necessary area per element for a multianode case. At ISABELLE we must be prepared to face rates of up to 10^5 GeV/sec/element. For a light yield of 200 p.e./GeV this would imply a surface area of 10 mm^2/channel. If microchannel plates could be made to saturate at lower gains, τ would be reduced.

Gas Sampling Calorimeters. Great advantage is to be gained with finely segmented calorimeters. Sampling, sufficiently fine to observe the shower shape not only improves position resolution but also greatly aids in particle identification. This is particularly true for neutral particle identification. Photons, neutral pions and eta mesons, cannot be distinguished at high energies by other means. Although ultimately limited by shower size, the resolving power achieved in most experimental detectors is determined by size of the sampling elements. This in turn is limited by overall cost. The much lower per channel costs of calorimeters employing gas sampling and amplification as compared to those using scintillator-photomultiplier combination makes them, in this regard, very attractive for use in large solid angle detectors. However, certain unfavorable characteristics associated with gas sampling calorimeters must either be accepted or overcome. These are listed below.

a. Loss of energy resolution: For a given average sampling, the energy resolution of gas calorimeters is about 50% worse than scintillator detectors (e.g., at 1/2 radiation length sampling in lead $\sigma \simeq 18\%/\sqrt{E}$ for the gas device versus a typical $12\%/\sqrt{E}$ sampling with scintillator). Though the reason for this loss of resolution is not entirely clear, the situation can be improved by operating the gas calorimeter at high pressure.[18]

b. Slow response: The length of the electrical signal is primarily determined by three things -- the charge collection time, the signal generation time or rise time, and the RC time of the detector/amplifier combination. Though a precise discussion is complex, two fundamental requirements for fast response are: small drift distances and small capacitance. These criteria are, however, difficult to meet and pulse lengths of more than 100 ns are typical. In addition, there is the problem of the extremely long tail generated by the slow moving ions that must be properly dealt with in high rate situations to minimize the effects of pileup.

c. Low density and difficult construction: The exponential dependence of the gas amplification on the field strength at the anode wire necessitates maintenance of strict tolerances upon all dimensions comprising the anode cathode geometry, in order to maintain uniform response. Practical tolerances lead to sampling layers that are thicker than those achievable with scintillator. For a given sampling, gas calorimeters are of lower average density than those using scintillator. The finer the sampling, the worse the discrepancy because the metal thickness becomes negligible compared to that of the gas. Since the shower size grows inversely to the density, this reduction in density can quickly obliterate the advantage to be gained through increased segmentation.

One other important consideration in evaluating the performance of calorimeters having fine segmentation in one-dimensional projections only is the degree of correlation between the energy measured for a given shower in each of the various projections. In designs providing only two projections, this is most critical because pulse-height matching between the two views is the only way to resolve ambiguities produced in multi-shower events. Clearly, devices in which the correspondence is exact, subject only to the limitations of electronic noise, are to be favored over simply interleaved views. The alternating samples make entirely independent measurements of the cascade with results differing according to sampling fluctuations. Detectors having projections, each of which samples a different part of the shower longitudinally, are of practically no use in complex events since the typically large variations in individual shower development can wipe out all pulse height correspondence between views, even to the extent of losing one view entirely. There is, nevertheless, considerable advantage to having separated pairs of interleaved or corresponding views at various longitudinal levels. The best position resolution and resolving power are obtained by measuring only the early part of the shower, before it has grown too large. Multiple levels are necessary to obtain high efficiency for late developing showers.

We are developing a new construction technique which will allow the simple and low cost assembly of high performance gas calorimeters. We believe that a gas sampling calorimeter built in this way will provide performance equal, or superior, to scintillator or liquid argon calorimeters in all respects except energy resolution. It is hoped that the energy resolution will remain sufficiently good that the considerable cost advantage will make this type of detector a clear choice for most ISABELLE applications. A mixture of equal volumes metal or metal oxide powders with acrylic monomer produces a low viscosity slurry which may be poured into molds of any desired shape before polymerization. The volume ratio and viscosity are variable to a large extent, making it possible to obtain castings of good uniformity over a range of densities. At BNL, the Department of Energy and Environment originally developed this technique using sand and crushed stone in place of the metal powder in order to obtain a high strength product which became known as plastic concrete. DEE, at our request, has made sample polymerizations incorporating lead and lead oxide powders. In both cases density of more than half that of lead metal may be achieved. Although the lead oxide product has lower density, it is harder. Both plastic combinations are good insulators ($>10^{13}$ohm-cm); however, the lead product has twice as high a dielectric constant ($\epsilon \sim 20$) and becomes suddenly and irreversibly conducting if a high enough field is

applied. In the case of PbO the final product has an approximate assay of 84% Pb, 6% O and 10% PMMA by weight.

We are presently preparing to cast the PbO plastic into sheets as shown in Figure 18. We will then plate the surface with conducting cathode strips running perpendicular to the grooves. After placing anode wires centered in the half cylindrical grooves, these plates may be stacked so the grooves are arranged in a close-packed hexagon. Alignment is easily maintained by sacrificing the endmost groove to an alignment rod. We hope to find a private company to construct for all plate fabrication including plating. The molds used for making the sheets are actually themselves molded from a single machined metal plate having the same surface features as desired for the final product. In this way a high production rate for high tolerance final plates can be achieved.

The two projection readout with the beam in position (a) in Fig. 18 is obtained by joining rows of anode wires in one view and cathode strips in the other. Note that in this way the X and Y pulse height measurements are equivalent as they see exactly the same charge. In this design the largest capacitance around is that coupling adjacent cathode strips. We estimate this to be in the few hundred picofarad range. If we can keep this small enough we may be able to achieve pulse lengths dominated by the sum of the charge collection time (1.5 mm x 20 ns/mm = 30 ns) and the PWC rise time (~30 ns). Alternatively, the beam can be aimed at the device as indicated by (b) in Fig. 18. Then the cathode strips would integrate the shower longitudinally and could be arranged in towers. The

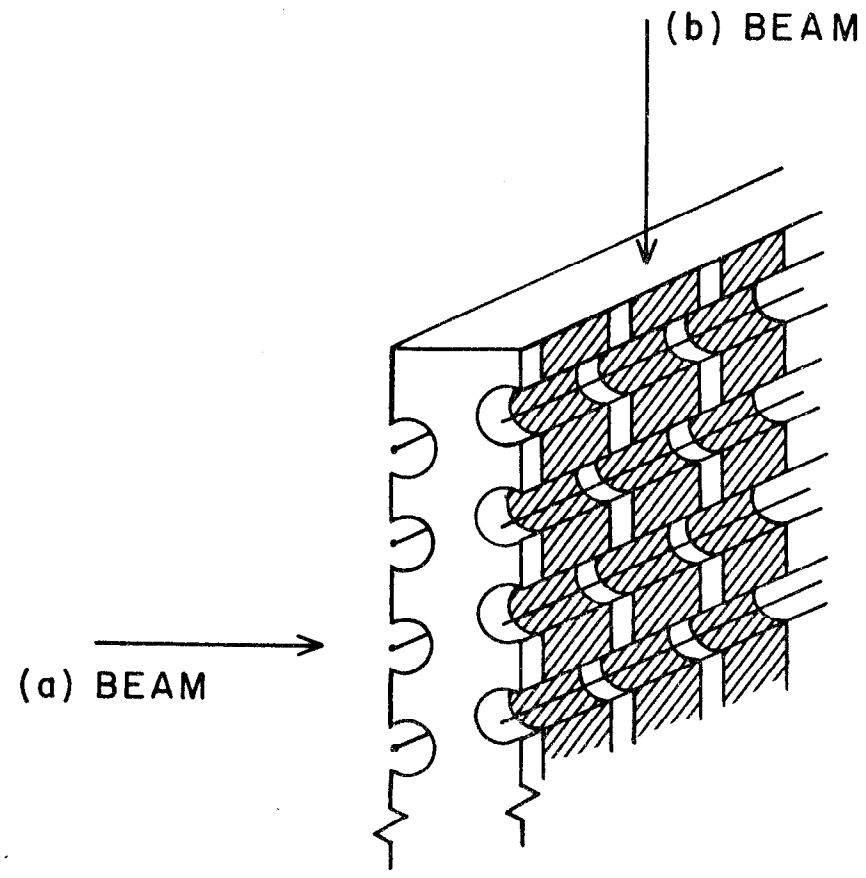

Fig. 18. Sheet of plastic loaded with heavy metal as model for construction of a calorimeter. Cross hatching indicates copper plating.

wires could be connected in bands of constant θ for a trigger proportional to the sum of the transverse momenta.

Note that for the dimensions shown in Figure 18, an initial PbO plastic density of 6 g/cc gives a final average density of 4 g/cc for the entire calorimeter. Monte Carlo (EGS) simulations of showers[19] indicate that this sampling arrangement is probably equivalent to a layered sampling of a 3 mm gas and 5.7 mm PbO plastic. This is about 1/2 r.l. sampling. Comparing this to a Pb scintillator calorimeter having layers of 3 mm and two crossed scintillator layers of 3 mm thickness each, one finds similar average density. Of course, the density of the scintillator calorimeter can be raised by increasing the lead thickness to 6 mm while still obtaining energy resolution similar to the gas device. If wave length shifting techniques are used the signals would also be of similar length ($\sim$60 ns).

In conclusion we believe that with these techniques gas sampling calorimeters may be constructed that provide performance statistics sufficiently close to scintillator devices that cost considerations alone will indicate their use in most ISABELLE applications. As a final comment we list several other salient features of this technique:

i) Materials other than PbO such as tungsten, iron, UO_2, or iron oxide may be used as the basic material. Although all dimensions and performance statistics will change according to the material, there may be other useful applications of the plastic casting technique.

ii) Uniformity is easier to obtain at edges than in the case of scintillator.

iii) Magnetic fields are of less concern than in the case of photomultiplier readout.

iv) Other casting techniques make the contemplation of non-planar structures appear reasonable.

One of the main problems of any calorimeter is fitting modules in a cylindrical or spherical geometry. This is because most designs use rectangular sheets. For an electromagnetic calorimeter with less than fifty samples, one can make each sheet of radiator and detector a slightly different size to fit into the desired geometry. However for a deep, fine sampled hadron calorimeter this quickly becomes overwhelming. One possibility is to use scintillating fibers as discussed by Borenstein et al.[14] as a sampling medium in a solid cast of plastic loaded with heavy metals or metal oxide. The fibers could be wound like wires in a PWC on frames and put into a mold. This mold could have sloping sides necessary to be a section of a solid figure. Since the fibers are coated, the material surrounding it should not affect the light output. To check the feasibility of this approach we constructed a modest model. The fibers of 2 mm diameter of NE102 were arranged in a close packed hexagonal array with distance between centers of 3.3 mm and the surrounding glass tube was filled with a mixture containing PbO. A phototube was placed on the end and the device was brought to a test beam. The results are shown in Figure 19. Unfortunately the trigger counters had a larger sensitive area than this device. However, there is clear peak in the distribution of pulse heights from π^- passing through the device. Although the electron beam was not extremely cleanly defined,

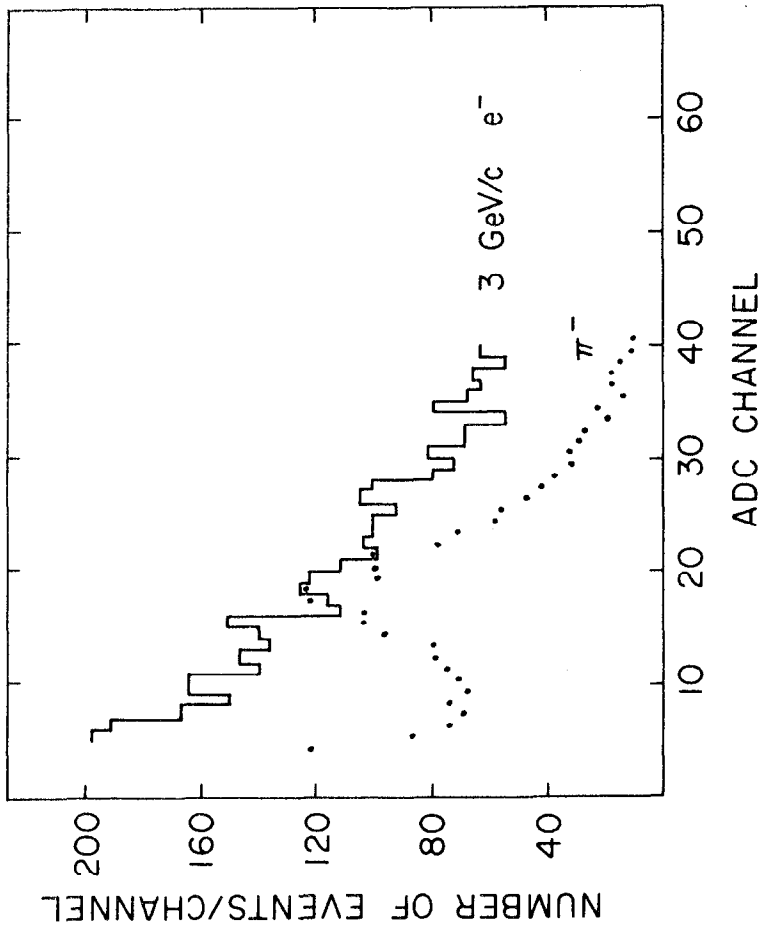

Fig. 19. Pulse height spectra for π^- and e^- traversing device.

there is evidence that the electrons give, on the average, larger pulse heights even though only part of a shower could be contained within this device. We imagine reading out the ends of the fibers parallel to the intersecting beams with waveshifter bars. However if a crinkle could be introduced in the fibers one could imagine arranging the fibers perpendicular to the beams and getting the light out of the back of the calorimeter with no shifting at all. Practicality questions abound: 1) what are the costs of this device; 2) how to make the mold release from the thousands of fiber ends; and 3) what are the variations in light output in various places in the solid.

We would also like to report on the idea of Polk, Smith and Willis[19] to instrument the iron poles of a magnet with a gas sampling calorimeter. The goal is to have moderately good energy resolution for hadron and electromagnetic showers and have magnetic properties of ordinary steel. T. Ludlam, et al. has constructed, and is now testing, a device of this type. The holes in the iron are in the pattern of a quincunz, 2 mm x 5 mm, so that a charged particle will be detected in 25% of the layers on the average. Test data should be available soon.

Another new idea in gas sampling is being implemented by the LBL-TPC group[20] shown in Fig. 20. By stretching nylon monofilament at right angles to the sense wires, a gas calorimeter can be operated in a limited discharge (Geiger) mode. This improves the energy resolution by minimizing the Landau fluctuations of individual charged particles in the shower up to the energy where two particles are likely to be found in a single cell. Still low energy δ-rays which may set off many cells can be detrimental to the energy resolution. Fig. 21 shows

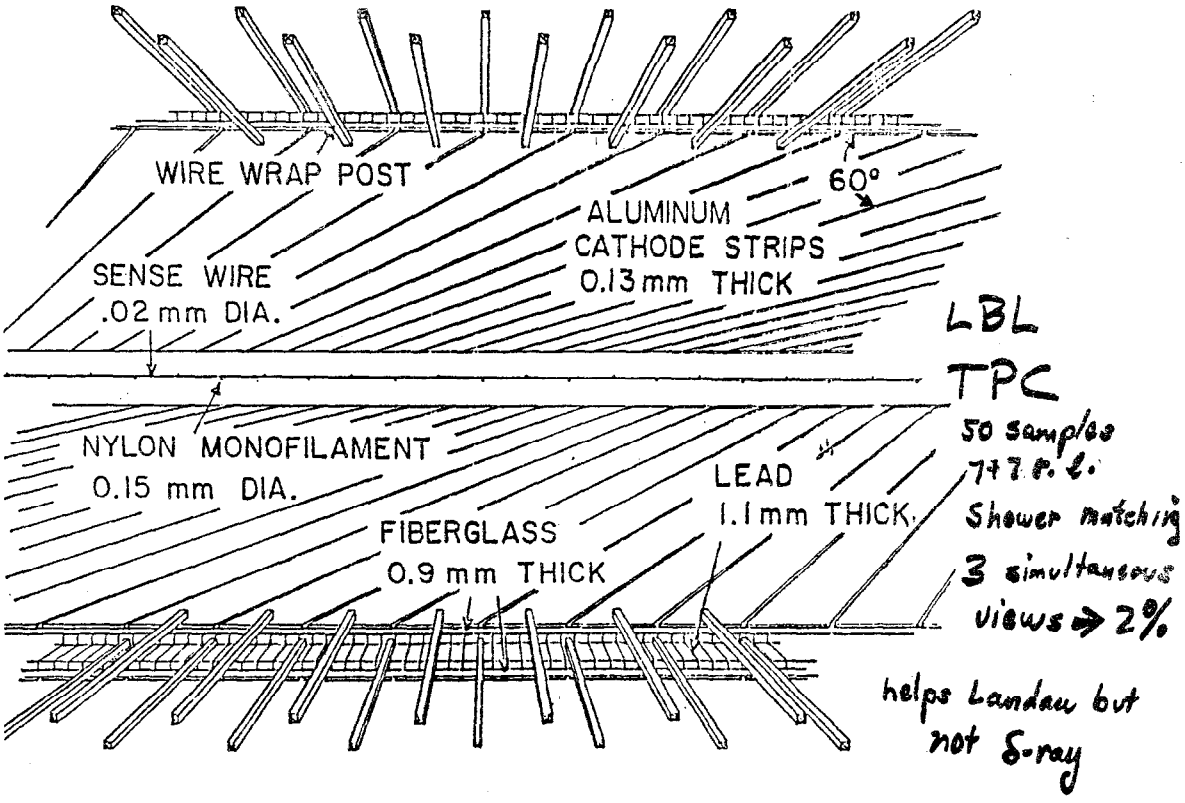

Fig. 20. End on view of the PEP-4 semi-Geiger mode electromagnetic shower detector.

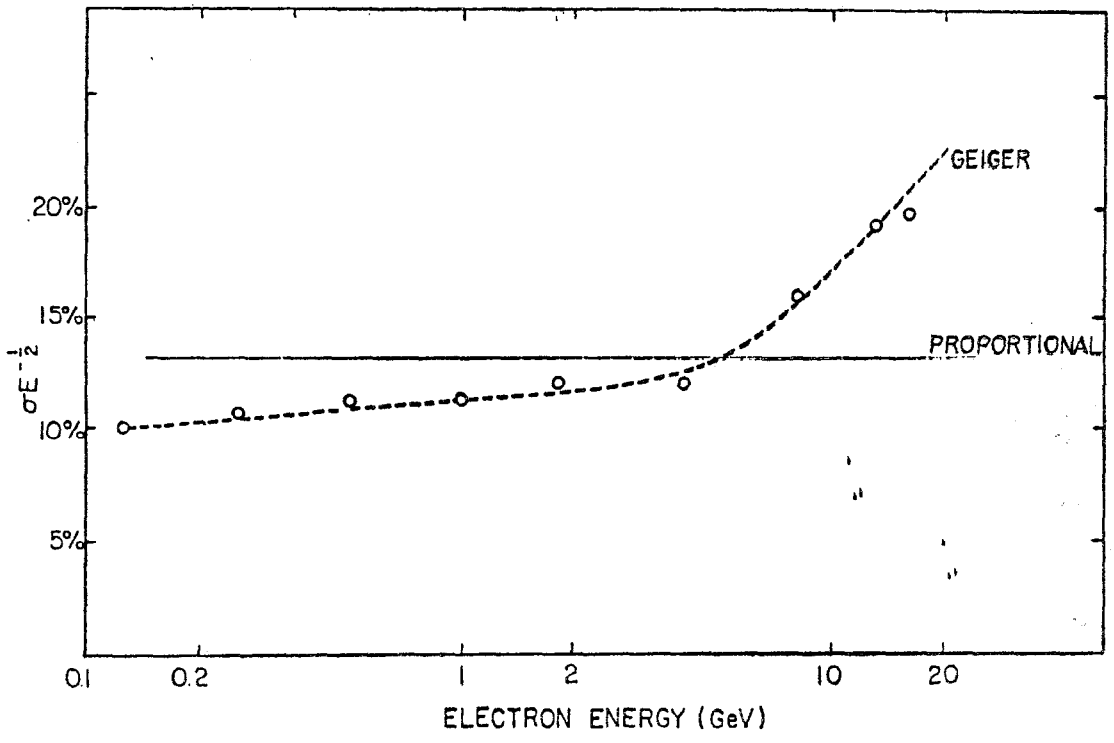

Fig. 21. Energy resolution for normal proportional mode calorimeters compared to a semi-Geiger mode device.

that the improvement in the energy resolution holds up to a certain energy where saturation occurs. This saturation means that it is likely for two electrons in the shower to be in the same cell. Another feature of this design is two sets of cathode strips at $\pm 60^{o}$ for each gap to allow excellent matching of showers.

Another new idea is the so called time projection calorimeter from Fischer and Ullaland[21] at CERN. Variations on this theme have been suggested by W. Carrithers at LBL and L. Price at ANL. The idea is that particles would enter an active region of gas which is divided by an absorbing medium into cells as displayed in Fig. 22. The charge particles would drift down to a readout plane of proportional wires and crossed cathode planes. With sophisticated electronics recording both the time of arrival, the location and pulse height, the details of the shower can be reconstructed. A prototype has been tested with $\sim 34\%/\sqrt{E}$ energy resolution. This technique does not have the advantage of high density or the ability to survive in a high rate environment.

This research was supported by the US Department of Energy under Contract No. DE-AC02-76CH00016.

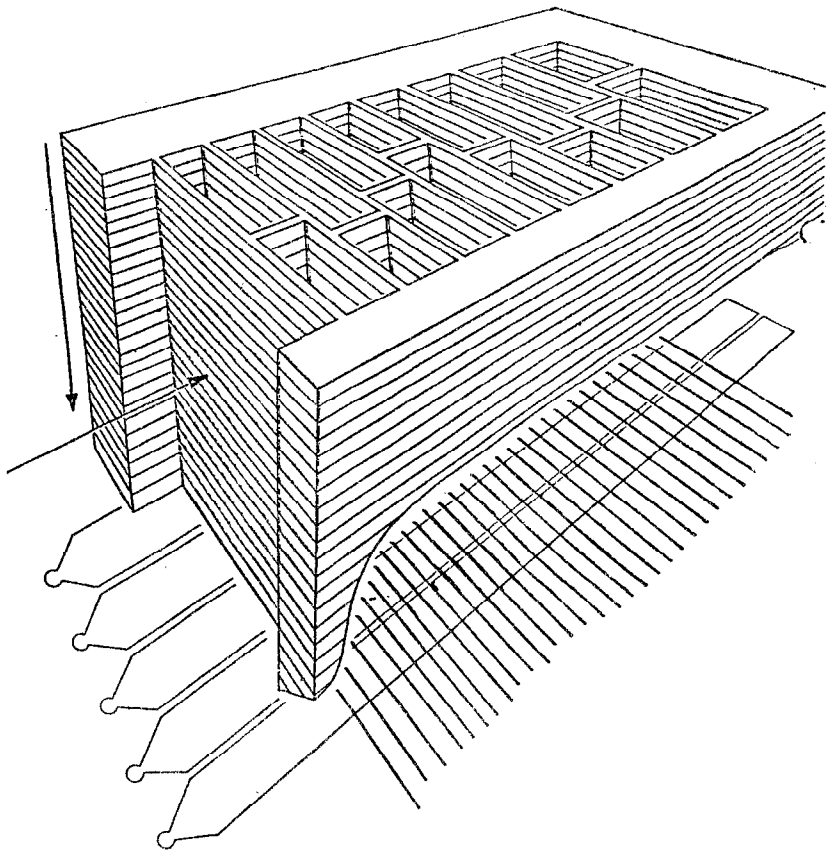

Fig. 22. Conceptual plan of the time projection calorimeter.

References

1. S. Iwata, Calorimeters (Total Absorption Detectors) for High Energy Experiments at Accelerators (A Review for a Tristan Workshop), DPNU-3-79 (February, 1979); see also Proceedings of the Calorimeter Workshop at FNAL (1975).

2. H.A. Gordon, R.B. Palmer and S.D. Smith, New Ideas in Calorimetry, Proceedings of the International Conference on Experimentation at LEP, Physica Scripta (to be published).

3. S.L. Stone et al., Nucl. Instr. and Meth. 151, 387 (1978).

4. G. Abshire et al., Nucl. Instr. and Meth. 164, 67 (1979).

5. D. Hitlin et al., Nucl. Instr. and Meth. 137, 225 (1976).

6. T.A. Gabriel, Nucl. Instr. and Meth. 150, 145 (1978).

7. J.P. Dishaw, The Production of Neutrinos and Neutrino-like Particles in Proton-Nucleus Interactions, SLAC-216 (March, 1979).

8. C.W. Fabjan et al., Nucl. Instr. and Meth. 141, 61 (1977).

9. A.L. Sessoms et al., Nucl. Instr. and Meth. 161, 371 (1979).

10. Baum et al., Proceedings of the Calorimeter Workshop at FNAL (1975).

11. See for example R. Johnson, Lawrence Berkeley Laboratory Report No. LBL-4610, 1975 (unpublished).

12. H. Gordon et al., "A Uranium Scintillator Calorimeter at the CERN ISR," presented at the International Conference on Experimentation at LEP, Uppsala, Sweden (June, 1980).

13. R.L. Anderson et al., "Tests of Proportional Wire Counter and Hadron Calorimeter Modules," SLAC-PUB-2039 (November, 1977).

14. S.R. Borenstein et al., Optical Fibers and Avalanche Photodiodes for Scintillator Counters, presented at the International Conference on Experimentation at LEP, Uppsala, Sweden (June, 1980).

15. R. Boie, BNL Instrumentation Division, private communication.

16. R.B. Palmer, A Conceptual Design of a Dipole Detector at ISABELLE, BNL preprint DD-1.

17. K. Oba and P. Rehak, Studies of High-Gain Microchannel Plate Photomultipliers, BNL preprint OG536A, submitted to 1980 Nuclear Science Symposium, Orlando, Florida (November, 1980).

18. Buchanan, Ticho, Wenzel, PEP4 Notes.

19. I. Polk, S.D. Smith and W.J. Willis, Development of Magnetic Calorimeters, ISABELLE Research & Development Proposal -- IRD1, BNL, 1978.

20. W.A. Wenzel et al., The PEP-4 (TPC) Facility -- A Status Report, Submitted to International Conference on Experimentation at LEP, Uppsala, Sweden (June, 1980).

21. G. Fischer, O. Ullaland, ibid.

PARTICLE IDENTIFICATION BY ČERENKOV AND TRANSITION RADIATION*

R. S. Gilmore

Stanford Linear Accelerator Center

Stanford University, Stanford, California 94305 USA

and

University of Bristol, H. H. Wills Physics Lab

Royal Fort, Tyndall Avenue, Bristol BS8 ITL, England

*Work supported in part by the Department of Energy, under contract DE-AC03-76SF00515, and in part by the University of Bristol.

1. INTRODUCTION

Particle identification requires a measurement of the particle's mass and the sign of its electric charge, the particles of interest having unit charge. Passing the particle through a magnetic field gives the sign, from the direction of curvature of the track, and also a measure of the particle's momentum from the radius of curvature. The momentum, p, is given by

$$pc = m\beta\gamma \tag{1}$$

where

$$\beta = v/c$$

$$\gamma = \left(1 - \beta^2\right)^{-\frac{1}{2}}$$

so if the velocity, v, is measured; the mass is obtained. The precision with which the mass is determined is given by

$$\left(\frac{dm}{m}\right)^2 = \left(\gamma^2 \frac{d\beta}{\beta}\right)^2 + \left(\frac{dp}{p}\right)^2 \tag{2}$$

If the momentum p is relatively well measured, then the resolution of particles with masses m_1 and m_0 requires velocity resolution, $\Delta\beta$, given by

$$\frac{\Delta\beta}{\beta} = \frac{m_1^2 - m_0^2}{2p^2} \tag{3}$$

At low velocities, β may be measured by Time-of-Flight techniques, but at higher velocities Čerenkov counters are more suitable.

2. ČERENKOV RADIATION

A particle with electric charge e and velocity v in a medium of dielectric $\varepsilon(\omega)$ generates fields in the medium which, at large distances, b, may be expressed as in Equation (4) below[1]

$$\text{Parallel Electric Field} \qquad E_1(\omega) = \frac{ie\omega}{c^2}\left[1 - \frac{1}{\beta^2\varepsilon(\omega)}\right]\frac{e^{-\lambda b}}{\sqrt{\lambda b}}$$

$$\text{Transverse Electric Field} \qquad E_2(\omega) = \frac{e}{v\varepsilon(\omega)}\sqrt{\frac{\lambda}{b}}\; e^{-\lambda b} \tag{4}$$

$$\text{Transverse Magnetic Field} \qquad B_3(\omega) = \varepsilon(\omega)\beta E_2(\omega)$$

where

$$\lambda = \frac{\omega}{v}\sqrt{1 - \beta^2\varepsilon(\omega)}$$

At low speeds this gives fields which fall off exponentially away from the particle, the energy being carried along with the moving charge. However, if $\varepsilon(\omega)$ is real, i.e., there is no absorption, there will be some speed such that $\beta^2\varepsilon(\omega)$ is greater than unity (provided $\varepsilon(\omega) > 1$). In this case λ is imaginary and the fields take the form of a travelling wave. This corresponds to the case where the particle is travelling faster than the electromagnetic radiation in the medium. The energy in the field cannot return to the particle and is radiated as a shock wave in the direction $\underline{E} \times \underline{B}$, making an angle θ with the particle direction, where

$$\cos\theta = \frac{1}{\beta\sqrt{\varepsilon(\omega)}} = \frac{1}{\beta n(\omega)} \tag{5}$$

where $n(\omega)$ is the refractive index of the medium.

The energy spectrum of the radiation is given by

$$\left(\frac{dE}{d\omega}\right) = \frac{e^2}{c^2}\,\omega\left(1 - \frac{1}{\beta^2\left(\varepsilon(\omega)\right)}\right) \tag{6}$$

One is more interested in the number of photons, energy $\hbar\omega$, emitted from length L in energy range dE. This is

$$N = \frac{e^2}{\hbar^2 c^2} \sin^2\theta \, LdE \, , \qquad (7)$$

$$= 370 \sin^2\theta \, LdE \; ; \quad L \text{ in cm, } dE \text{ in eV}$$

The intensity of Čerenkov radiation in the visible region is low, typically one thirtieth of that from a scintillator of similar thickness. One of the main problems in Čerenkov counter design is the very low signal strength, often giving as little as three or four photoelectrons.

Though the intensity in the visible region is low, the Čerenkov spectrum extends far into the ultraviolet, the spectrum being approximately constant with respect to photon energy as long as the refractive index n is roughly constant and greater than $1/\beta$. Figure 1 shows that the refractive index of a typical radiator is roughly constant at low photon energy, has pronounced maxima and minima at the region's anomalous dispersion near atomic resonances, where strong absorption will inhibit radiation, and finally is less than unity for high photon energies. There is no Čerenkov radiation in the x-ray region as the refractive index is here less than unity.

For good particle identification you require dm/m to be low; hence, from Equation (2), you must determine $d\beta/\beta$ well. If you measure the Čerenkov angle θ, you get the greatest sensitivity when $d\theta/d\beta$ is large. Figure 2 is a plot of Čerenkov angle against β for various refractive indices and shows that $d\theta/d\beta$ is greatest near the threshold value of β. Near threshold, however, the value of θ is low, so the signal intensity is low. Alternatively, you can operate at larger values of θ and obtain

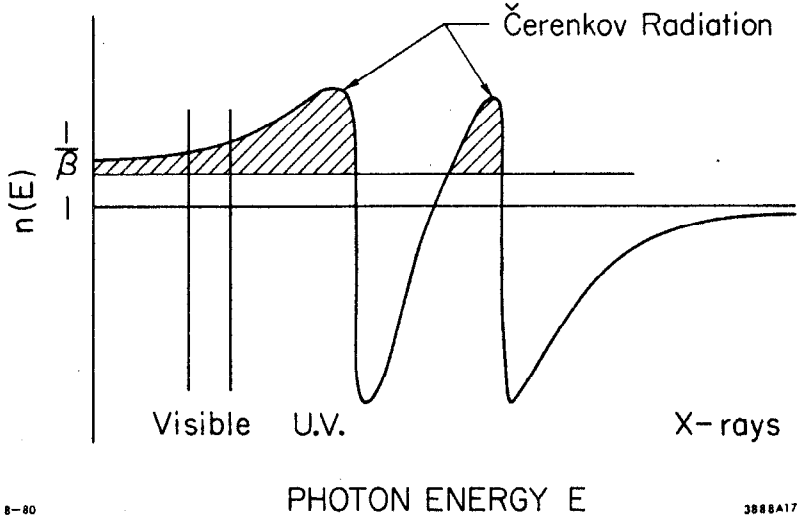

Fig. 1. Typical variation of refractive index with photon energy.

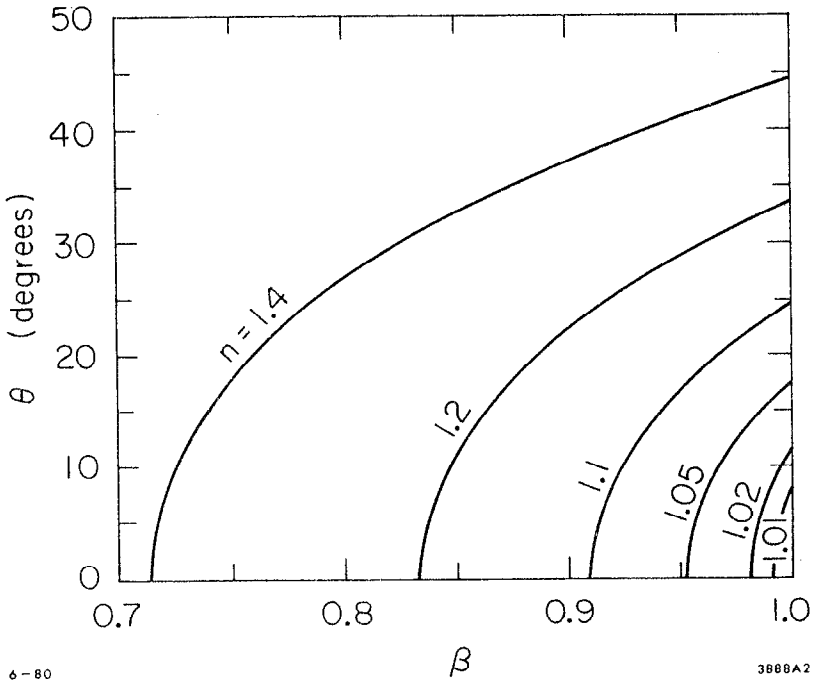

Fig. 2. Variation of Čerenkov angle θ with particle velocity β for several values of refractive index n.

more light, though dθ/dβ will be lower. These possibilities correspond to the two main classes of Čerenkov counter, as shown in Figure 3. The threshold counter detects particles which emit light, and sees only those above the threshold velocity, while the differential counter selects particles giving light at a predetermined value of θ. Reference 2 gives an extensive review of both types of counter, with further references for conventional Čerenkov types.

3. THRESHOLD ČERENKOV

This detects a particle which produces enough light, in principle if $\beta > 1/n(\omega)$, but in practice β must be somewhat higher to give a signal large enough to be detected. It will detect any particle with higher β, e.g., a kaon detector will also detect pions and electrons of the same momentum.

The threshold counter has only one adjustable parameter, the refractive index of the radiator. To control the β threshold you must control the refractive index (e.g., vary the pressure in a gas filled counter). Figure 4 shows the appropriate refractive indices for pions and kaons of varying momentum. At very low momentum liquids and solids may be used, and at high momentum gasses either at atmospheric pressure or at pressures which are easy to obtain. It is difficult to obtain gas radiators in the refractive index range from 1.01 to 1.2 and here Aerogel counters are being used.[3] Aerogel is a mixture of air and small particles of silica, of typical size 10-100 nm. These are small relative to the wavelength of light observed and result in an effective refractive index between that of air and silica.

$n = 1 + 0.21\ \rho$ where ρ is the density in g/cm^3 .

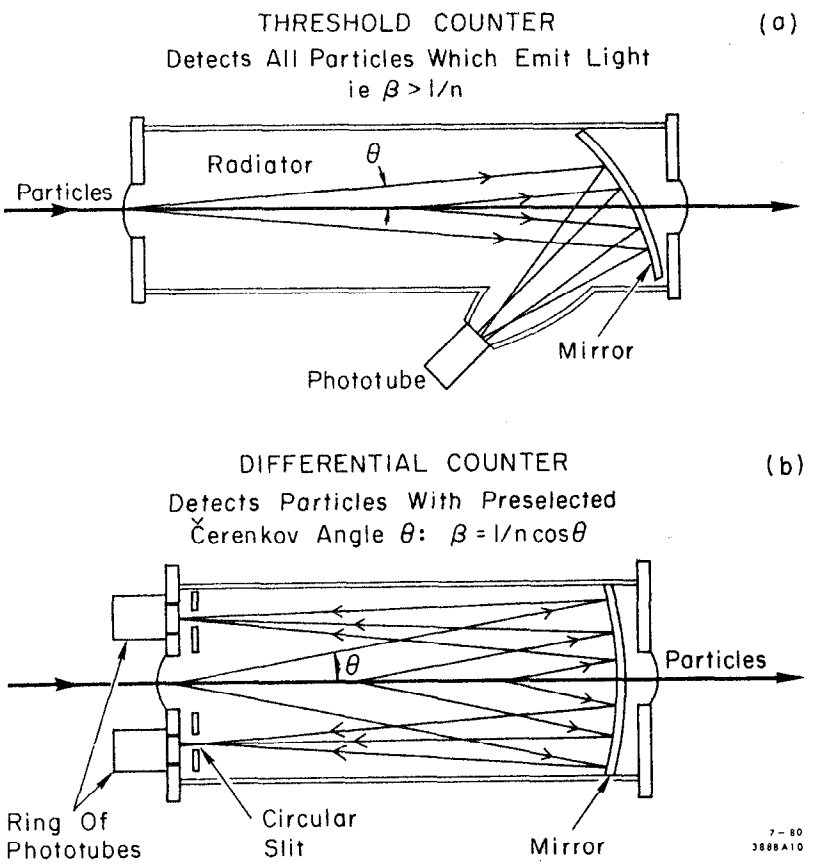

Fig. 3. The two principal classes of Čerenkov counter.

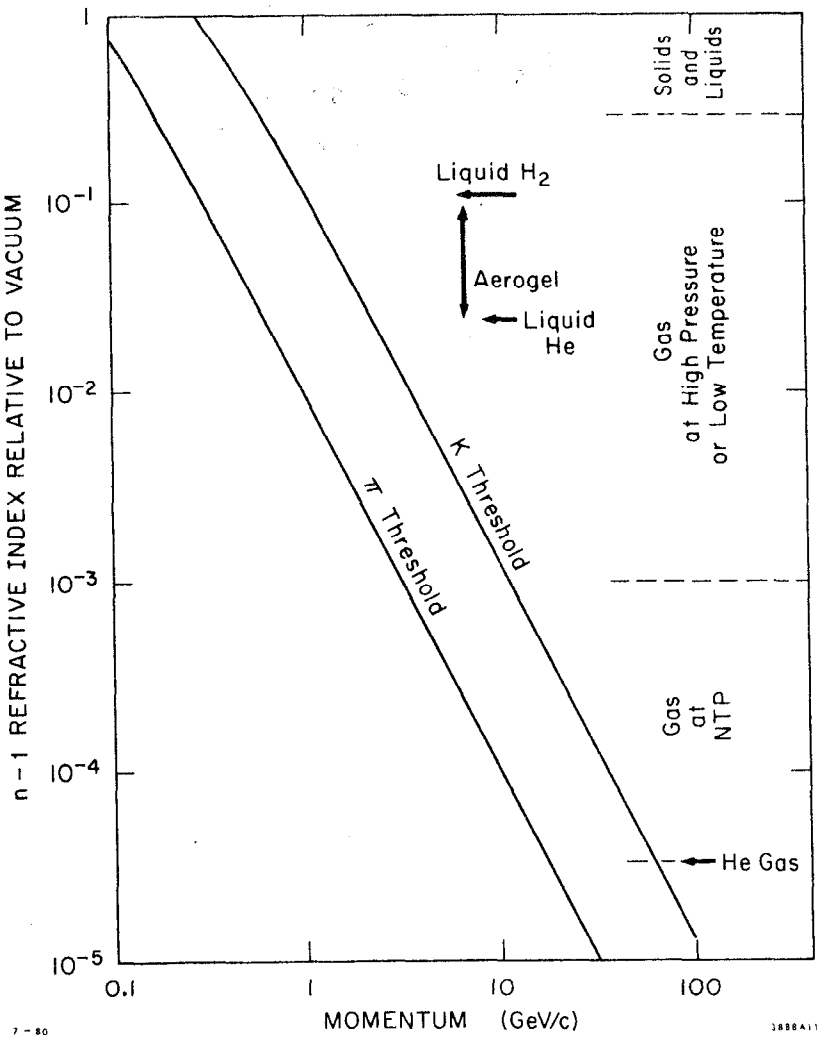

Fig. 4. The refractive index required so that of pions or kaons of given momentum be at threshold for Čerenkov radiation.

A pressure scan for a threshold counter[4] is shown in Figure 5. The detection efficiency for each type of particle arises gradually above threshold, showing that the resolution $\Delta\beta/\beta$ is limited. What effect limits the resolution? One contributing factor is the chromatic dispersion of the radiator medium, which will have a different refractive index for photons of different energy. The threshold β will vary with photon energy and give a spread, $\Delta\beta$, in resolution. For particles of different velocities β_1 and β_0 Equation (1) gives, for small values of θ,

$$\theta_1^2 - \theta_0^2 = 2(\beta_1 - \beta_2) = 2\Delta\beta \qquad (8)$$

The spread in Čerenkov angles due to dispersion is

$$\Delta\theta_{DISP} = \frac{n-1}{n\nu \tan\theta} \qquad (9)$$

where $\nu = (n-1)/\Delta n$ is the dispersive power of the medium.

The best signal is obtained for the detected particle by setting the slower particle exactly at threshold, where $\theta_0 = 0$ and it produces no light. Then you can show, using Equation (3), that

$$\frac{\Delta\theta_{DISP}}{\theta_1} \simeq \frac{1}{2\nu} \frac{m_1^2}{m_1^2 - m_0^2} \qquad (10)$$

For counters operating in the visible region, this is usually small, of the order of a few percent for particles of interest, and it is not strongly dependent on momentum. Chromatic dispersion does not significantly limit the resolution of a threshold Čerenkov.

The slow rise in the efficiency of a Čerenkov counter is dominated by statistical fluctuations in the small number of photoelectrons produced. If n photons give nq detected photoelectrons, the probability

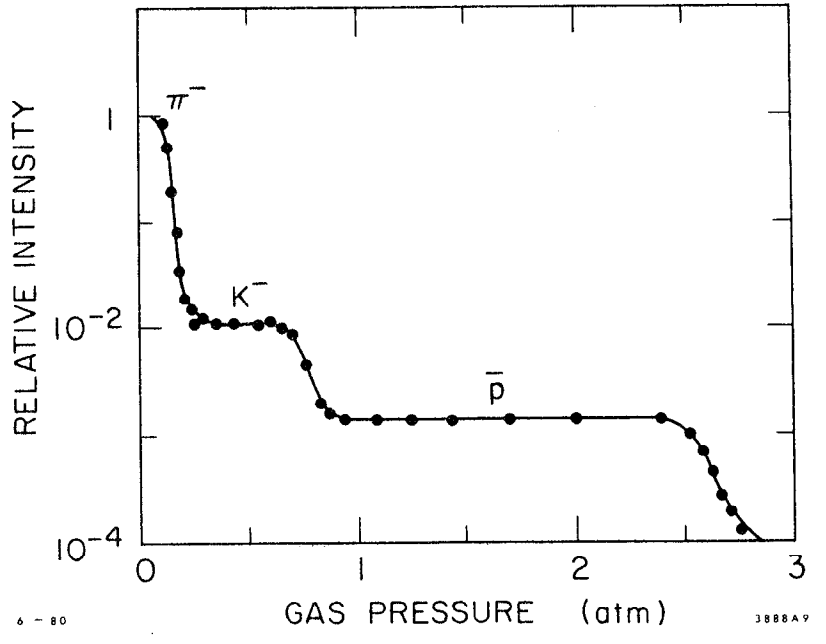

Fig. 5. Pressure scan for a five meter carbon dioxide filled threshold counter operating as a veto, for a beam of 20 GeV/c negative particles.

of detecting none is given by the Poisson expression e^{-nq}, so the efficiency is

$$\epsilon = 1-e^{-nq} \quad . \tag{11}$$

Figure 6 shows how the efficiency varies with the number of photons detected.

As the number of photons emitted is proportional to $\sin^2\theta$, we see from Equation (8) that the number of photons is approximately proportional to $\Delta\beta$, for a threshold counter with the unwanted particle set at threshold. As the particle momentum, and hence γ, increases, the $d\beta/\beta$ required for particle separation decreases, from Equation (2), and hence the photon yield decreases. To maintain a reasonable efficiency you must take steps to recover an adequate number of photons. This may be attempted by

(a) Optimising the collection of light by the phototubes with a suitable choice of reflecting surfaces and geometry. This should be done in any Čerenkov counter but becomes more critical at high momentum.

(b) Increasing the length of the radiator. As the photon yield is proportional to radiator length this gives a direct improvement. Threshold counters for use at high momentum are many meters long.

(c) Increasing the range of photon energies detected. This again gives a proportional improvement, but is not easy to achieve. Phototubes with ultraviolet transmitting windows or ultraviolet converting phosphors can increase the range.[5]

Threshold counters have the advantage of relatively simple construction, all that is required is a large volume of radiator medium and an optical system to focus the light onto the detectors. Figure 7 shows a Čerenkov counter used in an experiment at CERN.[6] The only rigid section

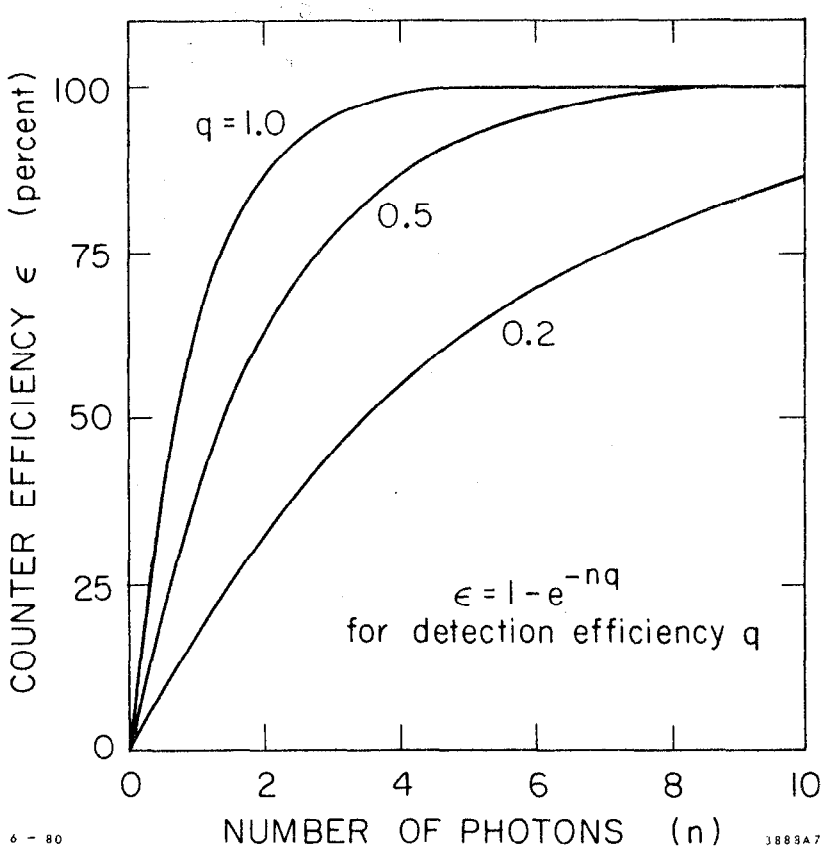

Fig. 6. Variation of the detection efficiency due to statistical fluctuations as a function of the number of photons.

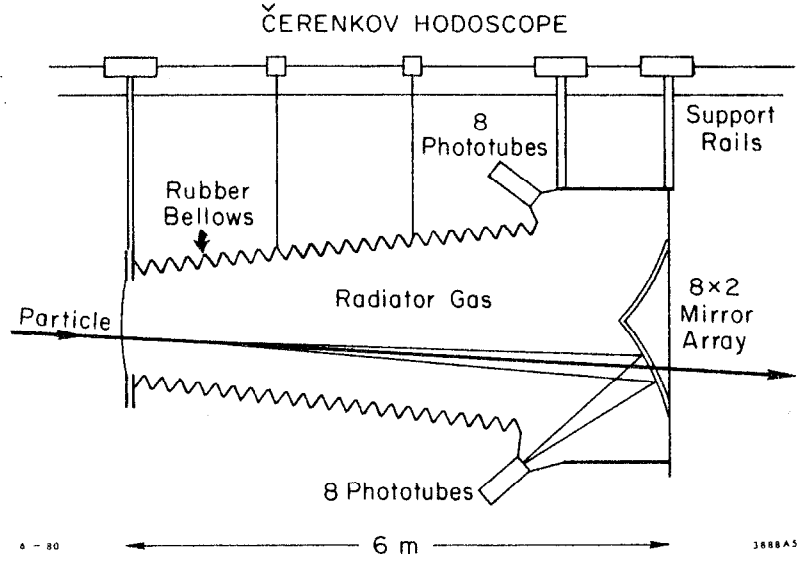

Fig. 7. Large modular threshold Čerenkov counter used in an experiment at CERN.

of this counter is the end box which holds the mirrors and phototubes. The main bulk of the counter is simply the radiator medium, and in this case is contained in a rubber bellows rather like an old camera, which can be folded up to allow access to other apparatus. The light collecting mirror is divided into sixteen sections, each of which is focused onto a different phototube. Such segmentation gives a threshold counter the ability to register several particles simultaneously, provided that they are sufficiently well separated that their Čerenkov light strikes different mirror sections.

4. DIFFERENTIAL ČERENKOV COUNTER

As Figure 3 shows, this uses a spherical mirror to produce a ring image for Čerenkov light at a given angle θ and detects the light corresponding to some angular range $\Delta\theta$ which passes through a circular diaphragm slit. This means that, unlike the threshold counter, for a given momentum p only one type of particle is detected.

The differential counter has two adjustable parameters — the refractive index, n, of the radiator and the detected Čerenkov angle θ. You can choose a larger Čerenkov angle for the detected particles than can be obtained with a threshold counter and consequently get more light. Because of the increased signal, the resolution of the differential Čerenkov counter need not be dominated by statistical fluctuations in the number of photoelectrons, but this means that various aberrations of the system now have significant effects on the resolution. Their effect is obtained from Equation (5) to be

$$\left(\frac{\Delta\beta}{\beta}\right)^2 = (\tan\theta\ \Delta\theta)^2 + \left(\frac{\Delta n}{n}\right)^2 \qquad (12)$$

Here $\Delta\theta$ includes contributions from

(a) the finite slit width, which allows a spread of angles $\Delta\theta$ to be detected;

(b) the spread in particle directions; and

(c) aberrations of the spherical mirror due to the particle track illuminating a large fraction of the aperture. Spherical aberration gives $\Delta\theta \sim 1/8(d/f)^3$ and coma gives $\Delta\theta \sim 1/8\ \theta(d/f)^2$. Here f is the focal length of the mirror and the diameter of the region illuminated.

The chromatic aberration, $\Delta n/n$, though negligible in threshold counters, is usually dominant in the differential variety. The velocity resolution of a differential Čerenkov counter may be an order of magnitude better than for a threshold counter of comparable length.

The light passing through the diaphragm is normally detected by a ring of photomultipliers behind the slit. To confirm that there is a ring image centered on the slit requires several tubes in coincidence. The resolution improves with the number, m, in coincidence, but the efficiency falls as

$$\varepsilon = \left(1-e^{-nq}\right)^m \qquad (13)$$

Figure 8 shows a pressure scan for a 10 m Helium filled counter[7] which gives $\Delta\beta/\beta$ of less than 2×10^{-6}.

It is possible to correct for chromatic and spherical aberrations and coma by using prismatic optical elements,[8] as indicated in Figure 9. Such counters are referred to as DISC counters and can give improvements in $\Delta\beta/\beta$ by an order of magnitude, i.e., $\Delta\beta/\beta \sim 4\times10^{-7}$. To achieve this value for resolution, uncorrected sources or error, such as the spread in particle directions, must be kept exceedingly small.

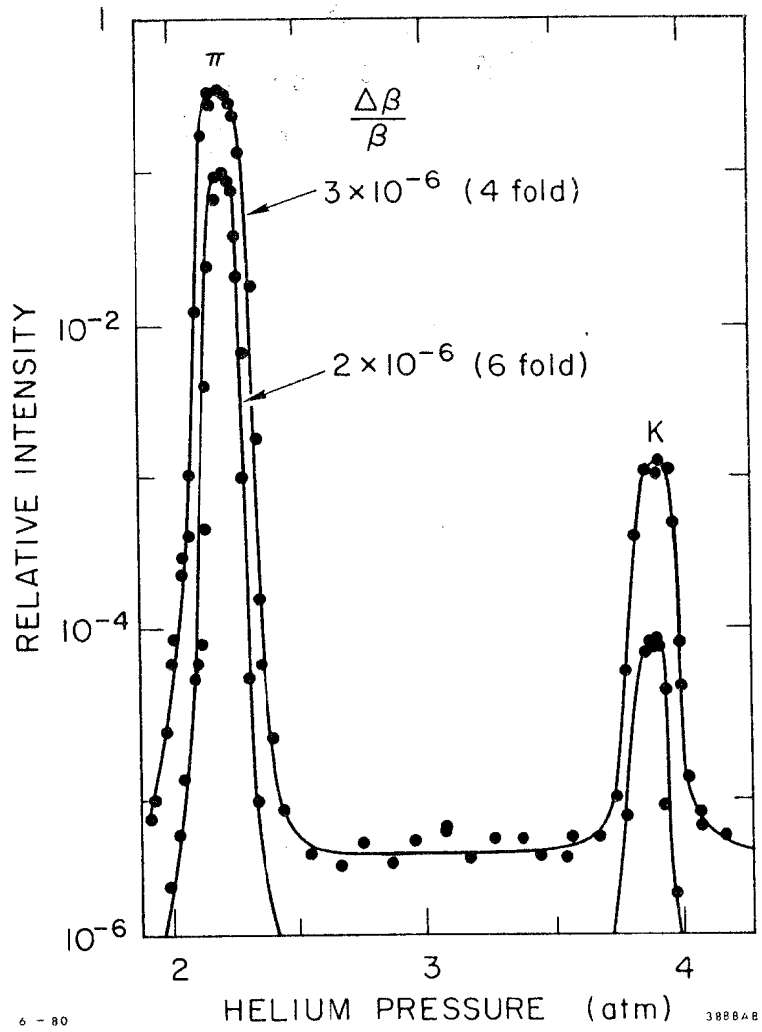

Fig. 8. Pressure scan for a ten meter helium filled differential Čerenkov counter in a 45 GeV/c beam. This shows how rejection of unwanted particles varies with the number of phototubes in coincidence.

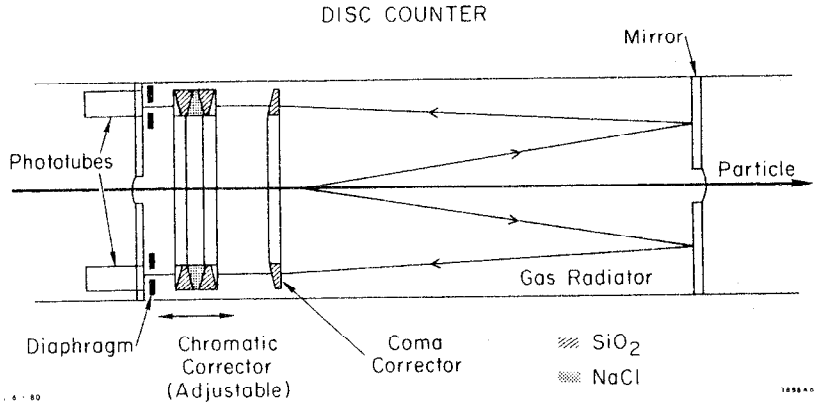

Fig. 9. Gas filled differential Čerenkov counter with optical elements to correct for chromatic aberration and coma.

5. COMPARISON OF DIFFERENTIAL AND THRESHOLD COUNTERS

The differential Čerenkov, operating as it does with larger values of the Čerenkov angle, gives more light for a given length of radiator and hence better $\Delta\beta/\beta$ in general. As shown in Figure 10, this means that the differential counter needed to resolve particles of a given momentum is shorter than the corresponding threshold counter. Other contrasting properties of the two types are listed below.

The differential counter:

- selects specific values of β within a range, $\Delta\beta$,
- imposes severe restrictions on the range of particle directions accepted,
- gives good rejection for unwanted particles.

These properties make the differential Čerenkov most suitable for particle identification in a beam line.

The threshold counter:

- detects all particles with β above threshold,
- can accept a moderate range of directions,
- with segmented optics and detectors it can register several particles simultaneously.
- can operate with the radiator inside a magnet.

The threshold counter is more suited for the detection of particles from an interaction.

6. TRANSITION RADIATION

Equation (2) shows that all Čerenkov counters will have problems at very high momenta, since the error in determining the mass blows up as γ^2. If, instead of determining β, you were able to measure γ

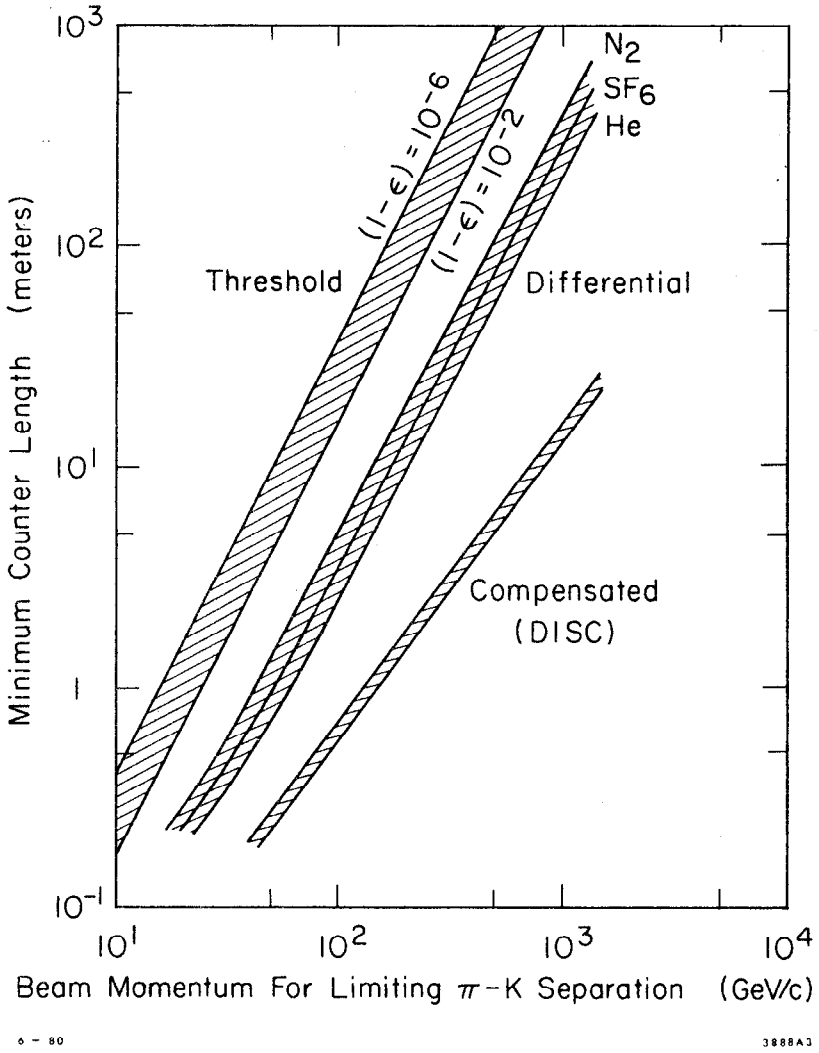

Fig. 10. This plot shows the minimum counter length which permits separation of pions and kaons as a function of momentum, for various counter types. The threshold counter band corresponds to a range of efficiencies ϵ.

directly, then the appropriate relation would be

$$\left(\frac{\Delta m}{m}\right)^2 = \left(\frac{1}{\beta^2}\frac{\Delta\gamma}{\gamma}\right)^2 + \left(\frac{\Delta p}{p}\right)^2 \qquad (14)$$

If $\Delta p/p$ is small, this gives a mass resolution at high momenta which is proportional to $\Delta\gamma/\gamma$. Ideally you would like a detector whose output is proportional to γ, and this is achieved with transition radiation.[9]

Transition radiation is emitted when a charged particle moves from a medium of refractive index, n_1, to a medium of different index, n_2. This may be thought of as due to the apparent acceleration of the charge. When you look at an object in an optically dense medium, such as a fish in a pond, it appears closer to the surface than it really is. If the fish moves steadily toward the surface it would appear to move more slowly than its actual speed. If, further, it manages by some means to continue to move steadily through the surface, then it would appear to accelerate suddenly. A charged particle moving through such an interface will similarly appear to accelerate and consequently will radiate. Unlike Čerenkov radiation, transition radiation can occur in the x-ray region as there is no requirement that n_1 or n_2 need be greater than one, only that they be different. The radiation can consequently be detected in a proportial chamber, which is an efficient, large area detector.

The energy spectrum for transition radiation between a medium and vacuum is[10]

$$\frac{dI}{d\nu} = \frac{e^2\gamma\omega_p}{\pi c}\left[\left(1+2\nu^2\right)\ln\left(1+\frac{1}{\nu^2}\right) - 2\right] \qquad (15)$$

where ω_p is the plasma frequency for the material and $\nu = \omega/\gamma\omega_p$.

The total energy emitted is then

$$I = \int_0^\infty \frac{dI}{d\nu}\, d\nu = \frac{e^2\gamma\omega}{3c} \sim \frac{\gamma}{3\times 137}\,\hbar\omega_p \qquad (16)$$

This is proportional to γ.

The photons originate from a region around the interface, over which the fields are coherent. This is the formation length D. D is of order $\gamma c/\omega_p$, typically $\gamma \times 10^{-6}$ cm. The angular spread of the transition radiation is very small, being of order $\theta \leq 1/n(\omega)\gamma$. Equation (16) gives the energy spectrum from a single interface, but in practice the radiation is emitted from a stack of foils and each foil has two sides. The spectrum is modified by interference effects, as shown in Figure 11(a), most of the energy being radiated near the frequency of the last maximum. As γ increases, the energy spectrum expands in proportion to γ. For the single interface this should continue indefinitely, but for a foil the output saturates when the energy of the last maximum is $\omega_{max} \sim \ell\omega_p^2/2\pi c$, where ℓ is the foil thickness. This saturation occurs because the increasing output from the single interface is accompanied by a proportional increase in the thickness of the formation length. When the formation length is comparable with the foil thickness it can no longer increase and the output saturates. Figure 11(b) shows the saturation of the γ dependence experimentally.[11]

From Equation (16) it may be seen that the number of photons produced per interface is small, of the order of the fine structure constant, 1/137, each photon having energy of the order $\gamma\hbar\omega_p$. To obtain a reasonable signal you need many interfaces, normally in the form of a stack of thin foils, but x-ray absorption in the material sets a

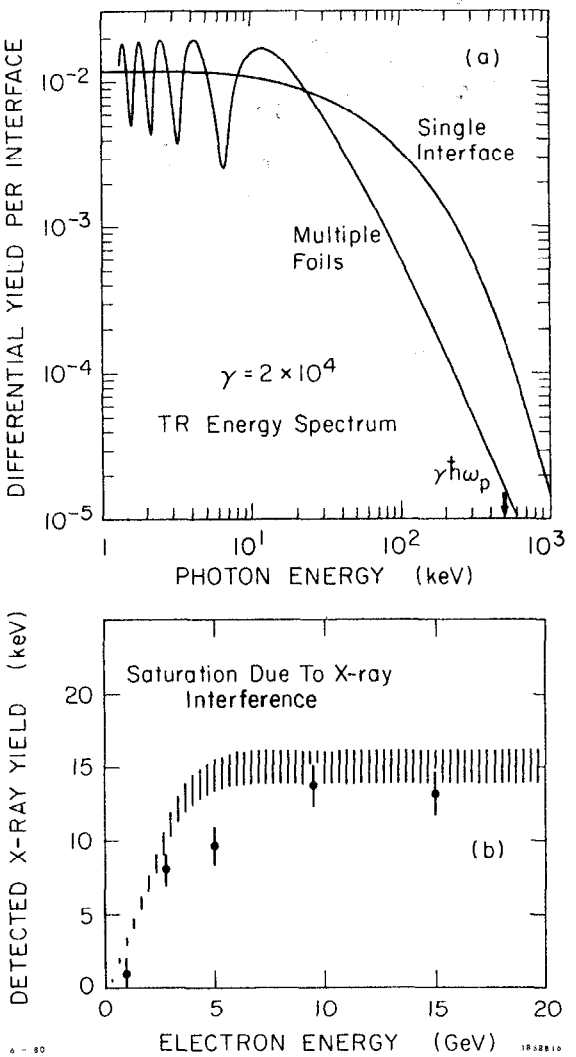

Fig. 11. (a) Transition radiation spectra for radiation from a single interface and from thin foils, showing interference effects. (b) Saturation effect due to foil thickness restricting the formation length.

practical limit on the number. Transition radiation detectors are currently limited by the very low signals obtained. A further problem with transition radiation detection is that the small emission angle means that the T.R. x-rays are not separated from the charged particle in the proportional chamber. You see the T.R. photons plus the ionization loss, dE/dn, for the charged particle.

This superposition of the T.R. photons and the ionizing particle may be avoided by placing a magnet in front of the detector to deflect the particles, as shown in Figure 12(a). In the absence of background due to ionization the x-ray spectrum may be well measured, as in Figure 12(c) which clearly shows interference effects.[12]

Normally the insertion of a deflecting magnet is not practicable and current practice is to optimise the T.R. signal relative to ionization[13] by using Lithium foils of low Z number, to reduce absorption, and thin Xenon filled proportional chambers to detect x-rays with minimum ionization signal. Figure 13 shows the difference in the signal amplitude for pions and electrons of the same momentum.

At present transition radiation detectors are used as electron identifiers,[14] operating with values of γ greater than 10^3 to give a useable signal with acceptable absorption. There is considerable demand for a detector which would identify hadrons at momenta below 100 GeV/c, i.e., with values of γ of the order of 100. The problem here is that the radiation is of lower energy and strongly absorbed. On the other hand, the formation length is small, of the order of a micron, so stacks of very thin foils could be used in principal, though they are difficult to make in practice. Attempts have been made to use polyethylene foams to obtain a large number of interfaces with low mass[15] with

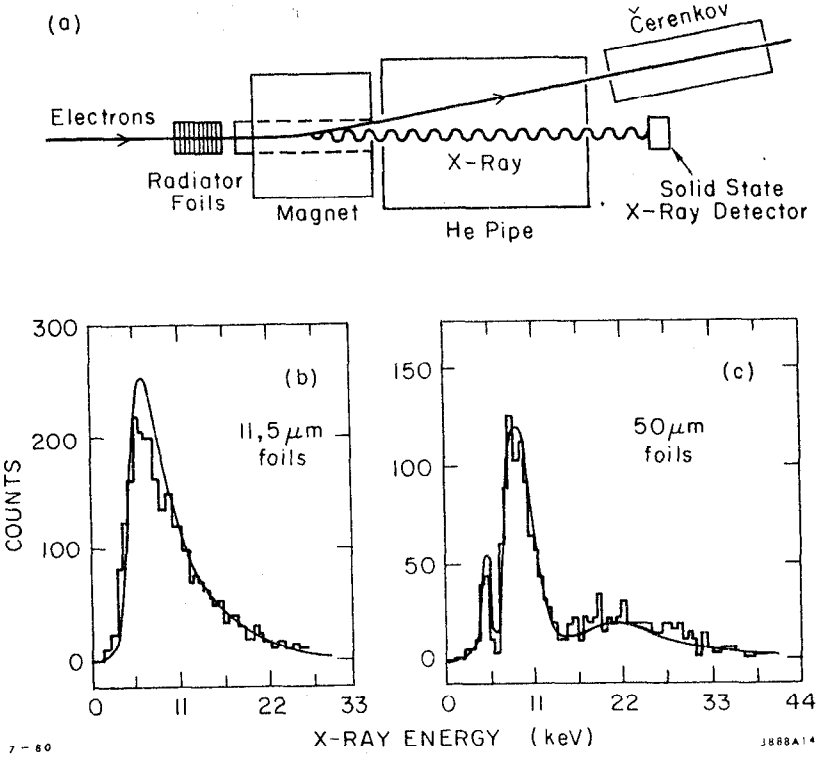

Fig. 12. (a) Detection system with a magnet to sweep particles away from the transition radiation detector; (b,c) show the detailed x-ray energy spectra obtainable.

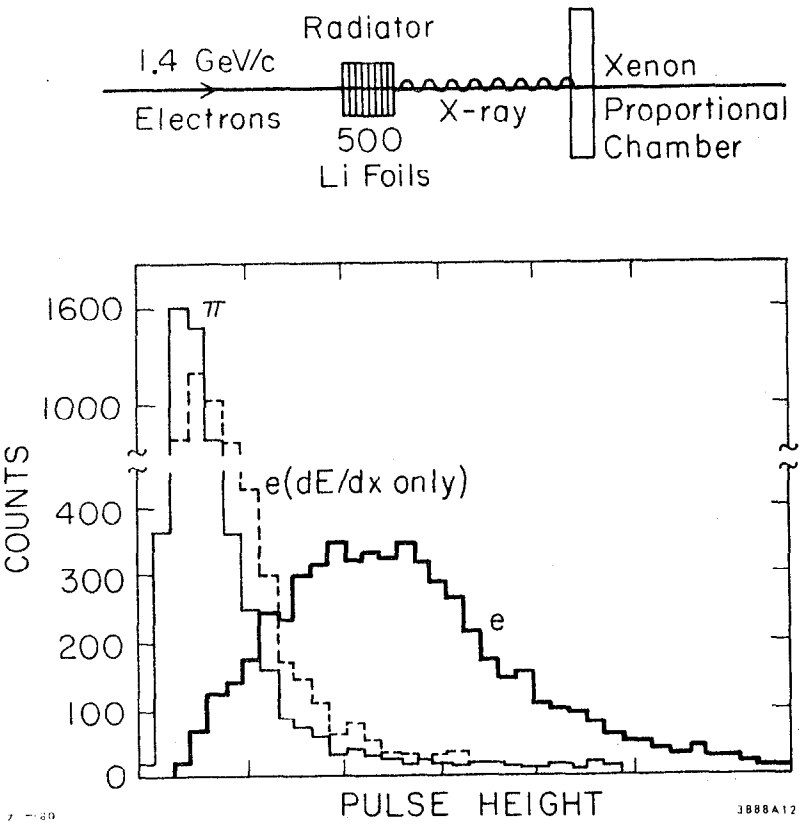

Fig. 13. Practical transition radiation detector with 200 μm Lithium foils; showing a comparison of signals from electrons and pions of 1.4 GeV/c.

some success. Another approach[16] is illustrated in Figure 14, where foils are separated by proportional chambers, so that each gap detects the x-rays produced with minimum absorption. Figure 14(b) shows the separation of protons and pions obtained at p = 200 GeV/c with a total of 18 gaps. With a greater number of gaps and perhaps several thinner foils between each one, it should be possible to obtain hadron separation at 50 GeV/c or lower.

7. RING IMAGING CERENKOV COUNTERS

Transition radiation detectors look good for high momentum particles, but in present high multiplicity events momenta of the order of 10 GeV/c are important and here the Čerenkov counter looks best.

Conventional Čerenkovs have drawbacks when used for identifying scattered particles. The restricted angular acceptance of a differential counter makes it virtually useless. Threshold counters are more practical, but even with molecular construction they are unable to distinguish between multiple particles when they are close together. In neither case does the detector give a measurement of the value of β for a range of possible values. The Čerenkov light contains a great amount of information, it is the detectors which limit it—the objective of the ring imaging Čerenkov is to produce a ring image with a spherical mirror, as in a differential Čerenkov, and then measure the position of each photon detected in this image,[17] as illustrated in Figure 15(a). This requires some form of detector which will give good precision in estimating the coordinates of the detected photons and also have a high efficiency for detecting photons, as the Čerenkov intensity is very low.

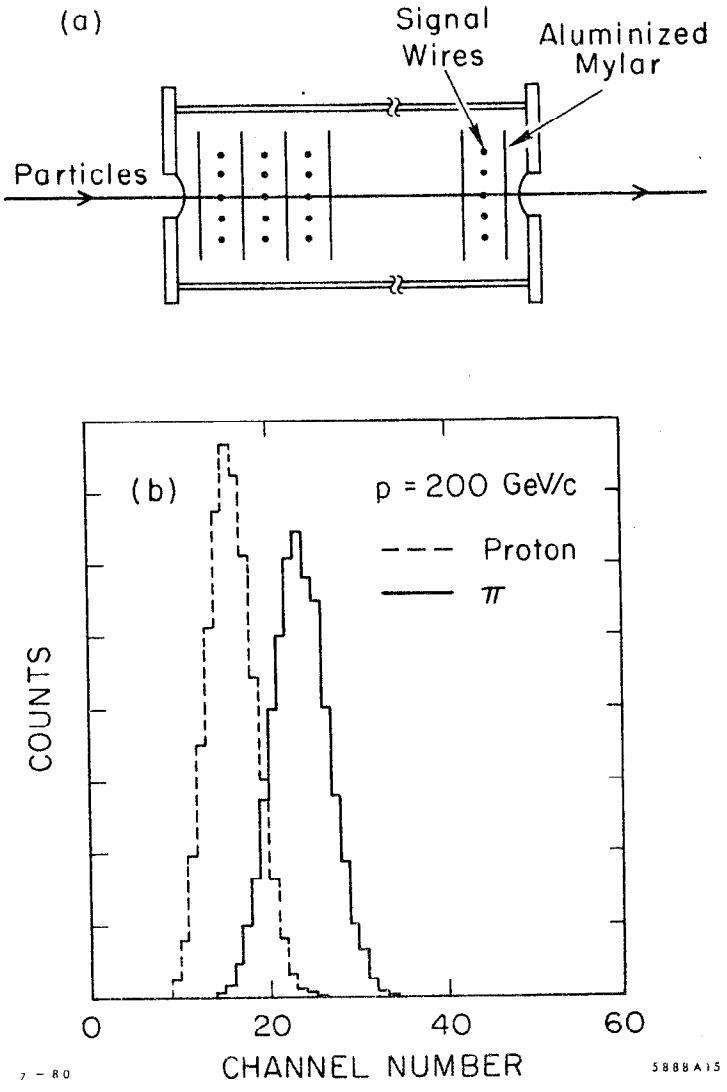

Fig. 14. (a) Prototype detector for hadron separation with 18 proportional chambers, having 4 mm gaps separated by 5 μm foils; (b) shows signals for pions and protons at 200 GeV/c.

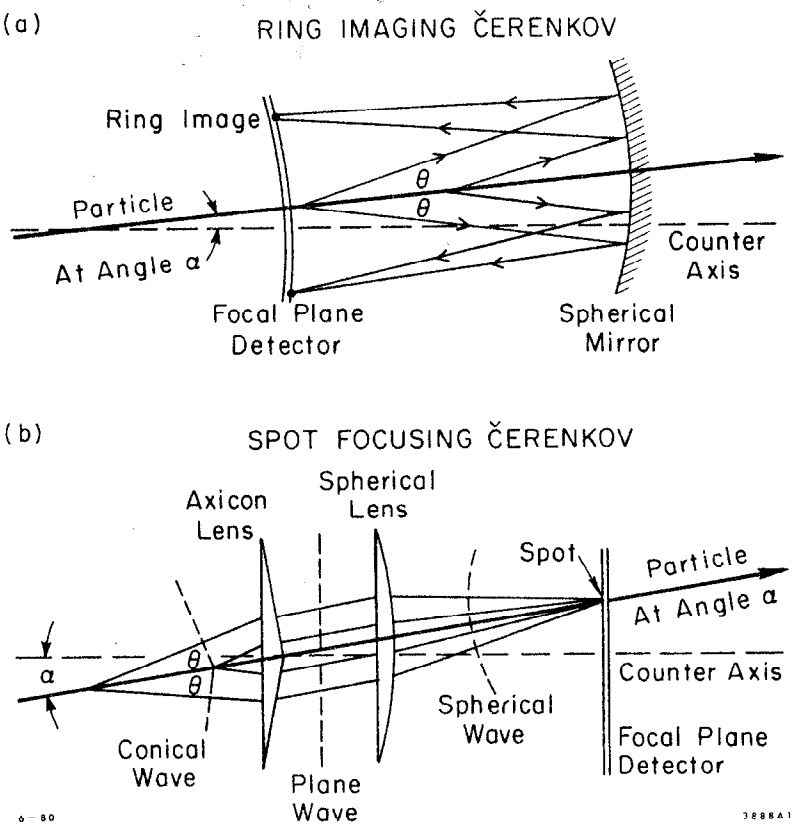

Fig. 15. (a) Principle of ring imaging Čerenkov with detector to measure the position of each photon recorded. (b) Spot focusing detector, which includes an axicon lens to subtract a fixed angle from the Čerenkov cone.

An intermediate concept is the spot focusing detector[18] as shown in Figure 15(b). This in effect subtracts some fixed angle from the Čerenkov cone with the axicon lens, giving a spot image for some preselected β_0. The relative variation of the image size with β around the value β_0 is enhanced, so the detector can be used with a relatively small number of pixels to identify particles with a small range of directions and velocities close to β_0. It is possible to get useable resolution for this device with a matrix of small diameter phototubes, but for the "standard" ring imaging concept, without any axicon lens, a high resolution detector with a much larger number of pixels is required.

The full ring imaging Čerenkov would provide a pattern of detected photons as in Figure 16(a), and fit these to appropriate rings for a number of particles (Figure 16(b)).

(a) This gives a measure of β for each particle detected.

(b) The angular range covered can be large if the mirror and detector are large.

(c) It can in principle resolve particles which are close together. On the other hand there are certain disadvantages. The device is likely to be slow, as the process of fitting rings requires extensive calculation, and it will also be expensive, as it needs an exotic photon detector.

One possibility for detecting the photons is to use an image intensifier[19]—a device with a photocathode similar to a photomultiplier, a microchannel plate to multiply the photoelectrons, and a charge coupled device (CCD) or charge dividing resitive anode[20] to give the coordinates of the photon. Such a system works, and has the advantage of using an established technology, but nevertheless the devices are delicate,

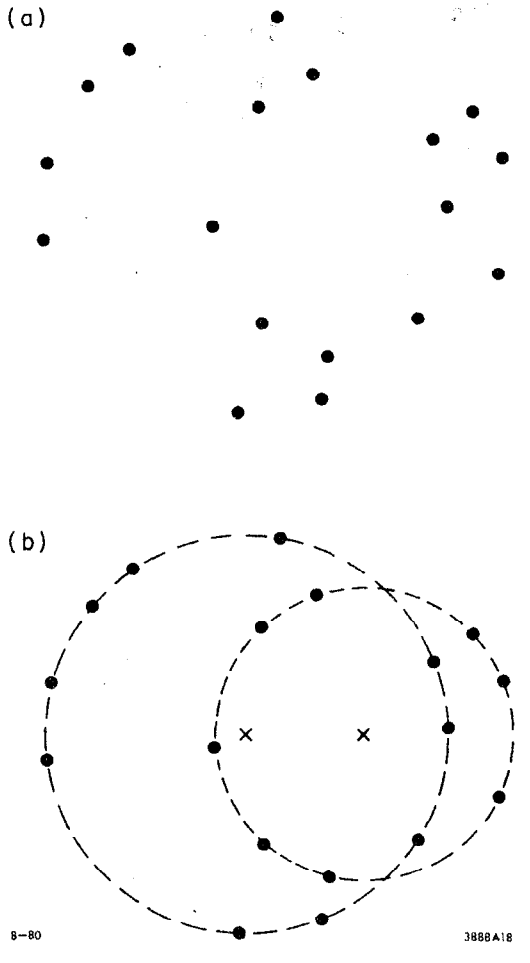

Fig. 16. (a) Possible pattern of detected photons in an imaging Čerenkov; (b) fitted to give Čerenkov ring diameters for two particles.

the quantum efficiency is not as high as for devices using a photoionizing gas, and the detector is small, which requires considerable demagnification of the ring image and limits the angular range of detected particles.

Another approach is the ultraviolet photon detector.[21] The Čerenkov spectrum extends well into the ultraviolet, giving photons with energy of 8 eV and above, which are capable photonionizing some gasses with a quantum efficiency which can be as high as 50%. These can be used in a proportional gas chamber to give a large area detector. The range of photon energies which can be detected is limited by the transmission cut-off of available window materials. Figure 17 shows that detection is possible over a useful band. The radiator also must transmit ultraviolet; in practice Nitrogen and a variety of noble gasses have been used.

The photoionizing gas may be included as the low ionization potential gas for a parallel plate avalanche chamber.[22] These chambers can give good high gain output for single photoelectrons, as shown by the single photoelectron pulse height distribution of Figure 18,[23] and the position of the electron avalanche may be detected by a variety of methods. A ring imaging counter can usefully work with a radiator of fairly high refractive index, such as liquid Helium,[24] giving many simultaneous photoelectrons. This means that the readout system must give a unique x,y position for each avalanche. Any system giving a set of x and y values, such as might be obtained with two crossed multiwire chambers, would give rise to many ambiguities. Possible schemes which have been considered are a multiwire proportional chamber,[25] a spark chamber with optical readout,[26] a multigap avalanche chamber with an

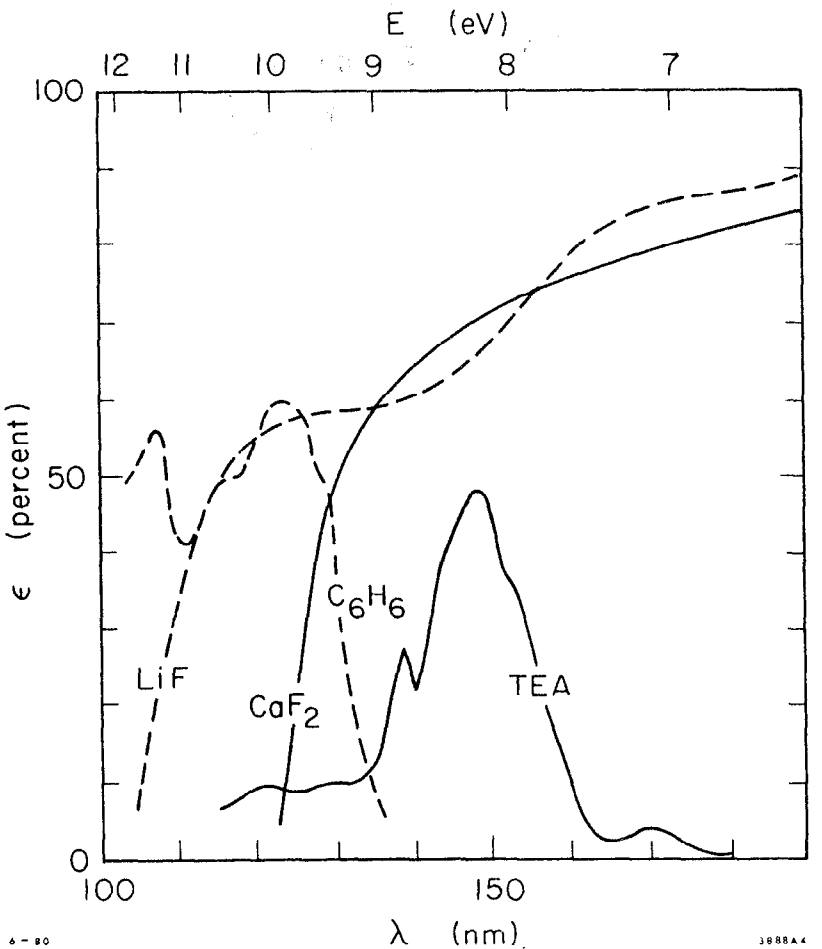

Fig. 17. Variation of photoionizing efficiency and window transmission with photon energy for some materials of interest.

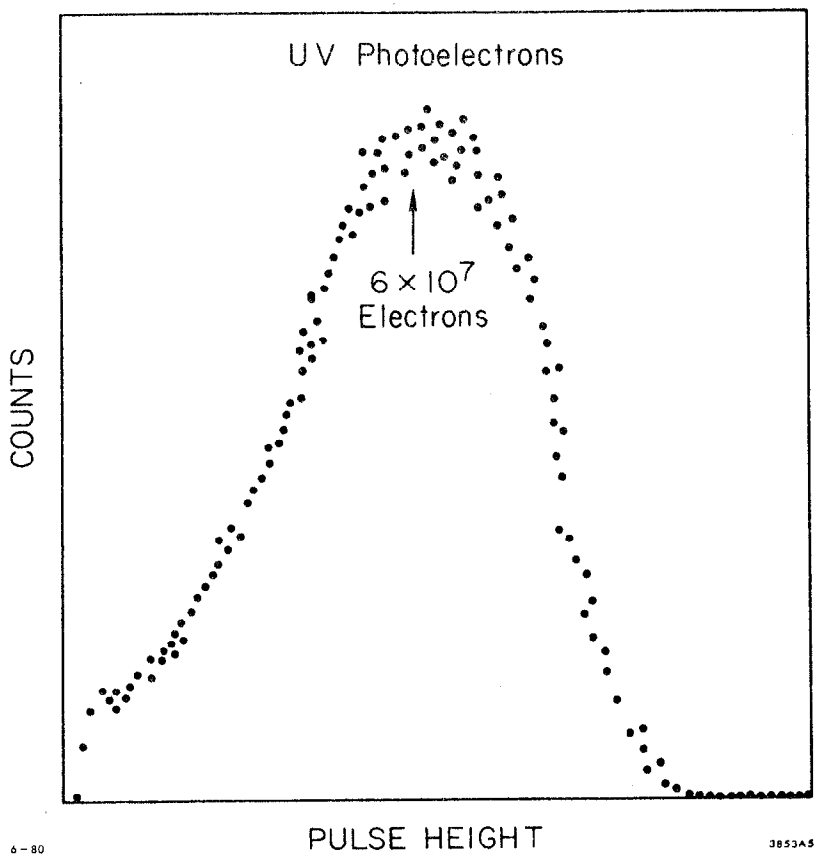

Fig. 18. Pulse height distribution for single photoelectrons amplified in a parallel plate avalanche chamber.

anode divided into small pads,[24] a needle chamber with Geiger amplification at the tips[27] and a lateral drift chamber.[28]

Figure 19 is a diagram of a proposed detector. As with the differential Čerenkov, the ring imaging Čerenkov has its resolution limited by aberration, according to Equation (12). For an ultraviolet detecting counter, chromatic dispersion, $\Delta n/n$, is more serious; for photons of 8 eV in Argon it is twice that in the visible region. The uncertainties in the angular term come from factors similar to those for the conventional differential, save that the slit width is replaced by the geometrical error in measuring the position of the photon and the spread in particle directions by the spread in directions for one particle, i.e., the multiple scattering in the radiator. The effect of these terms on the γ resolution (i.e., mass resolution) for kaons of various momenta is plotted in Figure 20, for a radiator one meter long and a precision of 0.6 mm for the photoelectron position. The liquid Helium line corresponds to $\Delta\beta/\beta$ of 5×10^{-4} and the line for the dense gas to $\Delta\beta/\beta$ of 5×10^{-5}.

The ring detector cannot readily be compensated for chromatic and spherical aberration, as with the DISC, but each detected photoelectron gives a separate measurement, so for N photoelectrons the error is reduced by a factor $1/\sqrt{N}$.

The resolution which might be obtained with a ring imaging detector is compared below with values obtained for other types, all counters being five meters long:

$$\text{Threshold} < 10^{-5}\ ,\quad \text{Differential} \sim 3 \times 10^{-6}\ ,\quad \text{DISC} \sim 4 \times 10^{-7}\ ,$$

$$\text{Ring Detector} < 2 \times 10^{-6}\ \text{(estimated)}\ .$$

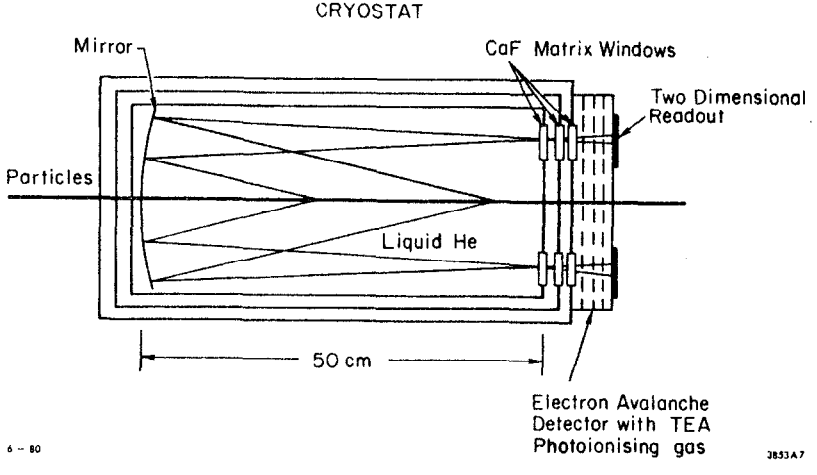

Fig. 19. A proposed prototype detector.

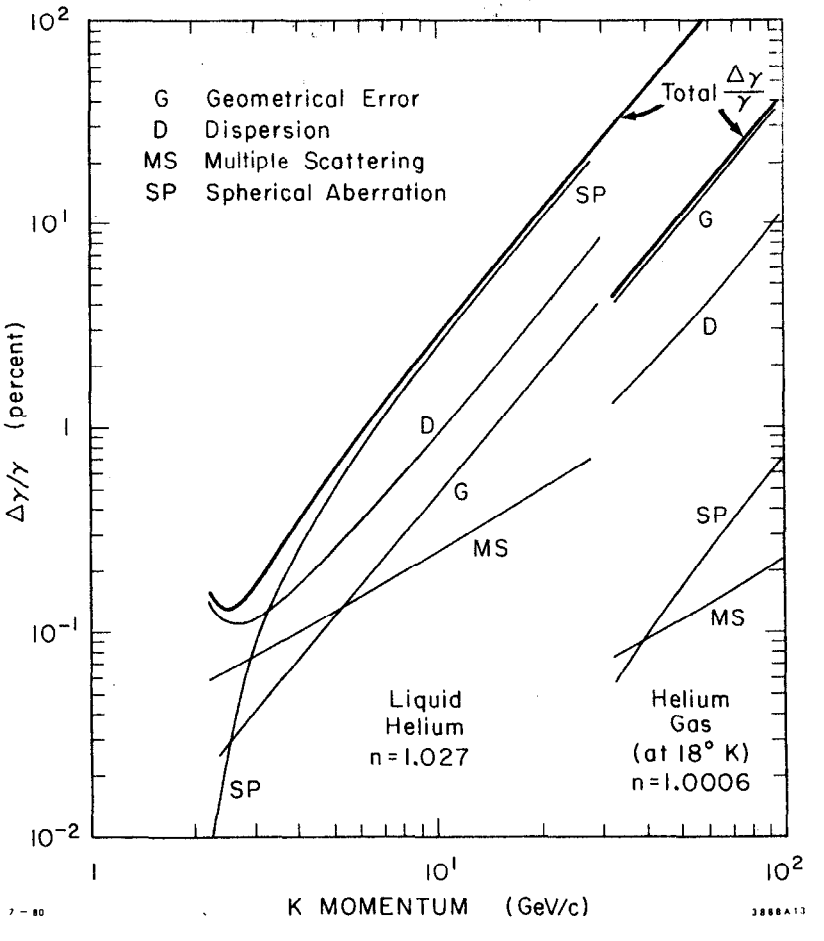

Fig. 20. Comparison of the effect of different sources of aberration on the resolution of an ultraviolet ring imaging Čerenkov counter one meter long, with a photon detector of 0.6 mm resolution.

The value estimated for the ring imaging Čerenkov assumes a low refractive index, with a consequent high β threshold. In practice it would normally be operated with a lower threshold, to give a wide coverage of β, and the resolution would be worse.

The resolution of the imaging Čerenkov is much poorer than that attainable with a compensated differential (DISC). Its advantages are in its wide angular coverage and ability simultaneously to measure the values of β for several particles of different velocities.

8. CONCLUSIONS

The Čerenkov counter has a role as a particle identifier for velocities which are too high for Time-of-Flight to be used, and too low for transition radiation detectors to give a useable signal. In beam lines the compensated differential counter is capable of giving the best resolution, but at high momenta the restriction on the spread of particle directions gives unacceptable limits on the beam acceptance. The transition radiation detectors being developed to identify hadrons at relatively low momentum do not have this restriction and might be used instead.

For particles produced in an interaction, the ring imaging type of Čerenkov should give the best coverage for multiparticle events, but a threshold counter is much simpler, cheaper and faster where it can give adequate separation. Again at high values of γ the resolution of Čerenkov counters will fail and some form of transition radiation detector will be necessary.

REFERENCES

1. J. D. Jackson, Classical Electrodynamics, Second Edition, John Wiley (N. Y.) 1975, p. 638.
2. J. Litt and R. Meunier, Ann. Rev. of Nucl. Sci 23, 1 (1973).
3. M. Cantin et al., Nucl. Instrum. Methods 118, 177 (1974); P. J. Carlson, K. E. Johansson and J. Norrby, IEEE Trans. on Nucl. Sci. NS-27, 96 (1980).
4. S. P. Denisov et al., Nucl. Instrum. Methods 85, 101 (1970).
5. P. Baillon et al., Nucl. Instrum. Methods 126, 319 (1975); P. J. Carlson, Nucl. Instrum. Methods 158, 403 (1979).
6. B. Alper et al., Phys. Lett. B94, 422 (1980).
7. S. P. Denisov et al., Nucl. Instrum. Methods 92, 77 (1971).
8. R. Meuniér, NAL Summer Study Rep SS/170, 85 (1970); C. Bovet, S. Milner, A. Placci, IEEE Trans. Nucl. Sci. NS-25, 572 (1978).
9. Proceedings of International Symposium on Transition Radiation of High Energy Particles, Yerevan, 1977; S. Iwata, report DPNU-31-79 (1979).
10. J. D. Jackson, op. cit., p. 691.
11. M. L. Cherry, G. Hartman, D. Müller and T. A. Prince, Phys. Rev. D10, 10 (1974).
12. C. W. Fabjan and W. Struczinski, Phys. Lett. 57B, 483 (1975).
13. J. Fischer et al., Nucl. Instrum. Methods 127, 525 (1975).
14. J. Cobb et al., Nucl. Instrum. Methods 140, 413 (1977).
15. C. W. Fabjan, Proceedings of International Symposium on Transition Radiation of High Energy Particles, Yerevan, 1977, p. 256.
16. A. G. Oganessian et al., Nucl. Instrum. Methods 145, 251 (1977).
17. A. Roberts, Rev. Sci. Instrum. 31, 579 (1960).
18. M. Benot, J. M. Howie, J. Litt and R. Meuniér, Nucl. Instrum. Methods 111, 397 (1973); M. Benot, J. C. Bertrand, A. Maurer and R. Meuniér CERN report CERN-EP/79-51.

19. B. Robinson, Report UPR-76E (1980), submitted to the Conference on Experimentation at LEP, Uppsala, 1980.

20. J. L. Alberi and V. Radeka, IEEE Trans. on Nucl. Sci., NS-23, 251 (1976).
J. W. Stümpel, P. W. Sanford, and H. F. Goddard, Journal of Physics E, 397 (1973).

21. J. Seguinot and T. Ypsilantis, Nucl. Instrum. Methods 142, 377 (1977).

22. G. Charpak and F. Sauli, Phys. Letters 78B, 523 (1978);
A. Breskin et al., Nucl. Instrum. Methods 161, 19 (1979).

23. R. S. Gilmore, D.W.G.S. Leith, S. H. Williams, paper submitted to IEEE 1980 Nuclear Science Symposium.

24. S. H. Williams, D.W.G.S. Leith, M. Poppe and T. Ypsilantis, IEEE Trans. on Nucl. Sci. NS-27, 91 (1980).

25. J. Seguinot, J. Tocqueville and T. Ypsilantis, Nucl. Instrum. Methods 173, 283 (1980).

26. G. Charpak, S. Majewski, G. Melchart, F. Sauli and T. Ypsilantis, Nucl. Instrum. Methods 164, 419 (1979).

27. G. Comby and P. Mangeot, IEEE Trans. on Nucl. Sci. NS-27, 111 (1980).

28. T. Ekelöf, J. Seguinot, J. Tocqueville and T. Ypsilantis, paper submitted to the International Conference on Experimentation at LEP, Uppsala, 1980.

TIME-OF-FLIGHT MEASUREMENTS*

William B. Atwood
Stanford Linear Accelerator Center
Stanford University, Stanford, California 94305

*Work supported by the Department of Energy, contract DE-AC03-76SF00515.

I. INTRODUCTION

Time of flight (TOF) measurements are used in high energy particle physics experiments to: 1) distinguish background from events and 2) identify particle types. An example of background separation is shown in Fig. 1.[1] These data come from a coincidence electro-production experiment performed at SLAC. The reaction being studied was $e + p \rightarrow e' + p' + X$ where the e(p) stand for an initial and detected electron (proton) and X is a produced but undetected final state with a mass in the ρ meson region. Plotted in Fig. 1 is the relative time between the detection of an electron and a proton in two of the spectrometers in End Station A. Data for two different kinematic settings taken in the experiment are shown. The time resolution has been partially corrected for the various flight paths through the instruments and the difference in time resolutions between the two settings results mainly from the incompleteness of this correction. The signal height above the background depends on the time resolution, $\Delta\tau$. The chance background is proportional to the product of the electron counting rate, the proton counting rate and $\Delta\tau$. Smaller $\Delta\tau$ means that higher electron and proton counting rates may be tolerated and result in a similar signal-to-noise ratio.

The second use of TOF measurements is to identify particle types. To utilize TOF measurements for particle identification requires that the momentum, p, of the particle also be measured. The time of flight difference for two particles of unequal mass is

$$\tau_1 - \tau_2 = \frac{\tau_o}{2}\left(\frac{M_1^2 - M_2^2}{p^2}\right) \qquad (1)$$

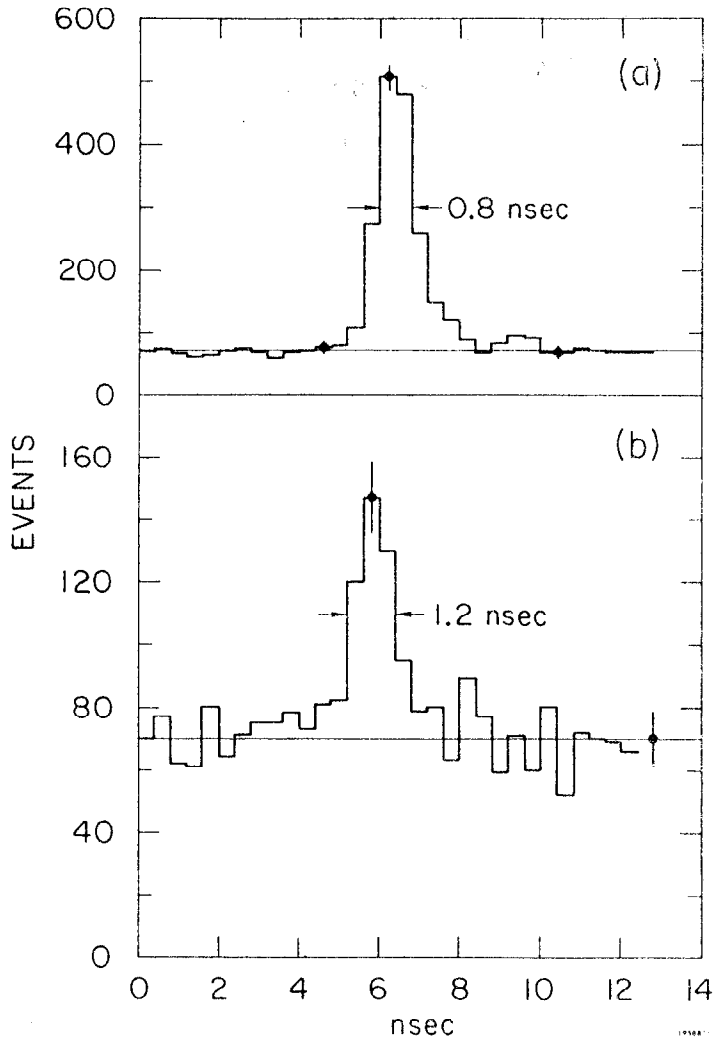

Fig. 1. Elimination of random background in $ep \rightarrow e'p'X$ using timing correlation. Plots (a) and (b) are two different kinematic settings.

where τ_o is the time for a particle travelling at the speed of light to traverse the same flight path (e.g., $\tau_o = d/c$ where d is the length of the flight path and c is the speed of flight.) Formula (1) has been used to produce the curves shown in Fig. 2 for various pairs of particles versus momentum. For these calculations a flight path of 1.5 meters was used ($t_o \simeq 5$ nsec) as this is a representative length for detectors used at storage rings.

The particle's mass is calculated using

$$M^2 = p^2\left(\frac{\tau^2}{\tau_o^2} - 1\right) \tag{2a}$$

and has an uncertainty of

$$\Delta M^2 = 2p^2\sqrt{\frac{M^2}{p^2} + 1}\left(\frac{\Delta\tau}{\tau_o}\right) \tag{2b}$$

due to the precision of the measurement of τ, $\Delta\tau$. Formula (2b) shows that particle identification using TOF measurements becomes worse as the square of the particle's momentum. To achieve the same mass resolution (and therefore the same level of particle identification) at twice the momentum requires a four-fold improvement in the TOF measurement ($\Delta\tau$ must be decreased by a factor of 4.)

To illustrate this technique, in Fig. 3 data from the Mark II collaboration are shown.[2] Clear bands of events occur at low momentum for π's, K's and P's. As the momentum is increased the bands broaden and eventually merge together at about 1 GeV/c. The TOF resolution for the counters used by the Mark II is quoted to be 300 psec for hadrons averaged over the entire system.

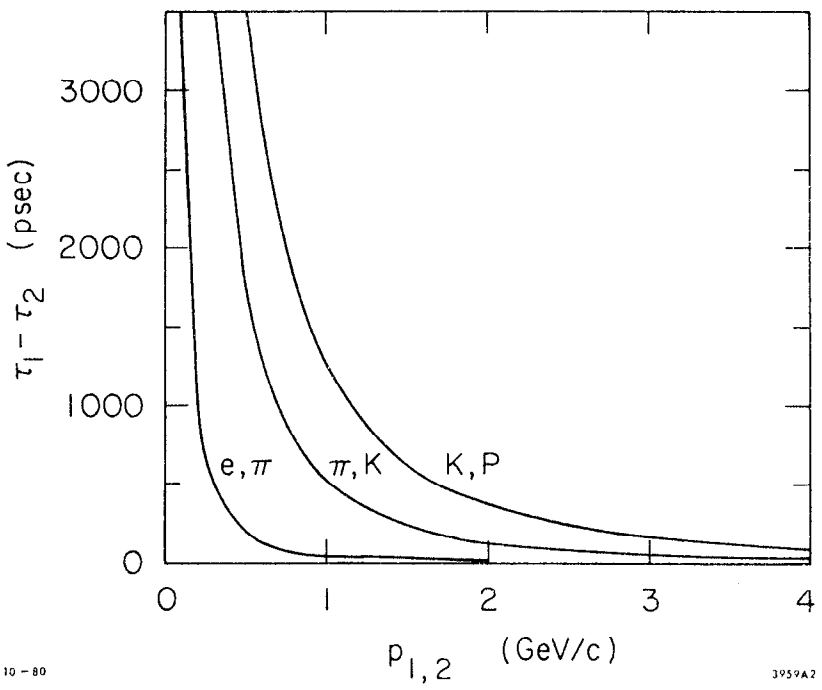

Fig. 2. Time-of-flight differences for various pairs of particles over a 1.5 m flight path versus momentum.

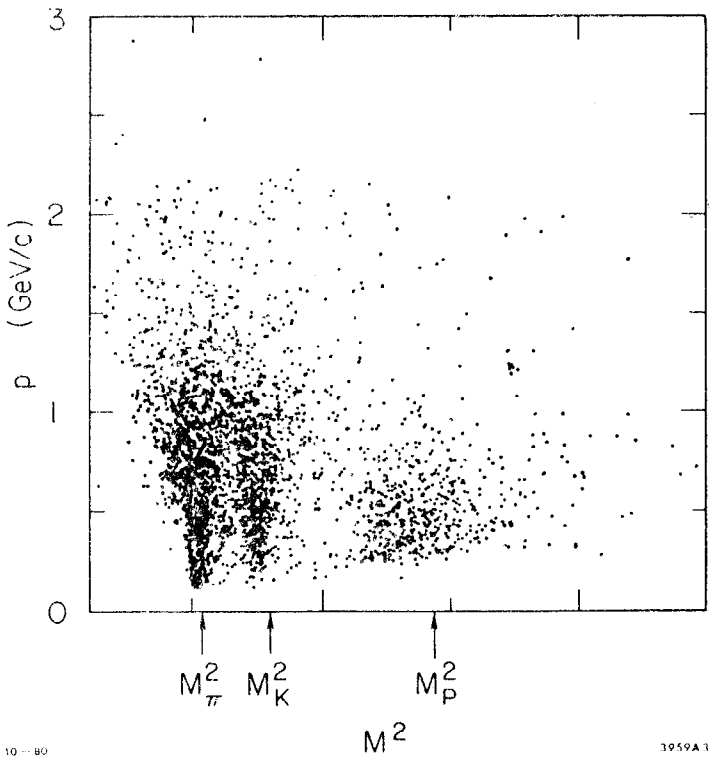

Fig. 3. Particle identification using time-of-flight and momentum measurements.

To place TOF measurements in perspective with other techniques for particle identification it is convenient to use the covariant velocity, $\eta(\equiv p/M)$. Using TOF measurements particles will be separable when

$$\eta \lesssim \sqrt{\frac{\tau_o}{2\Delta\tau}} \quad . \tag{3a}$$

Threshold Čerenkov counters will respond for

$$\eta \gtrsim \sqrt{\frac{1}{n^2 - 1}} \tag{3b}$$

where n is the index of refraction of the Čerenkov radiating medium. Energy deposition measurements (dE/dx) also scale in η and these three techniques for particle identification are shown in Fig. 4 versus η. Particles with η's to the right of the curve in Fig. 4a will be well identified. For threshold Čerenkov counters the range in momentum over which particles will be separated is $p_1 - p_2 = \eta(M_1 - M_2)$. For dE/dx measurements the range in momentum over which particles will be identified can be estimated by rescaling Fig. 4c by the appropriate particle masses; each particle type gives the same dE/dx curve shifted by an amount proportional to its mass. As such the curves for electrons, pions, kaons, and protons cross over each other in the momentum range of .8 GeV/c - 2 GeV/c.

π/K separation as a function of momentum and η is shown in Fig. 5 for these three techniques. This figure shows that the region where TOF measurements can play an important role is between 800 MeV/c and 2.0 GeV/c. This region is also covered by aerogel Čerenkov counters, but the advantage of being able to distinguish backgrounds (such as cosmic rays) from events and achievable granularity of detectors makes TOF measurements the method of choice for most experiments.

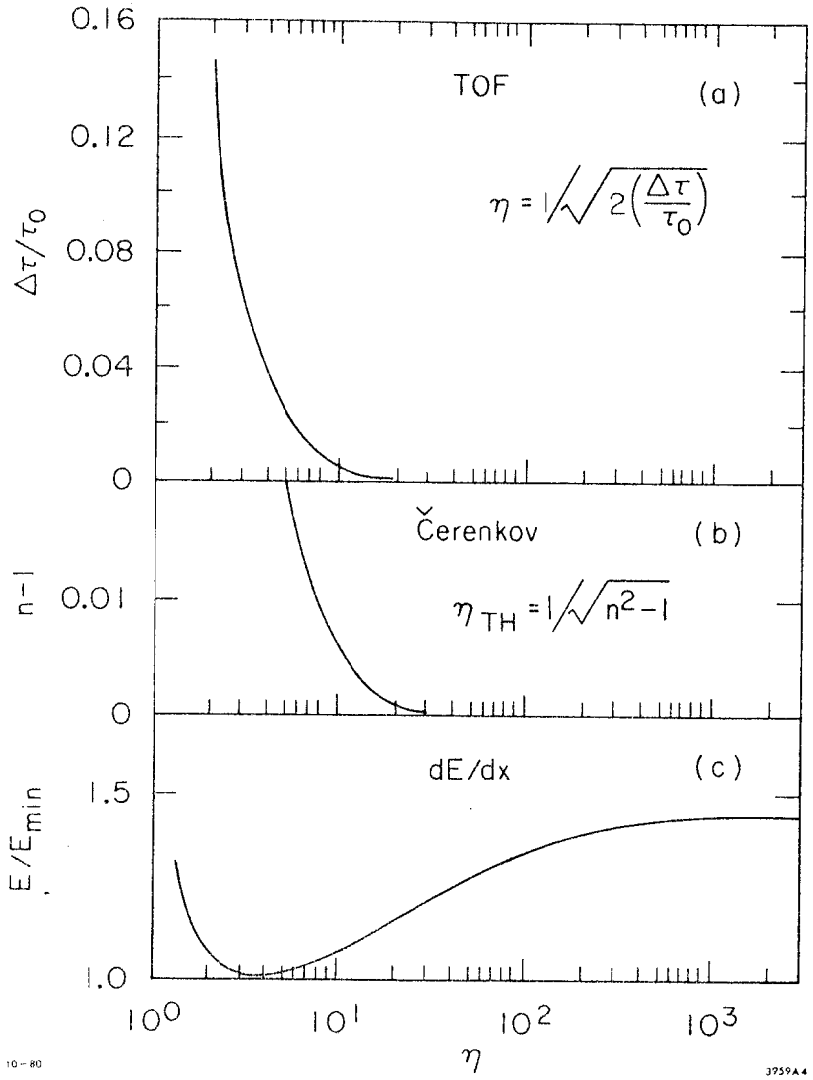

Fig. 4. Three techniques for particle identification:
(a) time-of-flight;
(b) threshold Čerenkov (n is the index of refraction); and
(c) dE/dx measurement.
The variable η is the covariant velocity $|\vec{p}|/M$.

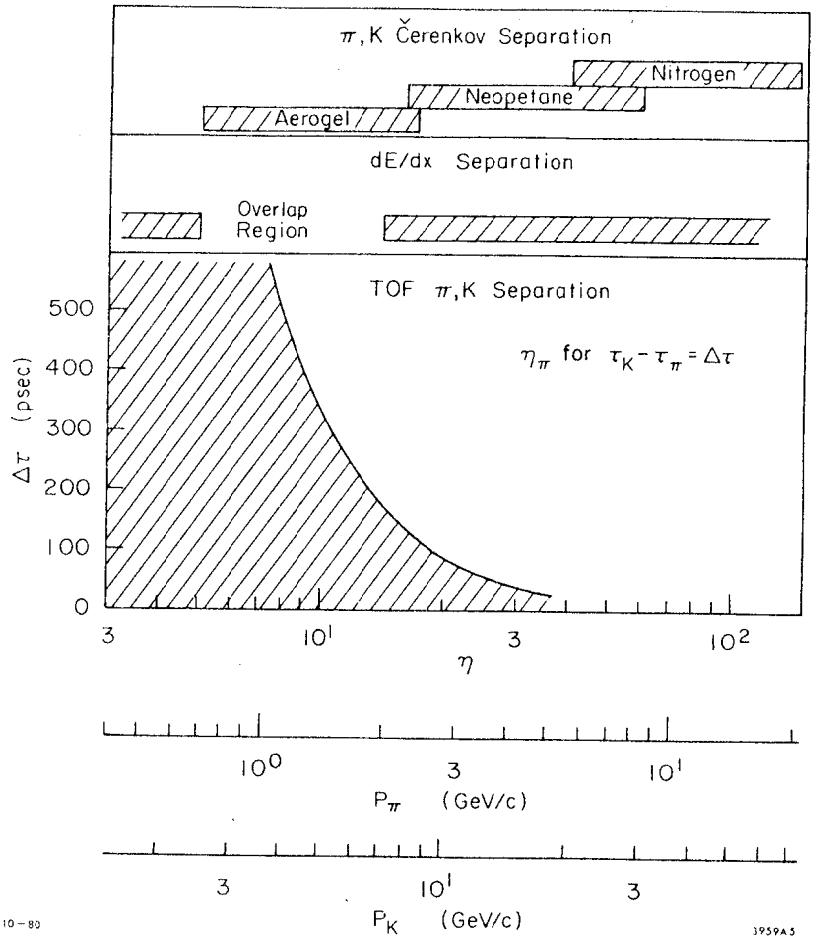

Fig. 5. π, K separation by 3 techniques.

In the following sections of these notes I will review two techniques for making TOF measurements: 1) conventional scintillation counters and 2) planar spark counters (PSC's).

II. SCINTILLATION COUNTERS

A typical scintillation counter is shown schematically in Fig. 6. The signals from each photomultiplier are pulse height analyzed. Its time of arrival is measured by first transforming it to a standard logic pulse in a discriminator and then using this pulse to stop a fast digital clock (TDC). If t_1 and t_2 are the respective signal arrival times from the discriminators connected to each end of the scintillator, then the location along the scintillator where the particle penetrated the counter is given by

$$x = \left(\frac{t_1 - t_2}{2}\right) v_{eff} \quad . \tag{4a}$$

v_{eff} is the effective propagation velocity of light in the scintillator and $t_{1,2}$ are assumed to be corrected for additive constants arising from delay cables, the photomultiplier delay time, light pipe delay time, etc. The time of penetration is

$$\tau = \left(\frac{t_1 + t_2}{2}\right) - \frac{L}{2v_{eff}} \tag{4b}$$

where L is the length of the scintillator. From Eq. (4a) we see that x is independent of τ and similarly from (4b) that τ is independent of x.

Now let us consider what some of the sources for fluctuation in τ may be. The scintillator light results from energy deposited by particles that penetrate it. Approximately one photon is produced for every 100 electron volts of energy deposited. For plastic scintillator a

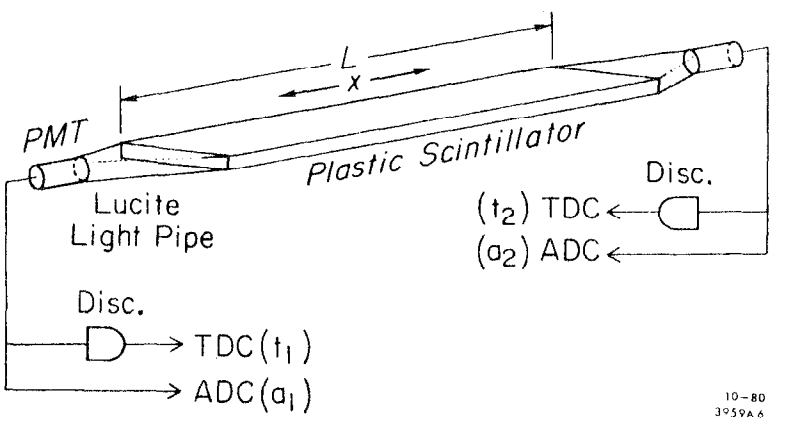

Fig. 6. Schematic diagram for a plastic scintillator, time-of-flight counter.

minimum of 2 MeV of energy is deposited per cm travelled for particles with unit charge which results in about 20,000 photons/cm being produced.

The time distribution for the light produced in three different types of scintillators is shown in Fig. 7 along with the time spectrum for Čerenkov light produced in lucite.[3] The latter is used to calibrate the response of the measuring apparatus.

The light pulses generated by the three scintillators shown in Fig. 7 are similar and a quantitative comparison is given in Table I.[3] Most groups building scintillator counter TOF systems have chosen NE110 or PILOT F. No significant difference in performance of these systems has been demonstrated.

After the light is produced it is transmitted to the photomultiplier via the scintillator plastic and a light pipe couples the round face of the phototube onto the usually rectangular scintillator cross-section. A calculation of the number of photoelectrons resulting from light that undergoes no bounces for typical counters (L = 300 cm × 2.5 cm thick) results in less than one. In fact much of the light bounces down the scintillator and light pipe at angles not much smaller than the total internal reflection angle. The "straight shot" light produced in the middle of the counter will require a time,

$$t_{min} = \frac{L}{2} \cdot \frac{n}{c} \qquad (5a)$$

to reach the light pipe. In Eq. (5a) n is the index of refraction for the scintillator and is approximately equal to 1.58. If the maximum angle away from the "straight shot" direction that light can make is given by the total internal reflection angle, $\Theta_{INT} = \sin^{-1}\left(\frac{1}{n}\right)$, then the maximum time for light transmission is

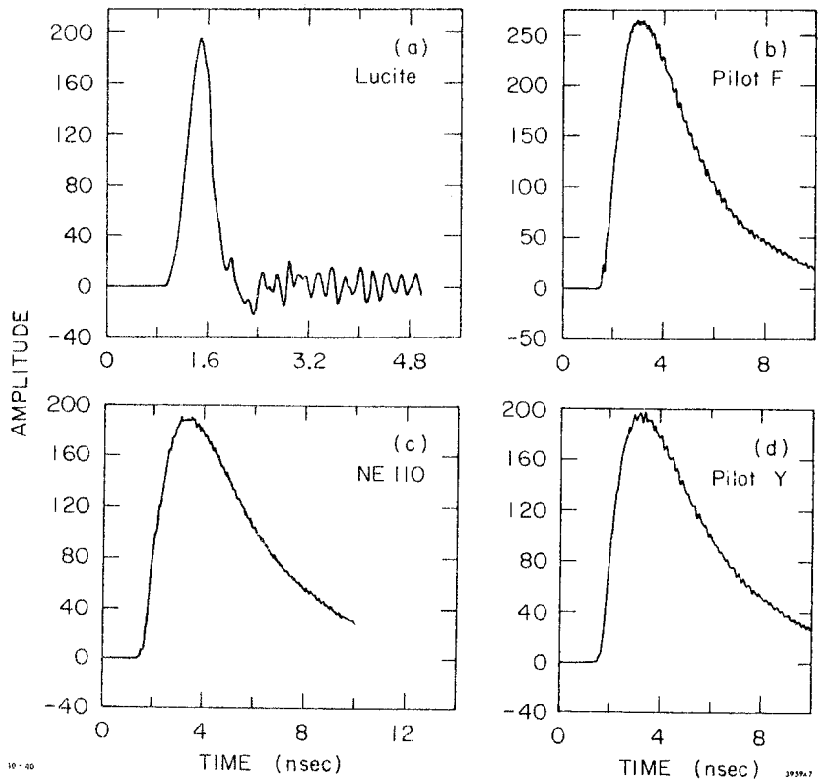

Fig. 7. Relative light output from various plastic scintillators. (a) shows the response of lucite used as a Čerenkov radiator for comparison.

TABLE I

Numerical evaluation of the plastic scintillators shown in Ref. 7.

Scintillator	Rel. Light Output	Rise Time (nsec)	Time for 10-90% Light Output (nsec)
Lucite	.05	.31	.51
PILOT F	1.00	.81	4.65
NE110	.88	.99	5.22
PILOT Y	.86	.88	5.13

$$t_{max} = \left(\frac{1}{\cos\theta_{INT}}\right) t_{min} \simeq 1.3\ t_{min} \quad . \tag{5b}$$

Equations (5a) and (5b) show that the light emerges over a time interval approximately equal to .3 t_{min}. This time interval is proportional to the length of the scintillator, L. As such the density of photons per unit time decreases as 1/L.

The effective transit time for light in scintillator TOF counters is measured by plotting the time difference $\left(\frac{t_1 - t_2}{2}\right.$ from Eq. (4a)$\left.\right)$ versus the measured position of penetration for particles. The result is shown in Fig. 8.[4] The data have been fit to a straight line and the slope measures the effective velocity of light in the scintillator. v_{eff} is found by this technique to be 16.3 cm/nsec. This value for v_{eff} is also found by others.[2] From this value we can calculate the typical angle away from the "straight shot" direction by

$$\cos\theta_{eff} = \frac{v_{eff}}{c/n} \simeq .84 \tag{6}$$

which gives $\theta_{eff} \cong 33°$ (compare to $\theta_{INT} \cong 39°$). In typical counters the light will have been internally reflected some 30 times before reaching the light pipe. This implies that the surface quality of the scintillator is very important.

The light pipe transmits the light emerging from the scintillator onto the photocathode. Usually the area of the photocathode is small compared to the cross-sectional area of the scintillator. Light will be lost in making this transition, but its important that these losses be minimized and uniform over the cross-section of the scintillator and that the transit time from all points on the end of the scintillator to the

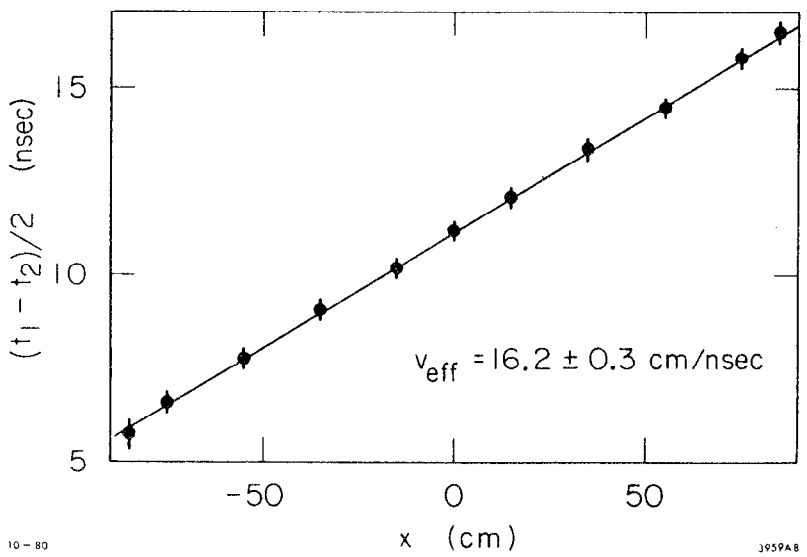

Fig. 8. Time difference versus position for a plastic scintillation counter.

photocathode be approximately equal. Monte Carlo computer programs are useful in modeling and optimizing the design of this piece of the system.[5]

The phototube produces the electrical signal that is measured by the electronics. Photons incident in the photocathode cause the emission of "photo-electrons" which are collected on the first of many dynode stages. These act as cascaded amplifiers. The time between light striking the photocathode to an output signal is about 30 nsec. Time jitter in phototubes comes about principally from different transit times of photoelectrons from different locations on the photocathode. These time differences have been measured to be about 190 psec for 2" tubes.[6] If a large number of photons strike the photocathode this jitter is reduced (for 100-photoelectrons the jitter is about 64 psec). To minimize this effect care should be used in designing the base for the phototube. The focussing elements between the photocathode and the first dynode have a significant effect on the time jitter. The voltage drop between the photocathode - first dynode is also important and a change of one part in a thousand can change the delay time by 20 psec. Some experimenters choose to stabilize this voltage drop by using zener diodes.[4]

The signals coming from the phototubes are processed by fast electronics producing a time of arrival and a measurement of the integrated charge in the pulse. Other schemes have been used, but this one is the most common and simplest to describe. It has been observed that the time of arrival is correlated with the pulse height. The principal correlation is sometimes modelled[4] to be

$$\tau = t - W\left(\frac{1}{\sqrt{a_o}} - \frac{1}{\sqrt{a}}\right) - \frac{x}{v_{eff}} \qquad (7)$$

where τ is the corrected time, t is the measured time minus any constant effects, W is a fitted parameter, a_o is a reference pulse height, a is the measured pulse height and x/v_{eff} is the position correction due to the delay time for light to travel down the scintillator. An example of $\frac{1}{\sqrt{a}}$ versus t is shown in Fig. 9.[4] The line in Fig. 9 indicates the fit for the parameter W.

Another method was proposed by M. Wollstadt[7] in which the dV/dt of the leading edge of the phototube pulse is measured. This is accomplished by using two discriminators with different threshold voltages, each connected to fast a TDC. The corrected time is then calculated by linearly extrapolating to V = 0. The impressively good results of Wollstadt using this method have not been successfully applied universally. Some report good success while others report no improvement.

We have now reviewed the major aspects of scintillation counter TOF systems and will now compare the results achieved by various groups. The discussion about how the light emerges from the scintillator indicated that the density of photo-electrons per unit time would be proportional to (N_e/L) where N_e is the average number of photo-electrons and L is the counter's length. I conjecture that the time resolution will be proportional to $(1/\sqrt{N_e/L})$ if the contribution from the phototube and electronics is negligible. The data for nine different counters is given in Table II. The time resolutions quoted are for particles crossing near the center of the counters and have been fully corrected for amplitude and position effects. In Fig. 10 these best time resolutions are plotted against $\sqrt{L/N_e}$. The straight line in Fig. 10 indicates the following "rule-of-thumb":

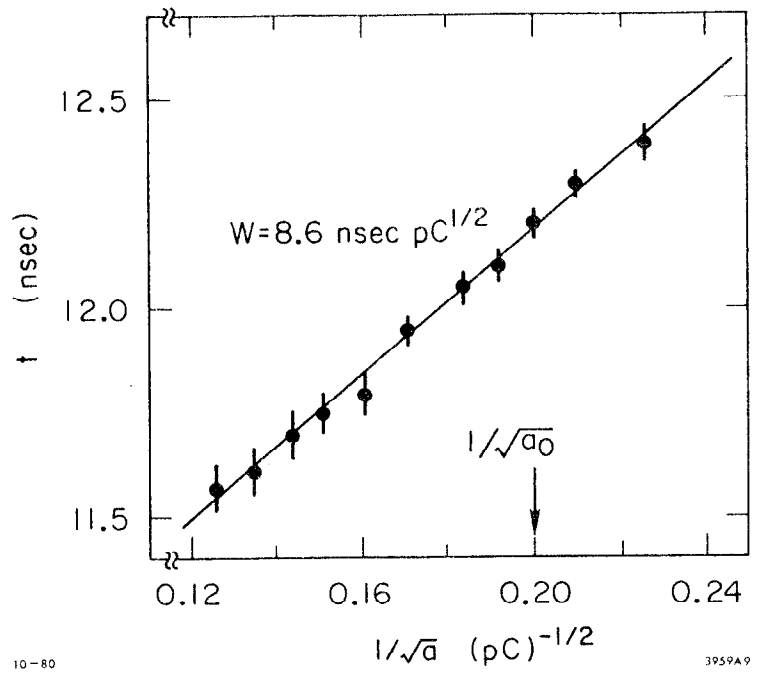

Fig. 9. Time correlation with pulse height a. a_0 is a reference pulse height.

TABLE II

Comparison of nine time-of-flight counters. L is the counter length and N_e is the average number of photo-electrons for minimum ionizing particles. Photoelectron yields which are starred (*) are my estimates based on the thickness of the scintillators. This was done when this information was unavailable from the references.

Counter	L(cm)	N_e	$\Delta\tau$(psec)
1) MARK II[2]	350	40	255
2) "Free Quark Search" (PEP-14)	315	90	166
3) DASP[4]	172	28*	212
4) F. Binon et al., N.I.M., 153, 409 (1978)	25	28*	92
5) M. Wollstadt[7]	100	39*	144
6) M. Wollstadt[7]	50	16*	152
7) MARK III[5]	300	120	140
8) M. Wollstadt[7]	100	260*	85
9) Same as 4)	~.2	4500*	48

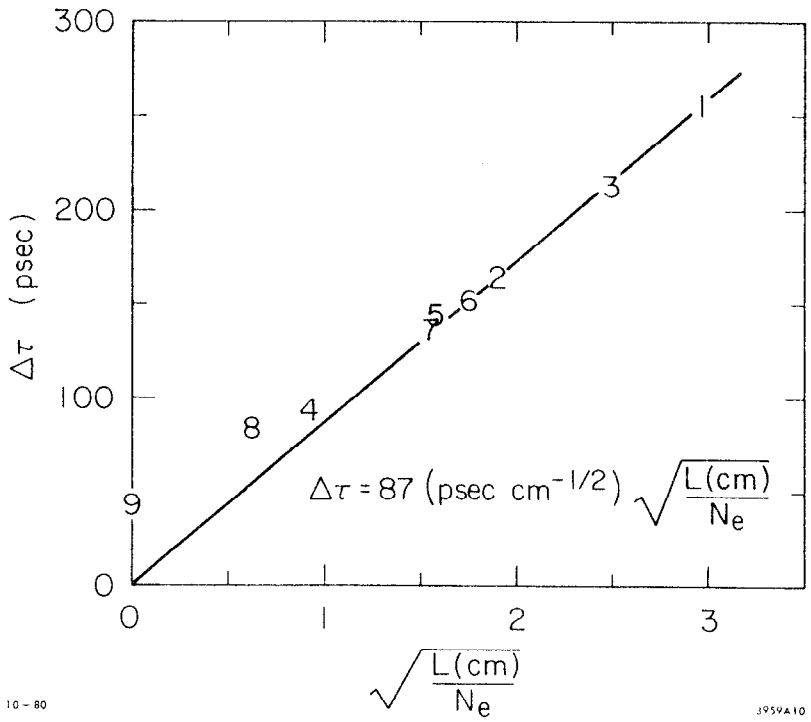

Fig. 10. A comparison of the time-of-flight counters listed in Table II. L is the length of the counter and N_e is the average photo-electron yield for minimum ionizing particles.

$$\Delta\tau = 87(\text{psec-cm}^{-\frac{1}{2}})\sqrt{\frac{L(\text{cm})}{N_e}} \quad . \tag{8}$$

Results from counters with expected resolutions $\gtrsim$ 100 psec agree well with Eq. (8). Below the 100 psec level other effects such as the photo-tube jitter certainly will contribute and will dominate the time resolution.

I have glossed over many important points and hope this will serve as an introduction to scintillation TOF systems. I have not described the necessary calibration procedures for large systems. Experimenters designing and constructing TOF systems are referred to the references I have given and should talk to these authors directly. The details of how they accomplished the results given in Table II are important.

III. PLANAR SPARK COUNTERS

Planar spark counters (PSC's) are considerably older particle detectors than plastic scintillators. J. Keuffel at CALTECH is usually given credit for their invention in 1949.[8] I will not describe the history of the development of these counters and refer interested people to the references. A major advance was the introduction of high resistance semi-conducting glass for one of the electrode surfaces. This glass sufficiently limits the discharges to minimize damage to the electrode surface.

A PSC is shown schematically in Fig. 11. The anode is made of semi-conducting glass with a volume resistance of 10^9 - 10^{10} Ω-cm.[9] Typical anodes used in test counters have had an area 9 cm × 9 cm to 30 cm × 30 cm and were 5 to 8 mm thick. The large flat surfaces are ground flat and polished. All corners and edges are

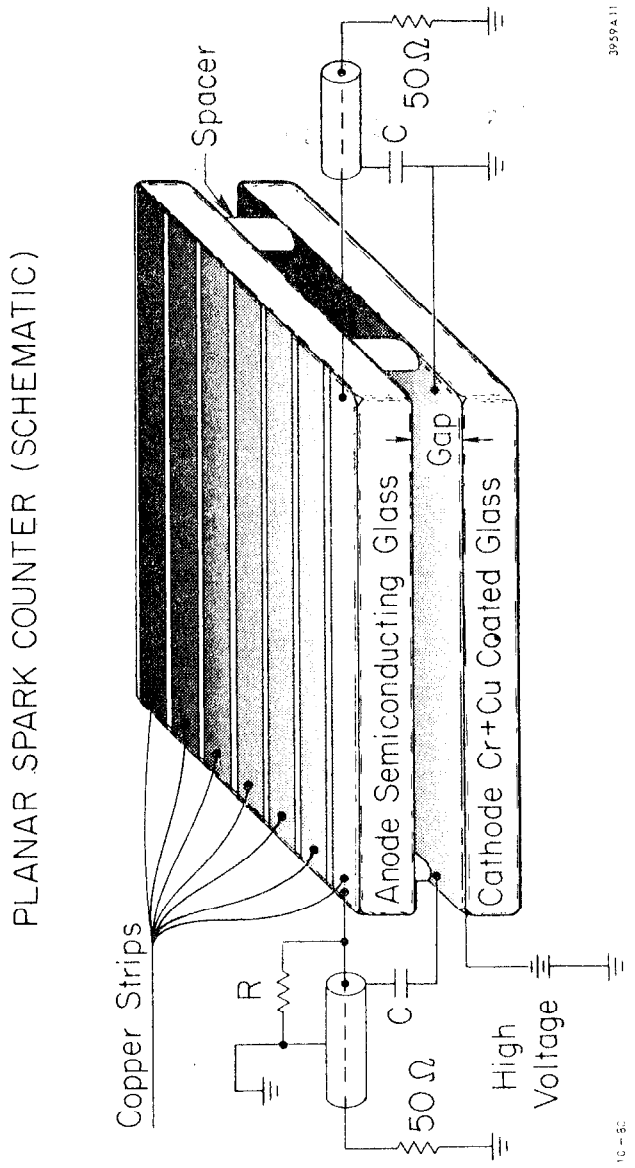

Fig. 11. Schematic diagram of a Planar Spark Counter (PSC).

rounded and polished. Copper strips are deposited over a thin layer of chrome on the surface opposite the electrode surface. The chrome is deposited first as it sticks well to glass; copper doesn't. The copper strips form one half of a transmission line that conducts the high frequency signals caused by sparks in the gap to the ends of the counter. The surface over which the strips are deposited should be polished to minimize the attenuation of high frequencies. The thickness of the copper should be $\gtrsim 5$ μm, a thickness which is several times the skin depth for the high frequency signals.

The cathode can be made from ordinary float cast, window glass. As with the anodes, edges and corners are rounded and polished. The electrode surface is formed by depositing a thin layer of chrome followed by a thick layer of copper. The deposition process is repeated with polishing and washing occurring before each Cr-Cu deposition. Typically 2-3 layers of copper are put on in this manner. The thickness of the copper is again $\gtrsim 5$ μm as this surface forms the other half of the transmission lines.

The two electrode surfaces are held apart to form a gap of 100-200 μm. The gap should be uniform to a few percent. To accomplish this two techniques have been used so far. The first, used by the experimenters at Novosibirsk,[10] consists of "outriggers" placed well away from the gap. The second, used by us at SLAC, are metallic shims placed inside the gap between the semi-conducting anode and copper cathode. This short circuits the gap at the spacer's location and the semi-conducting glass limits the current to <1 μA. The semi-conducting glass also grades the electric field from zero at the spacer to full value in a distance proportional to the thickness of the semi-conducting glass. The "outrigger" and "in-gap-spacer" schemes result in dead area and a more clever approach needs to be found.

Between the electrodes, gas at high pressure (6-10 Atmos) is circulated. Its composition is argon with 10% - 30% organic gases added to quench u.v. light. A typical gas mixture is 2% 1,3 butadiene, 2% ethylene, 10% isobutane (or propane), 5% hydrogen, and the balance is argon.

The strip lines are coupled to coaxial cables at each end of the counter. The anode side is connected directly to the center conductor and the cathode side, via a high voltage blocking capacitor, to the cable shield. A capacitor of a few hundred pico-farads is sufficient and is usually incorporated as a parallel plate capacitor with the copper cathode surface forming one half of the capacitor.

The sequence of events in a PSC which results in a spark begins with the counter in its quiescent state. The electric field strength, E, in the gap is large: $3\text{-}5 \times 10^5$ V/cm. Typical values of E/P (P is the gas pressure) range from 40-70 V/cm-torr. When a particle passes through the counter it creates N_o primary ion pairs. For the counters being described here N_o is in the range of 4-8 and is proportional to $P\delta$ where δ is the gap dimension. These initial ionizations quickly avalanche and this process can be described as a function of time, t, by

$$N(t) = N_o e^{\alpha v t} \tag{9}$$

where α is the number of ion pairs produced per unit length of drift for electrons (α is the first Townsend coefficient) and v is the electron drift velocity. The value $1/\alpha v$ is the time required for the avalanche

to grow by "e" and sets the time scale for these counters. "Fast" counters have large values of αv. The length for an avalanche to grow by "e" is $1/\alpha$ and is typically 1-2 μm for the operating conditions I am describing.

A streamer develops when space charge effects become important in the developing avalanche. This is called Meek's criterion[11] and occurs when there are $\sim 10^8$ electrons present in the avalanche. The streamer quickly propagates to both electrode surfaces, bridging the gap with a column of ionized gas. The subsequent spark depletes the surface charge on the electrodes. This causes the electric field in the region of the spark to fall almost to zero. The organic gases absorb u.v. photons produced in the discharge in a distance away from the spark which is short compared to the distance required for recovery of the electric field. The organic gases are crucial in ensuring the containment of the discharge to a small region about the spark. When the surface charges on the semi-conducting glass have been neutralized by the discharge, current ceases to flow. Gradually, the surface charges are reestablished on the semi-conducting glass. During this time the slower positive ions are gently swept from the gap. After a few milli-seconds the electric field is restored. During this process only that region of the counter in the vicinity of the spark is "out-of-action." The rest of the counter remains "live."

I will now discuss some of the operating characteristics of PSC's. Figure 12 shows the measured counting rate in a PSC with a gap of 185 μm, an area of 100 cm^2 and 6 atmospheres pressure.[10] This figure shows the non-coincident, or "singles" rate and the rate on the plateau part of the curve is consistent with the calculated cosmic ray rate

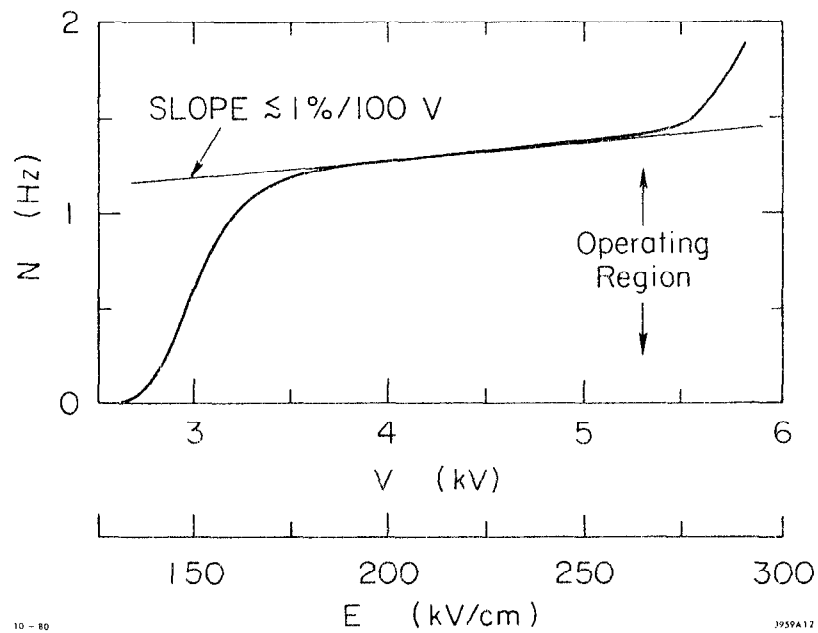

Fig. 12. Plateau curve for a PSC with a gap dimension of 185 μm and run at 6 atmos pressure. N is the singles counting rate and V is the voltage across the spark gap.

through the counter. In good counters the plateau extends to approximately twice the voltage at which signals are first observed and is very flat with a slope not exceeding 1%/100 volts.

The threshold voltage is determined by the gas pressure and composition and the gap dimension δ. If the distance an avalanche requires to form a streamer is Z_c, then at threshold $\delta = Z_c$. Only those electrons produced at the cathode surface will develop sufficient space charge, N_s, to induce a spark. The threshold curve can then be formulated as

$$\eta = 1 - e^{-N_o(1 - \frac{Z_c}{\delta})} \tag{10a}$$

where η is the probability for the counter to spark due to the passage of a charged particle and Z_c is calculated using

$$N_s = e^{\alpha Z_c} . \tag{10b}$$

The usual model for the first Townsend coefficient α is

$$\alpha = APe^{-BP/E} . \tag{10c}$$

The threshold portion of the plateau can then be fit to determine the parameters A and B in Eq. (10c). Typical values for these parameters are A = 6 cm^{-1} $torr^{-1}$ and B = 110 V/cm-torr.[10] I will use the value of B later on to estimate the time resolution attainable in PSC's.

The slow rise in the plateau curve is presumably noise which at low voltage is at a very low level but eventually increases abruptly at high voltage near the end of the plateau curve. In order to obtain the best time resolution from PSC's one operates as close to the end of the plateau curve as possible.

The output pulse shape for PSC's seems to be controlled by the high frequency characteristics of the counter. The final growth of the spark is very rapid and the subsequent current flow excites signals on the strip transmission lines. The signals propagate in both directions along the strip lines to the ends of the counter. The rise time of the leading edge of the subsequent output pulse is probably limited by the high frequency cut off of the strip lines themselves. We have measured the rise time for typical PSC's and find it to be ~300 psec for a 9 cm long strip line. The pulses are about 5 nsec wide and have an amplitude of several volts at the highest operating voltages. The pulse height distribution near threshold is very narrow and the sparks are probably being localized and quenched by the large resistivity of the semi-conducting glass. At the highest operating voltages the pulse height distribution has a much larger mean value and is about 100% FWHM. A typical pulse height distribution is shown in Fig. 13 at high voltage.

The maximum voltage obtainable for a fixed operating pressure depends on the u.v. light absorption properties of the gas. Ultraviolet photons must be absorbed by the gas before travelling far enough through the gap to regions of high electric field where a secondary spark may be induced through photo-ionization. The various organic gases mentioned earlier were selected to extend the u.v. absorption of the gas to long wavelengths. In particular the 1-3 butadiene and ethylene extend the absorption of u.v. light from 1600 Å (the isobutane cut off) to about 2250 Å. The u.v. absorption properties of these gases is shown in Fig. 14 (Ref. 12).

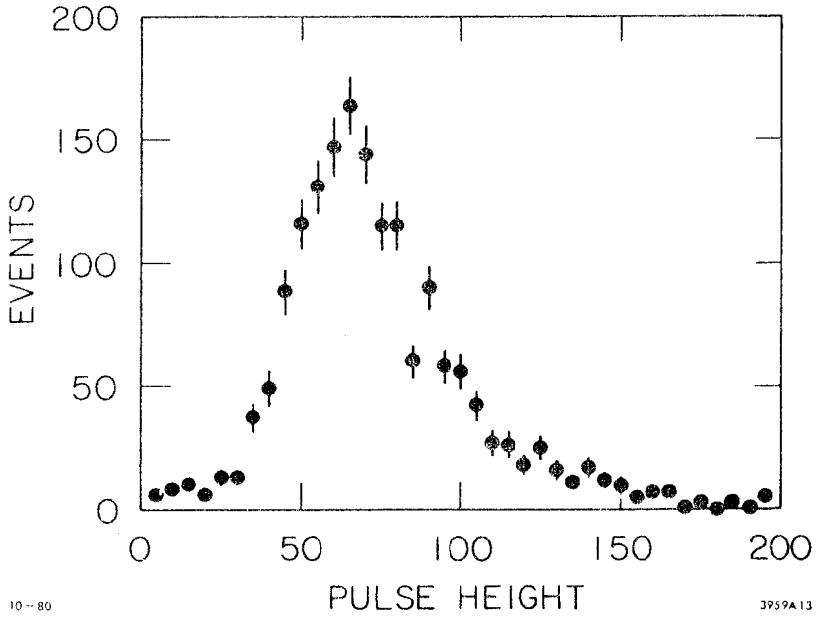

Fig. 13. Pulse height distribution for a PSC with a gap dimension of 180 μm run at 10 atmos, and 6800 volts.

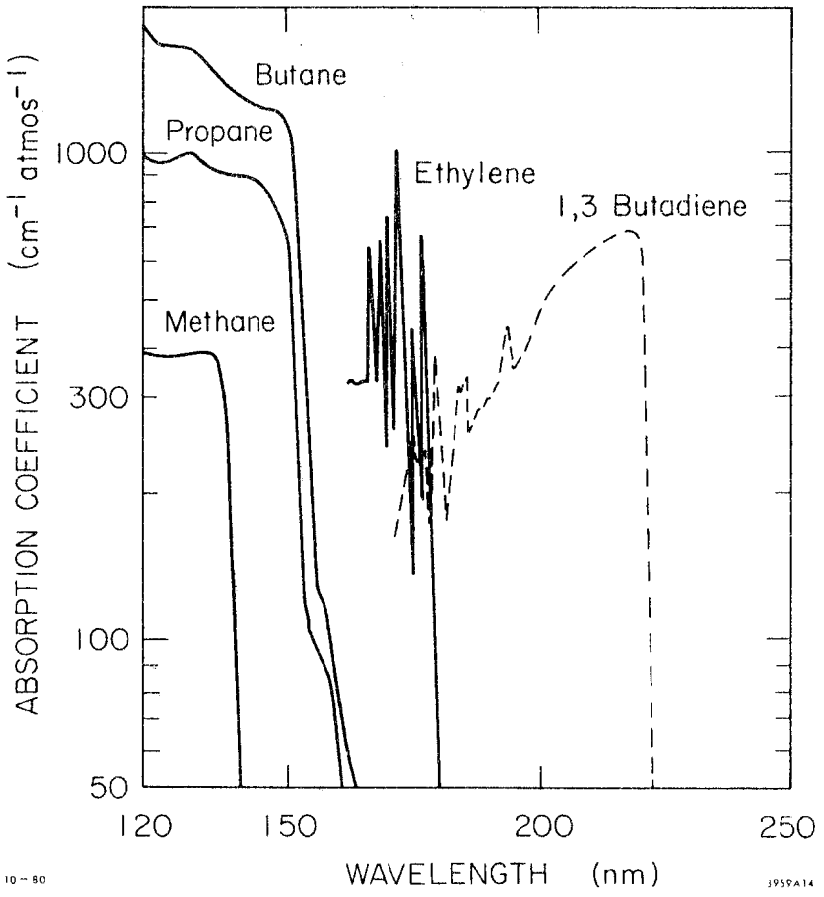

Fig. 14. u.v. light absorption coefficients for various organic gases used in PSC's.

The amount of charge in each spark has been measured by two techniques. The first is to integrate the charge in the signals from the strip lines.[10] The second method is to measure the total current drawn by the counter as a function of counting rate. The rate of increase in current with counting rate is interpreted as the charge per count. Both methods show that sparks at the higher operating points have a few nanocoulombs of charge.

The charge measurement can be used to estimate the size of the sparks, r_s. This is done by equating the spark's charge, Q_s, to an area times the surface charge density, σ_s:

$$r_s = \sqrt{\frac{Q_s}{\pi\sigma_s}} = \sqrt{\frac{Q_s}{\pi\varepsilon_o E}} \quad . \tag{11}$$

E is the electric field strength at the electrode surface $\varepsilon_o = 8.85 \times 10^{-14}$ farads/cm. Substituting numbers into Eq. (11) results in $r_s \simeq 1.3$ mm. In Ref. 10 a different calculation indicated a value for r_s of about 3 mm.

In any case the sparks are small, as they must be in order to minimize damage to the electrode surfaces. What is of real interest is not the spark size, but the size of the insensitive area about the location of a spark. In the counters constructed at SLAC, as mentioned earlier, the gap is "shorted" out by metal spacers at four locations. For semi-conducting glass thickness of 5 mm a "dropping-off" of the pulse height is observed for distances closer to the spacer than about 5 mm. In Ref. 10 the authors report calculated values of .35 cm^2 for the insensitive area. Our measurement for the insensitive area about the spacers is about .75 cm^2. As our measurement is around a D.C. short, it is probably an overestimate of the dead area caused by sparks.

The recovery time for the field in the gap after a spark has occurred is controlled by the resistance and thickness of the semiconducting glass. For the counters constructed at SLAC we calculate the recovery time to be about 10 msec. The recovery time should be kept long compared to the time necessary to sweep the positive ions left in the wake of a spark from the gap. This time is a few milliseconds.[10]

The delay time, t_D, after the passage of a charged particle through the spark gap until a streamer is formed is proportional to $\frac{1}{\alpha v}$. Variations in t_D can come from many sources but it is hard to imagine sources that don't also scale as $\frac{1}{\alpha v}$. In Ref. 10 measurements of both t_D and the time resolution are presented and a graph of these measurements is shown in Fig. 15. The ratio of t_D to the time resolution is approximately constant and both change very rapidly with increasing electric field strength.

An analytic model for $\frac{1}{\alpha v}$ can be formed by using Eq. (10) for α and the following model for v:

$$v = k\left(\frac{E}{p}\right) \quad . \tag{12}$$

k is a constant which depends on the gas. Thus

$$\frac{1}{\alpha v} \propto \frac{1}{E} e^{BP/E} \tag{13}$$

The lines in Fig. 15 indicate the variation in $\frac{1}{\alpha v}$ using the value of B determined from the fit to the threshold curve.

In Table III data for three different counters are given.[8,10] If B is assumed not to be strongly dependent on the composition of the gas, then a comparison of these counters is possible by introducing a correction for the various E/P values at which measurements were made. These

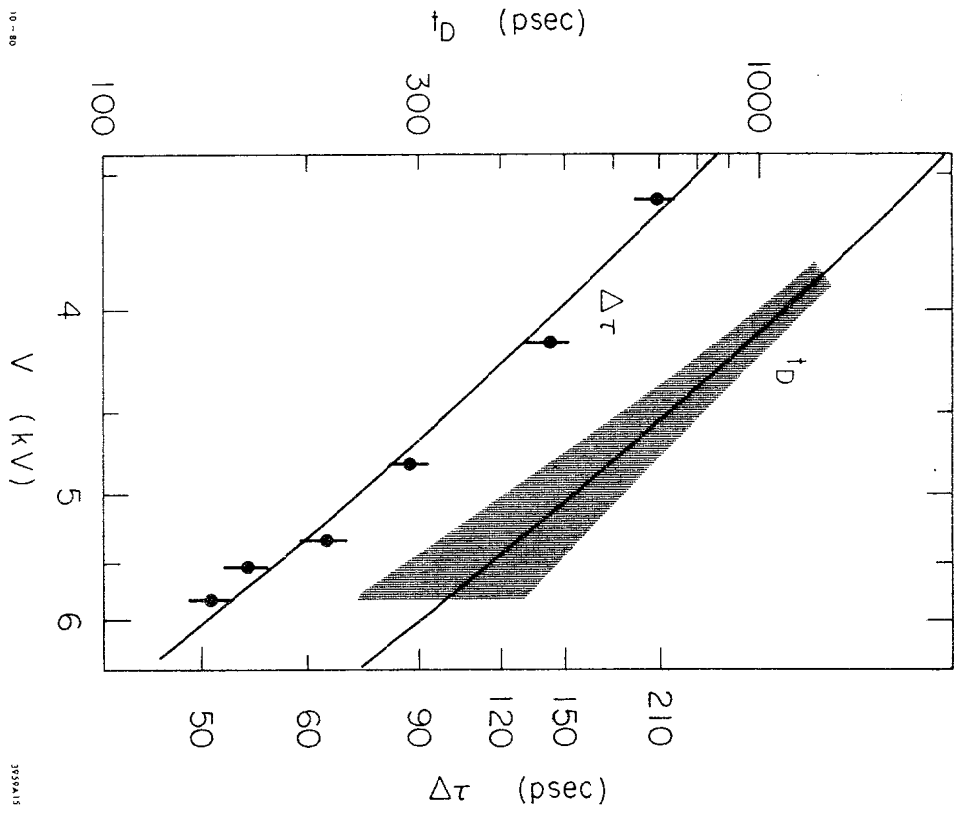

Fig. 15. The delay time between the passage of a particle through a PSC and the spark and the RMS time resolution of the same PSC versus the gap voltage V. The shaded area around t_D indicates the size of the measurement errors.

TABLE III

Operating properties of three PSC's. $\Delta\tau_{corr}$ is the time resolution corrected to E/P = 70 V/cm-torr using $\Delta\tau_{corr} = \Delta\tau \exp\left[B\left(\frac{1}{70} - \frac{P}{E}\right)\right]$. I used 110 V/(cm-torr) for B.

Reference	GAP(cm)	P(torr)	V(volts)	N_0	E(V/cm)	E/P(V/cm-torr)	τ(psec)	τ_{corr}(psec)
Ref. 8e	.10	755	5500	3.3	5.5×10^4	72.9	285	303.0
Ref. 10a-c	.0185	4530	5800	3.6	3.14×10^5	69.2	47	46.2
	.0185	4530	5500	3.6	2.97×10^5	65.6	51	45.9
	.0185	4530	5350	3.6	2.89×10^5	63.8	63	54.1
	.0185	4530	4850	3.6	2.62×10^5	57.9	88	63.4
	.0185	4530	4150	3.6	2.24×10^5	49.5	144	75.1
	.0185	4530	3580	3.6	1.94×10^5	42.7	210	76.9
Ref. 10d	.010	9060	6000	3.6	6×10^5	66.2	28	25.6

corrected values (to E/P = 70 V/cm-torr) are given in column 8 of Table III and are plotted against E in Fig. 16. A fit to these data gives the following "rule-of-thumb" for the time resolution of PSC's:

$$\Delta\tau(\text{psec}) \approx \frac{4.7 \times 10^6}{E^{1.03}(\text{volts/cm})} \; e^{110 \frac{P(\text{torr})}{E(\text{V/cm})}} \qquad (14)$$

One should note that N_o is approximately the same for all of the counters shown in Table III and so any dependence on N_o would not be revealed. It may in fact turn out that a major source of time fluctuations in PSC is controlled by the number of primary ion pairs and hence result in an overall $\sqrt{\frac{1}{N_o}}$ dependence. No good experimental evidence is yet available to confirm or debunk this conjecture.

The time resolution for a pair of 9 cm × 9 cm counters constructed at SLAC is shown in Fig. 17. These data were collected using a cosmic ray telescope equipped with drift chambers for particle tracking. Shown in Fig. 17 is the difference in the end-to-end time averages from the strip lines for the two counters. Both counters were run at P = 12 atmos. and had 185 μm gaps. The high voltage was 6800 volts in one counter and 7500 volts in the other.

A PSC can also provide a position measurement in much the same way as conventional scintillation TOF's do. This is done by taking the difference of the times measured at each end of the strip lines and correlating this with the measured location of the particle crossing. Using the drift chamber information from the cosmic ray telescope we can fit straight line trajectories for the particle tracks. The results of the difference from the fitted track location in the PSC to that predicted using the time difference (à la Eq. (4a) where v_{eff} is replaced with

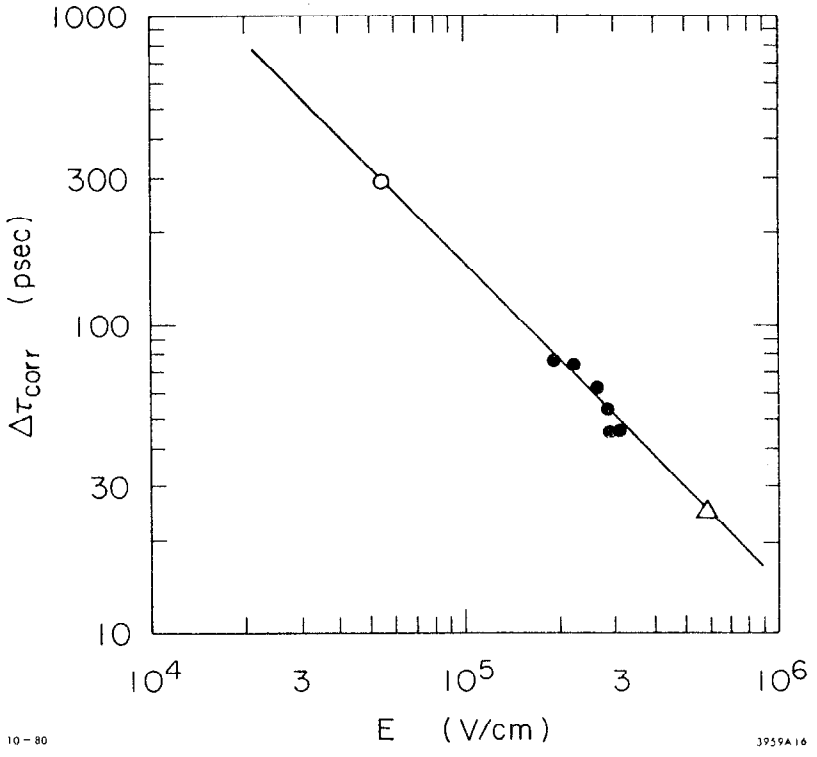

Fig. 16. Three PSC's run with different gaps and pressures: (○) 1000 μm gap, 1 atmos, (●) 185 μm gap, 6 atmos, and (△) 100 μm gap, 10 atmos.

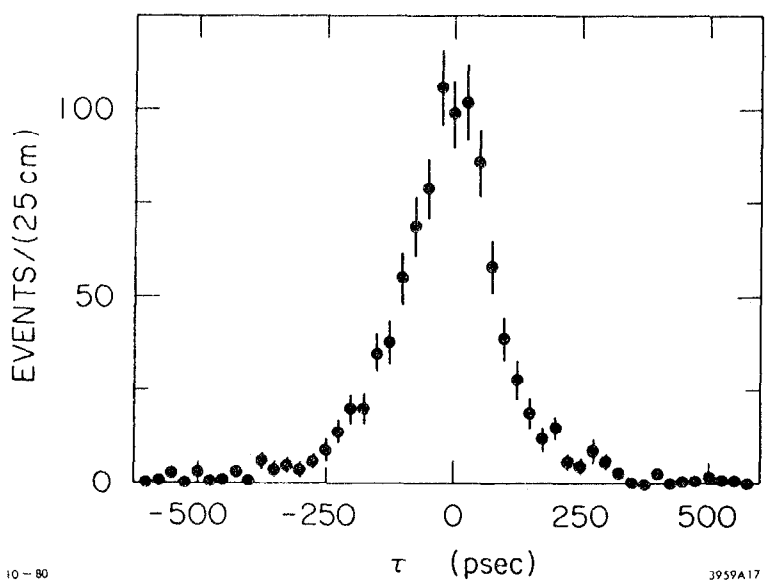

Fig. 17. Time difference spectrum from a pair of PSC's with 180 μm gaps run at 12 atmos. RMS resolution for a single counter is 55 psec. Data taken with cosmic rays.

the speed of signals in the strip lines: $v_{signal} \approx 15$ cm/nsec) is shown in Fig. 18.

The position accuracy in PSC's should not be correlated with the timing accuracy. This is because the timing accuracy is controlled by fluctuations in the delay time t_D. The same spark is the source for the signals at both ends and insofar as the spark occurs on a very fast time scale, the position resolution just reflects the timing accuracy of the electronics used to make the measurements. The measured position resolution of 2.4 mm can thus be interpreted as a time resolution of the electronics of about 16 psec RMS which is to be compared with the expected RMS of 14.4 psec arising from the 50 psec bin size in the TDC units used.

I have tried to explain what PSC's are and have glossed over many important points with respect to their construction. I will mention two before concluding this section. These counters are difficult to make and require a high standard of cleanliness not usually present in the workshops where particle detectors are constructed. The standards used in the manufacture of integrated circuits are closer to what must be achieved. The second point is that an extended "burning-in" period is required for PSC's. This is accomplished using an intense radioactive source to make the counter spark $\sim 10^5$ times per square centimeter. During the burn-in period the high voltage is slowly increased with attention to the singles rates which should be kept below about .04 Hz/cm^2. It has been conjectured[10] that during this initial period of use, a film of polymerized gas coats the electrode surfaces, covering up small imperfections that would otherwise lead to spontaneous breakdown.

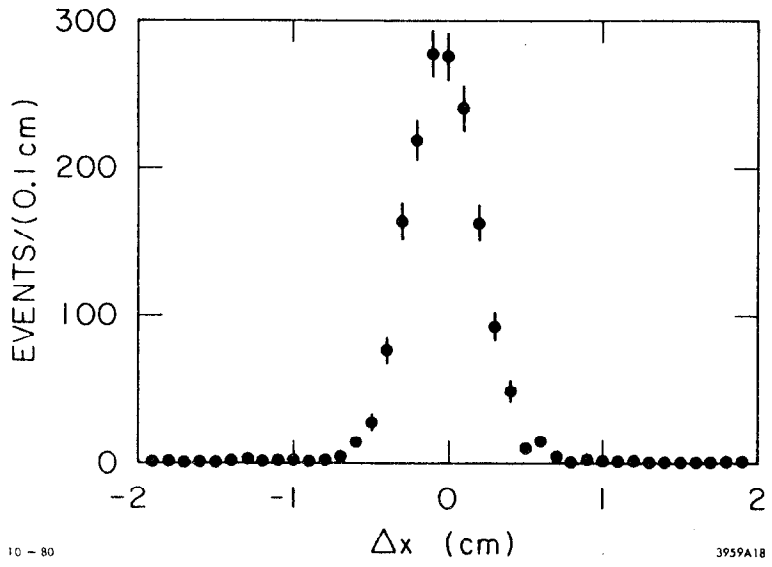

Fig. 18. Position determination in a PSC inferred from the difference in times measured on each strip. The location of particle penetrations was determined by reconstructing straight line trajectories from drift chambers.

No information yet exists on the maximum lifetime of PSC's. Greater than 10^7 sparks/cm^2 seem to not adversely affect the counter's performance. Whether or not PSC's can withstand the sometimes severe radiation environments present at storage rings is also unknown.

We are presently constructing 20 cm long PSC's here at SLAC and will then make 120 cm long counters. Our 9 cm × 9 cm counters have performed adequately enough to encourage us that these large counters can be made to work well with time resolutions at or below the 50 psec level.

Referring back to the introduction where particle identification using TOF was discussed, optimistically we might expect to be able to separate the various particle types using PSC's to momenta above 3 GeV. This would nicely complement the dE/dx technique using drift chambers by providing particle identifications in the "cross-over" region. The good position resolution along the strip lines in PSC's and the possible number of strip lines (limited by the number of TDC channels) could be made to result in a small number of ambiguous TOF measurements.

ACKNOWLEDGEMENTS

I gratefully acknowledge many useful discussions with Jeff Weiss of the Mark II collaboration and Dave Dorfan of Santa Cruz. I thank Art Ogawa for carefully reading this manuscript. I also wish to acknowledge the collaboration with Yuri Pestov from Novosibirsk during 1978 which made possible the construction of PSC's at SLAC.

REFERENCES

1. E. D. Bloom et al., SLAC-PUB-955 (1971).

2. J. Weiss (private communication).

3. J. Kadyk and M. Alam, MARK II Internal Note, Sept. 29, 1976.

4. W. Braunschweig et al., N.I.M. 134, 261-266 (1976).

5. D. Dorfan (private communication).

6. Branko Leskovar et al., IEEE Trans. on Nuc. Sci., Vol. NS-25, No. 1, 582 (1978).

7. Michael Wollstadt, BONN-IR-76-39, Universität Bonn (1976).

8. a) J. Keuffel, Rev. of Sci. Inst. 20, 202 (1949).
   b) F. Bellu and C. Franzinetti, Nuovo Cimento, X, No. 10, 1461 (1953).
   c) M. V. Babykin et al., Soviet Jour. of Atomic Energy, VI, 487-494, (1956).
   d) E. K. Zavoisky et al., Soviet Jour. of Atomic Energy, VI, 495-499 (1956).
   e) V. Parkhomchuck et al., N.I.M. 93, 269-270 (1970).

9. We have used semi-conducting glass made by U.S. Schott Optical in Dureay, Penn., glass type S8900. Alternate semi-conducting glass types are available from German Schott Optical.

10. a) V. D. Laptev et al., UDC 539.1.074.27, 1698 (1975).
    b) V. D. Laptev et al., UDC 539.1.074.27, 1703.
    c) A. D. Afanas et al., UDC 539.1.074.27, 1701.
    d) Yu. N. Pegtov et al., SLAC translation 184 (1978).

11. L. B. Loeb and J. M. Meek, The Theory of the Electric Spark, Stanford University Press, Stanford, California, Chapter II (1941).

12. H. Siebke, Diplomarbeit in Physik (in German), Aachen (1980).

August 1980

THE CERN LEP PROJECT

K.M. Potter
CERN, Geneva, Switzerland

1. Introduction

A Large Electron Positron project has been discussed by the European High Energy physics community in general [1] and at CERN in particular [2] since 1976. The European Committee for Future Accelerators (ECFA) has organized a number of studies on the physics programme which could be carried out with an electron-positron collider with beam energy around 100 GeV and, in parallel, feasibility and design studies [3, 4, 5] have been carried out at CERN with the collaboration of a number of other European Laboratories.

The LEP project has now reached a rather advanced stage and was officially presented to the CERN member states at their June meeting of this year.

This report outlines the reasons why the European High Energy Physics community has chosen to construct LEP, the general features of the machine with emphasis on the latest developments, a brief review of the experimentation which has been discussed in the various studies and finally the status and timescale of the project as of July 1980.

2. General Physics

This section will be rather brief as the reasons are very similar to those given for the choice of topic for this year's Summer Institute. Recent progress in the unification of the Weak and Electromagnetic interactions and the emergence of the Gauge Theories has made it extremely important to test these theories in the energy region where the interaction strengths become comparable. In the energy range up to 200 GeV, the standard Weinberg-Salam model [6] predicts the existence of both the neutral (Z^0) and charged ($W^{\pm}$) bosons which are needed to damp the rising Weak cross section.

The presence of the Z^0 pole will have a particularly spectacular effect as illustrated by the ratio R of the total to the point like cross-section, shown in figure 1. At present energies, as measured at

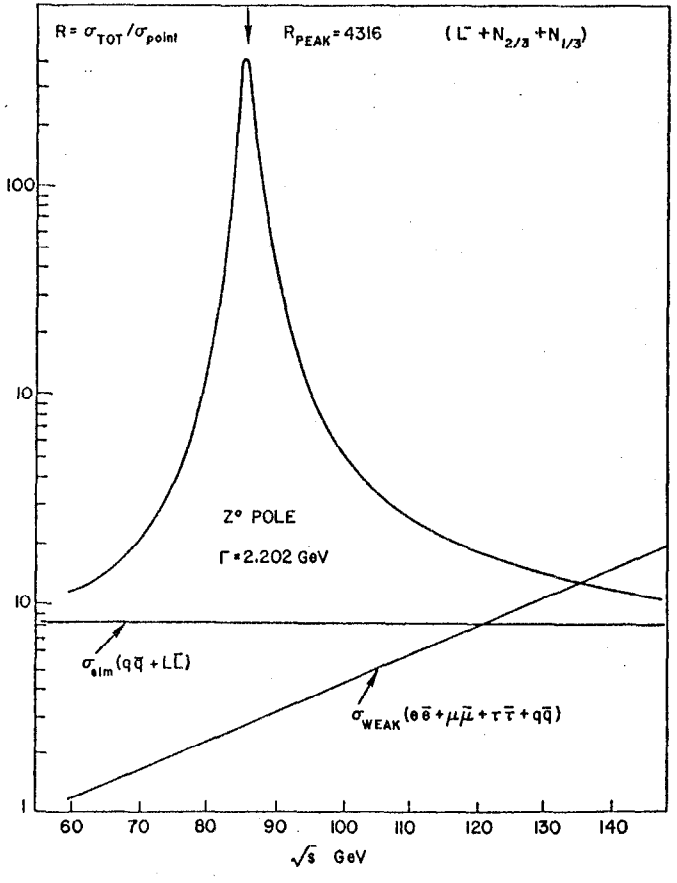

Figure 1 : The ratio R of the total annihilation to pointlike cross section calculated using the standard Weinberg-Salaam model with $\sin^2\theta_W = 0.25$. Also shown are the weak and electromagnetic cross sections with no Z° pole.

PETRA, R has a value of ~ 4 but will rise to over 4300 at the Z° mass value of 92 GeV in the Weinberg-Salam model with $\sin^2\theta_W = 0.23$. With the same parameters, the charged boson $W^{\pm}$ is expected to have a mass of 81 GeV [7].

However, since the large machine under discussion will take several years to build, it is anticipated that the existence of these particles will have already been established by experiments at the $p\bar{p}$ collider [8] at present under construction at CERN. The role of LEP will therefore be to carry out the detailed studies needed to verify or disprove the theories, detailed measurements which it will be impossible to make at the $p\bar{p}$ collider because of the "hadronic background."

An important question, to which there is no precise answer in the Gauge Theories, is how many quark-lepton families are there in nature ?

$$\begin{bmatrix} \nu_e \\ e \\ u \\ d \end{bmatrix} \quad \begin{bmatrix} \nu_\mu \\ \mu \\ c \\ s \end{bmatrix} \quad \begin{bmatrix} (\nu_\tau) \\ \tau \\ (t) \\ b \end{bmatrix} \quad \begin{bmatrix} \\ ? \\ \\ \end{bmatrix}$$

Experimental evidence exists for five quarks, but so far the expected sixth or top quark has not been seen at PETRA and PEP, and it is conceivable that LEP will be the first machine to observe the "toponium" states due to this quark. Further, complete families cannot be excluded and may well exist within the energy range up to 200 GeV in the centre of mass.

Another particle which is required by the theory in some form or other is the Higgs boson needed to induce symmetry breaking and generate the mass spectrum of the known quarks and leptons. Although it probably has a mass too high to be directly produced in a 200 GeV machine, it cannot be excluded that effects due to its existence could be observed.

These major predictions [6], which must all be verified in as detailed a manner as possible in order to constrain the theories, have set the energy scales for LEP, with a centre of mass energy of 100 GeV one studies the Z°, with 180 GeV, one studies W pair production and the maximum possible beam energy, is required for the Higgs Boson or Bosons.

These considerations have prompted the study of three different machines since 1976. The first was a feasibility study for a 50 km circumference machine with a beam energy of 100 GeV obtained with conven-

tional room temperature RF cavities [3]. This machine was extremely expensive and had a number of unsolved technical problems. The next had a circumference of 22 km and a beam energy of 70 GeV and was very successful from the machine point of view [4]. It became the basis for the present design for a circumference of 30 km with a beam energy approaching 90 GeV with room temperature RF cavities and the possibility to reach 130 GeV if superconducting cavities become technically feasible. The design report [5] for this machine was published last year and, in what follows, emphasis will be placed on developments since that report.

3. Status of the Machine Design

The present LEP machine [9] whose main parameters are given in Table I, has been optimized for a beam energy around 90 GeV and a luminosity of 10^{32} $cm^{-2}sec^{-1}$ to be obtained with room temperature RF cavities, this results in a circumference of 30.6 km. Physics experiments will be possible at eight interaction points of which half will have the design luminosity and a free space between low beta quadrupoles of ± 5 m, while the rest will have half the luminosity but a larger free space for experiments, ± 10 m.

The desirability of installing the enormous RF system in stages, with a view to the use of superconducting cavities as soon as they become available, has been considered from the start. Recently, this staged installation has been coupled with arguments to start physics as soon as possible with a minimum machine capable of studying the Z^0 with only four equipped interaction regions. This minimum machine has been called phase I and corresponds to the installation of 1/6th of the RF as shown in Table II. Further stages corresponding to 1/3rd and the complete 96 MW of RF are also shown. The final column corresponds to the performance when all the room temperature cavities have been replaced with superconducting cavities with 5 MV/m field gradients such that all the 96 MW is available for beam power.

The luminosity performance of the machine over its complete energy range is summarized in figure 2 where it can be seen that it is hoped to be able to limit the fall-off with energy E below the design maximum to be not faster than E^2 by the use of wigglers to maintain the optimum

TABLE I

LEP PARAMETERS AT 89 GeV

MACHINE CIRCUMFERENCE	30.6 km	
LENGTH OF LATTICE PERIOD	79 m	
INSTALLED RF POWER	96 MW	
NUMBER OF INTERACTION POINTS	8	
NUMBER OF BUNCHES PER BEAM	4	
HORIZONTAL TUNE	~ 97	
VERTICAL TUNE	~ 101	
SYNCHROTRON TUNE	0.10	
MOMENTUM COMPACTION FACTOR	1.46×10^{-4}	
HORIZONTAL DAMPING PARTITION N°	0.5	
BEAM LIFETIME	5.6 h	
CURRENT PER BEAM	8.4 mA	
FREE SPACE IN INTERACTION REGION	± 5	+ 10 m
VERTICAL AMPLITUDE FUNCTION	0.1	0.2 m
HORIZONTAL AMPLITUDE FUNCTION	1.6	3.2 m
BEAM-BEAM TUNE SHIFT	0.06	0.06
MAXIMUM LUMINOSITY / 10^{32}	1.0	0.5 $cm^{-2}s^{-1}$

TABLE II

STAGES OF LEP CONSTRUCTION

FRACTION OF RF INSTALLED	1/6	1/3	1	SUPERCONDUCTING RF
DESIGN ENERGY	49.4	62.3	89	130 GeV
LUMINOSITY	0.39	0.62	1.1	$1.0 \times 10^{32} cm^{-2} s^{-1}$
CURRENT	5.71	7.20	8.4	6.16 mA
RF POWER	16	32	96	96 MW
LENGTH OF RF	272	543	1629	1629 m
NUMBER OF FIVE-CELL ROOM TEMPERATURE CAVITIES	128	256	768	–

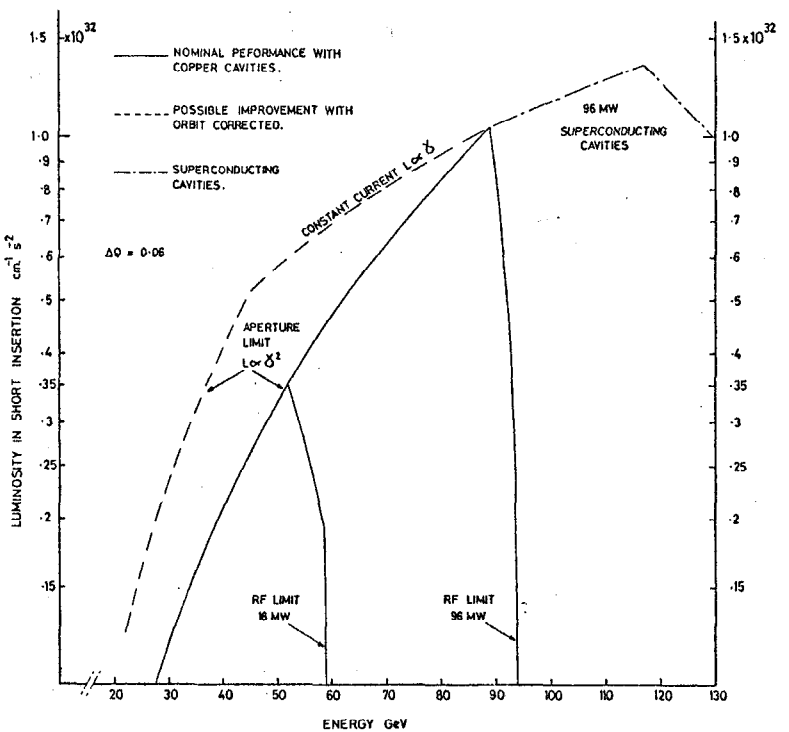

Figure 2 : Luminosity as a function of energy with 16 MW, and 96 MW of installed room temperature RF cavities. The extrapolation to 130 GeV assumes 96 MW of power available on the beam by the use of RF superconducting cavities.

beam size. A possible improvement in luminosity, at low energy, when maximum use is made of the machine aperture after correction of the orbit, is also indicated.

The whole machine, including experimental areas, will be constructed underground according to the layout of figure 3.

The tunnel is tangential to the CERN SPS and slightly below it so that it will be possible to inject protons from the SPS into a possible future proton ring (1 TeV per Tessla) in the LEP tunnel and also to allow e - p collisions at one interaction point, by constructing an SPS by-pass. A third overriding reason for this location results from a recent decision to use the existing PS and SPS complex as part of the electron-positron injector for LEP.

The ringed numbers on figure 3 show the positions of test drillings which have already been made to determine the depth of the molass rock which the tunnel will be cut in, as for the CERN SPS, by means of full face boring machines. The part under the Jura mountains will be in limestone and the dotted line indicates the trajectory of a reconnaissance tunnel which will be started shortly to obtain, as early as possible, information for this less well understood part of the tunneling programme. Approximately one-third of the tunnel will pass through limestone including interaction points 3, 4 and 5.

The cross section of the 4 m diameter standard tunnel is shown in figure 4. The details of this layout have been carefully studied to allow maximum space for installation in view of the 4 km between access points. Space has been reserved for a future proton machine as already mentioned and for the helium gas lines which will be needed for the superconducting RF cavities.

The underground experimental halls are proposed to be of similar design to that now under construction for the SPS collider at LSS4, but are somewhat longer as shown in figure 5. Access to halls 1, 2, 6, 7 and 8 will be by vertical shafts between 45 and 90 metres deep while halls 3, 4 and 5 which are deep under the Jura, will be reached by a combination of vertical shafts and nearly horizontal tunnels.

The magnet structure of LEP is a separated function FODO lattice with a cell length which has been made as long as possible on the argument that focussing elements are more expensive than dipoles. This is particularly true as it is intended to use an unconventional construction method for the dipoles which will halve the price. The field in the C shaped dipoles is only 0.123 T at 130 GeV and the return

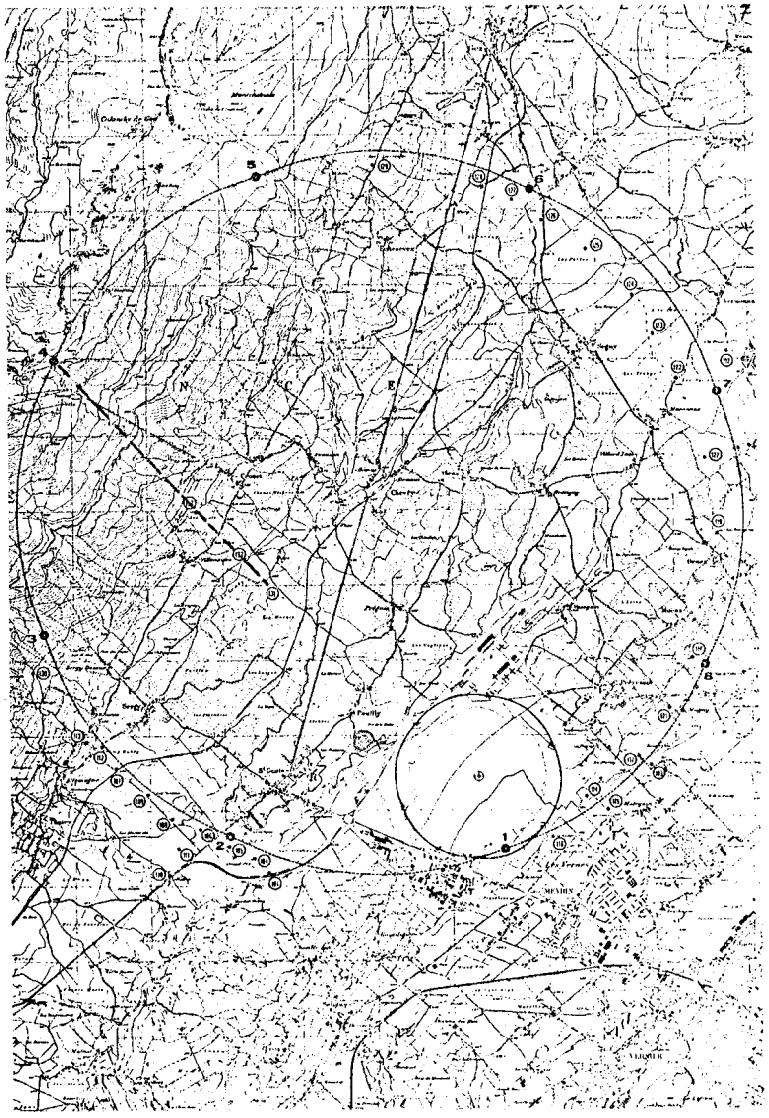

Figure 3 : Layout of LEP tangential to the CERN SPS showing the eight experimental areas numbered 1 - 8. The small numbered circles indicate test drillings which have already been carried out. The straight dotted line is a possible trajectory for a reconnaissance tunnel.

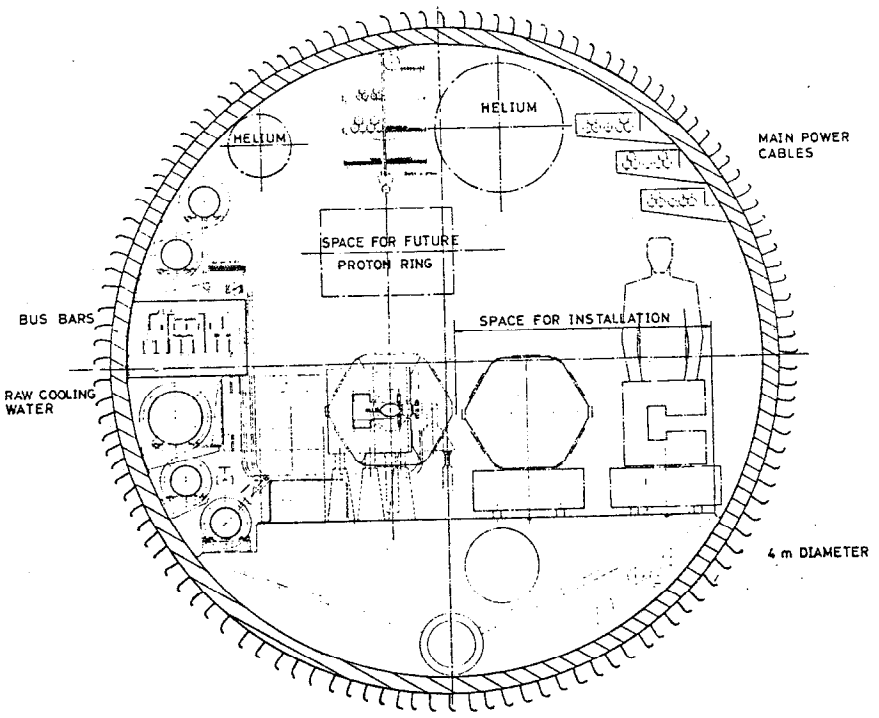

Figure 4 : Cross-section of the LEP 4 m diameter tunnel showing space reserved for a possible future proton machine, helium gas-lines for superconducting RF and space for installation.

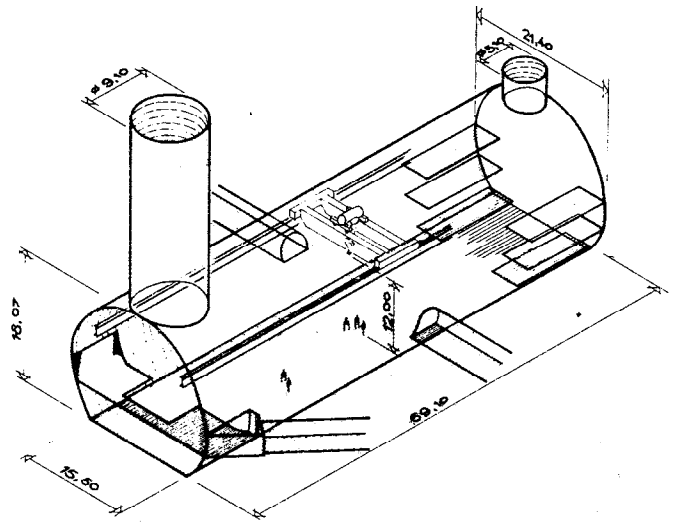

Figure 5 : A perspective of an underground hall 70 m long transverse to the beam which will accommodate two large experiments, counting rooms and associated electronics.

yoke of a conventional magnet would be far from saturated. A technique has been developed whereby conventional stamped laminations are given raised points in a number of places so that when stacked on prestressing rods the 1.5 mm thick laminations are spaced 4.1 mm apart. These spaces are then filled with concrete so that an extremely stable mechanical structure is obtained (figure 6). Two such full size dipoles [10] have already been built, tested and measured both mechanically and magnetically. Similar magnets built by industry will be delivered shortly.

Six of these magnet cores needed between each pair of quadrupoles, will be energised by two water cooled aluminium bars in place of conventional coils. The bars are situated above and below the median plane so that their insulation, consisting of clamp-on extruded plastic shells, will not be damaged by synchrotron radiation. Similar return conductors on the front of the magnets will compensate the stray magnetic field.

The cores of the quadrupoles and multipoles are of more conventional design but, for the coils, it is proposed to use anodised aluminium strip with water cooling on the outside. The quadrupoles and sextupoles have been designed to allow a beam energy up to 130 GeV.

The LEP vacuum chamber will be an aluminium extrusion with a linear ion pump, using the main magnetic field, similar to that of other electron machines [11] (figure 7). A special problem at LEP results from the higher critical energy of the synchrotron radiation ε_c = 400 KeV at 86 GeV and ε_c = 1.4 MeV at 130 GeV. Cooling of the chamber will require three water channels to avoid buckling due to uneven heating by the synchrotron radiation. A lead shield, as indicated in figure 7, will also be needed which will be applied by pressing preformed lead strips onto the chamber at temperatures just below the melting point of the lead.

The quantities of ozone and corrosive substances like nitric acid which will be produced by radiation escaping from this lead shield have been estimated [12] and are well below the acceptable limits. The production of neutrons in the vacuum chamber structure has also been estimated [13] and found to reach 10^9 neutrons/metre of bend/sec at 130 GeV. This neutron production starts just above a beam energy of 60 GeV due to the process $\gamma + d \rightarrow n + p$ on the naturally occurring deuterium in the cooling water of the vacuum chamber. This level of neutron production will not be serious for the machine but at high

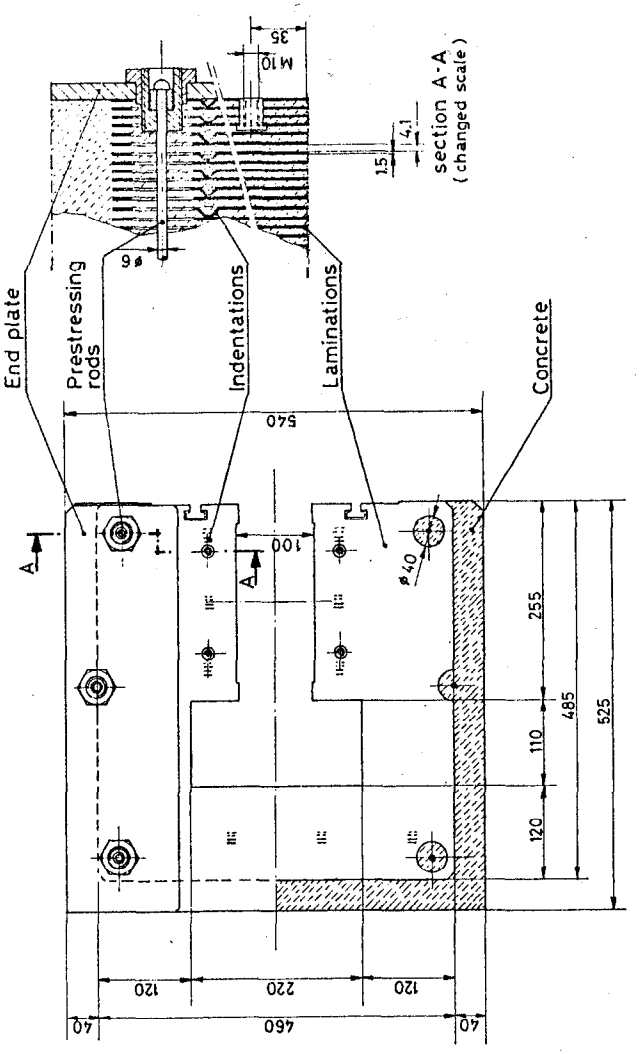

Figure 6 : A cross-section of the steel-concrete dipole magnet showing construction details.

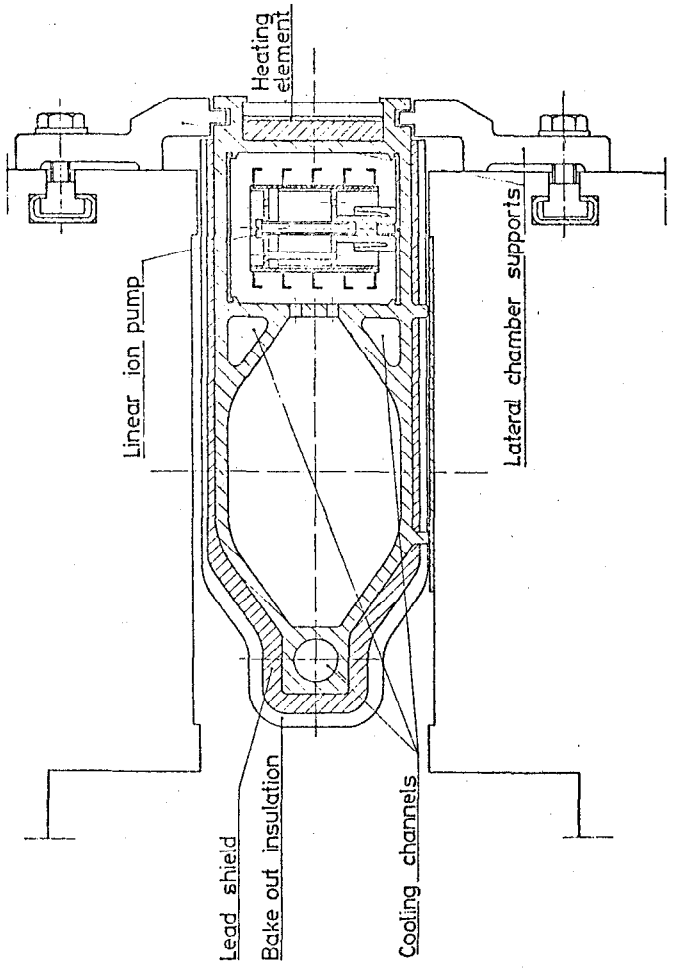

Figure 7 : Vacuum chamber cross-section with lead shielding and linear ion pumps.

energy a neutron shield will probably be needed at the end of the RF straight section to prevent background problems in the experimental areas.

The distributed ion pumps have also required a special development. They will be constructed in one metre lengths from five stainless steel strips with 5 cm diameter holes punched out to form the pump cells when the strips are assembled between titanium cathodes. The large diameter pump cells are needed to maintain adequate pumping in the low dipole field at injection.

The RF system of LEP has to make up for an energy loss of 1.37 GeV per turn at a beam energy of 86 GeV, making a total synchrotron power loss of 25 MW. The frequency of 353 MHz has been chosen for economic and beam dynamical reasons. It is proposed to use 768 five-cell cavities fed by 96 1 MW klystrons. Each five-cell cavity will be coupled to a low loss spherical storage cavity [14], as shown in figure 8. The stored RF energy then oscillates between the coupled systems spending on average half its time in the low loss environment of the storage cavity. This method decreases the power dissipation in the cavities by a factor of 1.5 allowing a higher beam energy to be reached for a given total power. The coupling of the cavities must of course be adjusted to ensure proper synchronisation with the bunch passage. The principle of operation has already been tested at low power and a 500 MHz storage cavity has been built to enable high power tests with an existing five cell cavity and klystron to start shortly.

Work on developing suitable superconducting cavities has started at both Karlsruhe and CERN. A single cell cavity constructed at Karlsruhe [15] will soon be installed in the storage ring DORIS at DESY while at CERN [16] accelerating fields of 4.6 MV/m have already been achieved in a single cell axial coupled model cavity.

A recent development in the machine project has been the adoption of a scheme [17] using the CERN PS and SPS as injectors for LEP. The electrons and positrons would still be produced in a 600 MeV Linac and accumulated in a small DC accumulator ring [18]. These two machines are being designed by the Linear Accelerator Laboratory at Orsay. Electrons or positrons from the accumulator ring which will have 1/7th the circumference of the PS, will be injected into the PS in opposite directions and accelerated to 3.5 GeV (figure 9). The positrons will be extracted from the PS and injected into the SPS via the existing proton transfer line for acceleration to 22 GeV. The electrons will pass via

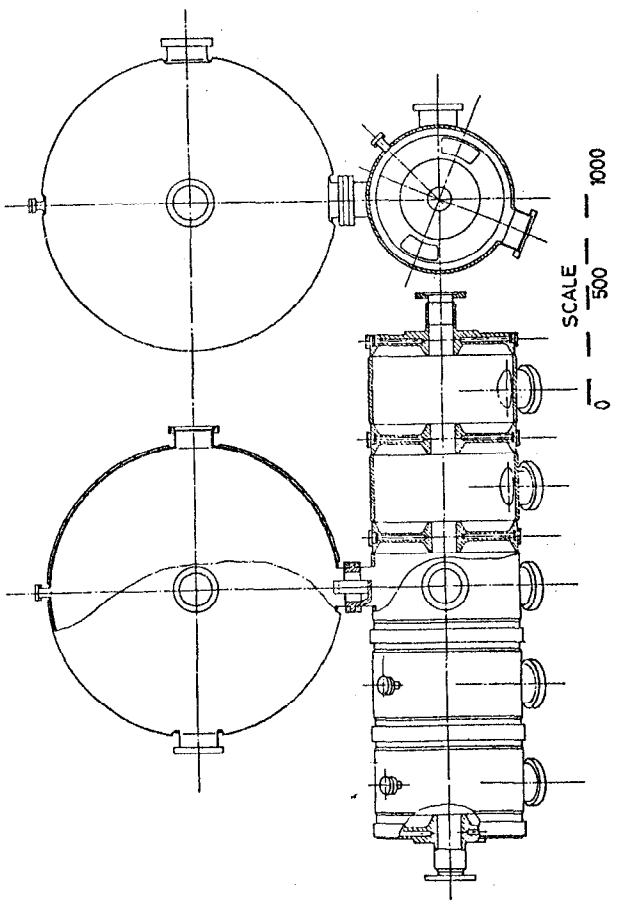

Figure 8 : A five-cell slot-coupled accelerating cavity with low-loss storage cavity.

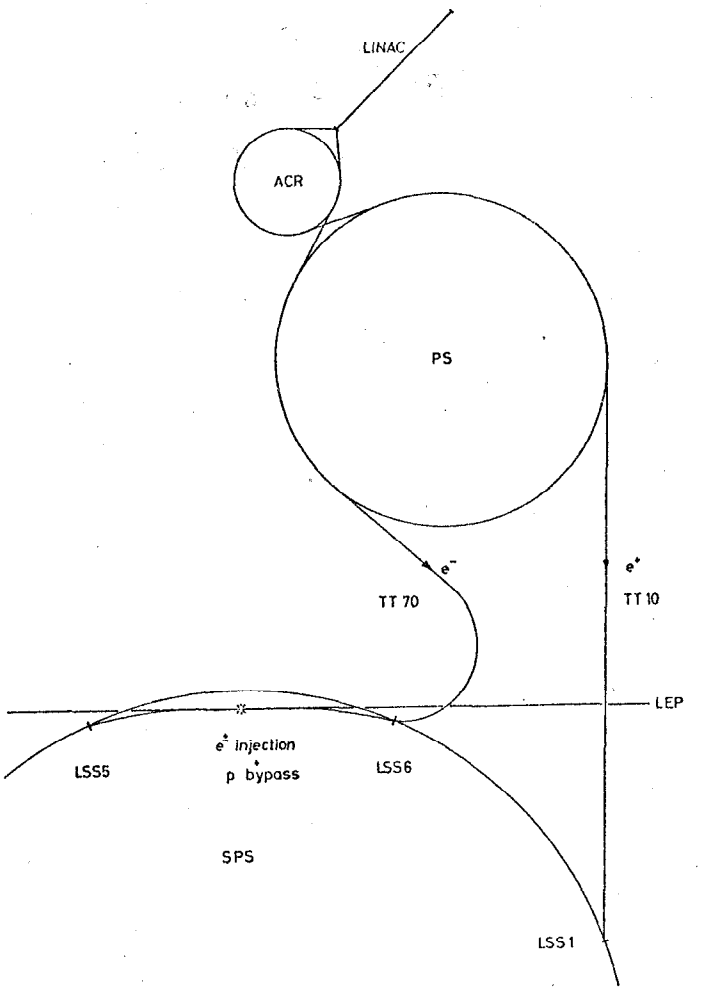

Figure 9 : Schematic of the injection system using the CERN PS and SPS.

the transfer line TT70 at present under construction for the antiproton project.

The effect of the synchrotron radiation on the machine components of the PS and SPS has been estimated [19] and found to be acceptable with the addition of a small amount of lead shielding at specific points.

The filling of LEP via transfer lines from the SPS which have not yet been fully designed, will be possible with almost no interference with normal proton operation of the SPS. The filling times will be ten minutes for electrons and ten minutes for positrons when using a filling mode with electron pulses interleaved with proton pulses. A dedicated electron filling could be achieved in two minutes but no shortening of the positron filling would be possible, as this will be limited by the production rate.

3. Experimentation at LEP

There has been a wide study of the anticipated experimental programme at LEP with the active participation of a large fraction of the European High Energy Physics community. This paper cannot possibly review all the detailed work in the various study reports [1, 20, 21, 22] but will merely pick out a few examples to illustrate the preparations which have already been made for an exciting LEP physics programme and to demonstrate the feasibility of experiments assuming little or no development of existing particle detection techniques.

Of prime importance at any accelerator is the event rate. Figure 10 shows the total number of e^+e^- annihilation events per day as a function of energy, assuming the design luminosity. In the standard model with three quark-lepton families, one can expect nearly 10^5 events/day at the Z° pole. If the Z° is absent, the rate will be no more than a few hundred per day. The high rate at the Z° pole will make many experiments relatively easy. The "data" points in the imaginary measurement [23] of the forward-backward charge asymmetry A_μ in the process

$$e^+e^- \rightarrow \mu^+\mu^-$$

shown in figure 11, represent 100 hours of running at each energy

$A_\mu = \frac{\text{Forward-Backward}}{\text{Forward+Backward}}$ and at the Z° pole $A_\mu = \left|\frac{v}{a}\right|$

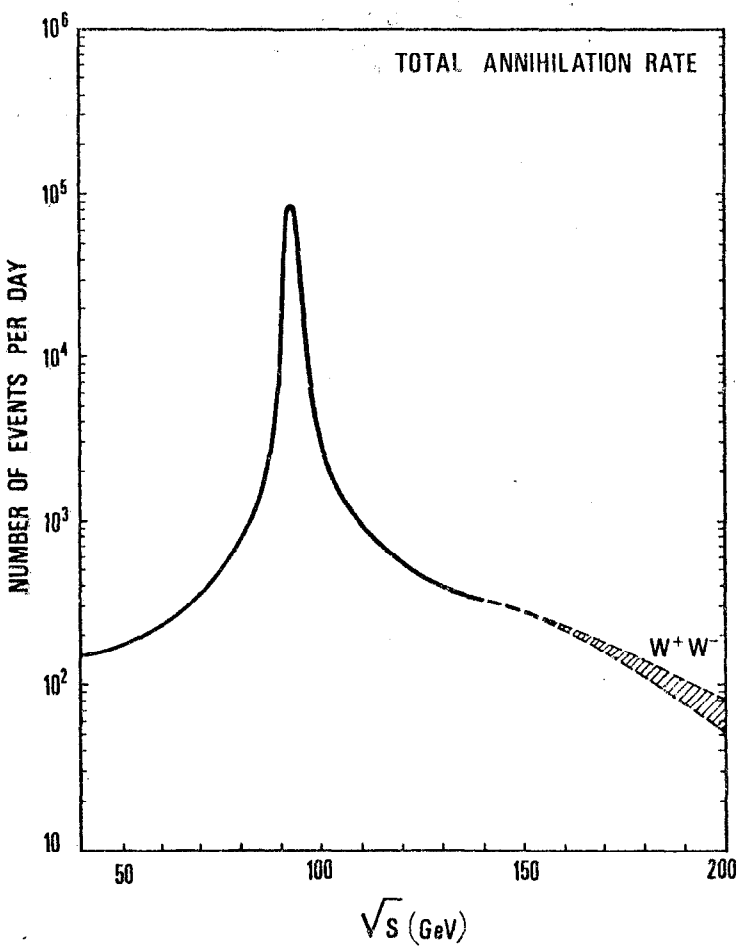

Figure 10 : The total annihilation event rate at LEP with the design luminosity and the standard model with $\sin^2\theta_W = 0.2$ and three quark-lepton families.

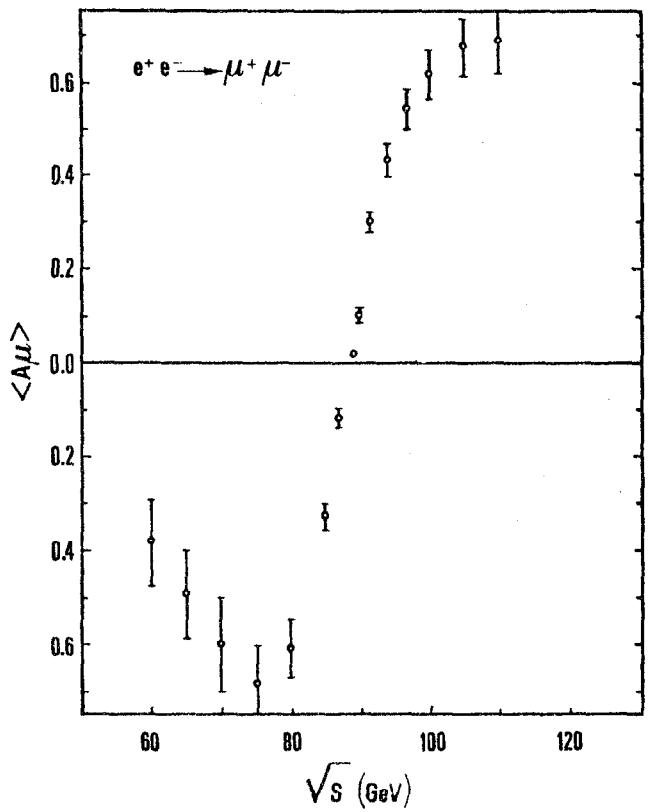

Figure 11 : Simulated measurement of the forward-backward charge asymmetry $< A_\mu >$ in $e^+e^- \to \mu^+\mu^-$ ($\sin^2\theta_W = 0.23$). Each "data" point corresponds to 100 h of running.

This experiment which is a measure of the axial and vector couplings, should be performed for all the fermions. As can be seen in figure 11, the data points close to the pole have very small error bars and precise measurements should be possible.

The charge ambiguity between the axial and vector couplings in this experiment could be resolved by measuring the helicity of the produced fermion which in the case of $\mu^\pm$ would require a 30 m long polarimeter according to an early study [1]. However, in the case of $e^+e^- \to \tau^+\tau^-$, there is not expected to be any great problem [23], the τ lepton's helicity being measured via the momentum distribution of its decay products

$$\tau \to e\, \nu_e\, \nu_\tau$$

or $$\tau \to \pi\, \nu_\tau$$

The τ leptons will be produced with a high $\gamma(\sim 25)$ at the Z° peak and the decay products will be almost collinear with the parent τ .

As already mentioned in the introduction, a search for new quarks will be of great interest at LEP and the methods which could be used have been extensively studied [24]. At low energy, the structures in R (figure 12) are extremely clear, the charm quark was first detected through the narrow $Q\bar{Q}$ states (J/ψ) preceding the step in R. At higher energies, such narrow states are expected to be considerably smaller and will not be easy to identify with a beam energy spread of 1.2×10^{-3}. Even with a smaller energy spread, very narrow peaks will be "washed-out" by radiative effects [25] as illustrated below. On the other hand, steps in R should be easier to measure precisely because of the higher multiplicity, the sphericity method used successfully at PETRA will also be possible if a good hadron jet detector is available.

Radiation by the incident e^+ and e^- will have extremely important effects at LEP as shown in figure 13 where the radiative effects on the Z° peak are shown. According to this calculation [23 26], 80 % of the raw events at a centre of mass energy of 140 GeV are in fact Z° production.

The detection and detailed identification of hadron jets will be of prime importance at LEP in view of the production of quark-antiquark pairs $e^+e^- \to q\bar{q}$ where the final state is only hadronic jets. At higher energies, the detection of W^+W^- pair production will also require a good jet detector. The W pair cross section in the standard

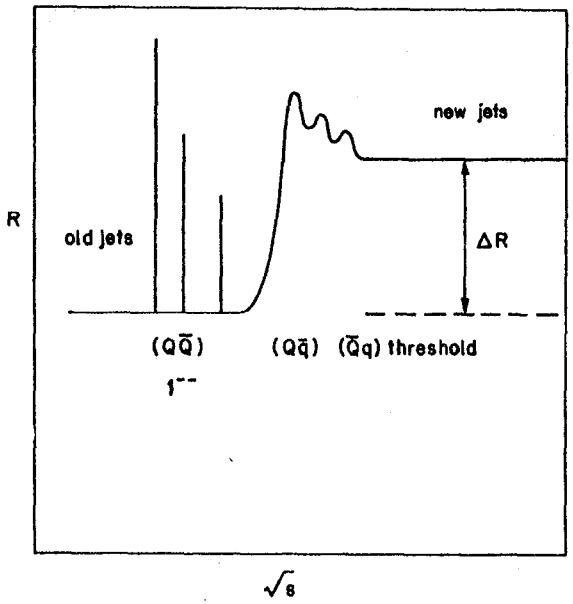

Figure 12 : Behaviour of R, the ratio of the total annihilation to pointlike cross-section at a new quark threshold.

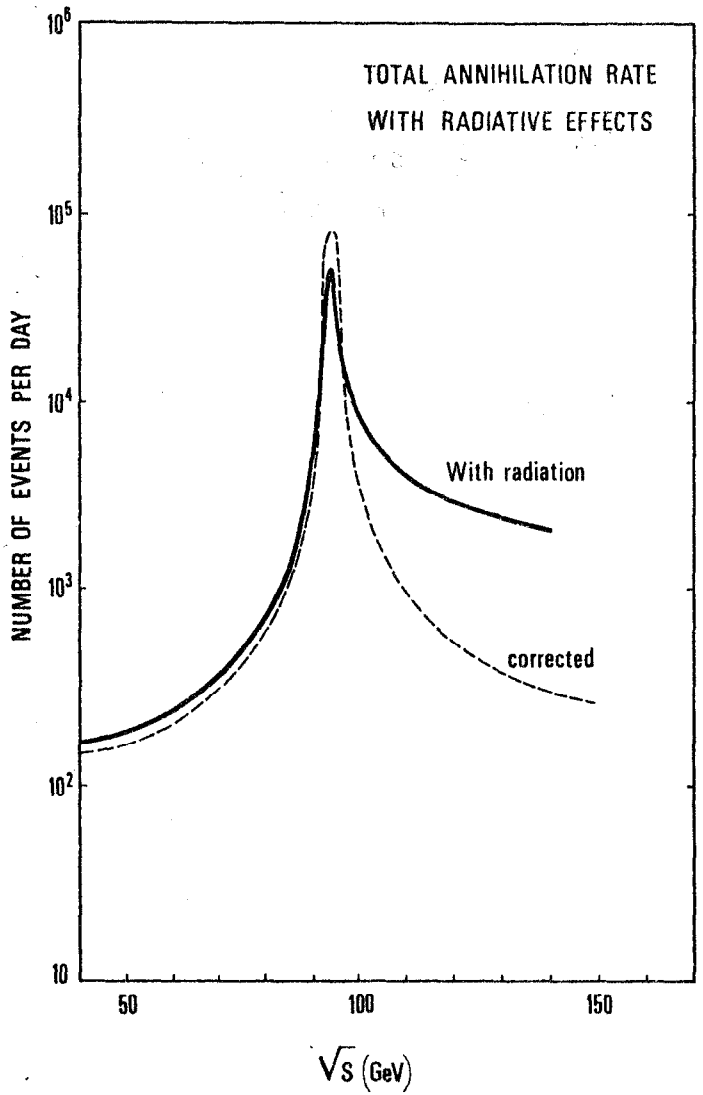

Figure 13 : The event rate at LEP around the Z° pole of the standard model before and after correction for the very important radiative effects.

model is shown in figure 14 where it can be seen that it reaches 1.8 x 10^{-35} cm^{-2} at 180 GeV (design energy with 96 MW of RF). At a luminosity of 10^{32} $cm^{-2}s^{-1}$, this gives 150 W pairs/day but with a branching ratio to hadrons expected to be around 0.8, the W pair events will yield :

100 "4 hadron jet" events/day
50 "2 jets + 1 lepton" events/day
5 "2 lepton" events/day

For these reasons, possible jet detectors have been extensively studied by the various working groups. The "hadronisation" of the quarks has been assumed to follow the Feynman-Field model and the resulting hadron jets have been used in Monte Carlo studies [27] of the behaviour of various detector configurations. This approach allows a careful analysis of the detector requirements in terms of granularity and energy resolution.

A proposed jet detector [24] is illustrated in figure 15 and is of a rather standard design. It is based on a solenoidal field of 1.5 T with an inner track chamber of 1.8 m radius of $\sim$ 6000 wires using Argon gas at 4 atmospheres. Such a detector would allow 100 samplings of dE/dx along a 1.25 m track to obtain good e/π and π/K separation over a wide momentum range (up to $\sim$ 50 GeV/c) [28]. An electromagnetic shower detector is placed immediately inside the magnet coil while the return yoke outside is adapted as a hadron calorimeter. An outer muon detector completes the system. The outer dimensions of this detector system are about 10 m x 10 m x 10 m and this has been used as the approximate size of experiments for the design of the experimental halls. Such a detector will fit very comfortably into the 21.4 m diameter cylindrical halls with space for transport above and around the detector. With a hall length of 60 m transverse to the beam, there will be plenty of room for electronics and cryogenic trailers.

Such a large detector would occupy the entire space between the low-β quadrupoles in a short insertion as shown in figure 15 where the quadrupoles are slightly inside the outer detector dimensions. For this type of installation so-called "slim" insertion quadrupoles have been designed [5,29] based on the superconducting magnets which will be installed at the ISR this summer. Provided the proper coordination of designs is carried out, this inclusion of quadrupoles into the detector should be perfectly possible and might even be taken further. A reduction of the free space between the quadrupoles should allow an increase in luminosity. In figure 15, it can be seen that there is no provision for compensation of the detector solenoid between the

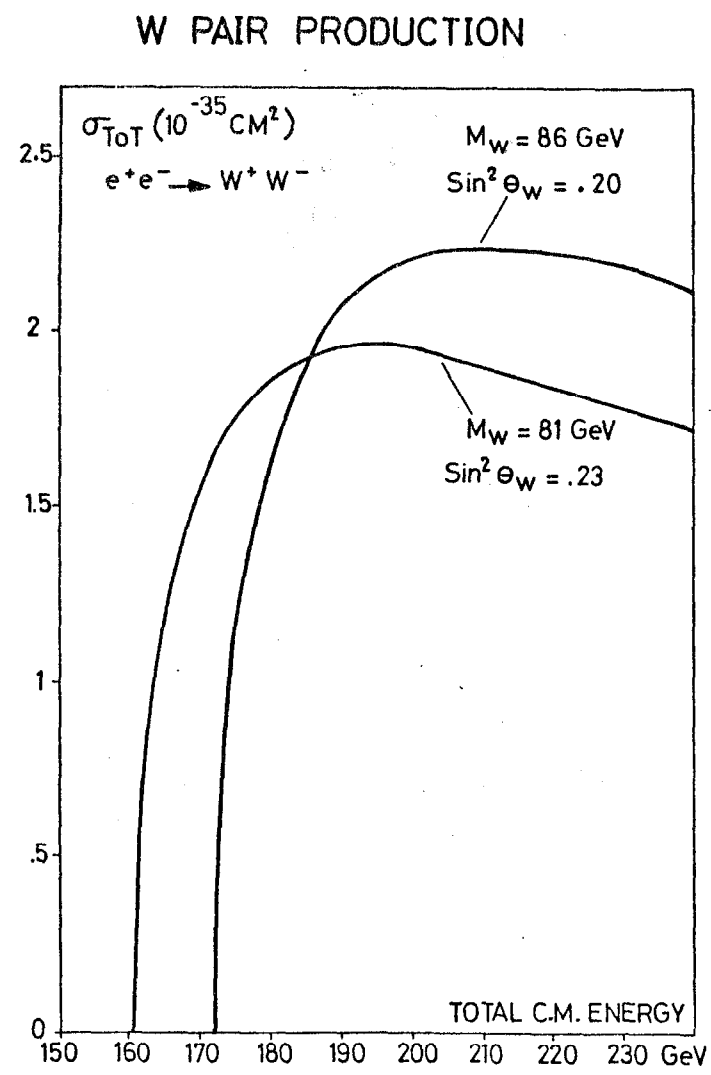

Figure 14 : The predicted [7] production cross section for W± pairs in the standard model for $\sin^2\theta_W = 0.23$ (present world average) and $\sin^2\theta_W = 0.2$

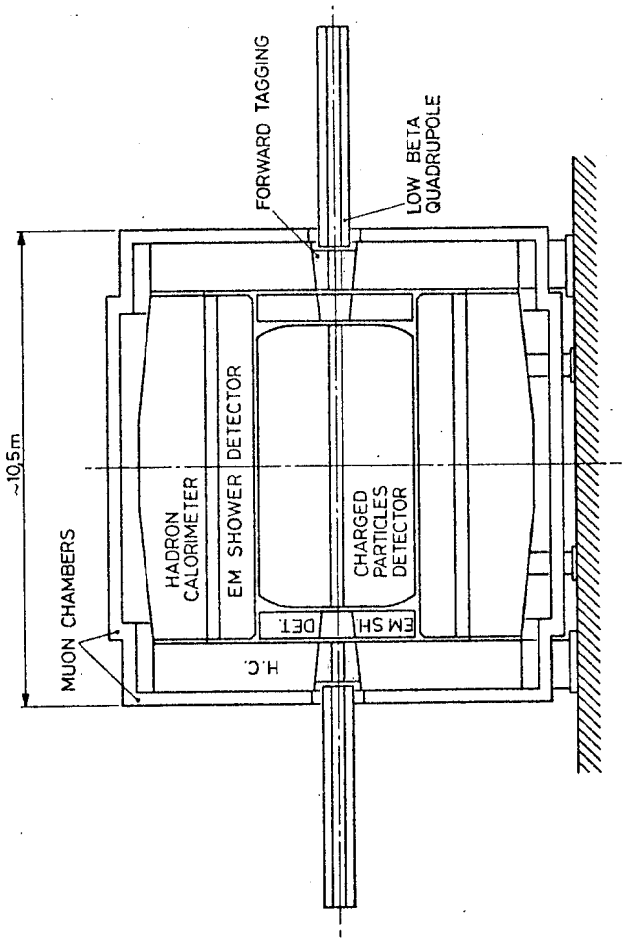

Figure 15 : The proposed JET Detector installed between slim superconducting insertion quadrupoles showing the limited space available for forward tagging detectors.

insertion quadrupoles. This will be done by means of skew quadrupoles in the adjacent straight sections.

Tagging of the forward electrons from two-photon processes will be very important at LEP since the two-photon cross section is increasing with energy while the QED annihilation goes as $1/E^2$. At a centre of mass energy of 100 GeV

$$\frac{\sigma_\gamma}{\sigma_{\gamma\gamma}} \sim 3 \times 10^{-4}$$

The two-photon process is expected to be a rich field of physics at LEP but, for other experiments, it will be considered a background, and for this reason studies [30 31] have been made of tagging efficiencies for various detector and insertion quadrupole configurations, including tagging behind the quadrupole. As an example, the tagging efficiencies which could be obtained behind three different quadrupoles are shown in figure 16. The slim quadrupole is not suited to this application but allows much better tagging around the magnet at angles in the range 55 - 300 mrad. With detectors in front of the quadrupole, angles down to 20 mrad or maybe even smaller can be reached depending on the diameter of the vacuum chamber.

In addition to event rate and suitability of detectors, it is necessary to consider backgrounds which may make experiments difficult or even impossible. As is well known, an important source of background at electron machines is the synchrotron radiation from the machine magnets. In the case of LEP, the radiation from the dipoles has a higher energy than in present machines. However, the machine layout with a 300 m straight section upstream of the crossing point will allow plenty of possibilities [4] for collimators to mask the detectors; in addition, the last dipole will have a lower bending power ($\sim$ 10 %) hence reducing the critical energy of the radiation which could reach the interaction region vacuum chamber. Much more important will be the radiation produced by the very powerful low-ß quadrupoles. The radiation from the last quadrupole has a critical energy of 0.25 MeV. Fortunately, it is produced in a reasonably small forward cone and, with a carefully designed vacuum chamber, will pass right through the interaction region. The bulk of this radiation will strike the machine vacuum chamber at distances greater than 50 m from the crossing point but even so the backscattered radiation will have to be taken into consideration when designing the interaction region vacuum chamber

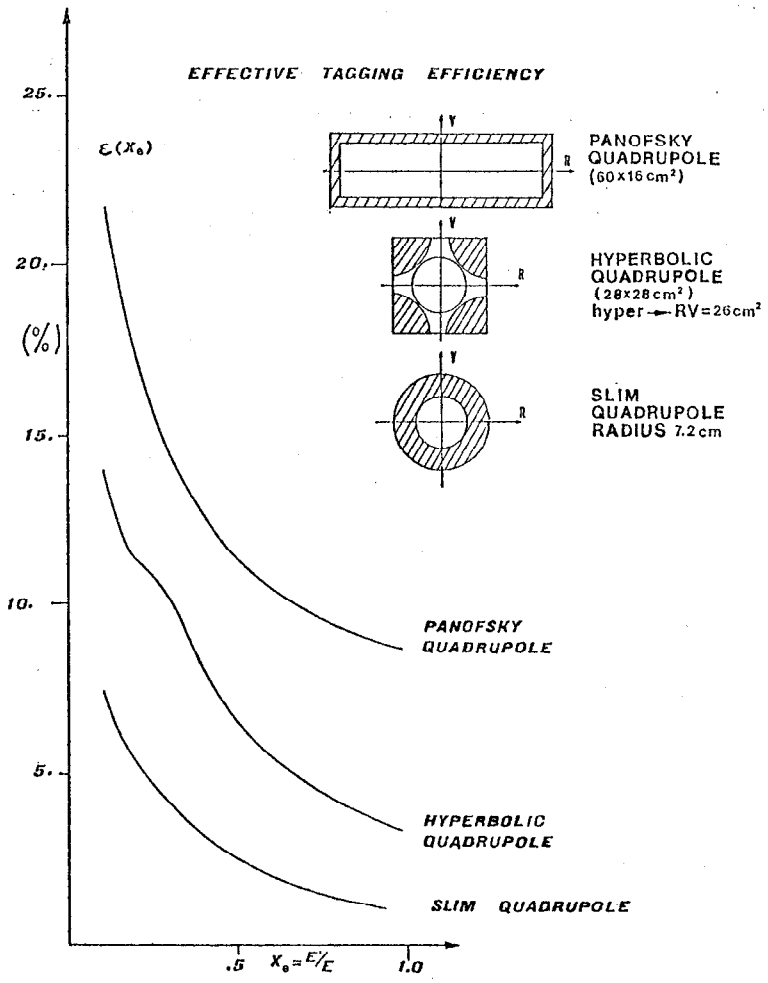

Figure 16 : Estimates of effective tagging efficiencies which could be achieved by placing suitable detectors behind the ± 5 m insertion quadrupoles for three different quadrupole configurations.

and radiation masks. The fraction of direct radiation intercepted by the vacuum chamber on the opposite side of the crossing region is shown in figure 17 as a function of the half-aperture.

Calculations [30, 33] have also been made of the rate of off-momentum beam particles which will be created by beam-gas bremsstrahlung in the RF straight section and final few bending magnets and which could be swept out of the vacuum chamber into detectors by the low-ß quadrupoles. This rate is a linear function of the residual gas pressure, the most important region being around the last bending magnets, a special effort will be needed to keep the gas pressure as low as possible at this point. It has been found that an inner radial collimator placed approximately 75 m before the interaction region effectively intercepts the higher energy part of this background. The approximate energy spectra of off-momentum particles are shown in figure 18 where it can be seen that the total rate in the crossing region itself is no more than one particle per hundred bunch crossings, assuming residual pressures equivalent to 10^{-10} torr of CO in the straight section and 10^{-9} torr in the bending magnets.

A third source of synchrotron radiation [5, 32] comes from the crossing point itself due to the influence of the electromagnetic field of one beam on the particles of the other (sometimes called beamstrahlung). In the case of LEP, some 3×10^{15} photons/sec will be produced with an energy spectrum characterized by a critical energy of $\varepsilon_c = 2.6$ MeV. These photons will be emitted in a very small forward cone and are themselves believed to be harmless but they will contribute to a considerable $e\gamma$ luminosity which will be as high as 5% of the e^+e^- luminosity. The $e\gamma$ interactions may cause additional background in the detectors via

$e\gamma \rightarrow e\gamma$ Compton scattering

$e\gamma \rightarrow e^+e^-e$ Pair production

These processes have been carefully calculated [34] and estimates made of the rate of particles, electrons and photons, leaving the vacuum chamber in the interaction region. High energy photons from Compton scattering could reach forward detectors but the calculated rate is only 3×10^{-4} per bunch crossing, the kinematics is illustrated in figure 19. A considerably higher rate ($\sim$ 5/bunch crossing) of low energy electrons ($<$ 100 MeV) will be created by the pair production process but all these electrons will curl up inside the vacuum chamber in the presence of a solenoidal field (figure 20).

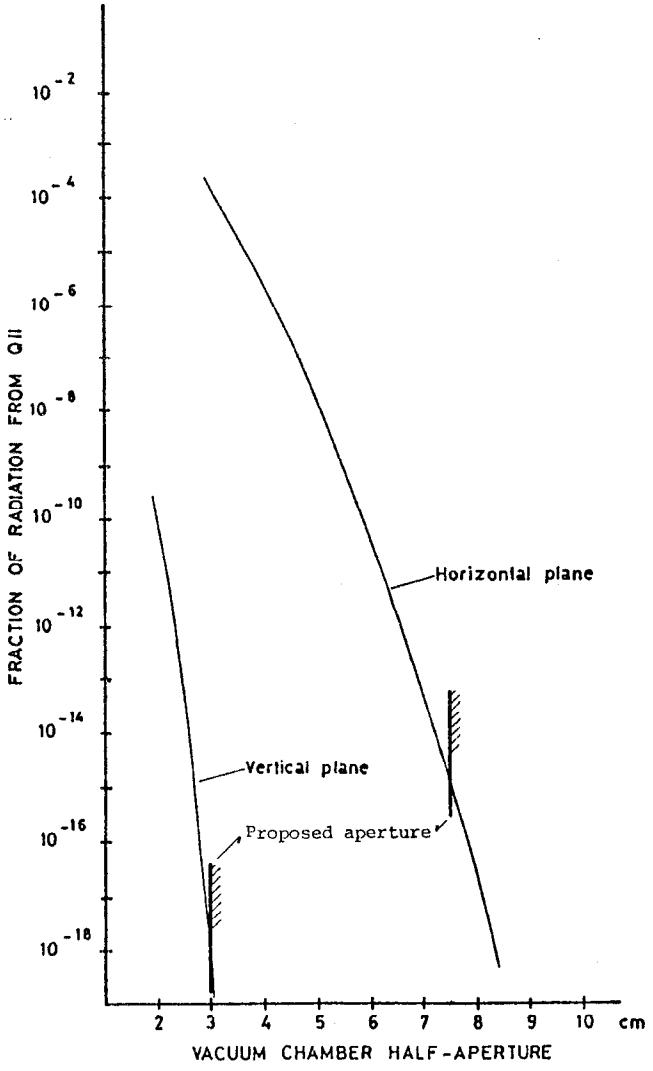

Figure 17 : The fraction of synchrotron radiation from the 5m insertion quadrupole intercepted by the vacuum chamber immediately in front of the opposite quadrupole, shown as a function of vacuum chamber half-aperture.

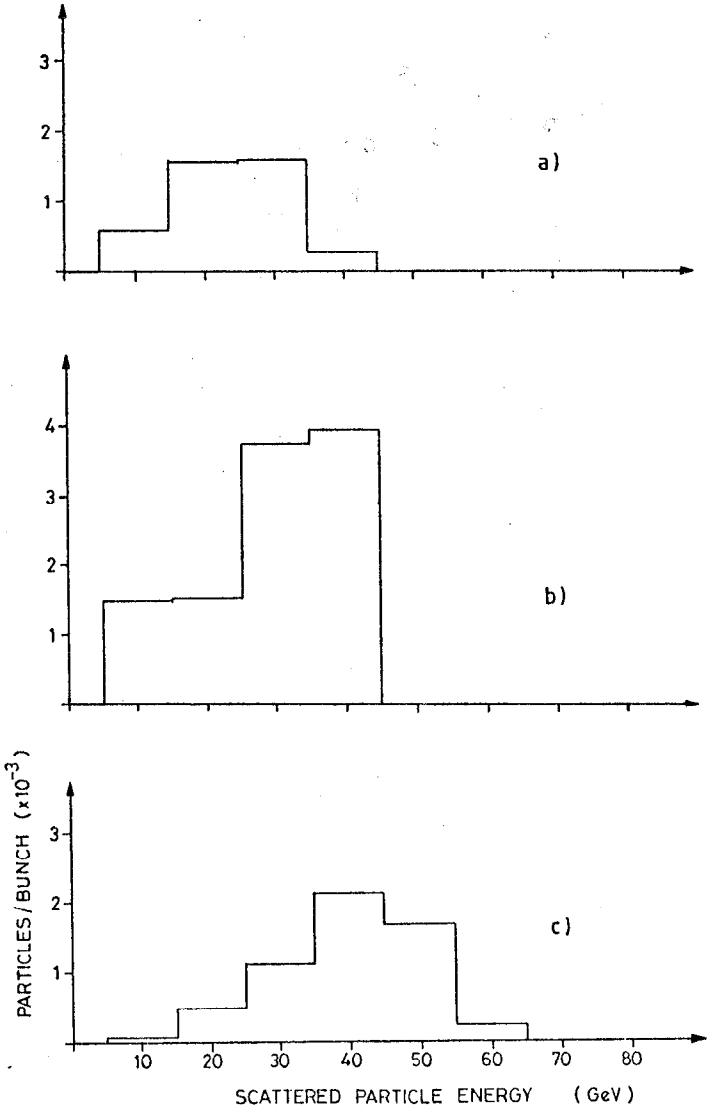

Figure 18 : Estimated energy spectra of off-momentum electrons reaching the vacuum chamber in three regions a) immediately upstream of the insertion quadrupole; b) between the quadrupoles; c) immediately downstream of the quadrupole. The high energy component has been effectively removed by a horizontal collimator 75 m upstream of the crossing point.

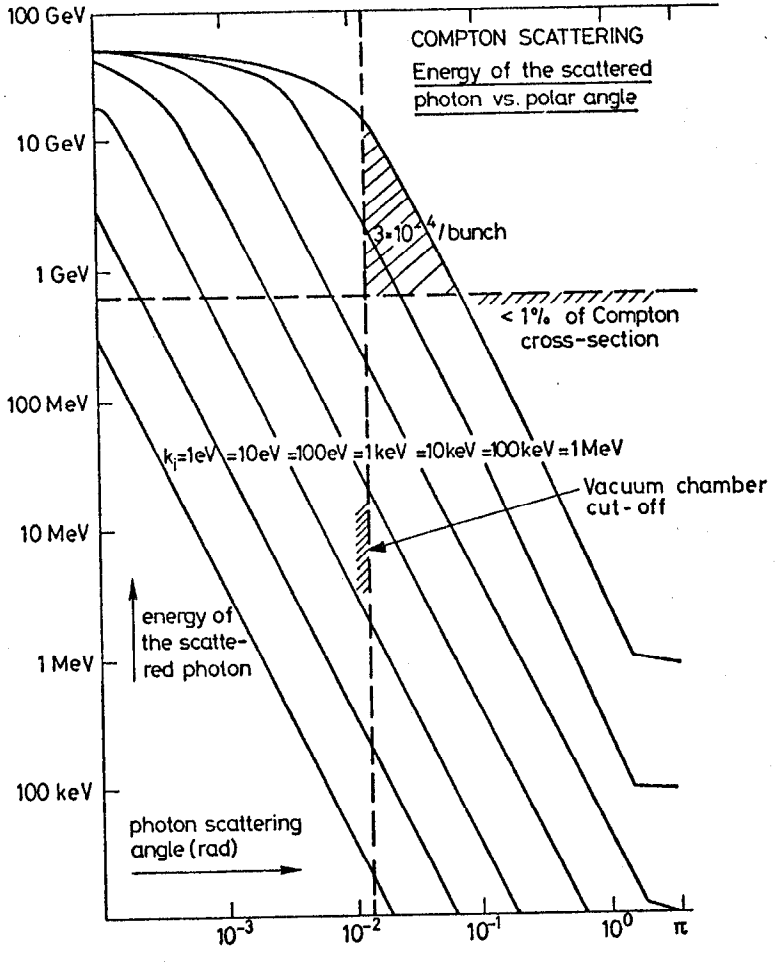

Figure 19 : Kinematics of the Compton scattering process $e\gamma \rightarrow e\gamma$ as a result of synchrotron radiation produced at the beam crossing point interacting with the opposite beam.

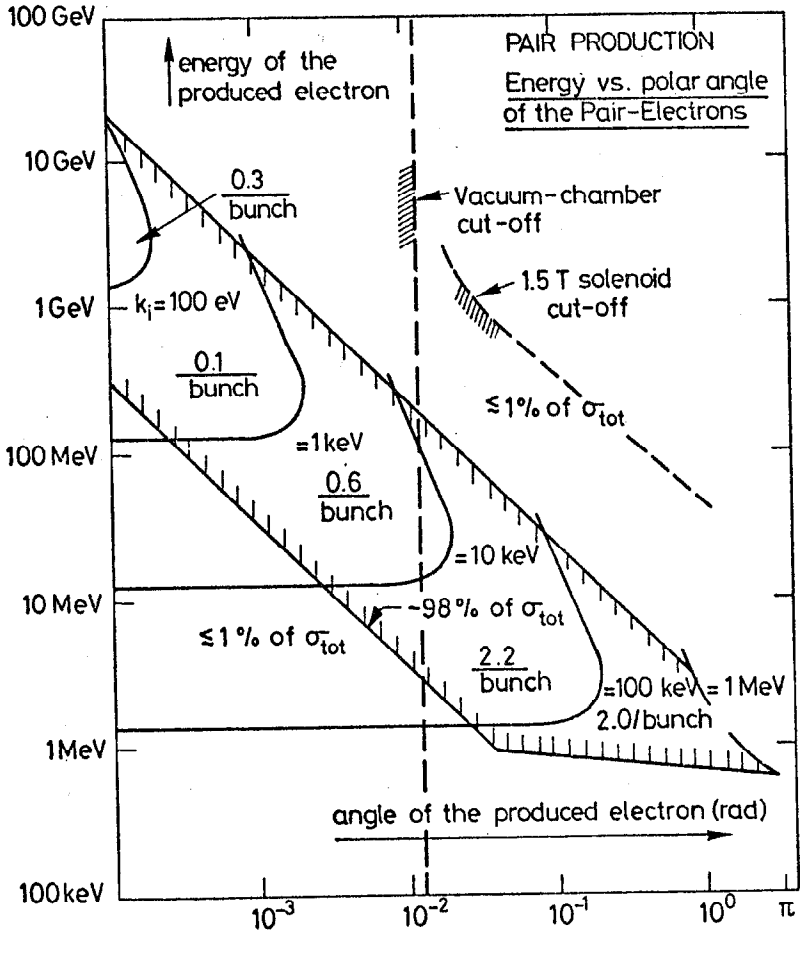

Figure 20 : Kinematics of electron pair production resulting from the synchrotron radiation produced at the beam crossing point interacting with the opposite beam.

4. Realisation of the Project

The construction of LEP was officially proposed to the Council of CERN at its June meeting of this year. The machine design report for the proposal is the so-called "Pink Book" [5] to which were added proposal documents concerning budget requirements and timescale. A phase I for the project was defined and agreed upon as the 1/6 RF stage (16 MW of installed RF power) with four equipped experimental areas. The RF stations would be at interaction regions 1 and 5 and the experimental areas at 1, 3, 5 and 7. A minimum of work would be performed elsewhere. It is proposed that with these austerity measures, it will be possible to construct LEP within the total CERN budget to achieve the first beams five years after approval. It is expected that this approval will be given in June 1981 so that it is hoped to start LEP physics in 1986.

It is apparent that with this timescale, it will be necessary to call for proposals for experiments almost immediately after approval of the project so that the preparation work which has been outlined in the latter half of this paper will be extremely important. The first round of detectors at LEP will have to be constructed with today's particle detection techniques.

Acknowledgements

This general review describes the work of a very large number of people. For the LEP machine design, a list of names appears in the "Pink Book" [5] while the various physics study reports [1, 20, 21, 22] contain similar lists of participants and authors of particular papers.

References

1. Discussions in the European Committee for Future Accelerators culminated in a recommendation in May 1977 that an electron-positron collider should be the next large European High Energy Physics project.
2. L. Camilleri et al., Physics with very High Energy e^+e^- colliding beams - CERN 76-18 (1976)
3. J.R.J. Bennett et al. - CERN 77-14 (1977)
4. The LEP Study Group - CERN Report ISR-LEP/78-17 (1978)
5. The LEP Study Group - CERN Report ISR-LEP/79-33 (1979)
6. S. Weinberg - Phys. Rev. Lett. 19, 1264 (1967)
   A. Salaam - Proc. 8th Nobel Symp. Stockholm 1968, ed. N. Svartholm (Almqvist and Wiksells, Stockholm, 1968) 367.
7. A. Martin - Report of SSG 20 - ECFA/79/39 (1980) 269
8. Design study of a proton-antiproton colliding beam facility - CERN report PS/AA/78-3
9. Recent summaries are :
   W. Schnell : Construction and Performance Plans for the LEP Collider, Presented at the Intern. Conf. on Experimentation at LEP, Univ. of Uppsala, Sweden 16-20 June 1980 - CERN report CERN-ISR-RF/80-11
   A. Hutton, Present Status of the LEP Project, Presented at XIth Intern. Conf. on High Energy Accelerators, CERN, Geneva July 7-11, 1980 - CERN Report CERN-ISR-TH/80-37
10. J-P. Gourber and L. Resegotti - IEEE Trans. Nucl. Sci. NS-26 (1979) 3185
11. U. Cummings et al., SLAC-PUB 797 /1970)
12. A. Perrot - LEP Note 225 (1980) unpublished
13. W.R. Nelson and J.W.N. Tuyn - CERN Report HS-RP/037 (1979)
14. W. Schnell, CERN report ISR-LTD/76-8 (1976)
15. W. Bauer and J. Halbritten - Primärbericht 08.02.03p01J - Kernforschungszentrum Karlsruhe (1980)
16. P. Bernard, H. Heinrichs, H. Lengeler, E. Picasso and H. Piel - LEP Note 209, (1980) unpublished
    V. Lagomarsino et al., IEEE Trans. Mag. 15 (1979)
17. Y. Baconnier, O. Gröbner and K. Hubner, LEP note 212 (1980) unpublished.

18. M. Sommer (ed) LAL Orsay report LAL 78/33 (1978)
19. G. Brianti - CERN report CERN/SPS/DI/80-3 - Rev. (1980)
20. Proceedings of the LEP Summer Study (Les Houches) - CERN 79-01 (1979)
21. ECFA-LEP Working Group 1979 Progress Report ECFA/79/39 (1980)
22. Proceedings of the International Conference on Experimentation at LEP, Univ. of Uppsala (1980) to be published in Physica Scripta
23. M. Davier, CERN 79-01 (1979) 61
24. K. Winter, CERN 79-01 (1979) 93
25. H. Boggild, Report of SSG 8, ECFA/79/39 (1980) 97
26. V.G. Goggi - ECFA-LEP/4 (1978) unpublished
27. D. Drijard, H. Grote and P.G. Innocenti - CERN 79-01 (1979) 133
28. A. Wagner, CERN 79-01 (1979) 165
29. C. Wyss, LEP note 169 (1979) unpublished
30. R. Del Fabbro and G.P. Murtas - LNF-79/23(R) (1979)
LNF-79/40(R) (1979)
31. P. Strolin, K. Potter - Report of SSG 6, ECFA/79/39 (1980) 59
32. A. Hofmann, E. Keil - LEP note 122 (1978) unpublished
33. A. Smith - LEP note 164 (1979) unpublished
P. Strolin, K. Potter ECFA/79/39 (1980) 59
34. J. Allaby et al. - CERN 79-01 (1979) 243

A High Energy e^+e^- Collider at Cornell Using Superconducting RF Cavities*

N. B. Mistry
Laboratory of Nuclear Studies
Cornell University, Ithaca, NY

We have begun a design study at Cornell for an e^+e^- colliding ring of sufficient energy to observe and study the Z^0—the neutral intermediate boson—and with sufficient luminosity to study in detail the weak interaction as well as rare decay modes of the various heavy particles produced at the Z^0.

This design study has not yet reached the status of a formal proposal for funds. As you will see, the design depends crucially on the successful development of superconducting RF cavities. For the present, we will put our major effort into the design and development of prototype superconducting RF cavities capable of being used in a high energy electron storage-ring.

Let me start with the question of what is a suitable optimum energy and luminosity. It is obvious that we cannot look towards a machine on the scale of the full LEP proposal. However, by restricting the design parameters to those sufficient to resolve some of the current important physics questions, we believe we can build a competitive U.S. facility.

What do we expect for the Z^0 mass? The standard Weinberg-Salam model relates the mass to two parameters: $\sin^2\theta_W$ and ρ, which can be measured in "low energy" experiments such as neutrino interactions and ed scattering, etc.

* Work supported by the National Science Foundation.

Thus

$$\hat{M}_z \sim (\sqrt{\rho}\ \sin\theta_w\ \cos\theta_w)^{-1}$$

with $\rho \simeq 1.0$.

Recent fits to experimental data yield values ranging from $\hat{M}_z = 87 \pm 8$ GeV for a two-parameter fit[1] to $\hat{M}_z \simeq 90 \pm 2$ GeV if we fix $\rho = 1.0$.[2]

Recently, however, higher order corrections have been estimated by Veltman and others[3] for diagrams involving Z^0 lines, for example:

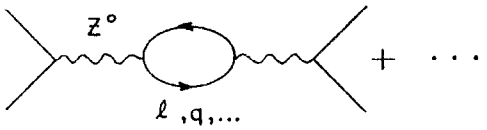

These lead to mass corrections such that the value $\hat{M}_z$ derived from measurements of $\sin^2\theta_w$ and ρ is lower than the mass of the Z^0 pole to be observed in e^+e^- collisions by 3.3 GeV to 5 GeV! The range of mass-values to be expected for a Z^0 resonance in e^+e^- collisions is shown in Figure 1. The curves were provided by Henry Tye at Cornell. Grand-unification schemes favor a value $\sin^2\theta_w \simeq 0.20$. Considering all this, we should be prepared for a mass as high as 98-100 GeV. In what follows, a nominal ring energy of 50 GeV per beam is assumed, but it is to be understood that the actual final design energy could be about 55 GeV.

What is the rate of hadronic events expected at the peak of the Z^0 resonance?

Defining $R \equiv \dfrac{\sigma(e^+e^- \rightarrow \text{hadrons})}{\sigma(\text{point-like})}$,

at the peak of the Z^0 we expect

$$R_{pk} = (9/\alpha^2) \cdot (\Gamma_{ee}/\Gamma_{tot}) \cdot (\Gamma_{had}/\Gamma_{tot})$$

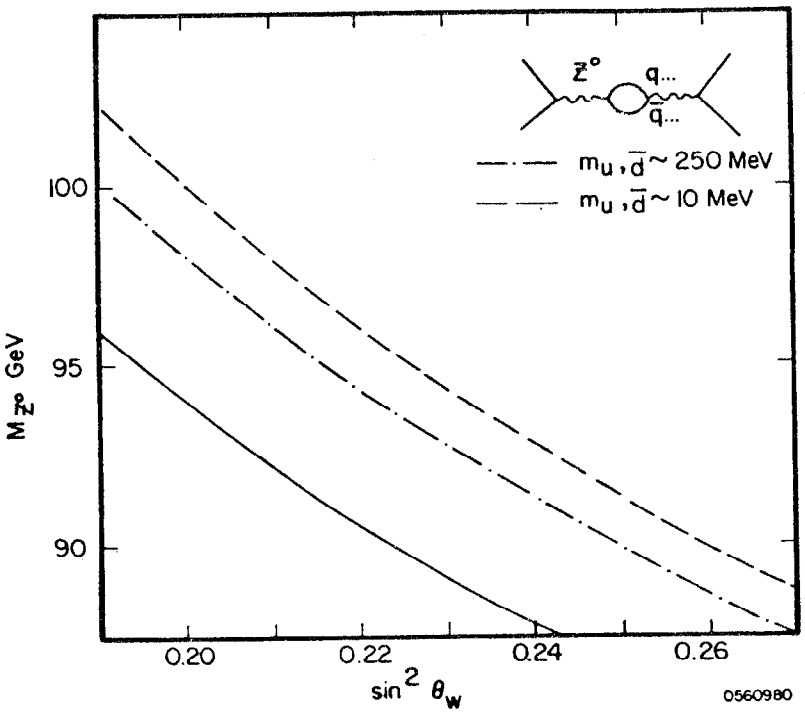

Figure 1. Mass of the Z^0 vs. $\sin^2\theta_w$ (solid curve). Broken curves show the effect of higher order terms.

The total width depends on the number of fundamental fermions N_i of mass $m_f < M_Z/2$. Using $\sin^2\theta_W = 0.23$, we get:

$$\Gamma_{tot} = 0.08 \text{ GeV } (1.0\ N_\ell + 2\ N_\nu + 4.4\ N_{1/3} + 3.5\ N_{2/3})$$

$\simeq$ 2.6 GeV, for $N_i = 3$ representing 3 generations each of leptons, neutrinos and quarks of charge 1/3 and 2/3. The coefficients of the N_i give the relative branching ratios. Thus the branching ratio into leptons is $\sim$ 0.03 and into hadrons is $\sim$ 0.73. Putting all this together yields $R_{pk} \sim 3800$, an enormous enhancement over the continuum value of $R \sim 4$-5. At the Z^0 mass the point-like cross-section is $\sim$ 0.011 nb. At a luminosity of $3 \times 10^{31} \text{cm}^{-2}\text{sec}^{-1}$, the hadronic event rate at the peak will be about 4500 per hour. Figure 2 shows the typical resonance curve. Note that the total width is a probe of the total number of generations of leptons. Since neutrinos associated with new generations of heavy leptons are unlikely to be very heavy (even though the leptons themselves may be heavier than $M_Z/2$), then $\Gamma_{tot} \propto 2\ N_\nu$; e.g., if there are five new generations of neutrinos Γ_{tot} increases from 2.6 GeV to 3.4 GeV, and R_{pk} drops to 2240.

We can now proceed to estimate rates for various interesting processes, assuming an average working luminosity $\langle \mathcal{L} \rangle \sim 10^{31} \text{cm}^{-2}\text{sec}^{-2}$ near the peak of the Z^0.

(a) The Z^0 will be a prolific source of heavy leptons and heavy quarks. Decays of heavy leptons and quarks will occur at ten per hour (leptons) to hundred per hour (quarks). Rare decay modes of heavy mesons at the 1% level can be observed at one per hour.

(b) Gluon jets produced with $Q\bar{Q}$ pairs are expected to be clearly separable at a rate of $\sim$ 1% of all events, yielding observable events at one per hour.

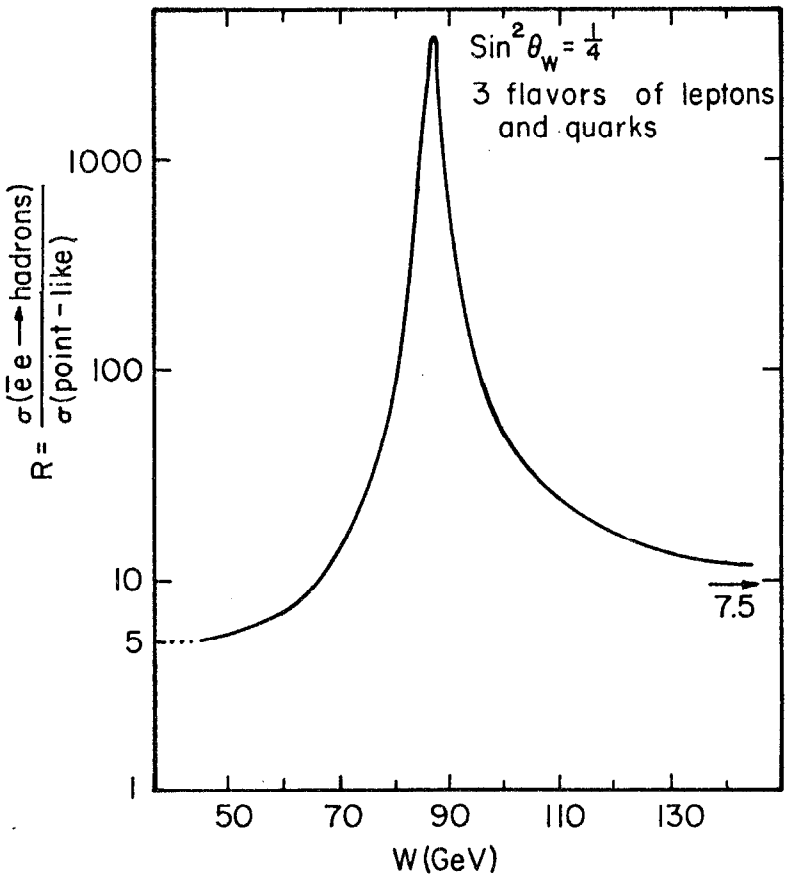

Figure 2. Z^0 resonance predicted using $\sin^2\theta_W = 0.25$.

(c) The branching ratio of $Z^0 \rightarrow$ Higgs + $\ell\bar{\ell}$ is expected to be $\sim 10^{-6}$ for $M_{Higgs} \sim 50$ GeV. This would yield an event every 10 days.

(d) Weak-electromagnetic interference can be measured through the forward-backward asymmetry in $\mu\mu$ or $q\bar{q}$ production as a function of energy. (See Figure 3.) At the peak of the Z^0, rates will be ~ 100/hr. However at $W \sim M_z/2$, rates will be less than one event per hour, using a scaled luminosity.

(e) Toponium states (^3S states of $t\bar{t}$) may yield $R_{pk} \sim 12$ at a toponium mass of 50 GeV. (This assumes Γ_{ee}(toponium) $\sim$ (12keV) $\times$ (t-charge)^2 and an energy resolution of 130 MeV at 100 GeV). A scaled luminosity of $7 \times 10^{30} cm^{-2} sec^{-1}$ at W = 50 GeV yields toponium rates of about ten per hour.

The conclusion to be drawn from all this is that the design luminosity at the peak should <u>average</u> at least $10^{31} cm^{-2} sec^{-1}$, and vary proportional to E^2 below the peak energy.

<u>Why superconducting cavities?</u>

The size of the ring and the choice of superconducting or normal RF cavities becomes evident on performing a cost optimization.[4, 5, 6] We separate the total cost C into fixed costs, C_0, which do not scale with the size of the ring or its luminosity, and scaled costs C' = (C-Co) which are to be minimized. The fixed costs include the costs of buildings, experimental halls, the injector and beam transport, etc.

The scaled costs can be expressed as follows:

$$C' = g_\rho \cdot \rho + (g_{cav} + \mathcal{L}_0 \cdot g_{\mathcal{L}}) E^4/\rho$$

where ρ is the radius, E the beam energy and $\mathcal{L}_0 \equiv \mathcal{L}/E$. The g_i are unit costs:

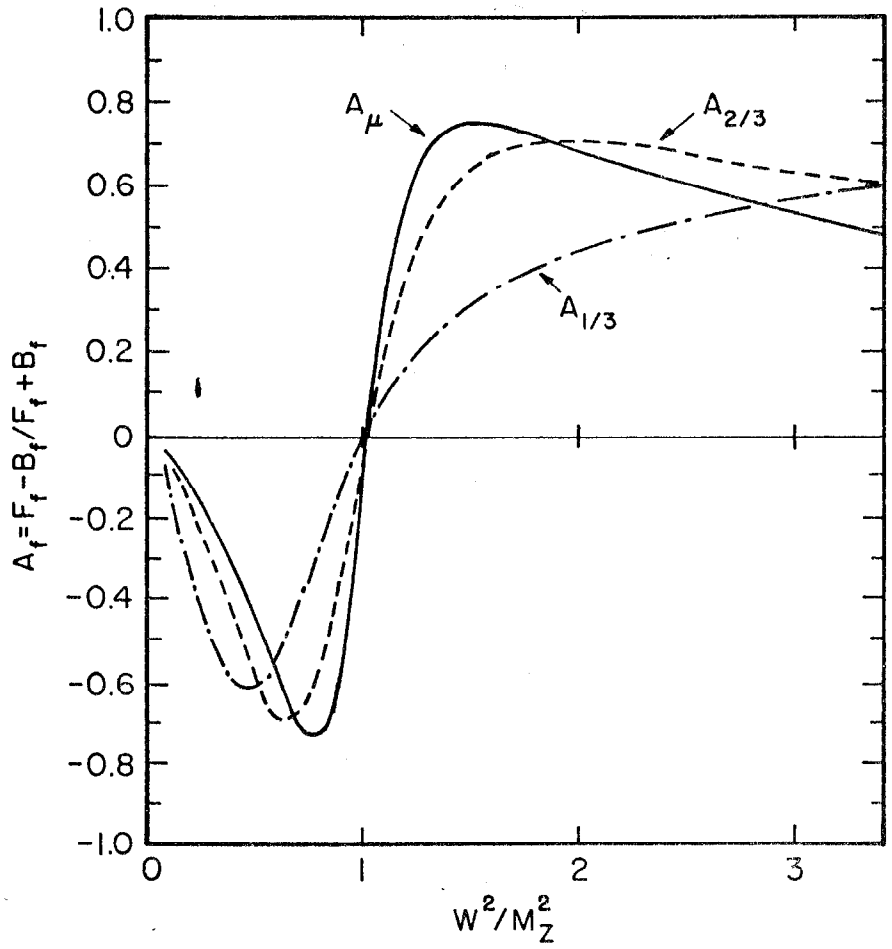

Figure 3. Forward-backward charge asymmetry in $\mu\mu$ or $q\bar{q}$ production, arising from weak-electromagnetic interference.

g_ρ is the cost per kilometer of components such as magnets, magnet power supplies, vacuum system, tunnel, controls, instrumentation, etc.

g_{cav} is the cost per unit of (E^4/ρ) for providing the accelerating RF voltage, with no power absorbed by the beams. This represents the cost of cavities, cryogenics, etc., and includes the 5-year cost of providing the power to make up cavity-wall losses. It is obvious that these power costs are very different for superconducting and normal cavities. As a result, g_{cav}(normal) is about ten times greater than g_{cav}(superconducting).

$g_{\mathcal{L}}$ is the cost of producing luminosity, i.e., of providing power to the beams. (Note: $\mathcal{L}_o \equiv \mathcal{L}/E$ is proportional to I_{beam}, and beam power $\sim E^4 I/\rho$). This includes the costs of klystrons, etc., and 5-year power costs.

The cost equation has a broad minimum when the two terms on the right hand side are equal. The optimum radius is then given by

$$\rho_o = \left[(g_{cav} + \mathcal{L}_o g_{\mathcal{L}})/g_\rho\right]^{1/2} E^2$$

Inserting unit costs extrapolated from operating machines like CESR, PEP and PETRA, with appropriate costs added for cryogenics, etc., for E = 50 GeV per beam and $\mathcal{L} = 3 \times 10^{31} cm^{-2} sec^{-1}$ at 50 GeV, we find

ρ_o(s-c) = 0.51 km and

ρ_o(normal) = 0.99 km

Thus for a storage ring using normal RF cavities, not only are the unit costs very high, but the ring diameter is almost twice as large as for the case with superconducting cavities. The total costs for a ring with normal RF are then much higher than for a ring with superconducting RF.

Table I shows the various cost terms for the "50 GeV" ring as proposed at Cornell. Table II shows the scaling part of the cost only, for various options of peak energy, luminosity and type of RF cavities. This illustrates the incremental cost for increased luminosity or energy and the penalty for using normal RF cavities.

The above considerations make it clear that for a given amount of money, the maximum potential in terms of energy and luminosity can be realized by using a superconducting RF system. Similar analysis for any large accelerator requiring high RF voltages makes the successful development of large-scale superconducting RF systems a high priority.

Parameters of the Storage Ring

The important input parameters for the design of the ring are peak energy E_o, luminosity $\mathcal{L}$ at E_o, the number of interaction regions and the free space between quadrupoles at the collision points. In general, significant increases in capital and operating costs result from any increase in these parameters. Another important parameter is the maximum obtainable transverse charge density at the collision point. A practical limit has been observed at all operating high energy e^+e^- colliding rings when the colliding beams begin to blow each other up and the beam lifetime is drastically reduced. This limit is characterized by a maximum linear tune-shift ΔQ of around 0.03. This is the value we have used in the design formulae.

Having chosen superconducting RF cavities, one has to decide on an achievable accelerating field in order to determine the total length of cavities needed. We choose $\mathcal{E}$ = 3 megavolts/meter as a reasonable field; in test cavities in the laboratory, fields of up to 4.5 MV/m have been measured. The RF frequency is tentatively chosen to be 1500 MHz, mainly from cavity-design considerations as will be seen later.

TABLE I

50 X 50 GEV STORAGE RING COSTS

(All costs in $ M, 1980 values, 20% contingency included)

Cost Linear with Circumference: Housing, Magnets, Vacuum, Instrumentation and Control	73
Cost to provide R.F. voltage using superconducting cavities with no energy supplied to the beam	22
Cost to supply energy to beam for luminosity	11
Total Storage Ring Cost	106
Fixed Costs:	
Injector	29
IR Halls and cranes	8
Site Work and Utilities	9
Auxiliary Lab and Office Space	12
Total Fixed Costs	58
TOTAL FACILITY COST	$ 164 M

TABLE II

CAPITAL COSTS OF VARIOUS STORAGE RINGS

Beam Energy GeV	Peak Luminosity (10^{32}/cm^2/sec)	Supercond. Cavities $ M	Normal Cavities $M
50	0.3	107	220
50	1.0	155	265
86	0.3	283	634
86	1.0	383	698

All costs in 1980 dollar values.

There will be four collision points. The interaction region straight-section lengths are chosen to be 100 m each, to allow room for polarization manipulation, wigglers, etc. The four RF region straight-section lengths are 187.5 m each.

Table III shows a list of significant parameters. Figure 4 shows the expected luminosity as a function of energy. Figure 5 shows a schematic layout of the ring.

Two possible sites are being considered for the location of the new storage ring. "Site A" is situated on land mostly owned by Cornell University next to the airport. The site is quite flat and a cut-and-fill operation is sufficient to construct the tunnels. This site is about five kilometers from the present CESR site. The injector for this site would be a 600 MeV linac filling a small 600 MeV accumulator ring, which in turn would lead to either a 10 GeV synchrotron in a tunnel separate from the main ring or a 20 GeV synchrotron housed in the same tunnel as the 50 GeV ring. An alternate site being considered is located within a kilometer of CESR, but is in rather undulating terrain. This site would use CESR as accumulator and injector, so that full-intensity bunches could be injected on the center line of the main ring. The drawback of this site is that two of the interaction regions are up to 50 meters underground, so that these experimental halls would have to be excavated deep underground. Tentative designs have been produced for all the underground and surface experimental areas as well as for RF installations and klystron buildings. A central laboratory building and smaller support buildings for each experimental area are being designed.

The vacuum chamber of the main ring will have a clear aperture of 45 mm x 30 mm. The linear power density of synchrotron radiation

TABLE III PARAMETER LIST

E_0: 50 GeV

$\mathcal{L}_{50\ GeV}$: $3 \times 10^{31} cm^{-2} sec^{-1}$

I.R.: 4

Expt. Space: 2 @ 4m
2 @ 6m

Length I.R. St.: 100 m each

ρ : 500 m

$\langle R \rangle_{ARCS}$: 690 m

Circumference: 5484 m

$\langle R \rangle = \frac{\sigma^{ce}}{2\pi}$: 873 m

ΔE /turn : 1.1 GeV

$\sigma_E / E : 1.9 \times 10^{-3} \times \left(\frac{E}{50}\right)$

$n_{bunches}$: 2/ beam

$N_{e^{\pm}}$/bunch : 2.1×10^{11}

I_{beam} : 3.7 mA/beam

$P_{radiated}$: 8.1 MW (2beams)

ϵ_c (synch rad) : 555 keV

β_H^* : 0.4m β_V^* : 0.04 m

σ_H : 0.11 mm σ_V : 0.011mm

Beam Aperture : 45 mm X 30 mm in Normal Cell

ΔQ_{max} : 0.03

R.F.

ΔV/turn : 1.5 GeV

$\mathcal{E}$: 3 MV/m

L_{CAV} : 500 m

Freq. : 1500 MHz

Power : 10 MW (includes ~ 2 MW higher mode loss)

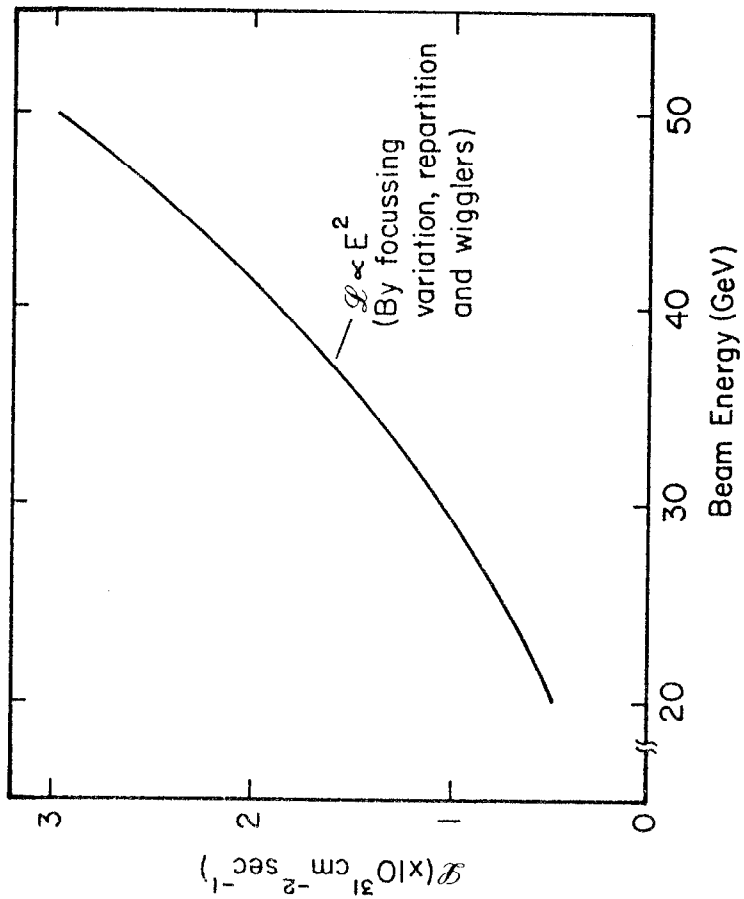

Figure 4. Luminosity vs. Beam Energy.

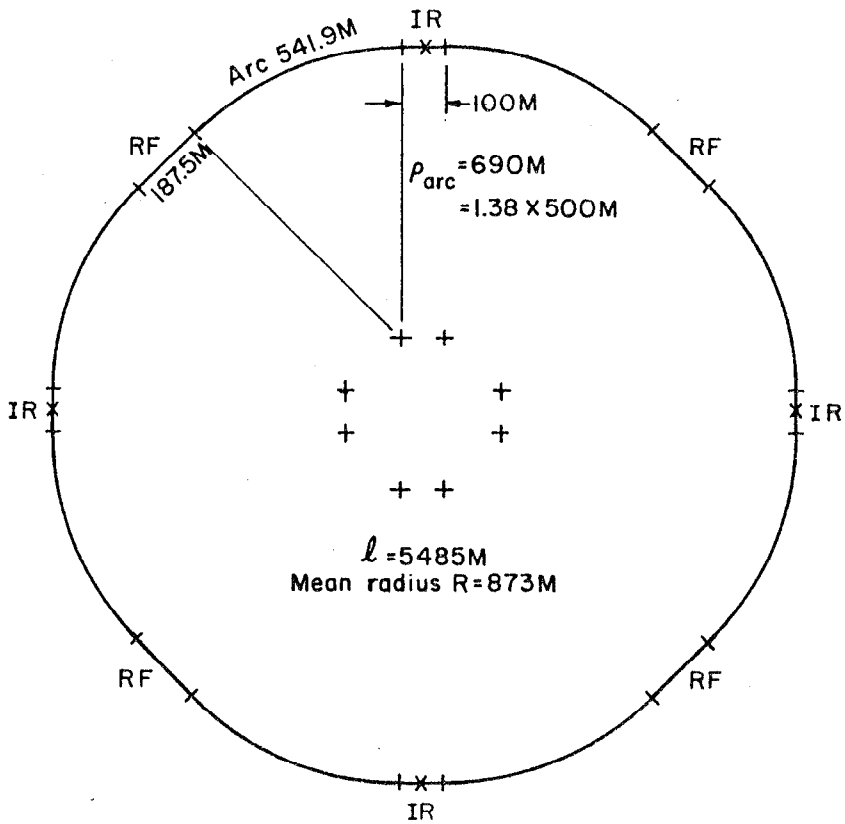

Figure 5. Schematic layout of the ring.

hitting the walls at 50 GeV and full beams is about 2.3 kW/m, which is about 50% higher than that in the CESR normal bends but considerably less than the intensity in the CESR high bend regions. The vacuum system is designed to operate at a pressure of approximately 3×10^{-9} Torr with full beams, to give a beam life-time of 10 hours.

Beam Polarization

The life-time for transverse beam polarization by spin-flip radiation is given by

$$\tau_p(\text{secs}) \sim 98.7 \cdot \rho^2 \cdot \langle R \rangle \cdot E_{GeV}^{-5} \quad \ldots.(\rho, R \text{ in meters})$$

$$\sim 69 \text{ seconds at 50 GeV}$$

However, integral depolarizing resonances occur at a spacing given by $\Delta Q(\text{integer}) = \gamma(g-2)/2$, i.e., every 440.65 MeV in beam energy. At best one can run at energy ± 220 MeV away from a resonance. At 50 GeV, the rms energy spread of the beams is 95 MeV, so that the polarization may not have too much of a chance. However, since $\sigma_E \sim E^2$, at a beam energy of 31 GeV the resonances can be a safe 6σ away ($\sigma_E \sim 37$ MeV) and the polarization life-time is still only 12 minutes. Thus one can expect good polarization in a limited energy range: 30 GeV down to about 25 GeV, where τ_p becomes as long as 37 minutes. Wigglers can be inserted in the long straights to reduce τ_p and extend the range.

Superconducting RF Cavities

Development of superconducting RF for accelerators has been going on at Cornell for several years. An 11-cell superconducting S-band accelerating structure was installed in the 12-GeV synchrotron in 1975 and used to accelerate beams to 5 GeV. The cavities were also successfully operated with 12 GeV beams in the ring, to provide a real test in the synchrotron-radiation and high-energy electron environment. More recent work has concentrated on the development of cavity shapes and fabrication techniques suitable for a large storage ring.

Some of the design considerations are presented below.

(1) Typical Wall Losses: The power absorbed in the walls can be expressed as $P_w = \mathcal{E}^2/R_{shunt}$. R_{shunt} has been measured using a niobium two-cell cavity to be 3.3×10^{12} Ω/m ($Q_0 = 3 \times 10^9$). This yields $P_w = 2.72$ watts/m. (In contrast, typical figures for a copper cavity operating at 350 MHz are: $R_{shunt} = 40 \times 10^6$ Ω/m, $\mathcal{E} = 0.6$ MV/m and $P_w = 225$ kilowatts/m.) Allowing for miscellaneous heat-loads of 2 watts/m for RF power inputs, etc., the load on a helium refrigerator is 5 watts/m. With an overall refrigerator efficiency of 10^{-3}, the mains power requirement is 5 kW/m. For copper-cavities, using 70% as the RF power conversion efficiency, 320 kW/m of mains power would be required.

(2) Choice of Frequency: Previous superconducting cavities used in the Cornell synchrotron operated at S-band, i.e., 3000 MHz, $\lambda = 10$ cm. However the resulting beam-aperture would be too small for use in a storage-ring. At 1500 MHz, the aperture would be adequate, allowing extra room for masking of synchrotron radiation.

What are the advantages and disadvantages of 1500 MHz relative to lower frequencies, say 500 MHz? The advantages of 1500 MHz are: (a) smaller size, easier to make and handle in large quantities for the complex surface treatment required, etc.; (b) higher accelerating field gradient for the same surface fields; (c) significantly less multipactoring, i.e., breakdown due to regenerative electron impact. The disadvantages are: (a) higher synchrotron-oscillation frequency; synchro-betatron instabilities could be serious, (b) short bunch

length, leading to larger higher-mode losses and instabilities due to induced fields, (c) lower klystron efficiency. These problems are being studied in detail. At present one can say that the "harmonic number" (number of RF wavelengths in the circumference) is the same as that for LEP, and this is supposed to mean that synchro-betatron oscillation problems should be the same for both machines. The bunch-size can be lengthened by using special cavities. The design of 1500 MHz klystrons is being commercially explored. Overall, the balance seems to be in favor of the 1500 MHz frequency, based on past experience in fabrication and operation.

(3) Coupling to beam: The cavities must supply about 20 kW/m to the beams at full energy and current. A single bunch extracts only about 10% of the stored energy, and will not significantly affect the fields. However, the geometry of the input coupling needs careful design in order to avoid exceeding locally the critical field H_c of the superconductor and to avoid local heating due to multipactoring at the coupling slot.

(4) Higher order mode heating: The passage of a bunch shock-excites many resonant higher modes in the cavity structure. Typically, about 4 kW/m deposited in this way by the beam must be removed from the cold cavity and absorbed in a room-temperature load. Further, this higher-mode coupling must not affect the fundamental accelerating mode in the cavity. Measurements with 5-cell copper cavities show that sufficient coupling can be achieved for the 6 modes studied at frequencies below twice the fundamental f_0. Modes with $f > 2f_0$ spill over from the cavity into the cut-off zones (refer to Figure 6) where liquid nitrogen absorber will be placed.

(5) Higher Mode Beam Instabilities: Instabilities can arise from

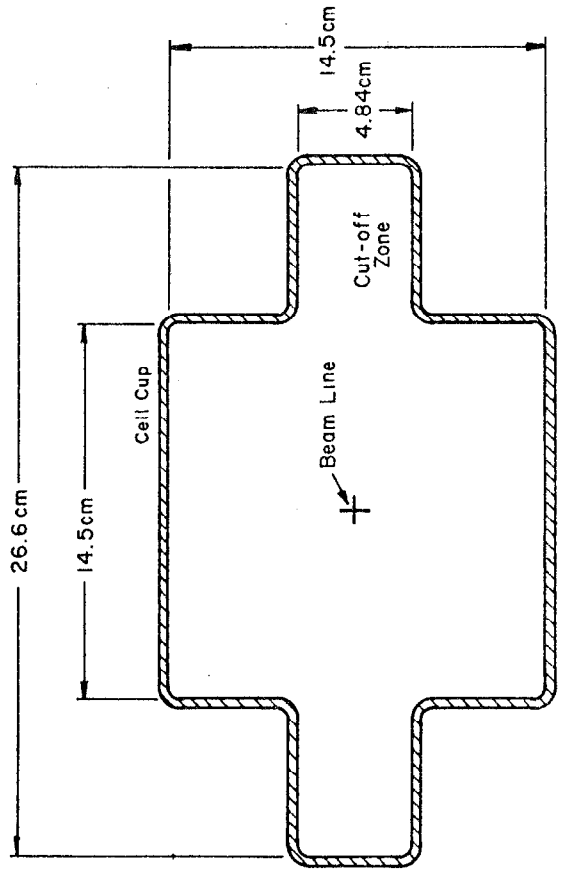

Figure 6. Cross-section of 1500 MHz cavity.

multibunch effects due to the wake-field of one bunch on the next, and from the single bunch multiturn effect of the wake-field of the same bunch on successive turns. Again, measurements using copper cavities show that sufficient coupling factors can be achieved to extract these modes and reduce the fields in the cavities to acceptable levels. A simplified way of looking at this problem is to realize that resonant build-up of higher mode fields can be avoided if the cavity is "loaded" by coupling to external loads such that $\tau_{decay} < 4.6\mu sec$ which is the bunch-passage interval. Typical loaded copper cavities show about one-fourth the minimum Q-value needed to make $\tau_{decay} = 4.6\mu sec$ for the lowest mode at 2000 MHz. Less coupling is needed to achieve the same result for higher frequencies.

Figure 6 shows a cross-section of the 1500 MHz cavity. Figure 7 shows a picture of a niobium two-cell structure used for tests.

Present Program of Cavity Development

The current program can be divided into three parts.

(a) Work on the basic superconducting structure. A two-cell niobium 1500 MHz structure has been used to achieve accelerating fields of up to 4.5 MV/m with $Q_0 = 3 \times 10^9$. The field is limited by multipactoring at the cup-bottom. Grooving of the cup-bottom is expected to reduce breakdown and allow higher fields to be reached. Multicell structures with realistic input-power couplers are being designed. The ultimate goal is to design a meter-long accelerating module for use in CESR. A preliminary design for such a module is shown in Figure 8.

(b) Mapping of fields and modes. A 5-cell copper structure at room temperature is used to make detailed higher-mode fieldmaps and shunt-impedance measurements. Couplings of higher-mode probes is also

Figure 7. Two-cell Niobium structure. The assembly shown achieved 4.5 MV/m at $Q = 3 \times 10^9$.

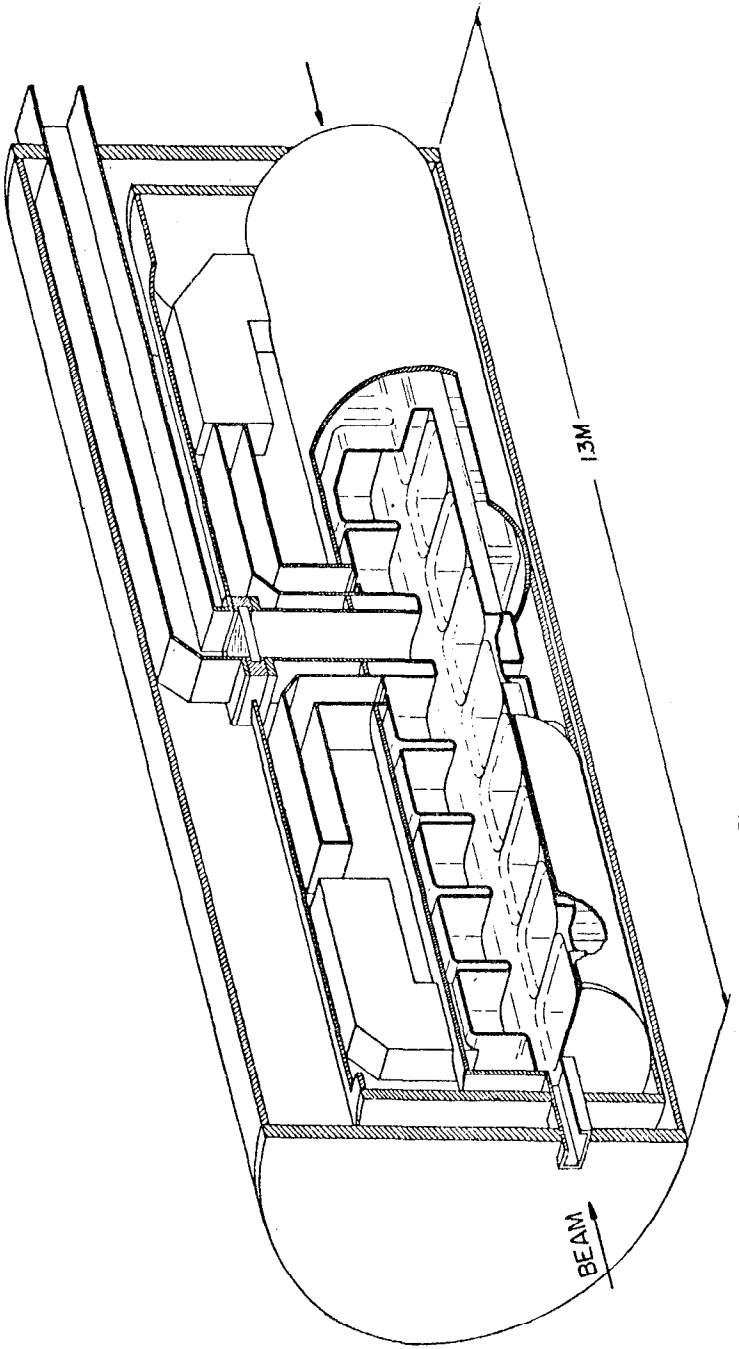

Figure 8. Sketch of one-meter accelerating module to be used in CESR.

studied.

(c) Tests in CESR at 5 GeV. Two meter-long modules will be installed in CESR and powered with 150 kW klystrons. This is expected to be a severe test of the entire concept in an environment of high-current beams and intense synchrotron radiation. In fact, for the full beam at 5 GeV, 150 kW/m has to be supplied to the beam instead of the 20 kW/m at 50 GeV. Similarly, 10 kW/m of higher mode power must be extracted rather than 4 kW/m for the 50 GeV ring. The aim is to install at least one module for passive tests in CESR by June 1981, with RF power to be applied as soon as a klystron is available.

Overall Schedule

While work progresses on the development of the cavities, the detailed design for the entire accelerator complex is also under way. A firm proposal is expected to be ready in early 1982. In order to be competitive with the first stage of LEP, the schedule is aimed towards a start of construction in 1983 and first operation with beams in 1986. The design of the ring, in particular the interaction regions and the facilities for experiments, will be crucially dependent on suggestions and advice from potential users. We hope you will all join in!

References

(1) P. Langacker et al., BNL Report #26498, Brookhaven National Laboratory, Upton, Long Island, N.Y.

(2) C. Geweniger, Moriond Conference, 1980.

(3) M. Veltman, CERN LEP-Theory Preprint 12 (1980);
F. Antonelli et al., University of Rome Preprint 174 (1980).

(4) B. Richter, Nuclear Instruments & Methods, 136, 47 (1976).

(5) D. Ritson, PEP Report 245, (1977), SLAC, Stanford, California.

(6) D. Ritson and M. Tigner, CLNS-406 (1978), Cornell University, Ithaca, N.Y.

A report was given to the SLAC Summer Institute by John Rees on the status of development of the PEP colliding-beam storage ring. The material presented corresponded entirely with that contained in a report presented to the Eleventh International Conference on High-Energy Accelerators at CERN in July 1980 by J. M. Paterson in behalf of the joint SLAC-LBL project group which designed and built PEP. That report is reproduced in the following pages.

P.E.P.*)

J. M. Paterson

For the PEP staff of Stanford Linear Accelerator Center, Stanford University, Stanford CA 94305 USA and Lawrence Berkeley Laboratory, Berkeley CA 94720 USA.

ABSTRACT

The design and construction of the PEP project is briefly reviewed. The initial testing of the storage ring system and its present performance is described. The short-range plans for continuing development are discussed.

INTRODUCTION

PEP is an 18-GeV positron-electron storage ring constructed at the Stanford Linear Accelerator Center as a joint venture of SLAC and the Lawrence Berkeley Laboratory, and sponsored by the U.S. Department of Energy. The official beginning of the project was in March 1976, with formal ground-breaking actually taking place in June 1977. The official completion date originally established by SLAC and DOE was April 1980. However, it appeared to us in 1976 that with some good luck we should be able to complete the construction six months earlier than that, and we set our internal schedule for completion as October 1979. We didn't have that good luck! Nevertheless, we did make the originally established date of April 1980, and also noteworthy is the fact that the project was completed within its initial cost estimate of 78 million dollars.

The schedule for installation of technical components and control systems was arranged in such a way as to allow some testing of subsystems before the entire ring was complete. In November and December of 1979, tests were carried out (on weekends in order not to interfere with the rest of the installation) which accomplished the transport of a positron beam from the linear accelerator through one-twelfth of the storage ring. These tests, although limited, were very beneficial, helping us understand the inter-relationships of the various technical systems. By the end of March 1980, all technical systems required to store a beam were complete and installed. We then started trying to get all of the systems operating properly, and together this took some two weeks' time — beam was first stored on April 16.

At that time, we limited the injection energy to 8 GeV because we were having problems with an injection component — the kicker magnet. (See below). During the remainder of April and May, hectic activity continued on completing and testing various technical systems, completing the installation of the first round of experiments in the interaction regions and testing the colliding-beam performance of the storage ring. In early June, the kicker

*) Work supported by the Department of Energy, contract DE-AC03-76SF00515.

(Invited talk presented at the XI International Conference on High Energy Accelerators, CERN, Geneva, Switzerland, July 7-11, 1980.)

magnet problem had been solved, and the injection and operating energy was raised to 11 GeV. Rapid progress was then made on all fronts. By the middle of June, the colliding beam performance reached a level where it became prudent to begin physics runs to allow the experiment groups time to check out their apparatus and to begin data acquisition at 11 GeV per beam.

REVIEW OF THE PEP DESIGN

The design of the Positron-Electron Project, PEP, has been described at prior conferences.[1,2] The more important parameters are listed in Table 1.

Table 1

Storage Ring Parameters

Characteristic	Value
Nominal Maximum Energy	18 GeV
Nominal Minimum Energy	4 GeV
Maximum Current per Beam at 15 GeV	55 mA
Number of Particles per Beam at 15 GeV	2.5×10^{12}
Number of Bunches	3
Design Luminosity per Interaction Region at 15 GeV and below at 18 GeV	10^{32} (E/15) cm^{-2} sec^{-1} 1×10^{31} cm^{-2} sec^{-1}
Number of Interaction Regions	6
Available Free Length for Experiments	19 m
Circumference	2200 m
Symmetry	6
RF Power Installed	5.5 MW
Number of Accelerating Sections	22
Number of 0.5 MW Klystrons	11
RF Frequency	353.2 MHz
Harmonic Number	2592

The lattice design has six-fold symmetry, with approximately 100-meter-long straight insertions (including 19-meter-long low-β insertions) which alternate with strong focusing arcs having short 5-meter straight sections at their midpoints. These latter sections are used for wiggler magnets (in three symmetric locations), transverse and longitudinal feedback equipment, optical monitoring and laser polarimeter systems. The radiofrequency

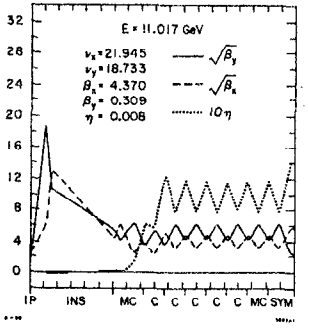

Figure 1

accelerating systems are distributed around circumference in three of the long straight sections. The lattice is flexible with the betatron functions and dispersion functions at the interaction points being tunable over a large range. Figure 1 shows the optical functions in one-twelfth of the lattice in a configuration which has been used in much of the early testing of the storage ring.

The chromatic corrections of the lattice parameters are achieved using up to nine separate families, or circuits, of sextupoles.[3] To date, we have operated over a range of betatron function at the interaction points from 0.5 m to .2 m in the vertical plane and from 5.0 m to 3.3 m in the horizontal. Several distributions of sextupole families have been used over this range. The mathematical lattice model of the storage ring in the control computer, which translate the optical parameters requested by the operator into hardware set-points, has proved quite accurate; in the lattice shown in Fig. 1, the measured betatron functions agree within 10% with what is computed from the model, and the betatron tunes agree to better than 0.1.

EXPERIENCE WITH TECHNICAL SYSTEMS

Transport and injection system[4]

Two beam transport lines take the positron and electron beams from the linear accelerator to the injection points in the storage ring. Beams can be injected at any operating energy of the storage ring between 4 and 15 GeV. The injection equipment includes four DC beam-bump magnets and three pulsed kicker magnets for each of the two beams. As mentioned earlier, we experienced electrical breakdown problems across ceramic supports within the vacuum tanks of two of the six kicker magnets. This problem limited the injection energy to 8 GeV during April and May. It is now corrected.

The rest of the transport and injection system has been reasonably trouble free and performs as designed. The one-nanosecond pulses transmitted through ±0.3% energy-defining slits contain at best approximately 10^9 electrons per pulse and 10^8 positrons per pulse. The injection repetition rate can be varied up to 180 pps, although, to date, less than 60 pps have generally been required to give filling times of a few minutes when the equipment was working properly. Positron injection is often difficult for reasons not yet understood.

The magnet and power supply systems[5]

The PEP main magnet system consists of approximately 200 each of bend magnets, quadrupoles and sextupoles which are powered in 19 separate circuits. There are nine sextupole curcuits, nine quadrupole circuits and one circuit which includes all the bends and the interaction-region quadrupoles. Each circuit is driven by thyristor-chopper power supplies running from common 600 VDC busses. In addition to the chopper supplies, there are about 120 bipolar transistor actuators for various trim and steering magnet circuits.

As a consequence of PEP's delayed and compressed installation schedule, the power supplies and their magnet circuits were not completed as systems until just before beam turn-on so that little time was available for testing, and system debugging was carried out simultaneously with beam tests throughout April and May.

Vacuum system[6]

So far, PEP has had only limited high-current, high-energy operation, and, therefore, there has been little testing of the vacuum system under heavy gas load, however, the system appears to be very good; the beam lifetime is several hours at the highest currents and energies at which we have run. On two occasions the RF sections have been vented to atmospheric pressure due to RF window failures. After purging with dry nitrogen and pumpdown, there has been no requirement for in situ bakeout.

Radiofrequency system[7]

The PEP 353-MHz radiofrequency accelerating system is comprised of 12 stations. Each station consists of a 500-KW klystron which feeds a pair of 5-cell accelerating cavities.

The SLAC-designed 500-KW klystrons have performed well, although the peak efficiency is a few percent less than the hoped for 70%. Some of the early tubes went soft while awaiting completion of installation after high power testing. This problem was traced to porosity developing in some stainless steel weldments due to faulty material. The tubes have been rebuilt and are back in service.

Only a fraction of the system is required for beam storage at low or medium energies; this was one of the items where contractors were able to defer a portion of their installation work until after beam start-up. As of July, eleven stations were operating, and the twelfth station is being installed in August.

Survey and alignment[8]

The PEP laser survey system proved to be rapid and reliable. The goal was to have residual alignment errors of less than 0.1 mm, and the orbit measurements would indicate that this goal was met. Typically, the orbit correction program can reduce the RMS orbit deviation to less than 2mm using less than 30 correctors with the maximum distortion being less than 4mm.

Instrumentation and control[9]

A description of the PEP control system and a discussion of its performance can be found elsewhere in these proceedings. The MODCOMP-IV has been supplemented with a VAX-11 in order to handle better the message traffic from the seven remote MODCOMP-II's and the desired multi-task service of interfacing with the operators.

BEAM PERFORMANCE

As mentioned earlier, the initial injection energy was 8 GeV. During the first injection tests, the lattice was set to a configuration with $\beta_y^* = 0.45$ metre and $\beta_x^* = 5.0$ metre. After beam was stored, the lattice functions were measured and found to be very severely mismatched around the ring. This was shown to be due to a reversed trim winding on an interaction region quadrupole, and when it was corrected, the ring proved to be quite symmetric.

Other than the expected head-tail instability, which occurs with negative chromaticity, no instabilities have been observed, with the following qualification: single-bunch currents greater than 5 or 6 mA have not been used. Both horizontal and vertical head-tail instabilities had threshold between 0.05 and 0.1 mA when the chromaticity of the respective degree of motion was negative. The coherent tune shift with current, which has been measured in the configurations used to date, to be of the order of $\Delta\nu_x \approx \Delta\nu_y \approx .0025/\text{mA}$, can affect the beam during injection, giving the impression of instability if the betatron tunes are near some lattice resonance.

Before studying colliding beams at 8 GeV, the vertical betatron function was lowered to $\beta_y^* = 0.35$ metre, and the wiggler magnet system was energized to a level equal to 70% of the design excitation at 8 GeV. The maximum linear beam-beam tune shift, computed from the maximum luminosity and current, always lay between $\Delta\nu_y = .02$ to $.03$. (The early luminosity measurements had large systematic errors while the measurement system was debugged.) Figure 2 shows the luminosity versus current for two cases: a) no excitation by the wiggler magnet system and b) the wiggler system powered to a level where the calculated emmittance of the beam had been increased by the wiggler by a factor of 2.4. To within the accuracy of the measurements at that time, the beam behavior was in good agreement with the predictions.

The maximum luminosity achieved at 8 GeV was 3.5×10^{29} cm^{-2} sec^{-1}. This was achieved both with one bunch per beam and with 3 bunches per beam. Experiments with lower β_y^* and with stronger wiggler magnet settings were curtailed when operation at higher energies became possible.

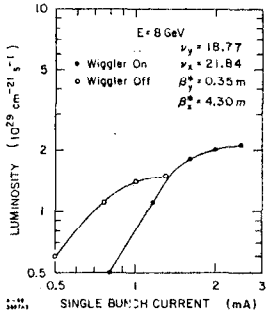

Figure 2

By the time operation at 11 GeV had settled down, many improvements in instrumentation and machine control had been implemented, and storage ring operation was reproducible. The betatron function was lowered to a $\beta_y^* = 0.30$ metres, and the sextupole correction system was changed to one where there were nine families instead of the two families used at the outset.

The maximum luminosity measured with the lattice configuration shown in Fig. 1 was 8×10^{29} cm^{-2} sec^{-1} with one bunch per beam, and 1.5×10^{30} cm^{-2} sec^{-1} with 3 bunches per beam.

The wiggler magnet system was set at a level where the calculated emittance was increased by 50% over that without the wiggler, and where it was 80% of the emittance assumed in the design at this energy. Typical curves of luminosity versus single bunch current are shown in Fig. 3.

The three-bunch data shown were taken during early physics runs in which the detector magnets of the Mark II, MAC and DELCO were operating. Over a wide range of current, the luminosity varies as $L \approx I^2$, indicating a constant emittance, and the luminosity per interaction region scales with the number of bunches.

Figure 4 shows the computed linear beam-beam tune-shift from this data. The $\Delta\nu_y$ per crossing increases linearly with current to values between 0.025 and .03. In the single-bunch mode, higher bunch currents were successfully collided with a visible increase in vertical beam size and the luminosity saturated. A limit on luminosity and current is reached when the lifetime

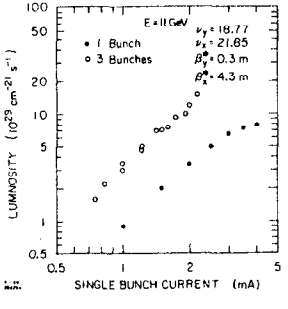

Figure 3

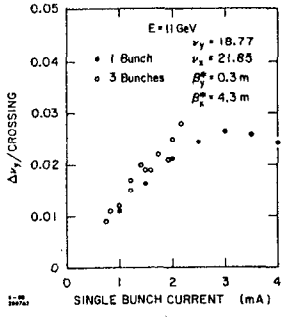

Figure 4

of one or both beams is significantly reduced. The three-bunch data have not, at this time, been extended into this regime.

SUMMARY AND FUTURE PLANS

After approximately three months of shakedown of the many engineering systems which make up the storage ring, the total system is beginning to operate as designed. Comparing present performance with the design assumptions indicates that the maximum beam-beam tune shift achieved, to date, is one half of the assumed 0.06. For the present lattice, all other parameters appear to reproduce the design values, and, after one allows for the lower maximum tune-shift, the luminosity is in agreement with the predicted value for this lattice.

In the design of PEP, much flexibility was allowed for in the lattice, and we must now begin gradually to explore the alternatives available. In the "standard configuration" of the design, the betatron and dispersion functions at the interaction points were: $\beta_y^* = 0.11$ m, $\beta_x^* = 2.8$ m and $\eta_y^* = -0.5$ m.

We will explore lower β^* values and non-zero dispersion to find the optimum operating conditions and to understand the scaling of the beam-beam limit as a function of these parameters. We will also explore alternate betatron tunes both to refine operating points and to study the use of smaller emittances. Higher energy operation is being pursued during this Conference, and our goal is to achieve 15-GeV operation this month.

ACKNOWLEDGEMENTS

As this is the first report on the operating performance of PEP since the completion of construction, I would like to thank all of the staff at the Stanford Linear Accelerator Center and the Lawrence Berkeley Laboratory who contributed to the design and construction of this project. Although this report is very preliminary, it is not without the encouraging indication that everyone's efforts are bearing and will continue to bear fruit.

* * *

REFERENCES

1) J.R. Rees, "The Positron-Electron Project-PEP," IEEE Trans. Nucl. Sci., NS-24, 1836 (1977).

2) H. Wiedemann, VI All-Union National Conference on Particle Accelerators.

3) M.H.R. Donald, P.L. Morton and H. Wiedemann, "Chromaticity Correction in Large Storage Rings," IEEE Trans. Nucl. Sci., NS-24, 1200 (1977).

4) J.M. Peterson and K.L. Brown, "The Sensitivity of the PEP Beam Transport Line to Perturbations," IEEE Trans. Nucl. Sci., NS-26, 3496 (1979).

5) R.T. Avery et al., PEP Insertion Quadrupole Design Features," IEEE Trans. Nucl. Sci., NS-26, 4033 (1979).
L.T. Jackson, "PEP Magnet Power Supply Systems," NS-24, 1245 (1977).
L.T. Jackson and W.S. Flood, "Hardware Implementation and Test Results of PEP Chopper Magnet Power Supply Systems," NS-26, 4072 (1979).

6) "Vacuum System of PEP," to be published in Proceedings of American Vacuum Society 1980.

7) M.A. Allen et al., "RF System for the PEP Storage Ring," NS-24, 1780 (1977).
H.D. Schwarz and J.N. Weaver, "The RF Reference Line for PEP," NS-26 3956 (1979).

8) J. Gunn et al., "A Precision Surveying System for PEP," NS-24, 1367 (1977).

9) "PEP Computer Control System," these Proceedings.
"PEP Computer Control System," NS-26, 3268 (1979).

A BRIEF REVIEW OF RECENT RESULTS FROM THE CRYSTAL BALL DETECTOR AT SPEAR*

E. D. Bloom
(Representing the Crystal Ball Collaboration)[1]
Stanford Linear Accelerator Center
Stanford University, Stanford, California 94305

*Work supported by the Department of Energy, contract DE-AC03-76SF00515.

INTRODUCTION

A large number of papers have been published recently by other members of the Crystal Ball Collaboration on the subjects covered in my topical conference presentation. Thus, when relevant publications exist, I have not repeated the results contained therein. For most subjects covered, this report will sketch the Crystal Ball results presented in my talk and refer heavily to these publications.

INCLUSIVE PHOTON SPECTRA FROM J/ψ and ψ' DECAYS

Inclusive photon spectra have been obtained from the decay of 810kψ' and 790kJ/ψ. These spectra are shown in Figs. 1 and 2. Recently published results[2,3] discuss two topics of interest.

The discovery of an $\eta_c(2980)$ candidate state is discussed in Ref. 2. The mass and width of this state are

$$M = 2978 \pm 9 \text{ MeV}$$

and (1)

$$\Gamma < 20 \text{ MeV}.$$

The branching fraction from the ψ' is

$$Br(\psi' \to \gamma\eta_c \text{ candidate}) = (0.43 \pm 0.08 \pm 0.18)\% \quad . \qquad (2)$$

The value for $Br(J/\psi \to \gamma\eta_c$ candidate) has not been published. The reason for this is illustrated in Fig. 3 where $Br(J/\psi \to \gamma\eta_c$ candidate) vs Γ is shown. Clearly the branching ratio is strongly dependent on the width of the η_c candidate. Depending on the width (Γ = 0-20 MeV), values for the branching ratio between 0.3% and 4% are possible. This range

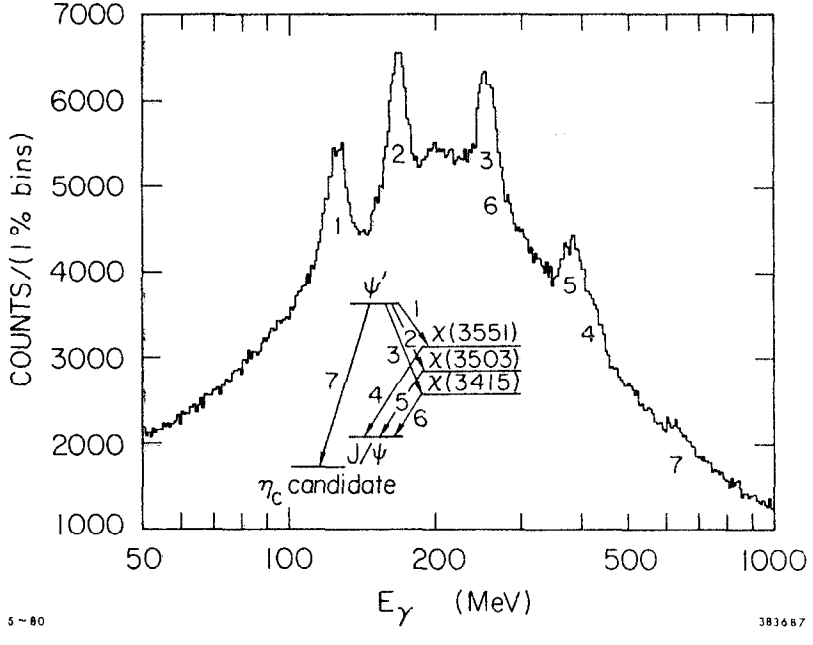

Fig. 1. The inclusive photon spectrum obtained from the decay of 800k ψ'(3684)'s. The analysis leading to this spectrum and that of Fig. 2 is described in Ref. 2.

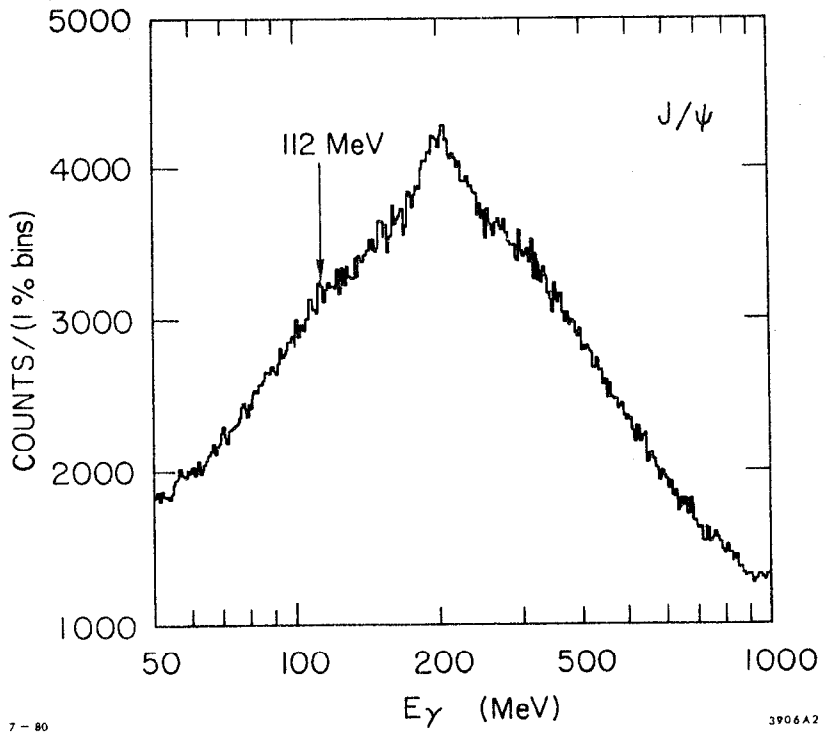

Fig. 2. The inclusive photon spectrum obtained from the decay of 900k J/ψ(3095)'s. The data are plotted vs ℓn E_γ since the resolution $\Delta E_\gamma/E_\gamma$ is slowly varying in E_γ.

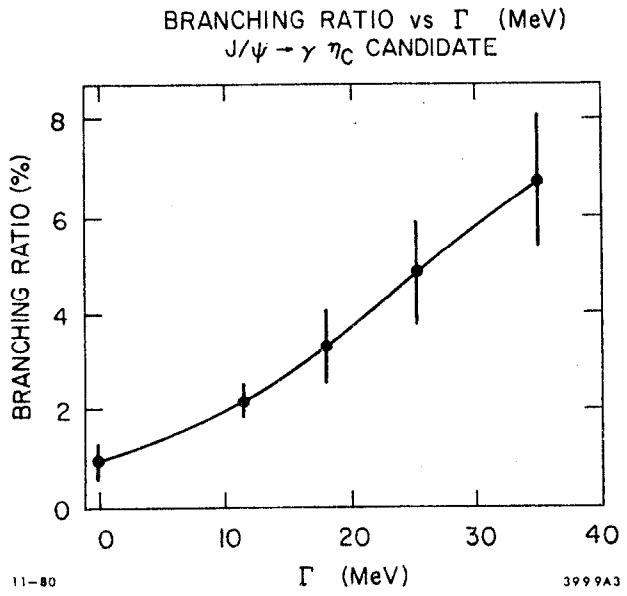

Fig. 3

Fig. 3. Br($J/\psi \to \gamma\eta_c$ candidate) (%) vs Γ of the η_c candidate as obtained from a simultaneous fit to the spectra of Figs. 1 and 2 in the region of the η_c candidate state.

includes the uncertainties introduced by the acceptance calculations (shown as the error bars in Fig. 3). Thus a good measurement of the width is needed before a branching ratio can be reliably obtained. This question is not relevant in the ψ' decay due to the high energy of the photon, $E_\gamma = 634 \pm 13$ MeV.

At present two measurements of the width exist as obtained from inclusive γ measurements and exclusive final state measurements of $\gamma\eta\pi\pi$ (the exclusive final state separation is discussed in Ref. 2). Figure 4 shows the results obtained from a simultaneous fit to the inclusive photon spectra of ψ' and J/ψ. Γ vs χ^2 is plotted, and the width obtained is,

$$\Gamma = 20 \begin{matrix} + 16 \\ - 11 \end{matrix} \text{ MeV}. \qquad (3)$$

Figure 5a shows Γ vs χ^2 as obtained from fitting a Breit-Wigner, folded with a Gaussian resolution function ($\sigma_{res.} = 5.0$ MeV @ 119 MeV), plus a constant background, to the exclusive $\gamma\eta\pi\pi$ data shown in Fig. 6. The $\chi^2(\Gamma)$ function prefers $\Gamma = 0$ with a 90% C.L. of $\Gamma < 8.5$ MeV. However, given the limited statistics of the exclusive final state data, we prefer to combine the $\chi^2(\Gamma)$ function of Fig. 3 with that of Fig. 4a, thus obtaining the function shown in Fig. 5b. This combined $\chi^2(\Gamma)$ function yields

$$\Gamma < 20 \text{ MeV (90\% C.L.)} \quad , \qquad (4)$$

which we presently take as the best estimate, from our data, of the width of the η_c candidate.

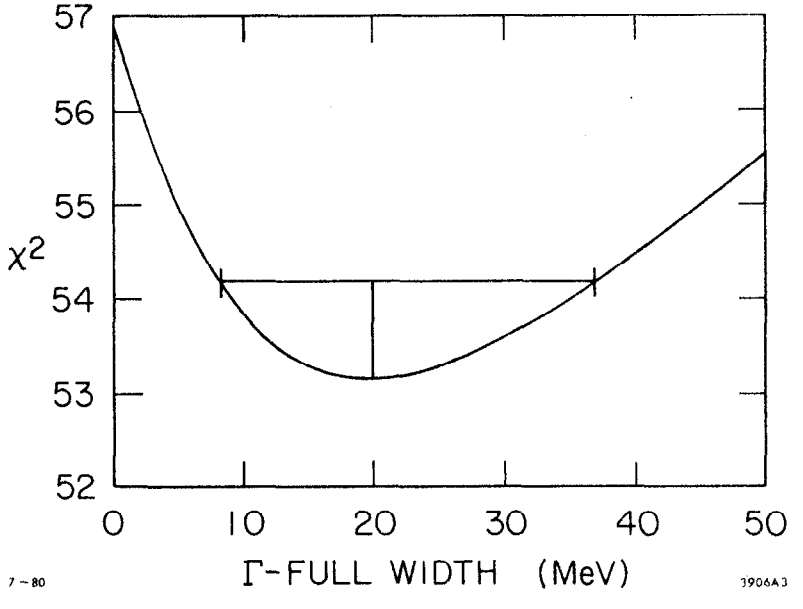

Fig. 4. χ^2 vs Γ resulting from the simultaneous fit to the inclusive spectra of Figs. 1 and 2 in the region of the η_c candidate state. This fitting procedure is described in Ref. 2.

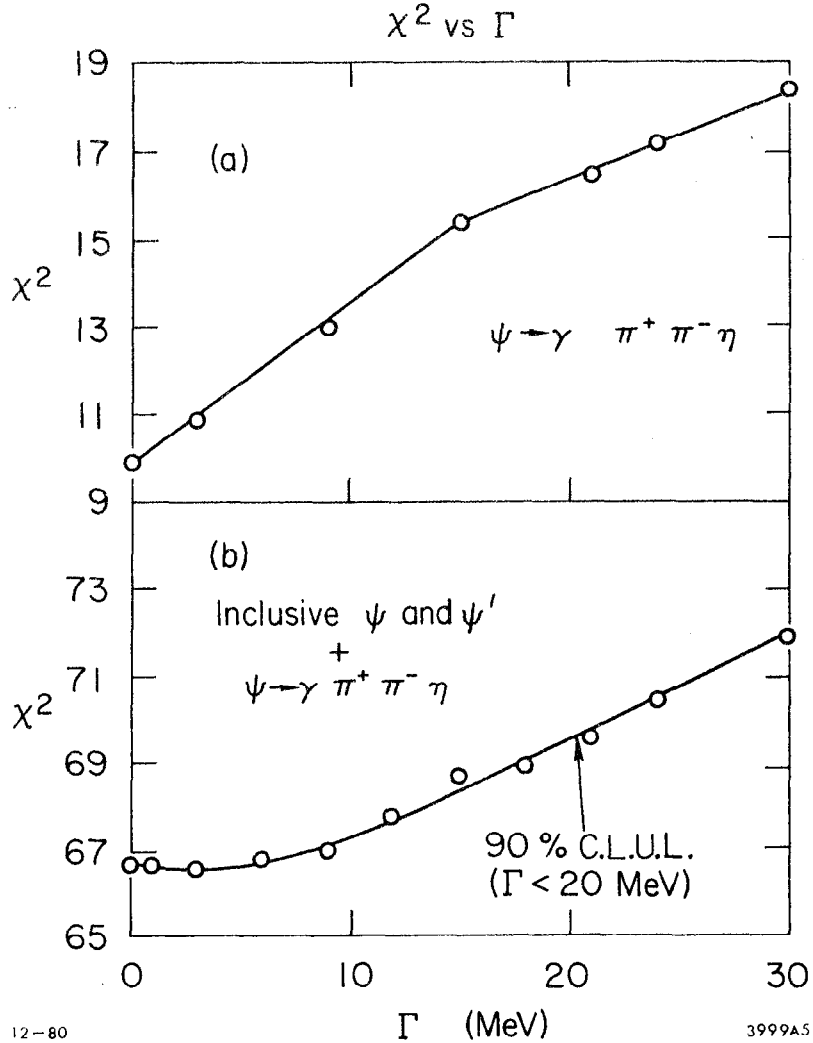

Fig. 5. a) Γ vs χ^2 obtained from a maximum likelihood fit of a Breit- Wigner, folded with a Gaussian resolution function (σ_{res} = 5.0 MeV @ 119 MeV), plus a constant background to the data of Fig. 6. b) The sum of $\chi^2(\Gamma)$ from Figs. 4 and 5a. This $\chi^2(\Gamma)$ function yields the best estimate of the width of the η_c candidate state from current Crystal Ball data. Γ < 20 MeV (90% C.L.).

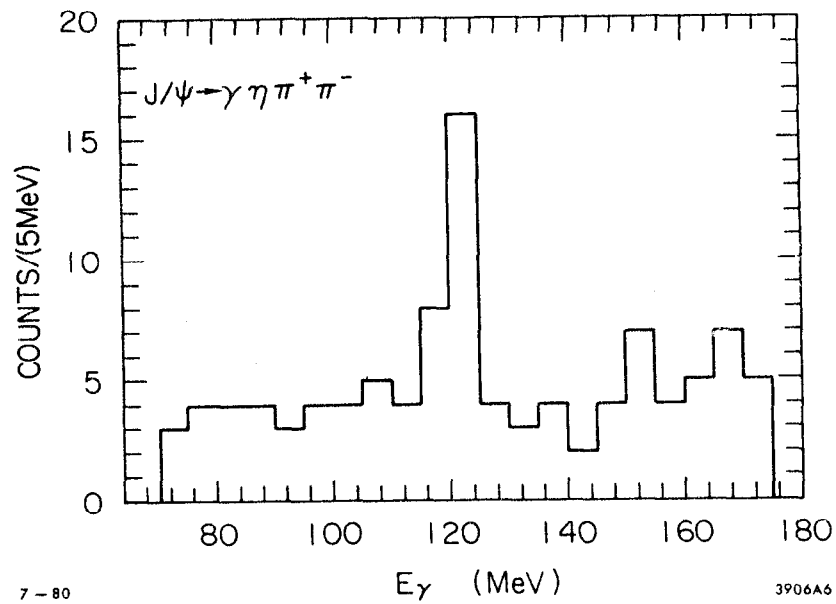

Fig. 6. Evidence for an exclusive final state signal for J/ψ (3095) radiative decay to ηππ. E_γ (MeV) vs events/5 MeV is shown for events in the mass range of the η_c (2980) candidate. A signal is evident at E_γ = 119 MeV corresponding to a mass, M_{η_c} = 2974 ± 2 ± 9 MeV where the first error is statistical and the second is systematic. See Ref. 2 for details.

The Mark II has also seen exclusive final state decays of the η_c candidate; these results are presented in Ref. 4. They obtain,

$$M = 2980 \pm 8 \text{ MeV}$$

and

$$\Gamma < 40 \text{ MeV (90\% C.L.)} \quad . \tag{5}$$

The radiative transitions from ψ' and J/ψ to ordinary hadrons are discussed in Ref. 3. Of particular interest is the nature of the bump in the inclusive photon spectrum of the J/ψ at $E_\gamma = 1220$ MeV ($M = 1420$ MeV) as shown in Fig. 7. This state is probably the E(1420); however, its strong production in J/ψ radiative decays has led to speculation that it may be a gluonium state. This possibility is discussed in detail in Ref. 3. The Crystal Ball has also obtained evidence for the decay

$$E(1420) \to K^+K^-\pi^0. \tag{6}$$

We obtain,[3]

$$Br(J/\psi \to \gamma E(1420)) * Br(E \to K^+K^-\pi^0) = (3.4 \pm 2.0) \times 10^{-4} \tag{7}$$

assuming the E is an isoscalar,

$$Br(J/\psi \to \gamma E(1420)) * Br(E \to K\bar{K}\pi) = (2.0 \pm 1.2) \times 10^{-3}. \tag{8}$$

This compares well with the Mark II result[3] of

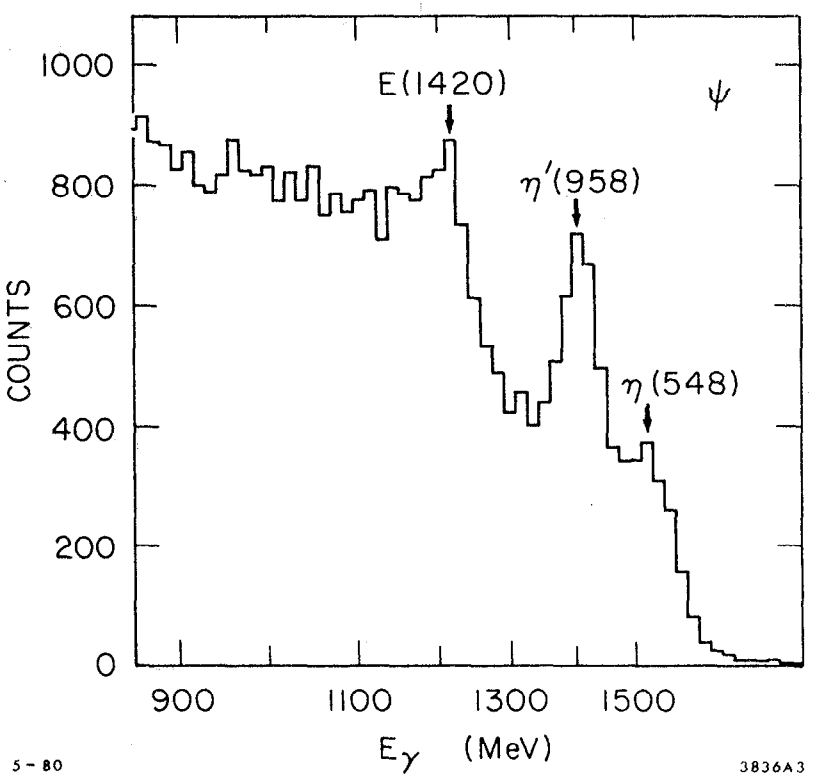

Fig. 7. The inclusive photon spectrum from J/ψ drawn to emphasize the endpoint region. The well-known states $\eta(548)$, $\eta'(958)$ are evident; $f(1240)$ is not evident in this spectrum though the process $J/\chi \to \gamma f$ has been observed in exclusive final states. Quite prominent is an indication for $J/\chi \to \gamma$ E(1420) leading to the speculation that E(1420) may have a gluonium component; see Ref. 3 for details.

$$Br(J/\psi \to \gamma E(1420)) * Br(E \to K\bar{K}\pi) = (3.6 \pm 1.4) \times 10^{-3}. \quad (9)$$

PHOTON CASCADE DECAYS OF THE ψ'

We have completed a study of the processes

$$\psi' \to \gamma\chi \quad \chi \to \gamma J/\psi \quad J/\psi \to e^+e^- \quad (10)$$

and

$$\psi' \to \eta(\pi^o) + J/\psi \quad \eta \to \gamma\gamma \quad J/\psi \to e^+e^- \quad . \quad (11)$$

The latter process is reported in Ref. 5. We find

$$Br(\psi' \to \eta J/\psi) = (2.18 \pm 0.14 \pm 0.35)\% \quad (12)$$

and

$$Br(\psi' \to \pi^o J/\psi) = (0.09 \pm 0.02 \pm 0.01)\% \quad (13)$$

where the first errors are statistical and the latter are systematic.

These values compare well to the Mark II values[6] of

$$Br(\psi' \to \eta J/\psi) = (2.5 \pm 0.6)\% \quad (14)$$

and

$$Br(\psi' \to \pi^o J/\psi) = (0.15 \pm 0.06)\% \quad . \quad (15)$$

However, the branching ratios, (12) and (14) above, are about a factor of two lower than all previous measurements.[7] The relatively large π^o branching ratio implies that isospin is violated in that decay.

Process (10) and (11) are the subject of the Ph.D. thesis of M. J. Oreglia, which can be obtained as Ref. 8. In particular the most complete treatment available from the Crystal Ball of process (10) is presented therein; though other sources also exist,[9] they are relatively incomplete.

We have determined that three χ states exist with cascade rates large enough to be detected with our present sensitivity. These are $\chi(3554 \pm 3$ MeV), $\chi(3509 \pm 4$ MeV), $\chi(3410 \pm 6$ MeV). The cascade branching fractions for these states along with measurements from other experiments are shown in Table I. The agreement among all experiments is excellent for the first two major states. Only the Crystal Ball has a clear indication for the cascade process for $\chi(3410)$; however, a strong signal is seen in the ψ' inclusive photon spectrum at this mass (see Fig. 1). Previously reported measurements indicating states $\chi(3455)$ and $\chi(3591)$ are in disagreement with Crystal Ball measurements. We see no indication for these states at the limits of our present sensitivity.

In addition to transition rates we have determined the multipolarity of the transitions for $\chi(3554)$ and $\chi(3509)$ and their spins. We find $\chi(3554)$ to have $J = 2$ and $\chi(3510)$ to have $J = 1$. In addition we have determined that the transitions in the cascades for these states are all dominated by electric dipole amplitudes; see Refs. 8,9 for details. This information, together with information on the hadronic decays[10,11] of the χ states yields parity plus for both states.

The Crystal Ball experiment has obtained preliminary evidence for the decays

TABLE I.

Observed branching fractions for the cascade process

$$\psi' \longrightarrow \gamma\chi \qquad \chi \longrightarrow \gamma J/\psi$$

from various experiments, including those from the Crystal Ball (C.B.). The mass values shown for the established states are obtained from Crystal Ball data. The upper limits are 90% C.L. limits.

Mass	$Br(\psi' \to \gamma\chi) \cdot Br(\chi \to \gamma\psi)$ 90%			
MeV/C (C.B.)	C.B.	Mk II[10]	Mk I[11]	DESY-Heidelberg[7b]
3554 ± 3	1.26 ± 0.22	1.1 ± 0.3	1.0 ± 0.6	1.0 ± 0.2
3509 ± 4	2.38 ± 0.40	2.4 ± 0.6	2.4 ± 0.8	2.5 ± 0.4
3410 ± 4	0.06 ± 0.02	<0.56	0.2 ± 0.2	0.14 ± 0.09
3455	<0.04 (e,μ final states) <0.02 (μ final states)	<0.13	0.8 ± 0.4	<0.25
3591	<0.04	--	--	0.18 ± 0.06

$$\chi(3554) \to \gamma\gamma \text{ and } \pi^o\pi^o; \quad \chi(3410) \to \pi^o\pi^o \tag{16}$$

by examination of the process

$$\psi' \to \gamma\gamma\gamma \text{ and } \gamma\pi^o\pi^o. \tag{17}$$

Some details of this analysis are presented in Ref. 9.

THREE-γ DECAYS OF J/ψ AND ψ'

Results from the crystal ball for the process

$$J/\psi \to 3\gamma \tag{18}$$

have been published[12] some time ago, and so I won't discuss these results here. A preliminary analysis has been recently completed of the process

$$\psi' \to 3\gamma\ . \tag{19}$$

We find 3γ decays to be much less probable from ψ' as compared to J/ψ. In particular,

$$\begin{aligned} Br(\psi' \to \gamma\eta) &< 10^{-4} \quad (90\%\ \text{C.L.}) \\ Br(\psi' \to \gamma\eta') &< 8 \times 10^{-4} \quad (90\%\ \text{C.L.}) \end{aligned} \tag{20}$$

where these upper limits are about a factor of 9 smaller than the observed branching fractions for γη, γη' from J/ψ. This somewhat surprising result is discussed in Ref. 3.

In addition, we find

$$Br(\psi' \to \gamma\eta_c(2980)\text{candidate}) * Br(\eta_c\text{candidate} \to \gamma\gamma) < 3 \times 10^{-5}(90\%\ \text{C.L.}) \quad (21)$$

using the Crystal Ball measurement of the inclusive photon branching fraction, e.g. (2), we find

$$Br(\eta_c\text{candidate} \to \gamma\gamma) < 10^{-2} \quad . \quad (22)$$

This upper limit does not impact the estimated theoretical value[13] of 1.3×10^{-3}.

INCLUSIVE η PRODUCTION

This subject is treated in great detail in Ref. 14. Thus I will only state the conclusions of our investigations of the process

$$e^+e^- \to \eta + X. \quad (23)$$

As is evidenced in Fig. 8:

1) We observe no strong variation of $R_\eta \equiv \sigma_\eta/\sigma_{\mu\mu}$ as a function of $E_{c.m.}$ for 3670 MeV < $E_{c.m.}$ < 5200 MeV (omitting ψ'), where by strong variation I mean no variation greater than 0.5 units of R. In particular, we estimate

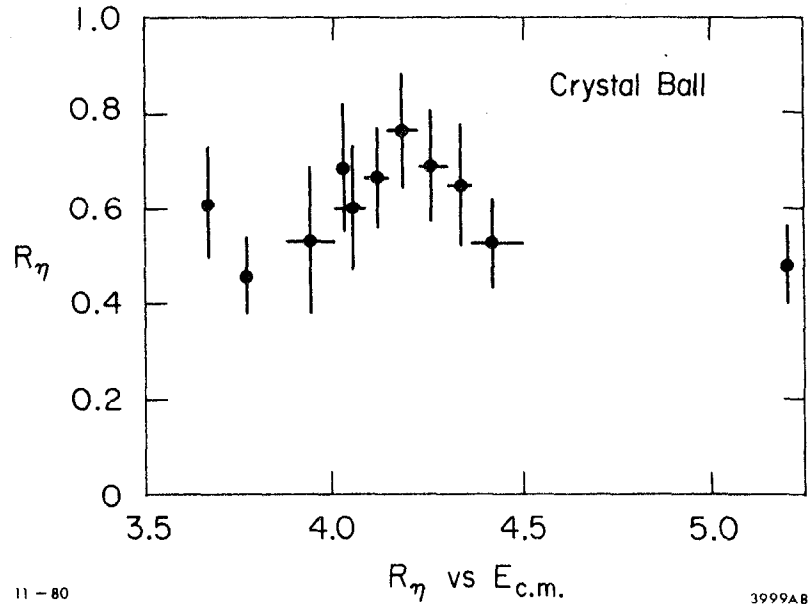

Fig. 8. The inclusive $R_\eta = \sigma(e^+e^- \to \eta X)/\sigma(e^+e^- \to \mu^+\mu^-)$ as a function of $E_{c.m.}$. R_η at ψ' is off scale; see Ref. 15 for details.

$$R(e^+e^- \to F\bar{F}X) \cdot Br(F \to \eta X) < 0.31 \ (90\% \ C.L.) \quad . \qquad (24)$$

2) From measurements at $\psi'(3772)$ we conclude that

$$Br(D \to \eta X) < 0.1 \quad . \qquad (25)$$

It thus appears that η production is not strongly correlated to charm production.

REFERENCES

1. Members of the Crystal Ball collaboration. California Institute of Technology, Physics Department: R. Partridge, C. Peck and F. Porter. Harvard University, Physics Department: A. Antreasyan, Y. F. Gu, W. Kollmann, M. Richardson, K. Strauch and K. Wacker. Princeton University, Physics Department: D. Aschman, T. Burnett (visitor), M. Cavalli-Sforza, D. Coyne, M. Joy and H. Sadrozinski. Stanford Linear Accelerator Center: E. D. Bloom, F. Bulos, R. Chestnut, J. Gaiser, G. Godfrey, C. Kiesling, W. Lockman, M. Oreglia and D. Scharre. Stanford University, Physics Department and High Energy Physics Laboratory: R. Hofstadter, R. Horisberger, I. Kirkbride, H. Kolanoski, K. Koenigsmann, A. Liberman, J. O'Reilly and J. Tompkins.
2. R. Partridge et al., Phys. Rev. Lett. 45, 1150 (1980).
3a. D. L. Scharre, To be published in the Proc. of the VI International Conf. on Experimental Meson Spectroscopy, Brookhaven National Laboratory, Upton, Long Island, N.Y., April 25-26, 1980; also SLAC-PUB-2519 (1980).
b. D. G. Aschman, To be published in the Proc. of the XV Rencontre de Morions, Les Arcs, France, March 15-21, 1980; also SLAC-PUB-2550 (1980).
4. T. M. Himel et al., Phys. Rev. Lett. 45, 1146 (1980).
5. M. Oreglia et al., Phys. Rev. Lett. 45, 959 (1980).
6. T. M. Himel et al., Phys. Rev. Lett. 44, 920 (1980).

7a. R. Brandelik et al., Nucl. Phys. B160, 426 (1979).

b. W. Bartel et al., Phys. Lett. 79B, 492 (1978).

c. W. Tanenbaum et al., Phys. Rev. Lett. 36, 402 (1976).

8. M. J. Oreglia, Stanford Ph.D. Thesis (1980), SLAC-236 (1981).

9a. T. H. Burnett, To be published in the Proc. of the XX International Conf. on High Energy Physics, Madison, Wisconsin, July 17-23, 1980.

b. M. J. Oreglia, To be published in the Proc. of the XV Rencontre de Moriond: Electroweak and Unified Theory Prediction, Les Arcs, France, March 15-21, 1980; also SLAC-PUB-2529 (1980).

10. T. M. Himel, Stanford Ph.D. Thesis, SLAC-223 (1979).

11. W. Tanenbaum et al., Phys. Rev. D17, 1731 (1978).

12. R. Partridge et al., Phys. Rev. Lett. 44, 712 (1980).

13. Two extensive reviews of the charmonium model and its comparison to experiment are: T. Appelquist, R. M. Barnett, K. D. Lane, "Charm and Beyond," Ann. Rev. Nucl. Part. Sci. 28 (1978); and E. Eichten, K. Gottfried, T. Kinoshita, K. D. Lane and T. M. Yan, "Charmonium: Comparison with Experiment," Phys. Rev. D21, 203 (1980).

14a. F. C. Porter, To be published in the Proc. of the XX International Conf. on High Energy Physics, Madison, Wisconsin, July 17-23, 1980; also SLAC-PUB-2593 (1980).

b. D. G. Coyne, To be published in the Proc. of the Vanderbilt Symposium on High Energy e^+e^- interactions, Nashville, Tennessee, May 1-3, 1980; also SLAC-PUB-2563 (1980).

RESULTS FROM CESR

Giancarlo Moneti
Syracuse University, Syracuse, N.Y., 13210

On behalf of the CLEO collaboration: D. Andrews, K. Berkelman, R. Cabenda, D.G. Cassel, J.W. Dewire, R. Ehrlich, T. Ferguson, T. Gentile, M.G.D. Gilchriese, B. Gittelman, D.L. Hartill, D. Herrup, M. Herzlinger, D.L. Kreinick, N.B. Mistry, E. Nordberg, R. Perchomok, R. Plunkett, R. Talman, H.G. Thonemann, and D. Weber (Cornell University); C. Bebek, J. Haggerty, J.M. Izen, W.A. Loomis, F.M. Pipkin, J. Rohf, W. Tanenbaum, and Richard Wilson (Harvard University); A.J. Sadoff (Ithaca College); D.L. Bridges (Le Moyne College); K. Chadwick, P. Ganci, H. Kagan, R. Kass, F. Lobkowicz, A. Melissinos, S.L. Olson, R. Poling, C. Rosenfeld, G. Rucinski, E.H. Thorndike, and G. Warren (University of Rochester); D. Bechis, J.J. Mueller, D. Potter, F. Sannes, P. Skubic, and R. Stone (Rutgers University); A. Brody, A. Chen, M. Goldberg, N. Horwitz, J. Kandaswamy, H. Kooy, P. Lariccia and G.C. Moneti (Syracuse University); M.S. Alam, S.E. Csorna, R.S. Panvini, and J.S. Poucher (Vanderbilt University) and the CUSB collaboration: G. Finocchiaro, G. Giannini, J. Lee-Franzini, R.D. Schamberger, Jr., M. Sivertz, L.J. Spencer, and P.M. Tus (The State University of New York at Stony Brook); T. Böhringer, F. Costantini, J. Dobbins, P. Franzini, K. Han, S.W. Herb, D.M. Kaplan, L.M. Lederman, G. Mageras, D. Peterson, E. Rice, and J.K. Yoh (Columbia University); G. Levman (Louisiana State University)

I plan to cover the following topics: a few data on the performance of the storage ring itself, CESR; a brief description of the CLEO and CUSB detectors; a summary of the detection and properties of the Υ and the first two excited states Υ' and Υ''; the discovery and

characteristics of the third excited state the T''', or 4S state, the first one above threshold for decay into bottom mesons; and a few very preliminary properties of the B mesons themselves.

I. The Storage Ring.

CESR, the Cornell e^+e^- storage ring, is built around the existing 10 GeV electron synchrotron and has only one electron bunch and one positron bunch, hence only two interaction regions. The South interaction region has room for a large, multipurpose detector and is occupied by CLEO; the smaller North region is occupied by the CUSB detector. CESR is designed for a 8 GeV beam energy, capable of being brought up to 10 GeV. The design luminosity was $10^{32}\ (E_b/8)^2\ cm^{-2}s^{-1}$. This figure should probably be revised to half that value because of the known limitations on the tune shift. For the actual performance the most interesting data are the following: the beam energy is up to 5.5 GeV; the best peak luminosity is $3 \times 10^{30}\ cm^{-2}s^{-1}$ at about that beam energy, i.e., about a factor of 8 down from the (revised) design luminosity. What is more important is the average luminosity per day which is now about 60 $nb^{-1}\ d^{-1}$ (taking already into account the dead time of the detectors) with peaks at 100 $nb^{-1}\ d^{-1}$.

II. The CLEO and CUSB detectors.

CLEO is a general purpose, magnetic detector built by the Cornell-Harvard-Rochester-Rutgers-Syracuse-Vanderbilt collaboration. In Fig. 1a we see a beam eye view of it. We notice first, around the beam pipe, a triplet of proportional chambers with axial wires and cathode strip loop readout in order to have a precise determination of the coordinates along the beam. Surrounding the proportional chamber we have a cylindrical drift chamber with 17 cylinders of 1.1 cm wide drift cells, 9 with axial wires, 6 at angles of $\pm 3^0$ with the axis. Proportional and drift chambers are in a magnetic field of 4.4 KG

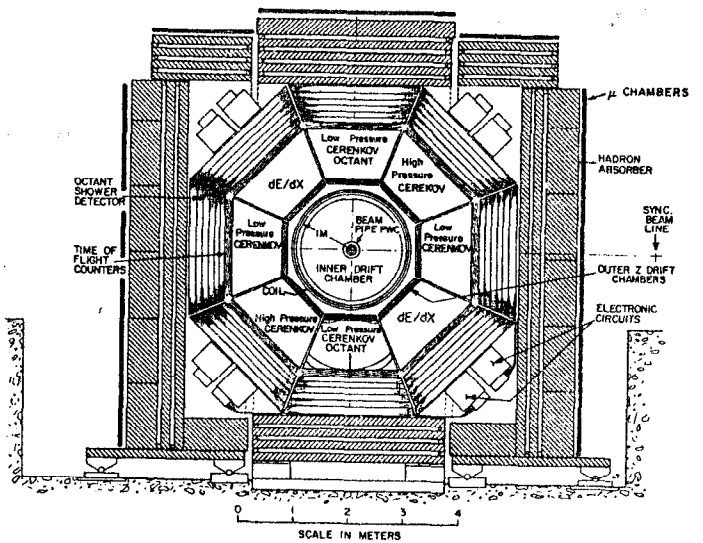

Fig. 1 (a) Beam eye view of the CLEO detector.

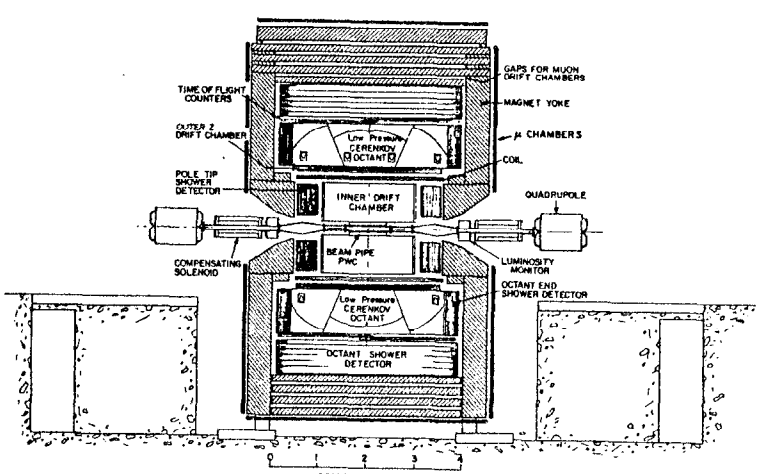

Fig. 1 (b) View of CLEO along the beam.

provided by an Aluminum coil 3 m long and with a radius of 1.05 m. The Al coil will soon be replaced by a superconducting coil (currently being tested) capable of generating a 15 KG field. Outside of the coil we find an octagonal symmetry. In each octant, starting from outside, we have a shower detector 12.7 radiation length deep, built as a proportional tubes and lead sheets sandwich. Preceding the shower counters we have time of flight scintillators and another detector for particle identification. Within about a year all octants will have a dE/dx measuring device constituted by pressurized proportional chambers sampling the ionization 117 times in the radial direction. Currently we have only two of them; the other octants are occupied either by high pressure Cherenkov counters (two octants) or by low pressure Cherenkov counters (four octants) which are only used in the identification of electrons. Immediately next to the magnet coil, each octant has a triplet of drift chambers in order to measure the coordinates of the tracks as they come out of the coil and also to determine if there was photon conversion in the coil and to determine the coordinates of the electron pair produced. Beyond the octants we have the iron yoke and additional iron (0.6 to 0.9 m thick) providing a filter for muon identification. All around this iron there are two layers of drift chambers, called the muon chambers, that provide the two coordinates for muons that filter through the iron. Additional layers of drift chambers are currently being installed in gaps within the iron shield.

In Figure 1b we see a view along the beam of the same detector. Here I wish to point out that there are electromagnetic shower detectors at each end of each octant and shower detectors also at the end of the drift chamber. They are all proportional tubes-lead sheets sandwiches.

Finally we see two small scintillator-lead sandwich shower counters that serve as luminosity monitor by detecting small angle Bhabba scattering.

Figures 2 and 3 show two examples of events obtained with CLEO as reconstructed by our reconstruction program and displayed through the computer. They are candidates, respectively for a mu pair and for a hadronic event. In the last one, one can observe two showers in the shower counters. The magnet coil has a thickness of about a radiation length, consequently a substantial number of photons convert in it and this is a likely example. The showers are preceded by hits in the time-of-flight counters and throughout the dE/dx proportional chambers and also in the drift chambers immediately before that, indicating the possible conversion of these two gamma rays in the magnet coil. In Table I is a summary of parameters of the CLEO detector.

While CLEO is a general purpose detector the CUSB (Columbia University, SUNY-Stony Brook, Louisiana State, Max Planck-Munich collaboration) detector, considerably smaller, has emphasis on measurement of the energy of photons and electrons and the direction of both photons and all charged tracks. It is somewhat in the same line of thought of the crystal ball: a crystal cube, if you like. In Fig. 4 we can see that immediately around the beam pipe there are 12 planes of drift chambers, to gather directions of all the charged tracks, surrounded by four layers of NaI crystals. They are followed in turn by two layers of lead-glass Cherenkov counters. Altogether the shower detectors are 16 radiation lengths deep. There are also proportional chambers interleaved with the NaI counters.

Table II gives a summary of the characteristics of the CUSB

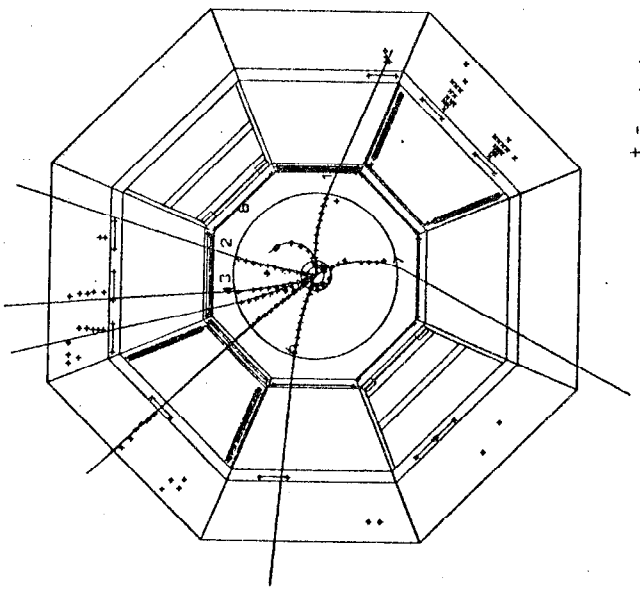

Fig. 3. A CLEO candidate event for e^+e^- + hadrons.

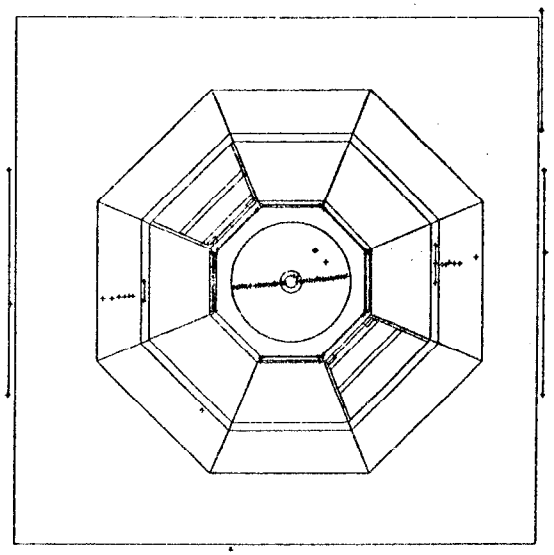

Fig. 2. A CLEO candidate event for e^+e^- + $\mu^+\mu^-$

TABLE I

CLEO PARAMETERS

Charged Particle Resolution:

$\Omega/4\pi$	.73 (good resolution)	.97(total)
$\Delta\theta$	.3 mrad	
$\Delta\phi$	.2 mrad	
$\delta p/p$ (B = .44 Tesla)	.03 × p (GeV/c)	

Photons:

Angular Resolution	7 mrad
2 photon separation	170 mrad
Energy Resolution	$.18\ E^{-1/2}$ Octant Shower Counters $.25\ E^{-1/2}$ End-cap Shower Counters
Material in front	∿ 1.5 rad. length
$\Omega/4\pi$ (total)	.78

Muons:

$\langle E_{min} \rangle$	1.3 GeV
$\Omega/4\pi$	.85

Hadron Identification:

	TOF	LPC	HPC	dE/dx
e/π	< .5	.3 to 3	.3 to 1.2	> .2 GeV/c
π/K	0.5 to 1.2		1.3 to 4	.4 to .7 GeV/c
K/p	< 1.7			.7 to 1.2 GeV/c
$\Omega/4\pi$ (per octant)	.07	.07	.05	.07
$\Omega/4\pi$ (total)	.56		.56	

$E_{min.}$ to get through coil: π > .2; K > .4; p > .6 GeV/c

Luminosity:

Absolute: $\lesssim \pm 8\%$ Relative: $\lesssim \pm 3\%$

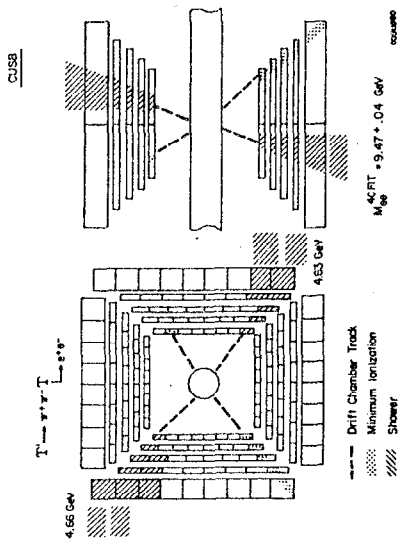

Fig. 5. A CUSB candidate event for $\Upsilon' \to \pi^+\pi^-\Upsilon$

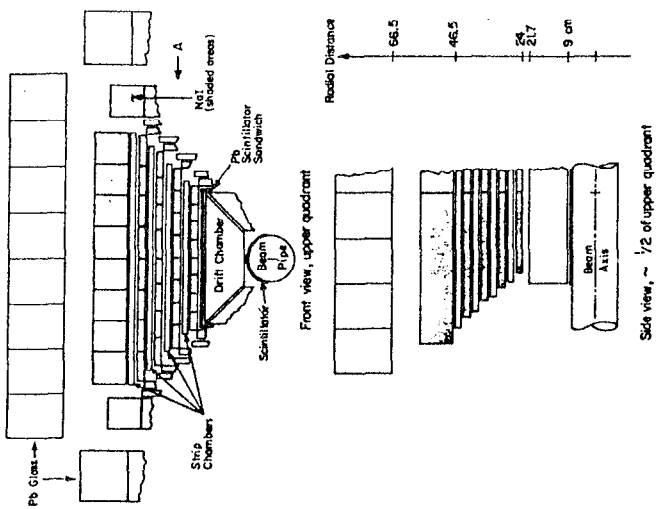

Fig. 4. The CUSB detector.

TABLE II

CUSB DETECTOR PARAMETERS

CURRENT:

MEASURE	USE	SOLID ANGLE $(\frac{\Delta\Omega}{4\pi})$	RESOLUTION (Expected) FWHM
$E(\gamma,\pi^0,\eta)$; $E(e^\pm)$	$\geq$ 8.6 r.l. NaI + $\geq$ 7 r.l. Pb glass	67%	$\sim$ 13% @ .2 GeV
$E_{(\text{stop }\pi^\pm)}$; $\frac{dE}{dx}\Big\|_{M.I.P.}$			$\sim$ 6% @ 1. GeV
θ,ϕ of tracks	4×12 Planes of Drift Chambers	80%	Accuracy of $\sim$ 1 mrad in ϕ $\sim$ 5 mrad in θ
θ,ϕ of shower centroids	4×4 Planes of Strip Chambers (PWC with Cathode Strip Readout)	67%	$\sim$ 1.5 mm $\perp$ $\sim$ 2.5 mm $\|\|$

FUTURE:

E	Segmented NaI End Caps	$\sim$ 30%	$\sim$ 10%
μ charge	Magnetized Iron + Drift Chambers	$\sim$ 25%	

detector, and Fig. 5 shows a candidate for the reaction $\Upsilon' \to \pi^+\pi^-\Upsilon \to \pi^+\pi^- e^+e^-$.

III. Υ states below threshold.

The first task that both groups successfully undertook was the search for the Υ and its exited states. There were and are excellent reasons to believe that they are bound states of a bottom quark-antiquark pair (bottomonium). The level diagram (Fig. 6) is expected to be quite similar to that of charmonium. The mass differences and certain decay rates can be calculated on the basis of the non-relativistic potential model[1]. It should be noticed that the non-relativistic approximation is much more reliable for the heavier bottom quarks than for charm quarks and that having found the shape of the potential from charmonium spectroscopy, it is possible to predict the properties of bottomonium and thus establish experimentally the flavor independence of the $q\text{-}\bar{q}$ potential.

The existence of the Υ and Υ' had been established by the Columbia-Fermilab-Stony Brook collaboration[2] and their mass difference and leptonic widths determined at DORIS[3]. For the Υ" only an approximate value of the mass was available[4] and it was still to be determined whether it is a narrow state below threshold for decay into bottom mesons.

The task was quite suitable as a first one for detectors not yet well known and in fact (as of December 1979) not fully assembled.

The search was made easier by the good c.m. energy (W) resolution of CESR: $(4.1 \pm 0.3\ \text{MeV}) \times (W/10\ \text{GeV})^2$, a factor of 2 better than at DORIS.

In order to find the Υ states we had to measure $\sigma(e^+e^- \to \text{hadrons})$ vs. center of mass energy. The criteria to select hadronic events in CLEO were the following. We requested that three or more charged

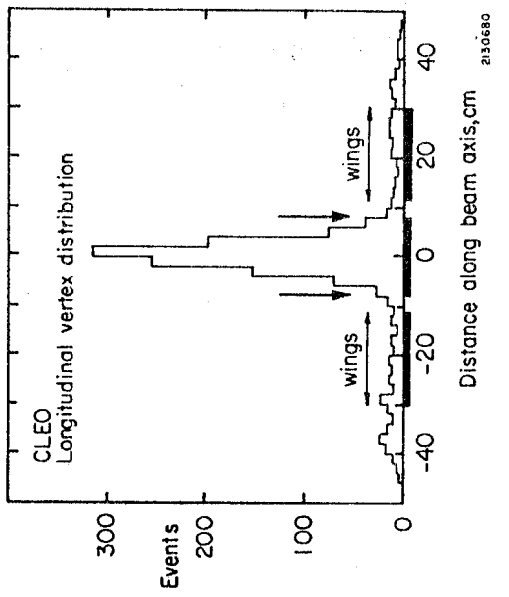

Fig. 7. Coordinate along the axis of the event vertex position.

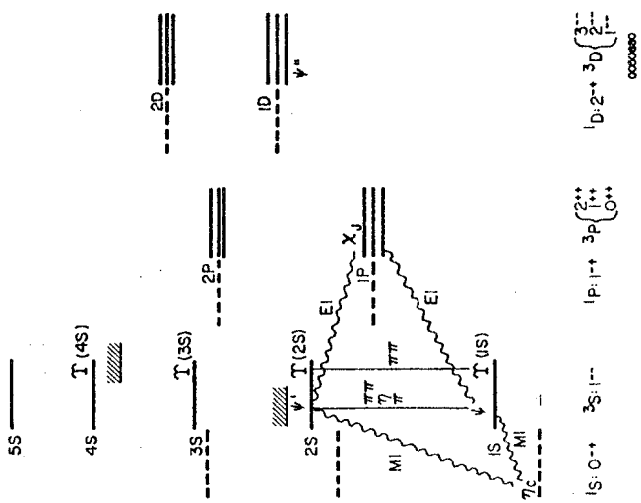

Fig. 6 Quarkonium energy levels.

tracks with a common vertex were found in the drift chamber, that the total charged energy was greater than 3 GeV and that the common vertex had to be within 2.5 cm of the beam line while the z coordinate, along the beam line, of the vertex had to be within 8 cm of the predicted beam crossing point. The actual distribution of the vertex point along the beam is shown in Figure 7. You can see clearly the peak due to the electron positron annihilation into hadrons superimposed on a background due to beam gas interaction. This curve was obtained last December and at that time the typical subtraction that had to be done to eliminate beam-gas and beam-wall interactions was 9%; beam-wall event rejection is considerably better now. Fig. 8 shows the CLEO updated results for the hadronic cross section in the Υ (L = 280 nb^{-1}), Υ'(L = 450 nb^{-1}), Υ''(L = 460 nb^{-1}). The fit is a superposition of gaussians, with the r.m.s. spread given above and including radiative corrections, over a continuum falling as W^{-2}. The cross sections are corrected for detection efficiency, which is expected to be different for continuum and for resonant events, as discussed below.

The hadronic yield vs. center of mass energy obtained with the CUSB detector in the November-December 1979 run[6] is shown in Fig. 9. Only half the detector was operational at that time, and the requirements for a hadronic events were: (i) energy deposited in the NaI counters greater than 0.42 GeV; (ii) at least one minimum ionizing track and (iii) two more tracks or showers. The fitted curve is calculated with the same criteria used by the CLEO group.

The numerical results for the masses and widths of the resonances are shown in Table III. The resonance masses are affected by a systematic error due to uncertainty in the absolute value of the beam energy. There seems to be a scale difference of $\sim$ 28 MeV

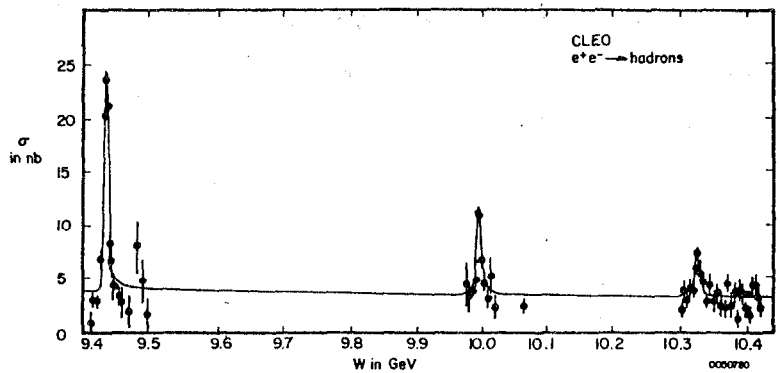

Fig. 8. $\sigma(e^+e^- \to \text{hadrons})$ vs. c.m. energy (CLEO).

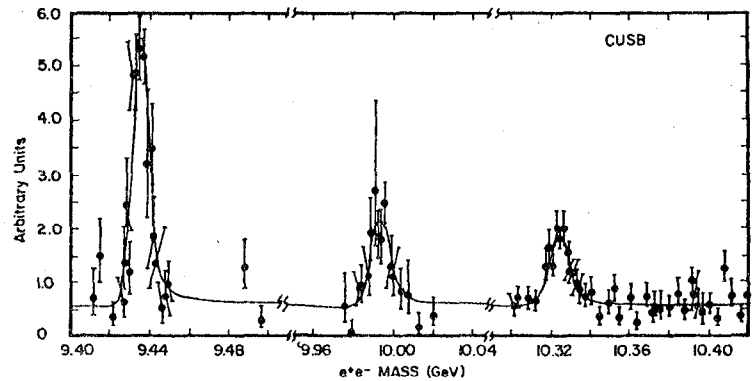

Fig. 9. $\sigma(e^+e^- \to \text{hadrons})$ vs. c.m. energy (CUSB)

Resonance	Mass (MeV)		$\Delta M(\Upsilon-\Upsilon(1S))$ (MeV)	
	CLEO	CUSB	CLEO	CUSB
$\Upsilon(1s)$	9433.6 ± 0.2 ± 28	9434.5 ± 0.4 ± 28	--	--
$\Upsilon(2S)$	9994.4 ± 0.4 ± 30	9993.0 ± 1.0 ± 30	560.8 ± 0.4 ± 3.0	559.0 ± 1.0 ± 3.0
$\Upsilon(3S)$	10323.1 ± 0.4 ± 30	10323.2 ± 0.7 ± 30	889.5 ± 0.5 ± 4.0	889.0 ± 1.0 ± 4.0
$\Upsilon(4S)$	10547.6 ± 1.1 ± 32		1114.0 ± 1.1 ± 5.0	1114.0 ± 2.0 ± 5.0

Resonance	$\Gamma_{ee}\cdot(\Gamma had/\Gamma tot) \equiv \Gamma'_{ee}$		$\Gamma'_{ee}/\Gamma'_{ee}(1S)$		Measured rms width (MeV)	
	CLEO	CUSB	CLEO	CUSB	CLEO	CUSB
$\Upsilon(1S)$	0.925 ± 0.06 ± 0.14	--	--	--	3.14 ± 0.20	
$\Upsilon(2S)$	0.468 ± 0.04 ± 0.07	0.51 ± 0.05 ± 0.05	0.39 ± 0.06		3.53 ± 0.22	4.0 ± 0.3
$\Upsilon(3S)$	0.221 ± 0.03 ± 0.05	0.31 ± 0.04 ± 0.03	0.32 ± 0.04		3.76 ± 0.24	
$\Upsilon(4S)$	0.221 ± 0.02 ± 0.03	0.24 ± 0.02 ± 0.03	0.25 ± 0.07		9.00 ± 0.82	8.1 ± 1.7

*The first error in each case is statistical, the second systematic.

between the CESR and the DORIS c.m. energy scales. The systematic errors on the mass differences are much smaller and those are the quantities that are to be compared with the predictions of the potential model.

The leptonic partial width is predicted by the non relativistic potential model through[7]

$$\Gamma_{ee} = 16\,\pi\,\alpha^2\,e_q^2\,\frac{|\psi(0)|^2}{M^2}\,(1 - \frac{16\pi}{3}\,\alpha_s), \qquad (1)$$

where α is the fine structure constant, e_q is the charge of the bound quark, $\psi(0)$ the value of the $q\bar{q}$ wave function at the origin and α_s is the QCD effective coupling strength. The value of Γ_{ee} is thus crucial in determining the charge of the quark involved.

Table III shows the experimental values of $\Gamma'_{ee} \equiv \Gamma_{ee}\cdot(\Gamma_{had}/\Gamma_{tot})$ obtained from the fits ($\Gamma'_{ee} \tilde{=} \Gamma_{ee}$ if $\Gamma_{had} \tilde{=} \Gamma_{tot}$). They are calculated through the relation:

$$\int \sigma(e^+e^- \to \Upsilon(nS) \to \text{hadrons})dW = \frac{6\pi^2}{M^2}\,\frac{\Gamma_{ee}\cdot\Gamma_{had}}{\Gamma_{tot}} \qquad (2)$$

where M is the mass of the $\Upsilon(nS)$[8] and Γ_{tot}, Γ_{ee}, Γ_{had} are its total width and partial widths for decay into e^+e^- and into hadrons, respectively. In order to determine Γ'_{ee} it is necessary to know the absolute value of the resonant cross section as a function of energy, so that the hadronic event detection efficiencies have to be accurately estimated. The efficiency for off-resonance (continuum) events is in fact different from the resonant event efficiency. Continuum events are clearly two-jet-like, as expected from annihilation into $q\bar{q}$, with a $(1 + \cos^2\theta)$ distribution of the jet axis relative to the beam; they have thus a tendency to miss our central detector and the detection efficiency has been determined by Monte Carlo simulation to be (61 ± 1)%. Resonant events are expected and found to be considerably

more isotropic and their detection efficiency is estimated to be (72 ± 1)%. In order to avoid the uncertainties associated with the efficiencies, we give in Table III the experimentally more accurate ratios $\Gamma'_{ee}(ns)/\Gamma'_{ee}(1S)$.

Notice the good agreement of the CLEO and CUSB results with the only slight exception of $\Gamma'_{ee}(2S)/\Gamma'_{ee}(1S)$. They also agree with the DORIS results for the $\Upsilon(1S)$ and $\Upsilon(2S)$[9] (see Table IV).

We should now compare the experimental mass difference and leptonic partial widths with the potential model predictions. Several such models have been formulated[1] going from the two-parameter, simple superposition of a Coulomb-like and a linear confining potential to the nearly parameter-free analytic formula of Richardson. They may differ in derivability from QCD and in predictive power, but the differences in numerical value of V(r) in the range of $q\bar{q}$ distances of interest are minimal, so that their predictions of mass differences and partial widths are very close. They are in good agreement with the experimental values, as shown in Table IV.

In order to determine the total widths Γ_{tot} it is necessary to measure the leptonic branching ratio $B_{\mu\mu} = B_{ee}$. As of today CLEO has only a very preliminary value of $B_{\mu\mu}$ for the $\Upsilon(1S)$. It is consistent with the DORIS results.

In Table V the average values are shown, as measured in the CLEO detector, of charged multiplicity, charged energy, and various "event shape" parameters for the continuum and the resonant events.

IV. The $\Upsilon(4S)$.

The spectroscopy of charmonium and bottomonium states (Fig. 6) are expected to be quite similar, but one of the main differences is the location of the threshold for free decay, not hindered by the OZI rule, into, respectively, charmed or "bottomed" mesons. In the case of

TABLE IV

Comparison of experimental values and theoretical predictions for the mass differences (in MeV) and the relative electronic widths of the first three excited Υ states. For the latter ones the experimental results are for $\Gamma'_{ee}(nS)/\Gamma'_{ee}(1S)$ which should be very close to $\Gamma_{ee}(ns)/\Gamma_{ee}(1S)$.

	M(2S)-M(1S)	M(3S)-M(1S)	M(4S)-M(1S)	$\Gamma_{ee}(2S)/\Gamma_{ee}(1S)$	$\Gamma_{ee}(3S)/\Gamma_{ee}(1S)$	$\Gamma_{ee}(4S)/\Gamma_{ee}(1S)$
CLEO	560.8	889.5	1114.0	0.51	0.31	0.24
CUSB	559.0	889.0	1114.0	0.39	0.32	0.25
LENA	552.6	-	-	0.50	-	-
DASP2	553.7	-	-	0.50	-	-
Eichten et al.	591	936	1213	0.36	0.25	0.20
Bhanot-Rudaz $\bar{m}_b$=3.5 GeV	561	881	1141	0.44	0.32	0.27
Bhanot-Rudaz $\underline{m}_b$=4.5 GeV	566	879	1123	0.43	0.29	0.24
Quigg-Rosner $\bar{T}$og	589	910	1140	0.45	0.29	0.21
Quigg-Rosner $\underline{C}$oul+lin	(560)	890	1150	0.38	0.27	0.22
Richardson	555	886	1146	0.42	-	-

TABLE V

Average values of various distributions observed in the continuum (between the $\Upsilon(3S)$ and $\Upsilon(4S)$) and for each of the upsilons with continuum subtracted. None of these averages are corrected for detector acceptance. (CLEO)

	Continuum	$\Upsilon(1S)$	$\Upsilon(2S)$	$\Upsilon(3S)$	$\Upsilon(4S)$
Charged multiplicity	6.55 ± 0.06	7.55 ± 0.05	8.28 ± 0.15	7.95 ± 0.18	8.48 ± 0.74
Charged energy, GeV	5.83 ± 0.07	5.2 ± 0.1	5.3 ± 0.1	5.1 ± 0.2	5.7 ± 0.2
Sphericity	0.232 ± 0.005	0.369 ± 0.005	0.38 ± 0.01	0.36 ± 0.02	0.38 ± 0.05
Thrust	0.848 ± 0.002	0.777 ± 0.003	0.77 ± 0.01	0.77 ± 0.01	0.76 ± 0.03
$R_2 = H_2/H_0$	0.458 ± 0.006	0.285 ± 0.005	0.26 ± 0.02	0.27 ± 0.02	0.26 ± 0.07
Oblateness	0.173 ± 0.003	0.195 ± 0.003	0.20 ± 0.01	0.22 ± 0.01	0.18 ± 0.02
Triplicity	0.946 ± 0.001	0.917 ± 0.001	0.908 ± 0.003	0.921 ± 0.004	0.90 ± 0.02

charmonium the threshold is just above the 2S state, while for bottomonium it is expected to be in the vicinity of the 4S state, and we have in fact observed the three states $\Upsilon(1S)$, $\Upsilon(2S)$, $\Upsilon(3S)$ to be narrower than the energy resolution of CESR, i.e., below threshold.

It was then most important to measure the hadronic cross section in the vicinity of the expected mass of the $\Upsilon(4S)$ state[1], about 1.12 GeV above the $\Upsilon(1S)$.

Because of the small charge of the bottom quark, all bottomonium resonances are much less prominent over continuum than the corresponding charmonium ones. A naive application of eq. (2) (assuming a Breit-Wigner shape of the resonance) tells us that the maximum resonant excess ΔR of $R = \sigma(\text{hadrons})/\sigma(\mu\mu)$ over its continuum value is

$$R = (9/\alpha^2) \cdot (\Gamma_{ee}/\Gamma_{tot}). \qquad (3)$$

For an expected $\Gamma_{ee}(4S) = 0.20$ keV and a "normal" hadronic width $\Gamma_{tot} = 100$ MeV that with mean $\Delta R = 0.34$, only a 9% increase over the continuum!

In fact a resonance close to threshold is not expected to have Breit-Wigner shape and, in the bottomonium case, the situation is further complicated by the closeness of the $B\bar{B}$, $B^*\bar{B} + B\bar{B}^*$ and $B^*\bar{B}^*$ thresholds. This has been pointed out by E. Eichten[10] and illustrated in Fig. 10. It shows that an accident of nature may make a resonance very hard or relatively easy to find. The accident has been in our favor this time.

Fig. 11 shows the updated CLEO results for $\sigma(\text{hadrons})$ in the region above the Υ''. A clear bump is found[11] at 10,547.6 MeV. Unfolding from the fitted width of the bump the energy resolution of the storage ring we find the total (natural width of this resonance to be $\Gamma_{tot} = 19.1 \pm 1.8$ MeV. CUSB measurements are shown in Fig. 12; the fitted mass value is identical to CLEO's, the (unfolded) natural total width is $\Gamma_{tot} = 12.6 \pm 6.0$ MeV (based on the February data[12]).

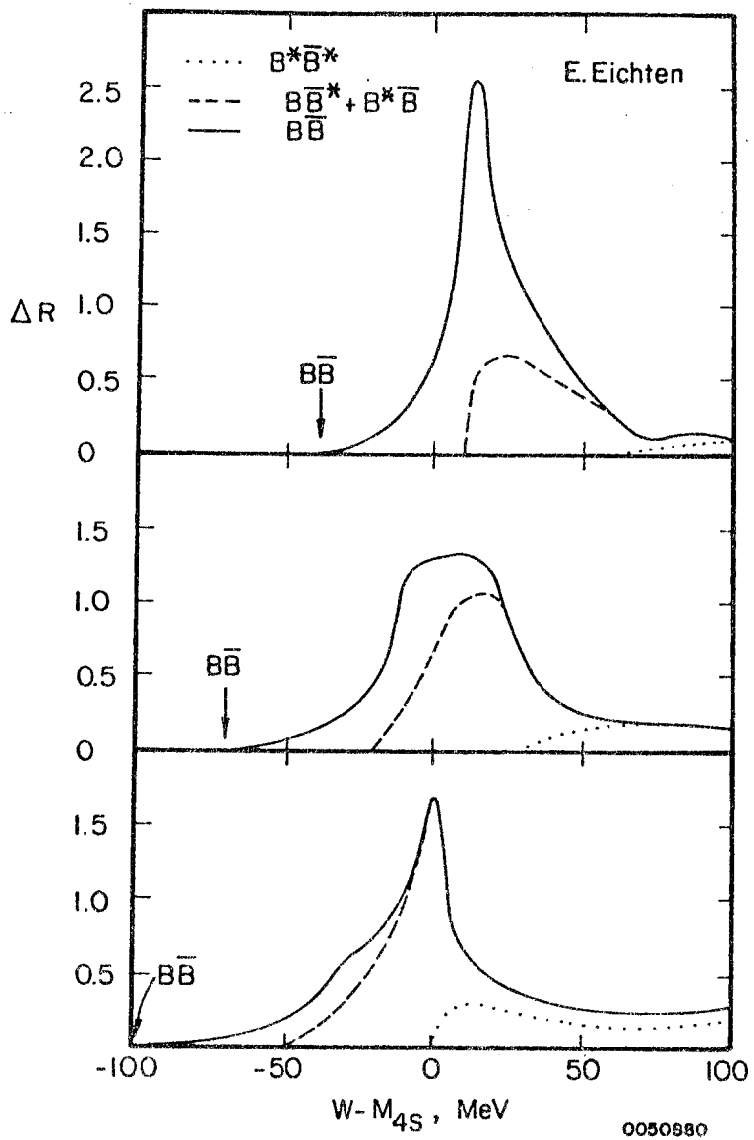

Fig. 10. Possible shapes of Υ(4S) resonant cross section vs. $E_{c.m.}$ in the vicinity of thresholds for decay into bottom mesons and their excited states[10].

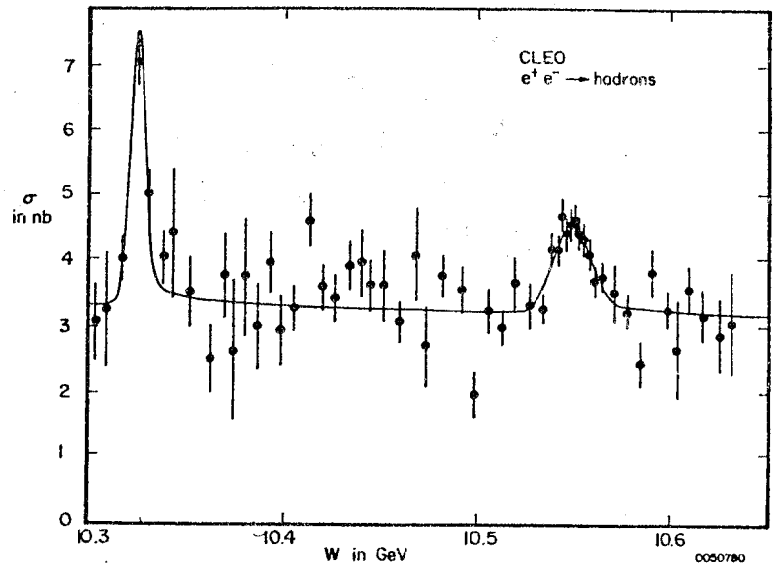

Fig. 11. $\sigma(e^+e^- \to \text{hadrons})$ vs. $E_{c.m.}$ in the Υ(3S) and Υ(4S) region (CLEO)

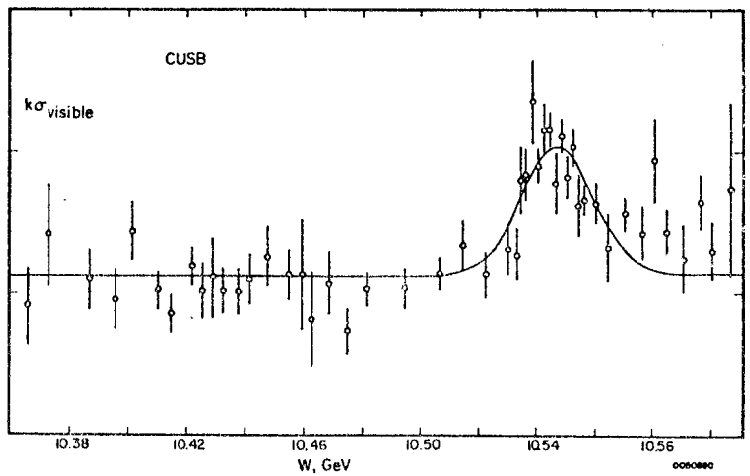

Fig. 12. $\sigma(e^+e^- \to \text{hadrons})$ vs. $E_{c.m.}$ in the region above the Υ(3S) (CUSB)

The two experiments establish beyond doubt that we are dealing with a resonance free to decay into hadrons, i.e., above threshold for decay into bottom mesons. We identify it with the $\Upsilon(4S)$. Its measured parameters are given in Tables III and IV.

Besides establishing beyond doubt the statistical significance of this bump in the hadronic cross section, we have the task of finding the characteristics of the resonant events. Specifically we wanted to see if they are consistent with the hypothesis of production of a pair of very slow moving bottom mesons and their approximately isotropic decay.

The CUSB collaboration used a modified thrust variable:

$$T' = (\Sigma|\vec{E}_{NaI} \cdot \vec{n}|)/(\Sigma E_{NaI}) \qquad (4)$$

where the summation is over all showers, $\vec{E}_{NaI}$ representing their energy and direction, while $\vec{n}$ is a unit vector in the plane normal to the beam, that maximizes the numerator. Fig. 13 shows the pseudo thrust distribution for events in the $\Upsilon(4S)$ region. The distribution has an excess of events at low values of T' as expected from isotropic events on top of the two-jet-like continuum. A cut at $T' < 0.85$ (Fig. 14, lower curve) removes 52% of continuum events but only 26% of resonant ones.

Very similar results were obtained by the CLEO collaboration[11] using the "shape parameters" H_ℓ introduced by Fox and Wolfram[13]:

$$H_\ell = \sum_{i,j} (|p_i||p_j|/W^2)\, P_\ell(\cos\phi_{ij}) \qquad (5)$$

where the summation is over all pairs of charged tracks, $|p_i|$ is the i^{th} track momentum, W the c.m. energy, ϕ_{ij} the angle between tracks i and j, and P_ℓ is the Legendre polynomial of order ℓ. The distribution of the ratio $R_2 = H_2/H_0$ is expected to be peaked near zero for isotropic events and near one for very jet-like events. The differential cross section $d\sigma/dR_2$ for events on and off the $\Upsilon(4S)$

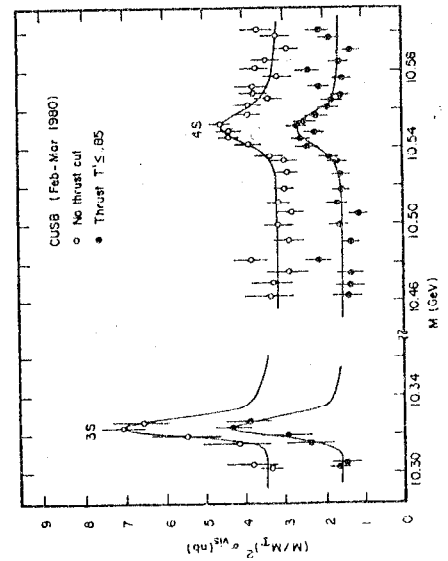

Fig. 14. Visible hadronic cross section vs. c.m. energy in the $\Upsilon(3S)$ and $\Upsilon(4S)$ region, without and with a pseudothrust cut.

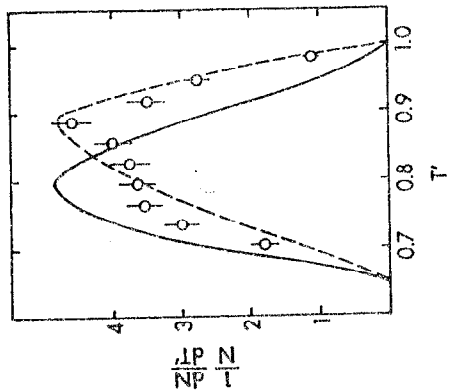

Fig. 13. Pseudothrust distribution (points) for events in the $\Upsilon(4S)$ region. Dashed line is such distribution for continuum events, solid line for events in the $\Upsilon(1S)$ region (CUSB).

peak region (defined as $5.270 < E_{beam} < 5.280$ GeV) is shown in Fig. 15a. A clear excess of low R_2 events is visible in the "on" sample. The difference (Fig. 15b) of the two distributions is in excellent agreement with the expectation of $B\bar{B}$ decaying essentially at rest.

The same situation prevails with respect to the sphericity (Fig. 16) and charged multiplicity (Fig. 17) distributions.

Having established that the 4S is above the threshold for decaying into bottom mesons, we still have to determine how far it is above threshold. There are two possible ways of obtaining information about this. One, already mentioned, uses the shape of the resonant cross section, the other one consists in spotting directly the presence of B^* decays. Let me start from the second one.

Shortly above the threshold for decay into $B\bar{B}$ there should be the threshold for $B\bar{B}^* + B^*\bar{B}$ decay and eventually $B^*\bar{B}^*$ decay. On the basis of the binding energy being inversely proportional to the mass of the constituent quarks, it is predicted[14] that

$$m(B^*) - m(B) = \frac{m_c}{m_b}[m(D^*) - m(D)] \qquad (6)$$

i.e., $m(B^*) - m(B) = 35$ to 50 MeV. The B^* would then decay through $B^* \to \gamma + B$ and, if the $\Upsilon(4S)$ were above threshold for decay into $B\bar{B}^* + B^*\bar{B}^*$, one should observe one $\sim$ 50 MeV photon per such decay and, if above the $B^*\bar{B}^*$ threshold, two $\sim$ 50 MeV photons per such event.

A preliminary spectrum of the soft single photons from the CUSB detector is shown in Fig. 18. In the same figure we also see how a peak of monochromatic photons in the quantity expected from the $B\bar{B}^* + B^*\bar{B}$ decay should appear. There is no sign of such a peak. The CUSB group concludes that the $\Upsilon(4S)$ is not above the $B^*\bar{B}^*$ threshold and that it is unlikely that it be above the $B\bar{B}^* + B^*\bar{B}$ threshold.

That we are close to the $B\bar{B}$ threshold can also be inferred from

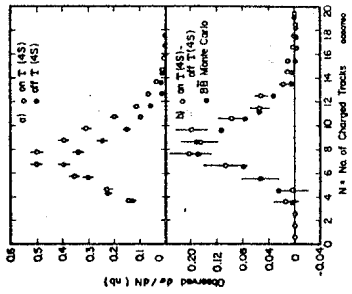

Fig. 17. Same as Fig. 15 for multiplicity distribution (CLEO).

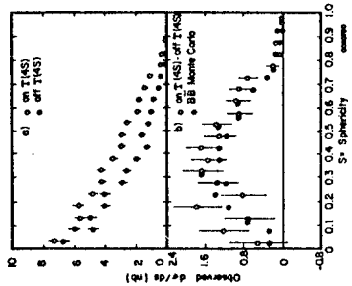

Fig. 16. Same as Fig. 15 for dσ/ds (CLEO).

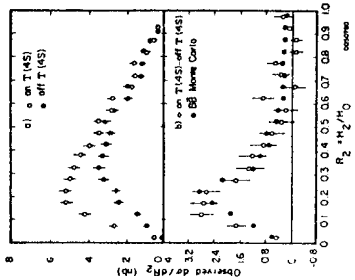

Fig. 15. Differential cross section $d\sigma/dR_2$ for events in and out of the $\Upsilon(4S)$ region (a) and their difference (b) compared with $B\bar{B}$ Monte Carlo (CLEO).

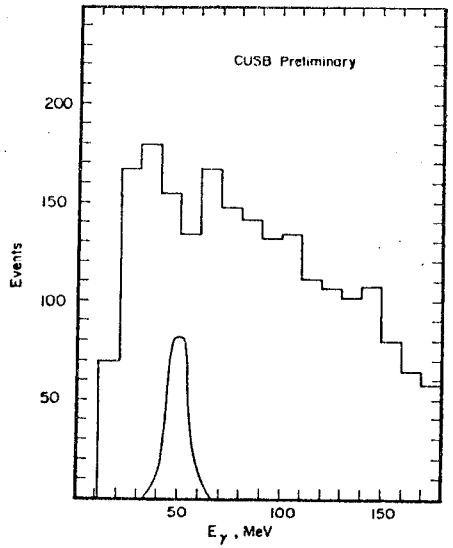

Fig. 18. Low energy photon spectrum from 827 T(4S) events, showing expected contribution from $B^* \to \gamma B$ decay if there were one B^* per T(4S) (CUSB).

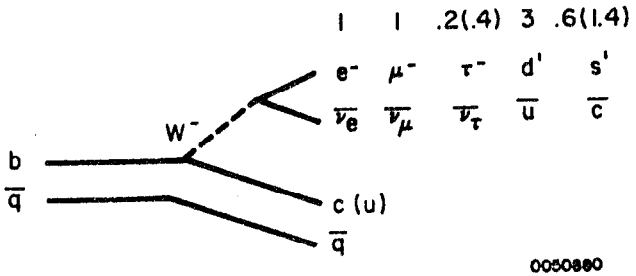

Fig. 19. Spectator model for bottom meson decay with estimated relative contributions of different final states.

the small total width of the 4S resonance. In fact the resonance should give considerably more information as 10. For the time being we do not have enough statistic mine such a shape!

V. Preliminary results on B decay.

It is fair to assume that the bump that we have ju is due to a $B\bar{B}$ resonance where B is a meson formed as a of a b quark and a u antiquark or a b quark and a d ant respectively, in two charge states, and similarly for t resonance is then a small factory of B and $\bar{B}$ mesons and a good observation point for their properties. The si quite similar to the ψ"(3770) but there is one very imp In the case of the ψ", because of the 2/3 charge of the the resonance is quite prominent over the continuum. the T(4S), because of the charge 1/3 of the bottom qua cross section is about 1/4 of the total cross section although we have a B factory, this is only a small fac anyway happy to have such a factory and let's see what able to produce with it up to now. I'll report about t results on the inclusive branching ratios for B decay into muons, and into $K^\pm$ mesons.

Let's start with the inclusive branching ratio in The simplest prediction, according to the spectator mo is that the branching ratio for the decay $B \to \ell\nu + X$ i 15 and 17% for each lepton[15]. In CLEO we can determ branching ratio by measuring the jump in the inclusive section for electron production and relating it to the ratio itself according to the following formula:

$$Br(B \to e\nu x) = \frac{\Delta\sigma_e^{vis}(P_e > 1\ GeV)}{2 \cdot \Delta\sigma_{had}^{vis}} \cdot \frac{1}{A_c \cdot \varepsilon_c \cdot \varepsilon_{an} \cdot f(p_e > 1)} \quad (7)$$

Here $\Delta\sigma_e^{vis}$ is the difference in visible cross section for the production of electrons of energy greater than 1 GeV on and off-resonance, $\Delta\sigma_{had}^{vis}$ is the similar difference for the annihilation into hadrons; A_c is the geometric acceptance of the Cherenkov counters, ε_c is the efficiency of the Cherenkov counters. The product $A_c \times \varepsilon_c$ has been estimated from Bhabhas and dimuons to be .31 ± .05. ε_{an} is the efficiency of the electron identification algorithm, which has been estimated from the data to be .68 ± .09. The factor of two is because we have both B and $\bar{B}$ decay and $f(P_e > 1)$ is the probability that a B decay produces an electron of energy greater than 1 GeV. This probability is model dependent; we have evaluated it to be $(70 \pm 5)\%$[16].

A charged particle with momentum above 1 GeV/c was called an electron (or positron) if it fired one of the low pressure Cherenkov counters, if the shower associated with it had an energy greater than half the momentum p, measured in the drift chamber, if at least 10% of the shower energy was deposited in the first 3.3 radiation lengths of the shower counter, if the width of the shower was consistent with that expected for electron showers and if the shower position agreed within ± 20 cm with the position of the track projected from the inner chambers.

In order to reject electrons from γ conversion we rejected events where an oppositely charged track forms an angle of nearly 0^0 with the electron candidate. In order to suppress events originated from Bhabha scattering, $\tau^+\tau^-$ production and two-photon processes, we required a charged multiplicity of 5 or greater.

Sources of background are charge exchange and photon conversion in the coil, random overlap of a charged particle track with electrons originated by photon conversion in the coil, and true electrons from D decays. The last ones may be responsible for about one third of σ_e^{vis} in the continuum region.

σ_e^{vis} ($p_e > 1$ GeV/c) as seen in CLEO is shown in Fig. 20. We observe a $\Delta\sigma_e^{vis} \simeq 35 \pm 8$ pb, an excess of about 5 standard deviations. Notice that in calculating $\Delta\sigma_e^{vis}$ we subtract both the continuum contribution and the accidental background. Since the B meson is expected to decay preferentially into charmed particles, we should observe also the electrons from D decays; however one can easily estimate that only about 10% of these electrons have $P_e > 1$ GeV/c and would be accepted in our analysis; the branching ratio below has been corrected for this effect. The spectrum of the electrons on resonance (continuum and background subtracted) is shown in Fig. 21; it is consistent with the expectation of the model of Fig. 19.

With a $\Delta\sigma_{had}^{vis} = 0.78 \pm 0.10$ nb we obtain for the branching ratio a preliminary value:

$$Br(B \to e\ \nu\ X) = (15 \pm 4 \pm 7)\%. \quad (8)$$

where the first error is statistical and the second systematic. Electrons were also identified in the two octants with the dE/dx measuring devices. The branching ratio obtained with them is very close to the above, but with considerably larger statistical error.

The CUSB collaboration has performed an analogous analysis and their preliminary results for σ_e^{vis} are shown in Fig. 22. They also conclude that

$$BR(B \to e\ \nu\ X) \simeq 10\%\ \text{to}\ 20\%. \quad (9)$$

Because of the $\sim$ 0.6 m iron shield around the detector, CLEO is also in a position to measure the inclusive muon yield and the branching ratio $BR(B \to \mu\ \nu\ X)$ from it. Our analysis in this case is still very

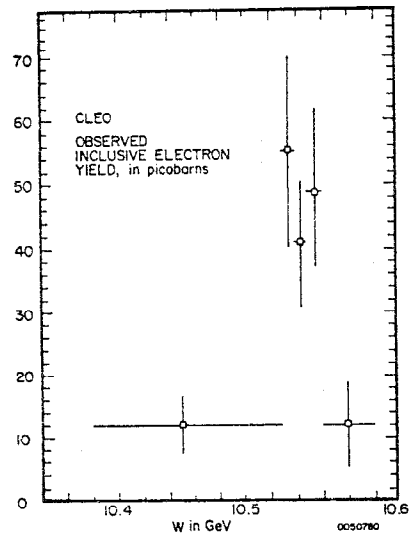

Fig. 20. Inclusive, visible cross section for production of electrons with $p > 1.0$ GeV/c, vs. c.m. energy (CLEO).

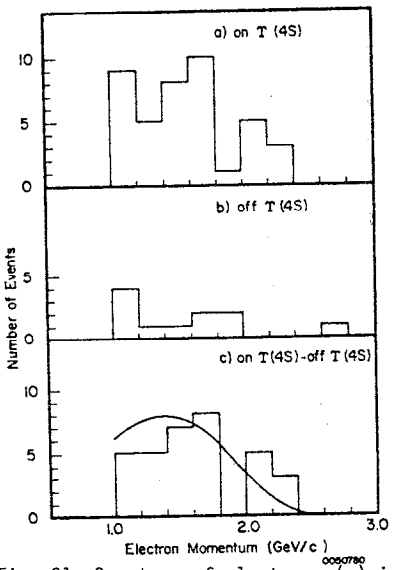

Fig. 21. Spectrum of electrons (a) in the T(4S) region, (b) in the adjacent continuum, and (c) their difference compared with expectation from spectator model.

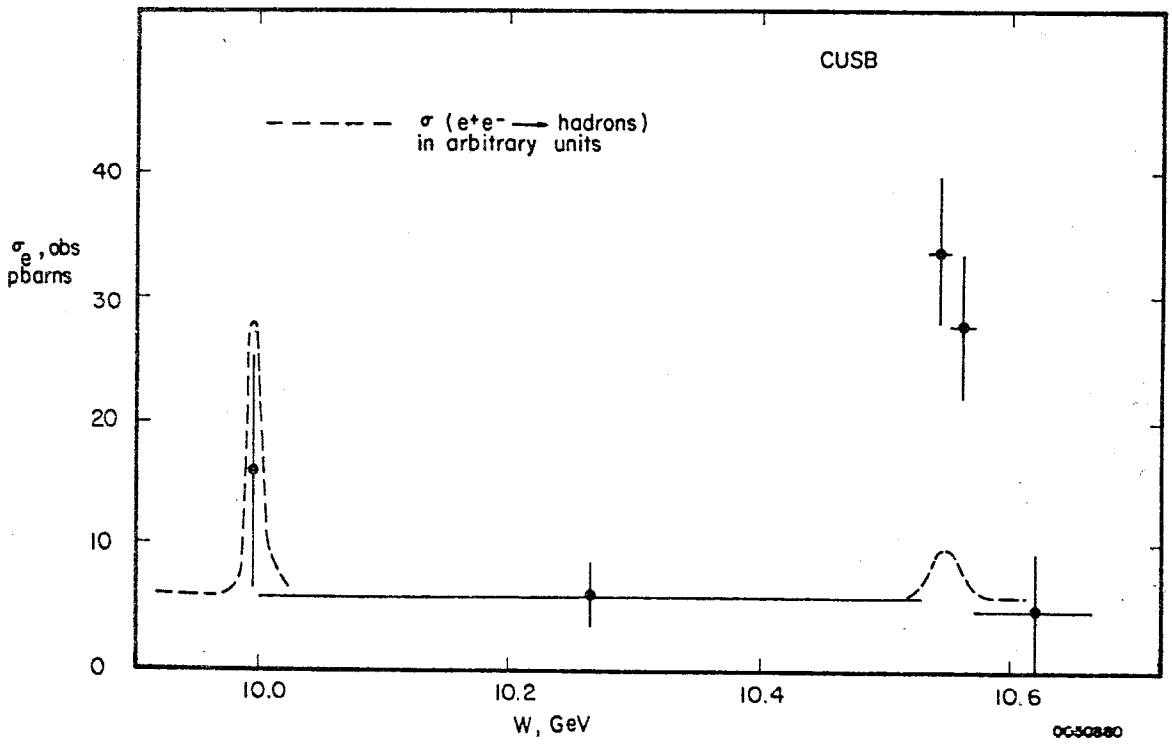

Fig. 22. Inclusive, visible cross section for production of electrons with $p_e > 1.0$ GeV/c vs. c.m. energy (CUSB).

preliminary. Muon candidates are identified by matching tracks extrapolated from the inner drift chamber and the (two-dimensional) coordinate of the hits in the muon chambers surrounding the iron. The distribution of the square of the distance between the two is shown in Fig. 23, together with the cut imposed. The minimum muon momentum accepted varies between 1.0 and 1.6 GeV/c, depending on direction. The combined geometrical and momentum acceptance has been calculated with a Monte Carlo based on the decay $b \to c\, W^-$ and found to be 0.39 ± 0.07 (it would be 0.54 ± 0.07 for the $b \to u\, W^-$ decay). The muon chamber efficiency was determined to be 0.90 ± 0.05 using cosmic rays, and the drift chamber tracking and extrapolating efficiency was found to be 0.80 ± 0.10.

The following backgrounds were evaluated and subtracted. Mixing tracks from different events, random matches were estimated to be 11%. π and K decay in flight and punch-through were estimated to be 12% and checked using $\Upsilon(1S)$ events. No candidates for $\psi \to \mu^+\mu^-$ were found. The contamination due to muons coming from $B \to DX$, $D \to \mu X'$ was estimated to be 15%. Muons from direct D production and decay were eliminated by subtracting the continuum.

The results for the visible muon cross section are shown in Fig. 24; it shows a clear enhancement at the $\Upsilon(4S)$. Putting together all the above numbers in a formula quite similar to (7) we get a very preliminary value for the branching ratio:

$$Br(B \to \mu\, \nu\, X) = (7.5 \pm 3.1)\%. \qquad (10)$$

From results (8), (9) and (10) we may conclude that we have evidence that the $\Upsilon(4S)$ decays strongly into particles that decay weakly with semileptonic branching ratios as expected from the naive spectator model approach. Models predicting very high semileptonic

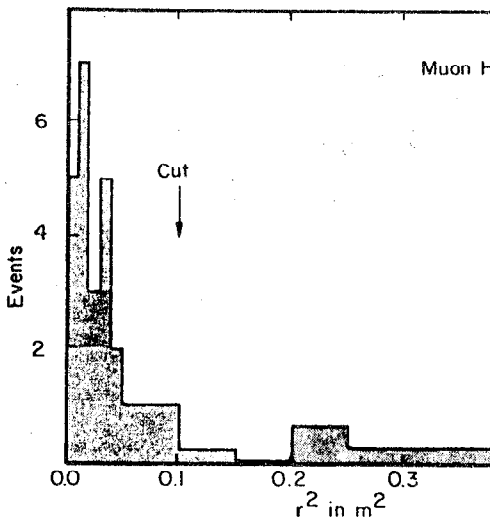

Fig. 23. Distribution of the square of the di polated drift chamber track and the in the muon chambers (CLEO).

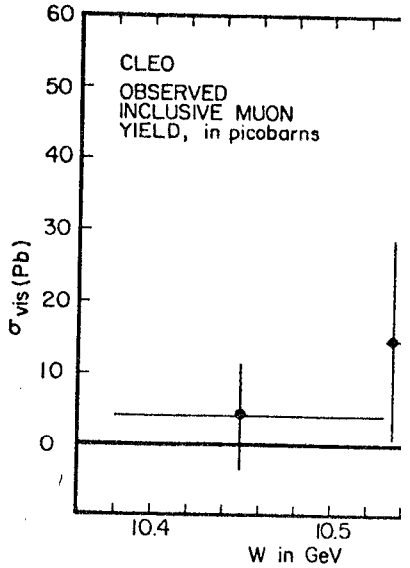

Fig. 24. Uncorrected inclusive muon yield as

branching ratios seem to be excluded.

The next piece of information that we have about the B decay is the inclusive branching ratio for decaying into K mesons. Figure 25 gives the very naive expectations for the number of strange quarks to be expected in the final state of respectively: (i) the continuum electron-positron anniliation into $q\bar{q}$ where we expect just one strange quark per event; (ii) for $B\bar{B}$-production with B decay via $b \to c\ W^-$ where we expect, according to the spectator model, 3.3 strange quarks per $B\bar{B}$ event; and finally (iii) for $B\bar{B}$ production with B decay via $b \to u\ W^-$ where we expect 1.3 strange quarks per $B\bar{B}$ event.

We can identify charged K mesons through time-of-flight and through ionization in the dE/dx modules. Since we have only two dE/dx modules for the time being we have to rely primarily on the time-of-flight information which covers the whole 2π azimuthal range. Preliminary results from the dE/dx measuring devices are completely consistent (on a track by track basis) with the ones obtained by time-of-flight. Fig. 26 shows the distribution of the difference between the predicted flight time for a K meson and the observed flight time in nanoseconds. The tracks selected have momentum between .6 and 1. GeV/c. One can see a prominent peak due to π mesons, a small peak due to $K^{\pm}$ mesons and a few events attributable to protons. The curve is a fit with 2 Gaussians, with r.m.s. resolution of 0.4 ns, that includes all sources of error; one Gaussian is centered over the π time of flight and the other on the K time of flight; the only unknown is the relative area of the two Gaussians. The non-Gaussian tail at large predicted flight times is due to errors in track length. Such tail cannot be present on the K side of the π peak because the shortest track length is a straight line from the vertex to the T.O.F. hit. Through the two-Gaussians fit one can obtain a number of

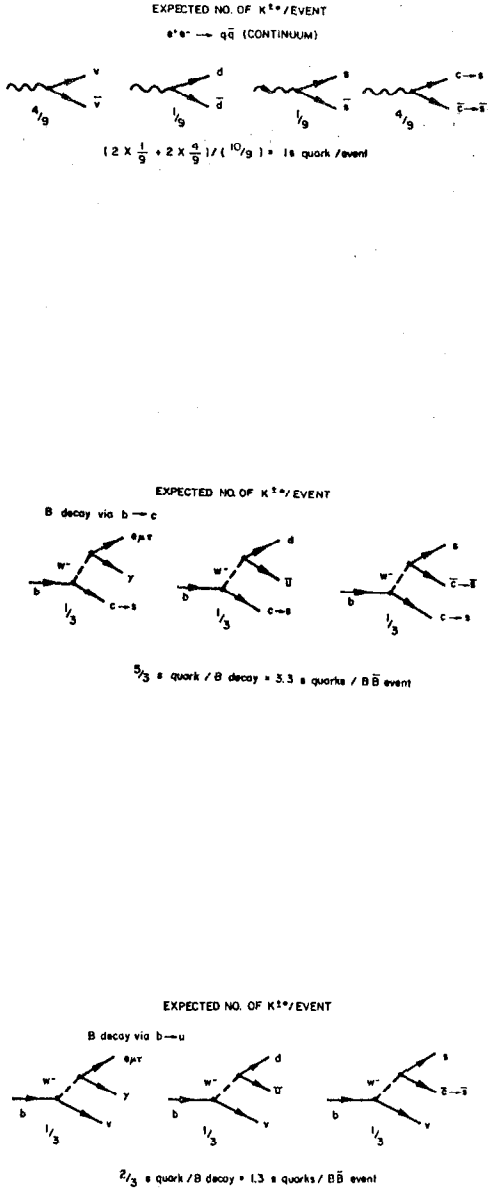

Fig. 25

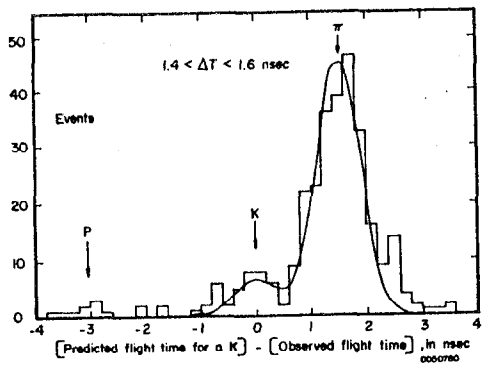

Fig. 26

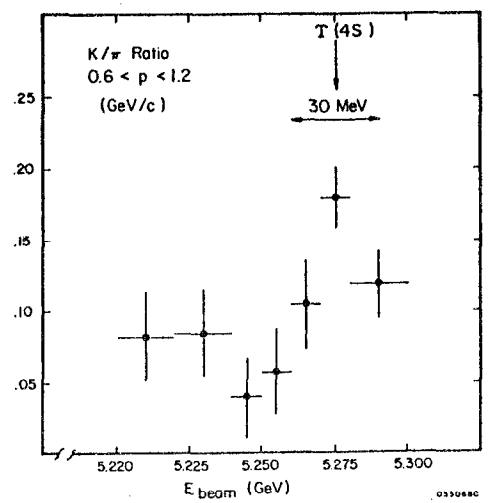

Fig. 27. Kaon to pion ratio as a function of c.m. energy.

kaons per pion and that result is shown in Fig. 27 as a function of beam energy. A clear, four standard deviation, peak is visible at the beam energy corresponding to the $\Upsilon(4S)$ resonance. The raw number of charged kaons per event comes out to be $0.033 \pm 0.004 \pm 0.003$ on the $\Upsilon(4S)$ and $0.012 \pm 0.003 \pm 0.003$ in the region off the resonance.

The product of solid angle acceptance and tracking efficiency is 0.25. The momentum acceptance (model dependent, according to the $b \to c\,W^-$ decay chain) was estimated to be 0.16. After correction for acceptance and subtracting the continuum from the on resonance events in proportion of the respective cross sections, we obtain the following preliminary number of charged kaons per $B\bar{B}$ event: $2.4 \pm 0.5 \pm 0.5$. This result should be compared with the prediction of a Monte Carlo based on the $b \to c\,W^-$ decay chain, 1.3 ± 0.2, and of that based on the $b \to u\,W^-$ decay, 0.36 ± 0.06. The latter seems to be excluded, while the data are marginally compatible with the former. Notice that the number of charged kaons per continuum event, $0.36 \pm 0.06 \pm 0.06$, agrees well with the corresponding Monte Carlo prediction, 0.48 ± 0.08.

At this stage we can conclude that the CLEO preliminary value for the $K^{\pm}$ yield from the $B\bar{B}$ events is higher than, but in rough agreement with, the one predicted by the theoretically preferred decay chain $b \to c\,W^-$.

There are still two other fundamental parameters of the B mesons on which we have some information: their mass and lifetime.

Accepting that the $\Upsilon(3S)$ is below $B\bar{B}$ production threshold and the $\Upsilon(4S)$ is above it, we can immediately conclude that $m(3S) < 2 \times m(B) < m(4S) - \frac{\Gamma}{2}$, i.e., $5.162 < m(B) < 5.270$ GeV. This is a very conservative interval. Indeed the measured total width of the $\Upsilon(4S)$ implies[10] that the threshold is either about 40 ± 10 MeV (i.e., $m(B) = 5.25 \pm 0.025$ GeV) below the $\Upsilon(4S)$ peak, the second value being unlikely

because of the failure of CUSB of observing the $B^* \to B\gamma$ decay at the $\Upsilon(4S)$.

Concerning the B lifetime, CLEO has measured the r.m.s. value of the distance of minimum approach to the beam axis of the reconstructed tracks. A value $\sigma = 1.4$ mm was found in continuum events after removing tracks with high multiple scattering ($p_e < 0.6$ GeV/c), K^0_S decay tracks and electron pairs. If B mesons (charged or neutral) move appreciably away from the production point before decaying, one should notice an increase of σ for the $\Upsilon(4S)$ resonating events of the order of $c\tau_B \beta_B = c\,\tau_B\sqrt{(W-2M_B)/M_B}$. Actually the observed value of $\sigma = 1.3$ mm in the resonant region. It is estimated that a $c\,\tau_B\,\beta_B = 2$ mm should produce a measurable broadening of σ. To translate this upper limit into one for τ_B we need to know $\Delta = W - 2M_B$. Assuming $\Delta > 20$ MeV[10] we arrive at the rough limit:

$$\tau_B \lesssim 1 \times 10^{-10}\ \text{s}.$$

This should be compared with the limit of 2×10^{-9} s (90% c.l.) for charged B found by JADE[17].

In summary we have determined the following preliminary values for the properties of the B meson.

Mass:	$5.16 < m(B) < 5.27$ GeV
Lifetime:	$\tau_B \lesssim 1 \times 10^{-10}$s
Leptonic branching ratio:	$Br(B \to e\,\nu\,X) + Br(B \to \mu\,\nu\,X) = (23\pm5\pm7)\%$
Decay chain:	$b \to c\,W^-$ favored over $b \to u\,W^-$.

This work was supported in part by grants of the U.S. National Science Foundation and Department of Energy.

REFERENCES

1. E. Eichten et al., Phys. Rev. D17, 3090 (1978) and D21, 203 (1980); C. Quigg and J. L. Rosner, Phys. Rep. 56C, 167 (1979); G. Bhanot and S. Rudaz, Phys. Lett. 78B, 119 (1978); J. L. Richardson, Phys. Lett. 82B, 272 (1979); see also K. Gottfried in Int. Symp. on H.E. e^+e^- Interactions, Vanderbilt Univ. (May 1980) (Cornell preprint CLNS 80/465).
2. S. W. Herb et al., Phys. Rev. Lett. 39, 252 (1977); W. R. Innes et al., Phys. Rev. Lett. 39, 1240 1640 (E) (1977).
3. J. K. Bienlein et al., Phys. Lett. 78B, 360 (1978); C. Berger et al., Zeit. f. Phys., C1, 343 (1979); C. W. Darden et al., Phys. Lett. 80B, 419 (1979).
4. K. Ueno et al., Phys. Rev. Lett. 42, 486 (1979).
5. D. Andrews et al., Phys. Rev. Lett. 44, 1108 (1980).
6. T. Böhringer et al., Phys. Rev. Lett. 44, 1111 (1980).
7. R. P. Van Royen, V. F. Weisskopf, Nuovo Cim. A50, 617 (1967); R. Barbieri et al., Phys. Lett. 57B, 455 (1975).
8. In using the spectroscopic notation nS, since I shall be concerned here only with triplet states, I shall omit the corresponding superscript.
9. H. Schröder, reported at VI Intern. Conf. on Exp. Meson Spectroscopy, Brookhaven, April 1980.
10. E. Eichten, Harvard U. Rep. NO. HUTP-80/A027 (1980) to be published.
11. D. Andrews et al., Phys. Rev. Lett. 45, 219 (1980).
12. G. Finocchiarro et al., Phys. Rev. Lett. 45, 222 (1980).
13. G.C. Fox and S. Wolfram, Phys. Rev. Lett. 41, 1581 (1978) and Nucl. Phys. B149, 413 (1979).
14. E. Eichten, K. Gottfried, Phys. Lett. 66B, 286 (1977); J. L. Rosner, in "Particles and Fields - 1979" (APS/DPF Montreal) p. 325 (1980).
15. D. Hitlin, these proceedings; M. S. Chanowitz, Intern. Symp. on H.E. e^+e^- Interactions, Vanderbilt Univ., May 1980, (LBL-10924); J. Ellis, M.K. Gaillard, D. Nanopoulos, Nucl. Phys. B100,313(1975); N. Cabibbo,L.Maiani, Phys. Lett. 73B, 418 (1979) and 79B,109(1978); M. Suzuki, Nuclear Phys. B145, 420 (1978).
16. See also, e.g., A. Ali, Zeit. für Phys. C1, 25 (1979).
17. JADE collaboration, reported at the Inter. Symp.on H.E. e^+e^- Interactions, Vanderbilt Univ., May 1980.

Highlights from PETRA Experiments*

Günter Wolf
DESY, Hamburg

* Talk presented at the 1980 SLAC Summer Institute on Particle Physics

1. Introduction

The experiments at the DESY e^+e^- storage ring PETRA presently are focussed on four major subjects,

- tests of quantum electrodynamics (QED) and search for weak neutral current effects;
- search for new particles such as heavy leptons and new heavy quark states;
- analysis of gluon bremsstrahlung in the hadron annihilation channel;
- two photon interactions.

Results on these topics have been presented at the 1980 Wisconsin conference[1-12].
This lecture concentrates on some of the topics. For more complete information the reader is referred to the conference reports and the published material.

1.1 PETRA

Since February of this year PETRA was operated with 60 RF cavities which allow beams to accelerate up to 19 GeV. Measurements were carried out up to c.m. energies of W = 2·18.3 = 36.6 GeV. The average luminosity collected per experiment over a period of several days varied from 100 nb^{-1}/day at W = 30-34 GeV to 30 nb^{-1}/day at W = 36.6 GeV. This lead to 30 and 8 hadronic annihilation events/day,respectively,accepted by an experiment. Up to June 1980 a total of ~6000 nb^{-1} were collected per experiment at c.m. energies between 12 and 36.6 GeV. The bulk of the data were taken near 12, 30 and 36 GeV.

At the end of this year the interaction regions will be shortened from 15.4 m to 8.6 m by adding quadrupoles. This so-called minibeta scheme is expected to increase the luminosity by a factor of 2-3.

1.2 Experiment

Five large detectors have been constructed and have taken data, CELLO, JADE, MARK J, PLUTO, and TASSO. CELLO and PLUTO share the same interaction pit in a push-pull fashion. PLUTO was data taking during 1979. At the beginning of 1980 CELLO took over.
All detectors have almost complete solid angle coverage for charged particles and photons, and, except for MARK J, employ a solenoid magnet filled with cylindrical drift and proportional chambers for charged particle tracking. The MARK J detector is a calorimeter.

Some rather new detector developments are worth mentioning. The JADE experiment uses as central tracking device a drift chamber (jet chamber) operated at 4 atm which samples tracks 48 times[13]. The high pressure combined with the large number of samplings permits a measurement of the energy loss of particles and thereby identifies them.
Fig. 1 shows part of an event picture. The dE/dx resolution (FWHM) so far achieved is 14 % for isolated tracks and 22 % for tracks in a jet. This permits the separation of $\pi^{\pm}$,$K^{\pm}$ and p,$\bar{p}$ at low momenta (<0.5 GeV/c) and of $\pi^{\pm}$ at higher momenta.

The TASSO detector in addition to the central detector has two so-called hadron arms designed to identify particles up to the highest PETRA momenta. They are equipped with three types of Cerenkov counters using aerogel (n = 1.025), Freon (n = 1.0014) and CO_2 (n = 1.0007), respectively, as radiator material[14]. The aerogel counters cover an area of 12 m^2. A β = 1 particle yields 3.9 ± 0.2 photoelectrons averaged over all aerogel cells. The hadron arms were complete by the end of 1979. Results on particle separated cross section will be discussed below.

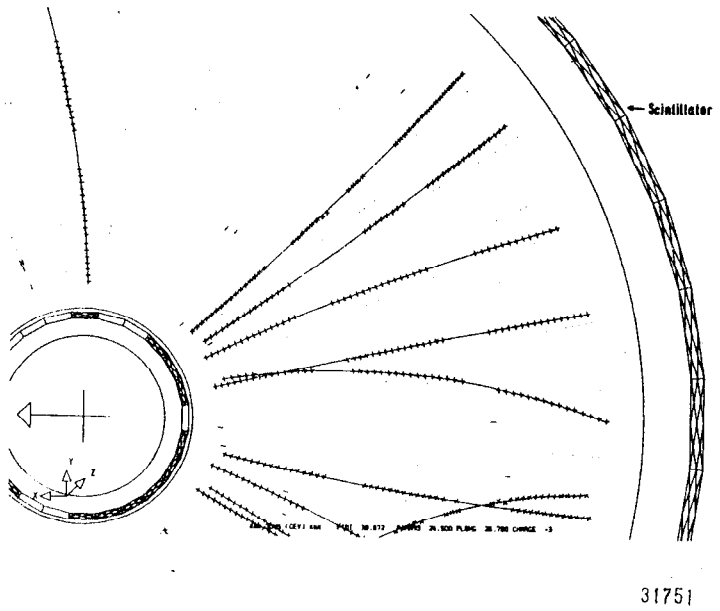

Fig.1 Cross sectional view of the JADE detector with the hit pattern of typical tracks.

Both CELLO and TASSO use liquid argon shower detectors to detect photons. In the CELLO counter the position and energy of photons is measured with lead strips. In the TASSO counter the lead is segmented into small towers subtending a small solid angle of 0.13 msterad each; the towers are directed towards the interaction point. This has the advantage that the energy of a photon is measured in one or at most a few towers; furthermore because of the small area over which the charge is collected the electronic noise level can be kept small. Fig. 2 shows an interesting but less than typical event where a hadronic event with an isolated photon of 9.3 GeV energy is detected. The photon energy is basically deposited in two front and the corresponding two back towers. The rms energy resolution (including the coil in front of the counter) as measured in the test beam is $\Delta E/E = 11\ \%/\sqrt{E}$ for $E > 0.3$ GeV. The analysis of Bhabha events ($e^+e^- \to e^+e^-$) yielded a resolution of $\Delta E/E = 4.9\ \%$ at $E = 15$ GeV. The rms noise level is less than 15 MeV.

List of References

1. W.Wagner, Two-Photon Results from PETRA, rapporteur talk at the XX International Conference on High Energy Physics, University of Wisconsin-Madison, 1980
2. E.Hilger, Rho Rho Production by Two-Photon Scattering, ibid.
3. D.Cords, Measurements of R and Search for New Thresholds at PETRA, ibid.
4. D.Pandoulas, Inclusive Hadron Production in e^+e^- Annihilation at PETRA, ibid.
5. S.L.Wu, Jet Studies by TASSO, ibid.
6. H.Oberlack, First Results from CELLO, ibid.
7. S.Yamada, Results from JADE on Jets, ibid.
8. V.Hepp, PLUTO Results on JETS and QCD, ibid.
9. H.Newman, Results from MARK J on Jets, ibid.
10. A.Böhm, Test of Electro-Weak Theories at PETRA, ibid, and Aachen preprint PITHA 80/9 (1980)
11. J.van Krogh, Quark Search in the JADE Experiment at PETRA, ibid.
12. B.H.Wiik, New e^+e^- Physics, plenary talk, ibid.

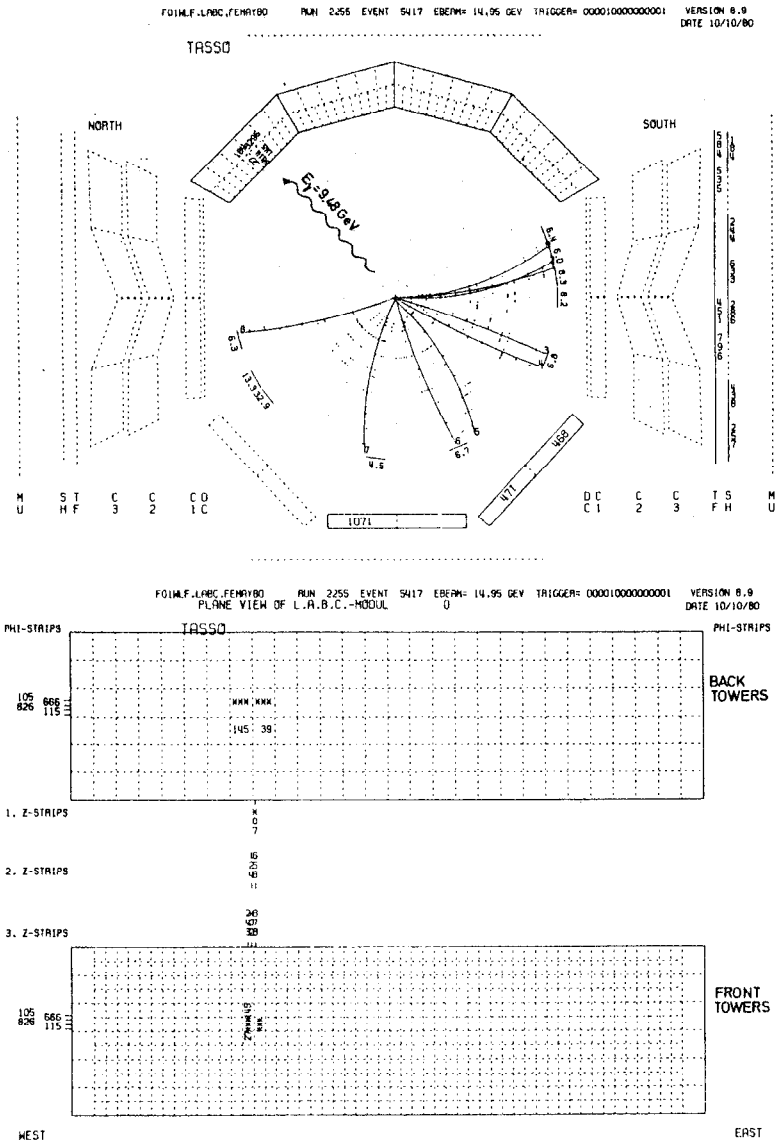

Fig.2 Cross sectional view of the TASSO detector. Indicated are the charged tracks as seen by the central tracking chambers and an isolate photon of 9.48 GeV detected in the barrel liquid argon counters. The shower energy measured in the towers is given in MeV. In the top view the energy is summed over rows of towers. In the bottom view the front and back towers are shown individually. The threshold for the towers was set at 20 MeV. Also indicated are the strips that had been hit.

13. H.Drumm et al., DESY Report 80/38 (1980)
14. H.Burckhardt et al., DESY Report

2. QED Tests and search for weak neutral current contributions

2.1 Electromagnetic processes

Purely electromagnetic processes can be calculated directly from QED. The PETRA data, taken at large values of the virtual photon mass squared Q^2 provide stringent tests of the theory. These tests were made for

Bhabha scattering : $e^+e^- \to e^+e^-$

two-photon annihilation: $e^+e^- \to \gamma\gamma$

μ-pair production : $e^+e^- \to \mu^+\mu^-$

τ-pair production : $e^+e^- \to \tau^+\tau^-$

Consider μ pair production which proceeds via timelike photon exchange.

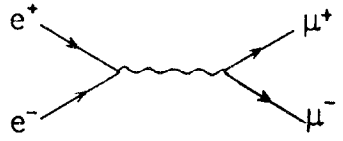

QED predicts for the differential cross section

$$\frac{d\sigma}{d\Omega} = \frac{\alpha^2}{4s}\,\beta_\mu\,\{(1+\cos^2\Theta) + (1-\beta_\mu^2)\sin^2\Theta\}$$

where $s = W^2$ and $\beta_\mu = P_\mu/E_\mu$. For $\beta_\mu = 1$

$$\frac{d\sigma}{d\Omega} = \frac{\alpha^2}{4s}\,(1+\cos^2\Theta)$$

and

$$\sigma_{\mu\mu} = \frac{4\pi\alpha^2}{3s} = \frac{86.8\ \text{nb}}{s} \qquad (s \text{ in GeV}^2)$$

Corrections of the vertices and the photon propagator can modify the QED cross section. These modifications can be parametrized by a cut-off parameter Λ,

$$\sigma = \sigma_{QED}\left(1 \pm \frac{Q^2}{Q^2 - \Lambda_\pm^2}\right)^2.$$

A fit of this form to the data yields Λ.

So far, no statistically significant deviation from QED was observed at PETRA[1]. Figs. 1 - 3 show comparisons between experiment and theory. Table 1 summarizes the 95 % confidence lower limits on the cut-off parameter Λ. The lower limits on Λ are found to be in the range between 50 and 200 GeV. Bearing in mind that the assumption was made that whatever modifies the photon propagator or the $\ell\ell\gamma$ vertex has the coupling strength e the results of Table 1 can be rephrased by saying that QED has been tested down to distances of $\approx 2\cdot 10^{-16}$ cm and/or that e,μ and τ are pointlike down to the same distances.

Table 1. QED cut-off parameters: 95 % confidence lower limits in GeV.

Experiment	$e^+e^- \to e^+e^-$		$\gamma\gamma$		$\mu^+\mu^-$		$\tau^+\tau^-$	
	Λ_+	Λ_-	Λ_+	Λ_-	Λ_+	Λ_-	Λ_+	Λ_-
JADE[2]	112	106	47	44	137	96	-	-
MARK J[3]	91	142	55	38	123	142	76	154
PLUTO[4]	80	234	46	-	116	101	74	65
TASSO[5]	150	136	34	42	80	118	115	76

2.2 Weak current effects

The standard theory predicts neutral weak current contributions via Z^0 exchange to the lepton pair production channels, $e^+e^- \to \ell^+\ell^-$ (see diagram).

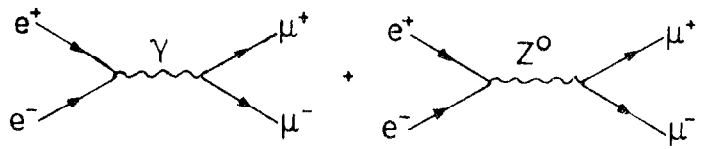

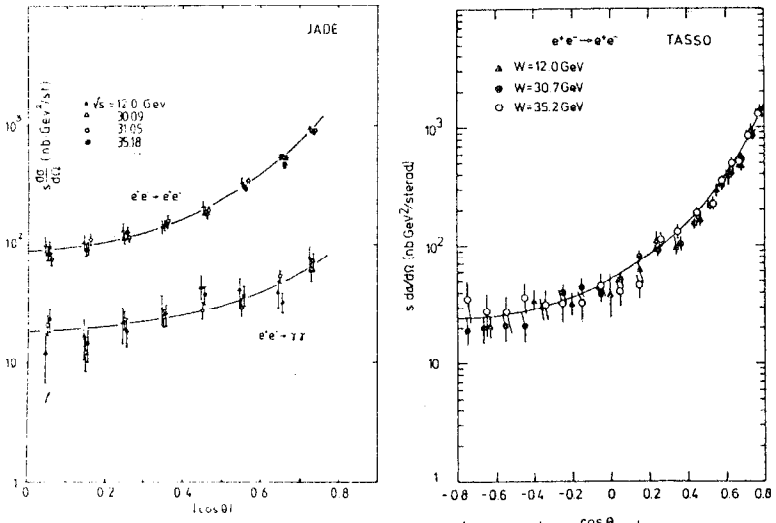

Fig.1 Differential cross sections for $e^+e^- \to e^+e^-$ and $e^+e^- \to \gamma\gamma$ as measured by JADE and TASSO.

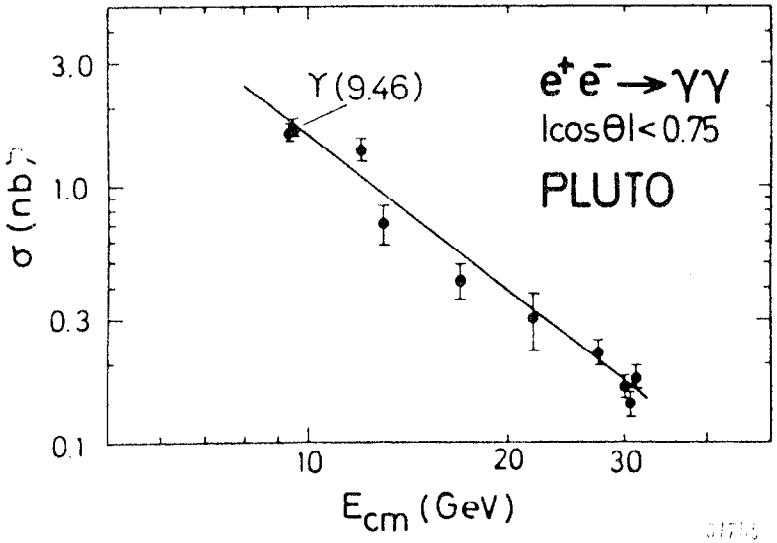

Fig.2 The cross section ee → γγ integrated over |cos| < 0.75. The solid line indicates the 1/s behaviour of the QED cross section.

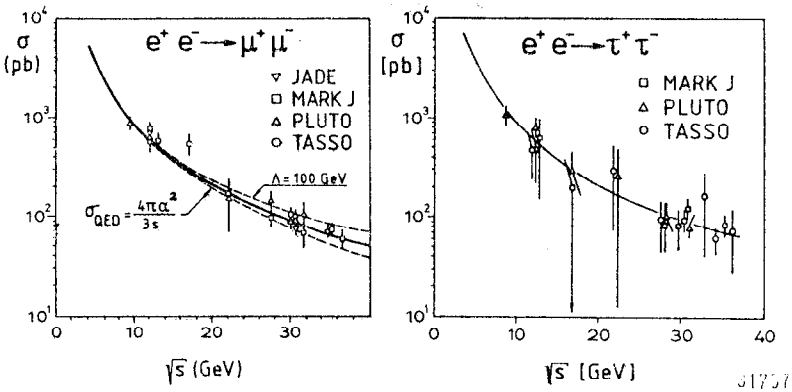

Fig.3 The cross sections for μ pair and τ pair production as a function of c.m. energy.

Even at PETRA energies these contributions are expected to be small. Consider μ pair production. The presence of Z^0 exchange supposedly will show up first via interference with the photon diagram. The standard theory predicts for the reduced vector and axial vector couplings at the $\ell^+\ell^-Z$ vertex

$$g_V = \frac{1}{2}\left(\frac{1}{4} - \sin^2\Theta_W\right) \quad \text{and} \quad g_A = -\frac{1}{2}$$

where Θ_W is the Weinberg angle. The current experimental value for Θ_W, $\sin^2\Theta_W = 0.23 \pm 0.02$ implies that g_V is small. The Z^0 contribution modifies the μ pair cross section and causes a forward-backward asymmetry:[6]

$$\sigma(\gamma + Z) - \sigma(\gamma) \sim g_V^2 \cdot s$$

$$A = \frac{F - B}{F + B} \sim -g_A^2 \cdot s$$

The predicted change in cross section at W = 30 GeV is ≈0.5 % and is much too small to be detected with present statistics. Integrated over the cosΘ acceptance of the muon detection systems the PETRA experiments should observe at W = 30 GeV an asymmetry A of -6 %.
Fig. 4 shows the angular distributions measured by the four experiments. They agree well with the QED prediction ~1 + $\cos^2\Theta$. The observed asymmetries (see Table 2) are compatible with zero but also with the prediction of the standard weak theory. The data shown in Fig. 4 represent roughly a hundred μ pair events per experiment. A sensitive test of the theory will require an increase in statistics by a factor of ~50.

2.3 Limits on weak current parameters.

In the standard theory Θ_W is the only free parameter. The measured cross sections on $e^+e^- \to \ell^+\ell^-$ put limits on $\sin^2\Theta_W$. The 95 % confidence upper limits on $\sin^2\Theta_W$ are

Table 2: Forward backward asymmetry $A_{\mu\mu}$ in μ pair production, measured and predicted by SU(2) x U(1) for the experimental acceptance (rough $|\cos\Theta| < 0.7$).

	JADE	MARK J	PLUTO	TASSO
$A_{\mu\mu}$ in %				
measured	-8 ± 9	0 ± 9	7 ± 10	-1 ± 12
predicted	-6	-6	-5.8	-6

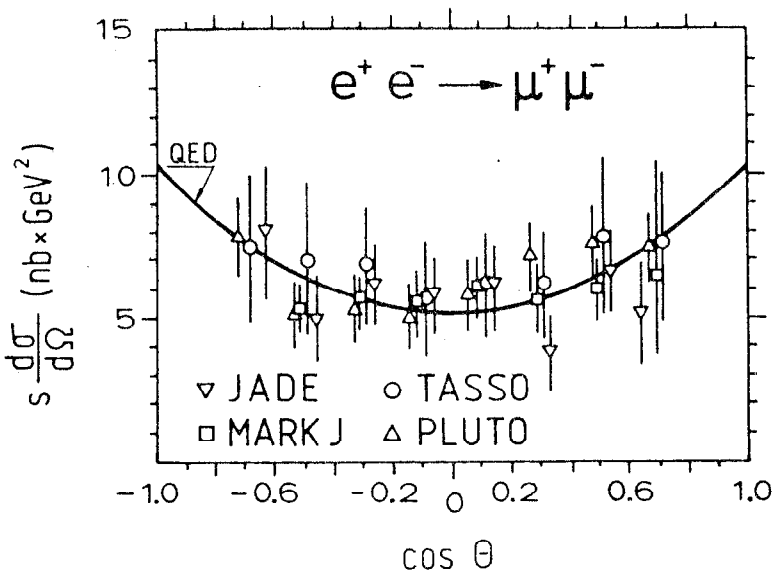

Fig.4 Angular distribution of μ-pair production measured by PETRA experiments at energies between 27 and 35 GeV.

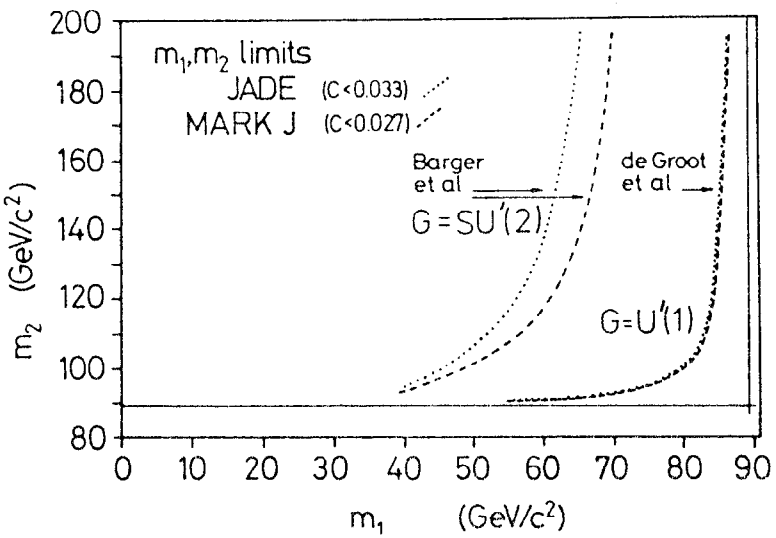

Fig.5 Limits on m_1 and m_2, deduced from a limit on C, for models with two Z^0-bosons.

JADE : $\sin^2\theta_W < 0.55$
MARK J: 0.42
PLUTO : 0.57
TASSO : 0.52.

The data provide tight bounds for models with two Z^0 bosons. De Groot et al.[7] assume two Z^0 but one $W^\pm$ boson, Barger et al.[8] assume two Z^0 and two W bosons. The range of mass values for Z_1^0 and Z_2^0 allowed by the data is shown in Fig. 5.

List of References

1. A.Böhm, rapporteur talk at the 1980 Wisconsin conference and Aachen preprint PITHA 80/9 (1980)
2. JADE Collaboration, W.Bartel et al., Phys.Lett. 92B (1980) 206 and data presented in Ref. 1.
3. MARK J Collaboration, D.P.Barber et al., Phys.Rev.Lett. 43 (1979) 1915 and Physics Reports 63 (1980) 337
4. PLUTO Collaboration, Ch.Berger et al., Z.Physik C4 (1980) 269; Phys.Lett. 94B (1980) 87 and data presented in Ref. 1.
5. TASSO Collaboration, R.Brandelik et al., Phys.Lett. 92B (1980) 199; 94B (1980) 259 and data presented in Ref. 1.
6. Explicit formulae can be found, e.g., in the 1975 PEP Summer study.
7. E.H. de Groot, G.J.Gounaris and D.Schildknecht, Phys.Lett. 85B (1979) 399; 90B (1980) 427 and Z.Physik C5 (1980) 127.
8. V.Barger, W.Y.Keung and E.Ma, U. of Wisconsin-Hawaii Reports, UW-COO-881-126 (1980), 133 (1980) and 138 (1980)

3. Search for new particles

3.1 The top quark

The presumed symmetry between leptons and quarks suggests the existence of a sixth quark ,t. The charge of the t is predicted to be +2/3 if one groups the quarks in weak isospin doublets, viz.

$$\begin{pmatrix} u \\ d \end{pmatrix} \begin{pmatrix} c \\ s \end{pmatrix} \begin{pmatrix} t \\ b \end{pmatrix}$$

The theoretical predictions for the t mass populate mass values between 10 and 40 GeV.

The presence of the t will manifest itself in e^+e^- annihilation in a variety of ways, e.g., as narrow $t\bar{t}$ bound states in the total hadron cross section, $\sigma(e^+e^- \to \text{hadrons})$, as a step in $R = \sigma(e^+e^- \to \text{hadrons})/\sigma_{\mu\mu}$ and as an abundance of spherical events.

The nonrelativistic model for heavy quarkonium[1-3] predicts 6 to 7 bound states $1^3S_1,\ldots,6^3S_1$ if the mass of the t is around 17 GeV (see Fig. 1). The peak height of the hadronic cross section near one of these states is given by

$$\sigma(e^+e^- \to V_t) = \frac{3\pi}{s} \frac{\Gamma_{ee}\,\Gamma_h}{(M_o - W)^2 + \Gamma^2/4}$$

This is reduced by the energy spread of the beams, ΔE, to

$$\sigma_{peak} \approx \frac{3\pi}{s} \frac{\Gamma_{ee}\,B_h}{\Delta W} \qquad B_h = \Gamma_h/\Gamma$$

where $\Delta W = 2\cdot\Delta E$. For PETRA $\Delta E/E = 6.5\cdot10^{-5}$ E, E in GeV. For a mass of 34 GeV (E = 17 GeV) the energy spread is 19 MeV. The leptonic width Γ_{ee} for the first state 1^3S_1 is predicted to be close to that of the J/ψ, Γ_{ee} = 5 keV. The hadronic branching ratio is expected to be around 0.7. Including radiative effects this yields

R_{peak} (34 GeV) ≈ 8.

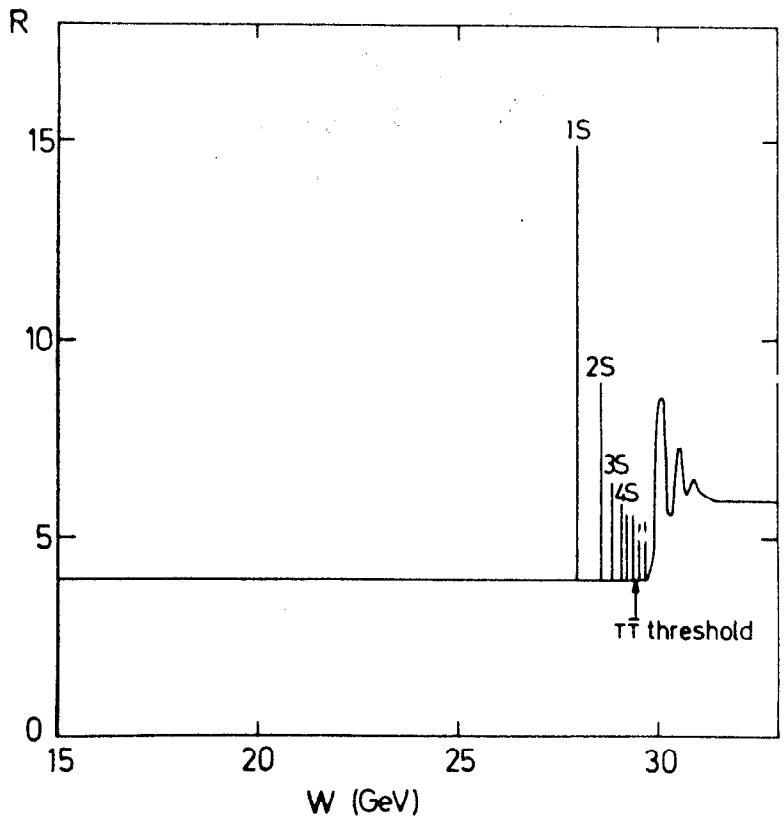

31747

Fig.1 The energy dependence of R expected near the $t\bar{t}$ threshold.

Energy scans in steps of 10 MeV have been conducted between 29.9 and 31.46 GeV and between 35.0 and 35.64 GeV. Fig. 2 shows the results from these scans. No evidence was found for any narrow signal of the expected height. The 95 % confidence upper limits on $B_h \Gamma_{ee}$ from the combined data are

W = 29.90 - 31.46 GeV[4-8] $\quad \Gamma_{ee} B_h < 0.7$ keV

35.0 - 35.64 GeV[9] $\quad \Gamma_{ee} B_h < 0.4$ keV

These upper limits are well below the 3.5 keV expected for the first $t\bar{t}$ state; they also disfavour the presence of a charge 1/3 quark, $Q_{1/3}\,Q_{1/3}$, bound state for which $\Gamma_{ee} B_h \approx 0.9$ keV.

The contribution of the t quark would increase R by at least $R_t = 3\cdot(2/3)^2 = 4/3$ to $R > 5$ if the c.m. energy is above the threshold for top meson production. The R data measured up to 36.6 GeV show no evidence for such a contribution (see next section): Within errors R is close to 4 between 17 and 36.6 GeV and compatible with the presence of the five quarks u,d,s,c,b alone.

The shape of hadronic events is very sensitive to contributions from the $t\bar{t}$ continuum. The $t\bar{t}$ events are expected to have a high particle multiplicity and a phase space like configuration. According to the Kobayashi-Maskawa generalized Cabibbo matrix[10] the favoured decay sequence for t quarks is $t \to b \to c \to s$. As a consequence the $t\bar{t}$ decays may have 14 or more quarks in the final state, presumably leading to a large hadron multiplicity. At threshold the $t,\bar{t}$ quarks are at rest and will emit hadrons more or less isotropically. As the energy increases the $t,\bar{t}$ quarks receive a boost and the events start to become two-jet like. However, this happens only well above threshold. For example a t quark of 15 GeV mass reaches a velocity of $\beta = 0.7$ only at

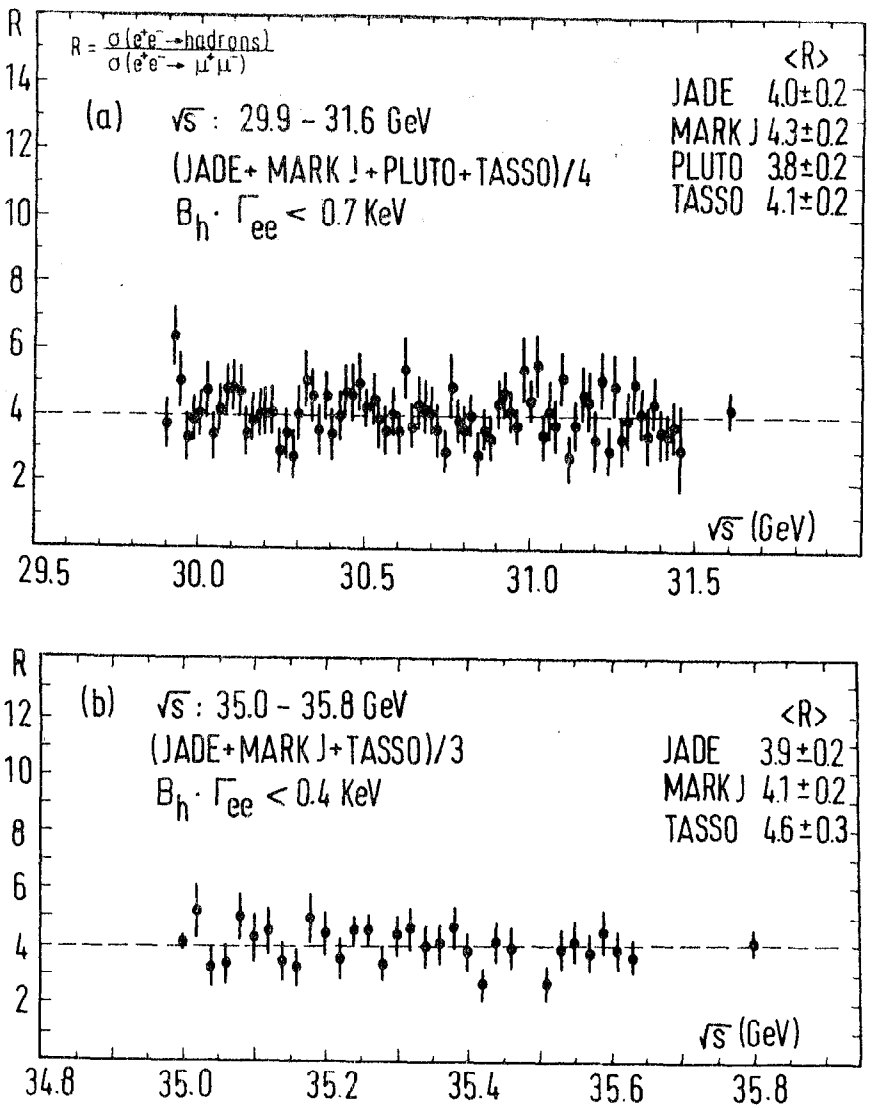

Fig.2 R values measured in small steps between 29.9-31.46 GeV und 35.0-35.6 GeV.

W = 42 GeV, i.e., 12 GeV above threshold. This implies that near threshold one cannot miss the $t\bar{t}$ continuum contribution.

As will be discussed in the next section the majority of the hadron events are two-jet events and tend to be collinear. A fraction of the events (5 - 10 %) have a three-jet structure and tend to be planar while phase space like events are noncollinear and nonplanar. The degree of collinearity is measured by sphericity S, that of planarity by aplanarity A (for the definition of S and A see next section).

Fig. 3 shows the event distribution in terms of S and A as measured by TASSO near 36 GeV. The sketch in Fig. 3a indicates the areas for collinear ($S \approx 0$), for noncollinear coplanar ($S \neq 0$, $A \approx 0$) and for spherical events (S and A large). Fig. 3b shows the event distribution expected from the $t\bar{t}$ contribution: the triangle plot is populated rather uniformly. Fig. 3c shows for comparison the distribution for events observed at W = 35.0 - 36.6 GeV. They concentrate in the collinear corner ($S \approx 0$) and only a few events are observed with S and A large. In Table 1 the observed and expected number of events for large S,A are compared for the TASSO and JADE experiments. The $t\bar{t}$ contribution is assumed to be $R_t = 4/3$. Several conclusions can be drawn from Table 1.

1. A $t\bar{t}$ continuum contribution with $R_t \geq 4/3$ can be excluded between W = 16 and 36.4 GeV by many s.d. The observed number of events is consistent with the contribution expected from u,d,.,b + gluon alone.
2. The presence of a new heavy quark with charge 1/3, $Q_{1/3}$, between W = 20 and 36 GeV appears unlikely if the $Q_{1/3}$ is assumed to decay in a manner similar to the t quark (i.e., into many hadrons).

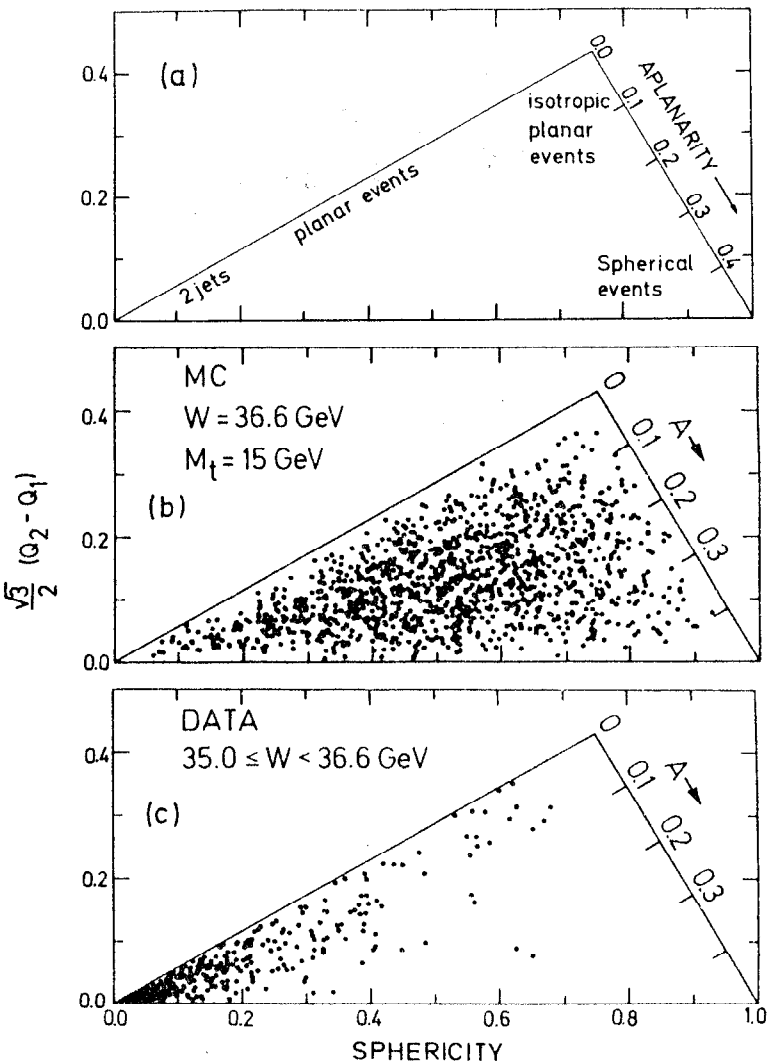

Fig.3 Distribution of events as a function of sphericity $S = 3/2\ (Q_1 + Q_2)$ and aplanarity $A = 3/2\ Q_1$.
(a) schematic diagram
(b) distribution expected from continuum production of $e^+e^- \to t\bar{t}$ at W = 36.6 GeV with the top threshold at $2m_t$ = 30 GeV.
(c) measured event distribution for $35 \leq W < 36.6$ GeV (from TASSO).

Table 1. Search for a heavy quark Q contribution assuming Q to decay as the top quark and $R_Q = 3e_Q^2$.

W(GeV)	experiment	Number of events observed total	observed after A cut		predicted u,..,b+gluon	predicted $Q\bar{Q}$, $e_Q = 2/3$	$Q\bar{Q}$, $e_Q = 1/3$
29.9 - 31.6	TASSO	816	A > 0.18	10	8.2 ± 1.0	m_Q = 8 GeV : 45 ± 3	m_Q = 10 GeV : 20 ± 2
30, 31.6	JADE	247	S > 0.55 A > 0.11	2		m_Q = 11 GeV : 26	
35.0 - 36.6	TASSO	469	A > 0.15	2	4.5 ± 0.5	m_Q = 15 GeV : 57 ± 2	m_Q = 15 GeV : 17.8 ± 0.5
35.0 - 36.6	JADE		S > 0.55 A > 0.11		3	m_Q = 15 GeV : 60	m_Q = 15 GeV : 15

Due to the cascade decay $t \to b \to c$ the $t\bar{t}$ contribution should yield also a fair fraction of multimuon events. The PLUTO group[11] investigated the prompt muon signal at W = 27.6 - 31.0 GeV and found consistency with c and b quark production alone. The same conclusion was reached by JADE[12]. The rate of prompt muons with P > 1.4 GeV/c at c.m. energies of 33.0 - 35.8 GeV was found to be 0.069 ± 0.024 per multihadron event to be compared with the expected rates from $c\bar{c} + b\bar{b}$: 0.084 ± 0.006 and $c\bar{c} + b\bar{b} + t\bar{t}$: 0.161 ± 0.009.

3.2 Search for free quarks

Using the dE/dx information in the central drift chamber the JADE group[13] has searched for free quarks produced in pairs, $e^+e^- \to q\bar{q}$, and produced together with ordinary hadrons, $e^+e^- \to q\bar{q}$ + hadrons at energies between 27 and 35 GeV. The ionization loss of a particle is proportional to the square of the charge. Hence for quarks of charge 2/3 dE/dx will be 4/9 of that of charge 1 particles--provided β is the same.

In the analysis the absorption of free quarks in the beam pipe was assumed to be negligible. Quark pair production was studied by analysing events with two collinear tracks. These events were divided into those where the tracks produced showers in the surrounding lead glass counters ("showering" tracks, mostly due to $e^+e^- \to e^+e^-$) and those where no showers were observed ("nonshowering" tracks, mostly due to $e^+e^- \to \mu^+\mu^-$). Fig. 4 shows for the two event types plots of the measured dE/dx for track 1 versus dE/dx for track 2. No events are found in the region where charge 2/3 quarks would contribute (see 2 s.d. circles in Fig. 4). The data place an upper limit of less than $R(q\bar{q}) < 0.01$ on the quark pair cross section (see Fig. 5).

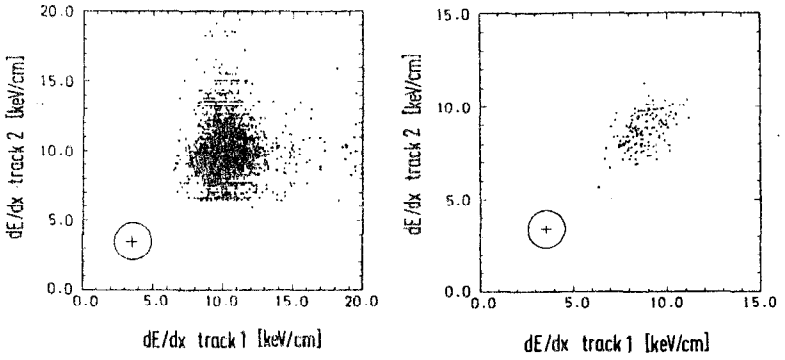

Fig.4 Energy loss of collinear two prong events. dE/dx of track 1 versus that of track 2 for a) showering and b) non-showering tracks. The cross indicates the expectation for Q = 2/3 particles and the circle the 2.5 standard deviation contour.

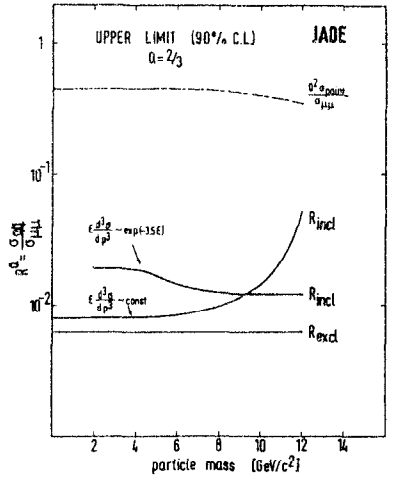

Fig.5 90 % confidence upper limits on $R^Q = \sigma_{q\bar{q}}/\sigma_{\mu\mu}$ for the exclusive and inclusive production of quarks with Q = 2/3 as a function of particle mass. The dashed line shows the curve expected for Q = 2/3, spin 1/2 pointlike particle.

The search for inclusive production of free quarks ($e^+e^- \to q\bar{q}$ hadrons) was also negative. The upper limit for the production cross section depends on the assumed momentum spectrum for the quark (see Fig. 5) and the quark mass. For quarks of mass less than 10 GeV $R(q\bar{q}\text{ hadrons}) < 0.02$.

Similar limits were put on the production of particles with charge 4/3 or 5/3, and on stable heavy particles of charge one (e.g., B meson).

List of References

1. C.Quigg and J.C.Rosner, Phys.Lett. 72B (1978) 462; G.Bhanot and S.Rudaz, Phys.Lett. 78B (1978) 119
2. H.Krasemann and S.Ono, Nucl.Phys. B154 (1979) 283
3. R.A.Bertelman and A.Martin, CERN Report TH 2772 (1979)
4. TASSO Collaboration, R.Brandelik et al., Phys.Lett. 88B (1979) 199
5. PLUTO Collaboration, Ch.Berger et al., Phys.Lett. 91B (1980) 148
6. JADE Collaboration, W.Bartel et al., Phys.Lett. 91B (1980) 152
7. D.P.Barber et al., MIT LNS Report 110 (1980)
8. P.Dittmann, rapporteur talk at the meeting of the Deutsche Physikalische Gesellschaft, Dortmund, March 1980
9. D.Cords, rapporteur talk at the 1980 Wisconsin Conference
10. M.Kobayashi and M.Maskawa, Progr.Theor.Phys. 49 (1973) 652
11. PLUTO Collaboration, Ch.Berger et al., Phys.Lett. 86B (1979) 413
12. JADE Collaboration, W.Bartel et al., DESY Report 80/86 (1980)
13. JADE Collaboration, W.Bartel et al., DESY Report 80/71 (1980)

4. Jet Physics

4.1 Introduction

Hadrons produced in e^+e^- annihilation are emitted into two back-to-back cones which become narrower as the c.m. energy increases. This two-jet structure was first observed in 1975 by the SLAC-LBL group[1] studying charged particles produced in e^+e^- collisions between 3.0 and 7.4 GeV at SPEAR. Subsequent experiments done in 1978 by the PLUTO group[2] at DORIS confirmed this behaviour and extended the measurements up to 10 GeV c.m. energy. In the latter experiments also the neutral component was analyzed and the jet axis of the neutral component was found to coincide with the axis determined with charged particles.

A marked deviation from two-jet production was observed at the position of the Υ by several DORIS experiments[3-5]. The analysis presented by the PLUTO group[6] strongly suggested that the direct decays of the Υ proceed via a three-gluon intermediate state leading to three hadronic jets in the final state[7]. Furthermore, the data preferred spin one for the gluons[8].

The commissioning of PETRA in 1978 opened the possibility to push the e^+e^- experiments to much higher energies. Studying nonresonant hadron production at energies around 30 GeV in 1979 the TASSO group[9] found a new process which leads to three-jet events. This observation was confirmed by the MARK J[10], PLUTO[11] and JADE[12] groups working also at PETRA. The properties of the three jet events matched well the warrant given by theorists for hard gluon bremsstrahlung[13].
A careful study of particle distributions between jet axes made by JADE suggests a difference between quark and gluon fragmentation. Two particle angular correlations measured by PLUTO indicate the importance of multiple and soft gluon emission for near back-to-back jets.
This section will review the experimental knowledge of jet formation in e^+e^- annihilation at high energies. Apart from the published material more information can be found in recent reviews[14,15].

4.2 Jet formation in the quark model

The quark model views e^+e^- annihilation into hadrons as a two step process (see Fig. 1); first a pair of quarks is produced (a) which then fragment into hadrons (b).

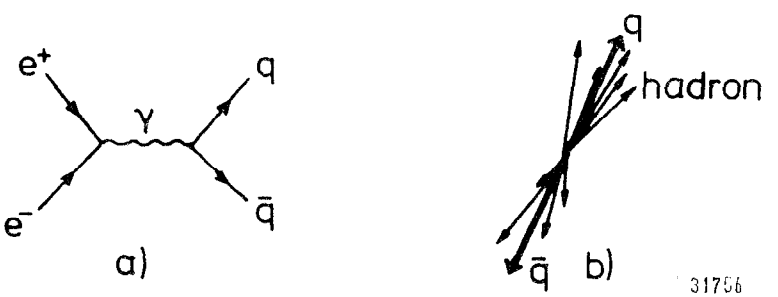

Fig. 1 e^+e^- annihilation in the quark model

The occurrence of jets is natural in this model. If the hadron momenta transverse to the quark direction of flight are limited and the number of produced hadrons grows only slowly with energy, the emitted hadrons will be more and more collimated around the primary quark direction as the total energy increases. Let W be the total c.m. energy, $\langle n \rangle$ be the average particle multiplicity, $\langle P_T \rangle$ and $\langle P_{II} \rangle \sim \langle P \rangle \sim W/\langle n \rangle$ the average transverse and longitudinal hadron momenta, then the mean half angle $\langle \delta \rangle$ of the jet cones can be estimated:

$$\langle \delta \rangle = \left\langle \frac{P_T}{P_{II}} \right\rangle \approx \frac{\langle P_T \rangle \cdot \langle n \rangle}{W} \sim \frac{1}{W}$$

The jet cones shrink roughly $\sim W^{-1}$. (Actually, in a realistic calculation of the quark model using the fragmentation functions of Field and Feynman[16] one finds $\langle \delta \rangle \sim W^{-1/2}$).

This simple picture of e^+e^- annihilation into hadrons is strongly supported by the data. Besides the jet structure of the events important tests in favour of the quark model are provided by the angular distribution of the jet axis and the size and energy dependence of the total cross section.

The angular distribution of the jet axis with respect to the beam direction was found to be of the form[1]

$$W(\cos\Theta) \sim 1 + \cos^2\Theta$$

which is what is expected if the primary partons have spin 1/2. For comparison, partons with spin zero would lead to $W \sim 1 - \cos^2\Theta$.

The total cross section is readily calculated. The cross section for producing a free $q\bar{q}$ pair is the same as for producing a $\mu^+\mu^-$ pair ($\sigma_{\mu\mu} = \frac{4\pi}{3}\frac{\alpha}{W^2}$) except that the quark charge e_q replaces the muon charge 1. Assuming that the produced $q\bar{q}$ pair turns into hadrons with unit probability the total cross section with respect to $\sigma_{\mu\mu}$ is found by summing the square of the quark charges,

$$R \equiv \sigma(e^+e^- \to \text{hadrons})/\sigma_{\mu\mu} = 3 \sum_{q=u,d,\ldots} e_q^2 \qquad (2)$$

where the factor 3 is the colour factor.

Fig. 2 summarizes the R measurements. The outstanding features of R are the spikes due to the excitation of vector states ($\rho,\omega,\ldots$) and the fact that in between the families of vector states ($\rho,\ldots$, $J/\psi\ldots$, $\Upsilon\ldots$) R is almost constant. The quark model, prediction (2), is in striking agreement (to within 30 %) with the data. Up to 3 GeV only u,d and s contribute and therefore R = 2. Above charm threshold (near 4 GeV) R should rise to a level of 3.3. Beyond the Υ family in addition the b quark contribution has to be included raising R to

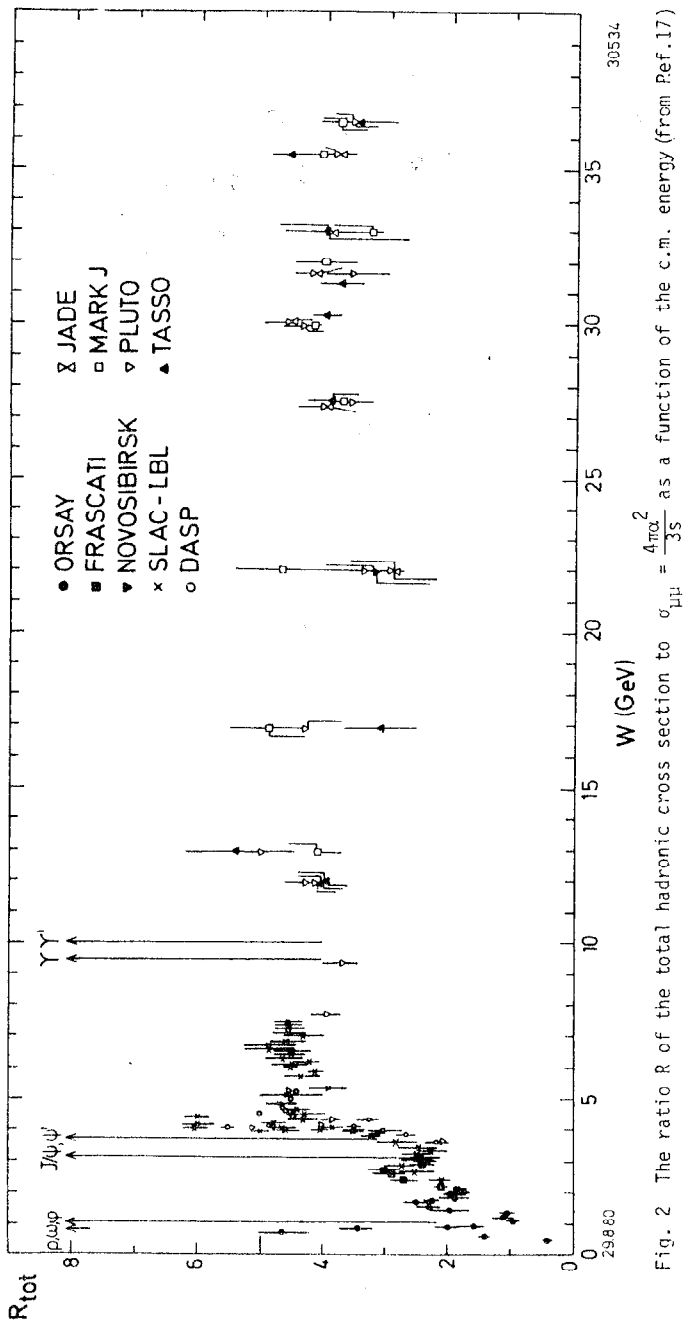

Fig. 2 The ratio R of the total hadronic cross section to $\sigma_{\mu\mu} = \frac{4\pi\alpha^2}{3s}$ as a function of the c.m. energy (from Ref. 17)

3.7 in accord with the data.

4.3 Jet measures

The jet axis and the amount of collimation is commonly determined in terms of sphericity[19], S, and thrust[20], T;

$$S = 3/2 \quad (\sum p_{Ti}^2)/(\sum p_i^2); \qquad T = \sum |p_{\parallel i}|/\sum p_i$$

$$0 \leq S \leq 1 \qquad 0.5 \leq T \leq 1$$

where p_{Ti}, $p_{\parallel i}$ are the transverse and longitudinal momenta relative to the jet axis which is chosen such that $\sum p_{Ti}^2$ ($\sum |p_{\parallel i}|$) is minimal (maximal) for sphericity (thrust). Sphericity measures approximately the square of the jet cone half opening angle

$$S \approx 3/2 \langle \delta^2 \rangle$$

and likewise $T \approx \sqrt{1 - \langle \delta \rangle^2}$.

Extreme jettiness ($\delta = 0$) leads to $S = 0$ and $T = 1$ while for spherical events $S \to 1$ and $T \to 0.5$.

4.4 Two-jet production

Fig. 3 shows the energy dependence of the average sphericity as measured at DORIS and PETRA. At low energies, $W \lesssim 4$ GeV, the observed $\langle S \rangle$ values are close to those predicted by phase space, $\langle S \rangle \approx 0.4$. Above 5 GeV $\langle S \rangle$ decreases rapidly with increasing W, i.e., the particles become more and more collimated in clear distinction to a phase space behaviour. A power law, $\langle S \rangle = 0.8\ W^{-1/2}$ describes the data well. The jet cone half opening angle as inferred from $\langle S \rangle$ shrinks from $\sim 31^\circ$ at W = 4 GeV to 17° near 36 GeV. Fig. 4 shows the sphericity distribution measured near 30 GeV. The strong preference for small S values is clearly seen. 80 % of the events have $S < 0.25$ or $\langle \delta \rangle \approx 23^\circ$. An analysis of the data in terms of thrust leads to the same conclusions (see Fig. 5).

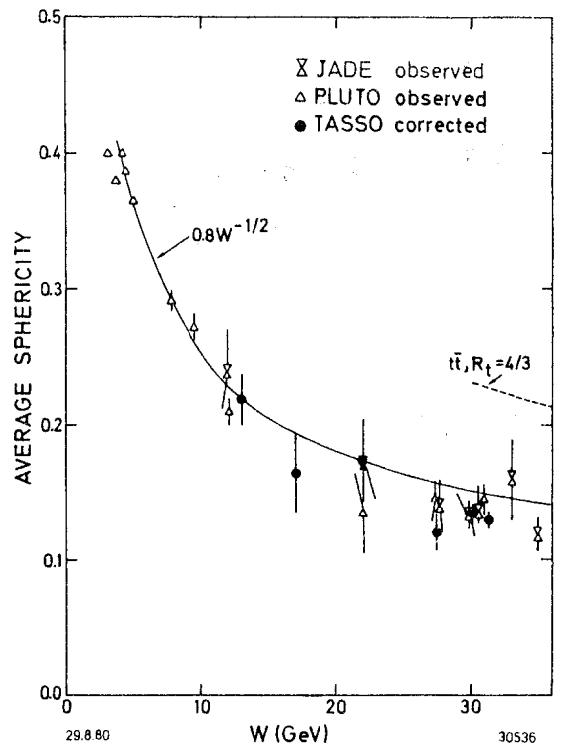

Fig.3 The average sphericity as a function of the c.m. energy.

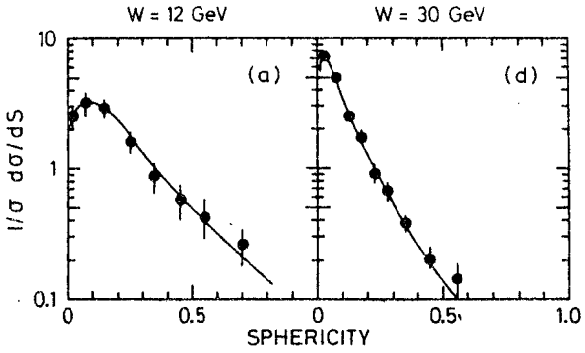

Fig.4 Sphericity distributions measured at W = 12 and 30 GeV (Ref. 37)

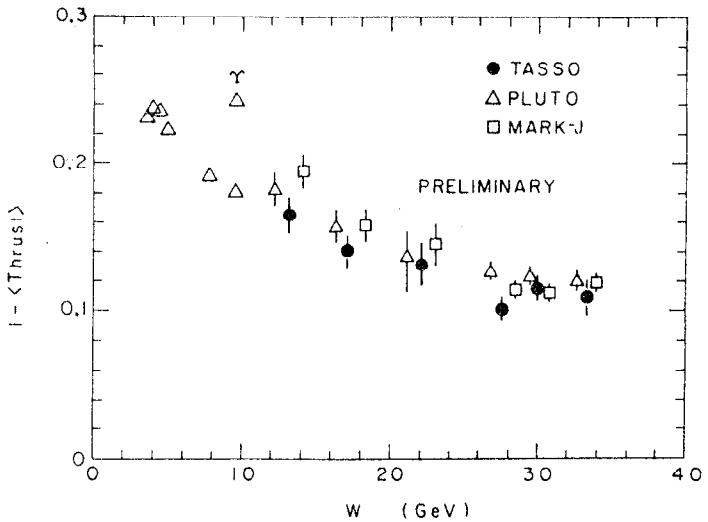

Fig.5 The average of 1-thrust as a function of the c.m. energy.

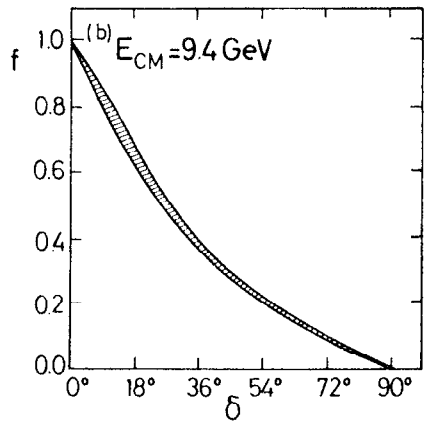

Fig.6 The average fraction of visible energy (f) outside a cone of half angle δ at 9.4 GeV (Ref. 21).

Despite the narrowness of the jet cone the spread of the particles around the jet axis is appreciable, in particular of the low energetic ones. This is illustrated by Fig. 6 which shows the fraction of energy f for charged plus neutrals observed outside a jet cone with half opening angle δ. The measurement was done by PLUTO at W = 9.4 GeV, where $\langle\delta\rangle \approx 24^0$. The energy flow around the jet axis has a long tail reaching out to the limit ($\delta = 90^0$).

4.5 Transverse momentum distribution and jet broadening

The transverse momentum distribution of hadrons produced in hadron scattering suggested a Gaussian p_T distribution for quark fragmentation into hadrons:

$$\frac{d\sigma}{dp_T^2} \sim e^{-\frac{p_T^2}{2\sigma_q^2}} \qquad (4)$$

The parameter σ_q e.g. for pions was found to be of the order of 250 MeV/c almost independent of the reaction energy. Deviations from a simple Gaussian behaviour-- a flattening of the p_T distribution-- were observed in pp collisions at high p_T values[23]. The e^+e^- annihilation data at energies up to 7.4 GeV were found to be consistent with an energy independent σ_q around 300 MeV/c [1]. However, when comparing data taken at 13, 17 GeV with those near 30 GeV the TASSO group found a large broadening of the p_T distribution with increasing energy[9]. The broadening was correlated with the appearance of planar events, some of which had a definite three jet structure. The properties of these events as well as their production rate agreed well with the predictions for gluon bremsstrahlung by Ellis, Gaillard and Ross[13].

We now discuss the experimental evidence for these jet events. Fig. 7 shows the normalized transverse momentum distribution $1/\sigma_{tot}\ d\sigma/dp_T^2$ evaluated with respect to the sphericity axis for 12, 13 - 17 and 27 - 32 and 35 - 36 GeV as measured by TASSO. The measurements for the three energies are in reasonable agreement for $p_T^2 < 0.2\ (GeV/c)^2$, but the high energy data are well above the low energy data for larger values of p_T^2 in contradiction to the naive parton model which assumes the quark to fragment with an energy independent transverse momentum distribution. The low energy data were fitted for $p_T^2 < 1\ (GeV/c)^2$ with the $q\bar{q}$ model[16] including c and b quarks . Increasing the parameter σ_q (eq. (4)) from its original value of 0.25 GeV/c to 0.30 GeV/c gave a good fit to the 12 and 13 - 17 GeV data. To fit the higher energy data with the same model σ_q had to be increased to 0.45 GeV/c. Fig. 8 shows the average p_T^2 as a function of W: it is seen to rise rapidly for $W \gtrsim 12$ GeV.

The widening of the transverse momentum distribution can have different origins:

1. the production of a new quark flavor. The data do not show any evidence for the production of a new heavy quark and we can dismiss that as a possible explanation.
2. the p_T distribution for quark fragmentation into hadrons is energy dependent: the average p_T grows as the energy increases. In this case the hadrons are still produced in two jets but the diameter of the "cigar" in terms of p_T^2 increases with energy (see sketch). Note also that both jets will grow in the same manner.

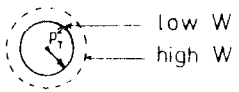

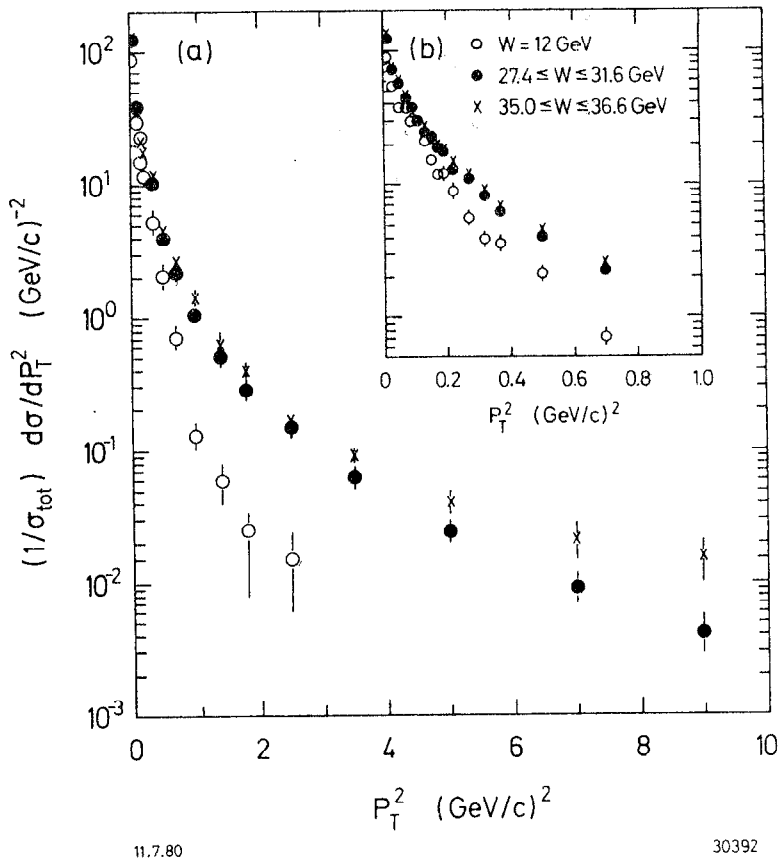

Fig.7 The p_T^2 distribution as measured by TASSO at c.m. energies of 12, 27.4 - 31.6 and 35.0 - 36.6 GeV.

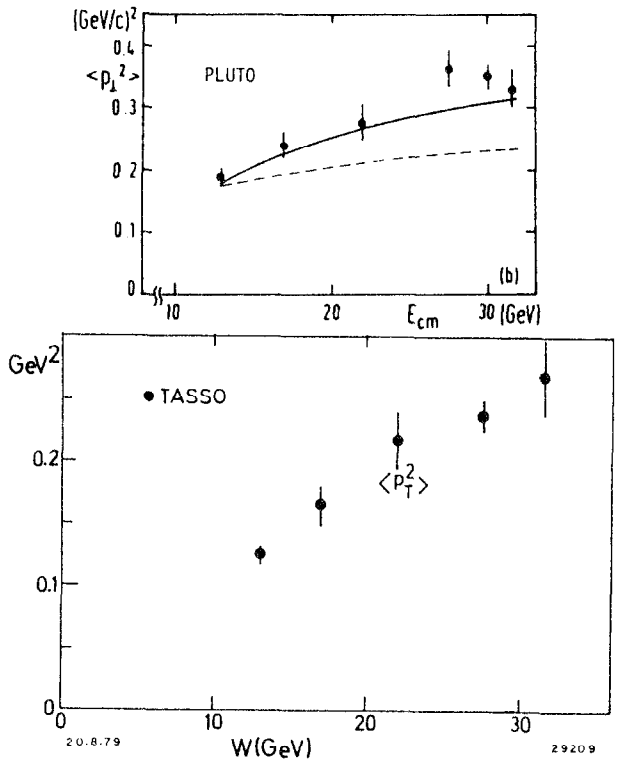

Fig.8 The average of the transverse momentum squared as a function of the c.m. energy measured by PLUTO and TASSO.

3. gluon bremsstrahlung from the outgoing quarks[13].

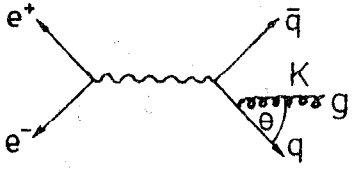

Schematic diagram for gluon emission

The radiated gluon carrying colour will turn into a jet of hadrons. The energy and angular distribution of the gluon is similar to that of a photon emitted by an electron.

Denoting by x_1, x_2 the fractional energies of the quarks, $x_i = 2E_i/W$, the cross section for gluon emission is given by

$$\frac{d\sigma(q\bar{q}g)}{dx_1\,dx_2} = \frac{2\alpha_s}{3\pi}\,\sigma_0\,\frac{x_1^2 + x_2^2}{(1-x_1)(1-x_2)} \qquad (5)$$

where σ_0 is the parton model cross section for quark pair production, $\sigma_0 = 3\sigma_{\mu\mu}\sum e_q^2$, and α_s is the strong (running) coupling constant,

$$\alpha_s(s) = \frac{12\pi}{(33-2N_f)\ln s/\Lambda^2} \qquad (6)$$

N_f = number of flavours (= 5 for u,d,...b)

$s = W^2$

Λ a constant

A crude approximation of eq.(5) yields for small Θ, K

$$\frac{d\sigma(q\bar{q}g)}{dK\,d\Theta} \sim \frac{\alpha_s}{K\sin\Theta}\,\sigma_0 \qquad (7)$$

where K is the energy and Θ the production angle of the gluon measured with respect to the quark. The average transverse momentum of the (hard) gluon jet is

$$\langle K_T\rangle \sim \frac{\alpha_s\cdot\sigma_0\iint\frac{K\sin\Theta}{K\sin\Theta}\,dK d\Theta}{\sigma_0\,(1+\frac{\alpha_s}{\pi})}$$

$\sim\alpha_s \cdot W$ (up to log terms)

(For the total cross section the first order QCD result, $\sigma_{tot} = \sigma_0 (1 + \frac{\alpha_s}{\pi})$ was inserted). The remarkable result is that contrary to many other predictions of QCD which lead to logarithmic deviations from the pure quark model and are therefore difficult to test experimentally, the transverse momentum is predicted to rise linearly with energy. If K_T is large compared to the typical transverse momentum of 0.3 GeV/c, then the event will have a three jet topology.

Detection of the gluon jet requires high c.m. energies for two reasons. Firstly, at low energies gluon and quark jets are broad and will overlap. Secondly, at low energies where $\alpha_s(s)$ is of order one, single as well as multigluon emission is important, and besides, perturbative QCD may not be applicable. The additional gluon jets aggravate the overlap problem at low energies. However, as the energy goes up the jets become narrower and $\alpha_s(s)$ becomes smaller; e.g., at the highest PETRA energies, $s \approx 1000\ GeV^2$, $\alpha_s(s)$ is around 0.2 such that the emission of several hard gluons can be neglected.

4.6 Planar events

The event shapes were studied by TASSO, PLUTO and JADE using the momentum tensor ellipsoid and by MARK J determining the oblateness.

Momentum tensor ellipsoid.

For each event one constructs the second rank tensor from the hadron momenta[19]

$$M_{\alpha\beta} = \sum_{j=i}^{N} P_{j\alpha} P_{j\beta} \qquad (\alpha,\beta = x, y, z) \tag{8}$$

summing over all N observed charged particles. Let $\hat{n}_1$, $\hat{n}_2$ and $\hat{n}_3$ be the unit eigenvectors of this tensor associated with the eigenvalues Λ_1, Λ_2 and Λ_3 which are ordered such that $\Lambda_1 < \Lambda_2 < \Lambda_3$. Note that

$$\Lambda_i = \sum (p_j \hat{n}_i)^2 \tag{9}$$

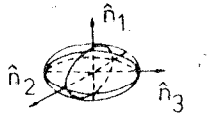

The principal axis is the $\hat{n}_3$ direction which is identical to the jet axis determined by sphericity; the event plane is the $\hat{n}_2$, $\hat{n}_3$ plane and $\hat{n}_1$ defines the direction in which the sum of the square of the momentum components is minimal.

Define the normalized eigenvalues

$$Q_i = \frac{\Lambda_i}{\Sigma p_j^2} = \frac{\Sigma(\vec{p}_j \cdot \hat{n}_i)^2}{\Sigma p_j^2} \tag{10}$$

which satisfy the relation

$$Q_1 + Q_2 + Q_3 = 1$$

Generally speaking the Q_i measure the

flatness (Q_1)

width (Q_2)

length (Q_3)

of an event.

The events will be characterized by the two variables aplanarity A and sphericity S

$$A = \frac{3}{2} Q_1$$

$$S = \frac{3}{2} (Q_1 + Q_2) = \frac{3}{2} (1 - Q_3) \tag{11}$$

Since $0 < Q_1 < Q_2 < Q_3 < 1$ all events lie inside a triangle.

Planar events

In Figs. 9-11 the distributions of

$$\langle p_{Tout}^2 \rangle = \frac{1}{N} \sum_{j=1}^{N} (\vec{p}_j \cdot \hat{n}_1)^2 \qquad (= Q_1 \Sigma p_j^2) \tag{12}$$

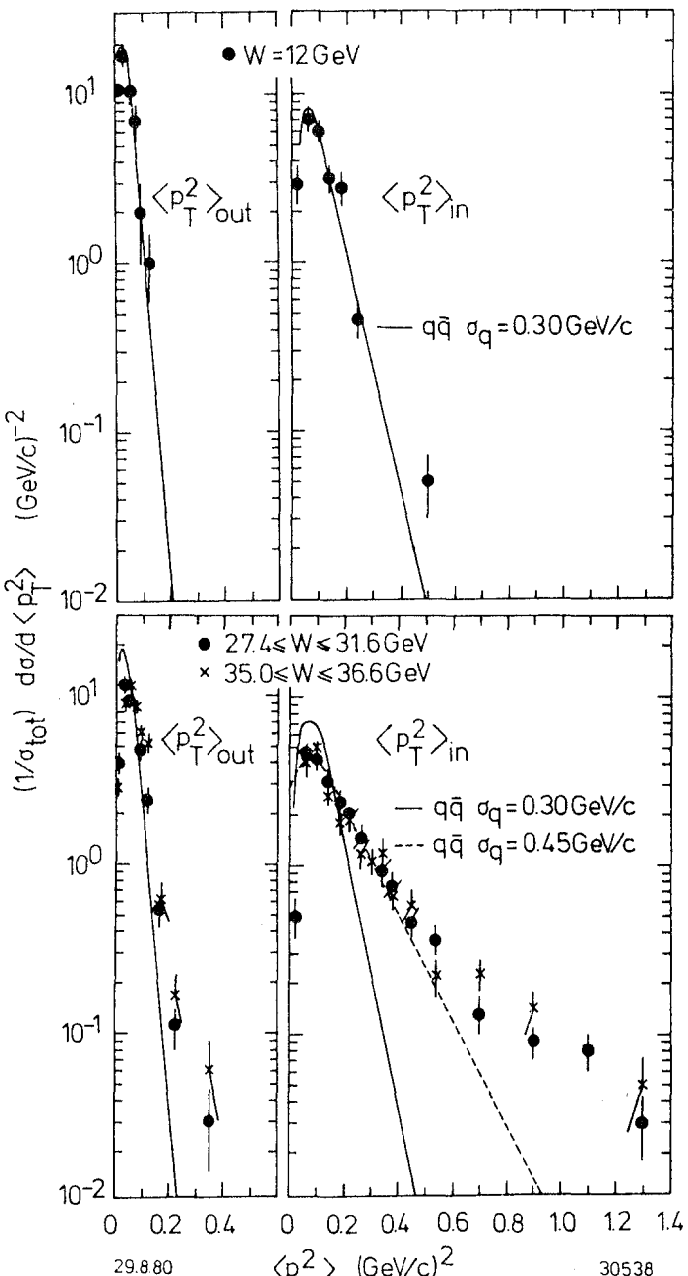

Fig.9 The mean transverse momentum squared normal to the event plane $\langle p_{Tout}^2 \rangle$ and in the plane $\langle p_{Tin}^2 \rangle$ per event as measured by TASSO.

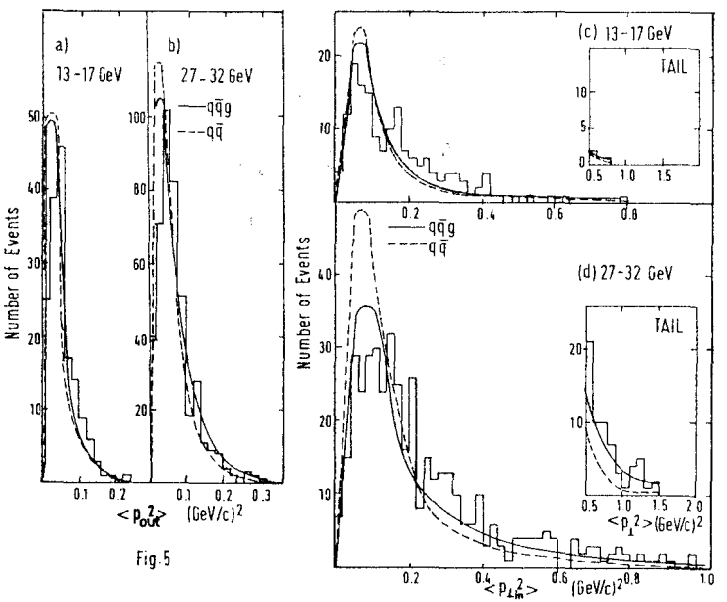

Fig.5

Fig.10 Distributions of $\langle p_{Tout}^2 \rangle$ and $\langle p_{Tin}^2 \rangle$ as measured by PLUTO (Ref.26)

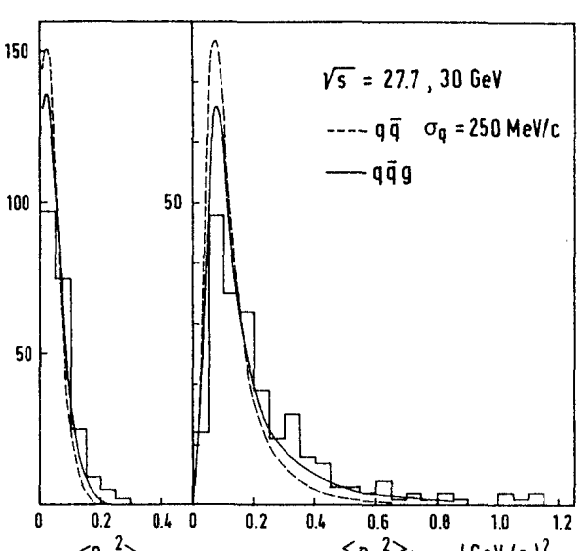

Fig.11 Same as Fig.10. Data measured by JADE (Ref.27).

(= square of the momentum component normal to the event plane given by $\hat{n}_2$ and $\hat{n}_3$) are compared with that of

$$\langle p_{Tin}^2 \rangle = \frac{1}{N} \sum_{j=1}^{N} (\vec{p}_j \cdot \hat{n}_2)^2 \qquad (= Q_2 \Sigma p_j^2) \qquad (13)$$

(= square of the momentum component in the event plane perpendicular to the jet axis). The data from TASSO[25], PLUTO[26] and JADE[27] show little increase in $\langle p_{Tout}^2 \rangle$ from low to high energy data. The distribution of $\langle p_{Tin}^2 \rangle$, however, becomes much wider at high energies; in particular there is a long tail of events with high $\langle p_{Tin}^2 \rangle$. The predictions of the $q\bar{q}$ model are also shown. Hadrons resulting from pure $q\bar{q}$ jets will on the average be distributed uniformly around the jet axis. However, some asymmetry between $\langle p_{Tout}^2 \rangle$ and $\langle p_{Tin}^2 \rangle$ is caused by statistical fluctuations. Fair agreement with the $q\bar{q}$ model is found at the low energy point. Thus the asymmetry observed at this energy can be explained by statistical fluctuations alone.

At high energy, one finds fair agreement for $\langle p_{Tout}^2 \rangle$ with the $q\bar{q}$ model with $\sigma_q \approx 0.3$ GeV/c, however, the long tail of the $\langle p_{Tin}^2 \rangle$ distribution is not reproduced by the model. This discrepancy cannot be removed by increasing σ_q. The result with $\sigma_q = 0.45$ GeV/c is also plotted in Fig. 9. The agreement is poor. One therefore must conclude that the data include a number of planar events that are not reproduced by the $q\bar{q}$ model independent of the assumption on the average p_T in that model.

The same conclusion was reached by the MARK J[28] group which studied the energy distribution ("energy flow") in the events. The coordinate system used is defined by the thrust axis ($\hat{e}_1$ = jet axis),

$$\text{Thrust} = \max. \frac{\sum_i |\vec{p}_i \ \hat{e}_1|}{\sum_i |p_i|}$$

where p_i is the energy flow detected by a counter; the major axis ($\hat{e}_2$) which is perpendicular to $\hat{e}_1$ and which is the direction along which the projected energy flow in that plane is maximized:

$$\text{Major} = \max. \frac{\sum_i |\vec{p}_i \ \hat{e}_2|}{\sum_i |p_i|} ;$$

the minor axis which is orthogonal to $\hat{e}_1$ and $\hat{e}_2$.

The difference Major - Minor is a measure for the planarity of an event and is called oblateness,

O = Major - Minor

The distribution of the oblateness is plotted in Fig. 12 together with the predictions of the $q\bar{q}$ and $q\bar{q}g$ models. The 17 GeV data are reproduced by both models. At the higher energies (27.4 - 31.6 GeV) an excess of events with large oblateness, i.e., planar events, is observed. This conclusion is reached independently of the value of σ_q used for the quark model.

The excess of planar events is readily seen at the highest PETRA energies from a plot of sphericity S versus aplanarity A (Fig. 13). In this kind of plot two jet events are found near S = 0, noncollinear planar events have S > 0 but small A while for spherical events both S and A are large (Fig. 13a). For illustration Fig. 13b shows the prediction of the $q\bar{q}g$ model (including u,d,s,c,b quarks) with gluon emission. The event distribution expected from a hypothetical t quark with a mass of 15 GeV which will lead to spherical events is plotted in Fig. 13c. The data shown in Fig. 13d cluster in the two-jet corner. In addition they populate a narrow band near A = 0 out to the highest sphericity values. This band of events is evidence for the presence of flat but wide = planar events.

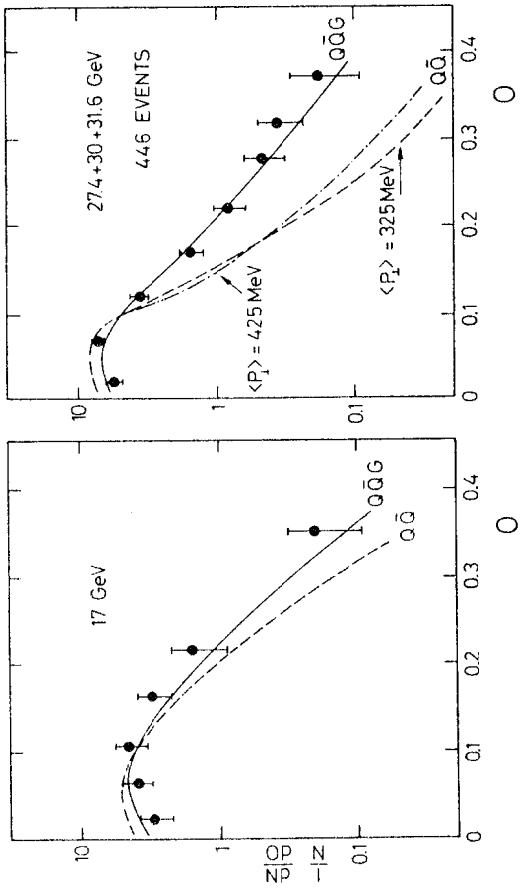

Fig.12 The oblateness distribution, O = Major - Minor, at 17 and 27.4 - 31.6 GeV (MARK J, Ref. 28).

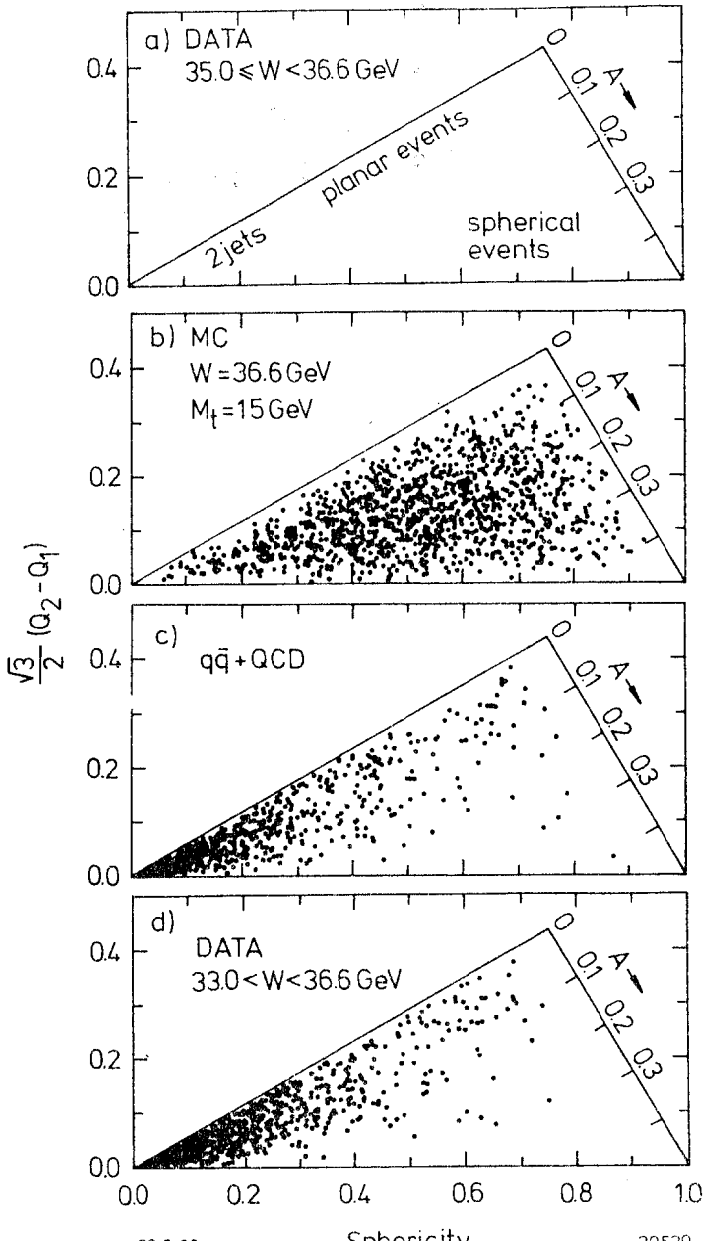

Fig.13 Distribution of events as a function of sphericity and aplanarity (TASSO).

4.7 Three jet structure

The data presented in the preceding paragraph demonstrated the existence of planar events. In order to check whether the particle momenta are distributed uniformly in the plane (disc like) or collimated into three jets the TASSO group adopted the procedure by Wu and Zobernig[29]. Each event is analysed as a three jet event. The particles are grouped into three classes C_1, C_2 and C_3 and for each class the sphericity is determined:

$$S_n = 3/2 \sum_{j \in C_n} \frac{q_{T_j}^2}{p_j^2}$$

The q_{T_j} are transverse momentum components in the event plane (defined by $\hat{n}_2$, $\hat{n}_3$) relative to the jet axis $\hat{n}_n$ for the group C_n which is chosen such as to minimize S_n. By considering all possible combinations one finds that grouping for which

$S_1 + S_2 + S_3$ = minimum.

This procedure was applied to planar noncollinear events selected by requiring $S > 0.25$, $A < 0.08$; out of a total of 777 events 77 satisfied these conditions. Fig. 14 shows the distribution of the squared transverse momenta p_T^2 of the charged hadrons for the 3 x 77 observed jets, where the p_T of each hadron is calculated with respect to the associated jet axis. It is compared with the corresponding distribution for events at 12 GeV analysed as two-jets and, therefore, without cuts in S or A. The p_T^2 behaviour is found to be the same in both cases, i.e., the particles from planar events at high energies are as collimated around three axis as particles from lower energy events around a single jet axis. The JADE group used the following procedure to demonstrate the existence of three-jet events. (See Fig. 15). For planar events from W ≈ 30 GeV selected by the condition $O_2 - O_1 > 0.1$ the thrust axis was determined. For the forward and backward (with respect

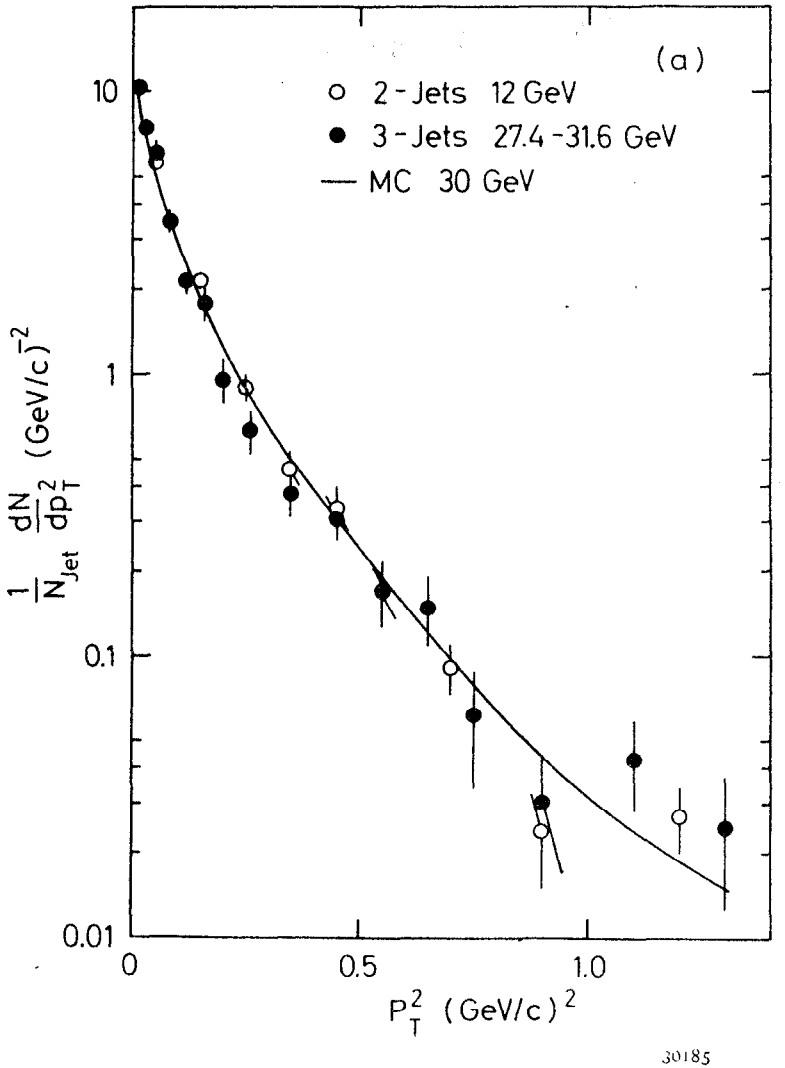

Fig.14 Distribution of the square of the transverse momentum relative to the jet axis at 12 GeV for all events analysed as two-jet events ϕ, and relative to the jet axes at 27.4 - 36.6 GeV for three-jet events ϕ (Ref. 37).

to the thrust axis) going particles the sum of the transverse momenta, Σp_{Ti}, was computed separately; the jet with the smaller Σp_T was called the slim jet and the other one the broad jet. The particles in the broad jet were Lorentz transformed into the rest system of the broad jet. In this system the thrust T_B of the broad jet was determined. The distribution of T_B is shown in Fig. 16 together with the thrust distribution of low energy events (W = 12 GeV) treated as two-jets. The two distributions are in good agreement which leads to the same conclusion drawn before from the similarity of the p_T^2 distributions of two- and three-jet events.

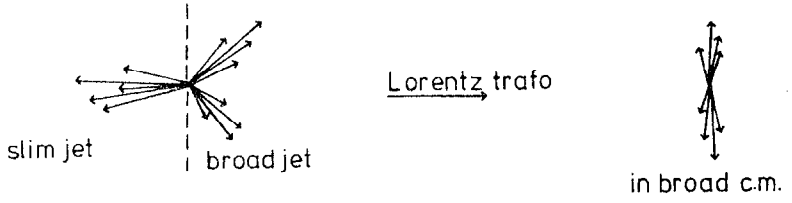

Fig. 15 Illustration of the procedure used by JADE

Fig. 17 shows a few typical three jet events.

4.8 Determination of α_s

The value of the quark gluon coupling strength, α_s, is directly related to the number of three jet events (see eq.(1)). In theory the determination of α_s is straightforward: after choosing a minimum angle between any pair of partons ($q,\bar{q}$ or g) the QCD cross section, eq.(5), can be integrated and compared to the corresponding observed three-jet cross section. In practise the analysis has to take into account the overlap between jets due to the hadronization, the omission of neutrals in the jet determination (at least in some of the experiments) plus

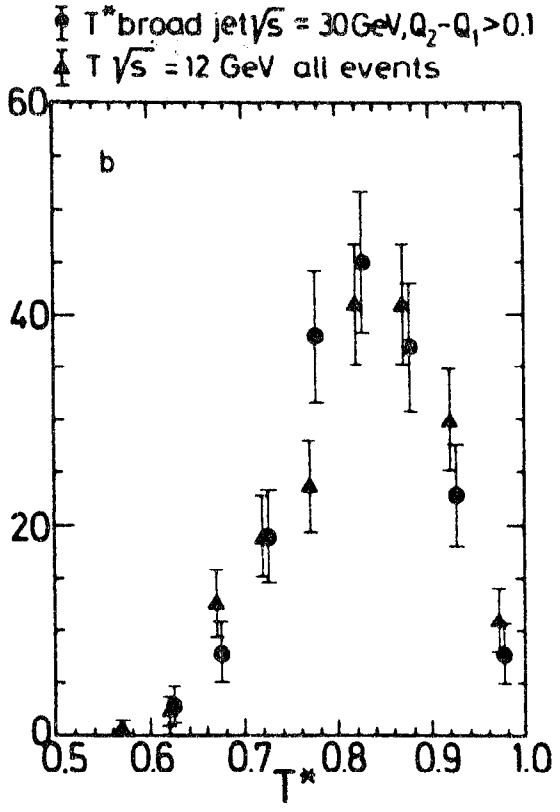

Fig.16 Distribution of thrust for the broad jet of planar events (at 30 GeV) compared with the two-jet thrust distribution at 12 GeV (JADE)

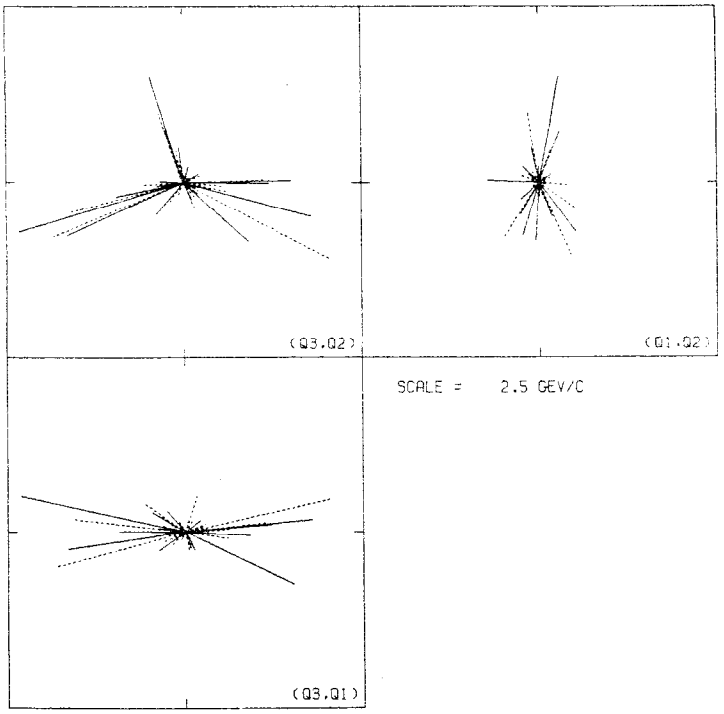

Fig.17a The three projections of a three-jet event. The solid lines indicate charged particles, the dashed photons (JADE).

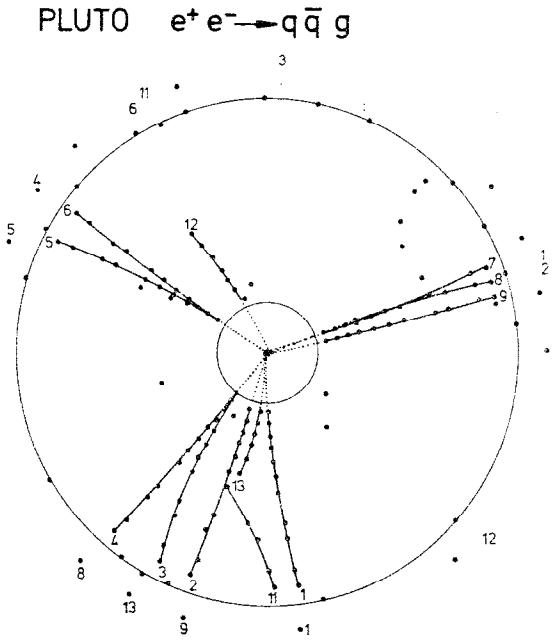

Fig.17b A three-jet candidate from PLUTO.

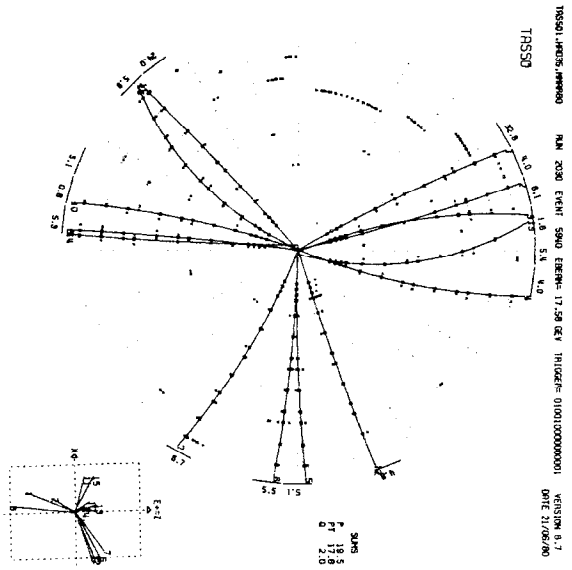

Fig.17c A three-jet candidate from TASSO.

the effect of the acceptance, the multijet contribution from semileptonic decays of the b quark, the corrections from higher order processes in α_s. To do this, elaborate Monte Carlo codes have been employed which describe the fragmentation of the quarks and gluons into hadrons[30-32] and simulate the effects of the detector. The fragmentation parameters were fine tuned by comparison with the data. Two Monte Carlo programs have played a major role in the results obtained so far, that of Hoyer et al.[30] and an extension by Ali et al.[31]. The framework of Field and Feynman[33] is used to describe the fragmentation of quarks into hadrons. The fragmentation process involves three parameters:

(i) a_F. The primordial fragmentation function $f^h(z)$ of a quark into a hadron h,

$$q \to q' + h$$

is taken to be

$$f^h(z) = 1 - a_F + 3a_F\,(1-z)^2, \qquad z = \frac{(p_\parallel + E)_h}{(p_\parallel + E)_q} \tag{14}$$

a_F is taken to be the same for u,d and s quarks;
for c and b: $a_F = 0$

(ii) σ_q. The distribution of the transverse momentum k_T of the quarks in the jet cascade is assumed to be $\exp(-k_T^2/2\sigma_q^2)$.

(iii) P/(P + V). Only pseudoscalars (π,K...) and vector mesons (ρ,K^*,...) are assumed to be produced. P/V is the ratio of pseudoscalar to vector mesons produced in the primordial cascade.

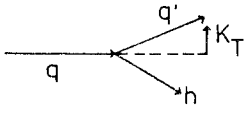

$q\bar{q}$ pairs are generated from the vacuum with the probability $u\bar{u} : d\bar{d} : s\bar{s} = 2 : 2 : 1$. Field and Feynman obtained a fair representation of hadron data with $a_F = 0.77$, $\sigma_q = 0.3$ GeV/c and $P/(P + V) = 0.5$.

In the Hoyer et al. program the gluon imparts its whole momentum to one of the two quarks (from $g \to q\bar{q}$). Therefore gluon and quark jets are the same. Ali et al. take the fragmentation function for gluons into $q,\bar{q}$, $g \to q\bar{q}$ to be[34]

$$f(z) = z^2 + (1 - z)^2, \qquad z = E_g/E_q \tag{15}$$

The quarks then turn into hadron jets according to the recipe given before.

Hoyer et al. consider only first order terms in α_s (diagrams a,b in Fig. 18);

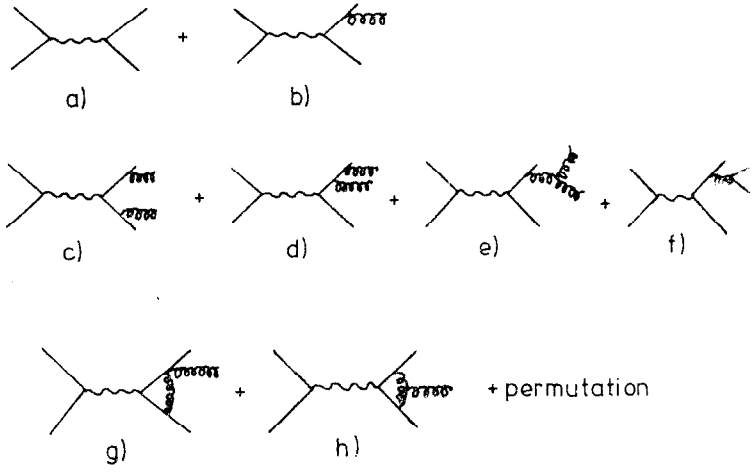

Fig.18 QCD diagram for hadron production up to second order in α_s.

Ali et al. include also all second order terms except for the diagrams of type 18g,h. In addition to the QCD diagrams QED corrections, particularly with hard photons in the initial state are important and have to be taken into account[35].

A first attempt to determine α_s at PETRA energies was made by the MARK J group using data taken around W = 30 GeV.[36] From the oblateness distribution of the broad jet (using the Ali et al. program) a value of $\alpha_s = 0.23 \pm 0.02$ (stat.) $\pm$ 0.04 (syst.) was obtained. A recent reanalysis adding data from 35 GeV and with the inclusion of hard photon corrections yielded a value of $\alpha_s = 0.19 \pm 0.02 \pm 0.04$ [36].

The TASSO group[37] found that α_s can be determined almost independently of the choice of parameter values describing the fragmentation by considering the events with large sphericity, S > 0.25. In this kinematical region three-jet events dominate and perturbative effects play a lesser role. Allowing a_F, σ_q, P/(P + V) and α_s to vary, α_s was found to be 0.16 $\pm$ 0.04 independent of the values of a_F, σ_q or P/(P + V).

In a second analysis the fragmentation parameters were determined using the events with small sphericity, S < 0.25. This region is dominated by two-jets and is insensitive to α_s. A simultaneous fit was made to

the x distribution (x = 2p/W) - most sensitive to a_F,

the $\langle p^2_{Tout} \rangle$ distribution - most sensitive to σ_q,

the charge multiplicity distribution - most sensitive to P/(P + V),

yielding

$a_F = 0.57 \pm 0.20$, $\sigma_q = 0.32 \pm 0.04$ GeV/c, $P/(P+V) = 0.56 \pm 0.15$

With these fragmentation parameters and turning again to the events with S > 0.25 a more precise value for α_s was obtained which is listed in Table 1.

The JADE group followed essentially the same procedure. Their preliminary value is[38] given in Table 1. A different method was developed by the PLUTO group[39]. The events were classified as 2-, 3-, 4-jet events according to the number of particle clusters observed. The value of α_s was determined by comparing the observed and Monte Carlo predicted number of three-jet events. The result is also given in Table 1.

Table 1. Determination of α_s around W = 30 GeV. First error is statistical, second systematic.

JADE[38]	$0.18 \pm 0.03 \pm 0.03$*
MARK J[36]	$0.19 \pm 0.02 \pm 0.04$*
PLUTO[39]	$0.16 \pm 0.03 \pm 0.03$*
TASSO[37]	$0.17 \pm 0.02 \pm 0.03$

* preliminary value.

All four experiments are seen to agree on the value of α_s.

Several cautionary remarks are in order.

- Although the value of α_s was found independently of the fragmentation parameters the analyses were based on a particular way of describing the hadronization process, namely the Field-Feynman model.
- The inclusion of the second order corrections seems to have a small effect on α_s. This may be seen from the TASSO results:

  $\alpha_s = 0.19 \pm 0.02$ with Hoyer et al., first order in α_s

  $= 0.17 \pm 0.02$ with Ali et al., including second order terms.

However the $O(\alpha_s^2)$ calculation does not include diagrams 18g,h, the effect of which is unknown.

Next we estimate the QCD parameter Λ using the relation

$$\alpha_s(Q^2) = \frac{12\pi}{(33 - 2N_f)\ln Q^2/\Lambda^2}$$

where N_f, the number of flavours, is taken to be $N_f = 5$.

It is theoretically an open question at which Q^2 value α_s is measured by the experiments discussed above. One possibility is to take Q^2 equal to the mass squared of the virtual photon, $Q^2 = S = W^2$, or $Q^2 \approx 900\ \text{GeV}^2$. Another choice is the mass squared p^2 of the quark that emitted the hard gluon.

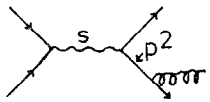

Fig. 19 shows the p^2 for the TASSO events with $S > 0.25$ used to determine α_s. The average p^2 is 140 GeV^2. Hence we find for

$$\alpha_s = 0.17 \pm 0.02 \pm 0.03$$

$Q^2 = s$: $\Lambda = 240 \begin{matrix} \nearrow 410 \to 730 \\ \searrow 130 \to 30 \end{matrix}$ MeV

$Q^2 = P^2$: $\Lambda = 95 \begin{matrix} \nearrow 160 \to 290 \\ \searrow 50 \to 12 \end{matrix}$ MeV

This range of Λ values may be confronted with the result from deep inelastic μp and γN scattering. The high Q^2 data indicate $\Lambda \approx 100$ to 500 MeV.

We close this section with a few figures in order to demonstrate how well the data are reproduced using the fragmentation parameters and the value α_s given above. Fig. 20 shows the measured sphericity, aplanarity and x distributions at W = 12 and 30 GeV together with curves calculated from the model. Note that only the W = 30 GeV data were used in the fit; at W = 12 GeV the curves are genuine predictions. Fig. 21 shows the fit to the $\langle p^2_{\text{tout}} \rangle$ distribution.

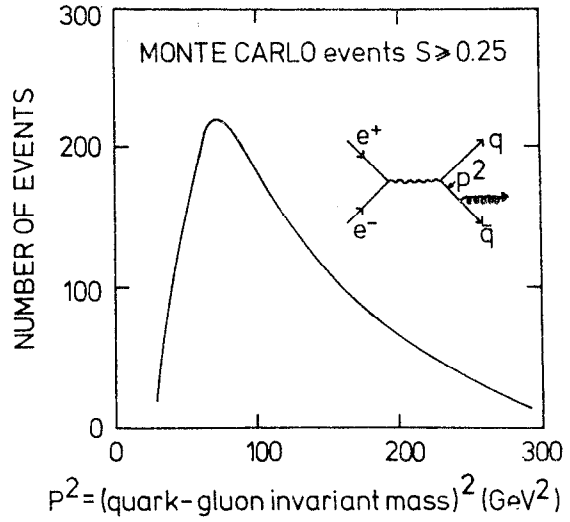

Fig.19 Distribution of the square of the quark-gluon mass as computed with the Monte Carlo of Ali at al. for events with large sphericity.

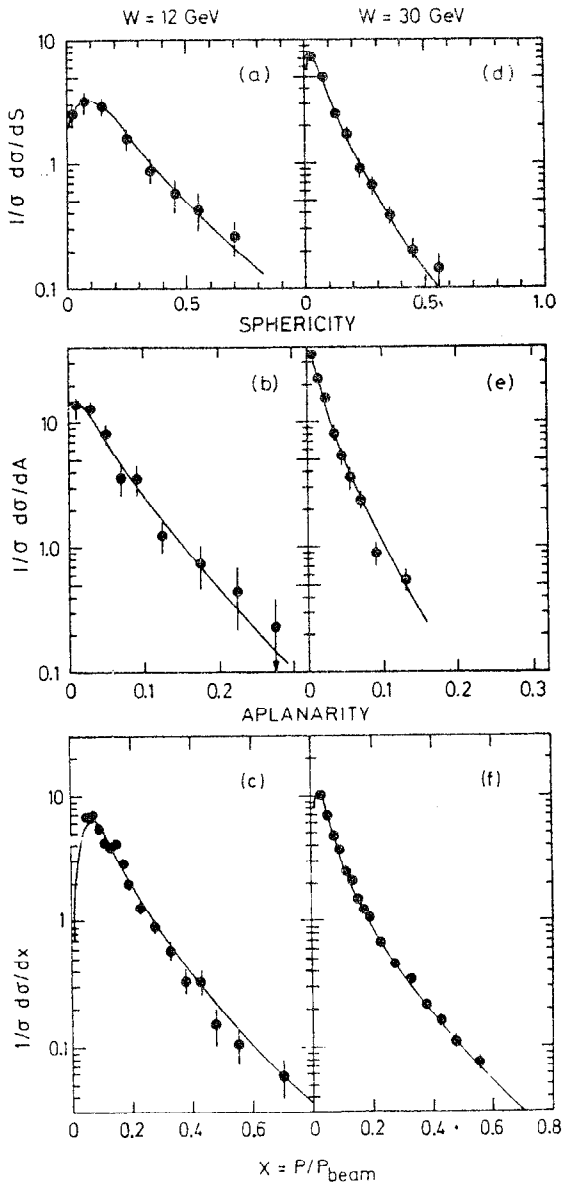

Fig.20 Comparison of the data for sphericity, aplanarity and the single particle inclusive x distribution for charged particles at 12 and 30 GeV with the QCD model (curves). From TASSO, Ref.37.

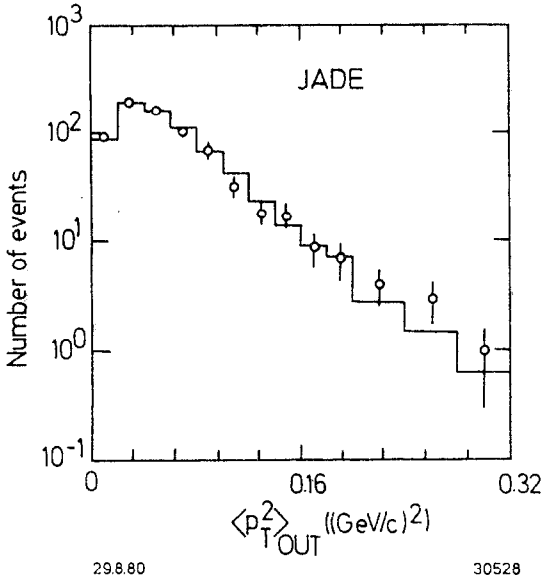

Fig.21 Comparison of the $\langle p_{T\,out}^2 \rangle$ distribution at 30 GeV with the QCD model (histogram). From JADE.

4.9 Gluon spin

The occurrence of three-jet events and their rate is consistent with the QCD prediction for bremsstrahlung of a hard gluon and is a major success of the theory. However, the existence and bremsstrahlung of gluons is a common property of field theories of strong interactions. The particular features of the QCD gluon are

- spin 1
- colour octet state
- the existence of the triple gluon coupling which is responsible for the nonabelion nature of the theory
- flavour independence of the coupling to quarks.

There is evidence from the PLUTO data as shown by Koller and Krasemann[40] that the gluons in the $T \to 3g$ decay have spin 1. However, one can argue that the gluons emitted in the T decay and in the bremsstrahlung process are of different types.

The TASSO group studied the angular correlation between jets in three jet events. The data were compared with the hypotheses for vector and scalar gluons. The cross section for $e^+e^- \to q\bar{q}g$ for the two alternatives reads[41] after averaging over production angles[42]:

for vector gluons (see eq.(5)):

$$\frac{d\sigma}{dx_1 dx_2} = \frac{2\alpha_s}{3\pi}\,\sigma_0\,\frac{x_1^2 + x_2^2}{(1 - x_1)(1 - x_2)} \qquad (16)$$

for scalar gluons:

$$\frac{d\sigma}{dx_1 dx_2} = \frac{\tilde{\alpha}_s}{3\pi}\,\sigma_0\,\frac{x_3^2}{(1 - x_1)(1 - x_2)} \qquad (17)$$

where as before $x_i = 2E_i/W$, $i = q,\bar{q},g$ and $\alpha_s,\tilde{\alpha}_s$ are the gluon quark couplings for the two cases.

The infrared divergencies in perturbative QCD are expressed by the $(1 - x_i)$ denominators. The vector expression has both collinear and soft divergences, while for the scalar case there is only the collinear divergence, causing a somewhat flatter behaviour as a function of x_i. Unfortunately, the difference between the two distributions is largest for the parton thrust x_1 near 1 where one approaches the collinear two jet singularity. In this kinematic region the cross section is sensitive to smearing effects caused by quark and gluon fragmentation. Moreover, for x_1 too close to 1, higher order terms become important.

The TASSO analysis used only the information from charged particles. This allows for a good determination of the jet axes and of the relative angles Θ_i between the jet directions (see Fig. 22a). The r.m.s. error on the Θ_i was found to be between 3^0 and 8^0. If the quarks and the gluon have negligible mass the x_i are determined by the Θ_i,

$$x_i = \frac{2\sin\Theta_i}{\sin\Theta_1 + \sin\Theta_2 + \sin\Theta_3}$$

After ordering such that $x_1 \leq x_2 \leq x_3$, x_1 measures the thrust T of the $q\bar{q}g$ system. Fig. 22b shows the angle $\tilde{\Theta}$ which was suggested to discriminate between vector and scalar gluons[43]. In this figure, the $q\bar{q}g$ system has been Lorentz boosted to the c.m. frame of partons 2 and 3. Assuming negligible quark and gluon masses,

$$\cos\tilde{\Theta} = \frac{x_2 - x_3}{x_1} = \frac{\sin\Theta_2 - \sin\Theta_3}{\sin\Theta_1}$$

In order to avoid the problematic area near $x = 1$ the TASSO analysis was restricted to events with $1 - x_1 > 0.10$ (248 events). With the help of Monte Carlo calculations smearing effects due to fragmentation and the leakage from two-jet events into the three jet class (which

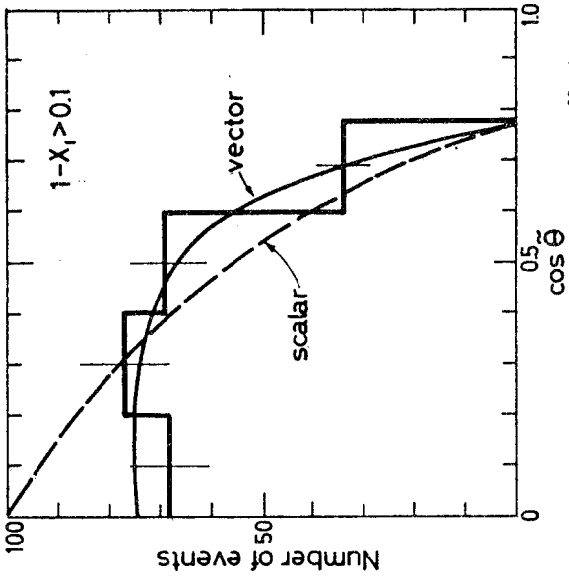

Fig.23 Observed distribution of the data in the region $1-x_1 > 0.10$, as a function of the cosine of the Ellis-Karliner angle $\tilde{\theta}$ defined in Fig.1b. The solid line shows the QCD prediction, the dotted line the prediction for scalar gluons, both normalized to the number of observed events (from TASSO).

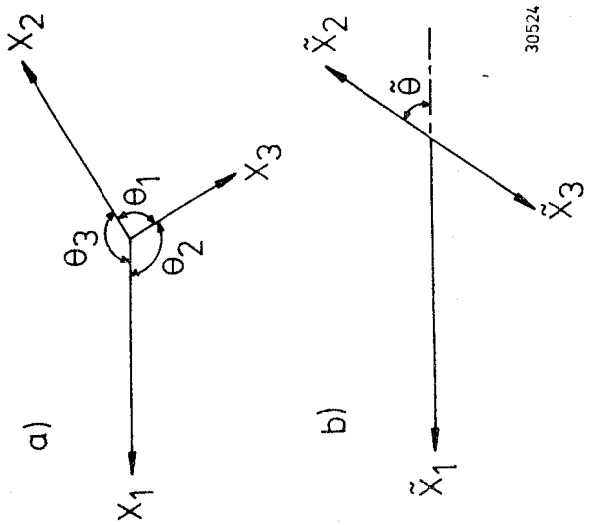

Fig.22 a) Momenta and angles of a $q\bar{q}g$ final state in the center-of-momentum frame.
b) The $q\bar{q}g$ final state transformed to the rest frame of particles 2 and 3.

amounted to 17-18 %) were studied. In order to eliminate any dependence of the spin analysis on the values of α_s, $\tilde{\alpha}_s$ these were treated as free parameters.

Fig. 23 compares the observed distribution of $\cos\tilde{\theta}$ with the predictions for vector and scalar gluons. The data clearly favour spin 1 over spin 0. Vector gluons are consistent with the data but scalar gluons are disfavoured by 3.8 standard deviations.

An analysis done by the PLUTO group[44] shows also preference for spin 1.

The data then confirm the first of the four properties predicted by QCD for gluons. Walsh[45] has given an argument which supports the second prediction, the colouredness of gluons. If gluons would be colourless then the T direct decay would proceed via a one-gluon intermediate state, which would turn into a $q\bar{q}$ pair and lead to two-jet final states-- such events are not observed by the PLUTO group[46].

Predictions three and four are yet to be tested by experiment.

4.10 Is there a difference between quark and gluon fragmentation?

There are several qualitative arguments which say that quarks and gluons fragment differently:

- A gluon before hadronization has to turn into a $q\bar{q}$ pair. Hence there are at least two quarks ($q = \bar{c}$) per gluon which then fragment into hadrons.
- The ggg coupling is 9/4 times stronger than than for $q\bar{q}g$ (9/4 α_s versus α_s). Therefore gluon emission is more frequent for gluons than for quarks.

Both arguments favour a higher hadron multiplicity for gluon jets.

Andersson, Gustafson and collaborators[47] suggested studying the yields of low energy particles emitted at large angles to the jet axes.

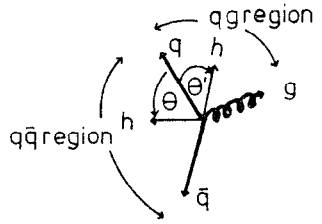

30558

The JADE group[48] performed the analysis using charged and neutral particles. Like before, planar events with $Q_2 - Q_1 > 0.07$ were grouped into the slim jet (q) and the two subjets which make up the broad jet. The subjet with the smaller angle relative to the slim jet was called the gluon jet (g), the other one the quark jet ($\bar{q}$). Monte Carlo studies indicate that in this way the gluon is correctly assigned for ~70 % of the events. The particle yield was then measured as a function of the angle Θ between the particle and the slim jet. In Fig. 24 the particle yield is shown as a function of Θ/Θ_{max} for the $q\bar{q}$ and the qg regions. One observes a significant difference (4 s.d.) near $\Theta/\Theta_{max} \approx 0.5$: the particle density is two times larger in the qg compared to the $q\bar{q}$ region. Fig. 24 was determined with charged and neutral particles. Charged particles alone reportedly give the same result. The Hoyer et al. MC does not predict a difference if the quark and gluon fragmentations are treated identically. The Lund MC[32] agrees with the data. This may be the first experimental indication that quarks and gluons fragment differently.

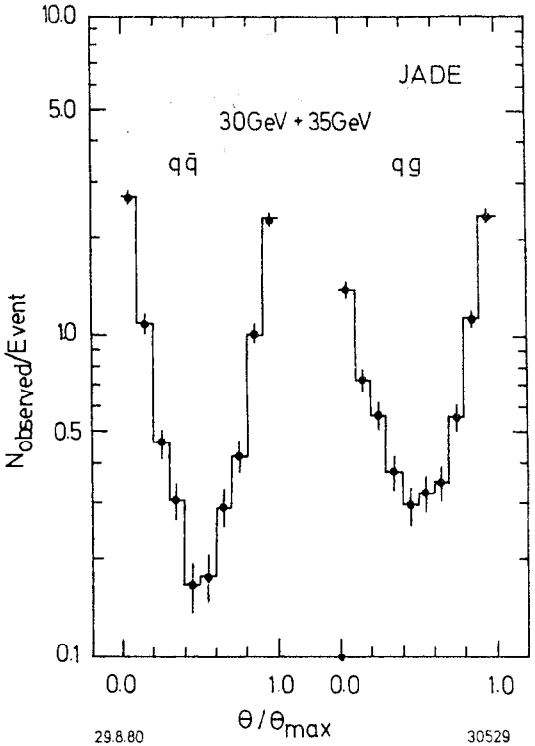

Fig. 24 Angular distribution Θ/Θ_{max} of particles between the jet axes (see text). From JADE[48].

4.11 Soft gluon emission

The previous section primarily dealt with effects due to the emission of a single hard gluon. This section considers the emission of soft gluons. For soft gluons α_s is no longer small but of order unity. Many (infinitely many) diagrams become important and should be summed. No rigorous theory does exist yet but a first step towards understanding these processes theoretically as well as studying them experimentally was made.

Consider again gluon bremsstrahlung in $e^+e^- \to q\bar{q}g$.

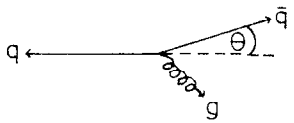

The cross section diverges as the angle Θ between the -q and $\bar{q}$ directions goes to zero,

$$\frac{d\sigma}{d\Omega} \sim \frac{1}{\Theta}$$

This divergence is cancelled by multigluon emission (see sketch).

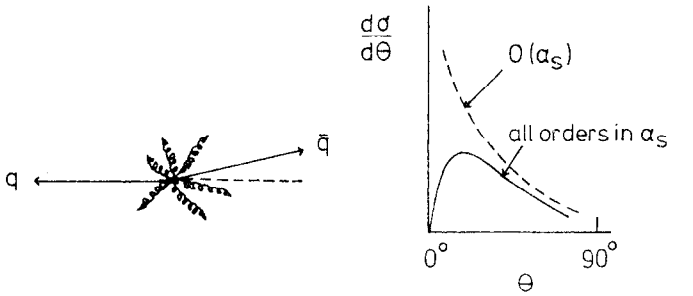

30557

The cross section approaches zero as $\Theta \to 0$: quark and antiquark are never emitted exactly back-to-back.

Dokshitzer, D'Yakanov and Troyan[49] proposed to relate the parton angular distribution to the two particle differential cross section:

$$\frac{1}{\sigma}\frac{d\Sigma}{d\Theta} = \sum_{a,b} \int dx_a\, dx_b\, x_a\, x_b \frac{1}{\sigma}\frac{d\sigma}{dx_a dx_b d\Theta} \qquad (18)$$

where a,b are any two particles emitted in the event with fractional momenta x_a, x_b, $x = P/E_{beam}$ and angle $(\pi-\Theta)$ between them, and summation is performed over all two particle combinations.

Through the factor $x_a x_b$ the higher momentum particles which supposedly know more about the primary quark directions are weighted more heavily.

The PLUTO group determined the two particle differential cross section $\frac{1}{\sigma}\frac{d\Sigma}{d\Theta}$ at energies between 9.4 and 31.6 GeV [50]. Fig. 25 shows the result at 31.6 GeV for the small angle region. The cross section tends to go to zero as $\Theta \to 0$; it goes through a maximum and falls off towards large angles.

The curves in Fig. 25 were computed by Ref. 51 at the quark level, i.e., hadronization was not considered. The curve labelled $O(\alpha_s)$ illustrates what was said before: the first order terms diverges as $\Theta \to 0$. The curves labelled $\Lambda = 0.2$ and $\Lambda = 0.8$ were computed in the leading log approximations to all order in α_s. They show explicitly the large cancellation near $\Theta = 0$ forcing the cross section to go to zero as $\Theta \to 0$. However, the hadronization process, which was not included in the calculation and which affects particularly the small Θ region, may change the whole picture.

Refs. 52 and 53 made an attempt to include hadronization effects. In Ref. 53 the PLUTO data at 9.4 GeV where hard gluon effects are

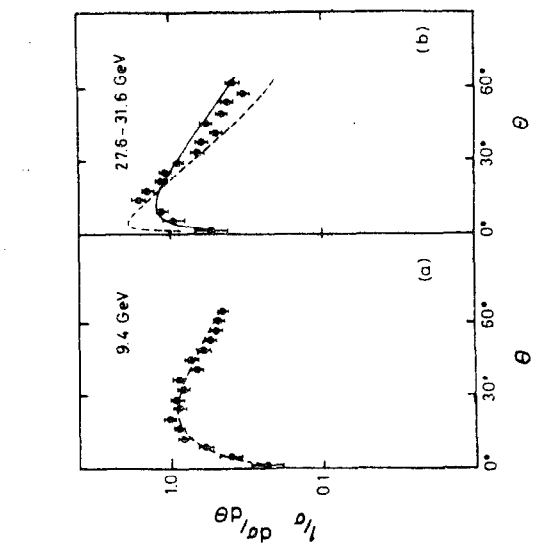

Fig. 26 The same quantity as in Fig.25 at 9.4 and 30 GeV. The dashed curve in (b) was calculated in the leading log approx., the solid curve includes hadronization[53].

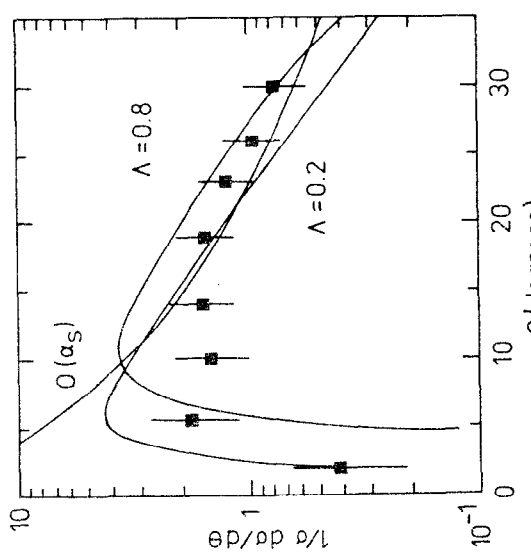

Fig.25 The two-particle cross section (eq.18) as measured at 30 GeV by PLUTO (Ref.50). The curves show the prediction of single gluon bremsstrahlung and of the leading log approximation without hadronization[51].

small were used to fix the parameters of hadronization. Assuming that after hard gluon emission the partons transform independently into hadrons the two particle differential cross section was predicted at 30 GeV using the leading log approximation and a QCD evolution technique.

Fig. 26 shows the input data at 9.4 GeV and the 30 GeV data together with their prediction (solid curve) which describes the data well. The dashed curve was computed without hadronization. The difference between the dashed and the solid curves demonstrates the importance of the hadronization process.
Two particle correlations at large angles were studied theoretically in papers cited in Ref. 54.

4.12 Gross features of the final states

As we saw above the final states in high energy e^+e^- annihilation are a result of quark and gluon induced jet formation. Correspondingly, by analysing the final state particles one should be able to piece the jet fragments together and reconstruct the properties of the primordial parton, such as charge, flavour, etc. This section summarizes briefly what is known on the final states produced at high energies.

4.12.1 Energy carried by neutrals

The JADE group[48,55] measured the fraction of energy carried by photons (either from π^0,n .. decay or from direct production) and by neutrals:

$$f_\gamma = \frac{\sum_i E_{\gamma_i}}{W}$$

and

$$f_{neutral} = 1 - \frac{\sum_i E_{CHi}}{W}$$

E_{CHi} energy of charged particle i. $f_{neutral}$ includes K^0_s and Λ particles. The result is given in Table 2 for energies between 12 and 35 GeV.

Table 2. Fraction of energy carried by photons and neutrals

W(GeV)	f_γ(%)	$f_{neutral}$ (%)
12	21.3 ± 7.0	31.2 ± 4.1
30.4	26.1 ± 5.9	37.5 ± 3.7
34.9	30.7 ± 6.0	43.8 ± 4.1

Furthermore, the fraction of energy carried by neutrinos, f_ν, was found to be less than 15 % (2 s.d.) at all energies. If free quarks of unit charge à la Pati-Salam exist f_ν should be equal to 20 to 30 %.

4.12.2 Charged particle multiplicity

In Fig. 27a the average charged particle multiplicty* $\langle n_{CH} \rangle$ is plotted as a function of c.m. energy[56-62]. Above 7 GeV the multiplicity is seen to rise (logarithmically) faster than at lower energies. The curves give the energy dependence for pp collisions[63] and $\bar{p}p$ annihilation[64]. They seem to bracket the e^+e^- data at high energies**.

* $\langle n_{CH} \rangle$ includes the $\pi^\pm$ coming from $K^0_s \to \pi^+\pi^-$ decay. This contribution amounts to 0.4 units at 7.4 GeV, 0.6 at 12 GeV and 1 unit at 30 GeV. In the pp and $\bar{p}p$ data shown by the curves the K^0_s contribution is not included.

** An interesting comparison between e^+e^- and pp data has been performed in Ref. 65 where the leading protons have been subtracted and the c.m. energy was rescaled. In this analysis a close correspondence between pp and e^+e^- data is obtained.

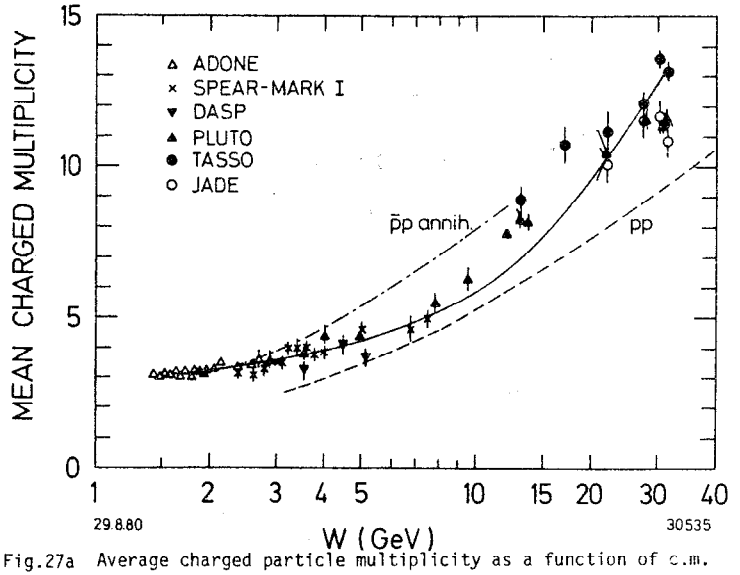

Fig.27a Average charged particle multiplicity as a function of c.m. energy.

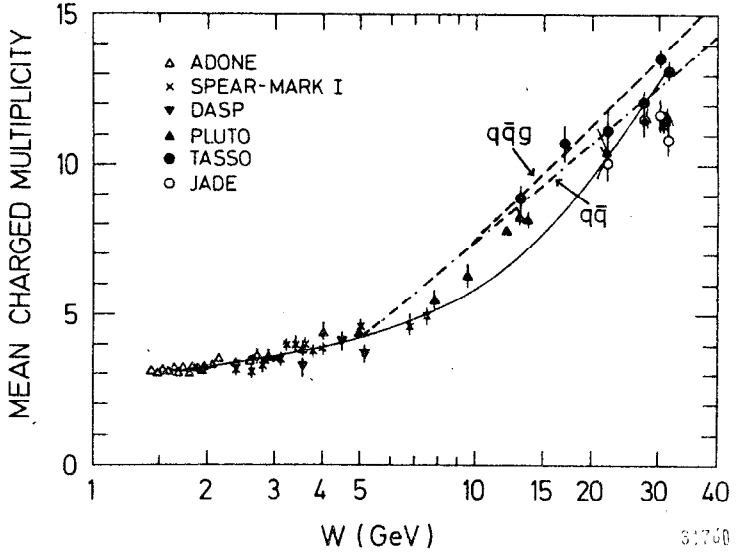

Fig.27b Same as in Fig.25. The dashed-dotted and dashed curves show the predictions of the $q\bar{q}$ and $q\bar{q}g$ models.

The simpliest form of scaling of charged particle production leads to $\langle n_{CH} \rangle = a + b \ln s$. This is certainly at variance with the data if the full energy range is considered. The observed rise of $\langle n_{CH} \rangle$ cannot be attributed to the onset of $b\bar{b}$ production which is found to yield an increase by ~0.2 units. In QCD an increase of $\langle n_{CH} \rangle$ over the scaling curve is predicted due to the additional contribution from gluon fragmentation. The exact form of the resulting energy dependence is not yet clear. If the result for infinitely heavy quarks is taken for guidance, one expects $\langle n_{CH} \rangle$ to grow like[66]

$$\langle n_{CH} \rangle = n_o + a \exp(b\sqrt{\ln(s/\Lambda^2)}).$$

Fits of this form reproduce the trend of the data[61,62]. One may therefore be tempted to attribute the rapid rise to hard gluon effects. However, Fig. 27b compares the $\langle n_{CH} \rangle$ data with the $q\bar{q}$ model, $e^+e^- \to q\bar{q} \to$ hadrons using the Field-Feynman fragmentation functions but without hard gluon contributions. The model accounts well for the rise seen above ~5 GeV (see dashed curve).* The inclusion of hard gluon emission raises the prediction by a negligible amount below 10 GeV; at 35 GeV it adds 0.8 units. We conclude therefore that the rapid rise of $\langle n_{CH} \rangle$ is mostly due to the growing phase space: the particle masses matter less as the energy goes up.

In Fig. 28a the PLUTO group[62] has compared the e^+e^- multiplicity distributions in a KNO plot[67] with pp and $\bar{p}p$ data. Plotted is $P_{CH} \cdot \langle n_{CH} \rangle$ where P_{CH} is the probability for observing a final state with n_{CH} charged particles versus $n_{CH}/\langle n_{CH} \rangle$. The e^+e^- data obey KNO scaling between 9.4 and 30 GeV. The distribution agrees well with the $\bar{p}p$ data but disagrees with the pp data which have a larger dispersion (see also Fig. 28b).

* At lower energies the model is presumably less reliable because of the approximations made for the fragmentation.

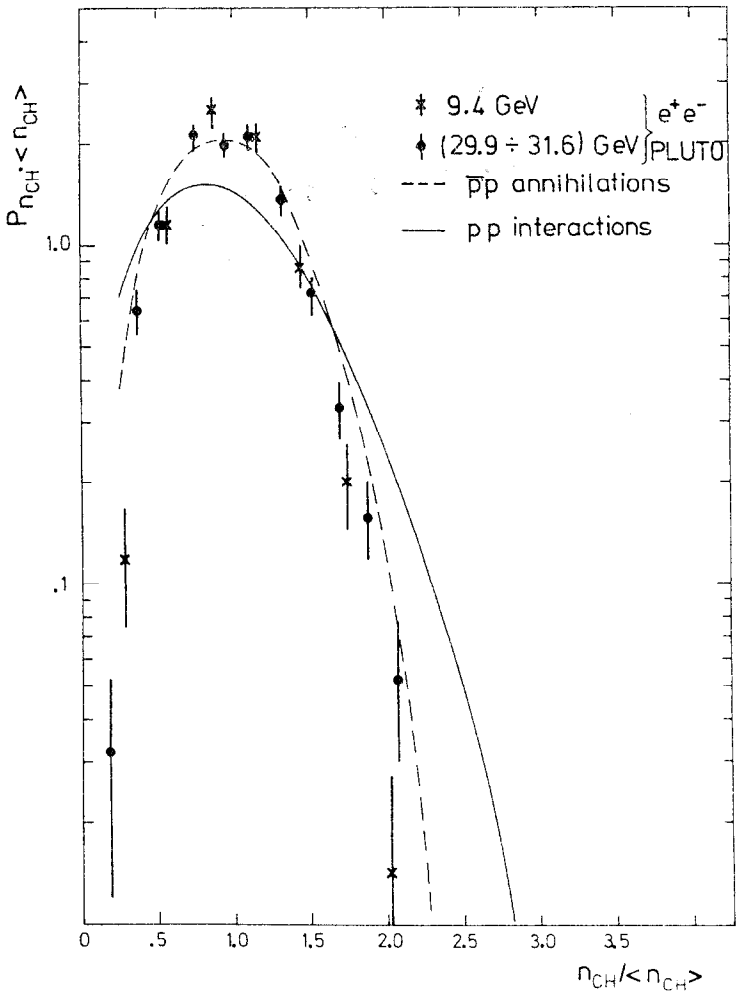

Fig.28a KNO plot for e^+e^- data as measured by PLUTO at 9.4 and 30.7 GeV[62]. The dashed curve is a fit to $p\bar{p}$ annihilation data. The solid curve describes high energy pp data.

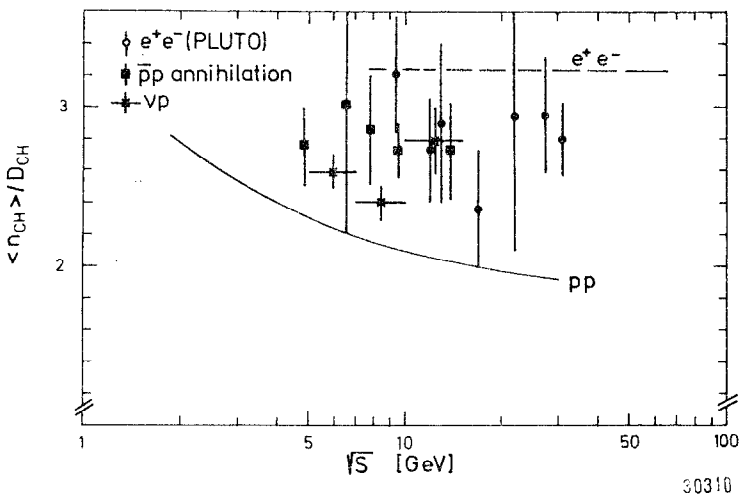

Fig.28b Energy dependence of the ratio $\langle n_{CH}\rangle/D_{CH}$ where $\langle n_{CH}\rangle$ is the mean charge multiplicity and D_{CH} is the dispersion of the multiplicity distribution, $D_{CH} = \sqrt{\langle n_{CH}^2\rangle - \langle n_{CH}\rangle^2}$. Also shown are the data for pp interactions, $p\bar{p}$ annihilations and νp interactions. (From PLUTO[62]).

4.12.3 Inclusive particle spectra without particle identification

The differential cross section for producing a particle h with momentum and energy P, E and angle Θ relative to the beam axis can be expressed in terms of two structure functions $\overline{W}_1$ and $\overline{W}_2$ which are closely related to W_1 and W_2 measured in inelastic lepton hadron scattering[68]

$$\frac{d^2\sigma}{dx d\Omega} = \frac{\alpha^2}{s}\,\beta\, x\,\{m\overline{W}_1 + \frac{1}{4}\,\beta^2\, x\,\nu\overline{W}_2\,\sin^2\Theta\} \qquad (19)$$

where m is the mass of h, $\beta = P/E$, $x = E/E_{beam} = 2E/\sqrt{s}$ and ν is the energy of the virtual photon as seen in the h rest system, $\nu = (E/m)\sqrt{s}$.

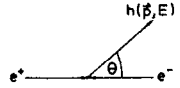

Diagram for inclusive particle production

At particle energies large enough that particle masses can be neglected, x can be replaced by the normalized momentum $x = P/E_{beam}$ and the scaling cross section reads

$$s d\sigma/dx \approx 4\pi\alpha^2\, x\,\{m\,\overline{W}_1 + \frac{1}{6}\, x\,\nu\overline{W}_2\} \qquad (20)$$

The structure functions in general depend on two variables, e.g., x and s. If scale invariance holds $\overline{W}_1$ and $\nu\overline{W}_2$ are functions of x alone and $s d\sigma/dx$ is energy independent.

Scaling behaviour is e.g. expected from the hypothesis of quark fragmentation: at energies large enough that particle masses can be neglected, the number of hadrons h produced by a quark q with fractional energy x, $D_q^h(x)$, is independent of s. This leads to

$$\frac{d\sigma}{dx}(e^+e^- \to q\bar{q} \to h) = \sigma_{q\bar{q}} \cdot 2D_q^h(x) = \frac{8\pi\alpha^2}{s}\, e_q^2 D_q^h(x) \qquad (21)$$

Fig. 29 displays the data on sdσ/dx measured by TASSO[69,70] at energies between 12 and 36 GeV. For x > 0.2 they are the same within errors and agree with those measured at low energy by DASP (Ref. 71, 5 GeV) and SLAC-LBL (Ref. 72, 7.4 GeV) to within 30 %. At low x values the particle yield shows a dramatic rise when the c.m. energy increases from 5 to 36 GeV. This rise is related to the growth of the multiplicity seen above.

Gluon emission will lead to scale breaking effects: the primary momentum is now shared by quark and gluon resulting in a depletion of particles at high x and an excess of particles at low x values. The effect becomes more pronounced as the energy rises, e.g., the 30 GeV data at x ≈ 0.2 are predicted to be higher by ~10 %, and at x = 0.7 lower by ~20 % than the 5 GeV data[73]. The measurements are not precise enough to test this prediction.

4.12.4 π, K and p,$\bar{p}$ cross sections

Inclusive $\pi^{\pm}$, $K^{\pm}$, K^{0}, $\bar{K}^{0}$, and p,$\bar{p}$ cross sections were measured at PETRA by the experiments listed in Table 3.

Fig. 30 shows the scaling cross section s/β dσ/dx for the sum of $\pi^{+} + \pi^{-}$ production for energies of 5.2 [71], 12 and 30 GeV as a function of x = 2E/W. The 12 and 30 GeV points agree with each other but appear to be lower than the 5.2 GeV data by ≈30 % for x < 0.2. There is a break in slope near x = 0.1 The data at lower x values have a larger slope.

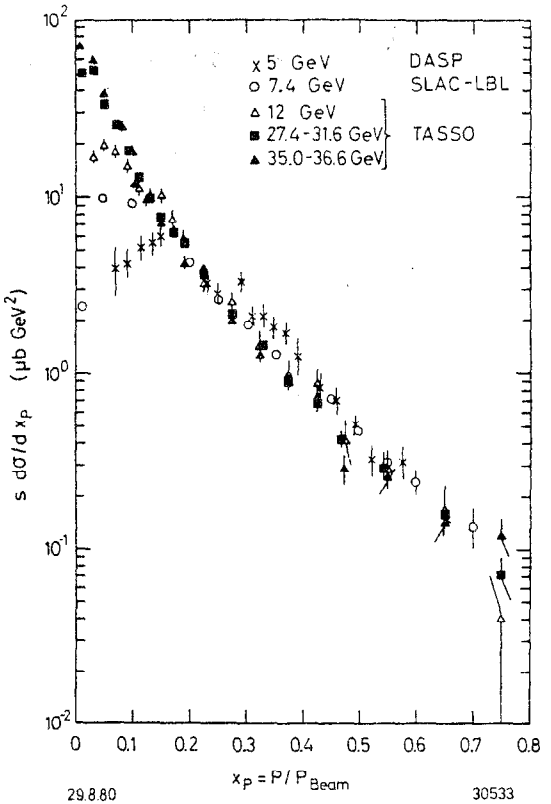

Fig.29 The scaling cross section sdσ/dx ($x=p/E_{beam}$) for inclusive charged particle production measured at energies of 5 GeV (Ref.71), 7.4 GeV (Ref.72) and between 12 and 36.6 GeV (Ref.69,70).

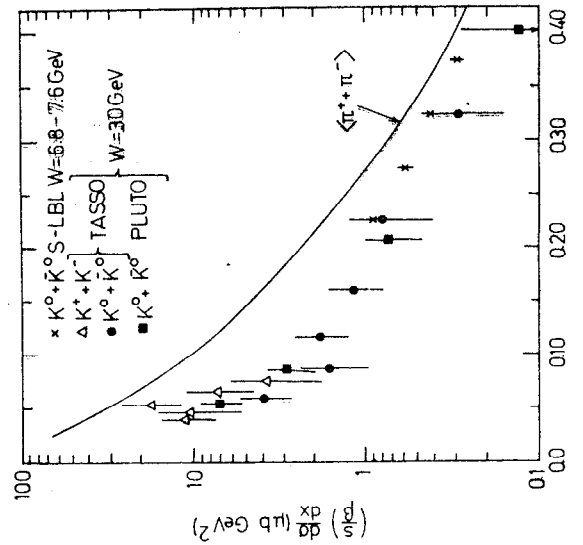

Fig.31 Same as in Fig.30 for $K^+ + K^-$ and $K^0 + \overline{K^0}$ production. (From Ref. 70).

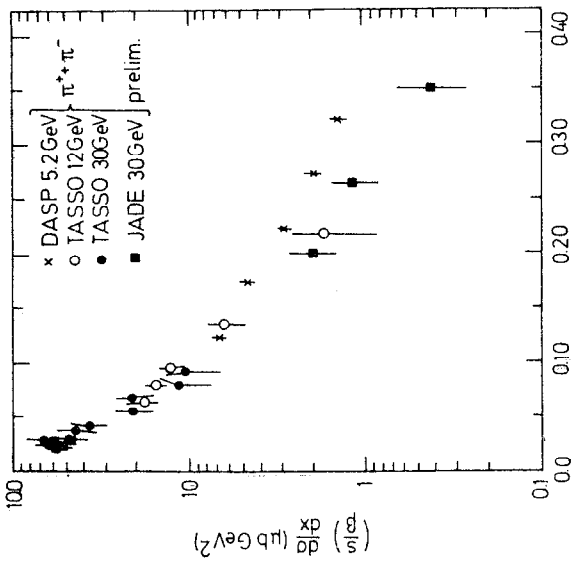

Fig.30 The cross section $(s/\beta)d\sigma/dx$ ($x = E/E_{beam}$) for the sum of $\pi^+ + \pi^-$ production. (From Ref. 70).

Table 3. Experiments measuring particle separated cross sections

type of particle	experiment	technique	momentum range (GeV/c)	remark
$\pi^\pm$	JADE	dE/dx[70]	<0.7, 2-7	preliminary
	TASSO	TOF[74]	<1.1	
		Cerenkov[70]	<5	preliminary
$K^\pm$	JADE	dE/dx[70]	<0.7	preliminary
	TASSO	TOF[74]	<1.1	
		Cerenkov[70]	<5	preliminary
K^0, $\overline{K^0}$	PLUTO	$K^0_S \to \pi^+\pi^-$[70]	all P	preliminary
	TASSO	" [75]	"	
p,$\bar{p}$	JADE	dE/dx[70]	<0.9	preliminary
	TASSO	TOF[74]	<2.2	
		Cerenkov[70]	<4	preliminary

In Fig. 31 the same quantity is plotted for $K^+ + K^-$ and $K^0 + \overline{K^0}$ production. Besides the PETRA data at 30 GeV measurements from 7.4 GeV[76] are shown also. For W = 30 GeV and $x < 0.1$ where $K^\pm$ data are available the $K^\pm$ and K^0, $\overline{K^0}$ yields appear to be the same. The K^0 data indicate a break in slope similar to that seen for the $\pi^\pm$ data. The curve in Fig. 31 is a hand drawn average through the high energy $\pi^\pm$ data (Fig. 30). The K yield is roughly a factor of 2 to 4 lower than the $\pi^\pm$ yield. Towards high x values the difference becomes smaller, i.e., the π and K yields approach each other.

In Fig. 32 the corresponding data are shown for $p + \bar{p}$ production. The data are rather scanty. The curve shows again the average of the $\pi^\pm$ data. Within the large error bars the K^0, $\overline{K^0}$ and the p,$\bar{p}$ yields appear to be the same. This rather large yield for p,$\bar{p}$ seems to be surprising.

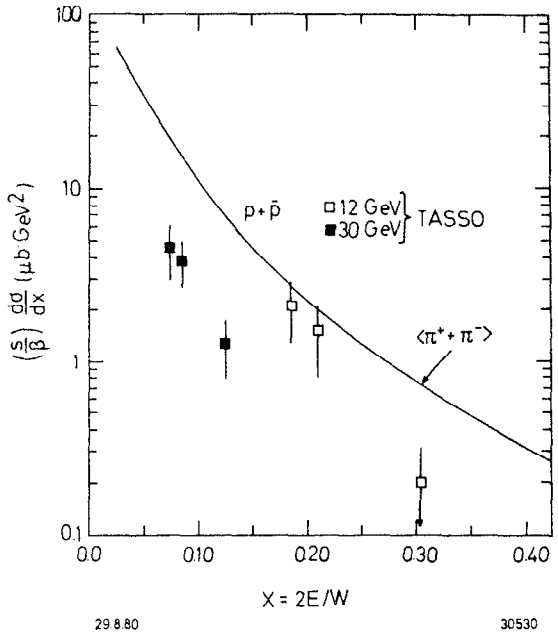

Fig.32 Same as Fig.30 for p + $\bar{p}$ production. (From Ref. 70).

Fig. 33 shows the relative fraction of $\pi^{\pm}$, $K^{\pm}$ and p,$\bar{p}$ as a function of particle momentum p at W = 30 GeV. The low momentum particles are basically all pions. As the momentum increases the fractions of $K^{\pm}$ and p,$\bar{p}$ rise, and for p ≈ 4 GeV/c there seem to be almost as many $K^{\pm}$ as $\pi^{\pm}$. An average event at W = 30 GeV has approximately 11 $\pi^{\pm}$, 1.4 K^{0}, $\overline{K^{0}}$, 1.4 $K^{\pm}$ and 0.4 p,$\bar{p}$ in the final state. Assuming that the number of n,$\bar{n}$ equals that of p,$\bar{p}$, out of 5 events two have a baryon antibaryon pair in the final state.

The number of K^{0}, $\overline{K^{0}}$ is a factor of 2 - 3 larger than observed in pp final states: at a c.m. energy of 24 GeV there are on the average 0.5 K^{0},$\overline{K^{0}}$ per event[77]. The excess of kaons in $e^{+}e^{-}$ annihilation is likely to be due to c and b quark contributions. Hence we may have had a first smell of primary quark flavours.

4.13 Summary

The dominant feature of $e^{+}e^{-}$ annihilation into hadrons is two jet production with the particle collimation becoming more pronounced as the energy increases. Concurrently with that a new phenomenon shows up at high energies which produces three-jet events. At 30 GeV roughly 5 - 10 % of the events have three distinct jets. The dynamic properties of these events as well as their rate is found to agree with hard gluon bremsstrahlung as predicted by QCD. The strong coupling constant, α_s, deduced from the data at 30 GeV has a value of 0.17 ± 0.02 ± 0.3.

The particle yield at large angles to the jet axes provided a first hint that quark and gluon may fragment differently into hadrons. An attempt was made to measure and interpret the acollinearity distribution between jets. Soft gluon emission combined with the effects of hadronization are able to describe the data.

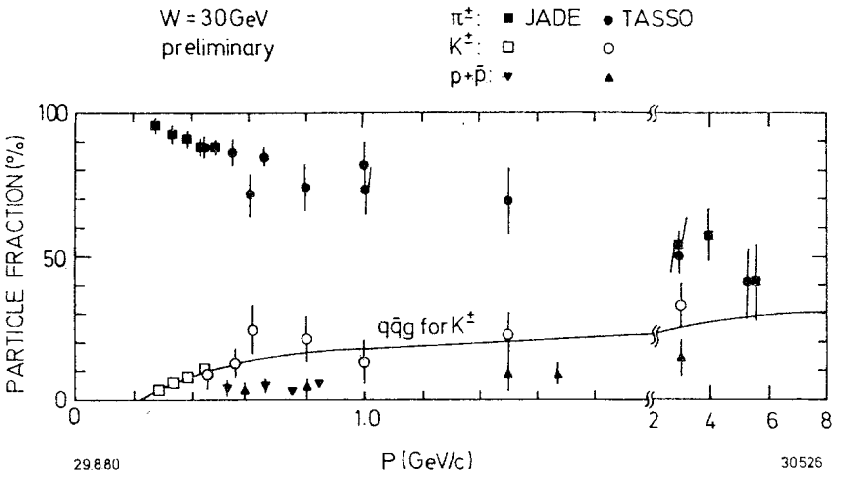

Fig.33 Charged particle fractions as a function of momentum. (From Ref. 70).

Acknowledgements: I am very grateful to Mrs E. Hell for her help with the manuscript.

List of References

1. R.F.Schwitters, rapporteur talk, 1975 Stanford Conference, p.5;
R.F.Schwitters et al., Phys.Rev.Lett. 35 (1975) 1320;
G.Hanson et al., Phys.Rev.Lett. 35 (1975) 1609

2. PLUTO-Collaboration, Ch.Berger et al., Phys.Lett. 78B (1978) 176

3. PLUTO-Collaboration, Ch.Berger et al., Phys.Lett. 82B (1979) 449

4. C.W.Darden et al., Phys.Lett. 80B (1979) 419;
W.Schmidt-Parzefall, 1978 Tokyo Conference, p. 260

5. K.J.Bienlein et al., Phys.Lett. 78B (1978) 360;
G.Heinzelmann, 1978 Tokyo Conference, p. 263

6. PLUTO group, data presented by S. Brandt at the 1979 EPS Conference, p. 338, and DESY-Report 79/41 (1979)

7. K.Koller and T.F.Walsh, Phys.Lett. 72B (1977) 227; 73B (1978) 504 and Nucl.Phys. B140 (1978) 449;
T.A. De Grand et al., Phys.Rev. D16 (1977) 3251;
S.J.Brodsky et al., Phys.Lett. 73B (1978) 203

8. K.Koller and H.Krasemann, Phys.Lett. 88B (1979) 119

9. B.H.Wiik, Proceedings of the Intern. Neutrino Conference, Bergen, Norway, June 1979, p. 113;
P.Söding, Proceedings of the EPS Intern. Conf. on High Energy Phys., Geneva, Switzerland, June-July 1979, p. 271;
TASSO.Conference, R.Brandelik et al., Phys.Lett. 86B (1979) 243

10. MARK J-Collaboration, D.P.Barber et al., Phys.Rev.Lett. 43 (1979) 830

11. PLUTO-Collaboration, Ch.Berger et al., Phys.Lett. 86B (1979) 418

12. JADE-Collaboration, W.Bartel et al., DESY-Report 79/80 (1979)

13. J.Kogut and L.Susskind, Phys.Rev. D9 (1974) 697, 3391;
A.M.Polyakov, Proceedings of the 1975 Intern. Symposium on Lepton and Photon Interactions at High Energies, Stanford, Aug. 21-27, 1975;
The first discussion on the experimental implications of gluon bremsstrahlung in e^+e^- annihilation was given by:
J.Ellis, M.K.Gaillard and G.G.Ross, Nucl.Phys. B111 (1976) 253 - erratum B130 (1977) 516;
T.A. De Grand, Yee Jack Ng, and S.-H.H. Tye, Phys.Rev. D16 (1977) 3251;
A. deRujula, J.Ellis, E.G.Florates and M.K.Gaillard, Nucl.Phys. B138 (1978) 387;
G.Kramer and G.Schierholz, Phys.Lett. 82B (1979) 102;
G.Kramer, G.Schierholz and J.Willrodt, Phys.Lett. 79B (1978) 249;
P.Hoyer, P.Osland, H.G.Sander, T.F.Walsh and P.M.Zerwas, DESY 78/21 (1978) to be published;
G.Curci, M.Greco and Y.Srivastava, CERN-Report 2632 (1979);
G.Kramer, G.Schierholz and J.Willrodt, DESY-Report 79/69 (1979)

14. see for example:
G.G.Hanson, 13th Rencontre de Moriond (1978), Vol. II, Gauge Theories and Leptons, edited by J.Tran Thanh Van and SLAC-PUB 2118;
B.H.Wiik and G.Wolf, Electron Positron Interactions, Springer Tracts in Modern Physics, Vol. 86 (1979);
G.Wolf, Lectures given at the 1979 CERN-JINR School, DESY-Report 80/13 (1980);
G.Flügge, Lectures given at the XIII Intern. Winter Meeting of Fund Phys., Spain, KF Karlsruhe Report KFK 2995 (1980);
G.Wolf, Invited talk, XI Intern. Symp. Multiparticle Dynamics Bruges, 1980, DESY Report 80/85 (1980)

15. T.Walsh, Talk given at the Vanderbilt Symposium on e^+e^- Interactions, 1980

16. R.D.Field and R.P.Feynman, Nucl.Phys. B136 (1978) 1

17. U.Timm, DESY-Report 80/70 (1980)

18. D.Cords, rapporteur talk at the 1980 Wisconsin Conference

19. J.D.Bjorken and S.J.Brodsky, Phys.Rev. D1 (1970) 1416

20. S.Brandt et al., Phys.Lett. 12 (1964) 57;
E.Fahri, Phys.Rev.Lett. 39 (1977) 1587

21. PLUTO-Collaboration, Ch.Berger et al., Phys.Lett. 78B (1978) 176

22. TASSO-Collaboration, R.Brandelik et al., Z.Physik C4 (1980) 87

23. see e.g. P.Darriulat, CERN Report EP/80-16 (1980), to be published in Ann. Rev. of Nucl. and Particle Science

24. M.Jacob, Lectures given at the 1979 JINR-CERN School

25. TASSO-Collaboration, R.Brandelik et al., Phys.Lett. 86B (1979) 243

26. PLUTO-Collaboration, Ch.Berger et al., Phys.Lett. 86B (1979) 418

27. JADE-Collaboration, W.Bartel et al., Phys.Lett. 91B (1980) 142

28. MARK J-Collaboration, D.P.Barber et al., Phys.Rev.Lett. 43 (1979) 830 and Phys.Lett. 89B (1979) 139

29. S.L.Wu and G.Zobernig, Z. Physik C2 (1979) 107

30. P.Hoyer, P.Osland, H.G.Sander, T.F.Walsh, and P.M.Zerwas, Nucl. Phys. B161 (1979) 349

31. A.Ali, E.Pietarinen, G.Kramer and J.Willrodt, DESY-Report 79/96 (1979), to be published

32. The Lund Monte Carlo, T.Sjöstrand, B.Söderberg, Lund-Report LU TP 78-18 (1978);
T.Sjöstrand, Lund Report LU TP-79-8 (1979)

33. R.D.Field and R.P.Feynman, Nucl.Phys. B136 (1978) 1

34. G.Altarelli and G.Parisi, Nucl.Phys. B126 (1977) 298

35. F.A.Berends and R.Kleiss, work to be published

36. MARK J-Collaboration, D.P.Barber et al., Phys.Lett. 89B (1979) 139

37. TASSO-Collaboration, R.Brandelik et al., Phys.Lett. 94B (1980) 437

38. S.Yamada, rapporteur talk at the 1980 Wisconsin Conference

39. V.Hepp, rapporteur talk, ibid.

40. K.Koller and H.Krasemann, Phys.Lett. 88B (1979) 119

41. J.Ellis, M.K.Gaillard and G.G.Ross, Nucl.Phys. B111 (1976) 253;
T.A.De Grand, Y.J.Ng and S.H.Tye, Phys.Rev. D16 (1977) 3251;
A.deRujula, J.Ellis, E.G.Florates, and M.K.Gaillard, Nucl.Phys. B138 (1978) 387

42. G.Kramer, G.Schierholz and J.Willrodt, Phys.Lett. 79B (1978) 249

43. J.Ellis and I.Karliner, Nucl.Phys. B148 (1979) 141

44. V.Hepp, talk presented at the 1980 Madison Conference

45. T.F.Walsh, talk presented at the 1980 Vanderbilt Symposium on e^+e^- Interactions, DESY Preprint

46. PLUTO Collaboration, Ch.Berger et al., Phys.Lett. 82B (1979) 449, and data presented by S.Brandt at the 1979 EPS Conference in Geneva, Vol. 1, 338

47. B.Anderson, G.Gustafson, Lund Preprint, LU TP 79-2 (1979); B.Anderson, G.Gustafson, Z. Physk C3 (1980) 223; B.Anderson, G.Gustafson, T.Sjöstrand, Lund Report LU TP 80-1 (1980); B.Anderson, G.Gustafson, C.Peterson, Nucl.Phys. B135 (1978) 273

48. W.Bartel and A.Petersen, DESY-Report 80/46 (1980) and S.Yamada, Ref. 38

49. Y.L.Dokshitzer, D.I.D'yakanov, S.I.Troyan, Phys.Lett. 78B (1978) 290

50. PLUTO-Collaboration, Ch.Berger et al., Phys.Lett. 90B (1980) 312

51. F.Halzen and D.M.Scott, Univ. of Hawaii and Univ. of Wisconsin preprint UH-511-379-80/UW-COO-881-130 (1980)

52. K.Kajantie and E.Pietarinen, DESY-Report 80/19 (1980)

53. R.Baier and K.Fey, Univ. of Bielefeld preprint BI-TP 80/10 (1980)

54. C.L.Basham, L.S.Brown, T.S.Ellis and S.T.Love, Phys.Rev. D17 (1978) 2298, and Phys.Rev.Lett. 41 (1978) 585; K.Konishi, A.Ukawa and G.Veneziano, Phys.Lett. 80B (1979) 259

55. S.Pandoulas, rapporteur talk at the 1980 Wisconsin Conference

56. C.Bacci et al., Phys.Lett. 86B (1979) 234

57. SLAC-LBL Collaboration, G.G.Hanson, 13th Rencontre de Moriond (1978), ed. by J.Tran Thanh Van, Vol. III

58. PLUTO-Collaboration, Ch.Berger et al., Phys.Lett. 81B (1979) 410; 78B (1978) 176

59. DASP-Collaboration, R.Brandelik et al., Nucl.Phys. B148 (1979) 189

60. JADE-Collaboration, W.Bartel et al., Phys.Lett. 88B (1979) 171

61. TASSO-Collaboration, R.Brandelik et al., Phys.Lett. 89B (1980) 418

62. PLUTO-Collaboration, Ch.Berger et al., DESY-Report 80/69 (1980)

63. W.Thomé et al., Nucl.Phys. B129 (1977) 365; see also the review by E.Albini, P.Capiluppi, G.Giacomelli, and A.M.Rossi, Nuovo Cimento 32A (1976) 101

64. Data given by R.Stenbacka et al., Nuovo Cimento 51A (1979) 63; see also S.Bashay, A.Fridman and P.Juillot, Phys.Rev. D15 (1977) 2702

65. M.Basile et al., CERB preprint (1980)

66. J.Ellis (private communication), motivated by W.Furmanski, R.Petronzio and S.Pokorski, Nucl. Phys. B155 (1979) 253

67. K.Zoba, H.B.Nielsen and P.Olesen, Nucl.Phys. B40 (1972) 317

68. see e.g. S.D.Drell, D.Levy and T.M.Yan, Phys.Rev. 187 (1969) 2159; D1 (1970) 1035, 1617, 2402

69. TASSO-Collaboration, R.Brandelik et al., Phys.Lett. 89B (1980) 418

70. D.Pandoulas, rapporteur talk at the 1980 Wisconsin Conference

71. DASP-Collaboration, R.Brandelik et al., Nucl.Phys. B148 (1979) 189

72. G.J.Feldman and M.L.Perl, Physics Reports 33 (1977) 285

73. R.Baier, J.Engels and B.Peterson, University of Bielefeld report BI-TP 79/10 (1979); W.R.Frazer and J.F.Gunion, Phys.Rev. D20 (1979) 147

74. TASSO.Collaboration, R.Brandelik et al., Phys.Lett. 94B (1980) 444

75. TASSO-Collaboration, R.Brandelik et al., Phys.Lett. 94B (1980) 91

76. V.Lüth et al., Phys.Lett. 70B (1977) 120

77. Dao et al., Phys.Rev.Lett. 30 (1973) 1151; Sheng et al., Phys.Rev. D11 (1975) 1733

Non-Conservation of Baryon Number*†

A. Zee††

Department of Physics, University of Pennsylvania
Philadelphia, Pennsylvania 19104

UPR-0151T 2/13/80

ABSTRACT

The possibility that baryon number may not be conserved is examined. We discuss the experimental and cosmological consequences of this possibility, emphasizing the various implications baryon number violation would have on our understanding of the physical world.

---

*Research supported in part by the U.S. Department of Energy under Contract No. EY-76-C-02-3071.

†Based in part on talks delivered at the 1980 Guangzhou Conference on Theoretical Particle Physics, at the 1979 Eastern Theoretical Physics Conference, at the 1980 SLAC Summer Institute on Particle Physics, at the 1980 DESY Grand Unification Workshop, and at a number of research institutions.

††Permanent address: Department of Physics, University of Washington, Seattle, Washington 98195

I. Symmetry in Physics

The possibility of proton decay has generated a great deal of interest over the last few years. In order to understand the significance of proton decay, we must view it in the proper physical and historical context. Thus, we will begin with an account of the rise and fall of symmetry in physics.[1] One major difference between the way physics is done in the 19th century and in the 20th century perhaps lies in the use of symmetries. Maxwell and his friends experimented with coils and magnets and distilled from their observations the correct equations of motions. It was not until later that Lorentz and others realized that Maxwell's Lagrangian possesses a deep symmetry of nature. It was Minkowski, apparently, who first recognized that one could reverse this chain of reasoning. By imposing the appropriate symmetry one could arrive at Maxwell's Lagrangian, from which then flows various experimental predictions. This profound shift in physicists' point of view towards symmetries has pervaded twentieth century physics. Minkowski's view apparently made a great impression on Einstein, who constructed a theory of gravity by imposing local coordinate invariance. Were one to follow the 19th century's line of attack, one would have to start with perihelion shift of mercury and the bending of light and construct a theory of gravity by adding successive corrections to Newton's theory. This can be, and has been, done.[2] But it is clearly more laborious and less elegant than imposing symmetries from the start. In this century, as physics become more abstract and complex, physicists have come to rely more and more on imposing a conjectured symmetry in their continued gropings for the fundamental laws of physics. Minkowski's view has now come to full flowering in the development of grand unified gauge theories of the non-gravitational interactions. For instance, by imposing SU(5) symmetry, Georgi and Glashow[3] wrote down a Lagrangian which predicts proton decay, probably the most stunning prediction of our times. (An even more extreme development in this direction is represented by supersymmetry and supergravity. These theories, however, do not appear to describe Nature. Perhaps that is because supersymmetry is not strongly motivated by experiment.)

Heisenberg introduced the concept of internal symmetry into physics by formulating the notion of isospin conservation. The implications of isospin conservation were developed by Cassen, Condon, Wigner and others. Nowadays, isospin conservation has lost some of its former aura and is regarded by particle physicists as almost an accident, more due to the smallness of the up and down quark masses compared to the hadronic mass scale than due to the smallness in the difference between the up and down quark masses. Why isospin proves to be such a good symmetry in nuclear physics is thus slightly mysterious after all. This question has recently been investigated.[4]

Beginning with isospin, physicists have explored larger and larger symmetries in the continuing search for the fundamental laws of Nature. Of course, these larger and larger symmetries are more and more badly broken so that their phenomenological manifestations are more and

more difficult to recognize. Nature appears to like symmetries deep down at heart but She also appears to enjoy breaking these symmetries. Perhaps the "reason" is that an exactly symmetric world is also a rather dull world. Feynman has commented that in his travels he has noticed that many architectural structures which at first glance look completely symmetrical are on closer inspection revealed to be in fact subtly asymmetrical. Architects appear to have a deep-seated need for both symmetry and asymmetry. The human face, with its slightly broken bilateral symmetry, furnishes another interesting example.

If what particle physicists have learned over the last two decades or so is to be summarized, one would probably have to say that the major lesson is that badly broken symmetries, provided they are softly broken, can be extremely useful. Understanding this point represents a tremendous advance; the older notion that only slightly broken symmetries are useful is too restrictive and not particularly illuminating. For example, one could always speculate on the breaking of almost any symmetry by a tiny term in the Lagrangian. In contrast, the concept of soft breaking, borrowed from the profound work of Ginsberg and Landau on superconductivity and developed by Gell-Mann, Levy, Nambu, Jona-Lasinio, and others, frees us to deal with badly broken symmetries and hence to explore physics at an energy scale beyond our grasp. Thus, the tremendously successful, but badly broken, SU(2) × U(1) symmetry of Glashow, Salam, and Weinberg[5] allows us not only to correlate all known weak and electromagnetic phenomena but also to master the physics on the scale of a few hundred GeV. In other words, the method of breaking symmetries softly so as not to mar the delicate structure of the theory and hence to destroy renormalizability, now known as the Higgs mechanism, allows us to at least discuss the physics of a mass scale much beyond our presently accessible mass scales. This freedom to discuss badly broken symmetries is perhaps one reason why physics is more interesting, to some people at least, than, say, architecture.

We are now faced with the dramatic possibility that Georgi and Glashow, with their SU(5) symmetry, have liberated us (or so say the enthusiasts) from our dreary existence among the debris of symmetry breaking to dream about the (hopefully) basic physics at 10^{16} Gev.

II. The Urge to Unify

In the long march towards a physical understanding of the world, we have finally reached the point of having a theory which, while it does not explain everything, is essentially consistent with all physical phenomena. This SU(3) x SU(2) x U(1) x Einstein theory is an amazing achievement indeed. (It is perhaps sobering to recall that the closest physicists have previously come to this situation is in the late nineteenth century, just before the specific heats of various substances were carefully measured at low temperatures. However, there were already some disturbing signs. For instance, the energy output of the sun was

certainly known to be inconsistent with the physics of the time. Possibly the most intrinsically disturbing sign of our times is the vanishing of the cosmological constant.)

In spite of, or perhaps because of, the success of the SU(3) x SU(2) x U(1) theory there are strong motivations to extend this theory to a grand unified theory. These include the desire (1) to understand charge quantization, (2) to have only one gauge coupling, and (3) to continue the trend towards unification started by Newton when he unified celestial physics with terrestrial physics.

We will now give the standard heuristic argument that grand unification tends (in general) to lead to proton decay. In a unified gauge theory based on a simple group the electric charge operator Q (being a generator of the simple group) must have zero trace. In other words, the electric charges of all the particles in a given representation must sum to zero. However, the charges of the known leptons (in a given family) sum up to $Q_\nu + Q_{\bar{e}} = -1 \neq 0$, while the charges of the known quarks (in a given family) sum up to $3(Q_u + Q_d) = 3(2/3 - 1/3) = +1 \neq 0$. It is difficult, on the other hand, not to notice that $-1 + 1 = 0$. Thus, if one is not allowed to invent fermions at will then one would have to put quarks and leptons into the same representation. It follows that there are gauge bosons transforming quarks to leptons and vice versa. In general, this leads to violation of baryon and lepton numbers. (We emphasize, however, that this heuristic argument certainly does not constitute a proof that grand unification necessarily leads to proton decay.[6])

An important point to note is that the grand unification mass scale is necessarily very high. This follows because (1) the strong, weak, and electromagnetic couplings, or more accurately, the SU(3), SU(2), and U(1) couplings, are very different at low energies, (2) according to renormalization group theory these couplings change with energy logarithmically slowly, and (3) thus one has to reach very high energies before the three couplings become equal. For the simplest SU(5) theory this mass scale turns out to be of order[7] 10^{15}Gev. This high mass scale in turn insures a very long life-time for the proton, consistent with the existing experimental limit of 10^{30} years. Thus, the first physical theory to predict an unstable proton also passes its first test: that of explaining the apparent stability of the proton. We will not discuss here all the other virtues of the simplest SU(5) theory; suffice it to say that this theory has a certain intriguing tightness and economy not shared by its competitors.

III. The Role of Exact Symmetries

Exact conservation of baryon number implies an exact symmetry in the Lagrangian. Now an exact symmetry can be either global or local.

While there is nothing in principle wrong with exact global symmetries, many people find them repugnant. For instance, if isospin is an exact global symmetry, then once the convention of defining which nucleon is the proton is

fixed at one point in space and time it is fixed throughout all space and time. To put it in another way, exact isospin symmetry means that the Lagrangian is invariant under an arbitrary notation of the proton state into the neutron state. But if isospin is an exact global symmetry, then the performance of a rotation here in the laboratory would require the performance of exactly the same rotation behind the moon. Mach, Einstein, and others were apparently quite disturbed by this requirement. (Think of rotational invariance, say. Does it imply that to leave the Lagrangian invariant one would have to rotate the whole Universe?) Considerations of this sort presumably led Einstein to formulate his general theory of relativity in 1915. Einstein's theory of gravity is the first theory to possess an exact local symmetry. This development inspired Weyl, in 1918-19, to try for a geometric theory of electromagnetism based on demanding invariance under a local change in the size or "gauge" of fields: $\psi \to (1 + \theta)\psi$. However, he did not insert the appropriate factor of i, a faux pas for which he could hardly be blamed considering that quantum mechanics was not invented till 1925. The factor of i was inserted by Fock and by London shortly after the invention of quantum mechanics, thus making gauge symmetry something of a misnomer for a phase symmetry.[8]

The central role of exact local symmetry in physics was thus established. The next important step was taken by Yang and Mills[9] in 1954 when they wrote down a Lagrangian with nonabelian gauge symmetry. The rest is history well known to us all. Thanks to a fascinating series of theoretical and experimental developments, we now believe that the strong, electromagnetic, weak, and gravitational interactions are all based on gauge symmetries.[10]

Viewed in this context, the notion of exact baryon conservation has long been puzzling to thinking physicists. For the reasons mentioned above, many people find it repugnant to think that proton stability is guaranteed by an exact global symmetry. On the other hand, if proton stability is based on an exact local symmetry, then there would be a massless gauge boson coupled to baryon number. As Lee and Yang[11] pointed out in 1955, the rather accurately known equality between inertial mass and gravitational mass, established by a series of experimenters starting with Bessel (1830), Eötvös (1889, 1922) and ending with Dicke et al. and Braginsky et al., implies a ridiculously small upper limit for the coupling of this massless gauge boson. Thus, the theoretical foundation of proton stability, already in the mid-fifties, appeared unsatisfactory to some people.

And so, when Pati and Salam[12] in 1973, Georgi and Glashow[3] in 1974, showed that the gauge principle when combined with notions on grand unification implies the decay of the proton, it meant, for many people, profound intellectual relief and satisfaction. A long-standing philosophical dilemma has been resolved.

Unfortunately, the actual calculated rate for proton disintegration is rather model-dependent and experiments designed to detect proton decay are by no means easy.

Several massive experiments[13] are now either under way or being constructed and we can only hope that the rate of proton decay is within the detectable range of these experiments. In any case, those who think philosophical and aesthetic prejudices are important in physics, and this author is amongst them, are already quite convinced that protons must decay.

It might also be mentioned that Pais[14] has suggested that exact baryon number conservation may be based on a spontaneously broken abelian gauge symmetry. However, this suggestion cannot be fitted into the framework of the SU(2) x U(1) gauge theory of electroweak interactions without generating anomalies which would spoil renormalizability.

IV. Why the Universe Is Not Empty

If baryon number is not conserved, then not only can baryons disappear, they could also appear. If protons will eventually die they could also have come into being in the early Universe. As pointed out by Yoshimura, Dimopolous and Susskind, Toussaint, Treiman, Wilczek, and Zee, Weinberg, and others[15], the interplay of three physical effects, (1) baryon number violation, (2) CP violation, and (3) disequilibrium in the early Universe could lead to a possible explanation of why the Universe contains matter at all.

The Universe is one vast emptiness, dotted here and there with a galaxy or two. With the discovery of the cosmic background radiation it has become possible to give a quantitative measure of this frightening[16] and almost inconceivable emptiness. By a variety of methods, it is possible to estimate, probably to within a factor of ten or so, the number density of baryons (protons and neutrons) in the Universe. The only possible dimensionless number one can consider is the ratio of the baryon number density n_B and the photon number density n_γ (which is rather accurately determined by the cosmic radiation measurements). This fundamental ratio n_B/n_γ turns out to be roughly[17] $10^{-9\pm1}$.

It is doubly remarkable that the Universe, while almost empty, is actually not empty: n_B/n_γ is small but definitely non-zero. It would appear that the very fact that we exist establishes the non-emptiness of the Universe. However, this statement requires some amplification and clarification.

Ever since Dirac's ideas about anti-matter were experimentally confirmed, people have speculated that the Universe has an equal amount of matter and anti-matter, segregated into domains. More precisely, it was asserted that all conserved quantum numbers of the Universe should be zero. In particular, since electric charge Q is known to be zero to a high degree of accuracy, it seems "aesthetically appealing" that baryon number B and lepton number L should also be zero. Unfortunately, the weight of observational evidence is against this supposition.[18]

If baryon number is absolutely conserved the small but non-zero matter content of the Universe is then simply a matter of initial conditions and its value presumably is a question outside the domain of physics. On the other hand, the non-conservation of baryon number opens up the exciting

possibility that the matter content of the Universe is actually something physicists can understand and hopefully even calculate.

The basic idea for explaining the matter content of the Universe is quite simple. It rests upon extrapolating the standard big-bang cosmology back in time, assuming the temperature becomes arbitrarily high or at least higher[19] than the grand unification mass scale of $\sim 10^{15}$ Gev. At that point, baryon number violating forces are comparable to the familiar interactions. (Thus, the proposed scenario depends on the baryon number violating interaction resulting from the exchange of heavy particles.) As the Universe cools, these forces become increasingly negligible and a net baryon number is generated, provided that a CP violation exists (at that time) which distinguishes matter from anti-matter.

It is also appealing that the small observed violation of CP in K-meson decay, which hitherto appears to have no connection with any other physical phenomena, may be after all intimately related to the non-emptiness of the Universe.

The subject is an active one, with a growing literature.[20] For further details we refer the reader to the papers cited[20]. Here we restrict ourselves to a few remarks.

(1) In the hot early Universe any net baryon number density will be quickly dissipated by baryon number violating forces. Thus, the initial condition "explanation" of the matter content of the Universe may be ruled out.

(2) Is it possible to actually calculate n_B/n_γ? Or failing that, is it possible to show, given the sign of CP violation in K-decay, that the Universe contains matter, rather than anti-matter? Unfortunately, the present state of the art does not allow us to answer these questions definitely. For instance, Barr, Segre, and Weldon[20] have shown that the simplest version of SU(5) theory with CP violation given by the Kobayashi-Maskawa mechanism[21] gives too small a value for n_B/n_γ but that the calculated value can be increased by complicating the Higgs sector. More detailed investigations have been carried out by Kolb and Wolfram.[20]

(3) Misner, Barrows, and Matzner[22] have shown that if the Universe started out in a chaotic state and subsequently smoothed itself out into a homogeneous isotropic state, the entropy per baryon would be much larger than the observed $n_\gamma/n_B \sim 10^9$. However, if n_γ/n_B is in fact determined by microphysics then one can no longer deduce from the observed value of n_γ/n_B that the Universe cannot have started in a chaotic state.[23] (It is remarkable that n_B/n_γ is a number which can be thought of as either very small or very large, and both views can be fruitful.)

(4) Since the formation of black holes may violate baryon number, one might think[24] that Hawking evaporation[25] of black holes may lead to the baryon asymmetry of the Universe, given the existence of CP violation. However, Toussaint et al.[15] showed that this is not the case unless baryon number is violated in the laws of physics.

Thus, it would appear that a rational explanation of the fact that the Universe is not empty would require baryon non-conservation. And so the enthusiasts amongst us would

argue that our very existence demands the decay of protons. Cooler minds, however, will insist that while proton decay implies baryon number non-conservation, baryon number non-conservation does not imply proton decay. Indeed, Segre and Weldon[27] have constructed an SU(5) theory with a stable proton but a non-conserved baryon number. The generation of baryon asymmetry in this model differs somewhat from the standard scenario.

We are indeed fortunate that we live in that epoch of the Universe after the birth of nucleons but before their eventual death. A physicist's logarithmic history of the world, assuming an open Universe, is shown in Fig. 1. We list on the right major events in the history of the Universe, and on the left various events of particular interest to humans. Time is plotted, on a logarithmic decay, starting with the Big Bang.

V. Proton Decay

We are now faced with a situation perhaps unprecedented in the history of physics. We have reasons to think that the "true" underlying physics occurs at a stupendous mass scale of order 10^{15} Gev while we live and explore at an energy scale of $\sim 10^{2}$ Gev amidst the debris of a smashingly broken symmetry. In the simplest version of SU(5) there is no new physics between 10^{2} Gev and 10^{15} Gev; between these two mass scales lies what Glashow has called a vast "desert." Many people find this scenario unpalatable; on the other hand, we must be reminded that while life may be linear,

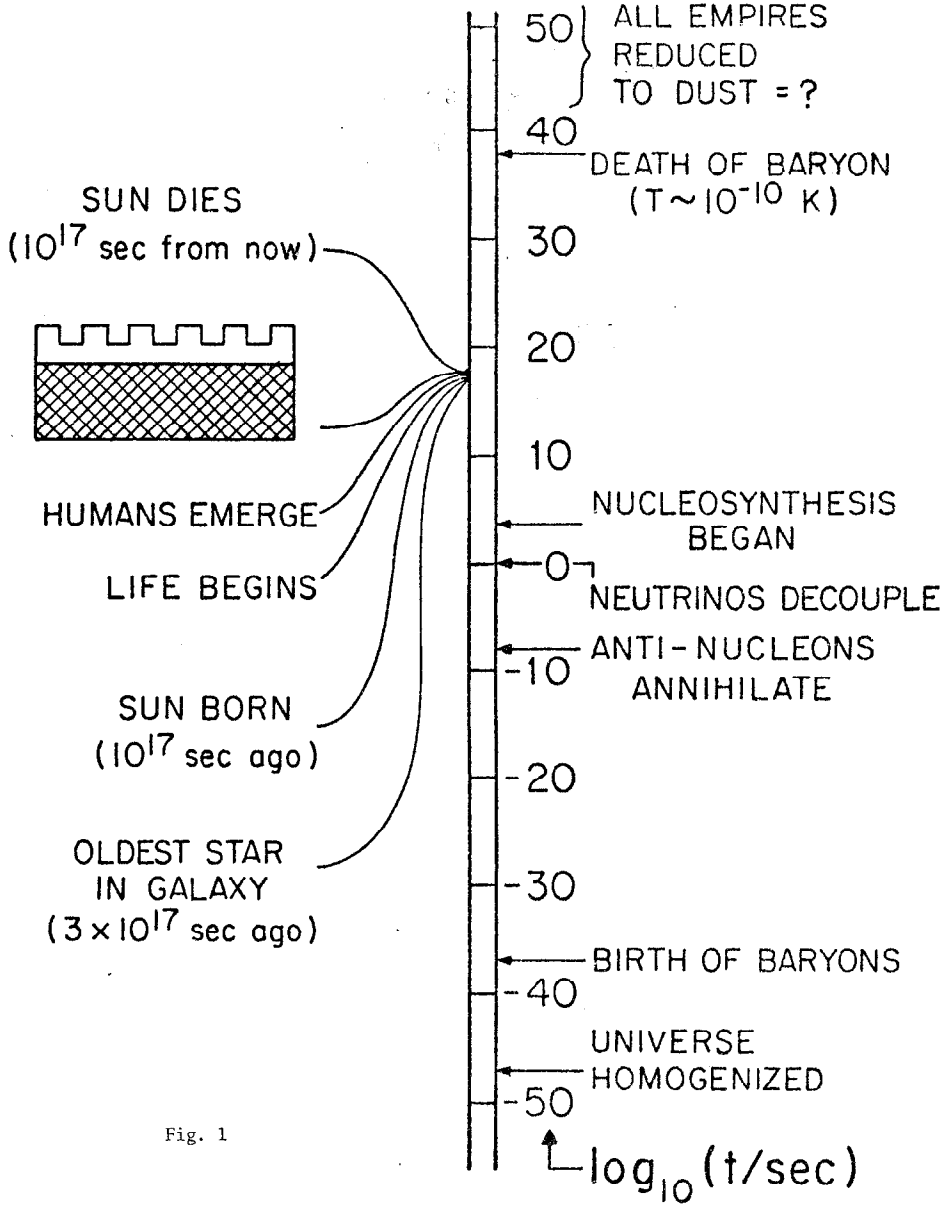

Fig. 1

physics tends to be logarithmic, as is evidenced by Fig. 1. We will come back to this issue later.

Perhaps amazingly enough, it is not hopeless for us to learn something about the physics at 10^{15} Gev. The neutral current parameter[7] $\sin^2\theta_w$, proton instability, and to a certain extent the early Universe[27] may all offer us a glimpse of grand unification physics.

In view of the far-reaching implications of the proton-decay experiments, it is clearly important to carry out a detailed phenomenological analysis[28,29] of the process. As is often the case in physics, it is appropriate to attack the problem from both sides. On the one hand, we would like to derive model-independent results in order to test the entire framework, rather than a specific model. On the other hand, we would also like to distinguish between competing models. A particularly accessible experimental signature which may allow us to distinguish between different models concerns the question of whether B-L (baryon minus lepton number) is conserved or not, or in other words, the question of whether the proton decays into a lepton (as in the mode $p \to \mu^-\pi^+\pi^+$) or into an anti-lepton (as in the mode $p \to \mu^+\pi^o$).

It turns out that a simple phenomenological analysis[28,29] is possible and proceeds as follows. We wish to construct an effective interaction Lagrangian to describe proton decay. Since the physics describing proton decay presumably occurs at a very large mass scale M_x (perhaps of order 10^{15} Gev) we could to a good approximation (to the extent that $M_w/M_x << 1$) treat SU(3) x SU(2) x U(1) as an exact symmetry. In other words, we could set $M_w = 0$. Theorists certainly think nothing of setting to zero the mass of a conjectured particle too massive yet to be discovered by experimentalists. The effective Lagrangian in question is to be constructed as a sum of operators formed out of quark and lepton fields (and possibly boson fields as well). The saving point is that we can restrict ourselves to operators of the smallest possible dimension. The reason is simply that operators of higher dimensions have to be multiplied by appropriately negative powers of masses so as to appear in the Lagrangian (which has mass dimension four, of course). However, M_w has been set to zero, and the only mass left in the game is M_x and so higher dimension operators are suppressed by powers of $1/M_x$. In order to form an operator transforming as a color singlet we must have at least three quark fields. In order to have a Lorentz scalar we must combine the three quark fields with another fermion field, either a lepton field or an anti-lepton field. The homework problem we assign ourselves is thus quite finite: find all Lorentz invariant four-fermion operators, either of the form $qqq\ell$ or of the form $qqq\bar{\ell}$, which transform as SU(3) x SU(2) x U(1) singlets and which violate baryon number. This is in fact analogous to the problem which Fermi[30] assigned himself and which he solved[31] in 1934: find all Lorentz invariant four-fermion operators which transform as singlets under the symmetry of 1934, namely the electromagnetic U(1).

The possible operators can be found readily. In the simplest case of including only one generation of quarks and

leptons, there exist only four operators. The Lorentz properties of two of these are such that they could arise from the exchange of a vector boson. The other two are such that they could arise from the exchange of a scalar boson. We will refer to these operators as vector and scalar respectively, in analogy to the famous SPVAT classification.

Physical consequences follow upon inspection of the list of operators.

(1) These operators all conserve B-L. Thus, B-L is conserved to lowest order in M_W/M_X, quite independent of model. In other words, any violation of B-L must be proportional to the breaking of SU(2) x U(1).

(2) $\Delta S \geq 0$ in proton decay.

(3) If the two vector operators dominate (as would be the case if Higgs exchange is suppressed because Higgs are composite and/or more massive than gauge bosons) further predictions follow. This is because the two vector operators involve oppositely polarized lepton fields and because the two vector operators have definite transformation properties under strong isospin. Therefore, predictions can be made concerning the polarization of the μ^+ in proton decay (which is said to be experimentally accessible). Also, isospin-like relations between different decay modes, such as between $0^{16} \to e^+X$ and $0^{16} \to \bar{\nu}X$, can be derived. These relations depend on the relative admixture of the two vector operators. It is at this point that model dependence comes in. The precise relative admixture can of course be determined in specific models such as SU(5), SO(10), etc. (The actual phenomenological value is subject to renormalization[32] down to 1 Gev from $\sim 10^{16}$ Gev). If the day should come when the world has witnessed hundreds of events of proton decay, these relations will help us to distinguish between competing models.

VI. Conservation or Violation of B-L

We learned in the last section that B-L is effectively conserved to a high degree of accuracy if no new physics exist between M_W and M_X. Thus, the observation of B-L violation in proton decay would have far-reaching implications bearing on the question of whether or not "oases" exist in Glashow's desert. Put another way, the theorem from the last section only states that B-L is conserved to order M_W/M where M is the next mass scale in the theory; with the existence of oases, M may be much lower than 10^{15} Gev.

Now that we have convinced ourselves that B and L are both violated, are we to let B-L stand as the last citadel upholding the notion of exact non-gauged symmetry. We have argued against, and Nature appears to abhor, exact symmetries which are not gauged; the only symmetries we know to be exact to a high degree of accuracy are color and electric charge. so, let us press onward and violate B-L.

We would do well by first examining some specific models. In the simplest and original version of SU(5), B-L turns out to be conserved exactly. This result can be traced back to the fact that with the minimal choice of Higgs fields the allowed Yukawa terms are so few that the Lagrangian ad-

mits a global U(1) symmetry. The global U(1) is broken by the Higgs vacuum expectation value which also breaks the SU(5) gauge symmetry (of course). However, it is clear that some linear combination of the global U(1) and a U(1) subgroup of SU(5) remains unbroken; this combination turns out to be none other than B-L. Thus, exact B-L conservation in this theory appears more or less "accidental" and in general would fail if additional Higgs fields are introduced.

The simplest choice[33] is a ten-dimensional Higgs field. The additional couplings allowed by the gauge symmetries remove the global U(1) symmetry. Decays changing B-L by two units, such as $n \to \mu^- K^+$, $p \to \mu^- K^+ \pi^+$, can now proceed. A characteristic prediction is that B-L violation in nuclear decay is accompanied by a strange particle. (One can in fact show[33] that this result is independent of the specific model under discussion by extending the analysis in the previous section to include dimension seven operators.) We should emphasize that the violation of B-L discussed here is quite consistent with the theorem derived in the previous section: the violation of B-L can indeed be computed in this specific model to be proportional to M_W but the mass M_W appears not divided by the grand unification mass but by the mass of the ten-dimensional Higgs.

The actual magnitude of B-L violation is beyond our present ability to predict; however, it can be shown that, with "reasonable" choice of parameters, one can have the B-L violating amplitude overwhelm the B-L conserving amplitude in proton decay.

Thus, while the observation of B,L violating nucleon decay would be most exciting, the observation of B-L violating and B,L violating nucleon decay would be doubly exciting. It might mean that "oases" exist in Glashow's desert. In our specific model, the "oasis" is none other than the additional Higgs structure.

Should proton decay violate B-L by two units, an amusing implication for the final state of an open Universe follows. Presumably, at the high temperatures when baryons were generated SU(2) x U(1) symmetry was restored and B-L was an exact symmetry. Thus, a universe born with all quantum numbers equal to zero would have $n_B = n_L$ in maturity, but could end up in old age with a net lepton number density if proton decay violates B-L.

With the violation of B-L all sorts of exotic processes, such as neutrino Majorana mass, and neutrinos oscillating into antineutrinos, all become possible.[35] A simple phenomenological way of incorporating these processes is to complicate the Higgs sector of the theory. Observation of these procedures would also shed important light on the questions discussed here.

VII. Unsolved Problems in Grand Unification

To conclude, the idea of grand unification liberates us from our dreary existence amidst the debris of symmetry breaking, freeing us to dream about the "true" physics at 10^{16} Gev in a magnificent leap of imagination probably unprecedented in the history of physics. Over the last few

years, the successful calculation of $\sin^2\theta_w$ and the possibility of explaining the content of the Universe have bolstered the believers of grand unification in their faith. Viewed in this context, the observation of proton decay would be most significant.

However, in our enthusiasm we should not be blind to the problems. To begin with, the present theory is only consistent with all physical phenomena; much remains to be explained. In particular, almost none of the physically interesting quantities can be calculated from first principles. There is of course also the matter of finding the correct grand unifying group and theory. We list here some outstanding conceptual problems, whose solution might help us in our search for the correct grand unifying theory.

(1) The breaking of grand unification symmetry and of SU(2) x U(1) symmetry apparently occur at vastly different mass scales. In the context of the Higgs mechanism, this implies vastly different vacuum expectation values, a situation which cannot be arranged "naturally" and which is unstable with respect to radiative correction. This is the so-called hierarchy problem.[36]

(2) Perhaps not unrelated to the hierarchy problem is the problem of dynamical symmetry breaking, about which nobody has anything substantial to say so far. A very interesting approach involves the concept of technicolor[37], which unfortunately generates additional problems. Technicolor may be an oasis in Glashow's desert. It should be noted that a theory without explicit Higgs fields typically possesses a number of global symmetries if fermions are assigned to several irreducible representations. Thus, any dynamical symmetry breaking scheme must address the problem of what to do with the multitude of Nambu-Goldstone bosons which would appear upon symmetry breaking.

(3) With spontaneous symmetry breaking, be it dynamical or due to explicit Higgs fields, there will in general be an energy (density) difference between the symmetric vacuum and the broken vacuum. This energy (density) of condensation appears as a cosmological constant in the presence of gravity.[38] If we normalize the energy scale so that the symmetric vacuum has zero energy then the cosmological constant would be enormous, of the order of the fourth power of a typical Higgs mass. This is surely the largest discrepancy between an observed value and a calculated value in the history of physics. We are of course faced with this problem even without grand unification, but grand unification exacerbates the situation. Does grand unification have anything to do with gravity?[39] How can we insure a phase transition with no latent heat?[40]

(4) The hierarchy of fermion masses is also difficult to explain.[41]

(5) Perhaps closely related to the above is the so-called family problem. Rabi's famous question, "Who ordered the muon?" has been escalated in our times to the puzzling question "Why does Nature repeat Herself, so needlessly and tediously?" To construct the physical world as we know it, only the first family of quarks and leptons is apparently

necessary. Cosmologists claim to have an upper bound on the number of different massless neutrinos. But perhaps neutrinos have small masses, increasing with each generation. Recently, people have begun to try to comprehend Nature's extravagance.

(5a) The simplest approach is to merely incorporate the repetitive structure phenomenologically, without any attempt to understand its origin. The idea is to introduce a so-called horizontal gauge symmetry under which the families transform into each other. One hopes to obtain relations between masses and mixing angles.[42] Some of the results obtained so far appear to be encouraging, but the approach suffers from a great deal of arbitrariness.

(5b) A more dynamical approach, proposed by Georgi[43], starts with an SU(N) gauge theory with N greater than five and with fermions assigned to some anomaly-free set of representations. The SU(N) gauge symmetry is supposed to break down to an SU(5) symmetry with the actual breaking mechanism unspecified. A plausible dynamical assumption is made that all fermions allowed to have SU(5)-invariant masses get masses of the order of 10^{15} GeV. The observation that there are no bare fermion mass terms in the standard SU(3) x SU(2) x U(1) and SU(5) theories provides the empirical basis for this assumption. In this way, one can, for a given initial choice of group and representations, determine how many generations of light fermions emerge at low energies.

(5c) A rather promising approach utilizes the spinorial representations of orthogonal groups. One aesthetically displeasing feature of the SU(5) theory is that fermions in each generation are assigned to two irreducible representations, a $\bar{5}$ and a 10. It seems reasonable to expect that in a truly unified theory all fermions should belong to a single irreducible representation. The SO(10) theory represents a slight improvement over SU(5) in this respect: at the cost of introducing a neutral lepton field for each generation, one can put all the fermions of a given generation in a single 16-dimensional spinorial representation. (In general, neutrino Majorana masses are induced as a result.[44]) However, the existence of families is still accommodated by merely having the 16-dimensional representation repeated. Now the spinorial representation of SO(2n) has dimension 2^{n-1}, in contrast to the tensor representation (of unitary and orthogonal groups) whose dimensions only increase like a power, rather than exponentially, with the rank of the group. Thus, we might imagine putting[45,46] all fermions into a single spinorial representation of some SO(2m+10) gauge theory which breaks down into an SO(10) theory. The 2^{m+4} dimensional representation of fermions would then decompose into 2^m spinors of SO(10). The outstanding virtue of this proposal is of course that the repetitive structure of fermion families emerges guaranteed by the mathematics. The number of families is determined to be a power of two: if we believe the cosmologists, there are four families. Unfortunately for this scheme, it turns out that only half of the 2^m spinorial representations have V-A weak interactions, the other half having V+A weak interactions. Perhaps the theory

is right after all: these V+A fermions may just have been too heavy to be seen. One (rather unnatural) approach[4] is to simply push up the masses of the unwanted fermions by the Higgs mechanism. A more interesting approach[45] invokes technicolor to confine the unwanted fermions.

This concludes our list of difficult problems. One wonders how many of these problems will have been solved, or at least will have been argued to be irrelevant, by the end of this decade just dawning on us. Most likely, the real problems are not even on this list. With this standard piety we come to the end of our brief survey of some of the issues debated by particle physicists today. It is remarkable and exciting that we are now talking about energy scales fourteen orders of magnitude beyond our experience and discussing issues which only a few years ago were thought to be outside the domain of physics.

Acknowledgment

We are grateful to many colleagues for discussions over the years, but most particularly to our frequent collaborator, Frank Wilczek. Much of what is described here is based on work done with him.

References

(This list of references is obviously not meant to be complete.)

1. Symmetries in physics are discussed in books by Weyl, Yang, and Sakurai. Our account follows closely a recent article of C. N. Yang (CERN preprint 1979).
2. D. Boulware and S. Deser, Ann. of Phys. 89, 193 (1975).
3. H. Georgi and S. L. Glashow, Phys. Rev. Letters 32, 438 (1974).
4. See e.g., P. Langacker and D. Sparrow, Phys. Rev. Letters 43, 1101 (1979).
5. S. Glashow, Nucl. Phys. 22, 579 (1961); S. Weinberg, Phys. Rev. Lett. 19, 1264 (1967); A. Salam and J. Ward, Phys. Lett. 13, 168 (1964).
6. In fact, for examples of grand unified theories which admit a stable proton, see P. Langacker, G. Segre, A. Weldon, Phys. Lett. 73B, 87 (1978); Phys. Rev. D18, 552 (1978); G. Segre and A. Weldon, Penn preprint 1980. However, these models always involve an imposed global symmetry.
7. H. Georgi, H. Quinn, S. Weinberg, Phys. Rev. Lett. 33, 451 (1974).
8. The brief account, which follows Yang (Ref. 1) is certainly not meant to be historically complete.
9. C. N. Yang and R. Mills, Phys. Rev. 95, 631 (1954); Phys. Rev. 96, 191 (1954).
10. For a review see for example E. Abers and B. Lee, Phys. Reports 9C, 1 (1973); D. Gress, in Methods in Field Theory, ed. by R. Balian.
11. T. D. Lee and C. N. Yang, Phys. Rev. 98, 1501 (1955).
12. J. Pati and A. Salam, Phys. Rev. D8, 1240 (1973); D10, 275 (1974).
13. In the U.S., a University of Pennsylvania experiment is now under way in the Homestake Gold Mine in South Dakota, and a Brookhaven-Irvine-Michigan experiment is planned for the Morton Salt Mine outside of Cleveland. There are also experiments planned in Europe. These are notably inexpensive experiments, and may be well-suited for countries such as China. The total integrated cost of the Pennsylvania experiment will run to a few x 10^5 U.S. $ (which incidentally is of the same order as the

the profit of the Homestake Mining Company per day with the present price of gold.)

14. A. Pais, Phys. Rev. (1973).

15. A. D. Sakharov, ZhETF Pis'ma 5, 32 (1967); M. Yoshimura, Phys. Rev. Lett. 41, 281 (1978), 42, 746(E) (1979); S. Dimopolous and L. Susskind, Phys. Rev. D18, 4500 (1978); D. Toussaint, S. Treiman, F. Wilczek, A. Zee, Phys. Rev. D19, 1036 (1979); S. Weinberg, Phys. Rev. Lett. 42, 859 (1979).

16. "Le silence éternel de ces espaces infinis m'effraie" - Pascal.

17. For a discussion and references, see e.g., S. Weinberg, Gravitation and Cosmology, Wiley.

18. G. Steigman, Ann. Rev. of Astron. and Astrophys. 14, 339 (1976).

19. It has been noted that 10^{15} Gev is roughly the kinetic energy of a typical bus. Thus, during this epoch of the Universe, to be hit by even a single proton is no laughing matter.

20. The literature includes M. Yoshimura, preprints. J. Ellis, M. K. Gaillard, and D. V. Nanopoulos, Phys. Lett. 86B, 360 (1979), 82B, 464(E) (1979); S. Barr, G. Segre and H. Weldon, to be published; D. Nanopoulos and S. Weinberg, to be published; A. Yildiz and P. Cox, to be published; A. Yu. Ignatiev et al., Phys. Lett. 87B, 114 (1979); M. S. Turner and D. Schramm, Nature 279, 303 (1979); E. W.Kolb and S. Wolfram, Caltech preprint. We recommend especially the paper by Kolb and Wolfram which exposes the weak points of some previous analyses.

21. M. Kobayashi and K. Maskawa, Prog. Theor. Phys. 49, 652 (1973).

22. C. W. Misner, Astrophys. J. 151, 431 (1968); J. D. Barrow, Nature 272, 211 (1978) and references therein.

23. M. Turner, Nature 281, 549 (1979); S. Bludman, private communication.

24. S. Hawking, Nature 248, 30 (1974); Comm. Math. Phys. 43, 199 (1975).

25. S. Hawking, as cited in B. J. Carr, Astrophys. J. 206, 19 (1976).

26. G. Segre and A. Weldon, to be published.

27. Besides baryon asymmetry see the recent work on monopoles in the early Universe. J. P. Preskill, Phys. Rev. Lett. 43, 1365 (1979); A. Guth and H. Tye, SLAC preprint 1979; M. Einhorn, D. L. Stein and D. Toussaint, preprint.

28. The analysis described here is due to S. Weinberg, Phys. Rev. Letters 43, 1571 (1979).

29. Several issues of great practical importance such as that of pion propagation through nuclei, are not touched on here. They have been investigated by D. Sparrow, preprint, C. Dover and L. L. Wang, preprint. A specific SU(5) analysis was performed earlier by M. Mahacheck, preprint.

30. E. Fermi, Z. Physik 88, 161 (1934).

31. Actually, his solution is incomplete. G. Gamow and E. Teller, Phys. Rev. 49, 895 (1936).

32. F. Wilczek and A. Zee, Ref. 3. J. Ellis, M. Gaillard and D. Nanopoulos, CERN preprint.

33. This section is based on F. Wilczek and A. Zee, Phys. Lett. 88B, 311 (1979). Similar remarks have been made by S. Glashow, HUTP-79 (A029).

34. H. Georgi, S. Glashow, S. Weinberg, private communication.

35. A. Zee, Penn preprint UPR-0150T.

36. E. Gildener, Phys. Rev. D14, 1667 (1976); S. Weinberg, Phys. Lett. 82B, 387 (1979); K. T. Mahanthappa, M. A. Sher, and D. G. Unger, Phys. Lett. 84B, 113 (1979). For a recent attempt to solve the problem, see T. P. Cheng and L. F. Li, to be published.

37. S. Weinberg, Phys. Rev. D13, 974 (1976); L. Susskind, Phys. Rev. D20, 2619 (1979).

38. M. Veltman, unpublished. J. Dreitlein, Phys. Rev. Lett. 33, 1243 (1974).

39. A. Zee, Phys. Rev. Letters 42, 417 (1979); L. Smolin, Nucl. Phys. B160, 253 (1979); S. L. Adler, IAS preprint 1980.

40. At the moment, the only glimmer of a hope involves supersymmetry and supergravity.

41. For a recent attempt in the context of grand unification, see S. Barr, to be published.

42. For a construction involving SU(3) x SU(2) x U(1) x SU(2) see F. Wilczek and A. Zee, Phys. Rev. Letters 42, 421 (1979). For a discussion at the grand unification level involving SU(5) x SU(2) see M. Gell-Mann, P. Ramond, and R. Slansky, Caltech preprint.

43. H. Georgi, Nucl. Phys. B156, 126 (1979); P. Frampton and S. Nandi, Phys. Rev. Lett. 43, 1460 (1979); J. Chakrabarti, M. Popovic, R. Mohapatra, CCNY preprint 1979.

44. M. Gell-Mann, P. Ramond, R. Slansky, unpublished; E. Witten, Harvard preprint.

45. M. Gell-Mann, P. Ramond, R. Slansky, unpublished.

46. F. Wilczek and A. Zee, preprint 1979.

NEUTRINO INSTABILITY

Henry W. Sobel, Frederick Reines, Elaine Pasierb

Presented by Henry W. Sobel

Department of Physics
University of California
Irvine, California 92717

Introduction

We have obtained indications of neutrino instability from our data on the processes:

$$\bar{\nu}_e + d \longrightarrow \begin{cases} n + n + e^+ & \text{(charged current)} \\ n + p + \bar{\nu}_e & \text{(neutral current)} \end{cases}$$

Although the deuteron reaction is not the ideal way to search for neutrino oscillations, it has a number of attractive features which allow us to side step many of the problems currently inherent in reactor neutrino studies. The reactor is a good source since it provides a very intense (2×10^{13} $\bar{\nu}_e cm^{-2} sec^{-1}$) pure source of $\bar{\nu}_e$'s at low energies (<10 MeV). The difficulty has been the uncertainty in the $\bar{\nu}_e$ spectrum.

Reactor Neutrino Experiments

The Reactor as a Neutrino Source

A power reactor produces neutrinos from the fission of ^{235}U, ^{238}U and ^{239}Pu. The neutrino spectrum of each component is different (Fig. 1). At the Savannah River Project (SRP) reactor where we work, ^{239}Pu produced less

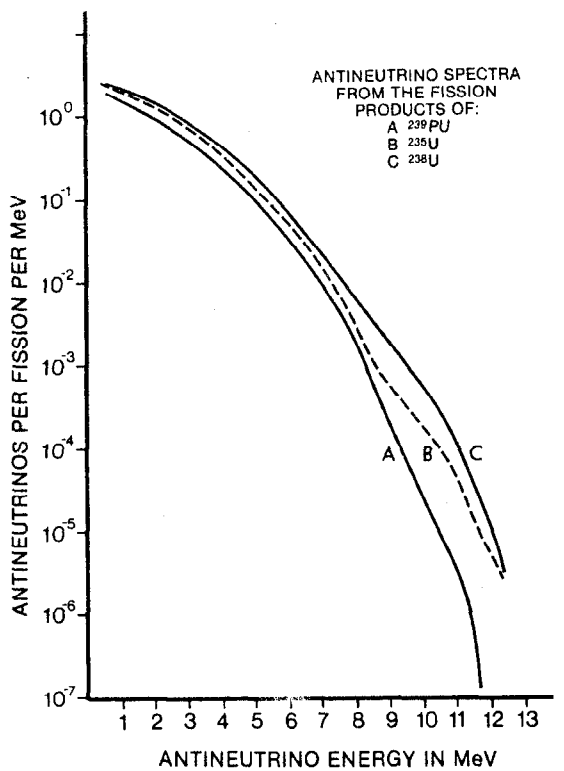

Fig. 1. Antineutrino spectra from fission products.

than 8% of the fissions during our experiment, and ^{238}U produced less than 4%. At the Grenoble reactor all the fissions come from ^{235}Pu.

Neutron activation of the reactor surroundings can also produce $\bar{\nu}_e$'s but they are less than $\sim$1.3 MeV.[1] Neutrino production in this mode is also possible with $\nu_e/\bar{\nu}_e \simeq .0005$ and $E_{\nu_{max}} = 0.8$ MeV.[2] Experimentally, the ratio $\nu_e/\bar{\nu}_e$ has been determined to be <0.02.[3]

The antineutrino spectrum itself is calculated by adding up the beta decay spectrum of all the fission products. Unfortunately, approximately 30% of the fission products involve unknown decay schemes, and as a consequence, the neutrinos from these decays require extrapolation and modeling. The two newest theoretical predictions for the antineutrino spectrum are shown in Fig. 2. They disagree to a level of about 30% depending on $\bar{\nu}_e$ energy.

$\bar{\nu}_e + p \rightarrow n + e^+$ Experiments

The inverse beta decay reaction has been studied in several different experiments and new experiments are being built. The data so obtained can be used in several ways.

1. Since the e^+ takes essentially all of the $\bar{\nu}_e$ energy in the reaction, a measurement of the e^+ spectrum determines the $\bar{\nu}_e$ spectrum. This neutrino spectrum can be used as input in other experiments.

2. The process can be used to study neutrino oscillations.

a. Experimental results can be compared with theoretical prediction: This technique suffers from the uncertainty in the predicted neutrino spectrum in that any

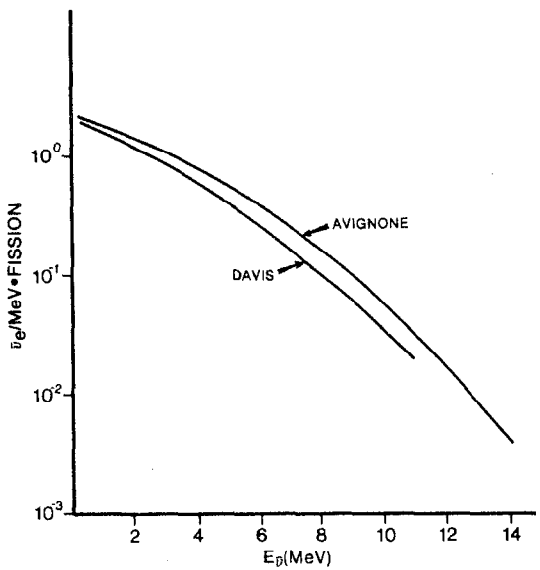

Fig. 2. Predicted $\bar{\nu}_e$ spectrum.

observed discrepancies can be attributed to that source.

b. We can compare the results of different detectors at various source to detector distances: These data are just beginning to be available in the required precision and analysis is incomplete.[4]

c. We can compare the results of the same detector taken at different distances: This clearly is the experiment of choice and two groups are actively pursuing this technique.

There are three data sets available at this time. They are the 6.5 meter data of Nezrick and Reines,[5] the 11.2 meter data of Reines, Gurr, and Sobel,[6] and the 8.7 meter data of the C.I.T.-Grenoble-Munich group.[7] Within one year, additional data are expected from a 38 meter point with the C.I.T.-Munich detector at a 2700 MW reactor near Zurich, a mobile detector at the SRP reactor which will span a 12 to 35 meter distance,[8] and a single point at 15.4 meters from the SRP reactor by a G.I.T.-U.S.C. group.[9]

Results from the 11.2 meter data are given in Fig. 3 and compared with the predicted positron spectrum of Avignone et al and Davis et al. We note that the observed data agree with the Davis prediction at β^+ energies $\gtrsim 2$ MeV but diverge below the prediction at higher energies.

All three experiments are compared in Table I. We list the ratio of the observed rates to those predicted by the Avignone and Davis spectra. In order to interpret these results in terms of neutrino oscillations we assume a simple two neutrino case.

Two Neutrino Approach

In this case a physical neutrino can be written as a

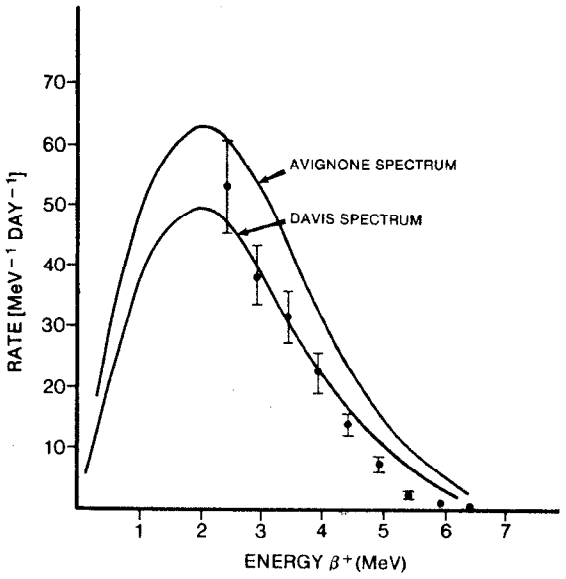

Fig. 3. 11.2 meter data from $\bar{\nu}_e + p \rightarrow n + e^+$.

super-position of two pure states, i.e.:

$$\bar{\nu}_e = \nu_1 \cos\theta + \nu_2 \sin\theta$$

and $$\bar{\nu}_{\mu/\tau} = -\nu_1 \sin\theta + \nu_2 \cos\theta$$

where θ is the mixing angle. Then, the probability of finding a $\bar{\nu}_\mu$ (or $\bar{\nu}_\tau$) at time t, given that we started with a $\bar{\nu}_e$ is:

$$\text{Prob.} = |a(t)|^2 = \tfrac{1}{2}\sin^2 2\theta \left[1 - \cos \frac{(\Delta)(t)}{2E_\nu \hbar}\right]$$

where $\Delta = |m_1^2 - m_2^2|c^4$, and the oscillation length

$$\lambda(m) = \frac{2.5E_\nu(\text{MeV})}{\Delta(\text{eV}^2)} \quad .$$

For $\bar{\nu}_e$ sensitive experiments, the ratio of counting rates with and without oscillations is given by:

$$R(d) = 1 - \tfrac{1}{2}\sin^2 2\theta \left[1 - \frac{\int N(E_\nu)\sigma(E_\nu)\cos(\frac{\Delta\, d}{2c\hbar E_\nu})\,dE_\nu}{\int N(E_\nu)\sigma(E_\nu)\,dE_\nu}\right]$$

where d = distance from source to detector

$N(E_\nu)$ = Neutrino flux

and, $\sigma(E_\nu)$ = Reaction cross section.

We can plot R(d) as a function of $\Delta \cdot d$ using $\sin^2 2\theta$ as a parameter for a particular process and energy interval. The result is a family of curves which can be used to imply Δ for any distance, d. In Fig. 4 for example, we plot such a family for the $\bar{\nu}_e + p$, charged current proton (ccp), reaction with a neutrino energy greater than 6.0 MeV. If we now use the Table I value $0.42 \pm .09$ (11.2 meters, $E_\nu > 6.0$ MeV, Avignone spectrum), Fig. 4 gives, for $\sin^2 2\theta = 1$, $\Delta = .42 \pm .04$ eV^2 and $\Delta = 1.1 \pm .05$ eV^2. We can con-

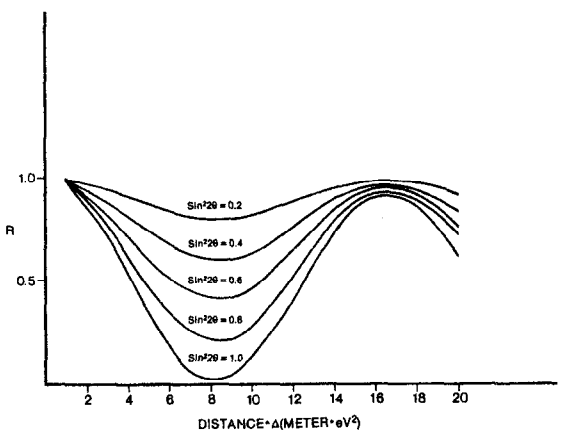

Fig. 4. R as a function of distance times Δ for ccp and $E_\nu > 6.0$ MeV.

Table I. Comparison of inverse beta decay results. The ratio of observed/predicted rates are tabulated.

Distance from Core Center (Meters)	Reaction	Neutrino Detection Threshold (MeV)	Ratio	
			Avignone Spectrum	Davis Spectrum
11.2	ccp	4.0	.68 ± .12	.88 ± .15
11.2	ccp	6.0	.42 ± .09	.58 ± .12
6	ccp	1.8	.65 ± .09	.84 ± .12
6	ccp	4.0	.81 ± .11	1.02 ± .15
8.7	ccp	3.0	.68 ± .15	.87 ± .14

tinue this procedure and generate a plot of Δ vs. $\sin^2 2\theta$, showing a region allowed by this measurement at the one standard deviation level (Fig. 5). Using the same data, if we compare instead to the Davis spectrum we get an allowed region shown in Fig. 6.

From this we can see that the conclusions we reach with this technique depend very strongly on the spectrum we use for comparison.

The Deuteron Experiment

As part of our reactor program, we have been studying the neutral current reaction,[10]

$$\bar{\nu}_e + d \rightarrow n + p + \bar{\nu}_e \quad \text{(ncd)}$$

and its charged current counterpart

$$\bar{\nu}_e + d \rightarrow n + n + e^+ \quad \text{(ccd)}$$

We have recently realized that this experiment could be used as a neutrino oscillation test. The neutral current branch is independent of ν type, while the charged current branch will only occur for incident $\bar{\nu}_e$'s. In addition, while the predicted rates of the individual branches are sensitive to the predicted neutrino spectrum (Fig. 7), the ratio of the predicted rates is not (Table II).

We choose to define the quantity:

$$R = \frac{\left(\frac{ccd}{ncd}\right)_{\text{experiment}}}{\left(\frac{ccd}{ncd}\right)_{\text{predicted}}} .$$

The denominator of this quantity has the following features:

1. It is independent of the reactor neutrino absolute

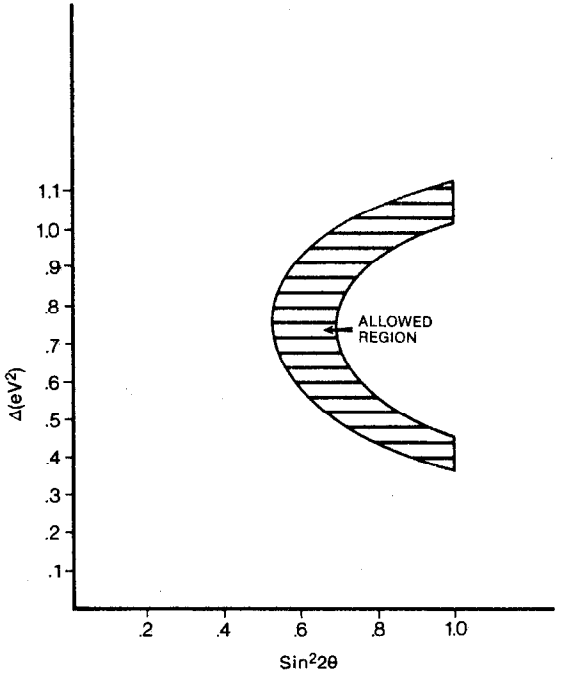

Fig. 5. $\Delta(eV^2)$ vs. $\sin^2 2\theta$ allowed region for 11.2 m ccp data; $E_\nu \geq 6.0$ MeV; Avignone spectrum.

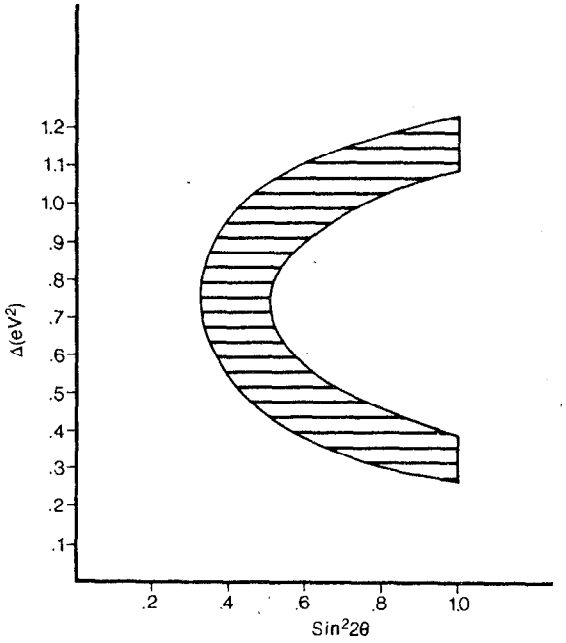

Fig. 6. $\Delta(eV^2)$ vs. $\sin^2 2\theta$ allowed region for 11.2 m ccp data; $E_\nu \geq 6.0$ MeV; Davis spectrum.

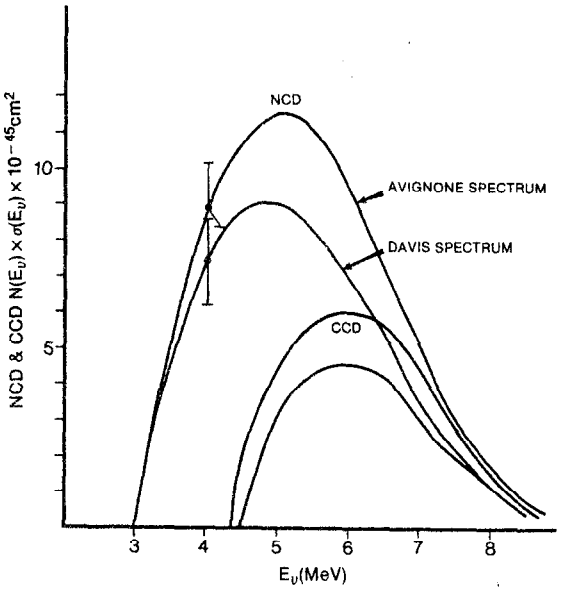

Fig. 7. Flux times cross section for ncd and ccd process as predicted from Avignone and Davis spectra.

Table II. Predicted cross sections for charged current and neutral current reactions, and the ratio of these predictions.

Cross section (cm^2/fission)	Davis Spectrum	Avignone Spectrum
ncd	2.87×10^{-44}	3.73×10^{-44}
ccd	1.21×10^{-44}	1.64×10^{-44}
Ratio $\frac{ccd}{ncd}$	0.42	0.44

normalization.

2. It is insensitive to the precise shape of the reactor neutrino spectrum.

3. The ncd process is independent of neutrino type.

4. The ccd process only occurs with $\bar{\nu}_e$'s.

5. Assuming the standard model, the ratio of the coupling constants is known to ~ 5%.[11]

The quantity, R, is expected to be unity. A value of R below unity would signal the instability of $\bar{\nu}_e$ as it traversed the distance (centered in this deuteron experiment at 11.2 meters) from its origin to the detector.

Experimental Approach

We have constructed a shielded volume at the reactor which has a greatly reduced neutron background. This shield made it feasible to search for the n.c. reaction by looking only at the product neutron, so avoiding the proton background problem of the earlier approaches.[12] The c.c. reaction is identified by detecting both product neutrons in a time window of 2 ms (the neutron capture time in this detector is 300 μs). Those cases in which only one of the two neutrons from the c.c. reaction was detected represented background for the n.c. reaction.

Detector Description

The target consists of 268 kg. of D_2O. Immersed in the D_2O are 10 cylindrical, helium-3 filled, neutron proportional counters. A side view of the detector is shown in Fig. 8. The target is enclosed in 10.2 cm of lead, 0.1 cm of cadmium and immersed in a 2200 liter anticoincidence detector. The detector is in turn surrounded by massive lead,

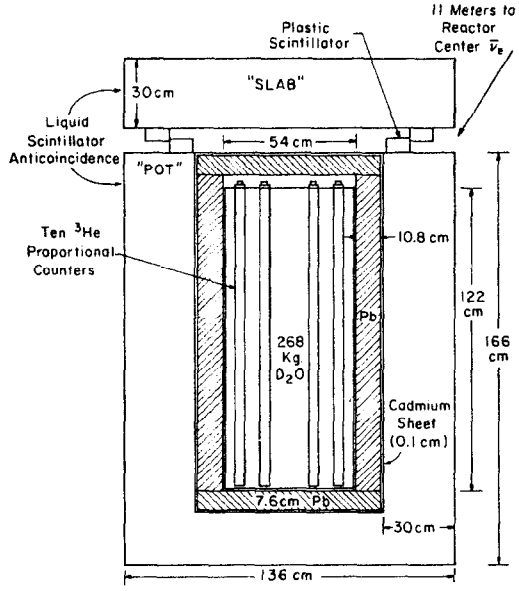

Fig. 8. Schematic diagram of the detector side view.

concrete and water shielding. Events arise from a neutron capture in the ^{3}He counters,

$$^3\text{He} + n \rightarrow p + {}^3\text{H} + 773 \text{ keV}$$

which meet the trigger requirements. All signals from the ^{3}He counters and the anticoincidence system within 2 ms before and after an event are recorded.

Neutron Detection Efficiency

The neutron detection efficiency was determined using Monte Carlo techniques and a ^{252}Cf source.

1. Monte Carlo. The neutron detection efficiency for our system is dependent on the energy spectrum of the neutrons under consideration. Accordingly, the efficiency is different for neutrons emitted from the ^{252}Cf source and those resulting from the lower energy n.c., c.c. or $\bar{\nu}_e + p \rightarrow n + e^+$ (I.B) background reaction.

The Monte Carlo computer code utilized for these calculations is one written by the Savannah River Laboratory. It has an extensive cross section library. Originally written for reactor geometries, it was modified to simulate the geometry of this experiment. The calculation is two dimensional, assuming an infinitely long array, and therefore a correction due to the loss of neutrons from the top and bottom of the detector must be made.

We find that the detection efficiency is relatively insensitive to neutron energy.

2. ^{252}Cf Source. We have checked the results of the Monte Carlo using a ^{252}Cf source positioned at various locations inside the detector.

a. A source calibrated to ± 3% was counted and

the results used to establish efficiency as a function of location.

b. The Cf source is a source of multiple neutrons, emitting on the average 3.73 neutrons per fission.

The numbers of single, double, triple and multiple neutron events were recorded for each source position. The neutron detection efficiency can be determined from ratios of these values without a knowledge of the absolute source calibration.

The efficiencies derived from the Monte Carlo, the direct neutron counting, and the neutron multiplicity method are in agreement within the uncertainties given below. The efficiencies for single neutrons produced uniformly throughout the D_2O are:

$$\bar{\eta}_{n.c.} = \bar{\eta}_{c.c.} = .32 \pm .02$$

$$\bar{\eta}_{^{252}Cf} = .28 \pm .02$$

and,

$$\bar{\eta}_{I.B.} = .36 \pm .02$$

The efficiency for detecting two neutrons in the c.c. reaction is $\overline{\eta^2} = 0.112 \pm 0.009$ where the two neutron efficiency is averaged over the D_2O volume.

During single neutron analysis, we use $\overline{\eta'} = .89\ \bar{\eta}$, the efficiency loss due to a background reduction, cut.

Data

We report the results of two data sets. Each data set consists of a number of reactor on and reactor off sequences alternating in time. Several time groupings were made from these sequences, each consisting of reactor on and off data. Reactor associated (reactor on minus reactor off) single and double neutron rates were obtained for each group. Some of the groups in data set 1 are shown in Table III. From this, we see that we have a reactor associated signal from both single and double neutrons. We now establish that this signal is due to neutrinos, and further, that they are due to the deuteron reactions in question.

Background Tests

1. Neutrons. Our neutron background was established by completely surrounding our detector with an additional neutron shield. The observed change in our signal implied a neutron background of $0.7 \pm 0.14\ day^{-1}$.

2. Gammas. The reactor associated gamma ray spectrum was measured with a 300 kg NaI detector in the same location as the D_2O target.

The background due to the (γ,n) reaction on the deuteron was calculated to be $0.05\ day^{-1}$.

3. $\bar{\nu}_e$ Background.

a. Our D_2O is not pure. The ratio of the number of protons to the number of deuterons is .0015. Since the inverse beta process has a relatively large cross section, this small contaminant gives a neutron background of $1.6 \pm 0.1\ day^{-1}$.

b. The liquid scintillator anticoincidence detector consists of $CH_{1.8}$ and is therefore a large source of proton targets for the I.B. process. We calculate that about $10^4\ day^{-1}$ are occurring in this detector. Most of the neutrons which are produced are thermalized in the scintillator, and captured on hydrogen or our cadmium

Table III. Sample neutron rates in data set 1.

	Group 1	Group 2	Group 3 . . .	Group 7	Weighted Mean
		Single Neutron Data			
Reactor on (day^{-1})	386.90 ±11.83	387.27 ±11.90	406.31 ± 6.72 . . .	439.95 ± 6.98	
Reactor off (day^{-1})	323.73 ± 7.32	320.01 ± 5.09	333.92 ±12.92 . . .	385.61 ± 5.66	
On-Off (day^{-1})	63.17 ±13.49	67.26 ±12.94	72.39 ±14.56	54.34 ±8.90	68.26 ±4.11
		Double Neutron Data			
Reactor on (day^{-1})	53.51 ±4.40	54.12 ±4.45	58.54 ±2.55 . . .	51.85 ±2.40	
Reactor off (day^{-1})	47.67 ±2.81	51.55 ±2.04	55.67 ±4.96 . . .	46.81 ±1.98	
On-Off (day^{-1})	5.84 ±5.22	2.57 ±4.90	2.67 ±5.58 . . .	5.04 ±3.11	3.66 ±1.52

shield. The probability of a neutron being seen by the ^3He detectors was calculated via Monte Carlo and measured with a neutron source immersed in the liquid scintillator. This probability varies from .0018 to .00056 as a function of source location, and implies a background of 34 neutrons per day.

The I.B. process occurs in a live anticoincidence, and as a consequence a large fraction (.77) of the background events are discriminated against by means of the energy deposition of the positron and its annihilation gammas. The residual background is thus 7.9 ± 0.7 day^{-1}.

The total background to the single neutron signal from these sources is therefore 10.2 ± 0.7 day^{-1}.

Deuteron Rates

We can now calculate the c.c.d. rate (R^{ccd}) and the n.c.d. rate (R^{ncd}) from the observed one neutron and 2 neutron signals (S_{1N}, S_{2N}).

$$R^{ccd} = \frac{S_{2N}}{\overline{\eta^2}} \quad \text{and} \quad R^{ncd} = \frac{S_{1N}^{ncd}}{\eta_{1N}}$$

where: $S_{1N}^{ncd} = S_{1N} - S_{1N}^{(BKGND)} - S_{1N}^{ccd}$

and, $S_{1N}^{ccd} = 2(\eta_{1N})(1 - \eta_{1N})R^{ccd}$

The experimental ratio of ccd to ncd is therefore:

$$r_{exp} = \frac{R^{ccd}}{R^{ncd}} = \frac{\overline{\eta^2}\, S_{2N}}{\overline{\eta^2}(S_{1N}-S_{1N}^{BKGND})-2(.89)(\bar{\eta}-\overline{\eta^2})S_{2N}}$$

and the error in r_{exp} is calculated from

$$\sigma^2_{r_{exp}} = \left(\frac{\partial r}{\partial S_{1N}}\right)^2 \sigma^2_{S_{1N}} + \left(\frac{\partial r}{\partial S_{2N}}\right)^2 \sigma^2_{S_{2N}} + \ldots$$

to be $r_{exp} = 0.167 \pm 0.093$.

We had that $R = \frac{r_{exp}}{r_{theory}}$

so, $R_{\substack{\text{Avignone} \\ \text{spectrum}}} = \frac{0.167 \pm .093}{0.44} = 0.38 \pm 0.21$

and, $R_{\substack{\text{Davis} \\ \text{spectrum}}} = \frac{0.167 \pm .093}{0.42} = 0.40 \pm 0.22.$

These represent a 3.0 to 2.7 standard deviation departure from unity, assuming that the σ_r calculated above is representative of a normal distribution.

In the same way as for the ccp experiments the allowed values of Δ and $\sin^2 2\theta$ are plotted in Fig. 9 for R = $.38 \pm .21$.

Consistency Checks

1. We have mentioned previously another experiment at the 11.2 meter position which measured the ccp process. This positron spectrum has been used to obtain a $\bar{\nu}_e$ spectrum for $E_{\bar{\nu}_e} > 4$ MeV (Fig. 10). The value for R deduced using this spectrum, extrapolated below 4 MeV, is $0.47 \pm .24$, a 2.2 standard deviation effect. If neutrino oscillations occur, with the parameters implied by the deuteron experiment, then the extrapolation of the neutrino spectrum to lower energies would be in error and the value of R reduced.

2. In Table IV we list the individual ccd and ncd

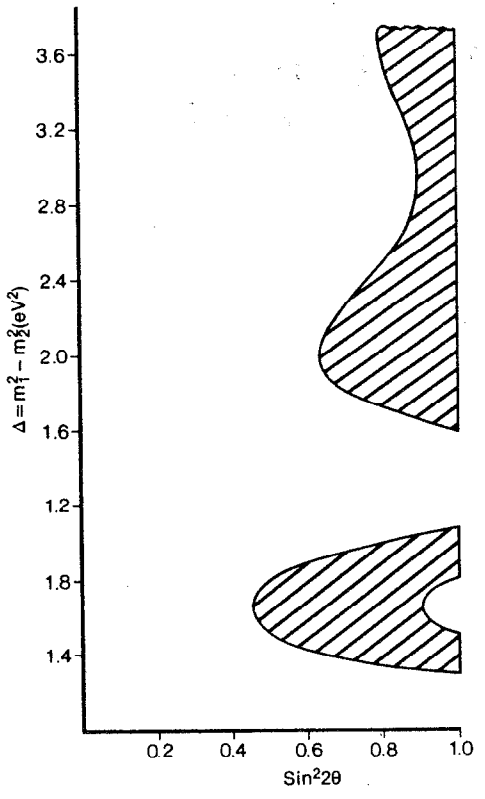

Fig. 9. $\Delta(eV^2)$ vs. $\sin^2 2\theta$ for R = 0.38 ± 0.21.

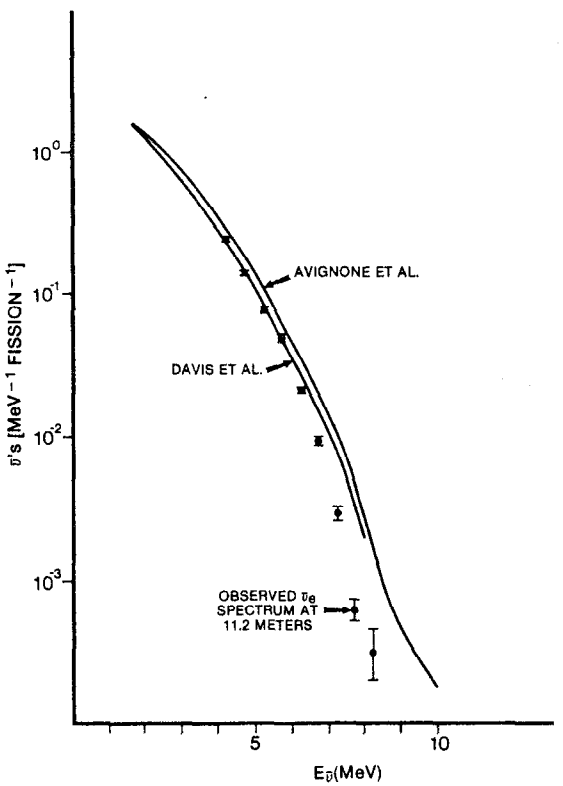

Fig. 10. The observed ν_e spectrum at 11.2 meters compared to Avignone and Davis predictions.

Table IV. Summary of Results for the Ratio $\frac{\bar{\sigma}_{expt.}}{\bar{\sigma}_{th.}}$

Distance from Core Center (Meters)	Reaction	Neutrino Detection Threshold (MeV)	Ratio		
			Avignone Spectrum	Davis Spectrum	Measured $\bar{\nu}_e$ Spectrum (preliminary)
11.2	ncd	2.2	.83 ± .13	1.10 ± .16	1.3 ± .22
11.2	ccd	4.0	.32 ± .14	.44 ± .19	.61 ± .29
11.2	ccp	4.0	.68 ± .12	.88 ± .15	≡ 1.0
11.2	ccp	6.0	.42 ± .09	.58 ± .12	≡ 1.0
6	ccp	1.8	.65 ± .09	.84 ± .12	-
6	ccp	4.0	.81 ± .11	1.02 ± .15	1.19 ± .27
8.7	ccp	3.0	.68 ± .15	.87 ± .14	-

rates, and other previously mentioned reactor results compared to the predicted rates using the Avignone spectrum, the Davis spectrum and the measured $\bar{\nu}_e$ spectrum at 11.2 meters.

Unlike the insensitivity of R to the reactor neutrino spectrum, all other ratios of experimentally determined rates to predicted rates are markedly dependent on the spectrum and normalizations. For this reason, we consider the precise values of these other ratios listed in Table IV to be of less significance. They can however be used to test consistency with R.

a. We note that since our measurement of the neutrino spectrum is only sensitive to $\bar{\nu}_e$ it should enable us to correctly predict the ratio for the charged current branch. Table IV indicates that the preliminary prediction for this ratio using the measured spectrum is 1.3 standard deviations from the expected value of unity. If the difference can be attributed to a normalization error between the two experiments it would have no effect on the ratio R. If, however, the difference is due to a statistical fluctuation and we therefore choose for the charged current the most likely value consistent with the two experiments, then the ratio R would become 0.62 ± 0.16. We note in this case that whereas R has increased, its error has diminished reflecting the greater precision of the prediction based on the measured $\bar{\nu}_e$ spectrum.

b. Allowed regions Δ vs. $\sin^2 2\theta$ can be drawn for each of the ratios listed in Table IV. For the Avignone spectrum there is an overlapping region consistent with all the experiments at 11.2 meters but not with the > 4 MeV data at 6 meters. We note that small changes in the normalization of the 6 meter data could give agreement. This yields

$$0.5 \leq \sin^2 2\theta \leq 0.8 \quad (32^\circ > \theta > 22^\circ)$$

and $$0.7 \leq \Delta(\mathrm{eV}^2) \leq 1.0$$

We find that the Davis spectrum yields no overlapping region at the level of one standard deviation. On the other hand it appears to predict more precisely the observed neutral current branch of the deuteron experiment.

c. If oscillations occur with these approximate parameters, then the observed spectrum at 11.2 meters should show evidence of spectral changes. In Fig. 11 we plot the ratio of the observed 11.2 meter data to the Avignone prediction as a function of neutrino energy. If oscillations do not exist and further if the Avignone spectrum is the correct one, then the ratio should be 1.0 independent of energy. For comparison, the predicted ratio for $\Delta = 1\ \mathrm{eV}^2$ and $\sin^2 2\theta = 1$ is plotted. The same comparison is made, this time to the Davis spectrum in Fig. 12.

Conclusions

The results of a reactor experiment comparing the observed rates of the charged current and neutral current interactions of reactor neutrinos with deuterons gives an indication of neutrino instability at the 2 to 3 standard deviation level.

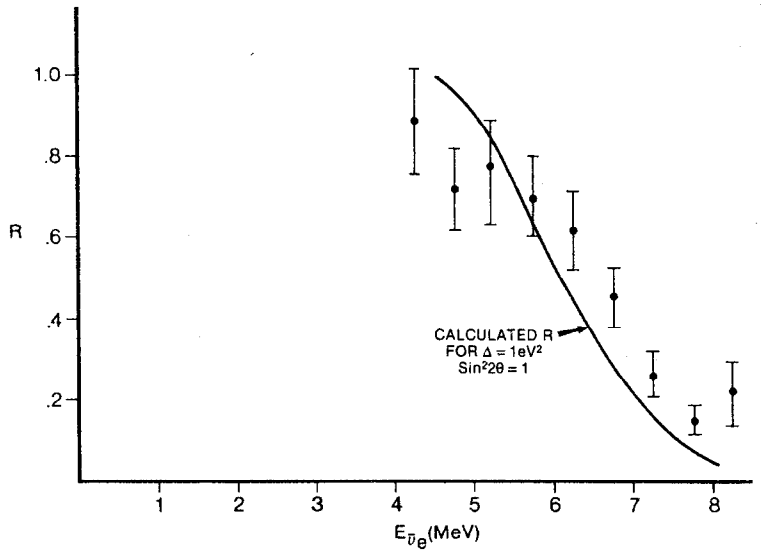

Fig. 11. The ratio of 11.2 meter ccp measured neutrino spectrum to that predicted by Avignone.

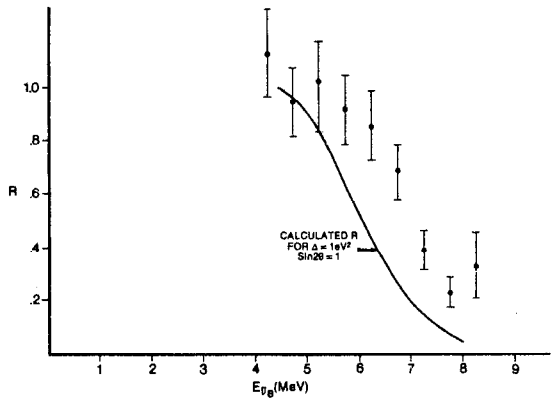

Fig. 12. The ratio of 11.2 meter ccp measured neutrino spectrum to that predicted by Davis.

References

1. S. Blankenship - UCI internal report, UCI-10P19-102 (1976).

2. S. Blankenship - UCI internal report, UCI-10P19-104 (1976).

3. R. Davis, Jr., and D.S. Harmer, Bull. Amer. Phys. Soc. (2) 4, 219 (1959).

4. A. Soni and D. Silverman, private communication.

5. F. Nezrick and F. Reines, Phys. Rev. 142, 852 (1966).

6. F. Reines, H.S. Gurr, and H.W. Sobel, Phys. Rev. Lett. 37, 315 (1976).

7. F. Boehm, private communication.

8. UCI internal reports - UCI-10P19-141 (1979), UCI-10P19-132 (1978), UCI-10P19-126 (1977).

9. S. Blankenship, Georgia Institute of Technology, private communication.

10. E. Pasierb, H.S. Gurr, J. Lathrop, F. Reines and H.W. Sobel, Phys. Rev. Lett. 43, 96 (1979).

11. R.M. Ahrens and L. Gallaher, Phys. Rev. D20, 2714 (1979) and private communication (1980). S.L. Glashow, J. Iliopoulos and L. Maiani, Phys. Rev. D2, 1285 (1970).

12. J.H. Munsee and F. Reines, Phys. Rev. 177, 2002 (1969).

A REVIEW OF PROTON DECAY EXPERIMENTS*

J. C. Vander Velde

Randall Laboratory of Physics
The University of Michigan
Ann Arbor, MI 48109

*Talk presented at the SLAC Summer Institute on Particle Physics, August 1980.

INTRODUCTION

I will review the status of preparations going on around the world to measure the lifetime for nucleons to decay via baryon number violating modes. After Tony Zee's beautiful talk[1] on the theoretical, cosmological, and philosophical aspects of these processes, I'm sure that I don't need to justify any further the flurry of activity that is presently aimed toward that end.

The subject itself is one of long standing but low profile, with several limits having been set as by-products of experiments primarily dedicated to other measurements. There is no substantive existing evidence for proton decay. The largest published lower limit comes from a recent reanalysis[2] of previous data which gives a limit of about $1x10^{30}$ years. The present intense interest in the subject began to penetrate our collective elementary particle consciousness about two years ago.

For orientation purposes we note the following calculation based on Avogadro's work:[3]

1 gm = $6x10^{23}$ nucleons

1000 Kg = 1 ton = $6x10^{29}$ nucleons

Suppose $\tau = 6x10^{30}$ yr (just above present limits)

Then one would get 10 decays/100 tons/yr ("present" detectors)

or 1 decay/0.1 ton/100 years (you)

One sees from this that one needs at least 100 tons of sensitive volume in order to make it worth the effort. Hence, there is a need for a new type of detector which is massive, yet cheap, and has good resolution (pattern recognition and track directionality) in the 1 GeV energy range.

Ultimately one will be limited in attempts to push lifetime limits by background due to "atmospheric" neutrinos interacting in the detector. This is quantified in Fig. 1, taken from the proposal of the Irvine-Michigan-Brookhaven (IMB) group. Atmospheric neutrino interactions above ~100 meV occur in all matter at an equivalent nucleon lifetime of $\sim 2x10^{30}$ yr. If the detector can make a total energy cut around the nuclear mass one gets about a factor of 10 improvement. A detector which can measure angles and track direction on two body events can get an additional factor of 100 improvement for modes such as $p \to e^+\pi^\circ$, $n \to e^+\pi^-$. At this point wide angle neutrino interactions such as $\nu+p \to e^+\pi^\circ n$ come in and limit the sensitivity to $\sim 3x10^{33}$yr. If we earthlings don't see proton decay at that level, then improved limits will only proceed proportional to the square root of the increased detector mass. In that case life will become very tough for intrepid experimenters who set out to push the limits upward. By going to a cavern under the surface of the moon one could get another factor of 100 in background reduction, since the moon has no atmosphere to act as a neutrino production target for cosmic rays. (An artificial satellite would need to be at several earth radii in order to diminish the earth's neutrinos.)

Nevertheless it seems one can improve the present limits by a factor of 1000 with a suitably designed earthbound experiment and, what is more exciting, perhaps detect several hundred events per year if the lifetime is in the range of current theoretical predictions.

After these general remarks we can proceed with descriptions of present experimental efforts. I will spend, perhaps, a disproportionate amount of time describing the IMB detector since I am most familiar with the details of that project and it in some sense sets a standard, being about a factor of 10 more massive (5000 tons fiducial volume) than the

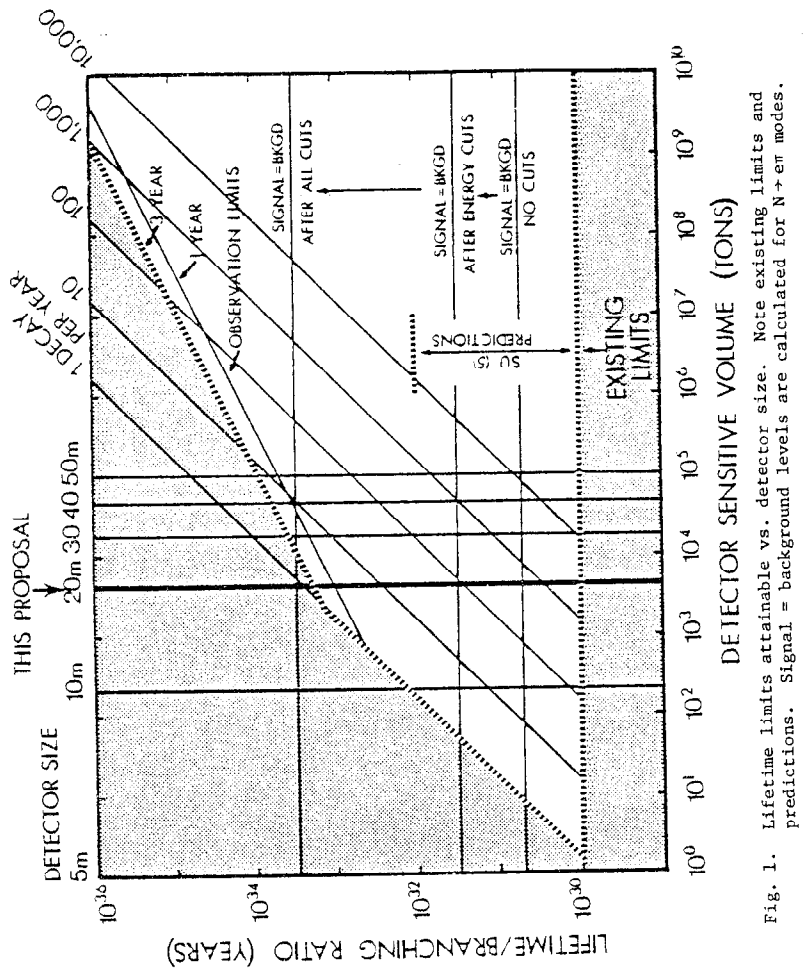

Fig. 1. Lifetime limits attainable vs. detector size. Note existing limits and predictions. Signal = background levels are calculated for N→eπ modes.

next in size. This is in no way meant to belittle the other experiments since the lifetime could be short enough so that smaller experiments which turn on earlier or use techniques better suited to certain decay modes might see the effect earlier or differently.

THE IMB DETECTOR

Current members of the Irvine-Michigan-Brookhaven group are:

C. Bratton	Cleveland State U.
M. Goldhaber	Brookhaven
T.W. Jones	U. Michigan/U. College (London)
W. Kropp	U.C. Irvine
J. Learned	U.C. Irvine/U. Hawaii
J. LoSecco	U. Michigan
F. Reines	U.C. Irvine (Co-spokesman)
J. Schultz	U.C. Irvine
D. Sinclair	U. Michigan
D. Smith	U.C. Irvine
H. Sobel	U.C. Irvine
J. Stone	U. Michigan
L. Sulak	U. Michigan
J. Vander Velde	U. Michigan (Co-spokesman)

Graduate Students:

B. Cortez	Harvard/Michigan
W. Foster	Harvard/Michigan
E. Shumard	Michigan
C. Wuest	Irvine

This group is building a 10,000 ton $(20\ m)^3$ water Cerenkov detector. The Cerenkov light from nuclear decay products comes out in cones of 42° half-angle and illuminates an array of hemispherical PM tubes spaced on a 1 m grid over the 6 faces of the cube. (See Fig. 2.) The fiducial volume will be $(16\ m)^3$ leaving a 2 m shield of water around it for rejection of cosmic ray muons and their interaction products. The size of the detector is limited not only by the considerations illustrated in Fig. 1, but also by the absorption length of light in water (maintainable at ∿30 m by reverse osmosis techniques) and by the practical size of stable caverns deep underground (and, of course, by dollars). The detector will be constructed in a special adit which has just been dug in the Morton Salt Mine east of Cleveland. The depth is 1900 feet (∿ 1600 mwe).

PROPOSAL FOR A NUCLEON DECAY DETECTOR

IRVINE/MICHIGAN/BROOKHAVEN

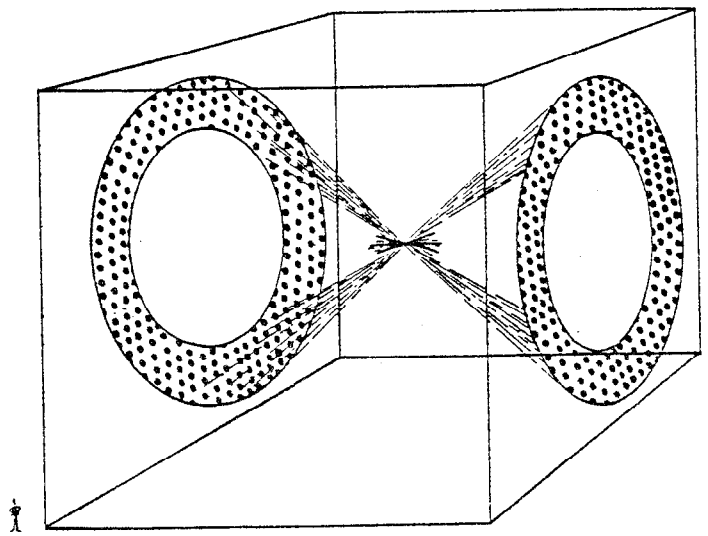

Fig. 2. The cover page of the IMB proposal depicting the two cones of Cerenkov light from a nucleon decay illuminating photomultiplier tubes on the faces of a 70 ft cube of water.

The reconstruction of particle tracks in such a detector takes place from the x, y, z, t, and pulse height information contained in each of the 100-200 PM tubes which light up in a typical nucleon decay. The Cerenkov cone from an idealized track is shown in Fig. 3a. One sees in Fig. 3b how the same track if tilted by 25° gives a different pattern with different time structure in the PM tubes.

In reality one must generate Monte Carlo tracks with multiple scattering, showering, etc. Fortunately this is straightforward in a homogeneous medium like water, which also has known Cerenkov and light absorption properties. A typical $p \rightarrow e^+\pi^\circ$ event is seen in Fig. 5. One sees that showering tracks give far from idealized annular pattern, and that in general one cannot separate $e^\pm$ from π° by patterns alone.

Nevertheless, reconstruction algorithms applied to events of the type shown in Figs. 4 and 5 indicate that satisfactory spatial and angular resolution can be achieved in order to reject background and identify nucleon decays at the desired level.

The detector also is able to distinguish showering tracks (π°,e) from non-showering tracks ($\pi^\pm$,μ) provided their energy is known approximately (see Fig. 6). Given a showering track, its energy can be determined to ±11% in the 2400-tube detector (see Fig. 7). This should produce ±7.5% energy resolution on the popular $p \rightarrow e^+\pi^\circ$ mode. One or more $\mu \rightarrow e$ decays can also be detected in a 5 μsec time gate opened by a possible nucleon decay trigger.

A summary of the calculated properties of this detector is presented in Table I.

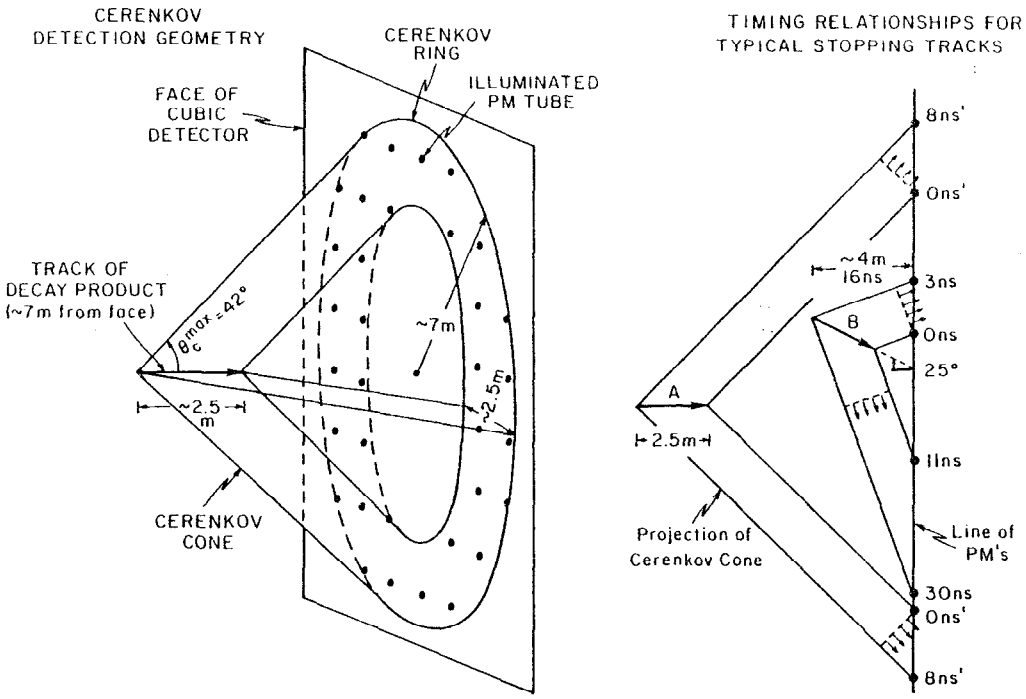

Fig. 3. Illustration of how the arrival time of various parts of a Cerenkov cone can determine track direction in the IMB detector. Similar techniques can be used in the volume arrayed HPW detector (see Fig. 14).

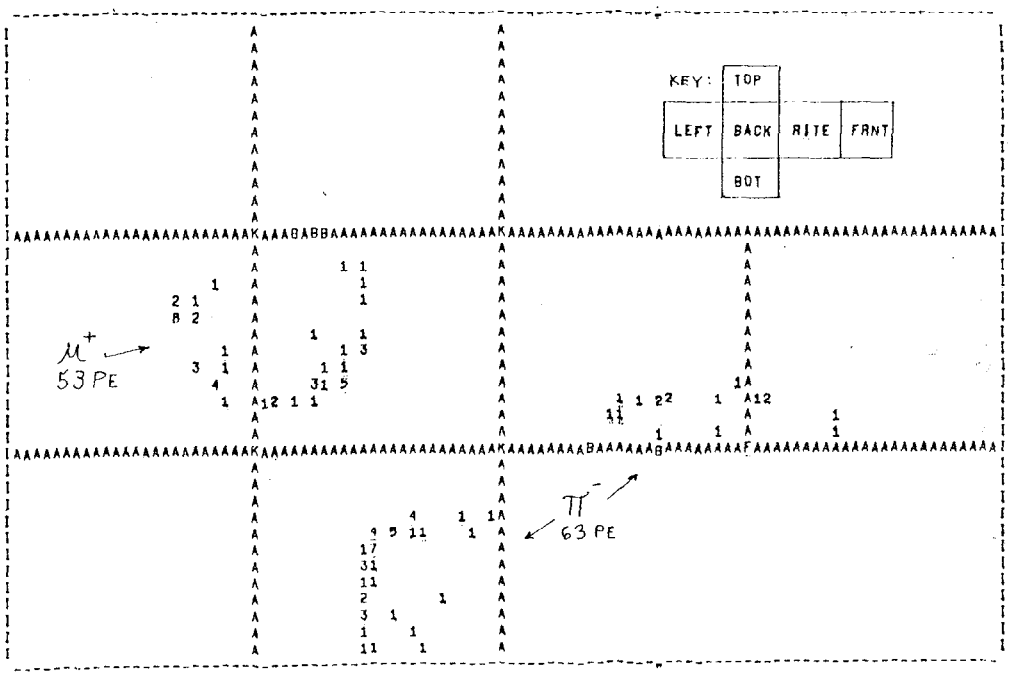

Fig. 4. PM tube response pattern from a $n \to \mu^+ \pi^-$ Monte Carlo event in the IMB detector. The numbers represent photoelectrons (pulse height) in PM tubes arrayed on the faces of an unfolded cube.

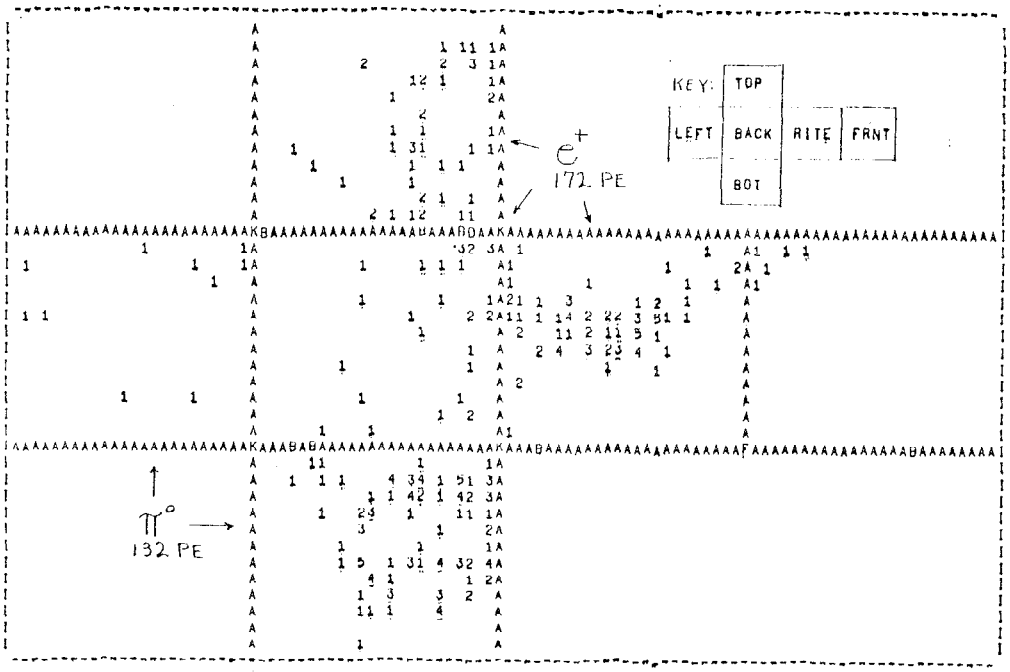

Fig. 5. Like Fig. 4 but for $p \rightarrow \pi^{o} e^{+}$. Events like this can be reconstructed with typical track angle errors of $\pm(15\text{-}20)^{o}$. (See Table I.)

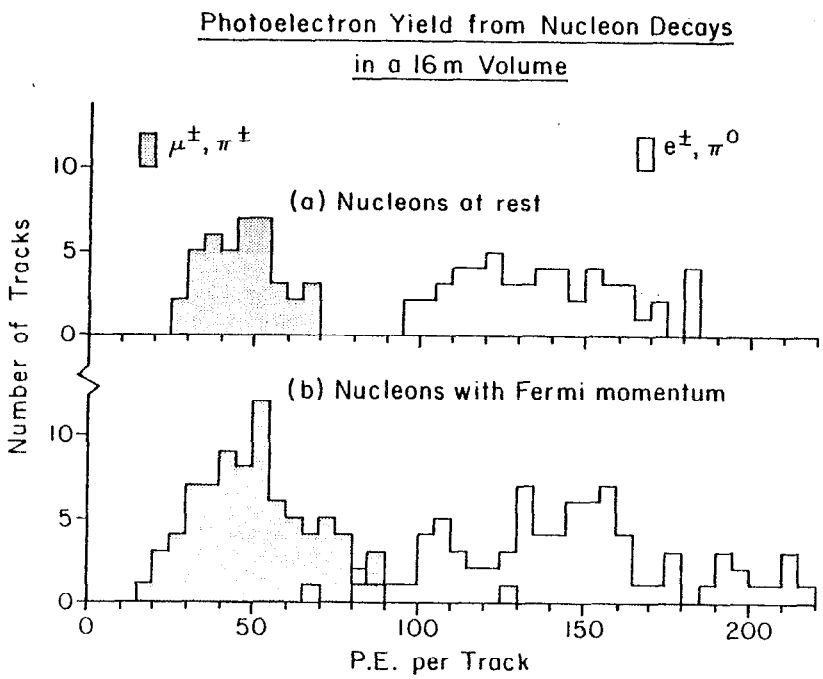

Fig. 6. Photoelectron yield from two body nucleon decays chosen at random in the IMB $(16\ m)^3$ fiducial volume. Note the discrimination between showering and non-showering tracks possible because of the approximately unique track energy.

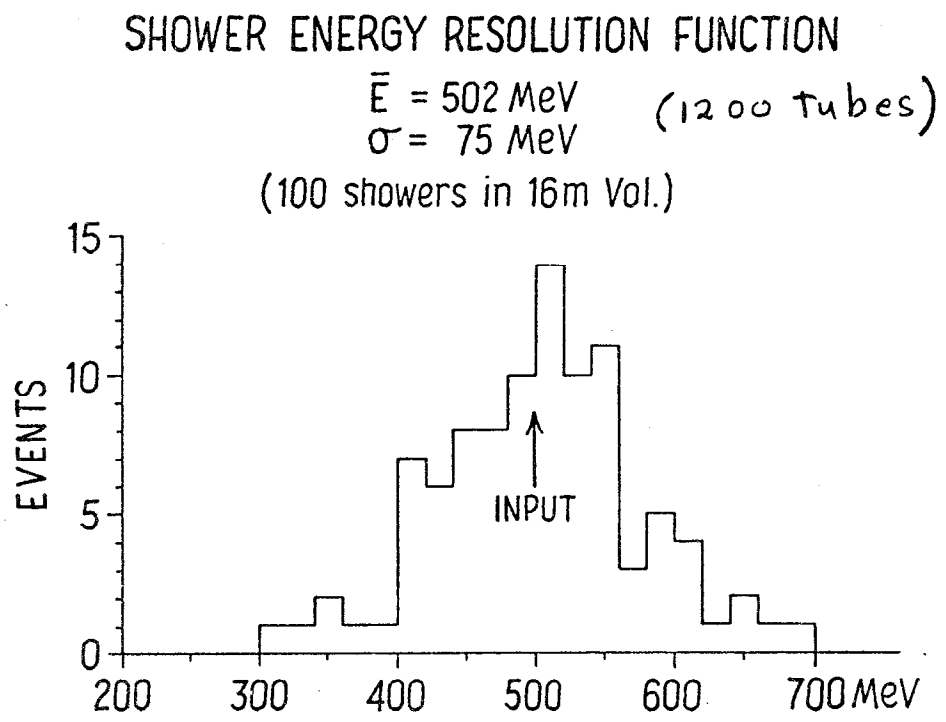

Fig. 7. Energy resolution calculated for 500 mev showering tracks (π^0 or e^+) in the IMB detector (with ½ final tube count). A 2400-tube detector should have 7.5% energy resolution on $p \rightarrow \pi^0 e^+$ events.

TABLE I

Summary of the IMB Detector Properties

Size:

Total volume = 6.5×10^{33} nucleons

Fiducial " = 2.5×10^{33} = (16 m)^3

Energy Resolution:

500 mev shower σ = 11%

300-450 mev/c $\pi^{\pm},\mu^{\pm}$ σ = 10-15%

Vertex Localization

σ = .5 m

Track Directionality

No ambiguity

Angular Resolution

Showers ($e^{\pm},\pi^0$) σ = 10-20°

Charged tracks $\sigma \lesssim 5°$

$\mu \rightarrow e$ Detection

>60% after trigger (Event thresh. ≈75 mev)

Several $\mu \rightarrow e$: OK

Position correlation: 1.5 m

e direction: ∿25°

BACKGROUNDS

In addition to the irremovable atmospheric neutrino background of ~0.2 event/ton/year one must deal with the more copious but less pernicious atmospheric muons. At the IMB depth (1600 mwe) and detector size they pass through the detector at a rate of 3.5/sec. The tube hit pattern for a typical muon passing in the top and out the bottom is shown in Fig. 8. One sees immediately that there is no trouble in distinguishing such events from nucleon decays, simply by the total light output or total tubes hit. For muons that pass through only a portion of the detector ("corner clippers") a more sophisticated rejection algorithm is needed. An example of the response of such an algorithm to 500 cosmic ray muons is shown in Fig. 9. The same algorithm passes virtually all of the nucleon decays, as can be seen in Fig. 10. Hence an immediate rejection factor of several hundred can be obtained from the raw hit pattern without making use of pulse height or timing information. Another immediate factor of ~100 can be obtained from pulse height, leaving a few thousand events per year which need to be dealt with using full blown fitting procedures which make simultaneous use of x, y, z, t and pulse height on all 50-100 PM tubes aided, perhaps, by visual techniques.

In addition to the cosmic ray muons themselves (typically in the hundreds-of-GeV region) coursing through the detector one must contend with events in which the muon misses the detector but makes a hadron or electron shower in the surrounding rock which then enters the detector. We expect about 20,000 such entering hadrons per year in the IMB detector. They come in, generally, at rather steep angles to the lateral faces so that a 2 meter thick "anti-region" of active detector surrounding the fiducial volume appears to be sufficient to reject them to a level such that further angle and energy cuts on the remainder reduce this background to a level below that due to neutrinos.

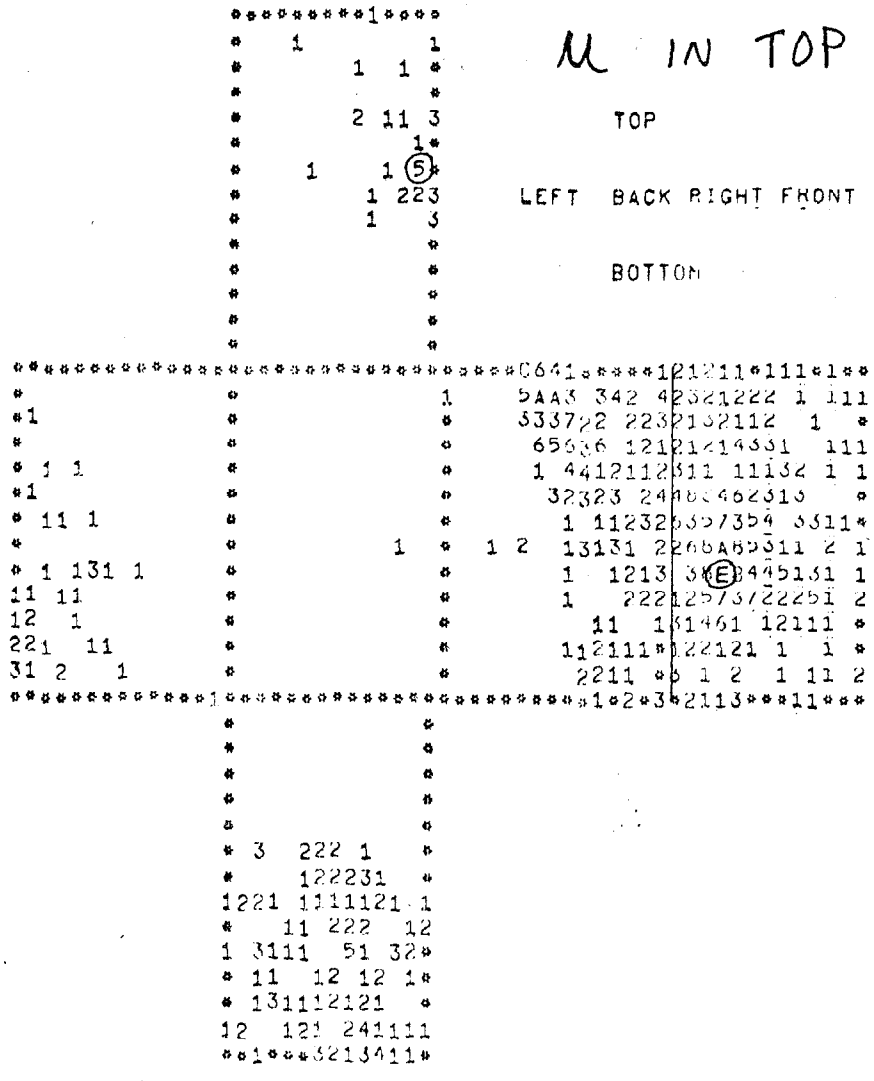

Fig. 8. PM tube response to a cosmic ray muon through the IMB detector. The muon enters near the "5" on the top edge and exits "E" on the front face.

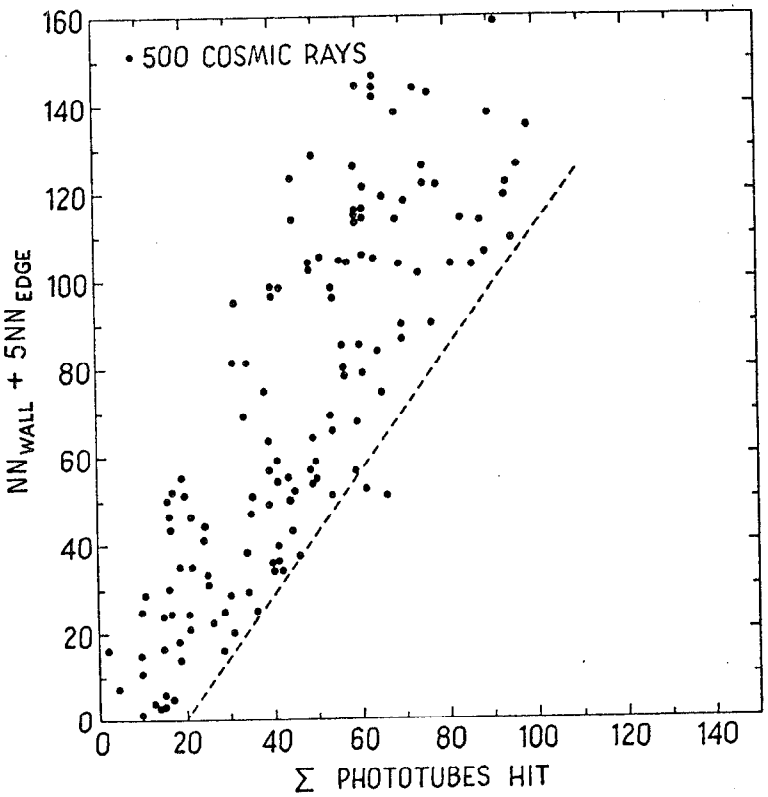

Fig. 9. Results of an algorithm for rapid rejection of cosmic ray muons. The algorithm makes use of the number of nearest-neighbor PM tubes that are lit. It does not use pulse height or timing data.

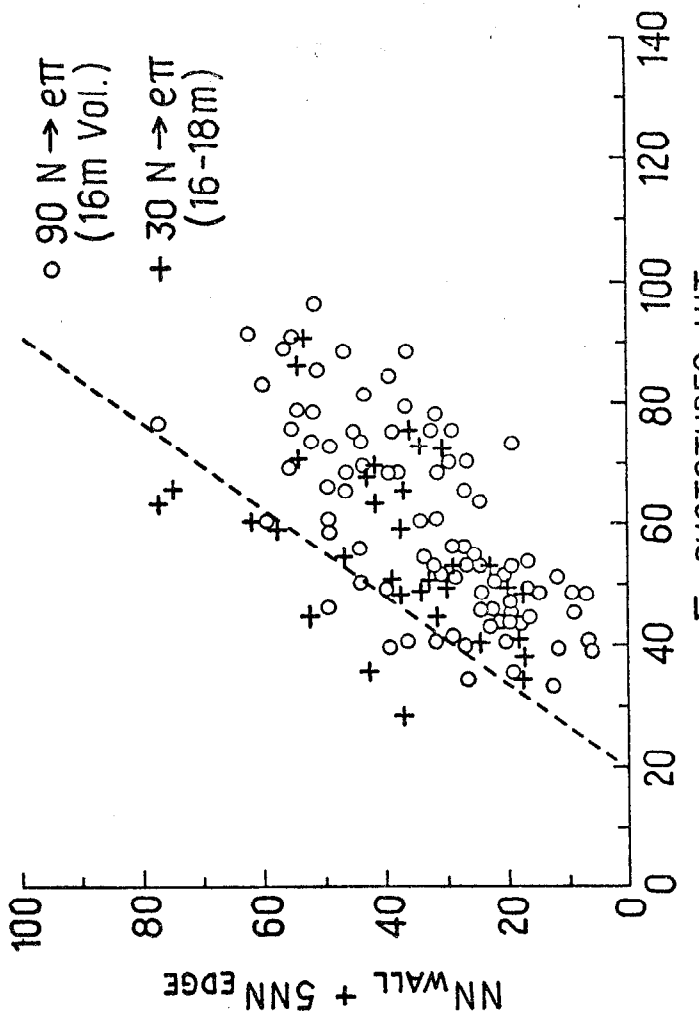

Fig. 10. Response of typical nucleon decays to the algorithm of Fig. 9. A negligible percentage of good events is rejected.

The irreducible neutrino background events above 100 meV occur at a rate of about 1000/yr in our detector. A rejection factor of 10 can be obtained by making total energy (total PM's plus pulse height) cuts on the data, equivalent to an energy window of about 100 meV around the nucleon mass. Stricter energy cuts are not feasible, due to fermi motion and nucleon interactions. Hence it is of little value to measure total energy to much better than 10%, and detectors with energy resolution but without pattern recognition will run into a neutrino induced apparent nucleon lifetime of $\sim 3 \times 10^{31}$yr (see Fig. 1).

Another factor of 100 in background rejection can be obtained by measuring track directions on two (or more) track events. The included angle between the products of a two body nucleon decay in a nucleus ranges from 145° to 180° (again, due to fermi motion). Only about 1% of the corresponding neutrino events (e.g., $\bar{\nu}p \rightarrow e^{+}\pi^{\circ}n$) have such a large included angle. Detectors which measure these angles to ±(10° to 20°) can push the neutrino background to a lifetime equivalent of 3×10^{33}yr. (Again, it is of little value to measure angles better than this.)

In the IMB detector we have 2.5×10^{33} nucleons in the fiducial volume and expect the neutrino background to range from 0.5 events/yr for the $e^{+}\pi^{\circ}$ mode to 1.4 events/yr for the $\mu^{+}\pi^{\circ}$ mode.

PROGRESS

Progress on the IMB detector has been achieved along various lines. Geometrical reconstruction algorithms have been developed and applied to signal and background Monte Carlo events generated in the water. The resulting resolutions are detailed in Table I.

The absolute response of PM tubes to cosmic ray muons in water has been measured in a 10 m horizontal tank depicted in Fig. 11. It is found

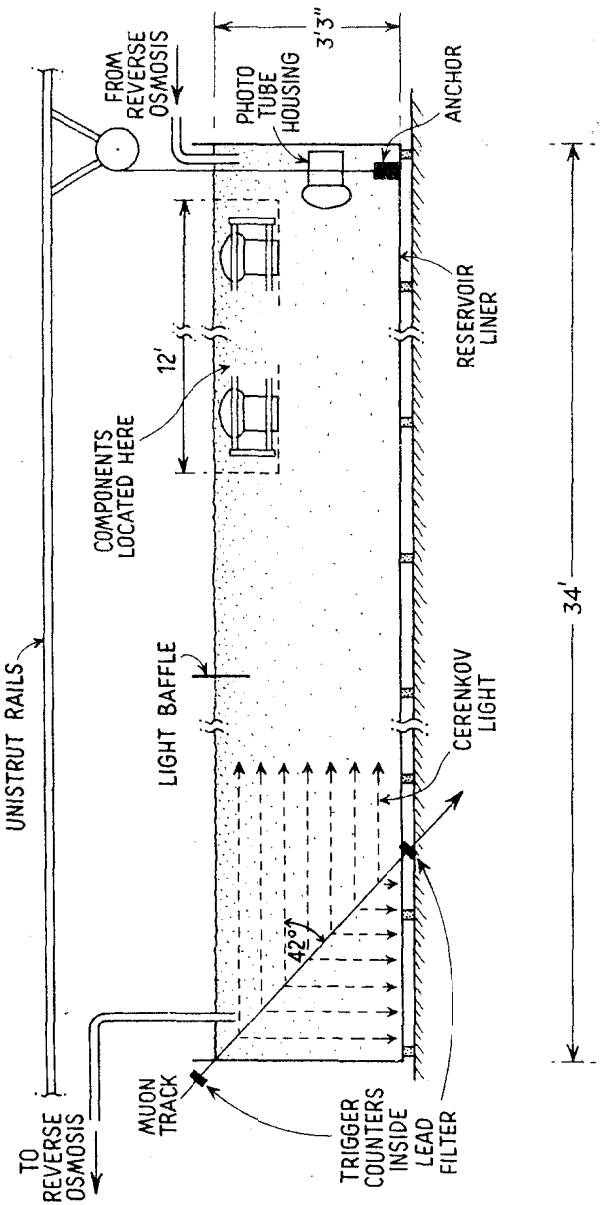

Fig. 11. Schematic of the IMB horizontal test tank facility in which absolute PM response to Cerenkov light was measured and water clarity maintenance was demonstrated.

that a 5-inch diameter hemispherical PM tube responds 70% of the time to a muon track 10 m away. This corresponds to an efficiency of 15% for photocathode response-times-collection for the tube at 400 nm. In the same tank, water has been maintained at an equilibrium clarity of 35 m absorption length (also at 400 nm) over long time periods using a recirculating reverse osmosis system.

Water-tight neutrally buoyant PM tube housings made of PVC have been developed and tested over long time periods in a 70-ft. vertical tank. This tank has also been used to test the extraction mechanisms for the tubes which will hang on nylon cords. The horizontal faces of the detector will be covered with tubes attached to neutrally buoyant PVC beams. These beams have been tested at full length complete with cables and PM tubes in a swimming pool.

A test setup is operating which determines noise levels, tube quality, and operating voltage for 16 PM tubes simultaneously.

A dark room containing 128 tubes has been set up in order to test the "home made" electronics and data acquisition system. A drawing of this "Disco" room is shown in Fig. 12. The tubes are first calibrated using a standard LED light pulser at two known times. The LED is then moved and fired at random times and single photoelectron light levels which correspond to nucleon decays. Initial results from this system are shown in Fig. 13. The spatial resolution in the two horizontal dimensions is typically ±2.5 ft. The vertical dimension (z) is somewhat worse due to the restricted height of the room and the absence of tubes on the top and bottom. These resolutions will be a factor of 0.75 smaller in water (due to longer flight time) for the same number of hit PM tubes (typically 10-15). (Actual nucleon decays will light up 50-200 tubes in a 2000 tube detector.)

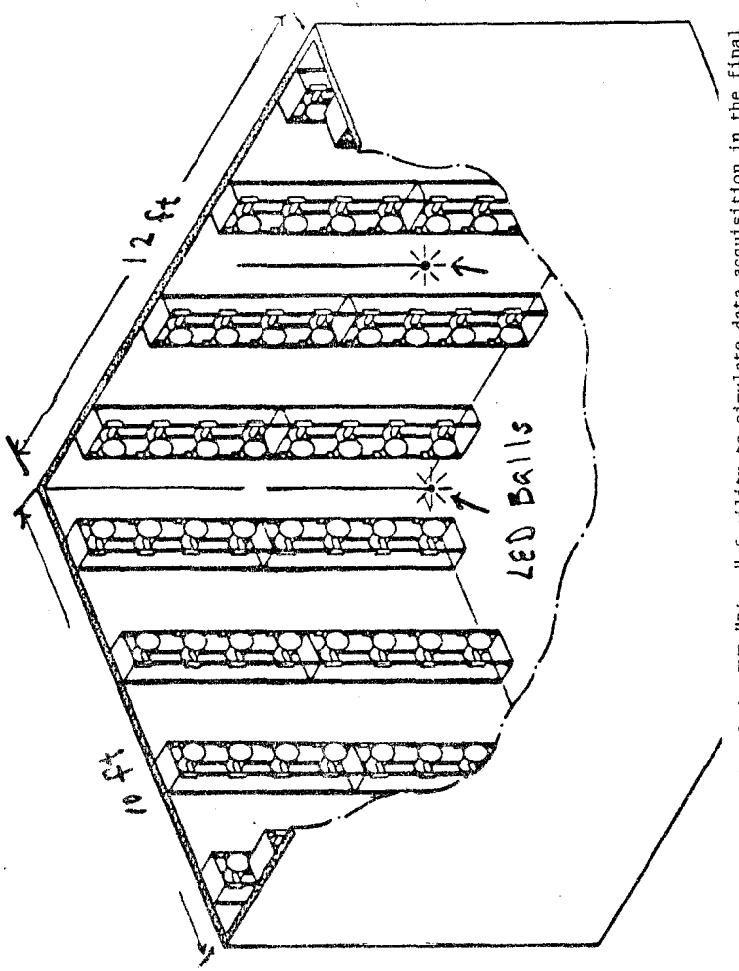

Fig. 12. Schematic of the IMB "Disco" facility to simulate data acquisition in the final detector. The LED balls are used to calibrate the PM tube/electronics system and also to simulate nucleon decays.

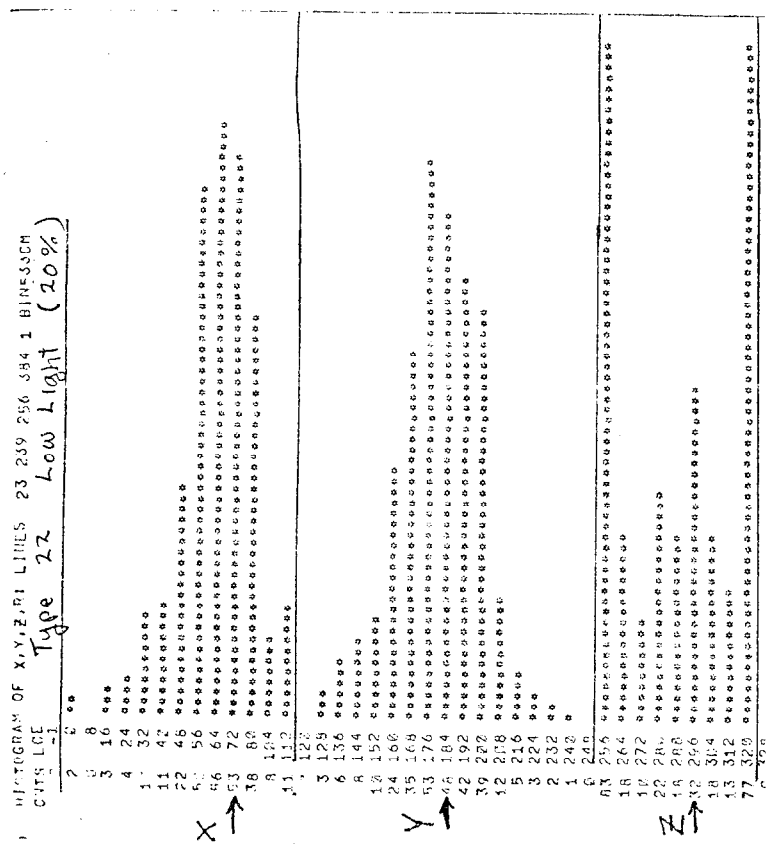

Fig. 13. Results on spatial reconstruction in the Disco.

The digging of the cavity in the Morton Salt mine has been completed along with wire meshing and rock bolting of the walls and ceiling. The laboratory will consist of a 18'x13'x350' tunnel plus a 40'x40' utility room, a 20'x60' electronics/operations area, and a 60'x80'x65' (deep) water container with 13' of head room over it. Physicists and students are presently preparing the walls of the cavity for the installation of the liner system to contain the water. During the next 3-4 months this cavity will (hopefully) be turned into a laboratory.

THE HPW DETECTOR

A Decay Mode Independent Search for Baryon Decay Using a Volume Cherenkov Detector*

J. Blandino [1], U. Camerini [3], D. Cline [3],** E. C. Fowler [2], W. F. Fry [3], J. A. Galdos [2], J. Innvaer [3], W. A. Huffman [1], G. Kullerud [2], R. J. Loveless [3], A. M. Lutz [1], J. Matthews [3], R. McHenry [2], R. Morse [3], T. R. Palfrey [2], I. Orosz [3], D. D. Reeder [3], C. Rubbia [1], A. Sarracino [3], A. H. Szentgyorgyi [3], H. Wachsmuth [3],*** R. B. Willmann [2], C. L. Wilson [2], D. R. Winn [1]

Harvard University [1], Cambridge, MA 02138
Purdue University [2], Lafayette, IN 47907
University of Wisconsin [3], Madison, WI 53706

*This is a revision of the proposal "A Multi-Kiloton Detector to Conduct a Sensitive Search for Baryon Decay."
**Spokesman for 1979-1980.
***Visiting Professor from CERN.

This detector is being constructed in the chamber formerly used by the Utah cosmic ray group near Park City, Utah. The chamber is at a depth of 1800 mwe. A cross section of the proposed detector is shown in Fig. 14. Aside from the fact that the detector volume is smaller (1000 tons) the principal features of the HPW detector which differentiate it from the IMB detector are these:

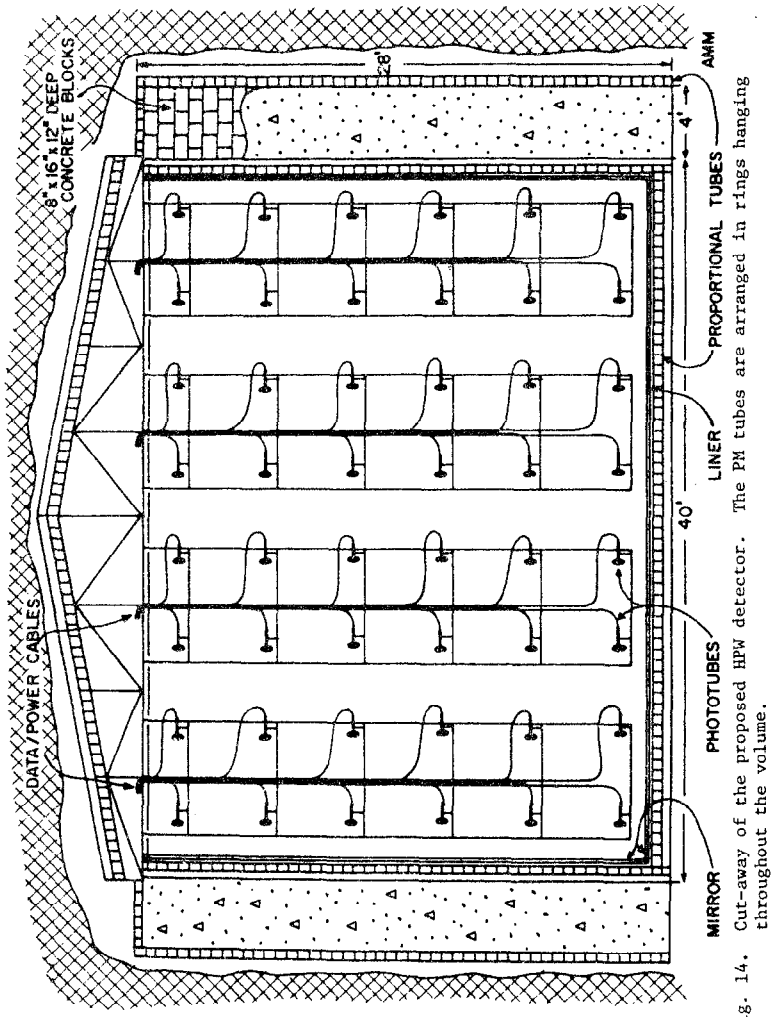

Fig. 14. Cut-away of the proposed HPW detector. The PM tubes are arranged in rings hanging throughout the volume.

(1) The 5-inch hemispherical PM tubes will be arrayed throughout the volume instead of on the surfaces.

(2) The detector will be surrounded by a layer of proportional tubes (top and bottom) and two layers separated by concrete (sides) in order to veto cosmic rays and their interaction products.

(3) The inner walls will feature mirrors in order to increase the total photon signal.

(4) A contemplated mode of operation is to introduce wave shifter into the water in order to further increase the collected photon count by a factor of ∿2, at the expense of geometrical reconstruction deterioration.

A sketch of a test setup at Purdue for this detector is shown in Fig. 15. Work is under way in the mine to prepare for the installation of the detector.

THE MINNESOTA DETECTOR

H. Courant, K. Heller, M. L. Marshak, E. A. Peterson
K. Ruddick and M. Shupe

School of Physics and Astronomy, University of Minnesota
Minneapolis, Minnesota 55455

The concept of this detector puts it into a class of tracking calorimeters. A schematic of a stack of detector modules is shown in Fig. 16. A single module consists of 8 gas proportional tubes, 1-inch in diameter, imbedded in heavy concrete. Five hundred such modules would give 50 tons of detector at a cost of about $50,000. About 1/2 of this amount will be installed by October 1 for initial operation in the Soudan mine in northeast Minnesota. The present site is at a depth of 1700 mwe and its dimensions limit the practical size of the initial version of this detector to about 50 tons.

Two stereo views of a $p \to e^+\pi^0$ decay in such a detector are depicted in Fig. 17. The large black circles represent the tubes that fire in each view. The design resolution has been chosen to be close to the minimum

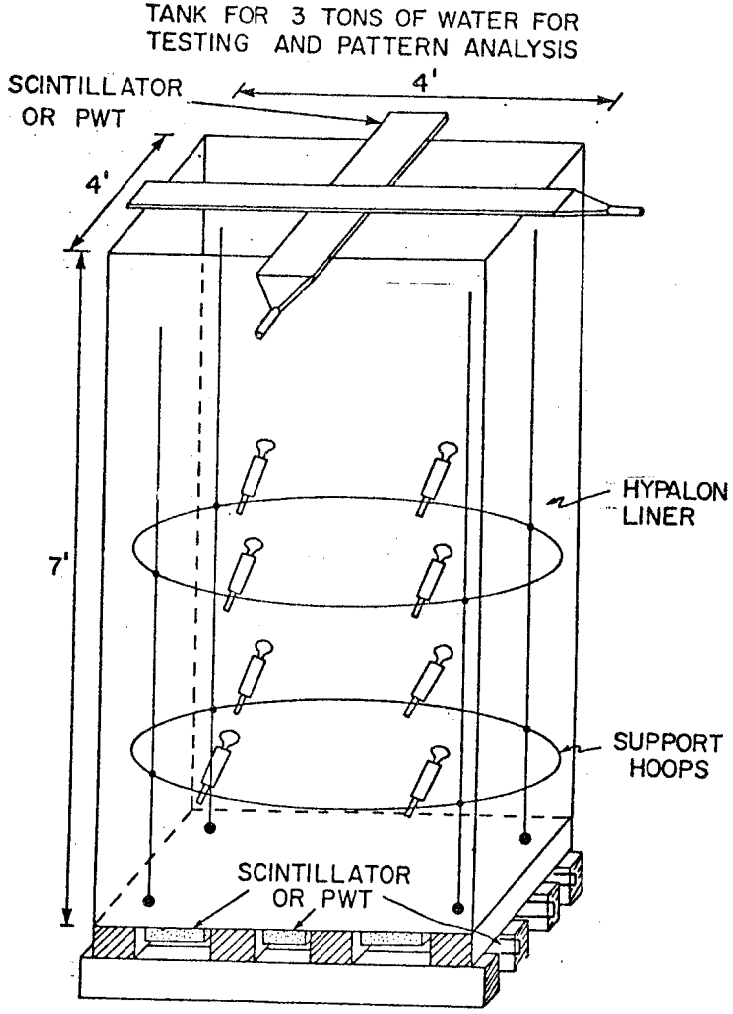

Fig. 15. Test facility for the HPW detector.

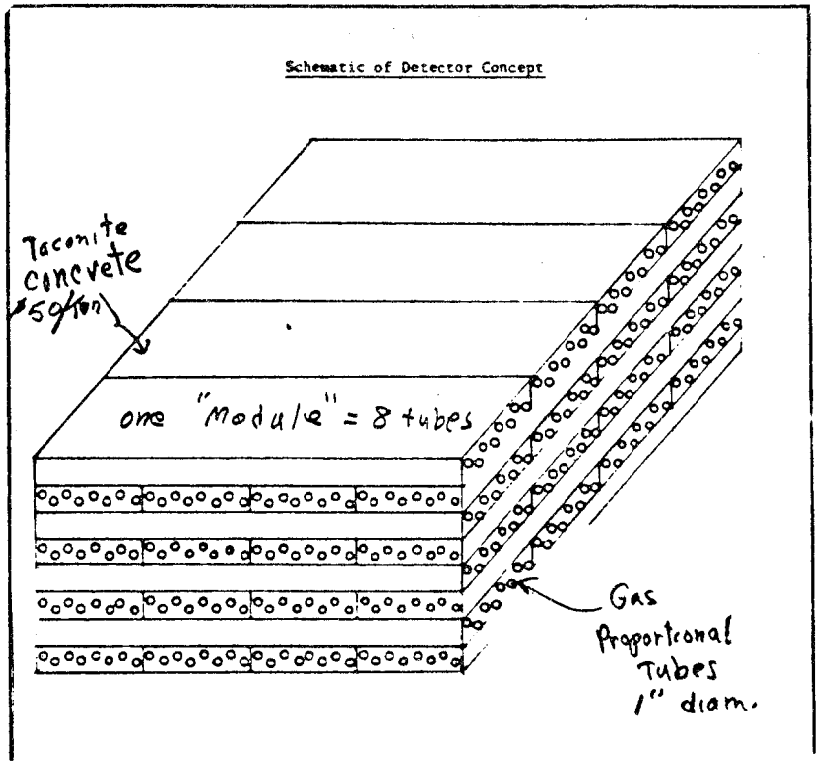

Fig. 16. Stacked modules of the Minnesota detector.

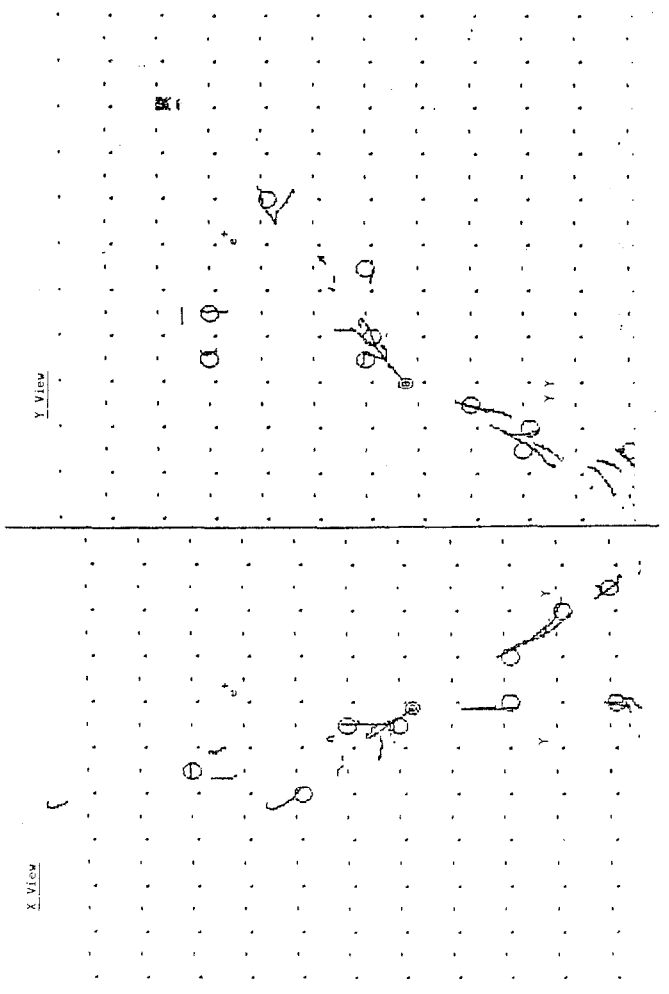

Fig. 17. Monte Carlo $p \to e^+ \pi^o$ event in the Minnesota detector. Circles represent firing proportional tubes.

necessary to recognize nucleon decays at a lifetime level just above present limits.

THE HOMESTAKE DETECTOR

In the Homestake gold mine in Lead, S.D. (4400 mwe), a group from the University of Pennsylvania has surrounded the ongoing solar neutrino experiment of Ray Davis et al. with a multipurpose detector to detect cosmic ray neutrinos, galactic neutrino bursts, cosmic ray muons, and nucleon decays. The detector consists of modules of wave-shifter doped water with four PMT's in each module. The total mass is about 400 tons. A sketch of the detector is shown in Fig. 18, taken from Ref. 4. Possible nucleon decays consist of a prompt pulse in neighboring modules followed by a $\mu \to e$ signature. The detection efficiency times branching ratio for nucleon decay is calculated to be .27. In $\sim$130 days of live time 89 events are seen, 2 of which could be nucleon decays. The calculated background from stopping cosmic ray muons is also 2 events. This gives a 90% C.L. upper limit on the nucleon decay lifetime of $\sim 1.5 \times 10^{30}$ years. (This result is unpublished as of this writing.)

THE NUSEX DETECTOR

This NUcleon Stability EXperiment is being assembled in the Mont Blanc Tunnel (5000 mwe) by the following group from CERN - Frascati-Milano-Torino.

G. Battistoni, E. Bellotti, G. Bologna, C. Castagnoli
V. Chiarella, D. C. Cundy, B. D'Ettorve, E. Fiorini (Spokesman),
E. Iarocci, G. P. Mannocchi, G. P. Murtas, P. Negri, L. Periale,
P. Picchi, M. Price, A. Pullia, S. Ragazzi, M. Rollier,
O. Saavedra, L. Trasatti and L. Zanotti

The detector will be a tracking calorimeter with a fairly fine granularity. The decaying material is primarily iron plates 1 cm thick separated by 1 cm × 1 cm limited streamer resistive tubes for track detection. A 150 ton version will be operating in the summer of 1981. A

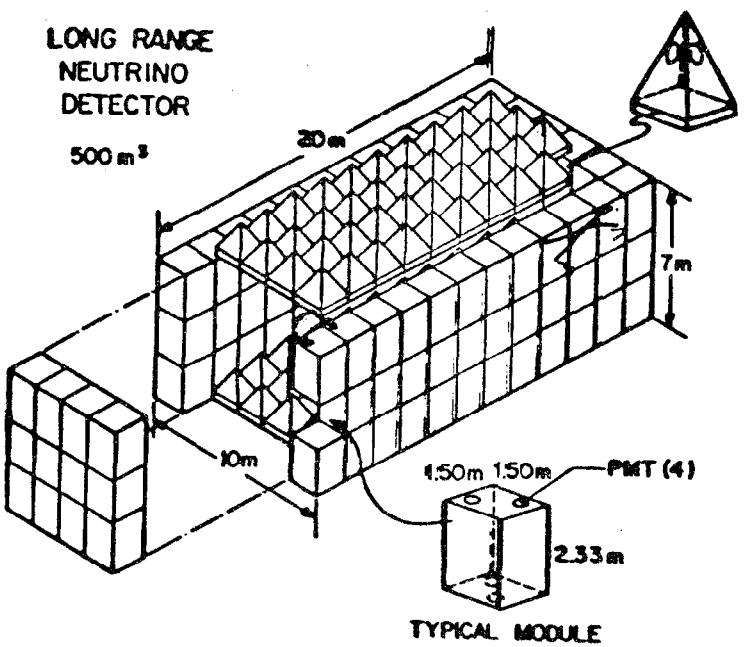

Fig. 18. Schematic of the existing Pennsylvania detector in the Homestake mine.

Monte Carlo $p \rightarrow \pi^0 e^+$ even in the detector is shown in Fig. 19. A full scale version is contemplated which would weigh 1200 tons and have 400,000 readouts.

THE FREJUS TUNNEL

The French government has dug an adit from one of the garages in the new Frejus tunnel on the Franco-Italian border. The room is large enough for a small scale detector or could be used as a staging area for a larger chamber. The depth is 4000 mwe. Physicists from Ecole Polytechnique, Orsay, Saclay, and CERN are considering and testing various possible detectors including flash-tube/iron sandwiches, limited Geiger tubes, and variations on the water Cerenkov idea. A collaborative effort on a large European experiment is being contemplated.

THE KGF EXPERIMENT

A group from the Tata Institute, Osaka, Tokyo which has ongoing experiments in the Indian Kolar Gold Field has proposed to do a nucleon stability experiment at a depth of 7000 mwe. At this depth the cosmic ray muon flux is down by a factor of 5000 from that at the IMB depth (1600 mwe). The authors of the proposal (dated May 1980) are as follows:

1. Tata Institute of Fundamental Research, Bombay, India
   (M. R. Krishnaswamy, M. G. K. Menon, M. K. Mondal, V. S. Narasimham, B. V. Sreekantan)
2. Osaka City University, Osaka, Japan
   (Y. Hayashi, N. Ito, S. Kazakami)
3. Institute for Cosmic Ray Research, Tokyo, Japan
   (S. Miyake)

The group plans to build a detector of 150 tons out of criss-crossed layers of 4"×4" proportional tubes separated by 1/2" iron plates. The overall dimensions would be 4m×4m×6m. A cut away of the detector is shown in Fig. 20.

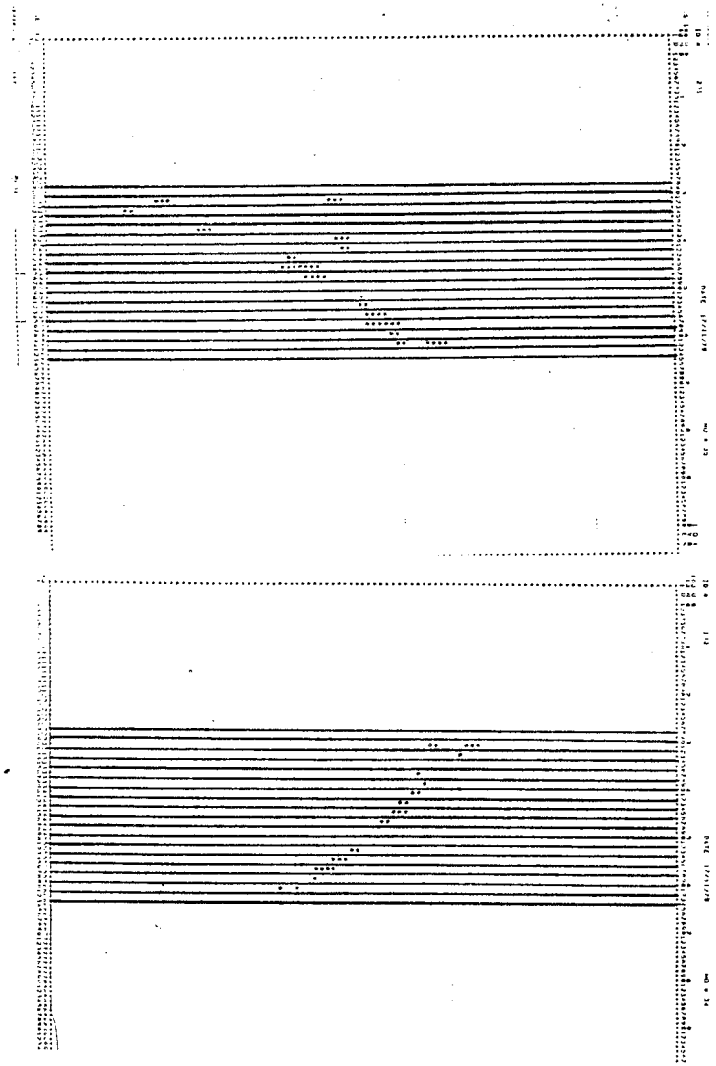

Fig. 19. Monte Carlo $p \to e^{+}\pi^{o}$ event in the Italian NUSEX detector. Dots represent firing limited-streamer resistive tubes.

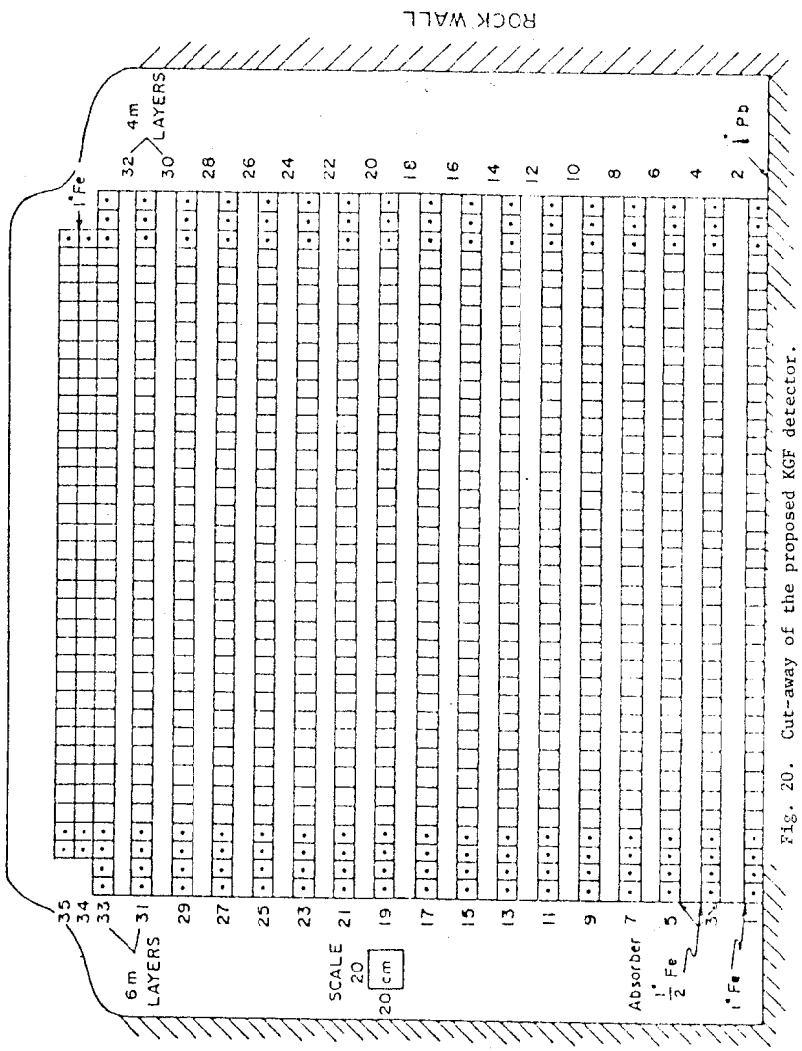

Fig. 20. Cut-away of the proposed KGF detector.

CONCLUSION

I have tried to give an up-to-date picture of the principal activity around the world to measure nucleon stability. It's obviously an exciting prospect that we may be on the brink of a whole new branch of physics.

ACKNOWLEDGEMENTS

I am greatly indebted to my cohorts, listed earlier, on the IMB experiment, as well as other colleagues, for long hours of discussion and sharing of ideas as we try to find our way in this new subject.

REFERENCES

(1) A. Zee (preceding talk at this conference).
(2) J. Learned, F. Reines, and A. Soni, Phys. Rev. Letters 43, 907 (1979).
(3) Amedeo Avogadro, b. Turin 9 June 1776, d. Turin 9 July 1856.
(4) M. Deakyne et al., Proc. of the Neutrino '78 Conference, Purdue University (Ed. by E. C. Fowler), pp.887-893.

RECENT RESULTS FROM THE CFRR NEUTRINO* EXPERIMENT AT FERMILAB

B. Barish, B. Blair, Y. Chu, B. Jin, D. MacFarlane, R. Messner, J. Lee, J. Ludwig, D. Novikoff, M. Purohit, F. Sciulli, and M. Shaevitz, California Institute of Technology, Pasadena, California 91125

D. Edwards, E. Fisk, Y. Fukushima, D. Yovanovitch, Q. Kerns, T. Kondo, P. Rapidis, S. Segler, R. Stefanski, and D. Theriot, Fermi National Accelerator Lab, Batavia, Illinois 60510

A. Bodek, R. Coleman, and W. Marsh
University of Rochester, Rochester, New York 14627

O. Fackler and K. Jenkins
Rockefeller University, New York, New York 10021

Talk presented by M. H. Shaevitz at the SLAC Summer Institute on Particle Physics (August 6-8, 1980).

ABSTRACT

Preliminary results from a new high-statistics study of neutrino and antineutrino interactions are presented. The full data sample includes 130,000 charged-current neutrino and 23,000 antineutrino events detected in the large-acceptance Lab E neutrino target at Fermilab with the N-30 dichromatic beam. Results based on a preliminary sample of one-third of the data are given for normalized cross sections, neutral currents, and like-sign dimuons.

* Supported in part by the U.S. Department of Energy under Contract No. DE-AC-03-79ER0068, San Francisco Operations Office.

INTRODUCTION

Deep inelastic neutrino scattering has long been a source of information concerning not only the weak interaction itself but also important details of nucleon structure, and more recently, new flavor production. Over the past five years, the experiments built to study these processes have become much larger, yielding increased data samples for analysis. With these new data, the errors have become dominated by systematic rather than statistical errors. In this paper, we report preliminary results from a new high-statistics experiment to measure neutrino interactions with good understanding of systematic effects.

DETECTOR

The Lab E neutrino detector is a separated-function device with a 690 ton target-calorimeter and 420 ton muon spectrometer (Figure 1). The target is composed of non-magnetized steel with transverse dimensions of 3m x 3m and is interspersed with scintillation counters every 10cm of steel and with spark chambers every 20cm. The non-magnetized nature of the target allows the precise tracking of the muon very close to the event vertex giving an angular resolution of

$$\sigma_{\theta}^{Proj}(\text{mrad}) = .14 + 57/P(\text{GeV}).$$

The muon spectrometer is made of solid iron toroids 12 feet in diameter with spark chambers and scintillation counters every 32" and 8" of steel respectively. The total field of the spectrometer corresponds to a P_t kick of 2.4 GeV. Figure 2 shows a computer reconstruction of a typical event with a muon traversing the spectrometer.

Absolute calibrations of the energy scale for the calorimeter and muon spectrometer have been performed using momentum-tagged hadron and muon beams coming into Lab E. The resolutions obtained in these cali-

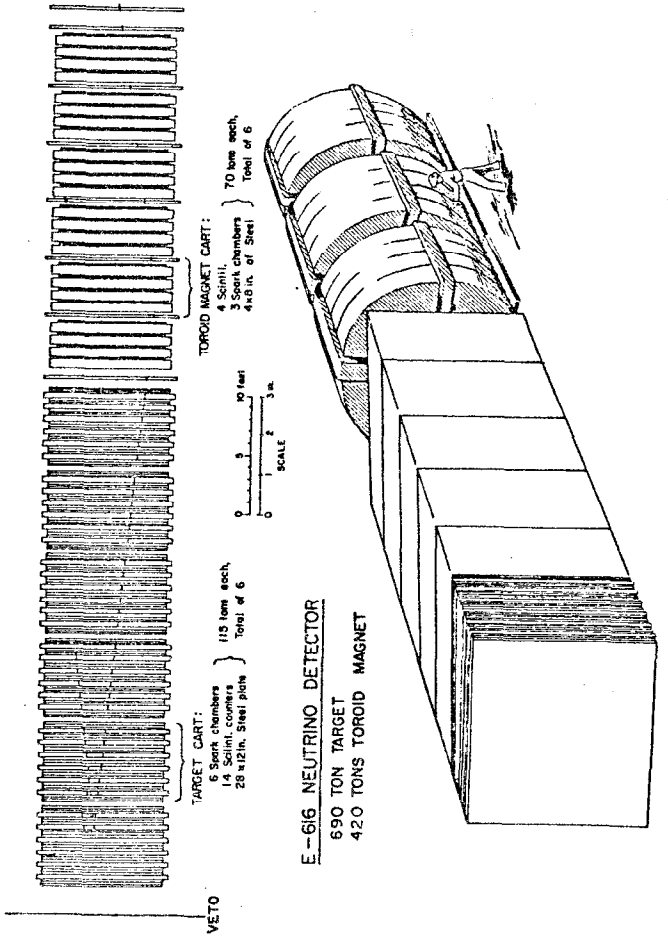

Figure 1: Lab E Neutrino Detector

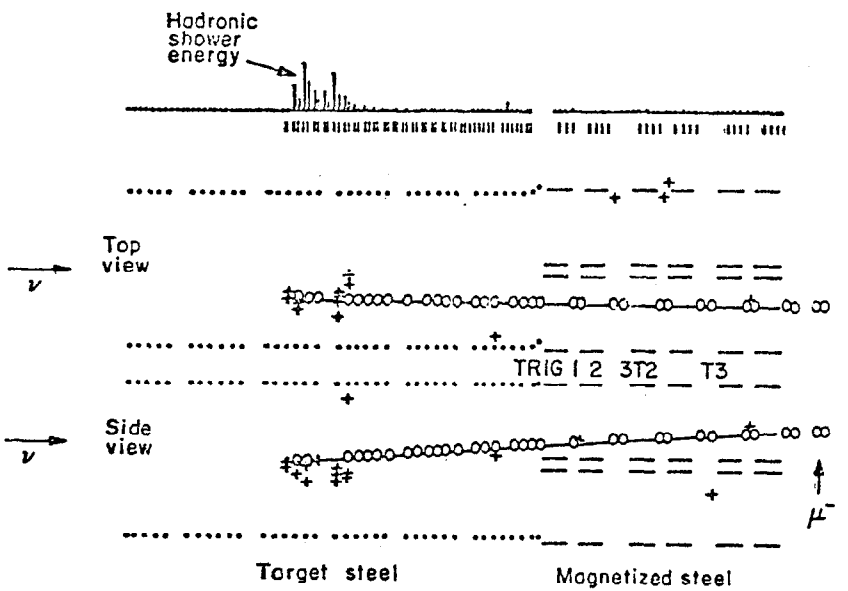

Figure 2: Computer reconstruction of a typical charged current event.

brations are

$$\Delta P_\mu/P_\mu = (.114^2 + (8.33 \times 10^{-5} P(\text{GeV}))^2)^{\frac{1}{2}}$$

and

$$\Delta E_H/E_H = .89/(E_H)^{\frac{1}{2}}$$

NEUTRINO BEAM AND FLUX MONITORING

The experiment uses the new N-30 dichromatic train at Fermilab. In this setup (Figure 3), a 400 GeV primary proton beam impinges on a BeO target, secondary particles are momentum and sign selected and then directed into a 340m evacuated decay pipe. The neutrino detector is located in Lab E, 910 meters downstream. The flux and energy spectrum of neutrinos at the detector is calculated from measurements of the number of pions and kaons in the decay pipe along with their energies and spatial distribution.

A combination of detectors is used to measure the flux of secondaries. The total flux (independent of particle type) is measured by ion chambers placed at two locations along the decay pipe. Each measuring station has three independent ion chamber gaps that allow cross checks to be made throughout the running period. The chambers are connected to the ADC's with sensitivities of either 20pC/count or 200pC/count. The calibration of the ADC's is continuously monitored by inducing pulses of known charge into the units.

The absolute calibration of the ion chambers is measured in two separate ways. First, the response of the chamber to a primary proton beam transported through the train is calibrated against a beam current transformer and RF cavity using a set of foil activation measurements as intermediate monitors. These measurements use a Cu foil of known thickness exposed to the primary proton beam. Although the foil

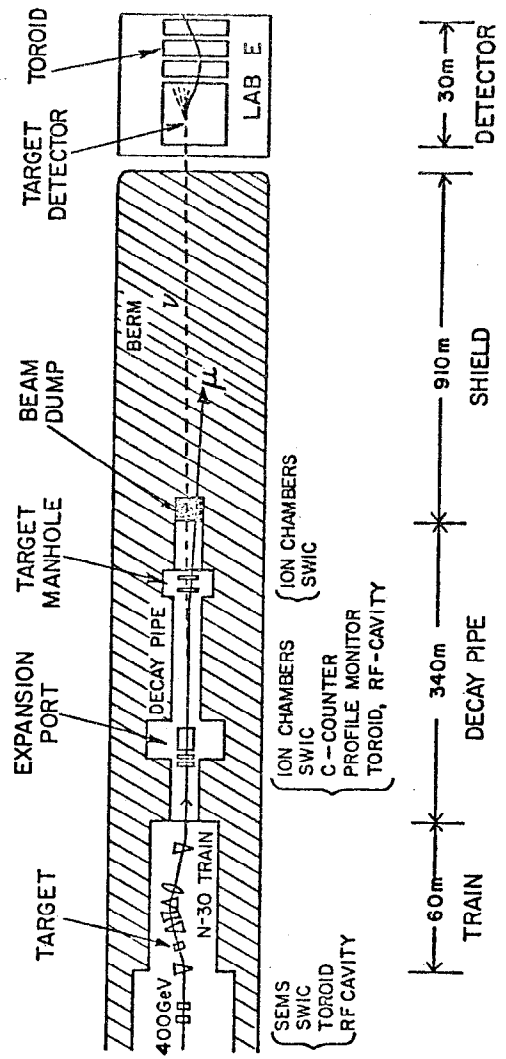

Figure 3: Layout of the Fermilab dichromatic neutrino beam line.

activation is only used to calibrate the ion chamber against the other devices, we do obtain the activation cross section as a by-product. The value of the cross section measured in this way for Na^{24} in Cu with incident 200 GeV protons is 3.90 ± .13 mb which agrees with previous measurements by our group. In the second method, we calibrate the ion chamber directly with a low intensity secondary beam and single particle counting. The calibration from this technique agrees with the first method to 3%. For the results presented in this paper, we estimate the total error for the ion chamber calibration including systematic errors to be 3.5%.

Particle fractions are measured with a differential Cerenkov counter using a He radiator; electronics integrate the counter's response over the entire beam spill. The counter has been calibrated by using a mono-energetic 200 GeV primary proton beam coming directly from the accelerator. This calibration provides a measurement of the gas index of refraction to better than .1% and also maps the counter response to a mono-energetic beam. The particle fractions measured with this counter at the different secondary momentum settings used in the experiment are given in Table I.

The flux monitoring system is designed to have many cross checks for the study of systematic errors. A segmented ion chamber (the "muon chamber") behind the beam dump (see Figure 3) measures the number and spatial distribution of decay muons and, therefore, the neutrino flux. At present this device has not been absolutely calibrated and can only be used to check the relative flux between different momenta and polarities. The pion fluxes obtained with this chamber agree with the above measurements using the Cerenkov counter and ion chamber to better than one percent for negative settings and five percent for positives.

TABLE I: Particle Ratios from Cerenkov Measurements

Beam Momentum (Positives)	K/π	π/P	Beam Momentum (Negatives)	K/π
			-250	.035 ±.002
+200	.145 ±.010	.224 ±.016	-200	.048 ±.003
+169	.135 ±.009	.403 ±.028	-169	.062 ±.004
+140	.128 ±.009	.640 ±.045	-140	.073 ±.005
+120	.109 ±.008	.895 ±.063	-120	.080 ±.006

For the preliminary results presented here, we estimate the systematic error in the neutrino flux to be below 10%. In the future, we should eventually reach errors of 2-3% with the additional information available from an absolute calibration of the muon chamber and the RF cavity placed in the decay pipe.

Knowledge of the energy spectrum of secondaries in the decay pipe is crucial for inferring the energy and flux of neutrinos at the detector. From measurements of particle yields for pions, kaons, and protons, energy spectra for each of the momentum settings are calculated. These spectra can be checked in two ways. First, for protons and kaons, the mean pressure observed in the Cerenkov counter is related to the mean momentum by

$$\text{Mean}\left(\frac{1}{(\text{Momentum})^2}\right) = \left(\frac{m^2_{K \text{ or } P}}{\langle\theta_c^2\rangle - 2K\langle\bar{P}\rangle}\right)^{-1}$$

where K and $\langle\theta_c^2\rangle$ are measured with the 200 GeV mono-energetic proton beam calibration and $\langle\bar{P}\rangle$ is the mean pressure. With this procedure, the energy can be measured to better than 1% and agrees with the value predicted from the particle yields at that level. An additional check using the measured energy of observed neutrino events also shows agreement to 1%.

TOTAL CROSS SECTION RESULTS

Neutrino and antineutrino data were recorded at five secondary energies (250, 200, 169, 140, and 120 GeV) over a period of eight months ending January 1980. The total sample includes 130,000 charged current neutrino interactions and 23,000 antineutrinos. The cross section results shown here are preliminary and correspond to about one-third of the above sample. All events are reconstructed by computer with fiducial and reconstruction cuts applied to limit the sample to regions with good acceptance and small background. With these cuts, the fiducial volume is restricted to 430 tons. Corrections are made for wide band background, cosmic ray contamination (1%), geometrical efficiency, and the unsampled region at high x and high y (3%). Geometrical inefficiency is corrected by a model independent method in which observed events are weighted by an efficiency factor. The efficiency factor is calculated by rotating the observed event around the beam direction as well as translating the event vertex along the beam direction and determining if the event would be accepted with the new vertex and orientation.

The method for extracting cross sections from the data uses both the events with the muon traversing the toroidal spectrometer (muon trigger events) and events where the muon stops or exits the side of the target before entering the spectrometer (hadron trigger events). The hadronic energy is measured for both types of events but the muon energy (and, thus, the total energy) is only measured for muon trigger events. Once the events are separated into interactions of neutrinos from either pion or kaon decay, the total energy for each event can be determined from its interaction point in the target due to the nature of the dichromatic beam. The separation of events into pion and kaon neutrinos is straightforward for both classes of events. For the muon trigger events, the total energy is measured and can be used for the separation. For hadron trigger events which occur at high y, the hadronic energy for kaon and pion neutrino interactions is sufficiently different to allow separation. With the events separated into radial bins and neutrino types, total cross sections for each beam setting are formed using the neutrino energy and flux distributions described previously.

For the final results shown in Figure 4, the different energy settings are combined; checks made in regions where different settings overlap show the cross sections to agree within statistical errors. The average total cross sections for the range from 40-200 GeV are:

$$\sigma_T^{\nu}/E_{\nu} = .733 \pm .005 \pm .073 \times 10^{-38} \text{ cm}^2/\text{GeV}$$

$$\sigma_T^{\bar{\nu}}/E_{\bar{\nu}} = .371 \pm .004 \pm .037 \times 10^{-38} \text{ cm}^2/\text{GeV}$$

where the first error is statistical and the second systematic. The results agree with our previous measurement[1] for neutrinos of (.700 ± .015 ± .035) taken with this beam and detector but are 15-20% higher compared to the world average of .63 ± .02 for neutrinos and .30 ± .01 for antineutrinos.

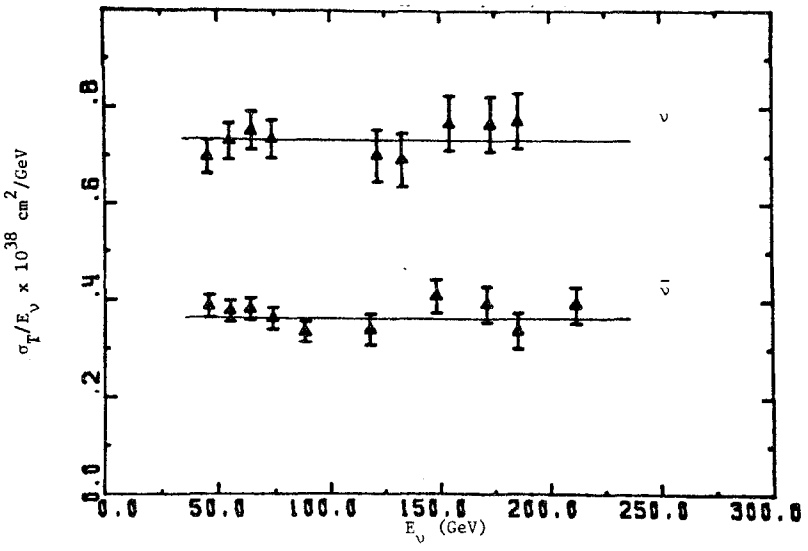

Figure 4: Total Cross Sections vs. Energy. Upper points are for incident neutrinos; lower points for antineutrinos.

NEUTRAL CURRENTS AND $SIN^2\theta_w$

The most precise measurements of $\sin^2\theta_w$ are from high statistics studies of deep inelastic neutrino scattering. The errors in these measurements are dominated by systematic uncertainties. Experimentally, large background subtractions are necessary to correct for wide band events, charged current events identified as neutral currents, and electron neutrino contamination in the beam. Theoretically, if one extracts $\sin^2\theta_w$ from the ratio of neutral to charged currents, corrections must be applied for scaling violations, anti-quarks, neutron-proton excess, and the experimental cut on the minimum detectable hadronic energy. We have chosen to measure $\sin^2\theta_w$ from the data by using the Paschos-Wolfenstein relations[2] with additional kinematic cuts in an effort to minimize some of the above uncertainties. In this method,

$$R- = \frac{\sigma^{\nu}_{NC} - \sigma^{\bar{\nu}}_{NC}}{\sigma^{\nu}_{CC} - \sigma^{\bar{\nu}}_{CC}} = \rho\ (\tfrac{1}{2} - \sin^2\theta_w)$$

and

$$R+ = \frac{\sigma^{\nu}_{NC} + \sigma^{\bar{\nu}}_{NC}}{\sigma^{\nu}_{CC} + \sigma^{\bar{\nu}}_{CC}} = \rho\ (\tfrac{1}{2} - \sin^2\theta_w + \frac{10}{9}\sin^4\theta_w)$$

These relations are true independent of any details of scaling violations or amount of anti-quark contribution and, thus, eliminate some theoretical corrections inherent in the simple ratio method.

Experimentally, this method demands that neutrinos and antineutrinos be normalized relative to one another and that the target nucleus be isoscalar; both requirements are satisfied by this experiment (small corrections are necessary for the neutron excess in Fe). The ratios, R^+ and R^- are independent of the particular kinematic region used and can, therefore, be evaluated in a domain where charged and neutral current events are clearly distinguished. The region of confusion is at high x and y where the outgoing muon exits the target before being identified. This region can be eliminated by a cut on Y_{NC} = (Observed hadron energy)/(Neutrino energy predicted from the dichromatic beam at the given radius). The cut depends on the event radius, r, and the length, L_{cut}, required to identify a muon in the detector and is given by

$$Y_{NC} < Y_{cut} = \frac{E_\nu\ \theta^2_{max}}{2M_p + E_\nu\ \theta^2_{max}} \quad \text{where } \theta_{max} = \tan^{-1}\frac{60''-r}{L_{cut}}$$

Figure 5 shows a length distribution before and after a Y_{cut}. With an L_{cut} = 210cm, it can be seen that the charged current contamination under the neutral current peak is substantially reduced; moreover, the shape agrees well with the Monte Carlo prediction. With this procedure, the charged current contamination in the neutral current sample is reduced to 4% for neutrinos and 2% for antineutrinos.

The preliminary results given here are for the 200 GeV momentum setting (about 1/3 of the total data) for neutrinos and antineutrinos from pion decay with L_{cut} = 210cm and E_{hadron} > 20 GeV. Small corrections as shown in Table II have been applied for the backgrounds mentioned previously giving the results:

$$R- = .258 \pm .035$$

$$R+ = .326 \pm .015$$

Additional corrections for strange/charm quarks, charm quark threshold effects, kaon neutrino contamination, and the small excess neutron content of the iron target amount to +3.4% for R- and +3.9% for R+. Converting these ratios to measurements of $\sin^2\theta_w$ gives the results:

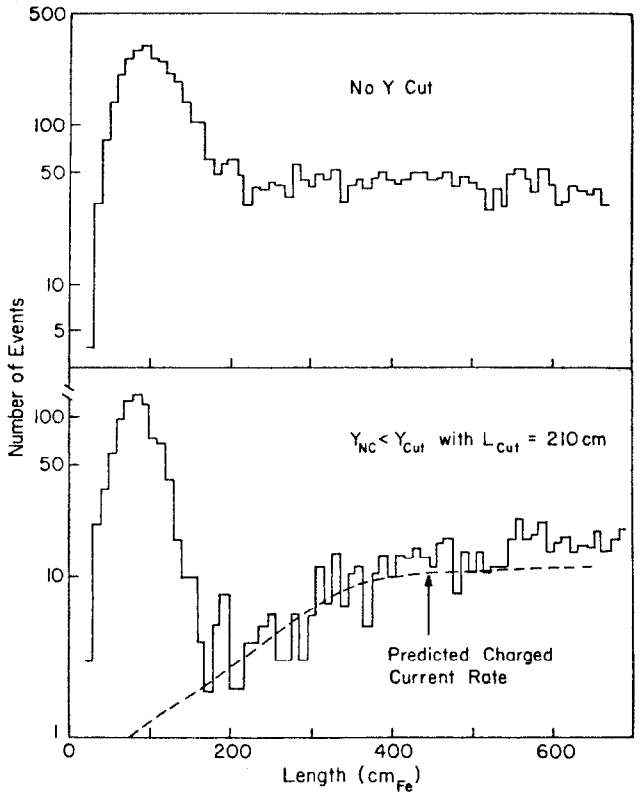

Figure 5: Length distribution for neutrino events The lower histogram has an additional cut on Y_{NC} with L_{cut} = 210cm (see text). The curve is a Monte Carlo prediction for charged current events with the same cuts.

Two Parameter Fit $\rho = 1.01 \pm .10$

$\sin^2\theta_W = .246 \pm .056$

One Parameter Fit $\sin^2\theta_W = .239 \pm .023$ with $\rho = 1.0$

TABLE II: Corrections to the Neutral Current Events

	Neutrinos	Antineutrinos
Charged Current Back	-3.9%	-2.0%
Cosmic Rays	-1.0%	-5.3%
Wide Band Background	-1.4%	-0.1%
Ke3 Background	-1.7%	-0.4%
π/K Decay in Shower	+0.1%	+0.1%
Other Corrections	+0.2%	+0.9%
Total	-7.7%	-6.8%

LIKE-SIGN DIMUON PRODUCTION

Over the past few years, several experiments[3,4,5] have observed the production of neutrino induced like-sign dimuon events at high energy. Two questions have arisen concerning these events. First, are the events associated with a prompt source and not just π/K decay? Second, if the events are prompt, what is the source? For the results presented here, we address these two questions.

The amount of π/K decay contamination in our sample of like-sign dimuon events is calculated using a novel approach which relies on experimental data as much as possible. The calculation separates the

background into two parts; a contribution from the decay of hadrons produced in the primary neutrino interaction and a contribution from the shower produced when these hadrons interact in the steel. The calculation utilizes a Field-Feynman quark jet simulation program[6] based on fits to neutrino-induced hadron final state data as measured in Neon bubble chamber experiments. This program provides the multiplicity and energy distributions for hadrons produced in the primary neutrino interaction. The contribution from subsequent interactions of these hadrons is determined using direct measurements of π-Fe interactions from another experiment[7] where both prompt muon and non-prompt muon rates have been measured at several incident hadron energies. This method uses empirical data except for first-generation decays where it assumes that ν-Ne distributions are the same as the ν-Fe distributions and that the Field-Feynman fits also represent the data at high hadron energies where the bubble chamber data are relatively poor. The procedure has been cross-checked by using new bubble chamber data[8] at higher energies directly instead of the Field-Feynman program. Figure 6 shows a comparison of these two methods along with the rate for muon production by incident pions. The two calculations agree on the amount of background in the dimuon sample to better than 20% and are close to the rate observed for pionic production

In a previous experiment (Experiment 482 at Fermilab) using the quad-triplet neutrino beam, we observed twelve like-sign events with $P_\mu > 9$ GeV and a calculated π/K decay background of 1.3 events. In the present experiment (with about one-third of the data analyzed), we have found nine like-sign events with 2.6 events background. (The difference in the ratio of signal to background for the two experiments is due to

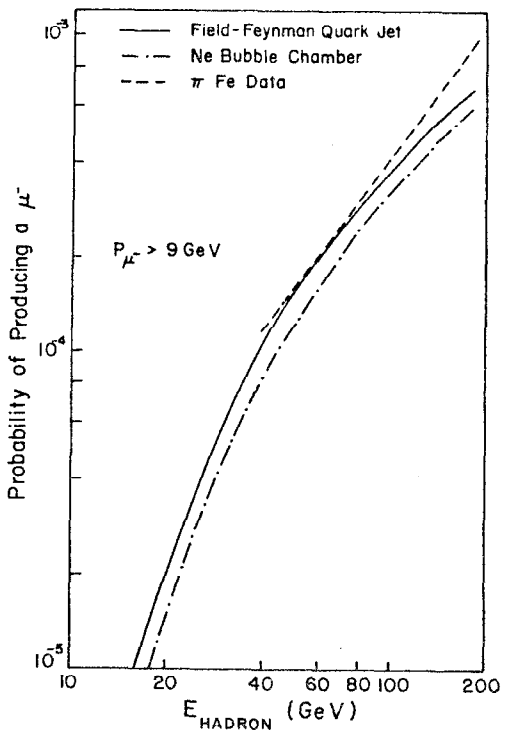

Figure 6: Comparison of the different methods of calculating the π/K decay background. The curves are the probability to produce a μ^- with $P_{\mu^-} > 9$GeV from π or K decay as a function of the hadronic energy. The solid curve uses the Field-Feynman quark jet program; the dot-dashed uses ν-Ne bubble chamber data directly. The dashed curve is production by incident pions.[7]

the like-sign events produced at neutrino energies above 250 GeV in the quad-triplet beam.) Clearly, a prompt signal of like-sign events is established; the probability that all the like-sign events originate from π/K decay is extremely small. The purity of these two samples is better than previous experiments in which the background is typically as large as the prompt signal. The reduction of the π/K decay background in this experiment is primarily due to the P_μ cut of 9 GeV, the high density of the target, and high energy beam.

Figure 7 shows the opposite- and like-sign rate versus neutrino energy for the two data samples. The event distributions have been corrected for geometrical efficiency and π/K decay background. The opposite-sign events show a sharp rise with energy around 50 GeV and flattening above 100 GeV characteristic of charm quark production convoluted with the experimental acceptance. In contrast, the like-sign events show a strong energy dependence over the entire range from 50-200 GeV. A large rise with energy is expected for the production of heavy mass particles and is most probably enhanced by the P_μ requirement. (A Monte Carlo calculation of $C\bar{C}$ production gives correction factors for the P_μ cut of 5 and 2 for E_ν = 100 and 200 GeV respectively.) A theoretical curve based on a first order QCD calculation of charm-anti-charm production via gluon bremsstrahlung and including experimental acceptance is also shown in Figure 7. The curve does show a large rise with energy but lies about two orders of magnitude below the observed data. There is an expectation that higher order corrections will raise this calculated rate substantially[9]. For this reason, $C\bar{C}$ production is still a possible source of the like-sign events.

Table III gives the average kinematic variables for the opposite- and like-sign samples. Several features are evident. The average ψ

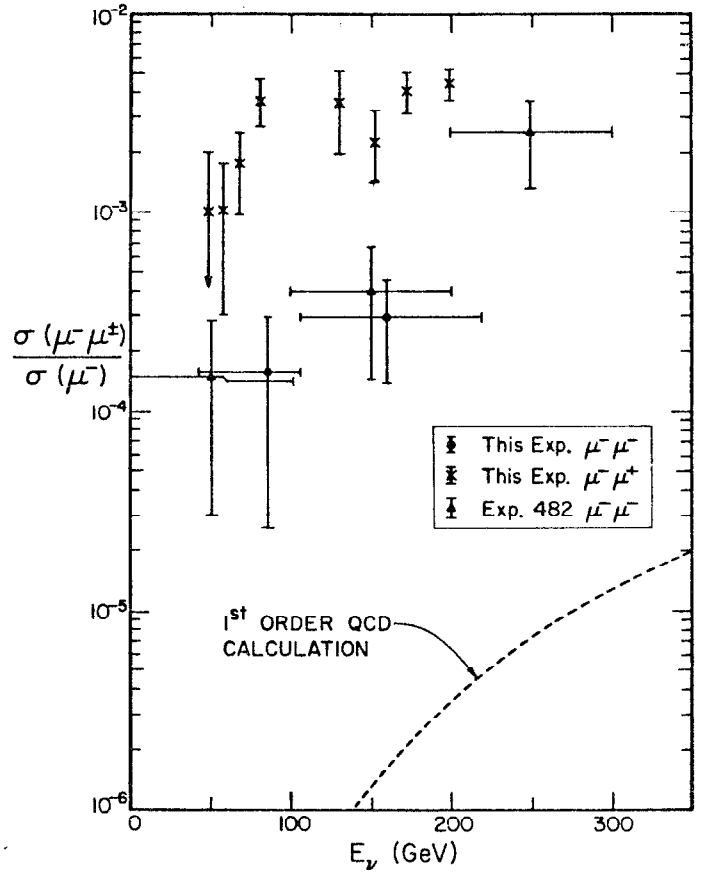

Figure 7: The prompt opposite- and like-sign dimuon rate with P_μ > 9 GeV versus energy. The curve is a QCD calculation of $C\bar{C}$ production with the second muon from the $\bar{C}$ decay.

TABLE III - Average Quantities for $\mu^-\mu^+$ and $\mu^-\mu^-$ Events

	This Exp. $\mu^-\ \mu^+$	This Exp. $\mu^-\ \mu^-$	Exp. 482 $\mu^-\ \mu^+$	Exp. 482 $\mu^-\ \mu^-$
Evis (GeV)	166 ± 5	154 ± 4	148 ± 6	179 ± 19
E_h (GeV)	76 ± 2	77 ± 4	62 ± 4	101 ± 14
$P_{\mu 2}$ (GeV)	23 ± 2	16 ± 1	19 ± 1	14 ± 2
$P^s_{\perp 2}$ (GeV)	.61 ± .05	.50 ± .04	.91 ± .07	.63 ± .14
φ (deg)	140 ± 4	135 ± 4	130 ± 5	131 ± 8
x_{vis}	.16 ± .02	.24 ± .03	.14 ± .01	.22 ± .07
y_{vis}	.61 ± .03	.60 ± .02	.59 ± .02	.63 ± .05
z_μ	.27 ± .02	.18 ± .02	.33 ± .02	.17 ± .04
W (GeV)	12.0 ± .3	10.8 ± .3	11.3 ± .4	12.7 ± 1.2

where

$E_{vis} = E_{\mu 1} + E_{\mu 2} + E_h$

$P_{\mu 2}$ is the momentum of the second muon

$P^s_{\perp 2}$ is the momentum of the second muon perpendicular to the hadron shower direction

$x_{vis} = 2E_{\mu 1} E_{vis} \sin^2(\theta_{\mu 1/2}) / (E_{\mu 2} + E_h)M_p$

$Y_{vis} = (E_h + E_{\mu 2}) / E_{vis}$

$z_\mu = P_{\mu 2} / (P_{\mu 2} + E_h)$

W is the invariant mass of the hadron system

angle and hadron energy, E_h, indicate that like-sign events are associated with the hadron vertex and, therefore, exclude heavy leptons as the source. The value for $P^s_{\perp 2}$ is smaller for the $\mu^-\mu^-$ sample compared to the $\mu^-\mu^+$ sample; this quantity should be larger if the $\mu^-\mu^-$ events are from the direct decay of quarks heavier than charm (bottom, top, etc.). The average z_μ for like-sign events is about one half the value for opposite-sign events as would be expected for $C\bar{C}$ production where the C and $\bar{C}$ quarks share the gluon energy. In general, the kinematic distributions of the like-sign events are consistent with the source being the hadronic vertex, and specifically from the decay of a charmed particle in associated production.

In conclusion, we have observed a large rate for the production of like-sign dimuons by neutrinos at high energy. Calculations indicate that the background from π/K decay is very small. The like-sign rate shows a steep rise with energy consistent with the production of a heavy mass state. While the source of the like-sign dimuons is still not known, it is not likely that they originate from either heavy leptons or quarks heavier than charm. Associated charm-anticharm production is one possible source that cannot be ruled out. Further studies with higher energies and statistics should help clarify this question.

REFERENCES

1. J. Lee, California Institute of Technology, Thesis (unpublished).

2. E. A. Paschos and L. Wolfenstein, Phys. Rev. D7, 91, (1973).
P. Q. Hung and J. J. Sukurai, Phys. Lett. 63B, 292, (1976).

3. A. Benvenuti et al., Phys. Rev. Lett. 41, 725, (1978).

4. M. Holder et al., Phys. Lett. 70B, 396, (1977).

5. J. G. H. deGroot et al., Phys. Lett. 86B, 103, (1979).

6. R. Field, private communications.

7. Data of Fermilab Experiment 379.

8. I. S. Chima, private communications, ν-Ne data from the BEBC collaboration.

9. G. L. Kane et al., Phys. Rev. D, 19, 1978, (1979).

SOME RESULTS FROM THE CHARM NEUTRINO EXPERIMENT AT THE CERN SPS

F. Niebergall*)
II. Institut für Experimentalphysik,
University of Hamburg, Hamburg, Germany

INTRODUCTION

The electronics detector of the CHARM Collaboration[1] has been taking data for about two years in the CERN SPS narrow- and wide-band neutrino beams (NBB and WBB). It was designed for a variety of applications which make it particular and different from other devices used in this field. In the first section the special features of this detector will be discussed. The four remaining sections are devoted to the discussion of physics results.

Section 2 treats the experiment on the reaction of inverse muon decay $\nu_\mu e \to \mu^- \nu_e$ and section 3 the measurement of the polarization of muons from the inclusive interactions of $\bar{\nu}_\mu$ with iron, $\bar{\nu}_\mu Fe \to \mu^+ X$, which was performed in collaboration with members of the CDHS group[2]. Both these experiments were performed with the main aim of studying space-time properties of weak interactions in leptonic and semileptonic reactions.

In section 4 some results of NBB running will be presented. Inclusive interactions of ν_μ and $\bar{\nu}_\mu$ are used to extract cross-section ratios and y distributions. The determination of the electro-weak mixing angle and the left- and right-handed coupling strengths confirms previously obtained results[3], with comparable precision but very different systematic uncertainties. Special emphasis is put on the extraction of y distributions for neutral current (NC) interactions which we compare with charged current (CC) y distributions obtained by the same procedure.

The last section treats results from a beam-dump experiment which was performed as the second of, as it now turns out, a whole series of experiments. The CHARM Collaboration did not participate in the first of these runs, where the existence of a prompt electron-neutrino flux was established by three different experiments[4]. The magnitude of the effect was, however, somewhat controversial and the existence of a prompt muon-neutrino signal could not be clarified. A new experiment was therefore performed with improved statistics and better control

*) Visitor at CERN, Geneva, Switzerland.

over background. The results of this run could eliminate earlier discrepancies and prove the existence of a prompt muon-neutrino flux. It yielded, however, new discrepancies as to the occurrence of prompt antimuon-neutrino production and the deviation of the electron-to-muon-neutrino flux ratio from the expected value of one. This led to the decision at CERN to perform yet another beam-dump experiment, which is currently being prepared.

1. THE CHARM NEUTRINO DETECTOR

The apparatus of the CHARM Collaboration[5] is an electronics detector consisting of two parts: a target calorimeter and a muon spectrometer. Figure 1 shows an over-all view of the set-up.

The design of the detector was largely determined by the main aim of the experiment to perform a kinematically complete measurement of NC inclusive interactions. This necessitates the determination of the energy and direction of the final-state hadronic system and the possibility of identifying muonless interactions on an event-by-event basis. These tasks can be performed by a relatively low density highly instrumented target calorimeter, which is surrounded by an iron magnet system.

Details of the detector are shown in Fig. 2. In the calorimeter part marble is used as target material. Its composition, $CaCO_3$, constitutes an isoscalar target and also has the desired feature of not depolarizing stopping μ^+. The marble plates of 3 m × 3 m lateral dimensions, 8 cm thick, are surrounded by 45 cm wide and 8 cm thick iron frames which can be magnetized such that a toroidal field of about 15 kG in the iron allows the determination of the momentum of muons leaving the detector at the side, or such that a dipole field of 58 G is created in the marble to precess the spin of stopping muons. The front face of the marble plates is covered by 20 scintillators, which are 3 m long, 15 cm wide and 3 cm thick. Behind the marble and also covering the iron frames are planes of proportional drift tubes[6]. One plane is composed of 128 tubes, which are 4 m long and have a cross-section of 3 cm × 3 cm. The calorimeter consists of 78 of these detector subunits with alternating orientation of the detector elements.

The first section of the toroidal iron end magnet is made up of 15 plates, 5 cm thick, instrumented with proportional drift tubes to measure not only muon tracks but also shower energy leaking out of the calorimeter. Five 15 cm thick plates are used for each of the three magnets that constitute the last part of the spectrometer. These

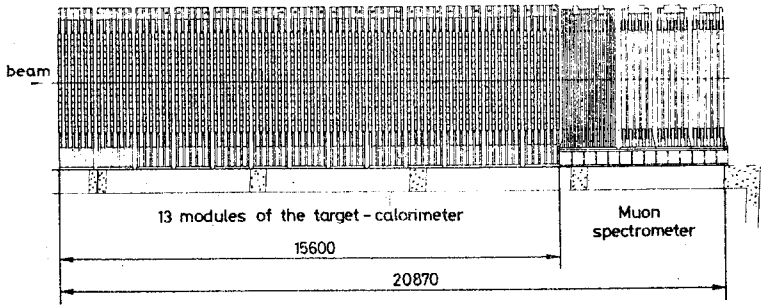

Fig. 1 The CHARM detector

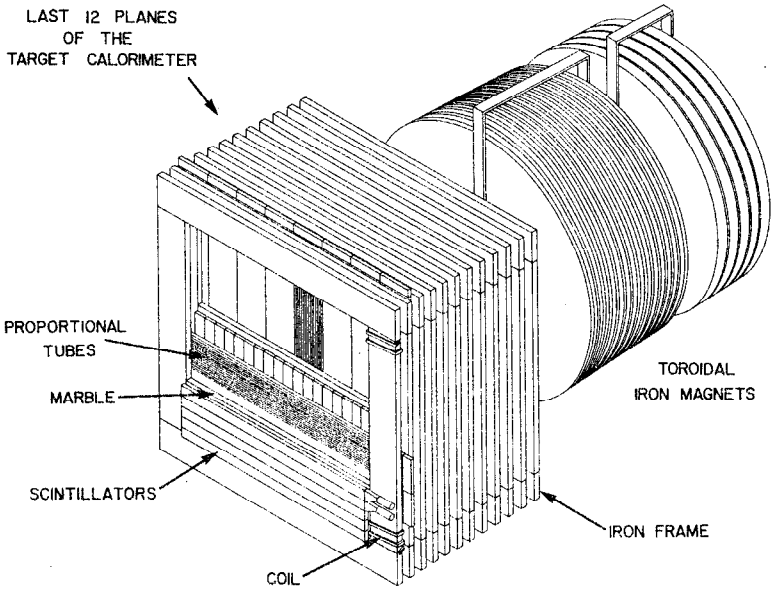

Fig. 2 Partial view of the fine-grain calorimeter and the muon spectrometer

magnets are equipped with scintillation counters to measure radiative losses of muons and interspersed with packages of proportional drift tubes to determine the coordinates of muon tracks.

The 1560 scintillation counters of the calorimeter are each equipped with a single photomultiplier. The signals are used to trigger the detector. They are recorded using two analog-to-digital converters (ADCs) for each channel. This provides a large dynamic range and high precision for measuring low pulse heights. Each of the 12,300 proportional drift tubes is equipped with an ADC and a time-to-digital converter (TDC) so that ionization and drift-times can be determined for individual tubes.

The detector combines the advantage of a relatively high fiducial mass of about 100 t with a high pattern recognition power. This is illustrated in Fig. 3, which shows a simplified on-line display of a CC neutrino interaction.

Data on detector performance are collected in Table 1. To these one has to add the following features:

- full trigger efficiency at low energies, $E_{shower} \geq 1.5$ GeV;
- good muon identification down to low momenta (a muon of 1 GeV/c momentum has a range of 20 target plates);
- 95% efficiency for muon charge determination for $p_\mu \geq 4$ GeV/c;
- electromagnetic showers can be distinguished from hadronic showers owing to the big difference in the widths of these shower types (see Fig. 4);
- CC interactions of ν_e and $\bar{\nu}_e$ can be identified.

The last feature is unique for an electronic detector. It found its first application in the analysis of the beam-dump experiment and will be explained in some more detail.

In contrast with hadronic showers, electromagnetic showers are extremely narrow (typically 2.5 cm FWHM, see also Fig. 4), and very regular in their longitudinal energy profile. To search for an electromagnetic component in a muonless neutrino event we define a band of the width of the scintillator elements (15 cm) which starts at the interaction vertex. The length of the band is typically restricted to about 10 radiation lengths (10 target plates), depending slightly on the energy found deposited in it. In the central part of the band, over a range of about 8 planes, the pulse height in each scintillator must be

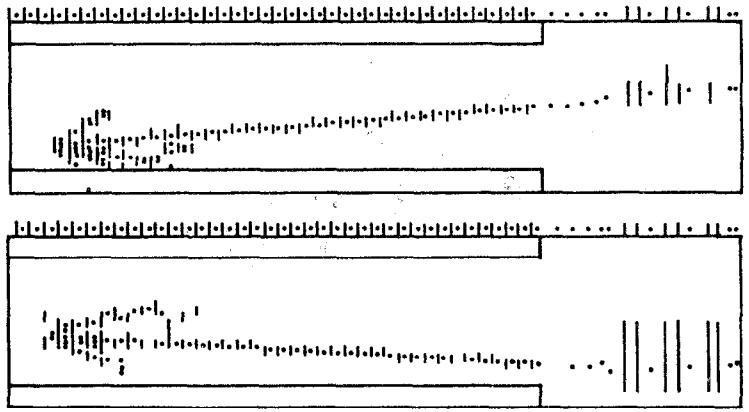

Fig. 3 Simplified on-line event display. Top and side view of a charged current neutrino interaction. Dashes and dots indicate hits in scintillators and proportional drift-tubes respectively.

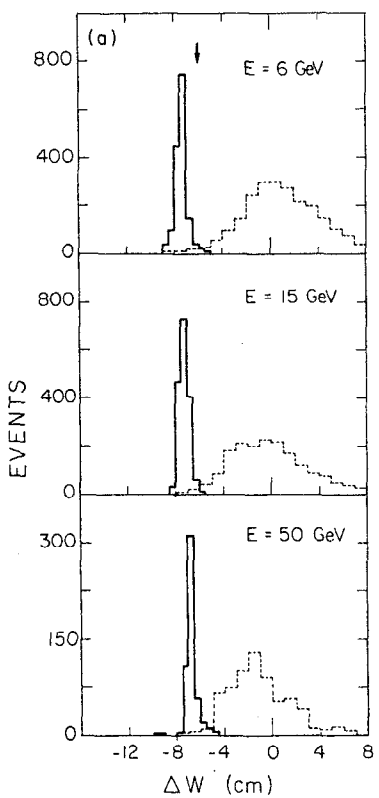

Fig. 4 Comparison of shower width (arbitrary units) for electrons (full-line histogram) and pions (dashed line histogram).

Table 1

Some characteristic features of the CHARM detector

Resolutions (E in GeV):	
energy (hadrons)	$\sigma(E) = 0.53\sqrt{E}$
" (electrons)	$\sigma(E) = 0.20\sqrt{E}$
shower angle	$\sigma(\Theta) = \left(\frac{0.16}{\sqrt{E}} + \frac{0.56}{E}\right)$ rad
vertex position (transverse)	$\sigma(y,z) = \left(\frac{19.5}{\sqrt{E}} + 0.003E_{shower}\right)$ cm
μ momentum, end magnet	$\frac{\sigma(p)}{p} = 16\%$
μ momentum, frame magnet	$\frac{\sigma(p)}{p} \approx 25\%$
μ angle	$\sigma(\Theta) \approx 2.5$ mrad
Average density	$\langle\rho\rangle = 1.3$ g/cm^3
Radiation length	$X_0 = 20$ cm
Absorption length	$\Lambda^{\pi}_{abs} = 93$ cm
Fiducial mass	100 t

higher than the equivalent of three minimum ionizing particles and the maximum of the pulse height must lie at a limited distance from the vertex.

In such a band we define four estimators of the total energy of the electromagnetic shower candidate: the maximum pulse height in a single scintillator, the pulse height measured in three longitudinally adjacent scintillators around the maximum, and the total pulse height for each of the two orientations of scintillator elements. These estimators have been calibrated in electron test beams for energies from 3 to 50 GeV. The combined resolution was found to be $\sigma_E/E = 0.25/\sqrt{E}$, comparable to the one obtained without spatial restrictions (see Table 1).

The four estimators are submitted to a test of whether they measure the same energy, and the band with the lowest χ^2 is retained as best candidate for containing an electromagnetic shower. We define the quantity η to measure the fractional energy of the hadronic part of the shower:

$$\eta = (E_{shower} - E_{em})/E_{shower} .$$

In the case of CC ν_e ($\bar{\nu}_e$) interactions η measures the inelasticity y.

Figure 5 shows the result of the method applied to a 50 GeV π^- beam, which was contaminated with electrons. Applying a cut in η, which retains 95% of the electrons, one obtains a contamination from π of about 2.5%.

To test the method we use CC ν_μ interactions, collected in the WBB run, and replace the μ track by a Monte Carlo generated electromagnetic shower of the same energy and direction. The y distribution of these events is approximately flat. Restricting the analysis to events with $y < 0.6$ yields the energy resolution shown in Fig. 6b as averaged over the electron spectrum of Fig. 6a.

The η distribution measured for muonless ν interactions in a beam composed of ν_e and ν_μ neutrinos consists of two parts:

a) A component from CC interactions of ν_e and $\bar{\nu}_e$, which depends on the y distribution and hence on the $\nu_e/\bar{\nu}_e$ flux ratio. For this part η is a good estimator of y if $y \lesssim 0.6$.

b) A background contribution from NC interactions of all kinds of neutrinos, which has approximately the shape of the π contribution shown in Fig. 5. The shape of this background contribution depends only on the shower energy. It can be determined from NC events in the WBB run where the contamination of ν_e and $\bar{\nu}_e$ is very low.

The relative contributions of parts (a) and (b) are fitted to the experimental η distribution for $\eta \leq 0.6$. The total rate of CC events from ν_e and $\bar{\nu}_e$ interactions can then be determined by extrapolation to $y = 1$.

2. THE INVERSE MUON DECAY REACTION[7]

The inverse muon decay

$$\nu_\mu e^- \rightarrow \mu^- \nu_e \qquad (1)$$

is the simplest example of a weak leptonic interaction mediated by the CC coupling. Its investigation yields information on the Lorentz structure of the weak leptonic coupling and the two-component character of neutrinos. A search for interactions with antineutrinos

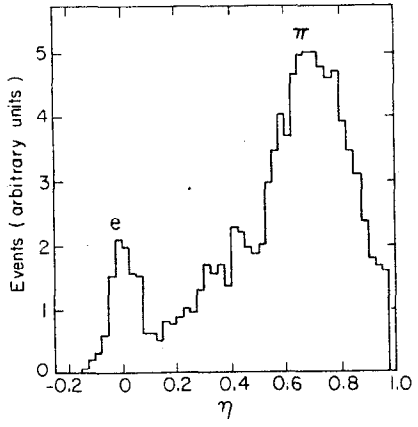

Fig. 5 Distribution of η for a 50 GeV pion beam contaminated with electrons

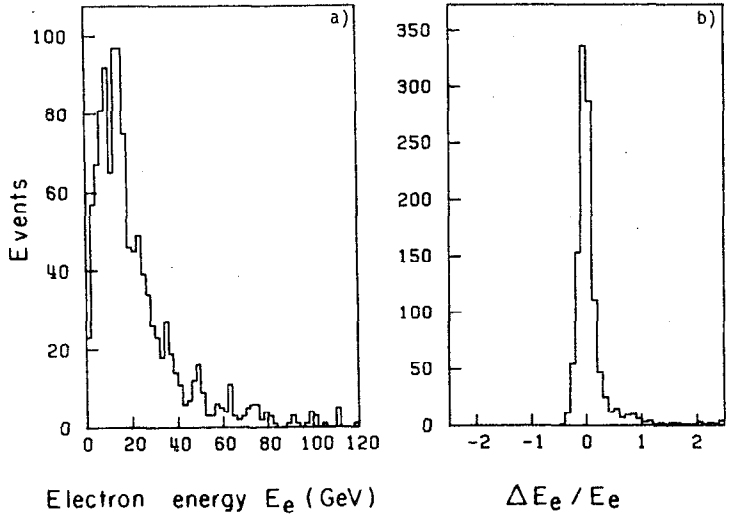

Fig. 6 a) Energy distribution of electron showers for CC ν_e events derived from CC ν_μ events of WBB data
b) Energy resolution for electrons from CC ν_e events with $\eta \leq 0.6$

$$\bar{\nu}_\mu e^- \rightarrow \mu^- \bar{\nu}_e \qquad (2)$$

can be used to set limits on the presence of interactions which are forbidden if the leptonic charge is additively conserved but allowed if the conservation law is of multiplicative nature.

The differential cross-section for interaction (1) can be written for $s >> m_\mu^2$ as[8]:

$$\frac{d\sigma}{dy} = \frac{G^2}{\pi} \frac{s}{8} \{(1 + P)(1 - \lambda)y^2 + (1 - P)(1 + \lambda)\} . \qquad (3)$$

Here y is the inelasticity $y = E_\mu / E_\nu$. The parameter λ can be expressed in terms of the vector and axial-vector coupling constants:

$$\lambda = -\frac{2 \text{ Re } g_V^* g_A}{|g_V|^2 + |g_A|^2} ,$$

so that for pure V - A interactions λ = 1 and hence the cross-section (3) is independent of y. P describes the polarization of the incident neutrino:

$$P = \frac{N(\nu_R) - N(\nu_L)}{N(\nu_R) + N(\nu_L)} ,$$

where $N(\nu_R)$ and $N(\nu_L)$ denote the number of right-handed and left-handed neutrinos, respectively, in the beam. So P = -1 for purely left-handed neutrinos.

The kinematics of the reaction is determined by the low mass of the target particle:

$$2m_e(1 - y) = E_\mu \Theta_\mu^2 ,$$

which restricts the outgoing muons to forward angles. For E_μ > 11 GeV (the threshold) Θ_μ < 10 mrad. Owing to the mass ratio $m_e / m_{nucleon}$ the total cross-section for reaction (1) is however more than three orders of magnitude smaller than that of the inclusive semileptonic process:

$$\nu_\mu N \rightarrow \mu^- X . \qquad (4)$$

The experiment is performed in the WBB. Events are selected with forward-going muons (Θ_μ < 10 mrad) which have no visible hadronic energy at the interaction vertex. The angle is measured with a resolution of ±2.5 mrad. Owing to limitations in energy measurement, quasi-elastic events of type (4) with $E_h \leq 1$ GeV may escape detection. One

can, however, determine the number of events from reaction (1) by comparing the q^2 distribution of the candidate events with the q^2 distribution of events

$$\bar{\nu}_\mu N \to \mu^+ X \qquad (5)$$

collected by the same criteria in the $\bar{\nu}_\mu$ beam. These events do not contain interactions from inverse muon decay [note the difference in the sign for reaction (2)], whereas the quasi-elastic part is energy independent and has the same q^2 dependence as channel (4) [9].

The result of the comparison is shown in Fig. 7. The two distributions are normalized to each other in the range $0.02 < q^2 < 0.1$ GeV^2. After corrections for acceptance, the low-energy excess of events attributed to inverse muon decay (1) is 171 ± 29 events. This result can be expressed as the rate of reaction (1) relative to the total inelastic rate (2) for energies above 10 GeV:

$$R_{exp} = \left.\frac{N(\nu_\mu e^- \to \mu^- \nu_e)}{N(\nu_\mu N \to \mu^- X)}\right\}_{E_{vis}>10\ \mathrm{GeV}} = (5.7 \pm 1.0) \times 10^{-4} ,$$

or, integrating the differential cross-section for the assumption of pure V − A coupling:

$$\frac{R_{exp}}{R_{V-A}} = 0.98 \pm 0.18 .$$

Figure 8 illustrates these findings in a graphical form and compares them with a result obtained previously by the Gargamelle Collaboration at CERN[10].

The agreement of the q^2 and momentum distributions of the excess events with predictions from the V − A model is shown in Fig. 9. Our results confirm the V − A structure of leptonic CC interactions and the two-component theory with left-handed neutrinos.

A search for events of reaction (2), which is forbidden if the leptonic charge is additively conserved, was performed in the antineutrino beam. We find 10 ± 10 events and derive from that a limit on the cross-section for reaction (2) of

$$R = \frac{\sigma(\bar{\nu}_\mu e^- \to \mu^- \bar{\nu}_e)}{\sigma(\nu_\mu e^- \to \mu^- \nu_e)} < 0.09 \ (90\%\ \mathrm{C.L.}) .$$

A similar result has recently been reported[11] from a search for the forbidden decay

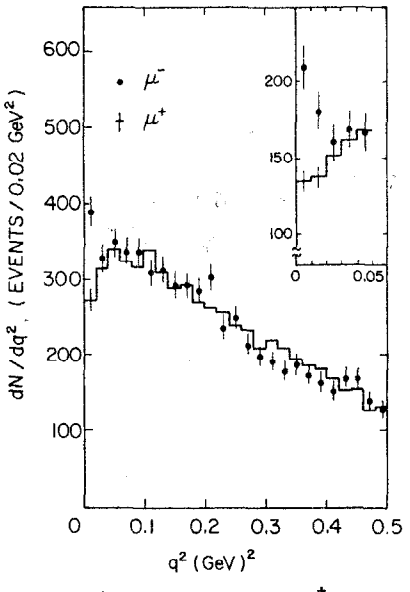

Fig. 7 q^2 dependence of single μ^- and single μ^+ events without visible recoil. The inset shows the same data in bins of 0.01 GeV^2.

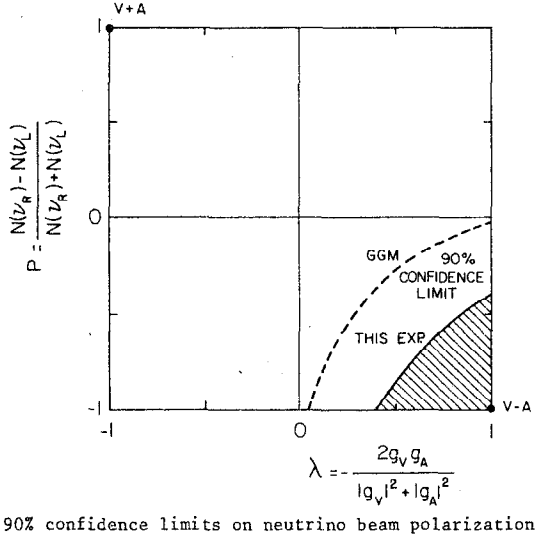

Fig. 8 90% confidence limits on neutrino beam polarization P and the parameter λ deduced from the observed rate of the inverse muon decay reaction. Also shown is a previous result obtained by the Gargamelle Collaboration[10].

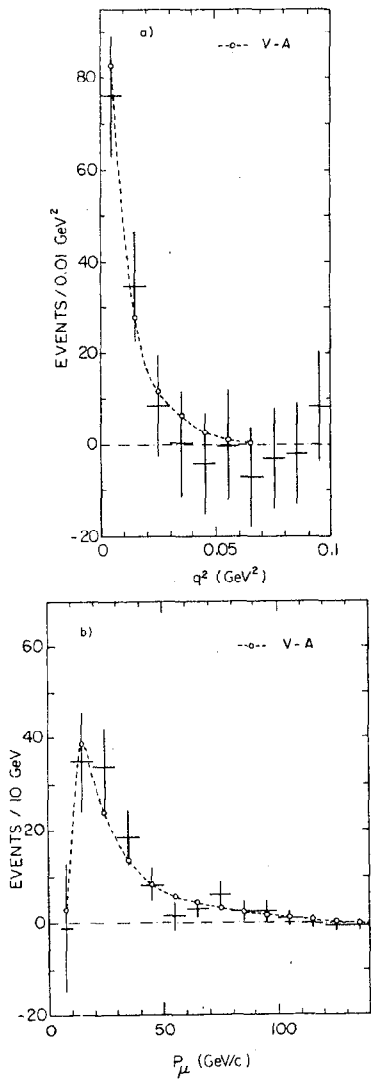

Fig. 9 Observed q^2 distribution of the difference $N_\nu(\mu^-) - N_{\bar\nu}(\mu^+)$ and observed μ^- momentum distribution of the difference $N_\nu(\mu^-, q^2 < 0.02\ GeV^2) - N_\nu(\mu^-, q^2 > 0.03\ GeV^2)$. The dashed lines are the V - A predictions for inverse muon decay.

$$\mu^+ \to e^+ \bar\nu_e \nu_\mu \ .$$

From the branching ratio for the forbidden decay BR = 0.001 ± 0.040 one can deduce R < 0.065 (90% C.L.).

These results can exclude models for which the lepton charge is only subject to a multiplicative conservation law.

3. POLARIZATION OF MUONS PRODUCED IN INCLUSIVE ANTINEUTRINO INTERACTIONS[12]

This experiment was performed jointly with the CDHS Collaboration[2].

The measurement of the μ^+ polarization for the reaction

$$\bar\nu_\mu N \to \mu^+ X \qquad (6)$$

can be used as a tool to investigate the space-time structure of high-energy, high-q^2 weak interactions. Vector (V) and axial-vector (A) interactions preserve the helicity of the lepton, whereas scalar (S), pseudoscalar (P) and tensor (T) interactions are accompanied by a spin flip. At low energies measurements of the muon helicity for pion[13] and kaon[14] decay have confirmed the dominance of V and A couplings for CC reactions and thus the positive helicity of antineutrinos in the beam used for the experiment. A deviation from positive helicity of the final state μ^+ in reaction (6) would therefore indicate S, P, and T contributions to the interaction.

The differential cross-section for reaction (6) can be written as[15]

$$\frac{2\pi}{mE}\frac{d\sigma}{dy} = 2(g_V - g_A)^2 + 2(g_V + g_A)(1 - y)^2 + (|g_S|^2 + |g_P|^2)y^2 + 32|g_T|^2\left(1 - \frac{y^2}{2}\right) + 8\ \mathrm{Re}\left\{g_T(g_S^* + g_P^*)\right\}y\left(1 - \frac{y}{2}\right) \qquad (7)$$

and measurements of the y distributions for high-energy ν_μ and $\bar\nu_\mu$ interactions[16] are compatible with the V - A structure of the interaction. It has, however, been pointed out[15,17], that such y distributions can also be described by appropriate mixtures of S, P, and T interactions. (Confusion theorem.)

To measure the polarization of reaction (6) the 1000 t CDHS detector[18] is used as a target. The toroidal field of this detector focuses μ^+ towards the CHARM calorimeter, which is used as polarimeter. The layout is sketched in Fig. 10. The spin of stopping muons is precessed in the 58 G dipole field which is produced by the iron frame

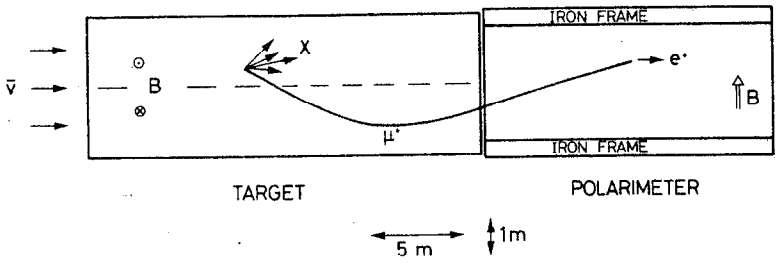

Fig. 10 Layout of the polarization experiment

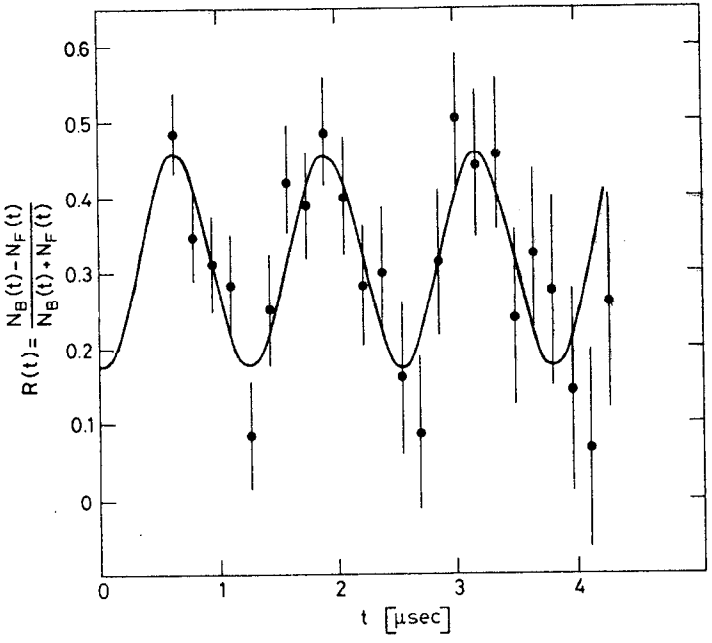

Fig. 11 Observed time dependence of relative forward-backward positron asymmetry. The curve is the result of a fit of equation 8 to the experimental points.

magnets. Decay positrons are detected either forwards or backwards of the marble plane in which the muon stopped. The time delay between the arrival of the μ^+ and the detection of the e^+ is recorded.

The experiment was performed in the $\bar{\nu}$ WBB. For about 13,000 events with stopping μ^+ 3,400 decay positrons were detected in the time interval from 0.56 μs to 4.38 μs. The time distribution yields a mean lifetime of $\tau = 2.16 \pm 0.08$ μs in good agreement with the expected value.

The time-dependent forward-backward asymmetry can be expressed as

$$R(t) = \frac{N_B(t) - N_F(t)}{N_B(t) + N_F(t)} = R_0 \cos(\omega t + \phi) + R_1 \quad . \qquad (8)$$

Here ω is the precession frequency (4.92 MHz in the 58 G field). The phase ϕ is expected to be $\phi = 0$ for negative and $\phi = -\pi$ for positive helicity. R_0 is the product of the analysing power α of the polarimeter and the absolute value of the polarization P. The quantity α was calculated by Monte Carlo methods using as input the geometry of the detector and taking into account a 10% depolarization of muons during their passage through the absorbing material. A correction R_1 has to be added owing to the fact that some of the muons stop in the scintillator material.

The experimental asymmetry distribution R(t) is shown in Fig. 11, together with a fit of Eq. (8) which yields the values:

$\phi = -3.1 \pm 0.2$ rad ($\phi = -\pi$ expected for positive helicity)
$P = 1.09 \pm 0.22$ (P = 1 expected for complete polarization) .

These values have been obtained for the average kinematical conditions of reaction (6):

$$\langle E_\nu \rangle = 27 \text{ GeV} \; ; \; \langle P_\mu \rangle = 16 \text{ GeV/c} \; ; \; \langle q^2 \rangle = 3.2 \text{ GeV}^2 \quad .$$

The results are compatible with pure V and A interactions and can be used to set upper limits on S, P, and T contributions to reaction (6) as

$$\frac{\sigma^{S,P,T}}{\sigma^{V,A}} < 0.18 \text{ (95\% C.L.)} \quad .$$

We are at present analysing more recent data for this reaction. The increased statistics will allow us to determine the polarization for various bins in y and as a function of q^2, which will increase the sensitivity for S, P, and T contributions.

4. INCLUSIVE INTERACTIONS OF NEUTRINOS AND ANTINEUTRINOS

The 200 GeV dichromatic neutrino beam was used to investigate the reactions

$$\nu_\mu N \to \begin{matrix}\mu^- X \\ \nu_\mu X\end{matrix}, \quad \bar{\nu}_\mu N \to \begin{matrix}\mu^+ X \\ \bar{\nu}_\mu X\end{matrix}. \qquad (9)$$

The emphasis of the experiment is on the investigation of NC interactions. At high energies not much is known about these reactions which goes beyond the determination of cross-sections. Bubble-chamber experiments are in general limited by statistics and poor resolution on the final-state hadronic shower, whereas previous electronic detector experiments suffer from poor pattern recognition power as well as from the missing information on the shower direction[19]. As mentioned in section 1 the CHARM detector was especially designed to overcome these difficulties.

The analysis of the data is not terminated; especially there are no results on NC structure functions yet, and the cross-section ratios and y distributions presented here are still preliminary.

The detector was triggered on a total scintillator pulse height corresponding to a visible energy of at least 500 MeV and hits in at least four detector planes. The trigger was fully efficient for energies above 1.5 GeV. For the analysis only events were retained which had a shower energy E_{sh} of at least 2 GeV. To keep corrections for energy leakage and background (especially of WBB origin) low, the fiducial mass was restricted to 65 t for neutrino interactions and even reduced to 37 t for antineutrino interactions.

Events were classified as CC candidates if they showed at least one track with a momentum of at least 1 GeV/c (corresponding to a minimum range of 20 target plates). The track should not show any visible interaction and should extrapolate to the event origin. All other events are classified as NC candidates. Table 2 shows the raw event numbers for reactions (9) and the corrections that have to be applied to the data. The corrections have two different sources:

a) Background from non-narrow-band components in the beam:
   - Wide-band beam contributions from π and K decay upstream of the magnetic beam channels (measured in runs with closed beam collimator)
   - K_{e3} decay contributions (calculated).

Table 2

Event numbers and corrections for inclusive interactions (9)

	ν		$\bar{\nu}$	
	CC	NC	CC	NC
Raw events	6503	2361	2751	1126
Corrections in %:				
WBB + cosmic-ray background	-1.7 ± 0.2	-4.0 ± 0.5	-8.9 ± 1.3	-12.8 ± 2.3
unidentified μ	1.5 ± 0.2	-4.1 ± 0.4	0.8 ± 0.8	- 2.0 ± 0.2
decay μ	-0.8 ± 0.2	2.3 ± 0.5	-0.6 ± 0.1	1.4 ± 0.3
K_{e3}	-	-7.2 ± 0.4	-	- 2.5 ± 0.2
Corrected events	6433.4 ± 84.3	2059.0 ± 53.5	2514.4 ± 63.7	948.3 ± 43.3

b) Wrong event classification:

- Muons from the decay of π and K mesons in the shower can fake CC events (measured for pion-induced showers).
- Muons that escape detection because they leave the detector at the side with a track length too short for identification, or with momenta below 1 GeV/c can fake NC events (calculated).
- Some cosmic-ray events can be mistaken for NC events (measured with beam off).

The intensity of the beam was monitored by a beam current transformer and solid-state detectors in the muon shield. The ratios p:K:π in the beam were determined experimentally[20].

Table 3 shows the results on the determination of cross-section ratios and slopes for the CC cross-section which were derived assuming

Table 3

Preliminary results for inclusive reactions (9)
for 20 GeV $\leq E_\nu \leq$ 200 GeV

$R = 0.320 \pm 0.010$	$R = NC/CC$; $E_{had} > 2$ GeV
$\bar{R} = 0.377 \pm 0.020$	$\bar{R} = \overline{NC}/\overline{CC}$; $E_{had} > 2$ GeV
$r = 0.491 \pm 0.019$	$r = \sigma_{\overline{CC}}/\sigma_{CC}$; corrected for cut in E_{had}
$\sigma_{CC} = 0.594 \pm 0.027$	$\times 10^{-38} \times E_\nu$ cm^2/GeV/nucleon
$\sigma_{\overline{CC}} = 0.292 \pm 0.015$	$\times 10^{-38} \times E_\nu$ cm^2/GeV/nucleon
$\sin^2 \Theta_w = 0.230 \pm 0.023$	$E_{had} > 2$ GeV, Paschos-Wolfenstein
$g_L^2 = 0.303 \pm 0.013$	$E_{had} > 2$ GeV, neglecting strange sea
$g_R^2 = 0.034 \pm 0.012$	$E_{had} > 2$ GeV, neglecting strange sea
$\alpha_{CC} = 0.17 \pm 0.03$	$E_{had} > 4$ GeV, neglecting strange sea
$\alpha_{NC} = 0.23 \pm 0.04$	$E_{had} > 4$ GeV, neglecting strange sea

scaling with energy. These results can be used to determine the electroweak mixing angle. Figure 12 shows a comparison with previous experiments[21]. The method illustrated in this figure requires a model-dependent extrapolation of the experimental results to the region with $E_h < 2$ GeV. A model-independent but less sensitive method due to Paschos and Wolfenstein[22] uses the relation (see Table 3 for definition of symbols):

$$\frac{R - rR}{1 - r} = \frac{1}{2} - \sin^2 \Theta_w ,$$

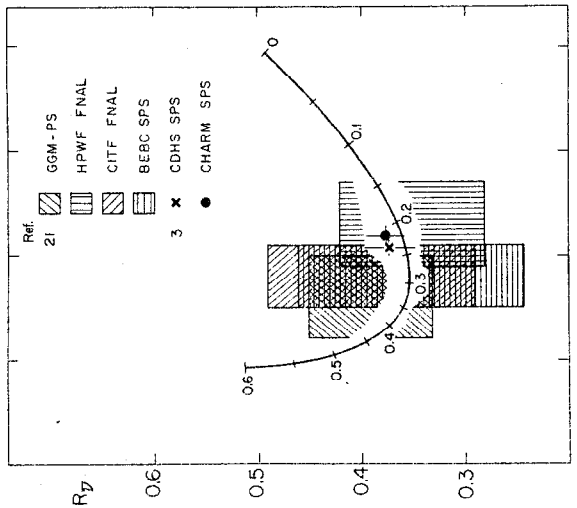

Fig. 12 Comparison of the results of various experiments on R and $\bar{R}$ with the Weinberg-Salam model. The data are taken with different cuts in shower energy. The cuts are 0 GeV, 4 GeV, 12 GeV, 15 GeV, and 10 GeV for the experiments GGM, HPWF, CITF, BEBC[21], and CDHS[3]), respectively. The CHARM data have a cut at 2 GeV, radiative corrections are not applied.

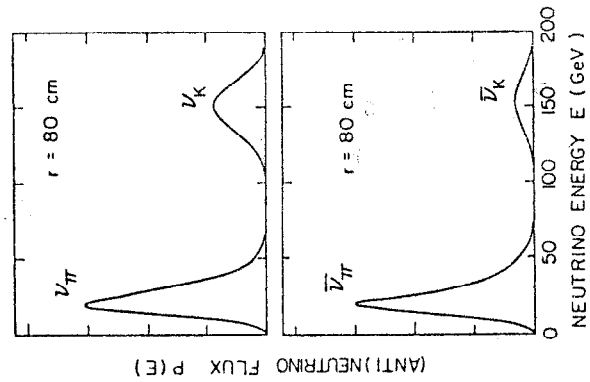

Fig. 13 NBB neutrino and antineutrino-spectra at a fixed radial distance of 80 cm from the nominal beam line

from which we obtain

$$\sin^2 \Theta_w = 0.230 \pm 0.023 \ .$$

The strength of the left-handed and right-handed chiral couplings can be extracted in a similar way[23]

$$g_L^2 = u_L^2 + d_L^2 = \frac{R - r^2\bar{R}}{1 - r^2} \ , \quad g_R^2 = u_R^2 + d_R^2 = r\,\frac{\bar{R} - R}{1 - r^2} \ .$$

The results are given in Table 3. They are consistent with previous results and confirm the presence of V + A (right-handed) couplings in NC interactions.

For CC events the inelasticity can be unambiguously measured as:

$$y_{CC} = \frac{E_h}{E_{tot}} = \frac{E_h}{E_h + E_\mu} \ ,$$

where E_h and E_μ are the hadron and the muon energy, respectively. In the case of NC events the final-state neutrino is undetectable and one has to use the knowledge in the dichromatic beam of the incident neutrino energy to determine the total energy E_{tot}. In this beam the neutrino energy is known as a function of the radial distance of the interaction from the axis of the beam. There is, however, the ambiguity of whether the neutrino comes from π or K decay. For a radial distance of 80 cm the situation is illustrated in Fig. 13. For all events with $E_h < E_{\nu_\pi}(r)$ a unique determination of E_{tot} is not possible. One has therefore to apply a statistical unfolding procedure to determine the y distribution.

We use the knowledge of the neutrino fluxes ϕ for each of the two sources to predict for the radial bins the hadron energy distribution for each of 10 bins in y:

$$\frac{dN}{dE_h} = \int f(y)\ \phi(E_\nu)\ dE_\nu \ . \qquad (10)$$

Assuming scaling behaviour, i.e. the shape of the y distribution is independent of E_ν, Eq. (10) can be rewritten as

$$\frac{dN}{dE_h} = \sum a_i \int b_i(y)_{y=y_i}\ \phi(E_\nu)\ dE_\nu \ , \qquad (11)$$

where the coefficients a_i constitute the y distribution. They are determined by a simultaneous maximum likelihood fit to all radial bins.

The result for each of the four reactions (9) is shown in Fig. 14. The CC events have been treated here exactly as the NC events, i.e., the knowledge of the muon momentum has not been used. All distributions are normalized to the total cross-section measurements.

For both CC and NC the y distributions are consistent with being equal for ν and $\bar{\nu}$ interactions at $y = 0$. This confirms charge symmetry for CC interactions and indicates identical initial- and final-state neutrinos for NC interactions.

Parametrizing the y distribution as

$$\frac{d\sigma^\nu}{dy} = \left[(1 - \alpha) + \alpha(1 - y)^2\right] \ , \quad \frac{d\sigma^{\bar{\nu}}}{dy} = \left[\alpha + (1 - \alpha)(1 - y)^2\right] \ ,$$

a fit to the data yields

$$\alpha_{CC} = 0.17 \pm 0.03 \ , \quad \alpha_{NC} = 0.23 \pm 0.04 \ ,$$

where the errors include systematic uncertainties. In the limit of negligible strange sea, α_{CC} measures the total antiquark content of the nucleon. Our result agrees with a previous determination[3,16], which was obtained in an experiment with very different systematic uncertainties. The near equality of α_{CC} and α_{NC} indicates that the Lorentz structure of the neutral currents is predominantly V - A.

Using the feature of our detector which allows us to measure the angle of the hadron shower we are currently analysing the data to extract structure functions especially for NC events. We hope to improve our results in the future by increasing the statistics of the experiment.

5. INVESTIGATION OF PROMPT NEUTRINO PRODUCTION IN A BEAM-DUMP EXPERIMENT

The second CERN beam-dump experiment was performed with increased statistics and better control over the background. The layout is shown in Fig. 15. The 400 GeV proton beam hit a 2 m long cylindrical copper target which was segmented so that different densities could be used by varying the distances between the discs. The target was followed by a 2 m long hadron stopper also made of copper. The CHARM detector was situated at a distance of 910 m from the dump.

Two different methods were applied to determine prompt neutrino fluxes. The first method used the possibility of disentangling "prompt" event rates from "non-prompt" event rates by measuring at two different

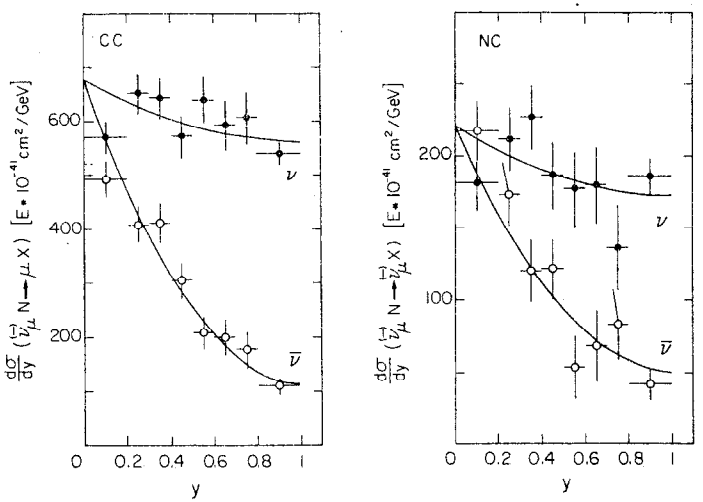

Fig. 14 Unfolded y distributions for charged and neutral current events. The error bars are statistical only, taken from the covariance matrix generated by the unfolding procedure. The distributions are normalized to the measured total charged current cross-sections.

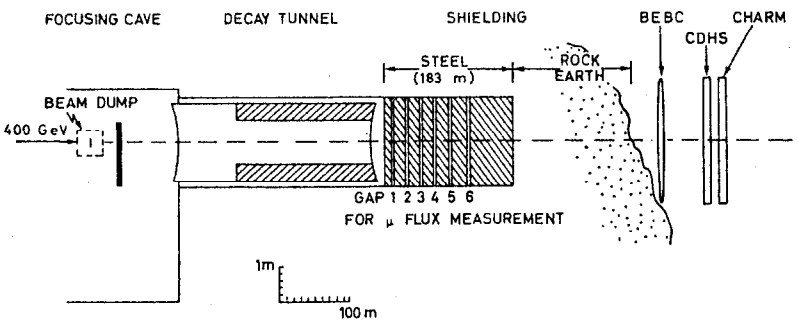

Fig. 15 Layout of the beam dump experiment

target densities, $\rho = 1$ (9 g/cm^3) and $\rho = 1/3$ (3 g/cm^3). The prompt signal is not affected by the density and can be determined by extrapolation to infinite ρ.

The second method consists in subtracting the non-prompt background based on the knowledge of conventional neutrino fluxes. These fluxes have been calculated[24] using two main sources of experimental information: the production rates of pions and kaons as measured for a long target, and the muon flux distribution from non-prompt decays which was determined by measurements in four different gaps in the steel shield (corresponding to range requirements of 23, 57, 94, and 136 GeV/c); the extrapolation technique is then applied to isolate the non-prompt rates based on measurements at three different target densities (3, 4.5, and 9 g/cm^3). The muon fluxes were continuously monitored throughout the experiment.

Both methods, extrapolation and subtraction, are subject to different uncertainties and a comparison of their results is therefore an important check of consistency.

Data were taken for 6.9×10^{17} protons-on-target (POT) with the full density dump and 2.60×10^{17} POT for the 1/3 density target. The detector was triggered as usual on a minimum energy deposition of 0.5 GeV (full efficiency at 1.5 GeV) and a minimum of four planes hit. Events with a total visible energy E_{vis} above 2 GeV and the event origin in a fiducial mass of 100 t (extending from target plane 3 to 70 and lateral dimensions of 2.4 m × 2.4 m) were selected for analysis.

Events are classified as one-muon candidates (1 μ) if they have at least one primary track with $p \geq 1$ GeV/c with no visible interaction and extrapolating to the vertex, and zero-muon candidates (0 μ) otherwise. For the total exposure we find 810 1 μ and 562 0 μ candidates. The numbers have to be corrected for wrong classification. Muons from π and K decay can simulate primary tracks. Muons with $p \leq 1$ GeV/c escape detection as well as those muons which leave the detector at the side before traversing enough material to be identified. Cosmic-ray events can simulate 0 μ events. Table 4 gives a list of these corrections.

The 1 μ events are essentially due to CC ν_μ ($\bar{\nu}_\mu$) interactions, whereas the class of 0 μ events is composed of a variety of different sources. The NC ν_μ ($\bar{\nu}_\mu$) interactions and all ν_e ($\bar{\nu}_e$) interactions are 0 μ events. Almost all ν_τ ($\bar{\nu}_\tau$) interactions also fall into this class,

Table 4

Event numbers and corrections

	$2 \leq E_{shower} \leq 20$ GeV			$E_{shower} > 20$ GeV	
	0 μ events	1 μ events	Systematic error	0 μ events	1 μ events
Raw events	291	469		271	341
Corrections:					
π/K decay	+ 3.7 ± 0.2	- 3.7 ± 0.2	±1.6	+ 7 ± 0.6	- 7 ± 0.6
soft μ loss	-23.3 ± 1.7	+23.3 ± 1.7	±4.0	-10.6 ± 0.4	+10.6 ± 0.4
side μ loss	-11.5 ± 0.5	+11.5 ± 0.5	±2.0	- 5.9 ± 0.3	+ 5.9 ± 0.3
cosmic ray	- 9.5 ± 1.5	0	0	0	0
Corrected events	250.4 ± 17.2	500.1 ± 21.7	±4.7	261.5 ± 17 ± 2	350.5 ± 18.7 ± 2

the exception being CC ν_τ ($\bar{\nu}_\tau$) interactions, where the τ ($\bar{\tau}$) decays into a μ (BR ≈ 17%). There is, however, a simple method to decompose the 0 μ signal into a ($\nu_\mu + \bar{\nu}_\mu$)-induced part and the rest. Since the ratio of NC to CC events in ν_μ and $\bar{\nu}_\mu$ interactions is a well-determined quantity (see previous section) the non-[ν_μ ($\bar{\nu}_\mu$)]-induced 0 μ signal can be determined as $N(0\ \mu) - \langle R \rangle N(1\ \mu)$. For the average ratio we use $\langle R \rangle = 0.324 \pm 0.006$ derived from our results obtained in the NBB experiment and a $\bar{\nu}_\mu$:ν_μ flux ratio derived from CC event rates in the beam-dump experiment $r = N(\mu^+)/N(\mu^-) = 0.185 \pm 0.035$.

Figure 16 shows the composition of the raw 0 μ event spectrum. The big fraction of NC $\nu_\mu + \bar{\nu}_\mu$ events can be reliably determined. The corrections due to misclassification of events are small and rapidly decreasing with energy. The fraction of non-prompt $\nu_e + \bar{\nu}_e$ contributions is known with an uncertainty of 21% [24].

The procedure of isolating the non-[ν_μ ($\bar{\nu}_\mu$)]-induced 0 μ signal was tested with events collected in the ν_μ and $\bar{\nu}_\mu$ WBB. Based on 6000 events which were mixed ν_μ and $\bar{\nu}_\mu$ events in the same proportion as found in the beam-dump exposure the subtraction $N(0\ \mu) - \langle R \rangle N(1\ \mu)$ yields no significant deviation from zero, confirming the reliability of event classification. This is illustrated in Fig. 17.

The prompt 0 μ event spectrum after subtraction of the $\nu_\mu + \bar{\nu}_\mu$ component and the non-prompt contributions from $\nu_e + \bar{\nu}_e$ interactions is shown in Fig. 18.

The most likely source of prompt neutrinos is the production and decay of charmed mesons. We test this hypothesis assuming $D\bar{D}$ production according to the differential distribution

$$\frac{d^2\sigma}{dx dp_T} \sim (1 - |x|)^n e^{-bp_T} \qquad (12)$$

(here p_T is the transverse momentum and $x = p_L/p_{L,max}$ the fractional longitudinal momentum). We use $n = 4$ and $b = 2$ (GeV/c)$^{-1}$ for the calculation. The dots in Fig. 18 show the model prediction normalized to the data above 20 GeV shower energy. The agreement is reasonable, but there is clearly an excess of events at low energies which the model does not describe. Assuming the cross-section to be proportional to the number of nucleons, one can use the comparison to evaluate, for 400 GeV p-Cu interactions, the product of cross-section and branching ratio for semileptonic decays as

$$\sigma_{tot}(pCu \to D\bar{D}X)BR(D \to \nu_e eX) = (1.5 \pm 0.5)\ \mu b\ .$$

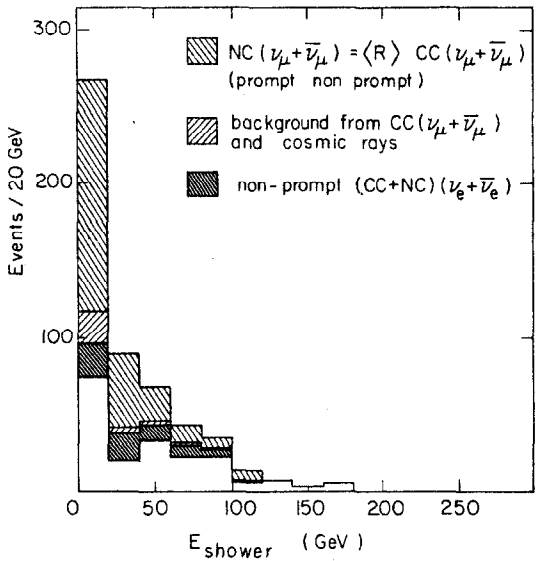

Fig. 16 Composition of the (0 μ) raw signal for the beam dump experiment for both densities together. The unshaded histogram constitutes the distribution of non-$\nu_\mu(\bar{\nu}_\mu)$-induced prompt (0 μ) events.

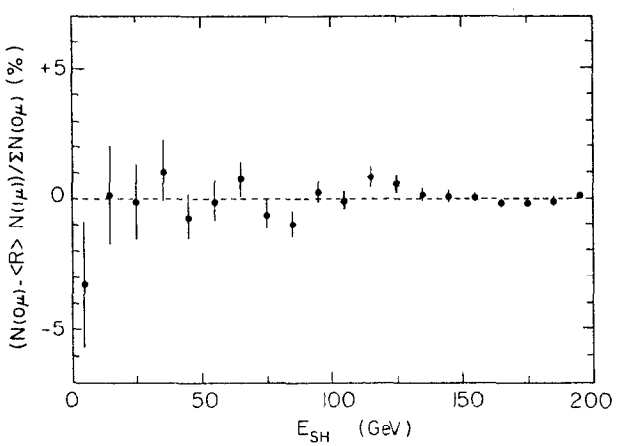

Fig. 17 Deviation of the fraction of muonless events from the expected contribution of NC interactions as observed in the horn-focused WBB. The data are composed of ν_μ and $\bar{\nu}_\mu$ induced events in the same proportion as the beam dump data.

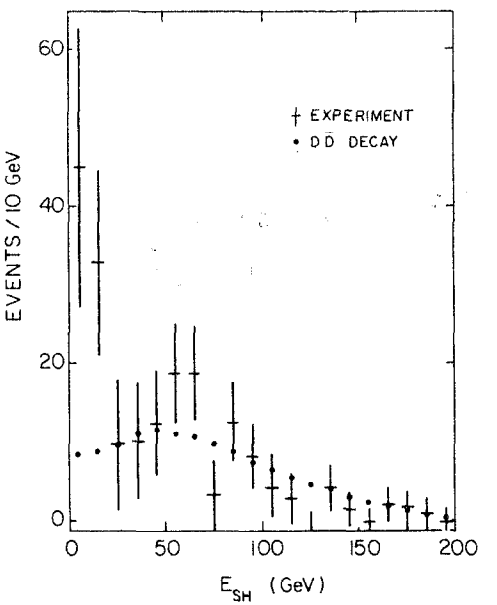

Fig. 18 Shower energy distribution of prompt muonless events in excess of muon neutrino NC interactions for ρ = 1 and 1/3. The points show the distribution of electron neutrino interactions expected from standard DD̄ production and decay. The content of the bin from 2 to 10 GeV is increased by a factor of 1.25.

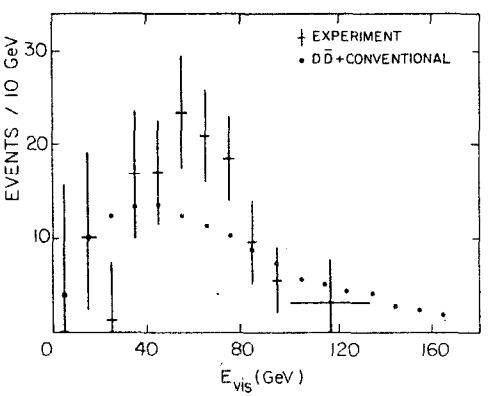

Fig. 19 Observed visible energy spectrum of CC ($\nu_e + \bar{\nu}_e$) events of prompt and non-prompt origin for ρ = 1 and 1/3. The content of the bin from 2 to 10 GeV is increased by a factor of 1.25. The sum of prompt CC ($\nu_e + \bar{\nu}_e$) events from standard DD̄ decay and of non-prompt CC ($\nu_e + \bar{\nu}_e$) events is also shown.

This comparison with the production model assumes that the prompt events in Fig. 18 are essentially due to ν_e and $\bar{\nu}_e$ interactions. As explained in section 1 we can also directly identify CC ν_e ($\bar{\nu}_e$) interactions. The result of such an analysis is shown in Fig. 19. The data points are compared with the model prediction (plus conventional background) retaining the normalization from Fig. 18. The agreement is again reasonable and thus supports the hypothesis of $D\bar{D}$ production as the source of these prompt neutrinos. It should, however, be stressed that Fig. 19 shows no evidence for a low-energy CC ν_e ($\bar{\nu}_e$) signal in excess of what is expected from $D\bar{D}$ production.

Table 5 gives the decomposition of the 0 μ signal for the two regions of shower energies, above and below 20 GeV, and compares the results obtained by subtraction of conventional background with those obtained by extrapolation. Within the limited accuracy the agreement is good.

Table 5

Decomposition of 0 μ signal

	$2 \leq E_{shower} \leq 20$ GeV	$E_{shower} > 20$ GeV
Corrected events	250.4 ± 17.2 ± 4.7	261.5 ± 17 ± 2
NC ν_μ ($\bar{\nu}_\mu$) prompt + non-prompt NC + CC ν_e ($\bar{\nu}_e$) non-prompt	162 ± 7 ± 3 19.7 ± 0 ± 4	113.5 ± 6.1 39.6 ± 8.2
Prompt events: by subtraction by extrapolation	 69 ± 19 ± 8 43 ± 38	 108 ± 18 ± 8.5 116 ± 37
Excess over expected $D\bar{D}$ decay contribution	54 ± 19 ± 9	

The 1 μ events have been analysed for $p_\mu \geq 4$ GeV/c, where the sign of the muon charge can be determined with high efficiency, and for neutrino energies $E_\nu = E_\mu + E_{shower} \geq 20$ GeV. The analysis using the subtraction method was restricted to data taken with the full density target to reduce the contributions of non-prompt background. (The data taken for $\rho \approx 1/3$ yield consistent results but, because of large uncertainties, do not improve the precision). The results are shown in Table 6, where again a comparison between the two analysis methods yields satisfactory agreement. These CC interaction rates can be used

Table 6

Prompt charge-selected 1 μ rates
Events/(ton·10^{17} POT)

Reaction	By subtraction	By extrapolation
$\nu_\mu N \to \mu^- X$	1.07 ± 0.27 ± 0.33	1.06 ± 0.54
$\bar{\nu}_\mu N \to \mu^+ X$	0.69 ± 0.15 ± 0.06	0.91 ± 0.29

to calculate the ratio of prompt $\bar{\nu}_\mu$ and ν_μ fluxes as

$$\frac{\phi(\bar{\nu}_\mu)}{\phi(\nu_\mu)} = 1.3 \pm 0.5\ (\text{stat})^{+0.4}_{-0.2}\ (\text{syst}) \quad \text{subtraction}$$

$$= 1.8 \pm 1.1 \quad \text{extrapolation}$$

which are consistent with 1 as expected for $D\bar{D}$ production.

We finally use the CC event rates to determine the ratio of $\nu_e + \bar{\nu}_e$ and $\nu_\mu + \bar{\nu}_\mu$ fluxes. The analysis is again restricted to $\rho = 1$ data with $E_\nu \geq 20$ GeV. For the muon-neutrino channel we find

$$N_{CC,\nu_\mu+\bar{\nu}_\mu} = 138 \pm 20 \pm 29 \text{ events} .$$

Two different methods are applied to determine the rate for CC $\nu_e + \bar{\nu}_e$ interactions:

- In the $D\bar{D}$ production model all 0 μ events above 20 GeV shower energy are ν_e- and $\bar{\nu}_e$ - induced and (83 ± 1)% of these events are CC interactions, so that

$$N_{CC,\nu_e+\bar{\nu}_e} = 67 \pm 12 \pm 3 \text{ events} .$$

- The CC events are directly identified and Fig. 19 yields after correction for non-prompt background and subtraction of the $\rho \approx 1/3$ contribution

$$N_{CC,\nu_e+\bar{\nu}_e} = 60.7 \pm 13 \pm 5.3 \text{ events} .$$

For the first method we can also apply the extrapolation procedure. From these numbers we obtain the flux ratios as given in Table 7. The different methods yield consistent results. The ratios are significantly different from unity, in contrast with expectations from the $D\bar{D}$ production model.

To conclude, we have observed prompt electron- and muon-neutrino production in 400 GeV proton-nucleus collisions. The results are

Table 7

Ratio of prompt fluxes $R = \phi(\nu_e + \bar{\nu}_e)/\phi(\nu_\mu + \bar{\nu}_\mu)$

$R = 0.48 \pm 0.12 \pm 10$	Model-dependent, subtraction
$R = 0.49 \pm 0.21$	Model-dependent, extrapolation
$R = 0.44 \pm 0.11 \pm 0.03$	Direct $CC_{\nu_e+\bar{\nu}_e}$, subtraction

consistent within large uncertainties with equal fluxes of ν_μ and $\bar{\nu}_\mu$. The prompt $\nu_e + \bar{\nu}_e$ flux above 20 GeV is only about half the flux of $\nu_\mu + \bar{\nu}_\mu$. This latter finding is at variance with predictions of a simple model of charmed meson production. The model can also not account for an excess of 0 μ events at low energies, whereas there is qualitative agreement as to the shape of this spectrum above E_{shower} = = 20 GeV for 0 μ events in general as well as for identified CC $\nu_e + \bar{\nu}_e$ interactions.

The second beam-dump experiment at CERN has not only eliminated some discrepancies that were left over from the first one[4], but has also shown a variety of interesting new findings that need further investigation in a third-generation experiment which is already being prepared. The new experiment will also clarify some discrepancies in the CHARM and CDHS results[25], especially as to the existence of prompt $\bar{\nu}_\mu$ production.

REFERENCES AND FOOTNOTES

1) CHARM Collaboration: M. Jonker, J. Panman and F. Udo (Amsterdam); J.V. Allaby, U. Amaldi, G. Barbiellini, A. Baroncelli, V. Blobel, W. Flegel, W. Kozanecki, K.H. Mess, M. Metcalf, J. Meyer, R.S. Orr, F. Schneider, V. Valente, A.M. Wetherell and K. Winter (CERN); F.W. Büsser, P.D. Gall, H. Grote, B. Kröger, E. Metz, F. Niebergall, K.H. Ranitzsch and P. Stähelin (Hamburg); E. Grigoriev, V. Kaftanov, V. Khovansky and A. Rosanov (Moscow); R. Biancastelli, B. Borgia, C. Bosio, A. Capone, F. Ferroni, E. Longo, P. Monacelli, F. de Notaristefani, P. Pistilli and C. Santoni (Rome).

2) J.G.H. de Groot, F.L. Navarria and A. Savoy-Navarro from the CDHS (CERN-Dortmund-Heidelberg-Saclay) Collaboration.

3) M. Holder et al., CDHS Collaboration, Phys. Lett. 71B, 222 (1977); C. Geweniger, CDHS Collaboration, Neutrino 79, Proc. Int. Neutrino Conf., Bergen, Norway, 1979 (eds. A. Haatuft and C. Jarlskog) (University, Bergen, 1980?), vol. 2, p. 392.

4) P. Alibran et al., Gargamelle Collaboration, Phys. Lett. 74B, 134 (1978);
T. Hansl et al., CDHS Collaboration, Phys. Lett. 74B, 139 (1978);
P.C. Bosetti et al., BEBC-ABCLOS Collaboration, Phys. Lett. 74B, 143 (1978).

5) A.N. Diddens et al., CHARM Collaboration, A detector for neutral-current interactions of high-energy neutrinos, preprint CERN-EP/80-63 (1980), to be published in Nucl. Instrum. Methods.

6) C. Bosio et al., CHARM Collaboration, Nucl. Instrum. Methods 157, 35 (1978).

7) M. Jonker et al., CHARM Collaboration, Phys. Lett. 93B, 203 (1980).

8) C. Jarlskog, Lett. Nuovo Cimento 4, 377 (1970).

9) Ch. Llewellyn Smith, Phys. Rep. 3C, 263 (1972).

10) N. Armenise et al., Gargamelle Collaboration, Phys. Lett. 84B, 137 (1979).

11) S.E. Willis et al., Phys. Rev. Lett. 44, 522 (1980).

12) M. Jonker et al., CHARM Collaboration, Phys. Lett. 86B, 229 (1979).

13) G. Backenstoss et al., Phys. Rev. Lett. 6, 415 (1961).

14) C.A. Coombes et al., Phys. Rev. 108, 1348 (1957).

15) R.L. Kingsley et al., Phys. Rev. D 10, 2216 (1974).

16) J. de Groot et al., Z. Phys. C1, 143 (1979).

17) B. Kayser et al., Phys. Lett. 52B, 385 (1974).

18) M. Holder et al., Nucl. Instrum. Methods 148, 235 (1978).

19) M. Holder et al., Phys. Lett. 72B, 254 (1977).
F.S. Merritt et al., Phys. Rev. D 17, 2199 (1978).
C. Baltay et al., Phys. Rev. Lett. 44, 916 (1980).

20) H.W. Atherton et al., Precise measurements of particle production by 400 GeV/c protons on Be targets, CERN 80-07 (1980).

21) J.B. Blietschau et al., Gargamelle Collaboration, Nucl. Phys. B118, 218 (1977).
P. Wanderer et al., HPWF Collaboration, Phys. Rev. D 17, 1679 (1978).
F.S. Merritt et al., CITF Collaboration, Phys. Rev. D 17, 2199 (1978).
M. Deden et al., BEBC-ABCLOS Collaboration, Nucl. Phys. B149, 1 (1979).

22) E.A. Paschos and L. Wolfenstein, Phys. Rev. D 7, 91 (1973).

23) L.M. Sehgal, Neutrino 78, Proc. Int. Neutrino Conf., Purdue University, 1978, (Purdue University, West Lafayette, Indiana, 1978), p. 253.

24) H. Wachsmuth, Neutrino and muon fluxes in CERN 400 GeV proton beam-dump experiment, preprint CERN/EP 79-125 (1979).

25) C. Geweniger, CDHS Collaboration, Contribution to this Conference.

RESULTS FROM THE CDHS NEUTRINO EXPERIMENT

C. Geweniger

Institut für Hochenergiephysik der Universität
Heidelberg, Germany

1. INTRODUCTION

Latest results from the CERN-Dortmund-Heidelberg-Saclay[1] neutrino experiment at the CERN SPS will be reported. The detector consists of a magnetized iron calorimeter equipped with drift chambers to measure muon momenta and shower energies from neutrino interactions in iron. It is in operation since December 1976 and is described in detail elsewhere[2].

The topics which will be covered by this talk are a beam dump experiment, the determination of nucleon structure functions from inclusive charged current interactions with an isoscalar target, and the analysis of opposite sign dimuon events. The data to be presented here are improved over previously published data of this group[3,4,5] from the statistical and the systematical point of view. Except for the beam dump experiment the results are mostly preliminary.

The analysis of structure functions is based on new samples of 65000 neutrino and 25000 antineutrino events taken in 200 GeV narrow band beams, compared to 23000 and 6200 events in 1977[4]. In addition 100 000 antineutrino events from a 350 GeV wide band beam exposure are used to extract the structure function of antiquarks. The dimuon sample comprises more than 10000 events, which augments the present world statistics by an order of magnitude.

2. BEAM DUMP EXPERIMENT

A first beam dump experiment was carried out at the CERN SPS in 1977 [3,6,7] with the aim of searching for "new" neutrinos. In such an experiment conventional neutrinos from the decay of pions and kaons are suppressed by absorbing the secondary hadrons from proton nucleus collisions in a solid block of copper before they decay. The flux of so-called "prompt" neutrinos which are produced either directly or via the decay of short lived particles (lifetimes $\lesssim 10^{-11}$ s) is not affected. The experiment found evidence for a new source of prompt electron neutrinos, which was attributed to open charm production in hadronic collisions.

The purpose of the present beam dump experiment was mainly to establish also the production of prompt muon neutrinos and to clear up a discrepancy in the rate of prompt electron neutrinos found by the CDHS group[3] and by the two bubble chamber groups from BEBC[6] and Gargamelle[7]. Data were taken in 1979 with a 400 GeV proton beam incident on a thick copper target. The angular acceptance of the experiment is restricted to a very small forward cone with an opening angle of ±2 mr. Three groups participated: CHARM, CDHS, and a group using BEBC[8]. Results from the CHARM collaboration have also been presented to this conference[9].

2.1 Prompt muon neutrinos

Muon neutrinos and antineutrinos are identified in the detector by their charged current interaction leading to a μ^- ($CC\mu^-$) or a μ^+ ($CC\mu^+$) in the final state. Even though conventional muon neutrinos are suppressed by roughly a factor of 2000 compared to an ordinary neutrino beam they are responsible for the bulk of the observed events. Hence, the subtraction of this background constitutes the main problem in the determination of a prompt signal.

Two methods are employed. With the first method-- the subtraction method --the conventional event rate is calculated and subtracted from the observed rate. This calculation has been done by H. Wachsmuth[10]. It is based on a cascade model for hadron nucleus collisions with experimental data adapted to the given conditions as input. Some parameters of the model are adjusted such as to explain the absolute muon spectrum measured in the shield behind the target. The uncertainty of this calculation is estimated at the level of 10%. An additional error arises from the total neutrino cross section when event rates are considered.

The second method -- the extrapolation method -- uses data from two runs with relative target densities of 1 and 1/3, respectively, in order to obtain the prompt rate by extrapolation to infinite density. The first method gives a smaller statistical error, whereas the second method is very safe from the systematical point of view.

The spectra of charged current events initiated by prompt neutrinos and antineutrinos are shown in Fig. 1. Points with error bars are obtained by the extrapolation method, the histograms result from the subtraction method. For neutrinos both methods give similar results, establishing a clear prompt signal. For antineutrinos, however, this is not the case: The extrapolation method, which is preferred for reasons of systematical reliability, yields a zero flux within errors. On the other hand, a small signal is found by the subtraction method. The integrated event rates are summarized in Table 1.

A $\bar{\nu}_\mu$ flux which is small compared to the ν_μ flux is in contradiction to a $D\bar{D}$ production model which predicts equal fluxes. One might be able to explain such an effect by a sizeable forward production of charmed baryons.

The small antineutrino rate is not confirmed by the CHARM and BEBC groups. The reason for that may be illustrated with help of Fig. 2, showing the normalized overall rates for the two target densities. The antineutrino rates of all three experiments are in reasonable agreement for the density 1 target, although the CDHS value is slightly below the other two. For the density 1/3 target, however, the results

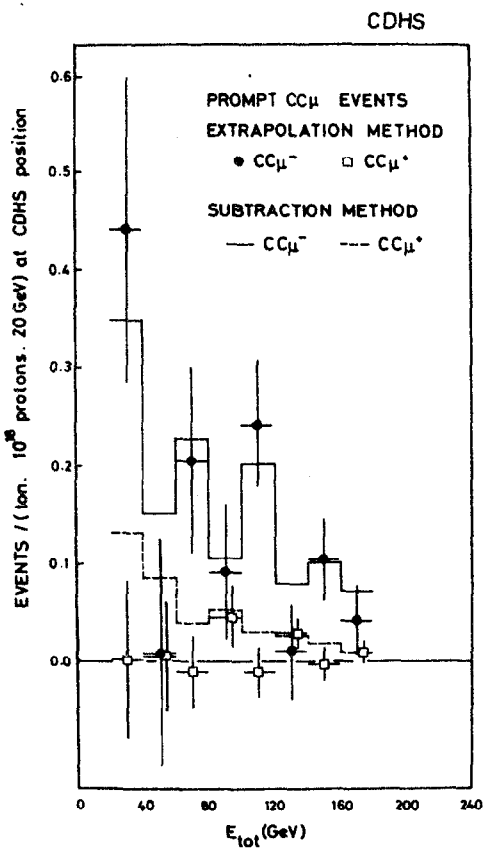

Fig. 1: Prompt ν_μ and $\bar{\nu}_\mu$ charged current events as a function of the total energy.

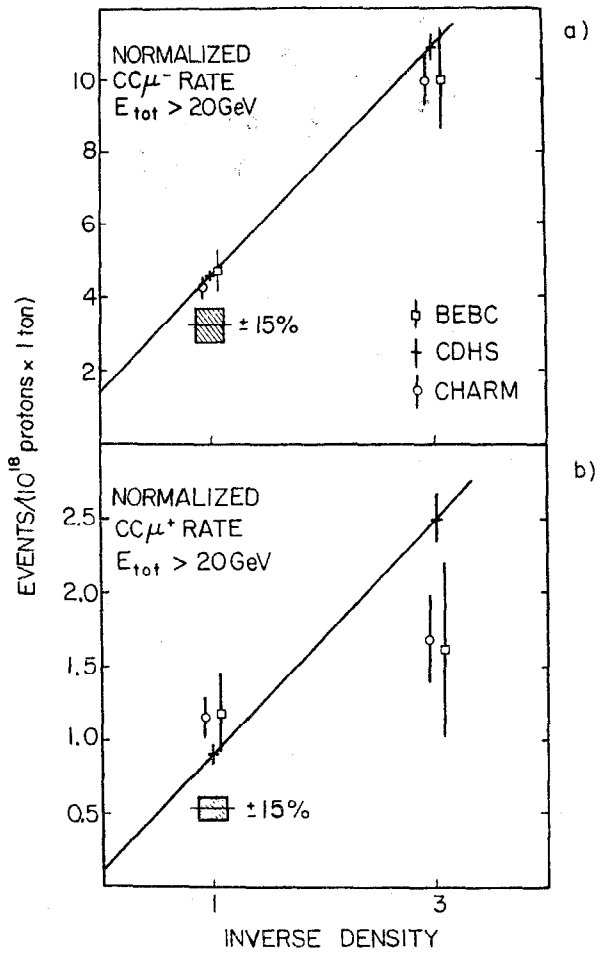

Fig. 2: Comparison of the overall ν_μ and $\bar{\nu}_\mu$ rates measured by three experiments. The straight lines indicate the extrapolation of the CDHS data to infinite density.

differ by about three standard deviations. The opposite sign of the difference for the two densities leads to a big difference in the extrapolation to zero inverse density. It should be noted, that the antineutrino events are measured simultaneously with the neutrino events, where the rates agree very well (Fig. 2a). So the difference is most likely due to a statistical fluctuation, rather than of systematical origin.

2.2 Prompt electron neutrinos

ν_e and $\bar{\nu}_e$ events in the CDHS detector are classified as events without muon (0μ). They cannot be identified, since in the calorimeter they look like neutral current events. Ordinary neutral current events initiated by muon neutrinos are easily determined from the measured 1μ events and subtracted from the 0μ rate. Fortunately the background of conventional electron neutrinos is small, unlike it is in the case of muon neutrinos. It can be calculated with adequate precision and it is also subtracted from the 0μ rate.

One is then left with an unexplained excess of 0μ events, which are attributed to charged and neutral current interactions of prompt ν_e and $\bar{\nu}_e$. This interpretation is supported by the bubble chamber experiment, where these events can be identified. The event spectrum as a function of visible shower energy is shown in Fig. 3 together with the prediction of a simple $D\bar{D}$ production model. The data are well described by the model; in particular, there is no excess over the prediction below $E_{sho} = 20$ GeV as found by the CHARM group[9]. The integrated rate of $\nu_e + \bar{\nu}_e$ charged current events is quoted in Table 1. It should be mentioned that all three groups agree well in this rate, and that the discrepancy in the 1977 experiment has been resolved in favour of the CDHS result.

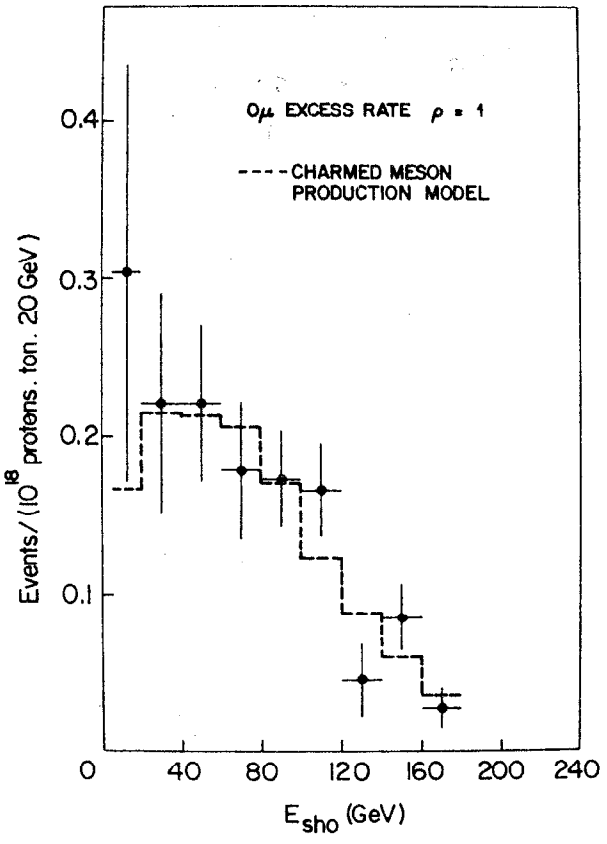

Fig. 3: Excess of 0μ events as a function of the shower energy. The dashed line is the predicted shape, if the events are interpreted in terms of electron neutrino events, originating from $D\bar{D}$ production.

2.3 Summary of beam dump results

Table 1: Rates of prompt events in beam dump experiment for $E_{tot} > 20$ GeV normalized to 10^{18} protons on target and 1t of detector at 890 m distance. First error is statistical, second error is systematical.

$CC\mu^-$	extrapolation	1.17 ± 0.26 ± 0.32
	subtraction	1.33 ± 0.13 ± 0.49
$CC\mu^+$	extrapolation	0.05 ± 0.12 ± 0.07
	subtraction	0.38 ± 0.06 ± 0.08
$CCe^- + CCe^+$		0.96 ± 0.09 ± 0.09
$\frac{e^+ + e^-}{\mu^+ + \mu^-}$	extrapolation	0.78 ± 0.20 ± 0.24
	subtraction	0.56 ± 0.07 ± 0.19

The measured prompt event rates are summarized in Table 1. The muon and electron neutrino rates have already been discussed in detail. One last item is the ratio of electron to muon neutrinos in Table 1. For both the extrapolation method and the subtraction method it is smaller than unity, but in view of the errors only the subtraction result is markedly different from unity. This ratio, however, depends critically on the calculated event rate from conventional muon neutrinos. An increase of 20% would be sufficient to make the prompt electron and muon neutrino fluxes equal. So we conclude that there is no compelling evidence for an anomalous e/μ ratio.

3. NUCLEON STRUCTURE FUNCTIONS

Neutrino experiments using isoscalar targets usually determine two structure functions out of three, which are given in terms of the charged current inclusive cross sections of neutrinos and antineutrinos by

$$F_2(x,Q^2) = \frac{\pi}{G^2 ME}\left[\frac{d^2\sigma^\nu}{dxdy} + \frac{d^2\sigma^{\bar\nu}}{dxdy}\right] \Big/ \left[1 + (1-y)^2 - R'y^2\right]$$

$$xF_3(x,Q^2) = \frac{\pi}{G^2 ME}\left[\frac{d^2\sigma^\nu}{dxdy} - \frac{d^2\sigma^{\bar\nu}}{dxdy}\right] \Big/ \left[1 - (1-y)^2\right] .$$

The third structure function $2xF_1$ is fixed relative to F_2 by specifying the parameter

$$R' = (F_2 - 2xF_1)/F_2 .$$

R' is small and vanishes if the Callan-Gross relation holds. New experimental information on R' is given in the next section. The structure functions can be interpreted in terms of the fractional momentum distributions of quarks and antiquarks:

$$q + \bar q = 2xF_1 = (1 - R')\,F_2$$
$$q - \bar q = xF_3 \qquad \text{(valence quarks)}$$
$$2\bar q = 2xF_1 - xF_3 \qquad \text{(sea quarks)}$$

Although the antiquark structure function $\bar q$ is mathematically derived from the difference of $2xF_1$ and xF_3, it is more directly determined from the antineutrino cross section at high y:

$$\frac{\pi}{G\,ME}\frac{d^2\sigma^{\bar\nu}}{dxdy} = \bar q + q(1-y)^2 .$$

For $y \gtrsim 0.5$ this cross section is dominated by antiquark scattering and a relatively small correction has to be applied for quarks using neutrino data.

The structure functions are displayed in Fig. 4 for a particular Q^2-bin. Antiquarks are confined to $x < 0.4$, hence xF_3 and $2xF_1$ become equal above $x = 0.4$ and can be combined since they are measured independently. The neutrino data are in good agreement with SLAC eD data on F_2 [11]. This is the only structure function measured by electron and muon scattering experiments with isoscalar targets.

All results which will be given in the following include radiative corrections to the cross sections according to Ref. 12, corrections for the small non-isoscalar component of the iron nucleus, and a small correc-

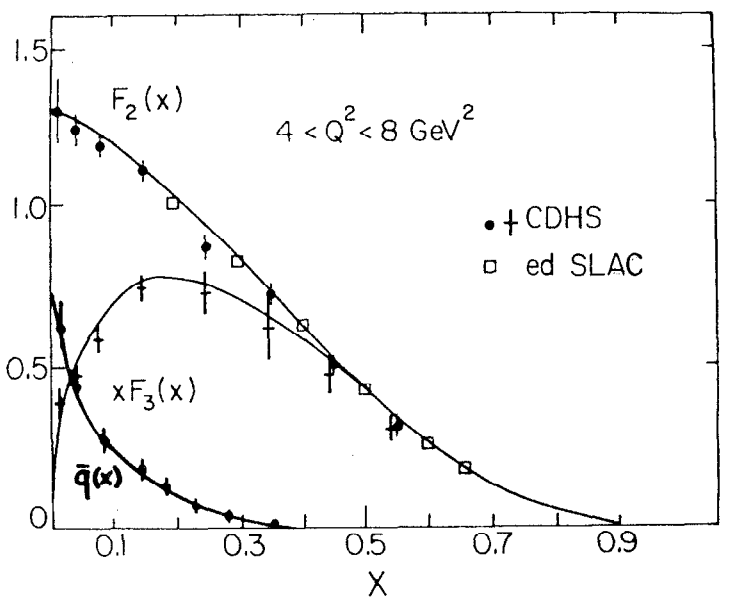

Fig. 4: The structure functions $F_2(x)$, $xF_3(x)$, and $\bar{q}(x)$ for a restricted domain in Q^2.

tion to F_2 caused by strange quarks. These corrections are omitted in the above formulae. The effect of Fermi motion is not unfolded.

3.1 The Callan-Gross Relation

Previously this group reported that the 1977 data are compatible with the Callan-Gross relation[13], the error, however, being rather large. On the other hand a small violation was found in an analysis based on electron scattering data from the SLAC-MIT experiments[14]. There the cross section ratio of longitudinally and transversely polarized virtual photons

$$R = \frac{\sigma_L}{\sigma_T} = \frac{(1 + Q^2/\nu^2)F_2 - 2xF_1}{2xF_1}$$

turns out to be $R = 0.21 \pm 0.10$. R and R' are related by

$$R' = (R - Q^2/\nu^2) \; / \; (1 + R) \; .$$

The present neutrino narrow band beam data have been used for a new determination of R by fitting the parameter R' to the y-distribution of the combined cross sections:

$$\frac{\pi}{G^2 ME} \left[\frac{d^2\sigma^{\nu}}{dxdy} + \frac{d^2\sigma^{\bar{\nu}}}{dxdy}\right] = F_2(x,Q^2) \left[1 + (1-y)^2 - R'y^2\right]$$

A possible distortion of the y-distribution caused by the scaling violations in F_2 is eliminated, if the fit is performed in bins of fixed ν. Results on R are given as a function of ν averaged over x (Fig. 5a), and as a function of x obtained from simultaneous fits to all ν-bins (Fig. 5b). In both cases the data are averaged over Q^2, and $\langle Q^2 \rangle$ increases proportionally to ν and x, respectively. No significant dependence upon x and Q^2 is observed, the average value being

$$R = 0.10 \pm 0.025 \text{ (stat.)} \pm 0.07 \text{ (syst.)} \; .$$

This is in good agreement with the SLAC-MIT result. In the subsequent analysis a constant value of $R = 0.1$ has been assumed to extract F_2 and the antiquark structure function $\bar{q}$.

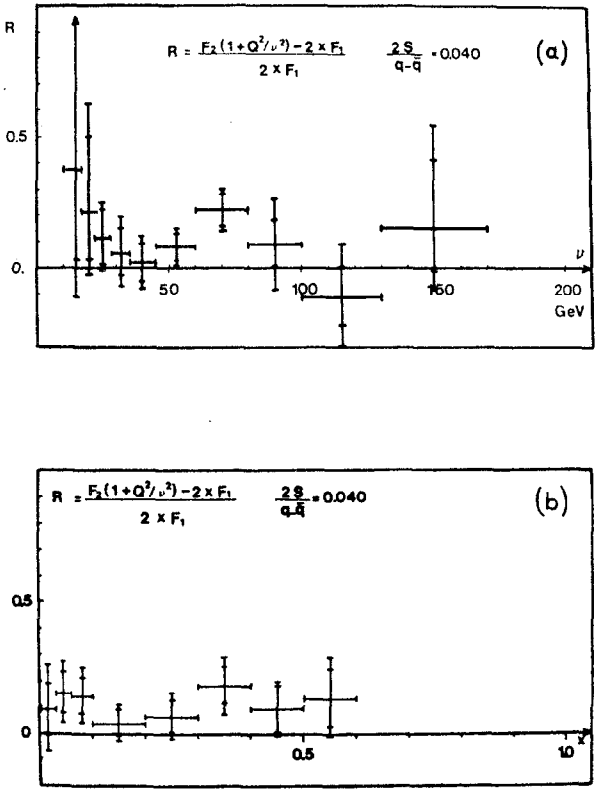

Fig. 5: $R = \sigma_L/\sigma_T$ as a function of ν and x, respectively.

3.2 The structure functions F_2 and xF_3

The structure function F_2 is given in Fig. 6 as a function of x and Q^2. The overall scale error is ±7%. It exhibits the well known pattern of scaling violations with much higher precision than previous data: a rise with Q^2 at small x which in QCD is explained by the increasing number of soft quark pairs produced by gluons, and a drop at large x caused by gluon bremsstrahlung. The agreement with the 1977 data[4] is very good.

The solid lines in Fig. 6 represent a first order QCD fit to the data using the method of Abbott and Barnett[15] to solve the Altarelli-Parisi equations numerically. Target mass corrections have been included. Such a fit provides at least a good phenomenological description of the data. For a proper comparison with perturbative QCD predictions, however, next to leading order corrections, finite quark mass effects (charm threshold), and higher twist terms have to be taken into account.

Second order corrections have been calculated and can in principle be included in the fits. Charm production affects F_2 mostly in the small x region, where the strange sea is concentrated. This can be avoided by going to larger x, or by using xF_3, which represents only valence quarks. xF_3 has the additional advantage that its Q^2 dependence can be predicted independently of the gluon distribution.

The most serious problem is posed by the higher twist terms which fall like powers of $1/Q^2$ in contrast to the logarithmic Q^2 behaviour of the structure functions predicted by perturbative QCD. They must be present, but their magnitude is not known, one only expects their relative contribution to increase with x. If QCD is to be tested one has to demonstrate, that the observed scaling violations are not due to higher twist terms only.

To illustrate the situation, xF_3 combined with $2xF_1$ for $x \geq 0.4$ is shown in Fig. 7 at large x. The solid lines result from the lowest order QCD fit and the dashed lines from a pure higher twist fit of the form

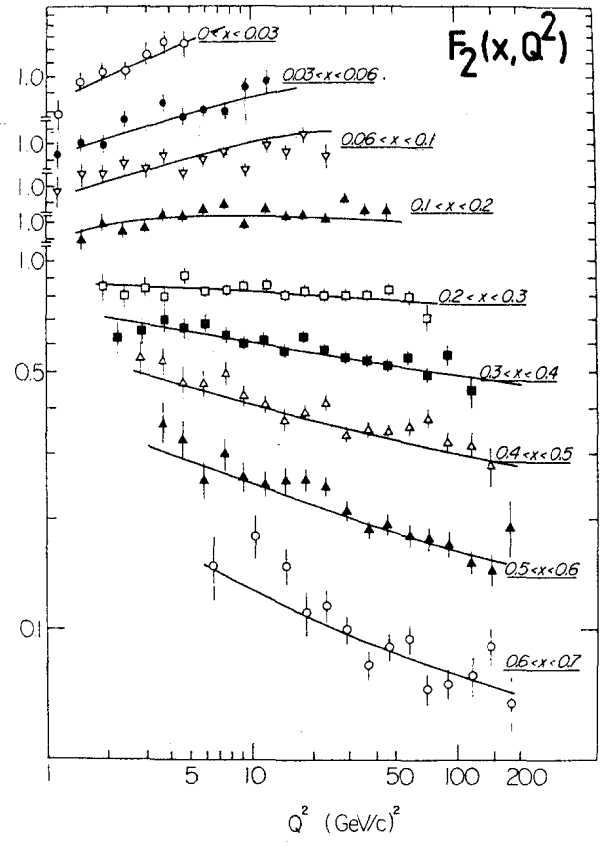

Fig. 6: The structure function $F_2(x,Q^2)$. The solid lines represent a first order QCD fit to the data, following Ref. 15.

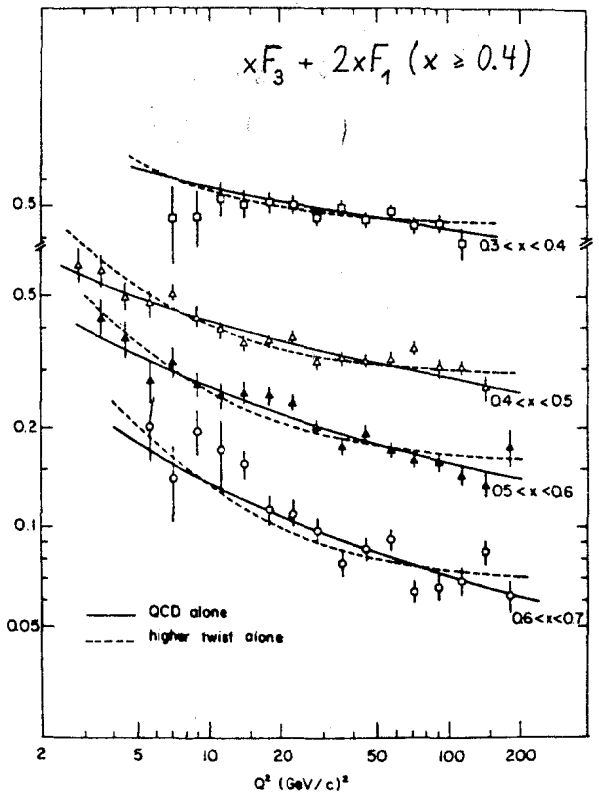

Fig. 7: The structure function $xF_3(x,Q^2)$ combined with $2xF_1(x,Q^2)$ for $x \geq 0.4$. The curves represent fits assuming first order QCD (solid lines) and higher twist terms only (dashed lines).

$$xF_3(x,Q^2) = F(x)\left[1 + \frac{ax}{(1-x)Q^2} + \frac{bx^2}{(1-x)^2Q^4}\right]$$

As can be seen, QCD predicts a continuous shrinkage of the structure function with Q^2, whereas pure higher twist terms ultimately lead to scaling. The preliminary results of this analysis are that lowest order QCD fits the data better than pure higher twists. Even better results are obtained by adding a $1/Q^2$ term to the QCD parametrization:

$$xF_3(x,Q^2) = xF_3^{QCD}(x,Q^2)\left[1 + \frac{ax}{(1-x)Q^2}\right].$$

This has to be made more quantitative in the future and there is a chance that these data can establish the presence of perturbative QCD effects.

The parameter Λ has been determined in lowest order from a fit to xF_3 combined with $2xF_1$ ($x \geq 0.4$) for $Q^2 > 10$ $(GeV/c)^2$. Target mass corrections and a propagator term with $M_W = 87$ GeV are taken into account. The result is

$$\Lambda = 0.27 \pm 0.08 \text{ (stat.)} \pm 0.10 \text{ (syst.)} \quad .$$

As mentioned before, the charm theshold and the gluon distribution don't enter here. Moreover, higher twist effects should be greatly reduced because of the rather high cut in Q^2.

3.3 The antiquark structure function

For the first time the scaling behaviour of the antiquark (sea quark) structure function has been measured. This structure function is of particular interest since it is directly related to the gluon distribution. 100 000 antineutrino events taken in a 350 GeV wide band beam and the narrow band beam sample of 25 000 antineutrino events have been analyzed. More precisely, in terms of the antiquark content the function $\bar{q}^{\bar{\nu}} = \bar{u} + \bar{d} + 2\bar{s}$ is measured. This is equivalent to $\bar{q} + \bar{s}$, if $q = u + d + s$.

Fig. 8 shows $\bar{q} + \bar{s}$ as a function of x and Q^2. The solid lines are the predictions from lowest order QCD parametrizations of F_2 and xF_3

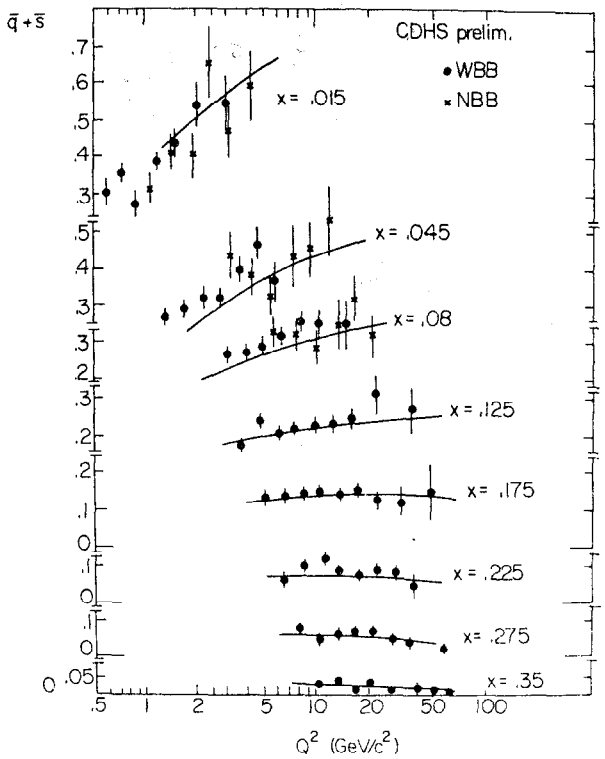

Fig. 8: The antiquark structure function $\bar{q}(x,Q^2) + \bar{s}(x,Q^2)$. The solid lines are predictions from fits to F_2 and xF_3.

obtained by fitting the narrow band beam data only. This demonstrates that a consistent set of structure functions from different data samples with different systematical errors is available. Strong scaling violations are observed at small x, indicating a shrinkage of $\bar{q} + \bar{s}$ with Q^2. This is confirmed by the decrease of the average fractional momentum $\langle x \rangle$ with ν (Fig. 9b). On the other hand, the integrated momentum fraction seems to increase (Fig. 9a).

Qualitatively, these observations are in agreement with expectations from QCD. Antiquarks originate from quark pair production by gluons, and the gluon momentum spectrum becomes softer with Q^2, whereas the total gluon momentum increases due to increasing gluon bremsstrahlung. It should be noted, however, that part of the effect could be caused by the threshold of charm production from strange antiquarks.

4. OPPOSITE SIGN DIMUON EVENTS

Opposite sign dimuon events produced in neutrino and antineutrino interactions are well described by the GIM-mechanism as the production of charmed quarks with subsequent semiletonic decay. In terms of the quark momentum distributions, the differential cross section for single charm production on an isoscalar target is given by

$$\frac{d^2\sigma^{(-)}_{\nu}}{dxdy} = \frac{G^2ME}{\pi}\left[\left(\bar{u}^{(-)}+\bar{d}^{(-)}\right)\sin^2\theta_c + 2\,\bar{s}^{(-)}\cos^2\theta_c\right]$$

Where θ_c is the Cabibbo angle. Since $\sin^2\theta_c \ll \cos^2\theta_c$, charm production by antineutrinos probes the strange sea quarks, whereas in the case of neutrinos the contributions from valence quarks and strange sea quarks are comparable.

Previous analyses were based on a few hundred events. Now samples of 8000 neutrino-induced and 1000 antineutrino-induced dimuon events after cuts are available. The cuts require a minimum muon momentum of 5 GeV/c and a total visible energy above 20 GeV. Even though the statistics has been improved by an order of magnitude, there is no need for any other process but charm production to explain the data.

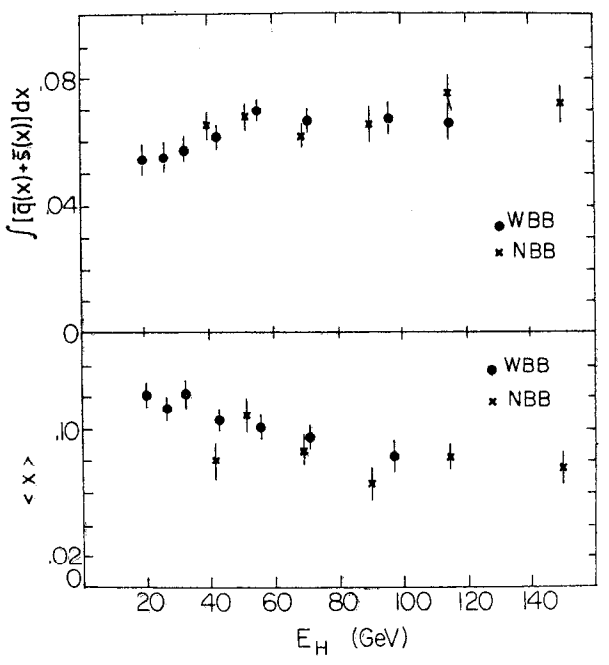

Fig. 9: Total and average fractional nucleon momentum carried by antiquarks as a function of ν (= E_H).

4.1 The strange sea

The x-distribution of strange sea quarks is simply given by the x-distribution of antineutrino-induced dimuon events. It is very similar to the x-distribution of all sea quarks (Fig. 10).

The x-distribution of neutrino-induced dimuon events can be understood as a superposition of the strange sea distribution and a Cabibbo suppressed valence quark distribution. This is demonstrated in Fig. 11. The strange sea distribution, taken from the antineutrino data, combined with a valence quark distribution, obtained from a Buras-Gaemers fit to xF_3 [16] (dotted line), is fitted to the neutrino x-distribution by varying the ratio of the two components. The fit (solid line) describes the data very well, and it is used to determine the relative fractional momenta of strange quarks and valence quarks.

The results on the strange sea contribution as a function of ν are given in Fig. 12. The four ν-bins correspond to an average Q^2 of 8, 13, 21, 40 $(GeV/c)^2$, respectively. For comparison the relative amount of non-strange antiquarks is indicated, which represents half of the non-strange sea. One observes scaling violations, which are relatively stronger for the strange than for the non-strange sea, and a suppression of the strange sea by a factor two to three. These results may indicate the presence of kinematical effects due to the threshold for single charmed quark production.

4.2 Transverse momentum of charm jets

In the framework of QCD, dimuon events are extremely useful to study gluon radiation off struck quarks. One expects that gluon radiation increases the transverse momentum of the current jet with respect to the current direction. In neutrino dimuon events the wrong sign μ^+ serves to identify the charmed quark, which gives rise to the current jet, and to measure its transverse momentum after the hadronization process. This is different from the usual situation, where the hadron carrying the primary quark is not identified.

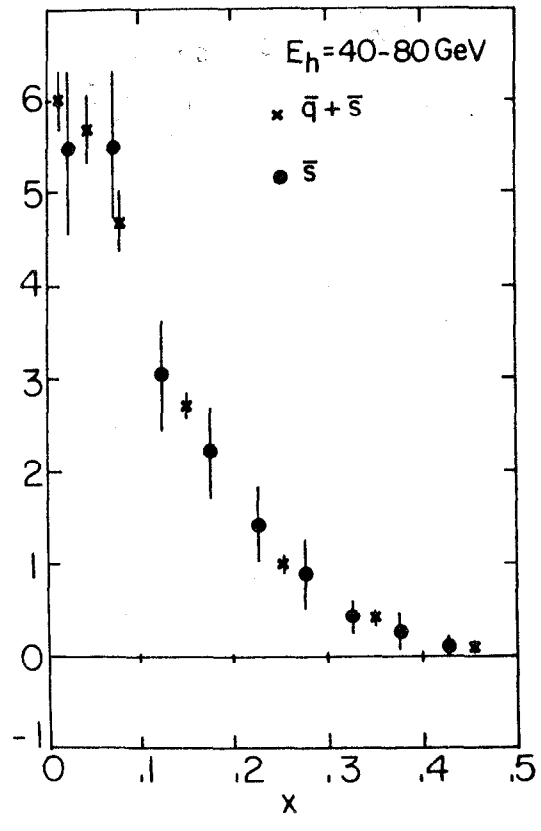

Fig. 10: x-distribution of strange antiquarks compared to all antiquarks.

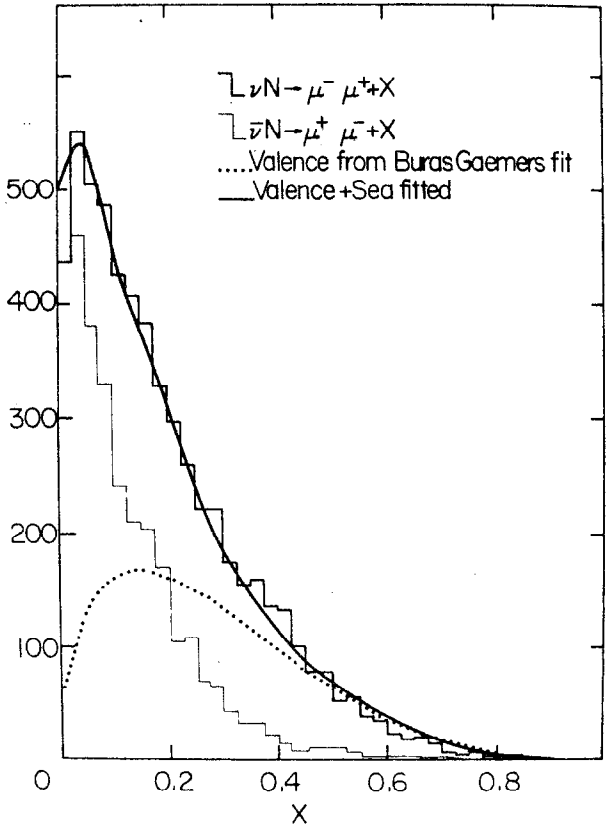

Fig. 11: Comparison of the x-distributions of neutrino- and anti-neutrino-induced dimuon events. The relative normalization is obtained from a fit to the shapes (solid curve), assuming that the difference is due to valence quarks (dotted curve).

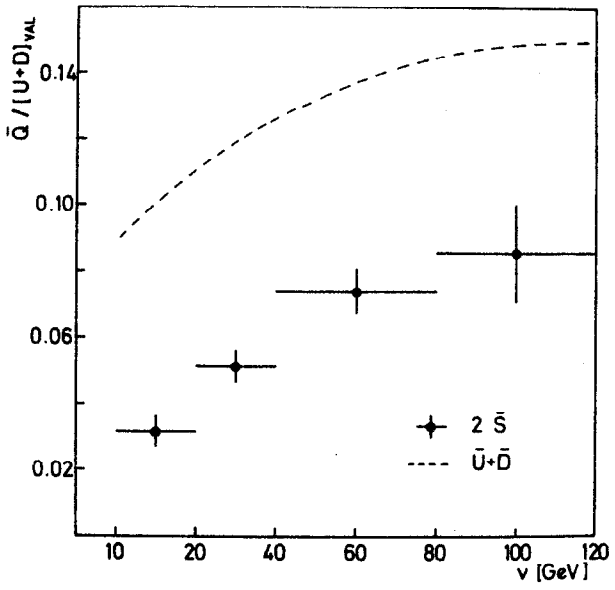

Fig. 12: Ratio of the fractional momenta of the strange sea to valence quarks. The corresponding ratio for non-strange antiquarks is indicated by the dashed line.

In first order QCD, according to Altarelli and Martinelli[17], the average transverse momentum squared of the quark should increase linearly with W^2, where W is the invariant mass of the hadronic system. This gluonic term adds to the intrinsic transverse momentum k_T of the quark. Denoting by z the fraction of the quark momentum carried by the μ^+, the more complete prediction for the transverse momentum of the μ^+ reads

$$\langle p_T^2 \rangle = z^2(\langle k_T^2 \rangle + C\alpha_s W^2) + \text{const.}$$

Here α_s is the strong coupling constant, and C is to a good approximation a constant, which can be calculated. For the electroproduction of light quarks it is $C = 3.1 \times 10^{-2}$ (Ref. 17). For the neutrino production of charmed quarks R. Moore[18] finds, that C depends upon the mass of the charmed quark m_c. Assuming $m_c \approx 1.25$ GeV/c^2, he obtains $C = 3.6 \times 10^{-2}$. The constant term in the equation arises from the quark fragmentation and the semileptonic decay of the charmed particle.

Experimentally, z is approximately measured by $z = E_{\mu+}/(E_{\mu+} + E_{had})$, and p_T is replaced by $p_{T,out}$, the transverse momentum of the μ^+ with respect to the production plane, since this quantity is better determined. In the limit of angular symmetry around the current direction, one has $\langle p_{T,out}^2 \rangle = \langle p_T^2 \rangle/2$. In Fig. 13 $\langle p_{T,out}^2 \rangle$ is given as a function of z and W^2. The predicted linear dependence upon W^2 is clearly exhibited by the data. A preliminary fit yields

$$\langle k_T^2 \rangle = \left[0.6 \pm 0.2(\text{stat.}) \pm 0.2(\text{syst.})\right] \ (\text{GeV/c})^2$$
$$C\alpha_s = \left[1.3 \pm 0.3(\text{stat.}) \pm 0.3(\text{syst.})\right] \times 10^{-2}$$

With $C = 3.6 \times 10^{-2}$, one calculates $\alpha_s = 0.36 \pm 0.12$, at an average Q^2 of 20 $(\text{GeV/c})^2$, consistent with other measurements of α_s.

4.3 Neutral current effects

The large sample of dimuon events makes it tempting to check the invariant $\mu^+\mu^-$-mass distribution for peaks from the decay of neutral vector mesons into $\mu^+\mu^-$. Of particular interest is the J/ψ -production via the neutral weak current, because it enables a test of the weak neutral-current coupling of the charmed quark.

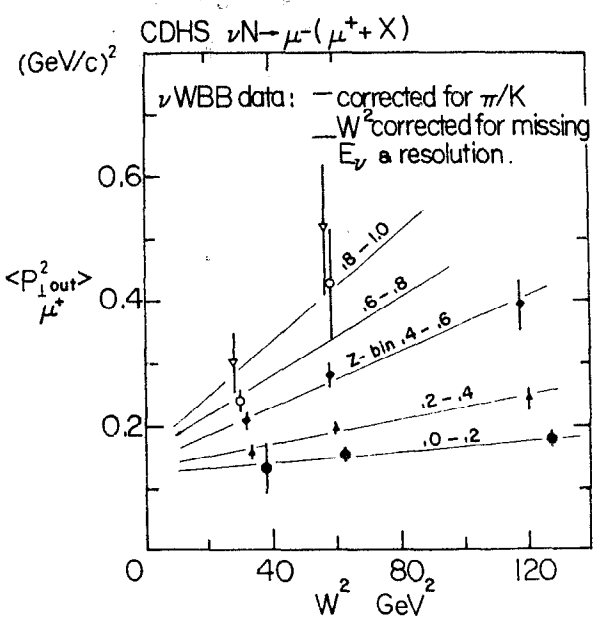

Fig. 13: Average $p_{T,out}^2$ of the μ^+ in neutrino-induced opposite sign dimuon events as a function of W^2 and z; $p_{T,out}$ is the transverse component of the momentum with respect to the production plane.

The J/ψ is expected to be diffractively produced, with little energy transferred to the hadronic system. Consequently, a cut in the hadronic energy $E_H < 6$ GeV is applied to the data. The invariant $\mu^+\mu^-$ mass distribution (Fig. 14) shows indeed a signal at the J/ψ mass, with a width expected from the experimental resolution. However, a statistical fluctuation is not yet excluded.

There is another peak in the ρ/ϕ-region, which becomes more prominent, if the cut in E_H is lowered. A lower cut in E_H, on the other hand, affects the J/ψ-signal, since, due to the rather large mass of the J/ψ, a finite momentum transfer to the rest of the hadrons is required.

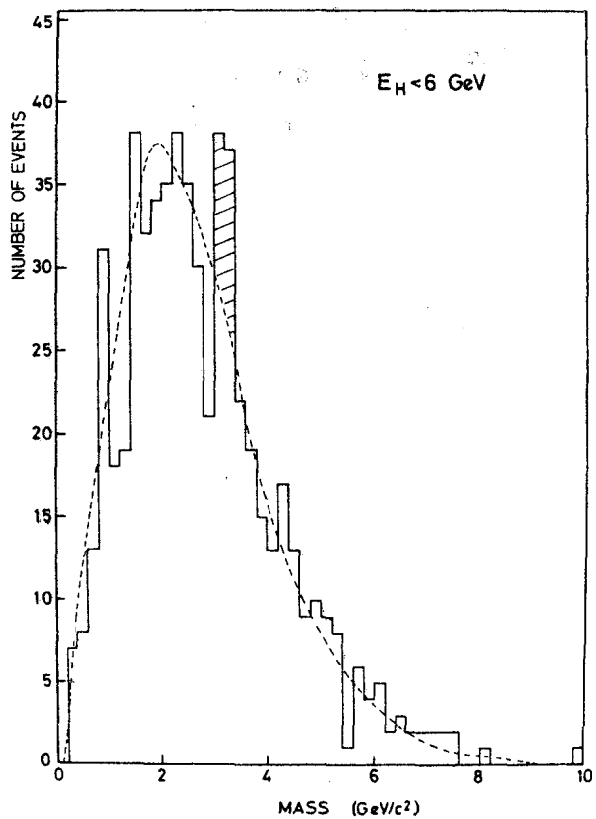

Fig. 14: Invariant dimuon mass of neutrino—induced $\mu^+\mu^-$ events for hadronic energies $E_H < 6$ GeV. The shaded area indicates a possible signal of J/ψ production by weak neutral currents.

REFERENCES

(1) The members of this collaboration are: H. Abramowicz, P. Bloch, J.G.H. de Groot, F. Dydak, F. Eisele, T. Flottmann, C. Geweniger, C. Guyot, J.T. He, V. Hepp, H.P. Klasen, K. Kleinknecht, J. Knobloch, J. Krolikowski, H. Lierl, S. Loucatos, J. May, J.P. Merlo, P. Palazzi, A. Para, B. Peyaud, B. Pszola, J. Rander, F. Ranjard, B. Renk, J. Rothberg, T.Z. Ruan, A. Savoy-Navarro, D. Schlatter, J.P. Schuller, J. Steinberger, H. Taureg, K. Tittel, R. Turlay, W. von Rüden, H. Wahl, H.J. Willutzki, J. Wotschack, and W.M. Wu.

(2) M. Holder et al., Nucl. Instr. Meth. 148 (1978) 235.

(3) T. Hansl et al., Phys. Lett. 74B (1978) 139.

(4) J.G.H. de Groot et al., Z. für Physik C1 (1979) 143.

(5) M. Holder et al., Phys. Lett. 69B (1977) 377.

(6) P.C. Bosetti et al., Phys. Lett. 74B (1978) 143.

(7) P. Alibran et al., Phys. Lett. 74B (1978) 134.

(8) Aachen-Bonn-CERN-Demokritos-London-Oxford-Saclay (ABCDLOS) Collab.

(9) F. Niebergall, these proceedings.

(10) H. Wachsmuth, Neutrino and muon fluxes in the CERN 400 GeV proton beam dump experiments, CERN/EP 79-125 (1979).

(11) E.M. Riordan et al., SLAC-PUB-1634 (1975).

(12) A. de Rújula et al., Nucl. Phys. B154 (1979) 394.

(13) A. Savoy-Navarro, Proc. Int. Conf. on Neutrinos, Weak Interactions, and Cosmology, Bergen, 1979, Vol. 2, p. 253.

(14) R.E. Taylor, Proc. 19th Int. Conf. on High Energy Physics, Tokyo, 1978, p. 285.

(15) L.F. Abbott and R.M. Barnett, Ann. Phys. 125 (1980) 276.

(16) J.G.H. de Groot et al., Phys. Lett. 82B (1979) 456.

(17) G. Altarelli and G. Martinelli, Phys. Lett. 76B (1978) 89.

(18) R. Moore, Dortmund University, private communication to the CDHS group.

RESULTS FROM CERN MUON SCATTERING EXPERIMENTS

H.E. Montgomery
CERN, Geneva, Switzerland

ABSTRACT

The status of experiments involved in muon scattering at CERN is reviewed. Special emphasis is given to recent results.

Presented at the Topical Conference of the SLAC Summer Institute July 28 - August 8 1980.

INTRODUCTION

There are two large muon experiments currently operating at CERN. They share a high quality beam, the critical elements of which are shown in fig. 1(a). The beam operates typically with 2×10^7 muons per 1.5 sec. spill at energies up to 280 GeV. The half width of the beam is approximately 2 cm at the experiments and the hard muon halo integrated over the face of the apparatus is of the order of 10-15% of the beam. As indicated in fig. 1(b) one experiment sits behind the other and under many circumstances the two experiments have taken data at the same time.

In sect. 1 of this paper the two experiments will be introduced and their results on nucleon structure function measurements summarised. In sect. 2 an attempt to measure the interference between weak and electromagnetic amplitudes is discussed. Sect. 3 covers results obtained on multi-muon final states and finally results for hadronic final states are discussed in sect. 4. Of the subjects covered only that of sect. 2 is directly related to the title of this school. The importance of the other results for strong interactions especially those on nucleon structure functions has however been emphasised several times during the course of the school, for example, by F. Sciulli in his lectures on neutrino interactions [1].

1. NUCLEON STRUCTURE FUNCTIONS

1.1 The BCDMS Collaboration (Bologna-CERN-Dubna-Munich-Saclay)

A side view of the apparatus is shown in fig. 2(a). The feature is the very long target of graphite which is surrounded by a modular iron toroid magnet. There are ten mechanically independent supermodules each with its own coils. The diameter of the toroids is 2.74m. The experiment is equipped with a total of 80 planes of proportional wire chambers with x and y orientations for the wires and also 20 planes of liquid scintillator hodoscopes. The hodoscopes are constructed to form concentric rings about the beam.

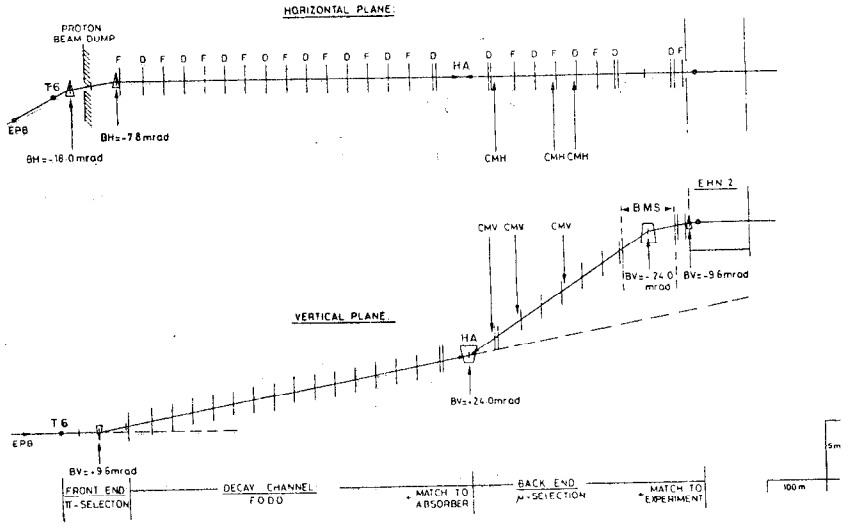

(a) SPS M2 Muon Beam Line Layout;

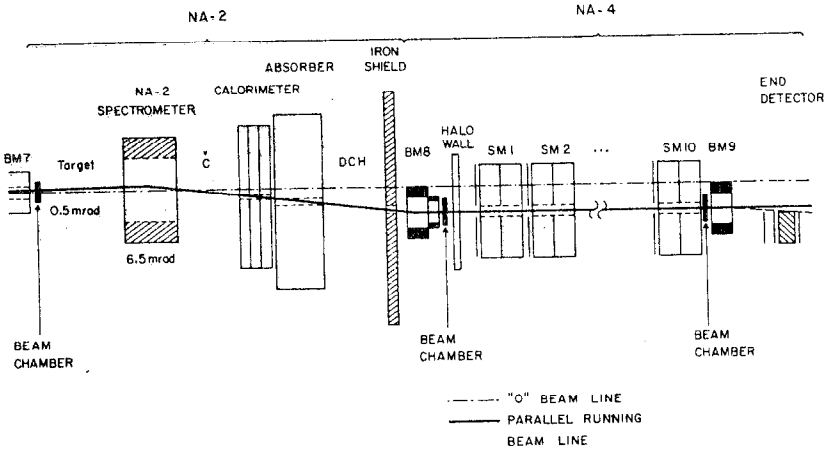

(b) Sketch showing relative positioning in Beam of EMC and BCDMS experiment.

Fig. 1

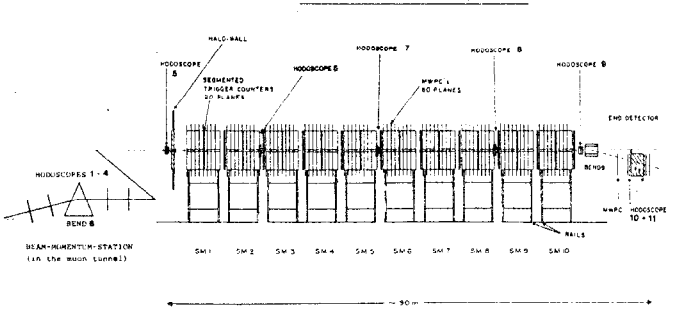

(a) Side view of BCDMS apparatus;

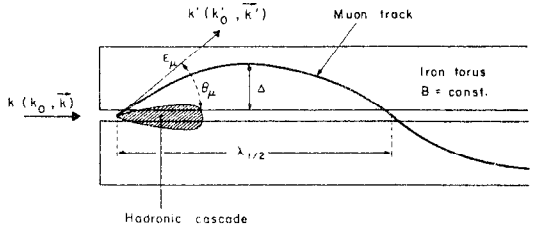

$$\lambda_{1/2} = 6.66\ k'_T / B$$

$$\Delta = \frac{Mp}{0.3B}\ \frac{q^2}{q^2_{max}}$$

(b) Trajectory of scattered muon in toroidal field;

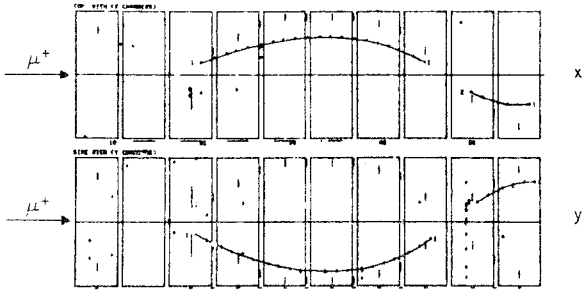

p = 92.1 GeV/c Q^2 = 96.0 (GeV/c)^2

(c) Reconstructed event (BCDMS) with Q^2 = 96 GeV^2.

Fig. 2

A muon incident along the axis of the system, after scattering, executes a series of oscillations in the toroidal field. The amplitude (see fig. 2(b)) of the oscillations is directly related to Q^2. This permits the use of the concentric scintillator rings in a trigger system which is directly proportional to Q^2. The track reconstruction for one event is shown in fig. 2(c).

Results on the measurements of F_2 were presented at the Madison Conference [2] for three beam energies, 120 GeV, 200 GeV and 240 GeV. A total of 300 000 events is involved and there is a minimum Q^2 which is 25 GeV^2 for 120 GeV and 50 GeV^2 for 240 GeV. The results are not corrected for Fermi momentum effects and so correspond to F_2(carbon)/12. Corrections are, however, made for radiative effects and, for the first time also, for the weak electromagnetic interference term. The ratio of longitudinal to transverse photon cross sections (R) is assumed to be zero. The results are shown in fig. 3(a) and (b) in which the 200 GeV data are in turn compared with 120 GeV and 240 GeV. The agreement is clearly good. Also shown on the figures are estimates of the excursions possible given present knowledge of the systematic uncertainties. The data show a weak but clear Q^2 dependence and a fit of the form

$$F_2 = \sum_{i=1}^{3} a_i (1-x)^{i+x} \left(1 + C \ln \frac{Q^2}{3} \ln \frac{1}{4x}\right)$$

yields C = 0.12 ± 0.03 (stat). The data are sufficiently extensive to allow construction of the n = 4 - 7 moments of F_2. As usual in estimating moments, extrapolations are required to both x = 1 and x = 0; however, the results shown in fig. 4 are confined to those moments and Q^2 values in which the measurements constitute at least 2/3 of the moment. The results are compared with those from CDHS [3]; no significant disagreement is seen but there are rather few neutrino points in the high Q^2 region relevant to these data.

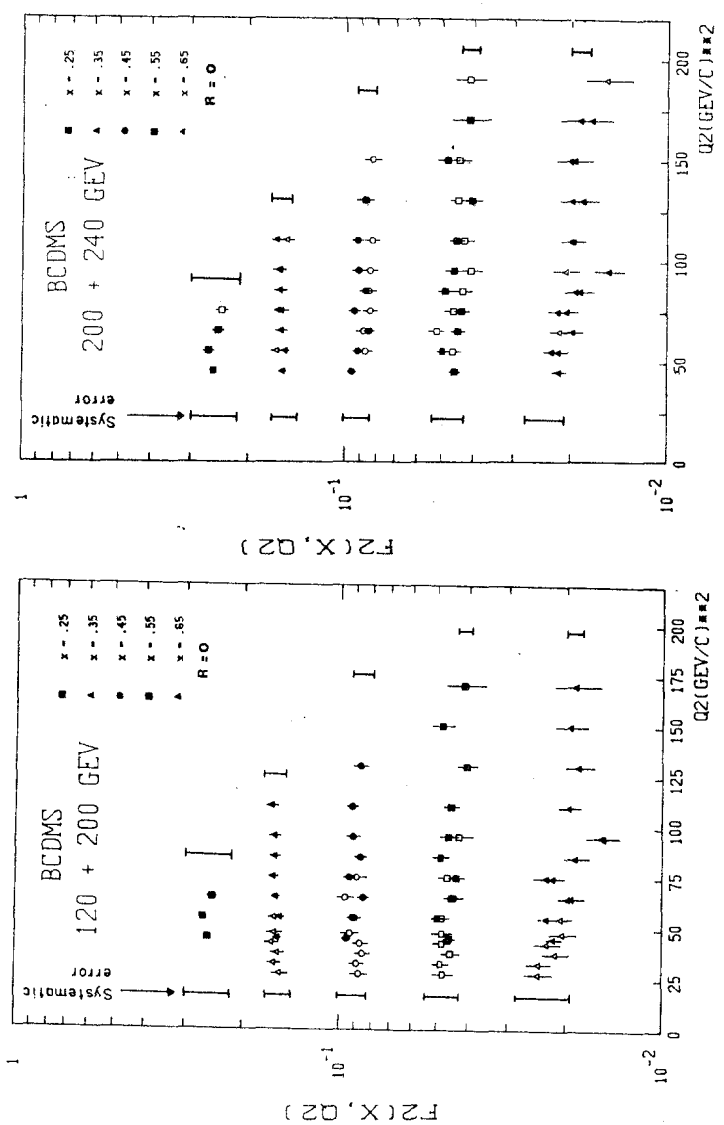

(a) F_2 (nucleon) from BCDMS closed symbols are 200 GeV, open symbols 120 GeV;

(b) F_2 (nucleon) from BCDMS closed symbols are 200 GeV, open symbols 240 GeV.

Fig. 3

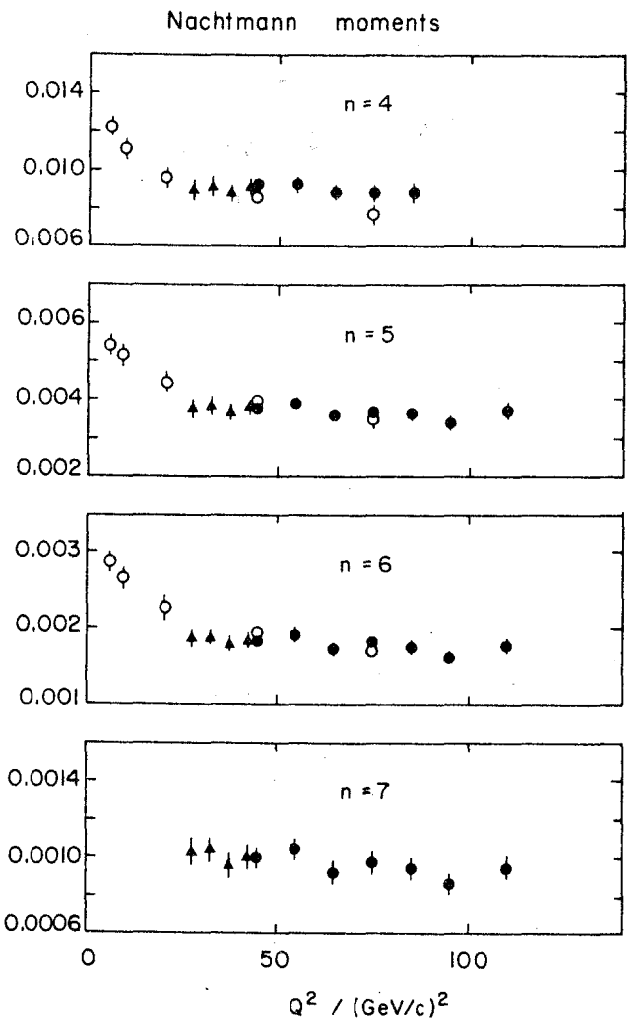

Fig. 4 Nachtmann moments of F_2, closed symbols from BCDMS, open symbols from CDHS(3).

1.2 The E.M.C.

(CERN-DESY-Freiburg-Kiel-Lancaster-LAPP-Liverpool-Oxford-Rutherford-Sheffield-Turin-Wuppertal)

In contrast to B.C.D.M.S., E.M.C. uses an almost "point-like" target (3 m Fe/Sc or 6m H_2) in conjunction with an open dipole magnet (4 Tm). A plan view of the layout is shown in fig. 5. There are 99 planes of wire chamber, both proportional and drift, distributed along the length of the system. The iron target is equipped for calorimetry and measures the total hadronic energy deposited with a resolution $\Delta E = 0.6\ E^{0.6}$. The front part of the hadron absorber is also in the form of a modular calorimeter, the front parts of which (22 X^0) measure electromagnetic showers.

Measurements of F_2 using the STAC target have been presented [4] for three energies, 120, 250 and 280 GeV (80K, 280K and 540K events respectively). The data have been corrected for radiative effects and for Fermi-motion, although the latter is only significant for $x > 0.5$. $R = 0.2$ is assumed in all E.M.C. analyses at the present time. There is an apparent overall discrepancy of 10% between the 120 GeV data and the high energy data, and the systematic uncertainties are estimated to be ± 10%. The combined data are shown in fig. 6; an adjustment of 5% on the data sets was used. In fig.7 the higher x data without Fermi motion corrections are compared with the statistical means derived from the three B.C.D.M.S. data sets. Agreement is excellent.

Measurements of F_2 (proton) [5] have also been made at 120 GeV and 280 GeV (150 K and 250 K events respectively). Corrections have been made for radiative effects and again $R = 0.2$ has been assumed. As shown in fig. 8 agreement between the two energies is good and (see fig. 9) so also is the agreement between the 120 GeV data and lower Q^2 data from SLAC [6]. Residual systematic uncertainties are approximately ±10%.

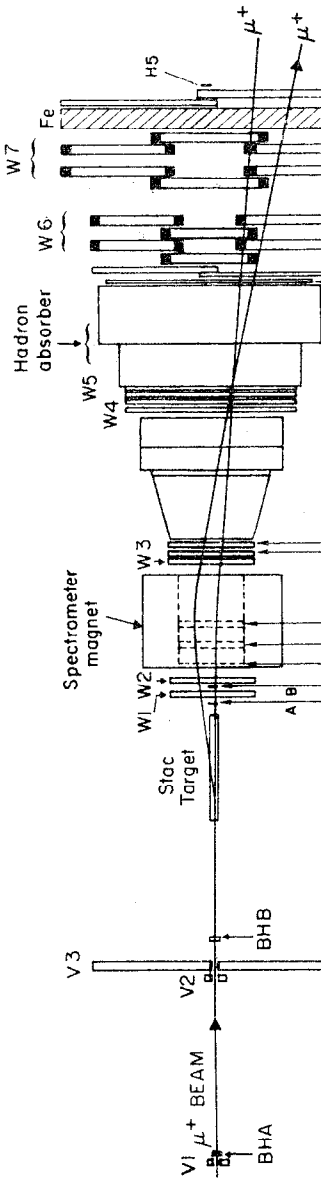

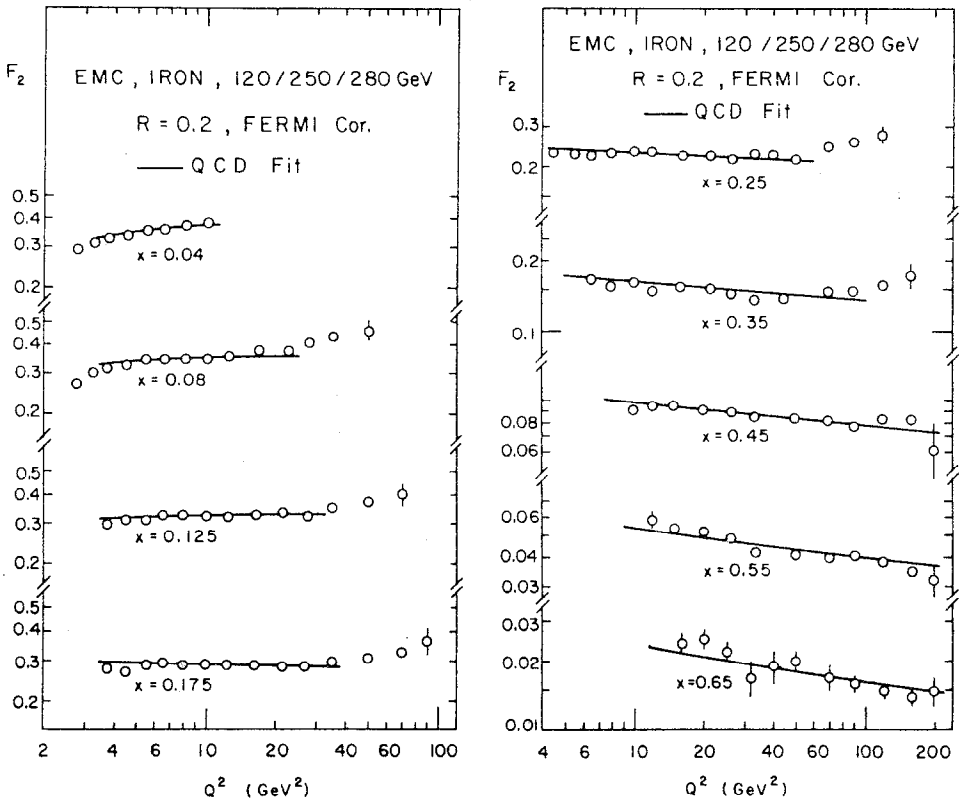

Fig. 6 F_2 (nucleon) as measured on iron by EMC, line is QCD fit, see text.

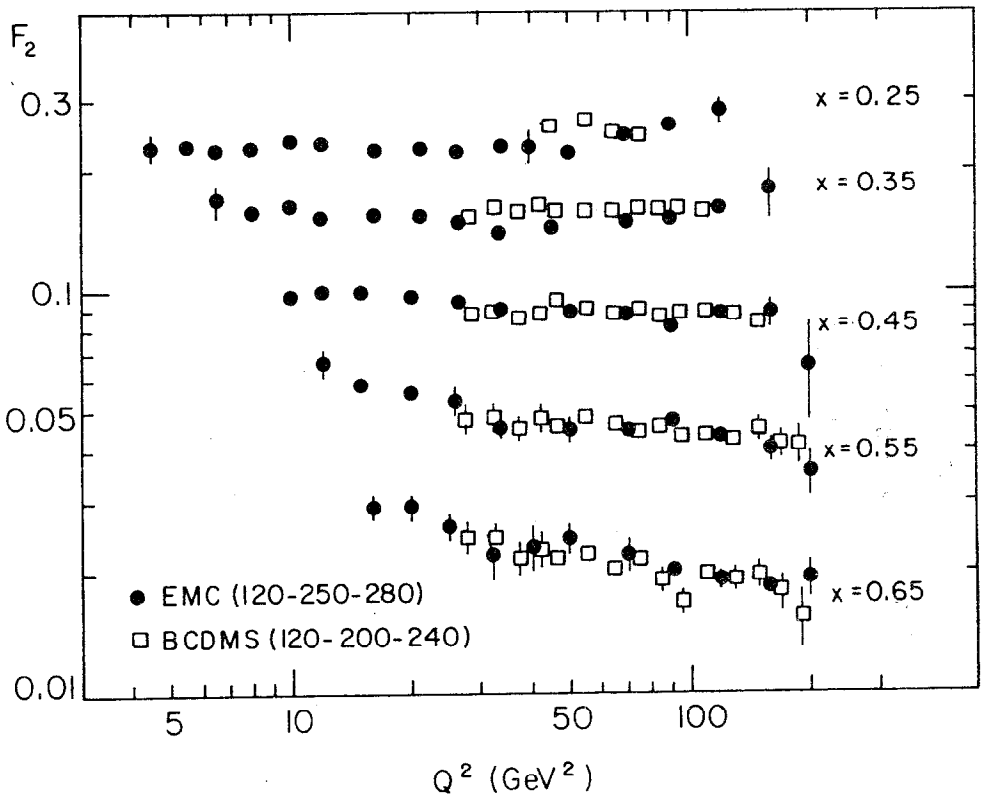

Fig. 7 Comparison of F_2 from EMC without Fermi motion corrections and from BCDMS.

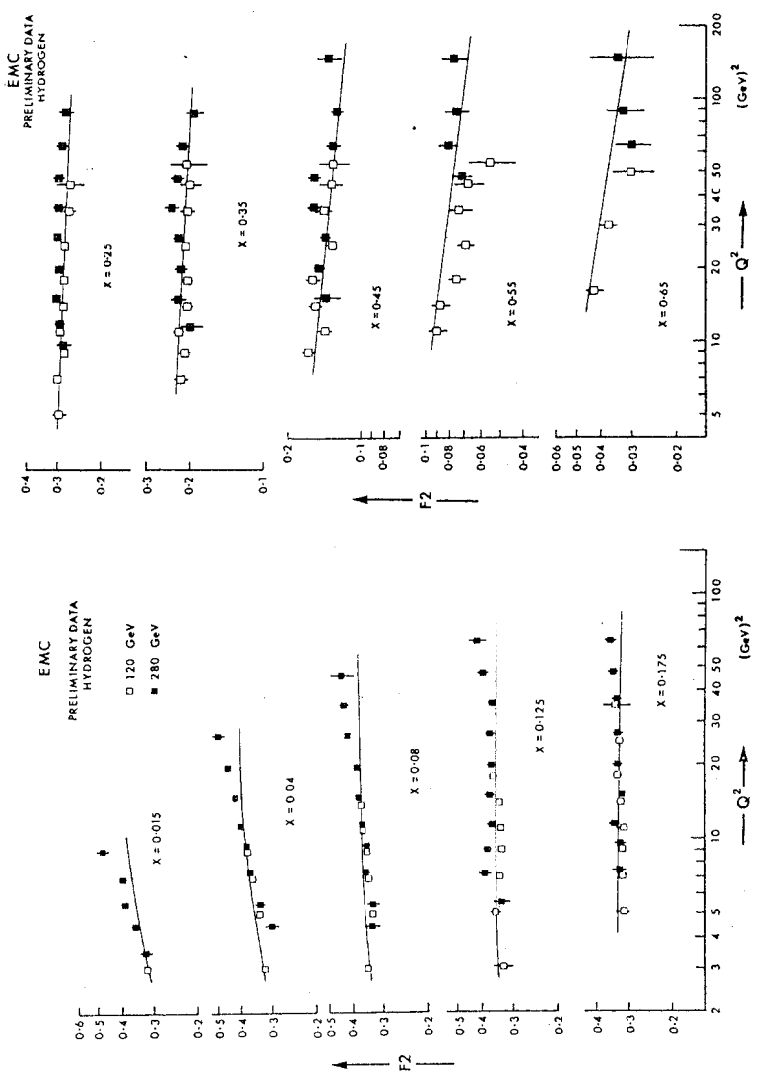

Fig. 8 F_2 (proton) from EMC at 120 GeV, open symbols, and 280 GeV, closed symbols.

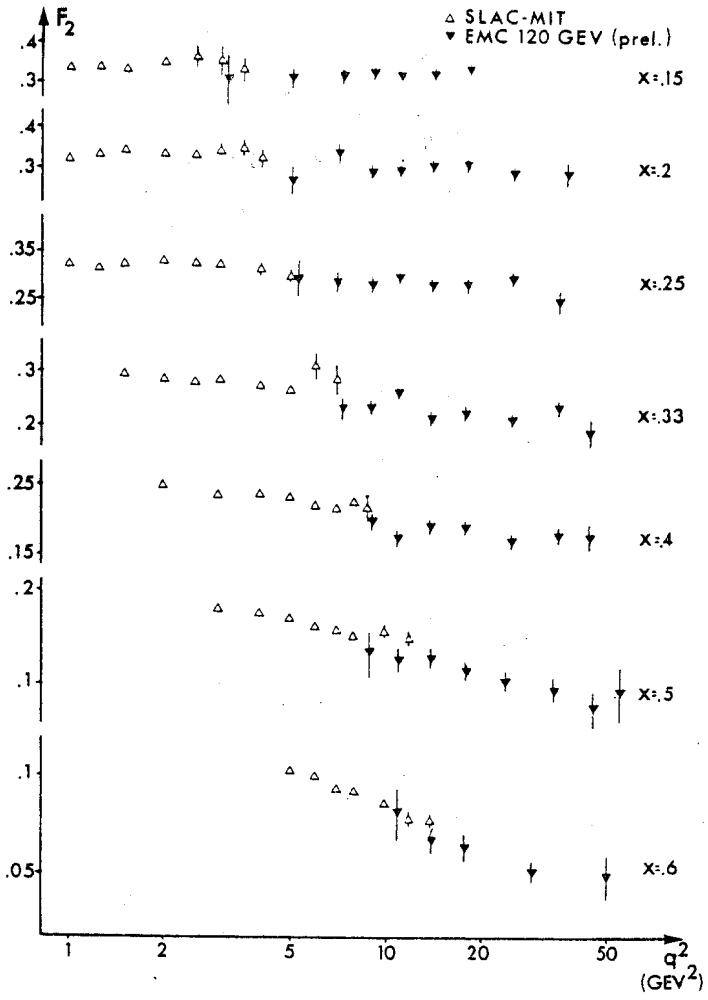

Fig. 9 F_2 (proton) from EMC at 120 GeV closed symbols and from SLAC (6) open symbols.

The lines shown in figs. 6 and 8 are the results of QCD fits using the program of Barnett et al. [7] based on direct use of the Altarelli-Parisi evolution equations [8]. An alternative analysis procedure due to Gonzalez et al. [9] has also been used [10]. The effective Λ obtained with both analyses was Λ = 100 MeV in first order. It is clear from the figures, however, that the fits are not good at low x. This is to be expected since no allowance was made for charm production which, as mentioned in the next section, is significant at low x. This low x region is also sensitive to the essentially unconstrained gluon distribution; these complications do not, however, generate the low Λ value since the same result was obtained when the fits were confined to $x \geq 0.25$. The conclusion on the strong interaction scale parameter at this stage of the analysis is therefore $\Lambda \simeq 100$ MeV, but with the existing systematic uncertainties a notional error of 100 MeV has to be assigned.

2. WEAK ELECTROMAGNETIC INTERFERENCE

High energy muon scattering experiments are usually analysed in terms of single photon exchange; however, at high Q^2 there is also a contribution from Z^0 exchange. The interference between the two amplitudes has a magnitude $\sim 10^{-4}\ Q^2\ (GeV^2)$ which comes from the relative values of the weak and electromagnetic couplings and the relative behaviour of the propagators. Assuming the standard model the effect is compared in fig. 10 with that due to normal radiative corrections. The B.C.D.M.S. group has attempted to measure this effect making use of the polarisation properties of the muon beam.

The muons produced by the decay of a momentum selected pion beam have a direct relationship between their laboratory momenta and their helicity. Therefore, momentum selection of the muons as occurs in the SPS M2 beam line (11) leads to a beam which is polarised. The various possibilities are given as follows:

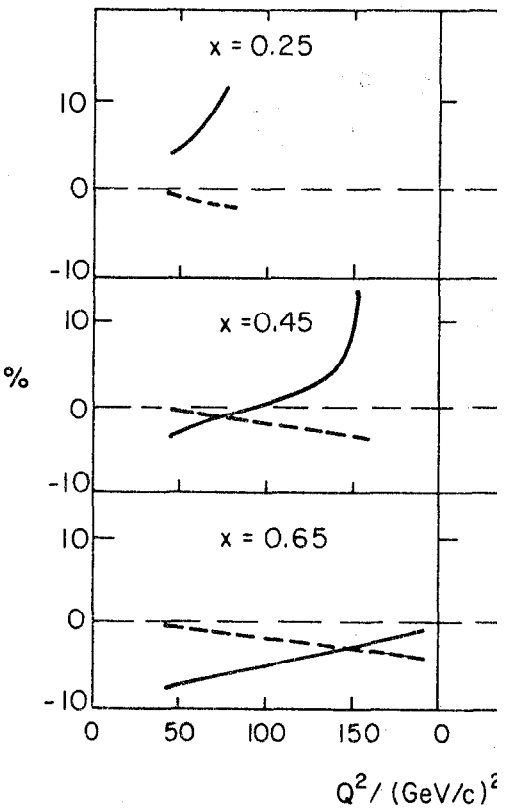

Fig. 10 Difference between measured and correcte
corrections (solid line) and weak em. ir

Particle	p_μ/p_π	Helicity	Rel μ yield per p for fixed μ mom.
μ^+	∿ 1	- 1	1
μ^+	∿ 0.5	+ 1	1/9
μ^-	∿ 1	+ 1	1/3
μ^-	∿ 0.5	- 1	1/27

The relative yields which are very approximate arise from relative production rates for π^+ and π^- and their energy dependence coupled with the acceptance of the beam line for the different relative μ to π momenta. Since statistics are important the choice of the two forward decay modes μ^+_L and μ^-_R is favoured.

An attempt is therefore made to measure the asymmetry

$$B = \frac{d\sigma^+ (\lambda \sim -1) - d\sigma^- (\lambda \sim +1)}{d\sigma^+ (\lambda \sim -1) + d\sigma^- (\lambda \sim +1)} \quad .$$

The significance of the measurement has been discussed by Klein [12] who shows that

$$B(\lambda) = K(a_\mu - \lambda v_\mu) A \quad ,$$

where a_μ and v_μ are the axial and vector weak couplings of the muon

$$K = \frac{G}{\sqrt{2}} \quad \frac{Q^2}{2\pi\alpha} = 1.79 \cdot 10^{-4} \; Q^2(GeV^2)$$

is the strength of the asymmetry, and

$$A = A_0 g(y) = \frac{xG_3}{F_2} \quad \frac{[1 - (1-y)^2]}{[1 + (1-y)^2]}$$

is a ratio of nucleon structure functions. The dependence of B on the helicity λ of the μ^- is shown in fig. 11 for the standard theory "μ^-_R"

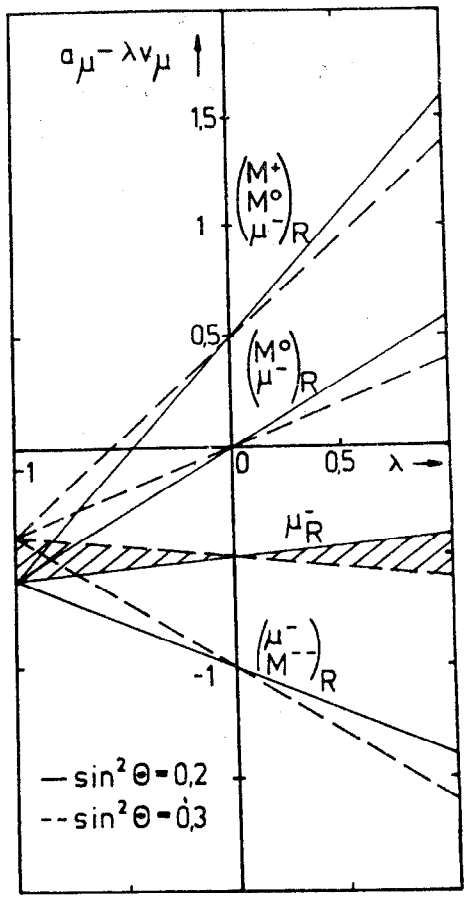

Fig. 11 Dependence of -B/kA on λ(μ^-) for different theoretical prescriptions.

and a selection of possible alternatives. The experiment as performed has $\lambda(\mu^-) \sim +1$ and so is particularly sensitive to the coupling (I_3^R) of the right handed u^-.

$$\frac{B(\lambda_{ij} - \sim + 1)}{- KA} \sim 2\ (I_3^R + \sin^2\theta_w)$$

within the lepton classification scheme presented at this school by H. Harari [13]; this was one of the experimentally not measured features.

The energy chosen for the experiment was 200 GeV; data for positive and negative muons totalling 2×10^6 events with $Q^2 > 40$ GeV^2 (4×10^4 $Q^2 > 100$ GeV^2) have been obtained. Data have also been taken at 120 GeV to permit a check on 2 γ exchange which can also contribute to the asymmetry.

Systematic effects will finally dominate the measurement, although the large uniform acceptance of the apparatus (see fig. 12(a)) is azimuthally symmetric and this reduces the effects of relative differences in, for example, the beam directions.

Differences in beam energy are magnified by about a factor 2 in the asymmetry and a careful check is necessary. Preliminary studies involving directing the beam into the live region of the toroids give a relative difference between the two signs of $(1.3 \pm 0.35) \times 10^{-3}$ in the "mean." Differences in distributions can be avoided by choosing the beam tracks; these are measured for individual particles.

The scattered muon momentum enters the asymmetry in a similar way to the incident momentum. The magnetic fields in the toroids have been checked over many cycles using a flux measurement and are found to be reproducible and symmetric at the level of 1×10^{-4}. Differences in energy loss are checked with those tracks for which two oscillations are visible. In the reconstruction only chambers present and efficient for both signs of beam are used to avoid apparatus bias.

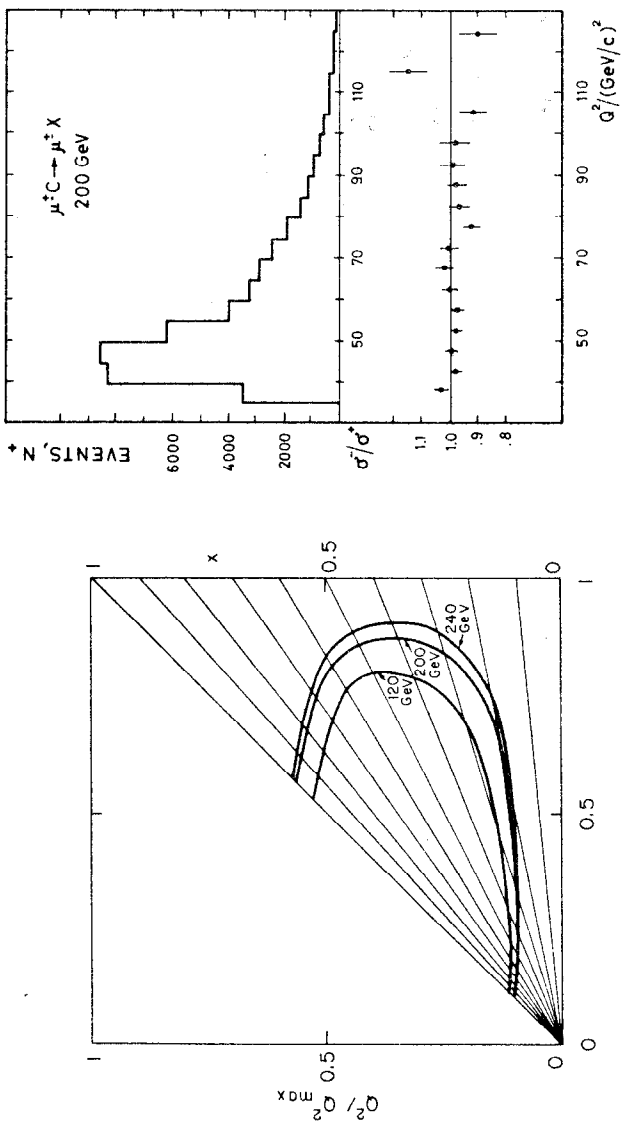

(b) Measured ratio of yields from positive and negative muons from BCDMS test run.

(a) Acceptance map for BCDMS apparatus: lines are 40% limits.

Fig. 12

Multimuon backgrounds are potential sources of asymmetry; however, they are estimated to contribute in less than 2×10^{-3} of the events presently used in the F_2 analysis. The implication is that the asymmetry will be much less than even this. Similarly, background from π and K decay is $\lesssim 10^{-4}$.

The data were taken with two signs of beam changed every few days (limited by SPS operational needs) up to June 1980. The results of a test measurement lasting $\sim$ 1 day are shown in fig. 12(b). No results of the systematic checks mentioned above were incorporated. It would seem that within about one year the weak coupling of the right-handed muon will no longer be unknown.

3. MULTI MUON PRODUCTION

Multimuon production final states have been measured by E.M.C. using the S.T.A.C. target. This permits the hadronic energy to be measured and the energy balance calculated event by event.

3.1 Dimuons

$$\mu^+ + N \rightarrow \mu^+ + \mu^\pm + \text{anything.}$$

The primary candidates for contributions to this process are π and K decay within the STAC and charmed particle decays. Charm decay is characterised by a mean missing energy of about 20 GeV.

$$E_{miss} = E_{Beam} - E_{\mu_1} - E_{\mu_2} - E_{STAC},$$

corresponding to the missing neutrino in the semi-leptonic charm decay. Such a signal has been observed by EMC [14] and has been found to fit well with the photon gluon fusion model. The basic diagram for this model is illustrated in fig. 13 (a); the underlying parameters are the scale of the strong interaction Λ, the charmed quark mass and the momentum distribution of the gluons. The satisfactory agreement can be obtained

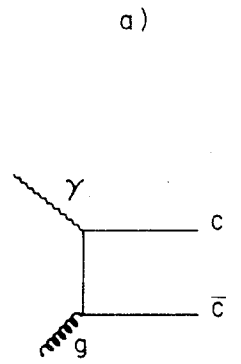

(a) Photon Gluon Fusion diagram for heavy quark-antiquark production;

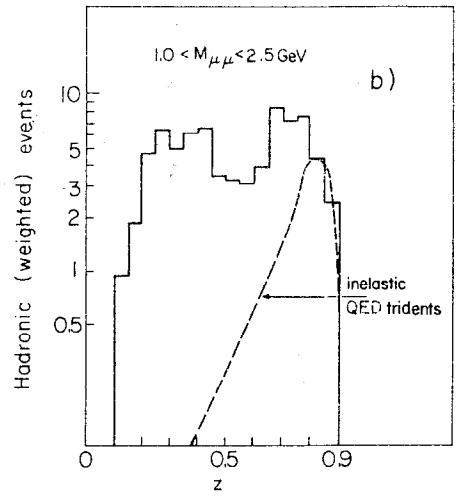

(b) $z = E_{\mu^+\mu^-}/\nu$ distribution for trimuon events dashed line is QED calculation;

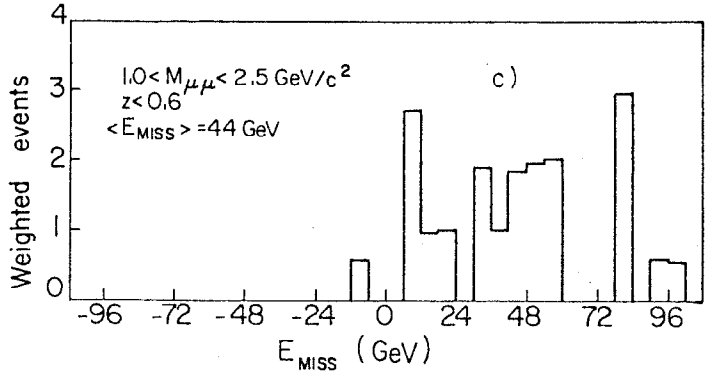

(c) Missing Energy distribution for fully measured trimuon events.

Fig. 13

without deviation from the "standard" values Λ = 0.5 GeV and M_c = 1.5 GeV for the first two and $G(\eta) = (3/\eta)(1-\eta)^5$ for the gluon distribution. The model and its application to similar data from BFP [15] is discussed in some detail by M. Strovink [16] at this conference. If used to estimate the contribution of charm to F_2 it can account for $\sim$ 30% of the low x rise with Q^2.

3.2 Tri muons

$$\mu^+ + N \rightarrow \mu^+ + \mu^+ + \mu^- + \text{anything}$$
$$E_{STAC}$$

Trimuon events have also been observed by EMC and a primary classification is made on the basis of the energy (E_{STAC}) deposited in the target.

"Elastic" events with E_{STAC} < 5 GeV can be understood on the basis of QED plus J/ψ production [17]. For the "inelastic" events an analysis of the target showers to determine whether they were hadronic or electromagnetic was performed. Above 20 GeV the separation was rather clean. It is found that with this energy cut the mass spectrum is not saturated by QED and J/ψ production. In fig. 13(b) the z distribution for events with 1.0 < $M_{\mu^+\mu^-}$ < 2.5 GeV is compared with the QED calculation; they are clearly not compatible. For those events in which the momenta of all three muons were measured the missing energy can again be calculated. A mean value of 44 GeV was obtained (see fig. 13(c)) and this constitutes strong evidence that charm production (in this case double semi-leptonic decay) is present. The kinematics of photon gluon fusion favour forward production of both charmed particles and, as shown in fig. 14, the distributions, for both the produced muon pairs and for the single negative muons, are rather well described by the model [18]. The same rather conventional set of parameters was used to calculate these curves which contain no arbitrary normalisation.

Inelastic J/ψ production [19] is clearly prominent; fig. 15(a) shows the mass distribution for the produced $\mu^+\mu^-$ pair for trimuon events with E_{STAC} > 5 GeV. The Q^2 dependence is shown in fig. 15(b) compared with the fit [17] to the elastic J/ψ production; there is no significant disagreement. The p_T^2 distribution fig. 15(c) is however much different.

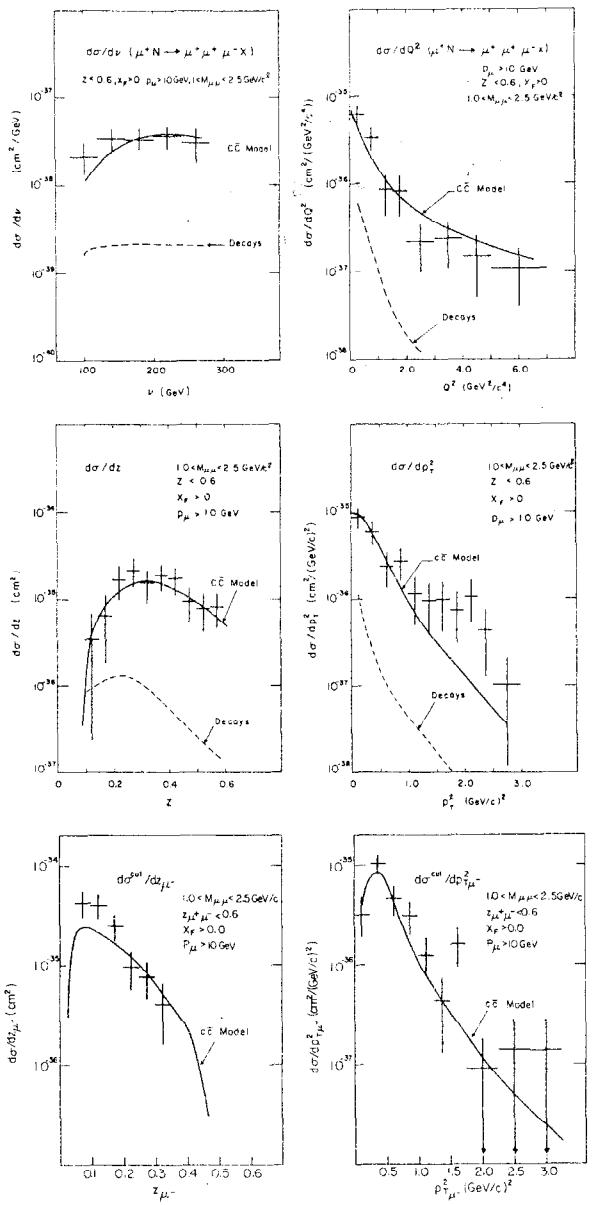

Fig. 14 Comparison of trimuon production distributions with the Photon Gluon Fusion ($c\bar{c}$) model.

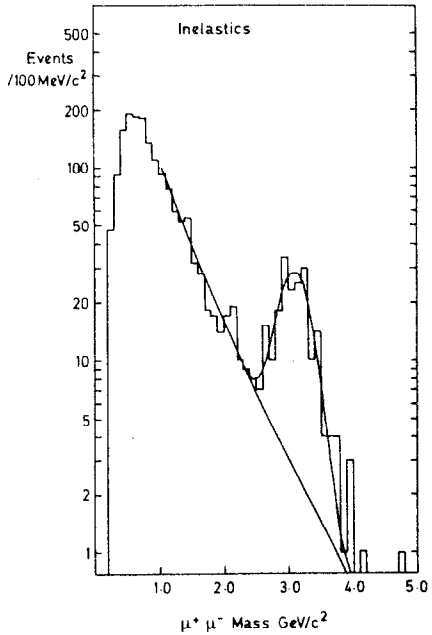

(a) Mass distribution for $\mu^+\mu^-$ pairs produced in inelastic trimuon events;

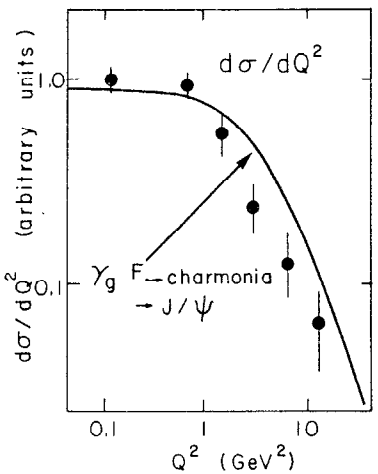

(b) Q^2 dependence for inelastic J/ψ production, the solid line is the fit to the elastic data (17);

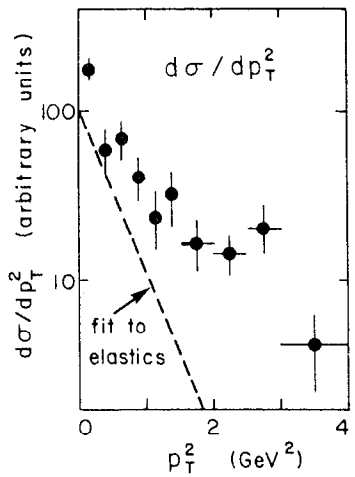

(c) P_T^2 dependence for inelastic J/ψ production, the dotted line indicates the behaviour of the elastic data (17).

Fig. 15

A low p_T^2 peak is present as for elastics but the rest of the distribution is much broader. There is also a difference in the energy dependence (fig. 16); whereas the elastics are fairly energy independent, the cross-section for inelastics continues to rise up to ν = 160 GeV.

If the production and subsequent decay of higher charmonia (ψ', χ etc.) were the major source of this "inelastic" signal such differences would not be expected. On the basis of the low p_T^2 peak and corroborative evidence from the STAC shower profiles the contribution from higher charmonia is now estimated to be much less than 50% (20). Speculation that some hard gluon emission could feed charm production from above to below open threshold [19] has now been replaced by a calculation [21] of higher order contributions to the photon gluon fusion graph which seems to reproduce the shape of the p_T^2 distribution.

Within the accuracy of the present data the photon gluon fusion model seems to come close to describing all the multimuon production which is not QED.

4. HADRONIC FINAL STATES

The open magnet configuration of the EMC apparatus allows the charged and neutral hadrons produced in the forward direction to be measured. Within the quark parton model for hadron production this covers the quark or current fragmentation region.

The results discussed here are based on ∿ 20 000 muon scatters with 280 GeV incident energy in which the muon vertex occurred in the downstream 2 m of the 6 m hydrogen target. The charged hadrons were momentum analysed in the forward spectrometer and the track selection was based on the closest distance of the track to the muon vertex. Acceptances were calculated using a cascade Monte Carlo model; the parameters of the model were varied to avoid model dependence in the results. The neutral hadrons were detected in the front electromagnetic modules of the calorimeter. Single clusters of electro-

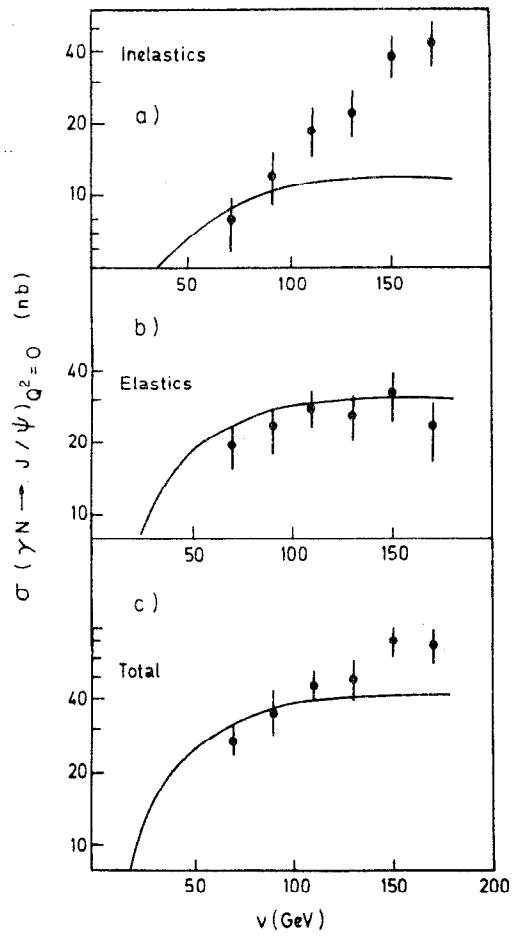

Fig. 16 Energy dependence of J/ψ production.

magnetic energy were identified using the interleaving of the sampling in two perpendicular directions. The modularity did not permit the separation of the two photons from π^0 decay. The acceptance calculation used the same model as for the charged hadrons and simulated calorimeter data were passed through the pattern recognition procedure. The results are to be identified as π^0 yields with an estimated 6% contamination from η. (This latter is dependent on the primary η/π^0 ratio which was assumed to be 0.5.)

The normalised $z = E_h/\nu$ distributions for the charged hadrons [22] are compared in fig. 17(a) with similar data from CHIO [23]. There is agreement within 20% which is the level of systematic uncertainty in the data. The dashed band in fig. 17(a) represents similar measurements from e^+e^- storage rings [24] and although the range of the e^+e^- data is limited they seem to be steeper. Comparison is made in fig. 17 between the neutral data and π^0 measurements [25,26] from much lower energy and Q^2 and there is good agreement. This implied lack of Q^2 dependence is demonstrated explicitly in fig. 18(a) where for $0.1 < x_{Bj} < 0.2$ data covering a range in Q^2 from 5 GeV^2 to 50 GeV^2 are superimposed. The quark parton model predicts that the yield of positive relative to negative hadrons should increase from low x_{Bj}, where scattering from the charge symmetry sea dominates, to high x_{Bj} where scattering from valence dominates. This difference is expected to be most prominent at high z if the fastest hadrons contain the struck quark. These two features are clearly demonstrated by the data in fig. 18(b).

From the z distributions no strong departure from quark parton model behaviour has been observed but this is not the case for the transverse momentum distributions. Transverse momenta do not occur in the pure quark parton model but are expected both from non-perturbative sources such as fragmentation and intrinsic p_T (fig. 19(a)) and from perturbative QCD corrections to the basic process (fig. 19(b)). This latter process is calculated [27] to have a linear dependence on W^2 from the phase space available for the gluon emission, while this may

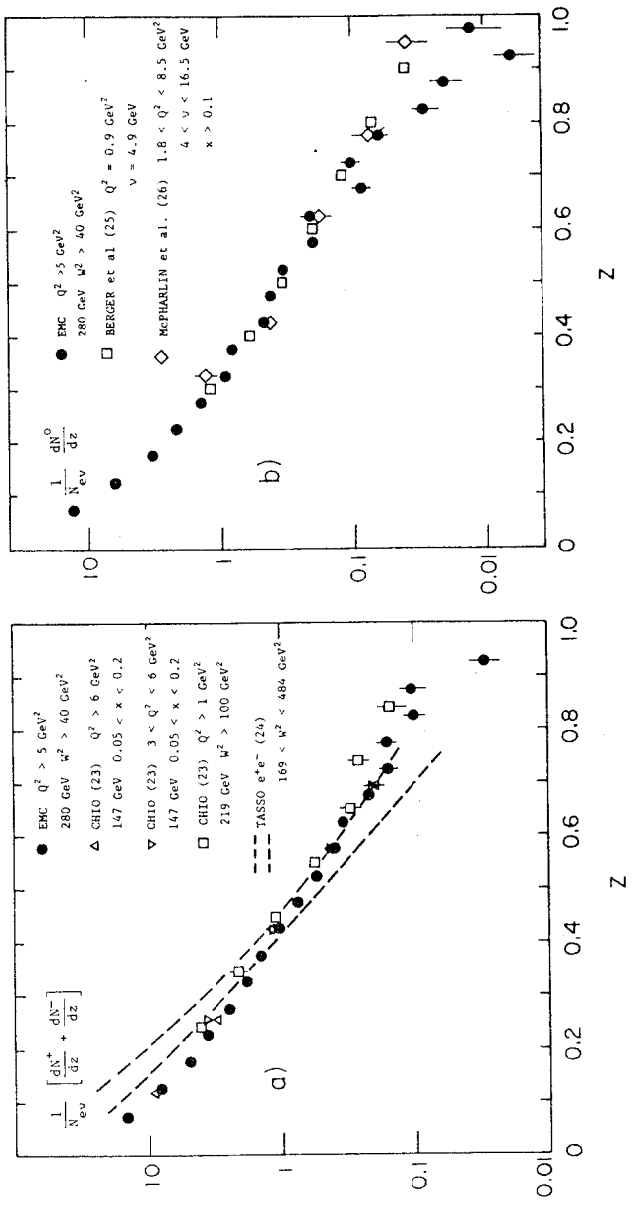

(a) Comparison of data from EMC, CHIO (23) and e^+e^- (24) on z distributions of charged hadrons;

(b) Comparison of neutral hadron measurements from EMC with low energy and Q^2 measurements of π^0 production.

Fig. 17

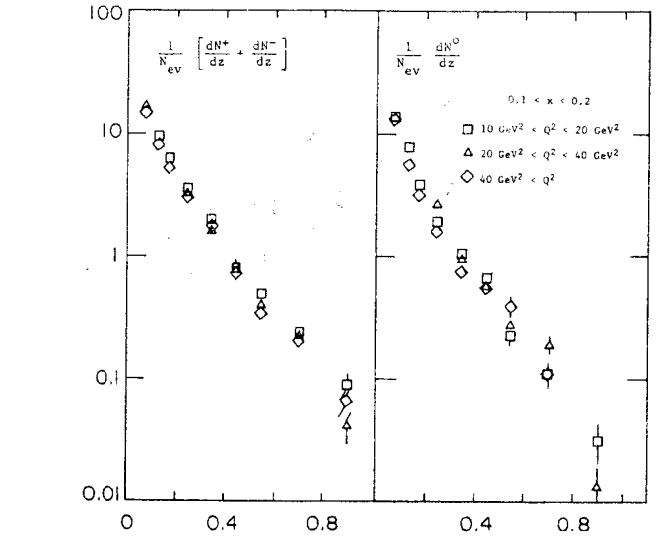

(a) Q^2 (in)dependence of z distributions for both charged and neutral hadrons at fixed x_{Bj};

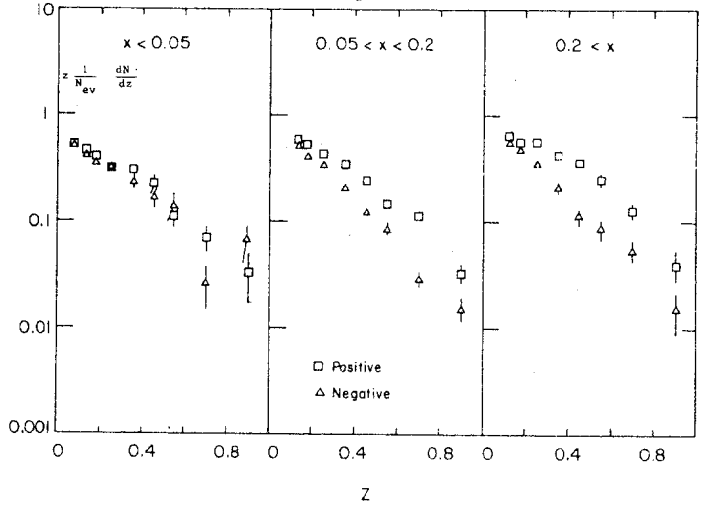

(b) x_{Bj} dependence of positive relative to negative hadrons.

Fig. 18

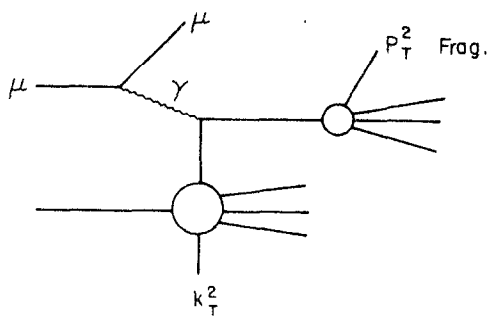

(a) Quark model diagram for hadron production;

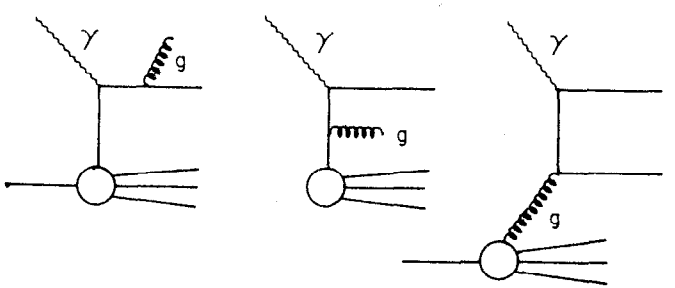

(b) Perturbative corrections to the Quark model diagram.

Fig. 19

not be the case for non-perturbative effects. A suggested description [28] for the behaviour of the mean p_T^2 of produced hadrons is

$$\langle p_T^2 \rangle = z^2 \langle k_T^2 \rangle + \langle p_T^2 \rangle_{Frag} + \langle p_T^2 \rangle_{QCD}$$

As shown in fig. 20 the data [29] in any given z range are well fitted by a constant non-perturbative part plus the calculated perturbative contribution. There is also good agreement with comparable measurements [30] from a lower energy neutrino experiment. The calculation [31] of the perturbative contribution used an effective coupling α_s with $\Lambda = 0.5$ GeV and although no fit with Λ as a free parameter has been made it is clear that the description is rather good.

The need for a z dependent non-perturbative contribution is shown in fig. 21 where the data are plotted versus z^2. Contribution from the fragmentation $p_T(\sigma = 0.35$ GeV) and the perturbative calculation do not saturate the data. At low z conclusions are difficult to make because of the complication of meson resonance production and decay. At high z the situation is clean and the data with $z^2 \geq 0.2$ have been fitted with the result $\langle k_T^2 \rangle = 0.6 \pm 0.1$ GeV^2. Whether or not this should be identified as the intrinsic quark momentum is not certain, however, such a high value certainly needs explanation.

The emerging picture of hadron production from these high energy data can be summarised by saying that to a large extent the quark parton model gives an excellent description of the data but that it needs to be supplemented both by perturbative corrections and also by large non-perturbative contributions to the p_T distributions.

I would like to aknowledge discussions with my colleagues, both BCDMS and EMC collaborations, and especially Joël Feltesse and Jörg Gayler for their reading of the manuscript.

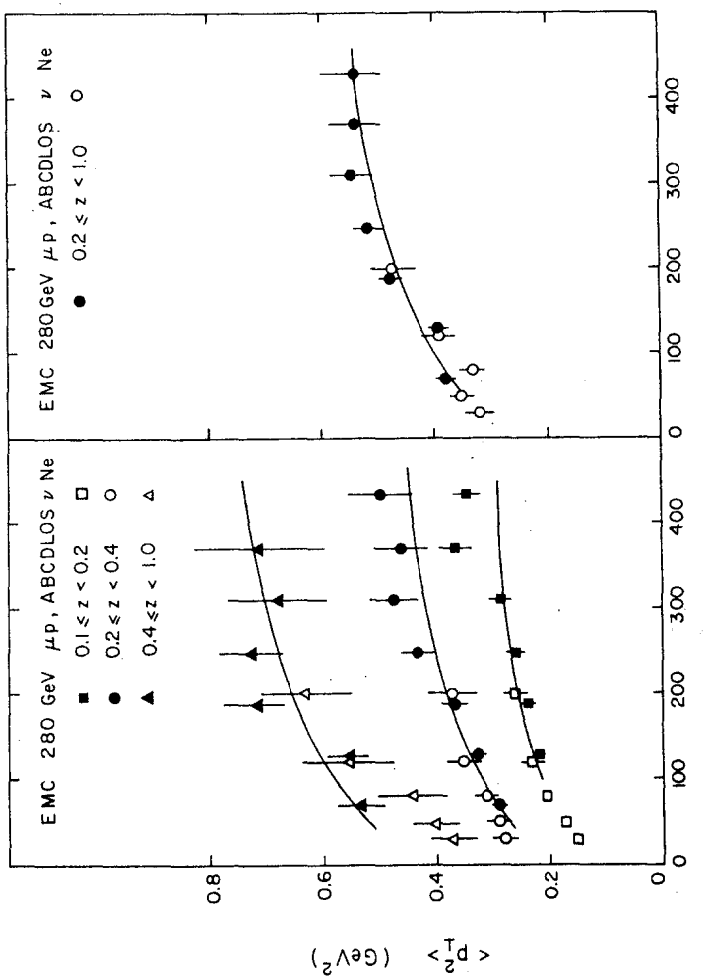

Fig. 20 W^2 dependence of $\langle p_T^2 \rangle$ for different z ranges, solid symbols EMC, open symbols BEBC data (30). Lines represent fits of a constant plus QCD calculation for each range of z.

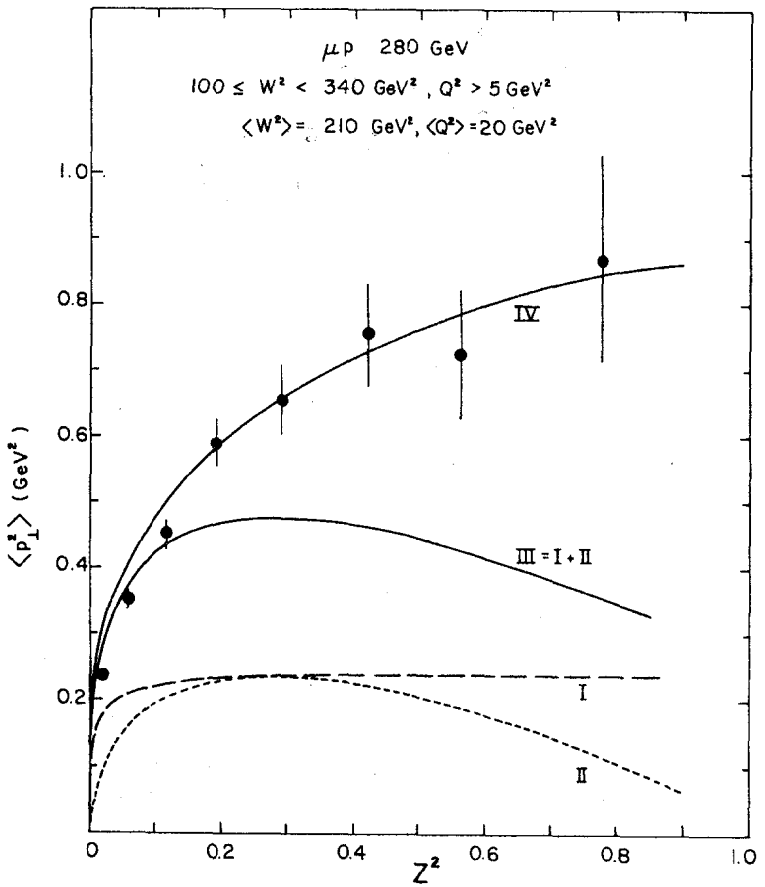

Fig. 21 z^2 dependence of $\langle p_T^2 \rangle$, curve I is the contribution from fragmentation, II the calculated perturbative QCD contribution and III is their sum, IV is a fit to $z^2 \geq 0.2$ with these elements and $\langle k_T^2 \rangle = 0.6$ GeV^2.

REFERENCES

[1] F. Sciulli, Neutrinos as Probes of Nucleons, Lectures at this School.

[2] D. Bollini et al., Deep Inelastic Muon-Nucleon Scattering at High Q^2. Contribution to the XXth Int. Conf. on High Energy Physics, Madison, July 1980.

[3] J.G.H. de Groot et al., Z. für Physik C 1 (1979) 143.

[4] EMC, J.J. Aubert et al., Measurement of the nucleon structure function F_2 by muon iron interactions at 280, 250 and 120 GeV, contribution to the XXth Int. Conf. on High Energy Physics, Madison, July 1980.

[5] EMC, J.J. Aubert et al., Measurement of the proton structure function F_2 in muon hydrogen interactions at 280 and 120 GeV, contribution to the XXth Int. Conf. on High Energy Physics, Madison, July 1980.

[6] A. Bodek et al., Phys. Rev. D20 (1979) 1471;
M.D. Mestayer, Ph.D. Thesis SLAC-214 (1978).

[7] L.F. Abbott and R.M. Barnett, SLAC-PUB-2325 (T/E)(1979), submitted to Annals of Physics;
R.M. Barnett, SLAC-PUB-2396 (T/E) 1979;
L.F. Abbott, W.B. Atwood and R.M. Barnett, SLAC-PUB-2400 (1979), submitted to Phys. Rev. D.

[8] G. Altarelli and G. Parisi, Nucl. Phys. B126 (1977) 298.

[9] A. Gonzalez-Arroyo et al., Nucl. Phys. B153 (1979) 161;
Nucl. Phys. B159 (1979) 512.

[10] EMC, J.J. Aubert et al., Scaling Violation in μN scattering and a possible interpretation, contribution to the XXth Int. Conf. on High Energy Physics, Madison, July 1980.

[11] R. Clifft and N. Doble, Proposed design of a high energy high intensity muon beam for the SPS North Experimental Area CERN/SPS 74-12 (1974).

[12] M. Klein, Muon induced weak neutral currents, Talk at the 1979 Int. School of Elementary Particle Physics, Kupari-Dubrovnik (Yugoslavia).

REFERENCES (Cont'd)

[13] H. Harari,, Quarks and Leptons, Lectures at this School.

[14] EMC, J.J. Aubert et al., Phys. Lett. 94B (1980) 96.

[15] A.R. Clarke et al., LBL-10747 (1980) submitted to Phys. Rev. Lett.;
A.R. Clarke et al., LBL-10879 (1980) submitted to Phys. Rev. Lett.

[16] M. Strovink, Virtual photoproduction of charm, Lecture at this Conference.

[17] EMC, J.J. Aubert et al., Phys. Lett. 89B (1980) 267.

[18] EMC, J.J. Aubert et al., Phys. Lett. 94B (1980) 101.

[19] EMC, J.J. Aubert et al., CERN-EP/80-84 (1980).

[20] EMC, R.P. Mount, Multimuon Production in 280 GeV μ^+ Iron Interactions. Presentation at the XXth Int. Conf. on High Energy Physics, Madison, July 1980.

[21] D.W. Duke and J.F. Owens, F.S.U.-HEP-800709 (1980).

[22] EMC, J.J. Aubert et al., CERN-EP/80-130.

[23] W.A. Loomis et al., Phys. Rev., D19 (1979) 2543;
C.S. Tao, Ph.D. Thesis, Harvard University, Cambridge Mass. 1979.

[24] R. Brandelik et al., Phys. Lett. 89B (1980) 418.

[25] C.H. Berger et al., Phys. Lett. 70B (1977) 471.

[26] T.P. McPharlin et al., Phys. Lett. 90B (1979) 479.

[27] G. Altarelli and G. Martinelli, Phys. Lett. 76B (1978) 89;
A. Mendez, Nucl. Phys. B145 (1978) 199.

[28] for example, P. Mazzanti, R. Odorico and V. Roberto, Phys. Lett. 81B (1979) 219.

[29] EMC, J.J. Aubert et al., CERN-EP/80-119 (1980), to be published in Phys. Letters.

[30] H. Deden et al., CERN-EP/80-66 (1980).

[31] P. Kroll (Wuppertal University) Private communications.

VIRTUAL PHOTOPRODUCTION OF HIDDEN AND OPEN CHARM

A.R. Clark, K.J. Johnson, L.T. Kerth, S.C. Loken, T.W. Markiewicz, P.D. Meyers, W.H. Smith, M. Strovink, and W.A. Wenzel

Physics Department and Lawrence Berkeley Laboratory
University of California, Berkeley, California 97420

R.P. Johnson, C. Moore, M. Mugge, and R.E. Shafer

Fermi National Accelerator Laboratory
Batavia, Illinois 60510

G.D. Gollin[a], F.C. Shoemaker, and P. Surko[b]

Joseph Henry Laboratories, Princeton University
Princeton, New Jersey 08544

presented by M. Strovink

A. Introduction

I shall begin by describing the Berkeley-Fermilab-Princeton multimuon spectrometer and the techniques used to analyze the data which it has collected. Notwithstanding the title of this talk, the first physics topic in fact will be relevant to weak interactions, the subject of this conference. Drawing from results now being prepared for publication[1], I shall present limits on the cross section with which possible heavy neutral or doubly charged muons are produced via right-handed charged currents. Turning to heavy-quark muoproduction, I shall outline next the relevant phenomenology, emphasizing the predictions of the vector dominance (VMD) and photon-gluon-fusion (γGF) models. The first heavy-quark data to be discussed will be the dimuon-mass spectrum observed in trimuon final states, which provides our published[2] limit on muoproduction of the T family. The bulk of the quarkonium results is devoted to J/ψ(3100) muoproduction. After briefly reviewing our original ψ results[3], I will focus on a combined analysis of the polarization and Q^2-dependence of elastically produced ψ's. These data have recently been submitted for publication[4]. The balance of my talk will be devoted to the muoproduction of open charm, observed in events with two muons in the final state. We have published[5] the cross-sections for diffractive charm muoproduction and photoproduction, and also the corresponding charm structure function and its substantial contribution to inclusive scale-noninvariance[6]. The conference organizers have asked that inclusive structure-function results not be emphasized here. Preliminary inclusive data from this experiment were reported at the 1979 Lepton-Photon Symposium[7].

Before proceeding, it is fitting to note that the Berkeley-Fermilab-Princeton experiment is to an unusual extent the product of graduate student research. The heavy-muon and T production limits, ψ results, and open-charm data presented here form part of the Ph.D. theses, respectively, of Wesley Smith, Thomas Markiewicz, and George Gollin.

B. Experimental Method

The muon spectrometer achieved the desired integrated luminosity ($\gtrsim 10^6$ nb^{-1}) by using a massive target ($\sim$5 kg/cm^2). High acceptance over the full target length made necessary a spectrometer magnet integral with the target. Its steel plates functioned also as hadron absorbers for calorimetry and muon identification. Full acceptance was maintained in the forward direction, with no blind "beam hole." Inability to find all the final state muons otherwise would have altered drastically the interpretation of many events. A dipole field configuration, requiring only one pair of coils for the full magnet, was most compatible with high forward acceptance. Proportional and drift chambers were able to withstand the full beam flux at Fermilab (typically 2×10^6 muons per 1-sec spill) without deadening in the beam area.

Construction of the apparatus depicted in Fig. 1 was completed in 1977. It consisted of 18 25-ton modules each containing 5 10-cm thick steel plates, 5 calorimeter scintillators (omitted in modules 16-18), and a pair of proportional (PC) and drift chambers (DC)[8]. Banks of 12 trigger scintillators (S_1-S_{12}) were located in even modules 4-18. The fiducial volume, 1.8×1 m^2 in area, extended 16 m in the beam direction. Within the central 1.4×1 m^2 area of each magnet plate, the 19.7 kgauss field was uniform to 3% and mapped to 0.2%. Located upstream of module 1 were one additional PC and DC, 63 beam scintillators, 8 beam PC's and 94 scintillators sensitive to accidental beam and halo muons.

Beam muons were momentum-analyzed by systems of proportional chambers and scintillator hodoscopes interspersed between magnets producing two separate beam deflections. Pulse heights from calorimeter counters within the spectrometer provided a tentative longitudinal ver-

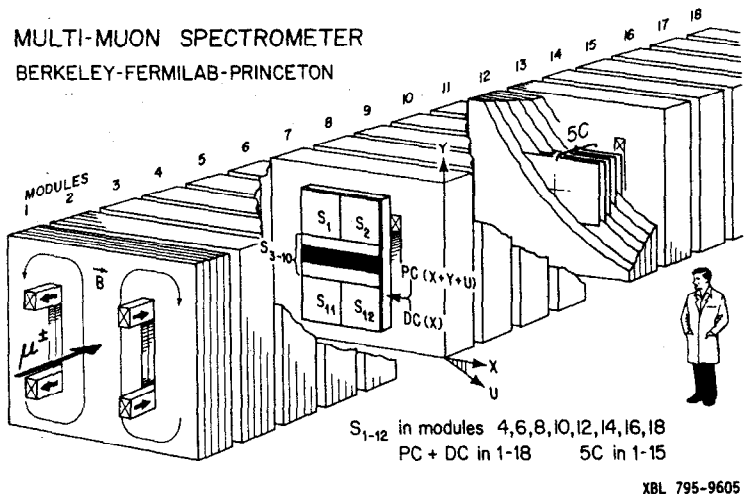

FIG. 1. Sketch of the multimuon spectrometer. The spectrometer magnet, serving also as a target and hadron absorber, reaches 19.7 kG within a $1.8\times1\times16$-m^3 fiducial volume. Over the central $1\times1\times16$ m^3, the magnetic field is uniform to 3% and mapped to 0.2%. Eighteen pairs of proportional (PC) and drift chambers (DC), fully sensitive over 1.8×1 m^2, determine the muon momenta typically to 8%. The PC's register coordinates at 30^o (u) and 90^o (y) to the bend direction (x) by means of 0.5-cm-wide cathode strips. Banks of trigger scintillators (S_1-S_{12}) occupy eight of the eighteen magnet modules. Interleaved with the 10-cm-thick magnet plates in modules 1-15 are 75 calorimeter scintillators resolving hadron energy E_{had} with rms uncertainty $1.5E_{had}^{\frac{1}{2}}$ GeV. Not shown upstream of module 1 are 1 PC and DC, 63 beam scintillators, 8 beam PC's, and 94 scintillators sensitive to accidental beam and halo muons.

tex position. The beam track then was traced forward to this vertex using the PC and DC hits. Outgoing tracks were recognized initially at their downstream end. Hits were added extending the tracks upstream to the vertex, making adequate allowance for Coulomb scattering and momentum uncertainty. In order not to interfere with rejection of halo tracks or later use of outgoing tracks to pinpoint the vertex, the transverse vertex position was not allowed to influence this upstream projection. At least 4 PC hits in two views and 3 hits in the third view were required for each accepted track. The small electromagnetic showers found along high energy muon tracks in iron, due mainly to direct production of electron pairs, contributed extra hits in the wire chambers which were not completely rejected at this stage. After the full track was identified, it was possible to apply a momentum-fitting algorithm capable of solving for the Coulomb-scattering angle in each magnet module, yielding a rigorous χ^2 for the track. By iteration, this algorithm identified and suppressed the false extra hits.

The beam and secondary tracks next were examined for consistency with a common vertex. The vertex position was moved by iteration in 3 dimensions to minimize the overall χ^2 while including all associated tracks. After the vertex was fixed, the coordinates and momentum of each track were redetermined, subject to the condition that it intersect the vertex point.

For analysis of 3μ final states the events were subjected to a 1-constraint fit demanding equality between the beam energy at the interaction point and the sum of muon and hadron shower energies in the final state. Using error matrices produced by the fits to individual tracks, the constraint perturbed all components of each track momentum. The resulting momentum resolution is 7%-12% (typically 8%) per track. At the ψ mass, the dimuon mass resolution is 9%. The uncertainty in Q^2 typically is 10%, but is bounded below by ~0.15 $(GeV/c)^2$ because of track

angle uncertainty.

The acceptance and resolution of the spectrometer were modeled by a complete Monte Carlo simulation. Coordinates of randomly sampled beam muons were used to represent the beam. Simulated muons underwent single and multiple Coulomb scattering, bremsstrahlung, and other energy-loss straggling in each magnet plate and were bent by the precisely mapped field. Simulated interactions occurred between muons and nucleons in non-degenerate Fermi motion, or coherently between muons and Fe nuclei. At low momentum transfer the effects of nuclear shadowing were taken into account. Coherent and elastic processes were attenuated by the appropriate form factors even for forward scattering (at $|t|_{min}$). Detector resolutions and efficiencies were included throughout. Monte Carlo events were output in the same magnetic tape format as raw data, and were reconstructed, momentum-fit and histogrammed by the same programs.

Data were accumulated during the first half of 1978 using $\sim 4\times10^{11}$ (gated) 209 GeV muons, of which approximately 90% were μ^+. Results presented here are based on 75% of this sample, except for the open-charm results, which represent 50% of the data.

C. Limits on Muoproduction of Heavy Neutral or Doubly Charged Muons

Considerable speculation has been devoted to the possible existence of heavy neutral gauge leptons. Variations of the standard SU(2)×U(1) model[9] have been proposed in which the known lepton doublets are coupled[10] to an M^0 or in which both right- and left-handed doublets exist and include[11] M^0's. Grand unification schemes frequently introduce M^0's, e.g., those[12] which embed $SU(2)_L\times U(1)_R$ in $SU(3)_L\times SU(3)_R$. In addition to the M^0, heavy doubly charged gauge muons (M^{++}) have been proposed in the context of an extended SU(2)×U(1) theory in doublets with the known singly charged leptons[11].

There exist few experimental limits on the masses of heavy muons. Studies of π and K decay[13] exclude the M^0 mass from the range $m_\mu<m_{M^0}<m_K$. Ref. 14 sets a 90%-confidence lower limit of 1.8 GeV/c^2 on the mass of the heavy muon M^-. Although there are 90%-confidence lower limits of[15] 2.4 GeV/c^2 and[16] 8.4 GeV/c^2 on the M^+ mass, the strongest experimental constraint on the M^0 mass is the limit[17] $m_{M^0}>1$ GeV/c^2.

Possible evidence for M^0 production has arisen from three experiments. Two μ^-e^+ events produced by $\nu_\mu N$ interactions below 30 GeV in the SKAT bubble chamber were attributed[18] to the production of an M^0 with $1.4<m_{M^0}<2.4$ GeV/c^2. In a cosmic ray experiment[19] deep underground, five events were analyzed as evidence for a heavy lepton with mass 2-4 GeV/c^2. Originally the observation of neutrino-induced trimuon events at Fermilab[20] prompted their interpretation as examples of M^0 production. Further experiments and analyses have failed to develop corroborating evidence for the interpretation of these phenomena as examples of M^0 production.

Using the simplest parton model with single W^+ exchange, invoking the Callan-Gross relation and considering only $\Delta S=\Delta C=0$ processes and isoscalar tragets,

$$\frac{d^2\sigma(\mu^+(L.H.)N\to\bar{M}^0X)}{dvdy}=\left(\frac{g_R}{g}\right)^2\frac{G^2Em_NF_2(x)}{\pi y}$$

where $v=Q^2/s$, $(1-y)$ is the fraction of the laboratory muon energy retained by the $\bar{M}^0$, and g_R/g is the ratio of possible right-handed to left-handed current amplitudes. The differential cross section is independent of $\bar{M}^0$ mass, except for kinematic restriction of the allowed area of the Q^2-ν plane. The differential decay rate for $M\to\mu^+\mu^-\bar{\nu}_\mu$, where the $\bar{M}^0$ is coupled to the μ^+ by a (V+A) current, is

$$\frac{d^5\sigma(\bar{M}^0\to\mu^+\mu^-\bar{\nu}_\mu)}{dx_-dx_\nu d\phi_\nu d\cos\theta_\nu d\phi_-}\propto x_\nu(1-x_\nu)(1-P\cos\theta_\nu).$$

Here $x_-(x_\nu)$ is $2p_{c.m.}/m_{M^0}$ for the $\mu^-(\bar{\nu}_\mu)$, θ_ν and ϕ_ν define the c.m. $\bar{\nu}_\mu$ direction relative to the $\bar{M}^0$ direction, θ_- and ϕ_- define the c.m. μ^-

direction relative to the $\bar{\nu}_\mu$ direction, and P is the $\bar{M}^0$ polarization along its direction of motion. Since the $\bar{M}^0$ carries the left-handed polarization of the incident μ^+, the two muons are emitted preferentially forward and together carry an average of 80% of the $\bar{M}^0$ energy in the laboratory.

Monte Carlo events were generated according to the above formulae at lepton masses of 1,2,3,6,9,12 and 14 GeV/c^2, and were binned[21] in Q^2 and in $p_\perp$, the daughter muon momentum transverse to $\vec{Q}$. Kinematic cuts were chosen individually for each heavy lepton type and mass in order to exclude data while retaining Monte Carlo M events. An empirical contour then was drawn for each Q^2-$p_\perp$ plot in order to contain all the data events on the low $p_\perp$, low Q^2 side. The Monte Carlo event populations on the high $p_\perp$, high Q^2 side of the contours then provide the cross section limits.

Figure 2 displays the mass-dependent limits[1] on $\bar{M}^0$ and M^{++} production. Also indicated are the expected products of cross section and branching ratio for the production of $\bar{M}^0$'s and M^{++}'s, where the $\mu\mu\nu$ branching ratio is assumed to be 0.1 and 0.2 for $\bar{M}^0$ and M^{++}, respectively. To 90% confidence the data exclude the production of an $\bar{M}^0$ and M^{++} coupled with Fermi strength to a right-handed current in the mass range $1<m_M<9$ GeV/c^2. Without a special mechanism to suppress pair production, doubly-charged leptons in this mass range would have been detected at PETRA. No comparable limits on M^0 production are available.

D. Phenomenology of Heavy-Quark Production by Muons

The theoretical framework for discussion of charm leptoproduction is evolving rapidly. In 1976 Sivers, Townsend and West[22] obtained a lower bound on the total ψN cross-section, requiring measurement of the ratio of cross-sections for forward ψ and total charm photoproduction. This bound depends only on unitarity and OZI[23] rules. Adding traditional vector-meson dominance (VMD) assumptions makes the ratio of

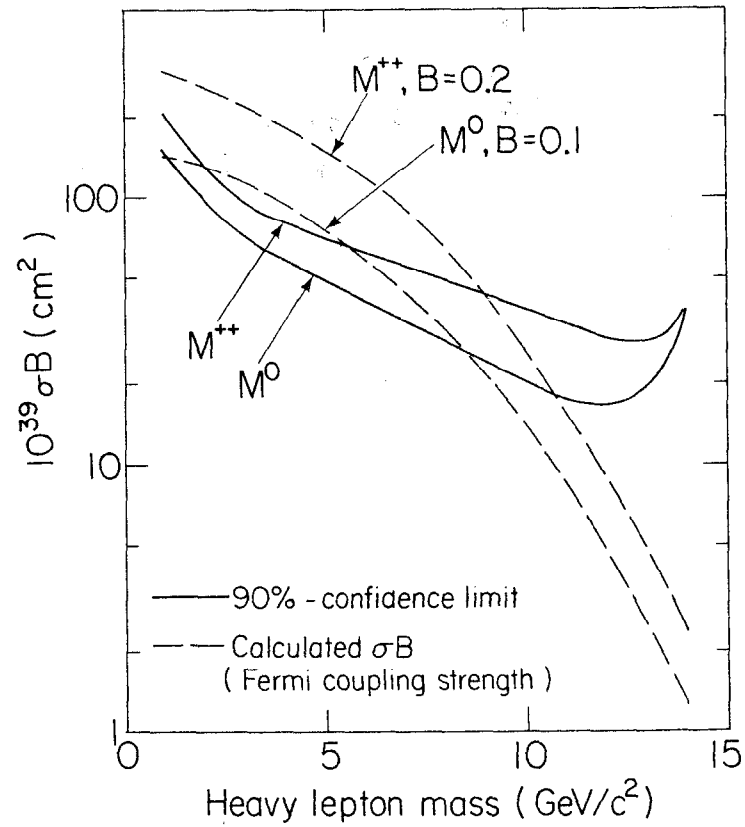

XBL 809-2016

FIG. 2. Experimental upper limits and calculated cross section-branching ratio products σB for heavy-muon (M^0 and M^{++}) production by 209-GeV muons, plotted vs. heavy muon mass. The calculation assumes $B(M\to\mu\mu\nu)$=0.1 (M^0) or 0.2 (M^{++}), and right-handed coupling of μ^+ to $\bar{M}^0$ with Fermi strength. With these assumptions, to 90% confidence the data rule out the existence of M^0 or M^{++} with mass between 1 and 9 GeV/c^2.

elastic to total ψN cross-sections nearly equal to the ratio of elastic ψ to total charm photoproduction. This ratio is evaluated in Ref. 22 as $(0.013\pm0.004)/\lambda$, where $\lambda\approx0.7$ is an off-shell correction. VMD connects charm photoproduction to muoproduction via a $(1+Q^2/m_\psi{}^2)^{-2}$ ψ propagator. The original data[24] on charm muoproduction were analyzed using a "photon dissociation" model of Bletzacker and Nieh (BN)[25].

With the advent of quantum chromodynamics, recent activity has centered on the photon-gluon-fusion (γGF) model[26], to which the right-hand graph in Fig. 3 refers. This is a Bethe-Heitler diagram for charmed-quark pair production with the nuclear photon replaced by a gluon. Not shown are the additional (presumably) soft gluon exchanges needed to conserve color. Comparison with the graph at left emphasizes the close connection between photon-gluon-fusion and the charmed sea. The large mass m_c associated with the internal quark line makes the gluon-exchange diagram finite and possibly the leading contributor to the charmed sea. Specific use of that mechanism makes it possible to allow sensibly for threshold effects due to m_c, and to predict the experimentally important correlation between the momenta of the two charmed quarks. In particular, the γGF model unifies the description of closed and open charm production via the quark pair mass $m_{c\bar{c}}$: charmonium production is taken to be dual to $c\bar{c}$ production with $2m_c<m_{c\bar{c}}<2m_D$, while open-charm production has $m_{c\bar{c}}>2m_D$. This makes the γGF charmonium calculations much more sensitive to m_c than are the open-charm calculations. Typically, one assumes $m_c=1.5$ GeV/c^2 and $\alpha_s=1.5/\ell n(m^2_{c\bar{c}}/\Lambda^2)$ with $\Lambda=0.5$ GeV/c^2. The distribution in gluon momentum fraction x is usually taken to be $3(1-x)^5/x$, with the exponent set by counting-rule arguments[27] and the coefficient by the integral over Bjorken $x_B=Q^2/2m_p\nu$ of the measured inelastic structure function $F_2(x_B,Q^2)$. The fraction of charmonia realized as the ψ is perhaps best regarded as a fit parameter[28] with the value 1/6. With these choices,

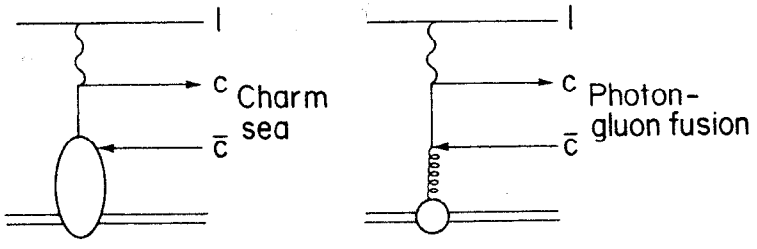

XBL 809-2015

FIG. 3. Illustration of the similarity between the "parton" picture in which the virtual photon is absorbed by a quark in the charmed sea, and the "photon-gluon-fusion" mechanism for pair production of heavy quarks. The latter process can be viewed as a prescription for generating the charmed sea, which predicts as well the correlation between $c(x)$ and $\bar{c}(x)$.

at 209 GeV the total cross section for (presumably primarily elastic) ψ muoproduction is 0.47 nb, and for open $c\bar{c}$ muoproduction is 5.0 nb. A similar calculation with bottom quarks of mass 4.7 GeV/c^2 and charge 1/3 gives 0.28 pb for T muoproduction at 275 GeV, or 0.13 pb at 209 GeV.

E. Limit on T Muoproduction

Figure 4 displays the spectrum in dimuon mass $M_{\mu^+\mu^-}$ from this experiment[2]. Events below 5 GeV/c^2 in $M_{\mu^+\mu^-}$ were reconstructed and momentum fit as previously described in Ref. 3. Above 5 GeV/c^2, the analysis of all events was checked by a hand reconstruction which was blind to the invariant mass. At all masses the assignment of beam-sign secondary muons either to the scattered muon or to the produced muon pair is the critical decision in the analysis. Incorrect pairing of muons from ψ or muon trident production can cause events which properly belong in the low-mass region to be misinterpreted as having a higher mass. Our muon pairing algorithm was selected primarily to minimize this problem. The scattered muon is chosen to be the one with the smaller value of the square of its scattering angle divided by its scattered energy. The alternative choice for the scattered muon would produce more than a one-order-of-magnitude exaggeration of the high-mass continuum near the T, as shown by the "mispaired" histogram segment in Fig. 4.

Despite the care exercised in muon pairing, Monte Carlo studies show that there remains a significant contribution in the region $4.7<M_{\mu^+\mu^-}<8.4$ GeV/c^2 from incorrectly analyzed lower-mass events. Allowance for these effects is most reliably made by use of an empirical fit to the mass continuum. The extrapolated continuum contains 1.8±1.0 background events in the T region $8.4<M_{\mu^+\mu^-}<11.1$ GeV/c^2, which in fact includes two observed events. With 90% confidence, there are fewer than 3.8 events above the extrapolated background.

The simulated T mass resolution and detection efficiency are 9%

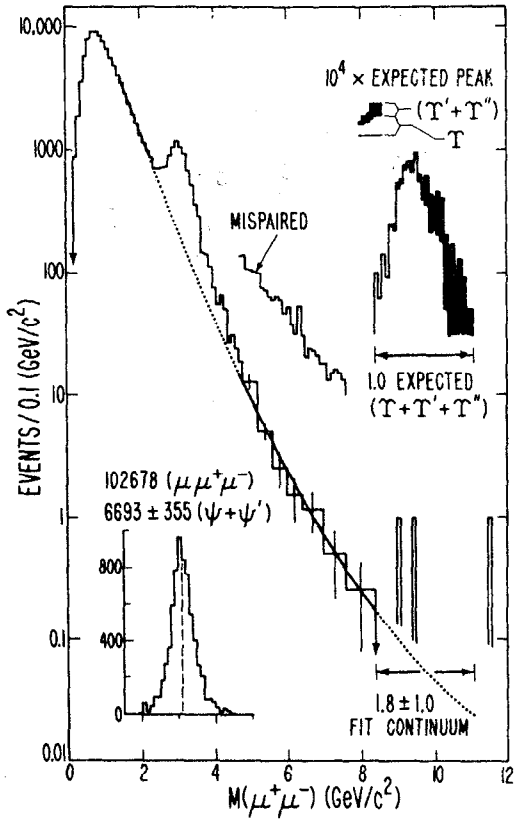

FIG. 4. Spectrum of 102 678 dimuon masses from 75% of the trimuon data. The background is fit by $\exp(a+bM+cM^2)$ in the regions of the solid curve with a χ^2 of 13.7 for 14 degrees of freedom, and is extrapolated along the dotted curve. The "mispaired" histogram segment illustrates the appearance of the mass spectrum if the alternative muon-pairing choice is made. The background-subtracted ψ peak is shown in the lower corner; the expected peak from $10^4\times$ the Monte-Carlo simulated T, T', and T'' sample is shown in the upper corner, with the contribution from T' and T'' in black. The extrapolated continuum contains 1.8±1.0 background events in the T region $8.4<M_{\mu^+\mu^-}<11.1$ GeV/c^2, which in fact includes two observed events. The additional event at 11.5 GeV/c^2 is interpreted as continuum background with 65% probability, or as part of the peak corresponding to known T states with 1% probability. With 90% confidence, there are fewer than 3.8 events above the continuum.

(rms) and 22%, respectively, and the simulated T cross section is normalized to the γGF value described above. The reconstructed peak corresponding to $10^4\times$ the expected signal is shown in Fig. 4; 1.0 events from all T states are expected in the data. Our 3.8-event limit, integrated luminosity, and detection efficiency combine to set the 90%-confidence limit $\sigma(\mu N\to\mu TX)B(T\to\mu^+\mu^-)<22\times10^{-39}$ cm^2. With $B(T\to\mu^+\mu^-)=(3.1\pm0.9)\%$[29], we obtain the 90%-confidence cross-section limit $\sigma(\mu N\to\mu TX)<0.79\times10^{-36}$ cm^2, including the error in the branching ratio. This limit lies above published predictions which use either the vector-meson dominance[30,31] or the γGF[32] models. Ignoring any γGF model uncertainty, this result rules out the choice $|q_b|=2/3$ with 85% confidence. With 67% confidence, the data disfavor the existence of similar bound states of a second charge 1/3 quark in the T mass region.

F. Original ψ-Muoproduction Results

The analysis in our early ψ publication[3] found the elastic data to be in agreement with a t-dependence of the form

$$d\sigma/dt(\gamma Fe\to\psi X)=G(t)\,d\sigma/dt(\gamma N\to\psi N)(t=0),$$

$$G(t)=A_e^{\,2}\exp(\alpha t)+A_e[(1-\varepsilon\delta)\exp(\beta t)+\varepsilon\delta\exp(\delta t)],$$

with nuclear shadowing factor $A_e=0.9$, coherent slope $\alpha=150$ (GeV/c)$^{-2}$, incoherent slopes $\beta(\delta)=3(1)$(GeV/c)$^{-2}$, and $\varepsilon=1/8$. Very recent fits now being finalized for publication have determined from the data alone a coherent fraction and average incoherent slope which are in close agreement with the above. All ψ results which I shall mention are corrected to a free-nucleon target.

In the initial publication[3], we observed a Q^2-dependence roughly consistent with ψ dominance ($\Lambda=2.7\pm0.5$ GeV/c^2). The observed ν-dependence of the effective cross section was in disagreement with the the available γGF prediction[33]. Subsequently, Weiler[34] and Barger, Keung and Phillips[28] obtained much better agreement with the data by parameterizing the gluon distribution as $C(1-x)^n/x$ at gluon four-momenta-squared of order m_ψ^2, rather than at smaller values. They fit $n=5.6^{+0.8}_{-1.2}$, and $n=4.6$, respectively; the latter authors found the observed Q^2-dependence to be consistent with $m_c=1.5$ GeV/c^2. At present, we are preparing for publication final combined fits to n and m_c. These fits favor significantly smaller m_c and larger n than mentioned above; I urge caution in use of the results of Refs. 34 and 28.

G. Polarization and Q^2-Dependence of Elastic ψ Muoproduction

Recently, we have measured[4] the polarization of muoproduced J/ψ(3100), analyzed by the decay $\psi\to\mu^+\mu^-$. These are the first data on the polarization of any charmonium state produced by real or virtual photon-nucleon collisions. Measurement of the ψ polarization is an essential component of the study of ψ-leptoproduction mechanisms. If ψ-N elastic scattering is helicity-conserving, the polarization of elastically leptoproduced ψ's in the vector-meson-dominance (VMD) picture[35] is simply related to that of the exchanged photon. In this case, the data measure R, the ratio σ_L/σ_T of ψ production cross sections by longitudinally and transversely polarized virtual photons (γ_L and γ_T). Since R must vanish at $Q^2=0$, it is a function of Q^2 which must be incorporated in any complete description of the Q^2-dependence of ψ leptoproduction.

Some aspects of the apparatus and analysis have been described briefly in sections B and F. For 3μ final states, the trigger demanded ≥3 hits in each of 3 consecutive trigger scintillator banks (Fig. 1). The trigger efficiency was uniform near the ψ mass, with a threshold below ∼1 GeV. A typical mass spectrum of $\mu^+\mu^-$ pairs already has been exhibited in Fig. 4. The analysis discussed in this section used a different muon pairing algorithm, which usually chose the unpaired muon to be the more energetic. Whenever the two like-sign muons differed by more than a factor of 2 in energy, the unpaired muon was chosen to make the smaller laboratory angle with the beam track. This pairing

algorithm retained 92% of the Monte Carlo ψ's in the mass peak, dispersing the remainder in a broad spectrum between 0.7 and 6 GeV, without producing important distortions in distributions of other variables.

The angular distributions of the decay products of lower-mass vector mesons[36] have been shown to be consistent with s-channel helicity conservation (SCHC) and natural parity exchange (NPE). With these assumptions, the distribution of dimuons from ψ decay is[37]

$$W(\eta,R;\theta,\phi)=[3/16\pi(1+\varepsilon R)]\{1+\cos^2\theta+\varepsilon(2R-\eta\cos 2\phi)\sin^2\theta+F\sin 2\theta\}.$$

Here θ is the polar angle of the like-sign daughter muon in the ψ rest frame, with $\theta=\pi$ in the direction of target recoil. The azimuthal "polarization angle" in this "helicity frame" is $\phi=\cos^{-1}(\hat{n}_d\cdot\hat{n}_p)-\cos^{-1}(\hat{n}_p\cdot\hat{n}_s)$, where $\hat{n}_s$, $\hat{n}_p$, and $\hat{n}_d$ are the unit normals to the incident muon scattering, ψ photoproduction, and ψ decay planes, respectively. We use ε to denote the ratio of γ_L to γ_T fluxes, and introduce the factor η to monitor the size of the $\cos 2\phi$ term: $\eta=1$ if SCHC and NPE are exactly obeyed. The function F, arising from the single spin flip elements of the density matrix, produces effects too small to be observed in these data.

To avoid statistical problems with low bin populations we have folded θ and ϕ into one quadrant, eliminating any sensitivity of W to F. The data were divided into a 4×5×3 grid in Q^2, $|\cos\theta|$, and $\phi_F=\frac{1}{2}\cos^{-1}|\cos 2\phi|$; dimuon-mass-continuum subtractions were performed in each of the 60 bins to obtain the acceptance-corrected ψ yields displayed in Table 1. Using the simulated average true values of Q^2, ε, $\cos^2\theta$, and $\cos 2\phi$ for each bin, these yields were fit to the product of $W(\eta,R)$ and the propagator $P(\Lambda)\equiv(1+Q^2/\Lambda^2)^{-2}$. Thereby, allowance was made for the possibility that the decay angular distribution is a function of Q^2 through the Q^2-dependence of R, e.g. $R\propto Q^2/m_\psi^2$ as suggested[35] by VMD. Since the experimental acceptance is not uniform in $\cos\theta$, such a dependence could have biased our measurement of Λ if

TABLE 1. Effective cross section, differential in $\cos\theta$ and ϕ, for the reaction $\gamma_V Fe\to\psi X$ (energy(X)<4.5 GeV), in arbitrary units. Data and statistical errors are given in 60 bins, defined by average Q^2 (top row), average $\cos^2\theta$ (left column), and one of three ϕ bins (second-left column). The average $\cos 2\phi$ in each ϕ bin is given vs. $\langle Q^2\rangle$ in the bottom three rows; values of average ε are in the right column. At lowest Q^2, average $\cos 2\phi$ in ϕ bin 1 (2) grows by 0.32 (0.23) as $\cos^2\theta$ rises from 0.02 to 0.54. The variation of average $\cos 2\phi$ with $\cos^2\theta$ is much weaker in other bins, and negligible at highest Q^2.

$\langle Q^2\rangle$ (GeV/c)^2		0.10	0.53	1.60	6.34	
$\overline{\cos^2\theta}$	ϕ bin	$d^2\sigma$(eff)/dϕd$\cos\theta$ (arbitrary units)				$\langle\varepsilon\rangle$
0.02	1	0.52(07)	0.37(09)	0.30(10)	0.05(07)	0.82
	2	0.55(07)	0.61(11)	0.36(11)	0.10(05)	
	3	0.59(06)	0.64(13)	0.44(09)	0.35(11)	
0.06	1	0.51(06)	0.24(07)	0.36(13)	0.05(04)	0.81
	2	0.61(07)	0.68(13)	0.35(10)	0.27(10)	
	3	0.50(06)	0.76(14)	0.54(11)	0.22(06)	
0.16	1	0.54(07)	0.25(11)	0.22(10)	0.04(05)	0.80
	2	0.64(08)	0.52(12)	0.36(11)	0.09(04)	
	3	0.52(07)	0.56(11)	0.49(11)	0.11(05)	
0.32	1	0.58(08)	0.32(12)	0.36(13)	0.04(06)	0.76
	2	0.46(08)	0.47(16)	0.27(09)	0.12(07)	
	3	0.62(09)	0.66(14)	0.39(10)	0.11(06)	
0.54	1	0.55(28)	0.91(34)	0.31(25)	0.12(10)	0.65
	2	0.67(20)	0.15(28)	0.48(22)	0.05(10)	
	3	1.09(29)	1.21(48)	0.35(28)	0.12(10)	
$\overline{\cos 2\phi}$	1	-0.09	0.54	0.73	0.80	
	2	-0.26	-0.11	-0.07	-0.03	
	3	-0.46	-0.72	-0.74	-0.81	

XBL 809-11762

the data had been summed over all angles.

The details of the fits are presented in Table 2. Three-parameter fits to η, R, and Λ are made both with $R \propto Q^2$ (fits 1 and 6) and with R=constant over the Q^2 range (fit 2). The parameter Λ describes the Q^2-dependence of the effective sum $\sigma_{eff} = \sigma_T + \varepsilon\sigma_L$ of γ_T and γ_L cross sections, or, in the case of fit 6, only of σ_T. An additional complication is the possible Q^2-dependence of any nuclear shadowing in the Fe target. We have used data which recently were summarized[38] for A=200, scaled the data to A=56, and fit a universal curve in $x' \equiv Q^2/(2m_M\nu + m_N^2)$:

$$A_{eff}/A(Fe) \equiv S(x') = (1-0.33\exp(-28x'))^{0.76}.$$

All fits in Table 2 are made both with S(x') included (multiplying W) and ignored.

The results of fits 1-4 are shown in Fig. 5. For purposes of this display only, the data and fits plotted vs. $|\cos\theta|$ (ϕ_F) are summed over ϕ_F ($|\cos\theta|$). The main feature of these angular distributions is a strong dependence upon ϕ_F, in the form predicted by SCHC. Unpolarized ψ's would yield a flat angular distribution (fit 3), which is ruled out. The data show no strong dependence on $|\cos\theta|$, slightly disfavoring R=0 (fit 4); significant Q^2-dependence of R is not required (fit 2). The photon-gluon-fusion (γGF) model[26], which has successfully described[28,34] other features of elastic ψ muoproduction, has yielded no prediction for the ψ polarization. This is due in part to complications associated with the exchange, required by color conservation, of at least two vector gluons.

Figure 6 presents the Q^2-dependence of σ_{eff}, summed over ν and normalized to unity at Q^2=0. For purposes of this display only, the data and fits to Λ are summed over $|\cos\theta|$ and ϕ_F. When the angular distribution is parameterized in the SCHC form with $R \propto Q^2$ and S(x') included, $\Lambda = 2.03^{+0.18}_{-0.12}$ GeV/c^2, where the statistical errors take into ac-

TABLE 2. Fits to the Q^2, ϕ, and θ-dependence of the effective cross section σ_{eff} for the reaction $\gamma_V Fe \to \psi X$ (energy(X)<4.5 GeV). The angular function $W(\eta,R)$, propagator $P(\Lambda)$, and nuclear screening factor $S(x')$ are defined in the text. Each of seven fits (numbered in the first column) is performed both with $S(x')$ included (multiplied "in") and ignored ("out") in the function fitted. Values of chi-squared and the degrees of freedom are given in the fourth column. Errors on the fit parameters Λ, η, and ξ^2 (fits 1 and 6) or R (fit 2) are statistical. Fit 6 is the same as fit 1 except that W is multiplied by $(1+\varepsilon R)$; Λ then parameterizes the Q^2-dependence of σ_T rather than σ_{eff}. Fit 7 compares the data integrated over ϕ and $\cos\theta$ with the Q^2-dependence predicted by γGF.

Fit No.	Function	$S(x')$	χ^2/DF	Λ(GeV/c^2)	η	ξ^2 or R
1	$W(\eta,R)\times P(\Lambda)$, $R=(\xi Q/m_\psi)^2$	in	45.4/56	$2.03^{+0.18}_{-0.12}$	$1.02^{+0.28}_{-0.23}$	$3.3^{+4.9}_{-3.0}$
		out	45.5/56	$2.18^{+0.18}_{-0.13}$	$1.04^{+0.28}_{-0.23}$	$4.0^{+4.8}_{-3.4}$
2	$W(\eta,R)\times P(\Lambda)$, R=constant	in	42.0/56	2.24±0.13	$1.09^{+0.31}_{-0.24}$	$.35^{+.26}_{-.18}$
		out	42.4/56	2.43±0.15	$1.10^{+0.31}_{-0.24}$	$.37^{+.27}_{-.22}$
3	$1\times P(\Lambda)$	in	73.3/58	2.06±0.11		
		out	73.3/58	2.22±0.13		
4	$W(1,0)\times P(\Lambda)$	in	48.6/58	2.21±0.12	≡1	≡0
		out	49.3/58	2.40±0.14		
5	$W(\eta,0)\times P(m_\psi)$	in	89.1/58	≡3.1	0.96±0.13	≡0
		out	68.5/58		0.93±0.14	
6	$(1+\varepsilon R)\times$Fit 1	in	47.0/56	2.08±0.24	0.86±0.17	$.24^{+.61}_{-.39}$
		out	47.6/56	2.20±0.29	0.87±0.17	$.34^{+.75}_{-.43}$
7	γGF -- Q^2 projection	in	32.1/8	$m_c \equiv 1.5$ GeV/c^2		
		out	14.6/8			

XBL 809-11763

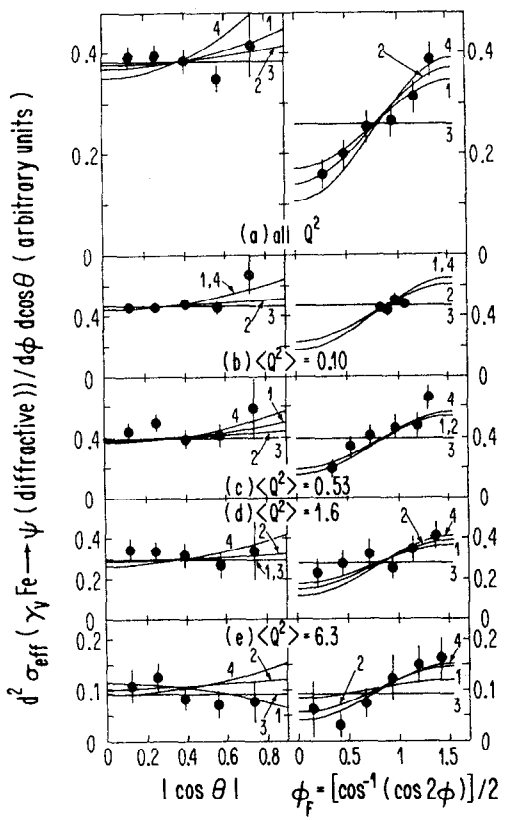

XBL 809-1801

FIG. 5. Angular dependence of the effective cross section for the reaction $\gamma_V Fe \to \psi X$ (energy(X)<4.5 GeV). Data and statistical errors are presented vs. $|\cos\theta|$ (left column) and ϕ_F (right column), with $\phi_F = \phi$ folded into one quadrant; θ and ϕ are defined in the text. All data ($\langle Q^2\rangle = 0.71$) are shown in (a); (b)-(e) divide the data into four Q^2 regions. Numbered solid lines exhibit the results of fits 1-4 in Table 2. Fits 1, 2, and 4 are to the SCHC formula with $\sigma_L/\sigma_T = \xi^2 Q^2/m_\psi^2$, constant, and zero, respectively; fit 3 corresponds to the production of unpolarized ψ's. Each fit is made to all the data with one adjustable normalization constant.

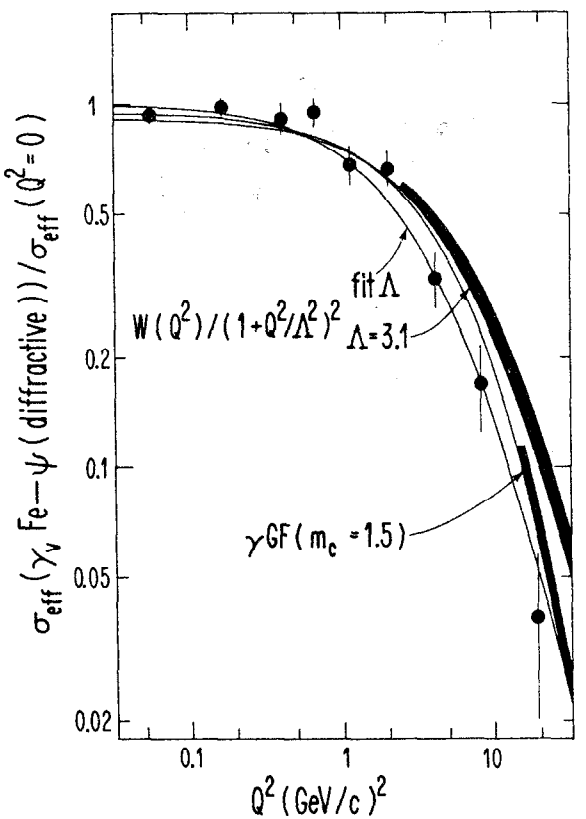

XBL 808-1800

FIG. 6. Q^2-dependence of the effective cross section for the reaction $\gamma_V Fe \to \psi X$ (energy(X)<4.5 GeV). Statistical errors are shown. Typical Q^2 resolution is 3.1 (0.6) (GeV/c)^2 at Q^2=17 (1.2) (GeV/c)^2. The data are fit to $(1+Q^2/\Lambda^2)^{-2}$ multiplied by the function $W(n,R)$ shown in Table 2. The weak Q^2-dependence of W results from the Q^2-dependence of $R=\sigma_L/\sigma_T$ and the particular average values of the angular factors $\cos^2\theta$ and $\cos 2\phi$, as given in Table 1. The best fits with free Λ (Table 2, fit 1) and fixed Λ=3.1 (Table 2, fit 5) are shown. The data are normalized so that fit 1 is unity at Q^2=0. Also exhibited is the γGF prediction (Table 2, fit 7). At high Q^2, the two latter fits are displayed as a solid band, with the upper (lower) edge including (omitting) the screening factor $S(x')$.

count the uncertainties in η and ξ^2 (Table 2, fit 1). If instead R=constant and $S(x')$ is left out, Λ=2.43±0.15 GeV/c^2 (fit 2). The other fits to Λ, either for σ_{eff} or σ_T (fit 6), are within this ±0.2 GeV/c^2 range, which accounts for the principal systematic error in Λ. We conclude that Λ is between 1.9 and 2.6 GeV/c^2. The simplest VMD prediction, $\Lambda=m_\psi$ (fit 5), is ruled out.

We also have fit the data in Fig. 6 to the γGF prediction (fit 7), assuming a charmed quark mass m_c=1.5 GeV/c^2 and a gluon distribution $G(x)=3(1-x)^5/x$. The data fall faster than the γGF curve, giving a barely acceptable fit (7% confidence) only if $S(x')$ is omitted. We have reached a similar conclusion[6] comparing γGF predictions with open charm muoproduction, using a different analysis. Varying m_c and the exponent of $(1-x)$ in $G(x)$ improves the γGF fit. We are in the process of making a combined determination of these parameters using the Q^2 and ν spectra of the ψ data.

To summarize this section, the azimuthal-angle distributions for muoproduced $\psi\to\mu^+\mu^-$ decay demonstrate that the reaction $\gamma_V N\to\psi N$ is helicity-conserving, and the polar-angle distributions suggest some longitudinally-polarized production, but do not rule out R=0. The Q^2-dependence of either σ_{eff} or σ_T clearly is steeper than $(1+Q^2/m_\psi^2)^{-2}$.

H. Cross Sections for Charm Production by Muons and Photons

The measurement of charm production in this experiment is similar to that in most neutrino experiments[39]. Charm states are identified by their ≥3-body decay into muons. Specified charmed hadrons are not resolved; they appear in the data weighted by their production cross section and leptonic branching ratio. This "continuum" signal is not well adapted to first observation[40] of charmed states, nor to the study of their decay systematics. However, once discovered in other reactions, charm production offers the only reasonable explanation for all but (19±10)% of the 20072 fully reconstructed single-extra- muon final states reported here. These statistics and signal-to-background level together with unambiguous determination of virtual-photon four-momenta make possible the study of charm-production mechanisms.

The ≥2μ trigger required a ≥20-GeV hadronic shower ≥2m upstream of ≥2 hits in each of three successive trigger hodoscopes (Fig. 1). Full tracking capability in an area including the beam produced a high, nearly Q^2-independent acceptance. In the analysis of same-sign dimuons, the more energetic muon was chosen to be the scattered muon. As inferred from $\mu^+\mu^-$ final states where the choice is obvious, this algorithm is successful for 91% of the same-sign events. The calorimeter was calibrated using the momentum-analyzed energy loss of high Q^2 single-muon triggers with a ≈3 GeV correction for the presence of a second muon.

Several analysis cuts were made to exclude regions of rapidly varying acceptance. Daughter muon energies were required to exceed 15 GeV, reconstructed vertices to fall between the centers of the first and eighth modules (Fig. 1), and hadronic shower energies to exceed 36 GeV. To avoid contamination from low-mass electromagnetically-produced muon pairs, the daughter muon was required to possess at least 0.45 GeV/c of momentum transverse to the scattered muon direction.

Monte Carlo charm events were simulated using the γGF model described in section D. For incoherent events the dependence on -t, not predicted by the model, was assumed to be as measured in the same apparatus for ψ production[3]. Likewise, the same nuclear parameters were used for coherent events. Carrying the full photon energy, charmed quark pairs with invariant mass exceeding the mass of two D mesons were transformed to D mesons using a fragmentation function $D(z)=(1-z)^{0.4}$ consistent with SPEAR data[41]. Here, z is the fraction of the parent quark's energy received by the charmed meson in the $c\bar{c}$ center of mass. The simulation assumed that neutral and charged D's are produced in a

2:1 ratio and decay to muons[42] with 4% and 20% branching ratios, respectively[43]. Production and decay of other charmed states were not explicitly simulated. These numbers imply a yield of 0.187 decay muons per charmed-quark pair. The $K\mu\nu$ ($K^*\mu\nu$) branching ratios were taken[43] as 0.61 (0.39). Charm decays to electrons with the same branching ratios were included to model missing energy from electron as well as muon neutrinos.

The major background to charm production is decay in flight of muo-produced π and K mesons. The corresponding Monte Carlo simulation used inelastic structure functions parameterized by the Chicago-Harvard-Illinois-Oxford collaboration[44]. From the same experiment[45] π and K production data were used to determine final state particle multiplicities and momentum distributions. Bubble chamber data[46] were used to parameterize secondary interactions between mesons in the showers and nucleons in the target. Because of this experimental input the Monte Carlo was free from dependence on models of hadron production. Showers were allowed to develop until no hadron energy exceeded 5 GeV. Hadron trajectories were simulated in the same detail as muon trajectories. The small yield of prompt muons from ρ decay, Drell-Yan processes and hadronic charm production in showers was neglected. The decay simulation was compared with a Caltech-Fermilab-Rockefeller (CFR) neutrino experiment's shower Monte Carlo[47], based in part on a model of hadron production. The CFR Monte Carlo predicted a rate 15% (35%) higher at W-boson energy of 130 GeV (180 GeV) than did this experiment's calculation for similar virtual photon energies.

To improve the ratio of signal to background, data with $\nu<75$ GeV were excluded. With this cut, absolute normalization of the π,K-decay Monte Carlo to the integrated beam flux fixes this background at 19% of the sample. The systematic normalization uncertainty in the shower Monte Carlo is determined to be ±50% in part by comparing the calculated π, K fraction with that obtained by representing the data as a combination of simulated π, K decay and charm events.

After the π,K-decay background is subtracted bin-by-bin from the data, the charm signal and the γGF prediction are compared in Fig. 7 (a)-(f). The muon-scattering vertex is modeled precisely in ν and adequately in Q^2. The longitudinal decay-muon variables (c) and (d) are in satisfactory agreement, as is the missing energy within the calorimeter calibration uncertainty. The daughter muon $p_\perp$ is higher in the data by 15%; however, this variable is sensitive to details of -t slope and charm decay systematics, which are not model predictions. Overall, the γGF model is an adequate basis for acceptance calculation.

Barger, Keung and Phillips[48] have discussed the potential background due to feed-down of trimuon final states due to electromagnetic production of muon pairs in which one muon is undetected. With our calorimeter energy requirement, their calculation predicts less than a 5% contamination from this source. Independently, contamination from feed-down of any background source of trimuons was checked by blinding the analysis to the softest muon in all detected trimuon final states otherwise satisfying the dimuon trigger and analysis requirements. These events, comprising 3.9% of the normal sample, amount to 100.1±5.3% of the Monte Carlo yield of detected muon decays from both D mesons. Thus, any other processes generating trimuons with the same muon detection efficiency as the charm signal can account for no more than 0.5% of the data. A standard calculation of $\tau\bar{\tau}$ production[48] and our γGF calculation of bottom quark pair production limit these "contaminants" to less than 0.1% and 0.03% of the sample, respectively.

The spectrometer's acceptance is by far most sensitive to the energy spectrum of produced muons. The γGF model describes quasielastic $c\bar{c}$ production[26] and predicts a ν distribution in excellent agreement with that observed in the subtracted data. Therefore, most of the model

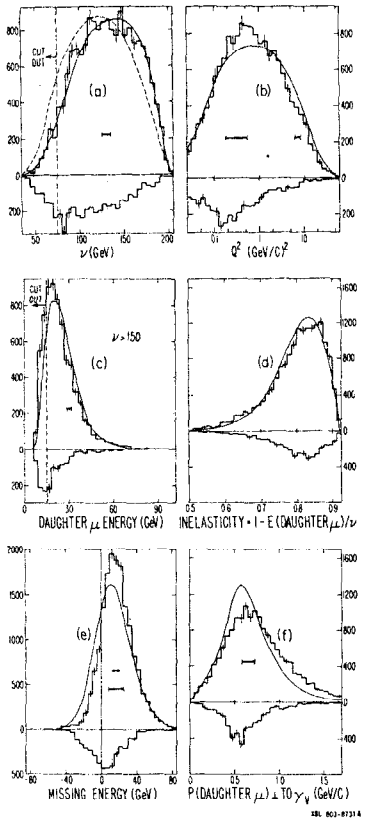

FIG. 7. Reconstructed distributions in (a) energy transfer, (b) momentum-transfer-squared, (c) daughter muon energy. (d) inelasticity, (e) missing (neutrino) energy, (f) daughter muon $p_\perp$. The ordinates are events per bin with acceptance not unfolded. Inverted histograms show the simulated π, K-decay background, absolutely normalized to the integrated beam flux. Erect histograms exhibit data after subtraction of this background; statistical errors are shown. The curves, normalized to the subtracted data, are the photon-gluon-fusion charm calculation. The dashed curve in (a) represents an alternate model in which $D\bar{D}$ pairs carrying the full photon energy are produced with a probability independent of ν. Events in (c) have $\nu>150$ GeV. The horizontal brackets exhibit typical apparatus resolution (rms). The arrow in (e) shows the shift caused by a ±2.5% excursion in calorimeter calibration.

dependence introduced in the analysis may be studied by varying the daughter muon energy distribution through changes in $D(z)$. Remodeling detector acceptance with $D(z)=(1-z)^3$ ($D(z)=(1-\min(z,0.99)^{-1.5}$) predicts mean daughter energies in five-standard-deviation disagreement with subtracted data and decreases (increases) the calculated acceptance by a factor of 1.24 (1.20). The agreement between subtracted data and γGF Monte Carlo is substantially worsened in many other distributions. The systematic errors quoted below are the sum in quadrature of excursions caused by the π, K normalization uncertainty and the fragmentation-induced changes in acceptance. After a relative acceptance correction of 26%, the ratio of opposite- to same-sign daughter muon events is 1.066±0.028 (±0.055), where the latter error is systematic.

The measured cross section for diffractive charm production is

$$\sigma_{\text{diff}}(\mu N\to\mu c\bar{c}X)=6.9^{+1.9}_{-1.4}\ \text{nb}.$$

"Diffractive production" refers to creation of $c\bar{c}$ pairs carrying most of the laboratory energy of the virtual photon, as in the γGF, VMD, and other peripheral models. The present analysis is insensitive to other possible mechanisms producing charm nearly at rest in the virtual photon-nucleon center of mass. This cross section is 137% of the γGF prediction. Corrected by a factor of 1.45 for the different beam energy, it is three times the cross section reported by the Michigan State-Fermilab group[49].

The muon cross section is expressed as an effective photon cross section σ_{eff} by factoring out the equivalent flux[50] of transversely polarized virtual photons. Figures 8 (a) and (b) show the extrapolation of σ_{eff} to $Q^2=0$ using a VMD propagator. The best-fit χ^2 values are approximately 1.8 per degree of freedom, due in part to a tendency for σ_{eff} to rise slightly with Q^2 near $Q^2=0.2$ (GeV/c)^2. Allowing for systematic error, the best fit propagator masses are $\Lambda=3.3\pm0.2$ and 2.9±0.2 GeV/c^2 at $\nu=178$ and 100 GeV, and the intercepts at $Q^2=0$ are

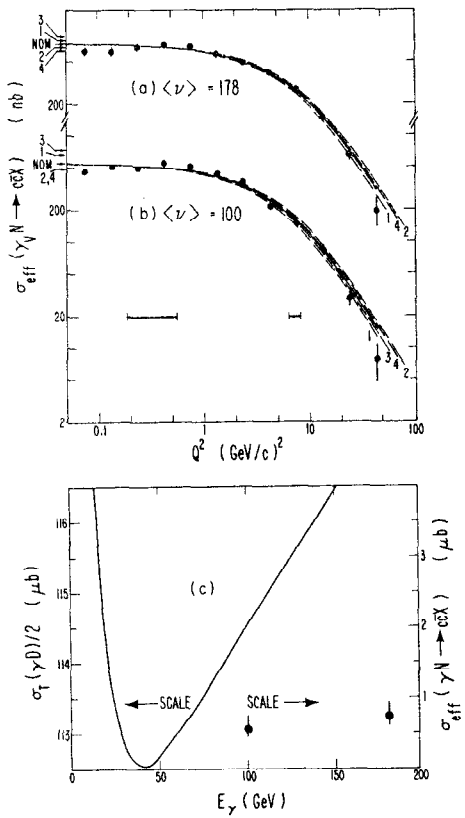

FIG. 8. Diffractive charm photoproduction cross sections and the rise of the photon-nucleon total cross-section. Parts (a) and (b) exhibit the extrapolation of the effective cross section for diffractive charm photoproduction to Q^2=0 at ν=(a) 178 and (b) 100 GeV. Statistical errors are shown. The solid curves are fit to $\sigma_0(1+Q^2/\Lambda^2)^{-2}$ with Λ=(a) 3.3 and (b) 2.9 GeV/c: the arrows labelled "NOM" exhibit σ_0. Systematic errors are parameterized by (1) decreasing, (2) increasing by 50% the subtracted π, K-decay background, and by recalculating the acceptance with a (3) softer, (4) harder quark fragmentation function as described in the text. Systematic effects on σ_0 are indicated by numbered arrows and effects on Λ are indicated by dashed curves, normalized to the same σ_0. Part (c) compares the extrapolated cross-sections for diffractive charm production by real photons (data points, right scale) with a fit (Ref. 51) to $\frac{1}{2}\sigma_T(\gamma d)$ (curve, left scale).

750^{+180}_{-130} and 560^{+200}_{-120} nb, respectively. The rise with ν of 190^{+34}_{-52} nb in the charm photoproduction cross section is significant, while the difference of 0.39±0.18 GeV in propagator masses is only suggestive. In all cases but the last, allowances for systematic uncertainties dominate the errors. The diffractive charm production rate is too small to saturate the rise[51] of the total γN cross section above 50 GeV (Fig. 8 (c)).

We have published[3] a value of 60±20 nb/GeV^2 for dσ/dt (γN→ψN) at t=0 and ν=100 GeV. With the observed -t slope, this corresponds to an elastic cross section of 25±8 nb. The results reported here fix the ratio of elastic ψ to diffractive charm production at 0.045±.022. The central value is approximately 2.5 times Sivers, Townsend, and West's VMD prediction[22]; in that particular picture our result would suggest that non-diffractive charm production may account for a significant fraction of the total charm-photoproduction cross section. Independent of VMD, using the results of Ref. 22, we obtain the 90%-confidence lower limit $\sigma_{total}(\psi N) \geq 0.9$ mb.

For the purpose of discriminating between charm-production models, Fig. 9 displays in more detail the dependence of σ_{eff} on ν in a range of Q^2 centered at 0.75 (GeV/c)^2. The insensitivity of σ_{eff} to Q^2 in this range decouples its Q^2- and ν-dependence. Again, the γGF model with gluon distribution $3(1-x)^5/x$ successfully describes the observed ν-dependence. However, as illustrated by the shaded band, systematic uncertainties prevent the data from ruling out the BN model[25], or the two alternate choices indicated for the gluon x distribution. The precision is sufficient to disfavor a flat ν-dependence.

I. The Charm Structure Function and Its Role in Scale-Noninvariance

The original signature[52] for scale-noninvariance in muon-nucleon scattering was the "shrinkage" of the structure function $F_2(x_B)$ with rising Q^2. As confirmed by subsequent muon[44] and neutrino[53] experiments, $\partial F_2/\partial Q^2$ is positive for fixed Bjorken $x_B \lesssim 0.1$ and negative for $x_B \gtrsim 0.25$.

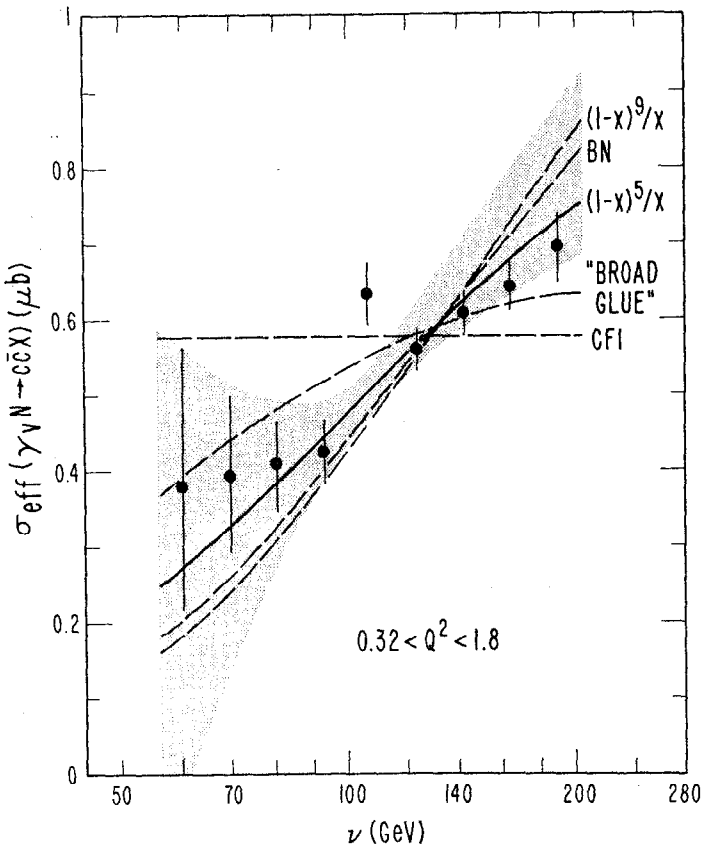

FIG. 9. Energy-dependence of the effective cross section σ_{eff} for diffractive charm photoproduction. For $0.32<Q^2<1.8$ $(GeV/c)^2$, σ_{eff} varies with Q^2 by $\lesssim$20%. Errors are statistical. The solid curve exhibits the ν-dependence of the photon-gluon-fusion model with the "counting-rule" gluon x distribution $3(1-x)^5/x$, and represents the data with 13% confidence. Other gluon-distribution choices $(1-x)^9/x$, and "broad glue" $(1-x)^5(13.5+1.07/x)$ are indicated by dashed curves. The dashed curve labelled BN is the phenomenological parameterization of Ref. 25, and the dashed line labelled CFI represents the energy-independence assumed by recent photoproduction analyses. Curves are normalized to the data. The shaded band exhibits the range of changes in shape allowed by systematic error. For clarity it is drawn relative to the solid curve. Data below ν=75 GeV are cut out.

If higher Q^2 is associated with greater resolving power of the exchanged boson probe, this shrinkage may be visualized as an increase in the number of resolved constituents sharing the nucleon momentum. Despite the general nature of this picture, the lepton-nucleon data have been widely interpreted as early confirmation of the specific predictions of quantum chromodynamics (QCD).

Ambiguities in the interpretation of scale-noninvariance in F_2 are different at high and low x_B. Effects of finite target mass conventionally are absorbed into redefinition[54] of x_B, which critically affects F_2 only at high x_B. "High twist" corrections for phenomena which are coherent over two or more constituents have been parameterized[55] as a power series in $(1-x_B)^{-1}$. These problems motivate the suggestion[56] that the stronger of the QCD predictions for F_2 is to be found at low x_B. However, available lepton beam energies limit Q^2 for $x_B \lesssim 0.1$ to values not greatly exceeding $m^2_{c\bar{c}}$. The proximity of this charm mass scale threatens to disrupt any low-x_B study of asymptotic scale-noninvariance. Earlier experimentation has provided only one estimate[57] of the charm contribution to F_2. It was given as a function of two phenomenological parameters which were not quantitatively determined.

In order to discuss the Q^2-dependence of charm muoproduction in connection with inclusive muon scattering, we define the charm structure function $F_2(c\bar{c})$ through the relation

$$Q^4 \nu d^2\sigma(c\bar{c})/dQ^2 d\nu = 4\pi\alpha^2(1-y+y^2/2)F_2(c\bar{c}).$$

Here y is ν/ν_{max} and $\sigma(c\bar{c})$ is the cross section for diffractive charm-pair production in muon-nucleon collisions. We label $\sigma(c\bar{c})$, $F_2(c\bar{c})$, and σ_{eff} as "diffractive" quantities because the analysis is sensitive mainly to $c\bar{c}$ pairs which carry off most of ν. In charm production $F_2(c\bar{c})$ plays the same role as would F_2 in inclusive scattering, if absorption of longitudinally polarized photons were negligible.

Figure 10 exhibits the dependence of $F_2(c\bar{c})$ on Q^2 at two values of

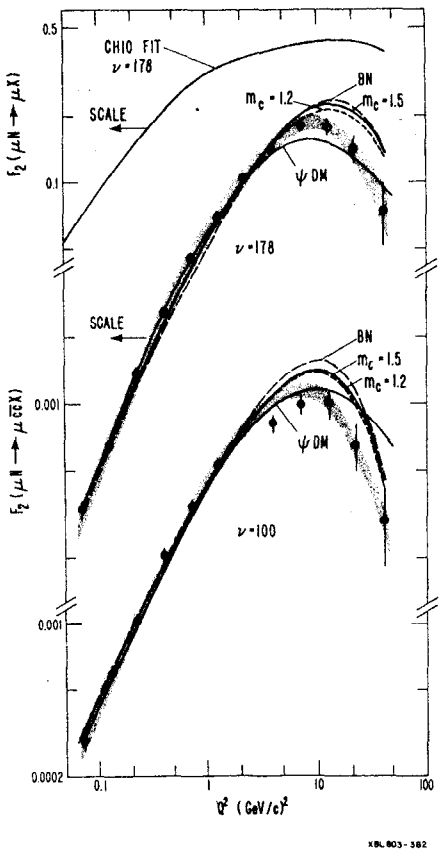

FIG. 10. Q^2-dependence of the structure function $F_2(c\bar{c})$ for diffractive charm muoproduction. At each of the two average photon energies, each curve is normalized to the data. Errors are statistical. The solid (short dashed) curves labelled m_c=1.5 (1.2) exhibit the photon-gluon-fusion prediction with a charmed quark mass of 1.5 (1.2) GeV/c^2. Solid curves labelled ψDM correspond to a ψ-dominance propagator, and long-dashed curves labelled BN are the model of Ref. 25. Shown at the top is a fit adapted from Ref. 44 to the inclusive structure function F_2 for isospin-0 μN scattering. The shape variations allowed by systematic errors are represented by the shaded bands.

fixed average ν. The charm structure function rises with Q^2 to a maximum at $Q^2 \approx 10$ (GeV/c)^2, above which it falls steeply. At the peak, $F_2(c\bar{c})$ is ≈4% of the inclusive F_2. None of the models depicted in Fig. 10 is an adequate representation of the data. The γGF shapes for m_c=1.5 and 1.2 GeV/c^2 are nearly degenerate. In that model[26] the Q^2-dependence is sensitive to $m_{c\bar{c}}$, which in either case is bounded below by $2m_D$. The maxima predicted by both the γGF and BN models shift with ν and curve with Q^2 like the data, but occur at values of Q^2 which are too high. The ψ-dominance predictions drop too slowly at high Q^2. Systematic errors are only weakly correlated with Q^2 and do not obscure the disagreement.

In the energy range of the data in Fig. 11, $F_2(c\bar{c})$ is manifestly scale-noninvariant for $Q^2 \gtrsim 10$ (GeV/c)^2, or $x_B \lesssim 0.07$. To model the charm contribution to F_2 for smaller photon energies, we multiply the γGF-model normalization by a factor of 1.37 and damp it at high Q^2 by the arbitrary factor $(1+Q^2/(10\ \text{GeV/c})^2)^{-2}$. The resulting family of dashed curves in Fig. 11 adequately matches the data where overlap exists.

To describe the full effect of charm production on F_2 we must include the charmonium contribution. The ψ-muoproduction rate[3] agrees with the unmodified γGF prediction if elastic ψ production accounts for 1/6 of all charmonium production[28]. This is close to the fraction expected if all charmonia are produced with equal likelihood. Adopting this model, we augment the measured $6.9^{+1.9}_{-1.4}$ nb open-charm cross section by 2.8 nb of bound charm production. Since charmonium production falls more rapidly at high Q^2 than open charm production, this augmentation increases the charm contribution to inclusive scale-noninvariance only by ≲15% in the region where it is most important.

To focus on the absolute charm contribution, published[44] fits at fixed x_B to the inclusive $\partial F_2/\partial \ell n Q^2$ are compared in Table 3 to $\partial F_2(c\bar{c})/\partial \ell n Q^2$ augmented for charmonium production. Although the latter

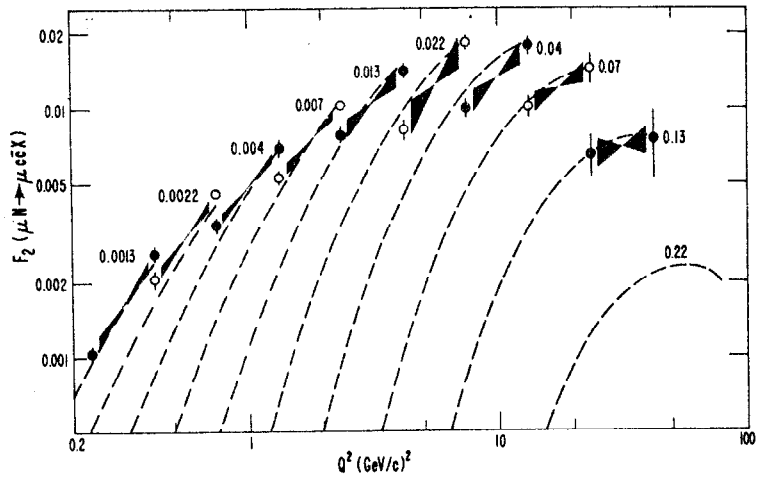

FIG. 11. Scale-noninvariance of $F_2(c\bar{c})$. Data points are arranged in pairs, alternately closed and open. The points in each pair are connected by a solid band and labelled by their common average value of $x_B = Q^2/2m_p\nu$. Errors are statistical. The dashed lines are the prediction of the photon-gluon-fusion model with $m_c = 1.5$ GeV/c^2 except that the model is renormalized and damped at high Q^2 as described in the text. The solid bands represent the slope variations allowed by systematic errors.

TABLE 3. Calculated $10^4 \partial F_2/\partial \ell n Q^2$ at fixed x_B vs. ν (top), Q^2 (left margin), and x_B (diagonals, right margin). For each Q^2-ν combination, two values are shown. The bottom value is fit to the structure function F_2 for μN scattering (Ref. 44). The top value is the contribution $F_2(c\bar{c})$ to F_2 from diffractive muoproduction of bound and unbound charmed quarks.

ν(GeV)	27	42	67	106	168	
Q^2 (GeV/c)^2	$\frac{10^4 \partial F_2(c\bar{c})/\partial \ell n Q^2}{10^4 \partial F_2(\mu N)/\partial \ell n Q^2}$					x_B
0.63	17 1070	30 1090	43 1110	54 1120	58 1130	
1.0	23 980	43 1010	63 1040	77 1050	84 1060	0.002
1.6	30 650	59 680	87 700	107 720	116 730	0.003
2.5	36 310	73 340	110 350	139 360	146 360	0.005
4.0	36 320	80 390	128 430	162 460	163 480	0.008
6.3	29 210	75 330	128 410	165 460	154 490	0.013
10	15 50	54 220	104 340	138 430	112 480	0.020
16	4 -130	27 50	64 230	90 360	52 440	0.032
25	-2 -189	7 -126	26 50	40 230	0 370	0.050
40	0 -31	-1 -171	6 -122	10 50	-22 240	0.080
63		0 -23	1 -154	1 -119	-16 50	0.130

XBL 809-11764

numbers are calculated rather than measured, we emphasize that the (γGF) model used has been made to agree with the diffractive charm-muoproduction data. In the region where charm scale-noninvariance is most important, the calculation is reliable to ≈±40%.

We conclude from Table 3 that diffractive charm production makes a contribution to inclusive scale-noninvariance which is very large compared to the ≲4% relative magnitude of its cross section. On average, in a region bounded by $2<Q^2<13$ $(GeV/c)^2$ and $50<\nu<200$ GeV and centered at $x_B \approx 0.025$, it contributes 1/3 of the total inclusive scale-noninvariance. This region embraces the data providing most of the original evidence[52] for scale-noninvariance in muon scattering. VMD arguments mentioned in section H raise the possibility that substantial non-diffractive charm muoproduction exists in addition to the diffractive production to which the analysis presented here is sensitive. A portion of any non-diffractive charm production might add further to the diffractive scale-noninvariance we have discussed.

We emphasize that the scale-noninvariance created by diffractive charm muoproduction is not a direct manifestation of asymptotic freedom or other fundamental theory. It is only a kinematic effect tied to the scale of the charmed quark mass. To study deeper implications of scale-noninvariance in muon scattering, one must include this effect in the model being fit, or subtract it from the data.

J. Acknowledgements

I wish to express thanks to the organizers for a very stimulating Topical Conference. This work was supported by the High Energy Physics Division of the United States Department of Energy under Contract Nos. W-7405-Eng-48, DE-AC02-76ER03072, and EY-76-C-02-3000.

References

[a]Present address: The Enrico Fermi Institute, 5630 S. Ellis Avenue, Chicago, Illinois 60637.
[b]Present address: Bell Telephone Laboratories, Murray Hill, New Jersey 07974.
[1]A.R. Clark et al., LBL-11663 (1980), submitted to Phys. Rev. Letters.
[2]A.R. Clark et al., Phys. Rev. Lett. 45, 686 (1980).
[3]A.R. Clark et al., Phys. Rev. Lett. 43, 187 (1979).
[4]A.R. Clark et al., LBL-11562 (1980), submitted to Phys. Rev. Letters.
[5]A.R. Clark et al., Phys. Rev. Lett. 45, 682 (1980).
[6]A.R. Clark et al., Phys. Rev. Lett. 45, 1465 (1980).
[7]A.R. Clark et al., in Proceedings of the 1979 International Symposium on Lepton and Photon Interactions at High Energy, edited by T.B.W. Kirk and H.D.I. Abarbanel (Fermilab, Batavia, Illinois, 1979), p. 135-148 (1979).
[8]G.D. Gollin, M.V. Isaila, F.C. Shoemaker, and P. Surko, IEEE Trans. Nucl. Sci. NS-26, 59 (1979).
[9]S. Weinberg, Phys. Rev. Lett. 19, 1264 (1967).
[10]F. Wilczek and A. Zee, Nucl. Phys. B106, 461 (1976).
[11]T. Cheng and L. Li, Phys. Rev. D16, 1425 (1977).
[12]S. Weinberg, Phys. Rev. D5, 1264 (1972); J. Schecter and Y. Ueda, Phys. Rev. D8, 484 (1973); Y. Achiman and B. Stech, Phys. Lett. 77B, 384 (1978).
[13]K.W. Rothe and A.M. Wolsky, Nucl. Phys. B10, 241 (1969).
[14]A.E. Asratyan et al., Phys. Lett. 49B, 488 (1974).
[15]T. Eichten et al., Phys. Lett. 46B, 281 (1973).
[16]B.C. Barish et al., Phys. Rev. Lett. 32, 1387 (1974).
[17]D.J. Bechis et al., Phys. Rev. Lett. 40, 602 (1978). This limit applies only to heavy muons which are long-lived because of some as-yet-undiscovered selection rule.
[18]D.S. Baranov et al., Phys. Lett. 81B, 261 (1979), and Sov. J. Nucl. Phys. 29, 622 (1979).
[19]M.R. Krishnaswamy et al., Phys. Lett. 57B, 105 (1975).
[20]B.C. Barish et al., Phys. Rev. Lett. 38, 577 (1977); A. Benvenuti et al., Phys. Rev. Lett. 38, 1110 (1977).
[21]Q^2 is defined for M^0 production by taking the like-sign final-state muon to be a scattered beam muon.
[22]D. Sivers, J. Townsend, and G. West, Phys. Rev. D13, 1234 (1976).
[23]S. Okubo, Phys. Lett. 5, 160 (1963); G. Zweig, report, 1964 (unpublished); J. Iizuka, Progr. Theor. Phys. Suppl. 37-38, 21 (1966).
[24]D. Bauer et al., Phys. Rev. Lett. 43, 1551 (1979), and references cited therein.
[25]F. Bletzacker and H.T. Nieh, SUNY-Stony Brook Report No. ITP-SB-77-44 (unpublished).
[26]J.P. Leveille and T. Weiler, Nucl. Phys. B147, 147 (1979), and references cited therein.
[27]S. Brodsky and G. Farrar, Phys. Rev. Lett. 31, 1153 (1973).
[28]V. Barger, W.Y. Keung, and R.J.N. Phillips, Phys. Lett. 91B, 253 (1980).
[29]K. Berkelman, summary of DORIS results presented to the XV Rencontre de Moriond (Les Arcs, Savoie, France, March 9-21, 1980).
[30]G. Aubrecht and W. Wada, Phys. Rev. Lett. 39, 978 (1977), make photoproduction predictions which, with γGF ν- and Q^2-dependence assumptions, correspond to 0.15×10^{-36} cm^2 of T muoproduction at 209 GeV.
[31]N. Bralić, Nucl. Phys. B139, 433 (1978), makes leptoproduction predictions which, with γGF energy-dependence assumptions, correspond to 0.07×10^{-36} cm^2 of T muoproduction at 209 GeV.
[32]H. Fritzsch and K. Streng, Phys. Lett. 72B, 385 (1978), make photoproduction predictions which, with γGF ν- and Q^2-dependence assumptions, correspond to 0.36×10^{-36} cm^2 of T muoproduction at 209 GeV.

[33]M. Glück and E. Reya, Phys. Lett. 79B, 453 (1978).
[34]T. Weiler, Phys. Rev. Lett. 44, 304 (1980).
[35]J.J. Sakurai and D. Schildknecht, Phys. Lett. 40B, 121 (1972).
[36]J.T. Dakin et al., Phys. Rev. Lett. 30, 142 (1972); W.R. Francis et al., Phys. Rev. Lett. 38, 633 (1977); R. Dixon et al., Phys. Rev. Lett. 39, 516 (1977).
[37]K. Schilling, P. Seyboth, and G. Wolf, Nuc. Phys. B15, 397 (1970); B. Humpert and A.C.D. Wright, Ann. Phys. 110, 1 (1978); T. Markiewicz, Ph.D. Thesis, Univ. of Calif., Berkeley, 1980 (unpublished).
[38]H. Miettinen, presented at the XX International Conference on High Energy Physics, Madison, Wisconin, July 17-23, 1980.
[39]See, for example, M. Murtagh, in Proceedings of the International Symposium on Lepton and Photon Interactions at High Energies, Batavia, 1979, edited by T.B.W. Kirk and H.D.I. Abarbanel (Fermilab, Batavia, 1979).
[40]G. Goldhaber et al., Phys. Rev. Lett. 37, 255 (1976).
[41]P.A. Rapidis et al., Phys. Lett. 84B, 507 (1979).
[42]We use the decay matrix elements of I. Hinchliffe and C.H. Llewellyn Smith, Nucl. Phys. B114, 45 (1976).
[43]J. Kirkby, in Proceedings of the International Symposium on Lepton and Photon Interactions at High Energies, Batavia, 1979, edited by T.B.W. Kirk and H.D.I. Abarbanel (Fermilab, Batavia, 1979).
[44]B.A. Gordon et al., Phys. Rev. D20, 2645 (1979).
[45]W.A. Loomis et al., Phys. Rev. D19, 2543 (1979).
[46]J.A. Gaidos et al., Nucl. Phys. B23, 10 (1973); P. Bosetti et al., Nucl. Phys. B54, 141 (1973); P. Bosetti et al., Nucl. Phys. B60, 307 (1973); G.A. Akopdjanov et al., Nucl. Phys. B75, 401 (1974); W. Morris et al., Phys. Lett. 56B, 395 (1975).
[47]M. Shaevitz, private communication. The CFR group also studied showers induced by pions incident on their detector.
[48]V. Barger, W.Y. Keung and R.J.N. Phillips, Phys. Rev. D20, 630 (1979).
[49]D. Bauer et al., Phys. Rev. Lett. 43, 1551 (1979).
[50]F.J. Gilman, Phys. Rev. 167, 1365 (1968).
[51]D.O. Caldwell et al., Phys. Rev. Lett. 42, 553 (1979).
[52]Y. Watanabe et al., Phys. Rev. Lett. 35, 898 (1975); C. Chang et al., Phys. Rev. Lett. 35, 901 (1975).
[53]See e.g. J.G.H. deGroot et al., Z. Physik C1, 143 (1979).
[54]See e.g. O. Nachtmann, Nucl. Phys. B63, 237 (1973).
[55]L.F. Abbott, W.B. Atwood, and R.M. Barnett, Phys. Rev. (to be published), and SLAC-PUB-2400 (1979).
[56]F. Eisele, presented at the XV Rencontre de Moriond (Les Arcs, Savoie, France, March 9-21, 1980).
[57]K.W. Chen and A. Van Ginneken, Phys. Rev. Lett. 40, 1417 (1978).

DIPOLE MOMENTS AND PARITY VIOLATING SPIN ROTATIONS OF THE NEUTRON

Norman F. Ramsey
Harvard University
Cambridge, Massachusetts

INTRODUCTION

In this report I shall discuss primarily four different categories of experiments involving slow neutrons. (1) The most recently completed experiments at the Institut Laue-Langevin (ILL) and at Leningrad which set an upper limit on the electric dipole moment of the neutron. (2) The new experiment now being assembled at the ILL to measure the neutron electric dipole moment with ultra-cold neutrons trapped by total reflection in a neutron bottle. (3) A recent measurement of the neutron magnetic moment at the ILL with an improvement in accuracy by a factor of more than one hundred. (4) The recent observation at the ILL of a parity violating spin rotation when neutrons pass through matter, due, presumably, to the parity violating weak interaction.

As is apparent, most of the experiments to be described were done at the ILL; they have involved an informal international collaboration of scientists which for various experiments includes the following: P. Miller and W. Dress of Oak Ridge National Laboratory; P. Perrin of the Centre European Nucleaire de Grenoble; W. Mampe of the ILL; M. Pendlebury, K. Smith, J. Byrne, R. Golub, and T. Sumner from Sussex University; K. Green and G. Greene of the Rutherford Laboratory; M. Forte of Euratom CCR-Ispra, and B. Heckel and myself from Harvard University.

COMPLETED NEUTRON ELECTRIC DIPOLE MOMENT EXPERIMENTS

A neutron electric dipole moment would occur if there were a slight bulge in the positive charge distribution in the neutron's upper hemisphere and of negative charge in the opposite hemisphere. It is easy to see

that the existence of such an electric dipole moment would violate both time reversal symmetry (T) and parity (P). The only means for specifying the orientation of a particle is by the orientation of its spin angular momentum, $\vec{J}$, so the electric dipole moment $\vec{\mu}_E$ must be given by

$$\vec{\mu}_E = C\,\vec{J} \qquad (1)$$

Therefore, if time is reversed, $\vec{J}$ is reversed and hence $\vec{\mu}_E$ is reversed. Consequently, the electric fields resulting from $\vec{\mu}_E$ would be reversed while ordinary electrostatic fields would be unchanged, so the magnitude of the resultant electric field would be different in the time reversed system and the physics in that system would be changed, contrary to the assumption of time reversal symmetry. Consequently, a search for an electric dipole moment of either the neutron or a proton is a test of T. A similar analysis shows that the existence of an electric dipole moment is also incompatible with P. For both of these reasons it was originally argued that the neutron could not have an electric dipole moment, but the author pointed out in two early papers[2,3] that both T and P symmetry were assumptions that should depend on experimental confirmation and that the neutron electric dipole moment provided a sensitive check. Subsequently, the work of Lee and Yang[4] and of Wu, Ambler, et al.[5] showed that P symmetry indeed was not valid for the weak interaction in beta decay. The later experiment of Fitch, Cronin, Christianson and Turlay[6] showed that there was a violation of CP symmetry in the decay of the long lived neutral kaon, K_L^o, and hence there should be a violation of T symmetry if CPT were conserved, as usually assumed. So far, all manifestations of T violation have been exclusively in the K_L^o and the possible discovery of a neutron electric dipole moment appears to be the most sensitive means for detecting a T violation in another particle. At present the low limit on the neutron electric dipole moment provides a severe restriction on many theories of particles and forces. For this reason, there is a continuing effort to reduce the limit on the neutron electric dipole moment as much as possible.

The reason that the neutron provides a more sensitive test than the proton is its zero charge. If a particle has an electric dipole moment its orientation dependent interaction energy is given by

$$W = -\vec{\mu}_E \cdot \vec{E} \qquad (2)$$

Consequently, an electric field is required to observe the electric dipole moment of a particle. But a charged particle will be accelerated out of the apparatus by an electric field and, even if the charged particle is the nucleus of a neutral atom, it will readjust its position in the atom until $\vec{E} = 0$. An exception to this statement can occur if the particle is acted on by another force. However, even in this case the electric field is almost cancelled and the neutron appears to be the hadron for which the lowest electric dipole limit can be established.

All of the neutron experiments I am discussing depend on the use of totally reflecting neutron mirrors, so let me first discuss some of the properties of such mirrors. Since a wave is associated with the neutron there is an index of refraction n when a slow neutron passes through matter. The index of refraction is given by

$$n = \left[1 - \frac{\lambda^2 N a_{coh}}{\pi} \pm \frac{\mu_M B}{\frac{1}{2} M v^2} \right]^{1/2} \qquad (3)$$

where λ is the neutron wave length, N the number of nuclei per cm^3, a_{coh} is the neutron coherent forward scattering length, μ_M the neutron magnetic moment, B the magnetic induction and $1/2\ Mv^2$ the neutron kinetic energy. As in the case of fibre optics, total reflection occurs for a glancing angle θ greater than the critical glancing angle θ_c where, as for light,

$$\cos \theta_c = n \qquad (4)$$

as shown in Fig. 1. A neutron conducting pipe can then be made to transmit all neutrons at a smaller glancing angle. The departure of n from unity increases with λ^2 so for very slow neutrons the neutron pipes are particularly effective.

Since the critical angles by Eqs. (3) and (4) depend on the orientation of the neutron spin in the magnetic induction B, a short length of magnetized mirror provides a highly effective polarizer and analyzer.

Finally, at neutron velocities below 6 m/sec there is total reflection even at normal incidence and the neutrons can be stored in a bottle for 30s or longer.

The most sensitive beam measurement of the neutron electric dipole moment is that of Dress, Miller, Pendlebury, Perrin and Ramsey.[7] References to less accurate earlier measurements have been published previously.[8] The apparatus of Dress, et al. is shown in Fig. 2. The neutron beam comes from the cryogenic moderator at the Institut Laue-Langevin (ILL) reactor in Grenoble, France. The neutrons are conducted from the moderator through a neutron conducting tube of rectangular cross section on whose surface they are totally reflected at glancing angles of two degrees or less. The use of such neutron conducting pipes markedly enhances the intensity by overcoming the normal diminution of beam intensity with the inverse square of the distance from the moderator. This gain of intensity is badly needed to compensate in part for the even greater loss of intensity by the selection of extremely slow neutrons.

As shown in Fig. 2, the neutron beam goes through a portion of the pipe in which the walls consist of magnetized iron. Depending upon the orientation of the neutron spin, there is total reflection at the walls for neutrons of one spin orientation while the neutrons with opposite spins are not reflected by that portion of the pipe and instead penetrate through the walls and are lost. Consequently following the spin polari-

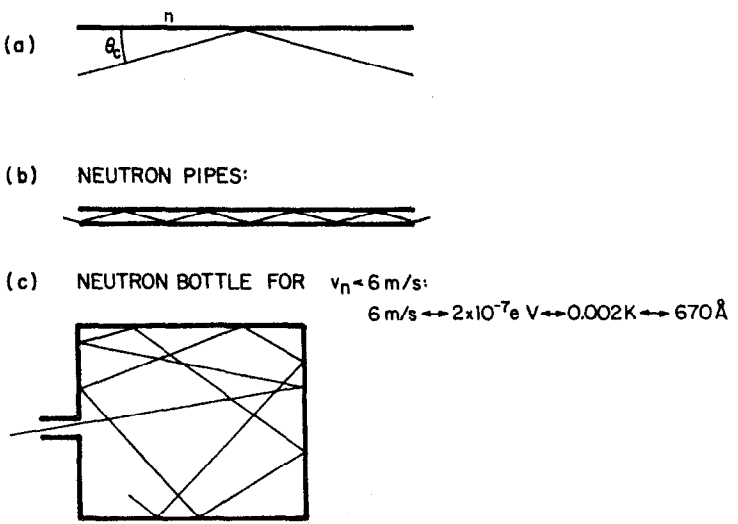

Fig. 1. (a) Total reflection of neutrons. (b) Neutron pipe and (c) neutron bottle.

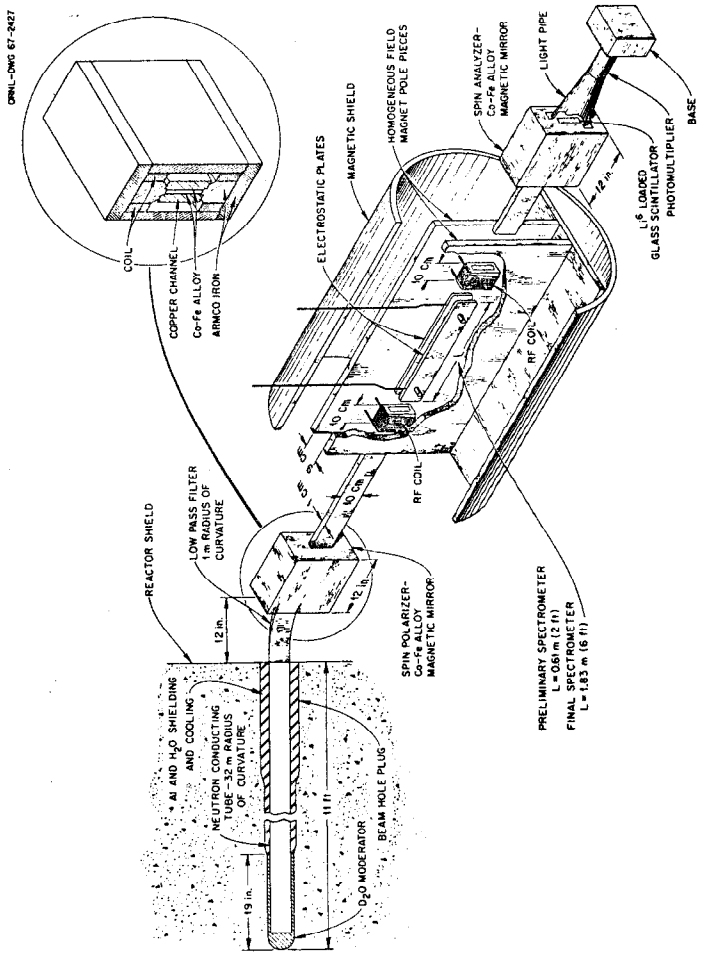

Fig. 2. Schematic diagram of neutron beam magnetic resonance apparatus

zing magnetic mirror, the neutrons are mostly polarized. The analyzing device to determine if there has been a change in the neutron spin orientation is a second spin analyzing magnetic mirror. If the neutron spin remains unaltered between the first and the second of these magnetic field regions, most of the neutrons will be transmitted by the second region. If, on the other hand, the neutrons have been reoriented by approximately 180 degrees between the two iron mirror sections, the neutrons whose orientation has changed will not be totally reflected in the second magnetic mirror, with a consequent reduction in beam intensity. Therefore, if the oscillatory fields are in phase, the minimum of detected beam intensity occurs at the precessional frequency of the neutron. On the other hand, as shown by the author,[9] if the oscillatory magnetic field is provided in two separate segments with a 90 degree phase shift between them, the shape of the resonance curve is that of a dispersion curve with the steepest portion of the slope at the spin precession frequency as shown in Fig. 3. If the frequency of the oscillator is set so that the detected neutron intensity is at the position of the steepest slope, the presence of a neutron electric dipole moment can be detected by successively reversing a strong electrostatic field. If there is an electric dipole moment the torque due to the electric field will increase the precessional frequency of the neutron for one orientation of the field and decrease it for the opposite. At a fixed frequency of the oscillator, this change in the precessional frequency of the neutron spin will then be detectable with high sensitivity as a change in the neutron beam intensity.

The electric field is applied over a length of 196 cm and typically has a value of about 100 kV/cm. The static magnetic field was about 17G and the neutron beam was 89% polarized.

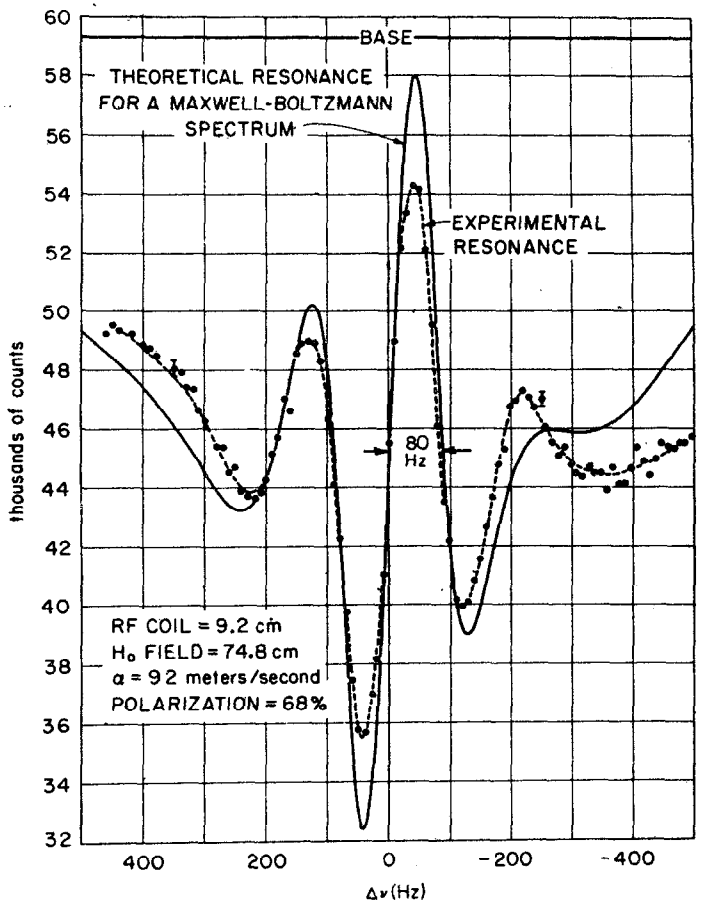

Fig. 3. Typical magnetic resonance with a 90° phase shift between the two oscillatory fields. The calculated transition probability for a Maxwell-Boltzmann distribution characterized by a temperature of 1K is shown in the solid curve. The departure of the experimental curve from the theoretical one when far from resonance is to be expected from the known departure of the beam velocity from Maxwell-Boltzmann distribution.

Great care in the experiment must be taken to avoid spurious effects which could either simulate a non-existent electric dipole moment or mask an existing one. Fortunately, a number of things can be done to eliminate or minimize such spurious effects. The relative phase of the two oscillatory fields, can be shifted from +90 degrees to -90 degrees in which case the slope of the curve at the resonance position is reversed with a consequent reversal of the effect of the electric field on the detected neutron beam intensity. This reversal in the electric dipole moment effects eliminates many possible spurious effects. The phase was reversed once per second. Fortunately, in addition, many of the possible spurious effects cancel themselves due to the parity or time reversal symmetry of the effect. For example, there can be an effect of the electric field upon the frequency due to the force from the electric field pulling the magnets together and thereby changing the magnetic field. However, this effect and many others go as E^2 and consequently cancel on subtracting of results with reversed electric fields. A check on the existence of such E^2 effects can also be obtained from observations at zero electric field. Likewise, to detect magnetic effects from the field reversing mechanism, the leads to the source of potential are reversed at intervals. In addition, measurements are made when no potential is present but when the reversing switches are successively changed.

An important source of a spurious effect was observed at one time in runs of high sensitivity. Whenever there is a spark across the electric plates, the accompanying current produces a slight magnetic field which in turn produces a very small residual change in the permament magnetic field due to the hysteresis of the iron. Even if the neutron counts during the period of the spark are excluded, the residual change in the permanent magnetic field can give a false result. This

trouble, however, can be eliminated if the existence of sparks is recorded and if care is taken to assure that equal amounts of measurements with the fields in opposite directions are utilized in each interval between sparks.

One of the most bothersome spurious effects is that due to motion of the neutrons with a velocity $\vec{v}$ through the electric field $\vec{E}$ since such motion produces an effective magnetic field $\vec{E} \times \vec{v}/c$. This effective magnetic field can then interact with the known neutron magnetic moment to produce an added precession frequency which will look like that due to an electric dipole moment since it will reverse with the reversal of $\vec{E}$. This effect is drastically reduced by making $\vec{E}$ parallel to $\vec{H}$. If exact parallelism could be obtained the effect would be completely eliminated since this spurious magnetic field would be perpendicular to the initial magnetic field with the result that the effect would go as $\vec{E}^2$ instead of $\vec{E}$. However, due to residual magnetism of ferromagnetic materials and magnetic shields, one can never be absolutely certain as to the direction of the magnetic field with the result that $\vec{E}$ and $\vec{H}$ cannot be made exactly parallel and the perpendicular component of $\vec{E}$ can produce an apparent electric dipole effect through the $\vec{E} \times \vec{v}/c$ effective magnetic field. The existence of such an effect, however, can be detected by changing the velocity of the neutrons since the spurious effects should be proportional to the neutron velocity. Consequently, all the data are analyzed in terms of an electric dipole moment and an apparent electric dipole proportional to the neutron velocity. The neutron velocity is altered in either of two ways. In some cases, the velocity is changed by changing the angle of neutron reflection from mirrors and in all cases the measurements are repeated many times with the direction of the neutrons through the apparatus reversed. For this reason, the basic neutron resonance apparatus is fastened to a turn-table which can be rotated to have the neutrons pass through the apparatus in opposite directions. The necessity for experiments at altered velocity greatly increases the running time of the experiment since the $\vec{E} \times \vec{v}/c$ effect must be measured with equal precision to that desired for the neutron electric dipole moment.

The results of the most recently completed measurements at the ILL are

$$\mu_E/e = (0.4 \pm 1.5) \times 10^{-24} \text{ cm}, \quad |\mu_E/e| < 3 \times 10^{-24} \text{ cm}. \qquad (5)$$

In other words, the neutron electric dipole moment, if it exists at all, is less than 3×10^{-24} cm.

The results of the above experiment have recently been confirmed and extended in Leningrad by Altarev, et al.,[10] who used a resonance experiment with neutrons stored in a double neutron bottle, as discussed briefly above and in greater detail below. The electric fields in the two halves of the double bottle are in opposite directions to provide first order cancellation of magnetic field fluctuations. A schematic diagram of their apparatus is shown in Fig. 4 and a typical resonance curve is shown in Fig. 5. Their final limit was

$$|\mu_E/e| < 1.6 \times 10^{-24} \text{ cm}. \qquad (6)$$

The small size of the above limits can be made apparent in several ways. Although nuclear physicists are accustomed to dealing with 10^{-24}, for them it is usually in units of cm^2. If 10^{-24} cm is squared to be in the same units it is 10^{-48} cm^2. The small size of the above limit can also be appreciated by noting that a μ_E/e of 10^{-24} cm corresponds to such a small bulge of the positive electric charge in the upper hemisphere of the neutron that even if the neutron were scaled up to the size of the earth the bulge would be only 0.01 cm.

The most relevant significance for the above results, however, is by comparison with the many theoretical calculations. Most theories that

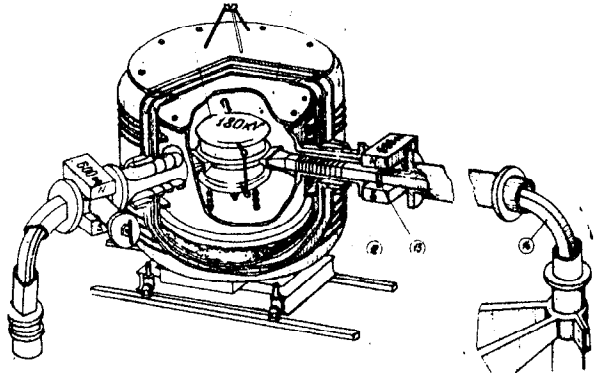

Fig. 4. General view of the Leningrad double bottle neutron magnetic resonance spectrometer.

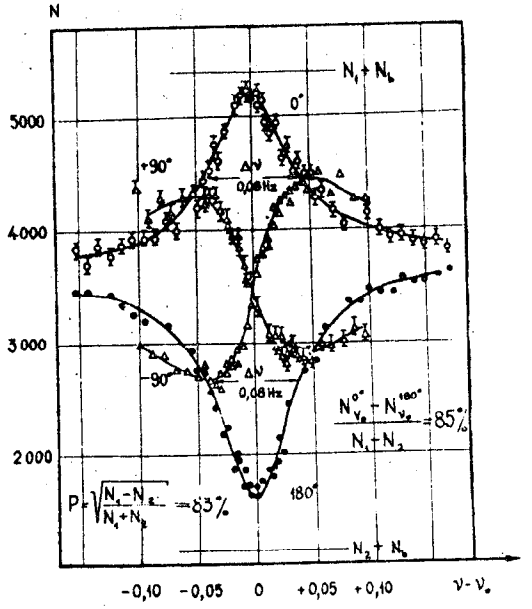

Fig. 5. Typical resonances with Leningrad Spectrometer

account for the CP violating decay of the K_L^o yield non-zero values for the neutron electric dipole moment. The predictions of these theories are shown in Fig. 6. Each lettered block in the figure corresponds to a different theory. It can be seen that the present limit of 1.6×10^{-24} cm already causes severe difficulties for many theories that predicted larger values.

Most of the current theories of the electric dipole moment are gauge theories. The standard model SU(2) x U(1) gauge theory of electro-weak interactions with four quarks, four leptons, three heavy vector bosons and a single Higgs doublet produces no CP violation.[11-13] Various procedures have been adopted to account for the observed CP violation in K^o decay and most of these predict non-zero values for the neutron electric dipole moment. (a) Kobayashi and Maskawa[1] and others[14] increase the number of quarks from four to six or more. (b) Weinberg[12] and others[15,16] increase the number of Higgs doublets to two or more. (c) Others[17] increase the number of vector bosons by going beyond the group SU(2) x U(1). (d) In some theories a CP violating term is added to the Lagrangian of quantum chromodynamics and the current algebra consequences are evaluated.[18] Most of these theories are in the category of milliweak theories since the CP violating interaction is approximately 10^{-3} times the ordinary weak interaction. In the case of models with additional quarks the factor of 10^{-3} arises from the smallness of the mixing angle connecting the new quarks with the old and μ_E/e is predicted[14] to be about $10^{-30\pm1}$ cm. On the other hand, theories with extra Higgs bosons acquire the 10^{-3} factor from the heavy masses of the extra particles and predict μ_E/e to be approximately 10^{-24} cm.[12,15,16] Other theories[17,18] have adjustable constants and encompass values including 0 and 10^{-24} cm or larger.

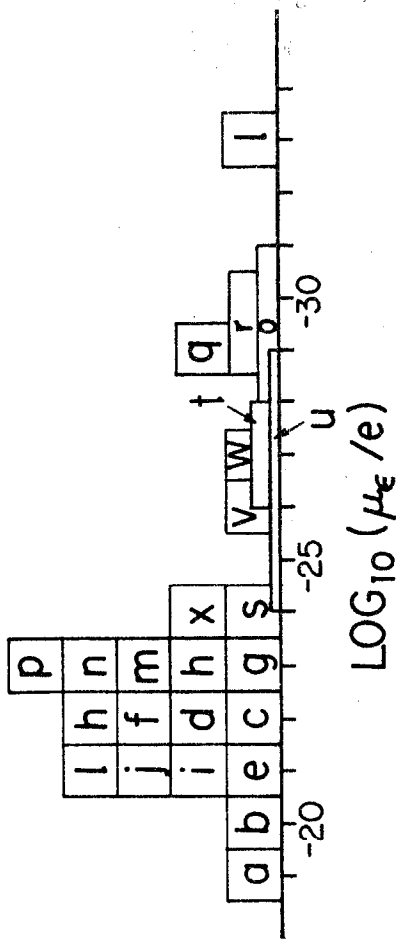

Fig. 6. Theoretical predictions of the neutron electric dipole moment. Each lettered block corresponds to a different theory with the references to the different theories being given elsewhere.[7,8] Normally, the rectangle indicating each theory is a square spanning one decade; where authors propose a wider spread, the height of the rectangle is reduced to give all theories equal area.

NEW ELECTRIC DIPOLE MOMENT EXPERIMENTS WITH BOTTLED NEUTRONS

Since the present experimental limit is in the midst of the theoretical predictions, there is a strong incentive for doing even more sensitive measurements and further experiments are planned at ILL, Leningrad and Argonne National Laboratory. At the ILL, R. Golub, W. Mampe, J. M. Pendlebury, N. F. Ramsey, K. Smith, T. Sumner and their associates plan to use bottled ultra cold neutrons. Such an experiment was proposed by the author[19] many years ago but a suitable beam with neutrons below 6 m/sec velocity did not exist at the ILL until recently. The method depends on using ultra cold neutrons of approximately 6 m/sec. These neutrons are led by a neutron conducting pipe into the apparatus shown in Fig. 7. The neutrons will be stored in a cylinder approximately 15 centimeters in diameter and 10 centimeters high with the top plates being metallic--probably beryllium--and the sides of the cylinder being of beryllia insulator. The oscillatory field is applied to the admission and exit tubes so the resonance can be observed by the previously described successive oscillatory field technique. The resonance will be observed in a similar fashion to the neutron beam experiment and observations will be at the steepest point of the resonance curve. The change in beam intensity correlated with the application of an electric field will then be examined to set a limit to the neutron electric dipole moment.

The use of stored ultra-cold neutrons possesses two particularly important advantages. The resonance curve for 30 second storage time of the neutron should be approximately 1300 times narrower than the neutron beam experiment with a corresponding increase in sensitivity. Furthermore, as mentioned earlier, a large fraction of running time in the beam experiment must be devoted to eliminating the $\vec{E} \times \vec{v}/c$ effect. Since it is the average value of $\vec{v}$ that is important, this effect is drastically diminished when the neutrons enter and leave by the same

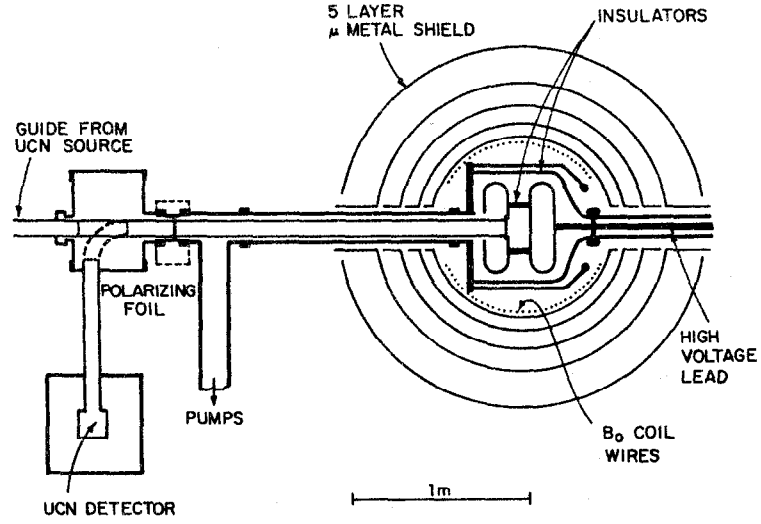

Fig. 7. Schematic diagram of apparatus for measuring the neutron electric dipole moment with bottled neutrons.

exit hole with a 30 second storage time instead of passing through the apparatus at a velocity of 80 m/sec. As a result of the reduced effective magnetic field from $\vec{E} \times \vec{v}/c$, it should also be possible to use a much weaker static magnetic field with an accompanying reduction in the field stability problem. A neutron beam resonance obtained at ILL with bottled neutrons is shown in Fig. 8 for neutrons stored for 20 sec. A comparison of Figs. 3 and 8 shows that the resonance with the bottled neutrons is 4000 times narrower than the previous neutron beam resonance.

Although the new experiment being planned will have the above marked advantages, it must be recognized that the experiment will still be an extremely difficult one. The limit has by now been pushed to such a low value that care must be taken to avoid all possible systematic effects. Although some of these are intrinsically reduced in an experiment with bottled neutrons, other serious problems will remain. For example, problems due to stray magnetic fields (especially when associated with reversals of the electric field) and to magnetic field changes resulting from electrical sparks can be just as serious with bottled neutrons as with neutron beams. These problems have already caused much difficulty in the beam version of the experiment and should be even more formidable in the bottled neutron experiment which seeks to lower the limit for the neutron electric dipole moment by a factor of 100 to 1000.

With an electric field of 30 kV/cm and a multilayer Mumetal or Moly-Permalloy magnetic shield, it should be possible initially to achieve a limit on the electric dipole moment of 10^{-25} cm even with the neutron densities of 0.6 n/cm^3 presently obtained. Two members of the collaboration (R. Golub and J. M. Pendlebury) have proposed[12] the use of cold liquid ^{4}He in a neutron bottle to accumulate much greater neutron densities. When these increased densities are available, a

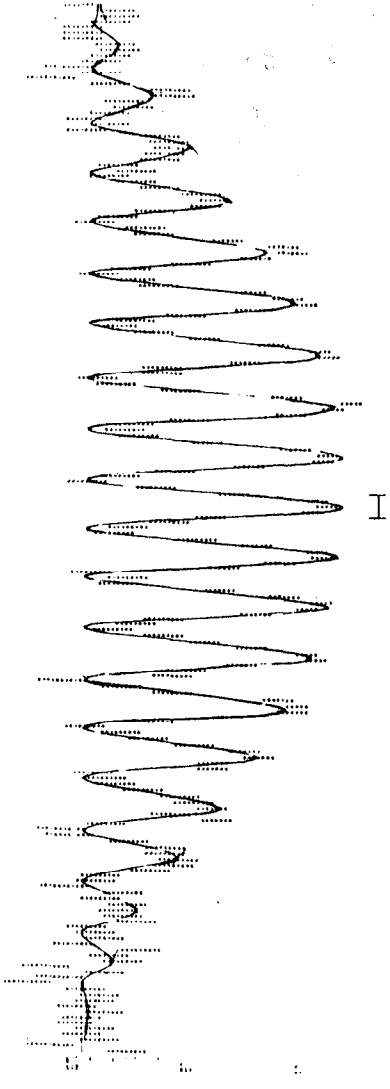

Fig. 8. Neutron magnetic resonance obtained experimentally with bottled neutrons. Two phase coherent but successive radio-frequency pulses are applied and the change in beam intensity is observed as the oscillatory frequency is varied. The observed resonance width of 0.022 Hz is to be contrasted to the 80 Hz width of Fig. 3.

limit of 10^{-26} cm should be obtained. Finally, with the use[13] of ^{3}He in the bottle as a magnetic field monitor a limit of 10^{-27} cm should eventually be obtained but this may also require the use of superconducting magnetic shields.

NEUTRON MAGNETIC MOMENT

The neutron magnetic dipole moment for some years has been the least accurately known of all the nucleon and lepton magnetic moments. The magnetic moments of the negative electron, the positive muon and the proton were all known to a fractional error less than 3×10^{-8} whereas the fractional error in the neutron moment was 1000 times greater or 3×10^{-5}. For this reason a measurement of the neutron magnetic moment has recently been completed at the ILL. Although the neutron beam apparatus at Grenoble was designed with the neutron electric dipole moment exclusively in mind, by coincidence it was also an appropriate design for measuring the magnetic moment of the neutron. Although the magnetic field was low, this disadvantage was more than offset by the large magnetic gap which permits an accurate calibration of the magnetic field because of the smaller inhomogeneities which result from the increased gap. In the previous most accurate experiment[18] the precision of the result was primarily limited by this field inhomogeneity and the consequent difficulty in calibrating the magnetic field accurately.

The magnetic moment was measured by Greene, Ramsey, Mampe, Pendlebury, Smith, Dress, Miller and Perin[20] in an apparatus which was essentially the same as that used in the above neutron electric dipole moment experiment. The 18 gauss magnetic field was calibrated by pumping water at high speed through a high magnetic field storage region to polarize the protons and then having the water pass through the neutron beam pipe at high velocity, with the resonance being observed by the separated oscillatory field method.[9] Proton resonances were taken with water flowing in the neutron guide or with water flowing through an adjacent monitoring tube while neutrons passed through the guide tube as shown in Fig. 9. By judicious alternation of tubes and by interspersed and nearly simultaneous determinations of the neutron and proton resonance frequencies, the field was averaged and drifts were accounted for. Appropriate corrections were made for diamagnetism of the water, nuclear magnetic shielding, etc.

The results of these measurements were:

$$\mu_n/\mu_p = -\ (0.68497935(17))\ (0.25\ \text{ppm})$$

or in nuclear magnetons μ_{NM}:

$$\mu_n/\mu_{NM} = -\ 1.91304184(88)\ (0.45\ \text{ppm}).$$

PARITY VIOLATING ROTATIONS OF THE NEUTRON SPIN

In 1914 F. Curtis Michel[21] pointed out that in principle a neutron spin polarized perpendicular to the neutron's velocity would precess about the velocity vector in a parity violating manner due to the weak force when the neutron passed through matter; a decade later L. S. Stodolsky[22] independently reached the same conclusion.

If ϕ_{pV} is the angle of rotation after passing through a sample of length ℓ, the rotation should be given[15,16,18] by

$$\phi_{pV}/\ell = (n_+ - n_-)/\lambda = -\ 2\pi N_a\ (a_+ - a_-)$$

$$= \sqrt{2}\ (\hbar/Mc)^2 N_a\ GM^2 W$$

where

$$W = ZC_{ne} + [ZC_{np} + (A-Z)\ C_{nn}]\eta$$

and

$$C_{ne} = 1.25\ (2\sin^2\theta_w - \tfrac{1}{2})$$

where n_+ is the index of refraction for the neutron wave with the spin in the direction of motion, ℓ the neutron wave length, N_a the number of

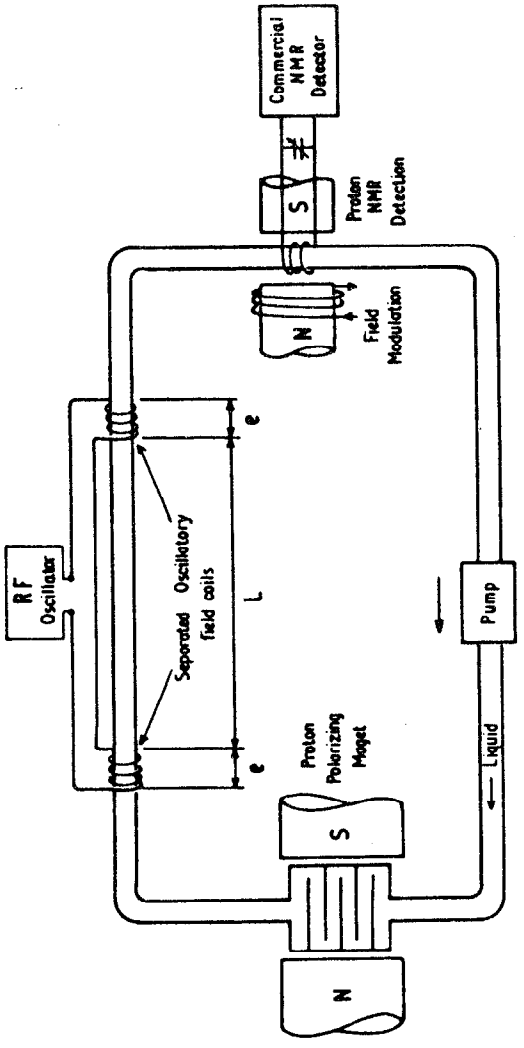

Fig. 9. Flowing water separated oscillatory field magnetometer

atoms/cm^3, a_+ the forward scattering length for the neutron spin in the direction of motion, M the neutron mass, G the Fermi constant = 1.02 x $10^{-5}/M^2$. W is the effective weak current charge where C_{ne} is the effective charge of the neutron electron interaction, C_{np} is the same for the n-p interaction, C_{nn} is the same thing for the neutron-neutron weak interaction and θ_w is the Weinberg angle.

For many years, the papers of Michel[21] and Stodolsky[22] were mostly ignored because of the anticipated smallness of the effect--about 1.4×10^{-8} radian per cm of bismuth traversed. Most experimentalists considered this rotation to be far too small to be observable. Nevertheless, when Stodolsky first called the author's attention to these calculations, it became apparent that the sensitivity for detecting the rotations of the neutron spin in the various neutron electric dipole moment experiments was greater than that required for detecting the parity violating rotations predicted by Michel and Stodolsky.

A proposal was made to the Institut Laue-Langevin to look for such a parity violating rotation in a $^{209}_{83}Bi$ rod of 1 m length where the predicted rotation was 1.4×10^{-6} radian. Bismuth had the attractive feature that its low cross section for slow neutrons permitted the use of long samples and hence provided high sensitivity. This originally proposed ^{209}Bi experiment is in fact just now starting a run at Grenoble. M. Forte of Ispra, Italy, later suggested[13] that due to a low lying 62 eV resonance, a much larger effect should be seen with $^{124}_{50}Sn$. Since the effect being looked for had never been seen before in any substance, it was clearly desirable to look for it first where it should be large. Furthermore, the effect proposed by Forte with ^{124}Sn should have been big enough to be seen with a weaker neutron beam and consequently could be looked for earlier.

As a result, Forte joined the group that made the original proposal and a search for the effect in $^{124}_{50}Sn$ was started at the end of the

calendar year 1979. By the time the experiment was actually to begin, Blayne Heckel, the Harvard graduate student doing most of the work, raised serious doubts as to whether there should be enhancement in ^{124}Sn; however, there were sufficient doubts, both about the theory and about the criticism of the theory that it seemed best to proceed with the experiment in any case.

A schematic diagram of the apparatus is shown in Fig. 10. Neutrons are polarized and analyzed by curved stacked magnetized foils. The neutron is left in a particular orientation after passing through the first current sheet and passes through the Sn sample where the spin is rotated by the weak interaction. The neutron passes through the second current sheet into a coil where the orientation of the magnetic field is perpendicular to the field in the first sheet. The neutron then passes to the analyzer. Any spin rotation then changes the number of neutrons transmitted by the analyzer. That the rotation is due to Sn can be seen by the use of the π coil which rotates the spin π radians about the coil axis and hence converts an increase in intensity to a decrease and vice versa if the Sn is in position 1. On the other hand, if the sample is in position 2 there is no change in intensity when the π coil is turned off or on.

Runs were planned both with a ^{124}Sn sample and with an ordinary Sn sample as a control. The result of the experiment by Forte, Heckel, Ramsey, Green, Greene, Pendlebury, Sumner, Miller and Dress[17] was no observable rotation of the neutron spin in the ^{124}Sn sample but, surprisingly, a significant rotation in the ordinary Sn sample being used as a control. The observed parity violating rotation of the neutron spin on passing through the ordinary tin was

$$\phi_{pv}/\ell = (+4.95 \pm 0.93) \times 10^{-6} \text{ rad/cm}$$

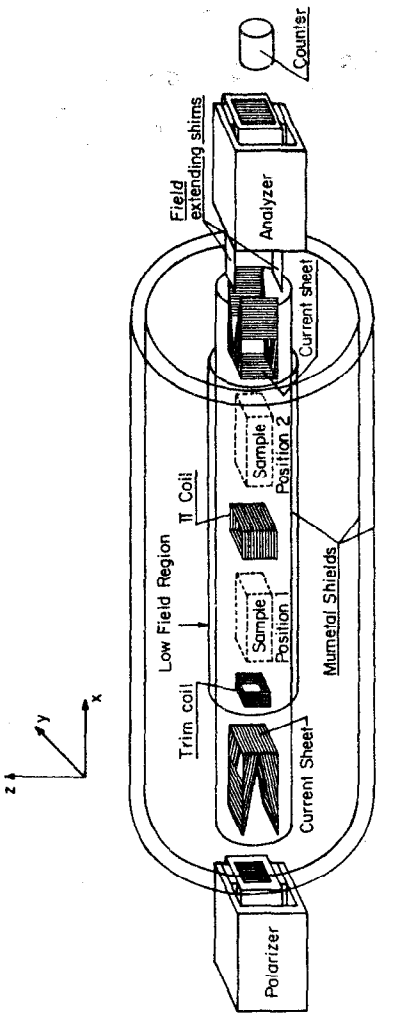

Fig. 10. Schematic diagram of the apparatus used to measure the parity violating rotation of the neutron spin due to the weak interaction.

Although this was only a five standard deviation effect, it was convincing and an abstract giving this result was published.[24]

After this unexpected result was obtained, the group decided the effect was possibly attributable to the 7.7% of ^{117}Sn in the ordinary Sn sample, since the neutron capture γ rays in the isotope also show a surprising large parity anomaly. Therefore, this spring, a run was made with ^{117}Sn and a very large effect was seen:

$$\phi_{pV}/\ell = (+36.8 \pm 2.7) \times 10^{-6} \text{ rad/cm}.$$

Although this large observation fully confirms the measurement with ordinary Sn, it is not of exactly the correct size for all of the ϕ_{pV} in ordinary Sn to be due to ^{117}Sn. This suggests that there may also be a contribution from ^{119}Sn, but this will have to be confirmed in later experiments.

The ^{209}Bi experiment is now just starting. With ^{209}Bi, the neutron-electron interaction will play a larger role. Since there is no nearby nuclear resonance, the theoretical interpretation of the observed results should be less dependent on nuclear theory complications. During the next few years, measurements of this new effect will be made on different materials with varying ratios of neutron, proton and electron constituents. It is hoped that by the study of the results with various materials, one can eventually measure separately the effects of the neutral and charged current. A particularly interesting substance to measure should be parahydrogen where complications of nuclear structure should be a minimum.

REFERENCES

1. E. Rutherford, Proc. Roy. Soc. A97, 374 (1920).
2. E. M. Purcell and N. F. Ramsey, Phys. Rev. 78, 807 (1950).
3. N. F. Ramsey, Phys. Rev. 109, 225 (1958).
4. T. D. Lee and C. N. Yang, Phys. Rev. 105, 1671 (1957).
5. C. S. Wu, E. Ambler, R. W. Hayward, D. D. Hoppes and R. P. Hudson, Phys. Rev. 105, 1413 (1957).
6. J. H. Christenson, J. W. Cronin, V. L. Fitch and R. Turlay, Phys. Rev. Letters 13, 138 (1964).
7. W. B. Dress, P. D. Miller, J. M. Pendlebury, P. Perrin and N. F. Ramsey, Phys. Rev. D15, 9 (1977).
8. N. F. Ramsey, Physics Reports 43, 400 (1978).
9. N. F. Ramsey, Molecular Beams, Oxford University Press (1956).
10. I. S. Altarev, Yu V. Barisov, A. B. Brandin, A. I. Egerov, V. F. Ezhov, S. N. Ivanov, V. M. Lobashov, V. A. Nazarenko, G. D. Porsev, V. L. Ryabov, A. P. Serebrov, and R. R. Taldaev, Leningrad Nuclear Phys. Institute, Preprint 430, 1 (1978).
11. M. Kobayashi and K. Maskawa, Prog. Theor. Phys. 49, 652 (1973).
12. S. Weinberg, Phys. Rev. Letters 37, 657 (1976).
13. L. Wolfenstein, Bull. Am. Phys. Soc. 25, 10 (1980).
14. D. V. Nanopoulos, A. Yildiz and P. H. Cox, Annals of Physics 126, (1980) and Phys. Letters 87B, 53 (1980).
15. T. D. Lee, Phys. Reports 9C, 143 (1974).
16. E. Eichten, K. Lane and J. Preskill, Phys. Rev. Letters 45, 225 (1980).
17. R. Mohapatra and J. C. Pati, Phys. Rev. D11, 566 (1975).
18. R. J. Crewther, P. DiVecchia, G. Venezianno and E. Witten, Phys. Letters 88B, 123 (1979).
19. V. W. Cohen, N. F. Corngold and N. F. Ramsey, Phys. Rev. 104, 283 (1958).
20. G. L. Greene, N. F. Ramsey, W. Mampe, J. M. Pendlebury, K. Smith, W. B. Dress, P. D. Miller and P. Perrin, Phys. Rev. D20, 2139 (1979).
21. F. Curtis Michel, Phys. Rev. 133B, 329 (1964).
22. L. S. Stodolsky, Phys. Lett. 50B, 352 (1974).
23. M. Forte, private communication and Inst. Phys. Conf. Ser. 42, 86 (1978).
24. M. Forte, B. Heckel, N. F. Ramsey, K. Green, G. Greene, M. Pendlebury, T. Sumner, P. D. Miller and W. B. Dress, Bull. Am. Phys. Soc. 25, 526 (1980).

A REVIEW OF EXPERIMENTS ON CHARMED PARTICLE LIFETIMES

J.H. Mulvey

Department of Nuclear Physics, University of Oxford, UK

1. INTRODUCTION

The lifetimes, branching ratios, decay modes, masses and other properties of charmed particles have a bearing on several fundamental questions of physics. These have been reviewed in the lectures by Harari and Hitlin printed elsewhere in these Proceedings. An accurate measurement of the lifetime, together with the leptonic branching ratio, is required for the determination of Kobayashi-Maskawa[1] mixing angles, which contain clues on the symmetry breaking mechanism responsible for fermion masses. The decay modes also provide another window on the character of the quark-gluon interaction and its description in terms of QCD.

There are several experimental approaches to the study of charmed particles produced on a fixed target:

(i) Bump Hunting. The existence of many decay modes, high multiplicities, missing neutrals and severe combinatorial smearing makes identification difficult and inefficient.

(ii) Leptonic Trigger. Parent identification is difficult; if an efficient muon detector is used little information on other decay products survives.

(iii) Decay vertex detection and parent identification. Both are essential for lifetime determination and also constitute an effective method for study of other properties, including the spectroscopy of higher mass states.

This review surveys recent experiments aimed at a determination of mean lifetimes and, in particular, considers the performance of some current and proposed techniques for the detection of short-lived particles.

2. THE DETECTION OF SHORT-LIVED PARTICLES

The experimental difficulties of decay vertex detection--in current experiments this usually means visual detection--can be illustrated by the following considerations.

The short-lived particles of "old" physics were easily seen in a bubble chamber. The K^o-meson, with a mean lifetime, τ, of $0.9\ 10^{-10}$s, has a mean flight-path, ℓ, given by:

$$\ell = \gamma\tau\beta c = \frac{p}{m}c\tau \sim \left(\frac{p}{m}\right) \times 3 \text{ cm};$$

where γ, β, and c have their usual meanings, p and m are the particle momentum and mass.

The charmed particles of "new" physics have mean lifetimes $\sim 10^{-13}$s (e.g., the D^o) and so flight-paths before decay, $\ell \sim \left(\frac{p}{m}\right) \times 30\mu m$. This reduction of scale by three orders of magnitude creates big difficulties for all techniques except for the photographic emulsion where the spatial resolution is more than adequate but the data are not easily accessible. For the heavier flavours, bottom or top, lifetimes may be even shorter.

However, a sizeable amplification seems available in the $\left(\frac{p}{m}\right)$ factor. A D^o of 2 TeV would travel a mean distance of $\sim$3 cms. But the gain in visibility of the decay with increasing momentum is not as great as might be expected.

The main factors determining visibility can be summarised as:

(i) Track Element Size (b, in μm)

For example grain diameter in photographic emulsion, or bubble diameter. The mean gap length is also important and should not be too large (say $\lesssim 4b$) or long gaps may frequently fake short-lived neutrals. These are the principal detector dependent factors determining the visibility of a decay vertex near the production point, and so limiting the sensitivity to short flight paths.

(ii) Scan Procedures

The difficulty of scanning large volumes of photographic emulsion to find the decays of neutral particles may lead to inefficiencies which increase with flight path. Track following of charged secondaries from the interaction, or following back from downstream detectors, is usually more efficient.

(iii) Production Process

This determines the momentum, $(\frac{p}{m})$, the multiplicity, n, the yield and whether production is single or associated. In associated production the efficiency for detection of the second decay is usually higher and can be more independent of lifetime and decay mode.

A crude characterisation of the performance of different devices for visual detection of a decay vertex with reasonable efficiency - say greater than ~30% - can be obtained by the following considerations.

2.1 Primary Vertex Confusion

Clear visibility of the decay vertex illustrated in Fig. 1(a) requires the flight path length to be greater than ℓ_c, the distance downstream of the production vertex which is obscured by tracks of particles in the forward cone. (In addition, for neutral decays ℓ must be greater than a few times the mean gap length.) To a rough approximation:

$$\ell_c \propto nb \quad ;$$

also

$$\ell_c \propto \frac{p}{p_T} \quad ,$$

where p_T is the average transverse momentum. The latter factor determines the forward collimation. So, clear visual observation of the

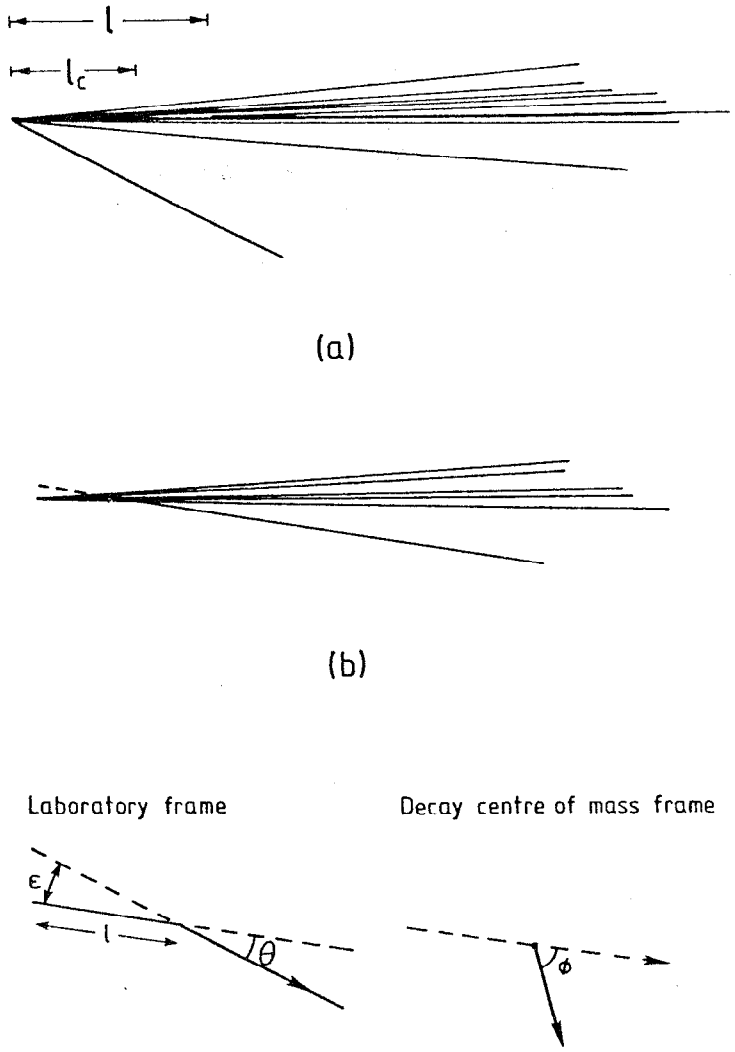

Fig. 1. Diagrams to illustrate vertex detection

decay vertex requires proper flight times, t, given by:

$$t \gtrsim K \left(\frac{m}{p_T}\right) \text{ nb}$$

where the constant K is characteristic of the production process rather than of the detection method. In the case of production by 340 GeV/c pions on hydrogen[2], for example, $K \sim 0.01$ (with b in μm); but a much smaller effective K may apply in the case of coherent $D\bar{D}$ production by photons (see Section 5). The point to note is that, in first approximation, the lower limit on proper time of flight is independent of the charmed particle momentum. Indeed the main reason for going to high energy incident particles may be to obtain higher yields, in spite of the slowly increasing confusion due to the logarithmic rise in n. Production at high p_T aids detection by taking the decay vertex out of the forward cone.

2.2 Kink Detection

A decay is often first noticed because the track of one of the decay products appears not to start at the production point (Fig. 1(b) and 1(c)). The perpendicular distance, ε, from the production point to the projected line of the secondary can also be used as a measure of the proper flight time.

$$\varepsilon = \ell \sin\theta$$

and

$$\tan\theta \sim \frac{1}{\gamma} \tan\frac{\phi}{2}$$

where φ is the centre of mass decay angle. This holds provided $\gamma > 1$ and the secondary is relativistic in the decay centre of mass. If the decay is isotropic in the centre of mass then:

$$\theta \sim \frac{1}{\gamma}$$

and

$$\varepsilon \approx ct.$$

As an approximate guide for efficient detection of a second vertex $\varepsilon \sim 3\sigma$, where σ is the error on a position measurement. For reasonable efficiency of visual detection $\sigma \sim 3b$, so

$$t \gtrsim \frac{3b}{c} \approx b(\mu) \times 10^{-14} \text{sec.}$$

Decays found in this way will not always have clearly visible vertices but accurate measurements on the tracks may reduce the uncertainty in ε by up to an order of magnitude and so may identify the accompanying secondaries of the decay.

Certain experiments rely on such measurements to detect a decay vertex; for example the attempts to set limits on the lifetime of particles produced and decaying within the vacuum pipe of an e^+e^- collider. These considerations show that the intrinsic position measurement error is the determining factor and production at higher momenta will not help (unless the parents emerge from the vacuum pipe).

2.3 Summary

The main factor determining the visibility of the decay vertices of short-lived particles is, not surprisingly, the size of the basic track element: bubble, grain or streamer. The increased flight path of high momentum parents does not prove to be much of an advantage; the character of the production process and decay kinematics make the detection efficiency almost independent of parent momentum. Table 1 gives rough performance characteristics of some detectors used in recent experiments. In spite of the possible improvement of resolution obtainable in bubble chambers through the use of holography (Section 5) there seems little chance of rivalling the photographic emulsion if proper flight-times in

the region of 10^{-15}s. to 10^{-14}s. are to be detected.

TABLE 1

ORDER OF MAGNITUDE PERFORMANCE FACTORS FOR DETECTORS USED IN RECENT EXPERIMENTS

Detector	Track Element Diameter (μm) b	Proper Time for Efficient Visual* Detection of Decay (10^{-14}s). $t_{min} \sim \frac{3b}{c}$	Confusion Length (Experiment Dependent). (mms)
Photographic Emulsion	0.5		0.01
LEBC[2] (1 Litre Hydrogen Bubble Chamber)	40		2 → 4
Streamer Chamber[4]	150		(Vertices found by measurement)
BEBC	500		10 → 30

* Measurement and track fitting may reduce this limit by up to a factor 10.

As an illustration of these considerations, Fig. 2(a) shows the appearance of an associated production event, D^0 and Λ_c^+, in a bubble chamber with 40μ bubbles. Perhaps this interpretation is rather more striking when one looks at Fig. 2(b) which is a drawing of the actual event, found in a photographic emulsion (Experiment WA58[3]).

3. A SURVEY OF RECENT EXPERIMENTS ON CHARMED PARTICLE LIFETIMES

As earlier reviewers[5] have noted, the main development of importance over the past year or two is the use of hybrid systems in which the spatial resolution of the detector is complemented by a

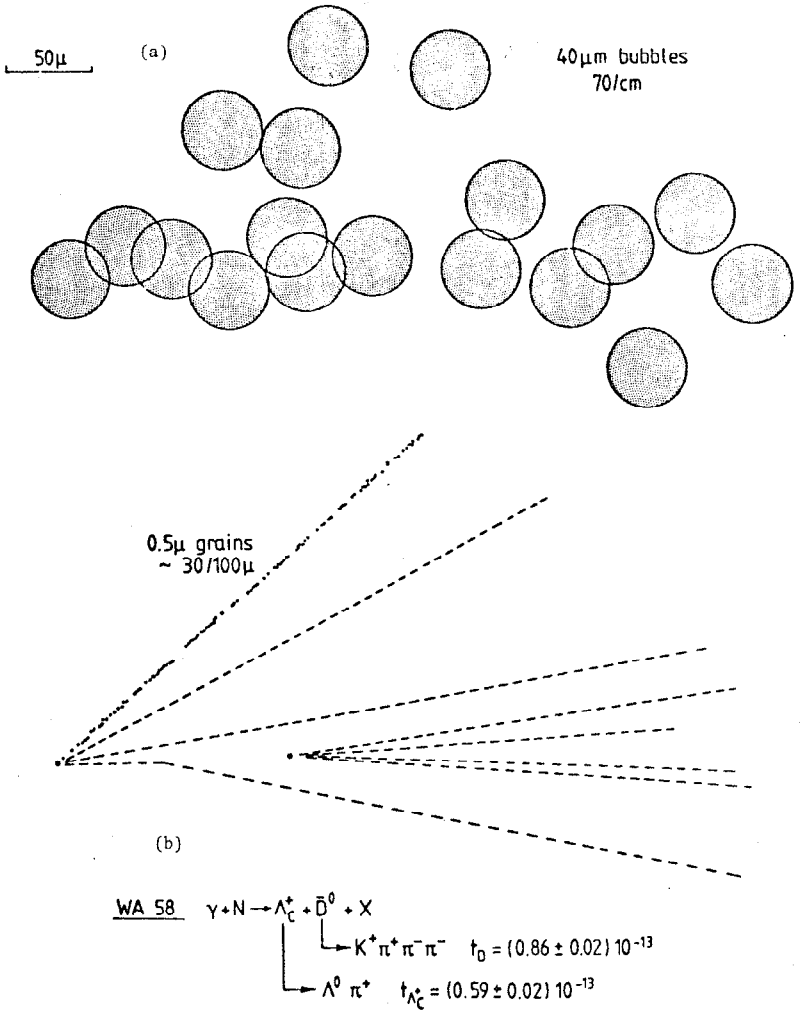

Fig. 2. An associated production event: (a) drawn as it might appear in a bubble chamber with 50 μm bubbles; (b) actual event as seen in photographic emulsion by experiment WA58[3].

powerful downstream spectrometer providing information on the decay products and so enabling the parent particle momentum and identity to be obtained. These experiments thus go beyond the early stages of observation and order of magnitude lifetime estimation to a first quantitative measurement of the lifetimes of specific charmed states.

This review of experiments is divided into two parts: first a brief summary is given of some of the experiments with little or no spectrometer information and secondly a description of four more recent experiments in which parent identification has been possible.

3.1 Experiments Without Parent Identification

Table 2 lists experiments which established the existence of short-lived particles with lifetimes in the 10^{-14}s. to 10^{-12}s. region. The experiment performed by Burhop and his collaborators[6] was the first to use a downstream system of electronic detectors to record the tracks of secondaries and so predict the location of interactions in a photographic emulsion stack. In other cases a muon identifier was used to select events or trigger a streamer chamber. The LEBC experiment[2], with an incident beam of 340 GeV/c pions, obtained a yield of associated production events on hydrogen consistent with a cross-section in the region of 40 μb. This and the streamer chamber experiment,[4] which obtained similar results, were essentially tests of new techniques for the detection of short-lived particles.

3.2 Experiments With Parent Identification

Four experiments able to detect short-lived particles and with spectrometer information making identification possible in favourable cases are summarised in Table 3. All used photographic emulsion as the production target. In the first three the charmed particles are produced

TABLE 2

EXPERIMENTS WITHOUT PARENT IDENTIFICATION

Experiment	Production Process	Detector	Number of Charm Candidates	Estimated Proper Flight Time or Mean Lifetime (10^{-13}s.)
Niu et al[7] 1971	Cosmic	Emulsion	1	0.2 → 0.4
Burhop et al[6] 1976, FNAL	Neutrino	Emulsion & Spectrometer	1	∿1
Japanese Collaboration[8] 1978/1979, FNAL	400 GeV/c Protons	Emulsion	7 (2 pairs)	0.2 → 10
Ballagh et al[9] 1980, FNAL	Neutrino	15' Bubble Chamber & EMI	4 (μe events)	0.6 → 10 (neutral) 1 → 10 (charged)
LEBC[2] 1980, CERN	340 GeV/c Pions	20 cm Hydrogen Bubble Chamber & Interaction Trigger	28 (10 pairs)	∿5 for σ ∿ 40 μb
Yale-FNAL[4] 1980	350 GeV/c Protons	24 atm. Neon-Helium Streamer Chamber & Muon Trigger	8	∿10 for σ ∿ 30 μb (charged)

TABLE 3

EXPERIMENTS WITH PARENT IDENTIFICATION

Experiment	Production Process	Vertex Detector	Downstream Detectors	Number of Charm Candidates		
				Neutral	Charged	Total
WA17[10] CERN	Neutrino	Emulsion	BEBC + EMI	3	5	8
E564[11] FNAL	Neutrino	Emulsion	15' Bubble Chamber + EMI	-	1	1
E531[12] FNAL	Neutrino	Emulsion	Spectrometer	10*	12*	22*
WA58[3] CERN	Tagged Photon	Emulsion	Omega-Spectrometer	3	7	10 (5 pairs)

* Identified parents only. These include 4 events identified since publication.[16]

by exposure to wide band neutrino beams, while in the fourth there was associated production by a high energy, tagged photon beam.

3.2.1 Experiment WA17

Photographic emulsion was exposed to the CERN wideband neutrino beam (average energy 30 GeV) at a position just in front of the beam entrance window of BEBC, as shown in Fig. 3. Behind BEBC is a two plane EMI (external muon identifier). The scintillation counter C provided a time correlation with the EMI and tagged the frame number of events occurring in the emulsion stack in anti-coincidence with the veto counter, V, in front of the stack. The location of events in the emulsion was predicted from track measurements in the bubble chamber and data from the MWPC. BEBC was filled with hydrogen and operated with a magnetic field of 35 kg.

31.5 litres of emulsion were exposed and a total of 206,000 pictures taken. These were scanned for event configurations in which at least three particles entered BEBC in directions diverging from a possible interaction point within the emulsion stack. At least one of these particles was required to have a momentum greater than 3 GeV/c. A candidate was found on about 1 in 40 pictures and these were all measured to obtain a prediction for the interaction vertex position. About 760 events expected to originate in the emulsion were searched for by a volume scan in the predicted region. 214 interactions were found, of which 169 were charged current events. The low efficiency (30%) for finding events was due largely to the low sensitivity of the photographic emulsion manufactured by Ilford; the grain density for minimum ionisation varied from 8 to 20 per 100μ.

The search for short-lived decays was carried out by following all minimum ionising, forward hemisphere tracks for at least 5 mms. Neutral decays were sought by a volume scan within a forward cone 30° extending

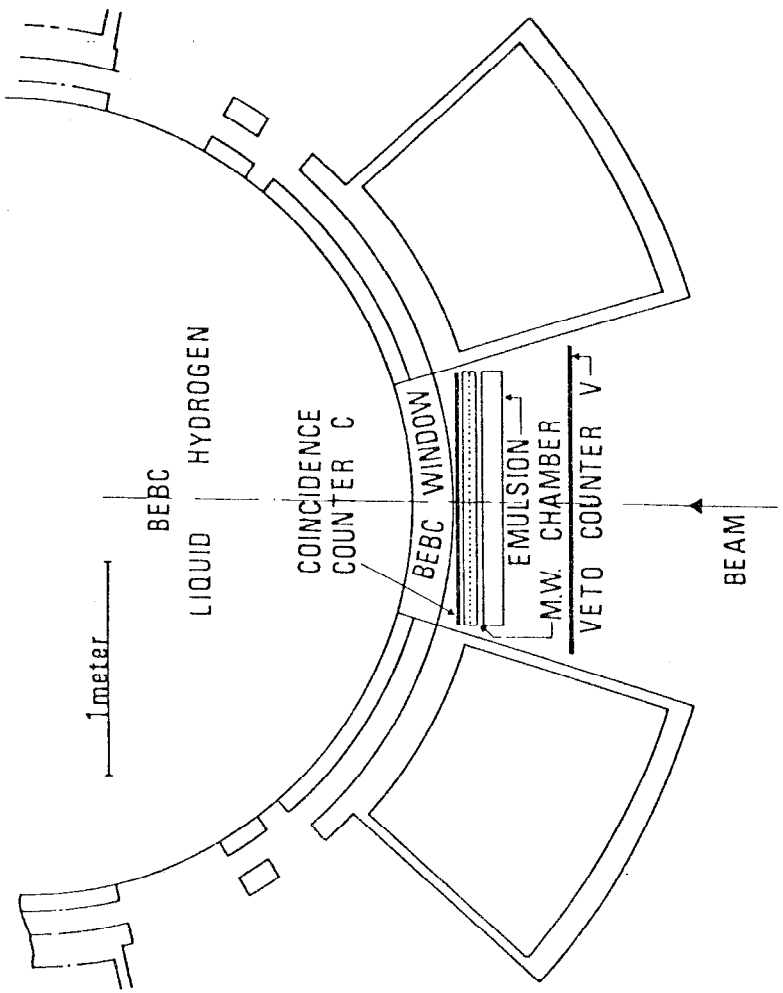

Fig. 3. Layout for experiment WA17.

up to 2 mms from the production vertex. No quantitative estimates of efficiency have been published.

Eight charmed particle candidates were found: 5 charged decays consisting of 3 with 3 prongs and 2 single prong; 3 neutral decays, all with 2 prongs.[10]

In only one event could the parent be identified. The interpretation is: $\Lambda_c^+ \to p + K^- + \pi^+$, based on identification of the proton, which makes an elastic scattering in the bubble chamber, and the K^-, through ionisation measurement. The mass obtained for the Λ_c^+ was 2260 ± 20 MeV and for the proper time of flight of the Λ_c^+ $(7.3 \pm 0.1)\ 10^{-13}$s.

An estimate of mean lifetime was obtained from the 3 neutral decays, which can be assumed to be D° or $\bar{D}^\circ$, by an analysis based on the relation $\varepsilon = ct$, since this is independent of the unknown parent momentum. The result obtained was:

$$\tau^\circ = (0.53^{+0.57}_{-0.25}).10^{-13}\text{sec.}$$

However, this result depends on the assumptions that both parent and secondaries (in the decay centre of mass) are relativistic and that there is negligible scanning bias (e.g., no loss of D° with long decay paths).

The charged decays (other than the identified Λ_c^+) were similarly treated although here there is ambiguity in possible parent identity between $D^\pm$, $F^\pm$ and Λ_c^+. Including a 3 prong decay found in a previous experiment by the same group, the lifetime obtained for this sample of 5 charged decays was:

$$\tau^\pm = (2.5^{+2.2}_{-1.1}).10^{-13}\text{s.}$$

3.2.2 Experiment E564

This experiment used the Fermilab 15' bubble chamber to detect particles emerging from a stack of photographic emulsion placed inside

the chamber liquid. The emulsion was enclosed in a stainless steel box, 0.6 cm wall thickness, located in the entrance "nose cone" of the bubble chamber. The chamber was filled with deuterium, equipped with a two plane EMI and the exposure was made in the single-horn wide-band neutrino beam. Twenty-two 1 litre stacks of cryogenic sensitised BR2 photographic emulsion manufactured in the USSR were exposed in this way and about 320,000 pictures taken.

The analysis of this experiment is not complete but one very interesting event has been published.[11] It is shown in Fig. 4 and interpreted as the production (in a charged current interaction) and subsequent decay of an F^+ meson. The identification was based on a 3C fit to the hypothesis: $F^+(2030) \rightarrow \pi^+\pi^+\pi^-\pi^0$ using information from the conversion of two photons assumed to originate from the π^0. Treating the F^+ mass as unknown a 2C fit gave its value as (2017 ± 25) MeV. The proper time of flight for the 50 μm path was $1.5.10^{-13}$sec.

3.2.3 *Experiment E531*

In this experiment the photographic emulsion was combined with a powerful downstream spectrometer providing accurate event location and detailed information on the decay products. The latter enables identification of a high proportion of the charmed parents, so states with different mean-lives can be distinguished and proper flight times determined. The success of E531 has set a standard by which to judge future experiments on charmed particle lifetimes.

The layout of the apparatus is shown in Fig. 5. The emulsion stacks are accurately located on a rigid plate mounted in front of a magnetic spectrometer using drift chambers. Time of flight is measured, with ±120 psec accuracy, by scintillator hodoscope planes immediately following the emulsion stacks and after the second set of drift chambers.

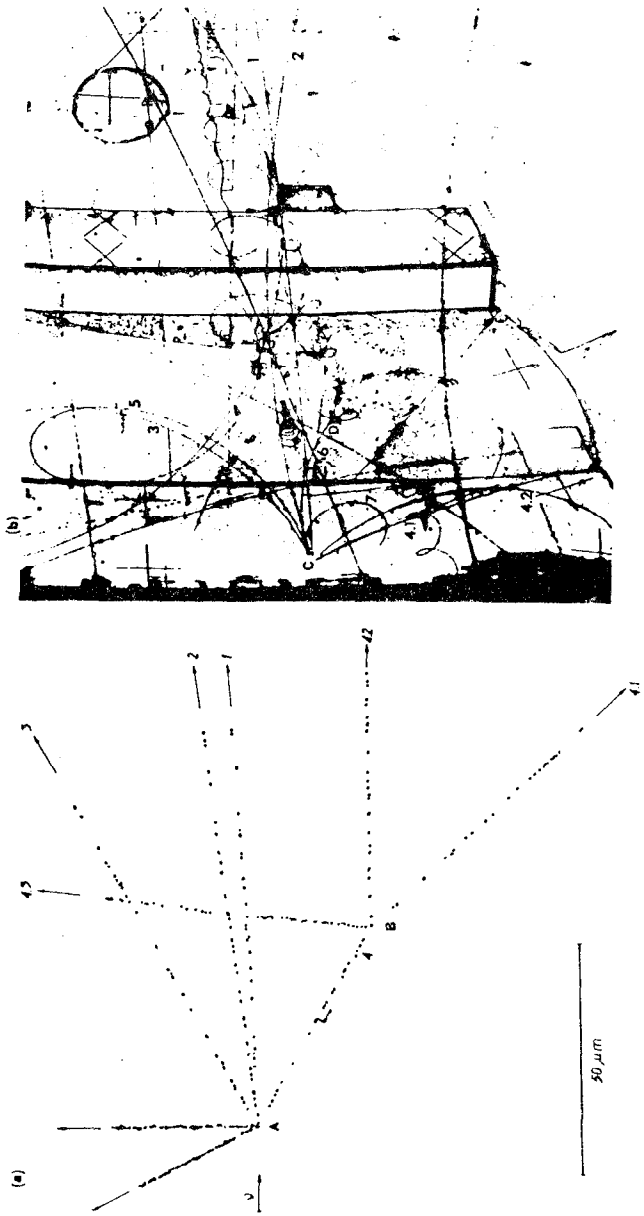

Fig. 4. Event interpreted as $F^+ \rightarrow \pi^+\pi^+\pi^-\pi^0$ in experiment E564.

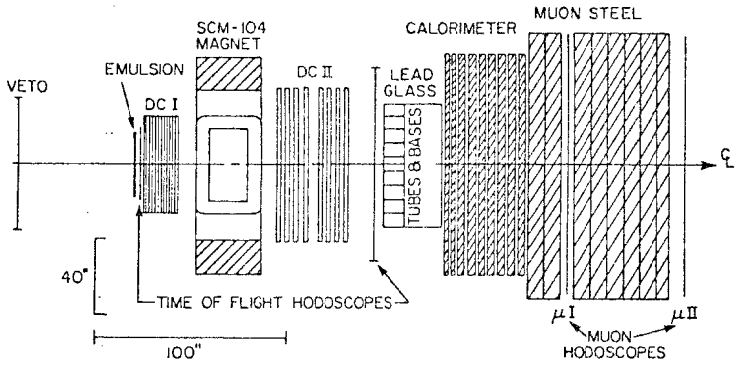

Fig. 5. Diagram of spectrometer for experiment E531.

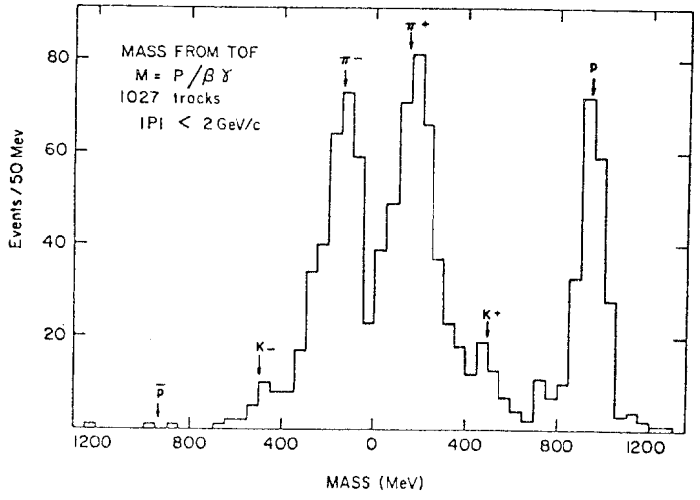

Fig. 6. Mass distribution from experiment E531.

This is followed by a 68 element lead-glass wall, an iron and scintillator hadron calorimeter and, finally, a muon identifier.

Data were recorded when 2 or more charged particles were detected in the time of flight hodoscope downstream of the magnet and in the absence of a signal from the upstream veto counter.

The emulsions, 23 litres, were exposed in two different geometries to the Fermilab wide band neutrino beam. Emulsion pellicles, 600 μm thick were arranged in the top half of the stack with their planes parallel to the incident beam; while in the bottom half, 330 μm emulsion sheets --sandwiching 70 μm polystyrene film-- were placed perpendicular to the beam. The stack dimension along the beam direction was 6 cm. and a fiducial sheet of emulsion was placed immediately downstream of it. This could be changed frequently, so the integrated exposure was low, and its position relative to the emulsion stack and track spectrometer was accurately determined by the marks left on it by Fe^{55} sources embedded in the mounting structure. The emulsions were manufactured by Fuji and the grain density was ~30/100μ for minimum ionisation.

The system's performance in particle identification is illustrated in Fig. 6 showing a mass histogram obtained from time of flight for momenta less than 2 GeV/c. Time of flight gives π/K separation at 1 s.d. up to 3 GeV/c and K/P separation up to 6 GeV/c. Ionisation measurements in the emulsion enable π/K separation to 0.8 GeV/c and K/P to 1.5 GeV/c. The lead-glass blocks are too large to separate the γ's from π^0s of momentum >5 GeV/c but the total energy and direction of neutral particles, including K^0_L, can be obtained.

Of 1077 events predicted and searched for (about 60% of the total data) 685 were found by a combination of volume scanning in the pellicles or track-following-- starting from the fiducial sheet -- in the case of the perpendicularly mounted films.

Decays were sought in two ways. In the pellicles charged tracks were followed for up to 6 mms and unmatched tracks found in the spectrometer were followed back, in the emulsion, towards the production point; a volume scan was made for neutral decays in a cylinder of 0.3 mm radius and 1 mm length from the vertex and, again, these could be found by following back unmatched charged tracks. For the perpendicular emulsion the decays, charged and neutral, were found by the method of following back tracks picked up in the fiducial sheet, using the spectrometer predictions.

A careful study of scan losses has been made for both neutral and charged decays. Vertex confusion causes losses below ~30 μm path length while for neutrals the volume scan in the pellicles is inefficient at long path lengths. These effects have been evaluated by estimation of confusion lengths in a sample of events and from the number of neutral decays (2) missed in the volume scan but found by following back tracks picked up in the spectrometer. The efficiencies obtained, as a function of path length, are shown in Figs. 7(a) and 7(b).

In the 685 events examined 25 multiprong candidate charm decays were found; 10 were neutral decays and 15 charged decays. An additional 24 single prong events were found but some are likely to be scatters and no analysis of these has been published; parent identification is less likely to be possible for such decays in any case.

Including 4 multiprong decays identified since their first publication[12] the collaboration has found[16] 10 D°, 5 $D^{\pm}$, 2 $F^{\pm}$ and 5 Λ_c^+. These are listed, together with their proper flight times, in Tables 4A, 4B and 4C.

Particles for which the identification is made with 90% confidence are underlined. For further details of the parent identification the

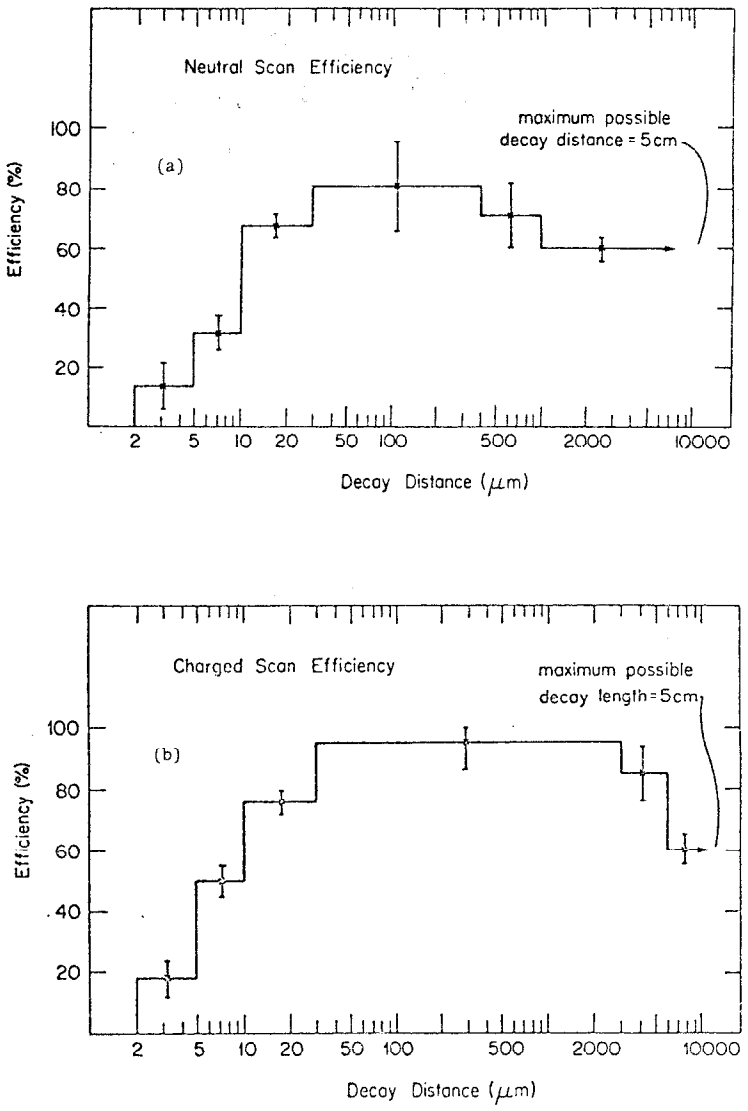

Fig. 7. Charm search efficiencies as a function of decay path E531: (a) neutral parents; (b) charged parents.

TABLE 4A

SUMMARY OF IDENTIFIED $D^\circ/\bar{D}^\circ$ DECAYS

Experiment	Decay	Fit Class or Mass	Flight Path (μ)	Momentum (GeV/c)	Proper Time of Flight (10^{-13}s)
E531	$K^-\pi^+\pi^+\pi^-\pi^-\pi^+$	0C	6.5	19.2	0.02
E531	$K^-\pi^+\pi^+\pi^-\pi^\circ$	3C	41	15.4	0.17
E531	$K^+\pi^-\pi^-\pi^+\pi^\circ$	3C	27	9.2	0.18
WA45	$K^+\pi^+\pi^-\pi^-$	1866 ± 6	123	33.7	0.23
E531	$K^-\pi^+\pi^\circ\pi^\circ$	3C	116	30.1	0.24
E531	$(K^\circ)\pi^-\pi^+$	0C	67	11.3	0.37
WA58	$K^-\pi^+(\pi^\circ)$	0C	267	26	0.65*
WA58	$K^+\pi^+\pi^-\pi^-$	0C	124	9	0.86
E531	$\pi^-\pi^+\pi^+\pi^-\pi^-\pi^+(\pi^\circ)$	0C	126	9.1	0.86
E531	$\pi^+\pi^-(K^\circ)$	0C	326	19.3	1.05
E531	$K^-\pi^+\pi^+\pi^-(\pi^\circ)$	0C	256	12.8	1.24
E531	$K^+\pi^-(\pi^\circ)$	0C	187	6.8(9.5)	1.71(1.2)**
E531	$K^-\mu^+(\nu)$	0C	2,647	38.7(22.8)	4.24(7.2)**

* Mean of two kinematic solutions

** Two solutions to kinematic fit.

NOTE: Decay particles in brackets not observed. For E531 particles underlined have been identified with 90% confidence.

TABLE 4B

SUMMARY OF IDENTIFIED CHARGED DECAYS

	Experiment	Decay	Fit Classification or Mass	Flight Path (μ)	Momentum (GeV/c)	Proper Flight Time (10^{-13}s)
Λ_c^+	E531	$\Lambda^\circ\pi^+\pi^-\pi^+$	3C	40.6	5.73	0.54
	E531	$P\pi^+\pi^-(K^\circ)$	0C	27.7	(2.9 (5.0	0.57*
	WA58	$\Lambda^\circ\pi^+$	(2280)	51	7	0.59
	E531	$K^-p\pi^+(\pi^\circ)$	0C	20.6	2.2	0.70
	E531	$(K_L^\circ)P$	0C	175	6.5	2.10
	E531	$\Lambda^\circ\pi^+\pi^-\pi^+$	3C	221	4.7	3.58
	WA17	$K^-p\pi^+$	2260 ± 20	354	4	7.2
$F^\pm$	E531	$K^+\pi^-\pi^+\bar{K}^\circ$	3C	130	9.7	0.91
	E564	$\pi^+\pi^+\pi^-\pi^\circ$	3C	50	2.4	1.5
	E531	$\pi^-\pi^+\pi^-\pi^\circ$	3C	670	12.3	3.7

* Average of two solutions

NOTE: Decay particles in brackets not observed. For E531 particles underlined have been identified with 90% confidence.

TABLE 4C

SUMMARY OF IDENTIFIED CHARGED DECAYS

Experiment	Decay	Fit Classification or Mass	Flight Path (μ)	Momentum (GeV/c)	Proper Flight Time (10^{-13}s)
$\underline{D}^{\pm}$ WA58	$\pi^+\pi^-\underline{\pi}^-$ (K^0)	OC	94	9	0.73*
E531	$K^-\pi^+\underline{\pi}^+\pi^0$	3C	457	10	2.8
E531	$K^-K^+\pi^+\pi^0$	3C	1,802	17	6.6
E531	$K^-\pi^+\underline{e}^+(\nu)$	OC	13,000	118	6.9
E531	$K^-\pi^+\underline{\mu}^+(\nu)$	OC	2,145	16	8.3
E531	$\underline{K}^+\pi^-\underline{e}^-(\bar{\nu})$	OC	2,307	9.4	15.3*

* Average of two solutions

NOTE: Decay particles in brackets not observed. For E531 particles underlined have been identified with 90% confidence.

reader is referred to the original publication. The lifetime results will be discussed in the next section.

3.2.4 Experiment WA58

This experiment at CERN used the Omega magnet and spectrometer to detect particles emerging from a single emulsion pellicle exposed to a tagged photon beam. The setup is illustrated in Fig. 8. A total of 6,000 emulsion pellicles were "shot," one at a time, into the position shown and each irradiated with $\sim 10^6$ photons of energy in the range 20 GeV to 70 GeV.

During exposure the 600 μm thick pellicles were inclined at an angle of 5°, presenting a maximum path length in the beam direction of ~ 6 mms. The spectrometer includes MWPC for track direction and momentum measurement, Cerenkov detectors, electron and photon detectors. The photographic emulsions, type BR2, were manufactured in the USSR and gave a grain density for minimum ionisation of $\sim 36/100\mu$.

A search was made in the emulsion pellicles in the regions predicted for interactions with three or more charged particles detected in the spectrometer.

The search for charged decays was made by following the tracks for up to 6 mms -- the maximum length available -- and the scan for neutrals extended for a distance ~ 300 μm unless one decay had already been found (associated production) or unmatched tracks had been observed in the spectrometer.

Results have been reported[3] on 5 pairs of short-lived particles found in 1,400 events. Only 5% of the exposed pellicles had at that stage been scanned. No quantitative estimate of efficiencies has been given. The five candidate pairs have decay multiplicities of: (4,1), (2,3), (3,3), (2,1), (3,1); the last two pairs were not associated with a

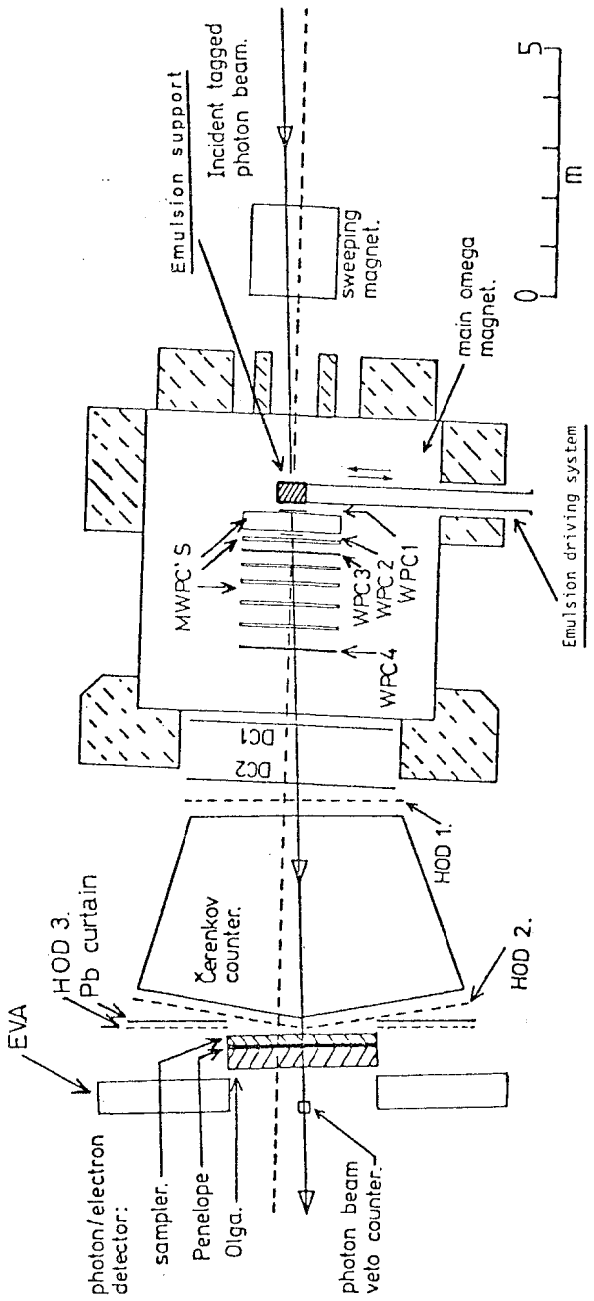

Fig. 8. The Ω-spectrometer used in experiment WA58.

spectrometer trigger and identification cannot be attempted; no fits were obtained for the third pair. In the first event the neutral decay mass is in good agreement with that of the $\bar{D}^0$ and the charged decay fits the Λ_c^+ mass using a Λ^0 detected in the spectrometer. The interpretation of the second event requires the assumption of two undetected neutrals (a K^0 and a π^0) for the D^- and D^0 assignments and gives two solutions for the parent momenta. All four decays are included in the summaries given in Table 4.

In an earlier run the same collaboration found a single neutral decay[13] and also reported two other possible short-lived particle decays at the Tokyo Conference of 1978[14]. After further analysis one of the latter, a 3 prong event, is now believed to be a close electron pair, or trident, while in the other the short apparent path length before decay, ~10 μm, is not significant compared to the errors estimated for the decay vertex location[15]

3.2.5 Biases and Backgrounds

(i) Scanning Losses

Determination of lifetime ideally requires a method with detection efficiency independent of path-length. However, decays after a short path can be missed due to vertex confusion while toward long path lengths the efficiency of volume scanning for neutrals tends to be low and the finite size of the detector becomes an ultimate limit. In experiment E531 a quantitative evaluation of detection efficiencies as a function of path-length has been made and used in the estimation of mean lifetimes.

Some feeling for the path lengths typical of the decays found is obtained from Table 4. The 300 μm limit for neutrals, unaccompanied by charged or shorter neutral decay, seems likely to lead to some loss of D^0 in WA58 as the typical momenta in this photoproduction experiment are

unlikely to be less than those in the three neutrino experiments; similarly the maximum emulsion path of ~ 6 mms may lead to a significant loss of $D^{\pm}$ at long path lengths.

(ii) Analysis

Parent identification is essential, not only to obtain proper flight times but also to distinguish between the different charged states which appear to have quite different lifetimes. The method of estimation based on the intercept ϵ will give rise to an underestimate of proper flight time if decay products not relativistic in the decay centre of mass are included. This is quite probable in the case of secondary kaons or protons from high multiplicity decays.

(iii) Strange Particle Background

K°_{S} decays can form a backgrond for neutral charm decays of charged multiplicity two. A very conservative upper limit for the number of such decays within ~ 3 mms of the production vertices examined in all four experiments is about one. Most of the observed two prong decays are not coplanar with the production point or show too large transverse momentum to be due to K° and the requirement of a mass consistent with the D° mass renders the possible background negligible. The situation for the charged decays used to obtain the lifetimes summarised in the next section is even clearer since all except one are three prong decays. The exception is the particle with a short, 50 μm path length seen in WA58 which has a parent mass of (2060 ± 20) MeV if the Λ° seen downstream is associated with its decay.

(iv) Secondary Interactions

In experiment E531, 13.9 m of charged track has been followed in the search for charmed decays. The E531 collaboration estimates that the number of 3-prong, recoiless interactions in their total sample does not exceed 0.8. If an estimate is made, on a similar basis, of the number of such interactions which might topologically simulate 3-prong decays in all four experiments together, the result is ~ 3. However, the chance that an interaction is included among the identified parents must be small.

The potential background among the neutral sample is more than an order of magnitude less because of the lower yield of stable neutral hadrons and the shorter distances scanned.

4. A SUMMARY OF RESULTS ON CHARMED PARTICLE LIFETIMES

The proper flight times of identified charmed particles obtained in the four experiments described in Section 2 are listed in Tables 4A, 4B and 4C.

In the determination of mean lifetime from such data correction must be made for the loss of events at short path lengths because of vertex confusion or at long path lengths because of the finite effective size of the detector or inefficiency of volume scanning. These factors have been included in the evaluation of lifetimes for experiment E531 which also has much the largest sample of events, all treated in a homogeneous manner. In view of the systematic differences in efficiency it is not correct to combine the events from all four experiments to obtain an overall average and so the results given in Table 5 are those of experiment E531 (including 4 events obtained since the first publication [16]).

TABLE 5

CHARMED PARTICLE LIFETIMES FROM E531[12,16]

Particle	Mass Used (GeV)	Number of Events	Mean Lifetime* τ (10^{-13}s)
Λ_c^+	2285	5	$1.36^{+0.85}_{-0.46}$
$F^\pm$	2030	2	$2.2^{+2.8}_{-1.0}$
	(Including the event of E564)	3	$1.9^{+1.7}_{-0.8}$
$D^\pm$	1868	5	$10.3^{+10.5}_{-4.1}$
D°, $\bar{D}^\circ$	1863	10	$1.01^{+0.43}_{-0.27}$

* Errors obtained from $\Delta\ln$ (Likelihood) = -0.5 ($\sim$1 s.d.)

Consistency of the data with the lifetimes obtained has been checked and found satisfactory for E531. One may next ask are the events found in the other experiments compatible with Table 5?

In the case of Λ_c^+, the event found in experiment WA17 has a proper flight time of 7.2 10^{-13} seconds. The probability of such a value in a sample of 7 is about 3.5% for a mean lifetime of 1.36 10^{-13}s. but rises to $\sim$20% if the mean lifetime is 2.2 10^{-13}s; this is about 1 s.d. higher than the E531 value and is also the mean lifetime obtained by including the WA17 event. Thus, there is no significant discrepancy.

Experiment WA17 estimates a lifetime for the D°:

$$\tau(D^\circ) = (0.53^{+0.57}_{-0.25})\ 10^{-13}\text{s}$$

from 4 events and by a method independent of the parent momentum. This result is consistent with that of E531; however, no allowance has been made for scanning loss and the method of analysis can be subject to a systematic error tending to cause an underestimate of the mean lifetime.

In the case of charged decays the WA17 value is:

$$\tau(\text{charged}) = (2.5^{+2.2}_{-1.1})\ 10^{-13}\text{s}$$

again from 4 events. This is not compatible with the E531 result for $\tau(D^\pm)$; however the parents in WA17 are not identified and are likely to be a mixture of Λ_c^+, $F^\pm$ and $D^\pm$.

The other events are quite compatible with the results of E531.

Before leaving this data, the following points are of interest (see the lectures by D. Hitlin).

(i) The results confirm by direct measurement of lifetimes the evidence for a large difference between the widths of charged and neutral D-mesons obtained from the leptonic branching ratios:

$$\frac{\Gamma(D^\circ)}{\Gamma(D^\pm)} = 3.1^{+4.2}_{-1.4} \quad \text{Mark II}^{(17)}$$

or

$$>4.3\ (95\%\ \text{C.L.})\ \text{DELCO}^{(18)}$$

(ii) The $F^\pm$ and Λ_c^+ lifetimes also appear short compared to that of the $D^\pm$ and closer to the D°-lifetime.

(iii) The naive model for charmed particle decay in which the associated quark is a spectator (Fig. 9(a)) leads to equal lifetimes for D°, $D^\pm$ and $F^\pm$. Observations (i) and (ii) suggest either suppression of the $D^\pm$ decays, through, for example, SU(4) 20-plet dominance in the weak interaction, or enhancement of non-leptonic D° (and Λ_c^+) decays by W-boson exchange (Fig. 9(b)) and of $F^\pm$ decays by weak annihilation (Fig. 9(c)). All these effects may well contribute.

(iv) Of the three $F^\pm$-mesons observed, two decay to final states of pions only and with no $s\bar{s}$ content. The absence of strange quarks in the

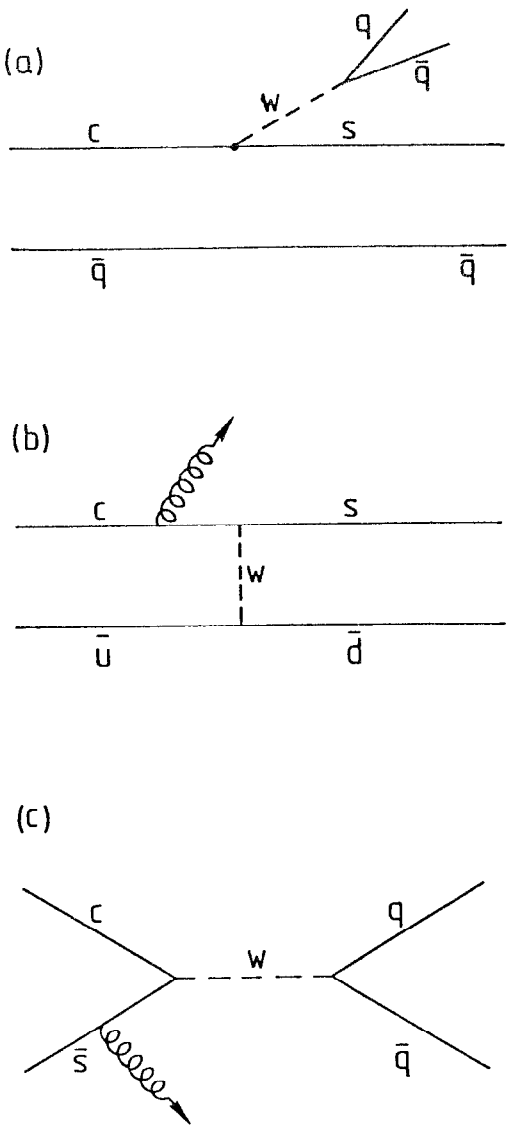

Fig. 9. Diagrams illustrating mechanisms for non-leptonic charmed hadron decay: (a) spectator model; (b) W-exchange; (c) W-annihilation.

$F^{\pm}$ decay products would be natural for a weak annihilation mechanism but not in the spectator model.

(v) Finally, in the presence of conflicting evidence from SPEAR and DORIS[19] on $F^{\pm}$-meson production in e^+e^--annihilation the three emulsion events, taken together with the results reported from the photoproduction experiment[20] in the Ω-spectrometer at CERN, provide the best evidence so far for the existence and mass of the $F^{\pm}$-meson.

5. CURRENT EXPERIMENTS AND FUTURE POSSIBILITIES

5.1 Current Experiments

Experiments which have recently taken data or are due to run within the next year include the following:

(i) The E531 spectrometer is being improved, especially the photon detection, and expects to run again in late 1980 or early 1981.

(ii) There will also be another run for E564, using the Fermilab 15' bubble chamber.

(iii) At CERN a new experiment (NA19) using photographic emulsion as detector coupled with an efficient muon identifier completed data taking in July 1980.[21] The layout is shown in Fig. 10. The incident beam is π^- of 340 GeV/c and the main aim is to search for evidence of "beautiful" hadrons decaying with short lifetime, $10^{-14} \rightarrow 10^{-13}$ seconds, to charmed hadrons. These would be apparent as a cascade of short-lived decays associated with a two or three muon signal.

(iv) The SLAC 40" hydrogen bubble chamber and associated spectrometer (Fig. 11) are being used[22] in a search for charmed hadrons produced by a mono-energetic 20 GeV photon beam generated by back

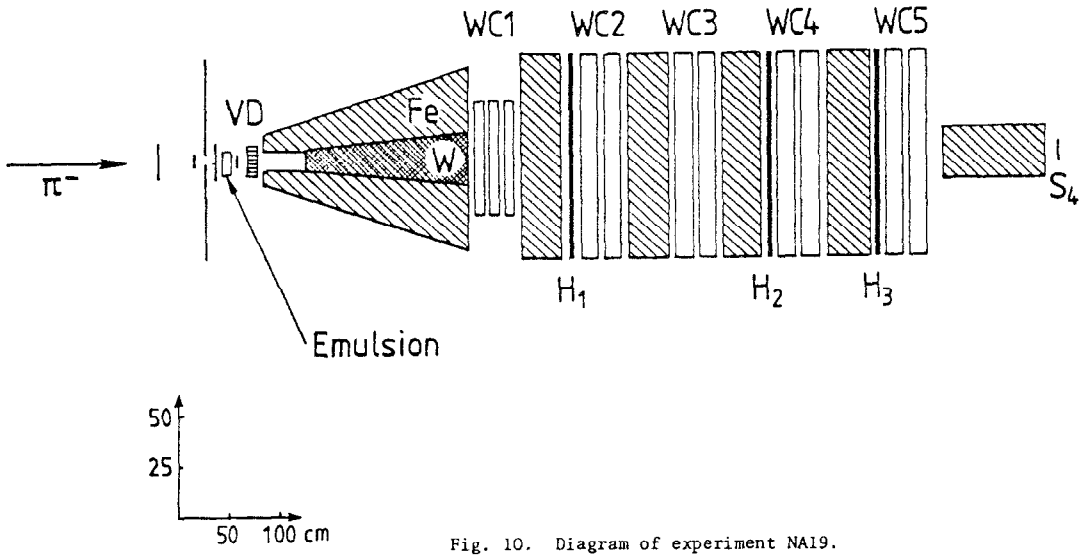

Fig. 10. Diagram of experiment NA19.

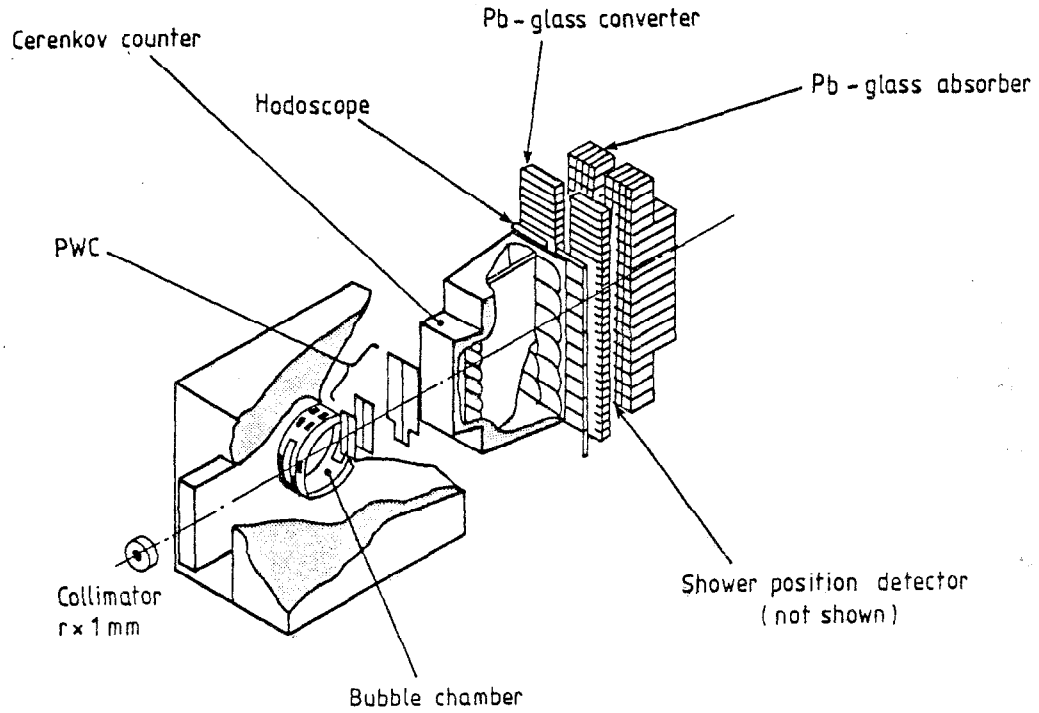

Fig. 11. The SLAC 40" bubble chamber hybrid system.

scattering from a laser. High resolution optics are used to photograph 60 μm bubbles.

(v) In a new approach to bubble chamber design and construction small hydrogen bubble chambers specially designed for high resolution optics have been built at CERN and used in two experiments to detect charmed particles produced by 340 GeV/c π^--mesons and protons. One, NA13, is listed in Table 2. The second, NA16, completed data taking in July 1980 and is described briefly below (5.2.1). Another very small bubble chamber called BIBC (Bern Infinitesimal Bubble Chamber) has been built by the Bern group[23] to search for short lived particle decays. It is about 5 cm in diameter, filled with freon and the bubble size is about 30 μm. Early in 1980 it was exposed to a high energy pion beam at CERN in a position just upstream of a streamer chamber placed inside a magnet to provide momentum determination for particles produced in the freon.[24]

(vi) At the Fermilaboratory further runs are planned using the streamer chamber developed by the Yale-Fermilab group. With new, laser triggered spark gaps and higher resolution image intensifiers track widths ~50 μm, or better, should be achieved[25].

5.2 Future Possibilities

The clear lesson gained from recent experiments and especially demonstrated by E531 is the need for better spatial resolution (that is, for all detectors except emulsion) and the requirement of parent identification. Given these, then higher statistics and sensitivity to smaller production cross-sections are essential, especially for the tasks of measuring beauty and τ-lepton lifetimes.

5.2.1 High Resolution with Small Bubble Chambers

The NA16 experiment at CERN[26] used a small hydrogen bubble chamber, LEBC (little European bubble chamber), constructed from lexan -- a transparent plastic material. This is effectively a "clean" chamber. It cycled at 30 Hz. The flash was initiated by a simple interaction trigger and a downstream spectrometer (EHS) provided momentum measurement, some particle identification -- by ionization measurement (ISIS) -- and photon detection. The chamber[27] is shown in Fig. 12. 1.3 million pictures were taken, half with a 340 GeV/c π^- beam and the other half with 340 GeV/c protons. A few hundred cases of associated charmed hadron production are expected to be found and the bubble size for most of the run was 40 μm.

An analysis of the efficiency of visual detection of short-lived hadrons in such an experiment has been made by the NA13 collaboration[2]. Fig. 13 shows the result as a function of lifetime for a bubble size ~50 μm. Clearly the efficiency is poor for mean lifetimes less than 5.10^{-13} seconds (as would be expected from the rule of thumb given in Section 2.2). The determination of D^0, $F^{\pm}$, Λ_c^+ lifetimes requires better resolution.

It was pointed out[28] several years ago that holographic photography could be used for bubble chambers. But the challenge of detecting charmed particle decays has stimulated renewed interest in this technique since it offers a means of obtaining higher resolution without incurring severe restriction in depth of field[29] and this has been demonstrated by recent tests carried out at the Rutherford Laboratory[30] and CERN[31]. It is instructive to make a simple comparison of the two methods.

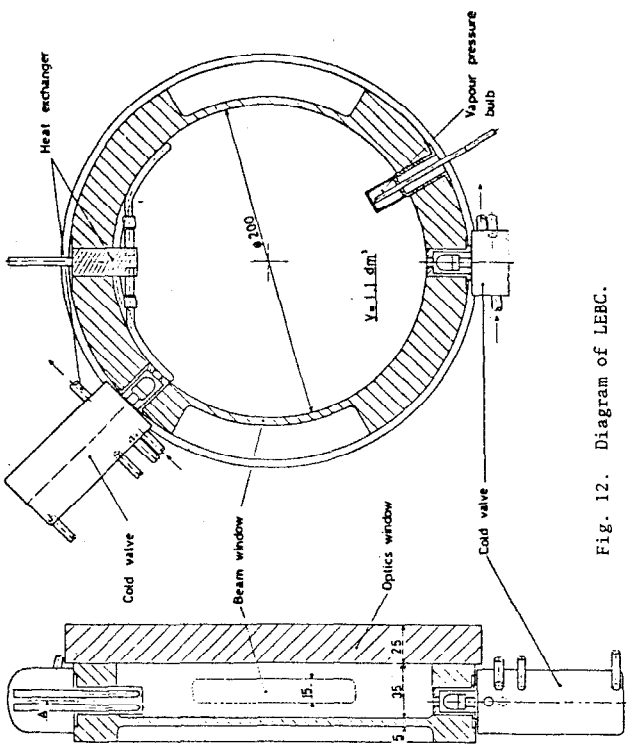

Fig. 12. Diagram of LEBC.

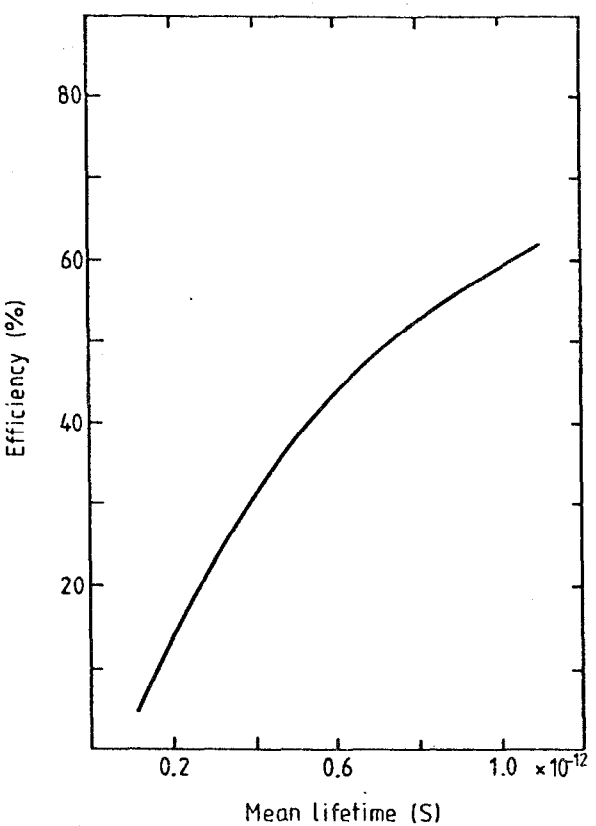

Fig. 13. Efficiency of short-lived particle detection as a function of mean-lifetime estimated for experiment NA13 with LEBC.

(i) Conventional Photography

With an optical system (Fig. 14(a)) of aperture 'A' the diffraction limited radius of the image formed of a point at distance D is:

$$d \sim \frac{1.2\lambda D}{A} ,$$

where λ is the wavelength (0.5 μm); and the depth of field, Δ:

$$\Delta \sim 3\lambda \left(\frac{d}{\lambda}\right)^2 .$$

In LEBC, with an apparent bubble diameter of about 40 μm the depth of field was ~5 mm. The practical limit of resolution for conventional optics in bubble chamber photography is held to be 15 μm to 20 μm, with a depth of field ~1 mm. This is not sufficient as an improvement in resolution and brings additional difficulty in the very small depth of field.

(ii) Holography

To illustrate this method, Fig. 14(b) shows the simplest optical arrangement, in-line Fraunhoffer holography, in which the film records the interference between the directly-transmitted wave front and that scattered by a bubble. The resolution is given by the same formula as before but now the aperture is the width of the holographic film. For example, with A ~7 cms and D ~30 cms a resolution of ~2 μm could in principle be obtained. The depth of field is now:

$$\Delta \sim \frac{L}{10}\left(\frac{d}{\lambda}\right)^2$$

where L is the coherence length of the laser used to illuminate the system; L may be 1 or 2 or 2 m resulting in a depth of field of several meters.

Thus the use of holography gives immediately two important advantages:

(a) spatial resolution sufficient to reach without difficulty lifetimes 5.10^{-14}s (or less with track measurements);

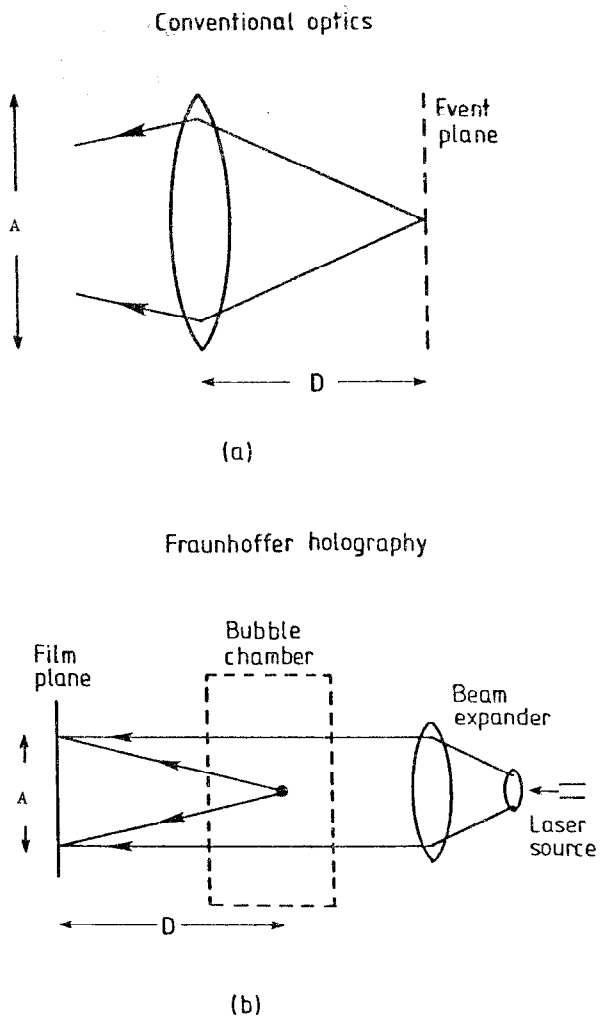

Fig. 14. Diagrams illustrating: (a) conventional optics; (b) Fraunhoffer holography.

(b) a depth of field which could allow an increase by some orders of magnitude in the incident beam intensity and so a corresponding improvement in sensitivity to rare processes.

As an illustration of the possible improvement in charmed particle detection, Fig. 15 shows the event already represented in Fig. 2, but now drawn with 5 μm bubbles.

(iii) The BIBC Test

The feasibility of holographic photography has been tested recently at CERN using BIBC the freon filled bubble chamber built by the Bern Group. In the test[31], carried out by a collaboration of CERN and the Institute of St. Louis, Bern, holograms were made, using a pulsed, monomode Q-switched ruby laser and particle tracks were recorded with bubbles of diameter ~8 μm. An image of the chamber can be formed by laser illumination of the hologram and examined by normal optical method. Fig. 16 shows a picture of an event in BIBC; it was made by viewing the holographic image with a TV camera attached to a microscope and then taking a photograph of the TV display screen. The bubble density in BIBC was 300 bubbles per cm.

(iv) Proposed Experiment

An experiment has been proposed at CERN which would use a LEBC-type hydrogen chamber and holographic photography in association with the EHS. The chamber and optical system will be designed to reach a resolution $\lesssim$ 5 μm. The bubble density needed is 300 → 400/cm and this may present difficulty as the necessary chamber operating conditions will be near the foam limit. However, the fact that the chamber construction is effectively "clean" is an advantage.

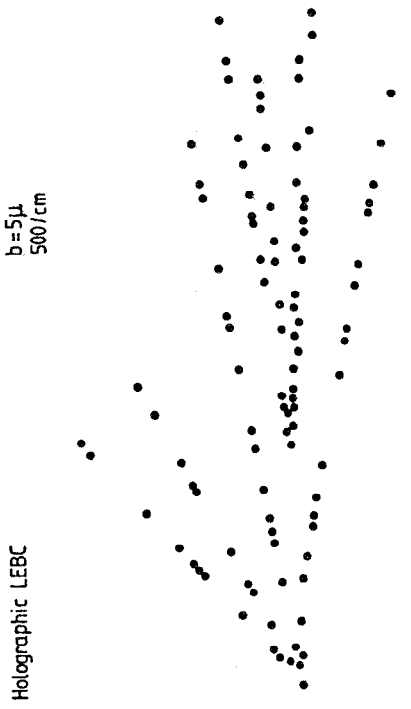

Fig. 15. The event shown in Fig. 2(b) as it might appear with 5 μm bubbles.

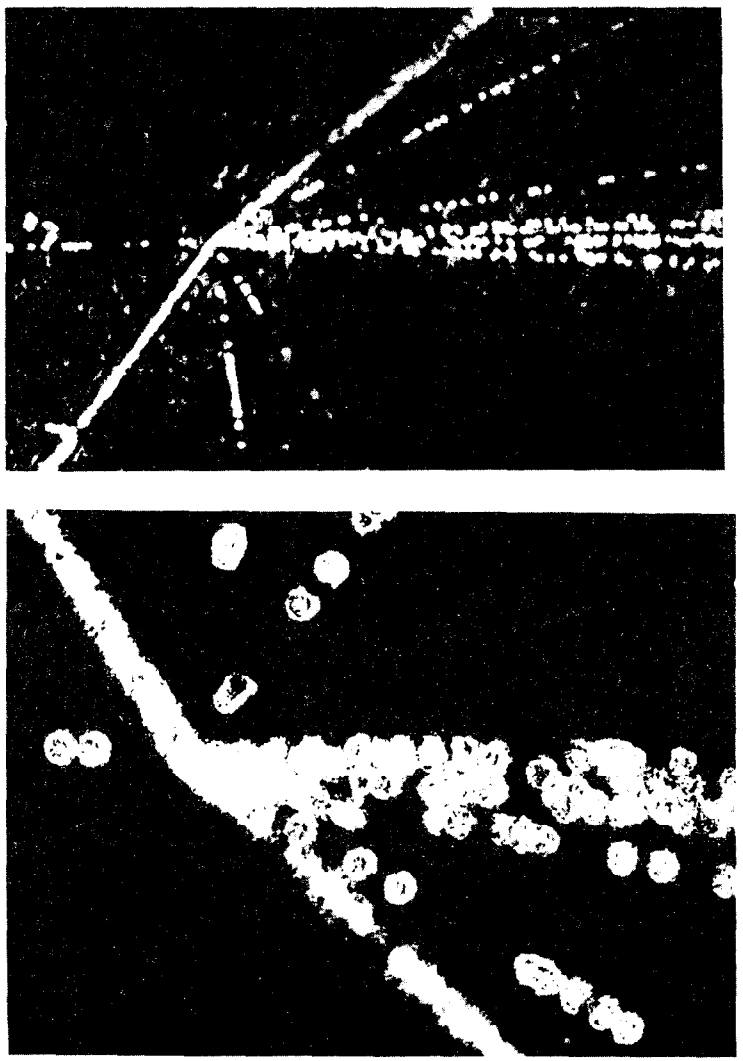

Fig. 16. Photographs of a holographic reconstruction of an event in BIBC. The bubbles are about 8 μm in diameter. (Both are of the same event taken at different magnification of the viewing optics.)

The problem of scanning and measuring the holographic images is now under study. It seems feasible to do this using a combination of optical enlargement and viewing with a TV camera, which may also provide digitised bubble-coordinates. One weakness is the relatively poor depth information; in the holographic image bubbles will remain in focus over a distance 100-200 μm. This situation could be improved by using a second system to enable stereoscopic reconstruction.

To take advantage of the large depth of field and increase the sensitivity requires the use of an efficient trigger for the laser illumination (coupled with labelling of the incident particle position). This must be achieved without compromising the spectrometer data.

5.2.2 Solid State Detectors

The use of solid state detectors to obtain high spatial resolution is being investigated actively. One approach has already been used in an experiment at CERN.

The vertex detector[32] developed for experiment NA1 consists of a series of forty thin silicon solid state counters. Each is a slice of n-type hyperpure silicon, 300 μm thick, coated on one side with an evaporated film of gold, to form a rectifying interface (Schottky barrier), and on the other an aluminium electrode. The diode thus obtained is reverse polarised to render the slice totally depleted. The discs behave essentially as ionization chambers and the amplitude of the pulse is proportional to the number of (minimum ionizing) particles passing through. The sensitive area is ~160 μm^2 and the discs are spaced ~100 μm apart. The associated electronics can handle 100 ns pulses and counting rates up to ~10^5 per s.

The detector is placed in a high energy photon beam (maximum energy 150 GeV) and followed by a spectrometer (Fig. 17). A very high incident

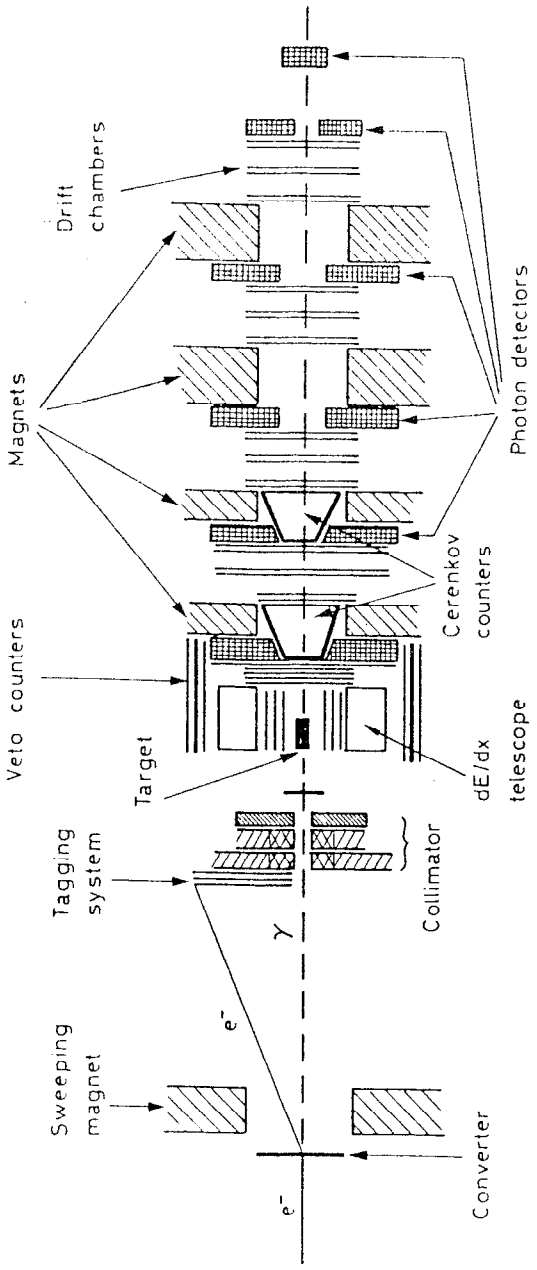

Fig. 17. The apparatus of experiment NA1.

intensity is used and the object is to select cases of coherent production of charmed hadron pairs on silicon nuclei. Such events may be identified by the following characteristic features of the data:

(i) A small signal in the disc where the production occurs, due to a nuclear recoil;

(ii) In the immediately following discs, either no signals (for D^0, $\bar{D}^0$) or pulses corresponding to two charged particles (D^+, D^-).

(iii) The decay of a charmed particle is manifest by a jump in pulse height by an appropriate multiplicity.

Figure 18 shows examples of pulse height distributions: (a) for an ordinary interaction; (b) and a candidate for coherent production of $D^0 + \bar{D}^0$.

A first run using this detector and spectrometer has taken place.[33] A point to notice is that by selecting coherent production, hence low primary multiplicity, the problem of vertex confusion is minimised (i.e., effectively, a very low value for K, Section 2.1) and the gain obtained from high ($^P/_m$) is realised. The thickness of the discs is a compromise between spatial resolution and the lower signal to noise and larger Landau fluctuations suffered with thinner discs.

The spatial resolution along the flight path is determined by the cell-size of 400μ. At 80 GeV/c, about the maximum momentum, the flight path is ~1200 μm, or about 3 cells, for a proper flight time of 10^{-13}s. So there is some loss for short flight times. The overall length, of 16 mms, is a little larger than the mean flight path for 80 GeV/c and a mean life of 10^{-12}seconds.

A large amount of data have been taken but the lack of resolution in the transverse direction leads to ambiguity in the association of tracks seen in the spectrometer with specific decay vertices. The lifetime analysis is not yet complete.

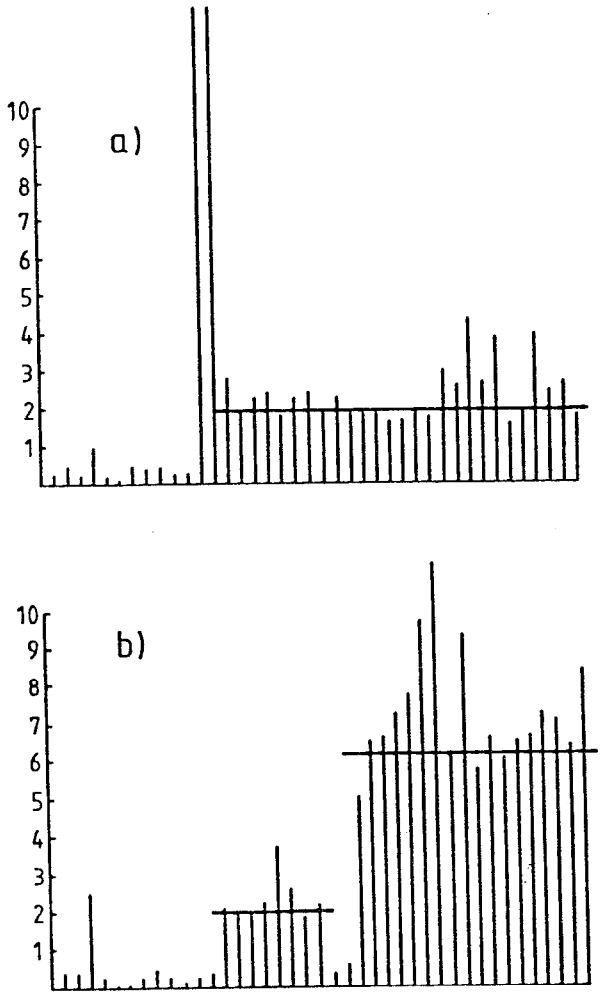

Fig. 18. Examples of data from the vertex detector of NA1; the vertical axis is pulse height and position of the silicon slice is shown horizontally. (a) shows very large pulses at the start of the event followed by a flat profile and is presumed to be an incoherent event; (b) starts with a small pulse consistent with a nuclear recoil which is followed by a gap and then a pulse height rising in two steps. This is the pattern expected for coherent production and decay of $(D^\circ + \bar{D}^\circ)$.

The Pisa group has extended this approach to obtain a multi-electrode silicon detector which operates as a miniature MWPC[34]. In this case the aluminium conductive layer has been etched away to leave strips of 300μ width and 300μ spacing (Fig. 19). This has been tested in a 60 GeV/c pion beam; the pulse height distributions show negligible cross-talk between adjacent strips. In principle it should be possible to make such detectors with much narrower strips, say ~1 μm.

6. CONCLUDING REMARKS

The measurement of heavy flavour lifetimes in the region of 10^{-13}s poses a double challenge to the experimenter. First is the need for spatial resolutions of a few microns or less and secondly, identification of the parent requires the momentum and identity of the decay products. In the last year hybrid experiments using photographic emulsion in conjunction with electronic detectors or a bubble chamber have yielded the first lifetime measurements on identified charmed particles.

Small bubble chambers may achieve the high spatial resolution required through the use of holography, and this could also enable a significant increase in sensitivity.

Recent developments in solid state detector technology are bringing a new approach to the challenge. But if the heavier flavours of hadrons and leptons have lifetimes less than 10^{-14}s. then the photographic emulsion seems the only technique at present able to tackle the task. The lead taken by the Japanese groups in automation of emulsion scanning and measuring techniques may well be followed by others.

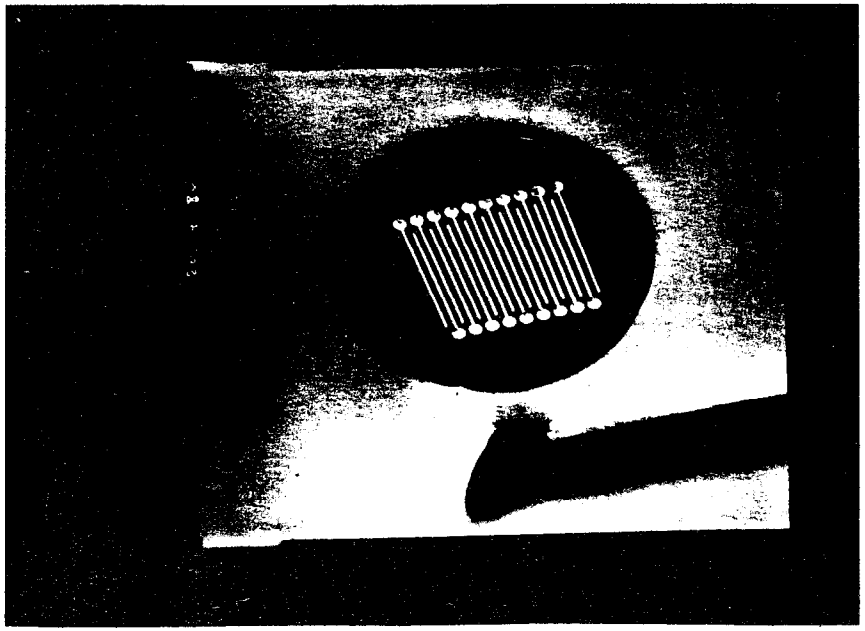

Fig. 19. Picture of a solid state MWPC developed by the Pisa group.

ACKNOWLEDGEMENTS

In preparing this review I have benefitted from discussions with several of those involved in these experiments and I am especially grateful for the help and advice given by Ron Sidwell, Colin Fisher, and my colleagues, Wade Allison and Paul Cartwright. It is also a pleasure to remember a very enjoyable Summer Institute and thank the organisers for inviting me and for their help while I was there.

REFERENCES

1. M. Kobayashi and K. Maskawa, Progr. Theor. Phys. 49 (1973), 652.
2. W. Allison et al, Phys. Lett. 93B (1980) 509.
3. Photon Emulsion and Omega Photon Collaborations; Contribution to 20th Int. Conf. on High Energy Physics, Madison, July 1980. Also G. Diambrini-Palazzi, private communication, July 1980.
4. J. Sandweiss et al, Fermilab-Pub-80/16-Exp. 7550.490, January 1980 and J. Sandweiss, Physics Today, October 1978.
5. D. Reeder, Proceedings of the 1979 International Symposium on Lepton and Photon Interactions at High Energies. Fermilab, August 1979, 553.
   L. Voyvodic, ibid, 569.
   P. Musset, Neutrinos-80 Conference, Erice, June 1980 and CERN-EP/80-161.
6. E.H.S. Burhop et al, Phys. Lett. 65B (1976) 299.
7. K. Niu et al, Prog. Theor. Phys. 46 (1971) 1644.
8. N. Ushida et al, Lett. Nuovo Cim. 23 (1978) 577.
   H. Fuchi et al, Phys. Lett. 85B (1979) 135.
9. H.C. Ballagh et al, Phys. Lett. 89B (1980) 423.
10. D. Allasia et al, CERN-EP/80-76, 29 May 1980. Submitted to Nuclear Physics.
11. R. Ammar et al, Phys. Lett. 94B (1980) 118.
12. N. Ushida et al, Phys. Rev. Letts. 45 (1980), 1049 and 1053.
13. M.I. Adamovich et al, Phys. Lett. 89B (1980) 427.
14. G. Diambrini-Polazzi, Proceedings of 19th International Conference on High Energy Physics, Tokyo 1978, 297.
15. G. Diambrini-Palazzi, private communication, July 1980.
16. R. Sidwell, private communication, July 1980.
17. R. Schindler, Ph.D. Thesis, Stanford University, SLAC Report No. 219, 1979.
18. W. Bacino et al, Phys. Rev. Lett. 45 (1980) 329.
19. E. Bloom, these Proceedings.
20. D. Hitlin, these Proceedings.
21. J.P. Albanese et al, NA19 "Experiments at CERN," CERN, August 1980.
22. J. Ballam, private communication, August 1980.
23. B. Hahn, E. Hugentobler and E. Ramseyer, Bern to be published.
24. A. Badertscher et al, NA18, "Experiments at CERN," CERN, August 1980.
25. J. Sandweiss, private communication, July 1980.
26. M. Aguilar-Benitez et al, NA16, "Experiments at CERN," CERN, August 1980.
27. H. Leutz to be published.
28. W.T. Welford, Applied Physics 5 (1966) 872 and Proceedings Int. Conf. on B. Ch. Techn., Argonne, 1970, 1024.
29. F.R. Eisler, Nucl. Inst. Meth. 163 (1979) 105.
30. C. Fisher, Vezeley Workshop, March 1980, CERN/EP/EHS/PH80-2,74 and private communication.
31. M. Dykes et al, CERN/EF 80-2 July 1980.
32. S.R.Amendolia et al, PISA 80-1, April 1980 and submitted to N.I.M.
33. E. Albini et al. Contribution to 20th Int. Conf. on High Energy Physics, July 1980 and L. Foa, private communication.
34. S.R. Amendolia et al, PISA 80-2, May 1980 and submitted to N.I.M.

NEUTRINOS AND COSMOLOGY

David N. Schramm

The University of Chicago

INTRODUCTION

In this lecture we will review the implications on neutrino physics from cosmology. However, to do this we will first give a brief overview of the particle physics-cosmological interface during the earliest history of the universe. With the general acceptance of the big bang model of the universe, has come the awareness that the earliest moments in the history of the universe were sufficiently hot that nuclear and elementary particle reactions occurred throughout the universe. We will review the arguments favoring the big bang and mention our trepidation as we push our calculations to earlier times and higher temperatures where the observational support is not obvious. We will then describe the big bang in chronological order beginning with the Planck time and quantum gravity and continue on through the era of grand unification where we expect the generation of baryonic matter to have occurred. Our chronologic history will continue on into the quark-hadron phase transition where the free quarks of the early universe combined to make hadrons. The decoupling of neutrinos at $\sim 10^{10}$ K will be described and the possible consequence of these relic neutrinos on the future dynamics of the universe. We will then go into the epoch of big bang nucleosynthesis where the observed abundance of ^{4}He and ^{2}D (and possibly ^{7}Li and ^{3}He) were produced. The sensitivity of this production to the baryon density will be discussed. It will also be shown that the He abundance can be used to set a limit on the number of neutrino types and thus also on the number of quark flavors. In looking at the interface with neutrinos and the big bang it is important to note that the extremely high and somewhat speculative temperatures are irrelevant to neutrinos in cosmology. In fact the neu-

trinos are only affected by events near to 10^{10} K where our understanding is somewhat more secure. This review will draw heavily on the previous papers of Turner and Schramm (1979), Schramm and Wagoner (1977), Schramm and Steigman (1980), and Yang, Schramm, Steigman and Rood (1979) and is an updated version of a similar review given by Schramm in Erice in April.

JUSTIFICATION OF THE HOT-DENSE EARLY UNIVERSE

The general acceptance of a hot-dense early universe (the big bang) began to happen with the discovery of the 3 K background radiation by Penzias and Wilson (1965). However, complete acceptance didn't occur until the experiments of Richards and co-workers (1973) showed that the background radiation had the appropriate thermal turnover at wavelengths of $\sim$ 1 mm. The existence of this radiation tells us that the universe was at one time at least $\gtrsim 10^4$ K. At $\sim 10^4$ K hydrogen would be ionized and the free electrons would easily scatter the photons. Thus the present observed radiation is merely the last scattered thermal radiation from $\sim 10^4$ K.

We actually have confidence that the universe was a good deal hotter than this. Gamow and his co-workers (1948) predicted that there would be this thermal background on the basis of assuming that nuclear reactions occurred in the big bang. To have nuclear reactions requires that the temperature had to be greater than $\sim 10^9$ K. The verification of a temperature at least as hot as 10^{10} K comes from the fact that the ^{4}He abundance is about 25% by mass. This helium abundance comes as a natural consequence of the standard big bang if the temperature was greater than $\sim 10^{10}$ K (see Schramm and Wagoner, 1977 and references therein).

There are at present no direct observational ties to earlier times in the universe when the temperature was even higher (unless one accepts the existence of matter as indication of grand unification decoupling at $\sim 10^{15}$ GeV). We do have some feeling that it is not totally absurd to discuss temperatures in the early universe as high as 10^{15} GeV or maybe even 10^{19} GeV. This lack of complete fear comes from the singularity theorems of Hawking, Ellis and Penrose (see Hawking and Ellis, 1973 and references therein). The theorems state that if the universe has a net free energy, then the world lines must have come out of a singularity. Since we know the universe is roughly homogeneous and isotropic, then the singularity becomes the global one which we call the big bang. The crux of these theorems is the present epoch of the universe. We have the 3 K radiation so we know there exists positive free energy and we can extrapolate our world lines back to higher densities and temperatures. The first place in our trek to earlier times where we really start to question the positive energy conjecture is at the quark-hadron transition. At this point the density is so large that the hadron bags overlap and free quarks exist throughout the universe. Since quark soup is not studied in the laboratory and since the nature of the gluon field at this transition is somewhat speculative (c.f. Schramm, Crawford and Olive, 1979), it may be that something occurs there which violates the positive energy condition. However, this transition occurs at $\sim$ 200 MeV when the density exceeds 10^{16} g/cm^3 and current physical ideas do not indicate anything that would violate the positive energy conditions.

The place where we are confident that the positive energy conjecture is in trouble is at the Planck time, 10^{-43} sec after the big bang, at a temperature of 10^{19} GeV. At this temperature, gravity becomes quantized and all bets are off. It may be that at the Planck time all of space-time is a foam of mini-black holes which are forming and exploding via the Hawking process on a Planck timescale. Such instantaneous black hole formation througout space-time would violate the positive energy condition and our extrapolation to higher densities and

temperatures must break down. However, we have already reached 10^{19} GeV; let's proceed from the big bang in chronologic order from such temperatures (see Table 1).

THE PLANCK TIME

Because we know that gravity must become quantized for temperatures greater than $\sim 10^{19}$ GeV which correspond to big bang model times of $\sim 10^{-43}$ sec after the classical big bang, and because there is no consistent quantum theory of gravity, it is obvious that we cannot talk in a scientific manner about times "earlier" than 10^{-43} sec. In fact the whole concept of space and time becomes jumbled at this epoch. Hawking refers to space-time being a foam of mini-black holes constantly bursting and reforming. Hartle and Hu (1979) using a semi-classical approach have suggested that the universe may be horizon-less at the Planck time. If this were the case, then many if not all of the causality problems associated with the big bang may be solvable. In particular, the standard model does not enable us to understand how the universe can be homogeneous and isotropic on scales that were never in causal connection. Whereas if the Planck time results in a vanishing of the horizon, then all of the universe might have been in causal connection and become homogenized and isotropized prior to the formation of the horizon.

One should remember that 10^{-43} sec is a model time. Earlier times really do not exist in the normal sense, or for that matter, there may be an inifinite amount of time "prior" to 10^{-43} sec. Our time extrapolation breaks down as we try to push beyond the Planck barrier.

We will see later that every time an interaction decouples from the rest of the universe during its expansion, we end up with an observable. The 3 K radiation, the n/p ratio (^{4}He abundance) and perhaps even the baryon/photon ratio are examples of this. One hope is that our expansion rate H_o and the deceleration rate q_o are consequences of the

TABLE 1. THE VERY EARLY UNIVERSE

Time	Temperature	Event	Observable
?	?	Domain of Quantum Gravity	?
10^{-43} sec.	10^{19} GeV	Planck Time - decoupling of Gravitons	Homogeneity-isotropy (?) (gravitons) H_o, Ω (?)
10^{-35} sec.	10^{15} GeV	Grand Unification Decoupling of X,Y	Matter to radiation ratio (perturbations?)
10^{-6} sec.	200 MeV	Quark-Hadron Phase Transition - Quark-Gluon confinement	Hadrons (n, p, π, K, . . .) (perturbations?)
1 sec.	1 MeV	Weak Interaction Freeze-Out - decoupling of neutrinos	n/p (neutrino background)
3 min.	10^9 °K	Big Bang Nucleosynthesis	H, D, ^{4}He (^{7}Li), (^{3}He)
10^5 yr.	10^5 °K	Recombination Decoupling of Photons - transition from radiation to matter domination.	3° background
$10^7 - 10^8$ yr.		Star and Galaxy Formation Heavy Element Synthesis	

"freeze-out" of quantum gravity. However, at the present time such hopes are more religious than scientific.

Before leaving the quantum gravity era, it is interesting to note a proposal by Cocconni (1980) that at temperatures greater than 10^{19} GeV the gravitational constant may vary like other gauge coupling constants do when one goes above the appropriate critical energy. In the case of gravity, such variation may be what causes the big bang in the first place and may be what prevents singularities from actually occurring. Thus while G may be constant for all normal interactions, its constancy above 10^{19} is not obvious.

Let us now move from the realm of total speculation into the direction of more developed ideas.

GRAND UNIFICATION AND THE ORIGIN OF MATTER

In this section we will discuss how recent developments in Grand Unification Theories may resolve the cosmological puzzle of $n_B/n_\gamma \sim 10^{-11} - 10^{-9}$ (where n_B is the baryon density and n_γ is the photon density). A little over a decade ago another puzzle, the large observed mass fraction of ^{4}He, was resolved by considering the role of nuclear physics in the early universe. Today, application of grand unified theories of particle interactions may explain the origin of baryons in the universe.

The striking success of gauge theories to describe particle interactions has motivated grand unified theories (GUTs), gauge theories which unify the weak, electromagnetic and strong interactions. A common feature of all these GUTs is that baryon number is no longer absolutely conserved. The necessity of baryon nonconservation is qualitatively easy to understand. In order to put quarks and leptons on equal footing (i.e., unification) they must be in the same multiplets and so symmetry operations (i.e., gauge transformations) exist which "rotate" a quark into a lepton, etc. These transformations correspond to interactions mediated by gauge bosons.

That baryon number might not be absolutely conserved is not too surprising. Unlike charge, which is believed to be absolutely conserved, baryon number has no long range force coupled to it. For this reason black holes do not conserve baryon number although they do conserve charge. To see this, consider the following example: Construct a black hole from charged baryons. An observer outside can determine the charge, mass, and angular momentum of the black hole, but no more. A hole made of baryons or antibaryons appears the same to an outside observer and therefore the baryon number that went into the hole is lost forever.

Baryon nonconservation is even more apparent when the black hole evaporates via the Hawking process by radiating a thermal spectrum of particles. The hole created from charged baryons will radiate a net charge equal to the charge that initially went into it; however, it will radiate equal number of baryons and antibaryons. In the process of creating a black hole and its eventual evaporation charge, angular momentum and energy are all conserved, but baryon number is grossly violated.

In the simplest of the GUTs, SU(5) there are the six usual quark flavors (u,d,s,c,t,b), the six usual leptons ($e^-,\nu_e,\mu^-,\nu_\mu,\tau^-,\nu_\tau$) and 24 gauge particles, the photon $W^\pm$, Z_o, 8 gluons, and 12 new superheavy gauge particles which mediate baryon nonconservation. In addition to the usual light ($\sim$ 200 GeV) Higgs particles which generate masses for the quarks, leptons, $W^\pm$, and Z_o there are superheavy Higgs particles which generate masses for the superheavy gauge particles. These superheavy Higgs particles can also mediate baryon nonconservation. The mass of a superheavy Higgs or gauge boson, m_x, is of the order of 10^{15}

GeV/c^2.

At present energies (hundreds of GeV) baryon nonconserving processes are almost negligible (almost, but not quite since these theories do predict proton decay with lifetimes at $\sim 10^{32}$ yrs) and are effectively a point interaction, with interaction strength, G, given by

$$G \sim \alpha/m_x^2 \sim 10^{-25} G_{WEAK}$$

where G_{WEAK} is the Fermi constant of the weak interaction ($G_{WEAK} m_p^2 \sim 10^{-5}$). However, at energies of the order of the unification mass, m_x, these processes will be roughly as strong as all the other interactions. Energies of the order of 10^{15} GeV occur in the very early universe when the temperature was of order 10^{28} K. In the standard model this corresponds to a time of 10^{-35} sec after the singularity. Since the baryon nonconserving interactions are so strong at very early times, it seems reasonable that a baryon-symmetrical universe (zero net baryon number) might evolve a net baryon number. However, two additional ingredients are necessary.

The first is particle-antiparticle asymmetry or C and CP violations. An arrow is needed to specify the direction of the violation. To see this, consider the following two reactions which violate baryon number,

$$A + B \rightarrow C + D \qquad \Delta B_1 \neq 0 \qquad \text{rate } r_1,$$
$$\bar{A} + \bar{B} \rightarrow \bar{C} + \bar{D} \qquad \Delta B_2 \neq 0 \qquad \text{rate } r_2,$$

in the second reaction, particles have been replaced by their antiparticles. Both processes violate B (baryon number), and $\Delta B_1 = -\Delta B_2$. If C and CP are good symmetries, then the rates, r_1 and r_2, will be equal and the effect of the two reactions is no net baryon generation. If C and CP are violated then r_1 does not have to be equal to r_2 and there can be a net generation of baryon number. CP and C violation occur in nature (the $K^o - \bar{K}^o$ system) and also occur naturally in GUTs.

The final ingredient is departure from thermal equilibrium at some point in the early universe. Such departures occur naturally during the evolution of the universe. This ingredient too is essential as it has been shown by several authors that if CPT is a good symmetry and if a system is in equilibrium, then regardless of B, C, and CP violations the net baryon number will remain equal to zero (Weinberg, 1978 and Toussaint, Wilczek and Zee, 1979 and Susskind and Dimopoulos, 1979 and references therein).

The exciting and amazing result is that when GUTs are used to describe the interactions in the very early universe ($kT \gtrsim m_x c^2$), an initially baryon symmetrical universe can evolve a net baryon excess of about $10^{-10\pm1}$ per photon for reasonable parameters of the GUT. This point has now been worked out in detailed calculations by Fry, Olive and Turner (1980). Much later, when the baryons and antibaryons annihilate ($T \sim 10^{12}$ K) this excess leaves the one baryon per $10^{10\pm1}$ photons we see today. Before GUTs, baryon number was believed to be absolutely conserved so that an initially baryon symmetrical universe would remain symmetrical (contrary to the apparent lack of antimatter in the universe) and the near completeness of baryon-antibaryon annihilations would leave a baryon/photon ratio of only $\sim 10^{-18}$ (Steigman, 1979 and references therein).

Cosmological generation of baryons has some important astrophysical implications. In the scenario described above (and in all but one of the scenarios suggested) the baryon/entropy ratio is determined only by the parameters of the GUT. Therefore, independent of any primordial temperature fluctuations, the baryon/entropy ratio will be constant

throughout the universe (unless the fluctuations were so large that some parts of the universe were never hot enough to have had X, $\bar{X}$-bosons). This bears directly upon the question of galaxy formation and clustering. In the gravitational instability theory of galaxy formation initial density fluctuations are needed. These fluctuations are of two basic types: adiabatic and isothermal. In an adiabatic fluctuation both the radiation and matter participate, with the baryon entropy ratio remaining constant. In an isothermal fluctuation the radiation does not participate, i.e., the temperature remains constant. One can see that if the baryons were cosmologically produced as outlined above, only adiabatic initial fluctuations would be permitted. There is a way around this restriction and it involves primordial black holes and the Hawking process (Turner and Schramm, 1979). In this scenario an initial spectrum of primordial black holes evaporates producing entropy (photons) and X, $\bar{X}$-bosons which produce a net baryon excess as before. However, in this case isothermal fluctuations can also occur. In addition, the lower limit on m_x for appreciable baryon production can be circumvented, because mini-blackholes evaporate at a time determined by their mass. Mini-black holes in the proper mass range will radiate X-bosons when the surrounding universe is cool ($kT \lesssim m_x c^2$); the presence of these X-bosons is a highly nonequilibrium situation and thus their free decays produce a baryon excess.

The baryon/photon ratio can be turned upside-down and viewed as a photon or entropy/baryon ratio of $10^{10\pm1}$ indicating an apparent large entropy per baryon. Some years ago, Misner suggested an alternate explanation based on this idea. He proposed that the universe may have started with cold baryons and a very chaotic geometry (rather than the isotropic and homogeneous geometry it has today) and through dissipation, the large entropy/baryon of $10^{10\pm1}$ and the isotropy and homogeneity were produced. However, Penrose and others have argued that the amount of entropy/baryon that could have been produced by a chaotic geometry being smoothed by dissipation is more like 10^{40}; and so, they conclude that our <u>apparent</u> large entropy/baryon is in fact very small, indicating the initial geometry was very close to being isotropic and homogeneous. However, if the grand unification ideas are correct, this potential probe of the initial geometry, the baryon/entropy ratio, does not remain constant and could easily have been raised from 0 ($\approx 10^{-40}$) to the present $10^{-10\pm1}$ by cosmological baryon generation. Therefore, the baryon/entropy ratio cannot be used as a "footprint" of the initial geometry and so our relatively small entropy/baryon ratio (compared to 10^{40}) cannot be used to infer that the universe has been isotropic and homogeneous <u>ab initio</u>. In fact, the initial geometry could have been quite chaotic (see Turner, 1979).

One cosmological problem associated with GUTs has been the generation of monopoles (c.f. Presskil, 1979 and Fry and Schramm, 1980 and references therein). Since monopoles are not observed and yet they may be generated by the GUT in the early universe one would like some method of suppressing the monopole production. A variety of schemes has been proposed and these are summarized by Presskil and by Fry and Schramm. Perhaps the most intriguing is that the monopoles may gravitationally cluster before the universe becomes matter dominated. This can occur because of their large mass to charge ratio whereas normal matter cannot gravitationally cluster until the transition from radiation domination. If monopoles do cluster early, then they could be the seeds that stimulate galaxy formation and they may have been concentrated in galactic cores. Let us now continue our chronologic evolution of the universe from $T \sim 10^{15}$ GeV down to $T \sim 200$ MeV where the quark soup condenses into normal hadrons.

QUARK-HADRON PHASE TRANSITION

As the universe expands it will eventually drop below the density where the quarks are so close together that they interact with the entire sea of quarks to where the quarks only interact in color triplets or in quark anti-quark pairs. At very high densities, hadrons overlap and lose meaning as individual particles. We may then refer to the universe as being a quark-gluon fluid. It is expected that this transition occurs when the total number density of hadrons is greater than 10 times nuclear density, n_o.

A heavy ion collision experiment can be proposed to explore this transition. Such an experiment may in fact yield a signature for quark matter (see Olive, 1980 and references therein). Using the nuclear fireball model for heavy ion collisions, it is expected that a region of quark matter may exist temporarily in a collision of sufficiently high energy. However, there are two major differences between the transition in the big bang and a heavy ion collision. These are: 1) the net baryon number of the system and 2) the effect of surface radiation in the fireball. The net baryon number in the big bang is quite negligible, while in a heavy ion collision this is no longer the case. The effect of surface radiation is not quite as obvious. In the big bang it is obviously not relevant since one has a near infinite fluid. For our purposes we will neglect this correction as it should not affect the qualitative existence of a quark signature.

If no transition occurs, the ratio of antibaryons to baryons in the spectrum should approach unity as the fireball temperature is increased. In addition, the relative abundance of pions should steadily decrease. The reason for these effects is simply that at higher temperatures, more baryon particle-antiparticle pairs will be produced and will eventually overshadow the net number of baryons. The relative numbers of pions seen will decrease, since more of the higher resonance ~~mesons will~~ be produced. Thus by comparing the ratio of antinucleons to nucleons and abundances of pions at various energies, one should be able to determine whether or not a transition occurred.

Another current problem in cosmology is the question, where do galaxies come from? In fact we know that on very large scales, the universe appears to be very homogeneous and isotropic. The average density is not the 1 gm/cm^3 of water; so it's clear that the universe is not completely homogeneous and isotropic; there are large variations in density. And the question is why? Why did we have these fluctuations? Why did we have these fluctuations that ended up producing stars, galaxies, planets, people, etc. To make galaxies, one needs some sort of fluctuation, and it has to be of sufficient amplitude to become gravitationally bound so that that fluctuation remains even though the universe is expanding to lower densities.

The fluctuations must be bound at a particular time. The reason is this: the universe is dominated by radiation early in its history, gravitational contraction cannot occur. Galaxies cannot form. So the universe had to have a fluctuation that had grown in amplitude sufficiently to make a bound fluctuation after the universe was no longer radiation dominated, and also after recombination, after the time the photons freely propagated. We do know that the 3° radiation is relatively uniform and isotropic, so sometime after that recombination there had to have been a fluctuation of matter density that was sufficient to be a bound fluctuation. The question is, where do these fluctuations come from? What is their origin? What some people have done in trying to make galaxies is to assume some sort of arbitrary spectrum of primordial fluctuations coming out the big bang singularity. A major goal has been to find a mechanism for the production of these fluctuations after the singularity. One such process we are very interested in is this quark-hadron phase transition. Could what happens

at the phase transition be of a nature that might stimulate clustering of some sort?

Remember this phase transition is from a quark soup to lower densities at which hadrons are formed. Current ideas on quark confinement tell us that the quark-quark color interaction is stronger the farther apart the quarks are. Therefore, as three quarks are removed from the quark soup to make a baryon, it may be that this lower quark density site is maximally unstable to further hadron condensation. In addition, the removing of a triplet of quarks reduces the Debye-color screening of the remaining quarks in the vicinity and thus enables those particular quarks to have longer range interactions. It thus seems that the quark-hadron phase transition may be unstable to the growth of density fluctuations.

Let us now look at events near the decoupling of the weak interaction at $T \sim 1$ MeV.

THE DECOUPLING OF THE WEAK INTERACTION AND RELIC NEUTRINOS

During the early evolution of the universe, all particles, including neutrinos, were produced copiously. In the following we will allow for the possibility that the neutrinos have a small rest mass $m_\nu c^2 << 1$ MeV. Neutrinos with full strength, neutral current, weak interactions were produced by reactions of the type,

$$e^+ + e^- \leftrightarrow \nu_i + \bar{\nu}_i; \; i = e, \mu, \tau.$$

At high temperatures ($kT > m_\nu c^2$), these neutrinos were approximately as abundant as photons.

$$n_{\nu_i}/n_\gamma = 3/8(g_{\nu_i})$$

g_ν is the number of neutrino helicity states. For massless spin ½ neutrinos with $\bar{\nu}_e \neq \nu_i$ then $g_\nu = 2$. If the neutrinos have a mass then each spin ½ particle would have 2 helicity states, thus for $\bar{\nu}_e \neq \nu$, $g_\nu = 4$ However, because known neutrinos appear to be only left handed then, if massive, they may be of the Majorana type ($\nu_i \approx \bar{\nu}_i$), in which case g_ν is still 2. A numerical factor of 3/4 comes from the difference between Fermi-Dirac statistics (neutrinos) and Bose-Einstein statistics (photons); the remaining factor of ½ is from the number of photon spin states ($g_\gamma = 2$).

For light neutrinos ($m_\nu << 1$ MeV), equilibrium was maintained until $T \approx 1$ MeV. (For massive neutrinos with $m_\nu \gtrsim 1$ MeV, they will annihilate for temperature less than m_ν but $\gtrsim \frac{1}{4}$ MeV, thus ν's with $m_\nu \gtrsim 1$ MeV will not be as abundant, see Gunn et al., 1978 and references therein.) At lower temperatures the weak interaction rate is too slow to keep pace with the universal expansion rate so that few new neutrinos are produced and, equally important, few annihilate. Thus, for $T \approx 1$ MeV, the neutrinos decouple; at this stage their relative abundance is given above. When the temperature drops below the electron mass, electron-positron pairs annihilate heating the photons but not the decoupled neutrinos. The present ratio of neutrinos to photons must account for the extra photons produced when the $e^\pm$ pairs disappeared (c.f. Steigman, 1979)

$$N_\gamma(T < m_e) = 11/4 \, N_\gamma(T > m_e); \; (n_\nu/n_\gamma)_o = 3/22 \, g_\nu.$$

From the present density of photons and the above, we obtain the present number density of neutrinos. If the neutrinos have mass we can obtain the mass density, ρ_ν, by

$$\rho_\nu = \sum_i (g_{\nu_i} m_{\nu_i}/200\ h_o^2)\ (T_o/2.7)^3.$$

In this equation and subsequently, m_ν, is in eV and the sum is over all neutrino species with $m \ll 1$ MeV, h_o is the Hubble constant in units of 100 km/sec/Mpc. We have implicitly assumed that the neutrinos still exist today and thus have a lifetime greater than the age of the universe for decay into anything other than neutrinos. This assumption is supported by the astrophysical lifetime-mass constraints on neutrinos (Gunn et al., 1978) and the recent work of Kimball et al. (1980).

It is interesting to compare this density to the critical density of the universe, $\rho_c = 3H_o^2/8\pi G$. The ratio Ω is defined as $\Omega = \rho/\rho_c$. For $T_o \lesssim 3$ K and $h_o < 1$ and assuming Majorana mass neutrinos with $g_\nu = 2$ we find that

$$\Omega_\nu \geq 0.014\ m_{\nu_i}$$

We will show later that from big bang nucleosynthesis, the upper limit on baryon density parameter Ω_b is 0.14. We obtain the relationship with $g_{\nu_i} = 2$

$$\Omega_\nu/\Omega_b \geq \sum_i m_{\nu_i}/1.4$$

which is independent of h_o and T_o. Therefore <u>if neutrinos have masses of the order of eV or greater, then neutrinos are the dominant mass component of the universe today</u>.

Massive neutrinos gravitate and they will have participated in gravitational clustering (see Gunn et al., 1978). However, since neutrinos are non-interacting, their phase space density is conserved and they will cluster only in the deepest potential wells; the slowest moving (i.e., the heaviest) will cluster most easily. Tremaine and Gunn (1979) have shown that neutrinos with $m_\nu \geq 10$ eV will contribute to the mass in binary galaxies, B and small groups, SG. But from above, $\Omega_\nu \geq 0.14 \geq \Omega_{B,SG}$ if $m_\nu \geq 10$ eV. As a result, the heaviest neutrino is probably at this order or lighter so that it may avoid clustering on the scale of single galaxies. Because of the uncertainties with regard to $\Omega_{B,SG}$ it is marginally allowable for neutrinos to have masses from 10 to 20 eV but in clustering on the scale of single galaxies seems to be ruled out if standard ideas for gravitational clustering prevail. For this reason Schramm and Steigman (1980) assert that m_ν is probably < 20 eV.

Tremaine and Gunn point out that neutrinos lighter than ~ 3 eV will not cluster at all due to the fact that the phase space constraints on neutrinos in clusters will give these low mass neutrinos velocities greater than escape. In between these two limits there is a small but crucially important window for the neutrino mass. Neutrinos with a mass between 3 and 10 eV will contribute to the mass of clusters of galaxies (the deepest potential wells) but not (significantly) to the mass on smaller scales. But recall, the scale on which the missing mass problem truly emerges is that of clusters of galaxies. It has been shown by Schramm and Steigman following the review of Faber and Gallagher that baryons could explain the "missing mass" or "missing light" problem up to scales of binaries and small groups but probably not on the scale of large clusters. (As you may recall the missing mass or light problem comes from the fact that the dynamics of galaxies implies a larger mass than that directly seen.) Schramm and Steigman, therefore, proposed that the dominant contribution to the mass of clusters of galaxies (and to the mass of the universe) is from relic neutrinos with a finite mass $3 < m_\nu < 20$ eV. (Note that experimentally m_{ν_e} and m_{ν_μ} must be < 1 MeV, however the experimental limit on

m_{ν_τ} is $\lesssim$ 250 MeV so in principal it may escape our present constraints. However, if it has a mass $\gtrsim$ 10 MeV it must have a lifetime $\lesssim 10^3$ sec from the astrophysical arguments of Gunn et al. and Falk and Schramm (1979).

Obviously, if Ω_ν were > 1 the Friedman universe would be closed by neutrinos. Current estimates put $\Omega_{cluster} < 1$ and thus Ω_ν would probably also be constrained to be < 1 however the uncertainties are sufficiently large that closure by neutrinos cannot be completely excluded. Note that with $g_\nu = 2$, if

$$\Sigma m_{\nu_i} > 100\ h_o^2 (2.7/T_o)3 \text{ eV}$$

then the Friedman universe with $\Lambda = 0$ is closed. With $h_o = 0.4$ and $T_o = 3$ we see that for a $\sum_i m_{\nu_i}$ as small as 12 eV closure is in principal conceivable, however we feel that $\Sigma m_{\nu_i} \geq 25$ would be more conclusive. As we showed before, the limits on Ω imply $m_{\nu_i} \lesssim 20$ eV. The total number of such species is constrained by arguments of the types to be discussed in the next section.

BIG BANG NUCLEOSYNTHESIS

The results of big bang nucleosynthesis depend on two basic assumptions.

1. The Equivalence principle, that is, the local validity of special relativity in all free-falling reference frames. This principle has been verified to a high degree of accuracy in a variety of experiments.

2. The temperature of the universe was at one time greater than a few 10^{10} K. This enables equilibrium to be assumed as an initial condition.

In addition the results of the standard model calculations make the following four assumptions.

a. The cosmological principle, that is, the isotropy and homogeneity of the universe. The 3 K radiation and galaxy counts support this assumption. However, calculations with anistropic, inhomogeneous models have been performed.

b. The universe is composed primarily of matter and contains negligible amounts of antimatter. Steigman (1979) has discussed the evidence for this assumption in detail.

c. No particle species was degenerate (most importantly, the neutrinos). Neutrino degeneracy severely affects the ^{4}He abundance and is discussed by Schramm and Wagoner (1977) and Schramm and Steigman (1979).

d. The expansion rate of the universe is given by the general relativistic formula (although General Relativity need not be the correct theory of gravity).

The time evolution of the scale factor for the universe R(t) at very early times is governed by

$$H \equiv \dot{R}/R = (8\pi G\rho/3c^2)^{\frac{1}{2}}$$

where G is Newton's constant and ρ is the total energy density of the universe. The expansion rate H(5) has dimensions of t^{-1} and this time t is approximately the time it takes for the universe to double its size and is also roughly the age of the universe. For early times the energy density is determined by the number of relativistic species present. If a species is relativistic ($kT > mc^2$), then that particle and its antiparticle wil be as abundant as photons (modulo statistical weight factors of order unity) and will contribute to the energy density like a photon, that is, its contribution to the energy density if $\rho \sim aT^4$ (energy density associated with black body photons). During the epoch of nucleosynthesis, kT was much less than the rest energy of a baryon, so that there was only one baryon for $\sim 10^9$ photons. While

each baryon contributed $\sim$ 1000 MeV to ρ and each photon contributed only a few MeV, the small number of baryons made their contribution negligible. Today, there is still only one baryon for $\sim 10^{10}$ photons, but the average energy of a photon is only milli eV, and so, matter density dominates the total energy density.

At a temperature of 10^{11} K (kT $\sim$ 10 MeV) the particles present were: n, p, e^+, e^-, ν_e, $\bar{\nu}_e$, ν_μ, $\bar{\nu}_\mu$, ν_τ, $\bar{\nu}_\tau$ and γ and possibly other as yet undiscovered particles. As mentioned before these constituents were maintained in statistical equilibrium by the weak and electromagnetic interactions. The fact that the universe was in thermal equilibrium at 10^{11} K means that its future evolution is independent of its history before this temperature. At this temperature, the ratio of neutrons to protons, governed by the Saha equation, $n/p = \exp[-(m_n - m_p)c^2/kT]$, was close to unity. As we've already seen departures from equilibrium were extremely important in the early universe.

As we mentioned in the previous section, when the temperature of the universe dropped to about 10^{10} K (kT $\sim$ 1 MeV) the neutrinos ceased to be in equilibrium with the other particles. Thereafter the neutrinos expanded freely, and maintained an equilibrium distribution corresponding to a temperature inversely proportional to R(t). (Their numbers remained constant, the volume element $\propto R(t)^3$ and their wavelengths were redshifted $\propto R(t)^{-1}$, so that their energy densities $\propto R(t)^{-4}$, corresponding to a temperature $\propto R(t)^{-1}$.)

At about the same temperature the weak reactions which maintained the equilibrium ratio of neutrons to protons ($n + e^+ \rightleftarrows p + \bar{\nu}_e$, $n + \bar{\nu}_e \rightleftarrows p + e$, and $n \rightleftarrows p + e^- + \bar{\nu}_e$) were no longer effective and the neutron/proton ratio "froze-out" at the value corresponding to this temperature

$$n/p \simeq \exp[(m_p - m_n)c^2/kT_f],$$

a ratio of about 1/6 and then decreased to a value of about 1/7 by the time of nucleosynthesis due to neutron decays. The "freeze-out" temperature, T_f, and the time from "freeze-out" to nucleosynthesis will be very important.

When the temperature dropped to approximately 10^9 K (kT $\sim$ 0.1 MeV) nucleosynthesis occurred very rapidly. Two important things can happen at this temperature. First, the radiation is cool enough so that deuterium can be formed and is not immediately photo-disintegrated. Second, the temperature is high enough so that two deuterium nuclei can overcome their coulomb barrier and can come together to form ^{4}He. At this time essentially all the neutrons form into deuterium and all the deuterium combines into ^{4}He. The result of nucleosynthesis is that the ^{4}He mass fraction is given by

$$Y \equiv (2n/p)/(n/p + 1)$$

Small amounts of deuterium, ^{3}He and ^{7}Li, were also synthesized. Nucleosynthesis beyond ^{7}Li is prevented by the lack of stable isotopes with atomic mass 5 or 8. This simplified picture is borne out by the very careful calculations done by Wagoner, Fowler and Hoyle (1967). It is interesting to note that the mass fraction of deuterium produced depends critically on the present baryon density. This fact has been exploited to determine the present density and is discussed in detail in Schramm and Wagoner (1977 and references therein).

The ^{4}He mass fraction Y depends critically upon the neutron/proton ratio at nucleosynthesis and less sensitively upon the baryon density. The neutron/proton ratio in turn depends upon the value of n/p at freeze-out and the time from freeze-out to nucleosynthesis during which neutrons are decaying. Freeze-out is determined by the weak reaction rates Γ which maintain this ratio in equilibrium and

the expansion rate of the universe and roughly occurs when $\Gamma \approx H$. The total energy density ρ comes from the relativistic particle present, which around freeze-out ($T \approx 10^{10}$ K) are: the photon, e^+e^- pairs, and all the neutrinos:

$$\rho = \rho_e + \rho_\gamma + \rho_{\nu_\mu} + \rho_{\nu_e} + \rho_{\nu_\tau} + ? = K\, aT^4,$$

where K is proportional to the number of species, photons contributing 1 to K and each neutrino species contributing 7/8 to K. The reaction rate $\Gamma \sim \sigma n v$ is $\propto T^5$ since $n \propto R^{-3} \propto T^3$ and $\sigma \propto (\text{energy})^2 \propto T^2$. This fact implies that freeze-out occurs at a higher temperature when K is larger (i.e., more relativistic particles) and therefore, the neutron/proton ratio freezes out at a higher value. In addition, when K is larger, the expansion rate H is faster, so there is less time for neutrons to decay. Both these effects increase the n/p ratio at nucleosynthesis when more particle species are present and the result is increased ^{4}He production. The number of relativistic particles also affects D, ^{3}He, and ^{7}Li production, however, these abundances are more difficult to determine and interpret and ^{4}He will be the most useful in obtaining constraints on new particle species.

We will discuss the ^{4}He constraints on new neutrino types (i.e., in addition to the standard e, μ and τ neutrinos), however, with minor modification, these arguments apply to any new light ($mc^2 \lesssim 1$ MeV), stable particles. In order to make use of these results, the mass fraction Y must be known. This is a bit of a problem since ^{4}He is made in stars as well as in the big bang. Stars forming now may be contaminated by as much as $\Delta Y \approx 0.06$ "new helium." The best estimates for Y give a value of between 0.20 and 0.25 with 0.25 as an upper limit (see Yang et al., 1979). A very conservative upper limit including "contaminated stars" would be 0.29. Present galactic dynamics suggest a lower limit on the present density of about 2×10^{-31} g cm^{-3} (≈ 0.04 of closure density for $H_o = 50$ kms^{-1} Mpc^{-1}). However, as noted in the previous section, it is conceivable that this mass is not from baryons but from leptons. For the present let us assume that this lower limit on $\Omega_{B,SG}$ is from baryons. We will later examine what happens if $\Omega_{B,SG}$ is in the form of leptons. A lower limit on the baryon density of half this value and $Y \lesssim 0.25$ constrains the number of additional neutrino types (beyond ν_e, ν_μ and ν_τ) to 1.

Standard particle physics models have quark/lepton symmetry, that is, for each lepton and neutrino pair (or generation) there is associated a quark pair. At present there is evidence for three quark/lepton generations: (u,d), (c,s), (t,b), and (ν_e,e^-), (ν_μ,μ^-), (ν_τ,τ^-). There is some evidence for the τ neutrino, but no evidence for the "t" quark. Thus, in these standard models with $Y \lesssim 0.25$ and $\rho_b > 10^{-31}$ g/cm^3 there can be at most one additional generation (eight quark flavors total). A limit of $Y \lesssim 0.29$ implies at most four new neutrino types (in addition to ν_τ) and, therefore, at most 14 quarks.

It is also interesting to note that for a fixed upper limit on Y, as the number of neutrino types increases the upper limit on the present baryon density (allowed by ^{4}He production) decreases. For $Y \lesssim 0.25$ and only e, μ and τ neutrinos the baryon density must be less than 0.14 of the closure density. That is, the universe cannot be closed by baryonic matter.

These ^{4}He constraints have been generalized to massless particles that couple more weakly than the usual neutrinos. In this case a species may not contribute a "full aT^4" to ρ because its temperature may be less than the temperature of the photons and neutrinos. This is because the photons and neutrinos may have been heated (relative to these particles) by other particle annihilations in the same way that the photons were heated relative to the neutrinos by e^+e^- annihi-

lations. However, these particles (if they exist) still contribute to ρ and affect the expansion rate and ^{4}He production. Steigman, Olive and Schramm (1979) have obtained limits on the numbers of hyperweak neutrinos and other such particles that are allowed.

The major uncertainties in the above limits on numbers of neutrino flavors come from:

1. The half life of the neutron which affects the rates that determine n/p. Examination of the uncertainties here allows a variation of $\sim \Delta 1$ on the limit of excess neutrinos.

2. The exact temperature of the thermal background since the relation between density and temperature scales at T^3. The sensitivity here is small compared to the uncertainty listed in 4 below.

3. The limits on the primordial helium abundance. The upper limit of 0.25 is clearly an upper bound but it may be that it could be reduced to less than 0.22 which would force us to discuss baryon densities less than 10^{-31} g/cm^3 and thus focus attention on 4, below.

4. The lower limit on the baryon density may be below that inferred from galactic dynamics if the bulk of the matter measured by dynamics were not baryons but were instead neutrinos with mass. Such a solution would be demanded if the primordial helium abundance were proven to be less than 0.22 or if the mass of the neutrinos were shown to be greater than 10 eV. (Neutrino masses less than 10 eV will not contribute on the scales of binaries and small groups and will thus not effect the argument).

If one is forced to say that the ρ implied from binaries and small groups is not in baryons then we must ask what is the lower limit to ρ_b. A clear lower limit is from stellar matter but that only gives $\rho_b \gtrsim 10^{-32}$ g/cm^3. If we note that the centers of galaxies are probably baryons since neutrinos would require masses $\gtrsim$ 100 eV to be trapped there (note neutrinos are not able to radiate so they can't fall and stay in the deeper potential wells of the galactic centers unless they were trapped there primordially) then we can use internal galactic dynamics to argue that $\rho_b \gtrsim 5 \times 10^{-32}$ g/cm^3. This limit, coupled with $y \leq 0.25$ allows a total of nine 2-component neutrinos (e, μ, τ, and six more. If the neutrinos have Dirac masses and thus four components, the limits become 4 and e, μ and τ and one more are again all that are allowed. However, this limit of 5×10^{-32} from internal galactic dynamics has some observational uncertainties. If it goes much lower then no limits are obtainable for $y < 0.25$. In fact if it were shown that the only lower limit on ρ_b was stellar matter then there would definitely be no possible limit on the number of neutrinos from big bang nucleosynthesis (see Olive, Schramm, Steigman, Turner, and Yang, 1980).

In any case it is obvious that the primordial helium abundance and the neutrino mass are extraordinarily important to the understanding of this problem.

Before leaving the subject, it is important to note that the ideas are testable by experiment. In particular, if the width of the neutral intermediate vector boson, Z^o, is measured in colliding beam machines, then it will tell us the number of neutrino flavors. It is fascinating that one of the most important tests of our cosmological ideas will come from accelerators rather than telescopes.

CONCLUSION

To date, the interdisciplinary effort involving cosmologists, nuclear physicists and particle physicists has produced some exciting results. The ^{4}He abundance fixes an upper limit of eight quark flavors on models with quark/lepton symmetry and a baryon dominated universe. The grand unification ideas may resolve the puzzle of one baryon for every 10^{10} photons. If neutrinos have mass then the bulk of the mass of the universe may be in the form of leptons. As our knowledge of the fundamental particles and their interactions increases, and as our

determination of cosmological observables improves (or new observables are discovered) the close relationship of these two disciplines promises to continue to be an exciting one.

ACKNOWLEDGEMENTS

I would like to thank my collaborators Mike Turner, Gary Steigman, Keith Olive, Matt Crawford, Jim Fry, Eugene Symbalisty, Jongmann Yang, and Bob Wagoner for enabling me to draw on much jointly generated material. This work was supported by NSF grant AST 78-20402 and by NASA grant NSG 7212 at the University of Chicago.

REFERENCES

Cocconi, G (1980). Big and smaller bangs suggesting new physics. CERN preprint.

Dimopoulos, S. and L. Susskind (1978). Baryon number of the universe. Phys. Rev., D18, 4500-4509.

Faber, S.M. and J.S. Gallagher (1979). Masses and mass-to-light ratios of galaxies. Ann. Rev. Astron. Astrophys., 17, 135-187.

Falk, S.W. and D.N. Schramm (1978). Limits from supernovae on neutrino radiative lifetimes. Phys. Lett., 79B, 511-513.

Fry, J.N., K.A. Olive and M.S. Turner (1980). Evolution of cosmological baryon asymmetries. Submitted to Phys. Rev. D.

Fry, J.N. and D.N. Schramm (1980). Unification, monopoles and cosmology. Phys. Rev. Lett., 44, 1361-1364.

Georgi, H. and S.L. Glashow (1974). Unity of all elementary-particle forces. Phys. Rev. Lett., 32, 438-441.

Gunn, J.E., B.W. Lee, I. Lerche, D.N. Schramm and G. Steigman (1978). Some astrophysical consequences of the existence of a heavy stable neutral lepton. Ap. J., 223, 1015-1031.

Hartle, J.B. and B.L. Hu (1979). Quantum effects in the early universe. II. Effective action for scalar fields in homogeneous cosmologies with small anisotropy. Phys. Rev., D20, 1772-1782.

Hawking, S.W. and G.F.R. Ellis (1973). The Large Scale Structure of Space-Time. Cambridge University Press, Cambridge.

Kimball, M., S. Bowyer and B. Jacobson (1980). Berkeley preprint.

Lasher, G. (1979). Production of fluctuations in the early universe by the quark-nucleon phase transition. Phys. Rev. Lett., 42, 1646-1649.

Olive, K.A. (1980). A quark signature in the nuclear fireball model of heavy ion collisions. Phys. Lett., 89B, 299-302.

Olive, K., D.N. Schramm, G. Steigman, M. Turner, and J. Yang (1980). Submitted to Ap. J.

Penzias, A.A. and R.W. Wilson (1965). A measurement of excess antenna temperature at 4080 Mc/s. Ap. J., 142, 419-421.

Presskill, J.P. (1979). Cosmological production of superheavy magnetic monopoles. Phys. Rev. Lett., 43, 1365-1368.

Schramm, D.N. (1980). Proc. Erice Symposium on Nuclear Astrophysics. Ed. D. Wilkenson.

Schramm, D.N., M. Crawford and K.A. Olive (1979). Astrophysics perspectives on high energy nucleus-nucleus collisions. Proc. of the Workshop on Ultra-Relativistic Nuclear Collisions, LBL 8957, 241.

Schramm, D.N. and G. Steigman (1977) Lepton degeneracy and the cosmological constraints on numbers of neutrinos. Phys. Lett. 87B, 141.

Schramm, D.N. and G. Steigman (1980). A neutrino dominated universe. General Relativity and Gravitation, in press.

Schramm, D.N. and G. Steigman (1981). Relic neutrinos and the density of the universe. Ap. J., in press.

Schramm, D.N. and R.V. Wagoner (1977). Element production in the early universe. Ann. Rev. Nucl. Sci., 27, 37-74.

Steigman, G. (1979). Cosmology confronts particle physics. Ann. Rev. Nucl. Part. Sci., 29, 313-337.

Steigman, G., K.A. Olive and D.N. Schramm (1979). Cosmological constraints on superweak particles. Phys. Rev. Lett., 43, 239-242.

Toussaint, D., S.B. Treiman, F. Wilczek and A. Zee (1979). Matter-antimatter accounting, thermodynamics, and black hole radiation. Phys. Rev., D19, 1036-1045.

Tremaine, S. and J.E. Gunn (1979). Dynamical role of light neutral leptons in cosmology. Phys. Rev. Lett., 42, 407-410.

Turner, M.S. (1979). On the isotropy and homogeneity of the universe. Nature, 281, 549-550.

Turner, M.S. and D.N. Schramm (1979). The origins of baryons in the universe. Nature, 279, 303-305.

Turner, M.S. and D.N. Schramm (1979). Cosmoldgy and elementary particle physics. Physics Today, 32, no. 9, 42-48.

Wagoner, R.V., W.A. Fowler and F. Hoyle (1967). On the synthesis of elements at very high temperatures. Ap. J., 148, 3-49.

Weinberg, S., (1979). Cosmological production of baryons. Phys. Rev. Lett., 42, 850-853.

Woody, D.P., J.C. Mather, N.S. Nishioka and P.L. Richards (1975). Measurement of the spectrum of the submillimeter cosmic background. Phys. Rev. Lett., 34, 1036-1039.

Yang, J., D.N. Schramm, G. Steigman and R.T. Rood (1979). Constraints on cosmology and neutrino physics from big bang nucleosynthesis. Ap. J., 227, 697-704.

PARTICIPANTS

A:

Yoav Achiman
Gesamthochschule Wuppertal
Fachbereich 8 - Physik
Gausstrasse 20
5600 Wuppertal 1
GERMANY

Olaf Achterberg
Institut fur Experimentalphysik
Universitat Hamburg
Luruper Chaussee 149
2000 Hamburg 50
GERMANY

Jean Paul Albanese
EP Division
CERN
CH-1211, Geneva 23
SWITZERLAND

James Allaby
CERN
CH-1211, Geneva 23
SWITZERLAND

Pramudita Annggraita
Department of Physics and Astronomy
University of Hawaii at Manoa
2505 Correa Road
Honolulu, Hawaii 96822

Ramesh Anishetty
Department of Physics
Brandeis University
Waltham, Massachusetts 02154

Dikran Antreasyan
SLAC - Bin 98
P. O. Box 4349
Stanford, California 94305

Hideaki Aoyama
452-48
California Institute of Technology
Pasadena, California 91106

Ray Arnold
Department of Physics
American University
Washington, D.C. 20016

David Aschman
Department of Physics
Princeton University
Princeton, New Jersey 08540

David Aston
SLAC - Bin 62
P. O. Box 4349
Stanford, California 94305

W. B. Atwood
SLAC - Bin 96
P. O. Box 4349
Stanford, California 94305

B:

D. Badtke
Department of Physics
Johns Hopkins University
Baltimore, Maryland 21218

Andreas Baecker
Department of Physics
Harvard University
Cambridge, Massachusetts 02138

Jonathan Bagger
Department of Physics
Princeton University
Princeton, New Jersey 08544

J. Ballam
SLAC - Bin 80
P. O. Box 4349
Stanford, California 94305

Rose Mary Baltrusaitis
256-48
California Institute of Technology
Pasadena, California 91125

G. Baranko
Department of Physics
Indiana University
Bloomington, Indiana 47401

Guido Barbiellini
CERN
CH-1211, Geneva 23
SWITZERLAND

Michael Barnett
SLAC - Bin 81
P. O. Box 4349
Stanford, California 94305

Maurice Barnhill
Department of Physics
University of Delaware
Newark, Delaware 19711

P. Barringer
Department of Physics
Indiana University
Bloomington, Indiana 47401

J. Becker
Department of Physics
University of Illinois
Urbana, Illinois 61801

David Berley
U.S. Department of Energy
J-309
Washington, D.C. 20545

R. Blankenbecler
SLAC - Bin 81
P. O. Box 4349
Stanford, California 94305

Harold Bledsoe
Department of Physics
University of California
Santa Cruz, California 95060

M. Bloch
Commissariat a L'Energie Atomique
Division de la Physique
CEN-Saclay
B.P. No. 2 91190
Gif-sur-Yvette
FRANCE

Craig Blocker
Department of Physics
Harvard University
Cambridge, Massachusetts 02138

David Blockus
Department of Physics
Johns Hopkins University
Baltimore, Maryland 21218

Alain Blondel
Lawrence Berkeley Laboratory
One Cyclotron Road
Berkeley, California 94720

Elliott Bloom
SLAC - Bin 98
P. O. Box 4349
Stanford, California 94305

Gerard Bonneaud
SLAC - Bin 63
P. O. Box 4349
Stanford, California 94305

Michel Bonvin
Theoretische Physik
Eidgenossische Technische Hochschule
ETH-Honggerberg
CH-8093, Zurich
SWITZERLAND

A. Boyarski
SLAC - Bin 95
P. O. Box 4349
Stanford, California 94305

Eric Braaten
Department of Physics
University of Wisconsin
1150 University Avenue
Madison, Wisconsin 53706

J. Brau
SLAC - Bin 78
P. O. Box 4349
Stanford, California 94305

M. Breidenbach
SLAC - Bin 95
P. O. Box 4349
Stanford, California 94305

Stanley Brodsky
SLAC - Bin 81
P. O. Box 4349
Stanford, California 94305

Karl Brown
SLAC - Bin 94
P. O. Box 4349
Stanford, California 94305

Fatin Bulos
SLAC - Bin 98
P. O. Box 4349
Stanford, California 94305

Kirk Bunnell
SLAC - Bin 65
P. O. Box 4349
Stanford, California 94305

David Burke
SLAC - Bin 61
P. O. Box 4349
Stanford, California 94305

C:

Robert Cahn
Lawrence Berkeley Laboratory
One Cyclotron Road
Berkeley, California 94720

Daniel Caldi
Lawrence Berkeley Laboratory
One Cyclotron Road
Berkeley, California 94720

David J. E. Callaway
Department of Physics FM-15
University of Washington
Seattle, Washington 98195

Peter Cameron
Randall Laboratory, Room 2035
University of Michigan
Ann Arbor, Michigan 48109

Thomas Cardello
Department of Physics
Yale University
New Haven, Connecticut 06511

T. Carroll
SLAC - Bin 78
P. O. Box 4349
Stanford, California 94305

Ron Cassell
Department of Physics
University of Illinois
Urbana, Illinois 61801

V. Cautis
SLAC - Bin 78
P. O. Box 4349
Stanford, California 94305

Matteo Cavalli-Sforza
SLAC - Bin 98
P. O. Box 4349
Stanford, California 94305

George Chadwick
SLAC - Bin 94
P. O. Box 4349
Stanford, California 94305

V. Chaloupka
SLAC - Bin 78
P. O. Box 4349
Stanford, California 94305

Lee Chang
Department of Physics
Tsinghua University
Peking
PEOPLE'S REPUBLIC OF CHINA

Michael Chanowitz
Lawrence Berkeley Laboratory
One Cyclotron Road
Berkeley, California 94720

Alex Chao
SLAC - Bin 12
P. O. Box 4349
Stanford, California 94305

J. Chapman
Department of Physics
University of Michigan
Ann Arbor, Michigan 48104

Pisin Chen
Department of Physics
University of California
Los Angeles, California 90024

Jasbinder Chima
SLAC - Bin 78
P. O. Box 4349
Stanford, California 94305

Ting-wai Chiu
Department of Physics
University of California
Irvine, California 92717

Mark Coles
Lawrence Berkeley Laboratory
One Cyclotron Road
Berkeley, California 94720

Susan Cooper
Lawrence Berkeley Laboratory
One Cyclotron Road
Berkeley, California 94720

D. Cords
DESY
Notkestrasse 85
D-2000 Hamburg 52
GERMANY

D. Coward
SLAC - Bin 65
P. O. Box 4349
Stanford, California 94305

D. Coyne
Department of Physics
Princeton University
Princeton, New Jersey 08540

Huachang Cui
Department of Physics
University of Illinois
Urbana, Illinois 61801

D:

Shlomo Dado
Department of Physics
Technion - Israel Institute of Technology
Technion City
Haifa
ISRAEL

John D'Amore
Department of Physics
University of Cincinnati
Cincinnati, Ohio 45221

Dana Lawrence Day
Department of Physics and Astronomy
The University of Kansas
Lawrence, Kansas 66045

N. G. Deshpande
Institute of Theoretical Science
University of Oregon
Eugene, Oregon 97403

H. DeStaebler
SLAC - Bin 96
P. O. Box 4349
Stanford, California 94305

William Dieterle
Lawrence Berkeley Laboratory
One Cyclotron Road
Berkeley, California 94720

John Dillon
Lawrence Berkeley Laboratory
One Cyclotron Road
Berkeley, California 94720

Michael Dine
SLAC - Bin 81
P. O. Box 4349
Stanford, California 94305

Greg Donaldson
SLAC - Bin 63
P. O. Box 4349
Stanford, California 94305

J. Dorenbosch
SLAC - Bin 95
P. O. Box 4349
Stanford, California 94305

Jonathan Dorfan
SLAC - Bin 61
P. O. Box 4349
Stanford, California 94305

Persis Drell
Department of Physics
University of California
Berkeley, California 94720

Richard Dubois
BASQUE Group
TRIUMF
University of British Columbia
Vancouver, B. C.
CANADA V6T 1W5

Gary L. Duerksen
The Enrico Fermi Institute
The University of Chicago
5630 Ellis Avenue
Chicago, Illinois 60637

William Dunwoodie
SLAC - Bin 62
P. O. Box 4349
Stanford, California 94305

L. Stanley Durkin
SLAC - Bin 62
P. O. Box 4349
Stanford, California 94305

Alex R. Dzierba
Department of Physics
Swain Hall - West 117
Indiana University
Bloomington, Indiana 47405

E:

Mark Eaton
Lawrence Berkeley Laboratory
One Cyclotron Road
Berkeley, California 94720

Gad Eilam
Department of Physics
Technion - Israel Institute of Technology
Technion City
Haifa
ISRAEL

Martin B. Einhorn
Randall Laboratory of Physics
University of Michigan
Ann Arbor, Michigan 48109

Kevin Einsweiler
SLAC - Bin 65
P. O. Box 4349
Stanford, California 94305

R. Eisenstein
Department of Physics
University of Illinois
Urbana, Illinois 61820

E. Elsen
Institut fur Experimentalphysik
Universitat Hamburg
Luruper Chausee 149
2000 Hamburg 50
GERMANY

R. Erickson
SLAC - Bin 78
P. O. Box 4349
Stanford, California 94305

Andrew Eskreys
DESY
Notkestrasse 85
2000 Hamburg 52
GERMANY

F:

E. Farhi
SLAC - Bin 81
P. O. Box 4349
Stanford, California 94305

Gary Feldman
SLAC - Bin 61
P. O. Box 4349
Stanford, California 94305

Joe Feller
Department of Physics
Nevis Laboratories
Columbia University
P. O. Box 137
Irvington, New York 10533

C. Field
SLAC - Bin 78
P. O. Box 4349
Stanford, California 94305

Richard Fischer
SLAC - Bin 81
P. O. Box 4349
Stanford, California 94305

Geoffrey Forden
Department of Physics
Indiana University
Bloomington, Indiana 47405

Melissa Franklin
SLAC - Bin 61
P. O. Box 4349
Stanford, California 94305

Dieter Fries
Inst. fur Experimentelle Kernphysik
University of Karlsruhe und
Inst. fur Kernphysik des
Kernforschungszentrums
P. O. Box 3640
Karlsruhe
GERMANY

Rene Fries
SLAC - Bin 37
P. O. Box 4349
Stanford, California 94305

D. Fryberger
SLAC - Bin 20
P. O. Box 4349
Stanford, California 94305

Kanji Fujii
Department of Physics
Faculty of Science
Hokkaido University
Sapporo
JAPAN

Keisuke Fujii
Department of Physics
Nagoya University
Chikusa-ku, Nagoya
JAPAN

Masakazu Fujisaki
The Randall Laboratory of Physics
The University of Michigan
Ann Arbor, Michigan 48109

Noboru Fujiwara
SLAC - Bin 78
P. O. Box 4349
Stanford, California 94305

Yasutaka Fukushima
Fermilab
P. O. Box 500
Batavia, Illinois 60510

G:

John Gaiser
SLAC - Bin 98
P. O. Box 4349
Stanford, California 94305

Hrvoje Galic
"Ruder Boskovic" Institute
P.B. 1016
Zagreb 41001
YUGOSLAVIA

Lina Galtieri
Lawrence Berkeley Laboratory
One Cyclotron Road
Berkeley, California 94720

Chong-shou Gao
SLAC - Bin 81
P. O. Box 4349
Stanford, California 94305

C. Geweniger
Institute for High Energy Physics
University of Heidelberg
D-69 Heidelberg
GERMANY

F. Gilman
SLAC - Bin 81
P. O. Box 4349
Stanford, California 94305

Robin Gilmore
University of Bristol
Bristol BS8 1TL
ENGLAND

Nikos Giokaris
Department of Physics
University of Chicago
Chicago, Illinois 60628

L. Gladney
SLAC - Bin 95
P. O. Box 4349
Stanford, California 94305

Bruno Gobbi
Department of Physics
Northwestern University
Evanston, Illinois 60201

Gary Godfrey
SLAC - Bin 98
P. O. Box 4349
Stanford, California 94305

Joseph Goldman
Department of Physics
American University
Washington, D.C. 20016

H. Gordon
Brookhaven National Laboratory
Upton, New York 11973

Francesco Grancagnolo
Department of Physics
University of California
Santa Cruz, California 95060

Jean Paul Guillaud
Department of Physics
Indiana University
Bloomington, Indiana 47405

Jack Gunion
SLAC - Bin 81
P. O. Box 4349
Stanford, California 94305

Wlodzimierz Guryn
SLAC - Bin 43
P. O. Box 4349
Stanford, California 94305

Alan Guth
SLAC - Bin 81
P. O. Box 4349
Stanford, California 94305

H:

Gail Hanson
SLAC - Bin 61
P. O. Box 4349
Stanford, California 94305

H. Harari
Weizmann Institute of Science
Rehovot
ISRAEL

Neville Harnew
Department of Physics
University of Michigan
Ann Arbor, Michigan 48104

Jeff Harvey
452-48
California Institute of Technology
Pasadena, California 91125

Jay Hauser
256-48
California Institute of Technology
Pasadena, California 91125

Mitsuo J. Hayashi
Department of Physics
Tokai University
317 Kasumi, Numazu-city
410-03
JAPAN

Kenneth Hayes
SLAC - Bin 61
P. O. Box 4349
Stanford, California 94305

Ian Hinchliffe
Lawrence Berkeley Laboratory
One Cyclotron Road
Berkeley, California 94720

David Hitlin
Department of Physics
California Institute of Technology
Pasadena, California 91125

R. Hollebeek
SLAC - Bin 95
P. O. Box 4349
Stanford, California 94305

Keijiro Honda
Department of Physics
Hokkaido University
Sapporo
JAPAN

Alan Honma
SLAC - Bin 62
P. O. Box 4349
Stanford, California 94305

Roland Horisberger
SLAC - Bin 98
P. O. Box 4349
Stanford, California 94305

Tao Huang
SLAC - Bin 81
P. O. Box 4349
Stanford, California 94305

D. Hutchinson
SLAC - Bin 65
P. O. Box 4349
Stanford, California 94305

I:

Will Iley
Department of Physics
University of California
Davis, California 95616

Walter Innes
SLAC - Bin 61
P. O. Box 4349
Stanford, California 94305

George Irwin
SLAC - Bin 63
P. O. Box 4349
Stanford, California 94305

Chikashi Iso
Tokyo Institute of Technology
Ohokayama, Meguro-ku
Tokyo
152 JAPAN

J:

John Jaros
SLAC - Bin 61
P. O. Box 4349
Stanford, California 94305

Jere Jersak
Institut fur Theoretische Physik E
Technische Hochschule Aachen
5100 Aachen
GERMANY

William B. Johnson
SLAC - Bin 62
P. O. Box 4349
Stanford, California 94305

K:

Patricia Kalyniak
Department of Physics
University of British Columbia
Vancouver, B. C.
CANADA V6T 1W5

Sarbmeet S. Kanwal
452-48
California Institute of Technology
Pasadena, California 91125

Inga Karliner
Department of Physics
University of Hawaii
Honolulu, Hawaii 96822

Richard Kass
Rochester Group
Wilson Laboratory
Cornell University
Ithaca, New York 14853

Omer Kaymakcalan
Lawrence Berkeley Laboratory
One Cyclotron Road
Berkeley, California 94720

L. P. Keller
SLAC - Bin 20
P. O. Box 4349
Stanford, California 94305

Sam Kheifets
SLAC - Bin 12
P. O. Box 4349
Stanford, California 94305

Hiromichi Kichimi
SLAC - Bin 96
P. O. Box 4349
Stanford, California 94305

Jasper Kirkby
SLAC - Bin 63
P. O. Box 4349
Stanford, California 94305

Tetsuro Kitazoe
Department of Physics
Kobe University
Rokkodai, Kobe 657
JAPAN

Spencer Klein
SLAC - Bin 61
P. O. Box 4349
Stanford, California 94305

Jiro Kodaira
Research Institute for Fundamental Physics
Yukawa Hall
Kyoto University
Kyoto 606
JAPAN

Peter Koehler
SLAC - Bin 81
P. O. Box 4349
Stanford, California 94305

Kay Koenigsmann
SLAC - Bin 98
P. O. Box 4349
Stanford, California 94305

In-Gyu Koh
Department of Physics
Sogang University
C. P. O. Box 1142
Seoul
KOREA

Hermann Kolanoski
DESY
Notkestieg 1
2 Hamburg 52
GERMANY

Karl Koller
Theresienstrasse 37
Universität München
Sektion Physik
8000 Munich 2
GERMANY

David Koltick
Department of Physics
Purdue University
Lafayette, Indiana 47907

Paul Kooijman
SLAC - Bin 48
P. O. Box 4349
Stanford, California 94305

Sheila Kooijman
SLAC - Bin 48
P. O. Box 4349
Stanford, California 94305

Eve Kovacs
SLAC - Bin 81
P. O. Box 4349
Stanford, California 94305

W. Kozanecki
CERN
CH-1211 Geneva 23
SWITZERLAND

Paul Kunz
SLAC - Bin 62
P. O. Box 4349
Stanford, California 94305

L:

Kenneth D. Lane
Department of Physics
Ohio State University
Columbus, Ohio 43210

Willy Langeveld
NIKHEF
University of Amsterdam
Plantage Muidergracht 4
1018 TV Amsterdam
THE NETHERLANDS

Andrew Lankford
Lawrence Berkeley Laboratory
One Cyclotron Road
Berkeley, California 94720

Rudolf Larsen
SLAC - Bin 95
P. O. Box 4349
Stanford, California 94305

William Lavender
SLAC - Bin 62
P. O. Box 4349
Stanford, California 94305

Leon Lederman
Fermilab
P. O. Box 500
Batavia, Illinois 60510

Joel LeDuff
SLAC - Bin 12
P. O. Box 4349
Stanford, California 94305

David Leith
SLAC - Bin 62
P. O. Box 4349
Stanford, California 94305

M. Levi
Department of Physics
Harvard University
Cambridge, Massachusetts 02138

Lorne Levinson
SLAC - Bin 62
P. O. Box 4349
Stanford, California 94305

Bing An Li
SLAC - Bin 81
P. O. Box 4349
Stanford, California 94305

Wen-long Lin
Department of Physics
National Taiwan Normal University
88 Sec. 5, Roosevelt Road
Taipei, Taiwan
REPUBLIC OF CHINA

James Lindesay
SLAC - Bin 81
P. O. Box 4349
Stanford, California 94305

Steven Lindgren
SLAC - Bin 95
P. O. Box 4349
Stanford, California 94305

Stephan L. Linn
Randall Laboratory
University of Michigan
Ann Arbor, Michigan 48104

Bernard Lippmann
SLAC - Bin 81
P. O. Box 4349
Stanford, California 94305

Bill Lockman
SLAC - Bin 98
P. O. Box 4349
Stanford, California 94305

B. Loehr
SLAC - Bin 95
P. O. Box 4349
Stanford, California 94305

J. Loos
SLAC - Bin 48
P. O. Box 4349
Stanford, California 94305

V. Luth
SLAC - Bin 95
P. O. Box 4349
Stanford, California 94305

M:

David MacFarlane
California Institute of Technology
256-48
Pasadena, California 91125

Kaori Maeshima
Department of Physics
University of California
Davis, California 95616

Parthasarathi Majumdar
The Martin Fisher School of Physics
Brandeis University
Waltham, Massachusetts 02254

G. Mandelbaum
Lehrstuhl Prof., H. Fritzsch University
Theresienstrasse 37
D-8000 Munich 2
GERMANY

Tony Mann
Department of Physics
Tufts University
Boston, Massachusetts 02155

William Marsh
E-616, Lab E
Fermilab
P. O. Box 500
Batavia, Illinois 60510

Jay Marx
Lawrence Berkeley Laboratory
One Cyclotron Road
Berkeley, California 94720

Takayuki Matsui
Department of Physics
Nagoya University
Chikusa-ku, Nagoya
JAPAN

T. Matsuoka
SLAC - Bin 81
P. O. Box 4349
Stanford, California 94305

John Matthews
Department of Physics
Johns Hopkins University
Baltimore, Maryland 21218

Gerry McKeon
Department of Applied Mathematics
Faculty of Science
The University of Western Ontario
London
CANADA N6A 5B9

Larry McLerran
SLAC - Bin 81
P. O. Box 4349
Stanford, California 94305

Mac D. Mestayer
Department of Physics
University of Chicago
Chicago, Illinois 60637

D. Meyer
Department of Physics
University of Michigan
Ann Arbor, Michigan 48104

Hans-Jürgen Meyer
DESY - F33
Notkestrasse 85
2000 Hamburg 52
GERMANY

David Miller
SLAC - Bin 81
P. O. Box 4349
Stanford, California 94305

Nari Mistry
Newman Laboratory of Nuclear Studies
Cornell University
Ithaca, New York 14853

Kimio Miura
Nippon Medical School
Physics Department
2-297-2 Kosugi
Nakahara-ku Kawasaki
211 JAPAN

Michiko Miyamoto
11-2, 1-chome
Yamate, Nakasuji
Takarazuka City
Hyogo Prefecture
JAPAN 665

K. Moffeit
SLAC - Bin 78
P. O. Box 4349
Stanford, California 94305

Giancarlo Moneti
Department of Physics
Syracuse University
Syracuse, New York 13210

Hugh Montgomery
CERN
CH-1211, Geneva 23
SWITZERLAND

Robert Mozley
SLAC - Bin 65
P. O. Box 4349
Stanford, California 94305

John Mulvey
Nuclear Physics Laboratory
Oxford University
Keble Road
Oxford OX1 3RH
ENGLAND

N:

Morio Nakamura
Belcrest Hotel
624 Post Street
San Francisco, California 94109

J. Napolitano
SLAC - Bin 37
P. O. Box 4349
Stanford, California 94305

Homer Neal
Department of Physics
Indiana University
Bloomington, Indiana 47405

Adolfo M. Nemirovsky
Department of Physics
University of Kansas
Lawrence, Kansas 66044

Yee Jack Ng
Department of Physics and Astronomy
University of North Carolina
Chapel Hill, North Carolina 27514

Friedrich Niebergall
CERN
CH-1211, Geneva 23
SWITZERLAND

H. P. Nilles
SLAC - Bin 81
P. O. Box 4349
Stanford, California 94305

Pierre Noyes
SLAC - Bin 81
P. O. Box 4349
Stanford, California 94305

O:

Allen Odian
SLAC - Bin 65
P. O. Box 4349
Stanford, California 94305

A. Ogawa
SLAC - Bin 96
P. O. Box 4349
Stanford, California 94305

Harold Ogren
Department of Physics
Indiana University
Bloomington, Indiana 47405

Richard Oppenheim
SLAC - Bin 60
P. O. Box 4349
Stanford, California 94305

Harry Orbach
SLAC - Bin 81
P. O. Box 4349
Stanford, California 94305

Mark Oreglia
SLAC - Bin 98
P. O. Box 4349
Stanford, California 94305

P:

Chan Pang
Lawrence Berkeley Laboratory
One Cyclotron Road
Berkeley, California 94720

Sherwood Parker
Department of Physics
University of Hawaii
Honolulu, Hawaii 96822

R. Partridge
Department of Physics
California Institute of Technology
Pasadena, California 91125

Nello Paver
Instituto di Fisica Teorica
Universita degli Studi di Trieste
Strada Costiera 11
34014 Miramare-Grignano
ITALY

G. F. Pearce
Gruppe F22 (JADE)
DESY
Notkestrasse 85
2000 Hamburg 52
GERMANY

Laura Perasso
Instituto di Fisica
Universita di Pisa
Piazza Torricelli, 2
Pisa
ITALY

D. Perret-Gallix
SLAC - Bin 96
P. O. Box 4349
Stanford, California 94305

So-Young Pi
SLAC - Bin 81
P. O. Box 4349
Stanford, California 94305

C. E. Picciotto
Department of Physics
University of Victoria
P. O. Box 1700
Victoria, B.C.
CANADA V8W 2Y3

Dale Pitman
Department of Physics
University of Toronto
Toronto, Ontario
CANADA M5S 1A7

Rainer Pitthan
SLAC - Bin 96
P. O. Box 4349
Stanford, California 94305

Scott Plaetzer
Department of Physics
University of Illinois
Urbana, Illinois 61801

D. Pollard
SLAC - Bin 63
P. O. Box 4349
Stanford, California 94305

Frank Porter
Department of Physics
California Institute of Technology
Pasadena, California 91125

Keith Potter
ISR Division
CERN
CH-1211, Geneva 23
SWITZERLAND

Michael J. Puhala
Department of Physics
Iowa State University
Ames, Iowa 50011

Milind Purohit
California Institute of Technology
256-48
Pasadena, California 91125

R:

J. Rabin
SLAC - Bin 81
P. O. Box 4349
Stanford, California 94305

Norman Ramsey
Department of Physics
Harvard University
Cambridge, Massachusetts 02138

Kas Rangan
Department of Physics
Purdue University
Lafayette, Indiana 47907

Patricia Rankin
Imperial College
Blackett Laboratory
Prince Consort Road
South Kensington
London SW7 2AZ
ENGLAND

Blair Ratcliff
SLAC - Bin 62
P. O. Box 4349
Stanford, California 94305

Asim K. Ray
Department of Physics
Visva-Bharati University
Santiniketan 731235
West Bengal
INDIA

Zbigniew Rek
Department of Physics
12 Physics Building
Iowa State University
Ames, Iowa 50011

J. Richman
256-48
California Institute of Technology
Pasadena, California 91125

Burton Richter
SLAC - Bin 95
P. O. Box 4349
Stanford, California 94305

Robert Richter
SLAC - Bin 62
P. O. Box 4349
Stanford, California 94305

David Ritson
SLAC - Bin 94
P. O. Box 4349
Stanford, California 94305

L. S. Rochester
SLAC - Bin 96
P. O. Box 4349
Stanford, California 94305

Stephen Rock
Department of Physics
American University
Washington, D.C. 20016

J. Roehrig
SLAC - Bin 65
P. O. Box 4349
Stanford, California 94305

J. Rohlf
42 Oxford Street
Harvard University
Cambridge, Massachusetts 02138

Larry J. Romans
356-48
California Institute of Technology
Pasadena, California 91125

Oswald Römer
DESY
Notkestrasse 85
D-2 Hamburg 52
GERMANY

M. Ronan
Lawrence Berkeley Laboratory
One Cyclotron Road
Berkeley, California 94720

Francesco Ronga
INFN LNF
C.P. 13
0044 Frascati (Roma)
ITALY

Marc Ross
Department of Physics
Northwestern University
Evanston, Illinois 60201

Forest Rouse
Lawrence Berkeley Laboratory
One Cyclotron Road
Berkeley, California 94720

Andre Roussarie
SLAC - Bin 61
P. O. Box 4349
Stanford, California 94305

Shasanka M. Roy
Tata Institute of Fundamental Research
Homi Bhabha Road
Bombay 49 00 05
INDIA

D. Rubin
Department of Physics
University of Michigan
Ann Arbor, Michigan 48104

David Rust
Department of Physics
Indiana University
Bloomington, Indiana 47405

S:

Hartmut Sadrozinski
SLAC - Bin 98
P. O. Box 4349
Stanford, California 94305

O. H. Saxton
SLAC - Bin 96
P. O. Box 4349
Stanford, California 94305

Theo Schaad
Department of Physics
Harvard University
Cambridge, Massachusetts 02138

D. Scharre
SLAC - Bin 98
P. O. Box 4349
Stanford, California 94305

K. Schilcher
Department of Physics
University of California
Los Angeles, California 90024

D. Schiller
Universitat Gesamthochschule Siegen
Fachbereich 7
Naturwissenschaften I (Physik)
5900 Siegen 21
GERMANY

David Schramm
Enrico Fermi Institute and
Department of Physics
University of Chicago
Chicago, Illinois 60637

P. Schreiner
SLAC - Bin 48
P. O. Box 4349
Stanford, California 94305

Roy Schwitters
Department of Physics
Harvard University
Cambridge, Massachusetts 02138

Frank Sciulli
Division of Physics and Astronomy
California Institute of Technology
Pasadena, California 91125

Julia Sedgebeer
Department of Physics
Imperial College
Prince Consort Road
South Kensington
London SW7 2AZ
ENGLAND

M. Shaevitz
Lauritsen Laboratory
256-48
California Institute of Technology
Pasadena, California 91125

Stephen Shapiro
SLAC - Bin 62
P. O. Box 4349
Stanford, California 94305

Graham Shaw
Department of Theoretical Physics
The Schuster Laboratory
The University of Manchester
Manchester M13 9PL
ENGLAND

D. Sherden
SLAC - Bin 60
P. O. Box 4349
Stanford, California 94305

E. Shibata
Department of Physics
Purdue University
Lafayette, Indiana 47907

T. Shima
Randall Laboratory, Room 2035
University of Michigan
Ann Arbor, Michigan 48109

Tukuzo Shimada
Lawrence Berkeley Laboratory
One Cyclotron Road
Berkeley, California 94720

Toshiro Shimomura
SLAC - Bin 62
P. O. Box 4349
Stanford, California 94305

Kirk A. Shinsky
Laboratory of Nuclear Studies
Newman Laboratory
Cornell University
Ithaca, New York 14853

Ronald A. Sidwell
Fermilab
P. O. Box 500
Batavia, Illinois 60510

J. Siegrist
SLAC - Bin 95
P. O. Box 4349
Stanford, California 94305

Alan Sill
Department of Physics
American University
Washington, D.C. 20016

Milton Slaughter
T14 MS214
Los Alamos Scientific Laboratory
Los Alamos, New Mexico 87545

Elton Smith
Fermilab E-613
P. O. Box 500
Batavia, Illinois 60510

H. Sobel
Department of Physics
University of California
Irvine, California 92664

A. Soni
SLAC - Bin 81
P. O. Box 4349
Stanford, California 94305

Glenn Sowell
Department of Physics
Florida State University
Tallahassee, Florida 32306

Tony Spadafora
Department of Physics
University of Illinois
Urbana, Illinois 61820

James Spencer
SLAC - Bin 12
P. O. Box 4349
Stanford, California 94305

Stuart Stampke
356-48
California Institute of Technology
Pasadena, California 91125

Berthold Stech
Institut fur Theoretische Physik
Universitat Heidelberg
Philosophenweg 16
D-6900 Heidelberg
GERMANY

Lynn Stevenson
Lawrence Berkeley Laboratory
One Cyclotron Road
Berkeley, California 94720

Paul M. Stevenson
Department of Physics
University of Wisconsin
Madison, Wisconsin 53706

Harry Sticker
Department of Physics
Rockefeller University
66th Street and York Avenue
New York, New York 10021

R. Stiening
SLAC - Bin 95
P. O. Box 4349
Stanford, California 94305

Leo Stodolsky
SLAC - Bin 81
P. O. Box 4349
Stanford, California 94305

James Strait
Lawrence Berkeley Laboratory
One Cyclotron Road
Berkeley, California 94720

Karl Strauch
SLAC - Bin 98
P. O. Box 4349
Stanford, California 94305

Karl Streng
SLAC - Bin 81
P. O. Box 4349
Stanford, California 94305

J. D. Stroughair
Department of Physics
Case Western Reserve University
Cleveland, Ohio 44106

Mark Strovink
Lawrence Berkeley Laboratory
One Cyclotron Road
Berkeley, California 94720

Ryszard Stroynowski
SLAC - Bin 62
P. O. Box 4349
Stanford, California 94305

R. Sugahara
SLAC - Bin 78
P. O. Box 4349
Stanford, California 94305

Leonard Susskind
Department of Physics
Stanford University
Stanford, California 94305

A. Suzuki
SLAC - Bin 78
P. O. Box 4349
Stanford, California 94305

Shiro Suzuki
SLAC - Bin 62
P. O. Box 4349
Stanford, California 94305

Zenon Szalata
Department of Physics
American University
Washington, D.C. 20016

T:

K. Takahashi
National Laboratory for
High Energy Physics
KEK, Oho-machi
JAPAN

Mitsuyoshi Tanaka
Department of Physics, 510C
Brookhaven National Laboratory
Upton, New York 11973

Takáo Tanuma
Department of Physics and Astronomy
University of Maryland
College Park, Maryland 20742

Giora Tarnopolsky
SLAC - Bin 62
P. O. Box 4349
Stanford, California 94305

R. E. Taylor
SLAC - Bin 96
P. O. Box 4349
Stanford, California 94305

John Thaler
Department of Physics
University of Illinois
Urbana, Illinois 61801

Serge Theberge
Department of Physics
University of British Columbia
Vancouver, B.C.
CANADA V6T 1W5

Jan Timmer
SLAC - Bin 57
P. O. Box 4349
Stanford, California 94305

Walter Toki
SLAC - Bin 65
P. O. Box 4349
Stanford, California 94305

John Tompkins
SLAC - Bin 98
P. O. Box 4349
Stanford, California 94305

Luca Trentadue
Department of Physics
Stanford University
Stanford, California 94305

T. Trippe
Lawrence Berkeley Laboratory
One Cyclotron Road
Berkeley, California 94720

Y. S. Tsai
SLAC - Bin 81
P. O. Box 4349
Stanford, California 94305

T. Tsao
SLAC - Bin 81
P. O. Box 4349
Stanford, California 94305

George Tzanakos
Department of Physics
Syracuse University
Syracuse, New York 13210

U:

Yoshinobu Unno
SLAC - Bin 65
P. O. Box 4349
Stanford, California 94305

V:

J. Vander Velde
Department of Physics
University of Michigan
Ann Arbor, Michigan 48104

J. Va'Vra
SLAC - Bin 20
P. O. Box 4349
Stanford, California 94305

Martin Veltman
University of Utrecht
THE NETHERLANDS

R. Vidal
SLAC - Bin 95
P. O. Box 4349
Stanford, California 94305

Francesco Villa
SLAC - Bin 65
P. O. Box 4349
Stanford, California 94305

G. von Dardel
EP Division
CERN
CH-1211, Geneva 23
SWITZERLAND

W:

Klaus Wacker
SLAC - Bin 98
P. O. Box 4349
Stanford, California 94305

Bob Wagner
Fermilab
P. O. Box 500
Batavia, Illinois 60510

W. Wagner
Physics Institute of Aachen
Physikzentrum
D-51 Aachen
GERMANY

Shuqin Wang
SLAC - Bin 96
P. O. Box 4349
Stanford, California 94305

Tai Chieh Wang
SLAC - Bin 37
P. O. Box 4349
Stanford, California 94305

Yun-yong Wang
Lawrence Berkeley Laboratory
Berkeley, California 94720

B. Ward
SLAC - Bin 81
P. O. Box 4349
Stanford, California 94305

T. Watanabe
SLAC - Bin 81
P. O. Box 4349
Stanford, California 94305

Bruce Weeks
SLAC - Bin 81
P. O. Box 4349
Stanford, California 94305

Alan Weinstein
SLAC - Bin 98
P. O. Box 4349
Stanford, California 94305

Marvin Weinstein
SLAC - Bin 81
P. O. Box 4349
Stanford, California 94305

J. Weiss
SLAC - Bin 95
P. O. Box 4349
Stanford, California 94305

M. Werlen
SLAC - Bin 95
P. O. Box 4349
Stanford, California 94305

Raymond Willey
Department of Physics and Astronomy
University of Pittsburgh
Pittsburgh, Pennsylvania 15260

Crispin Williams
Department of Physics
University of California
Davis, California 95616

Stephen Williams
SLAC - Bin 62
P. O. Box 4349
Stanford, California 94305

Mark Wise
SLAC - Bin 81
P. O. Box 4349
Stanford, California 94305

Bill Wisniewski
Department of Physics
University of Illinois
Urbana, Illinois 61801

Stanley Wojcicki
SLAC - Bin 63
P. O. Box 4349
Stanford, California 94305

Günter Wolf
DESY
Notkestrasse 85
2000 Hamburg 52
GERMANY

Dan-di Wu
Department of Physics
Harvard University
Cambridge, Massachusetts 02138

Y:

A. Yamaguchi
Department of Physics
Tohoku University
Sendai
JAPAN 980

Richard K. Yamamoto
Laboratory for Nuclear Science
575 Technology Square, Room 408
Massachusetts Institute of Technology
Cambridge, Massachusetts 02139

W. K. Yan
SLAC - Bin 63
P. O. Box 4349
Stanford, California 94305

Chih-yuan Yao
SLAC - Bin 95
P. O. Box 4349
Stanford, California 94305

Edward Yen
Department of Physics
National Tsing Hua University
855 Kuang Fu Road
Hsinchu, Taiwan
REPUBLIC OF CHINA

George Yost
Department of Physics
University of California
Berkeley, California 94720

C. C. Young
SLAC - Bin 96
P. O. Box 4349
Stanford, California 94305

Z:

S. Zaidi
SLAC - Bin 81
P. O. Box 4349
Stanford, California 94305

Carl Zaiser
SLAC - Bin 61
P. O. Box 4349
Stanford, California 94305

Anthony Zee
Department of Physics
University of Washington
Seattle, Washington 98195

P. M. Zerwas
Institut fur Theoretische Physik
5100 Aachen
GERMANY

Guozhe Zhao
Lawrence Berkeley Laboratory
One Cyclotron Road
Berkeley, California 94720

USGPO-1981-789-715/99